Eastern Mediterranean University

ACE 2023

15th INTERNATIONAL CONGRESS ON ADVANCES IN CIVIL ENGINEERING

6 – 8 SEPTEMBER 2023

EASTERN MEDITERRANEAN UNIVERSITY • FAMAGUSTA • NORTH CYPRUS

PROCEEDINGS BOOK

Editors
Umut TÜRKER
Özgür EREN
Eriş UYGAR
Hamza SAEED

Umut Türker · Özgür Eren · Eriş Uygar ·

Hamza Saeed

Editors

Proceedings Book

15th International Congress on Advances in Civil Engineering

Famagusta, North Cyprus

Editors

Prof. Dr. Umut Türker
Eastern Mediterranean University
Department of Civil Engineering
Famagusta, North Cyprus Mersin 10
Turkey
umut.turker@emu.edu.tr

Prof. Dr. Özgür Eren
Eastern Mediterranean University
Department of Civil Engineering
Famagusta, North Cyprus Mersin 10
Turkey
ozgur.eren@emu.edu.tr

Assoc. Prof. Dr. Eriş Uygar
Eastern Mediterranean University
Department of Civil Engineering
Famagusta, North Cyprus Mersin 10
Turkey
eris.uygar@emu.edu.tr

PhD Candidate Mr. Hamza Saeed
Eastern Mediterranean University
Department of Civil Engineering
Famagusta, North Cyprus Mersin 10
Turkey
hamza.saeed@emu.edu.tr

PREFACE

Welcome to the 15th International Congress on Advances in Civil Engineering, ACE 2023, which took place in Famagusta, North Cyprus, from September 6th to 8th, 2023. It was an honour to witness the participation of all attendees, whose contributions, engagements, and scholarly exchanges enriched this esteemed gathering. The event served as a robust platform for disseminating academic and practical insights while fostering invaluable networking opportunities.

Traditionally convened biennially, ACE congresses had historically been a collaborative endeavour among esteemed partner universities: Bogaziçi University, Eastern Mediterranean University, Ege Üniversity, Istanbul Technical University, Karadeniz Technical University, Middle East Technical University, and Yıldız Technical University, supported by the Turkish Chamber of Civil Engineers. In 2023, the Cyprus-Turkish Chamber of Civil Engineers joined as an additional supporter, elevating the stature of this distinguished congress.

The ACE congress was a cornerstone for scholarly discussions on contemporary trends in civil engineering. It encompassed discourse on novel technologies, methodologies, theoretical frameworks, and industrial practices, gathering global researchers and industry experts to facilitate insightful exchanges across diverse facets of civil engineering. The event featured eminent Keynote Speakers and a diverse array of Social and Cultural Events that significantly enhanced the congress experience.

It was our sincere pleasure to have hosted all participants for this exceptional congress, fostering scholarly exchange and intellectual growth within the field of civil engineering.

Prof. Dr. Umut Türker

Congress Chair 15th ACE 2023

COMMITTEES

ORGANISING COMMITTEE

Umut TÜRKER
Özgür EREN
Eriş UYGAR

CONGRESS SECRETARIAT

Tolga ÇELIK

STEERING COMMITTEE

Gürkan YAĞCIOĞLU
Taner YÜZGE
Bilge DORAN
Cem AVCI
Engin ORAKDÖĞEN
Erdem CANBAY
Şemsi YAZICI
Şevket ATEŞ
Umut TÜRKER

SECRETARIAT ASSISTANTS

Hamza SAEED
Aria NOROUZI
Bashar ALIBRAHIM
Hussein A. MOUSSA
Iman YOUSSEFI
Muhammad RAJAB
Oğuz KARAYEL

SCIENTIFIC COMMITTEE

Abdullah EKİNCİ	Middle East Technical University
Abdulrezak MOHAMMAD	Conestoga College
Ahmed ALYOUSIF	University of Toronto
Ahmet BİRİNCİ	Karadeniz Technical University
Ahmet C. ALTUNIŞIK	Karadeniz Technical University
Ali ATEŞ	Bolu Abant İzzet Baysal University
Ali KOÇAK	Yıldız Technical Üniversity
Ali MOSABERPANAH	Cyprus International University
Ali R. REZAI	University of Warwick
Amin RIAZI	Seattle University
Anoosheh IRAVANIAN	- Aalto University - Near East University
Aria A. LANGROUDI	University of East London
Aslı P. GÜRGÜN	Yıldız Technical University
Atakan AKSOY	Karadeniz Technical University
Aydın ÖZTEMEL	Cyprus Turkish Chamber of Civil Engineers
Ayşe DALOĞLU	Karadeniz Technical University
Ayşe P. BALKIS	Cyprus Turkish Chamber of Civil Engineers
Ayşen ERGİN	Turkish Chamber of Civil Engineers
Bertuğ AKINTUĞ	Cyprus Turkish Chamber of Civil Engineers

SCIENTIFIC COMMITTEE

Cahit YERDELEN	Ege University
Ceren İNCE	Middle East Technical University
Changiz AHBAP	Eastern Mediterranean University
Cüneyt AYDIN	Atatürk Üniversity
Ece ÇELİK	Eastern Mediterranean University
Emre GÜRCANLI	İstanbul Technical University
Ertuğ AYDIN	European University of Lefke
Esin ÇEVİK	Yıldız Technical Üniversity
Feyza ÇİNİCİOĞLU	Turkish Chamber of Civil Engineers
Giray ÖZAY	Eastern Mediterranean University
Gözde OĞUZ	Cyprus Turkish Chamber of Civil Engineers
Gülay ALTAY	Özyeğin Üniversity
Gülben ÇALIŞ	Ege University
Hafzüllah AKSOY	Turkish Chamber of Civil Engineers
Hakan YALÇINER	Erzincan Üniversitesi
Halim CEYLAN	Turkish Chamber of Civil Engineers
Hasan ZAİFOĞLU	Middle East Technical University
Haseeb PAYAB	Drexel University
Hediye TÜYDEŞ	Middle East Technical University
Huriye BİLSEL	Cyprus International University
Hüseyin GÖKÇEKUŞ	Near East University
İbrahim BAY	European University of Lefke
İbrahim YİTMEN	Jönköping University
Iman AGHAYAN	Shahrood University of Technology
İrfan COŞKUN	Yıldız Technical University
İsmail SAFKAN	Cyprus Turkish Chamber of Civil Engineers
İsmail ŞAHİN	Yıldız Technical University
Kambiz RAMYAR	Ege University
Kemal D. TÖZER	Cyprus Turkish Chamber of Civil Engineers
Kezban ÖZLÜTAŞ	Girne American University
Khaled MARAR	Eastern Mediterranean University
Mahmood HOSSEINI	Eastern Mediterranean University
Mehmedali EGEMEN	European University of Lefke
Mehmet C. GENEŞ	Eastern Mediterranean University

SCIENTIFIC COMMITTEE

Mehmet M. KUNT	Eastern Mediterranean University
Melih YANMAZ	Middle East Technical University
Menteş ZORBA	Cyprus Turkish Chamber of Civil Engineers
Metin Hüsem	Karadeniz Technical University
Mohammad F. MOUSAVI	Bahçeşehir Cyprus University
Mohammad GHORBANZADEH	Girne University
Mohammad GOLHASHEM	International Final University
Mürüde ÇELİKAĞ	Eastern Mediterranean University
Mustafa ERGİL	Eastern Mediterranean University
Mustafa MAHAMID	-Technion-Israel Institute of Technology -University of Illinois at Chicago
Mustafa TOKYAY	Turkish Chamber of Civil Engineers
Nabi YÜZER	Yıldız Technical University
Nihat KABAY	Yıldız Technical Üniversity
Ninel ALVER	Ege University
Ömer YÜKSEK	Karadeniz Technical University
Oral YAĞCI	İstanbul Technical University
Osman SİVRİKAYA	Karadeniz Technical University
Perviz AHMEDZADE	Ege University
Pınar AKPINAR	Cyprus Turkish Chamber of Civil Engineers
Polen ÇİFTÇİOĞLU	Cyprus Turkish Chamber of Civil Engineers
Rıfat AKBIYIKLI	Turkish Chamber of Civil Engineers
Rıfat REŞATOĞLU	Near East University
Rouba ELDALATİ	Labanese University
Şakir ERDOĞDU	Karadeniz Technical University
Selim ALTUN	Ege University
Şeref ORUÇ	Karadeniz Technical University
Serhan ŞENSOY	Eastern Mediterranean University
Şerife Ö. SARPER	Eastern Mediterranean University
Şevket C. BOSTANCI	Cyprus Turkish Chamber of Civil Engineers
Shaban GHAT	Near East University
Suat AKBULUT	Yıldız Technical University
Şükrü ÖZÇOBAN	Yıldız Technical Üniversity
Tahir ÇELİK	Cyprus International University

SCIENTIFIC COMMITTEE

Tayfun DEDE	Karadeniz Technical University
Teoman ÖZER	İstanbul Technical University
Tolga ÇELİK	Eastern Mediterranean University
Tülin AKÇAOĞLU	Eastern Mediterranean University
Umut YILDIRIM	Eastern Mediterranean University
Vedat TOĞAN	Karadeniz Technical University
Yalçın YÜKSEL	Yıldız Technical University
Yasin FAHJAN	İstanbul Technical University
Yeşim GÜRTUĞ	Marmara University
Yusuf AYVAZ	Yıldız Technical University
Zafer KÜTÜĞ	Yıldız Technical Üniversity
Zalihe N. SEZAİ	Eastern Mediterranean University
Zekai CELEP	Turkish Chamber of Civil Engineers
Zeynep IŞIK	Yıldız Technical Üniversity

KEYNOTE SPEAKERS

Prof. Dr. İ. Özgür YAMAN

Middle East Technical University, Ankara, Türkiye.

Dr. İsmail Özgür Yaman received his undergraduate and graduate degrees from the Department of Civil Engineering at METU in 1993 and 1995 and earned his PhD in 2000 at Wayne State University, USA, with his work on the simulation of ultrasonic testing of concrete. He has been continuing his academic activities at METU Department of Civil Engineering since 2003.

Dr. Yaman's main research topics include the use of non-destructive testing methods in concrete; developments in cement and concrete technology. For the last ten years his focus is on concrete road construction technologies.

Having over 100 national and international publications, Dr. Yaman held various positions in international institutions such as TRB and EUPAVE, as well as national professional and research institutions such as IMO, TÜBİTAK, TÜRKÇİMENTO and THBB.

Prof. Dr. Abbas AMINMANSOUR

University of Illinois at Urbana-Champaign, USA.

Dr. Abbas Aminmansour is a member of the Structures Concentration faculty and Chair of the Building Performance Program in the School of Architecture at the University of Illinois at Urbana-Champaign. His areas of research and scholarship interest include design of steel structures as well as design of tall buildings.

Professor Aminmansour is an active member of technical committees in the American Institute of Steel Construction (AISC) and serves on AISC's Committee on Manuals and Technical Committee 4 of the AISC Committee on Specification. His work has been adopted by AISC several times and included in the AISC Manual. His most recent work is what is referred to as the super table in Part Six of the AISC Manual. He is the recipient of the 2015 Special Achievement Award from AISC. Professor Aminmansour is currently developing an integrated cloud-based book and software for the design of structural steel members.

Dr. Aminmansour is a current member and past Chair of the Chicago Committee on High-Rise Buildings (CCHRB). He is also an active member of the Council on Tall Buildings and Urban Habitat (CTBUH) where he serves on the Editorial Board of CTBUH's International Journal of High-Rise Buildings. CTBUH recognized Dr. Aminmansour as one of four 2022 Fellows selected globally for this honor.

KEYNOTE SPEAKERS

Prof. Dr. Manousos VALYRAKIS

University of Glasgow, UK.

Manos got trained as a Civil Engineer with focus on hydraulics, getting both his MEng and MSc degrees from Aristotle University of Thessaloniki. He got awarded his PhD in river engineering, from Virginia Tech (USA). After a one year postdoc, he joined the University of Glasgow, as an Assistant Professor in Hydraulic Engineering and manager of the Water Engineering Lab, where he has led hydraulics research and teaching, for more than a decade.

He has also held visiting Professor posts in several universities and aspires to help bridge theory with applications, by developing new flow and sediment transport measurement devices that allow to better observe and monitor these highly dynamical processes.

He serves the hydraulic engineering community through active memberships in professional societies, such as the International Association for Hydroenvironment Research (IAHR), the American Society of Civil Engineers (ASCE), the Institute of Civil Engineers (ICE). He has served in IAHR's Experimental Methods and Instrumentation (EMI) leadership team and ICE's Reservoir Safety Advisory Group (ReSRAG) aiming to bridge theory with practice.

Prof. Dr. Yasin FAHJAN,

Istanbul Teknik Universitesi

İstanbul Teknik Üniversitesi İnşaat Mühendisliği Bölümü'nde Yapı ve Deprem Mühendisliği alanında akademik ve araştırma faaliyetlerin şürdürmektedir. 1992 yılında Doğu Akdeniz Üniversitesi İnşaat Mühendisliği Bölümü'nden Lisans derecesini alan Yasin FAHJAN Master Derecesini 1994 yılında aynı bölümünden almıştır. 1998 yılında Boğaziçi Üniversitesi İnşaat Mühendisliği Bölümünde doktorasını tamamlamıştır. Deprem riski değerlendirmeleri, zemin-yapı etkileşimi, sıvı-yapı Etkileşimi konularında güçlü bir altyapıya sahiptir. Yapısal analizler, hızlı müdahale ve erken uyarı sistemleri, kuvvetli yer hareketi simülasyonları ile ilgili çeşitli eğitimsel ve ticari kodlar ve algoritmalar geliştirmiştir. Türkiye Afet ve Acil Durum Yönetimi Başkanlığı tarafından deprem sonrası kurtarma operasyonları ve ülke çapında risk değerlendirmesi ve yönetimi için işletilen AFAD-RED sisteminin ana geliştiricisidir. Ayrıca Türkiye'de ve yurt dışında birçok öncü mühendislik projesinde deprem mühendisliği danışmanı olarak çalışan Prof. FAHJAN, ulusal ve uluslararası düzeyde birçok araştırma projesinde ekip lideri olarak yöneticilikler yapmıştır. Birçok hakemli dergide ve konferanslarda önemli yayınları bulunmaktadır.

CONGRESS THEMES

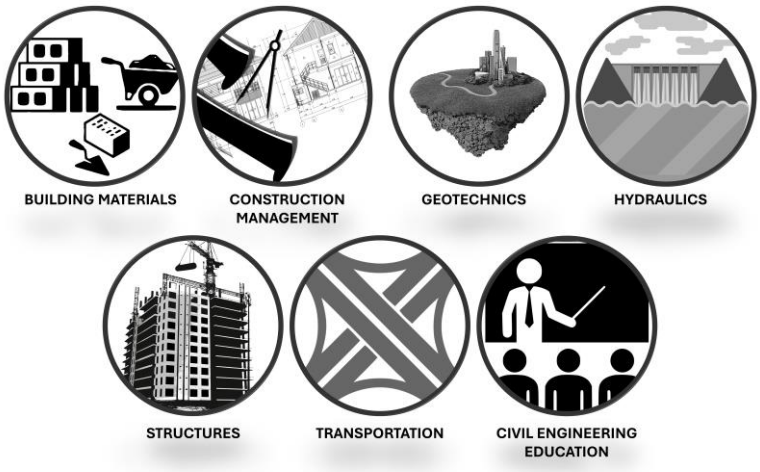

TABLE OF CONTENTS

BUILDING MATERIALS 1 – 146

Surface Treatment of Rubber Particles with Sodium Hydroxide Solution for Use in Cement Bound Base Course 1

Strength And Fresh Properties of Self-Compacting Concrete Containing Coarse Electric Arc Furnace Slag Aggregate 11

Mechanical Properties and Expansion Behaviour of ASR Affected Concrete 20

Properties of Ilmenite-Heavyweight Concrete Subjected to Elevated Temperature 30

Impact of Climate Change on Asphalt Binder Performance Selection in a Cold Region Environment 39

A Comparison and Review of Studies on Chemical Accelerator Admixtures in Concrete 61

Influence of Barite Sand on The Strength on Self-Compacting Concrete with Fly Ash 72

Development of Low-Carbon Oxalate Cement Using Copper Slag 81

Structures and Performance of Some Agro-Based Ternary Blends in Concrete – A State-of-the-Art Review 92

Investigation of the Effect of Asphalt Binder Modified with the New Synthesized TOBO Additive on Rutting Performance 103

A Review Paper About Test Methods Used/Developed for Fresh and Hardened Properties of High Strength Concrete 111

Effect of Reactive MgO Substitution on Strength Development and Microstructure Properties of Sodium Carbonate Activated Slag-Based Systems 121

Influence of Binary Use of Antifreeze Admixtures on The Early-Age Frost Resistance of Self-Compacting Concretes 131

CIVIL ENGINEERING EDUCATION 147 – 163

Education for the Use of BIM on the Example of Slovenian Higher Education 147

CONSTRUCTION MANAGEMENT 164 – 237

A Review of The Application of EVM in Construction Industry 164

Identification of Critical Factors in Design for Sustainability of Modular Constructions 175

A Systematic Literature Review on Blockchain Technology for Construction Contract Management 181

Quantification of Rework Causes in Turkish Construction Industry 192

Construction and Demolition Waste Processing for A Circular Construction Model: An Overview and Comparison Between On-Site and Off-Site Recycling....202

Resilience in Construction Industry and Its Role in Upgrading the Quality of Post-Earthquake Sheltering and Reconstruction....219

Supervisor's and Co-workers' Safety Climate of Building Construction Workers....230

GEOTECHNICS 238 – 405

Exploring the Effects of Cement and Eggshell Powder Stabilisation on the Engineering Characteristics of Expansive Soils: An Experimental Study....238

Improving Geotechnical Monitoring System Performances by Integrating Advanced Technologies for Data Acquisition and Elaboration....248

Micromechanical Modeling of the Dynamic Response of A Sand Deposit....258

Linear Equivalent Seismic Response of A Surface Foundation Excited by A Harmonic Rayleigh Wave....269

Effect of Colemanite and Glass Fiber on the Volume Deformation Behavior of Bentonite....278

Passive Earth Reinforcement for Lateral Equilibrium Optimization....283

An Assessment of Shrinkage Characteristics of Cementitiously Stabilized Granular Material for Pavement Layers....292

Active and Passive Pressures Acting on Smooth Circular Shafts....302

Automated Extraction of Geotechnical Data from PDF Reports and Kriging Application....312

Stability Analysis of Akaili Landslide (Jebha, Northern Morocco)....322

Prediction of the Simple Compressive Strength of Clay Soils Improved by Lime and Gypsum Using ANN Application....342

Investigation of Stability and Deformation Conditions of Slopes with Groundwater Level Changes by Precipitation Under Different Loads....351

Effect Of Stress History on Lateral Earth Pressure Coefficient At Rest Analysis Through Discrete Elements Method....362

Use of Recycled Aggregates from Derived Construction and Demolition Waste in the Highway Base Layer....386

Multiple Regression of Compression Index with Different Soil Parameters....397

HYDRAULICS 406 – 525

Trends of Standard Duration Maximum Precipitation Over the Last 30 Years in Kastamonu Province, Northern Turkey 406

Nonstationary Modelling of Low Flow in Çoruh Basin 417

Evolution of Low Flows in Çoruh Basin 425

Possible Effects of Climate Change on Seawater Temperatures: A Case Study for Sarıyer Meteorological Observation Station, Southwestern Black Sea 433

Examination of the Long-Term Drought Variability of the Continental Climate Regions Using Discrepancy Precipitation Index: The Case of Karaman Station Data, Türkiye 443

Tracking Climate Change Impact on Droughts in Northern Cyprus Through Standardized Precipitation Index 454

Estimation of Design Rainfalls in Cyprus Under Nonstationary Conditions 465

Introduction of a Computer Software (S-Hammer) Developed to Analyze Fluid Transients in Pipelines 476

Investigation of Interaction Between Pressure Relief Valve and Turbines During a Transient Flow in a Hydropower Plant 486

Determination of Sediment Yield of Çoruh River by Field Observation and RUSLE Method 495

Flood Risk Mapping with Entropy Based Methods 505

Investigating the Efficacy of Large-Scale Particle Image Velocimetry for Controlled Water Resource Management: An Experimental Approach 513

STRUCTURES & EARTHQUAKE 526 – 784

A Computational Model for the Analysis of 2D Beams and Frames Failure Based on Hardening and Softening Behaviors with an Incorporated Damage Model 526

Calculation Of Seismic Effects in the LIRA 10 Software Complex 536

Determining the Earthquake Behavior of the Historical Zonguldak Aziziye Mosque Minaret by Considering the 2022 Düzce-Gölyaka (Mw: 5.9) Earthquake 546

The Effect of Masonry Infills on the Performance of Steel Frames 563

A Simple Procedure to Approximate Fundamental Mode Period of Vibration 572

Testing of Concrete Masonry Infill Walls Subjected to In-Plane Lateral Load 586

Using Vertical Seismic Isolation by Dividing the Building's Structure into Interactive Parts 597

Comparison of the Seismic Behavior of RC Frame with Wide Beam and Deep Beam Non-linear Time History 607

A Nonlinear Study of The Influence of Strong Earthquake Ground Motion from The February 2023 Turkey Sequence (M = 7,8) 618

Adaptive Sliding Mode for A Semi Active Vibration Control 628

Corroboration of the Pre- and Post-Earthquake Assessment of the Buildings in 2023 Kahramanmaraş Earthquake Using Field Inspections and Street-Level Imagery 639

Effect of Mass Irregularity on Seismic Performance of a Base-Isolated RC Building 651

Effects of Configuration Changes on Live Load Carrying Capacity of Steel Railway Bridges with Same Span Length 660

Finite Element Analysis on Axial Compressive Performance of RHHCFST Short Columns with Longitudinal Stiffeners 678

Indicators Affecting the Design of Subway Stations to be More Responsive in Emergencies 689

Reviewing Prestress Losses in An Aged Spanish Concrete Bridge 699

Seismic Assessment of Bridges Under Aftershock Affects 709

The Effect of Foundations Uplift on The Seismic Behavior of Multi-Story Moment Frames Regular RC Buildings 718

Vision-Based Identification of Dynamic Characteristics Using Cameras: A Case Study on One of Tehran's Bridges 729

Shear Buckling of Corrugated Web Beams with Openings 740

Systems for Monitoring a Bridge Using Wireless Sensor Networks 751

Utilizing Shear Walls Constructed with a Blend of Crushed Waste Tire Rubber for Seismic Assessment and Retrofitting of an Existing RC Building 764

Seismic Response and Reliability Analysis of A High-Pier Rigid Frame Bridge 776

TRANSPORTATION 785 – 913

Financial and Structural Innovations in Mega Transportation Projects in Turkiye 785

Optimal Pavement Design and Maintenance Approach Using HDM-4 801

Investigation of the Effect of Bio-char and Activated Carbon on the Physical Properties of Asphalt Binder 829

The Effects of Nano Expanded Vermiculite on Asphalt Binder Properties 839

Modelling Shared Bicycle Demand Using Artificial Neural Networks 849

Development of Pavement Condition Prediction Models in Urban Areas Using Micro PAVER 860

Investigating the Tensile Properties of Geocell Reinforced Pavement System Using a 2D FE Model 870

An Evaluation of Electric Vehicle Performance in Extreme Weather Conditions and HVAC Use 884

Developing a Decision Support System for Roadside Restraint Systems (RRSs) Design 894

Investigation of the Usability of Basalt and Limestone Aggregates Obtained from Bitlis Region in Porous Asphalt Construction 904

Investigation of Rutting Performance of Asphalt Binder Modified with New Boron-containing Additive 914

BUILDING MATERIALS

pages: 1 – 146

Surface Treatment of Rubber Particles with Sodium Hydroxide Solution for Use in Cement Bound Base Course

Matija Zvonarić[1[0000-0002-7604-3002]], Martina Zagvozda[1[0000-0002-5334-3731]], Ivana Barišić[1[0000-0003-2635-1063]] and Lora Babić

[1] Josip Juraj Strossmayer University of Osijek, Faculty of Civil Engineering and Architecture Osijek, mzvonaric@gfos.hr

Abstract. Reduction of shrinkage and reduction in development of internal stresses of cement-stabilized aggregate is attempted to be achieved by using waste rubber in these mixtures. But, the incorporation of rubber leads to a reduction in the strength of the produced material due to the weak bonds between the rubber particles and the other materials within the mixture. Two forms of rubber were used, rubber granules and rubber threads. The rubber granules were used as a volume replacement for sand in a mixture comprising 5% of cement, while rubber threads were used as a 5% mass addition to a mixture comprising 7% of cement. Rubber particles were treated with a 5% sodium hydroxide (NaOH) solution as a measure of cleaning the surface of the rubber particles and neglection the negative impact of impurities with the aim of ensuring a better connection with other materials. Treatment of rubber with NaOH resulted in a significant increase in the specific surface area (SSA) of the rubber particle determined by the Brunauer, Emmett & Teller device (BET). The increase in SSA was supported by a significantly greater roughness of the particle surface observed by Scanning Electron Microscope (SEM). Mechanical properties examination included compressive strength (f_c) and indirect tensile strength (f_t) testing, as well as, dynamic modulus of elasticity (E_{din}) measurement after 7 and 28 days of curing regime. The obtained results were compared with the results of the same mixtures with untreated rubber, and it can be concluded that the treatment with NaOH achieved a significantly better effect on larger rubber particles, i.e. rubber threads.

Keywords: Cement Bound Base Course, Waste Rubber, Surface Treatment, Sodium Hydroxide, Specific Surface Area

1 Introduction

The use of rubber in cement–based composites has a dual role. On the one hand, utilization of waste material is ensured, while, on the other hand, rubber potentially reduces the development of internal stresses, which results in fewer cracks occurring in such materials. However, it has been shown that the use of waste rubber in concrete,

mortar, and cement stabilized aggregate (CSA) reduces the strength of such mixtures, mostly due to weak bonds between rubber and cement paste within the mixture matrix [1,2]. In addition to weak bonds, the decrease in strength is also contributed by the air–entrapment phenomenon on the rubber particles and rubber's hydrophobicity [3]. Therefore, researchers are approaching waste tire modification measures. Physical and chemical modifications of rubber particles can be distinguished. Thereby, physical modification implies cleaning rubber particles from hydrophobic impurities by various compounds, while chemical modification includes procedures for changing the rubber surface texture and morphology by different agents [4].

The most pronounced mechanical procedures include immersing or washing the rubber with water, exposure to different forms of radiation, or coating the rubber with some agent that can improve particle binding. When using chemical methods, knowledge of the chemical composition of the treated material is very important. At the same time, particular attention should be paid to the possible negative impact of the used chemical compounds on the environment. Mechanical modifications require minor changes in the technological process, but chemical modifications have proven to be more effective [5]. The simplest procedure for cleaning the rubber and increasing its hydrophilicity is submerging or rinsing the rubber with pressured water, followed by air–drying. However, this treatment does not provide significant improvement in the mechanical properties of concrete [2,6,7]. On the other hand, heating the rubber particles cleans the impurities on the rubber's surface and creates a hard surface membrane, which contributes to increased contact and more efficient load transfer within the concrete structure. Exposure of rubber to the temperature of 200°C for 1.5 hours has shown to be an effective measure to reduce the negative impact of rubber on the mechanical properties of concrete [8]. But creation of surface membrane on the rubber particle leads to decrease in its elasticity which is unwanted behavior due to tendency of increasing mixture's elasticity by rubber incorporation. The rubber particles can be coated with various materials. The use of fluorgypsum as a coating agent improves mechanical characteristics because fluorgypsum improves the transfer of mechanical stresses between rubber particles and cement paste. The reason for this lies in the fact that fluorgypsum neutralizes the negative impact of Zn present in the rubber, which slows the hydration of C_3S [9]. Furthermore, authors Najim and Hall [10] coated the rubber particles with cement paste and mortar and left them to air–dry for 28 days. This procedure also showed a positive effect on the mechanical properties of concrete. A more modern approach to the mechanical treatment of rubber highlights the exposure of the rubber to different radiations. Thus, it was shown that exposure of rubber particles to UV radiation resulted in a change in the surface energy of the rubber particle and, consequently, an increase in the ability to retain water on the surface of the particle and a better connection with the cement paste. Hereby, the best result was obtained by exposing the rubber to UV–C radiation [11]. In addition to UV radiation, morphological changes of the rubber particle surface can also be caused by gamma radiation exposure, which contributes to improving concrete's mechanical properties [12].

When speaking of chemical modification, the influence of chemical compounds based on acids, which change the surface of the rubber particle and increase adhesion

with the cement paste in concrete is the most researched. Sodium hydroxide (NaOH) was mostly used as a 10% and 5% solution to remove hydrophobic impurities and increase the porosity of the rubber particle surface [13,14]. The best results were obtained by treating the rubber with a NaOH solution concentration of 1 M for 24 hours [15], although it is emphasized that this modification did not significantly affect the behavior of concrete in terms of improving its physical and mechanical properties [16]. After the NaOH treatment, the decreasing trend of contact angle was observed indicating increase of hydrophilicity of rubber. By hydrophilicity increase, the prerequisites for development of stronger bonds are realized. As a result, the interfacial transition zone (ITZ) can be reduced and bonds between rubber particles and cement paste can be enhanced [17,18]. The modification of rubber particles with NaOH and potassium permanganate (KMnO4) proved to be effective in terms of improving the compressive and flexural strength of concrete, but for small amounts of rubber, while the formation of a cement coating on rubber particles is more effective for higher amounts of rubber [19]. Similar results were obtained for the modification of rubber particles with urea, whereby the resistance of concrete, among other things, to impact load was increased [20].

Mortar and concrete have a significantly higher amount of cement paste in comparison to CSA and, therefore, the influence of NaOH on the mechanical properties of such material has to be investigated separately. This research aims to test whether NaOH can neglect the negative impact of rubber on the mechanical characteristics of rubberized CSA. Two mixtures defined by previous research whose mechanical characteristics did not meet the requirements were taken as test mixtures. Likewise, the paper includes a microscopic analysis of the morphology of untreated and treated rubber to define the effectiveness of the treatment on the contact between rubber and cement paste as well as stress transfer. This research also analyzes the effect of NaOH solution on two different forms of rubber with different morphological characteristics and sizes.

2 Materials and Methods

Within this research four mixtures of rubberized cement stabilized aggregate (CSA) were conducted. The mixtures are composed of natural sand (0–2 mm) and natural gravel (0–4 mm, 4–8 mm, and 8–16 mm), granulated rubber (0–0.5 mm), and rubber threads (0.8–3 mm), Portland cement of grade 32.5R (CEM II B/M (P–S)) and an optimal amount of water determined according to [21]. The granulated rubber was used as a volume replacement for sand in mixtures comprising 5% of cement, while rubber threads were used as volume addition to aggregate in mixtures comprising 7% of cement. Different approach to the creation of mixture composition lies in the size and shape of the particles. Granulated rubber is similar in shape and size to sand and therefore, it was used as a replacement for sand. On the other hand, rubber threads differ from any used aggregate which is the reason for their use as an addition to the aggregate. The granulometric composition of the used aggregate is presented in Fig. 1. Based on previous research, 30% of granulated rubber as a replacement for sand (mixture C5R30)

and 5% of rubber threads as volume addition to aggregate (C7R5) were adopted [22–24]. These mixtures achieved almost satisfactory 7–days and 28–days compressive strength results and therefore, were selected as mixtures with the potential to achieve satisfactory strength through rubber modification. Based on market availability, sodium hydroxide (NaOH) was chosen. The granulated rubber and rubber threads were treated with 5% NaOH solution in such a way that the material was immersed in the solution for 1 hour. It was then washed under running tap water and dried in a dryer at 60°C for 24 hours. The rubber treatment procedure is shown in Fig. 2. a), b), and c). The treated rubber was then used for specimen preparation as described in [22, 23].

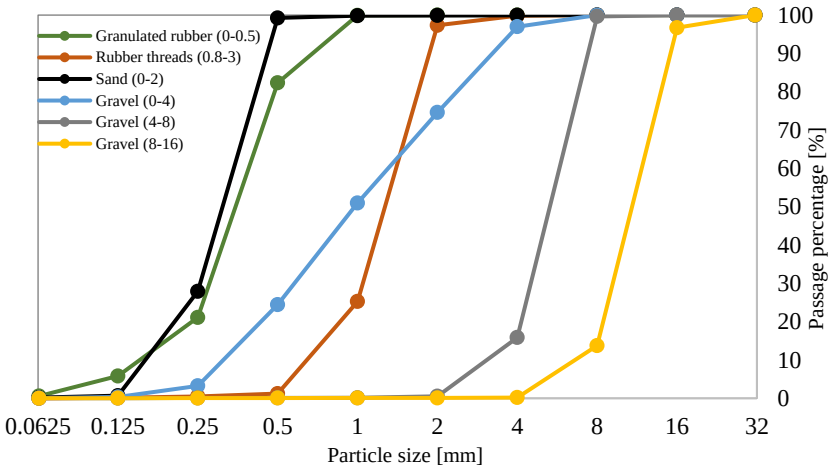

Fig. 1. Granulometric composition of aggregate

a) b) c)

Fig. 2. a) NaOH flakes; b) rubber immersed in solution; c) rubber drying.

The 7–days and 28–days compressive strength, indirect tensile strength, and dynamic modulus of elasticity of specimens were tested according to standards EN 13286 – 41 [25], EN 13286 – 42 [26], and EN 12504 – 4 [27], respectively. According to the standard, compressive strength is defined as the stress at the failure of the specimen

tested by the uniaxial load with free deformation. During the test, the sample is subjected to a compressive load continuously and without shock, so that the crack appears within a period of 30 to 120 seconds from the beginning of the loading. The maximum force at the break of the sample is recorded, and the compressive strength can be calculated.

To determine the indirect tensile strength of the CSA mixtures, the Brazilian method was used. During the test, the cylindrical specimen was exposed to a compressive load via a load band along two opposite supports until failure. With this type of load, relatively uniform tensile stress occurs perpendicular to the diametrical surface along which the compressive load is applied. After the recorded force at specimen failure, the indirect tensile strength can be determined.

The dynamic modulus of elasticity was determined by measuring the ultrasonic pulse velocity (UPV) through the specimen. The principle of this test is based on a pulse of longitudinal vibration emitted by an electro–acoustic transmitter in contact with the sample being tested. After passing through a sample of a known length, the vibration pulse is converted into an electrical signal on the receiver on the other side of the sample, and the time required for the pulse to pass through the sample is recorded. For modulus calculation, UPV, specimen density and Poisson's coefficient are needed. Given that the measurement of the Poisson's coefficient for these materials is imprecise and demanding due to the structure and unevenness of the specimen surface and the small influence of the coefficient on the results of the calculated dynamic modulus of elasticity, which is presented in detail in the paper [28], the Poisson's coefficient value of 0.25 was adopted. The UPV measurement precedes the compressive strength test on the same specimens. All conducted tests were carried out on three specimens of the same mixture to ensure the reliability of the results.

3 Results and Discussion

Before mixture preparation, untreated and treated rubber were analyzed by Scanning Electron Microscope (SEM). The SEM analysis showed that rubber treatment with NaOH solution resulted in a change particle surface morphology. As it is shown in Fig. 3. a) and b) and Fig. 4. a) and b), the treated rubber has a rougher surface compared to the untreated one. This claim applies to both, granulated rubber and rubber threads. With the more detailed analysis of the morphology of the rubber particles shown in the figures, it can be concluded that the rubber thread exhibits greater roughness and irregularity after treatment in comparison to the rubber granules. Changes in particle morphology prove that exposure of rubber to NaOH solution affects rubber particles. Namely, as a result of the contact between rubber and alkaline solution, the rupture of rubber molecules occurs, leading to the formation of cracks. Since the rubber is immersed in such a solution for 1 hour, the degradation of rubber is retained on the surface of the particles. During visual analysis, it seems that a greater effect was achieved when treating rubber threads, but to prove this, the specific surface area (SSA)

of rubber particles was determined by Brunauer, Emmett, and Teller machine according to ISO 9277:2010 [29] standard. The results of specific surface area analysis of untreated and treated granulated rubber particles and rubber threads is shown in Table 1.

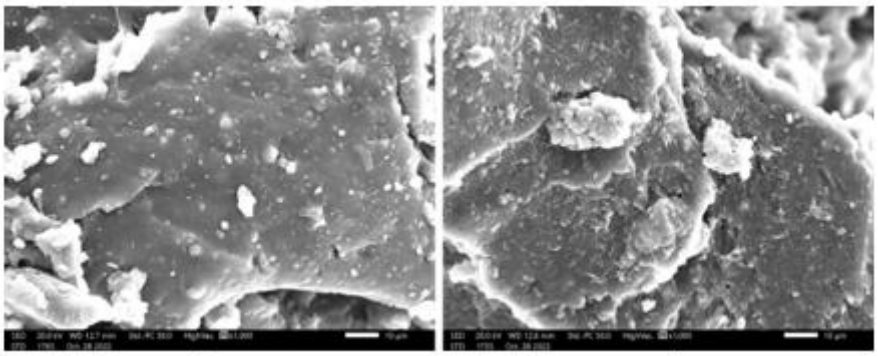

Fig. 3. SEM image of: a) untreated granulated rubber; b) treated granulated rubber.

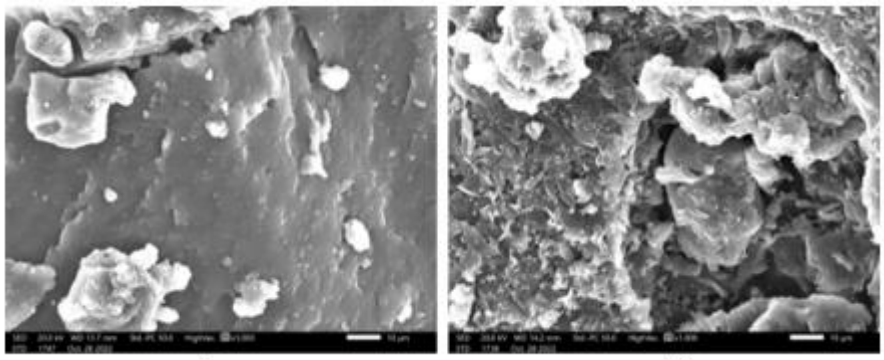

Fig. 4. SEM image of: a) untreated rubber threads; b) treated rubber threads.

Table 1. Results of mechanical characteristics

	SSA (m^2/g)	
	Untreated	Treated
Granulated Rubber	10,95	34,48
Rubber threads	16,58	58,64

The specific surface area of granulated rubber is 33.96% lower than of the rubber threads. By treating rubber with NaOH, the SSA increases for both types of rubber particles. The increase in the SSA is about 315% for granulated rubber and 350% for rubber threads after the NaOH solution treatment.

In addition to the analysis of the particle morphology and specific surface area, the mechanical properties of the rubberized mixtures were also examined. The results of compressive strength, indirect tensile strength, and ultrasonic pulse velocity along with the dynamic modulus of elasticity obtained in this research are presented in table 2. From the results with granulated rubber, it can be concluded that NaOH treatment resulted in a decrease in compressive and indirect tensile strength. The decrease for both strength types is more pronounced for shorter curing period. For the longer curing period, the strengths of treated mixtures decreased about 10%.

Table 2. Results of mechanical characteristics

Mixture	$f_{c,7}$ (MPa)	$f_{c,28}$ (MPa)	$f_{t,7}$ (MPa)	$f_{t,28}$ (MPa)	v_7 (km/s)	E_7 (GPa)	v_{28} (km/s)	E_{28} (GPa)
C5R30	1,56	1,94	0,32	0,45	1,75	5,47	2,19	8,59
C5R30-NaOH	1,03	1,74	0,22	0,41	1,65	4,87	2,22	8,86
C7R5	2,41	2,76	1,00	0,74	1,07	2,04	1,98	6,99
C7R5-NaOH	1,90	2,58	0,36	0,68	1,10	2,23	2,14	8,37

When observing only mixture with granulated rubber, a decrease in compressive and indirect tensile strength after 7 and 28 days amounts about 30% an 10%, respectively. While dynamic modulus of elasticity achieved 10% lower value for 7 days curing period and increase for 3% after 28 days curing period. When observing the rubber threads, the mixture obtained a lower drop in compressive strength in amounts about 20% for 7 days and 5% for 28 days. While indirect tensile strength is more negatively affected by this treatment in shorter curing period. The increase in dynamic modulus of elasticity is observed also for C7R5 mixture and this increase is more pronounced than for C5R30. Namely, the rough surface of the rubber is covered with the cement paste, which forms the rigid part of the mixture, and ultrasonic pulse pass through such material faster. Thus, the dynamic modulus of elasticity increased more for rubber threads due to higher increase in rubber surface in comparison to granulated rubber. The greater increase in specific surface area enabled a significantly higher contact surface between the rubber and cement paste, thereby facilitating better bonding and the formation of a stronger structure. Furthermore, sodium hydroxide positively influenced the hydrophilicity of the rubber and increased the adhesive properties of the rubber particle surface. The results of the specific surface area of the particles and the dynamic modulus of elasticity directly imply a connection between the stiffness of the mixture and the particle's surface properties, while the particle shape plays a lesser role on the development of the stiffness. Overall, the decreasing strength trend after NaOH treatment of the rubber loses strength over time for both mixtures. Thereby, this drop is much smaller after 28 days of curing, than after 7 days which means that hydration process is hindered at early age.

As a result of spreading the cement paste over the surface of the rubber particle, there is a lack of cement paste with the aggregate grains, which results in a lower strength of the mixture. Because of this, there is also a difference in the strength and stiffness (dynamic modulus of elasticity) trend, on which basis one can say that a new material was produced by treating the rubber. The differences in surface morphology and SSA proved to be an important factor affecting the optimal moisture content and maximum dry density of rubberized CSA mixtures [30]. The aim of rubber treatment was cleaning the rubber from impurities and lower the rubber's hydrophobicity. This should result with improved bonds between rubber and cement paste. However, this method is not as effective as in rubberized concrete, as a result of the difference in the amount of cement paste between these two materials.

4 Conclusion

Within this research, the possibility of improving the mechanical characteristics of rubberized cement stabilized aggregate (CSA) mixtures by chemical treating the rubber was examined. Immersion of the rubber in a 5% NaOH solution was chosen as the treatment method. This treatment was applied to two types of waste rubber, fine granulated rubber fraction and coarse elongated rubber threads. Apart from the mechanical properties, a visual comparison of the treated and untreated rubber was made using a Scanning Electron Microscope (SEM), and their specific surface area (SSA) was determined to determine the effect of the alkaline solution. Several conclusions can be drawn from conducted research:

- An increase in the roughness of the particle surface as a result of NaOH treatment was observed by SEM. The SSA of granulated rubber particles increased by 315%, while the SSA of rubber threads increased by 350%.
- Rubber treatment led to a decrease in compressive and indirect tensile strength, and this decrease was more pronounced for a shorter curing period. Contrary, a slight increase in the dynamic modulus of elasticity was observed.
- Obvious dependance between rubber surface properties and mixture's stiffness is observed.
- This procedure did not achieve the desired effect of strength increase due to the small amount of cement paste in CSA mixtures.

Acknowledgements
This research is supported by Croatian Science Foundation under the project UIP–2019–04-8195 "Cement stabilized base courses with waste rubber for sustainable pavements – RubSuPave".

References

1. Assaggaf, R.A., Ali, M.R., Al-Dulaijan, S.U., Maslehuddin M.: Properties of concrete with untreated and treated crumb rubber - A review. Journal of Materials Research and Technology 11, 1753–98 (2016).
2. Li, Y., Zhang, X., Wang, R., Lei, Y.: Performance enhancement of rubberised concrete via surface modification of rubber: A review. Construction and Building Materials 227 (2019).
3. Pham, N.-P., Toumi, A., Turatsinze, A.: Evaluating damage of rubberized cement-based composites under aggressive environments. Construction and Building Materials 2017, 234-241 (2019).
4. Zhang, R., Wang, H., Ji, J., Suo, Z., Ou, Z.: Influences of different modification methods on surface activation of waste tire rubber powder applied in cement-based materials. Construction and Building Materials 314 (Part B), (2022). https://doi.org/https://doi.org/10.1016/j.conbuildmat.2021.125191.
5. Tran, T.Q., Thomas, B.S., Zhang, W., Ji, B., Li, S., Brand, A.S.: A comprehensive review on treatment methods for end-of-life tire rubber used for rubberized cementitious materials. Construction and Building Materials 359 (2022).
6. Saloni, Parveen, Pham, T.M., Lim, Y.Y., Malekzadeh, M.: Effect of pre-treatment methods of crumb rubber on strength, permeability and acid attack resistance of rubberised geopolymer concrete. Journal of Building Engineering 40 (2021).
7. Youssf, O., Hassanli, R., Mills, J.E., Skinner, W., Ma, X., Zhuge, Y. et al.: Influence of Mixing Procedures, Rubber Treatment, and Fibre Additives on Rubcrete Performance. Journal of Composite Science 3 (2019).
8. Abd-Elaal, E.S., Araby, S., Mills, J.E., Youssf, O., Roychand, R., Ma, X. et al.: Novel approach to improve crumb rubber concrete strength using thermal treatment. Construction and Building Materials 229 (2019).
9. Rodrígues, R.S.L., Domínguez, O., Díaz, A.J.H., García, C.: Synergistic effects of rubber-tire-powder and fluorogypsum in cement-based composite. Case Studies in Construction Materials 14 (2021).
10. Najim, K.B., Hall, M.R.: Crumb rubber aggregate coatings/pre-treatments and their effects on interfacial bonding, air entrapment and fracture toughness in self-compacting rubberised concrete (SCRC). Materials and Structures 46, 2029-2043 (2013).
11. Ossola, G., Wojcik, A.: UV modification of tire rubber for use in cementitious composites. Cement & Concrete Composites 52, 34-41 (2014).
12. Martínez-Barrerad, G., del Coz-Díaz, J.J., Álvarez-Rabanal, F.P., Gayarre, F.L., Martínez-López, M., Cruz-Olivares, J.: Waste tire rubber particles modified by gamma radiation and their use as modifiers of concrete. Case Studies in Construction Materials 12 (2020).
13. Zhang, R., Wang, H., Ji, J., Suo, Z., Ou, Z.: Influences of different modification methods on surface activation of waste tire rubber powder applied in cement-based materials. Construction and Building Materials 314 (2022).
14. Dong, M., Elchalakani, M., Karrech, A., Yang, B.: Strength and durability of geopolymer concrete with high volume rubber replacement. Construction and Building Materials 274 (2021).
15. Shahzad, K., Zhao, Z.: Experimental study of NaOH pretreated crumb rubber as substitute of fine aggregate in concrete. Construction and Building Materials 258 (2022).
16. Copetti, C.M., Borges, P.M., Squiavon, J.Z., da Silva, S.R., de Oliveira Andrade, J.J.: Evaluation of tire rubber surface pre-treatment and silica fume on physical-mechanical behavior and microstructural properties of concrete. Journal of Cleaner Production 256 (2020).
17. Chou, L.H., Lu, C.-K., Chang, J.-R., Lee, M.T.: Use of waste rubber as a concrete additive. Waste Management & Research: The Journal for a Sustainable Circular Economy 25 (2007).

18. Guo, S., Dai, Q., Si, R., Sun, X., Lu, C.: Evaluation of properties and performance of rubber-modified concrete for recycling of waste scrap tire. Journal of Cleaner Production 148, 681-689 (2017).
19. Assaggaf, R.A., Maslehuddin, M., Al-Dulaijan, S.U., Al-Osta, M.A., Ali, M.R., Shameem, M.: Cost-effective treatment of crumb rubber to improve the properties of crumb-rubber concrete. Case Studies in Construction Materials 16 (2022).
20. He, L., Cai, H., Huang, Y., Ma, Y., Van den Bergh, W., Gaspar, L. et al.: Research on the properties of rubber concrete containing surface-modified rubber powders. Journal of Building Engineering 35 (2021).
21. European commitee for standardization. EN 13286-4:2021 Unbound and hydraulically bound mixtures - Part 4: Test methods for laboratory reference density and water content - Vibrating hammer. Brussels, Belgium: 2021.
22. Zvonarić, M., Barišić, I., Galić, M., Minažek, K.: Influence of Laboratory Compaction Method on Compaction and Strength Characteristics of Unbound and Cement-Bound Mixtures. Applied Sciences 11 (2021).
23. Zvonarić, M., Barišić, I., Dokšanović, T., Zagvozda, M.: Preliminary research on waste rubber application in cement bound base layer. 30th International Baltic Road Conference (IBRC 2021), (2021).
24. Barišić, I., Zvonarić, M., Netinger Grubeša, I., Šurdonja, S.: Recycling waste rubber tyres in road construction. Archives of Civil Engineering 67, 499-512 (2021).
25. European commitee for standardization. EN 13286-41:2021 Unbound and hydraulically bound mixtures-Pari 41: Test method for the determination of the compressive strenght of hydraulically bound mixtures. Brussels, Belgium: 2021.
26. European commitee for standardization. EN 13286-42:2021 Unbound and hydraulically bound mixtures - part 42: Test method for the determination of the indirect tensile strength of hydraulically bound mixtures. Brussels, Belgium: 2021.
27. CEN/TC104 TC. EN 12504-4:2021 Testing concrete - part 4: Determination of ultrasonic pulse velocity. 2021.
28. Barišić, I., Dimter, S., Rukavina, T.: Elastic properties of cement-stabilised mixes with steel slag. International Journal of Pavement Engineering 17, 753-762 (2015).
29. ISO. ISO 9277:2010 Determination of the specific surface area of solids by gas adsorption - BET method. Switzerland: 2010.
30. Zvonarić, M., Barišić, I., Netinger Grubeša, I.: Effect of rubber size and shape on Proctor elements of CBC mixtures. Case Studies in Construction Materials 17 (2022).

Strength And Fresh Properties of Self-Compacting Concrete Containing Coarse Electric Arc Furnace Slag Aggregate

Saeid Moghimi[1] [0000-0002-6563-9548], Cihat Yüksel[2] [0000-0002-1439-160x], Özge Andiç Çakir[3] [0000-0001-5662-3555] and Kambiz Ramyar[4] [0000-0003-2200-2691]

[1] Ege University, Civil Engineering Department, 35100, Bornova, Izmir, Turkey, saeid.moghimi@mail.ege.edu.tr
[2] Ege University, Civil Engineering Department, 35100, Bornova, Izmir, Turkey, cihat.yuksel@ege.edu.tr
[3] Ege University, Civil Engineering Department, 35100, Bornova, Izmir, Turkey, ozge.andic@.ege.edu.tr
[4] Ege University, Civil Engineering Department, 35100, Bornova, Izmir, Turkey, Kambiz.ramyar@ege.edu.tr

Abstract. With the increasing use of raw materials, natural resources are decreasing rapidly. In the construction sector due to the high demand for aggregate, which constitutes a large volume of concrete, there are shortages in natural aggregates in some regions as a result of excessive use of mines. In addition, with industrialization, more industrial by-products such as blast furnace slag or electric arc furnace slag (EAFS) aggregate are emerging. In this study 6 self-compacting concrete (SCC) mixtures were prepared. Three of these mixtures (control mixtures) were prepared from fine and coarse crushed limestone aggregate. The last three mixtures were prepared using 0-4 mm limestone aggregate as well as 4-8 mm and 8-16 mm coarse EAFS aggregate. In both control and EAFS aggregate- bearing mixtures 0, 20 and 40 w% of the cement was replaced with a Class F fly ash. The fresh properties of SCC mixtures like T50 and V-funnel flow times, L-Box ratio and segregation coefficient as well as 7-, 28- and 90-day compressive strengths were determined. The slump-flow, T50 flow time, V-funnel flow time and L-box ratio of the mixtures were adjusted to be SF1, VS2, VF2 and PA2, respectively in accordance with EFNARC classification. The slump flow, L-Box ratio increased with the increase of fly ash content in concrete mixtures, while T50 flow time and V-Funnel flow time decreased. The concrete mixture containing coarse EAFS aggregate and 40% fly was exhibited 69,2 MPa 90-day compressive strength (the highest compressive strength among all SCC mixtures).

Keywords: Self-compacting concrete; Fly ash; Fresh properties of SCC; Compressive strength.

1 Introduction

Waste materials (fly ash, bottom ash, slag, etc.) arising from activities of thermal power plants and iron- steel plant in Turkey can be used as supplementary cementitious material and/or aggregate in concrete. These materials are known to have pozzolanic and/or self-cementitious features in concrete. According to Turkey's Cement Producers Association data while the amount of fly ash emerging in the world is around 600 million tons per year, this amount is about 15 million tons/year in Turkey. There are currently 11 active thermal power plants in Turkey [1]. slag arises as a by-product during processing metals or ores containing metal, which is a complex of oxides and silicates lighter than metal, thus, accumulates on the surface of molten metal in furnace during metal production. In 2016 the total production of steel making slag in Europe was around 18.4 million tons, more than 30% of which consisted of Electric Arc Furnace Slag (EAFS) from stainless/high alloy steel production. The estimated use of the total steel making slag is 14.2 million tons per year, almost 50% being in road construction and about 5% in cement and concrete production [2].

EAFS is a by-product of the iron and steel making process in Electric Arc Furnaces. Calcium and iron oxides are the two major chemical constituents of this material, together with SiO_2, Al_2O_3, MnO and MgO. Typically, it has a quite stable crystalline structure, rich in magnetite and hematite, which makes it a suitable candidate for gamma-ray radiations shielding applications [3]. However, potential expansive reactions due to the presence of free lime and periclase may hinder a satisfactorily use of this material in concrete. These oxides can be prevented by an outdoor weathering of about 2–3 months before use and some daily cycles of wetting- drying conditions [4].

Revulta et al. prepared self-compacting heavy-weight concrete mixture and provided sufficient segregation and bleeding resistance. It was stated that this concrete with a slump-flow of 630 mm, a 500 mm spreading time (T50) of 3 seconds and a V funnel flow time (Tv) of 4 seconds, met the relevant self-compacting concrete criteria [5].

Maslehuddin et al. examined the radiation protection properties of concrete mixtures prepared by using EAFS and steel shots. Reference mixture included 100% steel shots as coarse aggregate. In the other mixtures 20, 35, 50 and 65% of steel shots were replaced with EAFSA. They reported that the maximum compressive strength at both 14 and 28 days was recorded on concrete samples with equal proportions of EAFSA and steel shots. The maximum gamma ray attenuation was measured in the specimen with 100% steel shots, while the minimum gamma ray attenuation was recorded in the concrete specimen with 35% steel shots and 65% EAFS [6].

Papayianni and Anastasiou aimed to produce high strength concrete containing high volume of industrial waste materials. They used high-calcium fly ash, ladle furnace slag and cement as binder material, crushed limestone and EAF slag as coarse aggregate. When EAF slag was used as coarse aggregate, the 28-day compressive strength increased by 9.5% compared to that of the reference concrete mixture including limestone fine and coarse aggregate. The corresponding value was 21,3%, when both

coarse and fine EAF slag aggregates were used. The combined use of ladle furnace slag as a binder and EAF slag aggregate gave the same 28-day strength as the reference mixture [7].

There are several studies on the properties of EAFS aggregate-bearing concrete mixtures. However, the studies on the behavior of EAFS produced in Izmir on the properties of concrete, particularly on the properties of special mixtures such as self-compacting or heavyweight concrete, is rare. In this study, the effects of Izmir EAFS aggregate on the fresh properties, compressive strength and modulus of elasticity of self-compacting heavyweight concrete mixtures with or without fly ash were investigated. The results were compared with those of the counterpart mixtures containing limestone aggregate.

2 Material and Methods

2.1 Materials

Within the scope of the study a CEM II A-L 42.5 R cement and a Class F fly ash were used. In this study 6 self-compacting concrete mixtures were prepared. Three of these mixtures (control mixtures) were prepared from fine and coarse crushed limestone aggregate. Depending on the inclusion level of fly ash, these mixtures were designated as C-0, C-20 and C-40, which indicates that 20 and 40 weight percent of cement are replaced by fly ash in C-20 and C-40 mixtures, respectively. The last three mixtures were prepared using 0-4 mm limestone aggregate as well as 4-8 mm and 8-16 mm coarse slag aggregate. These mixtures were designated as SL-0, SL-20 and SL-40. The chemical and physical properties of cement and fly ash are given Table1. The aggregate characteristics and concrete mix proportions are given in Table 2 and Table 3 respectively.

Table 1. Chemical and physical properties of cement and fly ash

Chemical composition	Cement (%)	(TS EN 197-1) Standard Limits	Fly ash (%)	(TS EN 450-1) Standard Limits (%)
SiO_2	18.90	-	57.17	-
Al_2O_3	4.07	-	23.81	-
Fe_2O_3	3.32	-	6.94	-
$SiO_2+Al_2O_3+Fe_2O_3$	-	-	87.92	Min 70
CaO	62.69	-	4.09	-
MgO	1.93	-	2.14	Max. 4
SO_3	3.13	**Max. 4%**	0.15	Max. 3
K_2O	0.59	-	1.96	-
Na_2O	0.28	-	1.44	-
Loss on ignition	4.71	**Max. 5%**	-	-
Cl -	0.01	**Max. 0.1%**	0.08	Max. 0.1
Free CaO	-	-	0.1	Max. 1.5
Physical properties				
Specific gravity	3.08	-	2.27	
Blaine specific surface (cm^2/g)	4252	-	-	
Residue on 45 µ sieve %	2.9	-	16.0	
Residue on 90 µ sieve %	0.1	-	-	
Initial setting time (min.)	190	**Min. 60**	-	
Final setting time (min.)	255	-	-	
Soundness (mm)	1	**Max. 10**	-	
Compressive strength (MPa)			**Strength activity index**	
2-day	24.5	**Min. 20**		
28-day	51.0	**Min. 42.5 – Max. 62.5**	81.0	Min. 75
90-day	-	-	91.0	Min. 85

Table 2. Characteristics of the aggregates

Aggregates	Specific Gravity	Absorption capacity (%)	Flakiness (%)	Los Angeles (%)
Coarse 4-8 limestone	2.66	0.60	21.00	26.50
Coarse 8-16 limestone	2.70	0.25	17.60	
Fine 0-4 limestone	2.64	0.9	-	-
Coarse 4-8 slag	3.40	2.50	2.43	14.40
Coarse 8-16 slag	3.40	2.00	1.44	
Filler-slag	3.20	-	-	-
Filler-calcareous	2.60	-	-	-

The mix proportions were designed to reach the following properties in accordance with EFNARC (2005) recommendation:

The slump-flow diameter of 600±50 mm (SF1),

T50 time more than 2 seconds (VS2),

V-funnel time between 9 and 25 seconds (VF2),

3 rebars L-Box test passing ability value (H2/H1 ratio) greater than 0.8 (PA2)

Table 3. Mix proportion of the concrete mixtures (kg/m^3)

Ingredient	C-FA0*	C-FA20	C-FA40	SL-FA0	SL-FA20	SL-FA40**
Cement	450	360	270	450	360	270
Fly ash	-	90	180	-	90	180
Water	202.5	202.5	202.5	202.5	202.5	202.5
Coarse 4-8 (limestone)	264	264	264	-	-	-
Coarse 4-8 (slag)	-	-	-	222	222	222
Coarse 8-16 (limestone)	173	173	173			
Coarse 8-16 (slag)				222	222	222
Fine 0-4 (limestone)	1085	1085	1085	1032	1032	1032
Filler-calcareous	203	203	203	170	170	170
Filler-slag				208	208	208
Super-plasticizer	4.38	4.20	4.07	5.4	4.7	4.2
Unit weight (theoretical)	2377	2377	2377	2506	2506	2506
Measured unit weight	2370	2372	2368	2497	2493	2500

*** Indicates the mixture containing 100% crushed limestone aggregate and 0 wt.% cement replaced with fly ash**

**** Indicates the mixture containing crushed limestone as fine aggregate and EAFS as coarse aggregate and 40 wt.% cement replaced with fly ash**

As it can be seen from Table 3 the superplasticizer content of C-FA20 and C-FA40 mixtures were lower than that of the C-FA0 mixture about 4 and 7%, respectively. Filler content of these three mixtures were kept constant, at 203 kg/m^3. In SL series the filler content was about 1.86 times greater than that of the control mixtures. The plasticizer requirements of SL-FA20 and SL-FA40 mixtures were 13% and 22% lower than that of the SL-FA0, respectively.

2.2 Test Procedures

The fresh properties of the concrete mixtures such as T50, V-funnel flow times, L-Box ratio and segregation coefficient determined according to relevant standards are given in Table 4.

Table 4. Fresh concrete properties and relevant standards

Test	Standard	Properties
Slump-flow	ASTM C 1611	Fluidity and workability
T50	ASTM C 1611	Fluidity and workability
V-funnel	EN 12350-9	Flowability
L box	EN 12350-10	Ability to pass through narrow sections
Segregation*	-	uniformity

* This test is not standardized yet.

3-compartment sieve set method was used to detect the resistance to segregation of the mixtures. In this test after application of the slump flow test, the 3-compartment sieve was carefully placed in the center of the fresh concrete. The plate was then removed carefully by inverting the sieve together with the bottom plate as shown in Figure 1.

After wet sieving of the concrete, the coarse aggregates (over 10 mm) in each compartment were weighed. In the 3-compartment sieve test, the difference between the masses of the coarse aggregate over 10 mm in the sieve compartments was quantified statistically using sieve segregation coefficient (SC_{sieve}) [8].

$$SC = \frac{\sqrt{\frac{\sum(\mathrm{Xi} - \mathrm{Xo})\hat{}2}{\mathrm{n} - 1}}}{\mathrm{Xo}} \quad (1)$$

In this equation SC: Segregation coefficient, xi: Mass of aggregate in each compartment (g), xo: The arithmetic mean of the aggregate masses in the layers of the sieve (g), n: Number of layers

Fig 1. Application details of the 3-chamber sieve test

7-, 28- and 90-day compressive strength and chord modulus of elasticity of the mixtures were determined according to TS EN 12390-3 and ASTM C 469 standards, respectively. For each experiment, 3 samples (100 × 200 mm cylinders) were tested, and the average values were reported.

3 Results and Discussion

3.1 Fresh Properties

The T50, V-funnel flow times, L-Box ratio and segregation coefficient test results of the mixtures are given in Table 5.

Table 5. Fresh properties of the concrete mixtures

Mixtures	Slump-flow (cm)	T_{50} (s)	V-funnel (s)	L-Box (H2/H1 ratio)	Sc (%) *
C-FA0	57	3.20	20.7	0.81	11.6
C-FA20	58	3.18	17.0	0.83	8.6
C-FA40	62	2.90	12.9	0.93	8.7
SL-FA0	63	3.20	16.5	0.91	6.5
SL-FA20	60	2.90	20.5	0.90	17.6
SL-FA40	58	3.40	16.9	0.83	16.3

***Segregation coefficient (3 compartment sieve)**

As it can be seen from Table 5 in control mixtures with increasing fly ash content slump-flow and L-Box ratio increased, however, the T_{50} and V-funnel flow times decreased. The opposite results were observed in the slump-flow, V-funnel flow time and L-Box ratio of the SL-FA mixtures. The segregation risk of SL-FA20 and SL-FA40 were higher than the other concrete mixtures. All the mixtures achieved the values recommended by EFNARC recommendations (explained in the section 2.1).

3.2 Compressive Strength and Modulus of Elasticity

The 7- 28- and 90-day compressive strength and modulus of elasticity test results of the concrete mixtures are given in Figure 2 and 3, respectively.

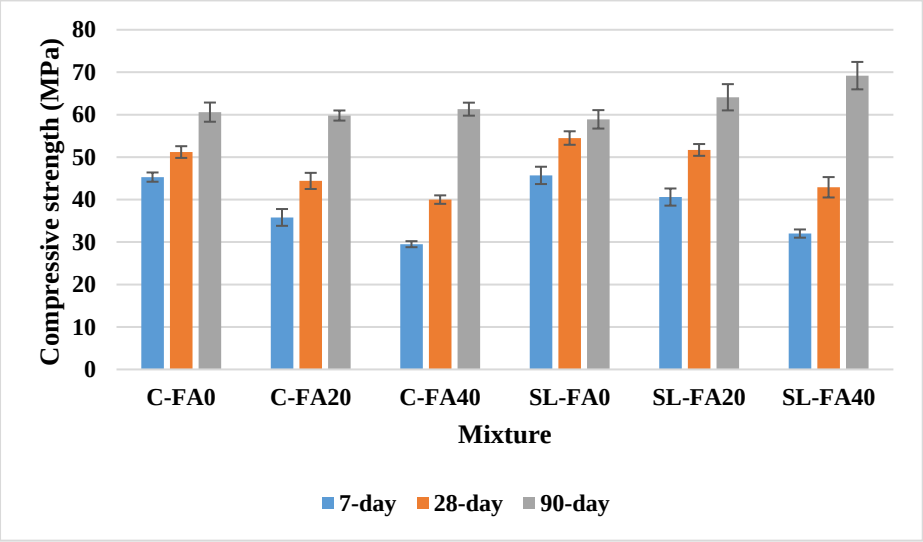

Fig 2. Compressive strength of concrete mixtures

It can be seen from Figure 2, The 28-day compressive strength of SL-FA20 mixture decreased about 5% compared to that of the SL-FA0. Whereas, 28-day compressive strength of C-FA20 was about 15% lower than that of the C-FA0. The rate of gaining compressive strength from 7- to 28-day in the C-FA0 and SL-FA0 was 12% and 17% respectively. However, strength gaining from 7- to 28-day in fly ash bearing mixtures was ranging from 20% to 27%. Increasing the fly ash replacement level decreased the 7- and 28-day compressive strengths of the control and slag aggregate-bearing mixtures. Whereas the 90-day compressive strength of control mixtures nearly were the same. The 90-day compressive strength of SL-FA20 and SL-FA40 was 9% and 17% higher than that of the SL-FA0, respectively.

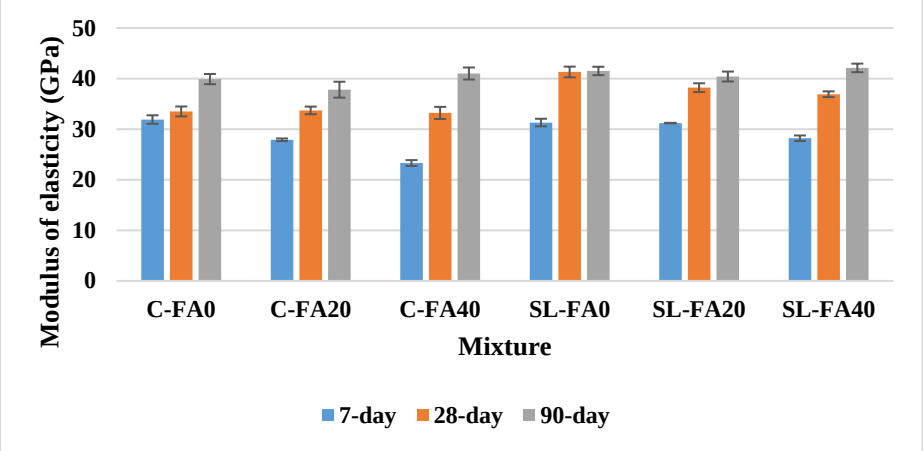

Fig 3. Modulus of elasticity of concrete mixtures

As shown in Figure 3 all of the slag aggregate-bearing mixtures exhibited higher modulus of elasticity than those of the counterpart control mixtures at all ages. Increasing the inclusion level of the fly ash decreased the 7-day modulus of elasticity of the mixtures. In SL series the fly ash-bearing concrete mixtures showed up to 12% lower modulus of elasticity than that of the SL-FA0 mixture at both 7- and 28-day ages. However, in the control mixtures the 28-day moduli of elasticity of the fly ash-bearing mixtures were higher than that of the C-FA0. SL-FA40 exhibited the highest 90-day modulus of elasticity among all the mixtures. The fact seems to be arisen in part from rough surface texture of the EAFs and in part from a useful chemical reaction (probably pozzolanic reaction) at the interface of EAFS aggregate and fly ash, both improving the ITZ.

4 Conclusion

Based on the materials utilized and the experiments conducted, the following outcomes were derived:

- All the fresh mixtures achieved the values recommended by the EFNARC recommendation for SCC.
- Increasing the fly content of the SCC mixtures decreased the superplasticizer requirement for the target properties. However, in the fly ash-bearing control mixtures the slump flow increased in spite of reducing superplasticizer content. The case was opposite in the EAFS and fly ash-bearing mixtures where the reduction in the superplasticizer content was accompanied by a reduction in the slump flow.
- The rate of compressive strength development from 7 to 28 days in the C-FA0 and SL-FA0 containing no fly ash was 12% and 17%, respectively. However, the corresponding percentages in the fly ash-bearing mixtures was in the range of 20 to 27%.

- The highest 90-day modulus of elasticity was observed in the mixture containing 40% fly ash and coarse slag aggregate.
- The compressive strength and modulus of elasticity of the electric arc slag aggregate-bearing mixtures were equal or higher than those of the counterpart limestone aggregate-bearing (control) mixtures at all ages.

References

1. Türkiye Çimento Müstahsilleri Birliği (TÇMB), Türkiye'deki uçucu küllerin sınıflandırılması ve özellikleri, July 2009, ANKARA (ISBN 975-8136-18-6), 2009.
2. Pomaro, B., Gramegna, F., Cherubini, R., De Nadal, V., Salomoni, V., & Faleschini, F.: Gamma-ray shielding properties of heavyweight concrete with Electric Arc Furnace slag as aggregate: an experimental and numerical study. Construction and Building Materials, 200, 188-197, (2019).
3. Faleschini, F., Brunelli, K., Zanini, M. A., Dabala, M., & Pellegrino, C.: Electric arc furnace slag as coarse recycled aggregate for concrete production. Journal of Sustainable Metallurgy, 2(1), 44-50, (2016).
4. Pellegrino, C., Cavagnis, P., Faleschini, F., & Brunelli, K.: Properties of concretes with black/oxidizing electric arc furnace slag aggregate. Cement and Concrete Composites, 37, 232-240, (2013).
5. Revuelta, D., Barona, A., & Navarro, D.: Measurement of properties and of the resistance to segregation in heavyweight, self-compacting barite concrete. Materiales de construcción, 59(295), 31-44, (2009).
6. Maslehuddin, M., Naqvi, A. A., Ibrahim, M., & Kalakada, Z.: Radiation shielding properties of concrete with electric arc furnace slag aggregates and steel shots. Annals of Nuclear Energy, 53, 192-196, (2013).
7. Papayianni, I., & Anastasiou, E.: Production of high-strength concrete using high volume of industrial by-products. Construction and building Materials, 24(8), 1412-1417, (2010).
8. Gökçe, H. S., Aksan, U., Andiç-Çakır, Ö.: Assessment of alternative segregation test methods for self-consolidating heavyweight concrete. Journal of Materials in Civil Engineering, 31(11), 04019277, (2019).

Mechanical Properties and Expansion Behaviour of ASR Affected Concrete

Saeid Moghimi [1][0000-0002-6563-9548], Cihat Yüksel [2][0000-0002-1439-160x] and Kambiz Ramyar [3][0000-0003-2200-2691]

[1] Ege University, Civil Engineering Department, 35100, Bornova, Izmir, Turkey, saeid.moghimi@mail.ege.edu.tr
[2] Ege University, Civil Engineering Department, 35100, Bornova, Izmir, Turkey, cihat.yuksel@ege.edu.tr
[3] Ege University, Civil Engineering Department, 35100, Bornova, Izmir, Turkey, Kambiz.ramyar@ege.edu.tr

Abstract. In this study the mechanical properties and expansion behaviour of ASR-affected concrete mixtures were investigated. For this purpose, four different concrete mixtures were prepared. In these mixtures, coarse (4-22.4 mm) reactive basalt aggregate was used, while non-reactive 0-4 mm crushed limestone, reactive 0-4 mm basalt and reactive 0-4 mm glass aggregates were used as fine aggregate. The fine aggregate of the first mixture was made of 100% basalt (100B), the fine aggregate of the second mixture was made of 100% non-reactive limestone (100L), the fine aggregate of the third mixture was consisted of 50% basalt + 50% glass (50B+50G), and the fine aggregate of the last mixture was 50% limestone + 50% glass (50L+50G). The ASR expansion of the concrete mixtures up to 20 weeks was recorded in accordance with RILEM AAR-4 accelerated testing method (60°C temperature and >90% relative humidity). Besides, the compressive strength and modulus of elasticity of the concrete specimens subjected to the accelerating curing were obtained at 4th, 6th and 8th weeks. For the sake of comparison, the compressive strength and modulus of elasticity of the 28-day standard-cured specimens were also determined. The strength loss, modulus of elasticity loss and ASR expansion in the mixtures containing 50% glass as fine aggregate (50L+50G and 50B+50G) were considerably more than those of the other two concrete mixtures subjected to the accelerated curing at 60ºC. The ASR damage was more pronounced on the modulus of elasticity than strength of concrete.

Keywords: Alkali silica reaction (ASR); Modulus of elasticity; Compressive strength; Waste glass aggregate.

1 Introduction

Durability of concrete is defined as its resistance to climatic conditions, chemical attack, abrasion or any other corrosive effect [1]. Alkali-silica reaction (ASR) is the reaction of reactive silica in concrete aggregates with hydroxyl and alkali ions in the

pore solution of concrete. This reaction leads to the formation of an alkali-silica gel in concrete which expands upon imbibing moisture. Tensile stresses, occurring in concrete as a result of expansion, lead to cracking [2].

The first damage caused by ASR in Turkey was detected in 1995 when widespread cracks were observed in some highway bridges in the Izmir region. Investigations revealed that the aggregates used in concrete from the beds and terraces of the Gediz and Nif Rivers contained over 3% reactive glassy rhyolite, which caused ASR [3]. Subsequent studies and investigations have shown that the reaction is not specific to the Izmir region [4], but also to Aliağa [5-6], Niğde [4, 7], Afyon [6], Sivas [7,8], Fırat basin [9], and Sakarya [2]. In recent years, it is known that some aggregates found in Gölcük, Aksaray and Kırklareli regions have been added to this list [10].

The first stage of the alkali-silica reaction occurs as a reaction between hydroxyl ions (OH-) in the pore solution and reactive silica in the aggregate. Silica in the aggregate does not react directly with alkali metals (Na+ and K+). Alkalis first react with the high concentration of hydroxyl ions in the void solution. Alkaline hydroxides react with reactive silica to form an alkali-silica gel. When weakly crystalline aqueous silica is exposed to a strong alkaline solution, an acid-base reaction occurs between the hydroxyl ions in the solution and the acidic silanol (Si-OH) groups as follows [11-12].

$$\equiv Si–OH + OH^- \rightarrow \equiv Si–O– + H_2O \quad (1)$$

As more hydroxyl ions enter the gel structure, some of the siloxane bonds (Si-O-Si) are attacked as follows [11]:

$$\equiv Si–O–Si\equiv + OH^- \rightarrow 2\equiv Si–O– + H_2O \quad (2)$$

According to Thomas [12], the dissolution rate is controlled by the alkalinity of the solution and the structure of the silica. The solubility of weakly crystalline or amorphous silica increases with the pH of the medium. Furthermore, few studies have been conducted to determine the minimum concentration of hydroxide required to initiate and sustain ASR in concrete. Diamond [13] reported that the reaction is unlikely to start when the hydroxide concentration is less than 0.25 mols, while Kollek et al [14] reported this value to be 0.20 mols. In general, portland cement is regarded as the main source of alkali in concrete. However, other components used in concrete (e.g., mineral admixtures, aggregates and chemical admixtures) can also increase the amount of alkali. Alkalis are present in portland cement in low percentages. The alkali content of typical cements ranges from 0.20% to 1.30% Na_2O. Nevertheless, the predominant ions present in the pore solution are alkali ions. From the beginning of hydration at normal temperatures, alkali ions are present in the pore solution along with other dissolved ions. The alkali concentration in the pore solution is influenced by a number of factors such as the alkali content of the cement, cement dosage and the degree of hydration. In a typical concrete mix, the alkali content ranges from about 0.15 to 0.85 mol/l. This causes the pH of the pore solution to vary between 13.2 and 13.9.

The level of expansion and the damage caused by ASR are influenced by many factors such as the alkali content of the concrete, the amount of reactive silica in the aggregate, ambient conditions and the distribution of reinforcement [12].

It is known that ASR gel formed in concrete swells by absorbing water. However, if the swelling of the gel continues after filling the voids, it may cause the formation of new cracks in the concrete or the growth of existing cracks. This adversely affects the dimensional stability and mechanical properties of concrete (Mohammadi et al., 2020). The total losses in the mechanical properties of concrete affected by ASR are influenced by several factors such as the size, quantity, physical and chemical properties of reactive aggregates [15; 16].

Mohammadi et al. [17] reported that the elastic modulus, flexural and tensile strength of concrete are more affected by ASR than the compressive strength of the same concrete.

There are several studies on the ASR expansion of concrete. However, studies on the mechanical properties (particularly elastic modulus) of concrete at various stages of ASR expansion are relatively less. In this study, the mechanical properties and expansion behaviour of ASR-affected concrete mixtures containing various reactive aggregates at different time intervals were investigated.

2 Material and Methods

2.1 Materials

The materials used in the experimental study and the experiments carried out are described in this section.

A CEM I 42.5R cement with high alkali content obtained from Soma Cement plant was used in the concrete mixtures. Chemical and physical properties of the cement are presented in Table 1.

Table 1. Chemical and physical properties of cement

Oxide composition	**%**	**TS EN 197-1 [24]**
CaO	63,95	-
SiO_2	20,14	-
Al_2O_3	4,70	-
Fe_2O_3	3,20	-
SO_3	3,04	Max. 4,0%
MgO	1,41	Max. 5,0%
Na_2O	0,48	-
K_2O	0,63	-
Equivalent Na_2O	0,90	-
Cl^-	0,01	Max. 0,1%
Loss on ignition	2,43	Max. 5,0%
Physical properties		
Specific gravity	3,11	-
Blaine fineness (cm^2/g)	4044	-
Soundness (mm)	1,0	Max. 10 mm
Residual on 45µm sieve (%)	2,1	-

To investigate the expansion and mechanical behavior of concrete as a result of ASR, 4 concrete mixes were prepared in accordance with RILEM AAR-4 "Detection of Potential Alkali-Reactivity- 60°C Test Method for Aggregate Combinations Using Concrete Prisms" standard. In all mixtures, basalt aggregate from Aliağa region, which is known to be reactive from previous studies [6, 18], was used as coarse aggregate, while non-reactive 0-4 mm crushed limestone, reactive 0-4 mm basalt and reactive 0-4 mm glass aggregate were used as fine aggregate. Fine aggregate of the first mix was 100% basalt (100B), the fine aggregate of the second mix was 100% limestone (100L), the fine aggregate of the third mix was 50% basalt + 50% glass (50B+50G) and the fine aggregate of the last mix was 50% limestone + 50% glass (50L+50G). The properties and sieve analysis results of the aggregates and TS 802 standard grading limits are given in Table 2 and Figure 1, respectively.

Table 2. Properties of aggregates

Aggregate	Water absorption capacity (%)	Specific gravity	loose unit weight (kg/m^3)	Compacted unit weight (kg/m^3)
limestone (0-4 mm)	0,9	2,65	1700	1895
Basalt (0-4 mm)	0,4	2,7	1790	1950
Basalt (5-15 mm)	0,65	2,8	1495	1555
Basalt (15-25 mm)	1	2,8		
Glass (0-4 mm)	0	2,43	-	-

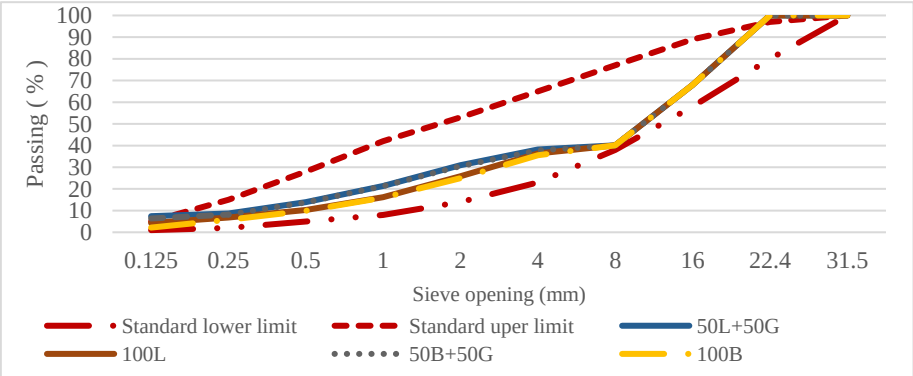

Fig. 1. Grading curves of the aggregates and their compliance with TS 802 Standard limits

2.2 Concrete Mixtures

The mix proportions and fresh properties of the concretes are given in Table 3 and Table 4, respectively. The W/C ratio of these mixtures was kept constant at 0.5 as stipulated in the RILEM AAR4 standard. The slump value of the mixtures was found to be in the range of 15±2 cm without any water reducing admixture. Prismatic (75*75*285 mm) and cylinder (100*200 mm) specimens were prepared from these mixtures. While some

of the cylinders were subjected to standard curing, the others were kept together with the prism specimens in a 60°C curing cabinet at 95±5% relative humidity inside the water and vapor-proof storage containers. The length of the prismatic specimens was measured at regular intervals for 20 weeks. The compressive strength and elastic modulus of the cylinder specimens subjected to accelerated curing were determined at weeks 4, 6 and 8. Thus, the effect of ASR expansion on concrete strength and elastic modulus was also investigated.

Table 3. Theoretical mix proportions of concrete mixtures (kg/m^3)

Mixture	Cement	Water	Fine aggregate (0-4 mm)			Coarse aggregate	
			Limestone	Basalt	Glass	Basalt (4-16 mm)	Basalt (16-22,4 mm)
100L	440	220	663	-	-	498	498
100 B	440	220	-	666	-	500	500
50B+50G	440	220	-	340	310	494	481
50L+50G	440	220	336	-	310	494	481

Table 4. Fresh properties of concrete mixtures (kg/m3)

Mixture	Slump (cm)	Theoretical unit weight	Measured unit weight
100K	15,5	2319	2325
100 B	15	2326	2320
50B+50C	14,5	2285	2240
50K+50C	14,5	2281	2233

2.3 Test Procedures

Prism expansion experiments
RILEM AAR-4.1 [19] standard is the test method developed by the RILEM committee. As stated in the standard, in the concrete mixtures 440 kg/m^3 cement, 220 kg/m^3 water and a combines aggregate consisting of 60% coarse aggregate and 40% fine aggregate were used. NaOH was added to the mixing water to increase the alkali content of the concrete mixtures to 1.25%.

Three 75*75*285 mm prisms were prepared from the concrete mixtures. These samples were placed in a storage container in a curing cabinet at a temperature of 60 ºC and 90% relative humidity for 20 weeks. The increase in length of the specimens at any age (e.g., at week 15) was calculated from the equation given below.

$$\% \text{ expansion} = ((l_{15}-l_0) / I_0) \text{ x}100 \quad (3)$$

Compressive Strength Tests

Concrete mixtures were subjected to compressive strength test in accordance with TS EN 12390-3 standard. Three 100*200 mm cylinder specimens of each mix were tested at each age and the average strength was reported.

Determination of Modulus of Elasticity

Three 100*200 mm cylinder specimens were tested in accordance with ASTM C469 standard. In order to eliminate the creep deformation that may occur in the specimens during the test and to ensure full contact of the specimen with the platens of testing machine, 3 loading and unloading operations were performed up to 40% of the compressive strength of the concrete, then the values required for the determination of chord elastic modulus of concrete (Equation 4) were recorded during fourth loading:

$$E = \frac{S_2 - S_1}{\varepsilon_2 - 0{,}00005} x100 \quad (4)$$

where E is the chord modulus of elasticity, S_2 represents the stress equal to 40% of the compressive strength of concrete, S_1 represents the stress corresponding to 0.00005 strain and, ε_2 represents the strain corresponding to S_2.

3 Results and Discussion

3.1 Compressive Strength and Modulus of Elasticity

The compressive strength and elastic modulus of 28-day specimens subjected to the standard and accelerated- curing are given in Table 5. The compressive strength and elastic modulus of the specimens subjected to accelerated curing for 28, 42 and 56 days are presented in Figure 2 and Figure 3, respectively.

Table 5. Compressive strength and elastic modulus of concrete specimens subjected to 28 days accelerated and standard curing

Mixture	Compressive strength (MPa)	Coefficient of variation (%)	Modulus of elasticity (GPa)	Coefficient of variation (%)
100L/ standard*	46,9	5,80	32,6	1,04
100L/ accelerated	45,2	1,83	32,5	0,15
100B/ standard	46,9	2,90	29,2	6,02
100B/ accelerated	44,3	2,97	29,3	5,90
50B+50G/ standard	46,3	2,70	32,1	3,07
50B+50G/ accelerated **	46,2	3,79	20,3	2,01
50L+50G/ standard	43,3	0,90	31,1	2,24
50L+50G/ accelerated	42,3	3,46	20,8	6,37

*100L/ standard: indicates that the fine aggregate of the mixture is 100% limestone and the samples are cured under standard conditions.

**50B+50G/accelerated: indicates that the fine aggregate of the mixture consists of 50% basalt and 50% glass and the specimens are subjected to accelerated curing (60°C curing cabinet at 95±5% relative humidity).

Table 5 shows that the compressive strength difference between the 28-day standard-cured and accelerated-cured specimens was about 0% to 5%. The reductions in the modulus of elasticity of these specimens as a result of accelerated curing ranged

between 0.3% and 36%. It was determined that the reductions in elastic modulus were higher in the mixtures containing glass fine aggregate. Moreover, the 28- day compressive strength of the specimens cured in standard conditions was very close to each other, regardless of the fine aggregate type. Mohammadi et al. [17] stated that the compressive strength of concrete is not a good criterion for ASR damage evaluation.

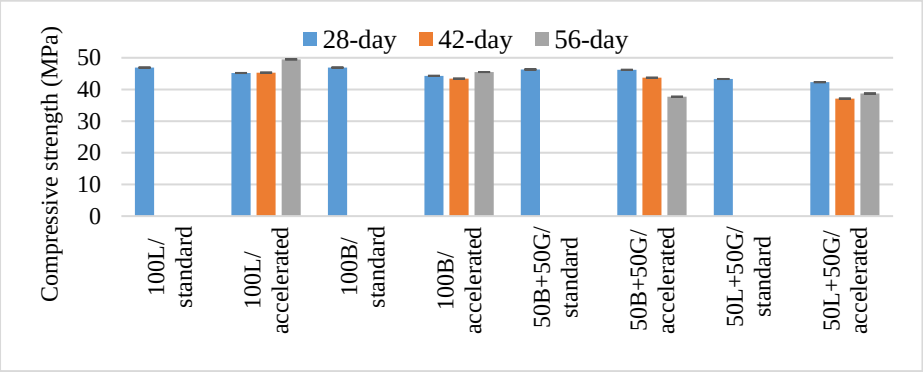

Fig. 2. 28-, 42- and 56-day compressive strength of concrete mixtures

As it was expected, in the specimens with 50% glass fine aggregate (50L+50G and 50B+50G), the strength loss upon accelerated curing was more pronounced by extending the curing time. However, a slight increase was observed in the compressive strength of the specimens with no glass fine aggregate when the accelerated curing period was extended from 28 days to 56 days.

As seen in Figure 3, with the exception of 100L mixture, a decrease in the elastic modulus of all specimens subjected to the accelerated curing was noticed. The highest loss of elastic modulus was observed in the 50B+50G and 50L+50G concrete mixtures.

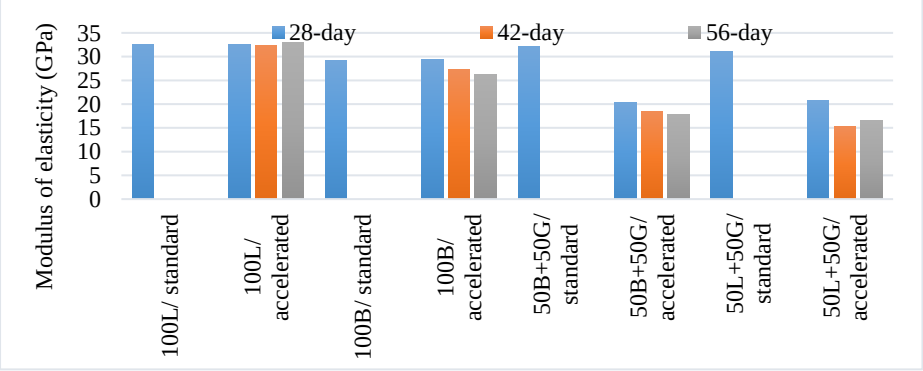

Fig. 3. Modulus of elasticity of concrete mixtures subjected to standard curing for 28-days or accelerated curing for 28, 42 and 56 days.

The elastic moduli of glass aggregate-bearing mixtures subjected to the accelerated curing were at least 10.3 GPa and at most 15.9 GPa lower than those of the standard-cured specimens. However, the elastic modulus of the accelerated- cured specimens in glass-free mixtures was found to be at most 3 GPa lower than that of the standard- cured specimens.

Figure 4 shows the 20-week expansion values of the mixtures. The figure also shows the maximum 20-week expansion limit (0.03%) set by the standard for concretes containing non-reactive aggregates. Among the mixes produced, 50B+50G and 50L+50G mixes containing 50% glass as fine aggregate showed the highest expansion. The 20-week ASR expansion of the mixture with 100% basalt (100B) as fine aggregate increased by 250% when 50% of the mixture was replaced with glass. The ASR expansion increase between the mixtures with limestone (100L) as fine aggregate and 50% limestone + 50% glass (50L+50G) was 775%.

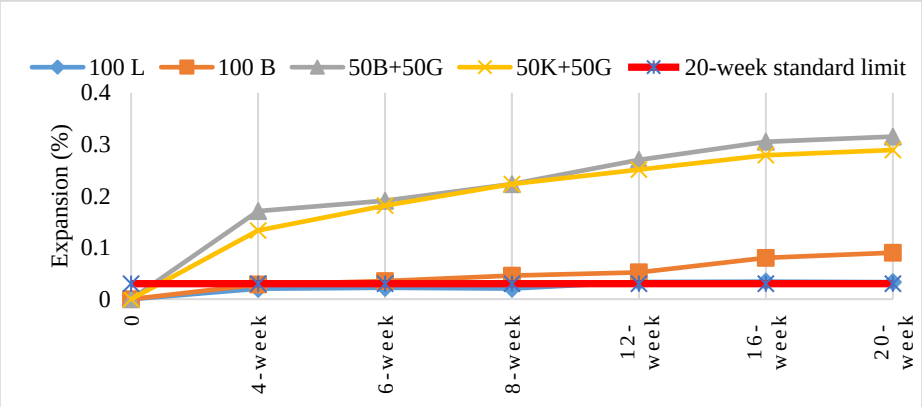

Fig. 4. ASR expansions of concrete mixtures

The highest expansion, resulting in the greatest loss of elastic modulus, was observed in the mixtures containing glass aggregate. Not surprisingly, the 100L mix, containing non-reactive limestone aggregate, showed the least expansion and resultantly the least elastic modulus loss. Table 6 shows the change in compressive strength and elastic modulus of the accelerated-cured specimens compared to those of the similar standard-cured specimens.

Table 6. Relative compressive strength and modulus of elasticity of specimens subjected to accelerated curing for 28, 42 and 56 days compared to those of 28-day standard- cured specimens (%)

Property		100L	100B	50B+50G	50L+50G
28-day	Compressive strength	-3,62	-5,39	-0,04	-2,48
	Modulus of elasticity	-0,51	0,23	**-36,83**	**-33,23**
42-day	Compressive strength	-2,63	-7,30	-5,63	-15,25
	Modulus of elasticity	-0,87	-6,78	**-42,82**	**-51,11**
56-day	Compressive strength	5,44	-2,85	**-15,38**	-10,66
	Modulus of elasticity	1,12	-10,21	**-44,76**	**-46,95**

When the relative compressive strength and elastic modulus of the mixtures were examined, it was understood that the elastic modulus was more affected by ASR. The elastic modulus of the mixtures that did not contain glass, and therefore expanded less, decreased by approximately 15% at most compared to the elastic modulus of the 28-day samples cured in standard condition. However, this decrease reached 50% in the mixtures containing glass. ASR is known to occur intensively in the transition zone (ITZ) of concrete. The decrease in the elastic modulus of the mixtures containing glass is thought to be the result of a further decrease in aggregate-matrix bond.

4 Conclusion

According to the materials used and the experiments performed, the following results were obtained:

- In concrete mixtures with 50% glass fine aggregate (50L+50G and 50B+50G), strength loss was occurred upon accelerated curing at 60ºC. The effect increased as the curing time increased. In these mixtures, 0.25% ASR expansion at the end of 12 weeks of curing caused a compressive strength loss of up to 15%. However, no strength loss was observed in the glass-free 100L and 100B mixtures, although an ASR expansion of 0.05% occurred during 12 weeks.
- The loss of compressive strength arisen from ASR expansion was considerably lower than the loss of modulus of elasticity of the concrete mixtures.
- While the modulus of elasticity of the less expanded mixtures without glass exhibited a maximum decrease of approximately 15% (compared to that of the 28-day standard–cured specimens), this decrease reached 50% in the mixtures containing highly reactive glass aggregate.

References

1. Tang, S.W., Yao, Y., Andrade, C., Li, Z.J.: Recent durability studies on concrete structure. Cement and Concrete Research. 78, 143–154 (2015).

2. Ramyar, K.: Betonda alkali-silis reaksiyonu: bir derleme, Ready Mixed Concrete Congress, Istanbul, 70-82 (2013).
3. Katayama, T., Bérubé, M. A., Fournier, B., & Durand, B.: Alkali-aggregate reaction in the vicinity of Izmir, Western Turkey. In Alkali Aggregate Reaction in Concrete, Proc. 11th International Conference, Quebec, Canada pp. 365-374 (2000, June).
4. Kocacitak, S.: A note of information regarding to alkali-Aggregate reactions in Turkey, Symp. Alkali-Aggregate Reaction, Preventive Measures, Reykjavik, 259-262 (1975).
5. Andiç-Çakır, Ö., Çopuroğlu, O., & Katayama, T.: A review of alkali-silica reactivity in Turkey: a case study from Izmir, west Anatolia. In Proc. 14th International Conference on Alkali Aggregate Reaction, TX, Austin. Vol. 10 (2012, May).
6. Çopuroğlu, O., Andiç-Çakir, Ö., Broekmans, M. A., & Kühnel, R.: Mineralogy, geochemistry and expansion testing of an alkali-reactive basalt from western Anatolia, Turkey. Materials Characterization, 60(7), 756-766 (2009).
7. Korkanç, M., & Tuğrul, A.: Evaluation of selected basalts from Niğde, Turkey, as source of concrete aggregate. Engineering Geology, 75(3-4), 291-307 (2004).
8. Erik, D., & Mutlutürk, M.: Alkali-silica reactivity features of gravel-sand aggregates in Koç River (Hafik-Sivas). In ROCKMEC 2004–VIIth Regional Rock Mechanics Symposium (2004).
9. Aşık, İ., Şen, H., Ergintov, Y., Ünsal, A., Şentürk, E., & Bayrak, E.: Alkali silis reaksiyonu yönünden zararlı olan bir ocağın iyileştirilmesi, Beton kongresi, Ankara bildiriler kitabı, 1-10 (2004).
10. Yüksel, C.: Alkali agrega reaksiyonu performans test metotlarının geliştirilmesi. Ege Üniversitesi Fen Bilimleri Enstitüsü, Doktora Tezi (2020).
11. Dent Glasser, L.S. and Kataoka, N.: The chemistry of alkali-aggregate reactions, Proceedings of the 5th International Conference on Alkali-Aggregate Reaction, Cape Town, S252/23 (1981).
12. Thomas, M.: The effect of supplementary cementing materials on alkali-silica reaction: A review. Cement and Concrete Research, 41(12), 1224-1231 (2011).
13. Diamond, S.: ASR-another look at mechanisms. In Proc. of the 8th Int. Conf. on Alkali-Aggregate Reaction in Concrete. pp. 83-94 (1989).
14. Kollek, J.J., Varma, S.P., Zaris, C.: Measurement of OH− concentrations of pore fluids and expansion due to alkali-silica reaction in composite cement mortars, Proceedings of the 8th International Congress on the Chemistry of Cement, Vol. 3, Rio de Janeiro, pp. 183–189 (1986).
15. Saint-Pierre, F., Rivard, P., & Ballivy, G.: Measurement of alkali–silica reaction progression by ultrasonic waves attenuation. Cement and Concrete Research, 37(6), 948-956 (2007).
16. Giaccio, G., Zerbino, R., Ponce, J. M., & Batic, O. R.: Mechanical behavior of concretes damaged by alkali-silica reaction. Cement and Concrete Research, 38(7), 993-1004 (2008).
17. Mohammadi, A., Ghiasvand, E., & Nili, M.: Relation between mechanical properties of concrete and alkali-silica reaction (ASR); a review. Construction and Building Materials, 258, 119567 (2020).
18. Andiç-Çakır, Ö.: Alkali agrega reaktivitesinin tespitinde kullanılan deney metotlarının İncelenmesi. Ege Üniversitesi Fen Bilimleri Enstitüsü, Doctora Tezi (2007).
19. RILEM AAR-4.1.: Detection of Potential Alkali-Reactivity – 60°C Test Method for Aggregate Combinations Using Concrete Prisms, in: Nixon, P.J. and Sims, I. (eds.), RILEM Recommendations for the Prevention of Damage by Alkali-Aggregate Reactions in New Concrete Structures State-of-the-Art Report of the RILEM Technical Committee 219-ACS, Springer, 99-116pp (2016).

Properties of Ilmenite-Heavyweight Concrete Subjected to Elevated Temperature

Ahmed Mounir[1], Alaa Mohsen[1], AbdelMonem Soltan[2], Mohamed Kohail[1*]

[1] Faculty of Engineering, Ain Shams University, Cairo, Egypt
[3] Faculty of Science, Ain Shams University, Cairo, Egypt
m.kohail@eng.asu.edu.eg

Abstract. The advancement of technology in the medical and energy industries has resulted in a rise in the usage of radiation-based devices in recent years. Unfortunately, exposure to this radiation endangers human health and causes environmental degradation. As a result, preventing the spread of this dangerous radiation is a top priority, particularly in facilities holding such equipment, such as nuclear power plants and hospitals. The use of heavyweight concrete in the construction of those structures results in much higher radiation shielding capability. The purpose of this study is to explore the density and compressive strength of ilmenite aggregates before and after being treated to elevated temperatures. In this study, heavyweight concrete was made from ilmenite brought from Egypt's eastern and western deserts. Ilmenite Concrete mix was made with 400 Kg/m3 cement, a W/B ratio of 0.35, 10% silica fume of the binder weight, and 2% superplasticizer of the binder weight, fine aggregate is siliceous sand, and ilmenite coarse aggregate. According to the test findings, the ilmenite concrete was obtained as heavyweight concrete in accordance with TS EN 206-1, since, a density reached 3.12 t/m3. As a result, the 28 days compressive strength of the ilmenite concrete mix was lower than normal-weight concrete. As well as, The Ilmenite concrete mix had lower compressive strength than normal-weight concrete after being treated at 300°C and 600°C, but it had higher compressive strength at 900°C.

Keywords: Heavyweight concrete; Ilmenite, Density; Elevated temperature

1 Introduction

In recent years, there has been a movement in the medical profession to widely use radiation-emitting equipment in the hospital, as well as in the energy industry to replace traditional energy sources with green resources like nuclear energy. As a result, the Egyptian government intends to use nuclear power to produce electrical energy in the next decades, hence, Egypt’s first nuclear energy plant will be El-Dabaa by 2026.

Exposure to the radiation emitted by those sources endangers human health because of high penetration energy that may penetrate the human body and ionize human cells, producing cancer, as well as the radiation endangers the health of the environment. As a result, avoiding the seepage of this hazardous radiation from structures containing such devices is critical.

Using heavyweight concrete is one of the high-performance solutions. The density of Heavyweight concrete surpasses 2.6 t/m^3[1], which may be achieved by substituting normal weight aggregate by heavyweight aggregates with heavyweight minerals such as e.g. (calcium magnesium, barium, silicon, iron, and barium). Aggregate minerals influence aggregate physical and mechanical characteristics, for example, (shape, water absorption, density, surface texture, particle size, and pore system). As a result, the nature of the aggregates has a significant impact on the characteristics of heavyweight concrete in both the fresh state, for example (setting time and workability), and hardened state (radiation shielding, density, tensile strength, modulus of elasticity, and compressive strength).

One of the most important properties that should be investigated on the shielding concrete is the Thermal degradation behavior due to the high danger of exposure to high temperature from the nuclear reactor core due to collision of reactor radiation with concrete as well as the possibility of explosion any nuclear reactor devices. As a result, investigating the heavyweight concrete behavior at various heatin g temperatures is critical. According to Sakr [2] ilmenite concrete has the best mechan ical characteristics after firing compared to baryte and gravel concrete, and coated mat erial increases fire resistance up to 500°C. According to Horszczaruk [3] the concrete mix containing magnetite aggregate performs the best against increased temperatures when compared to standard normal-weight aggregate.

In this study, heavyweight concrete was made with ilmenite aggregates. The ilmenite aggregate was brought from the deserts of eastern and western Egypt. The density and compressive strength of the concrete was measured before and after exposure to various rising temperatures and compared to normal-weight concrete prepared using dolomite aggregate.

2 Methodology of Research

2.1 Materials

Portland Cement 42.5N obtained from Torah cement company. Mineral admixtures were used such as silica fume from Edfo, Aswan used to improve the mechanical and physical characteristics for concrete, as well as, superplasticizer sika viscocrete-3425 to improve the workability of concrete. Fine aggregate is dolomite for all mixes, two mixes with dolomite coarse aggregate as control concrete mix and other with ilmenite coarse aggregate were prepared. Table 1 showing the materials specific gravity.

Table 1. Materials specific gravity.

Material	Cement	Water	Super plasticizer	Silica fume
Specific gravity	3.15	1	1.08	2.2

Ilmenite local heavyweight aggregate ($FeTiO_3$) is the main material adopted in the research to examine the feasibility of create heavyweight concrete compared to dolomite ($CaMg(CO_3)_2$) as a control. Ilmenite aggregate is a type of heavyweight aggregate collected from the western and eastern deserts. Coarse aggregates were sieved for three different sizes (14mm,10mm, and 5mm). The specific gravity of aggregates was determined, Table 2 shows the results. Ilmenite aggregate had higher specific gravity 4.8, while dolomite aggregate had a specific gravity of 2.65. also Table 2 shows aggregate water absorption.

Table 2. Aggregates characteristics.

Property	Dolomite	ilmenite
Specific gravity	2.65	4.8
Water Absorption (%)	2	1.3
Abrasion by water (%)	99.0	98.6

2.2 Mix Proportions

The American Concrete Institute (ACI) absolute volumes approach [4] was used to design the concrete mixture, as follows: 400 kg/m3 cement, 0.35 W/B ratio, (0.6 coarse aggregate:0.4 fine aggregate), silica fume 10% of cement [5], and superplasticizer 2% of cement [6]. Table 3 shows the amount (Kg/m^3) of material utilized in each mixture.

Table 3. Amount of material utilized (Kg/m^3).

Concrete mix	Cement	Water	Super plasticizer	Dolomite Coarse aggregate	Ilmenite Coarse aggregate	Dolomite Fine aggregate	Silica fume
Dolomite	400	154	8	1103.5	------	735.7	40
Ilmenite	400	154	8	------	1509.1	1006.1	40

2.3 Mixing, Curing and Testing Specimens

The mixing sequence is as follows, as detailed below:

- Prepare the needed amount from each material.
- Coarse aggregate was washed to eliminate harmful elements and chloride contamination, and then allowed to dry for 24 hours.
- Place fine and coarse aggregates in the mixer and mix for 2 minutes, or until observed the uniformity of the mix.
- Add silica fume and cement to the dry batch then mix for 2 minutes to ensure even distribution.
- Pour 80% of the water into the dry mix and mix for 1 minute.
- Lastly, dissolve the superplasticizer with the remaining water then add to the solution, continuing to mix for 1 minute.

- Filling the molds in three compacted layers, compacting them carefully to guarantee the mold cast is free of air bubbles.

Time for Mixing should be kept as short as possible to prevent segregation because of the high aggregate density, which has a higher tendency to segregate. All specimens were removed from moulds after 24 hours and then kept in water for 28 days. Each concrete mix, moulded into 12 cubes, specimen details presented in Table 4.

Table 4. Specimen detail for each concrete mix

Tests	Specimen type	Dimension (mm)	Number
Compression test after 28 days	Cubes	100x100x100	3
Fire resistance	Cubes	100x100x100	9 (3 for 300 °C) (3 for 600 °C) (3 for 900 °C)

2.4 Compressive Strength

Compressive strength is a necessary characteristic of concrete. Since the test shows indication of concrete mix quality at the hardened stage. In this test, three 100x100x100 mm cubes were evaluated after 28 days. Ten tons hydraulic jack load capacity was used to perform the test. The compressive strength is calculated in accordance with ECP 203-2020 [7]:

$$fc = \frac{P}{A} \tag{1}$$

where: fc: compressive strength. P: failure load. A: cross section area subjected to load

2.5 Fire Resistance

To examine the mechanical characteristic of heavyweight concrete after subjected to high temperatures, particularly the compressive strength, three 100x100x100mm cubes were prepared from two mixes of dolomite concrete as well as ilmenite concrete. After 28 days the cubes being exposed to increased temperatures of 300°C, 600°C, and 900°C, the elevated temperatures met the ASTM 119E [8] criteria.

The weight of the cubes was measured before placed in the electric furnace as shown in Fig.1. Reference to ASTM 119E standards [8], the temperature was raised for one hour to the desired temperature, then held steady for one hour. After two hours, the furnace was shut off, then the temperature gradually lowered until the cubes could be handled and transported outside the electric furnace.

Fig. 1. Concrete cubes placed in electric furnace.

3 Results and Discussion

3.1 Density of Concrete

Concrete density has a major impact on the radiation shielding capabilities of concrete. it is one of the most critical factors to consider when using high-weight concrete. reference to TS EN 206-1, heavy-weight concrete has a density more than 2.6 t/m^3. Since aggregate takes a place with rough 40% to 60% of the concrete mix weight, aggregate density has a considerable impact on concrete density. Fig.2. depicts hardened concrete density after 28 days. The ilmenite concrete had a maximum density 3.12 t/m^3. The dolomite concrete, on the other hand, had the lowest density 2.59 t/m^3. Results matching with the fact of the heavy weight aggregate has a major effect on the concrete mix density due to high weight participation on the concrete mix.

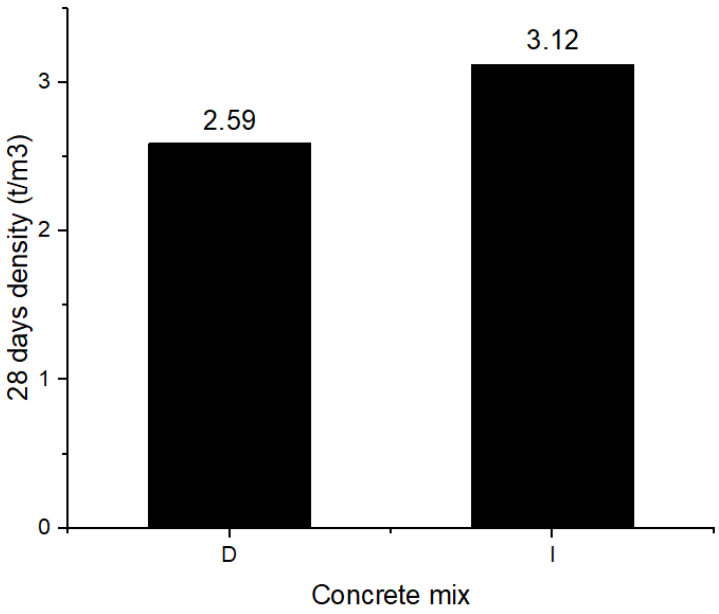

Fig. 2. 28 days concrete mix density

3.2 Compressive Strength

Compressive strength is a necessary characteristic that shows an indication for concrete quality, since, it is dependent on the hydrated component at ITZ as well as the uniformity of ITZ, moreover, the physical and mechanical characteristics and aggregate shape. After 28 days, the compressive strength of concrete mixes was tested on cubes 100x100x100mm. Three cubes were tested and averaged. The dolomite concrete has the highest compressive strength, whereas the ilmenite concrete mix has the lowest. Ilmenite and dolomite concrete had compressive strengths of 24.10 and 41.60, respectively.

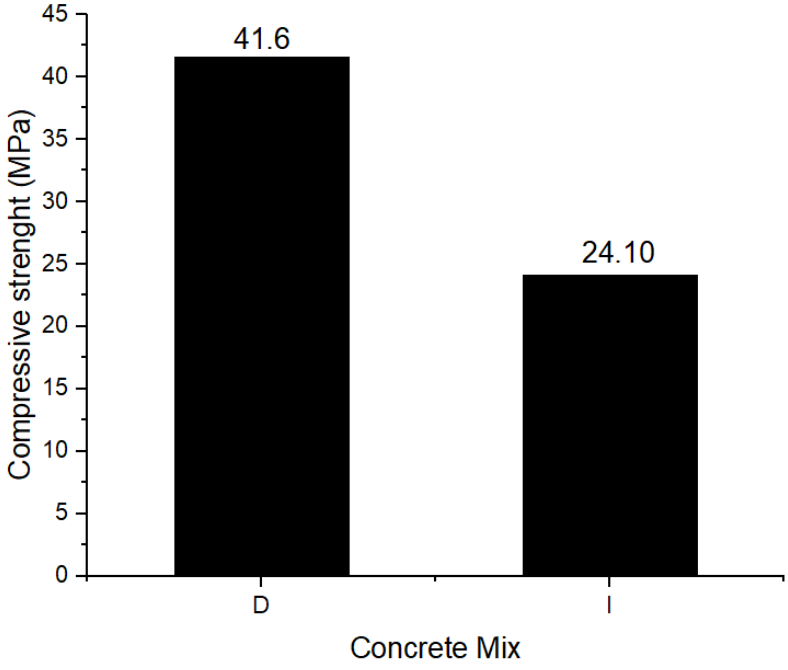

Fig. 3. Concrete mix compressive strength

3.3 Fire Resistance

Three concrete cubes from each concrete mix were prepared and exposed to increased temperatures of 300°C, 600°C, and 900°C after 28 days. The concrete cubes were burnt at 300 °C, no cracks appeared on the cubes, however minor cracks were noticed at 600 °C and 900 °C, as well as two dolomite concrete cubes was spalling in the electric furnace while exposed to 900 °C. Fig.4. depicts the results of a compressive strength test performed on concrete cubes to measure the fire resistance of concrete mixtures

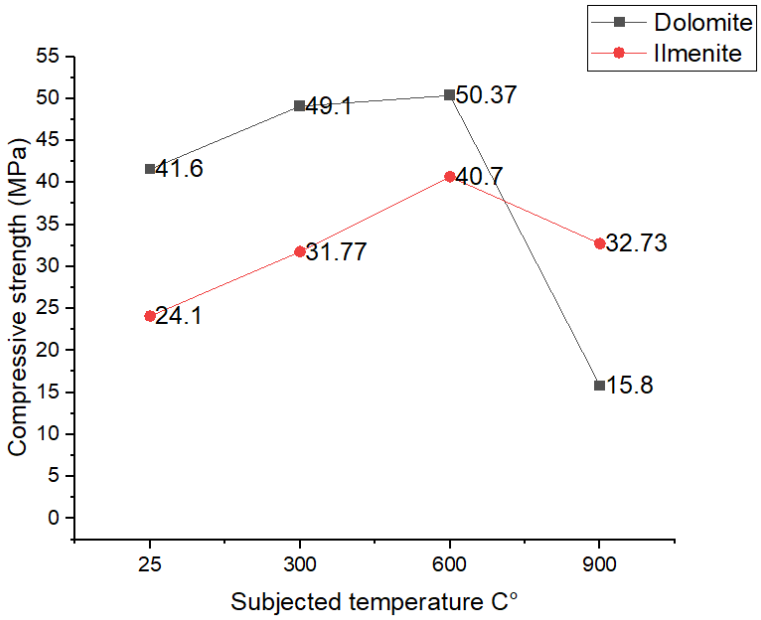

Fig. 4. Compressive strength with subjected temperature °C

The results reveal that after being exposed to temperatures of 300°C and 600°C, all concrete mixtures had enhanced compressive strength. This finding can be explained by still existing unhydrated components in the concrete mix, after that the concrete was exposed to elevated temperatures, which forced the water to transfer and reach with unhydrated components, making more C-S-H to be released, causing the compressive strength to increase.

Dolomite concrete has the highest compressive strength at room temperature with 41.6 MPa, at 300°C with 49.1 MPa and at 600°C with 50.37 MPa. Hence the compressive strength decreases to the lowest with 15.8 MPa at 900°C. Nevertheless, the ilmenite concrete mix had the lowest compressive strength at all temperatures except 900°C, reaching 32.73 MPa.

4 Conclusions and Recommendations

Aggregate Properties Conclusions

- Dolomite aggregate has the lower specific gravity compared to Ilmenite aggregate by 55%.
- Dolomite aggregate has the lower water absorption compared to Ilmenite aggregate by 154%.
- Dolomite aggregate has the lower water absorption resistance compared to Ilmenite aggregate by 100.5%.

Physical Properties of Heavy Weight Concrete

- Dolomite concrete mix showed lower density at 28 days compared to Ilmenite concrete by 83%.
- Ilmenite concrete mix can consider heavy weight concrete reference to TS En 206-1.

Compressive Strength of Heavy Weight Concrete

- Ilmenite concrete obtain lower 28 days compressive strength compared to dolomite concrete mix by 58%.

Effect of Elevated Temperature on Heavy Weight Concrete Compressive Strength

- At 300°C, ilmenite concrete showed lower compressive strength compared to dolomite concrete mix by 65%.
- At 600°C, ilmenite concrete showed lower compressive strength compared to dolomite concrete mix by 81%.
- At 900°C, dolomite concrete mix showed lower compressive strength compared to ilmenite concrete mix by 50%.

References

1. T. S. En and M. Önsöz, “TÜRK STANDARDI,” no. 112, 2014.
2. K. Sakr and E. El-Hakim, “Effect of high temperature or fire on heavy weight concrete properties,” Cem. Concr. Res., vol. 35, no. 3, pp. 590–596, 2005, doi: 10.1016/j.cemconres.2004.05.023.
3. E. Horszczaruk, P. Sikora, and P. Zaporowski, “Mechanical properties of shielding concrete with magnetite aggregate subjected to high temperature,” Procedia Eng., vol. 108, no. December, pp. 39–46, 2015, doi: 10.1016/j.proeng.2015.06.117.
A. C. I. C. 211, “Standard Practice for Selecting Proportions for Normal, Heavyweight, and Mass Concrete,” no. Reapproved, 1991.
A. S. Ouda, “Development of high-performance heavy density concrete using different aggregates for gamma-ray shielding,” Prog. Nucl. Energy, vol. 79, pp. 48–55, 2015, doi: 10.1016/j.pnucene.2014.11.009.
4. H. S. Gökçe and Ö. Andiç-Çakır, “Bleeding characteristics of high consistency heavyweight concrete mixtures,” Constr. Build. Mater., vol. 194, pp. 153–160, 2019, doi: 10.1016/j.conbuildmat.2018.11.029.
5. “Egyptian Code of Practice for Reinforced Concrete No. 203; 2007,” 2020.
6. American Society for Testing and Materials, “ASTM E119 - Standard test methods for fire test of building construction and materials.,” ASTM - Am. Soc. Test. Mater., vol. 552, no. 1, p. 36, 1992, [Online]. Available: www.aslm.org

Impact of Climate Change on Asphalt Binder Performance Selection in a Cold Region Environment

Osama A. Abaza[1*], Alexander Litvinchuk[2], Jesse Batac[3]

[1]Department of Civil Engineering, University of Alaska Anchorage, 2900 Spirit Drive, Anchorage, Alaska 99508, USA
oabaza@alaska.edu
[2]Department of Civil Engineering, University of Alaska Anchorage, 2900 Spirit Drive, Anchorage, Alaska 99508, USA
alitvinchuk@alaska.edu
[3]Department of Civil Engineering, University of Alaska Anchorage, 2900 Spirit Drive, Anchorage, Alaska 99508, USA
jesse.batac@outlook.com

Abstract. The concentration of greenhouse gases in the atmosphere has increased, resulting in the trapping of heat and changes in long-term weather patterns and temperatures worldwide. This change is expected to impact the design, construction, and maintenance of roadway infrastructure, particularly in cold regions where roadways are built on permafrost, and hot mix asphalt surfaces may develop premature ruts due to temperature changes if appropriate measures are not taken. This study focuses on the impact of climate change, particularly temperature changes, on the design of asphalt hot mixtures in cold regions such as Alaska. The research aims to quantify the effect of climate change, including its projections and extreme events, on the selection of binder grades for asphalt based on the SuperPave performance grading system. The study analyzed temperature projections for different regions of Alaska as a prototype for a cold region and found a significant increase in the low temperature thresholds by 1.63°C by 2037. However, based on current design practices, the overall temperature projections are not drastic enough to warrant changes in binder selection. Nevertheless, the study found a high probability of low temperature extreme events, which may cause premature failures beyond the projected models, necessitating changes in the binder selection strategy for cold regions.

Overall, this study highlights the potential impact of climate change on roadway infrastructure, particularly in cold regions, and provides valuable insight into the appropriate binder selection strategy for asphalt hot mixtures in response to these changes. The research findings may inform decision-making processes for designing and maintaining roadway infrastructure in cold regions and mitigate the impact of climate change on infrastructure.

Keywords: Binder selection, Climate change, Cold regions.

1 Introduction

Concentrations of greenhouse gases in the atmosphere such as carbon dioxide (CO2), methane (CH4), and nitrous oxide (N2O) have increased substantially since the beginning of the industrial era in the middle of the 18th century. Solar radiation absorbed at Earth's surface is radiated back to the atmosphere as heat. However, increasing concentrations of these gases increase the absorption of outgoing radiation by the atmosphere and trap heat. This change has caused measurable changes in the long-term temperature and weather patterns around the globe. The primary objective of this study is to assess the impact of climate change on asphalt binder grade selection based on the SuperPave specification for a cold regions environment using Alaska as a prototype example with its three geographic regions (Central, Northern, and Southcoast) per Alaska Department of Transportation and Public Facilities (AKDOT&PF) regional boundaries as shown in Fig. 1. Historical climate data from the last 100 years will be analyzed to determine the extent of the changes to the present day and predict future changes in temperature that will need to be accounted for including the probability of occurrence of extreme events. The study's findings will further help define design practices and improve the performance of pavement designs around Alaska. This will extend pavement life and reduce the premature pavement deterioration.

Fig. 1. DOT&PF's regional boundaries.

2 Literature Review

Global historical climate change data is seen rising at a rate of 0.2 degrees Celsius (°C) per decade (Hansen et al., 2006). However, the North American region, especially more northern latitudes, is experiencing a higher rate of temperature increase than the global temperature change. The higher temperature increase in northern latitudes can be attributed to a decrease in sea ice and land snow cover, leading to a lower surface albedo level (Hansen et al., 2006) (Gerd & Shulski, 2009). Several studies have run simulations for multiple scenarios of global CO2 levels, with each scenario producing an increase in global temperature (Peacock, 2012).

A 50-year study of Alaska's temperatures was conducted between the years 1949 to 1988 using data collected from the Alaska Climate Research Center, NOAA National Data Center, and the National Weather Forecast office (Stafford et al., 2000). From all the stations that data was collected, 25 stations were selected throughout Alaska based on the location, consistency, and quality of the data collected at each station. It is important to note that each of the 25 stations is below 527 meters to reduce the altitude's impact on the temperatures collected (Stafford et al., 2000). The data collected for Alaska was separated into four regions: the Arctic, the Western, the Interior, and South/ Southeastern Alaska. This was done to understand the regional differences in temperature change, as areas closer to water are less susceptible to significant temperature shifts due to water's high thermal inertia (Hansen et al., 2006). The data collected consisted of the mean, minima, and maxima temperatures and precipitation averaged per season for 50 years (Stafford et al., 2000). The study results show that the most significant increase in temperature happens during the winter, followed by spring and summer. Autumn values indicate a decrease in temperatures as seen in Fig. 2.

The most significant mean temperature increase occurs in the interior region where the city of Fairbanks is located. The temperature in Fairbanks was studied in the period 1906 to 2006 using one of 21 first-order stations. First-order stations are stations of the same measuring equipment and are regularly maintained by meteorologists increasing data accuracy and consistency (Gerd & Shulski, 2009). The mean temperatures for each year are plotted, and a linear fit is calculated to find the change in mean temperature. It was found that the increase in mean temperatures in 100 years in Fairbanks is 1.4 °C (Gerd & Shulski, 2009). 1.4 °C is far higher than the global increase of 0.8 °C over the same time frame (Gerd & Shulski, 2009).

A study conducted in 2014 analyzed the Diurnal Temperature change in the continental United States. The United States was then divided into four regions separated by 40-degree latitude and -100-degree longitude (Qu et al., 2014). The data collected consisted of the daily minimum, daily maximum, and mean temperatures. Each region's min, mean and max temperatures were plotted between 1911 and 2012 to find the changes in each temperature. The data was also binned in seasons to study how the DTR changed (Qu et al., 2014).

Results show an increase in yearly temperatures mean and max for all regions and seasons (Qu et al., 2014). However, the annual increase in minimum temperatures can be seen increasing more rapidly than yearly maximum temperatures. This difference in

rates of change is causing a decrease in the DTR of -0.04658 degrees per decade with an overall reduction of DTR of -0.465 degrees over the century (Qu et al., 2014). When each season is analyzed, the summer season is shown to have the most significant decrease in DTR at a rate of -0.0105 degrees per year or -0.1 degrees per decade (Qu et al., 2014). Table 1 gives more details about the changes in in Diurnal Temperature Range per year.

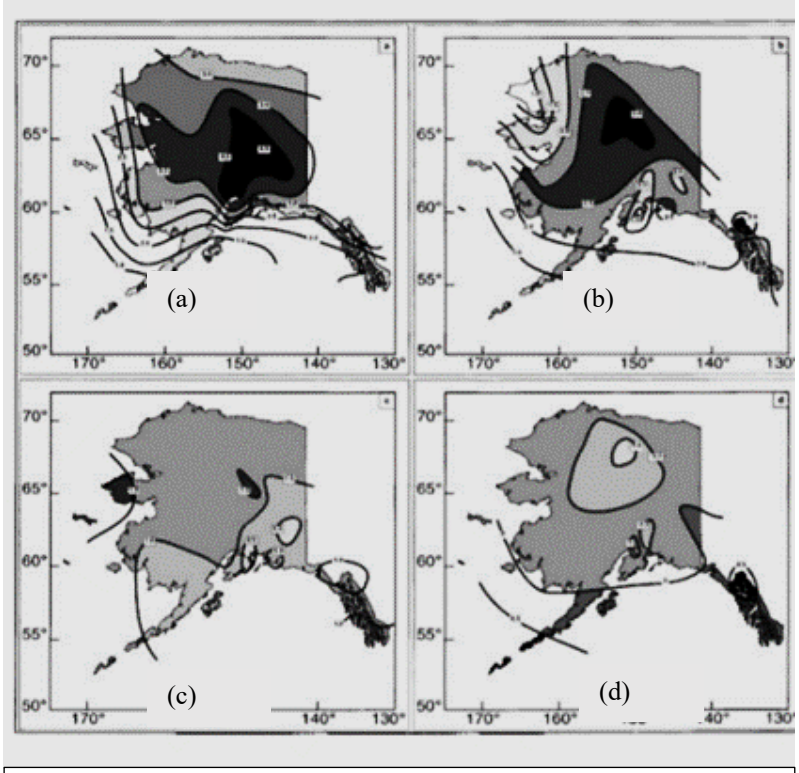

Dark indicates increase in temperature, white indicates decrease in temperature could be helpful since some images show localized increases and decreases.

Fig. 2. Increases in seasonal temperatures, winter (a) shows the highest increases, followed by spring (b) and summer (c). Decrease in temperatures are shown in autumn (d) (Stafford et al., 2000).

Table 1. Change in Diurnal Temperature Range per year.

Trends of seasonal average daily maximum temperature (TMAX), minimum temperature (TMIN), and Diurnal air Temperature Range (DTR) (unites: °C/yr) of continental USA.

	Season			
Variable	Spring	Summer	Fall	Winter
TMAX	0.007170	-0.000701	-0.000761	0.007740
TMIN	0.009669	0.009893	0.00455	0.008576
DTR	-0.002499	-0.010594	-0.005116	-0.00837

(Qu et al., 2014)

Looking at interior Alaska, DTR change is occurring at a higher rate with a decrease of DTR of 2.2 °C over 50 years., Another hotspot of the decline has happened in the southeastern part of the state as shown in Fig. 3, reducing 1.8 °C between 1949 and 1997 (Stafford et al., 2000).

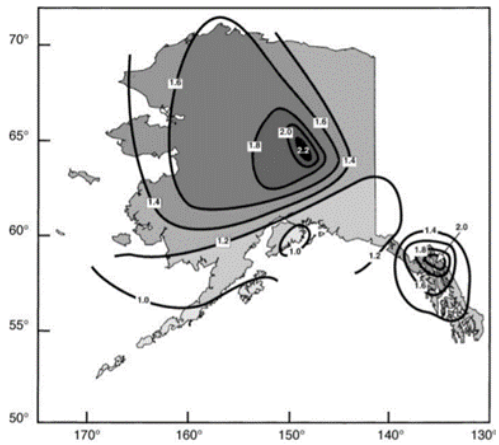

Fig. 3. Degrease in DTR between 1949 and 1947 (°C) (Stafford et al., 2000).

This decreasing DTR trend can be better seen when looking at the temperature data in Fairbanks (Gerd & Shulski, 2009). The number of frigid days, below -40 °C, has decreased from 14 days annually to only eight days. The increase of very hot days, above 26.7 °C, has only gone up slightly from 11 days a year to 12 days a year (Gerd & Shulski, 2009). The decrease of frigid days frequency compared to the only slight increase in very hot days shows a reduction in DTR (Gerd & Shulski, 2009).

Four scenarios based on predicted radiative forcings were run to project climate change over the next century to create a climate model (Peacock, 2012). The four scenarios, low, medium-low, medium-high, and high, were based on predicted CO2 levels in the next century. A 1300-year preindustrial control run was used to have a baseline to compare future temperature changes. To test the accuracy of each model, the data collected were superimposed on the predicted change of temperatures. The

temperatures for both Alaska and Canada follow the prediction well. However, the data collected from the lower 48 deviate from the projection after 2000.

Analysis of the results shows the temperature to increase in all scenarios. It should be noted that temperature change increases with latitude, with the most significant increase occurring in the summer months (Peacock, 2012). A shorter study was run to understand better which scenario collected data most fit. It was found that after running three separate systems, from conservative to no change in emissions, the current temperature change lands between the two extremes (Hansen et al., 2006). The most conservative projections show an increase of 1 to 3 °C, while the most extreme scenario shows an increase of up to 8 °C over the next century (Peacock, 2012).

The Alaska Department of Transportation & Public Facilities (AKDOT&PF) divided the state into three geographic regions consisting of the Southcoast Region, Central Region, and Northern Region as shown in Fig. 1. The Southcoast Region encompasses the eastern panhandle of the state and the Aleutian Chain. Central Region covers the western half of Prince William Sound, Cook Inlet, and extends west to Bristol Bay. Northern Region encompasses the eastern portion of Prince William Sound, all of interior Alaska, the North Slope, and much of western Alaska. The purpose of splitting the state into three regions is to split the authority for highway program development and in turn any subsequent projects into three similarly sized groups. Grouping the projects together by region ensures that much of the same environmental, climactic, and topographical demands will be experienced across projects in the region.

Even though each region has many of their own unique design practices the Alaska Highway Preconstruction Manual, Alaska Flexible Pavement Design Manual, and the Standard Specifications for Highway Construction apply to all regions and among other things serve as the core guidance for pavement design and specifications in Alaska. Pavement structures in Alaska are designed in accordance with the policies and design procedures in the Alaska Flexible Pavement Design Manual (AKFPD 2020). The AKFPD Manual guides designers through the comprehensive computerized method for the design of Alaskan pavement structures using the Alaska Flexible Pavement Design method version 2 computer program. Essentially, the manual Provides specific guidance on the input variables and other decision criteria necessary to run the AKFPD software and complete a design. The Alaska Highway Preconstruction Manual (AKHPM 2020) states that Hot Mix Asphalt (HMA) is the predominant type of wearing course used on AKDOT&PF roadways. Sections 402 and 702 of the Standard Specifications for Highway Construction (SSHC 2020) state that all HMA pavement structures must meet the standards specified by AASHTO M 320, Standard specification for Performance-Graded Asphalt Binder.

The Performance Grade (PG) system is the method of categorizing an asphalt cement binder used in asphalt pavement relative to its rated performance at different temperatures. It was originally developed during the Strategic Highway Research Program (SHRP) in the early 1990's and was called SuperPave. Performance grading is based on the concept that asphalt binder properties should be related to the conditions under which the binder is used, AASHTO M 320 covers asphalt binder performance graded where designations are related to the average seven-day maximum pavement

design temperature and the minimum pavement design temperature. This is important to the research because if temperatures change significantly, the performance grading of the binder will no longer be sufficient. The current Standard Specifications for Highway Construction (SSHC 2020) identifies PG 52-28 as the typical grade used in asphalt pavements, when no other grade is specified. In this case, the first number (52) indicates that the binder meets high temperature physical properties up to 52 °C. The last number (-28) indicates that the binder meets low temperature physical properties down to -28 °C.

However, pavement design and binder selection is much more involved and complex than simply matching the expected temperatures to the correct performance grading. In the Northern Region PG 52-40 is often used. In Central Region, PG 64-40 and PG 52-40 along with PG 52-28 are often seen depending on the roadway. In the Southcoast region PG 58-28 and 64-28 are most commonly used. As shown by the various binder grades used throughout Alaska, typical binder high temperature classifications range from 52 to 64 and the low temperature classifications range from -28 to -40.

One thing that the SuperPave system does not properly disclose about a pavement design is various modifications efforts that aim to combat some of the most common pavement design problems in Alaska like rutting. Modification efforts have focused on increasing the PG grades of asphalt binder at various situations by adding polymers and additives. Several studies indicated that the Superpave PG grading system does not reveal adequate information about modified asphalt binders in terms of potential performance. This research however was focused on the performance of the binder based on the temperature. Analyzing various topics related to binder selection and additives may be addressed for future research per types of expected premature pavement failures.

Swarna et al. (2021) conducted research to assess the impacts of climate change on asphalt binder grade selection and implications. 10 climate change models from the pacific climate database were analyzed and the maximum and minimum temperature data was extracted to determine the new asphalt binder for 16 test sites across 10 Canadian provinces. The purpose of the study was to quantify the impact of climate change on pavement performance, estimate the change in binder grade due to temperature increases, and to quantify the influence of upgraded binder grade on pavement performance and service life. It was found that of the 16 sites that were analyzed, all but three sites required at least a single step increase in binder grade to account for temperature changes based on the models. In addition, 2 locations required double step increases. Ultimately, the study concluded that upgrading asphalt binder was a cheap and effective strategy to combat climate change temperature increases.

Basit et al. (2021) conducted research to evaluate the impact Climate Change Implications for Asphalt Binder Selection in Pavement Construction across Ontario. In this study, the latest long-term pavement performance (LTPP) model was used to determine the asphalt pavement surface temperatures. For different representative concentration pathways (RCP), the relative impact of climate change on pavement temperature extremes and thereby appropriate PG to meet projected pavement temperatures was assessed using the LTPP models. The results of this study indicate that in the future, climate variations will cause changes to asphalt binder grades across

the examined locations in Ontario, which depend on the severity of the projected warming. This research offers useful suggestions that can be incorporated by the road agencies and designers towards adaptation of pavement construction materials suitable to the changing climate.

Viola and Celauro (2015) analyzed the daily temperature records for a total of 71 weather stations provided by the Italian Air Force Meteorological Service from 1984 to 2013. This historic data was then used to detect and model trends using several statistical procedures including both parametric and non-parametric techniques. Based on current temperatures and design practices, PG 64-22 binder proved to be the most common grade encompassing about 55% of the Italian territory. The future model was then calibrated to analyze the temperature in the year 2033 to deduce any changes from the current year. As far as the scenario 2033 was considered, the PG 64-22 was again the most common grade and covered approximately 60% of the needs for Italy, while again the first four binder cover the 90% of the range of climate conditions. The substantial difference is that, due to climate change, a significant shift of PG towards highest design temperatures is shown. Even though it hasn't exceeded enough to classify for the next Performance Grading, the fact that it approached to the next grading shows that it could occur if the temperature model is modified, or timeline is extended.

Similarly, another study, Delgadillo et al. (2020) investigated the correlation between climate change and performance grading binder selection in Chile. The researchers analyzed data from 94 weather stations spanning different regions of Chile and acquired historical the historical trends from these stations from 1970 until 1999. The researchers then applied an advanced predictive algorithm known as MIRCO5-WRF, and extrapolated weather data for a 30-year time span into the future (2030-2059). Using these future climate predictions, it was found that between 10 and 40 percent of all weather stations may require changes in their upper bound performance grades and 5 and 10 percent of station may require change in their current lower bound performance grades depending on the Representative Concentration Pathway scenario through 2030-2059.

3 Methodology

The methodology of this research consists of three phases to determine the impacts of climate change on asphalt binder grade selection in all three AKDOT geographic regions of Alaska. Due to the sheer size and extreme climate variations within each region, three locations were selected to give a more comprehensive look at the climate and corresponding predicted asphalt binder grade changes experienced in each region. These locations were: Northern Region- Fairbanks, Central Region- Anchorage, and Southcoast Region- Juneau. Each of the three locations were selected to represent the three regions defined in Fig. 1 per to the size and importance of the location for each region and the localities with most roadway mileage in the state.

The first phase of the study includes the collection of maximum and minimum temperature predictions from the National Oceanic and Atmospheric Administration's

(NOAA) National Centers for Environmental Information (NCEI). The Global Historical Climatology Network - Daily (GHCN-Daily) dataset integrates daily climate observations from approximately 30 different data sources. This database contains station-based measurements from over 90,000 land-based stations worldwide many of which include historic daily temperature data going back to the beginning of the 20th century. From this database, the minimum and maximum daily temperatures for each location were taken as far back as the records were available. For the Northern Region, the Fairbanks records extracted dated back to 1929. For Central Region, the station used was Anchorage International Airport (AIA) however, this was supplemented by records from the Merrill Field airport which dated back to 1916. Lastly, for Southcoast Region, records from the Juneau Airport were used and dated back to 1936.

From the NCEI database, the temperature records were extracted in a comma separated values (CSV) format and transferred to excel. For each location, the station identification tag, station name, latitude, longitude, elevation, date of observation, maximum observed daily temperature, minimum observed daily temperature, and average daily temperature. From this, the minimum, maximum, and maximum 7-day average temperature for each year were extracted and placed in a separate database. This information is important in the SuperPave performance grading system and asphalt binder selection which is based on the minimum pavement temperature over the design period and maximum 7-day consecutive temperature experienced during the design life of the pavement. Records spanned almost 100 years in each of the regions creating a high level of confidence in the trends observed from the data.

After extraction of the annual minimum, maximum, and maximum 7-day average temperature for each year, a linear regression model was applied to the data in order to determine the change in temperature over the historic period. Developing this regression model will determine estimates for temperature projections over the study period. Because the typical design period for a pavement in Alaska is 15 years per the input from Alaska DOT&PF, this was applied to the regression model to determine the change in temperature for a pavement designed in the current year. Actually, pavement life in the state are well below this limit due to the premature failure of pavement structures due to studied tire use especially on main arterials (Abaza, 2019). Worst case scenarios of 15 years were taken into consideration in this research.

Finally, after obtaining the historic trends for each region, a 15-year projection could be made using the linear regression models obtained in phase 2. These estimates assume that the change in climate can be modeled by the best fit linear regression and that the temperatures will change at the same historic rate. Furthermore, extreme historic minimum, maximum and 7-day was considered over the study period to account for extremes beyond the15 years projection based on the probability of occurrence considering 95 percent confidence level. Lately, extreme events related to high spikes in temperatures beyond the lowers and higher norms as well as other climate change extreme events such droughts and high intensity rain events were depicted. Extreme events are occurrences of unusually severe weather or climate conditions that can cause devastating impacts on communities and agricultural and natural ecosystems. Weather-related extreme events are often short-lived and include heat waves, freezes, heavy downpours, tornadoes, tropical cyclones and floods. Climate-related extreme events

either persist longer than weather events or emerge from the accumulation of weather or climate events that persist over a longer period of time. Examples include drought resulting from long periods of below-normal precipitation or wildfire outbreaks when a prolonged dry, warm period follows an abnormally wet and productive growing season (USDA, 2022). For the purpose of research extreme temperatures where considered. Using the designations of the current local PG binder used for each region, the changes in future temperature will warrant a change in PG binder over the 15-year design period as well as the historic extremes over the study period for a typical roadway in Alaska. The methodology incorporated in this research will be recommended for local organizations as well as Nordic countries and other localities for future PG binder selection.

4 Data Analysis

4.1 Analysis of Temperature Data

Data collection and analysis of the previous year's average, minimum and maximum temperatures as well as extreme events had to be examined and study the temperature trends. Temperature data was collected using the NOAA Global Historical Climatology Network for three locations in Alaska. Fairbanks was chosen as the location to represent the Northern Region, Anchorage for South Central, and Juneau for the Southcoast. The data gathered consists of temperature minimum, average, and maximum temperatures dating back to 1929 for both Anchorage and Fairbanks while Juneau's temperature data only dates back to 1936. The temperature data for all three locations were analyzed and plotted to obtain a best fit for each region.

Analyzing at the data collected from Fairbanks, an increase in both the historic high, historic low and 7-day historic high temperatures can be seen in Fig. 4, Fig. 5 and Fig. 6. The best fit relationship was developed for all three relationships where the high temperature is climbing at a rate of 0.067°C per year, the low temperature climbing at a rate of 0.0595°C per year, and the 7-day maximum average rising at a rate of 0.005°C per year. Further examinations of the relationships for Fairbanks, the historical minimum temperature is rising at a rate almost 9 times greater compared to the rate that the historical maximum is rising. In addition, it can be seen that the historical 7-day average temperature is increasing at a rate of 0.005°C per year.

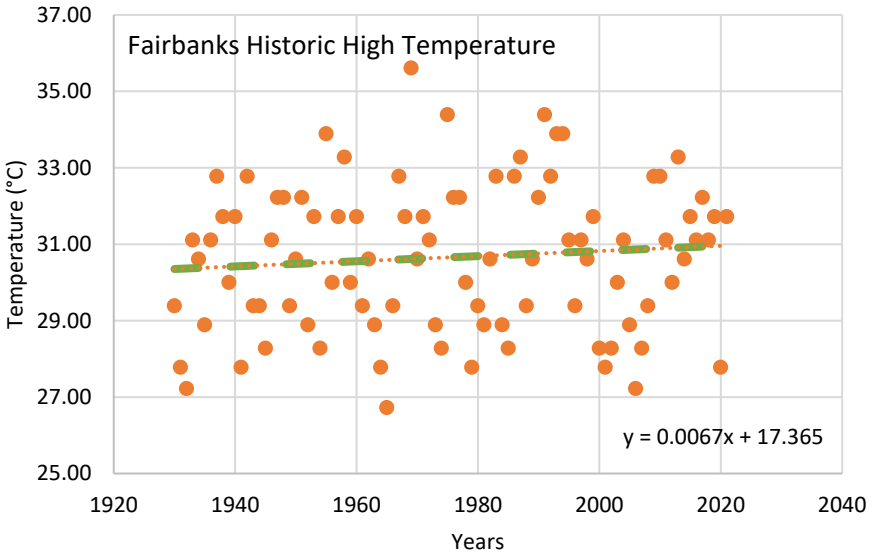

Fig. 4. Fairbanks Historic High Temperatures from 1929.

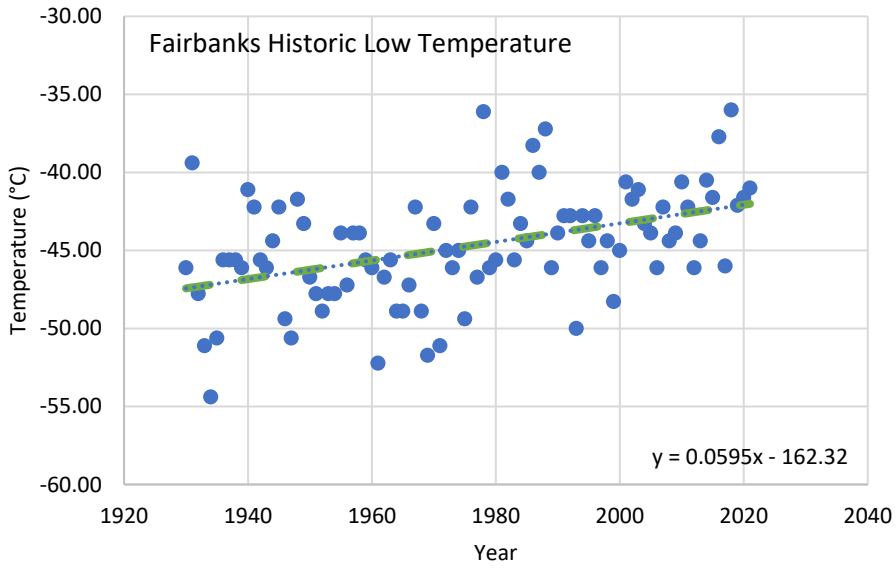

Fig. 5. Fairbanks Historic low Temperatures from 1929.

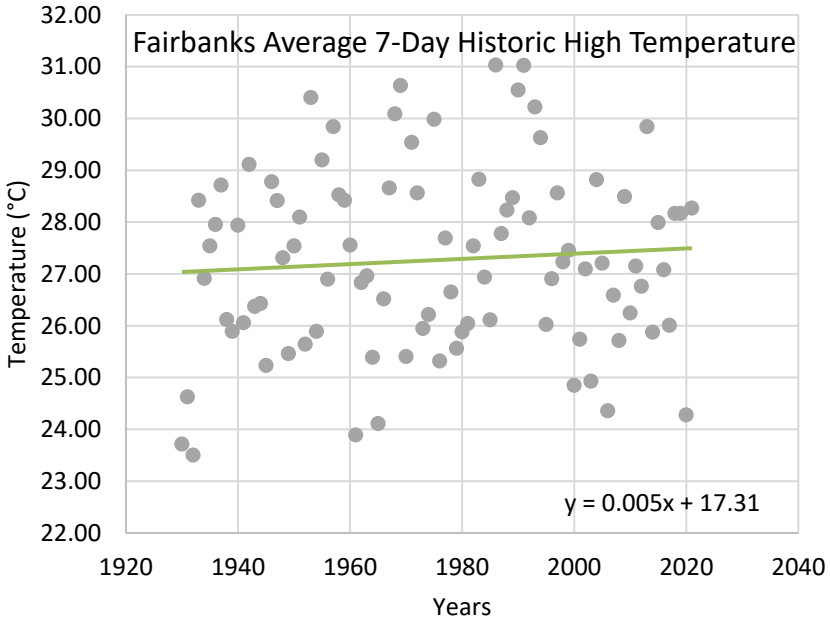

Fig. 6. Fairbanks Historic 7-day average high Temperatures from 1929.

The data collected from AIA and Merrill Field Airport in Anchorage shows the same trend as the data from Fairbanks. Where the minimum, maximum, and seven-day average temperatures were graphed per Fig. 7, Fig. 8 and Fig. 9, the maximum temperature and 7-day maximum temperatures can be seen rising at a slower rate compared to the rise in minimum temperatures. The rise in the average maximum and 7-day maximum temperature is 0.0019°C per year and 0.01°C per year.

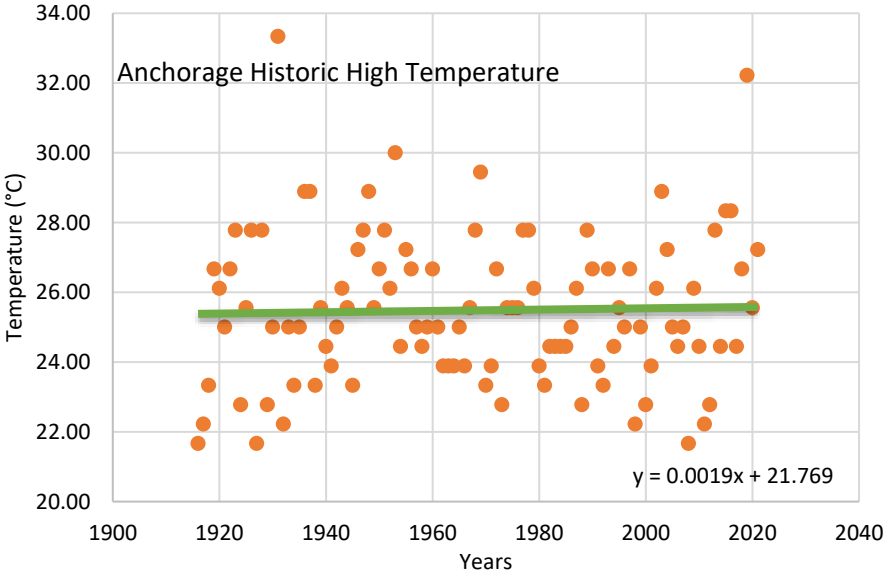

Fig. 7. Anchorage Historic High Temperatures from 1929.

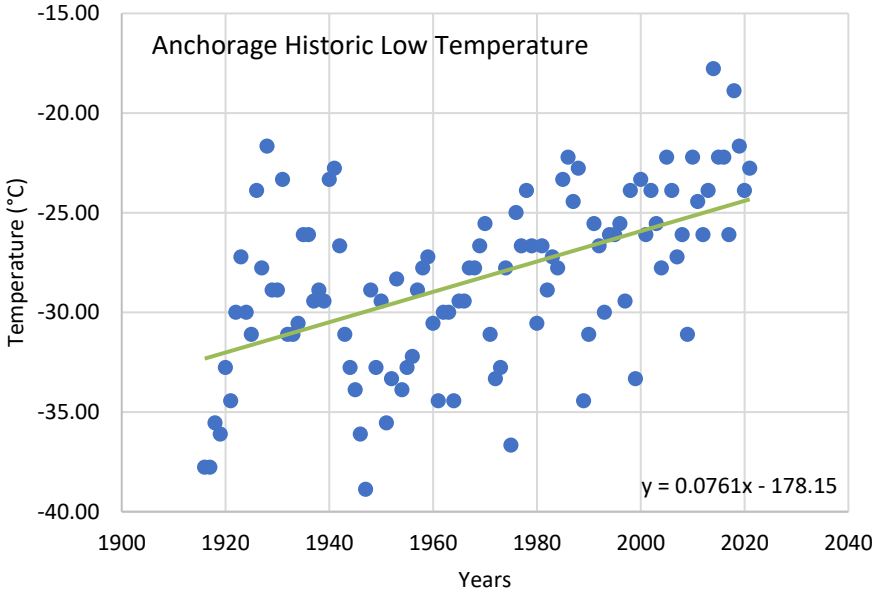

Fig. 8. Anchorage Historic Low Temperatures from 1929.

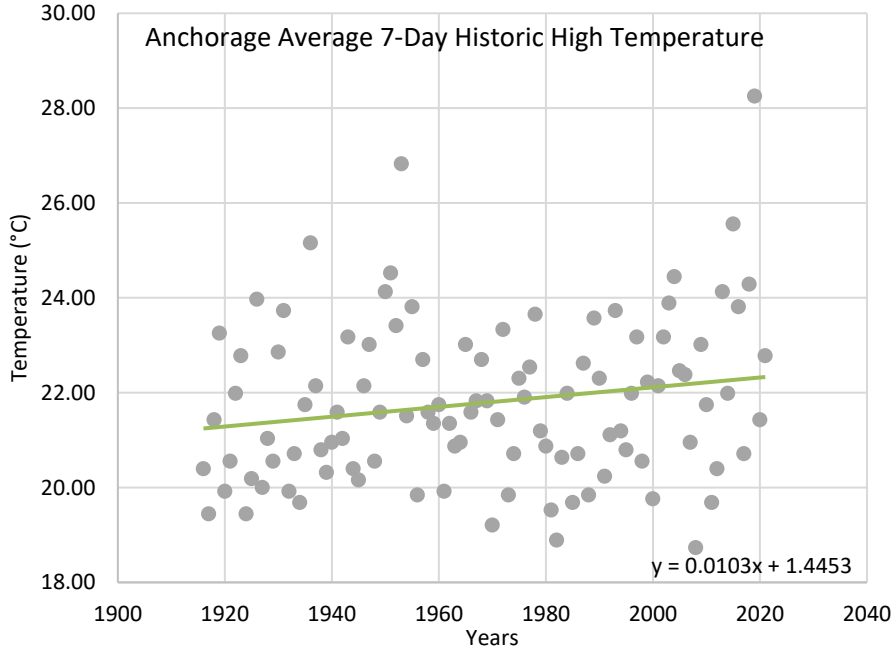

Fig. 9. Anchorage Historic 7-day average high Temperatures from 1929.

Southeast Alaska, where Juneau is located, shows the largest decrease in the historical diurnal temperature range as shown in Fig. 10. Fig. 11 and Fig. 12. The rise in the historic high temperatures and historic 7-day high temperatures are increasing at a rate of 0.008°C per year and 0.005°C per year. This rate of temperature change is lower compared to the increase in historic low temperatures of 0.186°C per year. The temperature increases of the historic low temperatures in Juneau is 23 times greater than the historical increase of high temperature. This difference in rates shows a fast decline in the diurnal temperature range which can be seen in all regions where data was collected. In general, the rate of increase in the low temperature decreases going south from Fairbanks to Juneua.

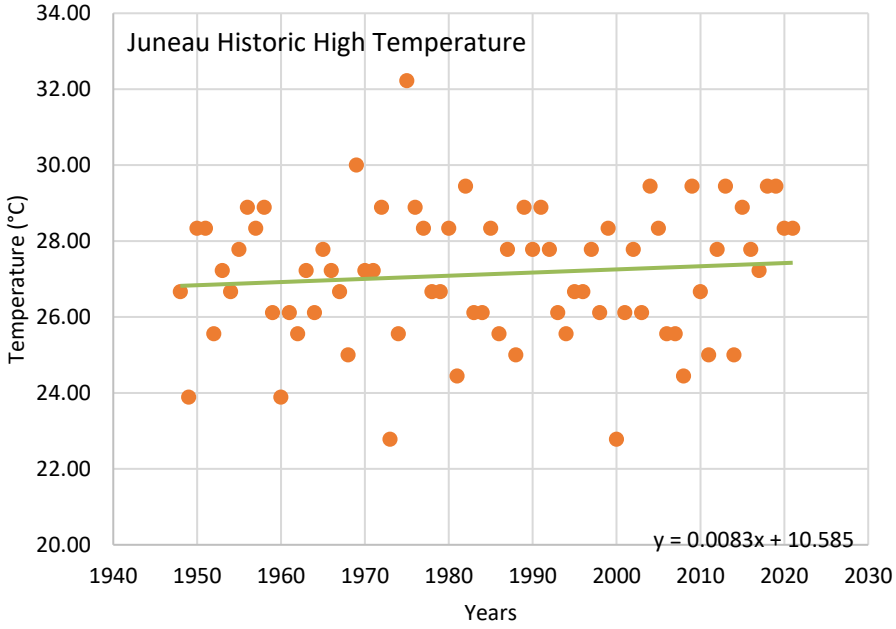

Fig. 10. Juneau Historic Low Temperatures from 1936.

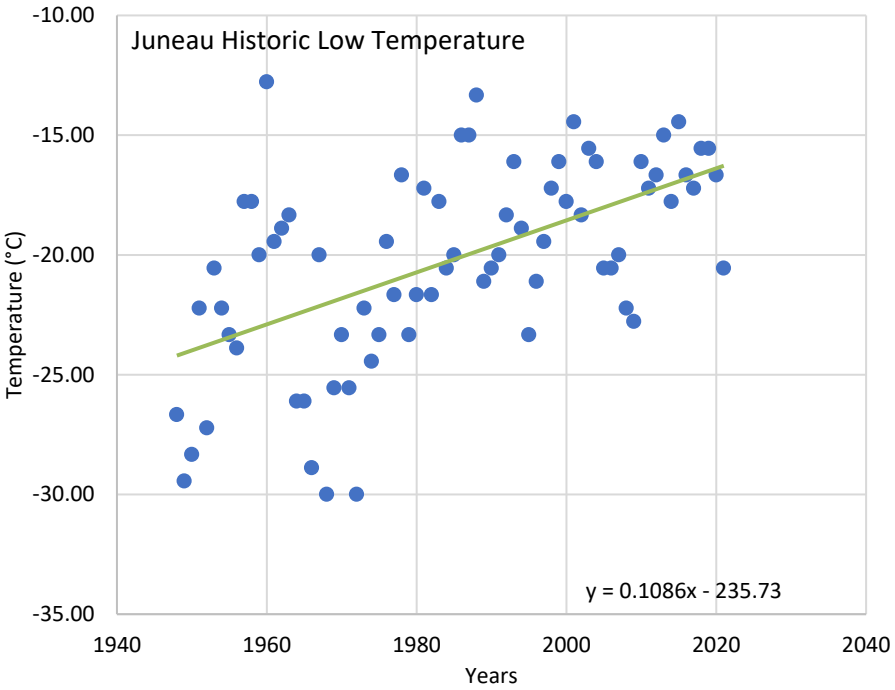

Fig. 11. Juneau Historic Low Temperatures from 1936.

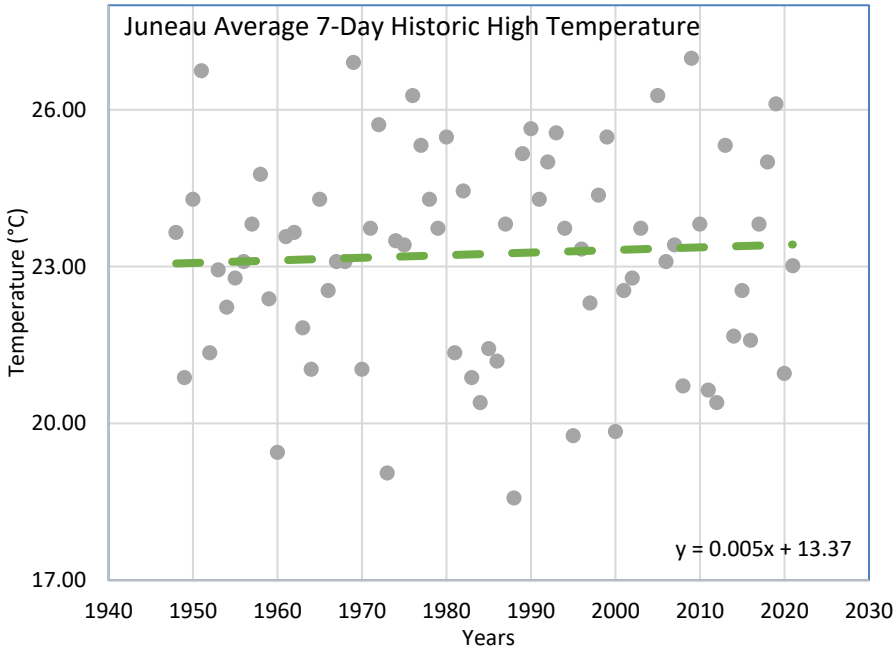

Fig. 12. Juneau Historic 7-day average high Temperatures from 1936.

4.2 Future Temperature Projections

Applying the regression models developed with the historic observations for the predicted minimum and 7-day average maximum were developed for all three locations for the next 15 years which represents the typical design life for pavement structures in the state. This is the basic input into the SuperPave performance grading and binder selection. Fig. 13 shows the general trend with little variations in the 7-day average maximum temperature between the three regions basically due to latitude, proximity to shore areas and elevation. In the case of low temperatures the differences are significant mainly due to latitude with Fairbanks being the closest to the Arctic Circle.

Projecting the minimum, and 7-day maximum temperatures of Fairbanks show slight increases in all temperatures while the minimum temperature is projected to increase by 0.89°C by 2037. The maximum temperature is projected to increase by 0.1°C, and the 7-day average temperature is projected to increase by 0.07°C by 2037. Looking at future temperatures for Anchorage, the regression model projects an increase of 1.15°C in minimum temperature, an increase of 0.03°C for maximum temperatures, and an increase of 0.15°C for the maximum 7-day temperatures. Projecting the minimum, maximum, and 7- Day average temperatures for Juneau shows a large increase in projected low temperatures compared to Anchorage and Fairbanks. The minimum temperature is projected to increase 1.63°C by 2037. The maximum temperature is projected to increase 0.02°C by 2037 and the 7-day maximum average to increase 0.07°C by 2037. The projected temperatures from all three locations show a high increase in the low temperatures compared to the increase in high and 7-Day

maximum temperatures. Juneau is projected to have the highest increase in low temperature with a temperature increase of 1.63°C by 2037. Fairbanks is projected to have the highest increase in high temperatures with a temperature increase of 0.1°C.

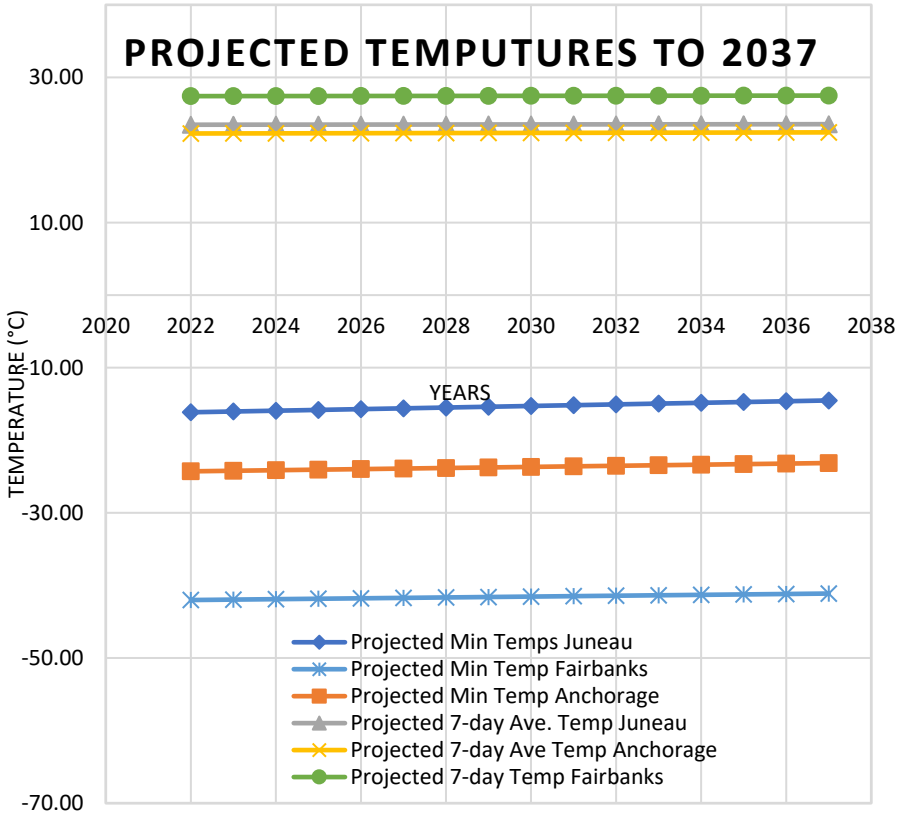

Fig. 13. Projected temperatures to 2037 for the three regions.

Based on the temperature projection models, consideration of a fifteen year design period, the and the current binder selection adopted by public agencies in the state, the changes in PG binder selection are not warranted to account for any potential project period change. The impact of any low temperature change based on the projection models will cause insignificant increase in the low temperature and will not impact the integrity of the pavement structure with respect to thermal cracking. On the other hand, binder selection at low temperature above the current selection will not reflect any cost savings as well. In addition, the projected average maximum seven-day temperature reflects a steady trend well below any limit to warrant changes and in turn will not cause any premature failure during the prescribed design period. Public agencies need to track and calibrate the models with time to make sure binder selection strategies are in line

with the projected low and 7-day average temperatures expected for the regions under consideration.

Analysis of extreme events can be defined using either of two approaches. The first approach examines the probability or chance of an event of a given magnitude occurring within a certain reference period (e.g., 1961 - 1990); here an extreme event has a low probability of occurring at a given location (< 10%) and is typically of a high intensity. This type of probabilistic approach is applied in extreme event attribution to determine whether global warming is driving changes in the frequency and intensity of extreme events (USDA, 2022). The second approach is more widely applied by the climate adaptation community and uses impact-related thresholds to determine if an event is extreme, and to inform adaptive solutions. A common example here is the number of consecutive days over 100˚F, which can be used to quantify heat waves. Of course, impacts associated with a 100˚F threshold will vary according to location – what might be an extreme event in one place (e.g., Burlington, VT) may be within the normal range somewhere else (e.g., Phoenix, AZ). Thus, thresholds are often location-specific (USDA, 2022). In this research the first method was used considering the engineering application as well as the detailed data extracted for each of the regions analyzed in the state of Alaska as defined earlier. Table 2 shows the eight and ninety fifth percentile of temperatures data for low, high and 7-day average high temperatures in each of the three regions.

Table 2. Eighty and ninety fifth percentile of temperature data in the three studied region of Alaska.

85% in the study period			
	85% High	85% Low	85% 7-Day Average High
Anchorage	17.78	-13.89	17.54
Fairbanks	20.61	-27.22	20.46
Juneau	16.67	-5	16.67
95% in the study period			
Anchorage	20.56	-21.11	19.76
Fairbanks	25.00	-36.72	23.83
Juneau	21.11	-12.78	19.60

The ninety fifth compared to the eighty fifth percentile for high temperatures shows significant differences with relatively higher differences for Fairbanks and Juneau compared to Anchorage. In addition, the differences are even much higher, reaching about twice as much for low temperatures compared to the high temperatures with Fairbanks being the highest compared to Anchorage and Juneau. Furthermore, the 7-day average high temperatures shows lowest changes as the extreme events level off

over the seven day period with Anchorage having the lowest difference. This outcome indicates that the temperature change for extreme events showing higher change or spikes relative to the general temperature projections developed earlier as shown in Fig. 13. The differences are more significant at the low temperature threshold used in the binder selection compared to the 7-day average high temperatures as the spikes level off over the seven day period for high temperatures. This is more notable in Fairbanks relative to Anchorage and Juneau with all will warrant consideration in future binder selection having a direct impact on the pavement thermal cracking during the designated fifteen year design period used by the state agencies. Though the 7-day average high temperatures is warranted as well but it will have a lower impact on the pavement structure as rutting caused by higher temperature are not of concern for the AKDOT considering the much higher rut development in the state caused by the abrasive action of studded tires (Abaza, 2019).

Table 3 shows further analysis of examples of the current PG binder selection in the three Alaskan regions with historic exceedance for low temperatures for each with consideration of the project design period.

Table 3. Historic Exceedance Probability for low temperatures in the three Alaskan regions.

Region	PG	Historic Exceeded Low Temperature (°C)	Exceedance Probability Low Temperature
Anchorage	64-28	51	48.11%
Fairbanks	52-40	84	91%
Juneau	58-28	5	6.76%

It is clear the exceedance probability percentages gets higher towards the arctic region with Fairbanks and Anchorage on the high side and Juneau being the lowest. In the case of Fairbanks, the lowest temperature considered in the example shown in Table 3 represents the actual use of PG binder selection in that region being -40 °C which is lower than the historic exceedance of low temperature by about 44 °C. This difference might not give much of an indication for the adopted low temperature in the PG binder selection but the possible occurrence of such temperature using the exceedance probability is a strong indication of possible change which is in this case reaches 91 percent. The same terminology can be applied for the other two regions with Anchorage and Juneau showing about 48 and 7 percent of exceedance probability respectively. The exceedance probability for these examples considering maximum the 7-day average high temperatures shows very low values approaching zero. In general, in the case of these examples and the three regions considered, the low temperature in the binder selection is warranted for Fairbanks and Anchorage and the maximum 7-day average temperature is not warranted in all regions.

5 Conclusion and PG Binder Recommendations

Based on the results of the research and the consideration of the three Alaskan regions the following can be concluded:

1. Climate change in the form of temperature projections over almost one hundred years and current design practice the changes are not drastic enough to warrant an increase or change in the PG binder selection within the design life of a pavement. This applies for low and the 7-day average high temperatures. With current designs ranging from PG 52-28 to PG 64-40, binders are sufficient to handle the temperature changes across the state. In the research it was shown that a pavement designed in 2022 with a design life of 15 years would still be sufficient even after the slight increases in maximum and minimum temperatures anticipated in by 2037.
2. Climate change in the form of extreme events defined in this research as the probability or chance of an event of a given magnitude occurring within the pavement design period of fifteen years, the binder selection process is warranted for low temperature in the areas approaching the arctic region. In the case of this research Fairbanks and Anchorage are considered areas where the low temperature in the binder selection are warranted.
3. Climate change in the form of extreme events for the 7-day average high temperatures used in the PG binder section are not warranted across the state as the exceedance probability of such an events are approaching zero. This is considered normal as the extreme maximum consecutive seven day temperature will level off dismissing extreme maximum temperature beyond the prediction models developed as part of this research.

It recommended that state agencies especially the ADOT&PF to consider the following in their future PG binder selection strategies:
1. Develop a temperature project database using existing weather stations across the state to qualitatively assess temperature changes over the available historic database in each of these stations to define parameters needed for PG binder selection for the projects in the locality.
2. Adopt a policy for binder selection based on temperature projection as well as extreme events to better preserve pavement assets and avoid possible premature pavement failure that might reduce pavement life or pose risks to roadway users.
3. In addition to the above, continue the efforts on the addition of modifiers that will improve pavement performance against rutting, thermal cracking and other pavement distresses which might reduce pavement life in Alaska. As mentioned previously, pavement design in Alaska is much more complex than simply selecting the appropriate PG binder based on temperatures. Various efforts to modify the binder and improve performance against certain actions like rutting and thermal cracking are not captured in the simple selection of PG binder through temperatures.

References

1. Abaza, O. (2019). Survey and Economic Analysis of Pavement Impacts from Studded Tire Use in Alaska. Report No. FHWA-AK-RD-4000(175), (pp. 1–95). Anchorage, Alaska.
2. Alaska Flexible Pavement Design Manual (2020), Alaska Department of Transportation and Public facilities (AK DOT&PF). chrome-extension://efaidnbmnnnibpcajpcglclefindmkaj/https://dot.alaska.gov/stwddes/desmaterials/assets/pdf/pvmtdesign/flexpvmt_mnl.pdf (July 15, 2022).
3. ASCE (American Society of Civil Engineers). (2014) Minimim Design Loads for Buildings and Other Structures, Standard ASCE/SEI 7-10. Third printing. ASCE, Reston, VA.
4. Basit, A, Shafiee, M, Bashir, R and Perras, M A (2021). Climate Change Implications for Asphalt Binder Selection in Pavement Construction across Ontario. International Conference on Transportation and Development 2021, 2021, pp 289 – 301. American Society of Civil Engineers 1801 Alexander Bell Drive, Reston, VA United States 20191-4400.
5. Burka, L. P. (1993). "A hypertext history of multi-user dimensions." MUD history, <http://www.ccs.neu.edu> (Dec. 5, 2013).
6. Climate Hubs, United States Department of Agriculture, https://www.climatehubs.usda.gov/content/extreme-weather, (November 2022).
7. Committee on Curtain Wall Systems. (2014). Curtain Wall Systems: A Primer, ASCE Manuals and Reports on Engineering Practice No. 126. Memari, Ali M., ed. ASCE, Reston, VA.
8. Delgadillo, Rodrigo, Arteaga, Leandro, Wahr, Carlos, and Alcafuz, R. (2020). The influence of climate change in Superpave binder selection for Chile. Road Materials and Pavement Design, Volume 21, Issue 3, 2020, pp 607-622.
9. Dhillon, Gurpreet S., Surinder Kaur, Ajila C. M., Brar, Satinder K., and Surampalli, Rao Y. (2013). "Greenhouse Gas Contribution on Climate Change." Chapter 3 in Climate Change Modeling, Mitigation, and Adaptation, Rao Y. Surampalli, Tian C. Zhang, C. S. P. Ojha, B. Gurjar, R. D. Tyagi, and S. M. Kao, eds. ASCE, Reston, VA, 26-61.
10. Hansen, J., Sato, M., Ruedy, R., Lo, K., Lea, D. W., and Medina-Elizade, M. (2006). "Global temperature change." Proceedings of the National Academy of Sciences, 103(39), 14288–14293.
11. Garrett, D. L. (2003). "Coupled analysis of floating production systems." Proc., Int. Symp. on Deep Mooring Systems, ASCE, Reston, VA, 152-167.
12. Gerd, W., and Shulski, M. (2009). "A century of climate change for Fairbanks, Alaska." Arctic Institute of North America, <http://climate.gi.alaska.edu/sites/default/files/papers/Arctic62-3-295.pdf> (Mar. 31, 2022).
13. Peacock, S. (2012). "Projected twenty-first-century changes in temperature, precipitation, and snow cover over North America in Ccsm4." Journal of Climate, 25(13), 4405–4429.
14. Qu, M., Wan, J., and Hao, X. (2014). "Analysis of diurnal air temperature range change in the continental United States." Weather and Climate Extremes, 4, 86–95.
15. Stafford, J. M., Wendler, G., and Curtis, J. (2000). "Temperature and precipitation of Alaska: 50 Year trend analysis." Theoretical and Applied Climatology, 67(1-2), 33–44.
16. Standard Specifications for Highway Construction (2020),), Alaska Department of Transportation and Public facilities (AK DOT&PF). chrome-extension://efaidnbmnnnibpcajpcglclefindmkaj/https://dot.alaska.gov/stwddes/dcsspecs/assets/pdf/hwyspecs/sshc2020.pdf (June 18, 2022).
17. Singh, Vijay P. (2014). Entropy Theory in Hydraulic Engineering: An Introduction. ASCE Press. ASCE, Reston, VA.
18. Stahl, D. C., Wolfe, R. W., and Begel, M. (2004). "Improved analysis of timber rivet connections." J. Struct. Eng., 130(8), 1272-1279.

19. Swarna, S, Hossain, K, Pandya, H and Mehta, Y (2021). Assessing Climate Change Impact on Asphalt Binder Grade Selection and its Implications. Transportation Research Record: Journal of the Transportation Research Board, Volume 2675, Issue 10, 2021, pp 786-799.
20. Viola, F. and Celauro, C. (2015). Effect of climate change on asphalt binder selection for road construction in Italy. Transportation Research Part D, Elsevier: Transport and Environment, Volume 37, Issue 0, 2015, pp 40-47.
21. Zhou, H. and Attard, T. (2014). "Simplified Anisotropic Plasticity Model for Analyzing the Postyield Behavior of Cold-Formed Sheet-Metal Shear Panel Structures." J. Struct. Eng., 10.1061/(ASCE)ST.1943-541X.0001152, 04014185.

A Comparison and Review of Studies on Chemical Accelerator Admixtures in Concrete

Farzin Asgharpour[1][0000-0003-3380-8359] and Khaled Hamed Marar[2][0000-0001-5650-2980]

[1] Eastern Mediterranean University, Civil Engineering Department, North Cyprus, Türkiye, farzin.asgharpour@emu.edu.tr
[2] Eastern Mediterranean University, Civil Engineering Department, North Cyprus, Türkiye, khaled.marar@emu.edu.tr

Abstract. Today today's world, according to the advance of technology especially in civil engineering and materials science significant progress in concrete has been witnessed in structures, highways, offshore structures, dams etc. Accelerators can be used in concrete to increase the rate of its early strength and facilitate faster setting and hardening. Rapid repair and retrofit of structures by using accelerating admixtures in the construction materials division, and also their effects on the physical properties and hydration in the last few decades, is desired and have been studied and taken into consideration. However, using the best accelerator admixtures and improving them is one of the favourite topics among researchers due to the construction need. In this paper, the most common admixtures which are incorporated in the concrete as an accelerator have been studied and their compressive strength, resistance against sulphate attack, water absorption, and modulus of rupture in different periods and dosages are reviewed. In this review paper, it needs to be mentioned that, by using different dosages of accelerators, increasing the compressive strength is not certain but it is witnessed that a significant improvement in water absorption, modulus of rupture and it can change the merits consideration of using accelerators in the construction. Hence, the use of accelerators should be carefully considered and applied in accordance with relevant standards to avoid negative effects on their long-term performance and high dosages of accelerators are particularly harmful for durability.

Keywords: Accelerator Admixture, Construction, Hydration.

1 Introduction

Concrete is a widely used building material, but its slow curing process and lower early-stage strength can pose challenges in construction projects. One solution to this issue is high early strength concrete (HESC), but it is often costly and not easily producible [1]. Another approach involves the use of concrete accelerators, which are chemical admixtures that expedite the curing process and reduce setting time. These accelerators affect the hydration process by altering the dehydration speed of concrete components, such as tricalcium silicate and tricalcium aluminate. Non-chloride accelerators, such as calcium formate, have also been explored as alternatives [2].

The use of accelerators is particularly critical when pumping concrete and improving structures, as it affects the early age of concrete [3]. One method of increasing cement strength involves reducing the water-to-cement ratio. However, this approach is not suitable for concrete pumping, which is commonly employed in high-rise buildings where water reduction is not feasible [4].

Accelerators play a vital role in altering the setting time and facilitating faster construction processes, repairs, and the use of concrete in low-temperature conditions [5]. They also contribute to the production of "green cement" and are beneficial in sprayed concrete technology [6],[7],[8].

In recent years, new techniques, and fields of research, such as additive manufacturing (AM) and supplementary cementitious materials (SCMs), have received significant attention [9]. They also contribute to the production of "green cement" and are beneficial in sprayed concrete technology [10]. Additionally, the adoption of supplementary cementitious materials (SCMs) has gained attention for reducing CO_2 emissions and improving construction processes [8],[11],[12].

SCMs, such as fly ash and blast furnace slag, can replace cement types 2 and 3, but they may increase setting time [10],[13]. The use of SCMs aligns with the global effort to reduce clinker consumption and its associated CO_2 emissions. These advancements in concrete technology and materials offer promising alternatives for sustainable and efficient construction practices [11],[12].

2 Classification of Accelerator Concrete

Accelerator concrete is a well-known additive admixture used for rapid construction or achieving early strength in concrete [14]. These accelerators can be categorized into two main groups: organic and non-organic compounds. Their primary function is to modify the setting time and promote hardening in concrete. Understanding the composition, action, and various applications of accelerators is crucial. Additionally, concerns about the environmental impact of cement production have prompted researchers to explore alternatives that are cost-effective, easier to produce, and possess superior durability and mechanical properties. Recent investigations have specifically focused on the use of non-chloride hardening accelerators, which have demonstrated significant enhancements in the durability and mechanical properties of Portland cement. These findings highlight how chemical admixtures can optimize the setting time, particularly during early strength development, and improve the overall durability of Portland cement by mitigating common cracking issues and preventing failures [15], [16], [17]. According to the type of accelerator used in the concrete, it can be classified into four different categories, such as:

2.1 Calcium Chloride Accelerator

Calcium chloride ($CaCl_2$) is an inorganic accelerator that has a significant impact on strength development at low temperatures. However, when using this type of accelerator, it is important to consider the potential negative effects by increase the

dosages of the accelerator, such as reduced durability, increased susceptibility to sulfate attack and freeze-thaw damage, as well as increased shrinkage [18].

2.2 Non-Chloride Accelerator

The non-chloride accelerator or Chloride-free is a viable alternative additive to calcium chloride in concrete. It offers notable benefits, including increased compressive strength and enhanced hydration, particularly in the initial days of the curing process [19]. It is important to emphasize that the non-chloride accelerator is commonly employed in chloride-sensitive environments or when the use of calcium chloride is prohibited because it may hurt the steel rebars and structures [20].

2.3 Alkali-Free Accelerator

Alkali-free accelerators are organic compounds used in concrete to accelerate setting and hardening. They alter the ionic equilibrium by consuming Ca^{2+} and SO_4^{-2} ions from the liquid phase, promoting early strength development. These accelerators provide an alternative method for rapid concrete curing without the risk of alkali-aggregate reactions or harmful gel formation. By modifying the chemistry of the concrete mixture, they speed up the setting process, allowing for faster construction and earlier structural loading. It is important to follow manufacturer guidelines to ensure proper usage and compatibility with the specific concrete application [21], [22].

2.4 Silicate- Based Accelerator

Unlike alkali-free accelerators, this type of additive admixture contains alkali silicates, such as sodium or potassium silicate. The advantages of using this kind of accelerator include increased early-age strength and fast pozzolanic reaction [23].

3 Methodology

3.1 Compressive Strength

The compressive strength test is a widely recognized mechanical test used to determine the maximum load a material can withstand before failure. For this study, both cubes and cylinders were considered as potential specimens for testing, with the load being gradually applied [24].

Standard cube dimensions of 150*150*150 mm were selected for the compressive strength tests. The tests were conducted at specific time intervals (3, 7, and 28 days) after incorporating Alccofine and non-chloride accelerators into the concrete. The chemical properties and characteristics of the accelerators were determined in accordance with the guidelines presented in IS: 516-1959. To ensure reliable results, four dosage levels were investigated, with three cubes allocated for testing the compressive strength at each dosage.

It is worth noting that the use of $Ca(NO_2)_2$ at varying dosages can potentially induce a corrosion reaction in reinforced or high-strength concrete. Additionally, an increase in carbonation of hydration can influence alkali carbonates, consequently affecting compressive strength by reducing it.

Based on the data presented in Fig. 1, the compressive strength values from seven different papers are compared, considering different dosages of $Ca(NO3)_2$ over a period ranging from 1 to 28 days. The results indicate that compressive strength generally increases over time. However, it is important to note that increasing the dosage of $Ca(NO_3)_2$ is not necessarily a guarantee of achieving the highest compressive strength in a shorter timeframe.

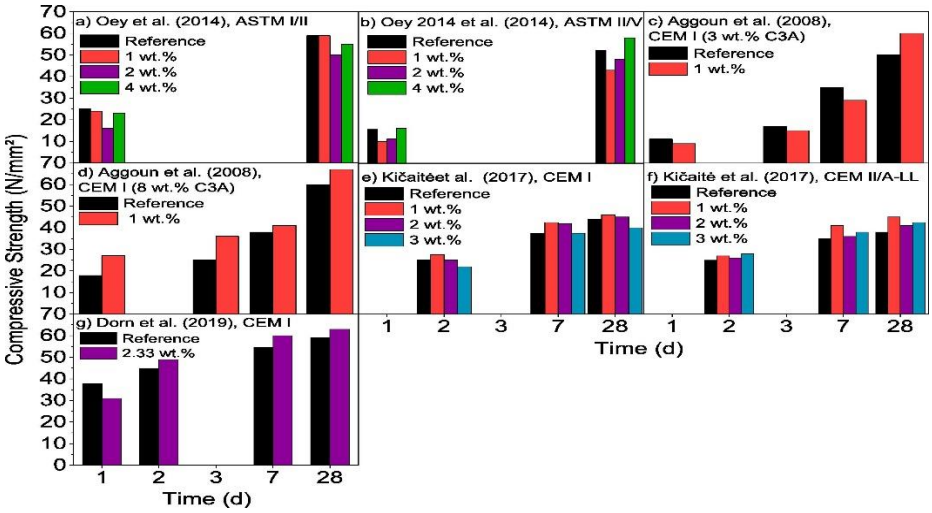

Fig. 1. Compressive strength development of cement mortar and concrete at different $Ca(NO_3)_2$ dosages [13]. a, b) [25]; c,d) [26]; e,f) [27]; g)[28].

Fig. 2 illustrated a study on the influence of alkali carbonates revealed that the addition of 4% Na2CO3 led to a remarkable 120% increase in compressive strength after two days [29]. However, it is crucial to consider that increased carbonation of hydration may impact the presence of alkali carbonates, potentially resulting in reduced high strength in later ages due to hydration with CaO.

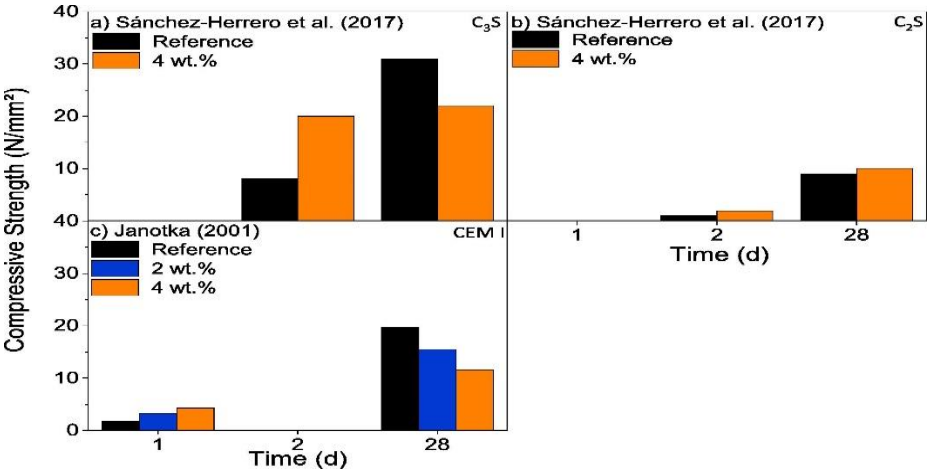

Fig 2. Compressive strength development of C3S, C2S, and OPC paste at different Na_2CO_3 dosages [13]. a, b) prisms of synthesized C3S and C2S paste [30]; C) [31].

3.2 Split Tensile Strength

This test is one of the most common and important tests that shows the extent and size of cracking in concrete samples. It is an indication that the concrete is weak, especially in terms of tensile strength.

Table 1. Split tensile strength while using non-chloride accelerator [32].

Accelerator content	Split tensile strength per N/mm^2		
%	7 Days	14 Days	28 Days
M20- 0	1.56	2.54	3.25
M20- 0.8	1.62	2.57	3.52
M20- 1	2.17	3.53	3.14
M20- 1.2	3.13	5.15	5.5
M25- 0	2.56	3.54	4.83
M25- 0.8	2.6	3.58	4.93
M25- 1	2.92	3.99	5.13
M25- 1.2	4.11	4.64	6.83

Based on the findings presented in Table 1, it has been reported that the utilization of non-chloride accelerators, coupled with an increase in dosage, leads to the attainment of the highest split tensile strength. Furthermore, it is noteworthy that M25 class concrete exhibits more favorable outcomes with prolonged curing periods.

By using Alccofine and non-chloride accelerators in concrete as accelerators, cylinder specimens of size 150*300 mm were used, and the code for this test was based on IS 5816-1999. Two different periods were chosen (7 and 28 days). For this test, the

cylinder was placed in the lengthwise direction, and then a load was applied to the sample until a crack was visible.

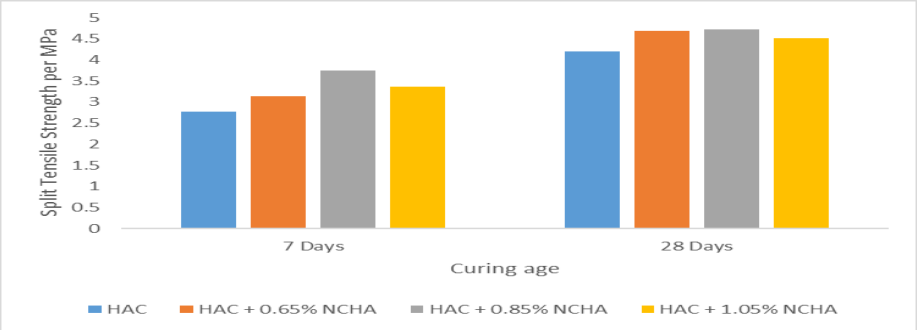

Fig. 3. Split tensile strength of Alccofine concrete with different proportion of NCHA. [1]

Based on the above figure (Fig. 3), it is concluded that the split tensile strength with different dosages of NCHA was compared at 7 and 28 days. As expected, the strength increases with time. However, it need to be mention that 0.85% of NCHA give the best strength after comparison between different dosages in both 7 and 28 days.

3.3 Water Absorption

The other common test which is very important is water absorption. The size of the cylinder sample used for this test was 150mm, and the test with Alccofine and non-chloride accelerators was investigated at 7 and 14 days. First, the samples were dried in a special drying room at 105 °C or 221°F, for one day and after this step, the cylinders were immersed in water at 23°C for two days.

Water absorption test is using for testing the durability of concrete, however, according to Fig.4 it is believed that after comparison the different dosages of accelerator, the water absorption is decreased.

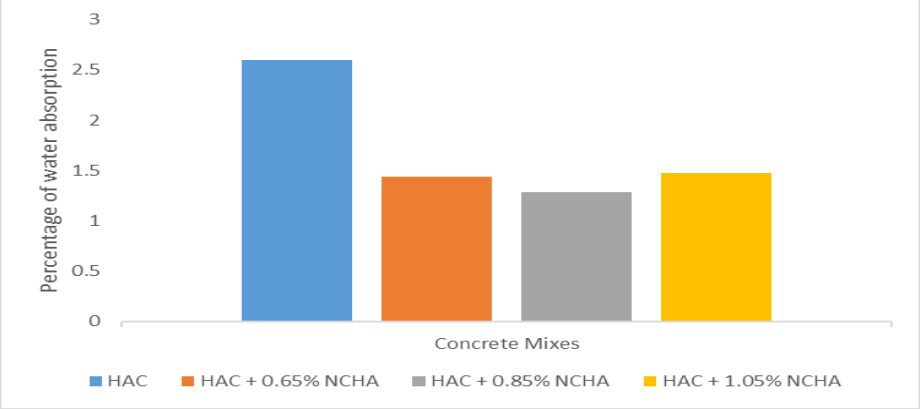

Fig. 4. Percentage of water absorption of Alccofine concrete with NCHA [1].

However, when formic acid is utilized as an accelerator concrete, the water absorption of different dosages (0%, 0.5%, 1.0%, 2.0%, and 3.0%) over a period of 60 minutes is recorded as following: 11.3%, 9.9%, 8.5%, 11.6% and 14.3% respectively [33].

Furthermore, while Alumino-silicate used in the concrete as an accelerator, how much we use more accelerator, it reduced the water absorption [34].

3.4 Modulus of Rupture

One of the other tests that has received attention in recent years is the modulus of rupture test, which measure the amount of load or force a sample can withstand before failure in bending. The modulus of rupture is also known as the maximum strength of the sample before failure, which indicates the flexibility of the sample before bending in the test. The machine used for the modulus of rapture test is shown on the page below.

Fig. 5, presents the modulus of rupture outcomes for concrete mixes with a water-binder ratio of 0.45, comparing the effects of including or excluding a non-chloride hardening accelerator (NCHA) at 7 and 28 days. The results demonstrate that the reference concrete exhibited lower modulus of rupture values compared to the concrete mixes with the same water-binder ratio. During the early stages, by increasing dosages of accelerator, displayed significant improvements in modulus of rupture, showing increases of 7.24%, 29.03%, and 26.66%, respectively, compared to the reference Alccofine concrete mix. However, at later stages, the modulus of rupture for mixes 0.65%, 0.85%, and 1% remained similar to that of the reference mix.

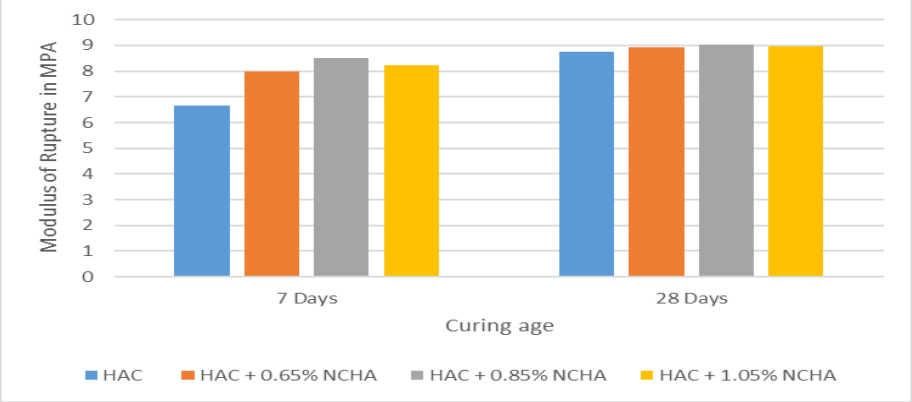

Fig. 5. Modulus of rupture measurements for Alccofine concrete with varying proportion of non-chloride hardening accelerator (NCHA) [1].

Additionally, it is reported that by using Alumino-silicate, the highest dosage of the accelerator results in the highest modulus of rupture [34].

4 Conclusion

Upon careful assessment and analysis of comparisons and review papers delving into the utilization of accelerators within concrete applications. Several compelling conclusions have emerged from this comprehensive body of research. Notably it has been determined that incorporating Alccofine accelerators into concrete does not wield a significant impact on its mechanical properties during the initial days regardless of varying mix proportions or accelerator dosages implemented. However insightful observations highlight a reduction in water absorption when Alccofine is employed as an accelerator in comparison with non-chloride accelerating agents. This improvement can be attributed to the minute particle size intrinsic to Alccofine, which promotes concrete compaction and enhances its overall strength.

Furthermore, it has been discerned that both Alccofine and non-chloride accelerators serve to enhance concretes' resistance against sulfate attack. This suggests that these accelerators possess the capability to confer extended durability upon concrete structures. Nevertheless, it should be acknowledged that the spraying or pumping of concrete infused with accelerators might result in a heightened deterioration rate due to sulfate attack. $CaCl_2$ presents itself as an economical accelerator choice for concrete applications; however, its employment has experienced a downturn in recent years due to concerns surrounding chloride induced corrosion in reinforcement bars. As a result, $CaCl_2$ is predominantly deployed in scenarios involving non reinforced concrete applications where concerns germane to chloride ions are negligible. Propelling innovation forward are seeding accelerators such as C S-H PCE nanocomposites, which have emerged as a groundbreaking strategy for enhancing cements' setting time and early strength development. These materials exhibit remarkable potential in optimizing

hydration processes within an essential timeframe spanning from 6 hours up until 24 hours without undermining ultimate structural strength. Moreover, they offer benefits such as decreased superplasticizer dosages and enhanced workability.

Through the utilization of Alumino-silicate, it is observed that, after 1 day of air curing, the application of higher dosages of the accelerator results in the highest values for the module of rupture, module of elasticity, bulk density, and lowest water absorption.

In summary, this review paper indicates that the use of accelerators in concrete can have varying effects on different properties, such as compressive strength, resistance to sulfate attack, split tensile strength, water absorption and modulus of rapture. Each type of accelerator has its advantages and considerations, and their application should be carefully evaluated based on the specific requirements of the construction project.

References

1. P. N. Reddy and J. A. Naqash, “Development of high early strength in concrete incorporating alccofine and non-chloride accelerator,” SN Appl Sci, vol. 1, no. 7, 2019, doi: 10.1007/s42452-019-0790-z.
2. J. Nilimaa and V. Zhaka, “An Overview of Smart Materials and Technologies for Concrete Construction in Cold Weather,” Eng, vol. 4, no. 2, pp. 1550–1580, May 2023, doi: 10.3390/eng4020089.
3. Y. Tao, A. V. Rahul, K. Lesage, Y. Yuan, K. Van Tittelboom, and G. De Schutter, “Stiffening control of cement-based materials using accelerators in inline mixing processes: Possibilities and challenges,” Cem Concr Compos, vol. 119, May 2021, doi: 10.1016/j.cemconcomp.2021.103972.
4. Rahmani, M. Kazem. Sharbatdar, and M. H.A.Beygi, “A comprehensive investigation into the effect of water to cement ratios and cement contents on the physical and mechanical properties of Roller Compacted Concrete Pavement (RCCP),” Constr Build Mater, vol. 253, p. 119177, Aug. 2020, doi: 10.1016/j.conbuildmat.2020.119177.
5. P. C. Aïtcin, “Accelerators,” Science and Technology of Concrete Admixtures, pp. 405–413, Jan. 2016, doi: 10.1016/B978-0-08-100693-1.00019-9.
6. V. Kanchanason and J. Plank, “Effectiveness of a calcium silicate hydrate – Polycarboxylate ether (C-S-H–PCE) nanocomposite on early strength development of fly ash cement,” Constr Build Mater, vol. 169, pp. 20–27, Apr. 2018, doi: 10.1016/J.CONBUILDMAT.2018.01.053.
7. V. Kanchanason and J. Plank, “Effect of calcium silicate hydrate – polycarboxylate ether (C-S-H–PCE) nanocomposite as accelerating admixture on early strength enhancement of slag and calcined clay blended cements,” Cem Concr Res, vol. 119, pp. 44–50, May 2019, doi: 10.1016/J.CEMCONRES.2019.01.007.
8. G. N. L. J. Z. F.E. Townsend, “ASAPositionStatement_Underground_1”.
9. D. Marchon, S. Kawashima, H. Bessaies-Bey, S. Mantellato, and S. Ng, “Hydration and rheology control of concrete for digital fabrication: Potential admixtures and cement chemistry,” Cem Concr Res, vol. 112, pp. 96–110, Oct. 2018, doi: 10.1016/J.CEMCONRES.2018.05.014.
10. K. L. Scrivener, V. M. John, and E. M. Gartner, “Eco-efficient cements: Potential economically viable solutions for a low-CO2 cement-based materials industry,” Cem Concr Res, vol. 114, pp. 2–26, Dec. 2018, doi: 10.1016/j.cemconres.2018.03.015.

11. Han, K. Wang, Y. Wang, and J. Shi, "Study of aluminum sulfate and anhydrite on cement hydration process," Materials and Structures/Materiaux et Constructions, vol. 49, no. 4, pp. 1105–1114, Apr. 2016, doi: 10.1617/s11527-015-0561-2.
12. Hoang, H. Justnes, and M. Geiker, "Early age strength increase of fly ash blended cement by a ternary hardening accelerating admixture," Cem Concr Res, vol. 81, pp. 59–69, Mar. 2016, doi: 10.1016/J.CEMCONRES.2015.11.004.
13. T. Dorn, O. Blask, and D. Stephan, "Acceleration of cement hydration – A review of the working mechanisms, effects on setting time, and compressive strength development of accelerating admixtures," Construction and Building Materials, vol. 323. Elsevier Ltd, Mar. 14, 2022. doi: 10.1016/j.conbuildmat.2022.126554.
14. W. C. Wang, H. T. H. Duong, and C. H. Zhang, "Influence of accelerating admixtures on high early strength cement performance using heat curing method," Case Studies in Construction Materials, vol. 18, p. e01746, Jul. 2023, doi: 10.1016/J.CSCM.2022.E01746.
15. Narender Reddy, "A COMPREHENSIVE OVERVIEW ON PERFORMANCE OF NANO SILICA CONCRETE Investigation on Metakaolin and Silicafume Incorporated Concrete under Elevated Temperature View project AN INSIGHT INTO TEMPERATURE CHARACTERSTICS OF TERNARY BLENDED CONCRETE WITH PERLITE POWDER View project A COMPREHENSIVE OVERVIEW ON PERFORMANCE OF NANO SILICA CONCRETE," 2017. [Online]. Available: www.ijptonline.com
16. T. Narender Reddy A, "Behavior of ternary blended concrete under compression. Int J Civil Eng Technol 8(4):2089–2097," Civil Eng Tech, 2017.
17. S. D. S. S. Jindal BB, "Suitability of ambient cured alccofine added low-calcium fly ash-based geopolymer concrete. Ind J Sci Technol 10(12)," pp. 1–10, 2017.
18. V. S. Ramachandran, "Calcium Chloride in Concrete: Science and Technology," 1976.
19. Richardson, "Strength development of plain concrete compared to concrete with a non-chloride accelerating admixture," Structural Survey, vol. 25, no. 5, pp. 418–423, 2007, doi: 10.1108/02630800710838455.
20. T. Meagher, N. Shanahan, D. Buidens, K. A. Riding, and A. Zayed, "Effects of chloride and chloride-free accelerators combined with typical admixtures on the early-age cracking risk of concrete repair slabs," Constr Build Mater, vol. 94, pp. 270–279, Sep. 2015, doi: 10.1016/j.conbuildmat.2015.07.003.
21. P. Salvador, S. H. P. Cavalaro, I. Segura, A. D. Figueiredo, and J. Pérez, "Early age hydration of cement pastes with alkaline and alkali-free accelerators for sprayed concrete," Constr Build Mater, vol. 111, pp. 386–398, May 2016, doi: 10.1016/j.conbuildmat.2016.02.101.
22. Paglia, F. Wombacher, and H. Böhni, "The influence of alkali-free and alkaline shotcrete accelerators within cement systems," Cem Concr Res, vol. 31, no. 6, pp. 913–918, May 2001, doi: 10.1016/S0008-8846(01)00509-9.
23. K.-M. Kim, Y.-S. Heo, S.-P. Kang, and J. Lee, "Effect of sodium silicate- and ethyl silicate-based nano-silica on pore structure of cement composites," Cem Concr Compos, vol. 49, pp. 84–91, May 2014, doi: 10.1016/j.cemconcomp.2013.12.009.
24. N. Shanahan, A. Sedaghat, and A. Zayed, "Effect of cement mineralogy on the effectiveness of chloride-based accelerator," Cem Concr Compos, vol. 73, pp. 226–234, Oct. 2016, doi: 10.1016/J.CEMCONCOMP.2016.07.015.
25. Oey et al., "Comparison of Ca(NO3)2 and CaCl2 Admixtures on Reaction, Setting, and Strength Evolutions in Plain and Blended Cementing Formulations," Journal of Materials in Civil Engineering, vol. 27, no. 10, Oct. 2015, doi: 10.1061/(asce)mt.1943-5533.0001240.
26. S. Aggoun, M. Cheikh-Zouaoui, N. Chikh, and R. Duval, "Effect of some admixtures on the setting time and strength evolution of cement pastes at early ages," Constr Build Mater, vol. 22, no. 2, pp. 106–110, Feb. 2008, doi: 10.1016/J.CONBUILDMAT.2006.05.043.
27. Kičaitė, I. Pundienė, and G. Skripkiūnas, "The influence of calcium nitrate on setting and hardening rate of Portland cement concrete at different temperatures," IOP Conf Ser Mater Sci Eng, vol. 251, p. 012017, Oct. 2017, doi: 10.1088/1757-899X/251/1/012017.

28. T. Dorn, T. Hirsch, and D. Stephan, “Study on the Influence of Accelerators on the Hydration of Portland Cement and Their Applicability in 3D Printing,” 2020, pp. 382–390. doi: 10.1007/978-3-030-22566-7_44.
29. M. J. Sánchez-Herrero, A. Fernández-Jiménez, and A. Palomo, “C3S and C2S hydration in the presence of Na2CO3 and Na2SO4,” Journal of the American Ceramic Society, vol. 100, no. 7, pp. 3188–3198, Jul. 2017, doi: 10.1111/jace.14855.
30. M. J. Sánchez-Herrero, A. Fernández-Jiménez, and A. Palomo, “C3S and C2S hydration in the presence of Na2CO3 and Na2SO4,” Journal of the American Ceramic Society, vol. 100, no. 7, pp. 3188–3198, Jul. 2017, doi: 10.1111/jace.14855.
31. Janotka, “HYDRATION OF THE CEMENT PASTE WITH Na2CO3 ADDITION,” 2000.
32. P. Kathirvel, “Influence of Non Chloride Accelerator in Cement Concrete,” 2014. [Online]. Available: www.irjes.com
33. Y. Xiong, Z. Hu, Z. Jia, C. Liu, L. Ma, and Z. Liu, “Effect of formic acid as an accelerator on foam-stability, compressive strength, and pore size distribution of foam concrete,” Journal of Building Engineering, vol. 66, p. 105923, May 2023, doi: 10.1016/j.jobe.2023.105923.
34. P. CHAKARTNARODOM, P. SONPRASARN, S. POLSILAPA, N. KONGKAJUN, E. LAITILA, and W. PRAKAYPAN, “The influence of water-cement ratios and alumino-silicate based accelerator on the properties of fiber-reinforced cement composites,” Journal of Metals, Materials and Minerals, vol. 33, no. 2, pp. 75–80, Jun. 2023, doi: 10.55713/jmmm.v33i2.1633.

Influence of Barite Sand on The Strength on Self-Compacting Concrete with Fly Ash

Ksenija Janković[1][orcid ID 0000-0003-3744-3799], Marko Stojanović[1][orcid ID 0000-0003-1804-5138], Dragan Bojović[1][orcid ID 0000-0002-4900-6177], Anja Terzić[1][orcid ID 0000-0002-4762-7404], and Srboljub Stanković[2][orcid ID 0000-0001-6482-5448]

[1] Institute for Materials Testing, Belgrade, Bulevar vojvode Misica 43, 11000 Belgrade, Serbia
ksenija.jankovic@institutims.rs
[2] Vinča Institute of Nuclear Sciences, University of Belgrade, National Institute of the Republic of Serbia, Mike Petrovića Alasa 12-14, Vinča, 11000 Belgrade, Serbia

Abstract. This study compared the performance of self-compacting concrete (SCC) based on fly ash addition and limestone filler. A SCC prepared with Portland cement, river sand, and limestone filler was used as a reference sample. Additional experimental self-compacting concretes with different types of fine aggregates, fillers, and special additives for increasing freeze-thaw resistance were prepared and optimized. The correlation between mix design, i.e., percentage of barite sand and additives, on properties of hardened SCC (compressive and flexural strengths), were investigated and discussed.

Keywords: Mineral additives, Limestone filler, Barite, Strength

1 Introduction

The use of secondary raw waste-based materials such as recycled aggregate (i.e., crushed concrete), fly ash, various forms of slag, foundry sand, and so on is an appropriate modern solution for environmental difficulties as well as resource depletion challenges. Large quantities of waste and recycled materials available at reasonable prices all around the world provide an excellent answer for decreasing the carbon footprint of concrete. These compounds also serve as a binder for the stabilization of contaminated waste materials [1, 2].

Traditionally, the problem of industrial waste disposal has been tackled by the construction of planned landfills. However, landfills take up enormous expanses of land, and trash removal is usually complicated and costly. The use of industrial byproducts and waste materials such as fly ash in the construction of concrete overcomes the problem of their disposal, thus instead of generating new landfills, new ecological materials are developed [3, 4].

Cement is very expensive and energy-intensive component of concrete. Cement production accounts for 2.5 % of global CO_2 emissions from industrial capacities. One solution to this problem is the use of alternative secondary raw materials, such as fly ash, which is a byproduct of numerous manufacturing processes. Coal combustion residues (fly ash and bottom ash) are generated when coal is ignited in power plants.

Fly ash is a lightweight powdery raw material that is collected directly from a filter. Fly ash is composed primarily of spherical hollow particles. Coal ash comes in a variety of hues and features, depending on the type of coal, the geolocation of the deposit, the furnace structure, and the combustion procedure utilized in the thermal power plant [5].

When compared to ordinary vibrated concrete, self-compacting concrete (SCC) has a higher flow rate. High flowability is achieved by using a high proportion of extra fine mineral fillers in the mix design [6]. Given its availability and affordable cost, fly ash is one of the most frequently used mineral fillers in SCC. The components and their ratios, as well as the type and particle size of the filler, as well as the method of casting, production, and curing conditions of SCC, all have a considerable impact on the qualities of fresh and hardened concrete. The effect of fly ash on the properties of cementitious materials is defined as a combination of plasticizing (because to its spherical shape in tiny part sizes), micro-aggregate (related to its ability to infill), and active (thanks to its pozzolanic ability). This alters the properties of hardened SCC (strength, Young's modulus, water absorption, permeability, and so on) [7-9].

Heavyweight concrete used for radiation shielding in hospitals and/or nuclear facilities is usually made with barite aggregate. Concrete with barite powder as a sand substitute in the range of 0 % to 25 % lowered compressive strength at 28 days by only 10 %, elastic modulus at one year by 20 %, and tensile strength by up to 50 % [10]. The mixing method affects the grading curve of barite more than other aggregates. This changed the characteristics of concrete, increasing workability while decreasing compressive strength and modulus of elasticity [11]. Concrete with magnetite fine aggregate showed improved physico-mechanical characteristics than concrete based on barite and goethite. The compressive strength of high-performance heavy-density concrete including magnetite as fine aggregate was 23 % greater than that of sand-containing concrete [12-13]. The basic properties of regular concrete and heavy-weight concrete with barite were investigated in the context of their usage for gamma radiation shielding [14-16].

The purpose of this research is to assess the effect of filler (fly ash or limestone) and fine aggregate type (quartz, barite, or a combination of the two) on the properties of SCC.

2 Experimental Work

2.1 The Composition of Concrete

Portland cement CEM I 42.5R (specific density: 3100 kg/m^3) was utilized to produce self-compacting concrete. A considerable number of small particles are required to produce a self-compacting concrete mixture. Thereby, as fillers, two mineral additives were employed in this case. In particular, in the mix design of the referent concrete, limestone was used, but fly ash was used in the experimental SCC samples. Fig. 1 shows the chemical analyses of aggregates and mineral fillers. Specific densities for river aggregate and barite sand were 2610 kg/m^3 and 3770 kg/m^3, respectively. Fig. 2 illustrates the grain-size analysis of the fly ash and limestone. Properties of the milled fly ash sample are as follows: bulk density - 2310 kg/m^3, specific surface area –

7990 cm^2/g, pozzolanic activity/ flexural strength - 4.9 MPa, and pozzolanic activity/ compressive strength -14.1 MPa.

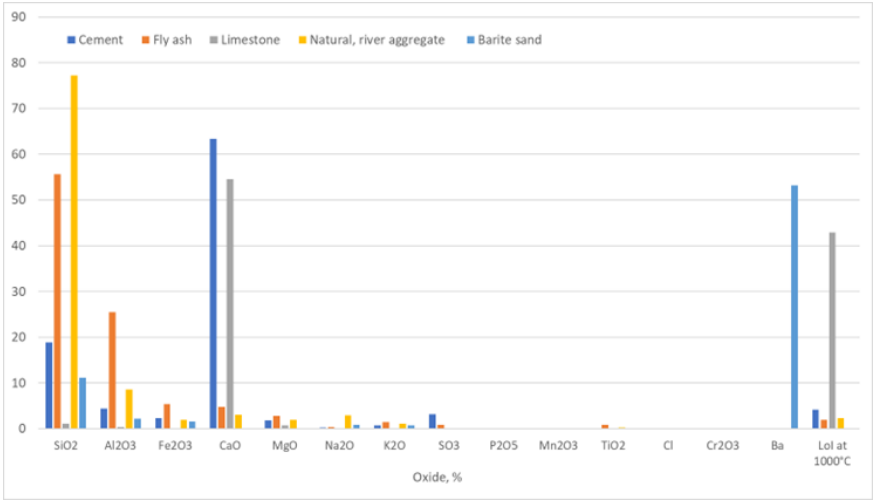

Fig. 1. Chemical compositions of SCC resource materials.

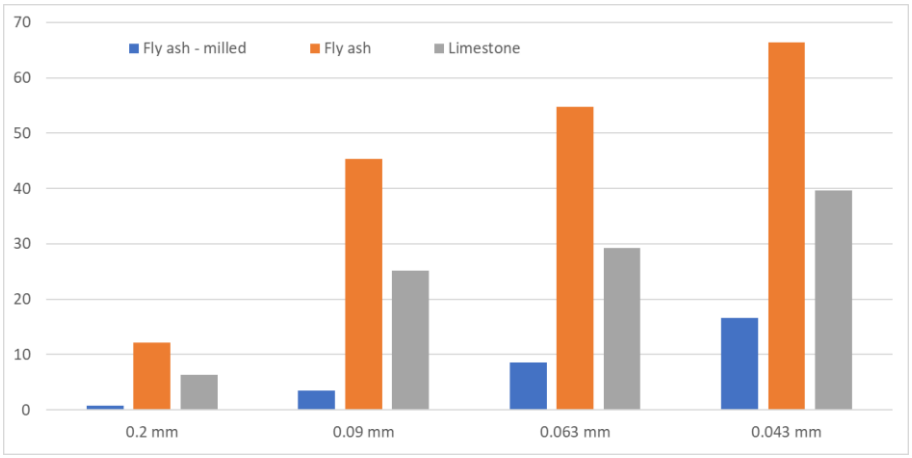

Fig. 2. Grain-size analysis of the fly ash and limestone.

In the mix-design of SCC-s, natural, separated river aggregate with 0/4, 4/8, and 8/16 mm fractions, barite sand, and combination (barite: river sand = 75:25 by volume) were employed. The percentage share of aggregate per fraction was 45 % for 0/4 mm, 20 % for 4/8 mm, and 35 % for 8/16 mm. Fig. 3. depicts a grain-size study of aggregate mixtures.

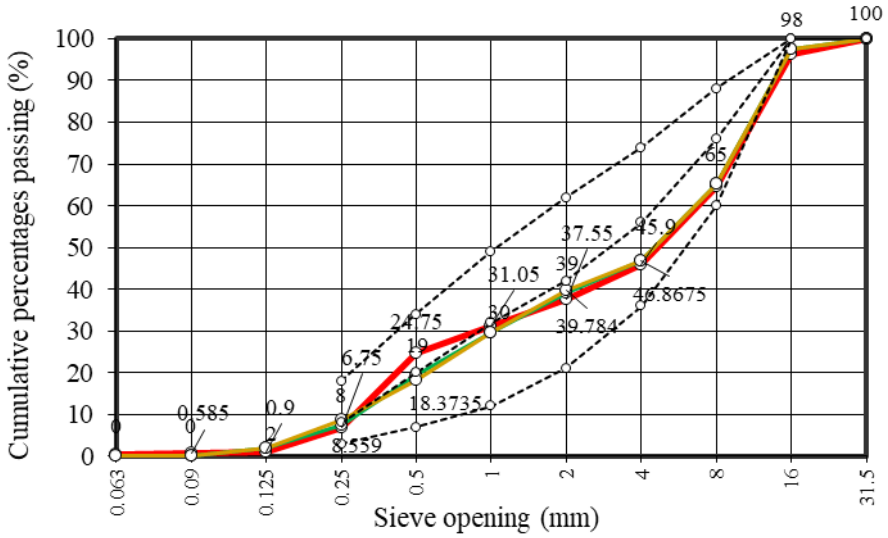

Fig. 3. Grading curves of aggregate mixtures for SCC samples (red mixture – natural aggregate; green mixture – 75% of barite and 25% of natural aggregate; and yellow mixture – barite).

2.2 Concrete Mixture

Five three-fraction self-compacting concrete mixtures were prepared for this experiment (Figure 4). Bulk densities of P301, P35, P37, P39, and P41 were 2383, 2739, 2743, 2606, and 2611 kg/m^3 respectively.

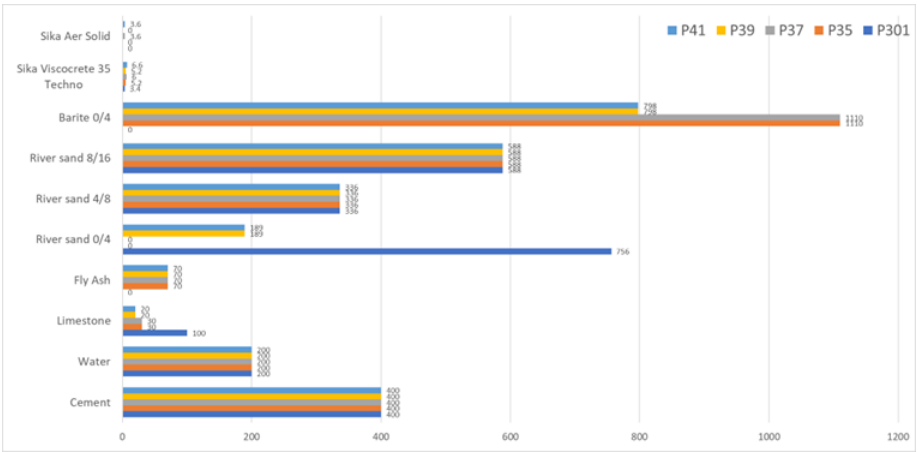

Fig. 4. Compositions of self-compacting concretes (values are given in kg/m^3).

Apart from the previously mentioned cement (CEM I 42.5R), mineral additives - limestone and fly ash, natural river separated aggregate (0/4, 4/8, and 8/16mm fractions), barite sand, and combination of barite and river sand, superplasticizer (Sika Viscocrete 35 Techno) and tap water were used as admixtures. In both combinations, a particular component (Sika Aer Solid) is used to boost freeze-thaw resistance. According to EN 206 requirements, fresh concrete was developed to meet the minimum needed qualities of self-compacting concrete. P301 reference concrete was made with limestone as a filler and natural river aggregate.

The combinations are intended to meet the following requirements: slump-flow 650 50 mm, t500 2s, V-funnel 9 - 25 s, L-box with 3 H2/H1 080 bars. All concrete kinds were created with w/c = 0.50. A sufficient amount of superplasticizer was applied to achieve the desired SCC characteristics in the fresh state.

3 Results and Discussion

3.1 Fresh Concrete Properties

Density, fluidity - slump flow test according to EN 12350-8, viscosity - t500 test according to EN 12350-8, V funnel test according to EN 12350-9, and the ability of the passage between the reinforcement - L box test according to EN 12350-10 were conveyed for the fresh concrete tests. The test results for concrete in the fresh state are shown in Fig. 5 and 6.

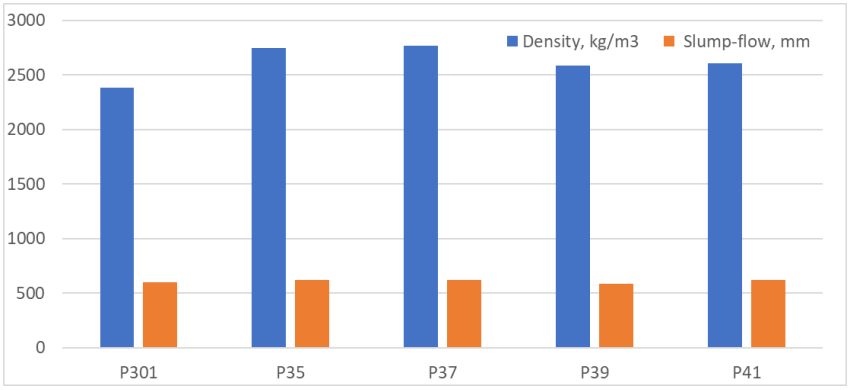

Fig. 5. Density and slump flow of fresh SCC samples.

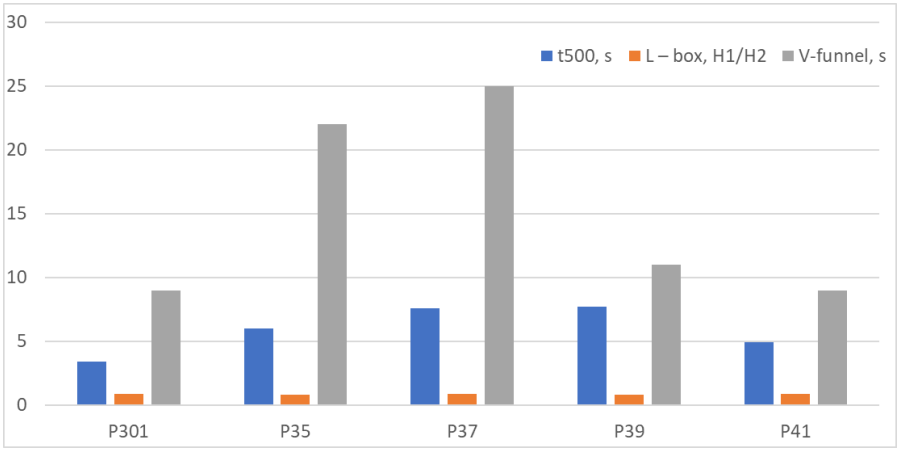

Fig. 6. Properties (T500, L-box, V-funnel) of SCC samples.

The slump-flow test, which is regarded the initial key characteristic of SCC, was employed to control the flowability of the mixture. The spreading measures of all concrete meet the SF1 class specifications, ranging from 590 to 620 mm.

V-the funnel is an experimental test that is used to determine the viscosity of a mixture. All concrete samples belonged to the VF2 category. The measured passing time ranges from 9 to 25 seconds. Segregation and water accumulation at the surface were not detected in any of the fresh concrete combinations examined.

The T500 property is defined as the time it takes for a fresh concrete slump to spread to the limit diameter of 500 mm. This property of fresh concrete is typically assessed during the slump-flow test. It denotes a specific approval of the viscosity of the combination. Concrete mixture t500 values ranged from 3.4 to 7.7 s. Intervals longer than 2 seconds were measured, and all tested mixes were classified as VS2.

The L-box test is used to determine the third key attribute of SCC, which is the ability of the mixture to move between reinforcing bars without being blocked. The height ratio of the concrete mixture at the ends of the L-box, which must be at least 0.80, was met by all mixtures. The mentioned combinations also met testing performance standards for their flow through three reinforcing bars, which is a significant criterion for densely reinforced constructions. As a result, all concrete is classified as PL2. The test results ranged from 0.80 to 0.88. The passage of aggregate grains between reinforcement bars was not blocked in any of the studies.

The preparation of the SCC mixture with fly ash and barite aggregate required more superplasticizer than the referent concrete for the same consistency class.

3.2 Compressive Strength

Concrete was compacted without vibration in metal cube-shaped molds with an edge length of d = 150 mm. Following that, the samples were cured in water at a temperature of 20 °C before being tested in line with the SRPS EN 12390-2 standard.

The compressive strength of concrete was tested at the ages of 2, 7, 28, and 56 days using the SRPS EN 12390-3 standard. The flexural strength of concrete was tested at 7, 28, and 56 days according to SRPS EN 12390-5. The hardened concrete's bulk density was determined using the SRPS EN 12390-7 standard. The bulk densities obtained ranged from 2320 to 2720 kg/m3. The results are shown in Fig. 7. and 8.

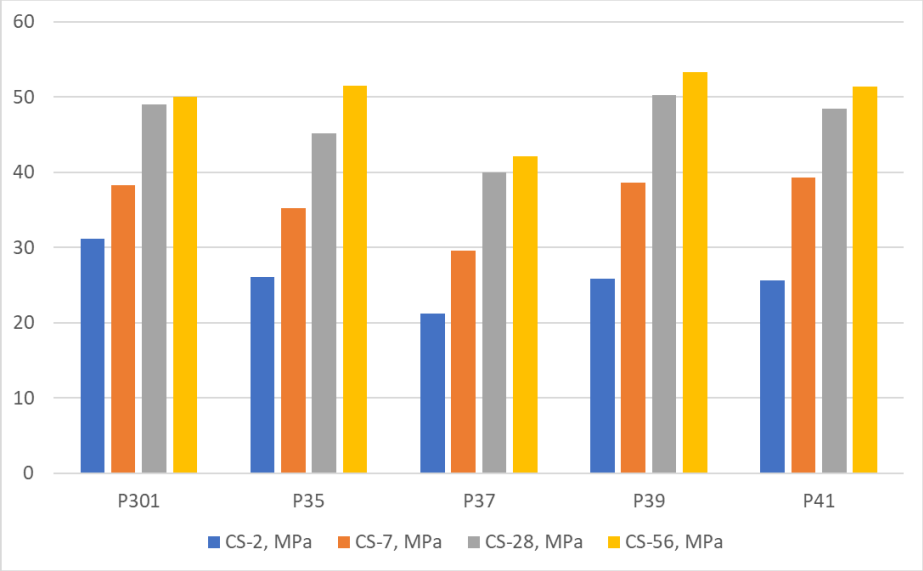

Fig. 7. Test results for concrete compressive strengths (CS) measured on cubic samples (d=150 mm).

Concretes made with the same aggregate and filler, but with Sika Aer Solid added, have slightly different strengths than concretes made with a combination of river and barite fine aggregate (P41 and P39). At 2 days, the strengths of concrete containing 19% barite sand (P37) began to decline. After 7 days of curing, the same thing happened to P35 concrete containing 16% barite sand.

At the age of 28 days, concrete samples made with barite sand had compressive strengths that were 10 to 22% lower than concrete made with river sand (reference concrete). Concrete with fly ash demonstrated a considerable drop in compressive strength compared to reference concrete with limestone at 2 days, which can be explained by differences in the pozzolanic activity of different fillers.

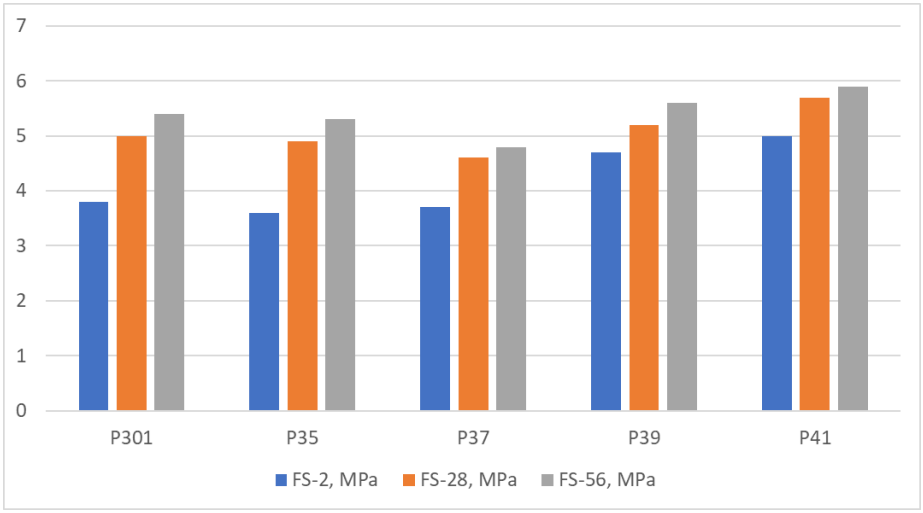

Fig. 8. Test results for concrete flexural strengths (FS) measured on cubic samples (d=150 mm)

4 Conclusion

Fly ash was employed successfully in the production of self-compacting concretes. All mixtures displayed SF1 flowability. All concrete samples belong to the VF2 viscosity class. All concrete mixtures are classified as VS2 based on t500 values. All concrete types are classified as PL2, because all mixtures satisfied the criteria for the height ratio of the mixture at the ends of the L-box. a larger quantity of superplasticizer was required for the production of the SCC in combination with Sika Aer Solid for the same consistency class. SCC with barite sand exhibits less strength than river aggregate concrete (reference concrete). The same tendency was also found at 2 and 7 days.

Acknowledgments
This investigation is financially supported by the Ministry of Science, Technological Development and Innovation of the Republic of Serbia (Contract No.: 451-03-47/2023-01/ 200012) and 2021-2023 bilateral cooperation project between Turkey and Serbia: "Tailor made self-compacting heavyweight concrete with waste materials".

References

1. Y.S. Feng, S.J. Zhou, A. Zhou, W. Xia, J. Li, S. Wang, Y. Du, Reuse of a contaminated soil stabilized by a low-carbon binder as roadway subgrade material and mechanical performance evaluation, Engineering Geology 303 (2022).
2. R. Chen, G. Cai, X. Dong, S. Pu, X. Dai, W. Duan, Green utilization of modified biomass by-product rice husk ash: A novel eco-friendly binder for stabilizing waste clay as road material, Journal of Cleaner Production 376 (2022) 134303.

3. C. Zhou, Z. Gong, J. Hu, A. Cao, H. Liang, A cost-benefit analysis of landfill mining and material recycling in China, Waste Management 35 (2015) 191-198.
4. Y. Zhao, L. Song, R. Huang, X. Li, Recycling of Aged Refuse from a Closed Landfill, Waste Management & Research 25(2) (2007) 130-8.
5. S. Alterary, N. H. Marei, Fly ash properties, characterization, and applications: A review, Journal of King Saud University - Science 33:6 (2021) 101536.
6. C. Shi et al., A review on mixture design methods for self-compacting concrete, Constr. Build. Mater. 84 (2015) 387–398.
7. P.L. Domone, A review of the hardened mechanical properties of self-compacting concrete, Cem. Concr. Compos. 29 (2007) 1–12.
8. Z. Zhang, S. Qian, H. Ma, Investigating mechanical properties and self-healing behavior of micro-cracked ECC with different volume of fly ash, Construction and Building Materials 52 (2014) 17-23.
9. EFNARC, ERMCO, EFCA, CEMBUREAU, bibm: The European Guidelines for SCC:Specification, Production and Use; May 2005.
10. K. Saidani, L. Ajam, M. Ouezdou, Barite powder as sand substitution in concrete: Effect on some mechanical properties, Constr Build Mater 95 (2015) 287–295.
11. M.A. Gonzalez-Ortega, S. Cavalaro, A. Aguado, Influence of barite aggregate friability on mixing process and mechanical properties of concrete. Constr Build Mater 74 (2015) 169–175
12. A.S. Ouda, Development of high – performance heavy density concrete using different aggregates for gamma - ray shielding. HBRC Journal (2014) http://dx.doi.org/10.1016/j.hbrcj.2014.06.010
13. A. S. Ouda, Development of high-performance heavy density concrete using different aggregates for gamma-ray shielding, Progress in Nuclear Energy 79 (2015) 48-55.
14. I. Ahmad, K. Shahzada, M. Imran et al., Densification of Concrete using Barite as Fine Aggregate and its Effect on Concrete Mechanical and Radiation Shielding Properties, Journal of Engineering Research 7(4) (2019) 81-95.
15. I. Akkurt, C. Basyigit, S. Kilincarslan, B. Mavi, A. Akkurt, Radiation shielding of concretes containing different aggregates. Cem Concr Comp 28 (2006) 153–157.
16. I. Akkurt, C. Basyigit, S. Kilincarslan, B. Mavi, A. Akkurt, The shielding of gamma – rays by concretes produced with barite, Prog Nucl Energy 46 (1) (2005) 1-11.

Development of Low-Carbon Oxalate Cement Using Copper Slag

Baki Aykut Bilginer[1], Sinan T. Erdoğan[2]

[1]Research Assistant, Materials of Construction Laboratory, Department of Civil Engineering, Middle East Technical University, Ankara, Turkey
[2]Professor, Materials of Construction Laboratory, Department of Civil Engineering, Middle East Technical University, Ankara, Turkey, aykutb@metu.edu.tr

Abstract. The high carbon footprint and energy consumption associated with the production of Portland cement poses a threat to the environment, contributing to climate change and global warming. Various low-carbon and low-energy alternative binders have been proposed in recent years, each with its own economical or technical advantages and disadvantages. Accelerated carbon sequestration into construction materials has also been proposed but this method is mostly suitable for precast applications due to the curing chamber used. Magnesium oxalate (MgOx) cement, a recently proposed alternative binder, can be made at room temperature using oxalic acid salts and calcined magnesia. Since oxalic acid can even be produced from captured CO_2, oxalate cements have the potential to be carbon neutral or even carbon negative. However, this goal is hard to achieve using calcined magnesia, due to the carbon emissions related with the decarbonation of magnesia and high-temperature calcination. This study evaluated the effect of partially replacing calcined magnesia with industrial wastes on the mineralogy and microstructure of MgOx. It is shown that environmentally and economically preferable cements can be made without sacrificing mechanical properties, through the formation of calcium oxalate and iron oxalate minerals.

Keywords: Magnesium; Oxalate Cement; Carbon; Sustainable Binder.

1 Introduction

Concern over the impact of carbon emissions on the global climate has increased in recent years. Accounting for almost 8 % of the total anthropogenic carbon emissions, the construction industry is under scrutiny by local and international authorities [1]. Therefore, it is vital to alleviate this environmental threat as much as possible. One way to decarbonize the construction industry is to replace portland cement systems with lower-carbon alternatives. There exist some alternative binders such as alkali-activated materials and low-calcium cements [2-5]. These alternatives are not feasible since they are not carbon-neutral or negative, or require higher-than-room temperature curing [6-8]. Recent studies focus on proposing an alternative carbon-neutral/negative binder with comparable mechanical properties to PC. Similar to the well-known magnesium phosphate cement (MPC) [9-12], magnesium oxalate cement (MgOx) has been

presented as a carbon-neutral/negative binder that can yield comparable mechanical and physical properties to PC-based materials [13-16]. MgOx is produced with calcined magnesia and an intermediate oxalic acid salt (obtained by reacting oxalic acid with fly ash, termed FAOx). Although this system yields products with comparable mechanical properties to ordinary portland cement (OPC), the use of calcined magnesia decreases its effectiveness based on energy consumption and carbon emission [13]. Hence, the main focus has been finding alternative alkaline materials to replace calcined magnesia. Ground granulated blast furnace slag was used as an alternative alkaline powder instead of calcined magnesia [17]. This alternative alkaline powder was tested for micro/macro level properties. Although this replacement yields promising outcomes concerning strength development and carbon footprint, its water resistance is significantly lower than the magnesium oxide counterparts. Therefore, in addition to being feasible in terms of sustainability and mechanical properties, the proposed alternative materials should also be effective in terms of durability. This study presents copper slag as the recent addition to alternative alkaline materials for oxalate cement production. Copper slag oxalate cement (CSOx) and magnesium oxalate cement (MgOx) were produced. Setting time, pH measurement, mineralogical investigation, strength development, and water resistance tests were performed.

2 Materials and Methods

2.1 Materials

Low-grade magnesia (MgO) was purchased in powder form. As this powder dissolves too quickly in an acidic solution, it was calcined for 1 h at 1500 °C to obtain calcined magnesia (MgO1500) [18]. After calcination, the hard mass obtained was ground to a powder. Copper slag (CS) was received in crushed rock form and milled to powder. Fly ash (FA) was obtained from the Afşin-Elbistan Thermal Power Plant in Turkey. Technical grade oxalic acid dihydrate (OxAc) was purchased from Balmumcu Chemical Industries in Ankara, Turkey. The oxide compositions of the main ingredients (low-grade magnesia, MgO1500, CS, and FA) determined using semi-quantitative X-ray fluorescence spectrometry (XRF, Rigaku ZSX Primus), are provided in Table 1.

Table 1. Oxide composition and density of the main ingredients

Oxide	Mass %			
	Low-grade MgO	MgO1500	FA	CS
MgO	81.30	82.80	2.26	6.75
SiO_2	9.35	10.60	40.09	18.9
Al_2O_3	0.06	0.08	16.24	6.87
Fe_2O_3	0.60	0.72	7.21	37.1
CaO	1.74	1.85	21.24	10.9
CO_2	6.89	3.82	-	-
NiO	0.12	0.13	-	-
K_2O	-	-	1.33	0.38
TiO_2	-	-	0.77	0.34
P_2O_5	-	-	0.40	0.58
SO_3	-	-	6.71	1.72
MnO	-	-	-	2.69
Density (g/cm^3)	3.10	3.40	2.00	4.00
Blaine's Fineness (cm^2/g)	10000	2000	3300	3000

2.2 Methods

This section presents certain tests to characterize oxalate cements produced.

Setting Time

Setting times of oxalate cement pastes are determined according to ASTM C191 [19] with small modifications. Water-to-binder ratio (W/B) is selected as 0.35 for all the mixtures. Mixing is done by hand using a scraper in two steps. Firstly, FAOx is mixed with water. Secondly, the alkaline powder is introduced and mixed to obtain a fresh paste. This freshly mixed paste is placed into the cylindrical rings with an inner diameter of 40 mm and a height of 40 mm. The measurement is made using a Vicat needle and penetration distance vs. time curves are obtained.

Strength Development

Compressive strength is determined on 50-mm mortar cube samples on mixtures shown in Table 2 according to ASTM C109 [20]. Since the workability of the mixtures is lower than those of Portland cement mortars, due to the fast reactions taking place, it is hard to utilize a standard mixing procedure. The most significant difference is that the mixture is mixed by hand using a scraper. FAOx is mixed with water to obtain a paste. Then, sand is introduced into the paste to get a fresh mortar and the alkaline powder is added. The samples are cured at ambient temperature until the testing time.

Table 2. Mortar samples used to determine strength development

Mixture	FAOx (F)	MgO1500 (M)	CS	Sand	Water
M3F7*	7	3	-	25	3.5
CS3F7*	7	-	3	25	3.5
M2.25CS0.75F7	7	2.25	0.75	25	3.5
M1.5CS1.5F7*	7	1.5	1.5	25	3.5
M0.75CS2.25F7	7	0.75	2.25	25	3.5

Raw material proportioning was performed based on carbon footprint estimates and performance-related expectations. Production of 1 g MgO directly from $MgCO_3$ with calcination emits ~1.1 g chemical CO_2. Assuming an additional 0.4 g CO_2 is released to obtain dead-burned MgO (at a temperature similar to PC clinker production) [21] brings the total CO_2 released to ~1.5 g per 1 g of MgO1500. FAOx (1 part FA and 1.5 parts OxAc) has FA:$C_2O_4^{2-}$ ~1.0, which means half of the FAOx mass is equivalent CO_2. Hence, carbon neutrality/negativity can be achieved only when FAOx:MgO1500 $\geq$ 3.0. Copper slag has a zero chemical carbon footprint, but operations like grinding make it slightly positive. Hence, with the proportions in Table 2 except for MgOx mortars, the mixtures can be carbon-negative. FAOx-to-alkaline binder ratio influences the mechanical properties and water resistance of oxalate binders, and the ratios in Table 2 were chosen based on [13]. W/B of 0.35 chosen for all mixtures is roughly the lowest value that allows adequate mixing and compaction of fresh mortars. The sand-to-binder ratio was chosen as 2.5 to give a paste/aggregate ratio similar to that in standard PC mortars.

pH Measurement

Changes in the pH of paste samples were measured on hardened paste samples (depicted with an asterisk in Table 2) at 24 h, with a pH meter (pH/CON 300, Oakton Instruments, USA). Hardened samples were ground with a mortar and pestle, and pH was measured on suspensions of 10 g of ground paste and 10 g of distilled water [22].

3 Results and Discussion

3.1 Setting Time

The setting times of the mixtures are given in Table 3.

Table 3. Final setting times of oxalate pastes

Mixture	Setting time (seconds)
M3F7	120
CS3F7	960
M1.5CS1.5F7	255

MgOx mixture has shorter setting time, which means the reactivity of MgO1500 is higher than copper slag. CSOx samples has setting time ~16 minutes, whereas MgOx sample has ~120 seconds. Fig. 1 shows the penetration depth versus elapsed time curves of the paste samples, obtained through the taken readings from the setting time test setup.

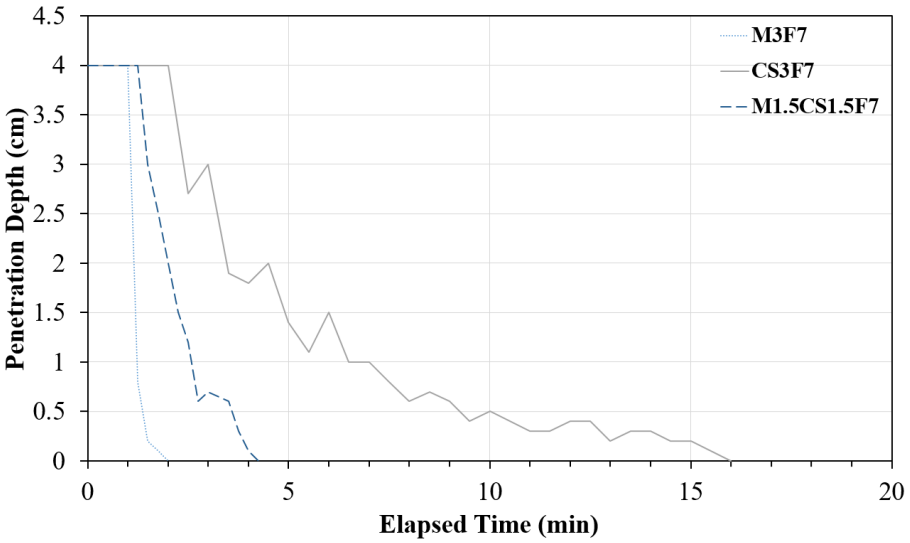

Fig. 1. Penetration depth of Vicat needle with the elapsed time

For all the samples, some time corresponding to a certain penetration depth can be determined to specify as the initial setting time. 1 cm of penetration can be assumed as the point where the initial set occurs. Since there is some correlation between the change in viscosity of the slurry and the setting time, it is possible to observe how fast the resistance to flow is changing for different samples.

3.2 Compressive Strength

Fig. 2 presents the strength development of oxalate cement mortars. MgO containing samples attain higher strengths than the others at all curing times. For MgOx sample, the strength gained after 7-d remain within the error bar (Figure 2), meaning that the sample complete its strength development at 7-d. CSOx sample complete its strength gain at 28-d. The 7-d strength of CSOx almost doubles at 28-d.

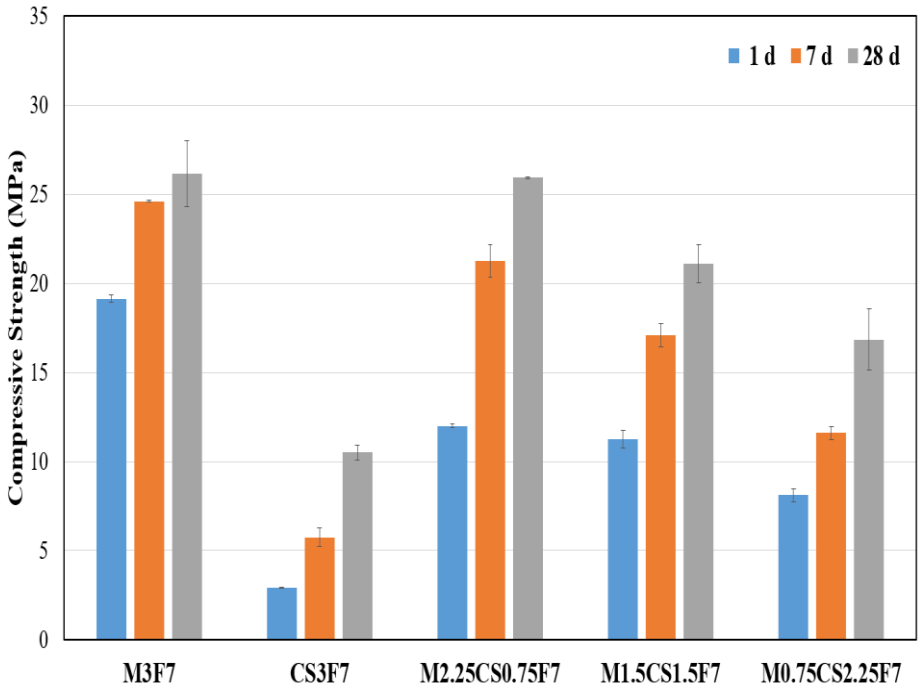

Fig. 2. Strength development of oxalate mortars

In MgO-CS hybrid scenarios, the strengths decrease in each curing period as the amount of CS in the system increases. Since strengths are very low for CSOx compared to MgOx (even less than half), it is expected that the strength will decrease with the increase in the amount of CS. These drops can be associated with a decrease in the amount of MgO. As the amount of MgO decreases, the amount of magnesium oxalates formed also decreases; hence, some decrease in the strengths is expected.

3.3 pH Measurement

The pH of the pastes is compared in Table 4.

Table 4. The pH of the pastes at different curing times

Mixture	pH		
	t = 0	1 d	7 d
M3F7	1.45	7.83	8.02
CS3F7	3.36	4.42	4.54
M1.5CS1.5F7	1.68	6.66	7.47

Table 4 gives the pH of the paste samples at different curing times. Considering the initial pH values, the rate of reaction of CSOx can be assumed to be greater than the other cements. Knowing the pH of the FAOx-water saturated solution is approximately ~1, starting condition for each case, the rate of reaction of the mixtures containing MgO

are slightly lower than CSOx. Looking at the 7-d results (Table 4), MgO-containing mixtures are alkaline (pH ~8-9) range, while CSOx sample has moderate acidity (pH ~4-5).

3.4 Mineralogical Investigation

Figure 3 compares the mineralogical development of the pastes. MgOx paste, as expected, contain a hydrated magnesium oxalate, glushinskite ($MgC_2O_4.2H_2O$) as its main reaction product (Figure 3 a). Some whewellite ($CaC_2O_4.H_2O$) and quartz are also found. These phases carry from the unreacted part of FAOx. Coming from unreacted calcined magnesia, periclase and forsterite are also present in the system. The diffractograms of the CSOx paste (Figure 3 b) show peaks corresponding to whewellite and humboldtine (an iron oxalate mineral) as well as some quartz. While humboldtine comes from the reactions taking place, whewellite and quartz carry from the unreacted raw materials.

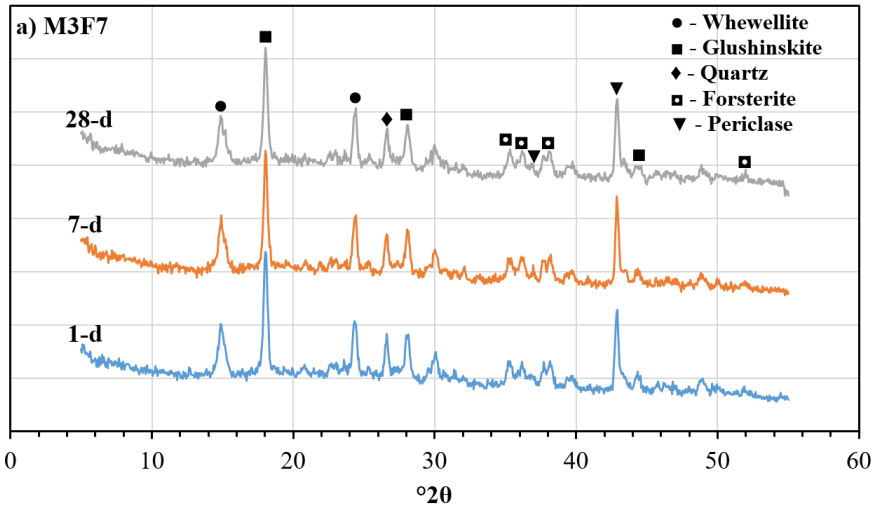

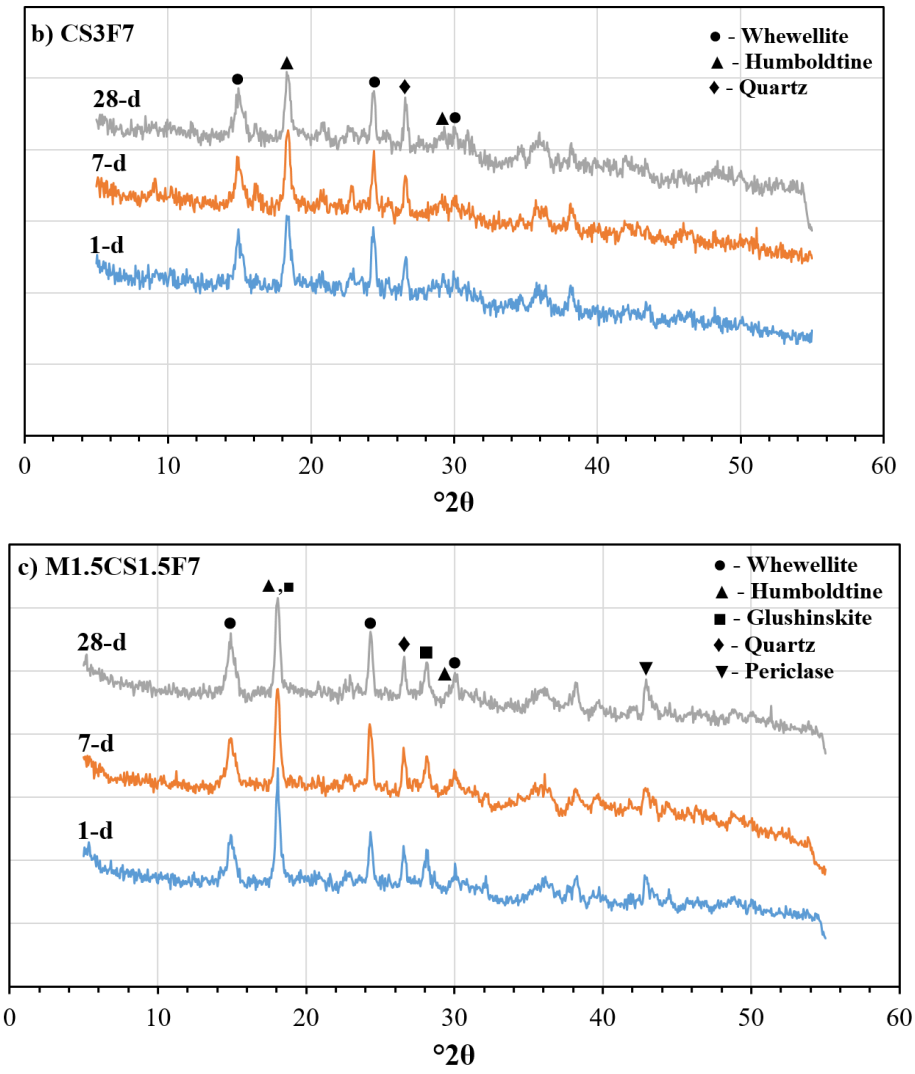

Fig. 3. The mineralogical evolution of the oxalate paste samples: a) M3F7, b) CS3F7, c) M1.5CS1.5F7

Hybrid paste contains glushinskite, humboldtine, whewellite, quartz, and periclase. While glushinskite and humboldtine represent the reaction products formed, whewellite, quartz, and periclase represent the unreacted raw materials (FAOx and calcined magnesia). Some undefined peaks, between 30-40 °2θ, may be related to forsterite from unreacted calcined magnesia. Also, due to the amorphous nature of copper slag, that portion possibly represents an amorphous phase.

3.5 Water Resistance

The resistance of MgOx, CSOx and the hybrid mortar to water are compared in Fig. 4. M3F7 do not show significant changes in compressive strength (observed differences being within experimental uncertainty). CSOx shows significant strength loss of around 70 %. This sample has poor water resistance, which limits its usage to indoor applications. Considering hybrid mortar, M1.5CS1.5F7 loses almost 60 % of its strength upon water curing.

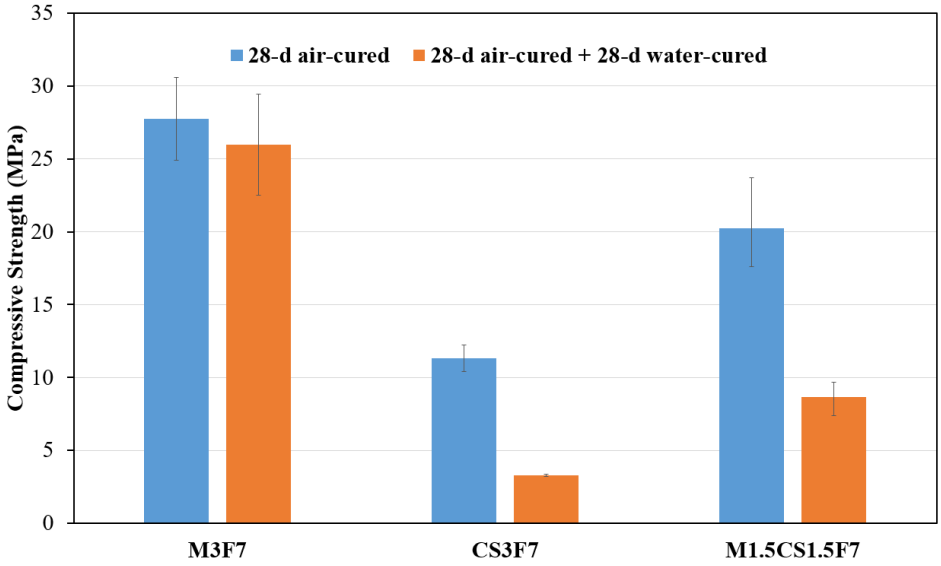

Fig. 4. The strengths of the oxalate mortars before and after water curing

4 Conclusions

Alternative oxalate cement mortars have been analyzed in terms of setting time, strength development, pH of the solution matrix, and water resistance. Following deductions can be drawn:

- MgOx has the lowest setting time, which is around 2 minutes.
- Copper slag can be used as an additive to increase the setting time of MgOx.
- CSOx mortar has low strength compared to MgOx mortar.
- The decrease in the amount of MgO1500 yields weaker product.
- While CSOx has moderate acidity, MgOx has alkaline environment.
- CSOx mortar loses ~70 % of its air-cured ultimate strength after water-curing. Hence, copper slag can only be used as magnesia replacement in small amounts.

References

1. T.A. Boden, R.J. Andres, G. Marland. Global, Regional, and National Fossil-Fuel CO2 Emissions. Carbon Dioxide Information Analysis Center, Oak Ridge National Laboratory, U.S. Department of Energy, Oak Ridge, Tenn., U.S.A, 2017. https://data.essdive.lbl.gov/view/doi:10.3334/CDIAC/00001_V2017.
2. J. Davidovits. Geopolymer chemistry and applications, third Ed., Institut Géopolymère, St. Quentin, 2008.
3. J.L. Provis, J.S.J. van Deventer. Geopolymers: structures, processing, properties and industrial applications, first ed., Woodhead Publishing, Cambridge, 2009.
4. F.P. Glasser, L. Zhang. High-performance cement matrices based on calcium sulfoaluminate–belite compositions, Cem. Concr. Res. 31 (2001) 1881-1886.
5. K. Scrivener, F. Martirena, S. Bishnoi, S. Maity. Calcined clay limestone cements (LC3), Cem. Concr. Res. 114 (2018) 49-56.
6. V. Meyer, N. de Cristofaro, J. Bryant, S. Sahu, Solidia cement an example of carbon capture and utilization, Key Eng. Mater. 761 (2018) 197-203. https://doi.org/10.4028/www.scientific.net/kem.761.197.
7. Carbon Built. https://www.carbonbuilt.com (accessed 01 December 2022).
8. Y.A. Criado, B. Arias, J.C. Abanades, Effect of the carbonation temperature on the CO2 carrying capacity of CaO, Ind. Eng. Chem. Res. 57 (2018) 12595-12599. https://doi.org/10.1021/acs.iecr.8b02111.
9. Liu, Y.; Chen, B. (2019) Research on the preparation and properties of a novel grouting material based on magnesium phosphate cement. Constr. Build. Mater. 214, 516-526. https://doi.org/10.1016/j.conbuildmat.2019.04.158.
10. Haque, M.A.; Chen, B.; Maierdan, Y. (2022) Influence of supplementary materials on the early age hydration reactions and microstructural progress of magnesium phosphate cement matrices. J. Clean. Prod. 333, 130086, https://doi.org/10.1016/j.jclepro.2021.130086.
11. Haque, M.A.; Chen, B.; Javed, M. F.; Jalal, F. E. (2022) Evaluating the mechanical strength prediction performances of fly ash-based MPC mortar with artificial intelligence approaches. J. Clean. Prod. 355, 131815. https://doi.org/10.1016/j.jclepro.2022.131815.
12. Haque, M. A.; Chen, B.; Liu, Y.; Farasat Ali Shah, S.; Ahmad, M.R. (2020) Improvement of physico-mechanical and microstructural properties of magnesium phosphate cement composites comprising with Phosphogypsum. J. Clean. Prod. 261, 121268, https://doi.org/10.1016/j.jclepro.2020.121268.
13. Erdoğan, S.T.; Bilginer, B.A.; Canbek, O. (2022) Preparation and characterization of magnesium oxalate cement. Engrxiv. https://doi.org/10.31224/2298.
14. Erdoğan, S.T. (2017) Oxalate acid-base cements as a means of carbon storage. American Geophysical Union Fall Meeting 2017, New Orleans, 11-15 December 2017.
15. Erdoğan, S.T. (2019) Magnesium oxalate cements for carbon reuse. American Geophysical Union Fall Meeting 2019, San Francisco, 9-13 December 2019.
16. İçinsel, N. (2020) Development of magnesium oxalate cements with recycled portland cement paste. M.S. Thesis, Middle East Technical University, Ankara, Turkey.
17. Bilginer, B.A.; Erdoğan, S.T. (2023) Development of magnesium/calcium oxalate cements. Mater. Construcc. 73 [350], e310. https://doi.org/10.3989/mc.2023.298122.
18. B.A. Bilginer, Development of magnesium potassium phosphate cement pastes and mortars incorporating fly ash, M.S. Thesis, Middle East Technical University, Ankara, Turkey, (2018).
19. ASTM C191. (2019). Standard Test Methods for Time of Setting of Hydraulic Cement by Vicat Needle, ASTM International, West Conshohocken, PA.

20. ASTM C109. (2020). Standard Test Method for Compressive Strength of Hydraulic Cement Mortars (Using 2-in. or [50-mm] Cube Specimens). ASTM International, West Conshohocken, PA.
21. E. Benhelal, G. Zahedi, E. Shamsaei, A. Bahadori, Global strategies and potentials to curb CO2 emissions in cement industry, J. Clean. Prod., 51 (2013) 142-161. https://doi.org/10.1016/j.jclepro.2012.10.049
22. M. Mahyar, Room-temperature phosphate ceramics made with afşin-elbistan fly ash, M.S. Thesis, Middle East Technical University, Ankara, Turkey, (2014).

Structures and Performance of Some Agro-Based Ternary Blends in Concrete – A State-of-the-Art Review

Christopher Fapohunda[1], Oluwatoyin Osanyinlokun[2] and Adekunle Abioye[3]

[1]Department of Civil Engineering, Federal University Oye-Ekiti, Nigeria.
ORCID No: 0000-0002-2448-6952, Email: christopher.fapohunda@fuoye.edu.ng
[2]Deparment of Civil Engineering, Bamidele Olumilua University of Education, Science and Technology, Ikere-Ekiti, Nigeria.
ORCID No: 0000-0002-0648-2587, Email: osanyinlokun.oluwatoyin@bouesti.edu.ng
[3]Deparment of Civil Engineering, Bamidele Olumilua University of Education, Science and Technology, Ikere-Ekiti, Nigeria.
ORCID No: 0000-0002-6154-7726, Email: abioye.adekunle@bouesti.edu.ng

Abstract. The field of structural engineering has in recent times; begin to widen its scope from the traditional analysis and design, into the development of new structural materials. This is because of the fact that the use of non-renewable materials in forming and framing structural project are raising serious environmental concerns bothering on sustainability of materials for the production of structural concrete. Of all the materials used for making concrete, cement has been found to be a major contributor to the greenhouse gases which affects the environment negatively. Research efforts are thus being directed towards finding sources of alternative cementing materials that will reduce dependence on cement. Wastes from both the industrial and agricultural industries are gradually becoming sources of such material for partial replacement of cement in concrete because of their pozzolanic properties. In particular however, the agro-based pozzolanic materials such as Rice husk Ash (RHA), Saw dust ash (SDA), Palm oil fuel ash (POFA) amongst other are such pozzolanic materials. To further widen the scope and resource base of pozzolanic materials for concreting, ternary blends consisting of two or more pozzolans, but in this case agro-based ash, are being researched into. But these researches need to be combined together to determine the extent of work done on such ternary blends and also present their relevant structural properties. This is with a view to help identify gaps in such research as a means of preventing wastage of research energies. This paper presented an up-to-date review of structural properties of some agro-based ternary blends use in structural concrete. It is concluded that more research effort is needed, especially in the development of practical and acceptable guidelines that will aid their application in concrete.

Keywords: Agro-based, Pozzolan, Rice husk ash, Structural properties, Sustainability.

1 Introduction

Of all the construction materials that are used in built environment, none has matched concrete in terms of acceptability in all lands. Its acceptability was based on many factors, which include: availability of materials of its production at every place, ability to be produced to have any desired specified strength, it enables builder and engineers to play with any geometric shapes, and excellent durability properties among others. However, this world-wide acceptability has its cost. Firstly, it leads to the exhaustion of the basic materials used for concrete productions. These materials like sand, gravel, limestone for cement manufacture are all non-renewable natural resources (Fapohunda, 2020, REF). The depletion of these materials for concrete production is having global environmental consequences and endanging the material existence of future generations. In addition to this, production of cement generates greenhouse gases like carbon dioxide (CO_2), nitrous oxide (NO_3), methane (CH_4), etc. into the atmosphere which are released into the environment, and with have been attributed to contribute significantly to the global warming (REF). During the production of cement clinker, $CaCO_3$ (calcium carbonate) is converted into calcium oxide (CaO) by means of calcination inside rotary klin to emit carbon dioxide (CO_2) as byproduct as in equation 1.

$$CaCO_3 + Heat = CaO + CO_2 \quad (1)$$

According to Summerbell et al., 2016; Adesina, 2020; and Miller et al., 2021, the contribution of concrete industry into the global gtreenhouse gas emissions is between 7 – 9%. Also cement has a very high embodied energy, that is, the energy consumed for raw material extraction, transportation, manufacture, assembly, installation, disassembly and deconstruction for any product system over the duration of a product's life (Praseeda et al., 2017). Apparently a material with low Embodied Energy is regarded more sustainable. It is against this background that researchers have been looking for ways to reduce greenhouse gas emissions attributed to concrete industry and embodied energy. One of the ways to achieve this is mass search for pozzolanic materials, especially from both industrial and agricultural wastes. These are to be used as partial replacement of cement to form binary blends. Some agricultural wastes in particular, that have been found to have pozzolanic properties are Palm Oil Fuel Ash (Jonida et al. 2023), Saw Dust Ash (Fapohunda et al., 2018), Rice Husk Ash (Fapohunda et al, 2017), Corn Cob Ash (Olafusi and Olutoge, 2012), Groundnut Husk Ash (Mahmoud et al. 2012), Banana Leaf Ash (Ndubuisi 2020), Sugarcane Bagasse Ash (Shuaibu et al. 2014 and Nasir Shafiq, et al. 2016), Palm Kernel Shell Ash (Ottos and Isaac 2018), and Bagasse Ash (Mrityunjay and Shivani, 2018) amongst others. While the usage of some of these as binary blends in concrete have resulted in improved structural and durability properties, others are inferior in quality and thus has limited or no application. It is in response to this that ternary blends were conceived by researchers to as a strategy to compensate for inferior pozzolans. Ternary blends by definition, contains cement with two other pozzolans with Portland cement, to form a binder in structural concrete as in equation 2.

$$\text{binder} = \text{Portland cement} + 2 \text{ pozzolanic materials} \quad (2)$$

Equation 2 was based on the possibility of obtaining a combined chemical composition from the two (2) pozzolanic materials that will yield cementitious paste capable of impacting adequate strength and durability properties to the resulting concrete. The use of ternary offers a wide range of possibilities because the two pozzolanic materials in the blend could be sourced from any of the at least five (5) categories as in Table 1. In addition, using ternary blends will thus help to address some of the sustainability issues associated with cement consumption in concrete production.

Table 1. Categories of Pozzolans in Ternary blends

Category	The two pozzolans
A	Both are industrial wastes
B	Both are agricultural wastes
C	One industrial waste + one agricultural waste
D	One industrial waste + others (geopolymer, quarry dust, metakaolin, etc.)
E	One agricultural waste + others (geopolymer, quarry dust, metakaolin, etc.)

Such concerns include reduction in the CO_2 emission and embodied energy as well as cost reduction. More importantly, increasing use of pozzolan in concrete industry will reduced its carbon dioxide emission significantly by 2050 and qualified to be classified as net-zero emissions industry. This work is on concrete containing agricultural waste ternary blends. Much research energy has been expended to discover possible ternary blends that are of agricultural origin. The results of these research efforts however appear to be scattered. Gathering such work together in form of a review will avail the researchers to know the extent of work done, uncover research gaps, reveal where supplementary research works are needed and enables overall understanding for effective application of the material. However, observation from Table 1 shows that at least five (5) different categories of ternary blends. **R**eviewing all of them in one work will be unwieldy. This work focuses on ternary blends of rice husk ash. Thus the aim of this paper is to carry out a critical review of works done by scholars on the potential usage of rice husk ash in ternary blends with other pozzolans in the production of structural concrete.

2 Methodology

The approach adopted for this work is to obtain all the scholarly works on concrete containing ternary blends of rice husk ash that are available on the internet. They were analysed for structural relevance. The summary of the structural features of Rice husk ash (RHA), being the pivot of this review was addressed first and then followed by its ternary blends with some agricultural waste. The results are discussed in the sections following.

3 The Review

3.1 Structural Properties of Rice Husk Ash (RHA) as Binary Blends in Concrete

Rice husk ash (RHA) is produced from rice husk, an agro-based waste material that is abundant in many parts of the world, especially in rice cultivating countries. Fapohunda et al. (2017 and Siddika et al., 2021)) did extensive review on scholarly work done that have confirmed its suitability as partial replacement of cement in the production of concrete. Its pozzolanic oxide composition (SiO_2 + Al_2O_3 + Fe_2O_3.) ranges from 73.13% to 95.77%; thus in the category of Class F fly ash (ASTM C618, 2005). Other notable findings from the review and others are that: (i) the paste containing RHA requires more water to achieve the standard consistency in comparison with the samples without RHA, and the water demand increased with increase in cement replacement with RHA, (ii) the workabilities measured both from the slump and compacting factor tests decreased with increase in RHA, which means more water is required to make the concrete workable. Other findings are decrease in the density of concrete specimens containing RHA with increase in the content of RHA at all water-binder ratios and development of densities with values of between 2200–2550 kg/m^3 are in the range for normal concrete applications. Also the compressive strength of concrete incorporating RHA developed later compressive strength that is higher than specimens without RHA as can be seen in Figure 1.

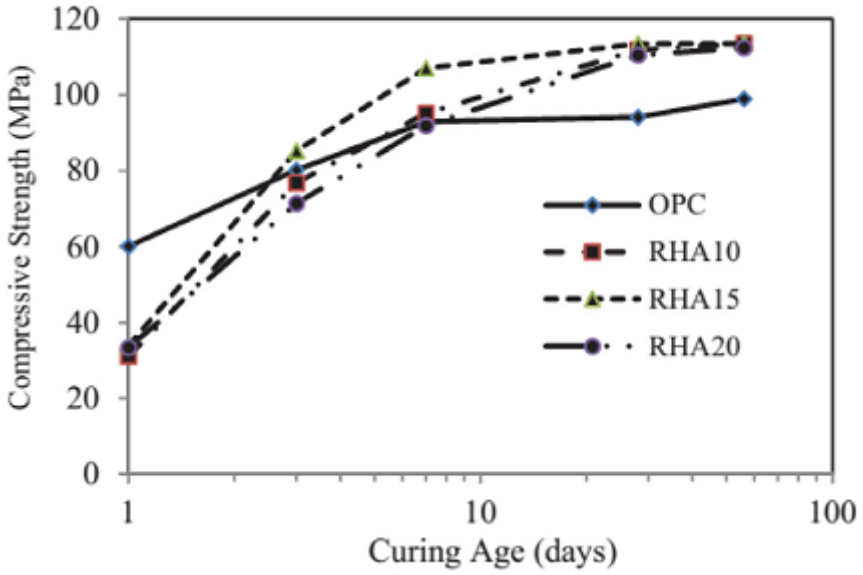

Fig. 1. Strength Development of concrete with Rice husk ash

It was however found out that the strength development of concrete containing RHA depends on the water-cement ratio (Al-Alwan et al., 2023), but at least up to 10% cement replacement with RHA resulted in strength development comparable to the control specimens. Further, RHA-concrete resulted in dense microstructure and thus impervious to agent of degradation like, sulphate attacks, chloride ingress, etc., as well exhibiting good shrinkage properties, giving it an overall structurally good and durable binary blends, when used with cement in concrete.

3.2 Ternary Blends of Rice Husk Ash (RHA) in Concrete

Rice Husk Ash and Corn Cob Ash Ternary Blends in Concrete

Corn cob is the hard thick cylindrical central core of maize (on which are borne the grains or kernels of an ear of corn). According to Adesanya and Raheem (2009a), corn cob as the agricultural waste product obtained from maize or corn; which is the most important cereal crop in sub-Saharan Africa. The documents of Food and Agriculture Organization (FAO, 2023) showed that 589 million tons of maize was produced worldwide in the year 2000. Corn Cob Ash (CCA) is obtained from the combustion of corn cobs either by open burning or the use of an incinerator. The results of Alake (2020) showed that the pozzolanic oxide composition ($SiO_2 + Al_2O_3 + Fe_2O_3$.) of CCA to be 78.34%, making it to be in the category of Class F fly ash (ASTM C618, 2005). In binary blends with cement, slump and compacting factor decreased with increase in CCA content, becoming less workable. Also, inclusion of CCA decreased the early age compressive strength but increase the latter ages compressive strength of concrete (Adesanya and Raheem, 2009b).

Alake also researched into the structural characteristics of ternary blends of rice husk ash (RHA) and corn cob ash (CCA) in equal amounts in concrete. The findings showed that the compressive strength increased with increase in curing age but decreased as the RHA and CCA contents increased; and the compressive strength were lower at early stages but improves significantly up to 56 days (Figure 2).

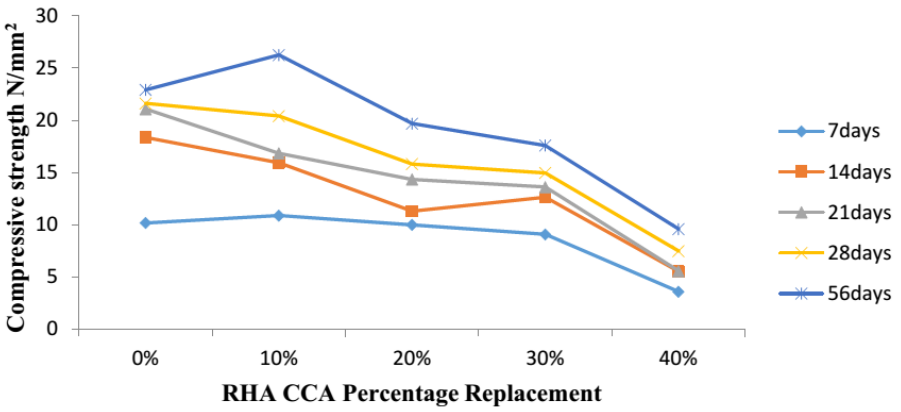

Fig. 2. Strength development of Ternary blends of RHA and CCA in concrete

However, up to 10% RHA and CCA content was considered to be the limit for the development of adequate strength. However, Kumari et a., (2023) were of the opinion that ternary blends of 10% RHA and 5% CCA to replace cement produced concrete with adequate structural strength. Kumari et al. (2023) carried out microstructural investigations with scanning electron microscopy (SEM) on ternary blends of RHA and CCA. Their analysis showed variation of behaviour with curing ages with a porous structure at early age which later turned into denser matrix at 28 days of curing

Rice Husk Ash and Sawdust Ash Ternary Blends in Concrete

Sawdust ash (SDA) is produced when saw dust, which is a waste material from the sawmill industry, is burnt into ashes. A review conducted by Fapohunda et al. (2018) revealed that SDA has a wide range pozzolanic oxide composition (SiO_2 + Al_2O_3 + Fe_2O_3.), between 50 and 70%, and thus are in the same category with the Classes C and F fly ash. It was also found out that with appropriate mix design, SDA can be used to partially replace cement up to 20% in the concrete mix to develop structural concrete that satisfies codes requirements.

The possibility of the combination RHA and SDA as ternary blends in structural concrete was investigated by Ettu et al., (2014). Equal proportions of RHA and SDA 5%, 10&, 15%, 20% and 25% were used in blends. They adopted curing days of 3, 7, 14, 21, 28, 50 and 90 days. Their results showed that compressive strengths at all the curing were higher than the control at 15% equal proportions of RHA and SDA in the mix. In his own investigation, James (2023) with equal replacement of RHA and SDA in the mix up to 15%, found out that the water requirement to achieve a standard paste increased with increase in the percent addition of RHA and SDA in the mix. He also found out the initial and final setting times followed the same trend. The results of James (2023) also confirmed earlier results by Ettu et al. (2014) that compressive strength increases with curing age.

Rice Husk Ash and Wheat Straw Ash Ternary Blends in Concrete

Wheat straw is obtained after harvesting the wheat crop on removal of stubbles. According to figures given by the Food and Agricultural Organization (FAO, 2022) of the United Nations, annual worldwide wheat production is about 734.5 million tons and for every production of kg of grain, about 1.3 to 1.5 kg of wheat straw is produced as waste on average (Pan and Sano, 2005). Its disposal either by indiscriminate dumping or uncontrolled burning is generating environment hazard. Wheat straw ash (WSA) is obtained by the controlled burning of wheat straw. In the work done by Goyal et al. (2007) Bheel et al. (2021) the pozzolanic oxide composition (SiO_2 + Al_2O_3 + Fe_2O_3.) of WSA was found to be between 78.14% and 80.03%, thereby falling into the category of Class F fly ash (ASTM C618, 2005). According to Babar et al. (2022), the use of WSA as binary blends in concrete resulted in increased compressive strength up to 10% replacement values and decrease in unit weight. Other findings are increased workability and water absorption with increase WSA content. Similar results were earlier obtained by Shar et al. (2019). The potential use of WSA with RHA, as ternary blends in concrete was investigated by Goyal et al. (2007). Three combinations of ternary blends of RHA and WSA in concrete were used, namely, (10+5) %; (5+10) %

and (7.5+7.5) %. Their results showed that ternary' blend with (7.5 + 7.5)% combination of RHA and WSA developed showed better strengths characteristics than control and other blends and proved to be the optimum combination for achieving concrete with better structural features. In their own investigation, Bheel et al. (2021) used ternary blends of RHA and WSA in equal proportions. Their results showed reduction in workability and density with increasing combined proportion RHA and WSA in the mix. The reported developed densities of between 2200 – 2300 kg/m^3 makes the resulting concrete useful for normal concreting. The results also showed that up to 10% ternary blends (5% RHA + 5% WSA) in the concrete mix, the compressive strengths and the tensile strengths measured through splitting test and modulus of rupture, were significantly enhanced at 28 days of curing. The pattern of the strength performance is shown in Figure 3.

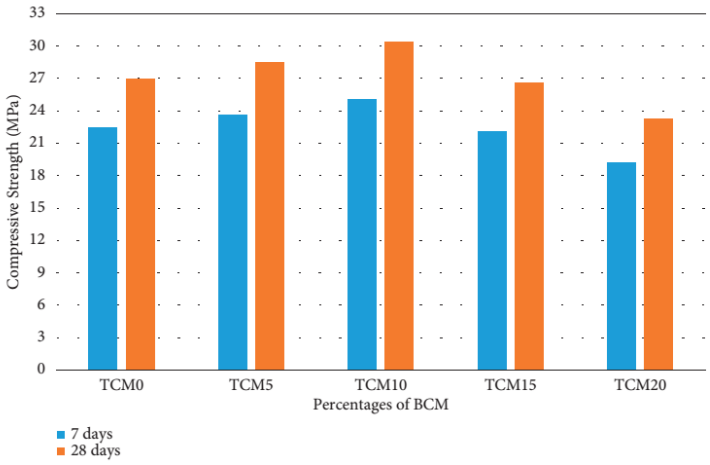

Fig. 3. Pattern of Strength development of ternary blends of RHA and WSA in concrete.

It can be observed in Figure 2 that strengths increased up to 10% of combined equal proportions of RHA and WSA, suggesting that using RHA and WSA in equal proportions at 10% replacement of cement will produce concrete having improved strength characteristic.

Rice Husk Ash and Ground Granulated Blast Slag Ternary Blends in Concrete

Ground granulated blast furnace slag (GGBFS), is a waste product obtained from steel industries. It is rich in SiO_2 and Calcium aluminates. Around 12 million tons of slags are produced by steel industries. The general trend of the effects of application of GGBFS in concrete from literature (Barnett et al., 2006; Srikanth et al., 2023; Rondón-Quintana et al., 2019) indicates that the partial replacement of OPC by GGBFS typically results in lower early strengths (7 to 28 days), but greater long term strengths. There is also enhanced workability, less bleeding, and lower heat of hydration. Other results include lower chloride ion permeability, less creep, improved resistance to sulfate attack and alkali silica reactivity (ASR) durability and increased steel corrosion

resistance. In furtherance to this, Dhinakaran and Sreekanth (2018) researched into the structural characteristics of ternary blends of RHA and GGBFG in concrete. They used 10 combinations of percentages of RHA and GGBFG in the mix as shown in Table 2

Table 2. Combination of RHA and GGBFS in Ternary blend with cement in Concrete (Dhinakaran and Sreekanth (2018)

Mix	Cement (%)	GGBFS (%)	RHS (%)
A	100	-	-
B	75	20	5
C	70	20	10
D	65	20	15
E	65	30	5
F	60	30	10
G	55	30	15
H	55	40	5
I	50	40	10
J	45	40	15

The strength investigated for the 10 combinations were compression and flexural strengths. Durability properties like sorptivity, porosity, and freeze-thaw, were also studied. The analysis of the results showed that the mix with 30% GGBFS and 5% RHA exhibited better structural and durability performance in comparison with control concrete. In addition, .it was also discovered that high-strength concrete, with 28-day compressive strength above 50 N/mm^2, could be produced with 35% replacement of cement either with 20% GGBFS and 15% RHA or 30% GGBFS and 5% RHA.

Rice Husk Ash and Others Ternary Blends in Concrete

Ternary blends of rice husk ash (RHA) with other materials were also found to have the potential for strength development for structural application. For example, ternary blend of rice husk ash (RHA) and silica fume (SF), investigated by Ahmed et a., (2022) showed a concrete with comparable structural features with the control, as well as providing strong resistance to alkali aggregate reaction at 5% SF and 20%RHA. Similarly, ternary blends of rice husk ash (RHA) and coconut husk ash (CHA) was researched into by Obokparo and Arum (2020). Their results showed that at 10% replacement the maximum compressive strength of 32.9N/mm^2 was obtained for the ternary blended concrete of RHA and CHA with cement at 56 days. This value, according to them, was 16.1% higher in strength than the control samples. In their own work, Al-Hashem et al. (2022) showed that ANN can be used to predict the 28-day strength of Rice husk ash (RHA) and Fly ash (FA) ternary blends in concrete.

4 Conclusions

From the above brief review of rice RHA-based ternary blends usage in concrete, it is obvious that such usage has the capacity to develop concrete with strength and durability characteristics that are adequate for structural application. More importantly, the usage will help achieve the status of net-zero in relation to greenhouse gas emissions in concrete industry. However, the development of national or professional technical standards to guide the use of the reviewed wastes as a component of concrete, which is not yet addressed, constitutes a major challenge that ought to be addressed by scholars. This is presented for further studies.

References

1. Adesanya, D. A. Raheem, A. A.: A study of the workability and compressive strength characteristics of corn cob ash blended cement concrete. Construction and Building Materials, 23(1), 311- 317 (2009a).
2. Adesanya D.A., Raheem A.A.: Development of Corn Cob Ash Blended Cement, Construction and Building Materials, 23,347-352 (2009b).
3. Adesina, A.: Recent advances in the concrete industry to reduce its carbon dioxide emissions. Environmental Challenges. https://doi.org/10.1016/j.envc.2020.100004.last accessed 2020/12/16
4. Ahmed, A., Ameer, S., Abbas, S., Abbass, W. Razzaq, A. Mohamed, A. M. and Mohamed, A.: Effectiveness of Ternary Blend Incorporating Rice Husk Ash, Silica Fume, and Cement in Preparing ASR Resilient Concrete. Materials, 15, 2 – 21 (2022). 2125. https://doi.org/10.3390/ma15062125
5. Al-Alwan, A. S. K., Al-Bazoon, M.., Mussa, F. I., Alalwan, H. A., Shadhar, M. H., Mohammed, M. M.,Mohammed, M. F.: The impact of using rice husk ash as a replacement material in concrete: An experimental study. Journal of King Saud University – EngineeringSciences, https://doi.org/10.1016/j.jksues.2022.03.002 last accessed 2023/03/22
6. Al-Hashem, M.N.; Amin, M.N.; Raheel, M.; Khan, K.; Alkadhim, H.A.; Imran, M.; Ullah, S.; Iqbal, M.: Predicting the Compressive Strength of Concrete Containing Fly Ash and Rice Husk Ash Using ANN and GEP Models. Materials, 15, 2 – 20 (2022).
7. Alake, O.: Strength Characteristics Of Rice Husk Ash And Corn Cob Ash Blended Cement Concrete. In Proceedings of 50th Builders Annual Conference and Annual General Meeting, Nigeria, (2020).
8. ASTM C618-05: Standard Specification for Coal Fly Ash and Raw or Calcined Natural Pozzolan for Use as a Mineral Admixture in Concrete. American Society for Testing and Materials International, West Conshohocken, Philadelphia (2005).
9. Babar, A. A., Lakho, H., Memon, M. A., Gul, H., Memon, F. A. and Siddiqui, F. H. (2022). The Impact Wheat Straw Ash as a Partial Replacement Material on Concrete Properties. 6th International Conference on Energy, Environment, and Sustainable Development, Mehran University of Technolgy Pakistan.https://eesd.muet.edu.pk/wp-content/uploads/2022/05/04_EESD2022_paper_74-OK.pdf. ; last accessed 2022/03/16
10. Barnett, S. J., Soutsos, M. N., Millard, S. G., Bungey, J. H.: Strength development of mortars containing ground granulated blast-furnace slag: Effect of curing temperature and determination of apparent activation energies. Cement and Concrete Research 36, 434 – 440 (2006)
11. Bheel, N., Ibrahim, M. H. W. Adesina, A., Charles, K., Shar, I. A.: Meahnical Performance of Concrete Incorporating wheat straw ash as partial replacement of cement. Journal

of Building pathology and Rehabilitation, Vol. 6, 4. https://doi.org/10.1007/s41024-020-00099-7 (2021)
12. Bheel, N., Awoyera, P., Shar, I. A., Sohu, S., Abbasi, S. A. Prakash, A. K.: Mechanical Properties of Concrete Incorporating Rice Husk Ash and Wheat Straw Ash as Ternary Cementitious Material. Advances in Civil Engineering, 13
https://doi.org/10.1155/2021/2977428 (2021)
13. Dhinakaran, G., Sreekanth, B.: Physical, mechanical, and durability properties of ternary blend concrete. Scientia Iranica A, 25(5), 2440{2450 (2018).
14. Ettu, L. O., Ezeh, J. C., Anya, U. C., Nwachukwu, K. C. Njoku, K. O.: Strength Of Ternary Blended Cement Concrete Containing Afikpo Rice Husk Ash And Saw Dust Ash.International Journal of Engineering Science Invention, 2(4),38-42 (2014).
15. FAO (2023). World Food Situation: http://www.fao.org/worldfoodsituation/csdb/en/. last accessed 2023/03/16
16. Fapohunda, C. A., Daramola, D. D.: Experimental Study of some Structural Properties of Concrete with Fine Aggregate replaced partially by Pulverized Termite Mound (PTM). Journal of King Saud University Engineering Sciences, 32(8), 484 – 490 (2020).
17. Fapohunda C. Akinbile, B. and Shittu, A.: Structure and properties of mortar and concrete with rice husk ash as partial replacement of ordinary Portland cement – A review. International Journal of Sustainable Built Environment 6, 675–692 (2017)
18. Fapohunda, C., Akinbile, B., and Oyelade, A. A.: Review of the Properties, Structural Characteristics and Application Potentials of Concrete Containing Wood Waste as Partial Replacement of one of its Constituent Material. YBL Journal of Built Environment, 6(1), 63–85 (2018).
19. Fapohunda, C., Kilani, A., Adigo, B., Ajayi, L., Famodimu, B., Oladipupo, O., Jeje, A.: A review of some agricultural wastes in Nigeria for sustainability in the production of structural concrete. Nigerian Journal of Technological Development, 18(2),76–87 (2021).
20. Goyal, A., Kunio, K., Ogata, H., Garg, M., Anwar, A. M., Ashraf, M. and Mandula, A.: Synergic Effect ofWheat Straw Ash and Rice-Husk Ash on Strength Properties of Mortar. Journal of Applied Sciences 7 (21), 3256-3261(2007).
21. James, O.: Effect of Rice Husk ash on Concrete produced with Saw Dust Ash. Repository.mouau.edu.ng; last accessed 2023/04/16
22. Jonida P, Ahmed A, John K, Fraser H. (2023). Palm Oil Fuel Ash as A Cement Replacement in Concrete. Mod App Matrl Sci 1(1). MAMS.MS.ID.000102. DOI: 10.32474/MAMS.2018.01.000102; last accessed 2023/03/16
23. Kumari, S., Singhal, D., Walia, R. And Rathee, A. Development of Ternary Concrete Utilizing Agricultural Waste Material. Research Square. DOI: https://doi.org/1 0.21 203/rs.3.rs-1 1 0751 5/v1; last accessed 2023/03/16.
24. Obokparo, I. S., Arum, C. N.: Properties of Ternary Cementitious Concrete
Matrix Containing Rice Husk Ash and Coconut Husk Ash. International Journal of Engineering Research & Technology (IJERT), 9(2), 863 – 870 (2020).
25. Olafusi, O. S., Olutoge, F. A.: Strength Properties of Corn Cob Ash Concrete. Journal of Emerging Trends in Engineering and Applied Sciences (JETEAS) 3 (2): 297-301 (2012).
26. Ottos, C. G., Isaac, O. E.: Palm Karnel Shell Ash as a Partial Replacement for Cement in the Production of Paving Blocks. International Journal of Trend in Scientific Research and Development (IJTSRD), 2(3), 12 -23 (2018).
27. Mahmoud H., Belel Z.A., Nwakaire C.: Groundnut shell ash as a partial replacement of cement in sandcrete blocks production. International Journal of Development and Sustainability, 1(3),1026-1032 (2012).
28. Miller, S. A., Habert, G., Myers, R. J., Harvey, J. T.: Achieving net zero greenhouse gas emissions in the cement industry via value chain mitigation strategies. One Earth, 1398 – 1411 (2021).

29. Mrityunjay, K., Shivani, S. D.: (2018) "Review on Effect of Baggase ash on Strength of Concrete" International Journal of Engineering Research and Technology (IJERT), 7(1), 202 – 204 (2018).
30. Pan, X., Sano, Y.: Fractionation of wheat straw by atmospheric acetic acid process. Bioresource Technology, 96 (11), 1256–1263 (2005).
31. Praseeda, K. I., Venkatanama-Reddy, B. V., Mani, M.: Life-cycle energy Assessment in Buildings: Framework, approaches, and Case Studies. Encyclopaedia of Sustainable Technologies, 113 – 136 (2017).
32. Shar, I. A., Menon, F. A., Bheel, N., Shaikh, Z. H. And Dayo, A. A. (2019). Use of Wheat Straw Ash as Cement replacement materials in the Concrete. In International Conference on Sustainable Development in Civil Engineering (MUET), Pakistan (2019).
33. Shuaibu, R. A., Mutukub, R. N., Nyomboic, T.: Strength Properties of Sugarcane Bagasse Ash Laterised Concrete. International Journal of Civil and Environmental Research (IJCER) 1(3), 110-121 (2014).
34. Siddika, A., Al Mamun, M. A., Alyousef, R. Hosseini, H. M.: State-of-the-art-review on rice husk ash: A supplementary cementitious material in concrete. Journal of King Saud University – Engineering Sciences 33, 294–307 (2021)
35. Srikanth, S., Krishna, C. B. R., Srikanth, T., Nitesh, K. J. N., Nadh, V. S., Kumar, S. and Thanappan, S.: Effect of nano Ground Granulated Blast Furnace Slag (GGBS) Volume% on Mechanical Behaviour of High Performance Sustainabnle Concrete. Journal of Nanomaterials, hhttps://doi.org/10.1155/2022/3742194; last accessed 2023/02/16.
36. Summerbell, D. L., Barlow, C. Y.: Potential reduction of carbon emissions by performance improvement. A cement industry case study. Journal of Cleaner Production, 135, 1327 – 1339 (2016)

Investigation of the Effect of Asphalt Binder Modified with the New Synthesized TOBO Additive on Rutting Performance

Hacer Yeşilçiçek[1][0000-0001-5474-7415], Şeref Oruç[2] [0000-0001-5788-890x] and Merve Gülfer Bozdemir [3][0000-0001-5868-6613]

[1] Karadeniz Technical University, Faculty of Technology, Trabzon, Türkiye, haceryesilcicek@ktu.edu.tr
[2] Karadeniz Technical University, Engineering Faculty, Trabzon, Türkiye, oruc@ktu.edu.tr
[3] Erzurum Technical University, Engineering and Architecture Faculty, Erzurum, Türkiye, merve.ozcan@erzurum.edu.tr

Abstract. The increase in the world population and the change in consumption habits, the increase in employment created by rapidly developing technology and industrialization in the economy have brought along many problems such as the depletion of raw materials and energy resources, and the increase in environmental pollution. The whole world has focused on the concept of sustainable development in order to solve the existing problems with the idea of saving from environmental concerns, economy and non-renewable energy resources. In recent years, researchers have been interested in waste and by-products due to their different properties obtained as a result of some processes from edible raw material sources. In this study, a new additive was obtained by chemically synthesizing tall oil, a by-product of paper production, together with boron oxide in the laboratory. The asphalt binder has been modified at certain rates with the synthesized new TOBO additive. Dynamic shear rheometer test (DSR) was applied to determine the resistance of the obtained modified binders against rutting. The experimental results showed that the TOBO additive improved the rutting parameter (G*/sinδ) of the original asphalt at high temperatures.

Keywords: Asphalt; Modification; Rheology; Tall oil.

1 Introduction

Bitumen adhesive, one of the products obtained from the distillation of crude oil, is a waterproof, dark brown or black colored material consisting mostly of hydrocarbons. For this reason, it is used together with aggregate in flexible layers in the construction sector, especially in coating engineering. Although the amount of bitumen (4-7%) used as a binder in flexible pavements is quite low compared to aggregate (90-95%), it is of great significance in terms of coating performance and behavior. Deterioration, such as

rutting and cracks, occur in the coating layer of pavements due to changing climatic conditions and the increase in traffic volume and load. In the studies in the literature, many additives of varying structural properties have been added to bitumen and/or bituminous mixtures in order to prevent such deterioration forms and improve coating performance. In this respect, styrene-butadiene-styrene (SBS), the most widely used thermoplastic elastomer additive, was found to improve high temperature stability [7,8] by increasing the rutting parameter [1-3], aging resistance [4-6] and complex shear modulus of bitumen. In addition, it was determined that mixtures modified with SBS had higher Marshall Stability values [1,9,10] and were more resistant to moisture damage [11]. Ethyl-vinyl-acetate (EVA) binder, another modifier, was found to contribute to physical [12-14] and rheological [15] properties, improve fatigue cracks in road pavements at low temperatures [16-18] and increase the viscosity of asphalt and the percentage improvement at high temperatures [19-21]. It was reported that low density polyethylene (LDPE) particularly improved the low temperature properties of bitumen, and the binder's resistance to cracking decreased as the concentration of LDPE added to the binder increased [22-24]. It was found that the use of bio-oil in bitumen modification improved the high temperature performance of the binder and increased its viscosity, deformation resistance, low temperature cracking resistance, and temperature sensitivity [25-29].

Studies conducted on the use of boron-containing additives in the modification of bitumen are very few. The first aim of the present study was to synthesize a new additive under laboratory conditions by adding boron oxide to tall oil, a by-product with long chain hydrocarbon content, and high unsaturated oil. The second aim of this study was to make the new additive chemically coordinate (interact with) with bitumen. In this context, Dynamic shear rheometer (DSR) test was carried out to determine the high temperature resistance the new additive with bitumen.

2 Materials and Method

2.1 Asphalt

In this study, 50/70 penetration grade asphalt obtained from the Tupras Izmit Refinery, Turkey was used. The properties of the asphalt used are given in Table 1.

Table 1. Properties of the original asphalt.

Properties	Value	Standard
Penetration (25°C, dmm)	56	ASTM D-5
Softening Point (°C)	50	ASTM D-36
Ductility (25°C, cm)	100 +	ASTM D-113
Specific gravity (gr/cm^3)	1.028	ASTM D-70
Viscosity (135°C, cP)	500	ASTM D-4402
Viscosity (165°C, cP)	100	ASTM D-4402

2.2 Synthesis of the Tall Oil Based New Boron Additive

The tall oil based new boron additive (TOBO) was chemically synthesized in a laboratory environment for the purpose of being used as a modifying asphalt binder. The synthesis process consisted of the reaction of sulfuric acid (H_2SO_4) catalyzed tall oil with boron oxide. The molecular weight (in terms of oleic acid) of the tall oil, which was obtained from Oyka Paper Factory, was 282 g/mol and. The boron oxide (99% purity) was obtained from Eti Mine Works and had a molecular weight of 69 g/mol.

The TOBO was chemically synthesized under laboratory conditions and used as a modifying agent in bitumen. The boron oxide (99% purity) was reacted with tall oil in the presence of a catalyst, namely H_2SO_4. Thus, the synthesized additive was originally considered to be a polyboric compound. A magnetic stirrer/heater and a 2000 ml glass beaker were used in the synthesis of the TOBO. This chemical treatment was carried out under controlled temperature conditions. 338 g tall oil was placed into the beaker and heated. Immediately after, 2 ml of H_2SO_4 was added and the mixture was mixed with a magnetic stirrer. The total amount of catalyst at the end of the reaction was approximately 20 ml. Next, 84g of boron oxide was gradually added as the temperature of the mixture reached 120 °C. Meanwhile, the mixing-heating processes were continuously carried out. The temperature was kept at 150 ± 5 °C and stirring was continued for 3 h. At the end of this period, the system was completely shut down and the additive was cooled to ambient temperature. The new additive was dissolved in gasoline to eliminate the amount of boron oxide remaining at the end of the reaction.

The solution obtained was filtered twice with filter paper. A vacuum aspirator was used to remove the gasoline in the body. The TOBO additive was then kept in a hermetically sealed glass beaker to be used in the modification of the bitumen [30]. The visual appearance of the TOBO additive is given in Fig.1.

Fig. 1. Visual of the additive.

2.3 Preparation of the TOBO Modified Binders

The original asphalt was turned into liquid by heating it in an oven at 150 °C. 1%, and 5% by weight of the TOBO was added to the binder that was poured into a mixing

vessel at the same temperature. The modification process was carried out with a high shear mixer for 30 min at 3000 rpm and 150 ± 5 °C. When this process was completed, the modified asphalt binder was made ready for testing. The description of the asphalt binders is given in Table 2.

Table 2. The description of the asphalt binders.

Sample Content	Code
AC 50/70 Asphalt binder	BA
AC 50/70 Asphalt binder + %1 TOBO	BA1
AC 50/70 Asphalt binder + %5 TOBO	BA5

2.4 Dynamic Shear Rheometer (DSR) test

Dynamic shear rheometer (DSR) testing is used to determine the resistance of asphalt to rutting at high temperatures [31-33]. Superpave rutting parameter G*/sin δ is obtained by measuring the complex shear modulus (G*) and phase angle (δ) of the asphalt binder under certain temperature and loading frequency [34]. In this study, Kinexus model rheometer was used. To find out the susceptibility the asphalt binder is to rutting, this test compares unaged and RTFO aged binder. Maximum shear stress level is 10%. In order to determine the high temperature performance, test temperatures were chosen as 58°C, 64°C, and 70°C. The loading frequency is set at 10 rad=s (1.59 Hz). Three samples were used for each asphalt configuration.

3 Results and Discussion

3.1 Results of DSR

The rutting parameter (G*/sinδ) of unaged-RTFO-aged asphalt binders was calculated, and the results are shown in Fig. 2 and Fig. 3 respectively. It is obvious that the addition of TOBO increases G*/sinδ for modified asphalt binders in comparison with base asphalt in the whole testing temperature range. Furthermore, the high temperature critical temperatures for BA, BA1, and BA5 at 1.0 kPa of G*/sinδ are 67.7°C, 70.2°C, and 73.0°C, respectively. This suggests that TOBO can significantly improve the high-temperature rutting resistance of base asphalt. More resistant asphalt binder against permanent deformation (higher G*) and a greater elastic component (lower δ) are desired for rutting resistance [35-37]. In addition, G*/sinδ values BA5 samples is slight at all testing temperatures, the influence of TOBO additive at 5% content ratios on rutting resistance of base asphalt binder is higher than at 1% ratios.

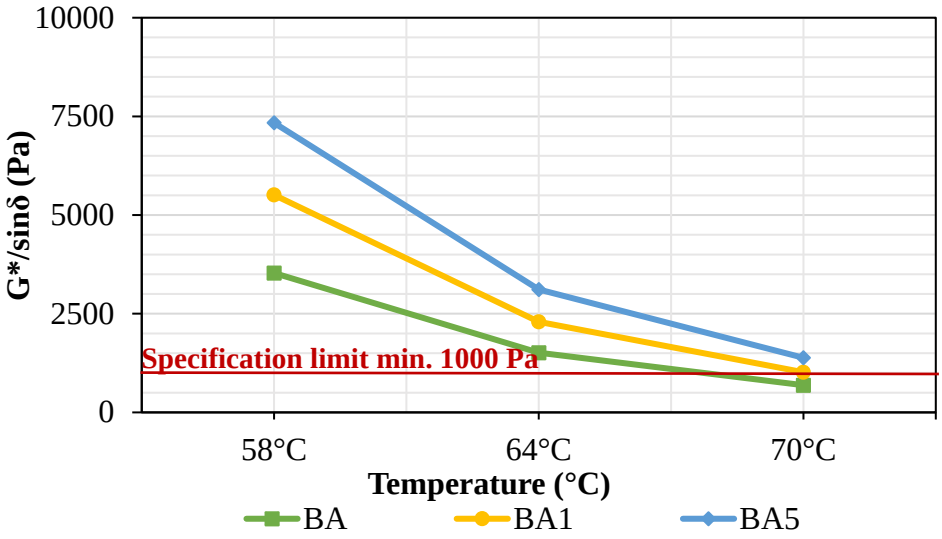

Fig. 2. G*/sinδ values of unaged asphalt binders at high temperatures.

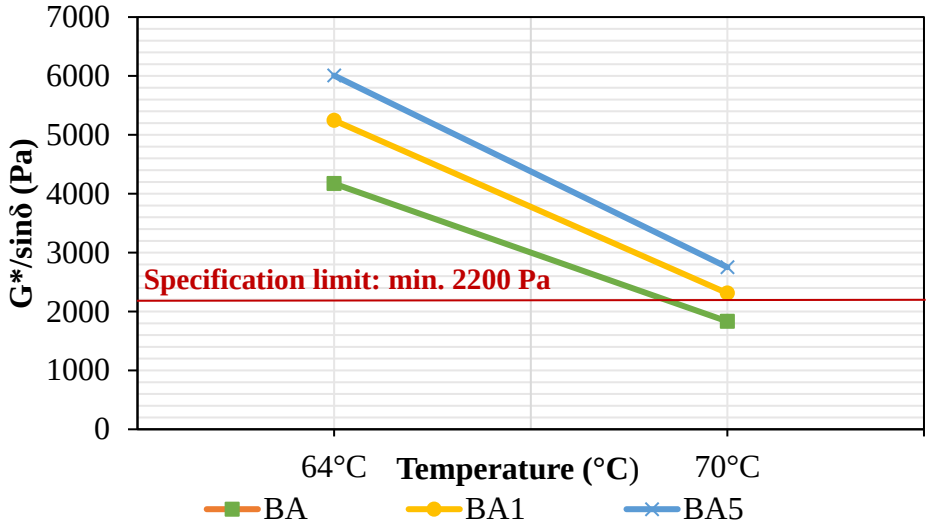

Fig. 3. G*/sinδ values of RTFO-aged asphalt binders at high temperatures.

As can be seen in Fig. 3, all modified asphalt binder samples should meet the minimum specification limit of 2200 Pa at both 64°C and 70°C. This means that the TOBO additive could prevent short-term aging at high temperatures.

4 Conclusion

In this study, a new additive containing tall oil-based boron oxide, namely TOBO, was chemically synthesized. Modified binders were obtained by adding 1% and 5% of the TOBO into bitumen. DSR test was performed to determine the rheological behaviors of the TOBO:

- When the results of the DSR (unaged and RTFO-aged) was examined, the TOBO was found to enhance the elastic properties of the asphalt binder, developing the rutting resistance at high temperatures.

References

1. Kök BV, Yılmaz M. :The effects of using lime and styrene–butadiene–styrene on moisture sensitivity resistance of hot mix asphalt. Construction and Building Materials 23, 1999–2006 (2009).
2. Galooyak SS, Dabir B, Nazarbeygi AE, Moeini A.: Rheological properties and storage stability of bitumen/SBS/montmorillonite composites. Construction and Building Materials 24, 300–7(2010).
3. Airey GD.: Rheological properties of styrene–butadiene–styrene polymer modified road bitumens. Fuel 82,1709–19(2003).
4. Chen JS., Liao, MC, Shiah MS.: Asphalt modified by styrene-butadiene-styrene triblock copolymer: morphology and model. Journal of Materials in Civil Engineering 14(3), 224-229 (2002).
5. Sengul EC, Oruc S, Iskender E, Aksoy A. : Evaluation of SBS modified stone mastic asphalt pavement performance, Construction and Building Materials 41, 777–783 (2013).
6. Zhao X, Wang S, Wang Q, Yao H. Rheological and structural evolution of SBS modified asphalts under natural weathering, Fuel 184, 242-247 (2016).
7. Weizhen S, Peng Y, Kaifu H, Kejian L, Daosheng L, Feng Y, Yi W. : The study of producing SBS modified asphalt by using Liaoshu high viscous crude oil, Petroleum Science and Technology 19(9-10), 1187–1196 (2001).
8. Cortizo SM, Larsen OD, Bianchetto H, Alessandrini LJ. : Effect of the thermal degradation of SBS copolymers during the ageing of modified asphalts, Polymer Degradation and Stability 86, 275-282 (2004).
9. Şengöz B, Işıkyakar G. : Analysis of styrene–butadiene–styrene polymer modified bitumen using fluorescent microscopy and conventional test methods. Journal of Hazardous Materials 150, 424–32 (2008).
10. Al-Hadidy AI, Tan Y, Ayman TH. : Starch as a modifier for asphalt paving materials. Construction and Building Materials 25, 14–20 (2011).
11. Görkem Ç, Şengöz B. Predicting stripping and moisture induced damage of asphalt concrete prepared with polymer modified bitumen and hydrated lime. Construction and Building Materials 23, 2227–36 (2009).
12. Isacsson U, Lu X. : Characterization of bitumens modified with SEBS, EVA and EBA polymers. Journal of Materials Science 34, 3737–3745 (1999).
13. Panda M, Mazumdar M.: Engineering properties of EVA-modified bitumen binder for paving mixes. Journal of Materials in Civil Engineering 11, 131-137 (1999).
14. Haddadi S, Ghorbel E, Laradi N. Effects of manufacturing process on the performances of the bituminous binders modified with EVA. Construction and Building Materials 22, 1212-1219 (2008).

15. Huseyin AI, Iqbal HM, Al-Abdul-Wahhab IH. Influence of Mw of LDPE and vinyl acetate content of EVA on the rheology of polymer modified asphalt. Rheologica Acta 45, 92–104 (2005).
16. Lu X, Isacsson U. : Artificial aging of polymer modified bitumens. Journal of Applied Polymer Science 76(12), 1811-1824 (2000).
17. Ameri M, Mansourian A, Sheikhmotevali HA. : Laboratory evaluation of ethylene vinyl acetate modified bitumens and mixtures based upon performance related parameters. Construction and Building Materials 40, 438–447 (2013).
18. Gonzalez O, Munaz ME, Santamaria A, Garcia-Morales M, Navarra FJ, Portal P.: Rheology and stability of bitumen EVA blends. European Polymer Journal 40(10), 2365-2372 (2004).
19. Liang M, Ren S, Fan W, Xin X, Shi J, Lou H. : Rheological property and stability of polymer modified asphalt: effect of various vinyl-acetate structures in EVA copolymers. Construction and Building Materials 137, 367-380 (2017).
20. Brovelli C, Hilliou L, Hemar Y, Pais J, Percira P, Crispino M. :Rheological characteristics of EVA modified bitumen and their correlations with bitumen concrete properties. Construction and Building Materials 48, 1202-1208 (2013).
21. Luo W, Chen, J. 2011. : Preparation and properties of bitumen modified by EVA graft copolymer. Construction and Building Materials 25, 1830-1835 (2011).
22. Jun L, Yuxia Z, Yuzhen Z. : The research of GMA-g-LDPE modified Qinhuangdao bitumen. Construction and Building Materials 22 (6), 1067-1073 (2008).
23. Ho S, Church R, Klassen K, Law B, MacLeod D, Zanzotto L.: Study of recycled polyethylene materials as asphalt modifiers. Canadian Journal of Civil Engineering 33(8), 968-981 (2006).
24. Othman A M. : Effect of low-density polyethylene on fracture toughness of asphalt concrete mixtures. Journal of Materials in Civil Engineering 22(10), 91019-1024 (2010).
25. Yang X, You Z. : High temperature performance evaulation of bio-oil modified asphalt binders using the DSR and MSCR tests. Construction and Building Materials 76, 380-387 (2015).
26. Sun Z, Yi J, Huang Y, Feng D, Guo C. : Properties of asphalt binder modified by bio-oil derived from waste cooking oil. Construction and Building Materials 102, 496-504 (2016).
27. Gong M, Yang J, Zhang J, Zhu H, Tang T. : Physical-chemical properties of aged asphalt rejuvenated by bio-oil derived from biodisel residue. Construction and Building Materials 105, 35-45 (2016).
28. Yang X, You Z, Dai Q, Milss-Beale J. : Mechanical performance of asphalt mixtures modified by bio-oil derived from waste wood resources. Construction and Building Materials 51, 424-434 (2014) .
29. Zhang R, You Z, Wang H, Ye M, Yap Y K.: The impact of bio-oil as a rejuvenator for aged asphalt binder. Construction and Building Materials 196, 134-143 (2019).
30. Yeşilçiçek H, Oruç Ş. and Bozdemir M G: Characterization and rheological properties of asphalt binder with a novel tall oil-based boron additive to enhance asphalt performance, Construction and Building Materials 359, 129510 (2022).
31. Yang, X., and Z. You. : High temperature performance evaluation of bio-oil modified asphalt binders using the DSR and MSCR tests. Construction and Building Materials 76 380–387 (2015).
32. Shoukat, T., and P. J. Yoo. : Rheology of asphalt binder modified with 5W30 viscosity grade waste engine oil. Applied Science 8 (7), 1194 (2018).
33. Bhat, F. S., and M. S. Mir. : A study investigating the influence of nano Al2O3 on the performance of SBS modified asphalt binder. Construction and Building Materials 271 (Feb), 121499 (2021).
34. Che, T., B. Pan, Y. Li, D. Ge, D. Jin, and Z. You. : The effect of styrene-butadiene rubber modification on the properties of asphalt binders: Aging and restoring. Construction and Building Materials 316 (Jan), 126034 (2022).

35. P. Ahmedzade. : The investigation and comparison effects of SBS and SBS with new reactive terpolymer on the rheological properties of bitumen. Construction and Building Materials 38, 285-291(2013).
36. J. Zhang et al. : Evaluation of the improved properties of SBR/Weathered coal modified bitumen containing carbon black. Construction and Building Materials 23, 2678-2687 (2009).
37. Bozdemir M G., Oruç Ş. and Yeşilçiçek H. : Physical and microstructural properties of new boron resin compound synthesized asphalt, Journal of Materials and Civil Engineering 35(2), 04022426 (2023).

A Review Paper About Test Methods Used/Developed for Fresh and Hardened Properties of High Strength Concrete

Farzin Asgharpour[1][0000-0003-3380-8359], Özgür Eren[2][0000-0002-5674-8697], Efecan Ünal[3][0009-0007-1666-3959] and Yahya Abdullah Mohammed Muaamar[4][0009-0004-0905-6585]

[1] Eastern Mediterranean University, Civil Engineering Department, North Cyprus, Türkiye, Farzin.asgharpour@emu.edu.tr
[2] Eastern Mediterranean University, Civil Engineering Department, North Cyprus, Türkiye, ozgur.eren@emu.edu.tr
[3] Eastern Mediterranean University, Civil Engineering Department, North Cyprus, Türkiye, efecan.unal@emu.edu.tr
[4] Eastern Mediterranean University, Civil Engineering Department, North Cyprus, Türkiye, ymuaamar1@gmail.com

Abstract. High-strength concrete (HSC) has become widely favored as a construction material for its remarkable mechanical attributes, long-lasting resilience, and attractive visual appeal. It's no wonder that HSC has gained such popularity among builders and architects alike. The assessment of HSC properties is critical in ensuring its safety and performance in construction. This review paper aims to provide an overview of the various test methods used and developed for assessing the fresh and hardened properties of HSC. The paper begins by discussing the properties of HSC and the importance of their evaluation. Next, it covers the different test methods used for assessing the fresh properties of HSC, including workability, flow, and setting time. the paper delves into an in-depth exploration of different test methods used to assess the hardened properties of high-strength concrete (HSC), including crucial factors like compressive strength, tensile strength, modulus of elasticity, and durability. Additionally, the paper thoroughly examines the challenges faced in these test methods and sheds light on future directions for evaluating HSC properties. It's important to mention that this review paper holds immense value as a valuable resource for researchers, engineers, and practitioners involved in the design and construction of structures using high-strength concrete.

Keywords: High-strength concrete, Workability, Compressive strength, Tensile strength.

1 Introduction

Concrete, a widely used construction material throughout history, has been enhanced by the addition of fibers to address some of its inherent disadvantages [1]. The

integration of fibers into concrete has demonstrated favorable outcomes in enhancing its mechanical characteristics and long-lasting resilience, thereby establishing it as a more dependable substance for construction purposes [2]. As the global population continues to grow, the demand for advanced construction materials capable of delivering superior outcomes has become increasingly pressing. One such material is high-strength concrete (HSC), which has made significant progress and is now extensively utilized. Additionally, ultra-high-performance concrete (UHPC) presents a cost-effective alternative that offers even better performance [3]. It is worth noting that the use of coal bottom ash and slag powder as fibers in concrete has not only demonstrated the ability to enhance its strength but also offers the advantages associated with HSC and UHPC, showcasing their potential to revolutionize the construction industry [4].

2 Test Methods Used and Developed for Fresh and Hardened Properties of HSC

Concrete testing is essential to ensure that it conforms to project specifications and meets quality requirements. Various tests are conducted to evaluate the properties of concrete, both in its fresh and hardened states. In this section, we will discuss specific test methods used for assessing the fresh and hardened properties of high-strength concrete.

2.1 Compressive Strength Test

The compressive strength test is a crucial and widely used method for evaluating the properties of concrete. It involves subjecting a cylindrical, cubic, or prism-shaped specimen to gradually applied loads to determine the maximum compressive load the material can withstand before breaking [5]. By doing this test the mechanical characteristics of the concrete can observed.

In order to ensure efficiency and sustainability in concrete production are attained, it is imperative that one optimizes the usage of time, energy ,and labor throughout the process .Simultaneously ,it becomes pivotal for one to enhance compressive strength levels as well while taking into consideration pertinent sources [6], [7]. It is critical noteworthiness lies in recognizing how tests may yield dissimilar results on account of various influential factors. Some examples include sample size discrepancies, differences in shape, washboard like forces arising from rough surface contact, maintenance temperatures over duration, and alterations made to load frequencies or routines. Therefore, it logically follows that one must always be cognizant of inherent variabilities present within a series of authenticated outcomes rather than relying predominantly on an isolated circumstance [8].

Several studies have utilized the compressive strength test to evaluate the effect of different additives on high-strength concrete. Li et al. [14] performed compressive strength tests on high-performance concrete using fly ash, silica fume, and polypropylene fiber additives. Smarzewski et al. [1] evaluated the mechanical behavior

of high-performance concrete with the additions of foundry sand and coal cinder. Moustafa et al. [9] examined the effect of tire scraps on the dynamic and mechanical characteristics of high-strength concrete. Tian et al. [10] conducted compressive strength tests to determine the dynamic and mechanical characteristics of high-strength concrete with lightweight aggregates.

2.2 Flexural Strength Test

The flexural strength test is used to evaluate the tensile strength of concrete. It measures the highest stress at the point of bending failure on the tension face of an unreinforced concrete slab or beam [11]. The flexural strength, also known as the modulus of rupture, is a critical factor in assessing the performance of concrete under bending and other tensile-inducing conditions.

Flexural strength tests can be conducted using third-point loading or center-point loading, and the results are reported as the Modulus of Rupture in MPa. It is important to use consistent specimen size and loading configurations to ensure reliable and comparable results [12].

The flexural strength test has practical applications, such as designing concrete pavements based on their flexural strength in relation to traffic loading and subgrade stiffness. Additionally, it is used to assess the tensile stress that leads to cracking in non-reinforced concrete and evaluate deflections at service loads [13].

In previous studies, the flexural strength test has been employed to evaluate the mechanical behavior and durability-related parameters of high-strength concrete with various additives. Li et al. [14] investigated high-performance concrete with fly ash, silica fume, and polypropylene fiber additives. Smarzewski et al. [15] evaluated the mechanical behavior of high-performance concrete with foundry sand and coal cinder additives. Moustafa et al. [9] examined the effect of tire scraps on the dynamic and mechanical characteristics of high-strength concrete. Tian et al. [16] determined the dynamic and mechanical characteristics of high-strength concrete with coarse aggregates of low absorption waste (LAW) prostrated water and lightweight aggregate (LWA) polymer emulsion.

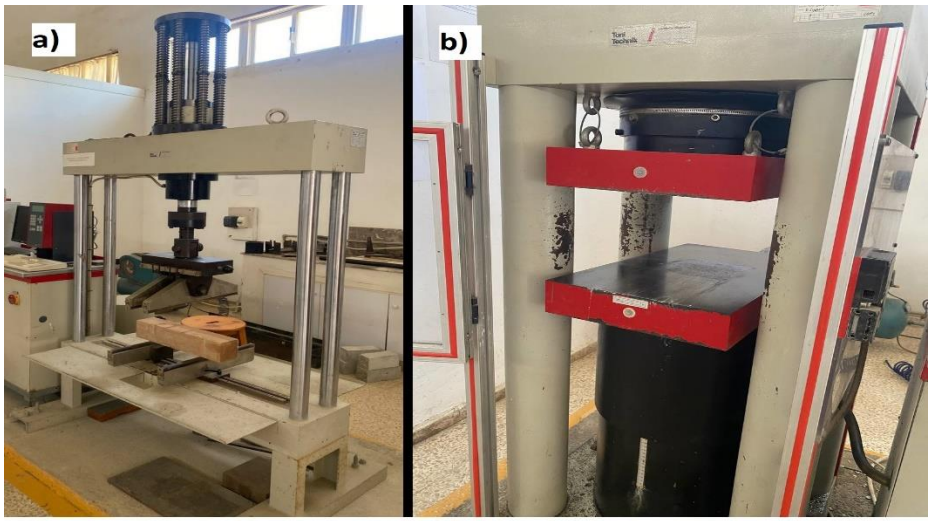

Fig. 1. a) Flexural strength testing machine; b) Compressive strength testing machine

Table 1. Review on the compressive strength test and flexural strength tests in high-strength concrete studies.

Source	Detail
Li. et al.	Investigated the performance of high-performance concrete with fly ash, silica fume, and polypropylene fiber additives [14].
Smarzewski. et al. [15]	Evaluated the mechanical behavior of high-performance concrete with foundry sand and coal cinder additives [15].
Moustafa. et al. [16]	Examined the dynamic and mechanical characteristics of high-strength concrete incorporating tire scraps [9].
Tian. et al.	Determined the dynamic and mechanical characteristics of high-strength concrete with LAW prostrated water and LWA polymer emulsion [16].

3 Experiment

In this section, we will discuss the experimental procedures and tests conducted to evaluate the properties of high-strength concrete, including the effect of aggregates, the splitting tensile test, bulk resistivity, rapid chloride permeability test, and workability tests.

3.1 Evaluation of Aggregate Effect on High-Strength Concrete Properties

A study conducted by Beushausen and Dittmer focused on evaluating the effect of two types of aggregates on the properties of high-strength concrete [17]. The compressive strength test and flexural tensile strength test were employed to assess the ultimate capacity of the material in compression and tension.

The compressive strength test was conducted following the SABS Method 861-2:1994. Three cubes were subjected to failure by applying a constant loading rate of 15 MPa per minute. The compressive strength was determined by breaking the cubes and recording the maximum load achieved.

Similarly, the flexural strength test was performed using a testing apparatus that applies a 4-point force on the sample and records the failure load. Two beam specimens were tested until failure, and the flexural strength was determined using the appropriate equation from the code.

3.2 Splitting Tensile Test

The splitting tensile test is a widely used method for evaluating the indirect tensile strength of concrete. This test is standardized and included in major international concrete standards such as ASTM C-496, ISO 4105, and BS 1881-117 [18]. It assesses the tensile behavior and properties of concrete by subjecting a cylindrical or prismatic specimen to nearly uniform tensile stress induced by compression along two diametrically opposed generators.

To conduct the splitting tensile test, thin strips, often made of plywood, are placed between the loading platens and the specimen to distribute the load evenly and prevent local failure in compression. The specimen fails by splitting due to the generated tensile stress state. The splitting tensile strength, considered a material property, is the maximum tensile stress estimated at failure based on the theory of elasticity.

The splitting tensile test has been widely used in studying the tensile behavior of concrete-like materials and assessing the true tensile strength of fiber-reinforced concrete (FRC) [19], [20]. It provides valuable insights for applications ranging from failure and deformation analysis to protective engineering.

3.3 Bulk Resistivity

electrical testing of concrete has garnered considerable attention from various organizations due to its ability to offer valuable insights into fluid flow characteristics. By employing the concept of bulk resistivity, we can effectively evaluate the electrical properties of concrete, specifically its conductivity. The beauty of electrical testing lies in its speed and simplicity, often requiring less than a minute to carry out. This allows us to quickly assess the electrical characteristics of concrete without any cumbersome or time-consuming procedures. It serves as a convenient and efficient method to determine how effectively concrete conducts electricity, which can have significant implications for various applications.

In this work, the variability involved in measuring the bulk resistivity along a cylinder's longitudinal axis after attaching electrodes to each end was investigated. The study involved ten laboratories and provided variability data for twelve concrete combinations at testing ages of 28, 56, and 91 days [21]. Electrical resistivity measurements offer valuable information related to chloride-induced corrosion in reinforced concrete structures [22].

3.4 Rapid Chloride Permeability Test

Chloride-induced corrosion of reinforcing steel is a common durability issue in concrete structures. The ingress of chlorides can occur through diffusion, evaporative transport, hydrostatic pressure, and capillary absorption, with diffusion being the predominant mechanism. Chloride ions penetrate the concrete and accumulate at the rebar level when the concentration on the outside exceeds the inside. When combined with wetting and drying cycles and the presence of oxygen, this can lead to reinforcement corrosion. The rate of chloride ion penetration is influenced by the interior pore structure of the concrete, which is affected by factors such as mix design, hydration level, curing environment, additional cementitious ingredients, and construction techniques.

The rapid chloride permeability test is used to evaluate concrete's resistance to chloride penetration. It involves subjecting concrete samples to an electrical potential and measuring the amount of charge passed through the concrete over a specified time period. The results provide an indication of the concrete's resistance to chloride ingress and its potential durability.

In this study, the ASTM C1202 test results were compared to surface resistivity test results at different ages. Both laboratory-made and field samples were tested to determine the correlation between the two methods. The surface resistivity measurements showed good agreement with the 56-day fast chloride permeability readings, with surface resistivity generally exhibiting less variability than the rapid chloride permeability test [23], [24].

3.5 Slump Test

Workability tests, such as the slump test, are commonly used to evaluate the concrete's consistency and workability before placement. The slump test is a cost-effective method that can be performed on-site without requiring laboratory equipment. It assesses variations in the construction ingredients, particularly the water-to-cement ratio [25].

The slump test measures the concrete's consistency at the middle workability level, indicating the amount of labor required for compaction and placement. The test ensures that the concrete's water content remains within the specified range. Significant changes in slump test results can be caused by factors such as improper water addition, aggregate batching variances, altered aggregate water requirements, and testing techniques [26].

During the creation and curing of test specimens, it is important to maintain a curing temperature between 22 and 25°C. Steel cube molds should not mix the sides and bases from separate molds.

3.6 Vebe Test

The Vebe test, also known as the Vee-Bee test, is used to evaluate the workability of fresh concrete. Named after its Swedish inventor V. Bahrner, the Vebe test assesses workability in terms of compaction and mobility. It indirectly determines the

workability by measuring the time required for compaction, which is related to the amount of work done [27].

In the Vebe test, the vibration process causes the concrete to shift from the slump cone form to the cylindrical form, known as the remoulding effect. The degree or seconds of VeBe are used to evaluate the remoulding effect.

The Vebe test is suitable for concrete with low slump values that cannot be accurately measured using the slump test. However, it may not be suitable for concrete with a slump higher than fifty millimeters due to intense vibration, making it difficult to measure or assess in seconds [28].

The Vebe test involves using a connected cylindrical cup with a slump cone inside. The cone is filled with concrete in four layers, compacted with a rod for 25 blows per layer. Excess concrete is struck off with a trowel to ensure proper filling. A clear glass disk mounted on a rotating arm is placed on top of the concrete, and the initial reading is recorded. The cone is then vertically removed, and the final reading is noted. The slump value, indicating the concrete's consistency, is calculated by subtracting the final reading from the initial reading. A vibrator is used to remold the concrete, and the time taken for complete remolding is recorded [29].

Fig. 2. fresh hardening concrete machine: a) VeBe test; b) Slump test

3.7 J-ring Test

The J-ring test is used to measure the passing ability of concrete, particularly self-consolidating concrete (SCC). It involves filling a J-ring with SCC and measuring the height of the concrete that passes through the ring. The results of the J-ring test for high-strength concrete (HSC) depend on various factors, including the mix design, aggregate properties, and testing conditions [30].

Achieving good passing ability in the J-ring test for high-strength concrete (HSC) can be challenging and depends on several factors, including the specific mix design, properties of the aggregates used, and testing conditions. Generally, HSC requires more attention and optimization to achieve satisfactory passing ability compared to lower strength concretes.

If the mix design of HSC has been properly optimized and the aggregates used have suitable particle size distribution and shape, it is possible to achieve good passing ability in the J-ring test. However, if the mix design is not tailored for optimal passing ability or the aggregates are not suitable for self-consolidating concrete (SCC), the results of the J-ring test may indicate poor passing ability.

The J-ring test is conducted by placing a base plate with a firm circle diameter of 500 mm on a leveled surface. The J-ring, which has a specific shape resembling the letter "J," is positioned on the base plate. SCC is poured into the J-ring until it is completely filled. The height of the concrete that passes through the J-ring is measured and recorded [31].

It is important to note that the results of the J-ring test for HSC can vary depending on the specific mix design, aggregate properties, and other factors. Achieving good passing ability requires careful consideration of these factors during the mix design process and thorough testing to evaluate the concrete's workability and flow characteristics [32].

4 Conclusion

In conclusion, the development and use of various concrete tests and methods are crucial for evaluating the properties and characteristics of concrete. Tests such as the slump test, Vee-bee test, J-ring test, and water absorption test provide valuable information about the workability, strength, and durability of fresh or hardened concrete.

Conducting these tests is essential to ensure that concrete meets the required specifications for a specific project. The results obtained from these tests play a vital role in identifying any issues or potential concerns with the concrete, allowing necessary adjustments and improvements to be made. It is important to perform these tests diligently, following the appropriate equipment, procedures, and industry standards to ensure accurate and reliable results. Inaccurate or inconsistent test outcomes can result in lower concrete quality, increased costs, and potential safety hazards.

Concrete testing holds significant importance in the construction industry. Keeping up with the latest methods and techniques is crucial for producing high-quality concrete that meets the desired specifications and complies with rigorous standards. By conducting thorough testing, construction professionals can ensure the durability and performance of concrete structures, contributing to the overall success and safety of construction projects.

References

1. Z. Yao, X. Li, C. Fu, and W. Xue, "Mechanical Properties of Polypropylene Macrofiber-Reinforced Concrete," Advances in Materials Science and Engineering, vol. 2019, 2019, doi: 10.1155/2019/7590214.
2. J. Liu, Y. Jia, and J. Wang, "Experimental Study on Mechanical and Durability Properties of Glass and Polypropylene Fiber Reinforced Concrete," Fibers and Polymers, vol. 20, no. 9, pp. 1900–1908, Sep. 2019, doi: 10.1007/s12221-019-1028-9.
3. S. Pyo and H. K. Kim, "Fresh and hardened properties of ultra-high performance concrete incorporating coal bottom ash and slag powder," Constr Build Mater, vol. 131, pp. 459–466, Jan. 2017, doi: 10.1016/J.CONBUILDMAT.2016.10.109.
4. M. Alkaysi, S. El-Tawil, Z. Liu, and W. Hansen, "Effects of silica powder and cement type on durability of ultra high performance concrete (UHPC)," Cem Concr Compos, vol. 66, pp. 47–56, Feb. 2016, doi: 10.1016/J.CEMCONCOMP.2015.11.005.
5. P. Samui, D. Kim, N. Iyer, and S. Chaudhary, New Materials in Civil Engineering. Elsevier, 2020. doi: 10.1016/B978-0-12-818961-0.00032-6.
6. H. Alghamdi, "A review of cementitious alternatives within the development of environmental sustainability associated with cement replacement," Environmental Science and Pollution Research, vol. 29, no. 28, pp. 42433–42451, Jun. 2022, doi: 10.1007/s11356-022-19893-6.
7. A. El-Sayed, I. N. Fathy, B. A. Tayeh, and I. Almeshal, "Using artificial neural networks for predicting mechanical and radiation shielding properties of different nano-concretes exposed to elevated temperature," Constr Build Mater, vol. 324, p. 126663, Mar. 2022, doi: 10.1016/j.conbuildmat.2022.126663.
8. U. J. Udi et al., "Efficiency of high performance fiber reinforced cementitious composites as a retrofit material for fire-damaged concrete," Mater Today Proc, vol. 61, pp. 477–486, 2022, doi: 10.1016/j.matpr.2021.12.278.
9. Moustafa and M. A. ElGawady, "Mechanical properties of high strength concrete with scrap tire rubber," Constr Build Mater, vol. 93, pp. 249–256, Sep. 2015, doi: 10.1016/j.conbuildmat.2015.05.115.
10. Y. Tian, S. Shi, K. Jia, and S. Hu, "Mechanical and dynamic properties of high strength concrete modified with lightweight aggregates presaturated polymer emulsion," Constr Build Mater, vol. 93, pp. 1151–1156, Sep. 2015, doi: 10.1016/j.conbuildmat.2015.05.015.
11. R. K. Dhir, J. de Brito, R. V. Silva, and C. Q. Lye, "Use of Recycled Aggregates in Road Pavement Applications," in Sustainable Construction Materials, Elsevier, 2019, pp. 451–494. doi: 10.1016/B978-0-08-100985-7.00012-1.
12. M. Y. Alabdulhady, M. F. Ojaimi, and A. H. Chkheiwer, "The efficiency of CFRP strengthening and repair system on the flexural behavior of RC beams constructed with different concrete compressive strength," Results in Engineering, vol. 16, p. 100763, Dec. 2022, doi: 10.1016/j.rineng.2022.100763.
13. Q. Tao, B. Niu, Y. Guan, J. Kong, C. Zhang, and Z. Kong, "Experimental and theoretical study on flexural behavior of high strength concrete encased steel beams with steel fibers," Structures, vol. 41, pp. 1359–1368, Jul. 2022, doi: 10.1016/j.istruc.2022.05.073.
14. Q.-F. Li and Z.-M. Song, "High-performance concrete strength prediction based on ensemble learning," Constr Build Mater, vol. 324, p. 126694, Mar. 2022, doi: 10.1016/j.conbuildmat.2022.126694.
15. P. Smarzewski and D. Barnat-Hunek, "Mechanical and durability related properties of high performance concrete made with coal cinder and waste foundry sand," Constr Build Mater, vol. 121, pp. 9–17, Sep. 2016, doi: 10.1016/j.conbuildmat.2016.05.148.

16. Y. Tian, S. Shi, K. Jia, and S. Hu, "Mechanical and dynamic properties of high strength concrete modified with lightweight aggregates presaturated polymer emulsion," Constr Build Mater, vol. 93, pp. 1151–1156, Sep. 2015, doi: 10.1016/j.conbuildmat.2015.05.015.
17. H. Beushausen and T. Dittmer, "The influence of aggregate type on the strength and elastic modulus of high strength concrete," Constr Build Mater, vol. 74, pp. 132–139, Jan. 2015, doi: 10.1016/j.conbuildmat.2014.08.055.
18. C. Rocco, G. V. Guinea, J. Planas, and M. Elices, "Review of the splitting-test standards from a fracture mechanics point of view," Cem Concr Res, vol. 31, no. 1, pp. 73–82, Jan. 2001, doi: 10.1016/S0008-8846(00)00425-7.
19. H. Ma, Z. Wu, H. Yu, J. Zhang, and C. Yue, "Experimental and three-dimensional mesoscopic investigation of coral aggregate concrete under dynamic splitting-tensile loading," Materials and Structures/Materiaux et Constructions, vol. 53, no. 1, Feb. 2020, doi: 10.1617/s11527-020-1447-5.
20. E. Denneman, E. P. Kearsley, and A. T. Visser, "Splitting tensile test for fibre reinforced concrete," Mater Struct, vol. 44, no. 8, pp. 1441–1449, Oct. 2011, doi: 10.1617/s11527-011-9709-x.
21. R. Spratt, J. Castro, T. Nantung, E. Paredes, and W. J. Weiss, "Variability Analysis of the Bulk Resistivity Measured Using Concrete Cylinders," 2011. doi: 10.5703/1288284314646.
22. P. Ghosh and Q. Tran, "Influence of parameters on surface resistivity of concrete," Cem Concr Compos, vol. 62, pp. 134–145, Sep. 2015, doi: 10.1016/j.cemconcomp.2015.06.003.
23. P. Joshi and C. Chan, "Rapid chloride permeability testing.," 2002.
24. T. D. Rupnow and P. J. Icenogle, "Surface Resistivity Measurements Evaluated as Alternative to Rapid Chloride Permeability Test for Quality Assurance and Acceptance," Transportation Research Record: Journal of the Transportation Research Board, vol. 2290, no. 1, pp. 30–37, Jan. 2012, doi: 10.3141/2290-04.
25. Y. Ghernouti, B. Rabehi, T. Bouziani, H. Ghezraoui, and A. Makhloufi, "Fresh and hardened properties of self-compacting concrete containing plastic bag waste fibers (WFSCC)," Constr Build Mater, vol. 82, pp. 89–100, May 2015, doi: 10.1016/j.conbuildmat.2015.02.059.
26. C. Dong et al., "Fresh and hardened properties of recycled plastic fiber reinforced self-compacting concrete made with recycled concrete aggregate and fly ash, slag, silica fume," Journal of Building Engineering, vol. 62, p. 105384, Dec. 2022, doi: 10.1016/j.jobe.2022.105384.
27. M. Hashemi, P. Shafigh, M. R. Bin Karim, and C. D. Atis, "The effect of coarse to fine aggregate ratio on the fresh and hardened properties of roller-compacted concrete pavement," Constr Build Mater, vol. 169, pp. 553–566, Apr. 2018, doi: 10.1016/j.conbuildmat.2018.02.216.
28. H. Rooholamini, A. Hassani, and M. R. M. Aliha, "Evaluating the effect of macro-synthetic fibre on the mechanical properties of roller-compacted concrete pavement using response surface methodology," Constr Build Mater, vol. 159, pp. 517–529, Jan. 2018, doi: 10.1016/j.conbuildmat.2017.11.002.
29. M. Nuruzzaman, J. O. Camargo Casimiro, and P. K. Sarker, "Fresh and hardened properties of high strength self-compacting concrete using by-product ferronickel slag fine aggregate," Journal of Building Engineering, vol. 32, p. 101686, Nov. 2020, doi: 10.1016/j.jobe.2020.101686.
30. G. H. Ahmed, H. Ahmed, B. Ali, and R. Alyousef, "Assessment of High Performance Self-Consolidating Concrete through an Experimental and Analytical Multi-Parameter Approach," Materials, vol. 14, no. 4, p. 985, Feb. 2021, doi: 10.3390/ma14040985.
31. "PRO_33_3rd_International_RILEM_Symposium".
32. X. Zhou, Y. Xie, G. Long, X. Zeng, J. Li, and F. Wang, "Simulating passing ability of self-compacting concrete in the J-ring test using cohesive particle liquid bridge model," Powder Technol, vol. 416, p. 118218, Feb. 2023, doi: 10.1016/j.powtec.2023.118218.

Effect of Reactive MgO Substitution on Strength Development and Microstructure Properties of Sodium Carbonate Activated Slag-Based Systems

Ömer Can Özen[1[0009-0004-9773-2984]], Didem Oktay[1[0000-0002-0093-1994]], Büşra Aktürk[2[0000-0003-1484-7758]]

[1] Yildiz Technical University, Civil Engineering Department, Istanbul, Türkiye,
omer.ozen@yildiz.edu.tr
dyasar@yildiz.edu.tr
[2] Istanbul Bilgi University, Faculty of Engineering and Natural Sciences, Istanbul, Türkiye,
busra.akturk@bilgi.edu.tr

Abstract. The high CO_2 emission and energy consumption caused by the production of cement, increases the need for more sustainable options today. Accordingly, replacing cement with natural pozzolans or by-products is a solution that reduces energy consumption and CO_2 emissions. Another alternative is alkali-activated materials (AAM), produced by calcium and/or silicon and aluminum-rich mineral additives instead of cement, and gaining strength after activation with alkaline activators. Sodium carbonate is one type of activator that can be obtained more easily compared to other alkaline activators has a high amount of reserves in Turkey. Drawbacks of sodium carbonate activation such as low early age strength and long setting times can be improved by using of various auxiliary materials such as slaked lime, sodium hydroxide or reactive MgO.

In this study, it is aimed to produce slag-based sodium carbonate-activated mixes, having sufficient early age strength and appropriate setting time values. To improve such properties, different amounts (0 - 15%) of reactive MgO were substituted with slag. One-part production method was applied for the mix productions. The consistency, setting time, compressive strength development properties of the produced mixtures were determined, and the microstructure properties were examined by X-ray diffractometry and scanning electron microscope at the age of 28th day.

The findings of the study revealed that substituting reactive MgO resulted in decreased consistency and setting time. However, a significant improvement in compressive strength, particularly at early stages, was observed. The reactive MgO/slag mixtures exhibited satisfactory compressive strength values, which can be attributed to their microstructure properties.

Keywords: Alkali-activated materials, sodium carbonate, compressive strength, microstructure.

1 Introduction

Portland cement is commonly chosen as the primary binder material for concrete production, given its widespread use in the construction industry. However, the production process of this cement, utilized in the concrete's structural composition, entails significant energy consumption during clinker production, resulting in substantial CO_2 emissions [1, 2]. Previous studies have revealed that these emissions account for approximately 7-8% of the total global CO_2 emissions from cement production [3]. For every ton of cement produced, around 1 ton of CO_2 is released [4]. Considering these statistics, there has been a growing trend in the industry to explore alternative binder systems, such as alkali-activated materials (AAM), which can form a binding matrix without relying on cement, thus mitigating the associated high energy consumption and CO_2 emissions. These alternative systems involve the use of amorphous alumina silicates, such as ground granulated blast furnace slag (GGBFS) and fly ash, in conjunction with alkali activators.

Various parameters play a crucial role in determining the properties of alkali-activated materials (AAMs), including the chemical structure and fineness of the binder material, the type and concentration of the activator, the mixing method, and the curing conditions [5-7]. Commonly used activators in alkali activation, such as sodium/potassium hydroxide and sodium silicate, are chosen for their ability to increase pH levels and facilitate binder dissolution. However, these activators are prone to fast setting times, leading to crack formation [8-9], and require significant energy during their production [10]. Sodium carbonate, on the other hand, presents a more environmentally friendly alternative as it demands less energy than other alkaline activators and can be sourced naturally. Nevertheless, systems employing sodium carbonate may exhibit lower pH values compared to those utilizing other activators, potentially resulting in reduced early age strength and delayed setting times [11,12].

Previous studies in the literature have highlighted the positive effects of incorporating reactive MgO in AAMs, enhancing compressive strength by establishing a stronger interface [13, 14, 15]. Although the use of sodium carbonate leads to slower strength development compared to other activators [16], it has been observed that incorporating MgO in slag-based systems, enhances early strength development to some extent [13, 17].

Existing literature on AAMs predominantly demonstrates the production of alkali activated mixes by preparing an alkali solution. However, this method poses challenges in real-life applications, as it necessitates an additional process compared to cement-based systems. Therefore, this study deviates from previous approaches by adding the activator in a dry powder form to the binder, subsequently incorporating water to the mixture. The study employed granulated blast furnace slag as the binder, with reactive MgO substituted accordingly. Furthermore, X-ray diffraction (XRD) and scanning electron microscopy (SEM) analyses were conducted to investigate the microstructure and hydration products in the study.

2 Experimental Study

2.1 Materials

In this study, ground granulated blast furnace slag (GGBFS) and reactive magnesium oxide (r-MgO) were used as binder materials. Sodium carbonate (NC) was employed as the activator in the system, added directly in powder form without the need for any solution preparation. The particle size distribution and chemical composition of the binders were assessed using Mastersizer and X-Ray Fluorescence analyses, as depicted in Figure 1 and outlined in Table 1, respectively.

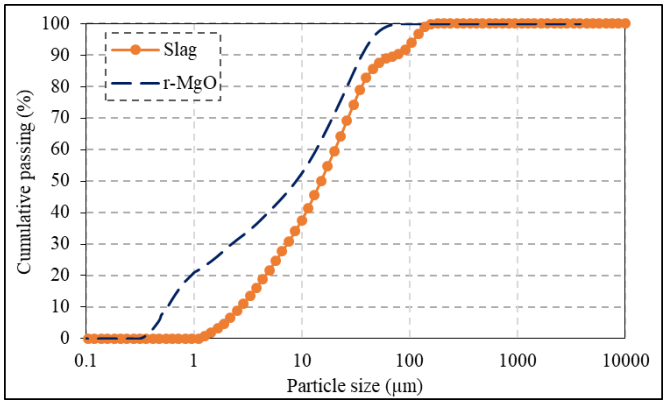

Fig. 1. Grain size distribution of slag and r-MgO.

Table 1. Chemical composition of binders.

Chemical composition (% by weight)	r-MgO	Slag
SiO_2	6.0	39.0
Al_2O_3	0.7	12.4
Fe_2O_3	0.3	1.2
CaO	7.9	33.7
MgO	83.6	7.5
SO_3	0.2	0.8
Na_2O	0.4	0.4
K_2O	0	0.6
Loss of ignition (%)	0.8	0.4
Specific surface area (m^2/kg)	1870	467
Relative grain density	3.55	2.88

2.2 Mix Proportions

In this study, both paste and mortar mixes were produced, and the corresponding mixing ratios can be found in Table 2.

As a reference, a mixture containing 100% GGBFS of binders was produced in both the paste and the mortar. Additionally, three different mixtures were created by substituting GGBFS and r-MgO at 5%, 10%, and 15% by weight. NC was used as the alkaline activator in these mixtures, with a consistent activator-to-binder ratio of 10% in all paste/mortar mixes. The water/binder ratio was maintained at 0.40 for paste mixes and 0.45 for mortar mixes. In mortar production, a silica-based fine aggregate with a maximum grain size of 2 mm was utilized at a volume rate of 50%, distinguishing it from the paste mixtures.

Table 2. Mixing ratios of paste mixes.

Mixes	GGBFS (%)	r-MgO (%)	NC (%)	Water/binder ratio
Ref	100	-	10	0.4
5Mg	95	5		
10Mg	90	10		
15Mg	85	15		

2.3 Testing Methods

Flow diameter. In order to assess the flow properties of the mortar samples, the freshly prepared mixtures were evaluated using a mini-slump cone (with an upper diameter of 70 mm, lower diameter of 100 mm, and height of 50 mm) in accordance with ASTM C1437.

Setting Time. The setting time of the paste mixtures was determined using an automatic Vicat apparatus in accordance with ASTM C191.

Compressive Strength. The compressive strength test was performed following the ASTM C109, and mortar specimens were produced as cube samples measuring 50×50×50 mm. After the demolding, the specimens were stored in a humidity cabinet maintained at a temperature of (21±2) °C and relative humidity of 65% until the testing days. The samples were tested on the 3rd, 7th, and 28th days, and the corresponding strength values for each respective day were recorded.

Microstructure Analysis

XRD Analysis. The hydration products of the paste samples were identified using XRD analysis, and the corresponding analysis was completed on 28 days. The paste samples were broken into small pieces and dried for 24 hours at 60°C. The *XPERT-PRO* X-ray diffractometer analyzer was used and the samples were gradually scanned at 0.02° 2θ step size and 1 s/step measurement duration from 5° 2θ to 70° 2θ diffraction angles.

SEM Analysis. SEM observations in back-scattered Electron (BSE) mode were performed on the *ZEISS EVO LS10* at an accelerator voltage of 15 kV. All samples are tested on the 28th day of the reaction. BSE images, which were gathered at a magnification of 5000×, were utilized to identify the non-hydrated slag particles and the gel structure of the mixtures.

3 Results and Discussion

3.1 Flow Diameter

The flow diameters of the mortar mixes shown in Figure 2. The flow diameter decreased with the increase of the amount of r-MgO substitution. In the *Ref* mixture, the observed flow diameter measured 210 mm, while in the *15Mg* mixture, it was recorded as 135 mm. On the other hand, the *10Mg* and *15Mg* mixes represented similar results.

The lower flow diameter with the r-MgO substitution attributed to the higher specific surface of r-MgO compared to slag (Figure 1) and its higher water absorption capacity [18].

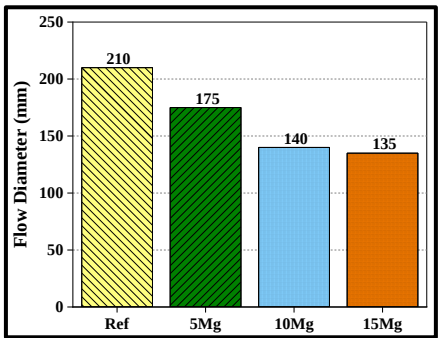

Fig. 2. Flow diameter values of mortar mixes.

3.2 Setting Time

The measured setting times of the mixtures are given in Figure 3. The initial setting time of the *Ref* mixes was found as 268 min, decreased by 75-85% with the substitution of r-MgO, resulting in a more rapid setting process. Comparing the *10Mg* and *15Mg* series, both exhibited similar setting times. As the ratio of slag-substituted r-MgO was increased to 10% and 15%, the initial setting time was approximately 35-50% shorter (reduced from 67 mins to 43 and 34 mins) compared to the *5Mg* series.

In terms of the final setting time, a similar trend was observed when comparing the different mixes. The *10Mg* and *15Mg* series exhibited the lowest final setting time at 90 minutes, while the *Ref* and *5Mg* series experienced final setting times of 420 and

200 minutes, respectively. The substitution of r-MgO significantly reduced the setting time, and lower values were obtained as the substitution rate increased.

Based on the findings of this study, it was observed that the substitution of r-MgO enhances hydration and corroborates the results reported in previous studies [19, 20]. Furthermore, there is a consistent correlation between setting time measurements and flow diameter values, indicating a similar pattern. (Fig. 2 & 3).

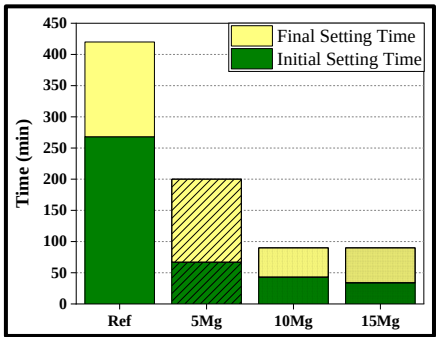

Fig. 3. Initial and final setting time results

3.3 Compressive Strength

The compressive strength values of the mixtures at 3, 7 and 28 days are given in Figure 4. The lowest strength values, measured as 0.69, 3.34, and 8.02 MPa in the *Ref* series, respectively, demonstrated significant improvement and reached higher values with the substitution of r-MgO. Notably, the *15Mg* series exhibited the highest compressive strength values (26.3, 34.4, and 39.0 MPa) on all test days.

Upon reviewing the results, it was observed that the substitution of r-MgO in the mixes resulted in significant improvements. Specifically, there was a 25-40 times enhancement in the 3-day results, and an approximately 5 times increase in the 28-day results compared to the *Ref* series.

Although it was seen in previous studies that NC-activated systems represent low early age strength and long setting times, it was observed that r-MgO substitution in slag-based systems significantly improved strength development [13, 16, 17, 21]. The results presented in this study also support the results of previous studies.

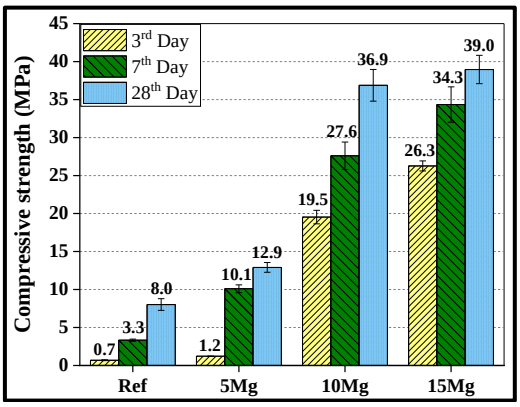

Fig. 4. Compressive strength results of mortar mixes

3.4 Microstructure

XRD patterns of the mixes at the 28th day is given in Fig. 5. It was found that the main hydration products are C-(A)-S-H, calcite, hydrotalcite, gaylussite and periclase.

Main binding phase C-(A)-S-H, reflected at 29.4° (2θ), was seen in all mixtures. At the same point, a peak was also found for calcite, which was also detected at 36°, 39°, and 43° (2θ), resulting from the interaction between slag and NC. Gaylussite was determined at approximately 14°, 28° and 33° (2θ), while hydrotalcite was determined at 12°, 23°, 34° and 39° (2θ).

It was observed that the intensity of the hydrotalcite and calcite peaks increased as the r-MgO substitution increased. This increase may explain the higher strength values observed in the MgO-substituted series.

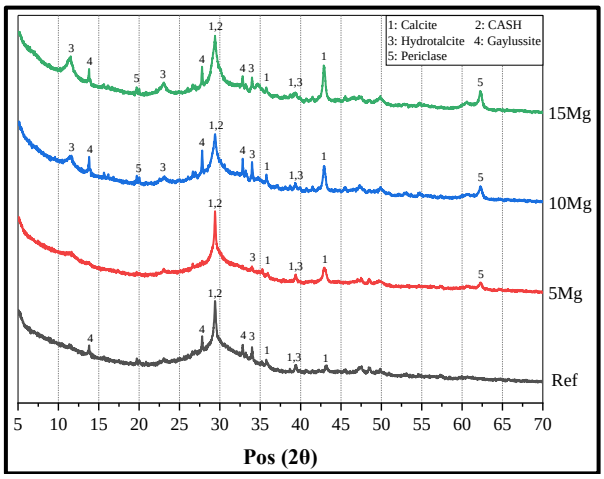

Fig. 5. XRD pattern of the 28th day.

The SEM images are captured from the paste mixtures at the 28th day of the reaction and shown in Fig. 6. As a result of the images obtained, it was seen that a less cracked and more void-free structure was obtained with the r-MgO substitution. These results can explain why the series with the highest compressive strength is *15Mg*, due to the direct ratio between the r-MgO amount and the compressive strength.

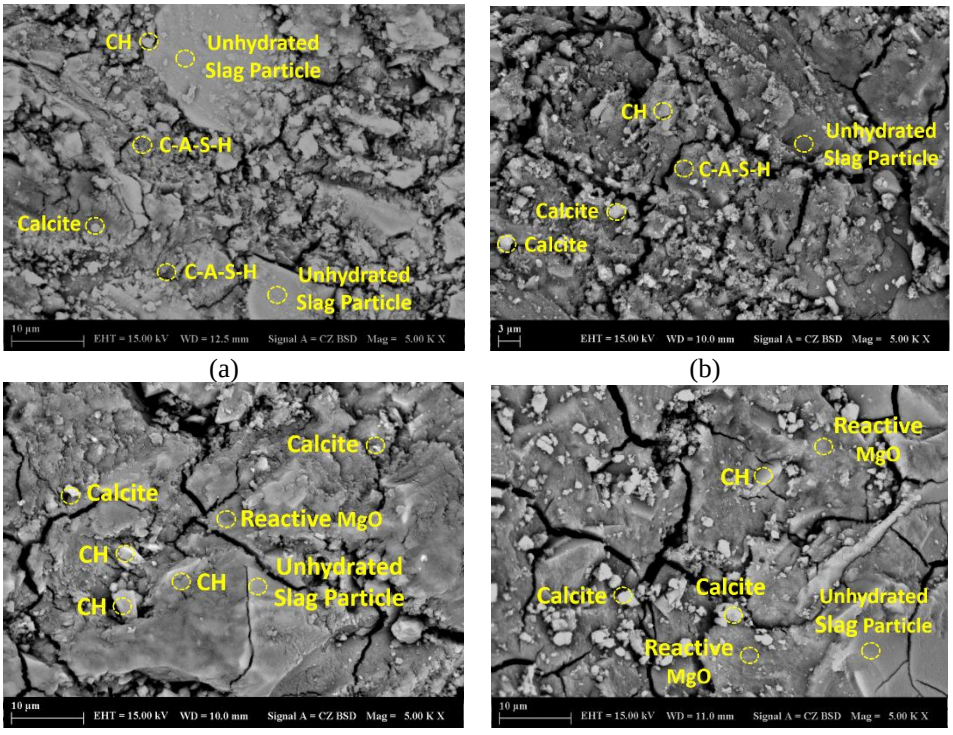

Fig. 6. SEM images for all specimens (a) *Ref*, (b) *5Mg*, (c) *10Mg*, (d) *15Mg*.

4 Conclusion

In this study, the effects of r-MgO substitution on NC-activated slag based systems were investigated.

It was observed that as the r-MgO substitution increased, the compressive strength increased and greatly accelerating the setting time. It was determined that the r-MgO substitution reduced the workability by causing a loss of flow diameter.

As a result of microstructural analysis, it was observed that calcite, C-(A)-S-H, hydrotalcite, gaylussite and periclase were the main reaction products, and the strength development in different mixes can be explained with the obtained data. Microstructural analysis results were found to be compatible with compressive strength results.

In addition, it has been seen that the alkali activator to be used in alkali-activated materials systems is more environmentally friendly when used as a one-part, and it shortens the time in terms of applicability and provides a great convenience in the production process.

Acknowledgments
This work was carried out within the scope of the projects titled "Production of Nano silica-added, Sodium Carbonate Activated Reactive MgO/Slag Based Binder Systems: Rheological, Microstructure Properties, Performance and Manufacturability by Digital Technologies " supported by Istanbul Bilgi University Scientific Research Projects (Project No: AK85096) and “Effects of Nano-Silica Additive on Hydration Mechanism and Mechanical Properties of Sodium Carbonate-Activated Reactive MgO/Slag Based Systems” supported by Yildiz Technical University Scientific Research Projects (Project No: FYL-2023-5636).

References

1. Bains, P., Psarras, P., Wilcox, J.: CO2 capture from the industry sector. Progress in Energy and Combustion Science, 63, 146-172 (2017).
2. Matalkah, F., Ababneh, A., Aqel, R.: Effects of nanomaterials on mechanical properties, durability characteristics and microstructural features of alkali-activated binders: A comprehensive review. Construstion and Building Materials, 336, 127545 (2022).
3. Forero, J.A.; Bravo, M.; Pacheco, J.; de Brito, J.; Evangelista, L.: Fracture Behaviour of Concrete with Reactive Magnesium Oxide as Alternative Binder. Appl. Sci., 11, 2891 (2021).
4. Deja, J., Uliasz-Bochenczyk, A., Mokrzycki, E.: CO2 emissions from Polish cement industry. International Journal of Greenhouse Gas Control, 4(4), 583–8 (2010).
5. Provis, J. L., Van Deventer, J. S.: Alkali activated materials: state-of-the-art report, RILEM TC 224-AAM (Vol. 13). Springer Science & Business Media (2013).
6. Khale, D., Chaudhary, R.: Mechanism of geopolymerization and factors influencing its development: a review. Journal of materials science, 42(3), 729-746 (2007).
7. Komnitsas, K., Zaharaki, D.: Geopolymerisation: A review and prospects for the minerals industry. Minerals engineering, 20(14), 1261-12773-5 (2007).
8. Yuan, X. H., Chen, W., Lu, Z. A., Chen, H.: Shrinkage compensation of alkali-activated slag concrete and microstructural analysis. Construction and Building Materials, 66, 422-428 (2014).
9. Lee, N. K., Lee, H. K.: Setting and mechanical properties of alkali-activated fly ash/slag concrete manufactured at room temperature. Construction and Building Materials, 47, 1201-1209 (2013).
10. Turner, L. K., Collins, F. G.: Carbon dioxide equivalent (CO2-e) emissions: A comparison between geopolymer and OPC cement concrete. Construction and building materials, 43, 125-130 (2013).
11. Dung, N.T., Hooper, T.J.N., Unluer, C.: Improving the carbonation resistance of Na2CO3-activated slag mixes via the use of reactive MgO and nucleation seeding. Cement Concr. Compos. 115, 103832 (2021).
12. Burciaga-Díaz, O.: Parameters affecting the properties and microstructure of quicklime (CaO)- Activated slag cement pastes. Cement Concr. Compos. 103, 104–111 (2019).

13. Akturk, B., Abolfathi, M., Ulukaya, S., Kizilkanat, A. B., Hooper, T. J. N., Gu, L., Yang, E., Unluer, C.: Hydration kinetics and performance of sodium carbonate-activated slag-based systems containing reactive MgO and metakaolin under carbonation. Cement and Concrete Composites, 132, 104617 (2022).
14. Taj, K., Akturk, B., Ulukaya, S.: Fresh state properties and compressive strength development of reactive MgO-based systems, Materials Today: Proceedings, Volume 65, Part 2, 1064-1069 (2022).
15. Wu, H.L., Zhang, D., Ellis, B.R., Li, V.C.: Development of reactive MgO-based Engineered Cementitious Composite (ECC) through accelerated carbonation curing, Construction and Building Materials, Volume 191, 23-31 (2018).
16. Akturk, B., Nayak, S., Das, S., Kizilkanat, A.B.: Microstructure and Strength Development of Sodium Carbonate–Activated Blast Furnace Slags, Journal of Materials in Civil Engineering, Volume 31 (2019).
17. Pu, L., Unluer, C.: Effect of Preconditioning on Carbonated Reactive MgO-Based Concrete Samples, Journal of Materials in Civil Engineering, Volume 32 (2020).
18. Vo, D. H., Hwang, C. L., Yehualaw, M. D., Liao, M. C.: The influence of MgO addition on the performance of alkali-activated materials with slag-rice husk ash blending. Journal of Building Engineering, 33, 101605 (2020).
19. He, J., Zheng, W., Bai, W., Hu, T., He, J., Song, X.: Effect of reactive MgO on hydration and properties of alkali-activated slag pastes with different activators. Construction and Building Materials, 271, 121608 (2021).
20. Jin, F., Gu, K., Al-Tabbaa, A.: Strength and hydration properties of reactive MgO-activated ground granulated blastfurnace slag paste. Cement Concr. Compos. 57, 8–16 (2015).
21. Li, Z., Zhang, W., Wang, R., Chen, F., Jia, X., Cong, P.: Effects of Reactive MgO on the Reaction Process of Geopolymer. Materials, 12, 526 (2019).

Influence of Binary Use of Antifreeze Admixtures on The Early-Age Frost Resistance of Self-Compacting Concretes

Ali Öz[1][0000-0002-6590-3775], Fatma Karagöl[2][0000-0003-1760-1972], Rıza Polat[3][0000-0002-8990-035X] and Cemal Karaaslan [4][0000-0002-8993-7566]

[1] Ataturk University, Civil Engineering Department, Türkiye, alioz@atauni.edu.tr
[2] Ataturk University, Civil Engineering Department, Türkiye, fatma.karagol@atauni.edu.tr
[3] Ataturk University, Civil Engineering Department, Türkiye, rizapolat@atauni.edu.tr
[4]Iğdır University, Iğdır, Türkiye, cemal.karaaslan@igdir.edu.tr

Abstract. This study investigates the impact of antifreeze admixtures on the early-age frost resistance of self-compacting concretes (SCCs). Antifreeze admixtures, including calcium nitrate and sodium thiocyanate, were used in binary combinations. The physical properties of SCCs, such as sorption coefficients and compressive strengths, were evaluated under different curing conditions. The results showed that antifreeze admixtures effectively reduced water absorption and improved the compressive strength of SCCs. The use of antifreeze admixtures mitigated the adverse effects of cold air exposure on the sorption coefficients and helped maintain higher compressive strengths compared to the reference samples. Additionally, pore analysis by nitrogen adsorption and Scanning Electron Microscopy (SEM) with Energy-Dispersive X-ray Spectroscopy (EDS) were conducted to assess the microstructural characteristics of SCCs.

Keywords: Self-compacting concrete (SCC); Cold weather concrete; Early-age frost damage; Antifreeze admixture; Binary use of admixtures.

1 Introduction

Concrete sets and gains strength as a result of hydration reactions between compounds of cement and mixing water. In order hydration reactions to take place, there must be sufficient water in the concrete and the concrete must be hot enough. In cold weather, the setting of the concrete is delayed and the rate of strength gain decreases, and as a result, the stripping times are prolonged [1]. At temperatures below 0 °C, moreover, the water in the capillary pores and larger voids can freeze. If the freezing event takes place before the concrete has set yet, there is an increase in the volume of the concrete as a result of the mixing water in the concrete turning into ice. As the water in the concrete converts to ice, there is not enough water for the hydration reactions. When at a later stage thawing takes place, the concrete can set and harden in such a case. However, even in this case, the enlarged pores due to the formation of ice cannot be sufficiently filled by the hydration products [1, 2]. Therefore, it becomes a concrete with low

strength and high-water permeability. Similarly, if freezing occurs following the concrete has set but before it has improved an appreciable maturity (compressive strength: ~3.5 MPa) [3], cracks occur in the concrete due to the freezing of the water in the capillary pores and causing the concrete to become a low-strength concrete [4].
The conditions of cold weather concreting exist when the air temperature drops to 4°C or below, during the protection period of the concrete from the adverse effects of cold weather [3]. Without additional precautions, this situation renders concrete casting impossible over an extended period in countries such as Turkey. For instance, in the province of Erzurum where this study was conducted, the average temperatures for the months of December, January, and February between 1929 and 2021 were -5.8 °C, -9.1 °C, and -7.7 °C, respectively [5]. To enable concrete casting during prolonged cold weather conditions, one solution is to heat the water and aggregates used in production to maintain a higher concrete temperature. However, excessively high concrete temperature increases heat loss rate and water requirement for a consistent workability, limiting the effectiveness of this approach [2]. The adverse effects of cold weather on concrete can be somewhat mitigated by employing high early strength cement, using a higher dosage of cement, and designing with a low water-cement ratio. Creating curing conditions that keep the concrete warm and utilizing accelerating admixtures are other methods that enable concrete casting in cold weather. Nevertheless, casting concrete in cold weather using these methods is generally more expensive due to the equipment requirements for protecting fresh concrete from freezing [6]. One of the effective methods that protects concrete from early-age frost damage is the use of antifreeze admixtures in the concrete. The application of this method is simple and relatively cheaper, and thanks to this method, concreting at lower temperatures is possible [6, 7]. It is known that Russia has been using antifreeze admixtures such as sodium chloride, calcium chloride, potash, sodium nitrite, calcium nitrate, urea, calcium nitrite nitrate and calcium chloride-nitrite-nitrate in cold-weather concreting for nearly 70 years [8, 9]. Antifreeze admixtures are commonly employed in cold weather concretes for the dual purposes of reducing the freezing point of water present in the concrete and accelerating hydration reactions [8, 10]. These admixtures ensure the protection of fresh or inadequately matured concrete from freezing by lowering the freezing point of the aqueous solution in the concrete to a temperature below the freezing point, thus safeguarding it from early-age frost damage. In addition, admixtures containing the same cations as C3S and C2S, such as calcium chloride, calcium nitrite and calcium nitrate, accelerate the hydration by forming the nucleating effect of such ions, thus enabling the concrete to reach sufficient maturity in an acceptable period [11]. Demirboğa et al. [9] revealed that in addition to the benefits stated above, urea reduces the permeability of concrete and fills the interfacial transition zone between cement paste and aggregate. Karagöl et al. investigated the impact of calcium nitrate-based antifreeze admixture on cold weather concretes and concluded that the addition of calcium nitrate not only lowers the freezing point of water but also significantly accelerates hydration reactions, promoting the rapid maturation of concrete and thus providing protection against cold weather conditions up to -20 °C. Polat investigated cold weather concretes by incorporating calcium nitrate and urea at a dosage of 6% of the cement weight and found that calcium nitrate was more effective than urea in

protecting the concrete from early-age frost damage. Khan and Kumar investigated the synergistic effects of calcium nitrate and sodium thiocyanate, which significantly contributed to the strength improvement of concrete under different curing conditions in cold weather. This finding provides a promising and practical solution for enhancing the applicability of concrete in cold weather conditions. In their study, Öz et al. [12] determined that calcium nitrate is more effective than sodium thiocyanate in protecting Self-Compacting Concretes (SCCs) from early-age freeze damage when used as individual additives.

Although there have been numerous studies on the use of antifreeze agents in conventional concretes, the utilization of antifreeze agents in SCCs has received relatively limited attention. In the present study, high-concentration solutions of calcium nitrate and sodium thiocyanate were employed as binary admixtures in self-compacting cold weather concretes. The capillary permeability coefficients and compressive strengths at 28 days were determined, and BET (Brunauer, Emmett and Teller) method and SEM-EDS (Scanning Electron Microscope and Energy Dispersive X-Ray Spectroscopy) analyses were performed to assess the characteristics of these concretes.

2 Experimental Program

2.1 Materials

Portland cement (CEM I 42.5R) in accordance with TS EN 197-1 [13] supplied from Aşkale Cement Factory (Erzurum-Türkiye) was used. The chemical composition of this cement is provided in Table 1.

Table 1. Chemical composition of cement (wt.%).

	SiO_2	Al_2O_3	Fe_2O_3	CaO	MgO	SO_3	Na_2O	K_2O	Cl
Cement	18.99	4.62	3.36	63.04	1.83	2.80	0.27	0.86	0.009

Sodium thiocyanate and calcium nitrate antifreeze admixtures in accordance with TS EN 934-2:2011+A1 [14] standard were used to increase the resistance of concrete against early-age frost damage. It should be noted that the concentration of these antifreeze admixtures used in this study is higher than that of the ones employed in the referenced study [12]. A polycarboxylate-based hyperplasticizer admixture was used in order for the SCC to have sufficient consistency. Table 2 presents some properties of these chemical admixtures.

Table 2. Properties of the chemical admixtures.

	CHRYSO FLUID HP 1106 (Hyperplasticizer)	**CHRYSO®LAB BET 11542 (Sodium thiocyanate)**	**CHRYSO®XEL AH 50 (Calcium nitrate)**
Appearance	Liquid	Homogeneous	Homogeneous
Colour	Light brown	Yellow	Brown
Density (gr/cm^3) (20 °C)	1.065	1.296	1.328
pH	6.00	7.74	6.11
Water soluble chloride (%)	<0.1	0.08	0.02
Solid content (%)	32.00	49.36	40.52
Alkali content (%)	<6	<5	<5

2.2 Production of SCC samples

Three SCC batches were produced, one as the reference mixture without antifreeze admixtures and the others containing both calcium nitrate and sodium thiocyanate admixtures. The mix proportions and IDs of these batches are provided in Table 3. The CN2-ST1 mixture had an additive ratio of 2% calcium nitrate and 1% sodium thiocyanate, while the CN1-ST2 mixture had an additive ratio of 1% calcium nitrate and 2% sodium thiocyanate. The water/cement ratio for each SCC mixture was kept constant at 0.326, and a constant 7.5 kg/m^3 of hyperplasticizer was used.

Table 3. Mix proportions (kg/m^3).

Mix ID	Cement	Water	Hyper-plasticizer	Calcium nitrate	Sodium thiocyanate	Sand (0 -5 mm)	Gravel (5 -15 mm)
Reference	500	163	7.5	-	-	1271	420
CN2-ST1	500	163	7.5	10	5	1247	412
CN1-ST2	500	163	7.5	5	10	1247	412

The workability properties of the fresh SCC mixes were evaluated following the methods specified in the European standard EFNARC [15]. Table 4 presents the workability properties of the Reference mix. According to EFNARC, this mix can be categorized as SCC and falls into the SF2 class in terms of consistency classification. Similarly, based on this standard, the mix is identified as VS2 and VF1 according to the T_{500} flow time and V-funnel time, respectively. Furthermore, the passing ability (PA) value of the SCC obtained using the L-box test exceeds the minimum limit of 0.8 [15]. The workability properties of the other SCC mixtures are not provided as they conform to this classification.

Table 4. Workability properties of the Reference mix test results.

Slump flow diameter (mm)	T_{500} flow time(s)	J-ring (mm)	L-box (PA)	V-funnel (s)
700	2.5	20	0.9	7

The freshly mixed SCC was placed in cylindrical molds with a diameter of 10 cm and a height of 20 cm. Three different curing regimes were applied to the freshly mixed SCCs: (i) standard curing conditions specified in TS EN 12390-2 [16], (ii) standard curing medium after 12 hours in a deep freezer at -5 °C, and (iii) standard curing medium after 12 hours in a deep freezer at -10 °C. The standard curing conditions involved keeping the samples covered with a damp tissue in the mold for 24 hours at 20±2 °C, followed by removal from the mold and immersion in a water tank saturated with lime at 20±2 °C until the testing day. The samples subjected to deep freezing were taken out after 12 hours and placed in the aforementioned water tank.

2.3 Test Methods

The capillary absorption coefficients of the SCC samples were determined on 28-day specimens following the guidelines of TS EN 113057 [17]. The 28 day compressive strengths of the SCCs were measured according to the relevant standard TS EN 12390-3 [18].
To assess the surface areas, pore volumes, and distributions of SCC samples with a porous structure, the Micromeritics3 Flex 3-port BET (Brunauer, Emmett, and Teller) surface area and micropore measuring device was employed. Additionally, the ZEIS Gemini Sigma 300 model scanning electron microscope (SEM) and energy dispersive X-ray spectroscopy (EDS) were utilized to examine the microstructure of the SCCs and determine their chemical composition.

3 Results and Discussion

3.1 Physical Properties

Figure 1 presents the variation of sorption coefficients for SCCs with different curing regimes over time. Initially, the water absorption by the concrete is relatively high, but it gradually decreases as the test progresses [2]. Consequently, while the sorption coefficient is initially high for all samples, it diminishes after 24 hours. In Figure 1, the sorption coefficients of SCCs incorporating antifreeze admixture are depicted, showing minimal influence from cold air exposure. Conversely, the SCC without antifreeze admixture exhibits a notable increase in sorption coefficient attributed to freezing temperatures.

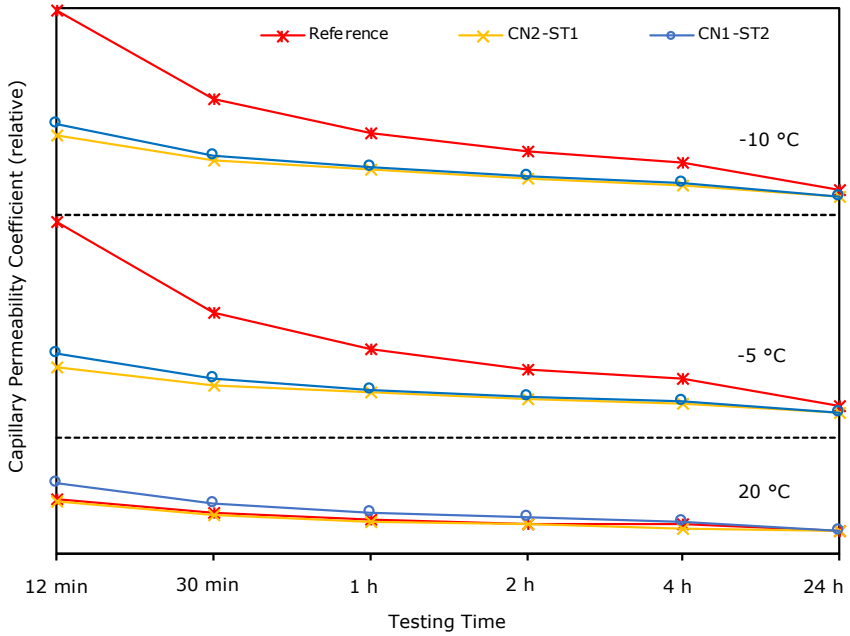

Fig. 1. Variation of sorption coefficients of SCCs under different curing conditions over time.

Figure 2 illustrates the sorption coefficients of self-compacting concretes (SCCs) during the 24-hour test period under various curing conditions. The sorption coefficients of the Reference samples cured under standard conditions range from 0.17 to 0.21 $kg/m^2.h^{0.5}$. Notably, reducing the curing temperature during the initial 12 hours from 20 °C to -5 °C and -10 °C resulted in a significant increase in the sorption coefficients of the Reference samples, namely by 68.1% and 83.5%, respectively.

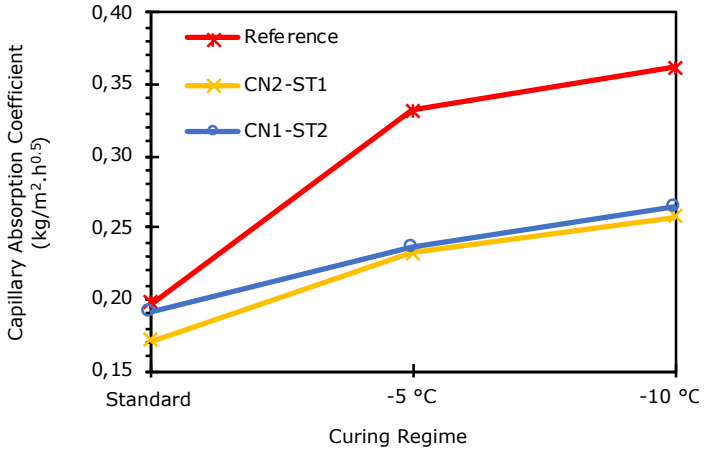

Fig. 2. Sorption coefficients of SCCs for the 24-hour test period under different curing regimes.

However, the samples with antifreeze admixtures exhibited limited increases in sorption coefficients under the same temperature variations. This water absorption primarily occurs through the capillary network, characterized by interconnected capillary pores within the fresh concrete structure. Freezing of water within these pores leads to expansion and increased connectivity of the capillary network. Nevertheless, the use of antifreeze admixtures lowers the freezing point of the aqueous solution in the capillary pores of SCCs, thereby mitigating the adverse impact of cold air.

3.2 Compressive Strength

The 28-day compressive strengths of the reference sample, CN2-ST1, and CN1-ST2 were determined as 31.1 MPa, 35.9 MPa, and 40.64 MPa, respectively. The incorporation of antifreeze admixture resulted in a significant improvement in the 28-day compressive strengths of SCCs, with increases of 15.3% (CN2-ST1) and 30.6% (CN1-ST2) observed [19].

Figure 3 shows the compressive strengths of all mixes after standard water curing. It is seen from Figure 3 that the results of mixes with antifreeze admixture were higher than reference samples. Figure 4 illustrates the compressive strengths of SCCs at deep freezer temperatures (-5 °C and -10 °C). For both temperatures, the compressive strengths of CN1-ST2 and CN2-ST1 samples were higher compared to the reference samples. Moreover, the residual compressive strength of SCCs containing antifreeze admixture was higher than that of the reference samples.

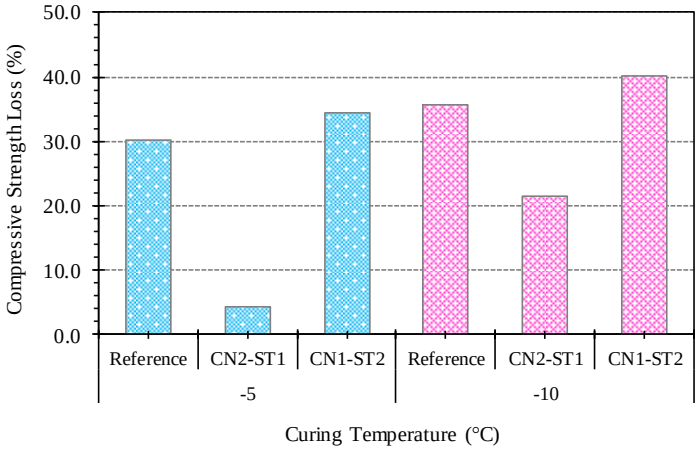

Fig. 3. Compressive strengths of SCCs exposed to standard cure.

3.3 Pore Analysis by Nitrogen Adsorption

BJH adsorption average pore diameters and pore volumes of SCCs assessed by BJH method are listed in Table 5. According to Table 5, adsorption average pore diameters increased with decline of temperature. As a result of micro cracks formed due to internal stresses caused by the transformation of water into ice, an increase in the void's diameter occurred in both groups. However, the pore diameter of the reference mix is higher than that of CN1-ST2.

Figures 5-6-7-8 show BJH adsorption cumulative pore volumes of reference and CN1-ST2 exposed to water curing and -10°C ambient temperature. The void structure in the cement paste significantly affects the mechanical and durability properties of the concrete. While macro voids reduce strength, the effect of microvoids varies according to their size. For example, pores below 20 nm are unharmful, and pores below 50 nm do not adversely affect strength [20]. In this context, Figures 5 and 6 illustrate the total cumulative pore volume rises from 0.035718 to 0.058241 in the reference mix. Furthermore, the cumulative pore volume below 10 nm of the reference in water curing is 0.031126, while that of the CN1-ST2 is 0.042747. Likewise, the cumulative pore volume below 10 nm of the reference mixture exposed to -10°C is 0.051210, "while that of the CN1-ST2 mixture is approximately 0.056015.

Table 5. The basic textural parameters of the SCCs.

Specimen	BJH adsorption average pore diameter (nm)	Single point desorption total pore volume of pores less than 40,3122* (cm^3/g)
Reference	16.5648	0.022457
Reference (-10 °C)	17.6195	0.035170
CN1-ST2	9.2811	0.049180
CN1-ST2 (-10 ° C)	15.4182	0.051531

*Single point adsorption: total pore volume of pores less than 40.3122 nm width at $p/p_0 = 0.9500$.

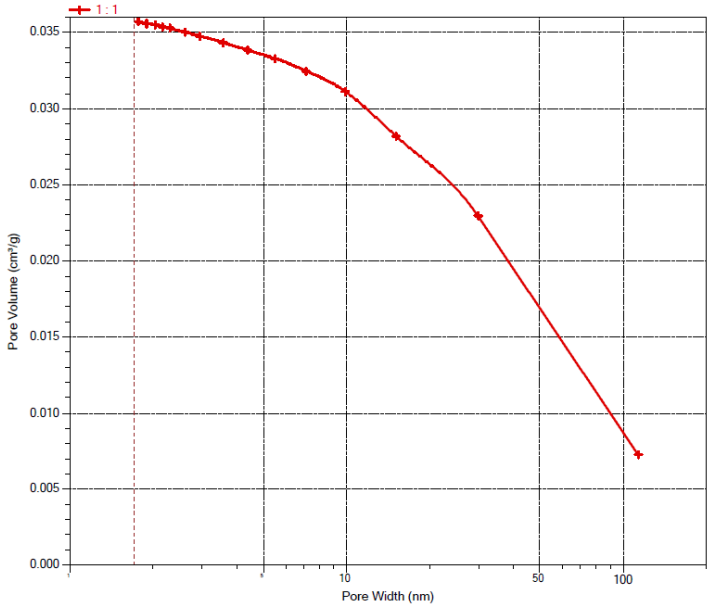

Fig. 4. BJH Adsorption Cumulative Pore Volume (Larger) of Reference

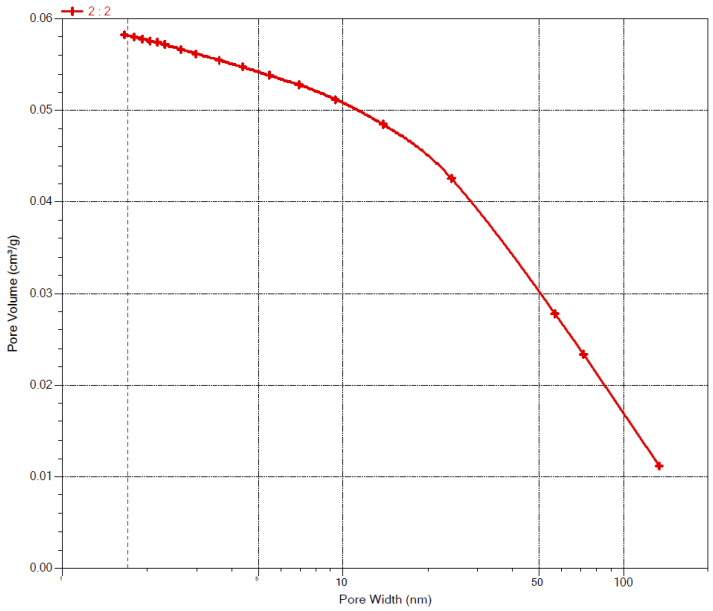

Fig. 5. BJH Adsorption Cumulative Pore Volume (Larger) of Reference (-10°C)

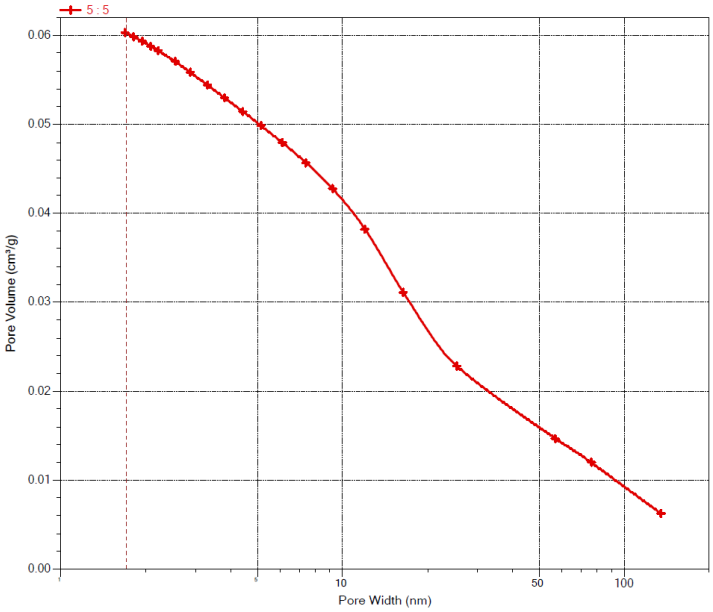

Fig. 6. BJH Adsorption Cumulative Pore Volume (Larger) of CN1-ST2

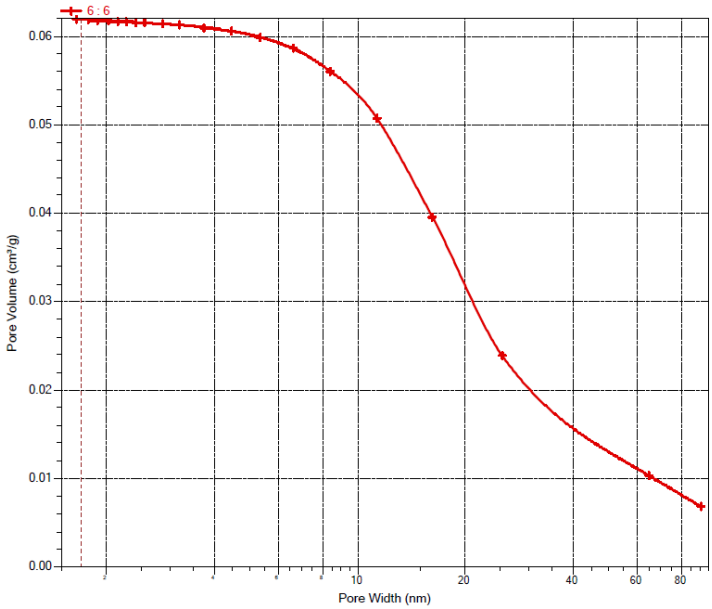

Fig. 7. BJH Adsorption Cumulative Pore Volume (Larger) of CN1-ST2 (-10°C)

The cumulative pore volume as a function of pore width was obtained using the BJH method and is given in Figure 9 [21]. In the Figure 8, although the total pore volume of all mixes increased due to cold weather, the pore volume below 10 nm in CN1-ST2 is higher than the reference. The cumulative pore volume above 50 nm at the reference is also higher than that of CN1-ST2. This situation coincides with both compressive strength results and SEM analyses.

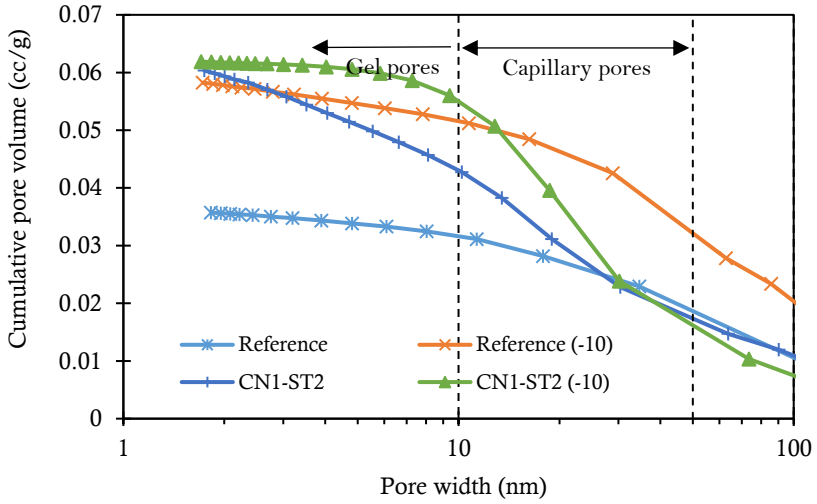

Fig. 8. Cumulative pore volume distribution of the SCCs as a function of pore width

3.4 SEM and EDS Analyzes

When the SEM images in Figure 10 are evaluated, there are differences in the internal structures of the reference samples in the standard water curing and exposed to freezing in the fresh state. According to ACI Committee 306R-88 and TS 1248, concrete must reach a strength of at least 3.5-5 MPa in order not to be damaged by freezing-thawing. However, high destruction is expected because of the freezing of water in the voids of the saturated fresh reference samples in plastic consistency in the experimental conditions applied in this study. In this context, while a denser structure is seen in standard water curing, it is seen that cracks and voids are formed as a result of internal stresses caused by the freezing water volume in samples subjected to cold weather. In addition, the decrease in crystal densities observed in the SEM-EDS analyzes of the samples exposed to freezing is due to the slowdown of the hydration reaction rate and the delay of the reactions.

When the SEM images and EDS analyses of the antifreeze-added CN1-ST2 mixture in Figure 11 were evaluated, cracks and voids occurred when the temperature decreased, as in the reference samples. However, it has been determined that the voids and cracks are fewer, the crystal peaks in SEM-EDS analyses are higher than the reference sample, and the peak differences at low temperatures are less than in the control sample.

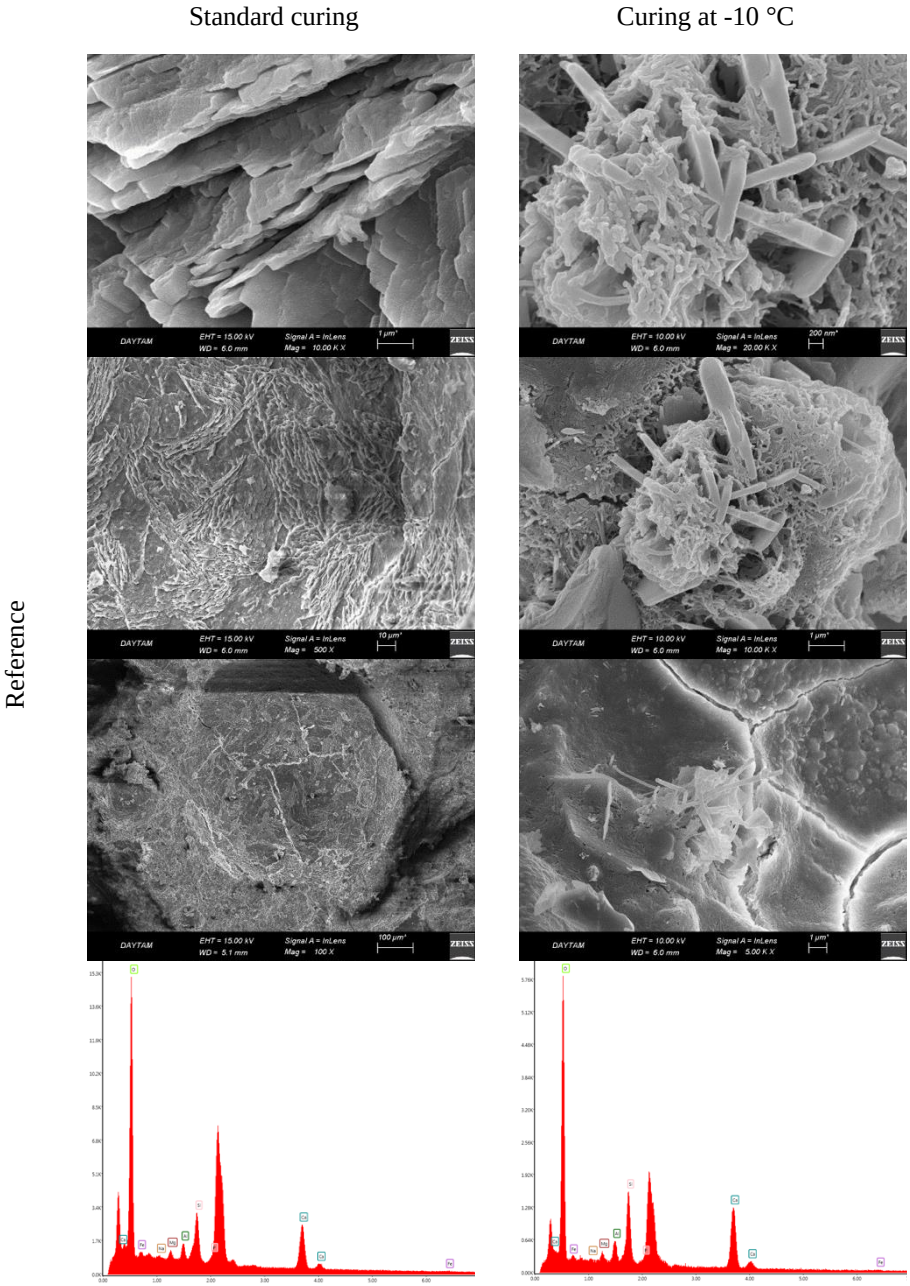

Fig. 9. SEM images and EDS analyses of the reference SCCs.

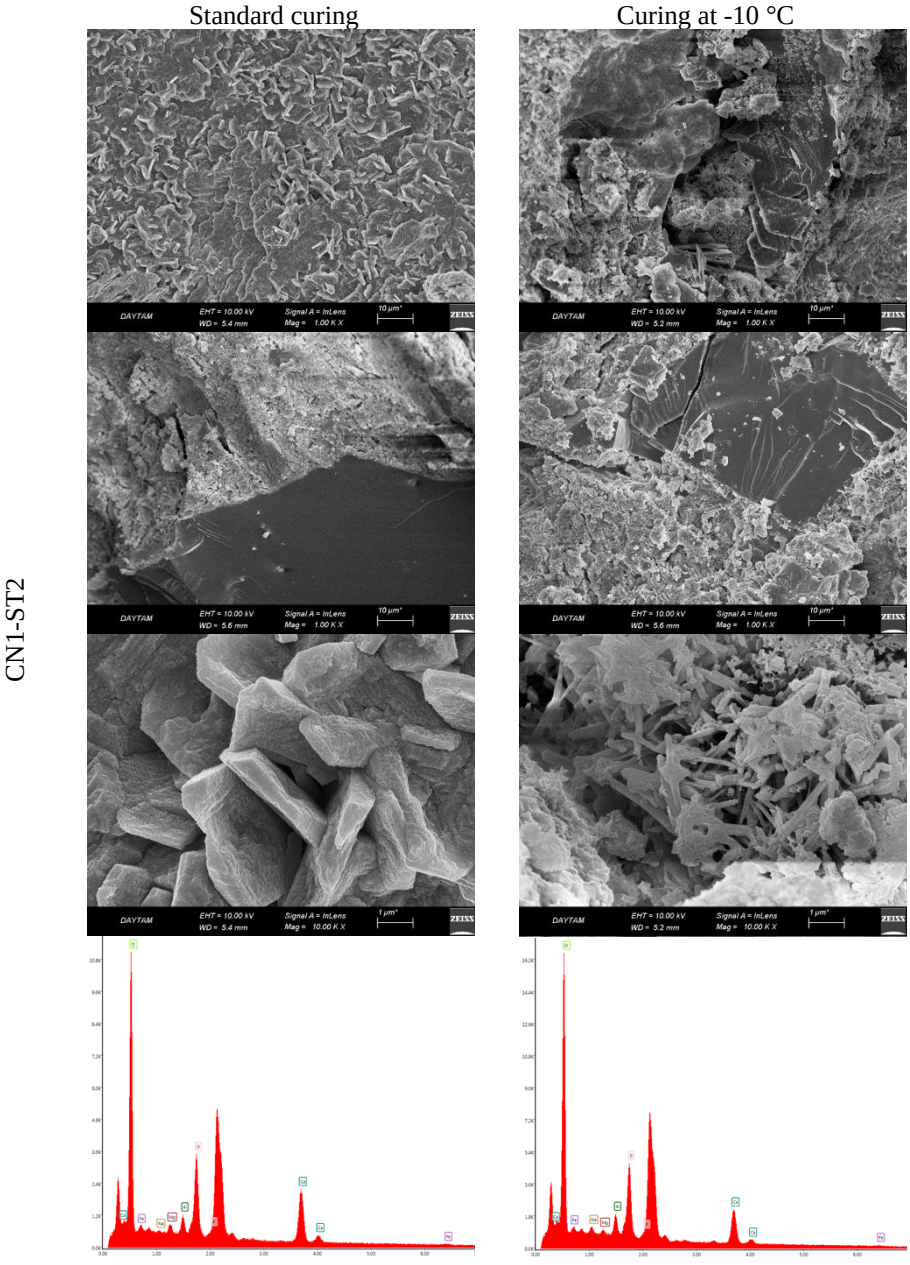

Fig. 10. SEM images and EDS analyses of the CN1-ST2.

4 Conclusions

Following results were obtained in this study:

— Capillary water absorption coefficients of all mixtures are higher in the first 30 minutes, but the coefficients decrease over time. In addition, when looking at the ultimate values, it was determined that the capillary water absorption coefficients of SCC concrete mixtures using antifreeze admixtures for all curing conditions decreased. These admixtures lowering the freezing point of water and the continuation of the strength development, though slowly, may have a positive effect on ensuring the impermeability of the concrete.

— When the strengths of SCC concrete with and without antifreeze admixtures were compared, it was determined that antifreeze admixture had a remarkable effect on the compressive strength of fresh concrete samples after water curing, -5°C and -10°C.

— According to the BET analysis results, although there was an increase in the pore volume in both mixes, as a result of the use of admixtures in SCC concrete with antifreeze admixtures, it is seen that the void diameters are smaller with lowering the freezing point of water. Furthermore, the pore volume below 20 nm, expressed as harmless, is higher in mixes containing antifreeze.

— In the SEM-EDS analysis results, although cracks are observed in both mixtures, it is seen that lesser diameter cracks are formed in SCC concrete with antifreeze admixtures, and even the losses in the crystal peaks are less.

— Besides, the compressive strengths support each other with the experiment results of capillary water absorption, BET, and SEM-EDS analysis.

References

1. Erdoğan, T.Y., Beton (Concrete). 6. ed. 2016, Ankara-Turkey: METU Press Publishing Company.
2. Mehta, P.K. and P.J. Monteiro, Concrete: microstructure, properties, and materials. 2014: McGraw-Hill Education.
3. 306R-10, A., ACI Committee 306, ACI 306R-10 Guide to Cold Weather Concreting, in American Concrete Institute, Detroit, Michigan (2010). 2010.
4. Neville, A.M., Properties of concrete. Vol. 4. 1995: Longman London.
5. Müdürlüğü, T.M.G. 2023; Available from: https://www.mgm.gov.tr/veridegerlendirme/il-ve-ilceler-istatistik.aspx?m=ERZURUM.
6. Polat, R., The effect of antifreeze additives on fresh concrete subjected to freezing and thawing cycles. Cold Regions Science Technology, 2016. 127: p. 10-17.
7. Saaki, K., et al., Antifreeze admixture developed in Japan concrete, non-chloride, non-alkaline admixture effectively prevents freezing of fresh concrete, in Concrete lnternational. 1991. p. 26-30.
8. Nmai, C.K., Cold weather concreting admixtures. Cement Concrete Composites, 1998. 20(2-3): p. 121-128.
9. Demirboğa, R., et al., The effects of urea on strength gaining of fresh concrete under the cold weather conditions. Construction Building Materials, 2014. 64: p. 114-120.

10. Korhonen, C.J., Antifreeze admixtures for concrete. Vol. 97. 1997: Cold Regions Research and Engineering Laboratory.
11. Karagöl, F., et al., The influence of calcium nitrate as antifreeze admixture on the compressive strength of concrete exposed to low temperatures. Cold Regions Science Technology, 2013. 89: p. 30-35.
12. Ali, Ö.F., Karagöl, Rıza, Polat, Cemal, Karaaslan, Kalsiyum Nitrat Ve Sodyum Tiyosiyanat Esaslı Antifriz Katkıların Kendiliğinden Yerleşen Taze Haldeki Betonların Don Direncine Etkisi, in Anadolu 11th International Conference On Applied Sciences. 2022: Diyarbakır.
13. TS-EN-197-1, Çimento - Bölüm 1: Genel çimentolar - Bileşim, özellikler ve uygunluk kriterleri (Cement- Part 1: Compositions and conformity criteria for common cements). 2002, TSE: Ankara-Turkey.
14. TS-EN-934-2:2011+A1, Kimyasal katkılar - Beton, harç ve şerbet için - Bölüm 2: Beton kimyasal katkıları - Tarifler, gerekler, uygunluk, işaretleme ve etiketleme (Admixtures for concrete, mortar and grout - Part 2: Concrete admixtures - Definitions, requirements, conformity, marking and labelling). 2011, TSE: Ankara-Turkey.
15. EFNARC, E.F.f.S.C.C.C.s., The European Guidelines for Self Compacting Concrete Specification, Production, and Use. 2005.
16. TS-EN-12390-2, Beton - Sertleşmiş beton deneyleri - Bölüm 2: Dayanım deneylerinde kullanılacak deney numunelerinin hazırlanması ve küre tabi tutulması (Testing hardened concrete - Part 2: Making and curing specimens for strength tests). 2019, TSE: Ankara-Turkey.
17. TS-EN-13057, Beton yapılar - Koruma ve tamir için mamul ve sistemler - Deney metotları - Kılcal su emmeye direncin tayini (Products and systems for the protection and repair of concrete structures - Test methods - Determination of resistance of capillary absorption). 2002, TSE: Ankara-Turkey.
18. TS-EN-12390-3, Beton-Sertleşmiş beton deneyleri-Bölüm 3: Deney numunelerinde basınç dayanımının tayini (Testıng hardened concrete-Part 3:Compressıve strength of test specımens). 2010, TSE: Ankara-Turkey.
19. Khan, J. and G. Kumar, Influence of binary antifreeze admixtures on strength performance of concrete under cold weather conditions. Journal of Building Engineering, 2021. 34: p. 102055.
20. Polat, R., A.W. Qarluq, and F. Karagöl, Influence of singular and binary nanomaterials on the physical, mechanical and durability properties of mortars subjected to elevated temperatures and freeze–thaw cycles. Construction Building Materials, 2021. 295: p. 123608.
21. Patel, S., et al., Effect of flue gas temperature on NO2 adsorption by aged recycled concrete Waste: DRIFTS, TGA and BET study. Chemical Engineering Journal, 2021. 420: p. 130413.

CIVIL ENGINEERING EDUCATION

pages: 147 – 163

Education for the Use of BIM on the Example of Slovenian Higher Education

Nataša Šuman [1][0000-0003-0470-7700], Zoran Pučko [1][0000-0002-5472-953X], Aleksander Srdić [2][0000-0003-2885-3550], Robert Klinc [2][0000-0002-0027-420X]

[1] Chair of Construction Management, Technology and Economics, Faculty of Civil Engineering, Transportation Engineering and Architecture, University of Maribor, Smetanova ulica 17, Maribor, Slovenia, natasa.suman@um.si
[2] Chair of Construction Management, Faculty of Civil and Geodetic Engineering, University of Ljubljana, Jamova 2, Ljubljana, Slovenia

Abstract. The construction industry is undergoing a digital transformation with the introduction of advanced technologies and methods of Industry 4.0, which are changing traditional project management. Building Information Modeling (BIM) is at the heart of modern construction project management, and educating professionals to use it is essential. The civil engineering curriculum at Slovenia's two largest universities has been adapted over the past decade to ensure that students are equipped with the necessary knowledge and skills to effectively use BIM in their future careers. This paper presents the experience of teaching and introducing BIM, advanced technologies, and Industry 4.0 methods as tools for modern construction project management. The courses introduced with the objectives and desired competencies, the learning and teaching methods, and the intended learning outcomes are presented. The importance of education at the frontiers of science is highlighted through reflections on the BIM -based courses and the number of graduates per year.

Keywords: BIM; education; study curriculum redesign; Construction 4.0.

1 Introduction

Project management, a scientific and professional discipline present across industries, has undergone radical changes in the last decade. We are in the era of Industry 4.0, where the rapid development of advanced technologies focused on digitalization and automation is reshaping the landscape. A major challenge lies in the transformation of traditional business models, shifting from material-centric products to information- and digital-centric products, data-driven approaches and intellectual business models [1]. This evolution is gaining momentum, and Industry 5.0 initiatives are already beginning to emerge, but it is important to note that the construction industry still needs to catch up in this area, as it is lagging behind in adopting these transformative advances [2]. To close these gaps and move the industry forward, there is an urgent need to bridge the gap and facilitate the adoption of Industry 4.0 principles, technologies, and

methodologies in the construction sector that would result in Construction 4.0 [1]. In doing so, we can unlock immense potential for efficiency, productivity and innovation, and ultimately foster a new era of construction that thrives at the forefront of technological advancement.

The European Union [3] has defined health, environmental protection and social development as global priorities for sustainable development. The construction industry is responding, as reflected in concepts such as green building [4], sustainable construction [5,6], circular economy [7], and smart cities and buildings [8]. In Slovenia, these goals are reflected in the Slovenian Smart Specialization Strategy S4 [9]. This strategy aims to create: 1. an inclusive, healthy, safe, and responsible society; 2. high levels of collaboration, competence, and managerial efficiency; 3. an intact natural environment; 4. an economy that creates value for all; and 5. lifelong learning.

Sustainable development strategies and tactics are essential to successful construction project management. Modern practises and technologies must be used throughout a project's lifecycle, from planning to execution to subsequent use. This is especially important in the digital age, where change is occurring rapidly around the world.

In order to stay relevant, the construction sector must keep pace with the latest trends and technological advances of Industry 4.0 [1]. These trends include Building Information Modeling (BIM), robotics, project management, advanced materials, offsite construction, occupational safety, surveillance, green building, 3D printing, and connected construction sites [10]. These innovations are recognized and discussed in both academic and professional circles [11].

The integration of Industry 4.0 technologies and methods requires civil engineering universities to incorporate modern content into the study process. For example, active learning, a teaching technique that includes interactive lectures, experiential learning, collaborative learning, and project-based learning, can be used to update learning content [12].

This paper provides an overview of formal and non-formal teaching and learning of methods and techniques of digitization and automation in civil engineering at the two largest universities in Slovenia, the Faculty of Civil Engineering, Transportation Engineering, and Architecture (FGPA) at the University of Maribor, and the Faculty of Civil and Geodetic Engineering (FGG), University of Ljubljana. We outline how digitization topics are integrated into the learning process, especially in subjects based on the BIM approach and Construction 4.0 technologies. A summary of digitization-based theses at both universities in the last 10 years will also be presented. With this contribution, we would like to share our experiences in teaching related to digital transformation with an international community of experts in order to foster discussions and suggestions for improvement.

2 Introduction to the Universities and Faculties Concerned

2.1 University of Maribor

The University of Maribor [13] was founded in 1975. With its 17 faculties, the University Library of Maribor and the dormitories, it is the second largest and second oldest university in Slovenia with a long tradition. During these years it has developed into a successful scientific institution whose main task and guiding principle is the dissemination and enrichment of knowledge. It is rapidly developing new areas of activity, testing new methods of study and seeking new ways of integration with its environment.

The Faculty of Civil Engineering, Transportation Engineering and Architecture (FGPA) [14] at the University of Maribor (UM) aims to transfer the knowledge and expertise in the fields of civil engineering, architecture and traffic engineering to students and professionals, thus contributing to their lives and careers as well as to the economy. In study year 2022/23 there are approximately 680 students at the Faculty studying in 6 undergraduate, 4 postgraduate programmes and 3 doctoral programmes. The Faculty also strives to develop innovative design and learning worldwide to contribute to the progress of society in these fields.

2.2 University of Ljubljana

The University of Ljubljana [15] is the largest university in Slovenia. It consists of 3 academies and 23 faculties offering more than 300 different bachelor's and master's degree programmes for over 40,000 students, making it one of the largest universities in Europe. With its research and scientific projects, researchers at the University of Ljubljana keep pace with the latest developments in the fields of art, science and technology, both at home and abroad. Currently, according to the Academic Ranking of World Universities (ARWU - "Shanghai Ranking"), the University is among the 500 best universities in the world and among the top 4% of European universities.

The Faculty of Civil and Geodetic Engineering (FGG) [16] is a part of University of Ljubljana (UL) since the very beginning in 1919, when the Department of Civil Engineering and the Department of Geodesy were active within the Faculty of Technology of the University of Ljubljana. Currently, UL FGG is represented by these two departments as well as by the Department of Environmental Civil Engineering. Also worth mentioning are the courses of study in Buildings and Spatial Planning. There are approximately 700 students studying at the Faculty in 5 undergraduate, 5 postgraduate programmes and 1 doctoral programme. The Faculty employs close to 200 full-time staff, including 90 teachers. UL FGG is one of only two faculties of civil engineering and the only faculty of geodetic engineering and water and environmental engineering in Slovenia. All three main areas of study programmes (Civil Engineering, Geodetic Engineering and Water Science and Environmental Engineering) thus have an important and direct impact on the human resources structure in business, state administration and municipalities.

3 Implementation of Digitalization and Automation in the Study Process

While the potential of computers in construction was recognised at the University of Ljubljana as early as the late 1960s and early 1970s [17], the importance and implementation of methods and technologies for digitization and automation have been systematically taught at both faculties since the 1990s, originally as part of the Chairs of Construction Informatics. Later, as the methods and applications of ICT were applied to other areas of AEC, the benefits were also recognised in the field of construction management and are now taught in the 1st and 2nd degree programmes. In principle, the importance of digitization is introduced in most professional teaching subjects. At the 3rd doctoral level, the importance of digitization is essentially included in all elective subjects, as the lecturers are competent professionals in their respective fields and follow the latest trends and research.

In the next sections, the efforts of the two largest Slovenian universities to implement BIM -based topics into the curricula of their respective degree programmes will be presented.

3.1 Faculty of Civil Engineering, Transportation Engineering, and Architecture

Since the 2015/16 school year, FGPA have been offering the 2nd level subject BIM - Building Information Modeling. This subject introduces the general concept of BIM, its role and technologies. In addition, we offer elective courses on digitization, including Computer Modeling of Construction Objects at 1st degree and BIM Project for Construction and Infrastructure at 2nd degree. At the Chair of Construction Management, Technology and Economics, we have included topics on digitization and automation in subjects such as Construction Management, Project Management in Construction, Operational Planning, Safety in Construction, Spatial Arrangement and Advance Planning, and Maintenance and Rehabilitation of Structures. Our colleagues also supervise theses on topics related to digitization and smart specialization in construction. Our work with students comprises three components: a) a BIM -supported learning process, b) learning processes with Industry 4.0 methods and technologies, and c) final theses on topics of digitization and smart specialization in construction.

Learning Process Supported by BIM Approach

The introduction of the BIM approach into the learning process has been carried out at FGPA for many years. The first working examples on BIM were introduced in the academic year 2015/16, when the students in the subject Project Management in Construction at the 2nd degree, i.e. Civil Engineering and Industrial Engineering, created a 4D and 5D model BIM for the first time for a garage house in Skopje. In all following years, students create 4D and 5D BIM models for different building construction projects for real building examples. Since the academic year 2019/20, such

work is also carried out in the professional study program Civil Engineering at the 1st degree.

The work with students in the subject of project management in civil engineering focuses on teaching the use of the basic 3D BIM model and its extension to 4D and 5D BIM models. Thereby, the 3D BIM, extended by the construction schedule, results in the 4D BIM, and the extension by the estimated construction costs results in the 5D BIM model. Students first acquire theoretical knowledge of modeling higher BIM dimensional levels, i.e., to create 4D, 5D and 6D BIM-models. Then they apply the acquired knowledge in a tutorial and a computer work in which they create 4D and 5D BIMs. The modules of Trimble Vico Office™ software [18] are used to create 4D and 5D BIMs. Some other tools are also used for support, such as local tool 4BUILD for cost estimation and MS Project [19] for scheduling. The paper [20] provides a more detailed description and schema for creating BIMs in the study process.

Over the years, students have created BIMs for various buildings such as a school gym, a single-family house with associated infrastructure, a commercial office building, a two-apartment house, an apartment building, a single-family house with an exterior and high-bay warehouse. One of the more comprehensive models was created in the 2021/2022 study year, when students created 4D and 5D BIMs for the construction of a single-family house. The input data was given as part of a conceptual design previously created using ArchiCAD BIM software. The original 3D model BIM was created by a student of the faculty, who also gave permission to use the 3D model BIM for study purposes. The 3D model BIM of a single-family house and the building site are shown in Figure 1.

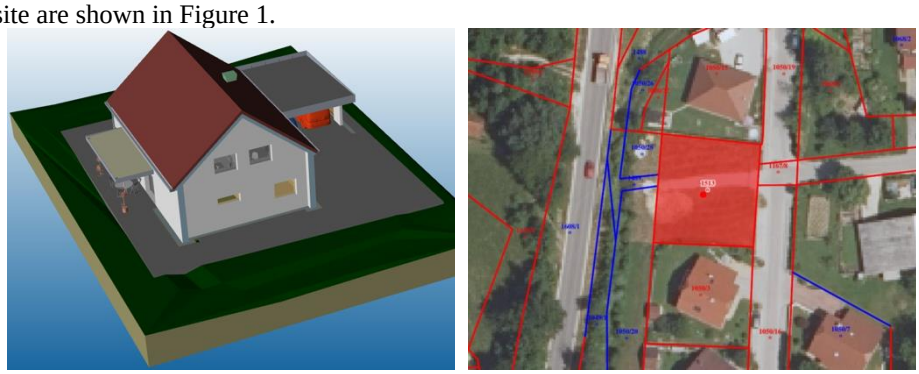

Fig. 1. 3D BIM model of a single-family house (left) and the building plot (right).

The creation of the 4D and 5D BIM model was done in groups of 3-4 students, there were 5 groups in total. Each group was assigned a set of building elements as shown in Table 1. The groups first analyzed their assigned elements (dimensions, materials, technology, quantity, etc.) in more detail and obtained the input data required for unit cost estimation and scheduling (market prices for materials, equipment and machinery, average wages, norms of work items). Then, in the Cost Planner module of the Trimble Vico Office™ software, a 5D BIM is first created. One of the biggest advantages of this software is the ability to link cost information directly and bidirectionally to the 3D BIM model elements. This means that when the geometry of the 3D BIM model

changes, the costs are automatically updated. Then the activities and their sequence are defined, which is the basis for building construction scheduling. With Vico Office software, time analysis is performed by creating a 4D BIM model in the Task Manager module. In time analysis, the advantage is also that the elements in the 3D BIM model are directly related to the activities in the schedule. The time analysis takes into account the connections between the activities and the assigned resources.

Table 1. Students group number assigned project tasks and visualization of building elements.

#	The topic of the project task	Visualization (set in Vico Office)
1	013_foundation slab 011_strip foundations 012_pad foundation 001_façades 015_façades - borders 016_gutters 017_steel construction 018_roofing of the garage and terrace	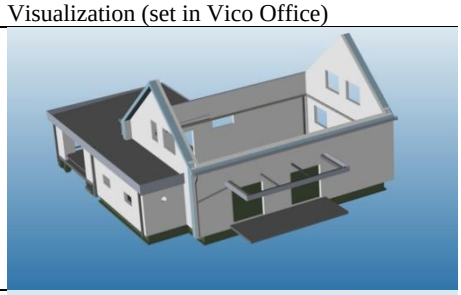
2	002a_external walls of the ground floor 002b_external walls of the 1st floor 003a_inner walls of the ground floor 003b_inner walls of the 1st floor 006_RC ties 007_RC stairs 008_RC slab above the ground floor	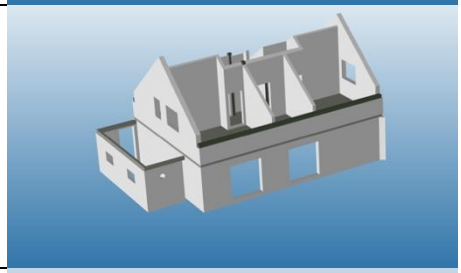
3	009_terrain 010_filling 026_curbs	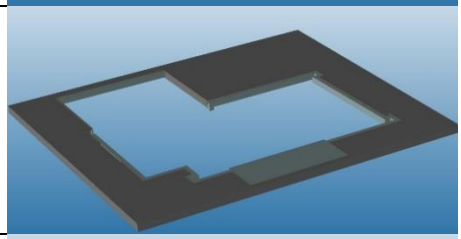
4	014_finishing floors - wood 022_housing equipment 024_doors 025_windows	
5	004_roofing 005_roof construction 019_wooden wall of the garage 020_chimney 021_glass roof 020a_chimney-coil	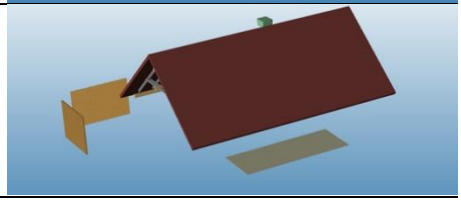

To conclude the course, a final presentation was held in January 2022 where each group presented their created 4D and 5D BIMs (Fig. 2). This presentation also included a presentation of the combined results of all groups in the form of a comprehensive 3D, 4D, and 5D BIM model (Fig. 3) to give students insight into the overall cost estimate and schedule for the single-family home. A simulation of the construction process was also created and presented to the students.

Fig. 2. Final presentation of the results.

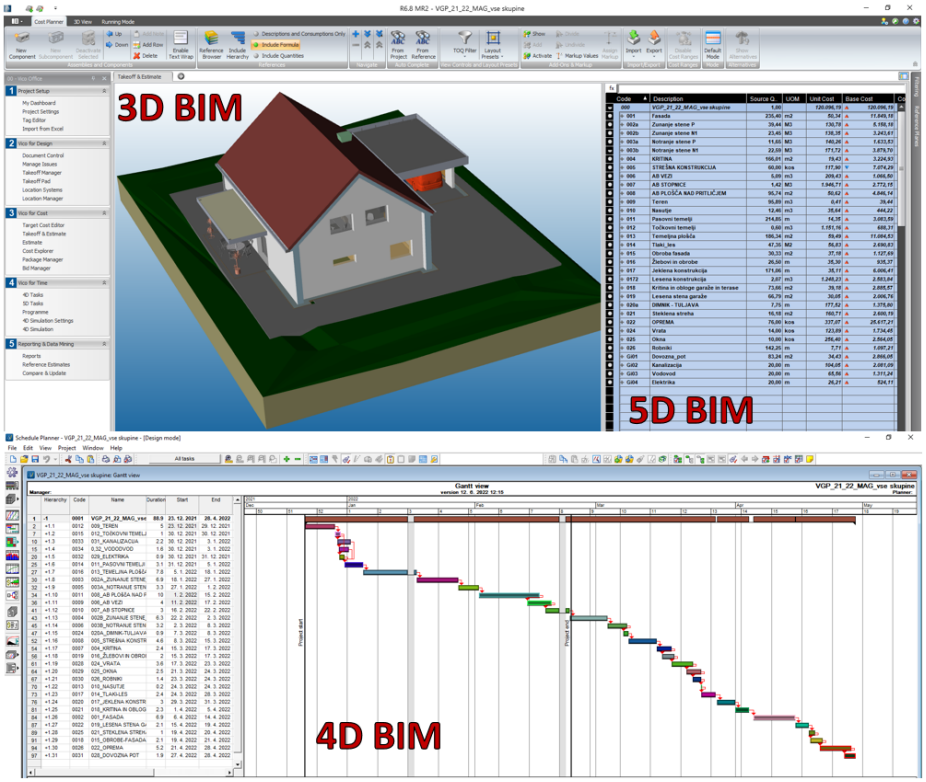

Fig. 3. Comprehensive 3D, 4D and 5D BIM model of the single-family house.

3.2 Faculty of Civil Engineering and Geodesy (FGG)

While the computer itself has been used in teaching at the FGG since the late 1970s, content related to construction informatics has been introduced into the curriculum at the FGG since the late 1990s, initially as part of general subjects such as Computer Science and Engineering Communication.

At FGG, special attention is given to motivating students to engage in deeper learning that ensures an optimal balance between the acquisition of concepts and skills, information processing, and the integration of fragmented knowledge components into complex structures. This is especially true for integrated and heterogeneous concepts such as BIM, where a linear approach to teaching is almost impossible.

Building Information Modelling (BIM) related content has been part of the study process since 2008, and even before that individual parts appeared in the context of product and process modelling. Later, after 2010, the first courses were accredited that dealt exclusively with modelling and processes within the BIM approach.

BIM Based Teaching Process at FGG

Until the Bologna reform, FGG teachers mainly taught students basic knowledge of computer science and engineering communication in subjects such as Computer Science, Programming, Automatic Data Processing, Engineering Documentation and Communication, and Descriptive Geometry. These subjects were taken primarily in the first years of study in civil engineering, surveying, and water engineering. Students were introduced to the latest developments, from object-oriented programming to web languages, Internet technologies, teleworking, computer-aided drafting and modelling, etc.

The Bologna reform has led to a thorough revision of the curricula, with emphasis on computer-integrated construction, advanced engineering communication, information modelling of products and processes, software engineering, complex 3D and 4D modelling, visualisation, etc. All of these topics are represented in the courses taught by FGG faculty, especially the staff of the Chair of Construction Informatics and the Chair of Construction Management, in the various FGG degree programmes: Digital Design, Engineering Communication, Information and Communication Technologies for Project Work, Building Information Modelling, Digital Design and Programming, Building Information Modelling, Data Processing, Programming, Project and Experiential Learning, Computer Integrated Construction, Computer Science, Information and Communication Technologies in the Built Environment, Computer Science and Informatics, Construction Management.

The redesign took into account the need to consider the nature of learning for quality teaching. We drew on the findings of Schneider and Stern [21] and their cognitive view of learning, summarised in ten key findings:

1. Learning is an activity carried out by the learner.
2. Optimal learning takes prior knowledge into account.
3. Learning requires the integration of knowledge structures.

4. Optimally, learning balances the acquisition of concepts, skills and meta-cognitive competence.
5. Learning optimally builds up complex knowledge structures by organizing more basic pieces of knowledge in a hierarchical way.
6. Optimally, learning can utilize structures in the external world of organizing knowledge structures in the mind.
7. Learning is constrained by capacity limitations of the human information-processing architecture.
8. Learning results from a dynamic interplay of emotion, motivation and cognition.
9. Optimal learning builds up transferrable knowledge structures.
10. Learning requires time and effort.

With this in mind, we have redesigned our teaching process toward an integration of problem-based learning and workshops to significantly enhance the educational experience. Through the use of problem-based learning, students are actively engaged in solving real-world challenges, which promotes critical thinking and problem-solving skills. On the other hand, workshops provide students with opportunities to apply theoretical knowledge in a practical way, which promotes deeper understanding and practical application of concepts. This combined approach fosters not only active learning, but also collaboration, communication, and creativity (all skills needed to train competent BIM professionals) who prepare students for real-world scenarios and improve their overall learning outcomes.

Project-Based Learning Approach

In the 1st year of the Master's programme, the course "Computer Integrated Construction" is taught, the main objective of which is to familiarise students with the importance of computer science as a connecting building block between the units of the construction industry and the processes that take place in it. The course introduces students to the theoretical and technological background of integration in the industry, deepens their understanding of the immediate and strategic aspects of computerization and, most importantly, provides them with the ability to think strategically and critically about the use and application of information technologies in construction. Seminar exercises in the course have been carried out in the past in the traditional manner, i.e., with blackboard and chalk, or, more recently, primarily with the use of a computer and pre-made computer presentations. After the theoretical part of the course, students were instructed to write a seminar paper on a topic of their choice, the results of which they presented to their classmates at the end of the semester. The seminar paper and presentation were graded, and the written exam was included in the course grade.

The redesign followed the guidelines of problem-based learning, in which students are first presented with a problem and learn by solving it. We create a scenario in which the teacher plays the role of investor, keeping the requirements as loose as possible. We set milestones for students to follow without adding requirements:

1. Team composition. Students can form teams independently, with each team consisting of up to three students, who must also choose the name of the team and become familiar with the skills of each team member.
2. Selection of a project site and preparation of the project.
3. Presentation of the project. The presentation takes place in front of classmates, who comment and evaluate the work at the end of each presentation.
4. Reflection. After the presentation, each student writes a reflection on their work, describing the dynamics of the group work, their attitude toward each decision, and their view of the project as a whole.

During each phase, joint mentoring sessions are organised to present the selected solutions and ideas. In this way, students are supported throughout the project and are able to bring the project to a successful conclusion with individual guidance.

Over the years, students have solved problems ranging from the design of single-family houses and shopping centres with associated transportation infrastructure to complex bridging structures. One such example is shown in Fig. 4.

Fig. 4. BIM model of the bridge leading to the Karavanke tunnel, created by the student team PONGO in 2020.

Workshop Approach

Workshops play a crucial role in engineering education by providing a hands-on learning experience that complements theoretical knowledge. Workshops offer students the opportunity to apply theoretical knowledge to real-world scenarios, bridging the gap between theory and practice. Through hands-on activities, students gain practical skills and experience that are vital for their future engineering careers.

The workshop principle is mainly used in undergraduate courses where students are not yet able to fully synthesize their knowledge and need more help and guidance.

Unlike the PBL approach, workshops are conducted exclusively in the classroom. Groups are formed (Fig. 5) in which students work on a set task. The workshops end with presentations (Fig. 6) where the groups present their findings, which are then commented on by the tutors, and the groups have the opportunity to compare results.

Fig. 5. Group work within the workshop.

Fig. 6. Workshop presentation with group findings presented on the wall.

BIM A+, European Master in BIM

In the academic year 2019/2020, a BIM A+ [22] Master's Course started, a European Master's in BIM, organised by the Faculty of Civil and Geodetic Engineering (FGG), Politechnico de Milano and the University of Minho. BIM A+ is a response to the growing demand of the EU market for BIM services that represent the future of design

and digitization of the construction process. The aim of BIM A+ is to offer an advanced education programme on BIM integrated design, construction and operation processes. In addition, emphasis is placed on the collaborative practises that form the cornerstone of such integration. The Master combines the diversity of expertise of leading European universities in the relevant fields. It also provides an education focused on a multidisciplinary understanding of virtual construction through the involvement of experts from complementary fields (engineers, architects, programmers and others).

The BIM A+ Master's programme has a duration of one academic year (60 ECTS) and is rotated between partners. This means that each student takes the courses in one partner institution and the thesis in another. The language of instruction and examination is English. The degree is a Master's degree awarded by the participating institutions as a double degree.

It provides up-to-date knowledge in the areas of modern design, project information management and design technologies, and advanced digitalization in the construction industry. The course is characterised by international collaboration, mobility, electronic content, compressed delivery, and modularity, allowing professionals who cannot be away from work for extended periods of time to continue their education on specific topics only and earn the appropriate credentials.

3.3 Learning Process Involving Technologies of Construction 4.0

In recent years, students at both facluties have also gained knowledge and skills about the use of advanced Industry 4.0 methods and technologies. One of these technologies is data collection of the environment using a 3D laser scanner, which is included in the learning content of several subjects, such as construction safety, spatial layout and advanced planning, and maintenance and rehabilitation of structures. A 3D laser scanner can be used for a variety of purposes, such as capturing the as-built condition of the environment, ensuring site safety, determining work progress, and creating a 4D as-built BIM model, etc. Students use the 3D laser scanner to collect point cloud data. Fig. 7 shows the acquired point cloud data for the selected site that the students acquired during the exercises in Spatial Arrangement and Advanced Planning course at FGPA.

Fig. 7. Acquired point cloud data by the students of FGPA.

The Fig. 8 shows a BIM model based on a captured point cloud created by students in the group named 1290ing in the Computer Integrated Construction course at FGG.

Fig. 8. The overlap between the captured point cloud and the BIM model, created by the 1290ing FGG student group in 2021.

In addition, students also gain knowledge and skills related to advanced augmented reality technologies. This is a combination of a real environment with digital elements that allows for a 1:1 scale visualization of the built environment. The technology is fairly new to the construction industry, and only a few applications can currently be demonstrated in practice. However, we believe that this technology has very great potential, and it is expected that more innovations in construction project management will be developed in the coming years. Fig. 9 shows an example of the use of advanced mixed reality in Construction safety course at FGPA.

Fig. 9. Use of advanced mixed reality during the study process.

3.4 Final Theses

The topics of the use of advanced technologies and trends in digitalization and automation become an ongoing topic for the final theses on all levels of education. The final theses deal with different areas of digitalization, mostly with the BIM approach, some topics deal with data collection and others with the use of advanced technologies such as object scanning, virtual reality, 3D printing, etc. Most of the papers involve not only theory but also the use of advanced technologies on real building examples.

An analysis of the final theses at FGPA showed that 38 final theses on the topics of digitalization and smart specialization were completed in the last 5 years. Of these, 22 final theses were in the bachelor's programs and 19 final theses were in the master's programs. Fig. 10 summarizes the analysis of final theses by topic from 2018 to 2022. The analysis shows that in the last few years, the number of final theses from data acquisition topics has increased.

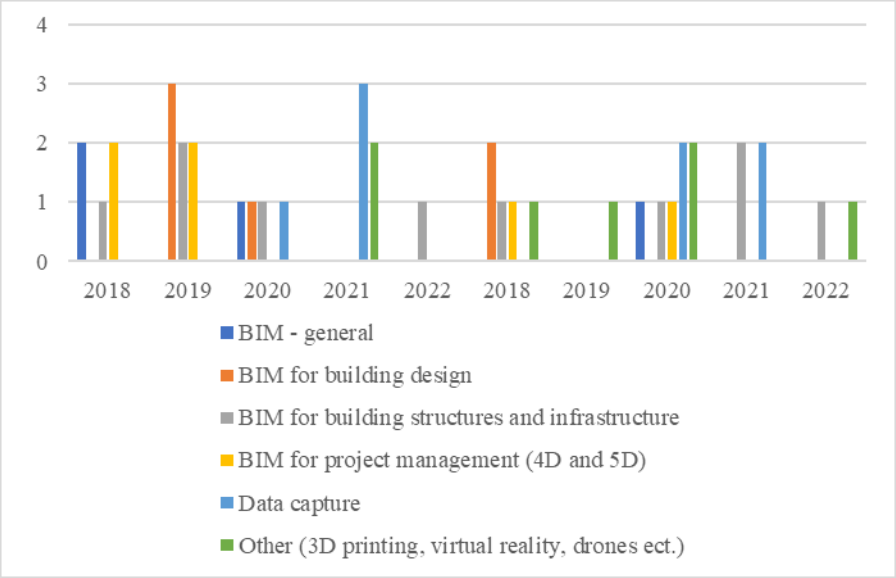

Fig. 10. BIM related final theses at FGPA from 2018 to 2022.

The analysis of final theses at the FGG (see Fig. 11) showed that since 2010, 93 final theses have been produced on all aspects of the BIM approach, 25 of them at the undergraduate level, 68 (35 of them in the BIM A+) at the postgraduate level, and 2 PhD theses have also been produced. BIM Final theses have also appeared earlier, with two doctoral theses on a topic closely related to BIM as early as 2003 and 2008.

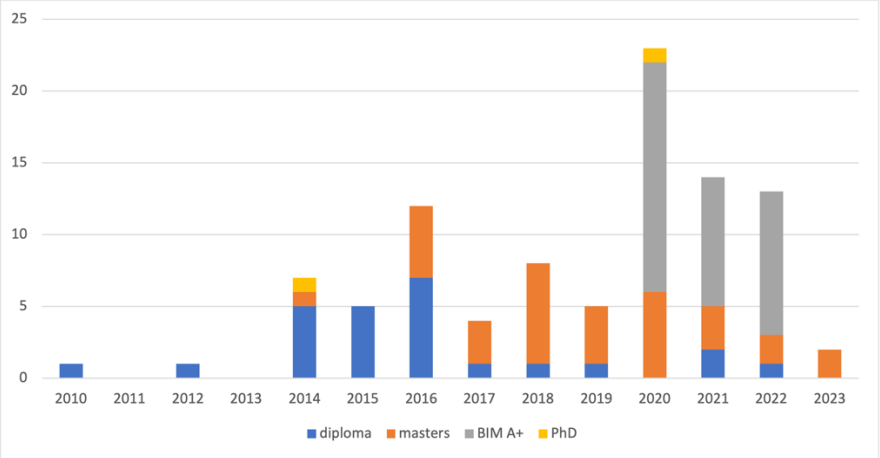

Fig. 11. BIM related final theses at FGG from 2010 to 2023.

3.5 Other forms of formal and non-formal learning

Many activities of other forms of formal learning and many forms of non-formal learning have been carried out at both faculties on the topic of digitalization and automation in construction. These activities can be combined into the following sets:

- participation in conferences and trade fairs,
- active participation in various professional events,
- excursions and site visits and
- involvement in various projects.

From 2022, both faculties are also official training centres for the buildingSMART Professional Certification Programme [23], which provides international validation that professionals are highly skilled and recognisably trained in digital ways of working. With the digital transformation in the construction industry, the need for advanced training is increasing. This means that people with extensive experience are in high demand and there is a need for a certification.

This bridges the gap between formal and lifelong learning, as these trainings expose practitioners to new methods, concepts and technologies, preparing them for the present and future. There is also added value for students, as the knowledge and experience gained and shared by faculty is incorporated into the subjects and topics taught by faculty.

4 Conclusions

The four main components of good university teaching, which also promotes a Deep Learning approach, are: Motivation, Activity, Interaction, and Structured Learning. An increasingly large and diverse student population is forcing educators to change, especially when teaching complex topics such as BIM. This is especially important for

"high quality" educators who not only impart knowledge to their students, but also engage them to think more deeply about the subject through a mentoring approach.

This paper presents an approach to teaching BIM and advanced technologies and methods of Construction 4.0 at two of the largest universities in Slovenia, as it is becoming increasingly clear that successful education in Building Information Modeling (BIM) at universities is crucial for preparing students for successful employment in the modern construction industry. By integrating BIM into the civil engineering curriculum, we equip students with the knowledge and skills necessary to effectively use this technology in their future careers. As we aim for a deep understanding of the subject, the focus of both faculties (in Maribor and Ljubljana) is on providing a comprehensive understanding of the principles of BIM, mastery of the software and practical application through hands-on projects and workshops.

In addition, a successful BIM education program should also emphasize the importance of interdisciplinary collaboration and communication skills, as BIM projects often involve multiple stakeholders, including architects, engineers, contractors, and facility managers. Therefore, we continually foster an environment that encourages teamwork, effective communication, and the ability to work across disciplines.

Other forms of formal and non-formal learning, such as student participation in conferences, trade shows, professional events, field trips, site visits, and involvement in projects, also make an important contribution to students' education. This is especially important in today's world where digital transformation is accelerating on a global scale. Therefore, we work closely with our Alumni to gain insight and continuous feedback on industry needs, which helps us refine the curriculum and ensure its relevance to the evolving needs of the construction industry. One of the outcomes of this process is the professional buildingSMART certification offered at both featured institutions.

Overall, the success of our approach is reflected in the number of BIM -related theses completed by our students, who find the topic of digitization and smart specialization in the architecture, engineering, and construction (AEC) industry relevant and interesting. We hope that by investing in comprehensive BIM education, we can play a crucial role in shaping the future generation of construction professionals in Slovenia, who will be able to effectively use technology to improve project outcomes and drive innovation.

References

1. Klinc, R., Turk, Ž.: Construction 4.0 – Digital Transformation of One of the Oldest Industries. Econ Bus Rev 21(3), 393–410 (2019); doi: 10.15458/ebr.92
2. Manyika, J., Ramaswamy, S., Khanna, S., et al.: Digital America: A Tale of the Haves and Have-Mores. McKinsey Global Institute; 2015.
3. European Union: New European Bauhaus: Beautiful, Sustainable, Together. n.d. Available from: https://new-european-bauhaus.europa.eu/index_en [Last accessed: 6/2/2023].
4. Li, Y., Rong, Y., Ahmad, U.M., et al.: A comprehensive review on green buildings research: bibliometric analysis during 1998–2018. Environ Sci Pollut Res 28(34), 46196–46214 (2021); doi: 10.1007/s11356-021-12739-7

5. Boyle, C.A.: Sustainable buildings. Proc Inst Civ Eng - Eng Sustain 158(1), 41–48 (2005); doi: 10.1680/ensu.2005.158.1.41
6. Pitt, M., Tucker, M., Riley, M., et al.: Towards sustainable construction: promotion and best practices. Constr Innov 9(2), 201–224 (2009); doi: 10.1108/14714170910950830
7. Norouzi, M., Chàfer, M., Cabeza, L.F., et al.: Circular economy in the building and construction sector: A scientific evolution analysis. J Build Eng 44,102704 (2021); doi: 10.1016/j.jobe.2021.102704
8. Ghaffarianhoseini, A., AlWaer, H., Ghaffarianhoseini, A., et al.: Intelligent or smart cities and buildings: a critical exposition and a way forward. Intell Build Int 10(2), 122–129 (2018); doi: 10.1080/17508975.2017.1394810.
9. Government of Slovenia. Izvajanje in prenova Slovenske strategije pametne specializacije - iz S4 v S5 | GOV.SI. 2021. Available from: https://www.gov.si/zbirke/projekti-in-programi/izvajanje-slovenske-strategije-pametne-specializacije/ [Last accessed: 6/2/2023].
10. Insights S. Top 10 Industry 4.0 Trends in 2023. 2020. Available from: https://www.startus-insights.com/innovators-guide/top-10-industry-4-0-trends-innovations-in-2021/ [Last accessed: 6/2/2023].
11. Hasan, S., Sacks, R.: Building Information Modeling (BIM) and Construction Tech Integration for Construction Operations: State of the Art. 2021; pp. 358–365; doi: 10.35490/EC3.2021.179
12. Lassen, A. K., Hjelseth, E., Tollnes, T.: Enhancing learning outcomes by introducing BIM in civil engineering studies – experiences from a university college in Norway. Int J Sustain Dev Plan 13(01), 62–72 (2018); doi: 10.2495/SDP-V13-N1-62-72.
13. University of Maribor. n.d. Available from: https://www.um.si/en/home-page/ [Last accessed: 6/7/2023].
14. UM FGPA. 2021. Available from: https://www.fgpa.um.si/en/ [Last accessed: 6/7/2023].
15. University of Ljubljana. n.d. Available from: https://www.uni-lj.si/eng/ [Last accessed: 6/2/2023].
16. Faculty of Civil and Geodetic Engineering | University of Ljubljana. n.d. Available from: https://www.en.fgg.uni-lj.si/ [Last accessed: 6/2/2023].
17. Reflak, J., Turk, Ž.: 50 years of construction informatics at IKPIR. Gradb Vestn 70(11/12), 249–263 (2021).
18. Trimbles. Vico Office. 2016. Available from: https://vicooffice.dk/en/, https://vicooffice.dk/en/ [Last accessed: 6/2/2023].
19. Microsoft. Project Management Software | Microsoft Project. n.d. Available from: https://www.microsoft.com/en-us/microsoft-365/project/project-management-software [Last accessed: 6/2/2023].
20. Pučko, Z., Šuman, N., Klanšek, U.: Teaching and Lifelong Education on BIM at FCETEA in Maribor, Slovenia. In: OTMC Conference 2019 Proceedings. (Ivica Završki, Anita Cerić, Mladen Vukomanović, et al. eds) Croatian Association for Construction Management: Zagreb, Croatia; n.d.; pp. 465–473.
21. Dumont, H., Istance, D., Benavides, F., et al., (eds): The Nature of Learning: Using Research to Inspire Practice. Educational Research and Innovation. OECD: Paris; 2010.
22. BIM A+, European Master in BIM - Building Information Modelling. n.d. Available from: https://bimaplus.org/ [Last accessed: 6/9/2023].
23. buildingSMART Professional Certification Program. n.d. Available from: https://education.buildingsmart.org/ [Last accessed: 6/9/2023].

CONSTRUCTION MANAGEMENT

pages: 164 – 237

A Review of The Application of EVM in Construction Industry

Muhammad Mubasher[1][0009-0001-9934-0675] Wei Tong Chen[2][0000-0001-9599-034] Theresia Avila Bria[2,3] (0000-0002-4265-5887) and Ferdinan Nikson Liem[2,3][0000-0001-7243-7306]

[1] National Yunlin University of Sci. & Tech., Department of Civil & Construction Engineering, Douliu, Taiwan, m11116029@yuntech.edu.tw
[2] National Yunlin University of Sci. & Tech., Graduate School of Engrg. Sci. & Tech., Douliu, Taiwan, chenwt@yuntech.edu.tw
[3] Department of Civil Engineering, State Polytechnic of Kupang, Kupang 85111, Indonesia

Abstract. Competition has increased in the construction industry in recent years as more and more contractors enter the market in hopes of landing lucrative project contracts. Recurring issues in the building business include budget overruns and work delays. Time and money differences are an issue in both first world and third-world nations. Across the 290 global projects studied, average cost overruns reached 73%. Over half (55%) of 137 projects in Nigeria had budget overruns of 5% to 808%. Earned value management (EVM) is a widely used approach to project management that provides early warning of potential problems and helps keep costs and schedules under control. The U.S. created EVM which is a method for evaluating a project's success that takes all its variable's time, money, and scope into account. EVM allows project managers to see forward based on projected and facts, and then adjust appropriately. Projects are now seen as interconnected nodes in a larger organizational network, leading to a surge in interest in construction project management (CPM) studies. This research aims to fill that void by analyzing 63 EVM articles published in eight scholarly journals between 2015 and 2023 to determine the current state of the field and identify promising avenues for further investigation. EVM enables project stakeholders to track expenditure and progress, enabling timely resource optimization.

Keywords: Earned value management analysis, Stakeholder theory, Construction project management; Review.

1 Introduction

Research using EVM in the field of CPM has grown rapidly over the past two decades. Motivated by the emerging view of projects as temporary network-based organizations, these studies sought to gain a deeper understanding of the management characteristics of construction projects. Construction project structures are transitory and short-lived in comparison to permanent organizations like corporations and public organizations;

yet they are purposefully created to accomplish the long-term aims and aspirations of the permanent organization or of a subset of the owners.

EVM, or earned value management, is a technique for managing projects that considers not just the budget but also the timeline and the quality of the work done. When EVM was first introduced as a contractual requirement, the United States government began using it to run its own internal projects. Since its inception in 1996, the EVM System (EVMS) has transformed the EVM from a requirement of government contracts to a practical best practice tool for project managers in the commercial sector worldwide "an integrated collection of rules, procedures, and practices to support programmed and project management as a decision enhancing tool and a crucial component of risk management" [1] is how an EVMS is described in the United States. According to Solomon and Young's interpretation, "EVM standard" is what EVMS stands for. Currently, EVM is the most widely utilized approach to evaluating project success. The EVM idea is also known as Earned Value Method, the Earned Value System (EVS), and Earned Value Analysis (EVA) among practitioners [2].

Although these names are mostly interchangeable [3]. EVM provides the project manager with a mechanism for doing regular, timely checks on the project's overall health [4]. The Methodology of EVM has been use for a variety of purposes, including, but not limited to, (1) cost and time estimation; (2) determining the cost and schedule impacts of known problems; (3) providing an accurate portrayal of the project's cost status; (4) identifying the root causes of problems; (5) depicting the project's schedule status; (6) providing timely information on projects, and (7) locating previously unrecognized trouble spots [5].

EVM is now commonly utilized in the business and governmental sectors for projects of all sizes [6]. It was discovered that the vast majority of EVM users have either completely or partly adopted an automated computer system to aid EVM procedures [7]. EVM software applications that integrate with other popular project management tools like Microsoft Project and Project Server, win sight, Cobra, and Open Plan have arisen in recent years to simplify the analytic procedures [8]. Staff augmentation, tool installation and training, and online EVM courses are all part of the EVM service package that several for-profit businesses have been offering [9]. Although there has been a steady flow of papers on EVM in the academic literature, there seems to be a lack of attention devoted to the need for a systematic evaluation of current research, which is what inspired this work [10].

- BCWS (Budgeted Cost of Work Scheduled) - PV (Planned Value)
- BCWP (Budgeted Cost of Work Performed) - EV (Earned Value)
- ACWP (Actual Cost of Work Performed) - AC (Actual Cost)
- SV (Schedule Variance): VP = EV – PV.
- CV (Cost Variance): VC = EV – AC.

2 Background of EVM

2.1 Terminology of EVM

Elements of the EVM have been extensively discussed and derived in several publications [11]. Key characteristics of EVM, such as planned value (PV), earned value (EV), and actual cost (AC), and EVM measurements are separated into these two groups in the practice standard [12]. Variances, indices and forecasts in addition, the development of EVM ideas has increased the discrepancies between fundamental metrics like earned schedule (ES) [13] and earned duration (ED) [14].

EVM relies heavily on performance indicators [15]. The EV method makes use of the schedule performance index (SPI) and the cost performance index (CPI) [16]. Cost and schedule management are linked, as shown by the critical ratio (CR) which is a composite statistic calculated by multiplying the CPI and SPI [17]. The weighted performance index is the sum of the SPI and the CPI, recognizing that the weights assigned to these two metrics may reflect the fact that cost performance and schedule performance are affected by distinct factors [18].

Researches and professionals in the field of EVM have been challenged for their use of the phrase. According to [19], the concept of earned value employs a jargon that is both antiquated and cumbersome. In the words of Cioffi, "only the real cost stays clear." The PMBOK® Guide in 2004 tries to streamline the language and pare it down to only two words per critical factor [20]. For instance, the term "earned value" might be used to refer to the amount of money spent on a project rather than the "budgeted cost of work produced" (BCWP) (EV) [21]. New nomenclature and formalism for EVM were introduced by [22]. A general formula for estimating the length of a project's completion time was published by Vandevoorde and Vanhoucke, who relied on three different techniques for doing so [12].

To calculate the "Actual Cost of Work Performed" (ACWP) and the "Budgeted Cost of Work Performed" (BCWP), "EVM" must be applied to construction projects with a consistent cost and time data log (often once weekly) [13]. In addition, the "BCWS," which stands for "Budgeted Cost of Work Scheduled," must be met before any construction work can begin; this number forms the foundation of both the work schedule and the associated cost plan [14].

Table 1. Terms relating EVM

EVM Metrics	Description of EVM Metrics
BCWS	BCWS, is the dollarized value of all work scheduled to be accomplished in each period. This most important variable symbolizes the planning function required by EVM. BCWS = % Complete (Planned) x Project Budget
BCWP	BCWP, is the dollarized (budgeted) value of all work accomplished in each period. The variable is also called EV and symbolizes the completion of work. BCWP is not 'earned' until the work is completed. The formula reads as follows: BCWP = % Work Performed (Actual) x Project Budget.
ACWP	ACWP, is the cost actually incurred and recorded in accomplishing the work performed within a given accounting period and is accumulated reported over time. The ACWP is reported by the contractor's accounting system in accordance with generally accepted accounting procedures. The formula reads as follows: BCWP = % Work Performed (Actual) x Project Budget.
BAC	BAC is a measure that is often used in EVM to track the actual cost of a project against its forecasted budget. It is calculated at the start of a project based on the project work and its individual components.
T	The planned period of the project.

Table 2. Additional EVM-Related Key Terms

Performance Metrics	Overview of Performance Metrics
SPI	SPI is a measure of the conformance of actual progress (EV) to the planned progress: SPI = EV / PV. In both above formulas, a value of 1.0 indicates that the project performance is on target. To find the schedule performance index, we must first find the planned value and the earned value. SPI is then calculated by dividing this earned value integer by the planned value integer. Therefore, the schedule performance index is a ratio of earned value to planned value.
CPI	CPI is a measure of the conformance of the actual work completed (measured by its earned value) to the actual cost incurred: CPI = EV / AC. SPI is a measure of the conformance of actual progress (EV) to the planned progress: SPI = EV / PV. CPI is a metric used to determine if tasks within a project use up more or less of the budget assigned to that project. If CPI is over 1.00 it means it's under-budgeted, and if it's below 1.00 it's over-budgeted.
SV	SV indicates how much a project is ahead or behind schedule. It measures whether a project is on track by calculating actual progress against expected progress. SV is used by the Program Manager and program personnel to determine how best to utilize their remaining resources. SV is part of EVM and helps project managers determine if a project is ahead of or behind schedule and by how much. To calculate SV, subtract project's PV from its EV: SV = EV – PV.
CV	CV is the difference between project costs estimated during the planning phase and the actual costs. In other words, it is how much actual costs vary from budgeted costs. Calculating cost variance is how project managers track expenses to see if a project is under or over budget. The cost variance formula is defined as the 'difference between EV and AC. (CV = EV – AC) Sometimes this formula is expressed as the difference between budgeted cost of work performed and actual cost work performed.

2.2 Cost and Schedule Estimate at Completion

Several performance indicators may be used to get the cost EAC and anticipated cost to finish the remaining work [15]. It can be shown from that EAC has the following universal formula:

EAC= AC+BAC-EV

Where BAC is the total budget and index is comprised mostly of a performance index and a regression index [16].

There are a few different ways to estimate how long a project will take, but the three most often cited are the planned value (PV) strategy, the earned duration (ED) technique and the earned schedule (ES) technique [17]. According to [18] provide a method for estimating the time it will take to complete a project in general:

EAC=AD+PDWR

2.3 Advantages and Disadvantages of EVM

By replacing the C/SCSC with commercial industry criteria and leveraging information technologies to promote timely data transfer between government agencies and contractors, the implementation of EVM has the potential to streamline the reporting requirements for projects, as noted by the General Accounting Office in 1997 [19]. According to [20] Valle and Soares outlined the primary advantages of EVM: There are six benefits to a well-implemented project control process, including: (1) a unified approach to managing budget, schedule, and progress; (2) enhanced insight into the project's scope and procurement; (3) prompt notification of issues; (4) the ability to anticipate trends in project deviations; (5) a reduction in the amount of time required to comprehend issues and find solutions; (6) encouragement of team members to actively participate in the control process; and (7) improved project outcomes [20].

However, empirical research has uncovered several barriers that may prevent EVM from being implemented, including:

(1) High cost, complicated and burdensome paperwork [21].
(2) Poor understanding of EVM; [22]
(3) Distrust and conflict between project managers, project consulting, and government [23].
(4) Pressures to report only good news [24]; and
(5) Contract in fixed price that makes EVM leery [25]

The result of EVM analysis is not directly tied to potential management action, and practitioners discovered that the accuracy of performance indicators may be problematic [26].

3 Empirical Studies of EVM in Construction

Various academic journals, international conferences, and books were utilized to compile this survey of EVM literature [27]. It was decided to divide the detected EVM papers into two categories: empirical and non-empirical [28]. Key challenges for empirical investigations include efficient EVM implementation, CPI behaviors, cost

control method accuracy, and time control technique accuracy. The topics of the theoretical investigations include SPI at various WBS levels, the precision of time control methods, and the combination of EVM with other project management approaches [29].

3.1 Effective Implementation of EVM

Successful implementation of EVM necessitates several extra key practices in planning, executing, and controlling process, in addition to adopting the project management principles defined in PMBOOK Guide in normal project management procedures [30]. According to research by, current Korean project control methods fail to provide accurate cost and schedule integrated data for EVM. Three key crucial success factors (acceptance, usage, and performance) were defined to improve the odds of a successful result for EVM adoption in the service of project success. Each component is then broken down into several smaller success sub-factors.

Cultural issues, such as a lack of openness to sharing negative information and an overly optimistic outlook on recovering from cost overruns, were also found to impede efficient project management. Specifically, the goal of contractor or government project managers may not be to discover the best accurate estimate, but rather to safeguard the project and the careers of its managers by hiding the "bad news”. A study argued that fixing "lingering cultural issues" is more important than improving EAC predicting accuracy.

3.2 Behaviors of CPI

Several studies were conducted to learn more about the CPI's behavior from the start to finish of the project. As discovered, after a project reaches 20% completion, the cumulative value of CPI stabilizes at about 0.10 and often declines from there. For extended projects lasting more than 6.7 years, which showed that Christensen and Heise's conclusion holds water.

3.3 Accuracy of Cost and Time Control Techniques

Numerous research on the reliability of the different methods for independent estimate at completion were prompted by the abrupt conclusion to the US Navy's A-12 Avenger Acquisition Program. Studies typically include comparing actual contract costs to EAC calculated using a variety of index-based techniques. EAC estimates based on CPI averaged over shorter periods were found to be somewhat higher, looked over 25 EAC studies and found that there is no conclusive evidence that either regression-based models or index-based models are inherently more accurate. How precise results are will be determined on the systems used and the contracts' current development state. According to previous research the cumulative CPI-based cost estimate at completion refers to the lower bound, which was the closest to estimation supported by contractor and government programmed managers, by analyzing data on completed contracts

extracted from the US Defense Acquisition Executive Summary database. However, in most cases, the average EAC calculated from the cumulative CR provided the most reliable results.

Evaluated data from real-world projects to assess the validity of three schedule forecasting approaches, and they found that the earned schedule method is more accurate at predicting the entire length of a project.

4 On-Empirical Studies of EVM in Construction

4.1 SPI at Different WBS Levels

The traditional SPI metrics have been questioned by Lipke [?] because they may provide erroneous and inaccurate time projections in the latter stages of a project. He proposed the idea of ES, which adds a temporal dimension to the financial metrics, and provided a modified schedule performance indicator [SPI (t)] for tracking progress over the course of a project's lifetime. If they are used at the activity level rather than the control account level or higher WBS levels, the SPI and SPI (t) are accurate measures of project performance. It was also investigated the impact of the false SPI values on the accuracy of three forecasting approaches, which even minor delays in key operations paired with significantly quicker progress in non-critical activities might result in a false SPI number.

Practitioners may only use the measurements at higher levels. A thorough schedule analysis, as pointed out by Lipke might place an undue amount of stress and disruption on the project team. Furthermore, Vanhoucke discovered that accurate measurement of project performance on high WBS levels is possible in the situation that the project network has a relatively serial structure that incorporates many key activities. On the other hand, Ding and Zhang presented a new approach to addressing this issue. They presented a float-based weighted SPI and a float-based criticality parameter to quantify the importance of each activity.

4.2 Accuracy of Time Control Techniques

In this context, comparing the efficacy of the PV technique, the ED method, and the ES approach is crucial. After comparing the outcomes of three approaches to project progress monitoring, Vandevoorde determined that the ES approach yields the most valid and accurate findings throughout the project's life cycle. When the SPI (t) value is false, however, Vanhoucke discovered that the ES approach underperformed the other two.

As a bonus, Vanhoucke introduced a simulation mode to look at how critical and non-critical activities in a network affect the precision of the three duration forecasting techniques. Results from simulations suggest that a greater criticality of project activities, as opposed to more parallel networks, may lead to improved prediction

accuracy. When plotted as a function of time, the intended value often follows an S-curve, according to the research. Throughout a project's lifecycle, the number of concurrent operations will fluctuate, which will cause project expenses to rise and fall along an S-shaped curve. However, EVM procedures often assume a linear relationship between the intended value and the actual value. Errors are conceivable because of this. Therefore, Cioffi created and investigated an analytic description for the shape in different contexts. The use of EVM is controversial when the project is exposed to extensive rework, as it may lead to wrong management choices and a decline in the cumulative value of CPI from the moment of stability until project completion. The "effective earned value" was created by Lipke [30] by combining the earned value idea with the assessment of schedule adherence. De Marco suggested a logistic-curve based technique that interpolates the nonlinear S-curve and allows the assessment of EAC (t) by considering the unique beginning behavior of a project's schedule, as an alternative to employing index-based calculations.

4.3 The Integration of EVM with Other Project Management Techniques

Intuitive principles were included into the 'percent complete' technique by Naeni and Salehipour [31], who offered EV indexes and estimations based on fuzzy logic. This method of EVM blends technical performance, cost performance, and schedule performance into the standard EVM framework, therefore satisfying product quality standards. To account for the unpredictability of project parameters, Pajares and López-Paredes [32] developed a new set of EVM indicators that serve as an early warning system for systemic and structural changes that might have a negative impact on the project's risk, cost, or schedule. The Kalman filter forecasting approach, which is based on the ES method and was created by Kim, may offer probabilistic estimates of the project's completion time. Estimates for future projects and the effectiveness of suggested fixes were calculated using the stochastic S-curves (SS curves). When evaluating the scheduling performance of construction projects stochastically, Nassar used Weibull analysis with the EVM. Lipke included the math of statistics into forecasting ultimate cost and length, since research on cost estimation at completion may be hampered by lack of available broad-based data.

5 Conclusions

To sum up, EVM is crucial to the overall management of the project's scope, timeline, and budget. More so, there are now rules for using this technique as a tool of control in future building projects. In this study, we survey the state of the talent in regard to current and well-liked EVM research paths. The article begins with an overview of the history of EVM, defining its key concepts and describing its terminology, performance analysis and forecasting metrics, and benefits and drawbacks. We suggest the retrieval

studies are organized using a categorization system that was devised. A vast amount of project data was evaluated to illustrate the behaviors of CPI and explore the accuracy of cost forecasting approaches, while case studies were utilized to emphasize the driving and hindering elements for efficient implementation of EVM.

We find our research the effectiveness of EVM has been enhanced by modelling and simulation techniques in non-empirical research. When brought into other nations, the EVM approach, which is widely used in the United States, may need certain structural modifications to fit in with local practices for managing projects. For the domestic market, it is important to establish a data representation model adequate for the gathering and processing of integrated data on both cost and schedule. The effectiveness of control during information integration is also influenced by the degree of detail of information, hence studies should be conducted to determine the optimal level of detail for different sized and kinds of projects. In last we say that Inaccuracies in implementing SPI (t) at higher WBS levels have been the subject of many research papers. A mathematical explanation and solution might be helpful in solving this problem, in addition to a qualitative one. However, in the meantime, the project team should use the right model to aid in doing a thorough schedule analysis and minimizing any negative repercussions. We suggest may possible mistakes exist in EVM outputs due to the linear intended value assumption. To better understand and forecast type-specific analytic expression, further investigation is required. In the last 30 years, several EAC investigations have been conducted. Prior research has relied heavily on information collected from military contracts.

Future studies should find the most accurate performance index for a given kind of project, since the formula's predicted accuracy is dependent on characteristics unique to the project at hand.

References

1. Defense Technical Information Center: DTIC ADA136382: Survey Relating to the Implementation of Cost/Schedule Control Systems Criteria within the Department of Defense and Industry. Phase I. 1983. Accessed: Feb. 06, 2023. [Online]. Available: https://archive.org/details/DTIC_ADA136382/mode/1up
2. Anbari, F.T.: Earned value project management method and extensions. Project Management Journal 34(4), 12–23 (2003).
3. Anbari, F.T.: Applications and extensions of Earned Value analysis method. Project Management Journal, 34(4), 12–23 (2001).
4. Barraza, G.A., Back, W., Mata, F.: Probabilistic forecasting of project performance using stochastic S curves. Journal of Construction Engineering and Management, 1(25), 0733-9364 (2004).
5. Chen S, Zhang Xue.: An analytic review of Earned Value Management studies in the construction industry. Construction Research Congress, (2012). ,https://ascelibrary.org/doi/abs/10.1061/9780784412329&ved=2ahUKEwiWma_I4rP_AhWEBIgKHWBwC0IQFnoECBIQAQ&usg=AOvVaw3m7_Ckq7Z6quLokryzAbQb

6. ASCE2012 Homepage, https://ascelibrary.org/doi/abs/10.1061/9780784412329&ved=2ahUKEwiWma_I4rP_AhWEBIgKHWBwC0IQFnoECBIQAQ&usg=AOvVaw3m7_Ckq7Z6quLokryzAbQb, last accessed 2022/03/12
7. Christensen, D.S.: Project advocacy and the estimate at completion problem. Journal of Cost Analysis, 13(1), 35–60 (1996).
8. Barr, Z.: Earned value analysis– A case study. Project Management Institute, 10(12), (1996).
9. Huang, J.W., Pan, H.M., Li, Y, Zhu, Y.T., Liao, Z.Y.: Cost/schedule monitoring and forecasting for project based on Earned Value Management (EVM). Advanced Materials Research, 919(921), 1437–1440 (2014).
10. Christensen, D.S., Christensen, and H.S.: Cost performance index stability. National Contract Management Journal, 25, 7-15 (1993).
11. Christensen, D.S.: The estimate at completion problem: A review of three studies. Project Management Journal, 24(1), 37–42 (1993).
12. Christensen, D.S.: Project advocacy and the estimate at completion problem. Journal of Cost Analysis, 13(1), 35–60, (1996).
13. Cioffi, D.: Designing project management: A scientific notation and an improved formalism for earned value calculations. International Journal of Project Management, (2006).
14. Cioffi, D.F: A tool for managing projects: An analytic parameterization of the S-curve. International Journal of Project Management, 23(3), 215–222 (2005).
15. Johnson, M.W., Christensen, C.M., Kagermann, H.: Reinventing your business model. Harvard Business Review Journal, 87(12), 52-60 (2008).
16. Christensen, D., Antolini, R.C., McKinney, J.W.: A review of estimate at completion research. Journal of Cost Analysis, (1995).
17. Adner, R., Kapoor, R.: Value creation in innovation ecosystems: How the structure of technological interdependence affects firm performance in new technology generations. Strategic Management Journal, 31(3), 306–333 (2010).
18. Marco, A., Briccarello, D., Rafele, C.: Cost and schedule monitoring of industrial building projects: Case study. ASCE Journal of Construction Engineering and Management, 135(9), 853-862 (2009).
19. Fleming, Q.W., Koppelman, J.M.: Earned value project management. 4th edition. Project Management Institute, Pennsylvania (2010).
20. MAJOR ACQUISITIONS significant changes underway in DOD's earned value management process. General Accounting Office, USA, 97-108 (1997).
21. Grace Commission: President's private sector survey on cost control (Grace Commission). Ronald Reagan, (1983). Available: https://www.reaganlibrary.gov/archives/topic-guide/presidents-private-sector-survey-cost-control-grace-commission.
22. Vandevoorde, S., Vanhoucke, M.: A comparison of different project duration forecasting methods using earned value metrics. International Journal of Project Management, 24(4), 289–302 (2006).
23. Kym, H.K.: Earned schedule in action. The Measurable News, 30, 23–28 (2005).
24. Henderson, K.: Earned schedule: A breakthrough extension to earned value theory? A Retrospective Analysis of Rea, 1(2), 13-23 (2003).
25. Abdel Azeem, S.A., Hosny, H.E., Ibrahim, A.H.: Forecasting project schedule performance using probabilistic and deterministic models. HBRC Journal, 10(1), 35–42 (2014).
26. Kerkhove, L.P., Vanhoucke, M.: Extensions of earned value management: Using the earned incentive metric to improve signal quality. International Journal of Project Management, 35(2), 148–168 (2017).
27. Kim, B.C, Reinschmidt, K.F.: Probabilistic forecasting of project duration using Kalman Filter and the Earned Value Method. Journal of Construction Engineering and Management, 136(8), 834–843 (2010).

28. Kim, E., Wells, W.G., Duffey, M.: A model for effective implementation of Earned Value Management methodology. International Journal of Project Management, 21(5), 375-382 (2003).
29. Kim, S., Park, C., Lee, S., Son, J.: Integrated cost and schedule control in the Korean construction industry based on a modified work-packaging model. Canadian Journal of Civil Engineering, 35, 225-235 (2008).
30. Lipke, W, A re-examination of project outcome prediction-Using Earned Value Management Methods. The Measurable News, 3, 14–16 (2005).
31. Naeni L. M, Shadrokh S, and Salehipour A: A fuzzy approach for the earned value management. International Journal of Project Management, 29(6) , 764-772 (2011).
32. Pajares, J., López-Paredes, A.; "An extension of the EVM analysis for project monitoring: The cost control index and the schedule control index. International Journal of Project Management, 29(5), 615–621 (2011).

Identification of Critical Factors in Design for Sustainability of Modular Constructions

Efkan Efekan[1][0009-0002-4761-6315], Tolga Celik[1][0000-0002-2513-6735] and Onur B.Tokdemir[2][0000-0002-4101-8560]

[1] Eastern Mediterranean University, Civil Engineering Department, North Cyprus, Türkiye, efkanefekan@emu.edu.tr
[2] Istanbul Technical University, Engineering Faculty, Istanbul, Türkiye,

Abstract. The circular economy emerged as a result of the search for resource efficiency and sustainability in various industries such as construction. Circular construction aims to reduce waste, extend the life of structures, and encourage the reuse and recycling of materials. Reversible design is an important approach to circular construction that focuses on creating flexible and adaptable structures that can be easily modified and disassembled. This article examines the important aspects of integrating reversible design into modular construction practices as part of the circular economy.

Keywords: Circular Economy, Modular Construction, Reversible Building Desing.

1 Introduction

With rising demand for construction materials, severe shortage, and increasing environmental concern, resource efficient construction is much discussed globally, especially after the concept of circular economy (CE) has emerged at various levels in recent years. Due to the concern of significant resource consumption regardless of limited resources, the transition of the construction industry towards a linear economy CE model is inevitable to conserve resources and promote efficient use of resources.

The transition to a circular economy in the construction industry provides an excellent opportunity to incorporate construction activities, processes and practices from limited natural resource consumption and environmental impacts. Circular construction uses interconnected models of narrowing, slowing, and closing resource cycles to reduce the extraction and wasteful use of natural resources, eliminate waste and pollution, make construction products and materials last longer, and keep products valuable after use. However, construction practitioners are struggling to successfully apply circular economy principles to construction projects.

The idea of reversible design and its incorporation into modular construction practices is crucial in applying circular economy principles in the built environment. The reversible design focuses on creating buildings that are adaptable, flexible, and easy to replace or dismantle to reduce waste and extend their lifespan. Reversible

design, combined with a modular structure using standardized components and off-site production, becomes a powerful tool for achieving circularity and sustainability goals. Moreover, it includes the use of modular construction techniques, standard or customized connections, and reversible assembly methods that facilitate the dismantling and recovery of materials for renovation or end-of-life. It entails designing structures that can be easily modified, disassembled, and reconfigured to meet changing needs and future uses. Reversible design solutions ensure high reuse potential of the building, systems, products, and materials, as well as high transformation potential (E. Durmisevic,2017).

This study addresses and demonstrates the importance of design principles for modular and prefabricated reversibility. The aim of the study is to indicate which factors can contribute to the circular economy when considering the design of modular construction. In this context, by examining the reversible design dimension of modular construction, it is an adaptable and applicable contribution to circular construction.

2 Overview of Circular Modular Construction Projects

Circular construction is pursued to manage resources, reduce negative environmental externalities (i.e., waste, pollution, and greenhouse gases), preserve natural capital, generate economic value, and engineer closed-loop systems of material inflow and outflow in building, civil engineering, and infrastructure projects (Giorgi et al., 2022). Circular construction combines CE principles, strategies, and objectives so that construction activities, operations and practices avoid limited resource consumption, economic inefficiencies, and negative social impacts (Ellen MacArthur Foundation, 2012). Thus, circular construction is rooted in the philosophies of industrial ecology, industrial symbiosis, reverse logistics, the cradle-to-cradle concept of effectiveness, cleaner production, and closed-loop material flows (Sehnem et al., 2019).

When implementing circular construction projects, developing a solid framework of relevant critical success factors (CSFs) can guide the project team in minimizing the risks of failure in circular modular construction projects (Wuni, 2022). Therefore, they conducted a very comprehensive study on an effective mechanism to improve Modular project success, critical success factors (CSFs) that can be prioritized in its implementation (O'Connor et al., 2014), (El-Abidi et al., 2019), (Wuni & Shen, 2022). According to the results (Wuni & Shen, 2022) obtained, the management of the "*Robust eco-design for reversible building, waste management, reuse and recycling*" and "*leveraging insights from demolition and design lifecycle stages*" factor in modular and prefabricated structures is vital for success factors. Since there is a limited study on reversible building design CSF in the literature and this factor is very important, the determination of the critical factors of this subject is detailed in the following section.

3 Reversible Building in Circular Modular Construction Projects

Circular construction facilitates reversible building design, improves the closed loop of material inflow and outflow from the building process, improves resource and waste management, minimizes pollution, and conceptualizes buildings as material banks through flexible, adaptable, and demountable buildings (Giorgi et al., 2022),(Guerra & Leite, 2021), (Antonini et al., 2020).

An architectural style known as a "reversible building" is one that was created specifically to allow for the transformation, disassembly, and reuse of building components. By removing, adding, moving, or substituting parts, transformations involve the conversion of one building form into another. They can happen at the spatial, structural, or material level of a building and are the result of the need to adapt the physical environment to human activities (Durmisevic & Yeang, 2009). Disassembly is the methodical dismantling of a building structure to salvage as many of its components as possible for future use. Reuse is the process by which abandoned construction materials are recycled (and occasionally improved according to the material structure) and used for the same purpose without being destroyed. This significantly lowers the cost, energy use, and carbon emissions associated with demolition, processing for recycling, and transportation to landfill and recycling facilities. It also preserves the invested embodied energy of deconstructed building parts, increases their useful life, and prolongs their lifespan (Durmisevic et al. (2017).

In the literature, there are several pilot studies on reversible building design carried out within the framework of the BAMB 2020 Horizon program, which is financed by the European Union. In addition, some researchers have studied the design of reversible buildings (Krohnert et al., 2022), (Antonini et al., 2020), (Yan et al., 2022), (Piccardo & Hughes, 2022). Determining the critical factors and adapting them to modular construction will help the companies producing in the market to prepare detailed documentation while preparing the environmental design, easy-to-apply, fast assembly and disassembly phase. Considering the technical aspects of reversible design, the critical factors are shown in Table 1.

Table 1. Critical factors in the technical aspects of reversible design

ID	Critical Factors
1	Reversible connections
2	The speed of assembly/disassembly (e.g., preassembly, fast connection techniques, etc.) the simplicity
3	Use and reuse of reclaimed building materials (e.g., recuperated finishing panels, profiles, etc.)
4	Damage beam sensitivity and load-carrying capacity of joints
5	Flexible integration of technical systems
6	Independence of the system (e.g., can one part be replaced?)
7	Low initial cost and environmental impact
8	High energy efficiency
9	Physical interaction with the digital Materials Passports Platform

1) **Reversible connections:** Reversible connections have the characteristics of making it possible to disassemble and reassemble modular construction components. Thanks to these features, modular building elements can be reused in future construction projects and can be easily separated without damage.
2) **The speed of assembly/disassembly:** By using pre-assembly and quick-connect methods, project times and productivity can be significantly reduced. Fast assembly/disassembly methods allow modular systems and standardized components to be connected to each other in a short time.
3) **Use and reuse of reclaimed building materials:** Modular structures gain a distinctive, rustic aesthetic when reclaimed building materials are used in their construction, which also improves sustainability and lowers costs.
4) **Damage beam sensitivity and load-carrying capacity of joints:** Considering the environmental conditions and the parts that may be additional attachments, attention should be paid to prevent damage to the structure.
5) **Flexible integration of technical systems:** The adaptability of modular construction to future technological advancements is made possible by the flexible integration of technical systems, which enables quick and simple maintenance as well as effective installation.
6) **Independence of the system:** The modular independence of the system allows for the replacement or replacement of individual components without disrupting the system, providing flexibility, cost-effectiveness, and maintenance.
7) **Low initial cost and environmental impact:** Reversible buildings have the benefit of having a low initial cost and minimal environmental impact because they are simple to disassemble, relocate, or repurpose, which minimizes waste and increases resource efficiency.
8) **High energy efficiency:** During construction, on the other hand, it is critical to prioritize high energy efficiency to minimize energy consumption, reduce environmental impact, and optimize the deconstruction process's sustainability.
9) **Physical interaction with the digital Materials Passports Platform:** By interacting physically with the Digital Material Passports Platform, it is possible to make wise decisions during the planning and execution of reversible building projects, integrate material information seamlessly, and manage resources efficiently.

4 Conclusion

A key element of the circular economy in the construction sector is a reversible design that accommodates modular construction. To adapt modular construction to the circular economy, this article emphasizes identifying the crucial elements for reversible building design and taking these elements into account. Buildings can become resilient assets that reduce waste and maximize resource efficiency by incorporating these factors into the design and construction processes. Reversible design and modular construction techniques will be crucial in producing a more sustainable and resilient built environment as the circular economy gains momentum.

This study aims to help companies make their transition to modular construction more effective and efficient and aims to support them in gaining competitive advantage and reaching their important goals faster with the time and cost saving, environmental impact, and flexibility of modular construction. The recommendations and strategies obtained will provide a practical roadmap for companies to successfully implement modular construction and contribute to their stronger position in terms of sustainability and efficiency and increase their long-term success. In the next study, current success criteria and data related to the design of sustainable modular construction will be analysed in detail and based on this information, critical success factors will be identified that will facilitate companies to adopt modular construction in accordance with their specific circumstances and goals.

References

1. Antonini, E., Boeri, A., Lauria, M., & Giglio, F. (2020). Reversibility and Durability as Potential Indicators for Circular Building Technologies. Sustainability, 12(18), Article 7659. https://doi.org/10.3390/su12187659
2. Durmisevic, E., Beurskens, P. R., Adrosevic, R., & Westerdijk, R. (2017). Systemic view on reuse potential of building elements, components and systems: comprehensive framework for assessing reuse potential of building elements. In Hiser International Conference: Advances in recycling and management of construction and demolition waste (pp. 275-280).
3. Durmisevic, E., & Yeang, K. (2009). Designing for Disassembly (DfD). Architectural Design(202), 134-137.
4. El-Abidi, K. M. A., Ofori, G., Zakaria, S. A. S., Mannan, M. A., & Abas, N. F. (2019). Identifying and Evaluating Critical Success Factors for Industrialized Building Systems Implementation: Malaysia Study. Arabian Journal for Science and Engineering, 44(10), 8761-8777. https://doi.org/10.1007/s13369-019-03941-4
5. Ellen MacArthur Foundation & McKinsey, "Towards the Circular EconomyVolume 1: Economic and Business Rationale for an Accelerated Transition," 2012, http://www.ellenmacarthurfoundation.org/business/reports/ce2012#.
6. Giorgi, S., Lavagna, M., Wang, K., Osmani, M., Liu, G., & Campioli, A. (2022). Drivers and barriers towards circular economy in the building sector: Stakeholder interviews and analysis of five European countries policies and practices. Journal of Cleaner Production, 336, Article 130395. https://doi.org/10.1016/j.jclepro.2022.130395
7. Guerra, B. C., & Leite, F. (2021). Circular economy in the construction industry: An overview of United States stakeholders' awareness, major challenges, and enablers. Resources Conservation and Recycling, 170, Article 105617. https://doi.org/10.1016/j.resconrec.2021.105617
8. Krohnert, H., Itten, R., & Stucki, M. (2022). Comparing flexible and conventional monolithic building design: Life cycle environmental impact and potential for material circulation. Building and Environment, 222, Article 109409. https://doi.org/10.1016/j.buildenv.2022.109409
9. O'Connor, J. T., O'Brien, W. J., & Choi, J. O. (2014). Critical Success Factors and Enablers for Optimum and Maximum Industrial Modularization. Journal of Construction Engineering and Management, 140(6), Article 04014012. https://doi.org/10.1061/(asce)co.1943-7862.0000842
10. Piccardo, C., & Hughes, M. (2022). Design strategies to increase the reuse of wood materials in buildings: Lessons from architectural practice. Journal of Cleaner Production, 368, Article 133083. https://doi.org/10.1016/j.jclepro.2022.133083

11. Sehnem, S., Vazquez-Brust, D., Pereira, S. C. F., & Campos, L. M. S. (2019). Circular economy: benefits, impacts and overlapping. Supply Chain Management-an International Journal, 24(6), 784-804. https://doi.org/10.1108/scm-06-2018-0213
12. Wuni, I. Y. (2022). A systematic review of the critical success factors for implementing circular economy in construction projects. Sustainable Development. https://doi.org/10.1002/sd.2449
13. Wuni, I. Y., & Shen, G. Q. (2022). Developing critical success factors for integrating circular economy into modular construction projects in Hong Kong. Sustainable Production and Consumption, 29, 574-587. https://doi.org/10.1016/j.spc.2021.11.010
14. Yan, Z. D., Ottenhaus, L. M., Leardini, P., & Jockwer, R. (2022). Performance of reversible timber connections in Australian light timber framed panelised construction. Journal of Building Engineering, 61, Article 105244. https://doi.org/10.1016/j.jobe.2022.105244

A Systematic Literature Review on Blockchain Technology for Construction Contract Management

Ahmet Karacığan[1][0009-0004-4763-0242] and Beliz Özorhon[2][0000-0002-4963-6937]

[1] Boğaziçi University, Civil Engineering Department, İstanbul, Türkiye,
ahmet.karacigan@boun.edu.tr
[2] Boğaziçi University, Civil Engineering Department, İstanbul, Türkiye,
beliz.ozorhon@boun.edu.tr

Abstract. Together with the Industry 4.0 concept, digitalization of the architectural, engineering, and construction (AEC) industries has accelerated. Blockchain technology has a strong potential to revolutionize the construction industry as it is gaining momentum in every other industry. The contract management procedure in the AEC industries is flawed due to a lack of information sharing, on-time payments, and an easily traceable supply chain. Implementation of the blockchain technology is expected to resolve such issues regarding contract management. In this respect, a comprehensive and systematic literature review has been conducted. In order to present the most recent state of blockchain-related research in the construction field, two of the largest databases have been analyzed. Based on an extensive literature review, application areas where blockchain technology has the potential to improve contract management processes were determined as "automated payments", "supply chain management", and "information management". Based on keyword analysis, search results from Scopus and Web of Science (WoS) databases have been examined via using VOSviewer software. Based on the analysis results, co-occurrence maps have been drawn for specific search results. The findings of the analysis showed the most important concepts that has been utilized together with blockchain implementation. It has also been observed that payments, supply chain management, and information management are the main application areas of blockchain technology within the construction industry. Findings of this study may guide the researchers who tries to explore the current state of literature regarding blockchain technology in the construction industry.

Keywords: Blockchain, Contract Management, Construction Industry.

1 Introduction

As technological advancement occurs and digitalization emerges, innovation becomes the main component of competitiveness for organizations. Digitalization is a key concern and the main driver for innovation and competitiveness for organizations [1]. Together with digital transformation, organizations have begun to adopt new technologies into their businesses and digitalized their traditional processes. In the last

decade, the construction industry has been undergoing a digital transformation process. Traditional design and construction processes are inefficient, and companies try to increase their productivity with Construction 4.0 applications. The Construction 4.0 term means not only the traditional construction upgraded with technological innovations but also a new way of perceiving and understanding construction through the light of innovation and increased productivity [2].

The construction industry is one of the largest industries in the world and has a significant number of processes that are yet to be digitalized. Although digital technologies such as Building Information Modeling (BIM), Artificial Intelligence (AI), Internet of Things (IoT), and many others now utilized in construction projects, the industry is still behind other industries in terms of digitalization based on a report by McKinsey & Company [3]. According to another report by McKinsey & Company [4]. digitalization has increased the productivity of the construction industry by only 1% in the last 20 years, whereas the average of other production industries is 3.6%. It is clear that there is an opportunity for the construction industry in terms of digitalization.

The construction industry still uses traditional contracts and inefficient payment applications [5] and has been suffering from time-consuming contracting processes. Construction contract management is a central part of project management since contracts include interrelated tasks and a broad range of risks to be managed [6]. Construction contract management requires dealing with multiple stakeholders for a variety of work processes such as payments, supply chain management etc. The lack of an efficient information sharing tool may result in delays and increased supply chain management costs [7]. Without a collaborative and secure information management system, it is difficult to overcome the challenges [8]. Medical, financial, and education industries have mitigated similar payment, supply chain, and information management issues with the use of blockchain enabled systems [8].

One of the emerging technologies enabling the digital transformation of the construction industry is blockchain. Blockchain is a form of digital distributed ledger technology (DLT) that has gained momentum after its introduction with the crypto currency Bitcoin in 2009. Although the implementation of blockchain is at the initial stages within the built environment [9, 10]. it has been considered to have a huge positive impact on the industry. Rugina [11] argues that the implementation of blockchain to regulate the contractual approach of construction parties reduces the number of disputes generated within a project. Blockchain has various application areas within the construction industry from smart payment systems to supply chain activities. It has been estimated that advancements in contracting processes may improve cost savings by up to 7% and productivity by up to 10% [12].

2 Literature Review

Blockchain technology can be used for information sharing in a trustable, traceable, transparent, and storable way among multiple parties [13, 14]. There are various studies in the literature regarding blockchain and its applications in the construction industry.

Turk and Klinc [15] conducted a study to investigate the potential applications of blockchain technology in the construction industry and argued that blockchain is able to improve the reliability of the any recorded information and securely store the data produced by sensors during the facility management phase. Another study conducted by Safa et al. [16]. argues that a combination of BIM and blockchain will enhance data transparency and shareability among construction parties.

An automated smart contract payment system has been proposed by Ahmadisheykhsarmast and Sonmez [17] to ensure the transparent and timely transactions of interim payments. Bousquin [18] argued that blockchain provides an information exchange system that enables stakeholders to transact automatically without any intermediary. Wang et al. [19] proposed a blockchain based system to track and validate supply chain information in real time. Moreover, in another study conducted by Lanko et al. [20], the research team stated that the integration of radio frequency identification (RFID) and blockchain promotes the data transparency throughout supply chain processes. Blockchain has the potential to improve supply chain management process thanks to its ability to store and share real time data securely [7].

Based on the literature, the application areas of blockchain in the construction industry can be categorized under three main headings. These are payments, supply chain management, and information management [21]. All these headings are a part of construction contract management practices. Therefore, contract management can be defined as one of the main application areas of blockchain for the construction industry.

2.1 Automated Payments

Payments are one of the most critical parts of construction project management practices. There are thousands of claims generated due to the late payment domino effect [22] that result in delayed schedules. The current payment system in the construction industry has its flaws. When the general contractor applies for an interim payment from the client, they first prove the completed work on site. After the agreement on the progress of the completed works, the client makes the payment to the general contractor. Once the general contractor receives the payment, the amount is paid to the subcontractors based on their progress of completed works. A huge amount of schedule delay occurs during the negotiations about the completed percentages. Project bank account (PBA) is another payment method where the payment is done by the client directly to the PBA and automatically transferred to the subcontractors and other parties. However, PBA creates high management costs and requires staff training [17]. Thus, the PBA system is not favored by the clients [23].

Blockchain technology and smart contracts concept have the potential to create an effective and automated payment system for the construction industry. There are several authors in the literature argued that the terms of a construction contract can be embedded into a blockchain based smart contract system which will then automatically execute itself [24, 25, 5]. In a study conducted by Luo et al. [26], a semi-automatic payment system has been proposed. Combination of a blockchain based payment system and BIM models may foster the benefits of an automated payment system.

Wang et al. [27] stated that a blockchain based automated payment system can reduce the number of disputes due to late payments and unfair payments to subcontractors.

However, there are some challenges that hinder the implementation of a blockchain based automated payment system. First of all, people tend to resist changes especially when it comes to payment related topics. Secondly, the applicability of the smart contracts for complex construction contracts may be difficult and time consuming [21]. In addition, selection of the currency that will be used for payments might be problematic due to the fluctuations of the cryptocurrencies. Das et al. [23] argued that the cost of implementing a blockchain based payment method will be higher than traditional payment systems.

2.2 Supply Chain Management

Supply chain management is one of the key concepts of project management. The process involves numerous stakeholders such as producers, vendors, warehouses, shippers, distributors, retailers, and subcontractors [21]. Thus, it is hard to manage such complex processes and a systematic approach needs to be followed. The main goals of a supply chain management systems are to improve efficiency and optimize resource materials which will result in cutting down costs [28].

The current supply chain management systems are based on the use of GPS and RFID technologies. The major problem with the current supply chain management systems is that each stakeholder keeps their own data in the system they have been using and this cause an interoperability problem with fragmented information among stakeholders [19]. Thus, it is hard to track and share sensitive information in a secure and transparent way. The lack of an efficient information sharing tool may result in delays and increased supply chain management costs [7].

Blockchain technology has the potential to improve the supply chain management process thanks to its ability to store and share real time data securely [7]. Wang et al. [19] conducted a study and proposed a blockchain enabled supply chain management system. The findings of the case study in that research showed that real-time information sharing, and monitoring are achieved thanks to blockchain technology. The study demonstrated that the delivery process of the precast components was improved, and the stakeholders were able to track the reasons for disputes.

There are also some limitations for blockchain technology to be combined with supply chain management. In an environment with a large number of stakeholders, the main issue would be the resistance to change to adopt such a new technology. It is not possible to implement a blockchain enabled supply chain management system without the participation of each stakeholder. In addition, the integration of huge amounts of GPS and RFID data may result in limited storage capacity and time-consuming transmission on a blockchain based system [29].

2.3 Information Management

Managing information in construction projects is a difficult and important task that requires attention. Storing and sharing data in a timely and accurate manner is challenging due to the lack of effective communication among stakeholders [30]. On

the other hand, information and data security concerns are hindering the adoption of digital technologies such as BIM, GIS or IoT in the construction industry [31].

Thanks to its ability for storing and sharing information transparently and securely, blockchain technology has the potential to overcome the current barriers regarding information management. A blockchain based information management system that is integrated into BIM may offer countless advantages from privacy to protection or transparency [16]. In this way, BIM data can be protected from manipulation [32, 33] which may result in unsolvable claims in the future. In a study conducted by Parn and Edwards [34], it has been argued that a blockchain based data management system has the potential to improve the security of the current common data environment.

Utilization of blockchain together with BIM implementation enables the project parties to track data creation and modification history in a trustable way and solve copyright and ownership issues [15]. In addition, the integration of blockchain and IoT technologies will help capturing, sharing, and updating real time data in a transparent, secure and liable way [35, 36].

On the contrary, there are also some barriers that hinder the implementation of blockchain technology in terms of information management. In a research study, Lee et al. [35] argued that transaction processing times will be intolerable especially when a public blockchain is used. Due to the large amount of BIM data used in construction projects, scalability might be a barrier. Moreover, since construction projects involve sensitive data such as design documentation, financial information, or legal contracts, private blockchains are more likely to be used. However, private blockchains are more open to being hacked compared to public blockchains if more than half of the users are controlled [37].

3 Methodology

Within the context of this study, two of the largest databases, Scopus and Web of Science (WoS) have been analyzed. First of all, special keywords have been decided and categorized. As the main keyword of the analysis the word “Blockchain” is used. Blockchain applications regarding the construction contract management have been summarized under three headings and these are “Payment”, “Supply Chain Management” and “Information Management” as mentioned above. Thus, these words are used as the sub-keywords. Finally, the word “Construction” is used as the focused keyword in order to obtain specific results from the searches. The search work is done by using the Title-Abstract-Keyword filter on the databases. A summary of the search results can be found in Figure 1.

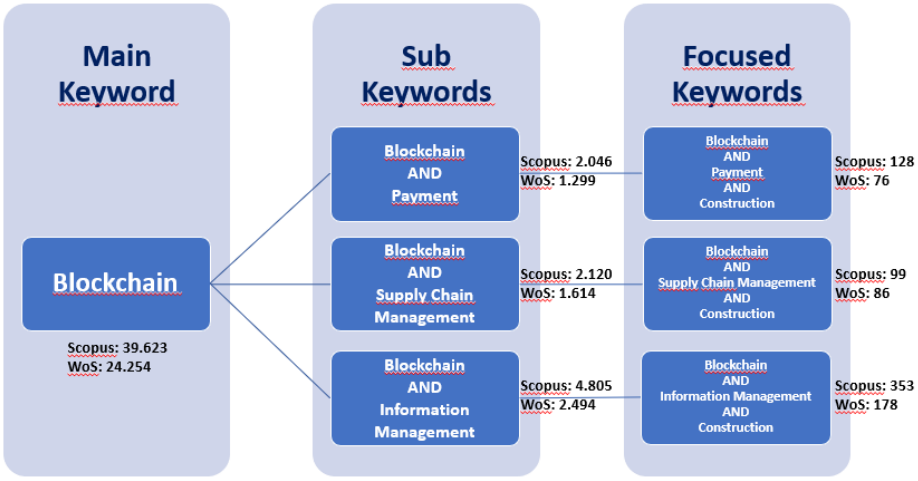

Fig. 1. Results of the Literature Search

The search results were then refined further by including only articles and conference papers that written in English language. As a result, 111 and 65 items were found on Scopus and WoS respectively for the search Blockchain AND Payment AND Construction, 76 and 67 items were found on Scopus and WoS respectively for the search Blockchain AND Supply Chain Management AND Construction and 273 and 146 items were found on Scopus and WoS respectively for the search Blockchain AND Information Management AND Construction.

These final results are then downloaded and analyzed by using VoSViewer version 1.6.18. The analysis is made based on the keyword cooccurrences. Only the keywords that have occurred 4 or more times were counted. In addition, a thesaurus file has been created for each search result to prevent the duplication of words due to spelling errors or different expressions of the same thing. For example, “Building Information Modeling” and “BIM” words or “blockchain” and “block-chain” words have been merged as a single word thanks to the thesaurus file.

Based on the analysis results, co-occurrence maps have been drawn for each of the search results. These maps help to understand the focus of the current literature. In other words, answers to such questions have been revealed, “what concepts were researched together with blockchain applications?”, or “which application of blockchain technology has been analyzed the most?”, or “what are the critical points to be discussed regarding the specific blockchain applications in the construction industry?”.

4 Results

The findings of the analysis showed that smart contracts concept is one of the most important concepts that has been utilized together with blockchain implementation. On the other hand, payments, supply chain management, and information management are the main application areas of blockchain technology within the construction industry.

Below, Figure 2 shows the analysis result for the search Blockchain AND Payment AND Construction. The literature is mostly focused on creating a blockchain based automated payment system that is expected to improve the efficiency of construction project management processes. It has been understood that most of the publications mentioned privacy and security concerns. On the other hand, integration of blockchain technology into construction management practices is also one of the biggest concerns.

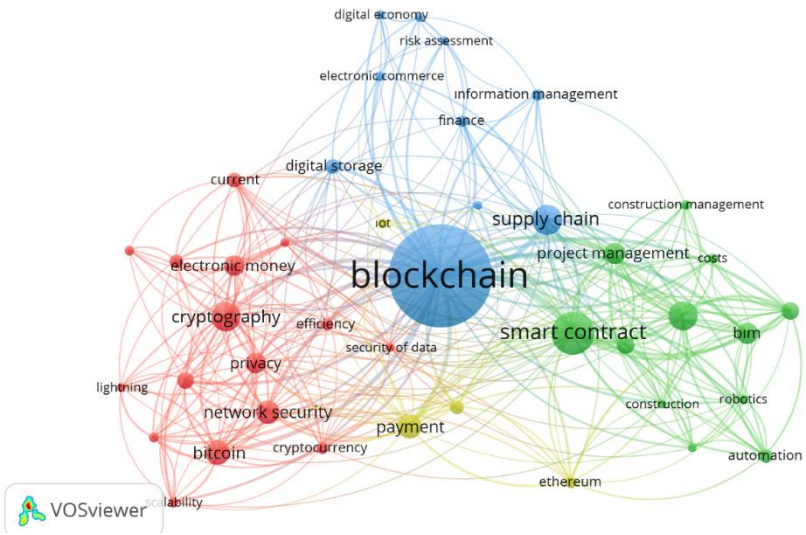

Fig. 2. Co-occurrence Map for Blockchain AND Payment AND Construction

Below, Figure 3 shows the analysis result for the search Blockchain AND Supply Chain Management AND Construction. The literature is mostly focused on creating a blockchain based supply chain management system which is expected to improve the traceability of the supply chain process and efficiency of construction management procedures.

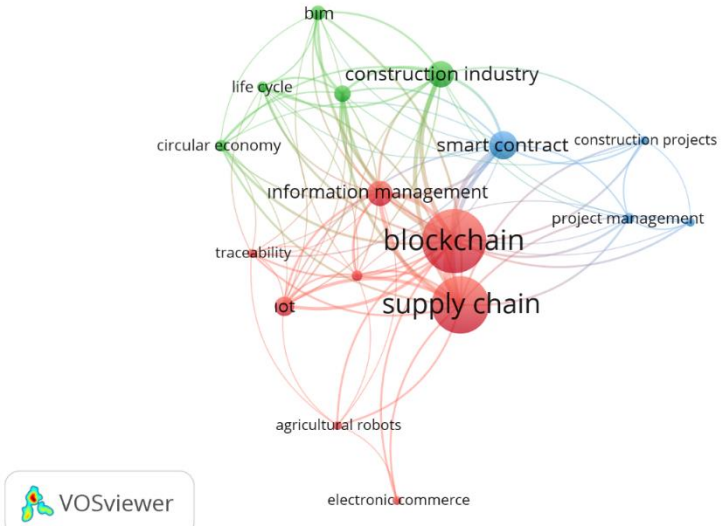

Fig. 3. Co-occurrence Map for Blockchain AND Supply Chain Management AND Construction.

Below, Figure 4 shows the analysis result for the search Blockchain AND Information Management AND Construction. Information management is main application area of blockchain technology since it provides an infrastructure for storing and sharing information safely and reliably. The map shows that information management is key for all the processes within construction management. The literature is mainly divided into 4 topics, and these can be categorized as "integration with other technologies", "possible applications within construction management", "implementation of the technology", and "digital infrastructure of the system".

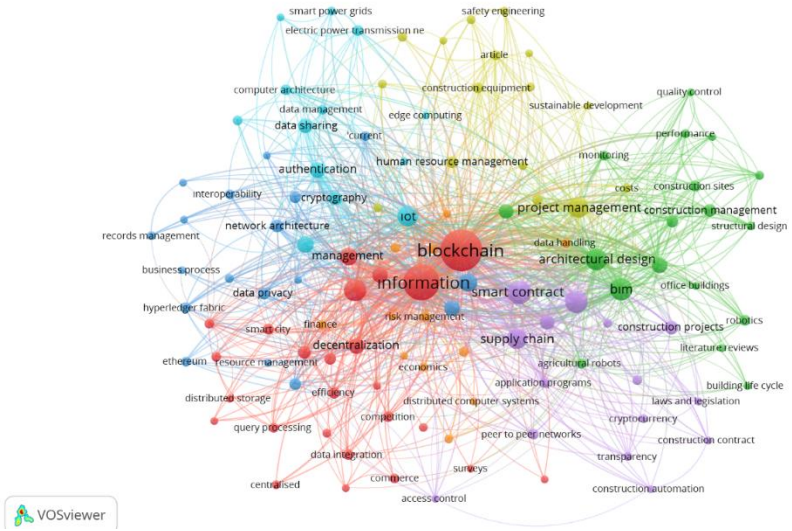

Fig. 4. Co-occurrence Map for Blockchain AND Information Management AND Construction.

Results also show that the literature is seeking for improving the efficiency of construction management practices by combining the opportunities that technology provides. There is no doubt that utilizing blockchain technology together with BIM, IoT and other digitalization tools will foster its benefits.

5 Conclusion

In this study, a systematic literature review has been conducted and results were assessed. In the literature, the number of studies regarding the integration of blockchain technology and the construction industry is increasing constantly. However, it is still in the initial stage and there is too much to explore. Most of the research studies are from the general perspective and about the possible applications of blockchain technology.

On the other hand, construction contract management is another popular research topic since the significance of claims and dispute resolution is increasing year by year for construction projects. Within the body of knowledge, there is a gap regarding the impact of the implementation of blockchain technology in the construction industry on contract management processes. Based on the systematic literature analysis, it can be argued that blockchain technology has the potential to overcome the challenges regarding construction contract management practices.

Findings of this study may guide the researchers who try to explore the current state of literature regarding blockchain technology in the construction industry. Significant subtopics were revealed to be focused on, and relevant studies may further examine the implementation of blockchain technology within the construction industry based on this literature review study.

Acknowledgements
This study has been supported by the TUBİTAK 2211-A Domestic Graduate Scholarship Program.

References

1. Allam, Z.: On Smart Contracts and Organisational Performance: A Review Of Smart Contracts Through the Blockchain Technology, (2018).
2. Forcael, E., Ferrari, I., Opazo-Vega, A., Pulido-Arcas, J. A.: Construction 4.0: A Literature Review. Sustainability, 12(22), 9755, (2020).
3. McKinsey & Company: Reinventing Construction: A Route to Higher Productivity, (2017).
4. McKinsey & Company: The next normal in construction, (2020).
5. Hamledari, H., Fischer. M.: Construction payment automation using blockchain-enabled smart contracts and robotic reality capture technologies, Autom. Constr. 132, (2021).
6. Greenhalgh, B.: Introduction to construction contract management, Oxfordshire, UK: Routledge, (2016).

7. Tezel, A., Papadonikolaki, E., Yitmen, I., Hilletofth, P.: Preparing construction supply chains for blockchain technology: An investigation of its potential and future directions, Front. Eng. Manage. 7 (4):547–563, (2020).
8. Das, M., Tao, X., Liu, Y., Cheng, J. C.: A blockchain-based integrated document management framework for construction applications, Autom. Constr. 133, (2022).
9. ARUP: Blockchain and The Built Environment, (2019).
10. Rathnayake, I., Wedawatta, G., Tezel, A.: Smart Contracts in the Construction Industry: A Systematic Review. Buildings, 12, 2082, (2022).
11. Rugina, C. R.: Smart Contracts Technology and Avoidance of Disputes in Construction Contracts. Lex ET Scientia International Journal. Vol 2, Pg 30-46, (2021).
12. Barbosa, F., Woetzel, J., Mischke, J.: Reinventing Construction: A Route to Higher Productivity. McKinsey and Company, (2017).
13. Penzes B.: Blockchain Technology in the Construction Industry, (2018).
14. Elghaish, F., Abrishami, S., Hosseini, M. R.: Integrated project delivery with blockchain: An automated financial system, Autom. Constr. 114, (2020).
15. Turk, Ž., Klinc, R.: Potentials of blockchain technology for construction management, Procedia Eng. 196, (2017).
16. Safa, M., Baeza, S. Weeks, K.: Incorporating blockchain technology in construction management, Strategic Direction 35 (10): 1–3, (2019).
17. Ahmadisheykhsarmast, S., Sonmez, R.: A smart contract system for security of payment of construction contracts, Autom. Constr. 120, (2020).
18. Bousquin, J.: Tech 101: Blockchain's benefits for construction, (2020).
19. Wang, Z., Wang, T., Hu, H., Gong, J., Ren, X., Xiao, Q.: Blockchain-based framework for improving supply chain traceability and information sharing in precast construction, Autom. Constr. 11, (2020).
20. Lanko, A., Vatin, N., Kaklauskas, A.: Application of RFID combined with blockchain technology in logistics of construction materials. In Proc., MATEC Web Conf, (2018).
21. Zhang, X., Liu, T., Rahman, A., Zhou, L.: Blockchain Applications for Construction Contract Management: A Systematic Literature Review, Journal of Construction Engineering and Management. Vol. 149-1, (2023).
22. Matt, V.: Late payments in the construction industry: Who's to blame?, (2020).
23. Das, M., Luo, H., Cheng, J. C.: Securing interim payments in construction projects through a blockchain-based framework, Autom. Constr. 118, (2020).
24. Cecconi, F. R., Dejaco, M. C., Moretti, N., Mannino, A., Cadena, J. D. B.: Digital asset management, In Digital transformation of the design, construction and management processes of the built environment, 243–253. Cham, Switzerland: Springer, (2020).
25. Li, J., Kassem, M.: Applications of distributed ledger technology (DLT) and Blockchain-enabled smart contracts in construction, Autom. Constr. 132, (2021).
26. Luo, H., Das, M., Wang, J., Cheng, J. C. P.: Construction payment automation through smart contract-based blockchain framework, In Vol. 36 of Proc., Int. Symp. on Automation and Robotics in Construction, 1254–1260. Hong Kong: International Association for Automation and Robotics in Construction, (2019).
27. Wang, J., Wu, P., Wang, X., Shou, W.: The outlook of blockchain technology for construction engineering management, Front. Eng. Manage. 4 (1): 67–75, (2017).
28. Qian, X. A., Papadonikolaki, E.: Shifting trust in construction supply chains through blockchain technology, Eng. Constr. Archit. Manage. 28 (2): 584–602, (2020).
29. Wan, P. K., Huang, L., Holtskog, H.: Blockchain-enabled information sharing within a supply chain: A systematic literature review, (2020).
30. Zhou, C., Ren, H., Zhang L.: Construction and empirical analysis of information management system of engineering investigation quality, J. Phys.: Conf. Ser, (2020).
31. Hargaden, V., Papakostas, N., Newell, A., Khavia, A., Scanlon, A.: The role of blockchain technologies in construction engineering project management, In Proc., 2019 IEEE

Int. Conf. on Engineering, Technology and Innovation (ICE/ITMC), 1–6. New York: IEEE, (2019).
32. Das, M., Tao, X., Cheng, J. C.: BIM security: A critical review and recommendations using encryption strategy and blockchain, Autom. Constr. 126, (2021).
33. Liu, Z., Jiang, L., Osmani, M., Demian, P.: Building information management (BIM) and blockchain (BC) for sustainable building design information management framework, Electronics 8 (7), (2019).
34. Parn, E. A., Edwards, D.: Cyber threats confronting the digital built environment: Common data environment vulnerabilities and block chain deterrence, Eng. Constr. Archit. Manage. 26 (2), (2019).
35. Lee, D., Lee, S. H., Masoud, N., Krishnan, M. S., Li, V. C.: Integrated digital twin and blockchain framework to support accountable information sharing in construction projects, Autom. Constr. 127, (2021).
36. Elghaish, F., Hosseini, M. R., Matarneh, S., Talebi, S., Wu, S., Martek, I., Poshdar, M., Ghodrati N.: Blockchain and the 'Internet of Things' for the construction industry: Research trends and opportunities, Autom. Constr. 132, (2021).
37. Yli-Huumo, J., Ko, D., Choi, S., Park, S., Smolander, K.: Where is current research on blockchain technology? A systematic review, PLoS One 11 (10), (2016).

Quantification of Rework Causes in Turkish Construction Industry

Eda Nur Erdem[1][0000-0002-7078-2234] and Gülden Gümüşburun Ayalp[2][0000-0002-7989-5569]

[1] Adana Alparslan Türkeş Science and Technology University, Department of Architecture, Adana, Türkiye, enerdem@atu.edu.tr
[2] Hasan Kalyoncu University, Department of Architecture, Gaziantep, Türkiye, gulden.ayalp@hku.edu.tr

Abstract. The construction industry suffers from time overruns, cost overruns, and quality failures, all of which are critical to the success of a construction project. These failures have a significant economic impact since the construction industry is an important constituent of the world economy. As a result, project performance is important and needs to be investigated in order to improve. One of the most recurring issues that have an adverse impact on project performance is rework. In the context of this study, "rework" is defined as redoing an activity as a result of errors, changes, or omissions that occurs during the design and construction phases. These unnecessary efforts result in time and cost overruns, contributing to poor project performance. Although there are studies in various countries to identify possible rework causes, there is no research in Turkey. Therefore, in order to fill the gap in the literature, this research focuses on the causes of rework in Turkish construction projects. To determine the causes of rework in construction projects, a comprehensive literature review was conducted, and 43 causes were identified. Rework causes were classified into six groups based on the conditions that led to their emergence. A total of 209 data were collected and statistically analyzed using the relative importance index to identify the most significant causes of rework. The findings revealed that client directed changes, changes in project scope, design changes by architects, client directed plan and scope extensions and poor communication are the five most vital causes of rework in the construction industry. It is noteworthy that all three causes are related to changes in projects demanded by different stakeholders. Based on these findings conceptual and managerial implications are recommended.

Keywords: Rework Causes; Turkish Construction Industry; Construction Management.

1 Introduction

Cost and time overruns in construction projects damage not only the projects and stakeholders but also the national economy [24]. Therefore, the primary objective of stakeholders is to improve project performance. One of the major risks that reduce the

performance of construction projects is rework [2]. Rework is the unnecessary effort spent to redo a task that was performed incorrectly the first time [15]. They can occur at any point and phase during a project, from the planning stage to the final delivery of the project, and are caused by various factors such as errors, omissions, or changes.

In recent years, there has been an increase in country-based studies on rework in construction. Studies show that the most critical rework factors differ depending on the country's unique circumstances. Love and Edwards (2004a) concluded that inadequate understanding of the end user, poor contract documentation, poor workmanship resulting in errors, lack of quality management and inadequate supervision were the most critical causes of rework. Shen et al. (2015) found that uncertain project process management, poor quality of construction technology and the use of poor quality materials are among the top factors that cause rework in construction projects in China. Ajayi (2017) concluded that clients are the group that causes the most rework in building projects in Nigeria. Although several researchers from developed and developing countries identified rework causes focusing on their country, there is no related study concentrated on rework causes in Turkish construction industry. Therefore, this study aims to define the most critical rework causes in Turkey that affect construction project performance.

2 Research Methodology

For this research, a questionnaire survey approach has been adopted to determine the influence of rework causes on project performance. The research method consists of five stages which are identification of the rework causes through a systematic literature review, preparation of the questionnaire, data collection, data analysis and evaluation of findings.

2.1 Identification and Categorization of Rework Causes

The first stage of the study was the identification and categorization of the rework causes. Conducting systematic literature review (SLR) literature is examined comprehensively.

Web of Science and SCOPUS databases were used to access scientific papers regarding rework in construction industry. The search parameters in the databases were determined using keywords. The search parameters were assigned as keywords: “rework” AND “reasons” AND “construction industry” and publications with a range of 2000-2021. A total of 64 journal articles were found in the initial search. Among the obtained studies 7 of them excluded because of not accessing the full-text. Remained 57 articles were read by two authors and 23 of them were chosen for a thorough examination for determining the rework causes.

The 23 selected articles coded to regarding the key study findings to specific rework causes taking into consideration the conditions that led to their emergence. Finally, 43 rework causes were identified (Table 1).

The rework causes are classified under six major categories as follows: client related factors, design team related factors, project manager related factors, labours related factors, site related factors and general - external related factors.

Table 1. Rework causes

Cause Group	Cause Code	Rework Causes	Sources
Client Related Factors	C1	Client directed changes	[1-3], [12], [16-17], [22], [24]
	C2	Poor communication	[2], [8], [18]
	C3	Client directed plan and scope extensions	[2], [10], [18]
	C4	Lack of client involvement	[1-2], [24]
	C5	Inadequate or weak feasibility study	[1-2], [18]
Design Team Related Factors	D1	Incomplete design	[1], [8], [18]
	D2	Errors and omissions in design	[2], [10], [22]
	D3	Design changes	[2], [18], [24],
	D4	Insufficient experience	[1], [17]
	D5	Lack of understanding of user	[2], [16], [22]
	D6	Poor contract execution	[2], [16]
	D7	Design management failure	[10], [18]
	D8	Fixed time for a task	[1], [16-17]
	D9	Lack of using modern technology and software	[1], [24]
Project Manager Related Factors	P1	Lack of experience of project manager	[2-3], [8], [18]
	P2	Failure to perform adequate document control	[16]
	P3	Poor planning and coordination	[1-2], [8], [18], [22]
	P4	Poor workload planning	[1], [26]
	P5	Ineffective management	[1], [16-17]
Labours Related Factors	L1	Lack of labour skills	[2], [8], [18], [26]
	L2	Time pressure	[1], [2], [18]
	L3	Poor workmanship	[1-2], [10]
	L4	Non-compliance with specifications	[18], [24]
	L5	Shortage of skilled labours required to complete work tasks	[1-3], [10]
	L6	Lack of motivation	[16-18]

Site Related Factors	S1	Poor site condition	[10], [26]
	S2	Complexity of design	[18]
	S3	Inaccurate or lack of site investigation	[1-2], [17-18]
	S4	Increase in project changes as the number of project stakeholders grows	[25]
	S5	Lack of safety considerations in the site	[1-2]
General External Related Factors	- G1	Schedule pressures	[1-2], [26]
	G2	Poor communication	[1], [8], [10]
	G3	Poor information flow	[22], [26]
	G4	Changes in project scope	[2], [18], [22] [24]
	G5	Inadequacies in contract documentation	[1], [16], [25]
	G6	Use of poor quality materials	[1], [17], [22]
	G7	Shortage of construction materials in market	[2-3], [22]
	G8	Wrong initial budget	[22]
	G9	Lack of technological equipment and Ineffective use of technology	[1-2], [8], [22], [26],
	G10	Change of laws	[8], [10]
	G11	Economic situation of the country	[2], [8]
	G12	Natural Disasters	[2-3], [22]
	G13	Changes in construction method to improve constructability	[1-3], [10], [18], [22], [26]

2.2 Data Collection

The target population of the current study is architects, civil engineers, and project managers, who are significant stakeholders of the construction industry. The questionnaire was distributed via face-face and e-mail to 690 construction professionals on 26 April 2022 and responses were accepted until 18 October 2022. A total of 209 data received from participants.

2.3 Data Analysis

Reliability Analysis

In order to perform statistical analyses of the data sets used in the study, the internal consistency of the data must first be measured. Cronbach's alpha (α) coefficient is the most widely used reliability criterion for assessing the internal consistency of data [23]. Cronbach's alpha (α) coefficient can be calculated using the following equation [5]:

$$a = \frac{k}{k-1}\left(1 - \frac{\sum s_i^2}{s_T^2}\right) \quad (1)$$

The α coefficient value range is 0–1. As a generally accepted rule, a Cronbach's alpha of 0.7 indicates an acceptable level of reliability [6;23].

Relative Importance Index Analysis

Relative importance index test was conducted in order to rank rework causes. Previous studies [8;9] used the same method to determine the most critical factors. Relative importance index can be calculated using the following equation:

$$RII = \frac{\sum W}{A\ x\ N} \quad (2)$$

Where; W is the weighting given to each factor by participants (ranging from 1 to 5); A is the highest weight (i.e., 5 in this case); and N is the total number of participants [20].

3 Findings

3.1 Reliability Analysis

Cronbach's alpha coefficient was calculated as 0.953 within the scope of the questionnaire survey for 43 criteria asked based on perception on a 5-point Likert scale. Since the value is greater than 0.9, internal consistency is considered to be excellent [20;21].

3.2 Relative Importance Index Analysis

A high RII value indicates that the relevant criterion is as important as the value it receives [9]. The following Table 2 illustrates the results of RII and rankings of rework causes.

Table 2. RII Results and Rankings of Rework Causes

Cause Group	Cause Code	RII (%)	Group Rank	Overall Rank
Client Related Factors	C1	83.60	1	2
	C2	73.21	3	18
	C3	82.42	2	4
	C4	63.69	5	39
	C5	69.67	4	27
Design Team Related Factors	D1	74.61	4	16
	D2	76.95	3	15
	D3	82.73	1	3
	D4	71.11	5	21
	D5	64.05	8	37
	D6	70.43	6	22
	D7	67.04	7	32
	D8	77.01	2	14
	D9	59.55	9	43
Project Manager Related Factors	P1	72.39	4	19
	P2	68.63	5	29
	P3	80.20	1	7
	P4	74.09	3	17
	P5	78.47	2	11
Labours Related Factors	L1	77.32	3	13
	L2	70.30	4	25
	L3	77.74	2	12
	L4	69.10	5	28
	L5	79.17	1	10
	L6	62.18	6	41
Site Related Factors	S1	65.02	5	35
	S2	70.37	1	24
	S3	67.18	2	31
	S4	66.97	3	33
	S5	65.76	4	34
General - External Related Factors	G1	80.00	5	9
	G2	82.19	2	5
	G3	80.09	4	8
	G4	85.23	1	1
	G5	70.39	7	23
	G6	70.25	8	26
	G7	62.14	13	42

G8	68.17	9	30
G9	64.24	10	36
G10	63.75	11	38
G11	81.18	3	6
G12	63.33	12	40
G13	71.90	6	20

After analyzing and ranking the rework causes of rework according to the RII, The five most important criteria are as follows:

- The “Changes in project scope” factor, with RII of 85.23%, is ranked as the most important rework causes.
- The “Client directed changes” factor, with RII of 83.60%, is ranked first within the client related factors category and second among all 43 rework causes.
- The “Design changes” factor, with RII of 82.73%, is ranked first within the design team related factors category and third among all 43 rework causes.
- The “Client directed plan and scope extensions” factor, with RII of 82.42%, is ranked second within the client related factors category and fourth among all 43 rework causes.
- The “Poor communication” factor, with RII of 82.193%, is ranked second within the general - external related factors category and fifth among all 43 rework causes.

Changes are almost inevitable throughout the life cycle of a project. The stage at which rework is recognized in the implementation process of projects affects the magnitude of rework [14]. Kermanshachi et al. (2018) found that the actual impact of late change orders on the project is often greater than expected. Aslam et al. (2019) found that design changes can affect the total construction cost at a rate ranging from 2.1% to 21.5%. Al-Janabi et al. (2020) and Trach et al. (2019) determined that design and scope changes made by the client are one of the most important factors causing rework. In the study conducted by Mohamad (2012), employers were the most important source of design changes in reinforced concrete structures. It is possible to manage these changes to prevent negative consequences.

Poor communication often results in incomplete and inaccurate information, which further increases the likelihood of rework occurrence. Communication failures may occur in projects due to various reasons such as foreign workers [11], large number of participants [25] or lack of managerial skills [28]. In the study conducted by Yap et al. (2020), it was found that the most critical cause of rework is inadequate communication. Mahamid (2016) found that the most important factors causing rework in residential projects in Palestine are poor communication of the client with project stakeholders. This study proved that poor communication among project stakeholders leads to conflicts and misunderstandings of document requirements, negatively affecting the workflow.

4 Conclusions and Recommendations

This study reveals the causes of rework in the Turkish construction industry from architects', civil engineers', and project managers' perspectives using data from 209 participants in industry. Through a comprehensive literature review, 43 rework causes were identified under six major categories client related factors (5 items), design team related factors (9 items), project manager related factors (5 items), labours related factors (6 items), site related factors (5 items) and general - external related factors (13 items).

Changes in project scope (G4), client directed changes (C1), design changes (D3), client directed plan and scope extensions (C3) and poor communication (G2) are top five causes of rework.

It should be carefully noted that the late changes in projects are damaging project productivity. Depending on the scope and scale of the changes needed, rework can range from minor corrections to major overhauls requiring rebuilding and demolition. Identifying requirements in the early stages of design process will help to reduce rework and increase project efficiency by preventing changes that may occur in later stages. Increasing the number of meetings to be held periodically between the teams will be useful for information sharing and updates.

On the basis of the outcomes of this research, it can be concluded that late changes and poor communication are significant risks that need to be managed to eliminate rework in the Turkish construction industry.

References

1. Ajayi, O. (2017). Occurrence of Rework on Components of Building Project in Lagos State, Nigeria. International Journal of Sustainable Construction Engineering and Technology, 8(1), 84–93. https://penerbit.uthm.edu.my/ojs/index.php/IJSCET/article/download/1719/1164
2. Al-Janabi, A. M., Abdel-Monem, M., & El-Dash, K. (2020). FACTORS CAUSING REWORK AND THEIR IMPACT ON PROJECTS' PERFORMANCE IN EGYPT. Journal of Civil Engineering and Management, 26(7), 666–689. https://doi.org/10.3846/jcem.2020.12916
3. Alwi, S., Hampson, K. D., & Mohamed, S. a. M. (2001). Effect of quality supervision on rework in the Indonesian context. Asia Pacific Building and Construction Management Journal, 6, 2–6. https://eprints.qut.edu.au/4153/1/4153.pdf
4. Aslam, M., Baffoe-Twum, E., & Saleem, F. (2019). Design Changes in Construction Projects – Causes and Impact on the Cost. Civil Engineering Journal, 5(7), 1647–1655. https://doi.org/10.28991/cej-2019-03091360
5. Bland, M., & Altman, D. G. (1997). Statistics notes: Cronbach's alpha. BMJ, 314(7080), 572. https://doi.org/10.1136/bmj.314.7080.572
6. Cronbach, L. J. (1951). Coefficient alpha and the internal structure of tests. Psychometrika, 16(3), 297–334. https://doi.org/10.1007/bf02310555
7. Erdem, E., N., and Gumusburun Ayalp, G. (2022), "Identifying the Universal Rework Factors in Construction Projects", In Proceedings of the 7th International Project and Construction Management Conference (IPCMC2022), Istanbul, Turkey, 20–22 October. pp. 54-65.

8. Enshassi, A., Sundermeier, M., & Zeiter, M. (2017). Factors Contributing to Rework and their Impact on Construction Projects Performance. International Journal of Sustainable Construction Engineering and Technology, 8(1), 12–33. http://penerbit.uthm.edu.my/ojs/index.php/IJSCET/article/view/1725/0
9. Gündüz, M., Nielsen, Y., & Özdemir, M. (2013). Quantification of Delay Factors Using the Relative Importance Index Method for Construction Projects in Turkey. Journal of Management in Engineering, 29(2), 133–139. https://doi.org/10.1061/(asce)me.1943-5479.0000129
10. Hwang, B., Zhao, X., & Yang, K. W. (2019). Effect of BIM on Rework in Construction Projects in Singapore: Status Quo, Magnitude, Impact, and Strategies. Journal of the Construction Division and Management, 145(2). https://doi.org/10.1061/(asce)co.1943-7862.0001600
11. Jarkas, A. M., & Bitar, C. G. (2012). Factors Affecting Construction Labor Productivity in Kuwait. Journal of the Construction Division and Management, 138(7), 811–820. https://doi.org/10.1061/(asce)co.1943-7862.0000501
12. Josephson, P., Larsson, B., & Li, H. (2002). Illustrative Benchmarking Rework and Rework Costs in Swedish Construction Industry. Journal of Management in Engineering, 18(2), 76–83. https://doi.org/10.1061/(asce)0742-597x(2002)18:2(76
13. Kermanshachi, S., Thakur, R., & Govan, P. (2018). Discovering the Impact of Late Change Orders and Rework on Labor Productivity: A Water Treatment Case Study Analysis Using System Dynamics Modeling. In Construction Research Congress 2018. https://doi.org/10.1061/9780784481295.069
14. Li, Y., & Taylor, T. G. (2014). Modeling the Impact of Design Rework on Transportation Infrastructure Construction Project Performance. Journal of the Construction Division and Management, 140(9). https://doi.org/10.1061/(asce)co.1943-7862.0000878
15. Love, P. E. (2002). Influence of Project Type and Procurement Method on Rework Costs in Building Construction Projects. Journal of the Construction Division and Management, 128(1), 18–29. https://doi.org/10.1061/(asce)0733-9364(2002)128:1(18
16. Love, P. E., & Edwards, D. (2004a). Determinants of rework in building construction projects. Engineering, Construction and Architectural Management, 11(4), 259–274. https://doi.org/10.1108/09699980410547612
17. Love, P. E., & Edwards, D. (2004b). Forensic project management: The underlying causes of rework in construction projects. Civil Engineering and Environmental Systems, 21(3), 207–228. https://doi.org/10.1080/10286600412331295955
18. Mahamid, I. (2016). Analysis of Rework in Residential Building Projects in Palestine. Jordan Journal of Civil Engineering, 10(2), 197–208. https://doi.org/10.14525/jjce.10.1.3536
19. Mohamad, M. I. (2012). Design Changes in Residential Reinforced Concrete Buildings: The Causes, Sources, Impacts and Preventive Measures.
20. Pallant, J. F. (2007). SPSS survival manual : a step by step guide to data analysis using SPSS for Windows. http://ci.nii.ac.jp/ncid/BA83963567
21. Polat, G., Damci, A., Turkoglu, H., & Gurgun, A. P. (2017). Identification of Root Causes of Construction and Demolition (C&D) Waste: The Case of Turkey. Procedia Engineering, 196, 948–955. https://doi.org/10.1016/j.proeng.2017.08.035
22. Shen, L., Jin, Z., Xia, B., & Skitmore, M. (2015). Analyzing Causes for Reworks in Construction Projects in China. Journal of Management in Engineering, 31(6). https://doi.org/10.1061/(asce)me.1943-5479.0000347
23. Tavakol, M., & Dennick, R. (2011). Making sense of Cronbach's alpha. International Journal of Medical Education, 2, 53–55. https://doi.org/10.5116/ijme.4dfb.8dfd
24. Trach, R., Pawluk, K., & Lendo-Siwicka, M. (2019). Causes of Rework in Construction Projects in Ukraine. Archives of Civil Engineering, 65(3), 61–74. https://doi.org/10.2478/ace-2019-0034

25. Trach, R., Trach, Y., & Lendo-Siwicka, M. (2021). Using ANN to Predict the Impact of Communication Factors on the Rework Cost in Construction Projects. Energies, 14(14), 4376. https://doi.org/10.3390/en14144376
26. Yap, J. T., Chong, J. W., Skitmore, M., & Lee, W. (2020). Rework Causation that Undermines Safety Performance during Production in Construction. Journal of the Construction Division and Management, 146(9). https://doi.org/10.1061/(asce)co.1943-7862.0001902
27. Yarnold, J., Banihashemi, S., Lemckert, C. J., & Golizadeh, H. (2021). Building and construction quality: systematic literature review, thematic and gap analysis. International Journal of Building Pathology and Adaptation. https://doi.org/10.1108/ijbpa-05-2021-0072
28. Zulch, B. (2016). A proposed model for construction project management communication in the South African construction industry. Acta Structilia : Journal for the Physical and Development Sciences, 23(1). https://doi.org/10.18820/24150487/as23i1.1

Construction and Demolition Waste Processing for A Circular Construction Model: An Overview and Comparison Between On-Site and Off-Site Recycling

Hanan Al-Raqeb[1][0000-0002-9761-4433], Hammadhu H.[2] [0000-0003-0985-4611], Seyed Hamidreza Ghaffar[3][0000-0002-4694-9508], Anjali G.[4][0000-0002-1729-4936]

[1,3]Department of Civil and Environmental Engineering, Brunel University London, Uxbridge, UB8 3PH, United Kingdom
Hanan.Alazemi@brunel.ac.uk
hammadhu@gmail.com
[2,4]School of Civil Engineering, Vellore Institute of Technology, Chennai, India
seyed.ghaffar@brunel.ac.uk
anjaligopakumar@vit.ac.in

Abstract. Construction and demolition waste (CDW) is one of the significant sources of environmental pollution and economic loss for the construction industry. Effective and efficient management of resources and waste is tedious and complex. After generation, CDW is usually disposed of at landfills or sent to processing plants for resource recovery after generation. Collection, transportation, and processing of CDW offsite incur a lot of cost and effort. The quality and quantity of secondary materials produced from the recycling process are highly impacted when the CDW gets mixed with other wastes. Pros of on-site processing of waste include proper separation and sorting which leads to higher recycling and recovery of secondary raw materials, lower disposal costs, and landfilling. On-site sorting can assist megaprojects inefficient material management, save costs and reduce environmental impact. Off-site sorting, however, will reduce the workload on the project teams and labour, save space while still utilizing sustainable solutions. However, the transportation costs and emissions resulting from the transport of demolition waste to recycling centres are an important issue. This paper will give an overview and comparison of the on-site and off-site recycling process which would help the projects to choose the appropriate method for CDW disposal.

Keywords: Construction Waste, Onsite Recycling, Offsite Recycling, Circular Construction

1 Introduction

The world's increasing population, rapid urbanization, and economic development have directly resulted in the increasing global generation of construction and demolition waste (CDW). Therefore, the construction industry, which accounts for 30% of the world's extraction of raw materials, plays an important role in this issue [1]. However, large CDW volumes, low recovery rates, and thin sales margins pose a major threat to the environment [2]. In fact, approximately 35% of CDW ends up in landfills, underscoring the urgent need for improved material recovery and recycling to mitigate negative environmental impacts. To meet this challenge, it is crucial to implement a circular economy (CE) model in CDW processing. This model is designed to minimize waste, maximize material value, and reduce environmental impact. Although various strategies and regulatory measures have been adopted globally to achieve CE in the construction industry, there is still a long way to go before optimal implementation [1]. Within CDW recycling, there are two main approaches: on-site and off-site recycling. However, a comprehensive comparison of the efficiency and sustainability of these two methods in the context of a circular construction model is currently lacking in existing research. Most studies have focused on either on-site or off-site recycling without considering the comparative advantages and disadvantages of both approaches. Thus, further research is needed to provide a comprehensive overview and comparison between on-site and off-site recycling for effective construction and demolition waste management in the context of a circular economy model.

The aim of this study is to provide a comprehensive overview of CDW processing for a circular construction model, with a specific focus on the comparison between on-site and off-site recycling. The following research questions guide the investigation of CDW processing within the context of a circular construction model:

- What is the significance of CDW recycling in a circular economy (CE)?
- How do CDW on-site and off-site recycling methods compare in terms of efficiency, environmental impact, and resource conservation?
- What are the barriers and challenges associated with implementing on-site and off-site recycling systems in different construction contexts, and how can they be overcome?
- How can the adoption of on-site and off-site recycling practices be optimized to achieve higher levels of sustainability and circularity in the construction industry?
- How can the adoption of on-site and off-site recycling practices be optimized to achieve higher levels of sustainability and circularity in the construction industry?

By addressing these questions, the review article aims to contribute to the understanding of sustainable waste management practices in the construction industry and encourage the adoption of more effective and efficient CDW processing methods in line with the principles of a circular economy.

2 Methodology

Fig. 1. Shows the outline of the methodology adopted in this study. After initial filtering of research and review articles from the selected database, suitable articles were identified and analyzed in this study.

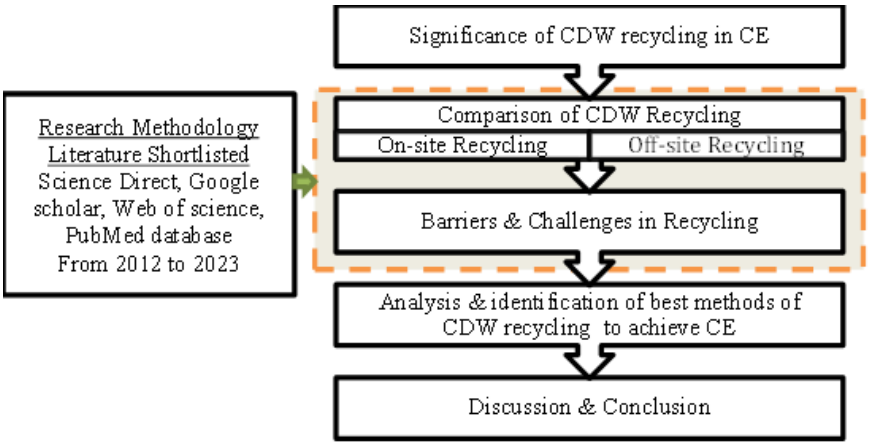

Fig. 1. Outline of the study methodology

To identify the most relevant research papers, a three-step strategy was adopted, namely database selection, sample search, and refinement. The methodology of the literature research is shown in Fig. 2.

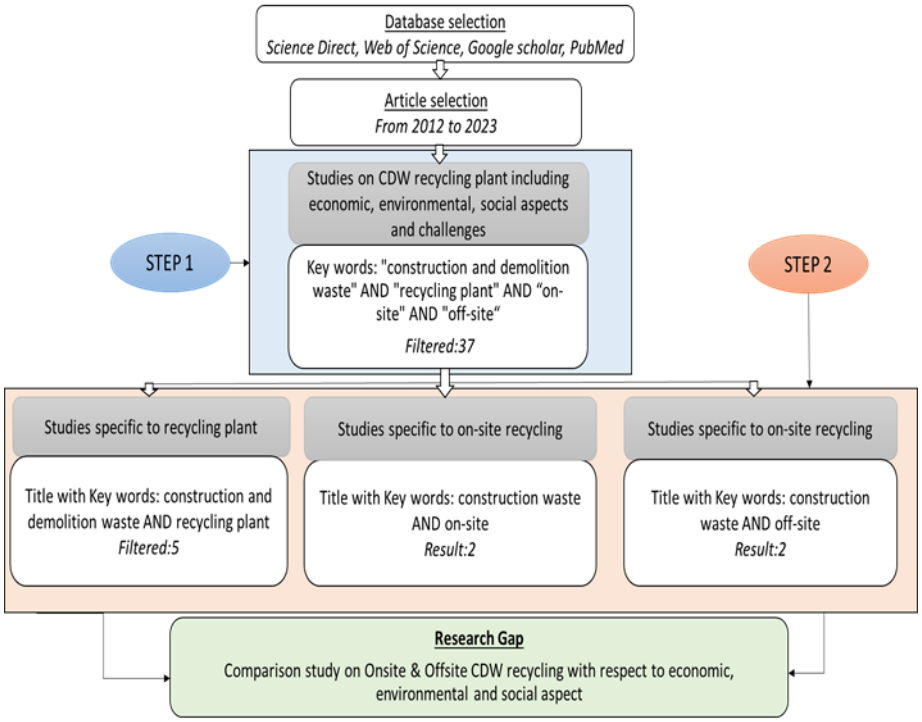

Fig. 2. Literature search methodology

3 Significance of CDW Recycling in Circular Economy

The significance of CDW recycling in a (CE) becomes evident when considering its potential for minimizing waste, maximizing material value, and reducing environmental consequences. Despite the existence of various strategies and regulatory measures, the implementation of CE in the construction sector still has room for improvement [1]. To truly establish a CE, it is crucial to shift the perspective of CDW from being seen as waste to recognizing its value as a resource. This can be achieved through effective management, including proper classification and processing of construction and demolition debris based on its nature and composition [6]. By recovering and recycling building materials from CDW, not only can effectively waste management be achieved, but it also opens up employment opportunities [7], [8]. To make circularity a feasible reality in the construction industry, a balance between material inflow and outflow needs to be achieved [9], [10]. In response to the challenges of construction waste management and the need for fire-resistant buildings, the "Development of an Innovative Insulation Fire Resistant Façade from the Construction and Demolition Waste" (DEFEAT) project has been launched in Cyprus. This project aims to develop a pilot scale of an innovative separation method for CDW. Additionally, it seeks to create a composite material made from CDW that exhibits low thermal conductivity, satisfactory mechanical properties, and fire resistance. The

resulting material can be used as a facade in both new and existing construction projects, addressing the challenges of CDW management and enhancing the fire safety of buildings [11]. This necessitates a transformation of the entire value chain, encompassing the building design process, the establishment of new markets, and the influencing of consumer behavior [12]. CDW is a significant contributor to environmental degradation due to its high generation volume, low recycling rate, and low revenue margins [13]. CE acts as a promising solution for issues associated with CDW.

4 CDW Sorting and Recycling Methods

Fig. 3. shows the overview of the volume of CDW ending up in landfill with and without different recycling processes. It is clear from the figure that the amount of waste ending in landfill is high without sorting and recycling.

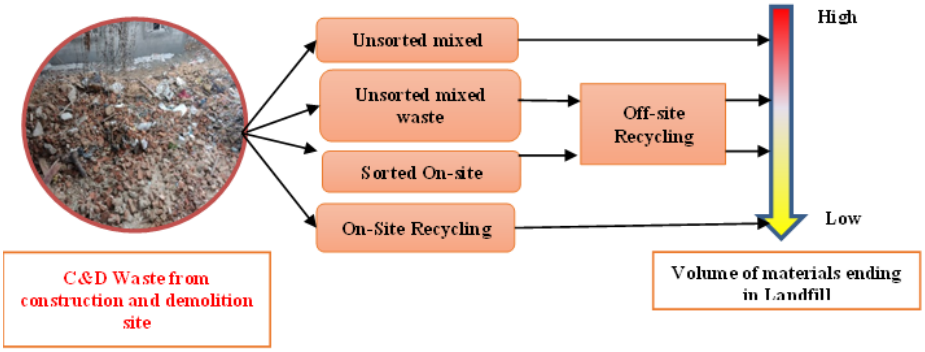

Fig. 3. Overview of the on-site and off-site recycling process (*Source: Authors original*)

On-Site Recycling of CDW. Waste sorting is one of the most successful strategies for waste reduction and material recovery [18]. On-site waste sorting, which involves the separation and classification of construction waste on worksites, allows for the collection of valuable materials for recycling and reuse [19]. On-site recycling of CDW involves processing waste materials on the project site through steps such as segregation, sorting, processing, storage, and transportation [20]. On-site recycling, also known as source-separated recycling, utilizes multiple dumpsters for different materials to minimize cross-contamination, ensuring the project's recycling goals are met [21], [22]. Examples of successful on-site recycling projects include the Louvre Abu Dhabi Museum and the Olympic Stadium in London. During the construction of the Louvre Abu Dhabi Museum, 3,700 tons of CDW were recycled on-site for road construction and landscaping [23], [24]. Similarly, approximately 90% of the CDW generated during the construction of the Olympic Stadium in London was recycled on-site for various construction purposes [25]. Benefits of on-site recycling of CDW

include reduced waste disposal costs, decreased environmental impact through resource conservation, and improved project sustainability [16], [26], [27]. However, limitations such as limited space, capacity constraints, increased project complexity, and stakeholders' reluctance may be encountered [28]– [30].

Off-site recycling of CDW. CDW generated from construction and demolition sites, or designated dumping places is transported to recycling plants by public or private parties. The off-site recycling process involves several steps to transform the waste materials into reusable products. Initially, the incoming waste materials undergo primary segregation to remove unwanted materials, such as plastics. Primary screening is then conducted to separate wood and other waste components like ceramics, glass, and metals. The materials are crushed multiple times and screened to obtain coarse and fine aggregates. Subsequent processes remove dust and clay, and the aggregates are sorted and classified by size. Additionally, the recycling process may involve the manufacturing of secondary products like paver blocks and bricks using the obtained recycled content. Various methods, including wet and dry processes, are employed in waste processing. Technological advancements continually introduce new recycling methods and facilities, leading to variations in capacity, quality, types of by-products, and processes [11]. Furthermore, the off-site recycling process is influenced by several factors, including policy support, policy enforcement, higher disposal charges, and the implementation of a trip ticketing system. [30]. Considering the location of the off-site recycling plant is crucial due to the significant environmental and economic impacts of transportation in the overall recycling process. Transportation distances exceeding 50 km result in increased prices for recycled products. However, environmental regulations concerning noise, air pollution, and other constraints, such as land availability, prohibit locating off-site recycling plants inside the city [31].

5 Comparison of On-Site and Off-Site CDW Recycling

When examining the effectiveness of CDW recycling methods. There are important factors to take into consideration. In this article. We will be exploring both on-site and off-site recycling techniques based on the sources provided. On-site recycling allows for the immediate reuse of materials resulting in fewer transportation costs and energy consumption associated with transporting CDW to off-site facilities. This type of recycling can also decrease the amount of time needed for waste removal providing a streamlined construction process [2]. Alternatively**.** Off-site recycling involves moving CDW components to specialized facilities for processing and reintroduction into production cycles. Despite the logistical effort that is required for this method. It has many advantages worth noting. Off-site facilities often have advanced equipment and technologies that permit the sorting and processing of CDW components in an efficient manner [32],[33],[34]. This allows them to achieve higher recovery rates of valuable resources as well as better control over recycled material quality. By processing larger volumes of waste via economies of scale these facilities can become more efficient at waste diversion rates and recycling rates [5], [35].

Evaluating efficiency involves considering factors such as waste diversion rates, recycling rates, or...Read More To conserve resources effectively evaluating different CDW management options necessitates considering recycling strategies carefully. On-site CDW recycling can significantly save resources by facilitating immediate reuse opportunities while minimizing waste generation. However, off-site CDW recycling represents a valuable approach that leverages advanced sorting/processing capabilities to recover a wider range of recyclable materials such as metals, concrete, and wood ultimately used across various industries [37]-[39].

To evaluate these processes further - Fig. 4 provides an overview comparing their pros/cons; it highlights major differences between on-site versus offsite plans tailored towards promoting better decision-making regarding effective CDW management**.**

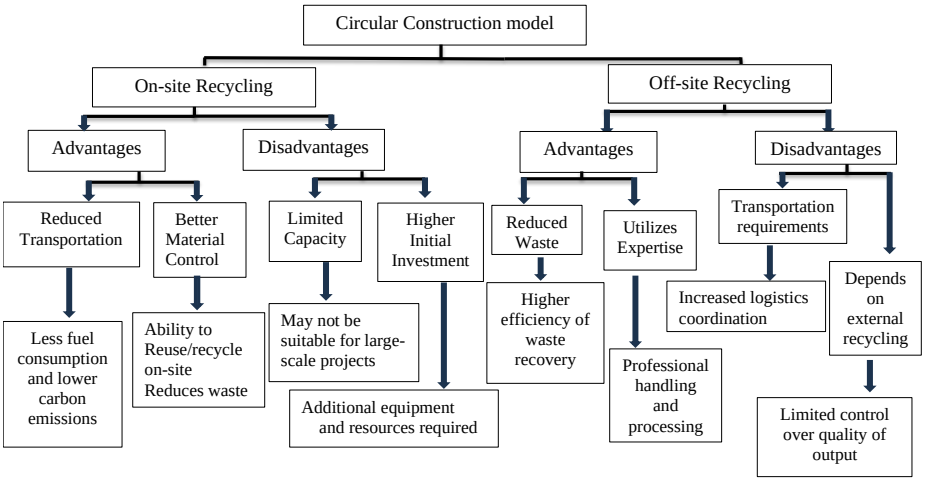

Fig. 4. The circular construction represents the comparison between On-site and Off-site recycling.

5.1 Challenges and Barriers in CDW Recycling

On-site recycling. Despite its numerous advantages, on-site recycling also presents certain challenges. One of the significant barriers is site space constraints, as it requires allocating space for equipment and storing recycled products [21], [40]. Additionally, on-site recycling necessitates the availability of cleaning facilities to ensure the production of high-quality recycled products. However, the limited availability of such facilities can result in poor-quality recycled products [40]. Another challenge lies in the lack of government policy support for implementing on-site recycling [22]. Optimizing site layout for recycling, customizing the recycling equipment for improved quality and improving the government support, and mandating onsite segregation help to promote onsite recycling of CDW [21]. These measures would help to address the challenges in on-site recycling.

Off-site Recycling. The practice of off-site recycling presents several challenges that hinder the effective management of (CDW). These challenges primarily revolve around the legal framework, policies, and operational issues associated with off-site recycling. Inadequate policies and legal frameworks for CDW management, the lack of clearly defined national goals, targets, and visions, and the absence of a standard reporting system and accessible data on waste generation are among the key factors impeding off-site recycling efforts. Furthermore, the absence of financial incentives, limited coordination among governmental agencies, and the absence of industrial norms or performance standards for waste management contribute to the complexity of the process.

Other challenges include poorly defined individual responsibilities, a lack of awareness among the public regarding waste management and resistance to waste segregation, and the mixing of Municipal Solid Waste (MSW) with CDW. The presence of hazardous substances and batteries further complicates the waste management process. In addition, the lack of proper funding to implement waste management technologies and practices, ineffective implementation at the ground level due to a lack of cooperation from the public, insufficiently trained workers, and inadequate technologies pose significant challenges. The absence of proper auditing for continuous monitoring and improvement, a lack of awareness about appropriate technologies and Public-Private Partnerships (PPP), and the need for stringent control and monitoring further contribute to the obstacles faced in the off-site recycling [16], [35], [41]– [47].

5.2 Overcoming Barriers and Opportunities in CDW Recycling

The effective implementation of CDW requires the collective effort of multiple stakeholders who need to take several approaches to overcome the challenges associated with it while taking advantage of this method's opportunities:

(a) Raising awareness amongst industry professionals, policymakers, and the public is essential [48], [49].

(b) Encouraging educational initiatives like training programs and industry events for promoting a culture geared towards sustainability would enable benefits linked directly with CDW recycling [51].

(c) Advocating for clear regulations will help incentivize keeping proper waste management guidelines in place while spearheading government policies that promote CDW recycling by setting targets thereby achieving sustainable construction practices [50].

(d) Investing in infrastructure development is a vital aspect. Allocation of resources towards establishing on-site recycling facilities and reducing transportation distances assist make necessities readily available leading up to cost-effective operations possible [51].

(e) Conducting comprehensive cost-benefit analyses could further highlight specific economic advantages leading up to investments from prominent construction companies into investing within CDW recycling productions along with creating new markets for recycled materials [50].

(f) Stakeholders should be encouraged to collaborate among themselves and lead by innovative solutions, sharing knowledge and experience that involves expert advice, together hand in hand establishing effective waste management practices becoming an industry standard [50].

(g) Lastly, governments can provide support towards regulating CDW through incentive funding opportunities and policies that will encourage the construction industries in reducing waste by dumping them in landfills for a cleaner environment while looking into investing more into recycled products that emulate profitability and sustainability measures [48], [49]. Programs like these work towards creating standards of high-recycled content that in turn generate more options within this marketplace's consumer base towards demanding their goods be predominantly made from recyclable products sourced from within their respective communities via a variety of methods including those derived from CDW.

Encouragingly still is usage at present which also incentivizes organizations with diverse roles such as offering financial incentives or tax credits while pre-purchasing preference policies ensure that substantial endeavors meet thriving industries' environmental goals leaning more towards responsible use than sustainable preservation addressing issues such as waste retention and preservation of scarce resources. Implementing established compliance standards is essential in ensuring that the CDW recycling processes are recognized as being effective in providing the higher goals of waste management and recycling while also holding true to values addressing future environmental needs.

6 Analysis and Discussion

6.1 Environmental and Economic Impact

The environmental benefits of CDW recycling are associated with various factors, including reduced transportation of waste, diversion from landfills, decreased demand for virgin materials, and lower energy consumption and greenhouse gas emissions. The extent of these benefits depends on the type of material and its potential applications. For example, non-inert materials like metals have high recycling potential, economic value, and versatile applications [52]. Recycling on-site reduces the amount of waste transported to off-site facilities, leading to lower transportation-related emissions and reduced traffic congestion [40]. It also minimizes the need for new landfills, preserving valuable land areas by diverting waste from landfill disposal to recycling [20]. Furthermore, on-site recycling conserves natural resources by reducing the demand for virgin materials in construction projects [40]. Off-site recycling plants can also contribute to dust emissions and leachate, which can negatively affect soil and groundwater [53], [52]. The offsite recycling process of CDW can have a significant impact on diesel consumption, particularly due to increased transportation distances and energy requirements compared to landfilling. However, the use of mobile equipment for on-site recycling can be energy-intensive, resulting in additional emissions. The choice between mobile and fixed plants for CDW treatment depends on

factors such as equipment costs, operational costs, labor costs, waste disposal costs, and the capacity of recycling facilities. Off-site sorting of CDW is not an effective method, and landfilling CDW after off-site sorting leads to significant environmental impacts. However, off-site recycling after on-site sorting has proven to be more successful in reducing environmental impact through improved material recovery and the reuse of secondary materials [54]. Achieving a zero-waste construction site by reusing materials solely within the closed loop of the site is often not feasible or too costly. However, zero waste can be achieved through off-site recycling, diverting materials to other projects, and participating in secondary material markets [31].

Implementing incentives for recycling enterprises can further reduce costs and improve overall income and investment returns [16], [50]. A study conducted by [56] compared the cost-benefit analysis of natural and recycled aggregates, revealing that manufacturing recycled aggregates is more cost-effective than extracting natural aggregates. Recycling aggregates help reduce greenhouse gas (GHG) emissions from concrete mixes by 26% and provide 97% more environmental benefits compared to using natural aggregates. Recycling coarse aggregate from CDW can reduce GHG emissions by up to 65% and decrease non-renewable energy consumption by 58% [56]. Recycling aggregates also reduce carbon emissions by a factor of ten and primary energy consumption by a factor of eight [57].

6.2 The Cost-Benefit Analysis of CDW Recycling Plants

A specific study focused on CDW management in Hanoi, Vietnam, highlights the increasing waste generation and the absence of a formal recycling industry, which exacerbates inadequate CDW management. The study assesses the potential for CDW recycling considering two recycling plant models: a stationary plant with a capacity of 1,000 tons/day and a mobile plant with a capacity of 360 tons/day. The findings indicate that the introduction of mobile recycling plants may require government intervention to internalize the positive externalities of recycling. Proposed supporting policies include a virgin material tax, green public procurement, and quality standard development. Successful CDW recycling models in Portugal and China demonstrate profitability and constraints associated with tipping fees, landfill fees, and land costs. The study also emphasizes the importance of a sustainable supply of input materials, economies of scale, and transportation distance in determining the viability and choice between stationary and mobile plants [58].

The stationary plant shows positive discounted cash flows after five years of operation. It demonstrates favorable financial and economic evaluations, with an Internal Rate of Return (IRR) of 18% and 38%, respectively. The Environmental Cost Accounting Factor (ECAF) of the stationary plant is more positive compared to the mobile plant. The stationary plant requires higher capital investment, accounting for approximately 8.3% of total costs. The initial capital unit cost in the stationary plant is half of that in the mobile plant. Economies of scale in the stationary plant result in a unit operating cost that is 1.7 times cheaper than the mobile plant. The main components of operating costs for both plants are the expense of waste concrete, followed by labor costs in the stationary plant and energy costs in the mobile plant. In

the financial evaluation, sales of recycled concrete aggregates (RCA) contribute 100% to the cash inflows of the stationary plant [58].

The mobile plant exhibits a negative Net Present Value (NPV) over its six years of operation. However, when considering the social-environmental benefits of recycling in the economic evaluation it becomes a viable investment option with an IRR of 43%. The mobile plant requires lower capital investment compared to the stationary plant but has higher initial capital unit costs. The operating cost per ton is higher in the mobile plant compared to the stationary plant. The major components of operating costs in the mobile plant are the input material and energy costs. In the financial evaluation, RCA sales contribute 54% to the cash inflows of the mobile plant [58]. Both recycling scenarios significantly reduce land occupation for landfills and greenhouse gas (GHG) emissions compared to the Business as Usual (BAU) scenario. Land occupation for landfills decreases by nearly 90% in the recycling scenarios, and GHG emissions decrease by 80% and 55% when the mobile and stationary plants are operational, respectively. These findings align with previous studies highlighting the environmental benefits of CDW recycling, including reductions in land use and GHG emissions [58].

6.3 Optimization of On-Site and Off-Site Recycling Practices

Deciding between on-site and off-site recycling methods for (CDW) requires careful consideration of several factors including project size, waste composition, local regulations/guidelines, and availability of recycling infrastructure. On-site recovery is suitable for smaller projects while Compositionist determines the immediate processing of the Waste. Local contexts play a crucial role; closer proximity to available recycling facilities positively affects the decision-making process hence accessibility adds significant value. It is therefore essential that all necessary factors are considered when making decisions concerning sustainable CDW management thus achieving maximum benefits entails adopting optimization strategies presented in Table 1 meant for optimizing on-site and off-site practices. Furthermore, using these optimizations leads ultimately to increased effectiveness and efficiency levels while promoting sustainability, resource conservation, and circularity within the construction sector leading toward long-term environmental benefits.

Table 1. Strategies for Promoting Sustainable Practices and CDW Recycling

Strategies	Description
Education and Awareness	Raise awareness about the benefits of on-site and off-site recycling practices among construction industry professionals, including contractors, architects, and developers. Promote the understanding of sustainable construction practices and their positive environmental impact.
Design for Disassembly and Reuse	Encourage architects and designers to incorporate principles of circular design into construction projects. Design buildings and structures with components that can be easily disassembled, reused, or recycled at the end of their lifecycle.
Waste Management Plans	Develop and implement comprehensive waste management plans for construction projects. These plans should prioritize waste reduction, segregation, and recycling. Set specific recycling goals and track progress throughout the project. [19], [21].
On-Site Recycling Facilities	Incorporate on-site recycling facilities within construction sites. These facilities can process and reuse CDW, such as concrete, bricks, and wood, on-site, reducing the need for off-site transportation and promoting resource conservation [21].
Collaboration and Partnerships	Foster collaboration between construction companies, recycling facilities, and government agencies. Encourage partnerships that facilitate the efficient collection, transportation, and processing of construction waste for recycling. [22], [19].
Regulatory Support	Governments can play a crucial role in promoting sustainable construction practices. Implement and enforce regulations that encourage the adoption of on-site and off-site recycling practices, such as waste reduction targets, recycling quotas, and incentives for using recycled materials in construction projects [22].
Innovation and Research	Support research and development efforts focused on improving recycling technologies, materials identification, and separation methods. Foster innovation in the construction industry to identify new ways to recycle and reuse CDW effectively [59].
Certification and Standards	Promote certifications and standards that recognize sustainable construction practices and encourage the use of recycled materials.
Economic Incentives	Provide economic incentives such as tax credits, grants, or subsidies to construction companies that adopt sustainable practices and demonstrate a commitment to on-site and off-site recycling. [60].
Market Development	Promote the development of markets for recycled CDW materials. This involves working with manufacturers, designers, and architects to increase the demand for recycled content in construction projects and raise awareness of the benefits of using recycled materials [60].

7 Conclusion

In this review article, we want to emphasize the significance of recycling CDW by highlighting its multitude of environmental, economic, and social benefits. It is essential to consider the specific factors of a project while choosing between on-site and off-site recycling methods. For example, on-site recycling is useful for immediate material reuse and reducing transportation-related environmental impacts. At the same time, off-site recycling benefits from specialized facilities, advanced technologies, and economies of scale that offer better resource conservation and higher recycling rates.

However, making an informed decision about selecting a method requires project-specific analysis and evaluation. Despite challenges and barriers in CDW recycling practices, implementing strategies such as education, collaboration with stakeholders, supportive regulations and policies, technological advancements, and financial incentives can help overcome these hurdles.

Integrating circular design principles into waste management plans to optimize both on-site and off-site recycling practices involving sharing knowledge through research and innovation together with certifications and economic incentives for businesses embracing sustainability goals – has vast potential to advance toward future sustainability goals in construction industries. We urge industry stakeholders together with policymakers to make CDW an environmental priority by promoting inclusive practices that value this material as being reusable rather than simply waste.

To ensure that we can successfully implement a circular economy model in the CDW sector – it is important to consider additional measures such as establishing standards plus certifications for secondary materials – while rewarding good practices within the construction industry by decentralizing waste management processes and further encouraging entrepreneurship diversity no matter the company size or background recognition is vital towards recognition of informal sectors. Additionally maintaining readability and transparent databases committed towards CDW sustainable solutions along with Lean Management Practices promotion plus design for deconstruction are all crucial in enabling a circular economy future beyond today's infrastructures network.

References

1. K. Kabirifar, M. Mojtahedi, C. Changxin Wang, and T. Vivian W.Y., "A conceptual foundation for effective construction and demolition waste management," Cleaner Engineering and Technology, vol. 1. Elsevier Ltd, Dec. 01, 2020. doi: 10.1016/j.clet.2020.100019.
2. Y. Yu, D. M. Yazan, V. Junjan, and M. E. Iacob, "Circular economy in the construction industry: A review of decision support tools based on Information & Communication Technologies," J. Clean. Prod., vol. 349, May 2022, doi: 10.1016/j.jclepro.2022.131335.
3. O. O. Akinade et al., "Design for Deconstruction (DfD): Critical success factors for diverting end-of-life waste from landfills," Waste Manag., vol. 60, pp. 3–13, Aug. 2017, doi: 10.1016/j.wasman.2016.08.017.
4. M. Ghufran et al., "Circular Economy in the Construction Industry : A Step towards Sustainable Development," Buildings, vol. 12, p. 1004, 2022.

5. M. Norouzi, M. Chàfer, L. F. Cabeza, L. Jiménez, and D. Boer, “Circular economy in the building and construction sector: A scientific evolution analysis,” J. Build. Eng., vol. 44, no. December 2020, 2021, doi: 10.1016/j.jobe.2021.102704.
6. G. Polat, A. Damci, H. Turkoglu, and A. P. Gurgun, “Identification of Root Causes of Construction and Demolition (C&D) Waste: The Case of Turkey,” Procedia Eng., vol. 196, pp. 948–955, Jan. 2017, doi: 10.1016/J.PROENG.2017.08.035.
7. L. A. López Ruiz, X. Roca Ramón, and S. Gassó Domingo, “The circular economy in the construction and demolition waste sector – A review and an integrative model approach,” J. Clean. Prod., vol. 248, 2020, doi: 10.1016/j.jclepro.2019.119238.
8. M. Yeheyis, K. Hewage, M. S. Alam, C. Eskicioglu, and R. Sadiq, “An overview of construction and demolition waste management in Canada: A lifecycle analysis approach to sustainability,” Clean Technol. Environ. Policy, vol. 15, no. 1, pp. 81–91, 2013, doi: 10.1007/s10098-012-0481-6.
9. J. Lederer, A. Gassner, F. Kleemann, and J. Fellner, “Potentials for a circular economy of mineral construction materials and demolition waste in urban areas: a case study from Vienna,” Resour. Conserv. Recycl., vol. 161, p. 104942, Oct. 2020, doi: 10.1016/J.RESCONREC.2020.104942.
10. A. Lismont and K. Allacker, “Turning the existing building stock into a resource mine: proposal for a new method to develop building stock models,” IOP Conf. Ser. Earth Environ. Sci., vol. 323, no. 1, p. 012070, Aug. 2019, doi: 10.1088/1755-1315/323/1/012070.
11. “C&D Waste Recycling Wash Plant - Construction & Demolition Waste - CDE.” https://www.cdegroup.com/applications/waste-recycling/c-d-waste-recycling
12. J. K. Seadon, “Sustainable waste management systems,” J. Clean. Prod., vol. 18, no. 16–17, pp. 1639–1651, Nov. 2010, doi: 10.1016/J.JCLEPRO.2010.07.009.
13. C. P. Ginga, J. M. C. Ongpeng, and M. K. M. Daly, “Circular Economy on Construction and Demolition Waste: A Literature Review on Material Recovery and Production,” Materials (Basel)., vol. 13, no. 13, p. 2970, Nov. 2020, doi: 10.3390/ma13132970.
14. J. A. Ferriz-Papi, E. Weekes, N. Whitehead, and A. Lee, “A cost-effective recycled aggregates classification procedure for construction and demolition waste evaluation,” Constr. Build. Mater., vol. 324, p. 126642, Mar. 2022, doi: 10.1016/J.CONBUILDMAT.2022.126642.
15. J. J. Abraham, R. Saravanakumar, P. E. Ebenanjar, K. S. Elango, D. Vivek, and S. Anandaraj, “An experimental study on concrete block using construction demolition waste and life cycle cost analysis,” Mater. Today Proc., vol. 60, pp. 1320–1324, Jan. 2022, doi: 10.1016/J.MATPR.2021.09.307.
16. B. Huang, X. Wang, H. Kua, Y. Geng, R. Bleischwitz, and J. Ren, “Construction and demolition waste management in China through the 3R principle,” Resour. Conserv. Recycl., vol. 129, pp. 36–44, Feb. 2018, doi: 10.1016/J.RESCONREC.2017.09.029.
17. J. Kirchherr, D. Reike, and M. Hekkert, “Conceptualizing the circular economy: An analysis of 114 definitions,” Resour. Conserv. Recycl., vol. 127, pp. 221–232, Dec. 2017, doi: 10.1016/J.RESCONREC.2017.09.005.
18. P. V. Saez, M. Del Río Merino, A. San-Antonio González, and C. Porras-Amores, “Best practice measures assessment for construction and demolition waste management in building constructions,” Resour. Conserv. Recycl., vol. 75, pp. 52–62, 2013, doi: 10.1016/j.resconrec.2013.03.009.
19. H. Yuan, W. Lu, and J. Jianli Hao, “The evolution of construction waste sorting on-site,” Renew. Sustain. Energy Rev., vol. 20, pp. 483–490, 2013, doi: 10.1016/j.rser.2012.12.012.
20. M. A. T. Alsheyab, “Recycling of construction and demolition waste and its impact on climate change and sustainable development,” Int. J. Environ. Sci. Technol., vol. 19, no. 3, pp. 2129–2138, 2022, doi: 10.1007/s13762-021-03217-1.
21. Z. Bao, W. M. W. Lee, and W. Lu, “Implementing on-site construction waste recycling in Hong Kong: Barriers and facilitators,” Sci. Total Environ., vol. 747, p. 141091, 2020, doi: 10.1016/j.scitotenv.2020.141091.

22. E. Lawson, “Best Practices for Construction Waste Management.” [Online]. Available: https://www.recycling-magazine.com/2020/03/30/best-practices-for-construction-waste-management/
23. T. N. Dao, P. H. Chen, and T. Q. Nguyen, “Critical Success Factors and a Contractual Framework for Construction Projects Adopting Building Information Modeling in Vietnam,” Int. J. Civ. Eng., vol. 19, no. 1, pp. 85–102, 2021, doi: 10.1007/s40999-020-00542-3.
24. The free encyclopedia Wikipedia, “Louvre Abu Dhabi.” https://en.wikipedia.org/wiki/Louvre_Abu_Dhabi
25. Deloitte, “Document information Resource Efficient Use of Mixed Wastes,” no. October, 2017.
26. C. K. Purchase et al., “Circular economy of construction and demolition waste: A literature review on lessons, challenges, and benefits,” Materials (Basel)., vol. 15, no. 1, pp. 1–25, 2022, doi: 10.3390/ma15010076.
27. J. Hao, F. Di Maria, Z. Chen, S. Yu, W. Ma, and L. Di Sarno, “Comparative study of construction and demolition waste management in China and the european union,” Detritus, vol. 13, pp. 114–121, 2020, doi: 10.31025/2611-4135/2020.14029.
28. U. A. Umar, N. Shafiq, and F. A. Ahmad, “A case study on the effective implementation of the reuse and recycling of construction & demolition waste management practices in Malaysia,” Ain Shams Eng. J., vol. 12, no. 1, pp. 283–291, 2021, doi: 10.1016/j.asej.2020.07.005.
29. M. Ramos and G. Martinho, “An assessment of the illegal dumping of construction and demolition waste,” Clean. Waste Syst., vol. 4, p. 100073, 2023, doi: https://doi-org.egateway.chennai.vit.ac.in/10.1016/j.clwas.2022.100073.
30. M. U. Hossain, Z. Wu, and C. S. Poon, “Comparative environmental evaluation of construction waste management through different waste sorting systems in Hong Kong,” Waste Manag., vol. 69, pp. 325–335, Nov. 2017, doi: 10.1016/j.wasman.2017.07.043.
31. W. Lu, Z. Bao, W. M. W. Lee, B. Chi, and J. Wang, “An analytical framework of ‘zero waste construction site’: Two case studies of Shenzhen, China,” Waste Manag., vol. 121, pp. 343–353, Feb. 2021, doi: 10.1016/J.WASMAN.2020.12.029.
32. A.Tighnavard Balasbaneh, & Mohd, and Z. Ramli, “A comparative life cycle assessment (LCA) of concrete and steel-prefabricated prefinished volumetric construction structures in Malaysia”, doi: 10.1007/s11356-020-10141-3/Published.
33. W. Lu and H. Yuan, “Off-site sorting of construction waste: What can we learn from Hong Kong?,” Resour. Conserv. Recycl., vol. 69, pp. 100–108, 2012, doi: 10.1016/j.resconrec.2012.09.007.
34. K. Osmun and C. Specialist, “On-site vs . Off-site Sorting : Which Construction Waste Recycling Method Is Best ?,” pp. 1–4.
35. S. Lockrey, H. Nguyen, E. Crossin, and K. Verghese, “Recycling the construction and demolition waste in Vietnam: opportunities and challenges in practice,” J. Clean. Prod., vol. 133, pp. 757–766, Oct. 2016, doi: 10.1016/J.JCLEPRO.2016.05.175.
36. N. Cho, M. El Asmar, and M. Aldaaja, “An Analysis of the Impact of the Circular Economy Application on Construction and Demolition Waste in the United States of America,” Sustain., vol. 14, no. 16, 2022, doi: 10.3390/su141610034.
37. B. I. Oluleye, D. W. M. Chan, A. B. Saka, and T. O. Olawumi, “Circular economy research on building construction and demolition waste: A review of current trends and future research directions,” J. Clean. Prod., vol. 357, p. 131927, Jul. 2022, doi: 10.1016/J.JCLEPRO.2022.131927.
38. C. S. Poon, A. T. W. Yu, S. C. See, and E. Cheung, “Minimizing demolition wastes in Hong Kong public housing projects,” http://dx.doi.org/10.1080/0144619042000213283, vol. 22, no. 8, pp. 799–805, Oct. 2010, doi: 10.1080/0144619042000213283.
39. C. S. Poon, A. T. W. Yu, and L. H. Ng, “On-site sorting of construction and demolition waste in Hong Kong,” Resour. Conserv. Recycl., vol. 32, no. 2, pp. 157–172, Jun. 2001, doi: 10.1016/S0921-3449(01)00052-0.

40. K. Kabirifar, M. Mojtahedi, C. Wang, and V. W. Y. Tam, "Construction and demolition waste management contributing factors coupled with reduce, reuse, and recycle strategies for effective waste management: A review," J. Clean. Prod., vol. 263, p. 121265, Aug. 2020, doi: 10.1016/J.JCLEPRO.2020.121265.
41. A. De Luca, L. Chen, and K. Gharehbaghi, "Sustainable utilization of recycled aggregates: robust construction and demolition waste reduction strategies," Int. J. Build. Pathol. Adapt., vol. 39, no. 4, pp. 666–682, Oct. 2021, doi: 10.1108/IJBPA-04-2020-0029/FULL/XML.
42. S. H. Ghaffar, M. Burman, and N. Braimah, "Pathways to circular construction: An integrated management of construction and demolition waste for resource recovery," J. Clean. Prod., vol. 244, p. 118710, Jan. 2020, doi: 10.1016/J.JCLEPRO.2019.118710.
43. S. S. Kolaventi, H. Momand, T. P. Tezeswi, and M. V. N. S. Kumar, "Implementing site waste-management plans, recycling in India: barriers, benefits, measures," https://doi.org/10.1680/jensu.21.00032, vol. 175, no. 1, pp. 30–51, Jul. 2021, doi: 10.1680/JENSU.21.00032.
44. J. Liu, E. Gong, and X. Wang, "Economic benefits of construction waste recycling enterprises under tax incentive policies," Environ. Sci. Pollut. Res., vol. 29, no. 9, pp. 12574–12588, 2022, doi: 10.1007/s11356-021-13831-8.
45. A. Mahpour, "Prioritizing barriers to adopt circular economy in construction and demolition waste management," Resour. Conserv. Recycl., vol. 134, pp. 216–227, Jul. 2018, doi: 10.1016/J.RESCONREC.2018.01.026.
46. Y. T. Negash, A. M. Hassan, M. L. Tseng, K. J. Wu, and M. H. Ali, "Sustainable construction and demolition waste management in Somaliland: Regulatory barriers lead to technical and environmental barriers," J. Clean. Prod., vol. 297, p. 126717, May 2021, doi: 10.1016/J.JCLEPRO.2021.126717.
47. H. Yuan, "Barriers and countermeasures for managing construction and demolition waste: A case of Shenzhen in China," J. Clean. Prod., vol. 157, pp. 84–93, Jul. 2017, doi: 10.1016/J.JCLEPRO.2017.04.137.
48. European environment agency, "Construction and demolition waste: challenges and opportunities in a circular economy," 16 Jan 2020. https://www.eea.europa.eu/publications/construction-and-demolition-waste-challenges
49. European Commission, "Construction and Demolition Waste management in United Kingdom," Resour. Effic. Use Mix. Wastes, vol. V2, no. September, pp. 1–68, 2015, [Online]. Available:
http://ec.europa.eu/environment/waste/studies/deliverables/CDW_UK_Factsheet_Final.pdf
50. R. Oliveira Neto, P. Gastineau, B. G. Cazacliu, L. Le Guen, R. S. Paranhos, and C. O. Petter, "An economic analysis of the processing technologies in CDW recycling platforms," Waste Manag., vol. 60, no. 2017, pp. 277–289, 2017, doi: 10.1016/j.wasman.2016.08.011.
51. U.-R. Aecom Development, "Construction and Demolition Waste Management and Recycling," no. April, pp. 1–272, 2018.
52. K. Chen, J. Wang, B. Yu, H. Wu, and J. Zhang, "Critical evaluation of construction and demolition waste and associated environmental impacts: A scientometric analysis," J. Clean. Prod., vol. 287, p. 125071, Mar. 2021, doi: 10.1016/J.JCLEPRO.2020.125071.
53. J. Jiang et al., "From prospecting to mining: A review of enabling technologies, LCAs, and LCCAs for improved construction and demolition waste management," Waste Manag., vol. 159, pp. 12–26, Mar. 2023, doi: 10.1016/J.WASMAN.2023.01.017.
54. C. Zhang et al., "Upgrading construction and demolition waste management from downcycling to recycling in the Netherlands," J. Clean. Prod., vol. 266, p. 121718, 2020, doi: 10.1016/j.jclepro.2020.121718.
55. O. Akinade et al., "Design for deconstruction using a circular economy approach: barriers and strategies for improvement," https://doi.org/10.1080/09537287.2019.1695006, vol. 31, no. 10, pp. 829–840, Jul. 2019, doi: 10.1080/09537287.2019.1695006.

56. E. A. Ohemeng and S. O. Ekolu, "Comparative analysis on costs and benefits of producing natural and recycled concrete aggregates: A South African case study," Case Stud. Constr. Mater., vol. 13, p. e00450, Dec. 2020, doi: 10.1016/J.CSCM.2020.E00450.
57. M. A. de B. Martins et al., "Evaluating the energy consumption and greenhouse gas emissions from managing municipal, construction, and demolition solid waste," Clean. Waste Syst., vol. 4, p. 100070, Apr. 2023, doi: 10.1016/J.CLWAS.2022.100070.
58. N. H. Hoang et al., "Financial and economic evaluation of construction and demolition waste recycling in Hanoi, Vietnam," Waste Manag., vol. 131, pp. 294–304, Jul. 2021, doi: 10.1016/J.WASMAN.2021.06.014.
59. A. T. Gebremariam, F. Di Maio, A. Vahidi, and P. Rem, "Innovative technologies for recycling End-of-Life concrete waste in the built environment," Resour. Conserv. Recycl., vol. 163, Dec. 2020, doi: 10.1016/J.RESCONREC.2020.104911.
60. S. Shooshtarian, T. Maqsood, S. Caldera, and T. Ryley, "Transformation towards a circular economy in the Australian construction and demolition waste management system," Sustain. Prod. Consum., vol. 30, pp. 89–106, Mar. 2022, doi: 10.1016/j.spc.2021.11.032.

Resilience in Construction Industry and Its Role in Upgrading the Quality of Post-Earthquake Sheltering and Reconstruction

Mahmood Hosseini[1][0000-0003-3142-4087], Yasamin O. Izadkhah[2*][0000-0003-0695-0181] and Peyman Pir-Ata[3]

[1] Professor, Dept. of Civil Eng., Eastern Mediterranean University (EMU), Famagusta, North Cyprus via Mersin 10, Türkiye
mahmood.hosseini@emu.edu.tr
[2] Associate Professor, Risk Management Research Center, International Institute of Earthquake Engineering and Seismology (IIEES), Tehran, Iran
izad@iiees.ac.ir
[3] Lecturer, Islamic Azad University, Birjand Branch, Birjand, Iran
peyman.pirata@gmail.com
*Corresponding Author

Abstract. In several developing countries, the construction sector is regarded as a pilot industry. On the other hand, many of these countries are subjected to earthquakes, as a threat to their development goals. As such, the governments of these countries have to consider earthquake as an inevitable issue in the process of development and take proper measures. In order to achieve these goals, and regarding the construction industry expansion in these countries, as well as their vulnerability against earthquakes, it seems necessary to revise the structure of the whole construction industry to be in more contingency with disaster risk management. In this article, it has been tried to emphasize, from the resilience point of view, the necessity of reinforcing the role of construction industry in all stages of disaster risk reduction, particularly post-earthquake sheltering and reconstruction. The proposed solution is using the resilience concept based on discovering and enriching quality in the structure of construction systems, called "disaster-resilience of construction industry". This characteristic aims at increasing the capability of a special system exposed to damage and reducing its vulnerability as well as increasing the rapidity of short- and long-term restoration processes. In this paper, first, the concept of resilience and its components have been introduced in general. Then, this idea has been addressed as a quality indicator in construction system in particular. Finally, the effects of this approach in mitigating the adverse consequences of natural disasters and improvement of the post-event conditions have been highlighted.

Keywords: Construction Sector in developing countries, Risk Management, Disaster Resilience.

1 Introduction

Earthquake is usually known as a natural massive destructive element that occurs in sudden and causes adverse effects and considerable damages. This element usually affects the physical structures at first. Although physical damages are common in all natural disasters, the difference in the case of earthquake is that human damages are mostly dependent on structural operation and destruction mechanism of physical environment and its consequent demolishing does not rely on the earthquake force itself. In other words, the phenomenon of earthquake is not too dangerous for homeless people but what makes the most damages and casualty is due to the low quality of structures. That is why similar earthquakes with the same duration and intensity cause different levels of damages in different locations. Despite the fact that earthquake consequences go further than damages, and it affects many other aspects of human life, such as social, economic, cultural, political, etc., its major characteristic, known as physical destruction, is more serious than the other aspects. This fact proves the important role of building industry and its specialists.

In recent decades, some attempts have been accomplished in order to enforce the role of building industry in crisis management, such as building lightening, improving building standards, codes, etc. However, many structural potentials of building industry for decreasing and restoring disaster consequences have been ignored and this fact overshadows the role of effective presence of building industry in many levels of crisis management. So far, enormous investigations have been conducted on earthquakes, their effects on structures, retrofitting and optimizing methods in order to reduce vulnerability. The results are very essential in improving and updating existing codes and developing new codes for new structural systems. It can also reduce human casualty and physical losses if it is implemented and supervised well.

Nowadays, mass production and industrial building construction has developed in a large scale. Mass industrial construction has always been considered as a solution of housing shortage crisis due to natural and man-made disasters. It makes it possible to reconstruct damaged spaces in a large scale, with shorter time and lower cost. Recently, many researches led to desirable process in lightweight structural and nonstructural elements. Since the building vulnerability depends on dead load to a large extent, these developments in lightweight construction make it possible that destructions caused by the future earthquake decline significantly. As Schneider has stated in 2002, “policy makers and stakeholders alike tend to underestimate hazard potentials. They see a low probability of hazard occurrence, are reluctant to impose limitations on private property, often unwilling to bear the costs incurred by mitigation plans, and frequently are ambivalent toward hazard mitigation, because they see it as being in conflict with other values and goals” [1].

In this regard, few questions arise: "Despite considerable experiences in the past and availability of necessary tools and technologies to mitigate future damages, where is the root of this neglect? Why construction industry does not accept responsibility in this regard? Which values or approach are assumed precedence over human lives? Today, in the era of post-modernism, we are encountered with another shift in human-

environment interaction. Our discourse is about effects of modernization on nature around us. In this situation, two more questions arise: Does the way we deal with natural disasters is at the same level of other components of industrial development? Can we propose a stable approach in facing earthquakes in the construction industry?

Many technical and hardware features can be identified to reduce the damages caused by natural disasters such as earthquakes and to help speeding up the recovery process. However, as Bosher et al. (2006) have mentioned, experiences over the past have proved that the construction industry has not been able to play an appropriate and effective role against disaster risks so far [2]. Maybe this fact is based on the lack of a coordinated management system. It is evident that individual developments usually do not lead to appropriate results unless they are used in an integrated management system meaningfully and coordinately. Unfortunately, the necessity for such a framework is not well understood by policy makers in construction industry and coordination between 'construction' and 'risk management' is therefore, neglected [1].

This paper is an attempt to provide a strategy in building industry in order to establish a sustainable coordinating management system to deal with earthquakes appropriately. The proposed solution is based on discovering and enriching quality in the structure of construction systems named by the authors 'the construction system resilience'. This factor manages the capability of a special system exposing to damage and reducing its vulnerability at its first step and repair the short-term and long term consequences in future actions. In this paper, first the crisis management approach is briefly discussed and its limitations which play a pivotal role in coordinating the construction industry dealing with natural disasters are explained. Then, the concept of resilience and its components will be introduced in general and the idea of resilience as a constructional quality in a construction system will be taken into consideration in particular. Finally, some deep influences of the mentioned approach on decreasing and resolving the shortages created by devastating natural disasters and improving the process of disaster management will be identified.

2 Disaster Management Process

Disaster management is the process of program planning and operation of authorities and public executive agencies that observes and analyzes disasters and tries to prevent the crisis after disasters. It takes advantages of available tools in an integrated, comprehensive and coordinated shape and makes efforts to reduce impacts, makes the necessary preparations and rapid relief and recovery to reach a normal situation in such cases**.**

Four main stages of disaster management are preparedness, response, recovery, and reducing the consequences. Many efforts have been done in order to highlight disaster management role in construction industry in recent decades and significant progresses have been achieved in this field. However, it seems that disaster management has not been able so far to create an appropriate framework for construction industry for playing a comprehensive and inclusive role in dealing with disasters. Some reasons for this failure are mentioned as follows:

- First, wide range of policymaking, planning and implementation efforts in disaster management makes it difficult to focus on details of the mechanisms involved.
- Second, despite the four stages of crisis management, which should cover both before and after the event plans, it seems that response and recovery phases are considered more important than those related to reducing the consequences of disasters. Disaster management is more likely to be raised temporarily in response to sudden disasters instead of working on long term preventive programs. Schneider [1] has stated that emergency management has largely been viewed as a reactive proficiency because hazard mitigation is rarely seen as urgent. It is evident that in crisis conditions, there is no good time for long-term planning. However, starting a development in this field should not wait for a disaster to happen.
- Third, on the one hand, due to the focus of disaster management on crisis mitigation in the aftermath of earthquakes, its communication with construction industry is one-directional, aiming at utilization of the construction industry's capacity for limiting the disaster's dimensions. On the other hand, review of development processes in construction industry indicates that the motivating factors have mostly been influenced by economic and industrial interests; and disaster management considerations do not have an active role in this regard.

Regarding the above reasons, although disaster management plays a very critical role in reduction of crisis, it cannot be expected to provide an appropriate framework for long-term planning of the construction industry in relation to disasters. As a result, different communities, especially those with more vulnerable infrastructure and structures are unable to use the maximum capacity of building industry in disaster management and, hence; are not fully capable to overcome the crises. This has led the investigators to look at natural disasters from different aspects, including resiliency, which is the focus of this paper as well.

3 Resilience and Its Role on Earthquake Risk Management

Disaster management approaches has been associated with many changes in recent years. One of the strategies that has received much attention in recent years is called 'resilience', which has been defined in different ways:

- "The ability that a person or institution has to recover quickly from a setback or misfortune …" [3]
- "Buoyancy, power of recover…" [4]
- "An ability to recover quickly from or adjust easily to misfortune, change or disturbance" [5].

Resiliency is a very broad and multi-dimensional term in disaster management which involves various aspects of the society. Bruneau et al. [6] have conducted extensive research on resiliency issue and have defined it as "the ability of a system to reduce the chances of a shock, to absorb such a shock if it occurs (abrupt reduction of performance) and to recover quickly after a shock (re-establish normal performance)". From Bruneau's perspective, resiliency has three purposes: 1) reducing failure probabilities, 2) reducing consequences from failures, in terms of lives lost, damage, and negative

economic/social consequences, and 3) reducing time to recovery (restoration of specific system or set of systems to "normal" functional performance).

Davis and Izadkhah [7] defined resilience as "the ability of communities, their physical, social, political systems and their buildings and settlements to withstand hazard generated forces and demands, to bounce back rapidly and to adapt to cope with future threats". They also added one more goal to those mentioned by Bruneau as "patterns of vulnerability that can develop during the process of reconstruction". Bruneau and Reinhorn introduce four components for resiliency [8]:

- **Robustness**: Strength, or the ability of elements and systems to withstand a given level of stress or demand without suffering degradation or loss of function;
- **Redundancy**: The extent to which elements and systems exist that are substitutable, i.e., capable of satisfying functional requirements in the event of disruption, degradation, or loss of functionality;
- **Resourcefulness**: The capacity to identify problems, establish priorities, and mobilize resources when conditions threatens to disrupt some element and system;
- **Rapidity**: The capacity to meet priorities and achieve goals in a timely manner in order to contain losses, recover functionality and avoid future disruption.
- In the following section these four components are discussed with regard to the construction industry.

4 Resilience in Construction Industry

In a large scale, resilience can involve all aspects of economic, social, political, technical and other dimensions involved in the disaster. This paper focuses on the resiliency of 'building systems' and 'construction industry', and 'disaster impacts' on them, and how 'resilience in construction industry' can be achieved. Considering the wide scope of application, it is necessary to determine clearly the scale and scope of these four terms and some related concepts used in this paper:

Construction industry: The construction industry is a vast field. This paper focuses on massive industrial construction systems. This area of the construction industry is not very advanced in terms of structural complexity, size, and height. Therefore, it is not applicable to large individual public buildings. These systems are usually used in projects with low complexity and high number of copies such as residential complexes with mass production.

Building systems: It is defined as a series of coordinated procedures for design and construction of a building/ part of a building. Building system can be discussed at micro/macro levels such as system of partitioning walls, finishing methods, roof systems, installations, etc., that can be considered as micro or sub systems, while all coordinated subsystem can be considered as a complete building system.

Disaster impacts: Impacts of disaster on the construction industry should not be considered just toward structural damages caused by disasters. Actually the rate of vulnerability of construction industry, the way it deals with high volume of housing demand, cost and speed of construction and many other issues, all together determine

the impacts of a disaster. It is also obvious that structural robustness will inevitably lead to reduction of vulnerability of the whole system as well.

Resilience in construction industry: According to Davis and Izadkhah in 2005, resilience in construction systems is defined as "the ability of a construction system to withstand hazard-generated forces and demands, to bounce back rapidly and to adapt to cope with future threats" [7]. Based on this definition, four goals are to be considered in the construction industry resilience:

1- Reducing buildings' performance failure probabilities in an earthquake;
2- Reducing negative economic and social consequences of buildings' failure;
3- Reducing building systems recovery time;
4- Reducing patterns of vulnerability related to long-term goals of settlement that can be developed during the process of reconstruction.

Since the construction industry is a complex set of skills, human resources, management, financial resources, construction details and methods, education, cultural and environmental issues, etc., enhancing resilience in the construction industry requires a full understanding of all aspects and how they are affected by the earthquake. This paper deals mostly with identifying the problem. The authors of this article believe that understanding and improving this quality can directly reduce depth of consequent damages caused by disaster in physical body of the society and increase the bouncing back speed to the normal level. In the following parts of the paper, four resilience components are discussed with regard to the construction industry.

4.1 Robustness

In connection with the construction systems, robustness can be defined as strength, or the ability of construction systems to withstand a given level of stress or demand without suffering degradation or loss of function. Apparently, this quality has been stressed more than any other component of resilience in the area of disaster management. In disaster management, mitigation is known as a main phase. The key task at this stage is to minimize vulnerability of structures against the seismic forces by increasing strength through building regulations and codes as well as compliance monitoring, in practice. Therefore, it can reduce the other side effects due to physical damages in terms of human and financial toll.

Despite the initial similarity between two views of retrofitting approach in disaster management and robustness in construction industry, the focus here is more on their differences and contradictions. Retrofitting, as its name suggests, is to reduce damages by increasing structural strength, and its priority is to protect human life. Robustness seeks to maintain construction system applicability in providing settlement. It is evident that, giving priority to maintain applicability of system does not mean to ignore the protection of people's lives. However, by increasing strength of the system to maintain its performance, safety of residents will noticeably achieve accordingly.

4.2 Redundancy

Despite developments made in increasing strength of structural systems, disruption in performance of buildings in a large earthquake seems to be inevitable. Consequently, society faces a high demand for housing and the limitation of time and resources after a disaster. Building systems must have redundancy quality in order to maintain their

performance and resilience in such circumstances. A system which has redundancy is able to fill the gaps caused by disaster and meets temporary space demands at an acceptable level (considering that expectations of affected people in temporary housing program are much lower than normal condition).

The importance of redundancy in construction system has been neglected to a large extent. Speed of common systems used in normal condition is much lower than what is expected in time of emergency. On the other hand, these systems provide a high level of welfare which is not predicted in emergency conditions. Therefore, in traumatic conditions, these systems temporarily lose their effectiveness in the system of supply and demand. Usually in such circumstances, employing construction systems at lower cost and complexity with higher quality, execution speed and simplicity, is recommended as a solution to urgent need for survivor's shelter. There are several systems and methods for providing temporary housing. Conex boxes, prefabricated panel systems, and in some cases deployable structures are few samples.

Actually, what we are looking for in redundancy is a dual performance capability which plays a crucial role in both permanent and temporary constructions. The role of redundancy in construction industry is to show flexibility in order to deal with new situation in the face of disasters. In most cases, achieving redundancy does not require modern technology and high cost. Some sort of traditional technologies which do not have a high structural resistance may show various degree of redundancy quality. It should be noted that here redundancy is regarded in relation to earthquake disaster. A system may show good performance of redundancy in face of earthquakes but not in other disasters. However, various structural systems have different degrees of this quality or they have the potential to enhance it. However, in most cases, it is not done deliberately in order to improve redundancy. For example, pre-fabricated and modular constructions are two features that strengthen redundancy.

4.3 Resourcefulness

Resourcefulness is the capacity to identify problems, establish priorities, and mobilize resources when existing conditions threatens to disrupt some elements and system. In fact, one of the main challenges for resilience is to manage an appropriate balance between temporary and permanent periods. Since construction in these two sections is completely different with conflicting requirements and demands, making balance between them is the most challenging aspect of resilience. It is necessary to perform some structural reforms in construction systems in order to create and improve a dual performance capacity (as proposed in redundancy stage). Economic justification and absorbing incentives to invest in this area demand extensive studies and creative ideas within each of construction systems. On the other hand, it is crucial to develop a comprehensive plan to coordinate with those agencies involved in related disaster management issues, such as disaster management headquarters, financial institutions, insurance companies, etc., in order to take advantage of technical capabilities of construction systems for controlling the lack and requirements for shelters after disasters. Resourcefulness oversees the richness of ideas raised to increase financial, technical and managerial feasibility of changes tack place in building systems in order to establish the redundancy. For the best results, these reforms should be carried out by manufacturers through increasing the capabilities of each system, which must be

identified and implemented. In this regard, insurance is one of the most effective and efficient strategies for distribution the cost of unexpected accidents in the long-term.

4.4 Rapidity

Rapidity is the capacity to meet priorities and achieve goals in a timely manner in order to cover losses, recover functionality and avoid future disruption. Acceleration in post-disaster housing program is one of the most critical and challenging issues in disaster management. However, its importance can vary depending on circumstances and priorities. The main objective of rescue phase is providing a minimum shelter in a slightest time. Speed is vital at this stage and in the case that weather is inappropriate, speed is measured by hours. In this stage, the quality criteria are far from normal conditions. In some cases, due to the large number of homeless people, and time constraints, the collective settlement is done. In the rehabilitation phase, the speed is measured by days and weeks. And finally, in reconstruction phase speed is measured by months and years. Prolongation of the rebuilding process is problematic in many ways. Therefore, policy-makers usually emphasize on accelerating the post-disaster reconstruction process in all cases. One of the most prevalent problems is unintended replacing of aforementioned trend to acceleration, which is a kind of rush in decision making and action. This rush is due to the lack of coordination in physical activities of each phase in post-disaster with the long-term and mid-term objectives. But rush into making decisions in every situation and phases, will cause destructive effect on planning and long-term objectives. In particular, the reliable or “disaster-avoiding” urban design, which is a very important issue in reconstruction of a city after a major earthquake as Hosseini [9] has mentioned would be adversely affected by the illogical too quick reconstruction. Obviously, rapid acceleration with logical management is as costly as other demands of disaster management. Since providing these costs is by governments, donors and the society, the financial helps reach to its higher level at the time of disasters and naturally it fades day after day and in the absence of rational management framework, this lack of coordination will increase the problem.

By enforcing resiliency in construction systems, it can be seen that most concerns about maintaining acceleration in construction and preventing rush at least in the area of housing can be decreased. For better performance of a construction system, it must coordinate itself with emergency programs of temporary housing which demands technological capabilities and special management. In fact, what makes the resilient systems distinctive from other systems, is that it emphasizes on ability to cover both temporary and permanent periods and also solve some complexity of systematic connection of these different scales in one construction system.

5 Construction Systems Resilience in Disaster Recovery Activities

Developmental Association Committee (DAC) related to Organization for Economic Cooperation and Development (OECD) has tried to codify some criteria to be used extensively in the evaluation of Humanitarian Relief Activities after disasters [10]. These criteria include communication, appropriateness, continuity, consistency,

coverage, efficiency, effectiveness and adverse effects. Based on these groups, increasing the resilience of construction industry can have the following positive impacts on the recovery, shelter actions, and reconstruction plans for heavily stricken cities, noted by Ghafory-Ashtiany and Hosseini [11] and Hosseini et al. [12].

1) Resiliency approach can be in line with policy of codifying temporary housing projects in disaster management to act before a disaster. This also increases the relevance and appropriateness, continuity, consistency and efficiency in the relief activities after disasters.

2) Temporary housing and reconstruction process usually requires a high level of technical and administrative facilities in which many cases (especially in more remote areas) exceeds the demands of the technical and administrative capacity of the area. Technical and administrative dependency to the services offered out of the region will cause management dependencies and policy making. Using systems with high resiliency has the benefit of reducing technical and technological dependency, and planning will be implemented at the area level, increasing the appropriateness and consistency, and reduces negative impacts on relief activities after disasters.

3) One of the problems of temporary housing is the lack of adaptation with cultural and architectural conditions dominated in the area and consequently, lack of consent of the people. Using systems with high resiliency in construction before disasters may be welcomed by damaged people due to their familiarity with the previous usage in area and its adaptation with the area condition. This increases the relevance and appropriateness of the relief activities after disasters.

4) One of the consequences of technical and administrative dependency to out-of-area services in temporary housing is that, after completing the construction of the units, necessary technical supports is nearly impossible. By resilient systems, technical knowledge, expert executive personnel and materials are needed to support future products and eliminate possible defects with continued presence in the area.

5) Access to the temporary housing phase is made by two ways: The first is materials and equipment sources in local market before a disaster (although these sources do not fully satisfy the requirements of reconstruction). The second source is materials which are used in damaged and destroyed buildings and depending on the level of destruction can be used in temporary housing or permanent reconstruction. In this case, the severity and type of damage is the usability factor.

6) Resilience approach of the construction systems makes the projection of the main policy making and planning possible in housing disaster management within the construction industry. This has many advantages, including reducing tensions and management problems of multiple organizations involved in disaster management, utilizing management experiences in construction projects in the face of crisis, facilitating synchronization of short-term and long-term objectives of reconstruction and development, reducing the ambiguities and complexities of counting, and accelerating estimation of damages after every disaster.

7) Experiences gained through past disasters prove that reconstruction policies are affected by pressures made by some donors. Through assigning the domain of temporary housing to construction industry, the donor’s charities can be directed to areas with less complexity and thus reduce the passive performance of policy makers.

8) In the resiliency approach, the method to design temporary housing is different from its traditional forms. In common methods, particularly in prefabricated box

systems, designers do not have direct contact with consumers which lead to ignoring the real needs of consumers and to design these needs based on the demands of aid groups (speed and ease of installation and transportation). Resilience-based approach with form-based design is a flexible system in which both temporary and permanent form plays crucial roles.

9) Using workforce of the survivors in reconstruction activities is highly emphasized. It also leads to the provision of required local manpower, motivated and confident, with no cost. It has also positive effects on the treatment of victims, and help to protect against the common mental disorders in such disasters and leads to the possibility of employing locals.

10) Temporary housing units remain in their places after passing the phase of temporary housing for some reasons, and this impose some problems and costs to the owner in permanent constructions and remain intact in their places or by attaching to permanent constructions, can create problems. If the temporary units or their component and materials can be used in reconstruction, the problem would be resolved. This way, there is no need to spend money to remove them, and remaining of these constructions does not harm the physical body of the reconstructed buildings.

6 Conclusion

Using the resiliency approach in construction industry and its positive impact on the operation of temporary housing and reconstruction after earthquakes is discussed in this paper. It is recommended that the construction industry authorities modify and correct the existing approaches and appropriately adapt them in criteria of resiliency approach. In this regard, recommendations for further research are as follows:

- Conducting more studies to explain the sustainable relationship of construction industry and management of post-disaster housing;
- Identifying potentials in construction systems to enhance resiliency capability;
- Developing criteria for resiliency capacity of construction industry;
- Evaluating the existing construction systems from resiliency capability point of view by means of correcting existing systems and from resilience perspective, in order to improve the construction systems in the long-term.

References

1. Schneider, R.O: Hazard mitigation and sustainable community development, Disaster
2. Prevention and Management Journal, 11(2), 141-147 (2002).
3. Bosher, L. Dainty, A. Carrillo, P. Glass, J. Price, A: The construction industry and emergency management: Toward an integrated strategic framework, Publisher: i-Rec information and research for reconstruction, https://hdl.handle.net/2134/12810 (2019).
4. Collins Dictionaries: http://www.collinsdictionary.com/. Last accessed 2022/6/4.
5. Oxford English Dictionary: http://www.oed.com/, Last accessed 2022/6/4.
6. UNISDR Resilience Definition: ‘The capacity of system, Community or society to resist or to change’, Hyogo Framework for Action 2005-2015 (2002).
7. Bruneau, Michel, Stephanie E. Chang, Ronald T. Eguchi, George C. Lee, Thomas D. O'Rourke, Andrei M. Reinhorn, Masanobu Shinozuka, Kathleen Tierney, William A. Wallace,

and Detlof Von Winterfeldt: A framework to quantitatively assess and enhance the seismic resilience of communities, Earthquake Spectra, 19(4), 733-752 (2003).
8. Davis, I. and Izadkhah, Y. O.: Building resilient urban communities. Open House International (OHI) (2005).
9. Bruneau, M. and Reinhorn, A: Overview of the resilience concept, Proceedings of the 8th National Conf. on Earthquake Engineering, San Francisco, USA (2006).
10. Hosseini, M: Reconstruction of towns and cities after destructive earthquakes: challenges and possibilities from the urban design point of view. In 9CCEE, Ottawa (2007).Overseas Development Institute, Evaluating humanitarian action using the OECD-DAC Criteria: An ALNAP guide for Humanitarian Agencies, London, (2006).
11. Ghafory-Ashtiany, M. and Hosseini M: Post-Bam earthquake: recovery and reconstruction. Natural Hazards 44: 229-241 (2008).
12. Hosseini, M., Y. O. Izadkhah, and P. Pir-Ata: Lessons learnt from shelter actions and reconstruction of Bam after the destructive earthquake of December 26, 2003. In 14th World Conference on Earthquake Engineering, China, pp. 12-17 (2008).

Supervisor's and Co-workers' Safety Climate of Building Construction Workers

Serkan Aydınlı[1][0000-0002-2897-4144] and Selman Aslan[2][0000-0002-6766-7315]

[1] Cukurova University, Civil Engineering Department, Adana, Türkiye, saydinli@cu.edu.tr
[2] Muş Alparslan University, Transportation Services Department, Muş, Türkiye, se.aslan@alparslan.edu.tr

Abstract. Safety climate is one of the major factors affecting safety behavior such as safety training, safety culture, safety motivation . Numerous studies have been conducted in many industries to explore the components of safety climate. In recent years, researchers have focused on the effects of supervisor's and co-workers' safety climate on workers' safety behaviors. Literature studies show that supervisor's and co-workers' safety climate have significant effects on safety behavior. This study employed widely used safety climate scale and focused on the supervisor's and co-workers' safety climate perception of building construction workers in Türkiye. Descriptive statistics of the survey data were presented and discussed. As a result, it is observed that co-workers' safety climate is slightly better than supervisor's. While co-workers' safety mentoring is the component of co-workers' safety climate with higher mean, supervisor's effort to improve safety is the lower component. This study also provides suggestions for future research directions on the effects of the safety climate on other safety factors.

Keywords: Occupational Health and Safety, Safety Climate, Workers' Perceptions, Building Constructions.

1 Introduction

The construction industry is one of the leading industries occupational accidents are frequently experienced. Social Security Agency of Türkiye reported 386 deaths in construction industry in 2021. In addition, it was stated that the accidents caused 58107 losses of working days [1]. The scientific world has been researching the causes of these accidents for years. While some researchers focused on mistakes in practice [2–4], others examined social and organizational factors affect occupational accidents [5,6]. In recent years, it has been revealed that factors have important effects on safety motivation and safe behavior. It has been discussed that important progress can be made in occupational health and safety statistics by controlling these factors.

Safety climate which is one of the leading concepts affecting safety motivation and behavior, is a multidimensional construct that measures an individual safety perception.

Safety climate is first introduced by Zohar [7] and is a specific form of organizational climate. The dimensions of the concept have changed in light of research over the years. Brown & Holmes [8] have tried to confirm Zohar's model and concluded that initial model does not supported by sample. The authors also conducted an explanatory factor analysis and decided that three-factor model is more practical for implementation. Dedobbeleer and Béland [9] first evaluated two- and three-factor models on construction workers. The results revealed that the two-factor model fitted better the sample of construction workers. The dimensions of the security climate have continued to change over time. Shea et al. [10] summarized the safety climate scale development process and listed dimensions commonly used as; safety systems, safety commitment, prioritization of safety, safety communication, safety involvement, safety training and safety rewards. Safety climate scales can also be implemented in different referents such as workplace, management, supervisor, co-workers and individual.

The relationships between safety climate and factors such as safety motivation, safety behavior, and safety performance have been investigated over the past decade. Studies show that the relationship of the safety climate with other safety factors may differ according to industries and cultures. Besides, it is explored that supervisor and co-workers have efficient roles in safety outputs. This paper aims to explore supervisor's and co-workers' safety climate in building construction industry. For this purpose, this paper is constructed as follows; 1) summarizing the literature investigating relationships between safety climate and safety outcomes, 2) introducing material and methods in research, and 3) presenting findings and discussion of results.

2 The Roles of Supervisor's & Co-Workers' Safety Climate on Safety Outputs

Supervisor's and co-workers' safety climates are significant safety environments based on human relations and have been investigated in many occupational health and safety studies. Both the supervisor's safety climate (SSC) and the co-worker's safety climate (CSC) affect the safety behavior of the employees [11].

From preliminary studies, Zohar and Luria [12] implemented three case studies to investigate supervisory practices on employees' safety behavior in manufacturing industry. As a result, it is observed that supervisory safety-oriented interaction increased workers' safety behavior and safety climate scores significantly. Michael et al. [13] investigated the impact of supervisor's leadership attitude on safety outcomes of blue-collar wood production employees. The results showed that supervisor's leadership is of great influence on safety outcomes. Lingard et al. [14] examined the effects of supervisors and co-workers' safety climate on reported injury frequency in Australian construction industry. Although the results showed that there are no significant differences between the injury frequency rates of workgroups with different

safety climate environments, the authors stated that the results should be confirmed with higher samples. Conversely, in another study, authors determined a link between subcontractor's supervisory safety response and injury rate [15]. Newaz et al. [16] also investigated the influence of SSC on workers' safety behavior and the authors concluded that mutual safety obligations between supervisor and workers should be fulfilled for safe behaviors.

Lingard et al. [17] aimed to explore the relationship between CSC and the workgroups' injury rate. Results show that neither aspect of co-workers' safety response was significantly correlated with workgroup injury rate. Brondino et al. [18] and Gao et al. [19] pointed to the effects and the mediation role of CSC on workers' safety behaviors. The authors highlighted that co-workers' safety behavior is strongly mediated by CSC.

3 Methodology

This study aims to evaluate the supervisor's and co-workers' safety climates of building construction workers in Türkiye. To this end, a questionnaire survey was constructed using scales developed by Brondino et al. [18] and Zohar & Luria [20]. This survey was implemented on 374 building construction workers employed mostly by small and medium-sized enterprises. Participants consist of workers and craftsmen who take part in various stages of construction from the site installation to the completion.

SSC survey is measured using a 10-items scale and it is of two main dimensions which are "Supervisor's effort to improve safety" and "Supervisor's reactions to worker's behaviors". On the other hand, CSC survey is measured using a 12-items scale and it is of four main dimensions which are "Safety communication", "Safety mentoring", "Safety values" and "Safety systems". All items of the questionnaire were scaled and applied with a 5-point Likert scale.

First, Cronbach's Alpha coefficients were calculated to check the reliability of the scales applied. Cronbach's Alpha is a coefficient ranging from 0 to 1 and measures the reliability of the scales used in survey studies. The reference intervals of Cronbach's Alpha coefficient and the meanings of these intervals are given in Table 1.

Table 1. Cronbach's Alpha coefficient intervals [21].

Cronbach's Alpha Score	Level of Reliability
0.00 – 0.20	Less Reliable
>0.20 – 0.40	Rather Reliable
>0.40 – 0.60	Quite Reliable
>0.60 – 0.80	Reliable
>0.80 – 1.00	Very Reliable

After the reliability of the scales was determined, the descriptive statistics of each dimension were analyzed and discussed.

4 Results and Discussion

4.1 Demographics of Sample

As stated before, 374 valid questionnaire data were obtained from construction workers from small and medium-sized construction enterprises. The general demographics of the participants are as follows. While 75.4% of the participants are married, 24.6% are single. When the participants are classified according to their educational status, it is seen that the majority of them are high school graduates. Participants work at various stages of building construction. In this regard, those who work in formwork and rebar works are the main ones. While obtaining data, care was taken to include participants of all ages and experiences. The average age of the participants was 37.98, and the average experience was 15.65.

4.2 Supervisor's Safety Climate of Building Construction Workers

In this part of the study, the results of the SSC questionnaire applied to the participants were presented and discussed. First, the reliability of the scales was determined by calculating Cronbach's Alpha coefficient. SSC is of two main dimensions which are "Supervisor's Effort to Improve Safety" and "Supervisor's Reactions to Workers Behaviors". Cronbach's Alpha coefficients of the aforementioned dimensions were calculated as 0.961 and 0.946, respectively. This shows that the scales are extremely reliable.

After the scale reliability was determined, the mean and standard deviation values, which are the basic descriptive statistics of all items of the scales, were calculated. Descriptive statistics of all items of SSC are given in Table 2.

The most striking item among the results is "Supervisor's care to worker's safety awareness" with higher mean (4.03) and lower standard deviation (0.98). This finding shows that supervisors aim to reach a high level of occupational health and safety awareness at the construction site. Safety awareness is a major factor affecting safety performance in construction industry [22] and one of the common problems in developing countries is that workers do not have enough awareness of occupational health and safety. In order to overcome this deficiency, it is necessary to provide an efficient training program, sustainable safety climate and culture. The development of the safety culture of the workers largely depends on the correct OHS practices and organizational culture of the enterprise. Moreover, social influence of colleagues is of great importance in safety awareness [23].

Table 2. Descriptive statistics of SSC dimensions.

Items	Mean	Std. Deviation
Supervisor's effort to improve safety		
Supervisor's care of safety rules when a delay in production schedule occurs	3.80	1.03
Supervisor's care for provide workers needed safety equipment	3.87	1.08
Supervisor's care to the use of safety equipment	3.88	1.10
Supervisor's care of safety rules when workers are tired	3.94	1.02
Supervisor's care to all safety rules	3.79	1.15
Supervisor controls the compliance of all the workers	3.92	1.02
Supervisor's reactions to workers' behaviors		
Supervisor discusses with workers on safety improvement	3.99	1.02
Supervisor's care for workers' safety awareness	4.03	0.98
Supervisor's coaching about safety care	3.92	1.05
Supervisor praise for very careful safety behaviors	3.91	1.12

Among the SSC items, the item with the lowest mean (3.79) is "Supervisor's care to all safety rules". It is seen that this item also has the highest standard deviation (1.15). This shows that there are differences between the opinions of the participants, some supervisors care about all security rules, while others do not. However, it is known that the supervisor's violation of the safety rules is reflected in the behavior of the workers due to social contagion [24]. In summary, the mean and standard deviation values of the dimensions indicate that, in general, workers are working in a satisfactory SSC environment.

4.3 Co-workers' Safety Climate of Building Construction Workers

In the second part of the study, CSC of the workers has been evaluated. In the construction industry, CSC is as important as SSC. The results of the CSC questionnaire applied to participants are as given in Table 3.

The results show that workers' perceptions of CSC are higher than SSC. In particular, the mean values of items belonging to the safety mentoring dimension are quite high. This is an important indicator showing that workers care about the safety of their team members. Similar to the SSC survey results, it is a significant finding that workers care about the safety awareness of their team members. The most crucial dimension both by the management and by the workers is "awareness". Awareness is one of the factors that directly affect safety performance [25]. On the other hand, the weakest dimensions of SSC are "safety communication" and "safety system". Findings regarding "safety communication" dimension show that there is no efficient communication between the workers about OHS practices. Efficient safety communication depends on an efficient

organizational safety climate [26].

Table 3. Descriptive statistics of CSC dimensions.

Items	Mean	Std. Deviation
Co-workers' Safety Communication		
Team members' speaking on safety on the week	3.77	0.89
Team members' discussing about incident prevention	3.97	0.84
Team members' discussion about safety hazard	4.03	0.78
Co-workers' Safety Mentoring		
Team members' emphasis on peers on safety care when under pressure	4.01	0.88
Team members' care of peers' safety awareness	4.12	0.71
Team members' mentoring to peers about working safely	4.04	0.77
Co-workers' Safety Values		
Team members' safety care at the shift end	4.05	0.85
Team members' safety care when tired	3.99	0.88
Team members' safety care when a delay in production schedule occurs	4.02	0.89
Co-workers' Safety Systems		
Team members care about other workers' safety equipment	3.84	1.05
Team members remind safety equipment use	3.91	1.00
Team members care about other members' safety compliance	4.06	0.88

It is clearly disclosed that the importance of "safety communication" and "safety systems" should be realized by construction organizations.

5 Conclusion and Future Directions

The construction industry is subject to many occupational accidents due to not paying enough attention to occupational health and safety climate and culture. This study focused on evaluating SSC and CSC in small and medium-sized construction enterprises. To this end, a questionnaire survey has been implemented for building construction workers and descriptive statistics of collected data were analyzed.

In summary, "safety awareness" is seen as the most important item in practice in both SSC and CSC. It is a known fact that the majority of employees with high safety awareness will have a positive effect on occupational safety performance [27]. The high importance given to safety awareness in the Turkish construction industry is a promising result for the future. On the other hand, it is clear that there are relatively weak items in both SSC and CSC. Major relatively weak items are "Supervisor's care of safety rules

when a delay in production schedule occurs" and "Team members' speaking on safety on the week". This result indicates that management should effort to improve safety communication and system in SSC and CSC.

There are also many potential future studies. The relationships of SSC and CSC with many indicators such as safety motivation, safety behavior and safety performance can be examined. It is of great importance to conduct region-based studies in order to observe how these relations change, especially in countries with different cultures. In addition, studies such as the determination of the validity of the scales in different cultures and the development of scales for each region/sub-sector are among important potential studies.

References

1. Social Security Agency. Ankara; (2022).
2. Manzoor, B., Othman, I., Manzoor, M.: Evaluating the critical safety factors causing accidents in high-rise building projects. Ain Shams Eng J 12(3), 2485–92 (2021).
3. Suraji, A., Duff, AR., Peckitt, SJ.: Development of causal model of construction accident causation. J Constr Eng Manag 127(4), 337–44 (2001).
4. Zhang, W., Zhu, S., Zhang, X., Zhao, T.: Identification of critical causes of construction accidents in China using a model based on system thinking and case analysis. Saf Sci 21, 606–18 (2020).
5. Jaafar, MH., Arifin, K., Aiyub, K., Razman, MR., Ishak, MIS.: Samsurijan MS. Occupational safety and health management in the construction industry: a review. Int J Occup Saf Ergon 24(4), 493–506 (2018).
6. Hoła, B., Nowobilski, T., Szer, I., Szer, J.: Identification of factors affecting the accident rate in the construction industry. Procedia Eng 208, 35–42 (2017).
7. Zohar, D.: Safety climate in industrial organizations: Theoretical and applied implications. J Appl Psychol 65(1), 96–102 (1980).
8. Brown, RL., Holmes, H.: The use of a factor-analytic procedure for assessing the validity of an employee safety climate model. Accid Anal Prev 18(6), 455–70 (1986).
9. Dedobbeleer, N., Béland, F.: A safety climate measure for construction sites. J Safety Res 22(2), 97–103 (1991).
10. Shea, T., De Cieri, H., Vu, T., Pettit, T.: How is safety climate measured? A review and evaluation. Saf Sci 143, 105413 (2021).
11. Fugas, CS., Silva, SA., Meliá, JL.: Another look at safety climate and safety behavior: Deepening the cognitive and social mediator mechanisms. Accid Anal Prev 45, 468–77 (2012).
12. Zohar, D., Luria, G.: The use of supervisory practices as leverage to improve safety behavior: A cross-level intervention model. J Safety Res 34(5), 567–77 (2003).
13. Michael, JH., Guo, ZG., Wiedenbeck, JK., Ray, CD.: Production supervisor impacts on subordinates' safety outcomes: An investigation of leader-member exchange and safety communication. J Safety Res 37(5), 469–77 (2006).
14. Lingard, HC., Cooke, T., Blismas, N.: Safety climate in conditions of construction subcontracting: a multi-level analysis. Constr Manag Econ 28(8), 813–25 (2010).
15. Lingard, HC., Cooke, T., Blismas, N.: Properties of group safety climate in construction: the development and evaluation of a typology. Constr Manag Econ 28(10), 1099–112 (2010).
16. Newaz, MT., Davis, P., Jefferies, M., Pillay, M.: Using a psychological contract of safety to predict safety climate on construction sites. J Safety Res 68, 9–19 (2019).

17. Lingard, H., Cooke, T., Blismas, N.: Coworkers' response to occupational health and safety. Eng Constr Archit Manag 1;18(2), 159–75 (2011).
18. Brondino, M., Silva, SA., Pasini, M.: Multilevel approach to organizational and group safety climate and safety performance: Co-workers as the missing link. Saf Sci 50(9), 1847–56 (2012).
19. Gao, R., Chan, A., Utama, W., Zahoor, H.: Multilevel safety climate and safety performance in the construction industry: Development and validation of a top-down mechanism. Int J Environ Res Public Health 8;13(11), 1100 (2016).
20. Zohar, D., Luria G.: A multilevel model of safety climate: Cross-level relationships between organization and group-level climates. J Appl Psychol 90(4), 616–28 (2005).
21. Hair, JF., Black, WC., Babin, BJ., Anderson, RE.: Multivariate data analysis. 7th ed. Upper Saddle River, New Jersey: Pearson; (2010).
22. Abdul-Rashid, I., Bassioni, H., Bawazeer, F.: Factors affecting safety performance in large construction contractors in Egypt. In: Boyd, D (Ed) Procs 23rd Annual ARCOM Conference. Belfast UK; p. 661–70 (2007).
23. Fung, IWH., Tam, VWY., Sing, CP., Tang, KKW., Ogunlana, SO.: Psychological climate in occupational safety and health: the safety awareness of construction workers in South China. Int J Constr Manag 23;16(4), 315–25 (2016).
24. Liang, H., Zhang, S.: Impact of supervisors' safety violations on an individual worker within a construction crew. Saf Sci 120, 679–91 (2019).
25. Tam, CM., Zeng, SX., Deng, ZM.: Identifying elements of poor construction safety management in China. Saf Sci 42(7), 569–86 (2004).
26. Pandit, B., Albert, A., Patil, Y., Al-Bayati, A.: Fostering safety communication among construction workers: Role of safety climate and crew-level cohesion. Int J Environ Res Public Health 28;16(1), 71 (2018).
27. Sawacha, E., Naoum, S., Fong, D.: Factors affecting safety performance on construction sites. Int J Proj Manag 17(5), 309–15 (1999).

GEOTECHNICS

pages: 238 – 405

Exploring the Effects of Cement and Eggshell Powder Stabilisation on the Engineering Characteristics of Expansive Soils: An Experimental Study

Reem Alqaisi[1[0000-0002-7470-0101]], Thang Minh Le[1[0000-0003-1104-014x]], and Hadi Khabbaz[1[0000-0001-6637-4601]]

[1]University of Technology Sydney (UTS), Sydney, Australia
Reemomar.alqaisi@student.uts.edu.au, minhthang.le@alumni.uts.edu.au, hadi.khabbaz@uts.edu.au

Abstract. The process of improving soil characteristics is commonly conducted through soil stabilisation. This study aims to explore using natural waste products to achieve this goal. The disposal of waste materials in landfills can cause pollution and attract pests. Therefore, this research investigates the utilization of eggshell powder (ESP) in combination with cement to stabilise expansive soils and decrease the negative impact of waste materials on the environment. Laboratory tests, including pH, linear shrinkage, and unconfined compressive strength tests, were conducted on artificially manufactured expansive soil samples to evaluate the effects of adding ESP and cement. ESP was obtained from various sources and added to 6% cement in four different proportions (0, 2, 4, 6 and 8% ESP) in the total dry mass of the soil mixture. The results indicate that the combination of eggshell powder and cement increases the pH value and soil strength while decreasing the linear shrinkage. This suggests that this combination can be employed to stabilise expansive soil and reduce energy consumption when used as a filling material for road subgrades. The study also identifies the ideal proportion of eggshell powder and cement required for soil stabilisation.

Keywords Cement stabilisation, Eggshell powder, Expansive soils.

1 Introduction

Expansive soils, which are found in many parts of the world, exhibit damaging volume changes due to variations in moisture levels. These changes are called swelling and shrinking and are caused by clay minerals within the soil. Swelling can cause structures to lift while shrinkage can lead to a settlement that exceeds the subgrade's capacity. Civil engineers face a major challenge when dealing with expansive soils as they are detrimental on construction, including pavements, highways, buildings, and canals (Alqaisi, Le & Khabbaz 2019; Ito & Wagai 2017; Ramos et al. 2015). Thus, expansive soils cause severe distress to structures and pose a major challenge to civil engineers in

areas where such soils are infested (Abbey et al. 2021; Jones & Jefferson 2012; Obianyo, Onwualu & Soboyejo 2020).

Research has focused on soil stabilisation in recent years, particularly through the addition of stabilisers such as cement and lime for paving works. To improve the strength resulting from these stabilisers, cheaper additives like recycled waste materials are being explored. Solid wastes from domestic, agricultural, and industrial activities such as ESP, rice husk ash, and bagasse ash are potential options for modifying soil characteristics. Utilising recycled waste materials not only enhances the sustainability of the construction industry but also provides the added benefit of waste management (Ahmed & Issa 2014; Cokca 2001; Dang, Fatahi & Khabbaz 2016; Edil, Acosta & Benson 2006; Kharade et al. 2014; Kumar & Gupta 2016). This investigation is mainly concerned with chemical stabilisation techniques using cement and domestic waste namely eggshell powder. Eggshell waste is an abundant source of bio-waste, derived from various domestic sources such as homes, poultries, hatcheries, and bakeries. In the past, this waste has been recklessly dumped in open landfills, posing severe environmental and health hazards through the generation of toxic gases (Pradhan & Sahoo 2017). However, recent research suggests that this waste material can be employed to foster sustainable and cost-effective construction practices.

Studies have been conducted on eggshells as a calcium-based waste for various purposes in civil engineering, such as partial replacement of cement in concrete (Basit, Sharma & Kishor 2019), as a fine aggregate in concrete (Raji & Samuel 2015), as a filler in hot mix asphalt (Erfen, Tun & Onn 2015); as a stabilising binder for soil improvement (Muthu Kumar & Tamilarasan 2014a). A case study (Oluwatuyi et al. 2018) was presented to determine the results of laboratory evaluation of laterite soils stabilised with ground eggshell, cement and a mixture of both in a ratio of 1:1 for possible use as highway construction material. In some cases, eggshell powder and quarry dust have been added to clay soil to improve its strength properties and act as a stabilising agent (Thabet & Thiab 2019). Other studies have examined the suitability of using eggshell powder and lime as modifiers or stabilisers for black cotton soil in road construction (Amu, Fajobi & Oke 2005; Barazesh et al. 2012; Muthu Kumar & Tamilarasan 2014b; Nyankson et al. 2013; Olarewaju, Balogun & Akinlolu 2011; Walia & Singh 2015). Nevertheless, few investigations have been carried out to tackle the concerns regarding the stabilisation of expansive soil utilizing cement and eggshell powder (Al-Rawas, Hago & Al-Sarmi 2005; Ampera & Aydogmus 2005; Ismaiel 2006; Saride, Puppala & Chikyala 2013).

This experimental research explores the novel concept of combining eggshell powder and cement with synthetic expansive soil, with potential advantages for geotechnical engineering applications. It is worth mentioning that the authors have already explored the effect of adding eggshell powder and lime to the expansive soil (Alqaisi et al 2021). This study presents that the addition of cement can also be effective in the treatment of expansive soil.

1.1 Materials

Expansive Soil: To commence the experimental investigations, artificial soil samples were meticulously prepared using a blend of kaolinite Q38, Bentonite Active Bond 23, and Sydney fine sand (KBS). Both kaolinite and bentonite underwent the linear shrinkage test, conducted in accordance with the rigorous Australia Standard ('(AS-1289.3.4.1-2008 2016)'). The findings revealed that the white-coloured kaolinite exhibited significantly lower linear shrinkage (LS) when compared to the darker grey-coloured bentonite, recording a mere 9% versus an astonishing 35%. The liquid limit values for kaolinite and bentonite were also established as 50.5% and 340%, respectively, based on the Australian standard (AS-1289.3.9.1:2015 (2015)). To emulate the characteristics of expansive soil in Queensland, a blend of artificial soils was prepared with a consistent 30% bentonite, 65% kaolinite, and a 5% fine sand ratio based on total dry mass. The resulting linear shrinkage value was measured at 21.8%, closely resembling the black soil collected from a Queensland road construction site. For a comprehensive overview of the expansive soil's index properties, please refer to Table 1.

Table 1. Fundamental engineering properties of artificial expansive soil

Property	Value
Sand (%)	7.85
Silt/clay (%)	74.62
Liquid limit (%)	154.95
Plastic limit (%)	30.92
Plasticity index (%)	124.03
Linear shrinkage (%)	21.23
Specific gravity	2.64
Optimum moisture content (%)	29.04
Maximum dry density (kN/m^3)	13.23
Soil classification	CH

Eggshell Powder and Cement: The eggshell powder used in this study was sourced from a commercial shop in New South Wales, Australia that supplies food restaurants. The eggshells were cleaned and dried at 110°C before being ground and sifted through a 0.075mm sieve to create a uniform powder. A consistent eggshell powder was generated, which was subsequently utilized in various geotechnical assessments with the objective of enhancing soil properties when integrated with cement. The eggshell powder contained approximately 1.7% moisture and had a specific gravity of 2.4. Moreover, its linear shrinkage was assessed to be approximately 1.5%. Values for the uniformity and curvature coefficients were obtained through the use of sieving analysis, with respective values of Cu=1.7 and Cc=0.96. Therefore, based on the unified soil classification system (USCS), the eggshell powder can be categorized as SP-SM. Cement Australia was the source of the General Purpose (GP) commercial cement utilized in the study. When calcium carbonate, alumina, silica, and iron oxide are combined and subjected to high temperatures through calcination and sintering, GP

cements are generated, which produce a novel set of chemical compounds that can react with water. The chemical composition revealed that the quality of cement was high, and 62% of its composition was calcium oxide.

Table 2. Physical properties and chemical composition of ESP and cement

Physical properties			Chemical composition		
Property	Value		Components	Content (%)	
	ESP	cement		ESP	cement
Specific gravity	2.4	3.13	Ignition loss	3%	2%
Bulk density (kg/m^3)	700-800	400-600	CaO	47.49	61.80
pH	11.3	12.0	SiO_2	0.11	20.01
			Al_2O_3	-	5.02
			Fe_2O_3	Traces	3.12
			MgO	-	3.10
			SO_3	0.38	1.89
			K_2O	-	0.49
			Na_2O	0.14	0.13
			CO_2	-	2.5

2 Experimental Method

2.1 pH Tests

The ASTM D6276 (2006) procedure was used to determine the optimum cement content to stabilise the expansive soil. Various percentages of cement were mixed with the untreated expansive soil, eggshell powder, and water to ascertain their corresponding pH values. The pH measurements were carried out using a probe-equipped pH meter calibrated with buffer solutions with pH values of 4 and 7 in a constant temperature room. Soil samples were air-dried, sieved, and mixed with cement or eggshell powder blended with cement. The specimens were stirred continuously for an hour to ensure uniformity of the soil mixtures, and pH values of the slurries were measured at a constant temperature of approximately 25°C.

2.2 Linear Shrinkage Tests

The shrinkage limit tests were conducted following the standard protocol outlined in AS-1289.3.4.1-2008 (2016). The soil samples were prepared in accordance with the procedure specified in AS 1289.1.1 (AS 2001) for the preparation of disturbed soil samples meant for Atterberg limits and linear shrinkage. To perform the linear shrinkage tests, moulds were first greased, and then wet soil, close to its liquid limit, was placed inside them. The moulds were filled carefully to remove any air bubbles. The tests were conducted on artificial expansive soil samples, both untreated and treated with eggshell powder after they were cured for either 7 or 28 days.

2.3 Unconfined Compressive Strength Tests

The study conducted unconfined compression tests on soil samples treated with cement and eggshell powder as additives, as well as untreated samples. The tests were carried out in accordance with AS 5101. 4 (AS 2008a) standard and involved compacting the samples in steel split moulds with a diameter of 50 mm and height of 100 mm. The preparation of the samples was based on the optimal moisture content obtained from compaction tests on untreated soil. The maximum dry density of the treated soils was determined before placing them in the moulds, and the samples were sealed in plastic covers to prevent moisture loss during the curing process. The tests were conducted after 7 or 28 days of curing at a temperature-controlled room set at 25°C and 80% relative humidity. The unconfined compression tests were conducted using a Tritech loading frame, and the results were recorded using a computer data logger. The tests were repeated 3-4 times for each mixture to obtain the unconfined compressive strength values, and the final value was calculated by averaging the results.

3 Results and Discussion

The following sections present a discussion of the findings from the investigations on pH, linear shrinkage, and unconfined compressive strength. The cement utilized in this study met the criteria outlined in either AS 3972-2010 for General Purpose (GP) and Blended Cements (GB) or NZS 3122:1995 for Portland and Blended Cements (General and Special Purpose), based on the appropriate regulations (Andrews 2006). The soil studied was filtered through a 2.36 mm sieve, and the majority of the soil particles were finer than 0.425 mm, resembling fine sand in size.

3.1 Influence of Additives on the pH Values of the Treated Expansive Soil

Fig. 1a demonstrates how pH values change depending on the amount of cement content in the soil. The pH values were determined using the Eades & Grim (1966) test method. Upon analyzing the pH values, it was discovered that the most effective cement content for soil stability is about 6%. The pH value increased from 11.01 for untreated soil to 12.35 for soil treated with 6% cement. After reaching this point, the pH value remained steady.

The variations in pH values in mixtures are depicted in Fig. 1b, as the eggshell powder content changes. Fig.1b shows a comparison of the pH values of a 6% cement-stabilised expansive soil with different proportions of eggshell powder added, at different curing times. Referring to Fig. 1b, the pH values of cement and eggshell powder tend to decrease as the curing time increases. This decline in pH values may be due to a reduction in the concentration of calcium (Ca^{2+}) and hydroxyl (OH^{-}) ions, which is caused by pozzolanic reactions and the formation of ettringite resulting from the interactions between the soil, cement, and eggshell powder. The study revealed that the ideal proportion of eggshell powder to cement in a mixture used for stabilising expansive soil is roughly 6% (with 6% cement already present in the mixture). It should be observed that the rise in pH value (above 9) in stabilised soils may produce a

corrosive atmosphere for infrastructure. Hence, particular emphasis should be placed on the planning stage of the chemical treatment of expansive soil with cement to avoid any such potential hazards.

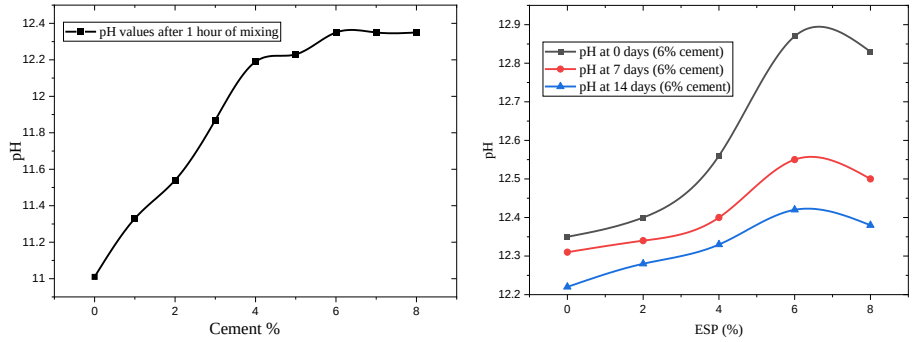

(a) (b)

Fig. 1. pH values: (a) cement stabilised expansive soil after 1 hour of mixing, (b) eggshell powder and 6% cement (ESP+ cement) stabilised expansive soil at different curing times.

3.2 Effects of Additives on Linear Shrinkage of Expansive Soil

Fig. 2a illustrates the impact of incorporating various ratios of eggshell powder into untreated expansive soil. The eggshell powder was added according to the soil's total dry weight, and the outcomes were measured after 7 and 28 days of curing. It is worth mentioning that the introduction of varying levels of eggshell powder resulted in a gradual reduction in linear shrinkage values. At the 7-day curing, linear shrinkage was found to decrease by 2.11%, 2.25%, 3.1%, and 4.99% by including 2%, 4%, 6%, and 8% eggshell powder, respectively. By adding eggshell powder during the 28-day curing process, there was a slight decrease in linear shrinkage. The addition of varying amounts of eggshell powder (2%, 4%, 6%, and 8%) resulted in reductions in linear shrinkage values of 4.1%, 5.31%, 6.67%, and 9.12%, respectively, after 28 days of curing.

To clarify, incorporating eggshell powder into the artificial expansive soil caused a decline in its linear shrinkage. This occurred due to the replacement of monovalent ions with divalent calcium ions, as found in studies by Bhuvaneswari et al. (2010) and Little (1995). Furthermore, the adsorption of calcium ions increased the pore fluid's viscosity, making more calcium ions available for ion exchange. This led to a rise in the concentration of electrolytes and the viscosity of the pore fluid. Another explanation is that the increase in electrolyte concentration in the pore fluid caused the diffused double layer (DDL) to decrease, as reported in research by Sivapullaiah and Jha (2014). Referring to Fig. 2b, it can be observed that adding 6% cement to the stabilised soil results in a further decrease in linear shrinkage (LS). This is because cement contains a high amount of calcium, which increases the availability of calcium ions. As a result, the addition of 6% cement led to a notable reduction in LS, decreasing from 21.2% to 13.1%, which is roughly an 8.1% reduction. The findings of the LS test indicate that

eggshell powder can have a significant impact on improving the shrinkage characteristics of cement-stabilised expansive soil after 7 days of curing, as demonstrated in Fig. 2b. When the eggshell powder was added to the cement-stabilised soil in concentrations ranging from 2% to 8%, the LS shrinkage decreased from 11.87% to 7.98%. The use of both eggshell powder and cement in soil stabilisation resulted in a greater reduction in LS compared to using cement or ESP alone. The addition of eggshell powder to the soil as an admixture result in the aggregation and flocculation of clay particles, which reduces the surface area of the clay. This phenomenon creates a coarser and less plastic soil admixture with less clay. Therefore, there is a significant decrease in linear shrinkage when increasing the amount of the additive during specific curing times.

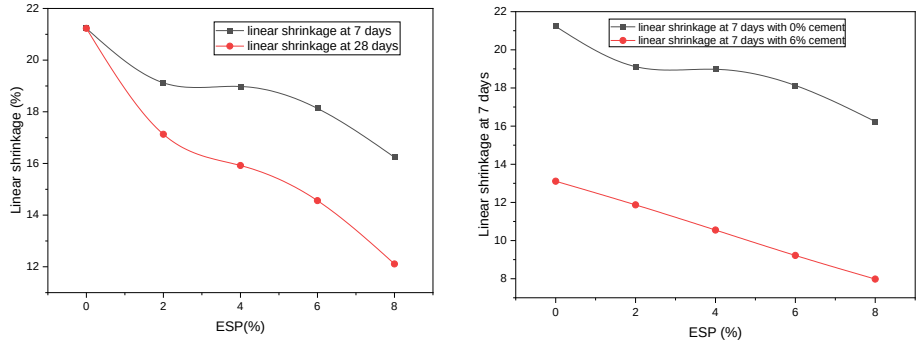

(a) (b)

Fig. 2. Linear shrinkage of the treated expansive soil versus (a) various ESP contents at 7 and 28 days of curing, (b) 6% cement and different ESP contents at 7 days of curing

3.3 Effects of Additives on UCS Values of Stabilised Expansive Soil

Fig. 3 and Fig. 4 demonstrate how the unconfined compressive strength of expansive soil samples changes when mixed with different amounts of eggshell powder and cement-eggshell powder, and then left to cure for 7 and 28 days, respectively. Fig. 3 shows how the flocculation process occurs in the soil specimens under these conditions. As can be observed in Fig. 3, there is an increase in the magnitude of UCS from 297 kPa to 339 kPa when 6% eggshell powder is added to the soil by dry weight. At 7 days of curing, it was found that the strength of the soil had improved by approximately 14%. However, it should be noted that the increase was not significant. Upon adding 8% eggshell powder to the soil, a sudden reduction in strength was noticed in contrast to its value at 6% eggshell powder addition. In other words, the addition of 8% eggshell powder resulted in a strength value of 302 kPa, which is still higher than the untreated soil. Nevertheless, the inclusion of 8% eggshell powder led to a minor 2% reduction in the strength of the stabilised expansive soil. After 28 days of curing, the unconfined compressive strength showed a significant increase with the addition of 6% eggshell powder, leading to a notable strength gain of around 25%. However, adding 8% eggshell powder resulted in a slight decrease in strength. Thus, it can be concluded that the optimal proportion of eggshell powder for stabilising the artificial expansive soil is

6%. Additionally, the soil's strength started to decrease beyond this point of addition. It seems that incorporating a small amount of eggshell powder boosted the soil's strength by hastening the rate of pozzolanic reaction, which resulted in increased strength. Nonetheless, as the percentage of eggshell powder increased, the soil's strength began to decline, according to Anoop et al. (2017).

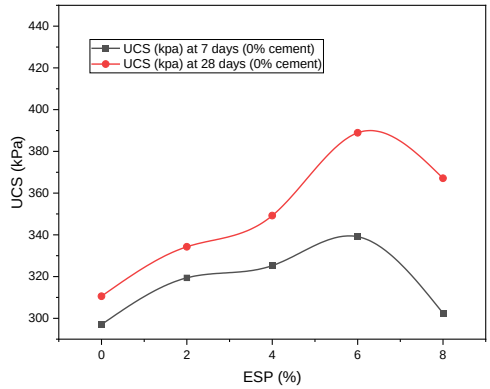

Fig. 3. Effect of eggshell powder on UCS of expansive soil samples after 7 and 28 days of curing

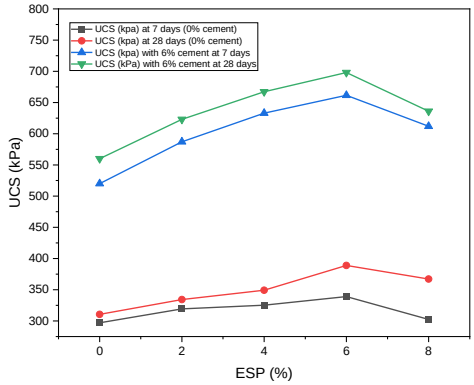

Fig. 4. Effect of eggshell powder and cement on UCS of treated expansive soil at 7 and 28 days of curing

The curves presented in Fig. 4 clearly show that the addition of cement to the expansive soil greatly increases the strength of the stabilised soil, with the strength rising from 297 kPa to 520 kPa after only 7 days of curing. Cement plays a critical role in speeding up the pozzolanic reaction, which leads to increased strength. Furthermore, supplementing the cement with 6% eggshell powder as a secondary additive resulted in an even greater increase in the strength of the stabilised soil, with the strength rising from 520 kPa to 662 kPa. However, the figure indicates that there is a limit to the amount of eggshell powder that can be added, as the strength of the soil began to decline when the percentage of eggshell powder increased. The results also show that longer curing times lead to higher UCS values, especially when 6% eggshell powder and 6%

cement are added. Increasing the curing time from 7 to 28 days resulted in a 5% increase in the UCS of soil samples treated with 6% eggshell powder and 6% cement. The findings indicate that the most effective combination for enhancing the strength of the stabilised expansive soil is 6% cement and 6% eggshell powder. The addition of large quantities of eggshell powder did not enhance the soil strength after 7 and 28 days of curing.

4 Conclusions

This study aimed to evaluate the effectiveness of eggshell powder (ESP) and its combination with cement as stabilisers for expansive soil. The results of the study showed that ESP had no significant impact on the geotechnical properties of stabilised expansive soils on its own. However, when used with cement, ESP had a remarkable effect on the shrinkage and strength of the soil. The optimal additive mixture for stabilising expansive soil was found to be 6% cement and 6% eggshell powder. The combination of ESP and cement had a significant impact on the linear shrinkage of stabilised soils, resulting in improved strength due to pozzolanic reactions between cementitious products associated with eggshell powder and clay particles. Soils stabilised with the ESP and cement combination displayed more flexibility than those treated with cement only. The best possible unconfined compressive strength (UCS) was achieved with the mixture of 6% cement and 6% eggshell powder, indicating its potential for stabilising problematic soil. This study shows that the use of eggshell powder and cement as Stabilisers for expansive soil is a promising approach that can improve soil strength and reduce linear shrinkage. Furthermore, the use of the cement-eggshell powder combination for expansive soil stabilisation could have the added benefit of reducing the environmental impact of domestic waste, such as eggshells.

References

1. Abbey, S.J., Eyo, E.U., Okeke, C.A. & Ngambi, S. 2021, 'Experimental study on the use of RoadCem blended with by-product cementitious materials for stabilisation of clay soils', Construction and Building Materials, vol. 280, p. 122476.
2. Ahmed, A. & Issa, U.H. 2014, 'Stability of soft clay soil stabilised with recycled gypsum in a wet environment', Soils and Foundations, vol. 54, no. 3, pp. 405-16.
3. Al-Kalili, A., Ali, A.S. & Al-Taie, A.J. 2022, 'A Review on Expansive Soils Stabilized with Different Pozzolanic Materials', Journal of Engineering, vol. 28, no. 1, pp. 1-18.
4. Al-Rawas, A.A., Hago, A. & Al-Sarmi, H. 2005, 'Effect of lime, cement and Sarooj (artificial pozzolan) on the swelling potential of an expansive soil from Oman', Building and Environment, vol. 40, no. 5, pp. 681-7.
5. Alqaisi, R., Le, T.M. & Khabbaz, H. 2019, 'Applications of recycled sustainable materials and by-products in soil stabilization', Springer, pp. 91-117.
6. Ampera, B. & Aydogmus, T. 2005, 'Recent experiences with cement and lime-stabilization of local typical poor cohesive soil', book: Veröffentlichungen des Instituts für Geotechnik der TU ergakademie Freiberg, pp. 2005-2.

7. Alqaisi, R., Le, M.T. and Khabbaz, H. (2021), Combined Effects Of Eggshell Powder and Hydrated Lime on the Properties of Expansive Soils. Australain Geomechanics Journal, Vol 56, No 1, pp. 107-118.
8. Amu, O., Fajobi, A. & Afekhuai, S. 2005, 'Stabilizing potential of cement and fly ash mixture on expansive clay soil', Journal of applied sciences, vol. 5, no. 9, pp. 1669-73.
9. Amu, O., Fajobi, A. & Oke, B. 2005, 'Effect of eggshell powder on the stabilizing potential of lime on an expansive clay soil', Journal of Applied Sciences, vol. 5, no. 8, pp. 1474-8.
10. Andrews, B. 2006, Guide to pavement technology: Part 4D: Stabilised materials.
11. Ashraf, M.A., Rahman, S.S., Faruk, M.O. & Bashar, M.A. 2018, 'Determination of optimum cement content for stabilization of soft soil and durability analysis of soil stabilized with cement', American Journal of Civil Engineering, vol. 6, no. 1, pp. 39-43.
12. Barazesh, A., Saba, H., Gharib, M. & Rad, M.Y. 2012, 'Laboratory Investigation of the Effect of Eggshell powder on Plasticity Index in Clay and Expansive Soils', European Journal of Experimental Biology, vol. 2, no. 6, pp. 2378-84.
13. Basit, K., Sharma, N.K. & Kishor, B. 2019, 'A review on partial replacement of cement by egg shell powder', Int. J. Innov. Technol. Explor. Eng.
14. Chen, F.H. 2012, Foundations on expansive soils, vol. 12, Elsevier.
15. Cokca, E. 2001, 'Use of class c fly ashes for the stabilizationof an expansive soil', Journal of Geotechnical and Geoenvironmental Engineering, vol. 127, no. 7, pp. 568-73.
16. Dang, L.C., Fatahi, B. & Khabbaz, H. 2016, 'Behaviour of expansive soils stabilized with hydrated lime and bagasse fibres', Procedia engineering, vol. 143, pp. 658-65.
17. de la Villa, R.V., Frías, M., de Rojas, M.I.S., Vegas, I. & García, R. 2007, 'Mineralogical and morphological changes of calcined paper sludge at different temperatures and retention in furnace', Applied Clay Science, vol. 36, no. 4, pp. 279-86.
18. Edil, T.B., Acosta, H.A. & Benson, C.H. 2006, 'Stabilizing soft fine-grained soils with fly ash', Journal of Materials in Civil Engineering, vol. 18, no. 2, pp. 283-94.
19. Erfen, Y.B., Tun, U. & Onn, H. 2015, 'The appropriateness of egg shell as filler in hot mix asphalt', J. Teknol. Malaysia.
20. Freire, M. & Holanda, J. 2006, 'Characterization of avian eggshell waste aiming its use in a ceramic wall tile paste', Cerâmica, vol. 52, pp. 240-4.
21. Gartner, E. 2004, 'Industrially interesting approaches to “low-CO2” cements', Cement and Concrete research, vol. 34, no. 9, pp. 1489-98.
22. Ismaiel, H.A.H. 2006, Treatment and improvement of the geotechnical properties of different soft fine-grained soils using chemical stabilization, Shaker.
23. Millogo, Y., Morel, J.-C., Traoré, K. & Ouedraogo, R. 2012, 'Microstructure, geotechnical and mechanical characteristics of quicklime-lateritic gravels mixtures used in road construction', Construction and Building Materials, vol. 26, no. 1, pp. 663-9.
24. Muthu Kumar, M. & Tamilarasan, V. 2014a, 'Effect of eggshell powder in the index and engineering properties of soil', Int J Eng Trends Technol, vol. 11, no. 7, pp. 319-21.
25. Muthu Kumar, M. & Tamilarasan, V. 2014b, 'Effect of Eggshell Powder in the Index and Engineering Properties of Soil', International Journal of Engineering Trends and Technology, vol. 11, no. 7, pp. 319-21.

Improving Geotechnical Monitoring System Performances by Integrating Advanced Technologies for Data Acquisition and Elaboration

Andrea Segalini[1[0000-0001-8023-9326]], Alessandro Valletta[1[0000-0001-9126-6717]], Marco Conciatori[1[0000-0002-8254-0347]], Andrea Carri[2[0000-0001-5800-7887]]

[1] Department of Engineering and Architecture, University of Parma, Parco Area delle Scienze 181/a, 43126 Parma, Italy,
andrea.segalini@unipr.it, alessandro.valletta@unipr.it, marco.conciatori@unipr.it
[2] ASE – Advanced Slope Engineering S.r.l., Via Robert Koch 53/a, 43123 Pilastrello (Parma),
andrea.carri@aseltd.eu

Abstract. In the present-day, there is a widespread recognition of the significance of monitoring activities in the geotechnical sector, offering numerous benefits in terms of safety assurance, validation of design assumptions, and risk management. Technological advancements have involved several elements of the geotechnical monitoring field, such as the introduction of multi-parameter sensors and automatic data loggers, and the implementation of high-performance calculators featuring increased computational power. Among the different available technologies, Internet of Things has become increasingly important in several fields of application, giving the possibility to connect different physical sensors through a communication network. In particular, these advantages play a key role in the development of Early Warning Systems (EWS) able to identify in real time the occurrence of a potentially critical event and disseminate appropriate messages. Another ground-breaking technology that has recently surfaced in the geotechnical field involves the implementation of algorithms based on Machine Learning into the data elaboration process. They deal with one of the main challenges posed by innovative instrumentation, related to the ability of sensors and monitoring techniques to provide a considerable amount of information, which should necessarily be addressed with automatic elaboration procedures. This study includes real-case examples and applications of these technologies, in order to highlight their importance in the monitoring process of different elements related to the geotechnical field.

Keywords: Geotechnics; Monitoring; Internet of Things; Machine Learning.

1 Introduction

When it comes to activities related to the geotechnical field, monitoring operations play a fundamental role to ensure safety, verify project assumptions, and collect useful information regarding the behavior of a specific element. These benefits are especially

important when man-made structures are involved, such as underground constructions [1-3], transport infrastructures [4-6], retaining walls [7,8], and civil buildings interacting with unstable slopes [9,10].

The increasing importance of these activities has been one of the main driving forces in the innovation process of the monitoring sector, ranging from the introduction of new sensors with improved performances to the implementation of advanced and methodologies for data elaboration and analysis [11]. The integration of these improvements has the main objective of providing efficient systems characterized by higher applicability, accuracy, and reliability compared to instrumentation based on more traditional approaches. In particular, the possibility to implement automatic processes allows to move towards a real-time monitoring approach, which is a key requirement when dealing with risk mitigation measures and early warning procedures [12].

2 Materials and Methods

2.1 Internet of Things (IoT)

One of the major advancements introduced by innovative instrumentations to overcome the so-called "manual philosophy" involves the integration of Internet of Things (IoT) technologies in the design process of automated monitoring systems. The basic principle of the IoT concept relates to the presence of a variety of sensors and devices that are able to communicate and interact with each other through an appropriate network to reach common objectives [13].

The integration of IoT-based devices results in a multi-layered architecture, where it is possible to identify four main components (Fig. 1). The first one is the perception layer, responsible for collecting the data thanks to a network of connected sensors. The following stage is dedicated to the transfer of collected dataset to the elaboration center for the subsequent processing operations. Therefore, the third layer involves dataset storage and elaboration, which is a fundamental step since traditional approaches are usually unable to manage the amount of data generated by an automatic system. Finally, the presentation layer allows to represent the monitoring outcomes through dedicated applications or web-based services.

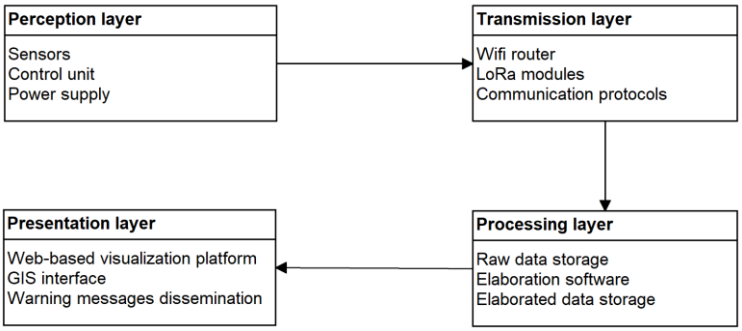

Fig. 1. Structure of a IoT-based monitoring system

A recent example of the integration of IoT technologies for improving monitoring system performances is represented by the Internet of Natural Hazards (IoNH) approach. IoNH represents a design concept where each component can interact and exchange data with each other, by exploiting a bidirectional remote control of different sensors and control units, and taking advantage of a cloud-based database, software, and representation platform. Moreover, the possibility to access and control by remote all connected devices significantly improve the system efficiency and functionality [14].

2.2 Machine Learning (ML)

Within the geotechnical monitoring framework, one of the most prominent challenges involves the ability of new sensors to provide a considerable amount of information. While this feature brings several advantages in the monitoring process, in turn it requires the development of specific processes for data management and elaboration.

A possible approach relies on the introduction of algorithms from the field of Machine Learning applied to the interpretation of available datasets. Machine Learning (ML) is a field of artificial intelligence that focuses on the development of algorithms and models that can learn from data, defining algorithms and techniques for automating solutions to complex problems that are hard to program using conventional programing methods [15]. ML techniques have key advantages in this context: since they learn directly from the examination of available datasets, they do not need explicit knowledge or models of the analyzed problem. They significantly benefit from the availability of large amount of information, improving their accuracy and applicability. Moreover, thanks to their adaptability, they can be customized to learn from many different sources like numeric measurements, images, text, or sound. This is especially important in more advanced systems, which often implement a multi-parameter approach to the monitoring activity, and therefore require technologies able to deal with different data typologies. The working principle of ML-based algorithms can be summarized in two distinct stages, named training and deployment (Fig. 2).

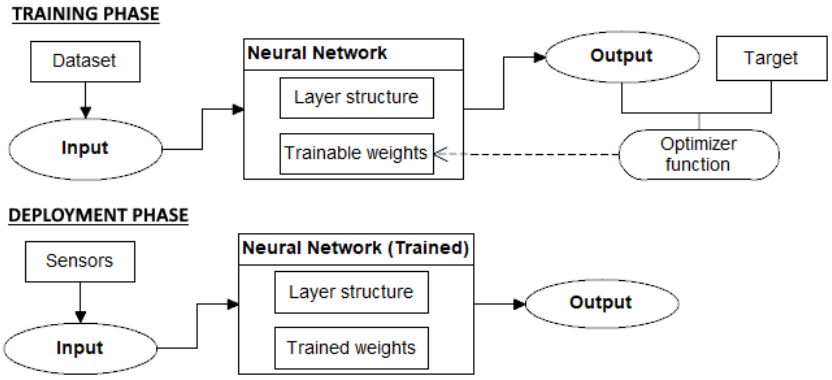

Fig. 2. Flow chart of the training and deployment phases

The training phase involves the transmission of all available data to the Neural Network (NN), which exploits this information to produce the desired output (e.g., forecasting the evolution of a specific, relevant parameters coming from monitoring activities). The loss function compares the outcome with the target and evaluates the network accuracy, while the optimizer function deals with the calibration of the NN in order to minimize the loss function value. The procedure aims to improve the ability of the model to interpret the behavior of the monitored element, allowing to achieve reliable outcomes from the elaboration of new datasets sampled during the monitoring activity.

At the end of the NN calibration process, the deployment phase relies on the trained Neural Network to analyze newly acquired monitoring data. Thanks to the short computational time needed for this task and taking advantage of the implementation of the previously discussed automatic procedures, the system is able to work with a near-real time approach.

3 Results and Discussion

3.1 Automatic Systems Integrating IoT Processes

This section reports an example of the integration of IoT-based technologies in a multi-parameter monitoring system, detailing the ability to detect specific events and disseminate appropriate messages. The case study here presented deals with the monitoring of a debris flow located near the Motorway A27 in Northern Italy, focusing both on the detachment and the transit areas in order to identify the landslide activation and evolution (Fig. 3).

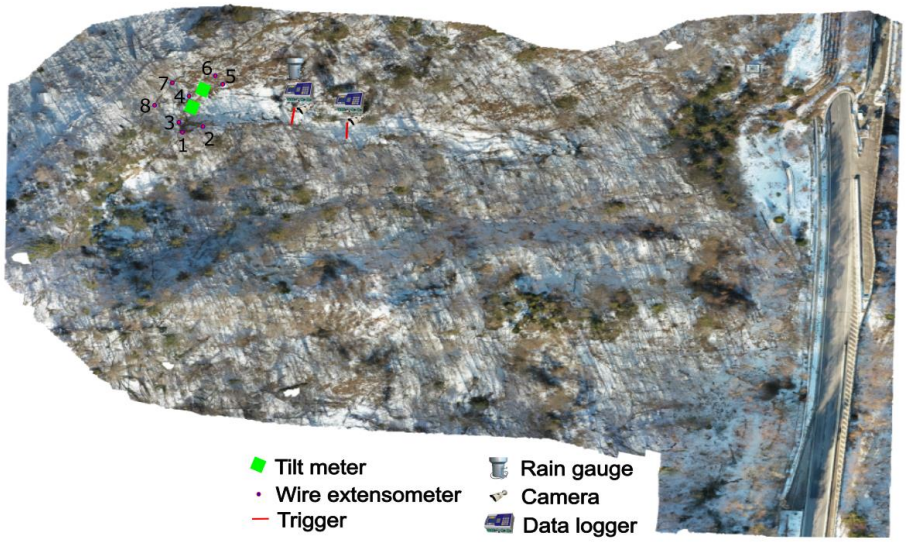

Fig. 3. Structure of the monitoring system installed near the A27 Motorway (Northern Italy)

The system integrates a total of 8 wire extensometers and 2 wireless tilt meters located in the upper part of the slope to study the behavior of the main scarp. The flow path is monitored with 2 devices, each one including a trigger and a camera, in order to identify the passage of debris in the channel. Finally, a rain gauge provides data regarding the rainfall in the area of interest. The presence of a multi-parameter automatic system based on different technologies and sensors makes it possible to compare the monitoring outcomes to find any correlation between available data.

The event here discussed dates back to 16th August 2021, when the rain gauge detected an intense rainfall event in the area, measuring close to 30 mm in a time span of a single hour. In the same time interval, information collected by other sensors located in different parts of the slope underlined the presence of an unusual behavior of the monitored element. In particular, one of the wire extensometers installed in the detachment area recorded a sudden deformation increase of 3.1 mm, while one of the trigger systems located in the transit area was activated by the passage of debris in the channel (Fig. 4). In turn, this caused the execution of two more operations: the camera connected to the activated trigger captured a picture of the debris flow channel, and an automatic message was disseminated to communicate the occurrence of the event. Finally, all collected data were uploaded on the dedicated web-based visualization platform. Thanks to the processes integrated in the monitoring system, all the previous operations were performed in near-real time, allowing the authorities responsible of the monitoring activity to obtain timely and reliable information regarding the evolution of the event.

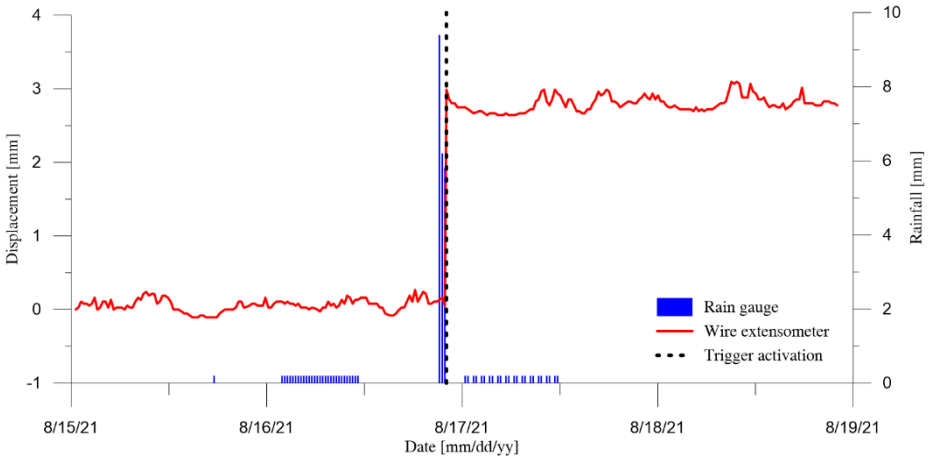

Fig. 4. Rainfall data and wire extensometer displacements recorded by sensors during the event occurred on August 16th, which caused the trigger activation

3.2 Training of ML-based algorithms

As previously stated, ML-based algorithms rely on the availability of previously collected monitoring data to train the Neural Network and improve its ability to generate reliable results. It is especially important to work with large datasets during the training phase, in order to provide a diverse range of examples and variations, enabling the model to capture a broader representation of the underlying patterns and relationships in the data. In this context, the ability of automatic systems to reach very high sampling frequencies plays a central role in the collection of large amounts of data in a relatively short time period.

The following example aims to underline the importance of these concepts, showing the evolution of the reliability of a Neural Network trained with datasets featuring different sizes. The case study deals with the monitoring of a retaining wall protecting a road that gave access to a tunnel in the French Alps. Two Vertical Array automatic inclinometers, integrating both MEMS sensors and piezometers, were installed on site to acquire information regarding the structure displacement and the water level variation over time [16].

In this case, the maximum amount of available information considered for the analysis includes the entire dataset collected during the monitoring period, amounting to 21621 records. From this, the corresponding training dataset was set as 70% of the total amount, thus obtaining 15134 values to carry on this stage of the process. Four additional scenarios were defined for the comparison, taking the total number of available data as the frame of reference. Specifically, new datasets were created by halving each time the number of data considered in the previous example, thus generating five datasets, with dimensions ranging from 15134 to 808 observations.

The evaluation of the performance for each training process was conducted by taking into consideration three different parameters, namely the loss function value, the Mean

Squared Error (MSE), and the Mean Absolute Error (MAE). The training procedure was repeated 10 times for each dataset, then the average value of the two best performing tests was considered for the comparison. Table 1 includes the number of values for each dataset and the outcomes of the corresponding training phase.

Table 1. Datasets dimension and corresponding outcomes for the training phase

Dataset ID	Number of training observations	Loss function	MSE	MAE
1	15134	0.00143	0.00075	0.00895
2	7567	0.00195	0.00102	0.01172
3	4305	0.01495	0.00794	0.06855
4	1782	0.02107	0.01133	0.08128
5	808	0.03574	0.02079	0.07634

It is possible to notice a steep increase in the loss function value as the number of available data is reduced, with a difference of one order of magnitude between Datasets 1 and 5. Moreover, as showed in Fig.5 a**,** the trend displayed by the parameter over the number of training observations follows an exponential behavior, with a coefficient of correlation equal to 0.89. As the training process aims to minimize the loss function value, it is quite evident how the low data availability negatively impacted the entire procedure, resulting in the creation of a Neural Network with lower reliability and precision.

A similar behavior, underlining the importance of the dataset dimension, emerges also from the analysis of the MSE and MAE values displayed in the bar plot in Fig. 5b. Once again, it is possible to note how the reduction of available information severely hindered the ability of the Neural Network of providing accurate predictions. In terms of MSE, Datasets 1 and 5 are separated by two orders of magnitude, with a similar trend compared to the one observed for the loss function. For what concern the MAE, the most substantial difference refers to the values obtained from Datasets 2 and 3, respectively equal to 0.01172 and 0.06885 as reported in Table 1.

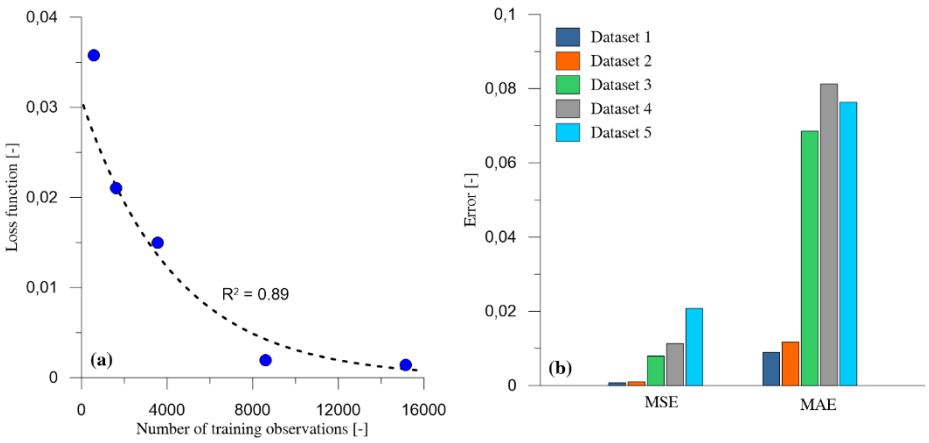

Fig. 5. (a) Loss function variation over the number of training observations; (b) Mean Squared Error (MSE) and Mean Absolute Error (MAE) values obtained for each dataset dimension

4 Conclusions

The introduction of a wide range of innovations, both in sensors and elaboration techniques, has proven to be a significant advancement in the field of civil engineering and monitoring systems. By integrating advanced technologies, engineers are better equipped to address the challenges posed by complex scenarios, giving the ability to take timely actions that can help prevent accidents, reduce maintenance costs, and prolong the lifespan of structures.

Examples included in this paper showed some of the practical benefits of the implementation of such technologies in monitoring systems. The possibility of integrating multi-parameter devices and IoT-based procedures gives the ability to derive meaningful cause-effect correlations between different factors, providing near-real time information regarding the evolution of a selected element. Moreover, they allow for the collection of consistent amounts of data in a relatively short time period, which is a key element for the training and application of advanced algorithms based on Artificial Intelligence and Machine Learning.

Acknowledgements
Project funded under the National Recovery and Resilience Plan (NRRP), Mission 4 Component 2 Investment 1.5 - Call for tender No. 3277 of 30/12/2021 of Italian Ministry of University and Research funded by the European Union – NextGenerationEU. Project code ECS00000033, Concession Decree No. 1052 of 23/06/2022 adopted by the Italian Ministry of, CUP D93C22000460001, “Ecosystem for Sustainable Transition in Emilia-Romagna” (Ecosister), Spoke 4.

References

1. Di Giulio, A., Sebastiani, D., Cinelli, M., Ginanneschi, R., Zanetto, G., Antonelli, A., Leone, C.: Performance evaluation and monitoring of the tunnel excavation with a Mobile Tunnel Borer. IOP Conf. Ser.: Earth Environ. Sci. 833, 012198 (2021). https://doi.org/10.1088/1755-1315/833/1/012198
2. Cuervas-Mons, J., Zêzere, J.L., Domínguez-Cuesta, M.J., Barra, A., Reyes-Carmona, C., Monserrat, O., Oliveira, S.C., Melo, R.: Assessment of Urban Subsidence in the Lisbon Metropolitan Area (Central-West of Portugal) Applying Sentinel-1 SAR Dataset and Active Deformation Areas Procedure. Remote Sensing. 14, 4084 (2022). https://doi.org/10.3390/rs14164084
3. Savi, R., Carri, A., Cavalca, E., Valletta, A., Segalini, A.: Application of innovative monitoring tools for safety and alert procedures in road tunnels. Transportation Research Procedia. 40, 1540–1547 (2019). https://doi.org/10.1016/j.trpro.2019.07.213
4. Anigacz, W., Beben, D., Kwiatkowski, J.: Displacements Monitoring of Suspension Bridge Using Geodetic Techniques. In: Conte, J.P., Astroza, R., Benzoni, G., Feltrin, G., Loh, K.J., and Moaveni, B. (eds.) Experimental Vibration Analysis for Civil Structures. pp. 331–342. Springer International Publishing, Cham (2018)
5. Hodas, S., Izvoltova, J., Chromcak, J., Bacova, D.: Monitoring the Geometric Position of Transition Zones to Increase the Quality and Safety of Railway Lines. Applied Sciences. 12, 6038 (2022). https://doi.org/10.3390/app12126038
6. Kiani, N., Abedin, M., Steputat, C.C., Mehrabi, A.B., Nanni, A.: Structural Health Monitoring of FRP-Reinforced Concrete Bridges Using Vibration Responses. In: Rizzo, P. and Milazzo, A. (eds.) European Workshop on Structural Health Monitoring. pp. 735–744. Springer International Publishing, Cham (2023)
7. Carlà, T., Macciotta, R., Hendry, M., Martin, D., Edwards, T., Evans, T., Farina, P., Intrieri, E., Casagli, N.: Displacement of a landslide retaining wall and application of an enhanced failure forecasting approach. Landslides. 15, 489–505 (2018). https://doi.org/10.1007/s10346-017-0887-7
8. Drusa, M., Vlcek, J.: Importance of Results Obtained from Geotechnical Monitoring for Evaluation of Reinforced Soil Structure – Case Study. Journal of Applied Engineering Sciences. 6, 23–27 (2016). https://doi.org/10.1515/jaes-2016-0002
9. Ciampalini, A., Bardi, F., Bianchini, S., Frodella, W., Del Ventisette, C., Moretti, S., Casagli, N.: Analysis of building deformation in landslide area using multisensor PSInSARTM technique. International Journal of Applied Earth Observation and Geoinformation. 33, 166–180 (2014). https://doi.org/10.1016/j.jag.2014.05.011
10. Liu, W., Yan, S., He, S.: Landslide damage incurred to buildings: A case study of Shenzhen landslide. Engineering Geology. 247, 69–83 (2018). https://doi.org/10.1016/j.enggeo.2018.10.025
11. National Research Council: Geological and Geotechnical Engineering in the New Millennium: Opportunities for Research and Technological Innovation. National Academies Press, Washington, D.C. (2006)
12. Valletta, A., Carri, A., Segalini, A.: Innovative monitoring instruments as support tools for natural risks management. ROL. 48/2019, (2019). https://doi.org/10.3301/ROL.2019.44
13. Atzori, L., Iera, A., Morabito, G.: The Internet of Things: A survey. Computer Networks. 54, 2787–2805 (2010). https://doi.org/10.1016/j.comnet.2010.05.010
14. Carri, A., Valletta, A., Cavalca, E., Savi, R., Segalini, A.: Advantages of IoT-Based Geotechnical Monitoring Systems Integrating Automatic Procedures for Data Acquisition and Elaboration. Sensors. 21, 2249 (2021). https://doi.org/10.3390/s21062249

15. Rebala, G., Ravi, A., Churiwala, S.: Machine Learning Definition and Basics. In: Rebala, G., Ravi, A., and Churiwala, S. (eds.) An Introduction to Machine Learning. pp. 1–17. Springer International Publishing, Cham (2019)
16. Segalini, A., Valletta, A., Carri, A., Cavalca, E.: Monitoring of a retaining wall with innovative multi-parameter tools. In: Proceedings of the 4th Regional Symposium on Landslides in the Adriatic—Balkan Region., Sarajevo, Bosnia and Herzegovina (2019)

Micromechanical Modeling of the Dynamic Response of A Sand Deposit

Said Derbane[1][orcid:0009-0003-7773-5806], Mouloud Mansouri[2][orcid:0000-0002-4179-7488], Salah Messast[3] and A. El Malki Alaoui[4][orcid:0000-0003-1357-8509]

[1,3] Department of Civil Engineering, LMGHU Laboratory, University of 20 August 1955 Skikda, BP 26, 21000, Skikda, Algeria
derbane_said@yahoo.fr
[2] Department of Civil Engineering, University of Ferhat Abbas Sétif 1, Sétf 19000, Algeria
mansouri_m@yahoo.com
[4] ENSTA Bretagne, IRDL, UMR 6027, CNRS, 29806 Brest, France

Abstract. This paper presents a numerical study of shear wave propagation in a vertical sand profile through micromechanical modeling. For this purpose, a 2D modeling by the Discrete Element Method (DEM) is carried out. The DEM model is based on molecular dynamics with the use of circular shaped elements. The intergranular normal forces at contacts are calculated through a linear viscoelastic law while the tangential forces are calculated through a perfectly plastic viscoelastic model. Rolling friction is incorporated to account for the damping of the grains rolling motion. Different boundary conditions of the profile have been implemented; a bedrock at the base, a free surface at the top and periodic boundaries in the horizontal direction. The sand deposit is subjected to a harmonic excitation at the base. The simulations carried out have well reproduced the elastic and damping features relative to shear wave propagation in a vertical soil deposit. The could be a good tool to assess the analytical solutions for highly damped situations.

Keywords: Sand Profile, Micromechanical Model, Discrete Element Method, Wave Propagation.

1 Introduction

The seismic wave propagation from the bedrock to the free ground surface depends strongly on the nature of the traversed soil layers. Especially, it is known that stiffness and damping of these layers have significant effects on the transmission of the motion. For granular soils these two properties i.e. stiffness and damping depend on the applied movement characteristics such as amplitude and frequency, as well as on certain soil state parameters, such as confining and density states. The classical methods used in the analysis of the movement transmission and its amplification from the bedrock to the surface are usually based on continuum mechanics. These methods work well for cohesive soils, however for granular soils, given the discontinuous nature of the

material, a discrete element modeling could provide more understanding to the involved mechanisms.

The modeling of wave propagation by the discrete element method is recently used to characterize the shear modulus and the damping of granular materials for low frequencies; Zamani and El Shamy [1]. A study of the parameters influencing the attenuation of wave amplitudes for a set of grains of the same diameter is presented in the work of Martin et al [2]. O'Donovan et al [3] have analyzed the micromechanical response of a granular material subjected to a dynamic wave propagation, they focused on grain displacements and intergranular contact forces. The influence of force chains has been treated to characterize wave scattering and attenuation in granular soils; Peters and Muthuswamy [4], Longlong and Shunhua Zhou [5].

In the present work, a 2D numerical study of the shear wave propagation in a vertical sand profile is performed. For this objective, a model of discrete elements is developed, numerical simulations have been carried out to study the response of the profile to movements with different amplitudes and frequencies. The analysis of the propagation is done in time domain, the nonlinear behavior of the material is inherently taken into account in this model. This numerical approach allows us to understand a number of essential characteristics of wave propagation, including motion amplification and damping.

2 Discrete Element Methods for Granular Materials Modeling

The discrete element method employed in this work is based on the molecular dynamics method. It models granular materials at the micromechanical scale using independent elements. The grains of the material interact at the contact points and each grain interacts with its neighbors and develops contact forces. It is assumed that the global deformation of the medium is mainly due to the relative motions of the grains considered as rigid bodies [6, 7]. The choice of a simple shape of the grains plays an important role in the optimization of the modeling time [8]. the most used shapes are discs for a two-dimensional 2D modeling and spheres for the three-dimensional 3D case. The contact forces are calculated through simple models based on a slight overlap of the grains [9, 10].

2.1 Equations of Motion

The movement of the grains controls the overall behavior of the medium, this movement obeys to the Newton's second law (equation 1), which is used to obtain the accelerations of the grains.

$$\begin{cases} m_i \ddot{\vec{x}}_i = \sum_j \vec{F}_{ij}^{contact} + m_i \vec{g} \\ I_i \ddot{\vec{\varphi}}_i = \sum_j \vec{M}_{ij}^{contact} + m_i \vec{g} \end{cases} \quad (1)$$

With $\vec{\ddot{x}}_i$ and $\vec{\ddot{\varphi}}_i$ represent respectively the translational and rotational accelerations of the grains, m_i and I_i are the mass and the moment of inertia respectively, $\vec{F}_{ij}^{contact}$ is the interaction force applied by a grain j in contact with grain i, $\vec{g}$ is the acceleration due to gravity and $\vec{M}_{ij}^{contact}$ is the moments caused with respect to the center of gravity of grain i by the contact forces $\vec{F}_{ij}^{contact}$.

2.2 Interaction Between Grains

Contact Forces

A simplified decomposition is used to study contact forces; a normal component $\vec{F}_n$ and a tangential component $\vec{F}_s$ included in the plane tangent to the grain at the point of contact [11].

The Normal Contact Force is presented by a viscoelastic model (Fig.1.a), $\vec{F}_n$ is given by [12]:

$$\vec{F}_n = (-k_n D_n - \nu_n V_n).\vec{n} \tag{2}$$

Where k_n is the elastic constant, ν_n is the viscous damping constant and V_n is the normal velocity.

The normal distance between two grains i and j denoted D_n is defined geometrically by:

$$D_n = \left\|\vec{x}_j - \vec{x}_i\right\| - r_i - r_j \tag{3}$$

In which r_i and r_j are the radii of grains i and j.

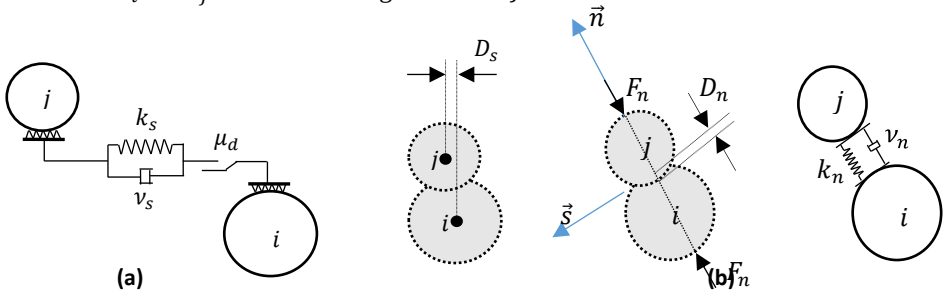

Fig. 1. Normal force (a) and shear force (b) between grains

The tangential contact force is computed through a viscoelastic model with friction (Fig.1.b) [12], $\vec{F}_s$ is given by:

$$\vec{F}_s = min(k_s D_s + v_s V_s,\ \mu_d F_n)\vec{s} \tag{6}$$

Where k_s is the tangential stiffness, v_s the viscous damping coefficient, μ_d is the inter-particle coefficient of friction, D_s is the grain deformation due to shear force. V_s is the tangential velocity of grain j with respect to grain i.

Contact Duration and Time Step Integration

The duration of a contact t_c and the integration time step Δt are given by [7]:

$$t_c = \pi\sqrt{\frac{m_{eff}}{k_n}} \text{ and } \Delta t_{max} \approx 0.1\pi\sqrt{\frac{m_{eff}}{k_n}} \quad (7)$$

Where m is the smallest effective mass in the system.

2.3 Wave Propagation Modeling

In the present work, a 2D modeling of shear wave propagation in a vertical sand profile is carried out. The model used for this purpose is based on a discrete element modeling and implemented in a C^{++} code.

The grains of the sand profile are pluviated under gravity to form a dense deposit. Different boundary conditions are considered: periodic boundaries have been introduced to represent an infinite profile in the horizontal direction, the upper surface is considered free and the profile is delimited and supported at the base by a wall which is considered as a bedrock. A chain of grains is introduced onto this bedrock, through which a controlled horizontal displacement is applied. The interactions between the grains of the chain and the deposit grains are treated with the same interaction models used in the interactions of the deposit grains.

In order to study the shear wave propagation in the profile, a harmonic displacement with specific amplitude and frequency is applied to the grain chain at the bottom of the profile. The deposit is divided into a defined number of layers in which the average displacements is monitored during the excitation of the profile.

3 Analytical Solutions of Wave Propagation in Soil Profiles

The results obtained by the DEM model will be compared with the analytical solution based on continuum model presented in [13]. The differential equation of motion for a damped medium is:

$$\frac{1}{c^2}\frac{\partial^2 u}{\partial t^2} = \frac{\partial^2 u}{\partial z^2} + \frac{2\xi}{\omega}\frac{\partial^3 u}{\partial t \partial z^2} \quad (9)$$

Where c is wave velocity, ξ is damping parameter, ω the pulsation.
For harmonic excitation, the final solution of this equation is:

$$\frac{A.u(z,t)}{u_0} = \cosh(ph)\cos(qh)\cosh(pz)\cos(qz)\sin(\omega t) + \sinh(ph)\sin(qh)\sinh(pz)\sin(qz)\sin(\omega t) + \cosh(ph)\cos(qh)\sinh(pz)\sin(qz)\cos(\omega t) - \sinh(ph)\sin(qh)\cosh(pz)\,\mathrm{coc}(qz)\cos(\omega t) \quad (10)$$

$$A = cosh^2(ph) - sin^2(qh) \quad (11)$$

p and q must be determined from the equations

$$p^2 + q^2 = \frac{\omega^2/c^2}{1+4\xi^2} \text{ et } 2pq = 2\xi\frac{\omega^2/c^2}{1+4\xi^2} \quad (12)$$

4 Results of Numerical Simulations and Discussion

4.1 Model Parameters

Fig.3 shows the sand profile model subjected to a base excitation, the different boundary conditions are indicated.

The properties of the grains as well as the micromechanical parameters used in the computation of the contact forces between the grains are presented in Table 1.

Table 1. Simulation parameters.

Parameters	Value
Grains number	5000
Grain radius r_i	$1.00\text{x}10^{-3}$ to $2.00\text{x}10^{-3}m$
Density G_s	2600 kg/m^3
Contact normal stiffness k_n	$1.2\ \text{x}10^6 N/m$
Contact shear stiffness k_s	$9.6\text{x}10^5 N/m$
Inter-particle friction coefficient μ	0.5

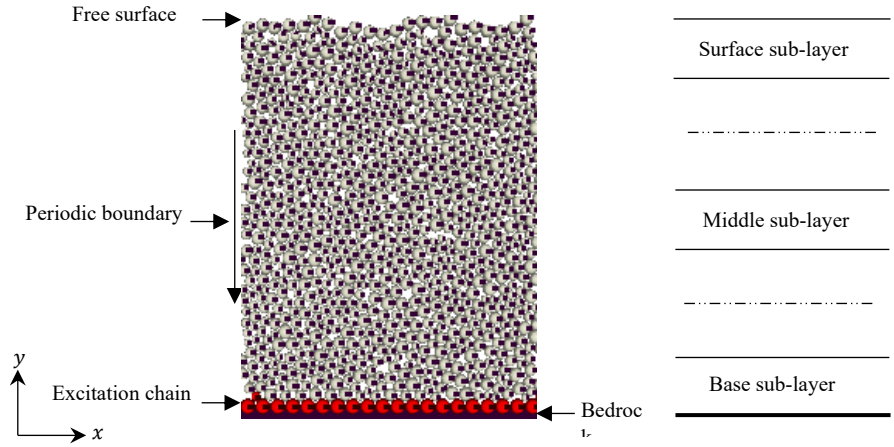

Fig. 2. Sand profile and boundary condition

This sand profile is built by pluviating grains under gravity and after stabilization of a number of 5000 grains throughout a 0.4 m large profile. The obtained profile is subjected to a harmonic excitation at its base $u(t) = a_0 \sin(ft)$ with $a_0 = 4x10^{-4}m$ and $f = 30Hz$. The dynamic amplification factor (DAF) at the free profile surface is defined as:

$$DAF = \frac{a}{a_0} \tag{15}$$

Where a denotes the displacement amplitude at the free surface; a_0 is the displacement amplitude at the bedrock i.e. the base excitation.

4.2 Analysis of Shear Wave Propagation in the Sand Profile

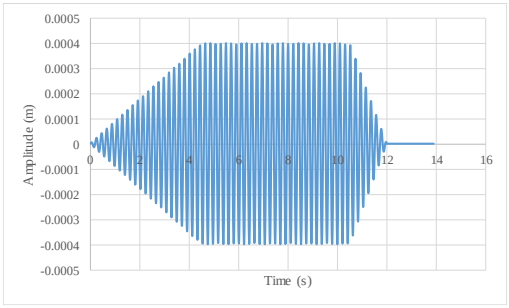

(a)

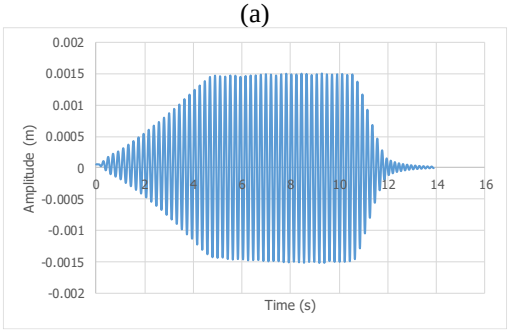

(b)

Fig. 3. Variation of the excitation amplitude at the bedrock and the response of profile

In order to avoid the perturbations due to transient response of the profile, the amplitude of the excitation is gradually increased during 4.5 seconds to reach a maximum of $4x10^{-4}\,m$, maintained for 6 seconds before gradually decreasing and reaching zero during 1.5 seconds (Figure 3a).

The propagation of the horizontal motion throughout the profile is carried out by dividing the profile into 10 sub-layers, in which the average displacement in each sub-layer is monitored. Fig. 3b presents the displacement at top sub-layer during the excitation. This figure shows that the soil experiences a damped vibration after ending the excitation, this means that the deposit exhibits an elastic damped behavior.

Fig.4 shows the response of the sand deposit at steady-state vibration i.e. between 4.5s and 10.5s.

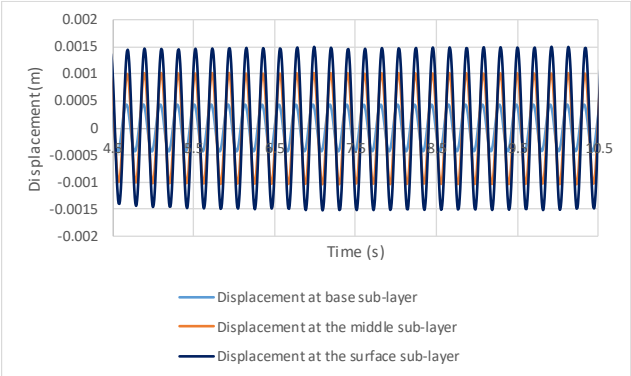

Fig. 4. Variation of displacement from the base to the surface

We note in these figure the presence of progressive amplification of the motion from the base to the surface. The amplification ratio (DAF) of the maximum displacement is at the top sub-layer with a value of 3.77.

Figure 5 shows the dynamic amplification ratio at different levels of the deposit.

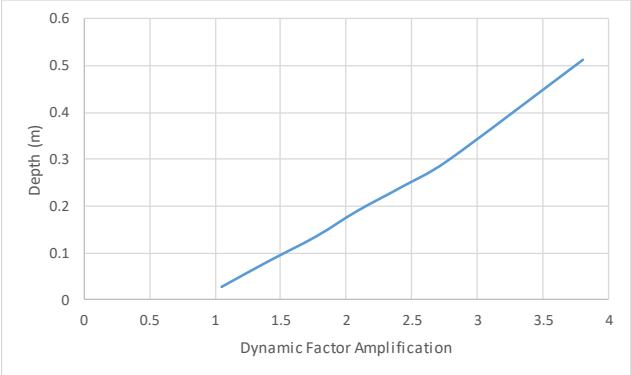

Fig. 5. Variation of the dynamic amplification factor

This figure clearly indicates that the movement increases with height. Such a remark reveals that the excitation frequency is lower than the first natural frequency (fundamental frequency) of the deposit.

4.3 Influence of the Profile Stiffness on Wave Propagation

In order to study the dynamic response of a deep layer, a variation of the stiffness of the sand profile is applied through an increase in gravity acceleration from $5g$ up to $25g$. An analysis of the displacement at the free-surface is made for the different values of gravity acceleration g (m/s^2). Fig.6 shows the influence of the increase in gravity acceleration on the displacement on the surface.

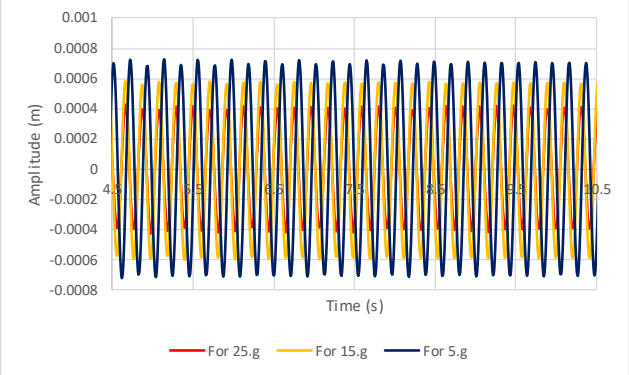

Fig. 6. Effect of the variation of gravity acceleration on the amplification of the displacement at the free-surface of the sand profile.

It is observed that the increase in gravity decreases the amplification of the displacement at the free surface. The variation of the vibration amplitude at the top layer of the deposit versus the gravity acceleration is shown in figure 7.

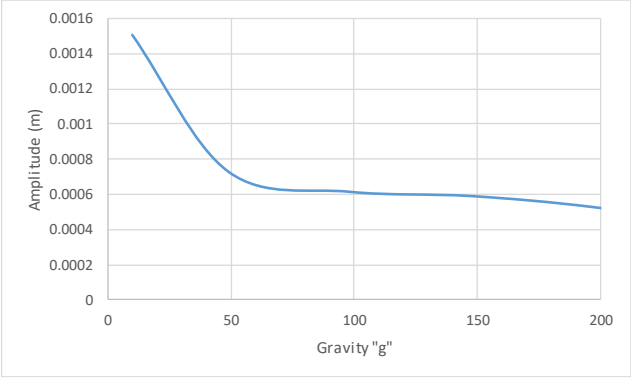

Fig. 7. Variation of the amplitude at the free-surface as a function of variation of gravity g

This figure 7 shows that the movement amplification decreases with the increase of gravity acceleration and tends to unit value for higher gravity acceleration values.
It could be concluded that the increase in gravity makes the sand profile stiffer, which greatly reduces the amplification of surface motion. This result is in accordance with theoretical knowledge which states that the most rigid profiles such as rocks do not amplify seismic movement.

4.4 Comparison of the Analytical Solution with DEM Modeling With

In a next step, the granular deposit is assumed a continuum with unknown stiffness and damping properties. In order to obtain these properties, we performed an inverse analysis by varying the parameters of the analytical model (wave velocity and damping, Eqt.10) until obtaining an analytical solution close to the results of the DEM modeling.

For the excitation frequency of 30rad/s, the displacements at the different depths of the analytical model are very close to the results of the DEM modeling for a wave velocity of 12.5 m/s and a damping of $\xi = 8\%$ for the analytical model. Figures 8 and 9 present respectively, the displacements at the different depths of the DEM model and those of the analytical solution for a soil with a wave velocity of 12.5 m/s and a damping of $\xi = 8\%$.

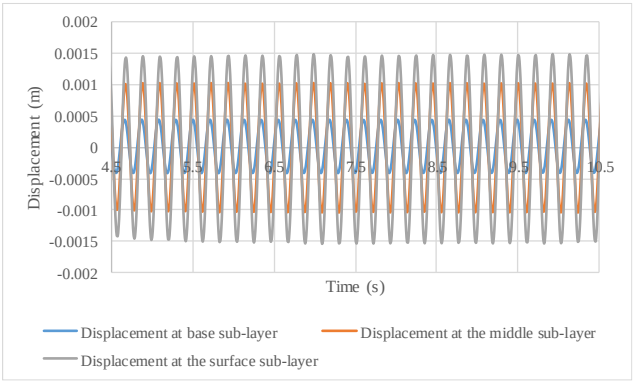

Fig. 8. Displacements at the different depths from the DEM model

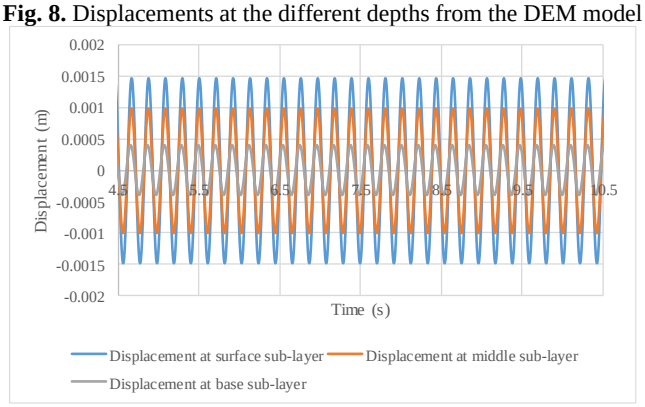

Fig. 9: displacements at the different depths from the analytical model

By comparing these graphical representations, the concordance between the two solutions is well demonstrated. It should be noted that with the obtained characteristic wave propagation of the deposit (12.5 m/s), the fundamental natural frequency is 38,17rad/s. This result confirms remark mentioned above, indicating that the excitation frequency (30rad/s) is lower than the deposit's fundamental frequency ($\omega_1 = \frac{\pi.c}{2.h} = 38{,}17 rad/s$).

It will be interesting in future works, to show by similar inverse analysis the effects of the movement parameters on the characteristic stiffness and damping parameters of the deposit. Moreover, it will be interesting to find up to which movement parameters, the analytical solution approximates well the displacements in the deposit.

5 Conclusion

The Discrete Element Model presented in this paper deals with a two-dimensional modeling of wave propagation in a granular material deposit. Several simulations have been performed to understand the response of granular materials under harmonic excitations applied at the bedrock. Dynamic responses of the deposit such as variation of displacement with time and depth, amplification of the motion and the effect of increasing profile stiffness were studied. In addition, an inverse analysis by varying the parameters of the analytical model (wave velocity and damping) until obtaining an analytical solution close to the results of the DEM modeling. The obtained results show the reliability of the use of the present DEM model to simulate the wave propagation in such a deposit. The simulations carried out, indicated that:

- The deposit exhibits an elastic damped behavior.
- The motion is amplified progressively from the bedrock until the top free surface.
- The increase of the gravity acceleration makes the sand deposit stiffer and decreases the amplification of the displacement at the free surface. The dynamic amplification factor tends to unit value for higher gravity acceleration values.

The inverse analysis carried out allowed the determination of characteristic stiffness and damping properties of the deposit. It will be interesting in future works, to show by similar inverse analysis the effects of the movement parameters on the characteristic stiffness and damping parameters of the deposit. Moreover, it will be interesting to find up to which movement parameters, the analytical solution approximates well the displacements in the deposit.

References

1. Natasha Zamani, Usama El Shamy (2011), Analysis of wave propagation in dry granular soils using DEM simulations. Acta Geotechnica (2011) 6:167–182
2. Martin H. Sadd, Gautam Adhikari, Francisco Cardoso (2000), DEM simulation of wave propagation in granular materials, Powder Technology 109 Ž2000. 222–233.
3. O'Donovan and al (2016), Micromechanics of seismic wave propagation in granular materials, Granular Matter (2016) 18:56
4. J. F. Peters, M. Muthuswamy (2005), Characterization of force chains in granular materia, Phys. Rev. E 72, 041307.
5. Longlong Fu, Shunhua Zhou (2023), Characterizing dynamic load propagation in cohesionless granular packing using force chain, Particuology 81 (2023) 135e143.
6. Pöschel T, Schwager T. Computational Granular Dynamics - Models and Algorithms, Springer-Vrlag: Berlin Heidelberg, 2005.
7. Mansouri M, El Youssoufi MS, Numerical simulation of the quicksand phenomenon by a 3D coupled Discrete Element - Lattice Boltzmann hydromechanical model, Int. J. Numer. Anal. Meth. Geomech. (2016), DOI : 10.1002/nag
8. X. Tang, J. Yang (2021), Wave propagation in granular material: What is the role of particle shape?, Journal of the Mechanics and Physics of Solids 157 (2021) 104605.
9. Richefeu. V, (2005), Approche par éléments discrets 3D du comportement de matériaux granulaires cohésifs faiblement contraints, thèse Université Montpellier II - Sciences et Techniques du Languedoc, 2005. Français. NNT: tel-00012112.
10. Cundall PA, Strack ODL (1979) A discrete numerical model for granular assemblies. Géotechnique 29(1):47–65.

11. J.Y. Delenne, M.S. El Youssoufi, F. Cherblanc, J.C. Bénet, Int. J. Numer. Anal. Methods Geomech. 28, 1577 (2004)
12. Fakih M, Delenne J-Y, Radjai F, Fourcaud T (2019) Root growth and force chains in a granular soil. Phys Rev E 99(4):042903.
13. Verruijt, A. (2009). An introduction to soil dynamics (Vol. 24). Springer Science & Business Media.

Linear Equivalent Seismic Response of A Surface Foundation Excited by A Harmonic Rayleigh Wave

Badreddine Sbartai[1][0000-0002-8784-3830] and Hamoudi Belkhir[2]

[1] Civil Engineering Department, LMGE Laboratory, Badji Mokhtar-Annab University, Algeria
badreddine.sbartai@univ-annaba.dz
[2] Civil Engineering Department, LMGHU, University of Skikda, Algeria
belkhir.doct2018@gmail.com

Abstract. The main objective of this paper is to analyse the effect of the non-linear behaviour of the soil on the seismic response of a foundation by taking into account the soil-structure interaction. The foundation is square-shaped, and rigid, resting on the surface of a homogeneous semi-infinite soil, and solicited only by the incident harmonic wave of Rayleigh. However, for higher deformations (during strong earthquakes), the behaviour of the soil will be characterised by a nonlinear behaviour law. The phenomenon of soil nonlinearity due to the seismic excitation imposed on the soil is reflect in the curve of reduction of the normalised shear modulus G/Gmax and the curve of increase of the normalised hysteretic damping coefficient ξ/ξmax as a function of the unit shear deformation γ/γr. This behaviour is obtaine by the equivalent linear method with the Masing model implemented in the one-dimensional (1D) computational code Caldynasoil. In this study, first, determine the nonlinear behaviour of a soil profile stressed by different levels of seismic accelerations applied at the bedrock level. The Caldynasoil computational code was use to find the variations of the nonlinear dynamic properties of the soil profile for different levels of seismic loading. Secondly, integrating the nonlinear dimensionless properties of the soil in a three-dimensional computational code Fonvib_Wave based on the boundary elements method combined with the theory of thin layers (BEM-TLM) in the frequency domain allows calculating the nonlinear displacements of a surface foundation. The obtained results represent the influence of the nonlinear behaviour of the soil on the vibration modes of a rigid foundation subjected to a Rayleigh wave R as a function of the dimensionless frequency, and PGA level. The conclusions that may predict from this research have shown the importance of the influence of the nonlinear behaviour of the soil, the PGA level and the angle of incidence of the Rayleigh wave on the response of the soil-foundation system compared to the linear case.

Keywords: Non-linear behavior, Equivalent Linear Method, Rayleigh wave, Soil, Foundation.

1 Introduction

The soil-foundation interaction plays a very important role in the seismic design of structures, which studied by many researchers for many years and until now. We can cite the works of Laysmer and Richart (1966), Scanalan (1976), Gazetas (1983), Wolf (1985), Boumekik (1985), Sbartai (2006, 2008), Wang et al (2014), Messioud et al (2016). But all these studies took into consideration the behaviour of the soil as a linear elastic or viscoelastic material. In the nonlinear case, very few investigations considered. We can cited the works of Borja et al. (1993, 1994) using numerical simulation in 2-D and in 3-D by the finite element method (MEF). They studied the dynamic response of a square foundation and based on Chatterjee and Basu (2008) viscoplastic semi-infinite soil; the soil-foundation interaction studied analytically on a perfect elastoplastic medium and determined the dynamic stiffness of the foundation. Gazetas and Apostolou (2004) investigated the response surface foundations with consideration of nonlinear soil behaviour, using the elastoplastic model of Mohr-Coulomb. However, Sbartai (2018) studied the variation of the dynamic impedance of a surface square foundation under the effect of nonlinear soil behaviour. The dynamic response of the foundation solicited by seismic harmonic waves, taking into account the nonlinear behaviour of the soil material, not very well developed in the literature.

In this paper, a numerical analysis of a nonlinear soil-foundation interaction system solicited by the incident wave Rayleigh presented.

2 Nonlinear Seismic Response of Foundations to Seismic Waves

2.1 Soil-Foundation System Response

The equivalent linear method that implemented in the Caldynasoil computation code Sbartai and Filial (2012) was used to analyze and predict the dynamic soil parameters (G/G_{max} and ξ/ξ_{max}) consistent with the nonlinear deformation of the soil. Thus, a soil characterized by its density ρ, its shear modulus G_{max}, its damping coefficient β and its Poisson's ratio v. The foundation is assumed rigid, square, placed on the surface of a semi-infinite homogeneous soil, and subjected to incident harmonic oblique seismic Rayleigh wave (Figure 1).

In the frequency domain, the following relation expresses the use of the thin layer method to obtain the Green functions, which link the soil displacements and the distributed traction on the elements at the soil-foundation interface:

$$\{u\} = [G] \times \{t\} \quad (1)$$

Where: $\{u\}$ and $\{t\}$ are the amplitudes of the displacement vectors and modal forces respectively at the soil-foundation interface. The matrix [G] represents the influence matrix involving the functions of Green.

According to the condition of compatibility between the soil and the foundation, (the foundation imposes on the soil displacements compatible with the rigid body

movement), the displacements of the foundation are connected by the displacements of the soil by the relation of the following condition of compatibility:

$$\{u\} = [R] \times \{\Delta\} \tag{2}$$

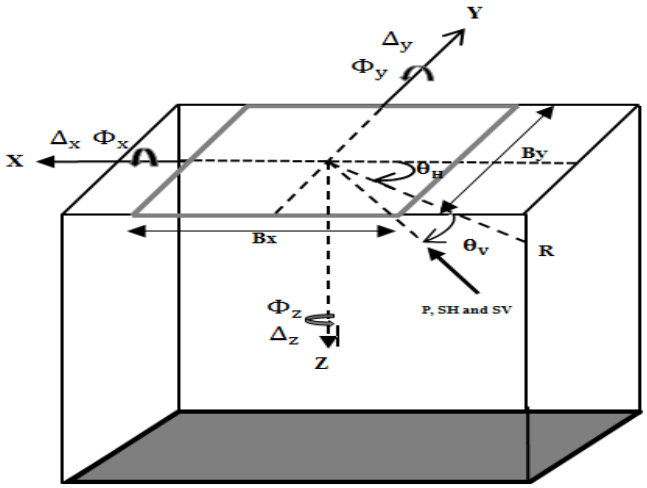

Fig. 1. The geometry of the foundation and the seismic harmonic *Rayleigh wave.*

Where: [R] is the transformation matrix, $\{u\}$ soil displacements at the soil-foundation interface, and $\{\Delta\} = \{\Delta_x, \Delta_y, \Delta_z, \Phi_x, \Phi_y, \Phi_z\}$ is the vector of displacement in the center of the foundation; $\Delta_i (i=x, y, z)$ represents the translations and $\Phi_i (i=x, y, z)$ the rotations (see figure 1).

The equilibrium between the vectors of the external loads P applied to the foundation and the traction $\{t\}$ at the soil-foundation interface is given by:

$$\{P\} = \quad [R]^t \times \{t\} \tag{3}$$

Where R is the size transfer matrix (6N * 3)

$$[R] = \begin{bmatrix} 1 & 0 & 0 & 0 & z & -y \\ 0 & 0 & 0 & -z & 0 & x \\ 0 & 0 & 1 & y & -x & 0 \end{bmatrix} \tag{4}$$

N: is the number of elements at the soil-foundation interface x, y and z are the position coordinates of the discretisation elements of the interface. When the foundation is superficial, z = 0.

By combining equations (1), (2) and (3), we obtain the dynamic stiffness matrix of the foundation given by:

$$\{P\} = ([R]^t \times [G]^t \times [R]) \times \{\Delta\} = [K(\omega)] \times \{\Delta\} \tag{5}$$

With, ω is the circular frequency of vibration and K (ω) the matrix of the impedance functions.

Consider the harmonic plane waves (P, SV, SV and R) characterized by the vertical angles of incidence θ_v and horizontal $\theta_H$respectively, (Figure 1). The free-field motion of the half-space due to seismic waves can expressed on the surface of the soil (z = 0) by the following relation:

$$\{uf\} = \{Uf\}\, e \tag{6}$$

$\{U^f\} = \{U_x^f U_y^f U_z^f\}$ is the vector of free-field motion amplitudes, $i=\sqrt{-1}$, c the apparent velocity of incident waves, $c=c_1/\cos\theta_v$or $c=c_2/\cos\theta_v$ for the P and S waves respectively, and is equal to c_R for the Rayleigh wave (c_R/c_1=0.9325 for a Poisson's ratio ν = 1/3). The presence of a surface foundation of a half space results in a diffraction of the total displacement field, which can be expressed by the following relation:

$$\{u\}= \{u^f\} + \{u^s\} \tag{7}$$

Where $\{u^s\}$ represents the scattered wave field, which satisfies the equation of motion (1). Combining equation (2) and (7) we obtain the displacement of the scattered field by the following formula:

$$\{u^s\} = [\mathrm{R}] \times \{\Delta\} - \{u^f\} \tag{8}$$

$$\{t\} = [G]^{-1} \times [\mathrm{R}] \times \{\Delta\} - [G]^{-1} \times \{u^f\} \tag{9}$$

Multiplying the two sides of equation (10) by the transpose of the transformation matrix

$$[R]^t \times \{\mathrm{t}\} = [R]^1 \times [G]^{-1} \times [\mathrm{R}] \times \{\Delta\} - [R]^t \times [G]^{-1} \times \{u^f\} \tag{10}$$

and substituting equation (10) in equation (11) yields:

$$\{\mathrm{P}\} = [\mathrm{K}] \times \{\Delta\} - [K\ ] \times \{U^f\} \tag{11}$$

Where,

$[K\ ]$: The motion matrix (6x3N) given by the following relation:

$$[K\ ] = [R]^t \times [G]^{-1} \exp\{-i\omega(\mathrm{x}.\cos\theta_H + \mathrm{y}.\sin\theta_H) / \mathrm{c}\} \tag{12}$$

The following alternative form can replace equation (11):

$$\{\Delta\} = [\mathrm{C}] \times \{\mathrm{P}\} + [S^*\ ] \times \{U^f\} \tag{13}$$

Where,

[C] = [K] is the dynamic compliance matrix (dynamic flexibility) (6 * 6). [S*] is the motion matrix (6 * 3) given by the following formula:

$$[S\ ] = [C] \times [K\ ] \tag{14}$$

When the foundation is only solicited by seismic waves, the external forces are zero ($P = 0$), the seismic response of the foundation in this case is obtained from equation (13) by the following expression:

$$\{\Delta\} = [S\ ] \times \{U^f\} \tag{15}$$

When the mass of the foundation is non-zero, replace [K] by [K] - ω^2[M] in the equations above, where [M] is the mass matrix of the foundation.

2.2 Linear Equivalent Soil Response

In this case, integrating the nonlinear behaviour of the soil in the analysis of the soil-foundation interaction by the linear equivalent method and comparing by a linear case. Due to the fact that the profile of the soil foundation is solicited by a large deformation (strong seismic excitation), the behaviour of the soil is described by curves giving the variation of the shear modulus G/G_{max} and the percentage of critical damping $\xi/\xi_{\max}$ compatible with the imposed deformation γ. The Caldynasoil computation code of Sbartai and Filali (2012) which uses the linear equivalent method with concentrated masses and the hyperbolic models of Hardin and Drnevich, Rambert and Osgood and Masing determine this behaviour. This procedure is iterative, which allows estimating the seismic response of a soil profile consisting of horizontal layers, subjected to any seismic acceleration at the level of the substratum. Figure (2) shows the mechanical model of the equivalent soil profile. Thus, considering each layer as linear and elastic modeled by a model with concentrated mass. The soil mass of this model is also concentrated above and below each layer.

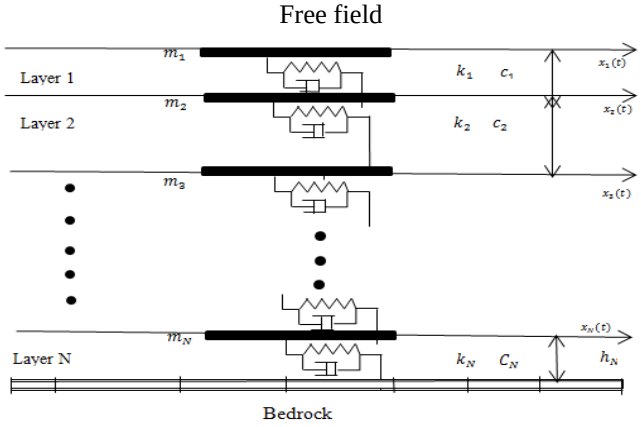

Fig. 2. The model with concentrated masses (Filali and Sbartai, 2017).

Where,

$$m_1 = \frac{\rho_1 h_i}{2},\ m_i = \frac{\rho_{i-1} h_{i-1} + \rho_1 h_i}{2} \quad (i = 2, 3 \ldots N) \tag{16}$$

m_i, ρ_i and h_i are the concentrated mass, the density and the thickness of the soil layer *i*.

In brief, we cite the analysis steps of the equivalent linear method with concentrated masses as follows:

Step 1: Estimate the initial physical parameters for each soil layer *i* (shear modulus G_{max}, density ρ, Poisson coefficient ν, hysteretic damping ζ_{max}). In this step, all soil parameters are found by in situ tests or laboratory tests with low deformation.

Step 2: Choose the number of soil layers for analysis.

Step 3: Calculate mass, stiffness and damping matrices.

Step 4: Solve the equations governing the motion of all soil layers considering the dynamic equilibrium for each layer:

$$[m]\,(\ddot{x}) + [c]\,(\dot{x}) + [k]\,(x) = -\,(m)\,\ddot{x}_r \qquad (17)$$

Where,

(x), $(\dot{x})$, $(\ddot{x})$: Vectors of displacements, velocity and horizontal accelerations of each layer with respect to the rock.

(m): Vector containing the mass of each soil layer.

$\ddot{x}_r$: Accelerogram at the rock level.

Step 5: For each layer *i*, the maximum shear unit deformations, $\gamma_{max\,(i)}$, are calculated from the maximum inter-layer displacements:

$$\gamma_{max(i)} = \frac{|x_i - x_{i+1}(t)|_{max}}{h_i} \qquad (18)$$

Step 6: Update the stiffness and the equivalent damping, from the maximum shear unit deformations calculated in step 5 we can update the effective shear modulus and the effective damping coefficient of each layer of soil. Generally a fraction of the maximum values of 2/3 is used, since the maximum deformation levels are reached only once during the dynamic response.

Step 7: Steps 3 to 7 repeated until convergence of rigidity and damping.

Generally, only a few iterations are sufficient to reach convergence.

3 Numerical Analysis

3.1 Soil response

In this study, a one-dimensional (1D) simulation by the Caldynasoil computation code based on the linear equivalent method with the Masing's hyperbolic model (1926) was used to determine the nonlinear behaviour at various levels of deformation. The soil profile is sandy with a height Ht = 10m, characterized by its density γ = 19.1 KN / m3, its shear wave velocity V_S = 100m/s. Five registered seismic accelerations (China - 0.01g, LomaPrieta-Diamond-0.10g, Nahanni-0.20-g, El-Centro-0.30-g, Los Anglos-0.40g) used. Finally, to find the reductions of the shear modulus and the increase of the damping compatible with each seismic excitation (Fig.3), and even also the values of the corresponding nonlinear properties of each seismic accelerogram. After applied the seismic accelerations of Loma Prieta-Diamond-0.10g, Nahanni-0.20-g, El-Centro-0.30g, Loma Preita-0.40g, Northridge -0.5g) on this soil profile, we have obtained its

nonlinear dynamic properties for each seismic excitation, where they recorded in Table 1.

3.2 The linear equivalent response of the soil-foundation system

The nonlinear seismic response of the soil-foundation system was calculated and compared by a linear case. The foundation solicited by harmonic Rayleigh wave, characterized by vertical and horizontal angle of incidence θ_V and θ_H respectively (Fig. 1). Fig. 4 represents the influence of nonlinear soil behaviour on the absolute values of displacement functions for angle of incidence of R wave θ_H= 0 as a function of the dimensionless frequency a_0 varying from 0 to 6. All the vibration modes of the foundation are calculated for different levels of nonlinearities of the soil following each seismic acceleration PGA (= 0.01g, 0.10g, 0.20g, 0.30g and 0.40g).

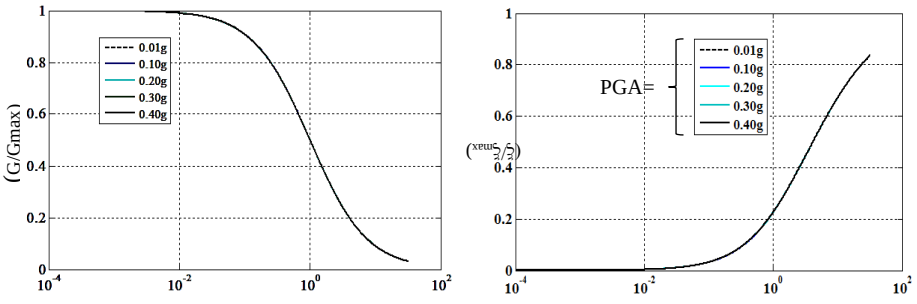

Fig. 3. Variation of the shear modulus (G/G_{max}) and damping coefficient (ξ/ξ_{max}) as a function of the shear strain ($\gamma/\gamma r$).

Table 1. Variations of the nonlinear dynamic properties of the soil vs the acceleration level of the earthquakes

Accelerogram(s)	G/G_{max}	ξ_g/ξ_{gmax}
Linear	1	0.05
Earthquake 0.1g	0.6	0.16
Earthquake 0.2g	0.26	0.43
Earthquake 0.3g	0.12	0.6
Earthquake 0.4g	0.04	0.68
Earthquake 0.5g	0.02	0.87

The influence of the nonlinear behavior of the soil on the response of the displacements of a square-shaped shallow foundation stressed by a Rayleigh wave has shown that the more the deformation of the soil increases, the more the displacements increase, especially for seismic accelerations between 0.3g and 0.4g. For a high non-linearity of the soil PGA (= 0.3g and 0.4g), the absolute values of the horizontal dimensionless displacement functions $|\Delta x/R_H|$ increase significantly with increasing dimensionless

frequency a_0. On the other hand, for small deformations of the soil PGA (= 0.1g and 0.1g) it was noted that the values of the displacements of the foundation approach those of the linear case.

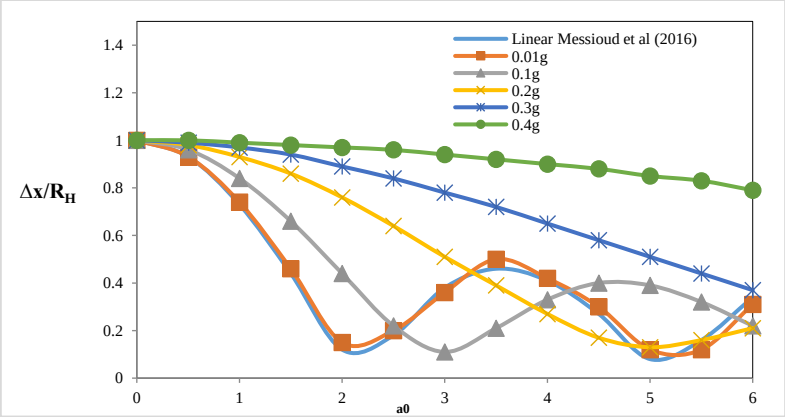

Fig. 4. Horizontal displacement $|\Delta x/R_H|$ f from the Rayleigh wave ($\theta_v = 0^0$, $\theta_h = 0^0$) .

4 Conclusion

The effect of nonlinear soil behaviour on the seismic response of the soil-foundation interaction was examined. The surface foundation was solicited by oblique harmonic plane Rayleigh wave. The hyperbolic model of the nonlinear behaviour of the Masing's soil (1926) implanted in the Caldynasoil calculation code of Sbartai and Filali (2012), Filali and Sbartai (2017) to determine the response of this system. The variation nonlinearity behavior of the soil was found for various levels of seismic accelerations imposed at the base of the soil profile. The response of the soil-foundation system was estimated using the coupled method BEM-TLM and compared with the elastic linear case. The main objectives of this study are:

- The nonlinear behaviour of the soil described by the decrease of the shear modulus (G/G_{max}) and the increase of the percentage of critical damping (ξ/ξ_{max}) as a function of the shear strain γ.
- The dynamic response of the foundation is strongly linked by the variations of the dynamic properties of the soil, the amplitude of the seismic acceleration, the angle of incidence of the wave, and dimensionless frequency a0.

Therefore, this study has shown the difference of nonlinear soil behaviour on the dynamic response of the soil-foundation interaction compared to linear case.

References

1. Borja RI, Wu W. Vibration of foundation on incompressible soils with no elastic region. Journal of Geotechnical Engineering 1994; 120:1570-1592.

2. Borja RI, Wu WH, Alexander P, Amies, Smith A. Nonlinear lateral, rocking, and torsional vibration of rigid foundations. Journal of Geotechnical Engineering 1994; 120:491-513.
3. Boumekik A. Fonctions impédances d'une fondation vibrante en surface ou partiellement encastrée dansun sol multicouche, Ph.D. Université libre de Bruxelles, Faculté des sciences, Bruxelles. (1985).
4. Chatterjee P, Basu B. Some analytical results on lateral dynamic stiffness for footings supported on hysteretic soil medium. Journal of Soil Dynamics and Earthquake Engineering 2008; 28:36–43. doi: 10.1016/j.soildyn.2007.04.004.
5. Filali K, Sbartai B A comparative study between simplified and nonlinear dynamic methods for estimating liquefaction potential. Journal of Rock Mechanics and Geotechnical Engineering2017; 9:955-966. doi.org/10.1016/j.jrmge.2017.05.008.
6. Gazetas G, Apostolou M. Nonlinear Soil–Structure Interaction: Foundation Uplifting and Soil Yielding. Proceedings Third UJNR Workshop on Soil-Structure Interaction 2004; 29-30.
7. Gazetas G. Analysis of machine foundation vibrations: state of the art. Soil Dynamic and Earthquake Engineering 1983; 2(1): 2-42.
8. Lysmer J, Richart FE. Dynamic response of footing to vertical loading. Journal of Soil Mechanics& Foundations Div, 1966, ASCE; (92).
9. Massing G.Eigenspannungen und verfestigungbeim messing. In: Proceedings of the 2nd International Congress of Applied Mechanics 1926; 332–335.
10. Messioud S, Sbartai B, Dias D. Seismic response of a rigid foundation embedded in a viscoelastic soil by taking into account the soil-foundation interaction. Structural Engineering and Mechanics 2016; 58(5):000. doi.org/10.12989/sem.2016.58.5.000.
11. Sbartai B, Filali K. Estimation of the Liquefaction's Risk of a Soil Deposit under Seismic Solicitations: Petrochemical Zone of Skikda city. Applied Mechanics and Materials 2012; 166-169: 2315-2320. DOI: 10.4028/www.scientific.net/AMM.166-169.2315
12. Sbartai B, Filali K. CALDYNASOIL: Software of seismic response and liquefaction potential deposit, 15th World Conference on Earthquake Engineering 2012; 24 to 28 September, Lisbon, Portugal.
13. Sbartai B. Dynamic Impedance Functions of a Square Foundation Estimated with an Equivalent Linear Approach. Springer International Publishing AG 2018; 461-470. DOI 10.1007/978-3-319-61914-9_35.
14. Wolf JP. Dynamic Soil Structure Interaction. Prentice Hall International Series in Civil Engineering and Engineering Mechanics 1985.

Effect of Colemanite and Glass Fiber on the Volume Deformation Behavior of Bentonite

Yusuf Batuge [1][0000-0002-8060-6664], Sukran Gizem Alpaydin [1][0000-0002-0784-2361], and Yeliz Yukselen-Aksoy[2][0000-0002-9145-765X]

[1] The Graduate School of Natural and Applied Sciences, Dokuz Eylul University, Turkey
ybatuge@hotmail.com
[2] Department of Civil Engineering, Dokuz Eylul University, Turkey

Abstract. Bentonite clay's low hydraulic conductivity properties, high swelling capacity and good self-sealing behavior make it the best candidate for use as a buffer material in the engineered barrier applications. However, it is undesirable for bentonite to rise to high swelling pressure values in the presence of water and to show high compressibility behavior under different stresses. In this study, colemanite and glass fiber additives were used to improve the compressibility and swelling properties of bentonite clay. For this purpose, the experiments were performed in an oedometer test device. According to the test results, colemanite additive decreased the compression and the swelling deformation amounts of bentonite, while glass fiber did not have a significant effect on the compression deformation and improved (decrease in deformation) the swelling behavior.

Keywords: Bentonite, Buffer, Colemanite, Glass fiber, Volume Deformation.

1 Introduction

Bentonite is a type of clayey soil that is widely utilized in various geotechnical engineering applications such as barrier systems and landfill liners as it provides very low permeability, sufficient thermal conductivity, and high swelling potential and water retention capacity. Therefore, comprehension of the volume deformation behavior of bentonite under different loading conditions is important for the stability and performance of such geotechnical structures. The compressibility behavior of expansive clays such as bentonite was investigated by former studies (Sridharan et al., 1986; Tripathy and Schanz, 2007). It is known that the saturated condition of the clays is considered as the higher water content values than their liquid limit values (Bag and Rabbani, 2017). Bag and Rabbani (2017) examined the consolidation behavior of bentonite at room and high temperatures. It was examined the compression index values between 432-1727 kPa and the result was found as 0.76. Different additives were used by researchers to improve the engineering parameters of bentonite and sand-bentonite mixtures used as buffer materials (Liu et.al., 2012, Al-Soud et al., 2022, Alpaydin and Aksoy, 2023). For example, Liu et al. (2012) investigated the effect of polymer additives in three different bentonite types in their study and observed that the polymer

increased the liquid limit values and swelling indexes of bentonites. However, the use of colemanite and glass fiber additives with superior engineering properties is not common. Boron is a natural compound and contains different proportions of boron oxide (Özkan et al. 1997). Colemanite, ulexite, and tincal are boron minerals commonly used in industry. The chemical formula of colemanite, a boron mineral, is $2CaO.3B_2O_3.5H_2O$ and its B_2O_3 content is between 27-32%. It increases the durability of materials to the maximum level (Etimaden 2019). Glass fiber is one of the most common synthetic fibers used to reinforce concrete and soils. It is used in many areas thanks to its low cost, high temperature resistance and high tensile strength. Mukherjee and Mishra (2021) reported that glass fiber additive decreased the compression index and increased the swelling index of the sand-bentonite mixtures.

In the present study, colemanite and glass fiber additives were added to improve the compressibility and swelling behavior of bentonite due to their superior properties. In this context, the compressibility and swelling behaviors of bentonite in the presence of colemanite and glass fiber were determined by oedometer tests.

2 Materials and Method

2.1 Materials

The bentonite clay used in the present study is powdered calcium bentonite activated at high temperature with NaCO3. According to the X-Ray Diffraction analyses results, mainly montmorillonite was observed in the bentonite content, as well as quartz, calcite, and albite minerals were observed. The bentonite sample' specific gravity value is 2.60, the natural water content is 7.5%, the liquid and plastic limit values are 270%, 63%, respectively. The colemanite additive was used in powdered form. Its specific gravity, plasticity index, and pH values are 2.42, 11%, and 9.26, respectively. Another additive material used in this study is glass fiber and the specific gravity, length, and diameter of glass fibers are 2.60, 3 mm, and 13 μm, respectively.

2.2 Methods

The oedometer tests were performed according to ASTM D2435, 2012. The bentonite-colemanite and bentonite-glass fiber mixtures were prepared by mixing an air-dried bentonite with different additive contents. The contents of the additives were determined according to the dry weight of the bentonite. The contents of the additives were 10% and 20% for colemanite, 0.5%, and 1.0% for glass fiber. The samples were prepared by mixing the air-dry bentonite and additives homogeneously and then using tap water with a water content of 1.5 times the liquid limit value of each mixture. For that reason, before performing the oedometer tests, the liquid limit values of the mixtures were determined by the Casagrande method and the results are given in Table 1.

The prepared samples in slurry condition at 1.5 times the liquid limit were placed in a sample preparation apparatus with a 70 mm diameter 19 mm height steel ring and a 30 mm height plexiglass cell on the steel ring and left to consolidate under 12.25 kPa

pressure for 14 days. At the end of 14 days, the sample in the ring was placed into the oedometer test device and the test was initiated. The samples were loaded from 24.5 kPa to 784 kPa with load increment ratio as 1.0 and then unloaded to 49 kPa. Each set of experiments was conducted at room temperature and lasted 2-3 months.

Table 1. Liquid limits of the mixtures.

Mixture	Liquid limit (%)
Ca-Bentonite	270.0
B-10 C	241.0
B-20 C	225.4
B-0.5 G.F.	269.0
B-1 G.F.	265.0

3 Results and Discussion

In the present study, the effect of colemanite and glass fiber additives on the compressibility and swelling behavior of bentonite were determined by oedometer tests. Initial void ratio values (e_0) of the mixtures vary between 4.68-6.85 and initial dry densities (γ_d) vary between 2.60-3.58 kN/m^3. The results were presented as void ratio-stress (e-logσ) plots (Figs.1 and 2).

The compressibility and swelling behaviors of the mixtures were evaluated in terms of total compression and swelling deformation amounts, compression and swelling indexes and the values are presented in Table 2. Compression index values were examined between 196 to 392 kPa and swelling index values were examined between 196-49 kPa load interval. According to the results, it was observed that 10% colemanite additive had a positive effect by reducing the compressibility. Addition of 10% colemanite reduced the compression index of bentonite from 2.79 to 1.90. As the colemanite content increased to 20%, the compression index decreased to 1.77. This is due to the high calcium content of colemanite and material displacement. In other words, the amount of bentonite was reduced as much as the amount of colemanite added while preparing the mixtures. For that reason, as the colemanite content increased, the compression index of the mixture increased. On the swelling behavior of bentonite, the contribution of colemanite decreased in both contents and caused an increasing trend in the swelling deformation amount. As the glass fiber content in the mixture increased, an increase in the total compression deformation was observed. This may be due to the fact that the glass fiber takes up less space in the sample than the bentonite particles. In other words, glass fiber is more compressible material than bentonite clay. On the other hand, glass fiber additives significantly increased the swelling behavior and provided improvement.

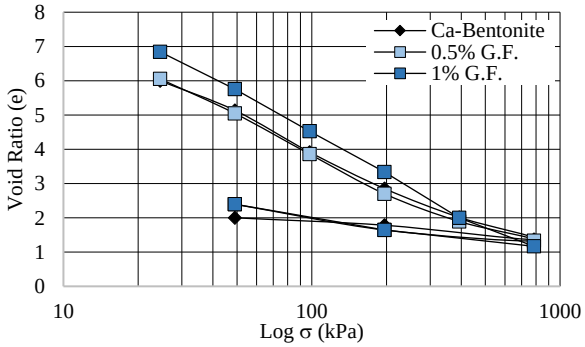

Fig. 1. Void ratio-stress relationships of bentonite in the presence of glass fiber

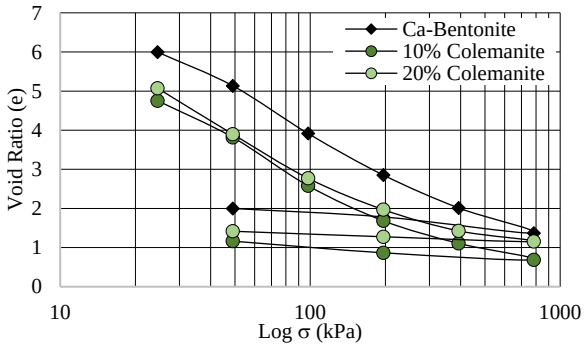

Fig. 2. Void ratio-stress relationships of bentonite in the presence of colemanite

Table 2. Total volume deformation of the mixtures.

Mixtures	Total Compression Deformation (%)	Total Swelling Deformation (%)	Compression Index (C_C)	Swelling Index (C_S)
Ca-Bentonite	53.27	7.24	2.79	0.36
B-10 C	42.02	4.93	1.90	0.49
B-20 C	55.03	3.68	1.77	0.23
B-0.5 G.F.	53.04	11.97	2.69	1.25
B-1 G.F.	58.03	17.03	4.44	1.86

4 Conclusions

In the present study, glass fiber and colemanite additives were added to bentonite and oedometer tests were performed. The total vertical compressibility and swelling deformation of bentonite mixtures were investigated. Considering the change in volume deformation behavior of the mixtures, 10% colemanite added bentonite mixtures showed promising behavior in terms of compressibility. Moreover, while glass fiber

additive did not affect the compressibility deformation of bentonite, it was determined to be beneficial in terms of swelling deformation. However, in future studies, the thermal and hydraulic behavior of bentonite should be investigated in the presence of these additives.

Acknowledgments
This study is supported by The Scientific and Technological Research Council of Turkey (TUBITAK) (Grant no:120M470). The authors are grateful for this support.

References

1. Al-Soud, M. S., Fartosy, S. H., Jabur, A. R., Majeed, M. W., Madhloom, H. M., Al-Ansari, N.: Sustainable improvement of bentonite clay characteristics by adding pulverized waste glass. GEOMATE Journal 23(95), 10-19 (2022).
2. Alpaydin, S. G., Yukselen-Aksoy, Y.: Investigation of shear strength of sand–bentonite mixtures with boron additives at high temperature for energy geo-structures. Environmental Earth Sciences, 82(10), 256 (2023).
3. Bag, R., Rabbani, A.: Effect of temperature on swelling pressure and compressibility characteristics of soil. Applied Clay Science, 136, 1-7 (2017).
4. Boron minerals (2019) http://www.etimaden.gov.tr/en/boron-minerals. (accessed 19 April 2019).
5. Liu, Y., Gates, W. P., Bouazza, A.: Improvement on the performance of geosynthetic clay liners using polymer modified bentonite. Geotech. Eng, 43(3), 43-45 (2012).
6. Mukherjee, K., Mishra, A. K.: Impact of glass fibre on hydromechanical behaviour of compacted sand–bentonite mixture for landfill application. European Journal of Environmental and Civil Engineering, 25(7), 1179-1200 (2021).
7. Özkan ŞG, Çebi H, Delice MD.:Bor minerallerinin özellikleri ve madenciliği. 2 Endüstriyel Hammaddeler Sempozyumu, İzmir, Türkiye, 224-228 (1997)
8. Sridharan, A.S.U.R.I., Sivapullaiah, P.V., Rao, A.S.: Swelling pressure of clays. Geotechnical Testing Journal 9.1, 24-33 (1986).
9. Tripathy, Snehasis, and Tom Schanz.: Compressibility behaviour of clays at large pressures. Canadian Geotechnical Journal 44(3), 355-362 (2007).

Passive Earth Reinforcement for Lateral Equilibrium Optimization

Tarik Solomon Teshome [1] [0009-0008-2094-9324], Zehra Nil Kutlu [2] [0000-0003-4813-588X], Aykut Şenol [3] [0000-0003-1832-3919], and İsmail Emrah Kılıç [4] [0000-0002-6514-2224]

[1] Istanbul Technical University, Civil Engineering Department, Istanbul, Turkiye, solomonteshome20@itu.edu.tr
[2] Maltepe University, Civil Engineering Department, Istanbul, Turkiye zehranilkutlu@maltepe.edu.tr
[3] Istanbul Technical University, Civil Engineering Department, Istanbul, Turkiye, senol@itu.edu.tr
[4] Maltepe University, Civil Engineering Department, Istanbul, Turkiye emrahkilic@maltepe.edu.tr

Abstract. Design optimization requirements on conventional and widely applicable structural retaining wall systems such as sheet pile walls, diaphragm walls, and bored pile wall structures have been increasingly growing to minimize the construction constraints, costs and duration. Passive side reinforcement may be referred to as a soil improvement performed on the passive side of a retaining wall with jet grouting. The purpose is to increase the passive earth pressure hence; reducing the total lateral forces acting on the wall, reducing the bending moments, and ultimately increasing the wedge angle. In this parametric study, finite element (FEM) analyses are performed using PLAXIS 2D to examine the influence of various passive zone reinforcement geometrical parameters on excavation's deformation and lateral force equilibrium modeled as a jet-grout equivalent soil-cement mixture block. The benchmark model is without passive side reinforcement, and two other models with different geometries of the reinforced zone are built. The effect of the passive side reinforcement is observed as significant reduction in the lateral displacements and the bending moment of the wall and also a shift in the active failure wedge zone. It can also be concluded that the location of the lateral force equilibrium gives the rough estimation for the soil-cement mixture block depth as L=5m for this specific study. The results of this study will be promising to guide geotechnical engineers in optimizing the proposed design by reducing total investment costs in case of high wall depths by introducing the Passive Earth Reinforcement for Lateral Equilibrium Optimization (PERLEO) methodology.

Keywords: Passive Side Reinforcement; Plaxis 2D; Soil-Cement Mixture Block

1 Introduction

Certain physical conditions of the soil in the construction site can make lateral support for the deep excavation very challenging or not feasible. Especially, when excavating deep pits in a densely populated urban environment, additional measures are often necessary to ensure the stability and safety of the neighboring structures by minimizing the displacements and settlements [1,2]. The most common methods applied in the engineering applications include zoned excavations [3,5], cross walls [5-7], and ground improvement with lateral support [8,9]. As an alternative solution the implementation of a soil-cement mixture block; using jet grouting or deep mixing; adjacent to the passive side of the wall prior to the excavation is beneficial to effectively reduce the displacement and bending moments on the flexible retaining wall which will have little or no effect on the nearby foundation systems [2, 10].

This study presents the Passive Earth Reinforcement for Lateral Equilibrium Optimization (PERLEO) methodology which is based on numerical analysis results for determination of the optimum dimensions of soil-cement block. Calculation results which was conducted using using Plaxis 2D software package and their evaluation are discussed. The present preliminary findings, in conjunction with the forthcoming studies, are expected to be beneficial in providing direction to geotechnical engineers for optimizing the proposed design by reducing the overall costs in the case of deep excavations, through the implementation of the PERLEO (Passive Earth Reinforcement for Lateral Equilibrium Optimization) methodology. In this regard, structural systems which compromise wall behavior turns as efficient solutions at relatively deep excavation pits and thus walls become critical infrastructures due to their importance in safety and sustainability of the construction activity.

2 Numerical Analysis

2.1 Model Geometry

The primary aim of the presented study is to evaluate the performance the soil-cement mixture block as a passive side reinforcement service condition performance under the mobilized earth pressures adjacent to an in-situ cantilever bored pile wall. In the present study, a benchmark model with no passive zone improvement (Figure 1a) and two different geometric patterns (L x B) for the soil-cement block for passive side reinforcement (Figure 1b & 1c) are studied to numerically determine the lateral displacements and bending moments on the cantilever bored pile wall placed in a fill and a loose sand soil profile. The dimensions used in the model is given in Table 1.

The depth of the excavation supported by the free height; H; of the bored pile wall is 20.0 m of a 35.0 m long bored pile wall. The reinforcement pattern is described by two parameters the depth; L and the width; B. Case 1 is the benchmark model when there is no reinforcement, Case 2, reinforcement in the passive zone is installed with the L=10 m and B=5 m and Case 3, the reinforcement pattern in the passive zone is L= 5 m and B=10 m as it is summarized in Table 1. The groundwater level is not considered

in this preliminary reference study for the ease of understanding the actual wall behavior.

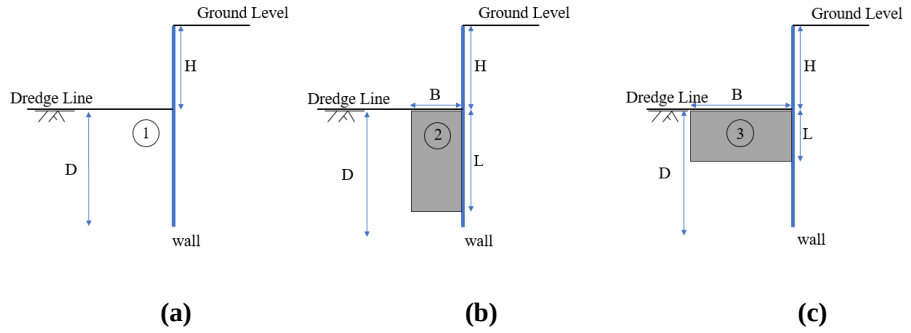

Fig. 1. Schematic plot of the passive zone reinforcement:
(a) Case 1, (b) Case 2, and (c) Case 3.

Table 1. Model Dimensions in Plaxis 2D

Property	Case 1	Case 2	Case 3
Free height of the wall, H (m)	20	20	20
Embedment depth of the wall, D (m)	15	15	15
Length of soil-cement block, L (m)	0	10	5
Width of soil-cement block, B (m)	0	5	10

The numerically determined lateral displacements and bending moments using the finite element software, Plaxis (2D) and the variation in the active zone geometry were compared to understand the effect of soil-cement mixture on the overall wall behavior. The 2D geometry model, meshes, and boundary conditions are shown in Fig. 2, to avoid the limit boundary effect the model size was 200 m in length by 100 m in width. The problem was divided into several groups of phases and staged construction was performed in the analysis to simulate the gradual mobilization of active earth pressure. The 2D geometry model, meshes, and boundary conditions are shown in Fig. 2.

2.2 Soil Model and Material Properties

The fill, the sand and the soil-cement block were modelled as a Hardening Soil (HS) model [11] with HS model parameters along with the effective shear strength parameters and unit weights as shown in Table 2. The HS model is necessary for this type of nonlinear analysis in Plaxis 2D due to the stress dependent stiffness characteristics of the defined problem [12, 13]

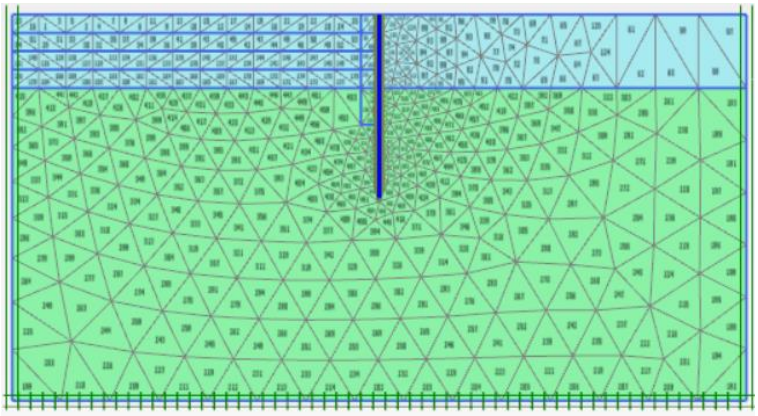

Fig. 2. 2D model geometry, meshes and boundary condition used in Plaxis 2D.

Table 2. Hardening Soil HS model parameters for numerical analysis.

Property	Fill	Sand	Soil-cement mixture block [14]
Saturated unit weight, γ_{sat} (kN/m^3)	20	19	19.4
Unsaturated unit weight, γ_{unsat} (kN/m^3)	19	18	18.4
Effective cohesion, c' (kPa)	0	1	492
Effective internal friction angle, ϕ' (°)	30	31	28
Reference secant rigidity, E_{50} (MPa)	30	20	347
Reference tangent rigidity, E_{oed} (MPa)	30	20	347
Reference rigidity, E_{ur} (MPa)	90	60	1040

The structural member used as a retaining wall was a concrete bored pile wall system and it was simulated as a plate element with the linear elastic material property. To effectively capture the behavior of the soil-plate element interaction the interface element was used. The parameters for the bored pile wall simulated with plate element can be found in Table 3.

Table 3. Equivalent plate element parameters for numerical analysis

Property	Value
Diameter, D (m)	1.5
Poisson's ratio, v	0.2
Axial stiffness, EA (kN/m)	34600000
Flexural stifness, EI (kN.m^2/m)	6120000

3 Numerical Analysis Results

The preliminary numerical analysis results are consistent and promising in understanding of the wall behavior for an efficient design under service loads with implemantation of a soil-cement mixture block as a passive side improvement regarding the lateral displacement and bending moments as given in Figure 3. In Figure 3-a the displacement vs depth variation plots are shown for the three cases studied. It can be clearly seen that the lateral deformation of the wall significantly reduced when passive side reinforcement is installed in the passive zone when comparing Case 1 (black line) with Case 2 (red line) and Case 3 (green line). Considering the results, the passive support from the soil-cement block has effectively reduced the lateral displacements of the wall by around 42% at top level.

The difference between reinforced cases (Case 2 & 3) and non-reinforced case (Case 1) clearly reveals the expected outcome of earth pressure distribution according to Rankine Theory. It may be seen that a much higher passive resistance is mobilized in the reinforced strata in compliance with its increased shear strength parameters, which eventually results in a lateral force equilibrium between active forces and passive resistance in a more shallow elevation (Fig.3a).

The evident difference in approximate turning points between reinforced cases and non-reinforced case, as well as the slope difference in the deflection curves of these cases are clear indicators of this phenomenon in Fig.3a. According to comparison of the deflections of the reinforced cases within eachother (Case 2 vs. Case 3), the difference in deflections has been observed to be much less and therefore comparable. This situation reveals two important outcomes depending on the observed difference where; *such difference being negligible* indicates that the passive earth resistance has been mobilized and has been able to oppose the active pressure until lateral equilibrium within the depth of L = 5 m. On the other hand, *such difference existing even if very slight* indicates that the more narrow configuration of the soil-cement bock (Case 2) has been forced to higher level of flexural effects as a discrete matrix in comparison to the wider configuration (Case 3) acting as a rigid body.

As shown in Fig. 3b, Case 2 being more prone to matrix bending has resulted in a slightly higher deflection curve along the reinforcement depth which has eventually resulted in a marginal deflection difference at top level of the wall between two cases. It should also be expected that the resultant earth force would be less in reinforced cases than the non-reinforced situation, which at the end results in significantly less bending action on the wall as shown in Fig.3b.

The plastic points and failure wedge with and without the installation of the soil-cement mixture block on the passive side of the wall is shown in Fig. 4. It is clearly be seen that the active failure wedge is shifted upward once the reinforcement soil-cement block is defined on the passive side. In Fig.4a the active zone wedge extends below the dredgeline. However after the instalment of reinforcement soil-cement block on the passive side, the active failure wedge is shifted upward and ends at a level around the dredge line (Fig. 4b-4c). Since there is no improvement measures on the active side,

the failure wedge angle remains the same for the unreinforced and two reinforced cases, but it relocates showing the decrease in the active earth pressures.

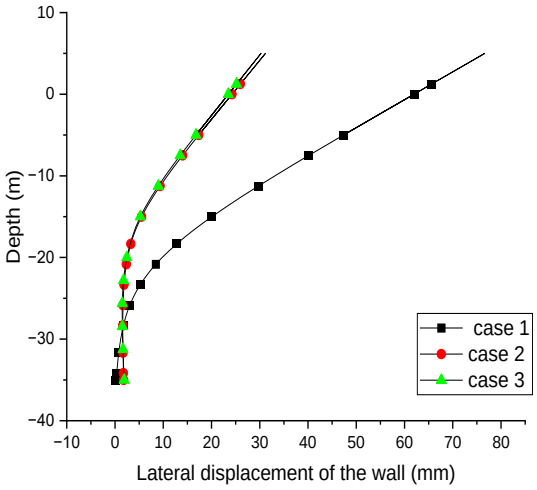

(a)

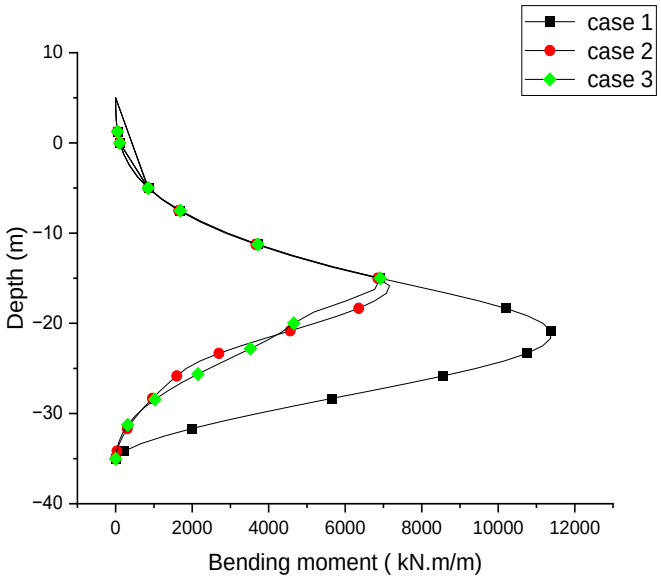

(b)

Fig. 3. Effect of the geometric parameters in passive zone reinforcement on (a) lateral displacement and (b) bending moment with depth of the bored pile wall.

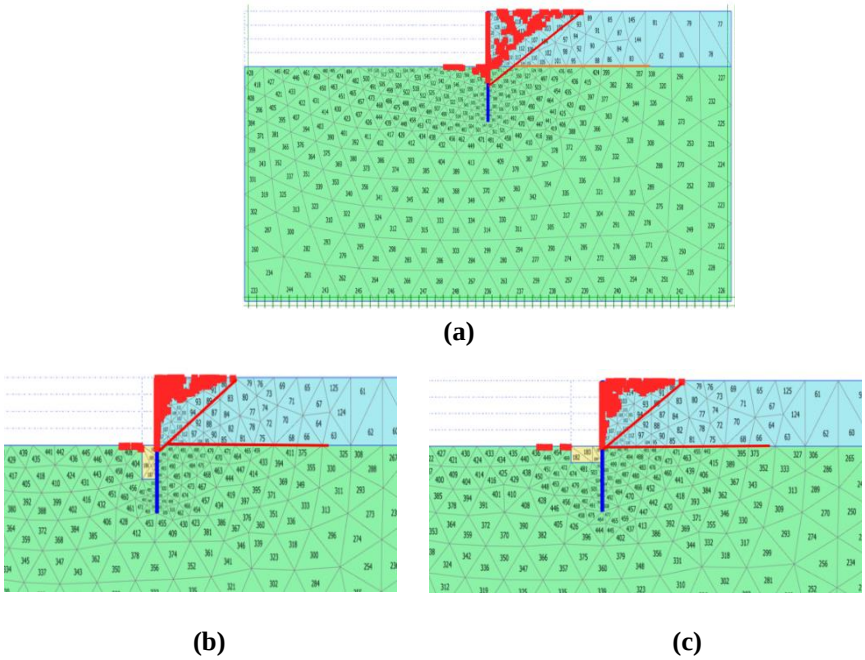

(a) **(b)** **(c)**

Fig. 4. Plastic point distribution and active failure wedge: (a) unreinforced Case 1, (b) reinforced Case 2, and (c) reinforced Case 3.

4 Conclusion And Discussion

The numerical analysis results performed to evaluate the demonstrated that the passive zone reinforcement successfully reduced the lateral displacement and the bending moments acting on the wall. Implemantation of the the passive side reinforcement significantly decreases the lateral deformation of the flexible wall and similar pattern were also obtained concerning the bending moment diagrams. These indicates that due to installation of a soil-cement mixture block on the passive side of the wall the overall stability and the model is improved significantly.

Upon examination of the effect of distinct geometrical configurations of the soil-cement block, the negligible difference in the mobilized lateral displacement distribution plots indicates that the length (depth) of the reinforcement block in Case 3, which is L = 5m, is sufficient for the mobilization of the increased passive resistance.

Furthermore, lateral displacement variation curves have turning points close to each other for two cases which shows that the earth pressure equilibrium is reached at a similar depths. In Case 1, the turning point is at lower depth compared to Case 2 and Case 3 due to less passive resistance mobilized to equilize the earth pressures.

The active wedge represents the contribution of the retained soil involved in the stability of the excavation. the active wedge is moved upward after the installation of the passive zone reinforcement proving that the active earth pressure acting on the retaining structure is decreased. Installing jet grout reinforcement in the passive side shifted upward the failure points in the model and increased the active wedge angle which signifies that the overall stability of the model is increased. For a better understanding of the effect of the geometric configuration of the reinforcement, more detailed analysis with different iterative changes in geometric configuration for the reinforcement in the passive zone must be conducted for future studies.

Acknowledgement
The first author would like to show his gratitude for the support offered to him by the coordination unit for scientific research projects of Istanbul Technical University (BAP, Project ID: MDK-2022- 43644).

References

1. Oztoprak, S., Cinicioglu, S. F., Oztorun, N. K., Alhan, C.: Impact of neighboring deep excavation on high-rise sun plaza building and its surrounding. Engineering Failure Analysis, 111 (2019).
2. Il'ichev, V. A., Gotman, Y. A.: Analysis of a soil-cement mass to reduce enclosure displacement by the method of optimal design. Soil Mechanics and Foundation Engineering 48 (4), 158-168, (2011)
3. Chen, R.P., Meng, F., Li, Z.C., Ye, Y., Ye, J.: Investigation of response of metro tunnels due to adjacent large excavation and protective measures in soft soils. Tunnelling and Underground Space Technology 58, 224–235 (2016).
4. Li, M.G., Zhang, Z.J., Chen, J.J., Wang, J.H., Xu, A.J.: Zoned and staged construction of an underground complex in Shanghai soft clay. Tunnelling and Underground Space Technology 67, 187–200 (2017).
5. Hsieh, P.G., Ou, C.Y., Lin, Y.L.: Three-dimensional numerical analysis of Deep excavations with cross walls. Acta Geotechnica 8 (1), 33–48 (2013).
6. Ou, C.Y., Hsieh, P.G., Lin, Y.L.: A parametric study of lateral wall deflections in deep excavations by the installation of cross walls. Computers and Geotechnics 50, 55–65 (2013).
7. Lim, A., Hsieh, P.G., Ou, C.Y.: Evaluation of buttress wall shapes to limit movements induced by deep excavation. Computational Geotechnics 78, 155–170, (2016).
8. Liu, G.B., Ng, C.W.W.M., Wang, Z.W.: Observed performance of a deep multi-strutted excavation in Shanghai soft clays. Journal of Geotechnical and Geoenvironmental Engineering ASCE 131,1004–1013 (2005).
9. Parashar, S., Mitchell, R., Hee, M.W., Sanmugnathan, D., Sloan, E., Nicholson, G.: Performance monitoring of deep excavation at Changi WRP project, Singapore. In: DiMaggio, J., Osborn, P. (eds.) In: Proceedings of the 7th International Symposium on Field Measurements in Geomechanics, pp. 1–12. ASCE (2007)
10. Li, S., Yao, A., & Ma, Y.: Failure Mechanism and Passive Earth Pressure on Foundation Pits with Skirt Reinforcement. Soil Mechanics and Foundation Engineering, 58(1), 25–33 (2021).

11. Schanz, T., Vermeer, P. A., Bonnier, B. G.: The Hardening Soil Model: formulation and Verification. Beyond 2000 in Computational Geotechnics - 10 years of PLAXIS, Balkema (1999)
12. Teo, P., Wong, K.: Application of the Hardening Soil model in deep excavation analysis. The IES Journal Part A: Civil & Structural Engineering (2010).
13. PLAXIS (2023). PLAXIS 2D Tutorial Manual. https//www.plaxis.com last accessed 2023/03
14. Bowles, J. E.: Foundation Analysis and Design. 5th edn. McGraw-Hill Education. Peoria, Illinois (2016).

An Assessment of Shrinkage Characteristics of Cementitiously Stabilized Granular Material for Pavement Layers

Samir Saurav[1] [0000-0002-3117-0729], Sanjeev Sinha[1] [0000-0003-1041-156X] and Anish Kumar[2] [0000-0002-5706-3219]

[1] Civil Engineering Department, National Institute of Technology Patna, Ashok Rajpath, Patna, Bihar, India.
samirs.phd20.ce@nitp.ac.in and sanjeev@nitp.ac.in
[2] Civil Engineering Department, Rajkiiya Engineering College, Azamgarh, Uttar Pradesh, India.
anish@gecazamgarh.ac.in

Abstract. The performance of pavement layers relies not only on their strength, but also on the shrinkage properties of the stabilized materials used in the base and subbase layers. Shrinkage cracking occurring in cementitiously stabilized layers (CSL) has a detrimental impact on pavement structures, causing distress and reducing their service life. Therefore, it is crucial to develop methods that effectively characterize the properties of cementitiously stabilized granular materials (CSGM) contributing to shrinkage cracking. Currently, there is a limited number of test methods available to comprehensively assess the shrinkage behavior of CSGM. Shrinkage in CSL mainly consists of ultimate drying shrinkage and autogenous shrinkage. The objective of this study is to characterize the strength and shrinkage properties of CSGM specimens. In particular, unconfined compressive strength tests were utilized to determine the optimal binder dose as specified by IRC 37 (2018) for the base and sub-base layers of the pavement. Furthermore, the study aimed to assess the shrinkage characteristics. The cement content was varied from 2% to 12% of the total dry mass of the CSGM sample. Results revealed that at 6% cement content, specimens exhibited more than three times the strength increase compared to those with 2% cement content. Additionally, the findings suggest that autogenous shrinkage strain is relatively small in comparison to ultimate drying shrinkage.

Keywords: Cementitiously Stabilized Granular Materials (CSGM); Unconfined Compression Strength (UCS); Ultimate Drying Shrinkage; Autogeneous Shrinkage.

1 Introduction

Due to the growing demand for natural resources, the availability of traditional paving materials is becoming limited, largely due to the construction and restoration of

pavements [1-3]. However, the scarcity of such resources necessitates the development of alternative paving techniques and the removal of environmental obstacles to resource exploitation [1, 4-6]. In recent studies of Biswal et al. [1] and Barik et al. [4], researchers have explored the feasibility by stabilizing moorum (a granular material) with a cement in terms of providing adequate structural performance at a lower cost. Generally, moorum is a residual soil formed in tropical regions by the weathering of basaltic rock [1]. The quality of India's hard moorum varies substantially from region to region [1, 4]. Despite their significant use in road construction, very few studies had been conducted to define the available moorum in India [3]. They consisted of varied-sized fragments of eroded rock, sand, silt, and clay. Instead of humus, iron oxides, aluminium oxides, and hydroxides created moorum [4]. The red colour was due to the presence of iron compounds. They are ideal for road construction. On the basis of moorum's geotechnical qualities, it is considered a good construction material for both subgrade and subbase, but control procedures had been proposed in various literature [6].This exploration of alternative materials is of utmost importance for sustainable construction practices, especially for both urban and low-traffic roadways.

As per standard practice of pavement layer stabilization, the unconfined compressive strength (UCS) is a crucial parameter for determining the suitability of stabilized materials in the base or subbase layer of pavements [1-5]. As per IRC 37 (2018), the required UCS value for acceptance in pavement layers is 1.7 MPa for the subbase and 3 MPa for the base layer. While other standards may have slightly higher or lower values, they do not exceed 4.5 MPa. Chamling et al. [9] investigated the performance of cement-stabilized granular lateritic soil from the eastern region of India, considering factors such as soil type, cement content, moulding moisture, and ambient temperature. Shankar et al. [10] reported a significant increase in the 7-day unconfined compressive strength (UCS) of Indian lateritic soil with the addition of 4% cement and pond ash. Caro et al. [11] studied the impact of water on the resilience modulus of untreated and treated Colombian sandy lateritic soil, recommending an optimal cement content of 6% for improved field performance. Additionally, Mengue et al. [12] assessed the improvement of fine-grained lateritic soil from Cameroon, determining suitable cement contents of 3% and 6% for sub-base and base layer applications, respectively.

Similarly, drying shrinkage that contributes most to the early-age shrinkage displacement and cracking in cement stabilized layer (CSL) [7-8]. Drying shrinkage is influenced by the initial water content. It has been found that the moisture content during compaction of CSL should be at the optimum or slightly below it but never above to minimize the shrinkage strain and cracking [8] and [9]. George [10] has also reported that shrinkage potential can be reduced by reducing molding moisture, increasing compaction density. Also, autogenous shrinkage results from the hydration reaction between water and cement molecules. The hydration products have smaller volume than the reactants, water and cement, which causes the autogenous shrinkage [11, 12].

Such investigations are essential to ensure their suitability and performance in real-world scenarios. Hence, this study focusses on assessment of strength along with the shrinkage strain at different cement proportion varying 2% to 12% of total dry mass.

2 Materials

This study adopts the experimental program presented in Figure 1. The moorum used in this study was sourced from a specific quarry site located in the eastern part of India. Samples were carefully collected from suitable depths within the quarries. The engineering and physical characteristics of untreated moorum are presented in Table 1 The gradation curves for the moorum are depicted in Figure 2. Based on the Indian soil classification system, moorum is classified as well-graded sand (SW). Additionally, according to AASHTO (2011) and Unified Soil Classification System (USCS) standard, moorum falls under the category A-1-a and SP respectively. For the stabilization process, grade 43 Ordinary Portland cement (OPC) was utilized.

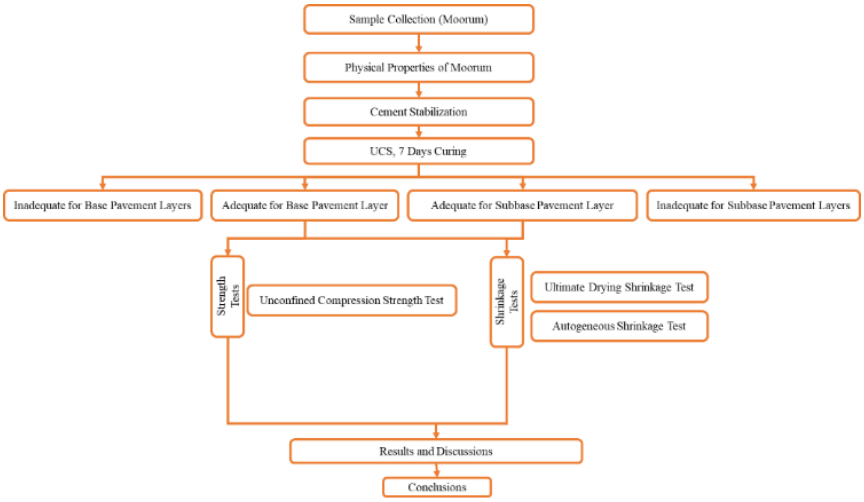

Fig. 1. The experimental programme methodology adopted in this study.

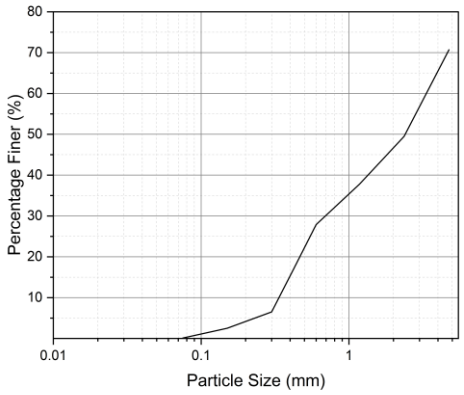

Fig. 2. A particle size distribution curve of collected moorum sample.

Table 1. Physical and engineering properties of moorum material.

Property	Indian Standard	Moorum
Soil Classification (as per USCS)	IS:2720 Part IV and ASTM D2487-11 (2011)	SW
Gravel (%)		9.99
Sand (%)		88.29
Silt (%)		1.72
Clay (%)		0.47
Finenes Modulus	IS 383	-
Type of Sand		-
Zone of Sand		-
Bulking (%)	IS 2386 Part II	-
Silt Content (%)		-
Specific gravity	IS 2386 Part III	2.68
Water Absorption (%)	IS 2386 Part III	10.72
Liquid Limit (%)	IS 2720 Part V	36.00
Plastic Limit (%)		32.90
Plasticity Index (%)		3.10
Maximum Dry Density (γ_d) in g/cc (MDD)	IS 2720 Part VII/ ASTM D1557 (2012)	1.94
Optimum Moisture Content (%) (OMC)	IS 2720 Part VII	9.82
UCS (Un-Treated Sample after 7-Day)- MPa	IS 2720 Part X	1.09
California Bearing Ratios (CBR) in %	IS 2720 Part XVI	5.82
Cohesion (C) in kN/m^2)	IS 2720 Part XIII	32.94
Φ in (º)		0.57
Permeability (m/day)	IS 2720 Part XVII	$2.21 * 10^{-3}$

3 Methodology

Modified Proctor tests were conducted on untreated moorum as well as moorum mixed with cement at concentrations ranging from 2% to 12%, following the guidelines of IS 2720 Part VII (2012) and ASTMD 1557 12 (2021), to determine the compaction parameters. To stabilize the moorum, varying percentages of cement were mixed based on the dry mass percentage of the moorum, with a maximum of 12% cement content. Before sample preparation, a specified amount of air-dried moorum and cement were thoroughly mixed to ensure homogeneity. Additionally, a obtained quantity of water was added to the mixture further.

The unconfined compression strength (UCS) test was conducted following the guidelines of ASTM D2166 (2016) and Indian Standard 2720 Part X (1991). To ensure sample integrity during extraction, a split mould was utilized to create cylindrical specimens measuring 100 mm in diameter and 50 mm in height for the unconfined compressive strength (UCS) test. For compaction, the samples were compacted in three layers, each receiving 25 blows, in order to achieve a dry density equivalent to the maximum dry density (MDD). The moisture content of the samples was determined by preserving a small portion of the sample (consisting of sand, brick, cement, and water).

Following extraction, the samples were covered in plastic to prevent moisture loss and cured for specific durations. Five cylindrical specimens were prepared for each cement content and cured for 7 and 28 days, respectively, before undergoing UCS testing.

Additionally, for ultimate drying shrinkage, the final drying shrinkage strain which indicates the material's characteristic of drying shrinkage after an extended period of drying, is of interest. To address this, adjustments were made to the humidity chamber based on available literature [16-18]. Consequently, the primary test was conducted immediately after compaction and demolding. For the ultimate drying shrinkage strain test, beam specimens measuring 101.6mm x 101.6mm x 285.75mm were used. The shrinkage of each specimen was measured in a humidity room using dial gauges attached to the specimen surfaces. The relative humidity (RH) and temperature values, as indicated in Table 2, were maintained during the test. Measurements continued until the shrinkage strain reached a stable condition. To minimize friction between the specimens and the bottom plate, a thin layer of plastic sheet was inserted between them. The selection of relative humidity (RH) and temperature was based on Indian yearly temperature and humidity conditions to simulate the prevailing variations in Indian circumstances. Notably, temperature and low or high RH conditions were evaluated, which had not been studied in prior research, to ascertain their effects on the results.

Autogenous shrinkage, which refers to the contraction of cement-stabilized materials (CSM) caused by the binder, is an important phenomenon to consider [16, 19]. To isolate the observed shrinkage strain resulting from the hydration of the cementitious binder and eliminate the influence of drying shrinkage due to evaporation, it is crucial to ensure proper sealing of the specimen throughout the test [16, 17]. The characterization of autogenous contraction strain in cement-stabilized materials does not have a universally accepted method yet. However, the standard method for measuring autogenous shrinkage strain in concrete involves using a strain transducer positioned in the middle of a concrete prism [20]. However, CSM specimens, unlike regular concrete specimens, undergo compaction before casting, making it unsuitable to use strain transducers during compaction due to their susceptibility to breakage.

For this experiment, an apparatus developed by Wang et al. [16] was adapted to measure the autogenous shrinkage strain of the specimens. To minimize moisture loss and drying shrinkage, the specimens were wrapped in plastic initially. However, it is challenging to achieve airtight sealing and prevent drying shrinkage with plastic wrapping alone. Therefore, wax was used as an alternative to protect the specimens. Wax was poured into plaster moulds, with holes at the bottom to allow excess liquid wax to escape. The specimens were coated with a thin layer of wax, taking advantage of the high viscosity and temperature-dependent solidification properties of wax. After removing the plaster mould, the specimens and wax were allowed to cool to ambient temperature. Dial gauges were attached to the ends of the prism samples to measure the amount of autogenous shrinkage.

Table 2 Designed relative humidity and temperature variations for measuring shrinkage characteristics.

Sl.No.	Relative Humidity (RH) in %	Temperature (T) in °C
1	30	30
2	40	20
3	40	40
4	50	32
5	65	20
6	65	40

4 Results and Discussion

UCS values after 7, 14, 28, 90 and 120 days of curing with varying cement content for moorum. The values increased from 0.14 to 1.5, with the increase in cement content from 2% to 12% by weight for moorum and remarkable change was noticed till 9% and not much afterwards at respective cement dosage. The strength for UCS in Biswal et al. [1] was shown no remarkable strength after 6% whereas in this study the increment till 9% had been observed. This indicates that the CSGM specimen becomes a stable stabilised material (i.e. the adverse effect of moisture does not increase) beyond 10% cement by weight. The average 7-day to 120 days strength was found to be above 6 MPa for moorum (Figure 3).

Similarly, study investigated the drying shrinkage of CSGMs under different relative humidity and temperature conditions. Specifically, three CSGM representative samples were prepared at varying relative humidity levels (65%, 50%, 40%, and 30%) and temperatures (20°C, 32°C, and 40°C) to determine the extent of shrinkage caused by the cement itself. The results revealed that drying shrinkage is rapid within the first 24 hours and slows down thereafter, with 90% of the final shrinkage occurring within three to five days, depending on the cement dosage. It was found that adding 2% to 4% of cement greatly reduces shrinkage, but the strain increases gradually when the cement content is increased to 6% or 12%. This may be attributed to the increase in pore size with higher cement content. The final drying shrinkage strain for cement dosages of 2% to 12% ranged from 0.001 to 0.009, with no observed strain exceeding 525 microstrain. The optimum moisture content of the CSGM specimen was found to be less than 13%, indicating that the soil has lower shrinkage in the long run. Additionally, drying shrinkage was found to increase with decreasing relative humidity and increasing temperature, as moisture evaporates more quickly under these conditions (Figure 4). An autogenous shrinkage test using the wax sealing method was employed (Figure 5). The results indicated that the autogenous shrinkage strain was less than the ultimate drying shrinkage strain. Overall, these findings provide valuable insights into the behavior of CSGM specimens under different environmental conditions and can inform the optimization of mix design and stabilization methods.

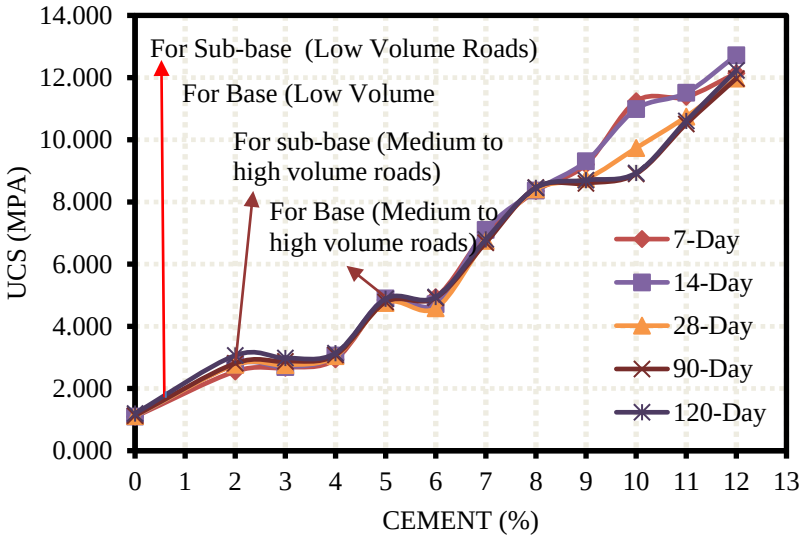

Fig. 3. Variation in UCS value from 7-day to 120-day curing with varying cement content for collected moorum sample.

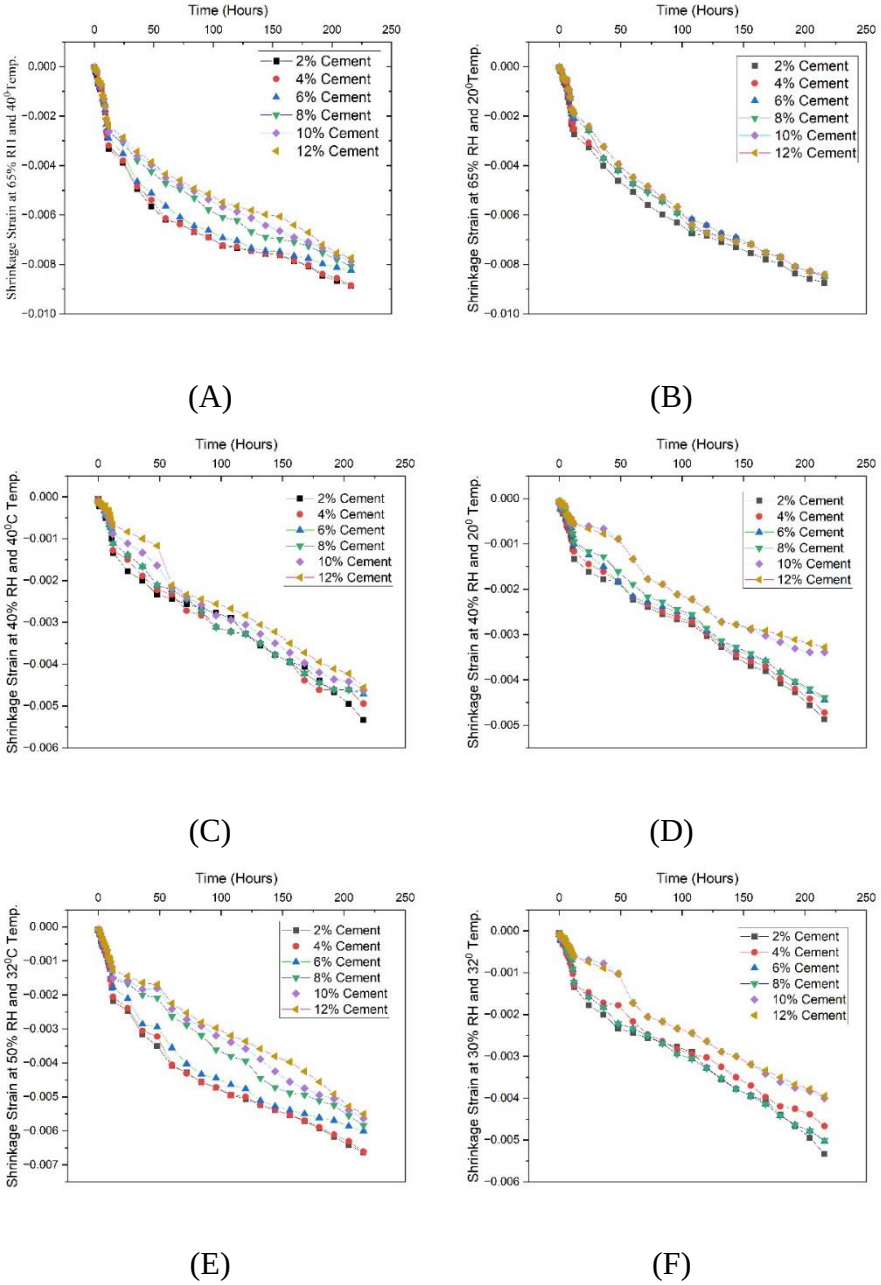

Fig. 4. The shrinkage strain at various cement percentage along with RH and Temp. variations under the ultimate drying shrinkage test.

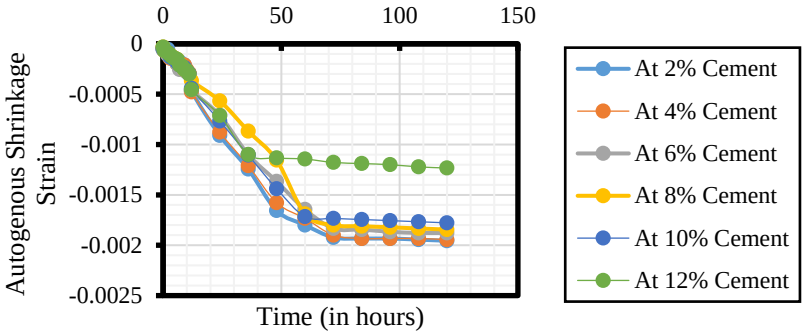

Fig. 5. The autogenous shrinkage strain at various cement percentages.

5 Conclusion

In this study, comprehensive laboratory tests were conducted on cementitiously stabilised granular materials (CSGM) moorum. It was found that a 7-day UCS value of 1.5 to 3 MPa is suitable for stabilised material containing 3% cement by weight, in the presence of water, as per standard provisions. After 7 days of curing, the UCS strength increases with increasing cement content up to approximately 9% by weight, after which the rate of increase slows. It was also determined that 5% cement by weight is suitable for use in the base layer, as per IRC (2012) and NCHRP (2004) standards.
The ultimate drying shrinkage test findings suggest that a lower relative humidity and higher temperature accelerated the drying shrinkage due to the rapid evaporation of moisture at lower or higher temperatures as a result of high moisture content. Further field testing is recommended to prevent the failure of stabilised pavement layers, which leads to cracks, and to check shrinkage strain in both methods. The use of ultimate and autogenous shrinkage tests can facilitate the improvement of mix design and selection of stabilisation techniques.

Acknowledgement
I would like to thank the lab staff for support and continuous guidance from PhD scholar Sachin Kumar towards this laboratory procedures.

References

1. Biswal, D. R., Sahoo, U. C., and Dash, S. R. (2020). “Fatigue Characteristics of Cement-Stabilized Granular Lateritic Soils.” Journal of Transportation Engineering, Part B: Pavements, 146(1), 04019038.
2. Biswal, D. R., Sahoo, U. C., and Dash, S. R. (2018). “Strength and Stiffness Studies of Cement Stabilized Granular Lateritic Soil.” Sustainable Civil Infrastructures, (April 2019), 320–336.

3. Biswal, D. R., Sahoo, U. C., and Dash, S. R. (2016). "Characterization of granular lateritic soils as pavement material." Transportation Geotechnics, Elsevier Ltd, 6, 108–122.
4. Barik, S. (2015). "Use of Locally Available Materials in Pavement Sub-Base".
5. Barik, Shubhakanta & Panda, Mahabir & Bhuyan, Prasanta. (2017). A Study on Use of Locally Available Moorum in Pavement Base and Sub-Base. 360-369. 10.1061/9780784480939.031.
6. Samuel, E., and Chukwuebuka, O. (2022). "Effect of Geochemical Composition of Lateritic Soils on their Geotechnical Properties." Indian Geotechnical Journal, Springer India.
7. Bofinger HE, Hassan HO, Williams RIT. The Shrinkage of Fine-Grained Soil Cement. TRRL Supplementary Report 398; 1978.
8. George KP. Shrinkage Characteristics of Soil-Cement Mixtures. Highway Res Rec1968;255:42–58.
9. Norling LT. Minimizing Reflective Cracks in Soil-Cement Pavements: A Status Report of Laboratory Studies and Field Practices. Highway Res Rec1973;442:22–33.
10. George KP. Characterization and Structural Design of Cement-Treated Base. In Transportation Research Record: Journal of the Transportation Research Board, No. 1288, Transportation Research Board of the National Academies, Washington, D.C.;1990, p. 78–87.
11. Mbaraga AN. Shrinkage Characterisation, Behavioural Properties and Durability of Cement-Stabilised Pavement Materials. PhD Dissertation. University of Stellenbosch, South Africa; 2015.
12. Agnello NM. Modelling the Shrinkage Behaviour of Recycled Concrete Aggregate and Cement Stabilised Materials. Master Thesis. Stellenbosch University, South Africa; 2018.
13. Consoli NC, Winter D, Leon HB, Scheuermann Filho HC. Durability, strength, and stiffness of green stabilized sand. Journal of Geotechnical and Geoenvironmental Engineering. 2018 Sep 1;144(9):04018057.
14. Mahalinga-Iyer U, Williams DJ. Properties and performance of lateritic soil in road pavements. Engineering Geology. 1997 May 23;46(2):71-80.
15. Joel, M., and Agbede, I. O. (2011). "Mechanical-Cement Stabilization of Laterite for Use as Flexible Pavement Material." Journal of Materials in Civil Engineering, 23(2), 146–152.
16. Wang J, Li X, Wen H, Muhunthan B. Shrinkage cracking model for cementitiously stabilized layers for use in the mechanistic-empirical pavement design guide. Transportation Geotechnics. 2020 Sep 1;24:100386. https://doi.org/10.1016/j.trgeo.2020.100386.
17. Pu S, Zhu Z, Song W, Wan Y, Wang H, Song S, Zhang J. Mechanical and microscopic properties of cement stabilized silt. KSCE Journal of Civil Engineering. 2020 Aug;24:2333-44.
18. Zhang J, Gao Y, Wang Z. Evaluation of shrinkage induced cracking performance of low shrinkage engineered cementitious composite by ring tests. Composites Part B: Engineering. 2013 Sep 1;52:21-9. http://dx.doi.org/10.1016/j.compositesb.2013.03.012.
19. Liu J, Tian Q, Wang Y, Li H, Xu W. Evaluation method and mitigation strategies for shrinkage cracking of modern concrete. Engineering. 2021 Mar 1;7(3):348-57. https://doi.org/10.1016/j.eng.2021.01.006
20. Zhang MH, Tam CT, Leow MP. Effect of water-to-cementitious materials ratio and silica fume on the autogenous shrinkage of concrete. Cement and Concrete Research. 2003 Oct 1;33(10):1687-94.

Active and Passive Pressures Acting on Smooth Circular Shafts

Abdelmadjid Meftah[1], Naima Benmebark[2], Sadok Benmebark[3]

[1] Constantine 1 University, Department of Geographical Sciences and Topography, Algeria.
abdelmadjid.meftah@umc.edu.dz
[2] Biskra University, Department of Civil and Hydraulic Engineering, Algeria.
benmebarekn@yahoo.fr
[3] Biskra University, Department of Civil and Hydraulic Engineering, Algeria.
benmebareks@yahoo.fr

Abstract. Several researchers have studied the lateral earth pressures acting on the vertical, rigid and circular shaft using experimental, theoretical and numerical methods of analysis, in this study a new retaining wall model under axisymmetric conditions with outward pressure is considered and can be widely used in the design of grain silos, buildings and road construction. The active and passive earth pressures are numerically studied by using the computer code FLAC-2D to evaluate the evolution of the distribution of earth pressure on a smooth cylindrical wall filled with granular material and subjected to radial displacement.
A parametric study is carried out in order to evaluate the distribution of the active and passive pressure on the wall as a function of the radius, the friction angle of the granular material. The numerical study found that: Firstly for the outward wall, increasing (r) has not effect on the active and passive earth pressures coefficients and is similar to plane strain conditions, secondly has not effect on the active and passive earth pressures coefficients and is similar to plane strain conditions, for the inward wall, increasing (r) has a fully clear effect on the active and passive earth pressures coefficients and is similar to plane strain conditions when r/f =33.33. Numerical results are discussed and compared with recent experimental results and theoretical solutions.

Keywords: Vertical circular shaft, Arching effect, Axisymmetric earth pressure, Numerical modeling.

1 Introduction

Several attempts have been made to study the lateral earth pressure distribution for cylindrical shafts in non-cohesive media. Westergaard, 1940 [20] and Terzaghi, 1943 [18], proposed analytical solutions; Prater, 1977 [13] used the limit equilibrium method; and Berezantzev, 1958 [3], Liu and Wang, 2008 [9], Liu et al., 2009 [10] used the slip line method. In contrast to classical earth pressure theory, where active and passive earth pressures are calculated using Coulomb, 1776 [5] or Rankine, 1857 [14]. Coulomb first proposed the limit equilibrium method by assuming a plane failure

surface, and this method can be used to determine the lateral earth pressure in general cases for cohesionless soil. Rankine's solution could potentially explain cohesive-friction backfill material bounded by a horizontal line, when the walls are vertical and there is no wall friction. Distributions obtained in axisymmetric conditions can vary significantly depending on the analysis method chosen. Xianfeng Mg et al 2021 [21] provided valuable knowledge on earth pressure distribution for the construction of circular deep shafts (e.g. 100m) in composite geological strata. Martin et al [12] concluded that the vaulting effect that develops in the ground and in the support makes circular shafts quite special with respect to the verifications classically defined for plane walls.

The objective of this study is to investigate the active and passive earth pressures on smooth cylindrical shaft linings installed in cohesionless ground and the required displacement for establishing active conditions by numerical approach using the explicit finite difference code FLAC [7] (Fast Lagrangian Analyses of Continua). The results are compared to published experimental results and many interesting conclusions are drawn, which cannot be found in existing research.

2 Numerical Modelling

2.1 Model Description

Studies with two numerical models were performed with the finite difference method (FDM) using FLAC 2D.

Two models were validated and a parametric study was performed to obtain changes in the earth pressure distribution in the cylindrical wall. In all case studies, axisymmetric conditions and plane strain were included in the simulations. The proposed modeling procedure of passive earth pressure distribution on a cylindrical shaft is performed in two steps:

- First, the shaft installation and geostatic stresses are calculated assuming that the fixed shaft is connected to the ground via an interface element. At this stage, the strength of the interface elements is set to zero and some stepping is required to bring the model to equilibrium.
- In the second step, radial velocity towards the shaft axis was applied to grid points representing wall shaft until smooth plastic flow was achieved (i.e. until a constant pressure on the shaft wall is reached). The level of error in such a FLAC calculation method depends on the speed used, so low speeds are recommended.

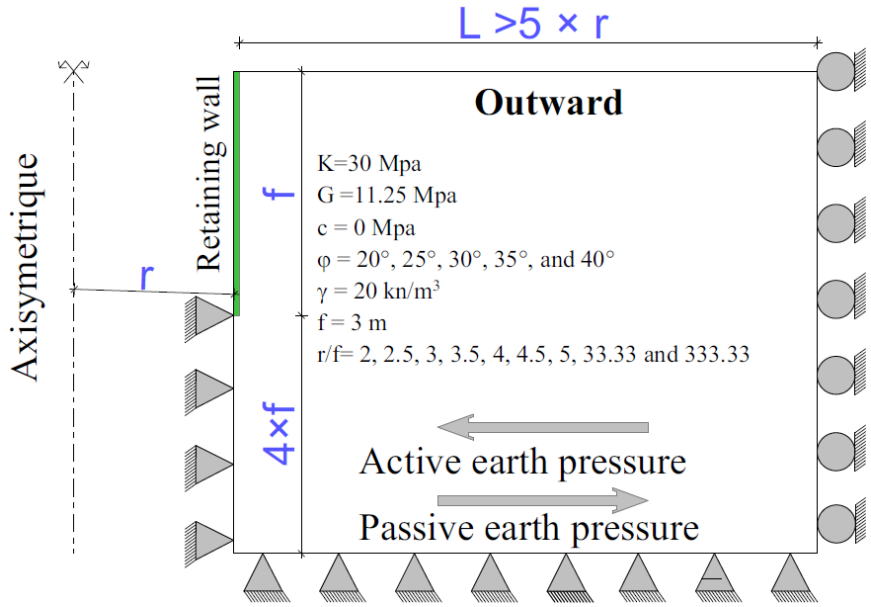

Fig. 1. Retaining Walls in Axisymmetric Condition: Outward Mechanisms active and passive earth pressures.

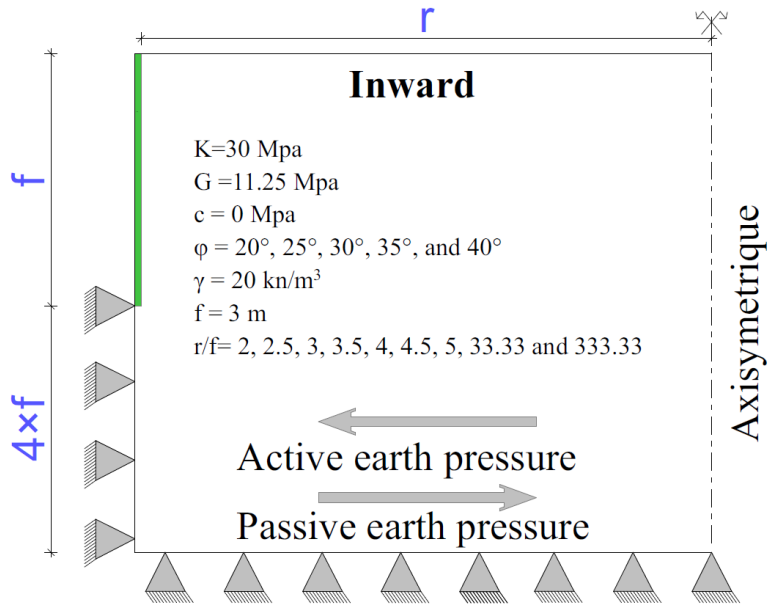

Fig. 2. Retaining Walls in Axisymmetric Condition: Inward Mechanisms active and passive earth pressures.

2.2 Active and Passive Earth Pressure Coefficients

There are many solutions based on the passive earth pressure problem in the literature.

- The limit equilibrium method [7-19]
- The slip line method [5-9]
- Limit analysis theory [12-17-18]

The tendency today in practice is to use the values given by Coulomb 1776 [5] and Rankine, 1857 [14].

2.3 Soil

Soil behavior is modeled by an elastic-perfectly-plastic Mohr-Coulomb model encoded in the FLAC code.

The mesh size is finer near the walls where strain is concentrated. Physical and mechanical characteristics assigned to the soil were: an elastic bulk modulus K=30 Mpa, an shear modulus G =11.25 Mpa, cohesion c = 0, internal friction angle $\varphi = 20°$, 25°, 30°, 35°, and 40°.

2.4 Boundary Conditions

To begin investigating and solving active and passive earth pressures in any geotechnical problem, the boundary conditions should first be determined. Fig. 1 and fig. 2 specifies the geometry of the retaining wall problem in active and passive cases. The principle of boundary conditions assumes that the lower bound is fixed in both directions, the left and right lateral boundaries are fixed horizontally.

The model has a height exceeds the sum of (4×f) below the level of the shaft toe, plus the height of the vertical shaft (f) and a length of five times the diameter of the vertical shaft from the center of the shaft. These dimensions were chosen to minimize the boundary effects on the performance of the vertical shaft.

2.5 Structural Elements

Structural elements built into FLAC do not support displacement loads. The shaft walls are therefore modeled by thin fixed membrane elements connected to the soil grid via interface elements attached on either side.

2.6 Damping

Previous research on the axisymmetric limit problem mainly considered the Mohr-Coulomb criterion as the limit condition.

The Mohr–Coulomb model are used to simulate the soil behavior with the corresponding soil parameters included in Fig.1 and 2. The Mohr-Coulomb model is an elastic perfectly plastic model. In geotechnical engineering, this model is widely used for modeling soil behavior. In the elastic region of the stress-strain curve, the model behaves linearly and its deformation is calculated based on Young and Poisson units.

2.7 Interface Elements

The shaft-soil interface is modelled with an interface element using the bilinear Mohr–Coulomb model.

Interface elements are used to describe the behavior of localized zones of deformation due to shear (slip surfaces) or in tension (cracks). Interface element is used on the contact surface between the retaining wall and soil.

3 Results and Discussions

The behavior of the ground is modeled by the elastic-perfectly plastic model of Mohr-Coulomb coded in FLAC code. All the following results are given for γ =20 kn/m^3, bulk modulus K = 30 MPa , shear modulus G = 11.25 MPa, angle of internal friction φ = 20°, 25°, 30°, 35° and 40° and cohesion c = 0.

3.1 Comparison with Other Studies

Tables 1, 2 and 3 compares the results of this study with those of other studies on plane strain and axisymmetric cases. For the active earth pressure coefficients ($K_{a\gamma}$) is shown in Tables 1, we compared our results with the both results of Liu & Wang [9] and Amin. K & Mohsen. E 2016 [2] for different values of radius (r_i) of 100 and 1000 m.

As can be observed, the results obtained in this study are in good agreement with those of Liu and Wang [9] and those of Amin. K and Mohsen. E 2016 [2]. Moreover, the results of this study for r_i = 1000 m are very close to those of Coulomb [5] and Abdul-Hamid Soubra, B. Macuh 2002 [15] for plane strain.

Similarly, for the passive earth pressure coefficients ($K_{a\gamma}$) is shown in Tables 2, and 3. Table 2 is shown for the axisymmetric inward and Table 3 is shown for the axisymmetric outward. As can be seen, there is very good agreement between the results of this study and the two results of plane strain Abdul-Hamid Soubra, B. Macuh 2002 [15] and Coulomb 1776 [5]. Moreover, the results of this study and the axisymmetric cases of Amin. K and Mohsen. E 2016 [1] are different.

Table 1. A comparison between the active earth pressure coefficients ($K_{a\gamma}$) in this study and other studies for the plane strain and axisymmetric inward cases (δ = 0°, r = 1000m, c = 0, γ = 20 kn/m^3 and H = 3 m).

	Inward wall						**Plane strain**		
φ (deg.)	**[9] r_i (m)**		**[2] r_i (m)**		**This study r_i (m)**		**This study**	**[5]**	**[15]**
	100	**1000**	**100**	**1000**	**100**	**1000**			
10°	0.696	0.708	0.681	0.701	0.691	0.693	0.702	0.704	/
20°	0.461	0.491	0.458	0.487	0.461	0.464	0.483	0.490	0.333
30°	0.300	0.332	0.299	0.329	0.307	0.310	0.325	0.333	0.217

Table 2. A comparison between the passive earth pressure coefficients ($K_{p\gamma}$) in this study and other studies for the plane strain and axisymmetric inward cases (δ = 0°, r = 1000m, c = 0, γ = 20 kn/m^3 and H = 3 m)

φ (deg.)	Inward wall				Plane strain		
	[1] r_i (m)		This study r_i (m)		This study	[5]	[15]
	100	1000	100	1000			
30°	6.69	6.58	3.02	3.03	3.02	3.00	3.00
40°	19.61	18.91	4.57	4.62	4.60	4.60	4.60

Table 3. A comparison between the passive earth pressure coefficients ($K_{p\gamma}$) in this study and other studies for the plane strain and axisymmetric Outward cases (δ = 0°, r = 1000m, c = 0, γ = 20 kn/m^3 and H = 3 m).

φ (deg.)	Outward wall				Plane strain		
	[1] r_i (m)		This study r_i (m)		This study	[5]	[15]
	100	1000	100	1000			
30°	6.74	6.59	3.00	3.00	3.02	3.00	3.00
40°	19.62	18.92	4.56	4.56	4.60	4.60	4.60

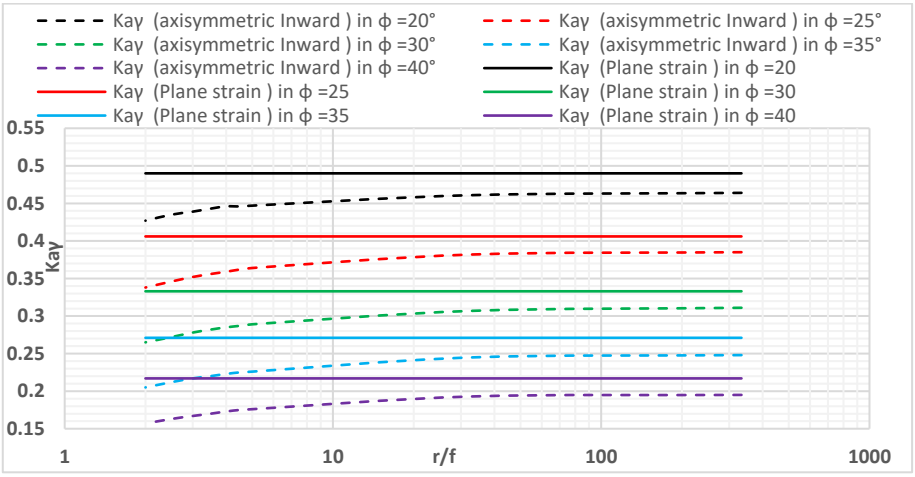

Fig. 3. Active earth pressure coefficients for Axisymmetric inward

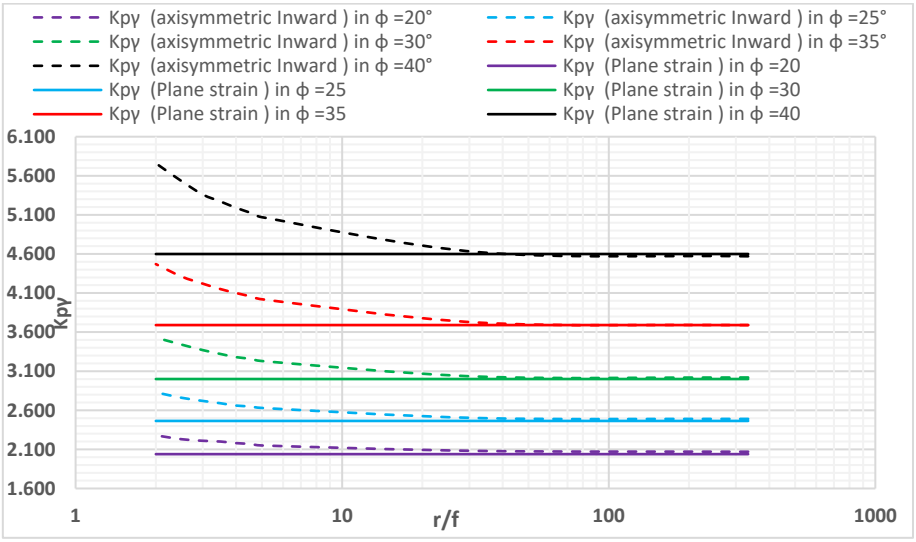

Fig. 4. Passive earth pressure coefficients for Axisymmetric inward

Table 4. Active earth pressure coefficients $K_{a\gamma}$ for axisymmetric outward cases

	r/f								
φ (deg.)	**333.33**	**33.33**	**5**	**4.50**	**4**	**3.5**	**3**	**2.5**	**2**
20°	0.469	0.470						0.469	0.470
25°	0.385	0.384						0.385	0.385
30°	0.309	0.309						0.310	0.310
35°	0.247	0.247						0.247	0.247
40°	0.194	0.194						0.195	0.195

Table 5. Passive earth pressure coefficients $K_{p\gamma}$ for axisymmetric outward cases

	r/f								
φ (deg.)	**333.33**	**33.33**	**5**	**4.50**	**4**	**3.5**	**3**	**2.5**	**2**
20°	2.06	2.06						2.05	2.05
25°	2.48	2.47						2.45	2.46
30°	3.00	2.99						2.98	2.99
35°	3.68	3.67						3.66	3.66
40°	4.56	4.56						4.55	4.57

Table 6. Active earth pressure coefficients $K_{a\gamma}$ for axisymmetric inward cases

	r/f								
φ (deg.)	**333.33**	**33.33**	**5**	**4.50**	**4**	**3.5**	**3**	**2.5**	**2**
20°	0.464	0.461	0.447	0.446	0.446	0.443	0.439	0.435	0.427
25°	0.385	0.382	0.364	0.362	0.359	0.356	0.352	0.346	0.338
30°	0.311	0.307	0.289	0.287	0.285	0.282	0.278	0.272	0.265
35°	0.248	0.245	0.226	0.225	0.223	0.220	0.217	0.212	0.205
40°	0.195	0.193	0.176	0.175	0.173	0.170	0.167	0.163	0.157

Table 7. Passive earth pressure coefficients $K_{p\gamma}$ for axisymmetric inward cases

	r/f								
φ (deg.)	**333.33**	**33.33**	**5**	**4.50**	**4**	**3.5**	**3**	**2.5**	**2**
20°	2.07	2.08	2.15	2.17	2.18	2.20	2.21	2.23	2.28
25°	2.49	2.50	2.63	2.65	2.66	2.69	2.72	2.76	2.83
30°	3.02	3.03	3.23	3.26	2.28	3.32	3.37	3.44	3.53
35°	3.69	3.72	4.02	4.06	4.10	4.15	4.22	4.31	4.47
40°	4.57	4.62	5.07	5.13	5.19	5.27	5.36	5.53	5.76

3.2 Implication and Explanation of Findings

Tables 4 to 7 summarize the results of the parameter investigation by numerical investigation of the active and passive earth pressure coefficient inward and outward the wall. These tables show the effect of parameters such as soil friction angle (φ) and retaining wall radius (r) on the active and passive earth pressure coefficients.

Figure 3 and Fig. 4 compares the results of axisymmetric and those of plane strain.

Tables 4 to 7 and Figures 3 and 4 illustrate that:

- There is an effect of the circular shape of the wall on the active and passive earth pressures in axisymmetric inward case.
- Inward case, the active and passive earth pressures, are decreased and increase respectively with increasing radius and tend to approach Coulomb values for very large radii.
- Outward case, the results indicated that no effect of the circular shape of the wall on the active and passive earth pressures.

4 Conclusions

Circular retaining walls are often used in deep excavation due to their structural advantages. However, employing plane strain results when designing circular retaining walls can be conservative and inaccurate. This study evaluated the axisymmetric active and passive lateral earth pressure of the retaining wall using the explicit finite difference code FLAC (Fast Lagrangian Continuum Analysis).

The results were presented and discussed in terms of earth pressures on the wall.

The following conclusions were drawn as follow.

- The results showed that the values of the lateral earth pressure for the outward and inward cases were very close to each other.
- In the outward case, the increasing (r) has not effect on the active and passive earth pressures coefficients and is similar to plane strain conditions.
- In the inward case, the increasing (r) a fully clear effect on the active and passive earth pressures coefficients and is similar to plane strain conditions.

References

1. Amin, K., and Mohsen, E.: Axisymmetric Passive Lateral Earth Pressure of Retaining Wall. KSCE Journal of Civil Engineering 21(5), 2332-2345) (November 11, 2016).
2. Amin, K., and Mohsen, E.: Axisymmetric Passive Lateral Earth Pressure of Retaining Wall. KSCE Journal of Civil Engineering 21(5), 2332-2345) (18 June 2016).
3. Berezantzev, V. G.: Earth pressure on the cylindrical retaining walls. M:Proc., Int. Soc. of Soil Mechanics and Foundation Eng. (ISSMFE) Conf. on Earth Pressure Problems, Butterworths, London, 2, 21–27 (1958).
4. Caquot, A., and Kerisel, J. Tables de poussée et de butée. Gauthier-Villars, Paris, 1948.
5. Coulomb, C.A.: Essai sur une application des regles des maximis et minimis a quelques problems de statique relatifs à l'architecture. Memoires de Mathématique et de Physique, Présentés à l'Académie Royale des sciences, par divers Savants, et lûsdans ses Assemblées, Paris, vol. 7, 343–382 (1776).
6. Duncan, J. M., and Mokwa, R.: Passive earth pressures: theories and tests. Journal of Geotechnical and Geoenvironmental Engineering, 127(3), 248–257 (2001).
7. FLAC Fast Lagrangian Analysis of Continua, ITASCA Consulting Group, Inc., Minneapolis, (2005).
8. Hettiaratchi, R. P., and Reece, A. R.: Boundary wedges in two-dimensional passive soil failure. Ge´otechnique, 25(2), 197–220 (1975).
9. Liu, F., and Wang, J.: A generalized slip line solution to the active earth pressure on circular retaining walls. Comput. Geotech, 35(2), 155-164 (2008).
10. Liu, F.Q., Wang, J.H., Zhang L.L.: Axi-symmetric active earth pressure obtained by the slip line method with a general tangential stress coefficient. Comput. Geotech, 36 (1–2), 352–358 (2009).
11. Lysmer. J.: Limit analysis of plane problems in soil mechanics. Journal of Soil Mechanics and Foundation Division, ASCE, 96(SM4), 1311–1334 (1970).
12. Martin, C., Nhat, H.N., Fahd, C., Maxime, F., Clément, S., Nicolas, U.: some practical considerations on the geotechnical justification of circular shafts. 11èmes journées nationales de géotechnique et de géologie de l'ingénieur, Institut National des Sciences Appliquées de Lyon [INSA Lyon], CFMS, CFMR, CFGI, (2022)
13. Prater, E.G.: An examination of some theories of earth pressure on shaft linings. Canadian Geotechnical Journal, 14(1), 91–106 (1977).
14. Rankine, W.J.M.: On the stability of loose earth. Phil. Trans. Royal. Society, London, 147(1), 9–27 (1857).
15. Soubra, A., and Macuh, B.: Active and passive earth pressure coefficients by a kinematical approach. Proceedings of the ICE Geotechnical Engineering, 155(2) 119-131 (2002).
16. Soubra, A.H., Kastner, R., and Benmansour, A.: Passive earth pressures in the presence of hydraulic gradients. Ge´otechnique, 49(3), 319–330 (1999).
17. Soubra, A.-H., and Regenass, P.: Three-dimensional passive earth pressures by kinematical approach. Journal of Geotechnical and Geoenvironmental Engineering, ASCE, 126(11), 969–978 (2000).
18. Terzaghi, K.: Theoretical soil mechanics. Wiley, New York (1943).

19. Weidong, H., Kangxing, L., Xinnian, Z., Xiaolong, T., Xiyu, Z.: Active Earth Pressure against Rigid Retaining Walls for Finite Soils in Sloping Condition considering Shear Stress and Soil Arching Effect. Advances in Civil Engineering 2020, 1-11 (2020).
20. Westergaard, H.M.: Plastic state of stress around deep well. Boston Society of Civil Engineers Journal, 27(1), 1-5 (1940).
21. Xianfeng, M., Chang, L., Lei, W., and Juyun, Y.: Analysis of earth pressure distribution on deep circular shafts in composite geological strata using centrifuge modelling. Bulletin of Engineering Geology and the Environment 80(2), 4089–4096 (2021).

Automated Extraction of Geotechnical Data from PDF Reports and Kriging Application

Nouhayla Bouayach[1[0009-0006-2640-921X], 2], Fouzia Kassou[1[0000-0002-6580-251X], 3], Mustapha Rguig[1[0009-0005-4206-2458], 4], Hajar Zoubir[1[0000-0002-7786-4953], 5]

[1] ERIC-(LAGCET), Hassania School of Public Works, Casablanca, Morocco
[2]Author E-mail: bouayach.nouhayla.cedoc@ehtp.ac.ma
[3]Corresponding Author E-mail: kassou@ehtp.ac.ma
[4]Author E-mail: rguig@ehtp.ac.ma
[5]Author E-mail: zoubir.hajar.cedoc@ehtp.ac.ma

Abstract. The need for accurate and timely data collection in geotechnical engineering is growing. However, the collection of data stored in large PDF reports is time-consuming and prone to errors if conducted manually. In this study, we use pattern recognition techniques and image processing and Optical Character Recognition (OCR) techniques to identify and extract relevant data, automating geotechnical test data extraction from PDF reports. The extracted data undergoes a thorough verification process, including random checks and outlier value analysis, ensuring its accuracy and reliability. Our study focuses on three types of geotechnical tests: PMT, CPT, and SPT. The study's practical applications are two-fold. Firstly, it converts unstructured PDF reports into a structured format, significantly enhancing the efficiency and reliability of data extraction. Secondly, as shown in an application, the extracted database can be leveraged for spatial analysis using kriging, a geostatistical technique for spatial interpolation and prediction. By automating the data extraction process and enabling advanced analysis techniques, our study highlights the importance of structured data in geotechnical and civil engineering.

Keywords: Geotechnical engineering, data extraction, PDF reports, automation, Kriging.

1 Introduction

Geotechnical engineering plays a vital role in ensuring the safety and stability of infrastructure projects, particularly in areas with complex soil conditions or significant uncertainties. The extraction and analysis of data from geotechnical reports are crucial for making informed decisions in engineering design and construction, especially in projects that require extensive data collection and analysis. While not all practitioners may encounter such situations, the ability to extract large amounts of data from geotechnical reports is particularly relevant for researchers and projects with significant data requirements. This data serves as a foundation for various applications, including machine learning algorithms, numerical simulations, and geostatistical analyses. By

automating the data extraction process from geotechnical reports, our approach offers an efficient solution for researchers and engineers who need to extract and utilize vast amounts of data for their work, enabling them to derive valuable insights and enhance the reliability of their geotechnical analyses.

Automated extraction of geotechnical data from PDF reports requires the use of various techniques and algorithms as these reports often contain a combination of text, tables, and graphical information. In the domain of automated data extraction from PDF reports, researchers have explored various approaches. One approach involves using text classification algorithms to categorize different sections of the reports. Bui et al. [1] developed a text classification algorithm that successfully classified text snippets into categories, enabling the extraction of relevant information. However, the classified categories such as “title”, “abstract”, “metadata”, are too general for our problematic and needs training on a labeled dataset. Downing et al. [3] developed automated text mining tools to extract chemical information from electronic chemistry theses. They used regular expressions to extract chemical names and terms, experimental procedures, and physical chemistry properties, and characterization data directly from PDF/DOCX electronic theses. This approach is effective but relies on specific document structures and is specific to the information sought from the document. Kallmes et al. [6] conducted a pilot survey to classify the structure and format of descriptive statistics reported in tables in the comparative medical literature, demonstrating the potential for automated extraction of quantitative evidence. In addition to text-based approaches, image processing techniques have been employed to extract data from images within the PDF reports. Optical Character Recognition (OCR) techniques, based on deep learning models, have been utilized to detect and extract text from documents and images. This has proven effective in extracting information from complex structured documents that incorporate images [15]. These approaches have shown promise in extracting information, but they may have limitations such as the need for training on labeled datasets or the reliance on specific document structures that do not match a geotechnical report’s structure.

In this study, we present an automated data extraction approach tailored to the specificities of geotechnical PDF reports. We address the challenge of working with geotechnical reports of diverse structures by leveraging manual exploring and spotting relevant general patterns within the documents. By incorporating OCR, image processing techniques such as edge detection and the Hough Line Transform [4], and regular expression search on text, we efficiently extract all the necessary geotechnical data from our reports, such as the PMT, CPT, and SPT measures and the lithological descriptions. This approach doesn’t call for training on labeled datasets and allows for the extraction of data in various origin formats, including both text and images, and is tailored to the specific nature of geotechnical reports and data. To ensure the accuracy and reliability of the extracted data, a verification process was conducted. The practical importance of this work is demonstrated through a case study involving the utilization of kriging [7] for spatial analysis on data extracted using our approach, showcasing the significance of structured data in geotechnical engineering.

2 Methodology

This section presents the method used to automate the extraction of geotechnical test data from PDF reports. The reports used contain results of geotechnical tests conducted on multiple regions in the north of Morocco, precisely in the section between the cities of Tangier and Assilah. Our geotechnical reports contain three different types of geotechnical tests: the Pressuremeter Menard Test (PMT), the Cone Penetration Test (CPT), and the Standard Penetration Test (SPT). The extracted data is then structured into separate tables for each test type. Verification methods are used to spot and correct the occurring extraction errors.

2.1 Libraries Used

In this project, several Python libraries were utilized to accomplish various tasks. PyPDF2 [1] was employed for PDF file manipulation, enabling the extraction and modification of content within PDF documents. For image processing and computer vision tasks, the cv2 library, also known as OpenCV [2], proved to be instrumental. It provided a wide range of functionalities for image manipulation and analysis. To convert PDF pages into images, the pdf2image library [10] was used, facilitating further image processing operations. For optical character recognition (OCR), pytesseract [13], a wrapper for Google's Tesseract OCR engine [9], was employed to extract text from images. In addition, the fitz library, based on the PyMuPDF library [11], allowed for advanced PDF operations. The Python Imaging Library (PIL) [16] was utilized for image processing tasks, offering an extensive set of functions. Numerical operations and array manipulation were made possible through the powerful numpy library [5]. For data manipulation and analysis, pandas [8] was employed, providing efficient data structures and analysis tools. Lastly, reportlab [14] was used to programmatically generate PDF documents.

2.2 Data Acquisition and Preparation

The geotechnical test data used in this study was obtained from large PDF reports that contained multiple test results (see Table 1). The report was stored as a PDF file, and the file path was provided as input to the code. The script employed the PyPDF2 library to extract pages from the PDF reports that contained the geotechnical test results. The identification of relevant pages was based on predefined patterns specific to each test type, such as the presence of specific words unique to the pages containing the results of a specific test type. The extracted pages were then saved as separate PDF files, namely "PMT.pdf," "CPT.pdf," and "SPT.pdf," for further processing.

Table 1. Different geotechnical tests included in the report.

Test type	Number of testing locations	Number of testing points
Pressuremeter Menard Test (PMT)	164	4434
Cone Penetration Test (CPT)	100	16330
Standard Penetration Test (SPT)	60	5934

2.3 Cone Penetration Test (CPT) Data Extraction

To process the CPT data, the script utilized the fitz library to open the "CPT.pdf" file. The text content of each page was extracted using the get_text() method. Regular expressions were employed to extract the desired information, including the test identifier (each test location has a unique test identifier), X, Y and Z coordinates, cone resistance and local friction. The data extraction followed the following steps:

- Extracting test identifier and coordinates from the PDF report: By carefully examining multiple geotechnical reports, manually identifying specific patterns of text that indicate the test identifier and its location coordinates on each page of the PDF. While this step may seem like a deviation from complete automation, it significantly simplifies the process of automating data extraction by leveraging regular expression matching. The identification of these general patterns unique to each information category can be efficiently accomplished within minutes by a human. The extracted data is saved in a structured table using a pandas DataFrame. As the Z coordinate was missing for many tests, the following step completes it using information from the AutoCAD MNT plan files.
- Creating an AutoCAD Script File and Extracting Elevations: creating an AutoCAD script file with a list of X and Y coordinates from tests with missing elevations, which is used as a command in AutoCAD to get the corresponding elevations from the MNT plan as an output. Then, matching the elevations with the corresponding X, Y coordinates in the table obtained in the previous step (see Table 2).
- Extracting CPT Measurements: extracting Test depth, Cone resistance, and Local friction for each test point (as multiple measurements are conducted in different depths in each test location), by searching for specific patterns of text to locate and extract the measurement values. The extracted data is saved in a pandas DataFrame (see Table 3).
- Combining the two tables to create a final DataFrame (see Table 4), stored in an Excel file.

Table 2. Extract of the table obtained in the first two steps for one CPT test location.

Test identifier	X	Y	Z
CPT_1	463792	569802	14,54

Table 3. Extract of the table obtained in the third step for one CPT test location.

Test identifier	Test depth	Cone resistance	Local friction
CPT_1	0	0	0
CPT_1	0,1	2,31	0,022
⋮	⋮	⋮	⋮
CPT_1	7,4	13,06	0,5347
CPT_1	7,5	19,49	0,514

Table 4. Extract of the final table featuring one CPT test location.

Test identifier	X	Y	Z	Test length	Cone resistance	Local friction
CPT_1	463792	569802	14,54	0	0	0
CPT_1	463792	569802	14,44	0,1	2,31	0,022
⋮	⋮	⋮	⋮	⋮	⋮	⋮
CPT_1	463792	569802	7,14	7,4	13,06	0,5347
CPT_1	463792	569802	7,04	7,5	19,49	0,514

2.4 Standard Penetration Test (SPT) Data Extraction

For the SPT data, the script followed a similar procedure. The "SPT.pdf" file was opened and the text content of each page was extracted. Regular expressions were employed to extract the relevant information, such as the test identifier, coordinates, blow counts, and dynamic resistance. The extracted information was stored as a table in an Excel file (see Table 5).

Table 5. Overview of the SPT database.

N°	Test identifier	X	Y	Z	Blow counts	Dynamic resistance
0	EXE-ZC-PS-AL Hamar-01	443553	534386	60,852	0	0
1	EXE-ZC-PS-AL Hamar-01	443553	534386	60,652	0	0
	⋮	⋮	⋮	⋮	⋮	⋮
5932	EXE-ZC-PS-R2114-20	453974	556168	57,194	44	222
5933	EXE-ZC-PS-R2114-20	453974	556168	57,394	43	217

2.5 Pressuremeter Menard Test (PMT) Data Extraction

The pressiometric test data required an additional step due to the presence of part of the test data in image form within the PDF report. The PMT data in text form (test identifier, coordinates X, Y, and Z, PMT modulus, limit pressure, and initial pressure) was extracted using a similar approach to the one described for the SPT and CPT data extraction. As for the data present in the report as an image (borehole lithology descriptions), the script utilized a combination of image processing techniques and optical character recognition (OCR) to extract the relevant data from these images. The data extraction from images followed the following steps:

- Preprocessing and Page Selection: Based on certain patterns on the text content of each page, the pages containing images were selected. Then, each selected page is checked for the presence of images not containing a specific color, as those are the images containing the lithology descriptions.

- Figure Extraction and Image Manipulation: The code uses the selected figure pages to extract and save the corresponding images from the PDF file as image files. The code crops the images based on the bounding coordinates obtained from the PDF file, keeping only the figure of the lithology representation. The cropped images are saved in a new folder and named based on the page numbers, to facilitate later access to the text content of the origin page of each image.
- Text Extraction: The code processes each cropped image and extracts text using the Tesseract OCR library. Tesseract's inclusion as a Python library facilitates its usage and integration within the code. While many OCR tools are available, Tesseract stands out for its ease of use, robustness, and compatibility with multiple languages, which is important as our lithology descriptions aren't in English. However, given the nature of the lithology descriptions and the potential for OCR errors, special attention was given to the extracted text. To ensure accuracy, a list of all unique words present in the extracted text was generated, and any occurring typos or errors in the lithology descriptions were manually rectified. This meticulous approach helped refine the extracted lithology information and enhance the quality and reliability of the resulting dataset.
- Line Detection: To identify the depth of the lines delineating the various lithology layers, the code analyzes each cropped image and detects horizontal lines using edge detection and the Hough Line Transform. The y-coordinates of the detected lines are obtained, which are transformed later to depths based on the scale used on the lithology representation.
- Lithological Data Extraction: The code combines the extracted text and line coordinates to extract lithological data from each image. Using the number of the report page from which each image was extracted, the lithological data is linked to the test identifier extracted from the pages' text content. The extracted data, including the test identifier, soil types, and depth boundaries, are organized in a DataFrame (see Table 6).
- Final database: The Lithological data is joined to the other PMT data in text form (test identifier, coordinates X, Y, and Z, PMT modulus, and limit pressure), and stored as a table in a an excel file (see Table 7).

In summary, the code performs preprocessing tasks, selects specific pages with relevant figures, extracts and manipulates images, and finally extracts and organizes lithological data from the processed images and links it to the other PMT data in a structured table.

Table 6. Overview of the Lithological Data.

Test identifier	Lithology description	Upper boundary depth	Lower boundary depth
EXE-SP-Loukkos-P30	marne verdâtre	0	1,989
EXE-SP-Loukkos-P30	vase	1,989	9,499
⋮	⋮	⋮	⋮
EXE-SP-PRO-2268-4	marne sableuse	0	11
EXE-SP-PRO-2268-4	pélite grisâtre	11	30,5

Table 7. Overview of the PMT database.

N°	Test identifier	X	Y	Z	Initial pressure	Limit pressure	Modulus	Lithology description
0	EXE-SP-Loukkos-P30	437653,46	505734,12	0,67	0	0,38	3,1	marne verdâtre
1	EXE-SP-Loukkos-P30	437653,46	505734,12	-0,83	0	0,17	3,1	vase
	⋮	⋮	⋮	⋮	⋮	⋮	⋮	
4432	EXE-SP-Loukkos-P9	438146,16	506795,82	-75,82	0,11	9,42	1313	pélite dure, grisâtre
4433	EXE-SP-Loukkos-P9	438146,16	506795,82	-77,32	0,11	9,78	323,3	pélite dure, grisâtre

2.6 Data Verification

To ensure the accuracy and reliability of the extraction method, a verification process was conducted on the extracted database, employing random checks and outlier value analysis. Random checks were performed on a subset of the extracted data, where a sample of data points was randomly selected and manually cross-validated against the original source documents. This procedure allowed for the identification of potential discrepancies or errors in the extraction process. Additionally, outlier values were examined to detect any extreme or anomalous data points that could indicate inaccuracies or inconsistencies (see Fig. 1). By carefully reviewing and validating the extracted data through these verification methods, the integrity of the dataset was enhanced, instilling confidence in the automated data extraction method used.

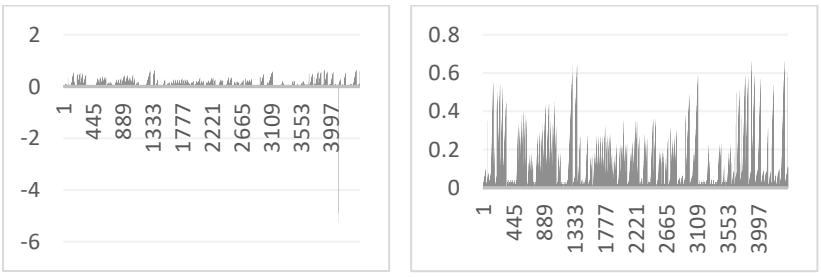

Fig. 1. Histogram plot of the PMT initial pressure values before outlier detection (left) and after outlier detection and correction (right) using values from the original PDF report.

3 Results and Applications

3.1 Data Extraction and Verification

The developed code successfully automates the extraction of relevant data from PDF reports containing test results. It efficiently parses the PDF files, identifies specific patterns, and extracts the necessary information. However, it is important to note that

the code's applicability is tailored to the specific structure and formatting of the PDF reports. Human intervention is required to identify and incorporate the relevant patterns into the code. The extracted data is subjected to a verification process that includes random checks and outlier value checks. These validation mechanisms ensure the accuracy and reliability of the extracted data, providing a solid foundation for subsequent analysis.

3.2 Structured Data for Improved Analysis

The automation of data extraction makes the task of transforming large hardly exploitable PDF reports into structured data more efficient and reduces the risk of human errors. Structured data allows for easy integration, comparison, and analysis across multiple geotechnical tests, enabling comprehensive insights into the tested parameters and their variations. The availability of organized data improves the overall quality of analysis and decision-making processes, which is highly beneficial for researchers and engineers.

3.3 Application of Kriging for Spatial Interpolation

One of the key applications enabled by the code is the utilization of the extracted database for spatial analysis using kriging. Kriging is a powerful geostatistical technique that allows for spatial interpolation and prediction. By applying kriging to the extracted database, researchers and practitioners can generate interpolated surfaces and predict values at unmeasured locations. To demonstrate the importance of having data in a structured and accessible format, an example of the Kriging spatial interpolation is given in Fig. 2. For the PMT modulus values of our PMT database. The standard error of this interpolation is 124. While not perfect, as nothing will be as exact as real measurements, Kriging enables us to have values at unmeasured locations based on the measurements at our georeferenced database, and is an easy-to-use technique for practitioners as it’s included in many user-friendly software such as ArcGIS. There are other spatial interpolation techniques used in the literature that might give better results than Kriging or be more adapted to a specific database, but these aren’t addressed in this study. By automating data extraction from PDF reports, the availability of geotechnical data in a structured way opens the door for the use of advanced spatial analysis techniques, providing valuable insights into the spatial distribution of soil properties or other variables of interest.

The combination of automated data extraction, verification, and the subsequent application of kriging highlights the significance of structured data in geotechnical engineering and related fields. It emphasizes the importance of moving away from PDF reports to structured data formats, enabling researchers and practitioners to unlock the full potential of their data and make informed decisions based on comprehensive analysis.

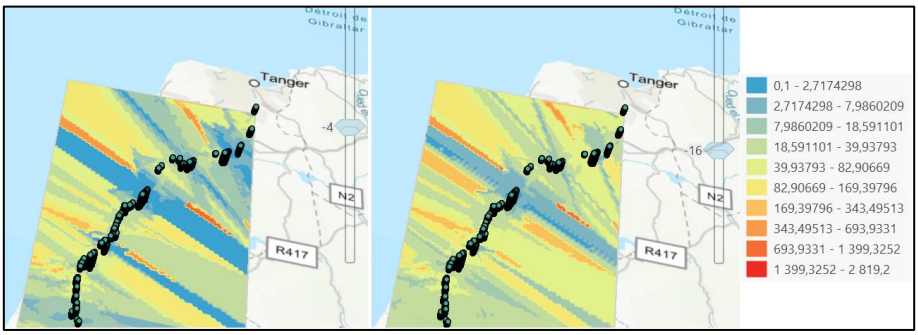

Fig. 2. Kriging 3D interpolation of the PMT modulus parameter, results for two different elevation values.

4 Conclusion

In conclusion, our study presents a practical approach to automate geotechnical data extraction from PDF reports, aimed at streamlining the data extraction process for geotechnical engineers. By combining OCR, image processing techniques, and text pattern recognition, we have developed a code that efficiently extracts the necessary data, offering a time-saving and error-reducing solution.

The reliability and accuracy of the extracted are verified. The comparison with manual extraction and the implementation of outlier value analysis have ensured the integrity of the extracted geotechnical data. This provides confidence in the usability and quality of the extracted data for further analysis.

The application of our code has practical implications for geotechnical engineering projects. By converting unstructured PDF reports into structured data, it facilitates easier data analysis and decision-making processes. One of the significant applications allowed by the availability of the extracted database is spatial analysis techniques, such as kriging, which helps us gain insights into the spatial distribution of geotechnical properties.

In summary, our study offers a valuable approach for geotechnical engineers and researchers to automate the data extraction process from large PDF reports. By automating the data extraction process and improving the quality of extracted data, our approach significantly enhances the efficiency and reliability of geotechnical engineering practices and provides a practical solution for extracting relevant information. One potential improvement is to automate the identification of patterns specific to each type of information, but this may require training on large labeled datasets of geotechnical reports and their corresponding extracted data. Additionally, the diversity of geotechnical reports and the lack of standardized formats pose challenges in creating a universally representative database. Therefore, the ideal scenario is for organizations and laboratories responsible for issuing geotechnical reports to adopt a structured format for storing and issuing test results right from the beginning, ensuring easier and more accurate data extraction. However, since this is rarely the case, our work serves as a guide for those seeking to extract data from

geotechnical PDF reports and highlights the importance of structured data storage in the field.

References

1. Bui, D. D. A., Fiol, G. D., Jonnalagadda, S.: Pdf Text Classification To Leverage Information Extraction From Publication Reports. Journal of Biomedical Informatics, (61), 141-148 (2016).
2. Bradski, G.: The OpenCV Library. Dr. Dobb's Journal of Software Tools (2000).
3. Downing J., Harvey M.J., Morgan P.B., Murray-Rust P., Rzepa H.S., Stewart D.C., Tonge A.P., Townsend J.A.: SPECTRa-T: machine-based data extraction and semantic searching of chemistry e-theses. J Chem Inf Model.;50(2):251-61 (2010).
4. Duda, R. O., & Hart, P. E.: Use of the Hough transformation to detect lines and curves in pictures. Communications of the ACM, 15(1), 11–15 (1972).
5. Harris, C.R., Millman, K.J., van der Walt, S.J. et al. Array programming with NumPy. Nature 585, 357–362 (2020).
6. Kallmes, K. M., Hardy, N., Kallmes, K. M.: Toward Automated Data Extraction According To Tabular Data Structure: Cross-sectional Pilot Survey Of the Comparative Clinical Literature. JMIR Form Res, 11(5), e33124 (2021).
7. Kriging Documentation, https://pro.arcgis.com/en/pro-app/latest/tool-reference/spatial-analyst/kriging.htm, last accessed 2023/03/18.
8. McKinney, Wes.: Data Structures for Statistical Computing in Python. 56-61. 10.25080/Majora-92bf1922-00a. (2010).
9. Ooms J (2023). Open Source OCR Engine Website, https://docs.ropensci.org/tesseract, last accessed 2023/03/18.
10. pdf2image Documentation, https://pdf2image.readthedocs.io, last accessed 2023/03/18.
11. PyMuPDF Documentation, https://pymupdf.readthedocs.io, last accessed 2023/03/18.
12. PyPDF2 Documentation, https://pypdf2.readthedocs.io, last accessed 2023/07/09.
13. pytesseract Documentation, https://pypi.org/project/pytesseract, last accessed 2023/03/18.
14. reportlab Documentation, https://docs.reportlab.com, last accessed 2023/03/18.
15. S, A. K. M.: Extract and Organize Information In Images With AI Using IBM Services. IJRASET, 7(10), 2031-2035 (2022).
16. Umesh, P.: Image Processing in Python. CSI Communications, 23 (2012).

Stability Analysis of Akaili Landslide (Jebha, Northern Morocco)

Houda Merouani[1][0000-0001-6217-8953], Abdellilah Dekayir[1], Mohamed Rouai[1], and Mohamed Ben Haddou[2]

[1] Geotech research team, Moulay Ismaïl University, Faculty of Sciences. PO. Box. 11201 Zitoune, Meknès, Morocco.
[2]CID, Technopolis Park, 11100 Sala El Jadida PO. Box. 1340 Rabat, Morocco.

Abstract. Located at the entrance of Jebha city in Northern Morocco, the Devonien-Silurien Akaili formation has experienced slope instability, causing disruptions in the traffic flow on National Road 16, also known as the Mediterranean ring road. This study aims to characterize the landslide through a multidisciplinary approach. It begins with a morphological investigation, followed by borehole investigations, and concludes with an empirical stability analysis using geomechanical classifications known as Bieniawski's Rock Mass Rating (RMR) and Romana's Slope Mass Rating (SMR).
The RMR is estimated using the empirical equation of Kincal & Koca [1], which relates to the Menard deformation modulus (EM):

$$\mathrm{RMR} = 38.043 \times \mathrm{EM}^{(0.3291)} \quad (1)$$

And the SMR was estimated from the basic RMR, using equations developed by Zakaria [2] and Hall [3]:

$$\mathrm{SMR} = 7.2251\mathrm{RMR}^{0.5207} \quad (2)$$

$$\mathrm{SMR} = 0.65 \times \mathrm{RMR} + 25 \quad (3)$$

The stability analysis of the SMR classification yields conclusive results that align with the natural conditions indicating that the weathered schists are responsible for slope instability. Based on these findings, slope reinforcement solutions involving berms and surface drainage are proposed.

Keywords: Stability analysis, Geomechanical classifications (RMR and SMR).

1 Introduction

The Internal Rif, or allochthonous zone of the Rif belt, consists of the large massifs on the Mediterranean coast between Sebta and Jebha and the Bokoyas. This zone is characterized by the presence of Palaeozoic, Mesozoic, and Cenozoic sequences, which include three main metamorphic complexes: the Sebtide, Ghomaride, and Dorsal complexes [4]. These complexes have been affected by alpine deformation and partial metamorphism since the Eocene-Late Oligocene. They exhibit thrusting toward the southwest, interacting with the Flysch units and External Zones. The Jebha fault, a

significant transfer fault formed during the westward emplacement of the Rif units, marks their southeastern boundary [5].

The Sebtide complex is composed of various metamorphic units, such as the Beni Bousera peridotites, overlain by granulites, gneisses, schists, Permian-Triassic phyllites, quartzites, and Triassic carbonates. The Ghomaride complex comprises four nappes of low-grade Paleozoic metasediments, covered by extensive unconformable Triassic red beds and thinner layers of Liassic, Paleocene-Eocene limestones, as well as Oligo-Miocene post-nappe detrital deposits [6]. The Dorsal complex consists of stacked Late Triassic-Liassic carbonate sheets, with a thin overlay of Jurassic-Late Cretaceous pelagic sediments and Tertiary detrital sediments.

The coastal range of the internal Rif has prompted several natural hazard studies [7] [8], particularly in the area upstream of the national highway N°16 or the Mediterranean Ring Road.

The initiation and reactivation of mass movements can be due to several internal or external factors. These factors may have geological, geomechanical, geometrical, hydrological, climatic, edaphic, or anthropogenic origins [8], and instability analysis must consider all these parameters.

There are several methods for studying and analyzing stability, including the geomechanical classifications form the basis of the empirical design approach and are widely used in rock engineering. There are various rock mass classification systems like the RMR [9], the Q system [10], and the GSI [11], frequently used for different purposes such as estimating the strength and rock mass and discontinuity properties, the deformability of rock masses, assessing the stability of rock slopes, tunneling, underground mining operations, etc..[12]. The classifications were adapted to the analysis of rock slope stability by Romana [13], who proposed a classification system called “Slope Mass Rating” (SMR) based on Bieniawski’s “Rock Mass Rating” (RMR) modified for slope conditions.

The present study area is the Jebha region, at the SE tip of the internal Rif, located in the Chefchaouen administrative region and known for its lithological diversity as well as for the manifestation of the sinistral Jebha wrench-fault in its NE termination [4], the entrance to this town has shown since 2019 signs of instability that have disrupted the traffic.

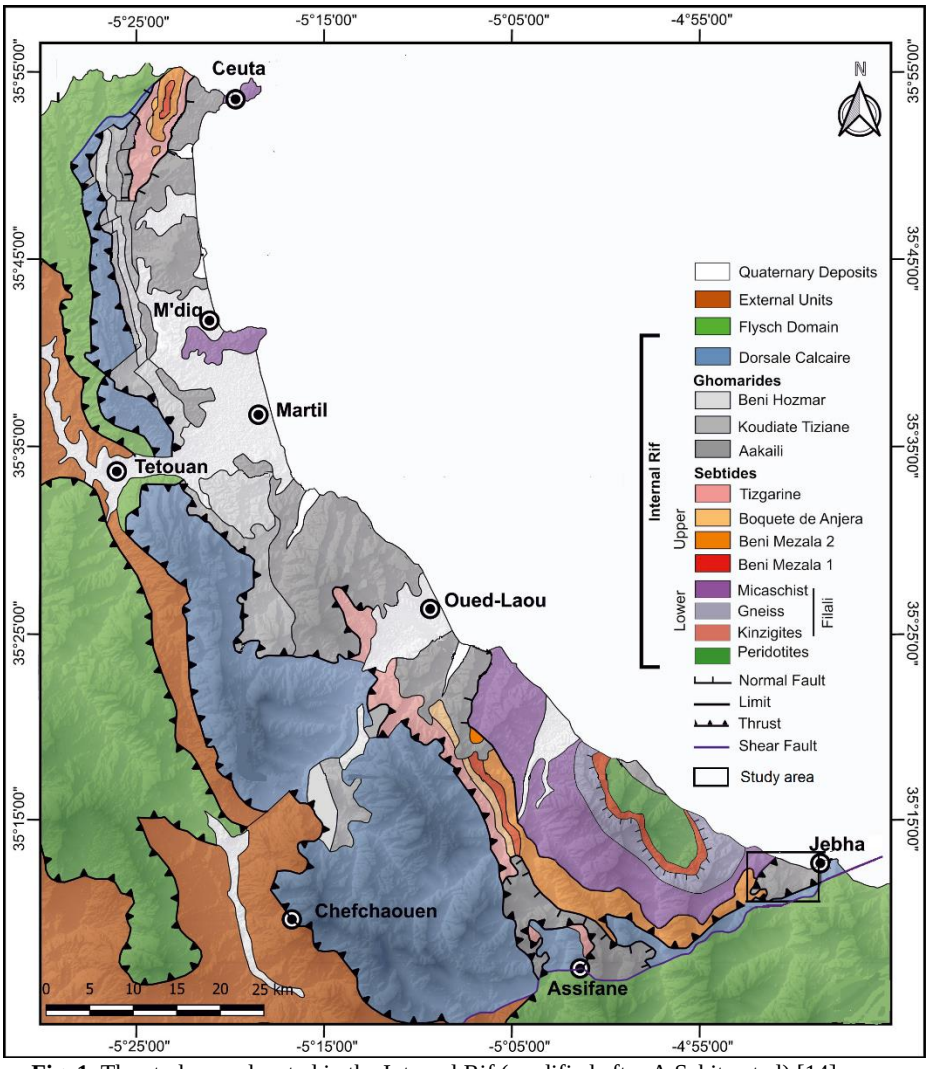

Fig. 1. The study area located in the Internal Rif (modified after A.Schito et al) [14]

2 Study Area

The study area is located at the entrance to the town of Jebha (35°.205N, 4°.6661W), Chefchaouen province. Jebha is characterized by a Mediterranean climate, with an average annual rainfall measured in the region over the last seventy years (between 1941 and 2012) of 337 mm, with an annual maximum of 528 mm [15]. Watercourses such as Oued Ouringa flow through the region into the Mediterranean Sea.

Fig. 2. Geographical location of the study area

Geologically, the studied zone is characterized by a tectonic superposition of several thrust sheets, from Southeast to Northwest: the Tisirene flysch, the Predorsalian, the Dorsal Calcaire (the external Dorsal to the west, the intermediate Dorsal, and finally the internal Dorsal to the east), the Ghomaride nappes, where there appear to be two nappes, dominated by the lower nappe of Akaili, and the nappe of Beni-hozmar [4].

The Jebha area is characterized by the sinistral Jebha wrench fault, which shows different dips in this sector, the NNW-SSE, and the ENE-WSW which separate the overlapping units. This area can be divided into two sectors [16], the eastern and the western sector, the landslide studied in this paper is located in the western sector over the Akaili Ghomaride nappe.

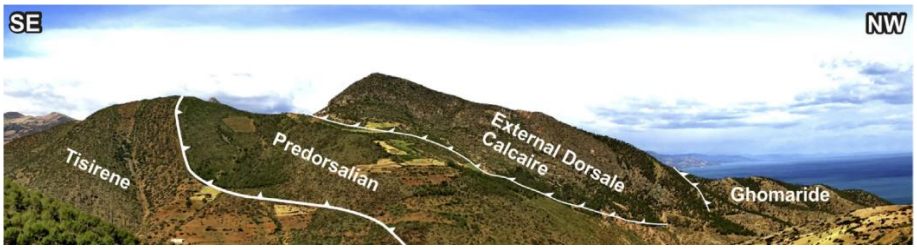

Fig. 3. Panoramic view of the Western area of Jebha [16]

The landslide studied affects a 124m high slope, which was reprofiled when the coastal road was built, with a 1H/1V (45°) slope and 3m long non-concrete berms every 6 m high. The slope is composed of the Devonian-Silurian of the Akaili nappe this formation is described by Olivier Philippe [4] as the sandstone-pelitic Silurian, which

easily disintegrates according to the main schistosity most often parallel to the stratification. Above, we find a Devonian series comparable to the calcareous flysch, with alternating calcareous beds on a 326egion326ral scale. These are the "Calizas albeadas".

This formation was marked by serval tectonic phases, the first noted by Olivier Philippe [4] and Chalouan [6], P2-S2, linked to the Bretonic phase (Eo-Variscan or Late-Acadian phase) [17]. Olivier distributes this phase to this formation with strong doubt since the structures linked to this phase are strongly dispersed by late tectonic phases, but Chalouan confirmed the presence of the Bretonic phase, describing the angular unconformity of a Visean conglomerate on Famennian "calizas alabeadas", S2 the flow cleavage of this phase shows a wide dispersion of direction forming a kind of trough between N50 and N130 with a slight dip [4], this would be related to the next tectonic phase, P4 S4, which occurred in the Eocene-Oligocene interval, which was responsible for the tectonic stacking of the Ghomaride Nappes. [16] P4 are folds of all scales, materialized in this zone by the large synforms of Devonian and Triassic terrain between Tarhassa and Jebha. The dip of the axial plane is most frequently N to N-NW, indicating a range from S to SE, and S4 is strain-slip cleavage.

Other alpine phases are given by researchers [17] [4] in this formation, such as the post-Aquitanian P'4 S'4 phase, which presents structures locally parallel to the P4 S4 phase structures due to the 90° rotation generated by the Jebha-Charafate accident, and the P''4 phase which is characterized by centimetric kink-bands oriented along two mean directions N60 and N130[4].

3 Materials and Methods

For our study of the Jebha landslide, we opted for a multidisciplinary approach:

First approach:
A morphological study of the landslide using multi-date Google Earth satellite photos of 2012, 2019, and 2020 and configuration of landslide features.

This approach enables the identification of landslide boundaries, mapping of features, measurement of surface displacements, and detection of temporal variations, it helps assess the size, spatial distribution, behavior, and progression of the landslide over time. It also aids in understanding potential triggers or causes of the landslide, contributing to a comprehensive assessment of its stability and associated risks.

Second approach:
A survey of the five boreholes installed on the landslide slope, combined with pressuremetric tests, using the Baud et Gambin Pressiorama[18] [19] [20] to describe and correlate the studied schist layers. This diagram [ln (p^*_{LM})/ln (E_M/p^*_{LM})] provides a representative overall picture of the formation or site from which the in-situ measurements originate, it is required to classify soils from very loose soils to very massive rocks, and in particular, to determine the value of the rheological coefficient

α. The Pressiorama is based on soil and weak rock classification suggested in French norms NF-P-94-261 [21] for shallow foundations and NF-P-94-262 [22] for deep foundations [23].

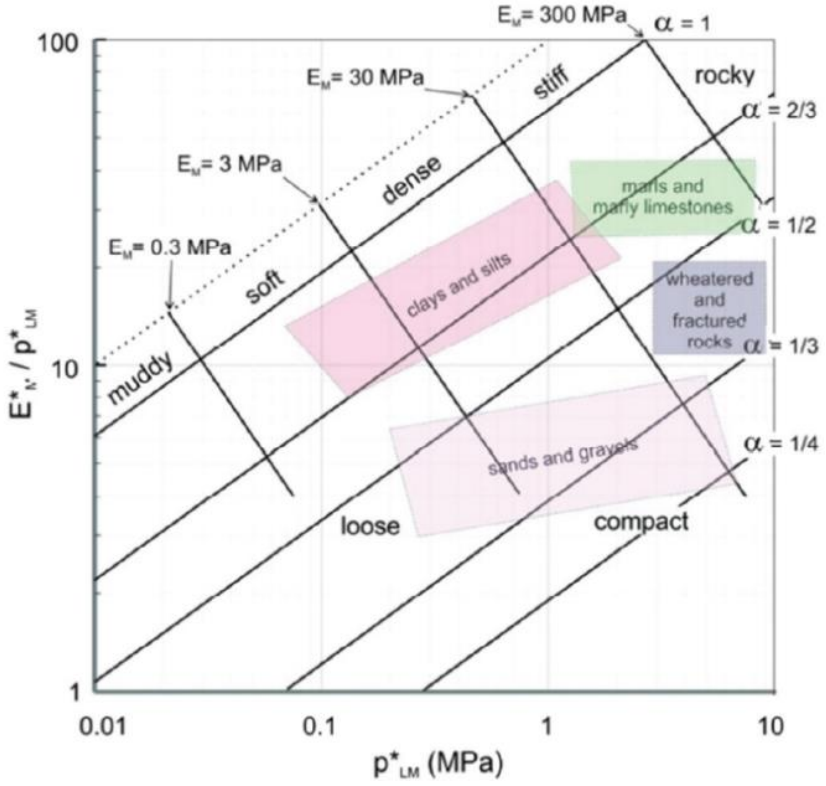

Fig. 4. Baud and Gambin's Pressiorama chart. P^*_{LM} : Net limit pressure (in Mpa); E_M : Menard 327egion327ral327er modulus; α: Rheological factor.

The installed boreholes were distributed as shown in Figure 5 The results of the 327egion327ral327er test in the five boreholes show that there are two layers of black shale, with the upper layer showing signs of weathering. Table. 1 shows the average 327egion327ral327er parameters of the Menard test in the detected layers.

Table 1. The average values of Pressiometric parameters in the five boreholes

Borehole	Test depth (m)	Lithology	P_f (Mpa)	P^*_l (Mpa)	E_M (Mpa)	E_M/P^*_l
SCP01	1,5-3	Weathered Schist	0,94	1,13	13,20	11,62
	4,5-15	Fractured Black Schist	3,98	4,40	243,88	55,42
SCP02	1,5-58,5	Fractured Black Schist	4,40	4,98	259,27	52,01
SCP03	1,5-34,5	Weathered Schist	3,46	4,50	112,69	25,00
	36-58,5	Fractured Black Schist	4,85	5.00	198,35	39,67
SCP04	1,5-13,5	Weathered Schist	4,19	4,88	317,40	65,04
	15-39	Fractured Black Schist	4,68	4,99	416,43	83,32
SCP05	1,5-12	Weathered Schist	4,19	4,53	151,50	33,41
	13,5-58,5	Fractured Black Schist	4,80	4,97	385,83	77,58

P_f, Pressure Creep; p^*_l, Net Limit Pressure; E_M: Menard Deformation Modulus.

Fig. 5. The layout of boreholes coupled with 328egion328ral328er tests.

Third approach:
The stability analysis of the Jebha slope was conducted using geomechanical classifications, with a particular focus on Bieniawski's Rock mass rating and Romana's Slope Mass Rating.

The rock mass rating classification is a widely used classification system for rock masses that helps assess their engineering behavior and stability. It takes into account five key parameters to calculate the RMR value in the classic method (RQD, UCS, Jw, Jr and Jn). The RMR value is calculated and classes are distributed to indicate the rock mass's quality and stability.

Table 2. Rock Mass Rating classes by Bieniawski [9]

Classes	**V**	**IV**	**III**	**II**	**I**
RMR Values	>20	20-40	40-60	60-80	80-100
Rock Mass Quality	Very Poor Quality	Poor Quality	Fair Quality	Good Quality	Very Good Quality
Cohesion (Kpa)	<100	100-200	200-300	300-400	>400
Internal friction angle (°)	<15	15-25	25-35	35-45	>45

The RMR system has been extended for new valuable applications while remaining part of the overall RMR framework. Romana, in 1985, contributed significantly to applying the RMR system in assessing rock slope stability. He introduced a factorial approach to incorporate a discontinuity orientation parameter into the RMR classification, based on field data. This approach addresses the importance of discontinuity orientation in rock slope stability.

The SMR classes provide valuable information about the stability, risk and design considerations associated with rock slopes. Classified according to their SMR values, these classes provide a comprehensive assessment of slope stability. Higher SMR classes indicate more stable slopes, while lower classes suggest potential instability and a higher risk of slope failure. The information conveyed by the SMR classes enables a comparative analysis between slopes, making it possible to prioritize stabilization efforts and identify slopes requiring closer monitoring. In addition, SMR classes help to determine the appropriate technical interventions according to the class assigned. By taking SMR classes into account, informed decisions can be made on slope stability management, ensuring that resources and efforts are allocated in such a way as to minimize potential risks.

Table 3. Recommended Support Measures for each SMR class [13]

Class	SMR	Support
la	91_100	None
Ib	81_90	None. Scaling
Iia	71_80	(None. Toe ditch or fence) Spot bolting
lIb	61_70	Toe ditch or fence. Nets Spot or systematic bolting
lIIa	51_60	Toe ditch and/or nets Spot or systematic bolting Spot shotcrete
IIIb	41_50	(Toe ditch and/or nets) Systematic bolting. Anchors Systematic shotcrete Toe wan and/or dental concrete
Iva	31_40	Anchors Systematic shotcrete Toe wan and/or concrete (Reexcavation) Drainage
Ivb	21_30	Systematic reinforced shotcrete Toe wan and/or concrete Reexcavation. Deep drainage
Va	11_20	Gravity or anchored wan Reexcavation

Classes	V	IV	III	II	I
SMR	0-20	21-40	41-60	61-80	81-100
Description	Very Bad	Bad	Normal	Good	Very Good
Stability	Completely instable	Unstable	Partially Stable	Stable	Completely Stable
Failures	Big planar of Soil-like	Planar or Big wedges	Some Joints or many wedges	Some Blocks	None
Failure probability	0,9	0,6	0,4	0,2	0

Due to the lack of essential elements required for the standard calculation, the RMR and SMR values in this study have been estimated. An empirical model (Figure 6) used in this study is based on the studies of several researchers, such as Kincal and Koca in estimating RMR values from Menard's deformation modulus [1], and ultimately Hall

and Zakaria [3] [2] for their empirical equations for calculating SMR from basic RMR values.

Fig. 6. Flowchart of the Empirical model used in Jebha's Akaili stability analysis

4 Results and Discussions

4.1 Results

Morphological Investigation

The study of multidate satellite images (Figure 6.) enables us to follow the evolutionary stages of the Jebha landslide. In 2012, the Tetouan Jebha section of national road 16 was freshly constructed, and the slope was reprofiled with berms. An area of triangular vegetation is visible with the point toward the road indicating water flow, this is ensured by the brownish color of the shale weathering just below this area.

As the vegetation zone scatters and open cracks appear, signs of instability begin to warn, in 2019 or perhaps earlier, of the failure of two masses, respectively 8000m2 and 7220m2 in surface area, in 2020, both sliding towards the NE.

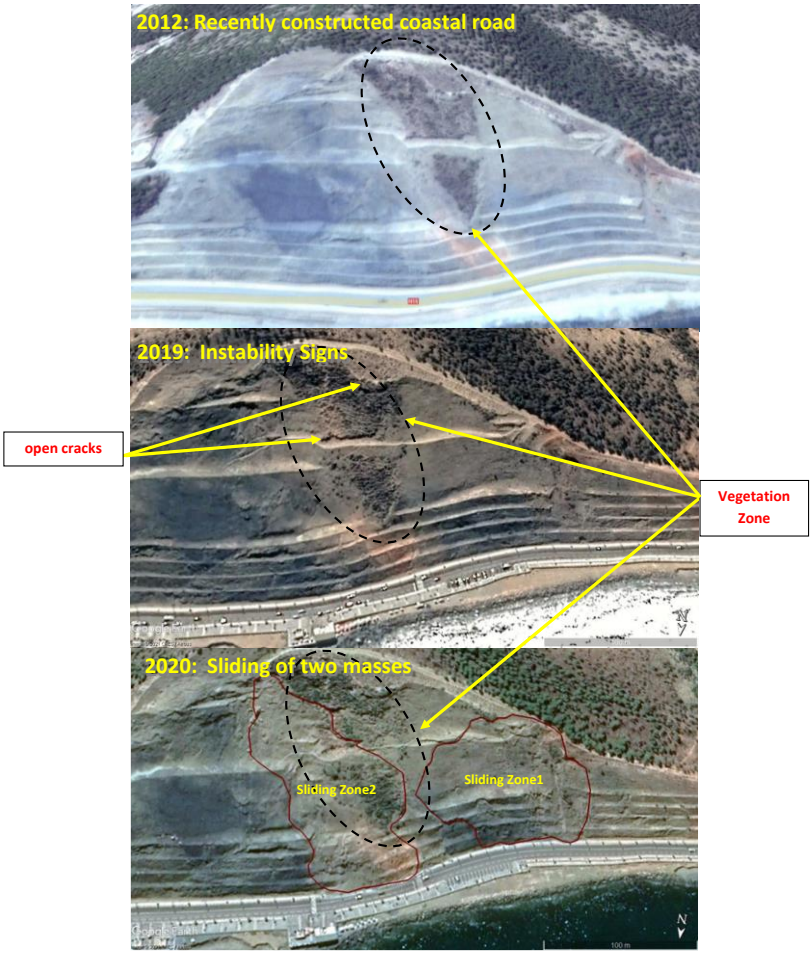

Fig. 7. Multidate satellite images of the Jebha landslide slope

In Figure 6, From top to bottom, we can see the landslide features, beginning from the instability cracks, the 2 m collapse of a berm forming a scarp, and the lifting of the sidewalk at the end forming the landslide tip.

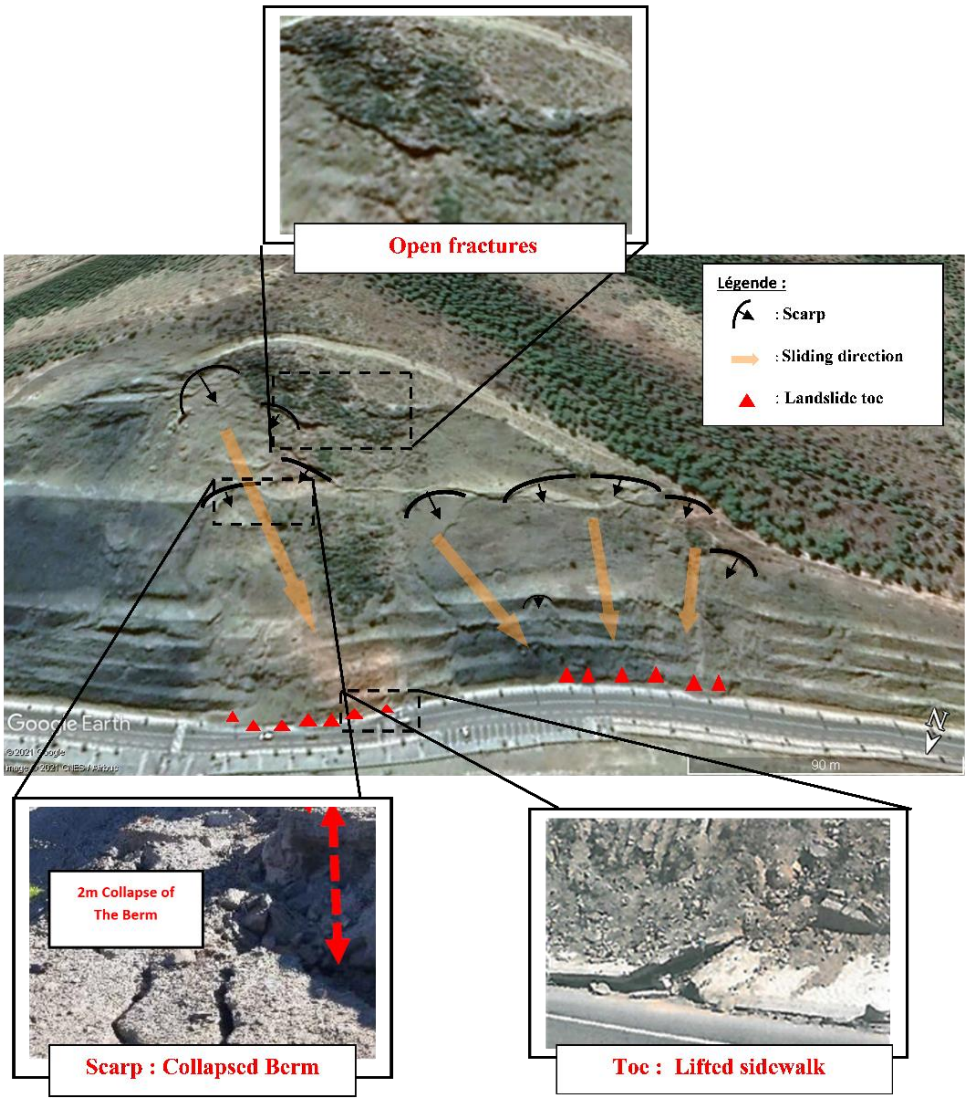

Fig. 8. Jebha landslide features

Pressiometric boreholes Investigation:

The characterization of the rock masses varies from surface to depth, and the pressiometric core boreholes distinguish between two schist layers: weathered schist and fractured fresh schist, after observing the cores and the pressiometric parameters provided by the laboratory, we were able to construct a correlation of the five boreholes

(considering SP04 to consist solely of the fresh schist layer since the characteristics of the two layers are similar in this case).

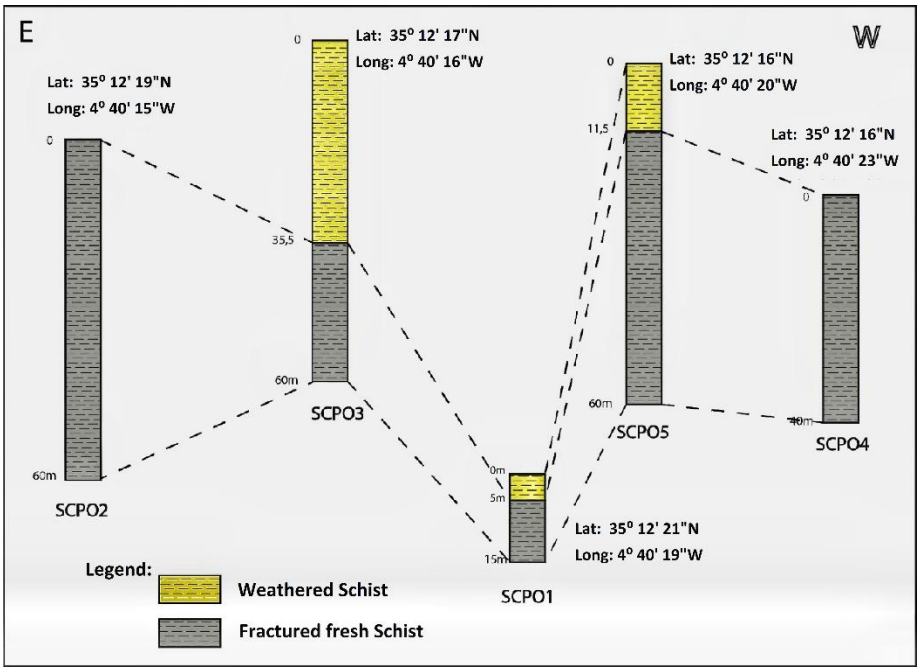

Fig. 9. Schematic boreholes correlations

We distribute to each layer an average value for the pressiometric parameters so that we can move on to classification using the Baud and Gambin Pressiorama.

Table 4. The average values of the pressiometric parameters of the schist layers

Layer	P_f (Mpa)	P^*_l (Mpa)	E_M(Mpa)	E_M/P^*_l
Weathered Schist(C1)	2,86	3,39	92,46	27,25
Fractured Fresh Schist(C2)	4,48	4,872	303,53	62,29

The first layer is a strongly to completely weathered rock mass showing a yellowish to brownish color and an almost total absence of carbonates (dissolution). According to Baud and Gambin's Pressiorama, layer 1 (C1) shows the behavior of 334egion334ral334er334ed soil, it is moderately hard and extremely tightly fractured ($a \approx ½$) (spacing < 6cm). Deeper down, the schist is dark gray and pale green with local color changes. Slightly to moderately weathered, according to the Pressiorama, the formation is hard (massive rock) and shows moderate ($\alpha \approx 2/3$) but very close fracturing (Spacing between 6 and 20 cm).

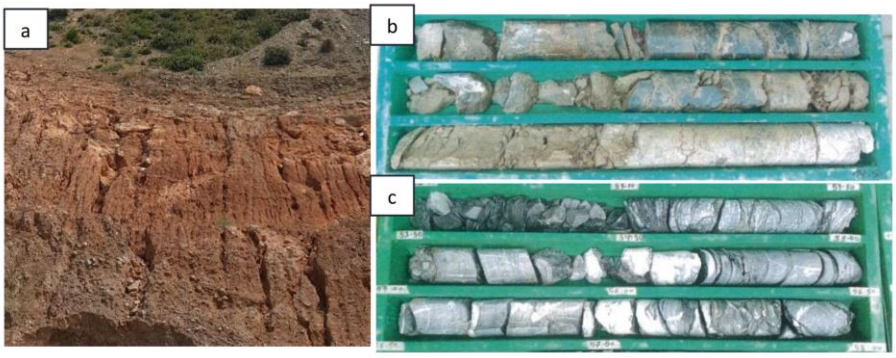

Fig. 10. A, The slope affected by the landslide; b, Schist of layer 1 (SCP3: 10.5-14.5m); c, Schist of layer 2 (SP3 53.5 -58m).

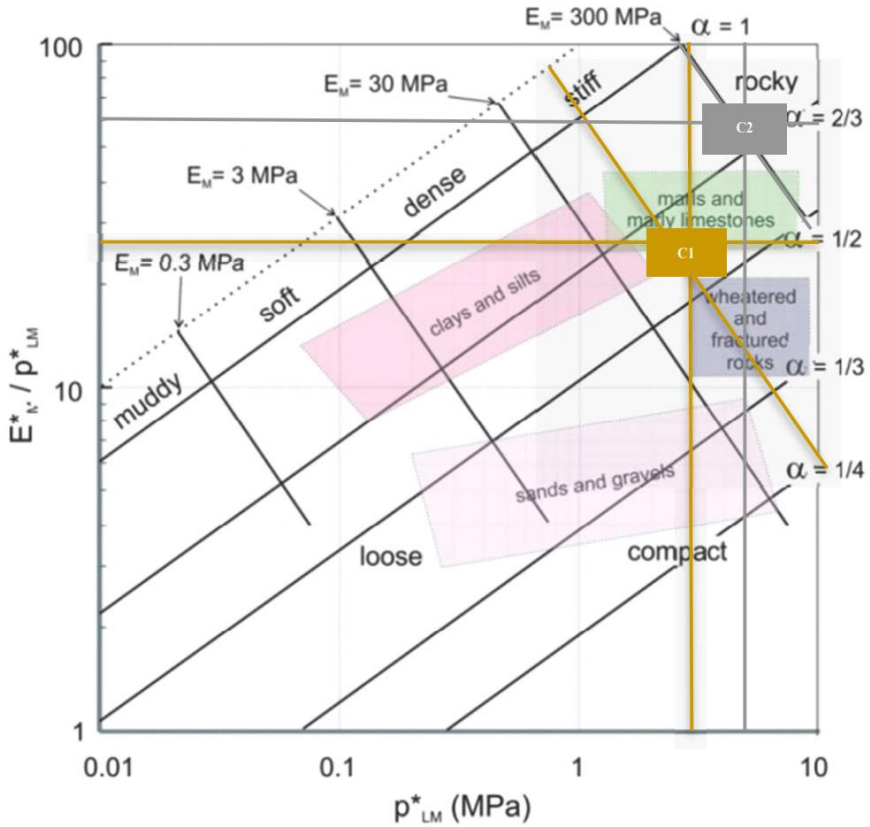

Fig. 11. Projection of 335egion335ral335er parameters average values for both layers on the Baud and Gambin Pressiorama. C1, layer1; C2, layer2.

Stability analysis: Application of the empirical model

the empirical model developed in this study, based on several empirical equations, is used to analyze and calculate slope stability at the Jebha area.

The first step is to calculate (estimate) the RMR values and classify both schist layers from the Menard deformation modulus. RMR is the basic parameter of the stability calculation, as it is included in the calculation of the SMR parameter for slope mass classification.

Table 5. Estimation of the RMR classes of schist layers

Layer	E_M (Gpa)	KINCAL & KOCA [1] $RMR = 38.043 \times EM^{(0.3291)}$	RMR Class	Quality
Weathered Schist	0.092	20	V	Very Poor
Fractured Fresh Schist	0.303	25.51	IV	Poor

The weathered schist has been classified as RMR Class V, indicating the rock mass's poorest quality and stability. On the other hand, the schist at the bottom has been classified as RMR Class IV, characterized by poor (moderate to fair) quality and stability.

The quality of the rock mass decreases from poor to very poor as a result of weathering, explaining the difference in RMR classes between the weathered schist (Class V) and the schist at the bottom (Class IV).

Stability analysis by Slope Mass Rating classification:

Table 6. The empirical calculating of SMR values based on RMR.

Layer	RMR	SMR according to Hall (1985) $SMR = 0.65 \times RMR + 25$	SMR according to Zakaria (2017) $SMR = 7.2251RMR^{0.5207}$	SMR Classes
Weathered Schist	18,01	36.7	33	IV
Fractured Fresh Schist	25,51	42	40	III

The two empirical equations, Hall's and Zakaria's, give comparable values and classify weathered schist and fresh fractured schist respectively in SMR classes IV and III.

Table 7. Romana's stability analysis of the schist layers based on SMR values [13]

Layer	SMR Classes	Stability	Probability of failure	Safe slope cut	Failures	Suggested Support Methods for SMR between 30 and 45
Weathered Schist	IV	Unstable	60%	<40°	Planar along joints and many wedges	Surface and deep drainage Shotcrete dental concrete ribs and/or berms toe walls
Fractured Fresh Schist	III	Partially stable	40%	45°	Planar or big wedges	

According to the Romana classification of rock slopes, weathered schist has poor stability characteristics, this layer is unstable with a 60% probability of failure, and the slope must be cut at 40° to stabilize this layer. At the bottom, in fresh fractured schist, stability characteristics are fair, the layer is partially stable with a lower probability of failure (40%) and a safe slope of 45°.

Romana has put forward guidelines for the application of SMR-based corrective measures. These recommendations serve as an initial approach for the project, specifically addressing slopes with SMR values ranging from 30 to 45. The proposed solutions under these guidelines include surface and depth drainage, shotcrete, ribs and/or berms, as well as toe walls.

Following a stability calculation using the Talren software, the results validated Romana's suggested guidelines. Consequently, the company has opted for a corrective measure involving a slope inclination of 3H/2V (34°) and the incorporation of berms, spaced at 10m intervals for every 30m of height. Additionally, a 10m oversize has been implemented to ensure stability.

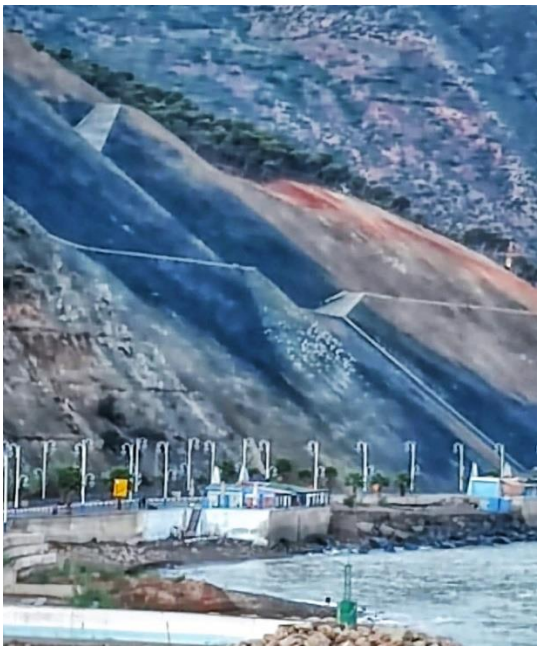

Fig. 13. The study area after the execution of the corrective solution

4.2 Discussion

the application of our empirical model in studying the Jebha landslide achieved favorable outcomes, The SMR classification yield results which are relevant and realistic.

The RMR values estimated by Menard deformation modulus E_M, is comparable to Mehrotra's finding [24]. Mehrotra's study incorporates both in situ and laboratory tests to determine the Rock Mass Rating (RMR) values of the Himalayan schist (Table 10). The measured RMR value of the shales in this study is approximately 25, which aligns with the calculated value for fresh schist in our own investigation. The observed lower RMR value in the first layer can be attributed to the impact of weathering, which results in a deterioration of its engineering properties.

Table 8. Comparison of shale RMR values in the Mehrotra study and in the present study

Studies	Type of rock	RMR
Mehrotra [24]	Schist	Nm:25-30
		S: 23-25
This Study		W: 18
		F:25

Nm, Natural moisture; S, Saturation; W, Weathered; F, Fresh

With regard to the results obtained by the SMR classification in stability terms, we can be sure, on the basis of the data from borehole SCP02, that the fresh shale layer remains stable at a slope of 45°, which corresponds to the natural terrain. Borehole SCP02, entirely composed of intact shale and located in an unaffected zone, confirms this.
(maybe a table)

5 Conclusion

In conclusion, this study aimed to investigate the morphology of the landslide that occurred at the entrance of Jebha, Northern Morocco, and to analyze the stability of the affected slope. Through a multidisciplinary approach, which started with multi-date Google Earth satellite photos interpretation, the survey of the pressiometric core boreholes, and the stability analysis with the empirical model at the end. Several key findings have emerged, providing a better understanding of landslide processes and valuable information for future slope management and risk mitigation strategies.

Firstly, we found that alongside the geological and tectonic factors affecting the Akaili Schist, the landslide was caused by the degradation of the geomechanical properties of the schist due to weathering processes. The weakening of the shale is attributed to the infiltration of water down the slope, as no drainage system had been installed since 2012 when the slope became destabilized due to road construction activities.

Secondly, by employing the empirical model for stability analysis, we could characterize the schist layers traversed by the boreholes, calculate their stability, and propose corrective solutions in two methods, the geomechanical classification materialized in the Slope Mass Rating by Romana, using estimated RMR form the Menard deformation modulus as input. The analysis demonstrated that the slope had a marginal safety factor prior to the failure, and indicated that the weathering schist layer significantly contributed to the slope instability. To address this, we recommend cutting the weathering schist layer at a lower slope and installing a drainage system to provide enhanced stability.

Moving forward, there are several avenues for future research in this area. It would be beneficial to conduct a more extensive study of the schist formation within the Akaili nappe of the Ghomaride region. This would involve a comprehensive investigation of the geological characteristics, structural geology, and mineralogical composition to better understand its behavior and susceptibility to instability.

Overall, exploring other unstable zones within the Internal Rif could provide a broader understanding of the regional landslide dynamics. Comparing and contrasting the geological and geotechnical characteristics of these zones with the Akaili Schist formation would enable us to identify common factors and develop more robust predictive models for landslide susceptibility assessment.

References

1. C. KINCAL and M. KOCA, "Correlations Of In Situ Modulus Of Deformation With Elastic Modulus Of Intact Core Specimens And RMR Values Of Andesitic Rocks: A Case Study Of The İzmir Subway Line," Bulletin of Engineering Geology and the Environment, pp. 12-13, 2019.
2. ZAKARIA.Z, OSCAR.A, SABILA.Z and JIHADI.L., "Modified Slope Mass Rating for Slope Design inOpen-Pit Mining," in EUROCK ., Ürgüp, Turkey, (2016).
3. I. PRASETYA, R. NARENDRA, A. WIRAMSYA and a. M. SOPHIAN.I, "RMR and SMR as Slope Stability Preliminary Studies of Rajamandala Limestone Mine Area," in 10th Asian Regional Conference of IAEG, Padjajaran, (2015).
4. P. Olivier, Etude Géologique et 340egion340ral de la 340egion de Jebha (Rif, Maroc). La terminaison NE de l'accident de Jebha-Charafate, Rabat: Editions du service géologique du Maroc, 1990.
5. F. Anahnah, J. Galindo-Zaldivar, A. Chalouan, J. Pous, P. Ruano, A. Pedrera, A. Constàn, M. Ahmamou, M. Benmakhlouf, P. Ibarra and E. Asensio, "Crustal resistivity structure of the southwestern transect of the rif cordillera (Morocco)," G3: Geochemistry, Geophysics, Geosystems., 2011.
6. A. Chalouan and A. Michard, "The Ghormarides Nappes, Rif Coastal Range, Morocco: A Variscan Chip In The Alpine Belt," Tectonics, 1990.
7. H. HARMOUZI, NEFESLIOGLU.H.A, ROUAI.M, SEZER.E.A, DEKAYIR.A and GOKCEOGLU.C, "Landslide Susceptibility Mapping Of The Mediterranean Coastal Zone," Arabian Journal of Geosciences, p. 18, 2019.
8. H. Tribak, M. Gasc-Barbier and A. E. Garouani, "Assessment of Ground Instabilities' Causative Factors Using Multivariate Statistical Analysis Methods: Case of the Coastal Region of Northwesten Rif, Morocco," Geosciences, 2022.
9. BIENIAWSKI.Z.T., Engineering Rock Mass Classifications, Hoboken: John Wiley & Sons, Inc., 1989.
10. N. Barton, R. Lien and J. Lunde, Engineering Classification of Rock Masses for the Design of Tunnel Support, Rock Mechanics 6(4): 189-236, 1974.
11. E. Hoek, Strength Of Rock And Rock Masses., ISRM News Journal 2(2): 4-16., 1994.
12. B. Singh and R. K. Goel, Engineering Rock Mass Classification: Tunneling, Foundations, and Landslides, Waltham: Butterworth-Heinemann , 2011.
13. M. ROMANA, New adjustment ratings for application of Bieniawski classification to slopes, Zacatecas: International Society of Rock Mechanics, 1985.
14. A. Schito, A. Atouabat, D. K. Muirhead, R. Calcagni, R. Galimberti, C. Romano, A. Spina and S. Corrado, "An insight on the polyphase thermal history of the Internal Rif (Northern Morocco) through Raman micro-spectroscopy investigation," Italian Journal of Geosciences, 2022.
15. H. HARMOUZI, A. DEKAYIR, M. ROUAI and M. AFECHKAR, "Analyse Géomorphologique Et Géologique Du Glissement De Terrain d'Akchour (Rif, Maroc).," Geo-Eco-Trop, p. 21, 2018.
16. S. VITALE, M. ZAGHLOUL, B. OUARAGLI, F. TRAMPARULO and S. CIARCIA, "Polyphase Deformation Of The Dorsale Calcaire Complex And The Maghrebian Flysch Basin Units In The Jebha Area (Central Rif, Morocco): New Insights Into The Miocene Tectonic Evolution Of The Central Rif Belt," Journal of Geodynamics ·, p. 19, 2015.
17. J. KORNPROBST, Contribution A L'étude Pétrographique Et Structurale De La Zone Interne Du Rif (Maroc Septentional), RABAT: Editions Du Service Géologique Du Maroc, 1974.
18. J.-P. BAUD, "ANALYSE DES RESULTATS PRESSIOMETRIQUES MENARD DANS UN DIAGRAMME SPECTRAL [LOG(PLM), LOG(EM/PLM)] ET UTILISATION DES

REGROUPEMENTS STATISTIQUES DANS LA MODELISATION D'UN SITE," in Symposium International ISP5-PRESSIO, Paris, 2005.
19. B. J.-P and G. M, "Détermination du coefficient rhéologique de Ménard dans le diagramme Pressiorama," in 18th International Conference on Soil Mechanics and Geotechnical Engineering, Paris, 2013.
20. J.-C. VERBRUGGE and C. SCHROEDER, Geotechnical Correlations For Soils And Rocks, London: ISTE Ltd, 2018.
21. AFNOR, French standard NF-P94-261, Paris, 2013.
22. AFNOR, French standard NF-P94-262, Paris, 2012.
23. J.-P. Baud, M. Gambin and R. Heintz, "50 Mpa Ménard PMTs Help Linking Soil and Rock Classifications.," in Proceedings of the 18th International Conference on Soil Mechanics and Geotechnical Engineering, Paris, (2013).
24. MEHROTRA.V, Estimation Of Engineering Parameters Of Rock Mass, Roorkee: University of Roorkee, (1992).
25. M. Khemissa, "METHODES D'ANALYSE DE LA STABILITE ET TECHNIQUES DE STABILISATION DES PENTES," in Journées Nationales de Géologie et de Géotechnique de l'Ingénieur JNGG , Lyon, 2006.
26. A. FAWAZ, E. FARAH and F. HAGECHEHADE., "STUDY AND RELATION BETWEEN THE PRESSUREMETER AND ELASTIC MODULI OF SOIL," Journées Nationales de Géotechnique et de Géologie de l'Ingénieur JNGG, pp. 1-10, 2014.
27. M. CASSAN, Les Essais In-Situ En Mécanique Des Sols: 1.Réalisation et Interpretaion., Paris: EYROLLES, 1988.
28. M. A. Bouhenniche, T. Messafer, M. A. Touzout and A. Nechnech., "Analyses Probabilistes De Stabilité Des Pentes – Etude De Cas," in Rencontres Nationales de Génie Civil et d'Hydraulique., Skikda, 2019.
29. T. B. SANTOS, M. S. LANA, A. E. S. SILVEIRA and L. R.C., "Applicability of geomechanical classifications for estimation of strength properties in Brazilian rock masses," Annals of the Brazilian Academy of Sciences, pp. 859-872, (2017).
30. Y. Xi, J. Zhao and L. Gang, "Inversion analysis of strength parameters of loess cutting high slope in Jijiayuan, Shanxi," Journal of Mountain Science, 2021.

Prediction of the Simple Compressive Strength of Clay Soils Improved by Lime and Gypsum Using ANN Application

Yasmina Kellouche[1*], Hamid Gadouri[1], Walid Teldjoune[1], Yazid Chetbani[2]

[1] Djilali Bounaama University, of Earth Science and Univers Department, 44225 Khemis-Miliana, Algeria, *y.kellouche@univ-dbkm.dz,
ORCID: 0000-0003-3052-844X
ORCID: 0000-0002-0753-3569
[2] Ziane Achour University, Science and Technology Faculty, Civil Engineering Department, Laboratory of Mechanics and Materials Development, POBox 3117 in the City of Djelfa 17000, Djelfa, Algeria, chetbani.yazid92@gmail.com

Abstract. Clay soils are considered poor materials, often requiring some stabilization to increase their physical and mechanical stability. Therefore, chemical methods of stabilizing clayey soils such as the addition of lime and gypsum are one of the preferable techniques to improve their geotechnical properties. The identification of the geotechnical parameters of clay soils improved by additions proves to be very costly, which has led the majority of researchers to move towards the prediction of these parameters using different techniques such as artificial neural networks (ANN) used in our study. The present paper aims to develop an efficient model based on ANN to predict the simple compressive strength (SCS) of soil stabilized with lime in the presence of gypsum. However, a database of 371 points comprising four parameters influencing SCS (lime, gypsum, initial SCS and curing time) collected from previous research. The results of training, testing and validation of the model developed in this study showed performance with a high correlation coefficient (R = 0.9257) and a low error (MSE = 0.009). The parametric study and the comparison of the predicted values with experimental results not included in the database proved the performance of the developed model. Therefore, this model can be used as a reliable tool to predict the SCS of clay soils stabilized with lime and gypsum.

Keywords: Clay Soils, Improvement, Lime, Gypsum, Prediction, Artificial Neural Networks.

1 Introduction

Unstable soils with problems and with poor geotechnical properties often require some stabilization to increase their physical and mechanical stability and improve their performance [1]. Soil improvement methods are one of available tools to solve the problems of stability or deformations occurring during the project execution. Therefore, chemical stabilization by the addition of lime, gypsum, cement or other cementitious additions remains the most used and the least expensive method [2]. The effect of additives is well known, but the prediction of properties such as strength gain and compressibility of stabilized soils remains impossible without carrying out long and costly laboratory tests. Recently, researchers focused on artificial intelligence technics to solve many geotechnical problems [3], pile bearing capacity [4], response parameters of kinematic soil-pile interaction [5], settlement prediction of shallow foundations on granular soils [6], unconfined compressive strength of a consolidated soil stabilized with cement and fly ash [7], the plasticity index, optimum moisture content and maximum dry density of lime-stabilized clayey soils [8], unconfined compressive strength prevision of expansive soils [9], CBR prediction of geotextile stabilized soils [10]. This study explores the utility of artificial neural networks (ANNs) as a self-contained machine learning tool in the stabilization of expansive clays and evaluates its ability to develop predictive model useful for performance evaluation of key properties of clay soils. The main objective of this work is to develop an ANN model to predict the simple compressive strength of clay soils stabilized with lime and gypsum. The accuracy of the model is guaranteed through data collection from several experimental research studies published in scientific journals.

2 Artificial Neural Network Overview

The significant progress realized in recent years in the field of artificial intelligence has made it possible to reduce the difficulties and overcome the limitations of linear models; artificial neural networks are one of these techniques. It is a technique that simulates biological neural systems in the human brain with the ability to learn, reason, and solve computational problems [11]. Training is a dynamic and iterative process for modifying the parameters of a network in response to the stimuli it receives from its environment. The type of learning is determined by how the parameter changes occur. Hence, learning a formal neural network consists in determining the optimal weights (of the optimal strength of the connection) according to the problem to be solved. It is a phase in the development of a neural network during which the behavior of the network is modified until the desired behavior is obtained. In terms of learning algorithms, two main classes have been defined according to whether learning is said to be supervised or unsupervised. This distinction is based on the form of the learning examples. In the case of supervised learning, the examples are couples (Input, Associated output) while we only have values (Input) for unsupervised learning. The multilayer perceptron (MLP) is a network composed of successive layers. The connections between neurons in each layer include associated weights that are

iteratively adjusted by the learning algorithm to minimize the risk of error and produce accurate predictions. The input layer reads the incoming signals, a neuron per input x_j, an output layer provides the system response. One or more hidden layers participate in the transfer. A neuron from a hidden layer is connected at the input to each of the neurons of the previous layer and at the output to each neuron in the next layer [12] (See Fig. 1).

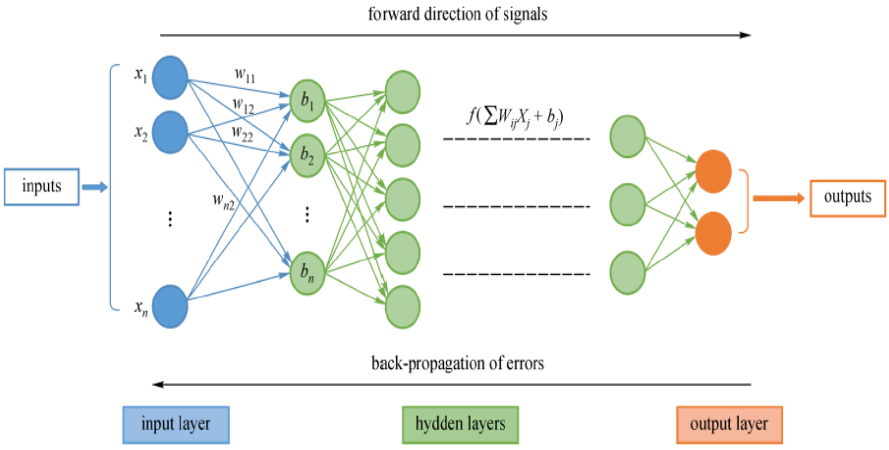

Fig. 1. Artificial neural network process [12].

Each neuron j of the hidden layer calculates the sum of n input neurons symbolized by $x_i\,(i = 1, \ldots\ldots\ldots\ldots.., n)$ and weighted by the synaptic weights ($w_1, w_2, \ldots\ldots\ldots\ldots, w_n$) after adding the bias b, the result will be multiplied by the transfer function (f) to give the output y as showing in Eq.1.

$$y = f(\sum_{i=0}^{n-1} w_{ji}x_i + b) \qquad (1)$$

Generally, the most used functions are: 'threshold', 'linear', and 'sigmoid' functions.

3 Data Collection and Analysis

The database is made up of 371 results collected from several experimental studies on soils stabilized with lime and gypsum published in the literature [13 - 23]. Gypsum content ($CaSO_4$), lime content (L), initial simple compressive strength of non-stabilized soil (SCS0) and age (t) were selected as input neurons and the simple compressive strength (SCS) as output neuron in the architecture of the model.

The variation percentage of each input parameter is given in Table 1. This table can help us know where the majority of the data is for each input parameter, which will tell us in which range of variation our model will perform better [12].

Table 1. Variation range of data.

Input parameters	Variation range of data	Distribution of data (%)
$CaSO_4$ (%)	0-10	83
	10-20	13
	20-30	4
Lime (%)	0-5	57
	5-10	33
	10-15	10
RCS0 (kPa)	9.2-359.2	65
	359.2-709.2	32
	709.2-1059.2	3
Cure period (j)	0-149	97
	150-299	2
	300-499	1

4 Model Development

The neural network used in this study is the multilayer perceptron (MLP) trained with the backpropagation algorithm. The learning function used for training the ANN is the Levengberg-Maquardt the fastest training algorithm for the MLP and the least convergent in the prediction of nonlinear parameters [12]. After data collection and processing (data filtering and normalization), the backpropagation training starts. The model training process will be iterated until the best validation results obtained by optimizing the network parameters (number of hidden layers, number of neurons in each hidden layer, optimal error, transfer function, fraction of data designed for learning, testing and validation). The database wase divided into three parts: the training dataset to train the ANN model, the validation dataset to stop the training process, and the test dataset to evaluate the performance of the model after completion of the training process. The next step is the normalization of the data between [–1; +1] before their introduction to ANN model to make them consistent with the limits of the tangent sigmoid transfer function used in the process. The Mean Squared Error (MSE) that specifies the error generated during training is calculated by using (Eq.2):

$$MSE = \frac{1}{N}\sum_{1}^{i=N}(O_{EXP} - O_{ANN}) \quad (2)$$

Where; N is the total number of data, O_{EXP} is the experimental value of the output and O_{ANN} is its predicted value.

The architecture of the best model consists of a single hidden layer with 16 neurons (see Fig.2). The lime content, percentages of $CaSO_4$, the curing period (T) and the initial simple compressive strength RCS0 were considered as input parameters and the compressive strength (RCS) the output of the model.

We note that the most efficient model with the highest correlation coefficient (R=0.9257) and the lowest MSE error (MSE = 0.009) is showed in Fig.3.

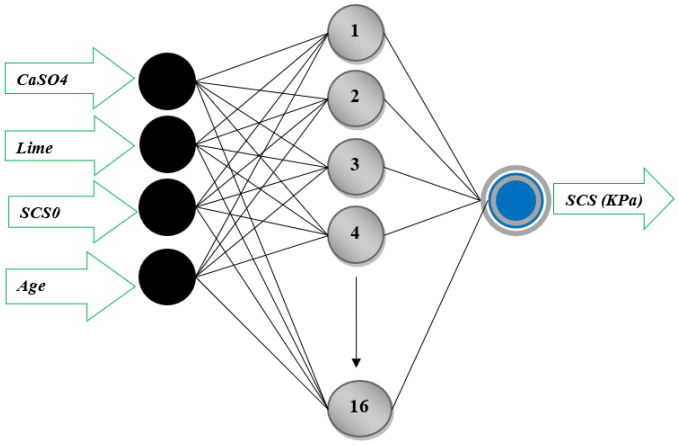

Fig. 2. Architecture of the selected model.

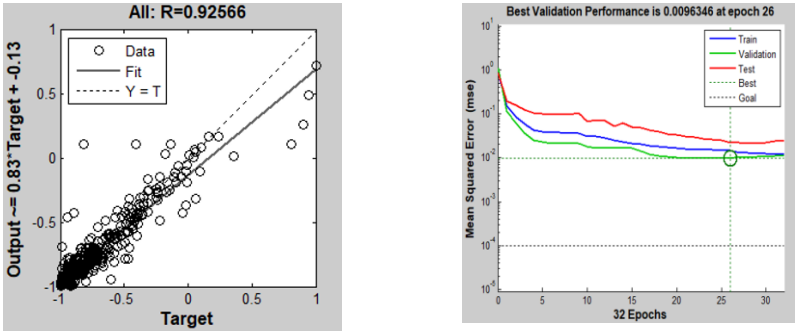

(a) (b)

Fig. 3. Performance of the model: a) Regression coefficient and b) MSE.

5 Sensitivity of the Model

It is necessary to establish a parametric study in order to highlight the variations of the SCS of the stabilized soils with the variation of lime and gypsum content.

5.1 Effect Of Lime on the SCS

To see the influence of the lime content alone on the simple compressive strength, we fixed SCS0 (200kPa) and $CaSO_4$ (0%) and we varied the percentage of lime (4, 5, 6, 7, 8 and 9%) at different ages (3, 7, 14 and 28 days) as shown in Fig.4a. Indeed, the simple compressive strength increased from 500 KPa to 676.45 KPa and from 641.60 KPa to 754.20kPa with the addition of 9% of lime at 3 days and 28 days of curing, respectively. It is known in the literature that the treatment of clay soils with lime causes a

considerable increase in the simple compressive strength, this behavior has been mentioned by several researchers [23] [24] [25].

5.2 Effect of Gypsum on the SCS

The effect of gypsum content alone on the simple compressive strength was observed by variyng the percentage of $CaSO_4$ (0, 2, 4, 6, 8 and 10%) at different ages (3, 7, 14 and 28 days) for RCS0 (200kPa) and 0% of lime content as shown in Fig.4b. As indicated, the compressive strength increased from 255.166 KPa to 1424.803 KPa between 3 and 28 days for a gypsum content of 6%, followed by a slight decrease of SCS for 8% of gypsum at 3.7 and 14 days of cure. This behavior is consistent with the results obtained by several researchers [14] [15] [17].

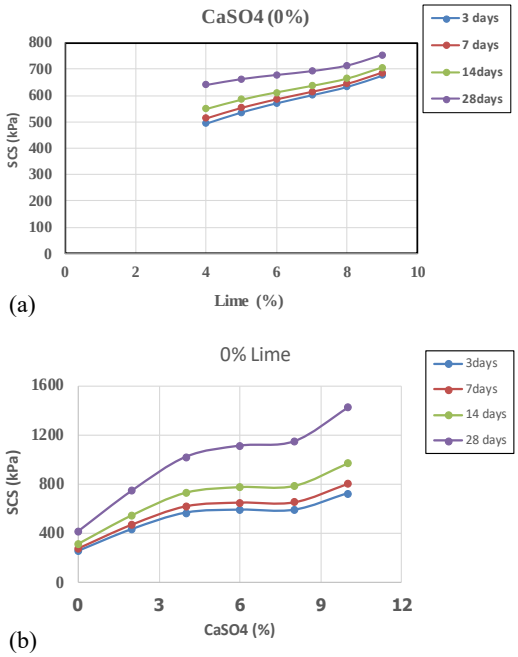

Fig. 4. Effect of a) lime and b) gypsum on SCS.

5.3 The Combined Effect of Lime and Gypsum on the SCS

Figure 5 presents the simple compressive strength results for different lime rates with different gypsum contents. Fig.5a shows a significant increase in SCS up to 6% CaSO4 then it decreases beyond this rate for 4% lime at all ages. For 6% lime, the SCS increases from 572.166 KPa to 1666.598 KPa between 3 and 28 days for gypsum contents between 0 to 6%, beyond this dosage it decreases significantly (Fig.5b). Figure 5c shows an increase in RCS of soil treated with 8% lime between 0 to 6% CaSO4. Beyond 6% gypsum, we notice that the SCS decreases at 3, 7 and 14 days of cure. At 28 days of cure, the SCS increases for 0 to 7% of CaSO4 then it decreases beyond 7%

of gypsum. For the soil treated with 10% lime, a slight increase in simple compressive strength was noticed after the addition of 6% CaSO4 for 3 to 28 days of curing. Beyond 6% of $CaSO_4$, the SCS decreases progressively for all the periods of cure (Fig.5d). From these results, it was observed that there is a significant increase in SCS for the dosages of 0 to 6% of $CaSO_4$ with the different lime contents, and beyond 6% of gypsum, the SCS decreases for all ages. The same observations have been noted by some researchers [21] [27]. It is known that the addition of lime improves the geotechnical properties of soils. However, in many cases, when gypsum is present in lime-treated soils, adverse effects have been observed. To understand the mechanisms involved in the stabilization of gypsum soils by lime, a series of macro and micro tests with different parameters (gypsum and percentages of lime, water content, curing conditions) are necessary to establish before stabilization [27].

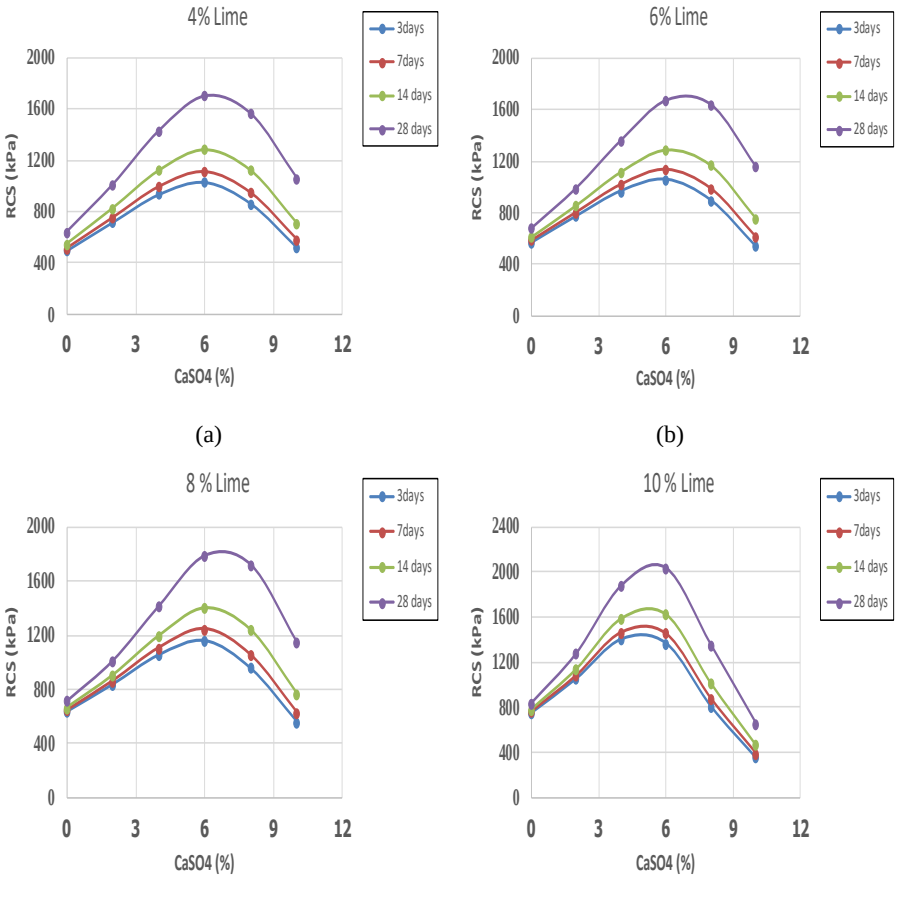

Fig. 5. The Combined effect of lime and gypsum on SCS.

6 Conclusion

This work has been established to develop an ANN model for predicting the simple compressive strength of clay soils stabilized with lime and gypsum. The most efficient model with the highest correlation coefficient (R=0.9257) and the lowest MSE error (MSE = 0.009) was selected to predict the SCS. The parametric study established is in agreement with the literature and showed the ability of the model to generalize in a well-specified range of data. On the other hand, the optimization of the chosen architecture can be done with a hybrid system for example by using the genetic algorithm with the ANNs to reach higher levels of performance.

References

1. Negi, C., Yadav, R.K. and Singhai, A.K., 2013. Effect of silica fume on index properties of black cotton soil. International Journal of Scientific & Engineering Research 4(8): 828–833
2. Kolias, S., Kasselouri-Rigopoulou, V. and Karahalios, A., 2005. Stabilisation of clayey soils with high calcium fly ash and cement. Cement and Concrete Composites 27(2): 301–313. doi:10.1016/j.cemconcomp.2004.02.019
3. Cal, Y., 1995. Soil Classification by Neural Network. Advances in Engineering Software 22(2): 95–97. doi:10.1016/0965-9978(94)00035-H
4. Lee, I.M. and Lee, J.H., 1996. Prediction of Pile Bearing Capacity Using Artificial Neural Networks. Computers and Geotechnics 18(3): 189–200. doi:10.1016/0266-352X (95)00027-8
5. Ahmad, I., Hesham, El Naggar, M. and Khan A.N., 2007. Artificial Neural Network Application to Estimate Kinematic Soil Pile Interaction Response Parameters. Soil Dynamics and Earthquake Engineering 27(9): 892–905. doi: 10.1016/j.soildyn.2006.12.009
6. Shahin, M.A., Maier, H.R., and Jaksa, M.B., 2003. Closure to "Predicting settlement of shallow foundations using neural networks" by Mohamed A. Shahin, Holger R. Maier, and Mark B. Jaksa. Journal of Geotechnical and Geoenvironmental Engineering, 129(12): 1175–1177. doi:10.1061/(ASCE)1090-0241(2003)129:12(1175)
7. Chen, M., Yang, G. and Fanny, Y., 2013. The Use of Artificial Neural Network for Predicting the Unconfined Compressive Strength of Infrastructures: Innovative Infrastructure Geotechnology 284–296. doi:10.1007/978-3-319-61902-6_22
8. Taleb Bahmed, I., Harichane, K., Ghrici, M., Boukhatem, B., Rebouh, R. and Gadouri H., 2017. Prediction of geotechnical properties of clayey soils stabilised with lime using artificial neural networks (ANNs). International Journal of Geotechnical Engineering 5: 1–13. doi:10.1080/19386362.2017.1329966
9. Tabarsa, A., Latifi, N., Osouli, A., & Bagheri, Y. (2021). Unconfined compressive strength prediction of soils stabilized using artificial neural networks and support vector machines. Frontiers of Structural and Civil Engineering, 15(2), 520-536. Tailliez, S. (1998). Etude expérimentale du comportement mécanique des sols granulaires injectés (Doctoral dissertation, Châtenay-Malabry, Ecole centrale de Paris).
10. Jeremiah, J. J., Abbey, S. J., Booth, C. A., & Kashyap, A. (2021). Results of Application of Artificial Neural Networks in Predicting Geo-Mechanical Properties of Stabilised Clays—A Review. Geotechnics, 1(1), 147-171.
11. Lippmann, R.P., 1987. An Introduction to Computing with Neural Nets. IEEE ASSP Magazine 4(2): 4–22. doi:10.1145/44571.44572

12. Kellouche Y., Boukhatem B., Ghrici M., Tagnit-Hamou A., (2017). “Exploring the major factors affecting fly- ash concrete carbonation using artificial neural network.” Neural Comput & Applic, DOI 10.1007/s00521- 017-3052-2. Kosko, B., 1994. Neural networks and fuzzy systems: a dynamical systems approach to machine intelligence. Prentice Hall, New Delhi.
13. Wild, S., Kinuthia, J. M., Jones, G. I., & Higgins, D. D. (1998). Effects of partial substitution of lime with ground granulated blast furnace slag (GGBS) on the strength properties of lime-stabilised sulphate-bearing clay soils. Engineering Geology, 51(1), 37-53.
14. Degirmenci, N. (2008). The using of waste phosphogypsum and natural gypsum in adobe stabilization. Construction and Building Materials, 22(6), 1220-1224.
15. Yilmaz, I., & Civelekoglu, B. (2009). Gypsum: an additive for stabilization of swelling clay soils. Applied Clay Science, 44(1-2), 166-172.
16. Ahmad, I., Hesham, El Naggar, M. and Khan A.N., 2007. Artificial Neural Network Application to Estimate Kinematic Soil Pile Interaction Response Parameters. Soil Dynamics and Earthquake Engineering 27(9): 892–905. doi: 10.1016/j.soildyn.2006.12.009
17. Pekmezci, B. Y., Kafesçioğlu, R., & Agahzadeh, E. (2012). Improved performance of earth structures by lime and gypsum addition. METU JFA, 2, 205.
18. Islam, S., Haque, A., Wilson, S. A., & Ranjith, P. G. (2014). Improvement of acid sulfate soils using lime-activated slag. Proceedings of the Institution of Civil Engineers-Ground Improvement, 167(4), 235-248.
19. Aldaood, A., Bouasker, M., Al-Mukhtar, M. (2014). “Impact of wetting–drying cycles on the microstructure and mechanical properties of lime-stabilized gypseous soils.” Engineering Geology. 174, pp. 11–21. 2014.
20. Kolay, P.K. and Ramesh, K.C., 2016. Reduction of expansive index, swelling and compression behavior of kaolinite and bentonite clay with sand and class C fly ash. Geotechnical and Geological Engineering 34(1): 87–101. doi:10.1007/s10706-015-9930-4
21. Tilak, B., Dutta, R. K., & Mohanty, B. (2015). Strength characteristics of bentonite–lime–gypsum mix reinforced with coir fibres. European Journal of Environmental and Civil Engineering, 19(9), 1108-1135. DOI: 10.1080/19648189.2015.1005159
22. Saberian, M., & Rahgozar, M. A. (2016). Geotechnical properties of peat soil stabilised with shredded waste tyre chips in combination with gypsum, lime or cement. Mires and Peat, 18(16), 1-16.
23. Gadouri, H., 2017a. Influence of the presence of sulfates on the treatment of clayey soils by mineral additions. Doctoral dissertation, Yahia Farès University of Medea, Algeria.
24. Sahoo, J.P. and Pradhan, P.K. (2010), Effect of Lime Stabilized Soil Cushion on Strength Behaviour of Expansive Soil, Geotech Geol Eng., Vol. 28, pp. 889–897.
25. Kavak, A. and Baykal, G. (2012), Long-term behavior of lime-stabilized kaolinite clay, Environ Earth Sci., Vol. 66, pp. 1943–1955.
26. Pekmezci, B. Y., Kafesçioğlu, R., & Agahzadeh, E. (2012). Improved performance of earth structures by lime and gypsum addition. METU JFA, 2, 205.
27. Aldaood, A., Bouasker, M., & Al-Mukhtar, M. (2021). Mechanical behavior of gypseous soil treated with lime. Geotechnical and Geological Engineering, 39(2), 719-733.

Investigation of Stability and Deformation Conditions of Slopes with Groundwater Level Changes by Precipitation Under Different Loads

Baran Toprak[1[0000-0003-4726-0531]], Murat Pinarlik[2[0000-0001-8783-825X]]

[1] Kırıkkale University, Faculty of Engineering and Architecture, Department of Civil Engineering, Yahşihan, Kırıkkale, Türkiye,
barantoprak@gmail.com
[2] Gazi University, Faculty of Technology, Department of Civil Engineering, Beşevler, Ankara, Türkiye,
muratpinarlik@hotmail.com

Abstract. Slope stability problems have become a common problem worldwide to the decreasing of availability construction areas. The ever-increasing loads imposed by modern buildings further compound the challenges faced in areas already prone to slope instability. In addition, one of the most significant factors affecting slope stability problems is changes in groundwater level (GWL) based on by precipitation. In this study, the amount of increase in the water level has been revealed and the effect of this situation on the stability of the slope has been evaluated. Furthermore, the effect of the amount of increase in the groundwater level on the stability of the slope under increasing loads was investigated. Depending on all these data, the deformation of the area containing the stability problem was also examined by finite element analysis. As a result, how the area deforms under time-dependent precipitation has been comparatively demonstrated. It has been noticed that the increasing groundwater level impacts the stability of the slope, while the additional loads create the issue of slope stability combined with settlement.

Keywords: Slope stability, Finite element analysis, Time dependent precipitation, Groundwater level.

1 Introduction

The stability of slope is significant for engineering projects and human activities like building highways, railways, excavations for foundations, creating embankments, constructing dams, and levees [1]. With the impact of climate change, many countries experience prolonged and more intense rainfall [2]. In our country, located in a semi-arid climate region, the occurrence of landslides is accelerated, particularly due to the changing groundwater levels resulting from spring rainfall and snowmelt [3].

The change in the groundwater level is the most important factor affecting the stability on the slopes. The underground water level, which rises and falls due to

precipitation, brings along some slope problems. Deformation analysis is one of the important elements that show slope behavior in slope stability. The occurrence of load changes creates some stability problems even on slopes that appear stable. These load changes can be caused by the rising and falling ground water level, as well as the possible loads on the slope. In this study, it is planned to examine slope stability and deformation analyzes for the mentioned cases. Finally, it is planned to have information about slope behavior by performing deformation analyzes for different situations on slopes.

2 Modelling Details

Firstly, the coordinates where the model will be created are entered. Slopes and elevations were determined. The slope boundaries and the depth of the unit to be investigated underground were also determined. Coordinates of model is shown in Table 1.

Table 1. Coordinates of Model.

Number of Points	x [m]	z [m]
1	0,00	0,00
2	20,00	0,00
3	37,32	10,00
4	60,00	10,00

Low and medium plasticity clay ground is used in the model. Details of clay with low or medium plasticity (CL, CI), soft consistency are : Unit weight: $\gamma = 20{,}00$ kN/m^3, Stress-state: effective, Shear strength: Mohr-Coulomb, Internal friction angle: $\varphi_{ef} = 19{,}00$ °, Ground cohesion: $c_{ef} = 12{,}00$ kPa, Saturated unit weight: $\gamma_{sat} = 22{,}00$ kN/m^3.

A permanent 10, 20, 50 and 100 kN/m^2 surcharge load on the land is included in the model. This surcharge load starts 40 m away from the slope end point and is considered to be 10 m long. The groundwater level is assumed to be 5 m deep to represent the unfavorable situation.

2.1 Analysis for the Control Model

In the literature, several conventional limit equilibrium methods are employed, including but not limited to Bishop's modified method [4], Janbu's generalized procedure of slices [5], Morgenstern and Price's method [6], and Spencer's method [7]. Numerical analysis methods, such as the finite element method [8], finite difference method [9], and discrete element method [10], are commonly employed for slope analysis. In this study, Geo5 Geotechnical Software was used in [11].

The sample selected as the control model was designed for the most favorable situation. No groundwater condition or surcharge load was determined in the control model for the sloped terrain passing through the predetermined coordinate points. All of the values found as a result of the circular slip surface analysis were found to be above the 1.5 safety factor. Table 2 shows that all values are more than 1.5 and the slope is safe.

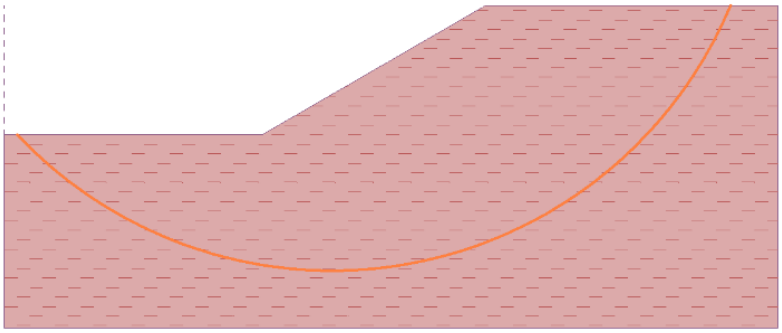

Fig. 1. Circular slip surface for control model

Table 2. FS values of Control model

Verification method	FS Found	FS Wanted
Bishop	2,36	>1,50
Fellenius / Petterson	2,02	>1,50
Spencer	2,36	>1,50
Janbu	2,36	>1,50
Morgenstern-Price	2,36	>1,50

2.2 Analysis of the Model with 1 m Underground Water Level

In the second case, the analysis of the model containing the ground water level at 1 m depth was made. As the underground water level gets closer to the surface, the slopes have an extremely inconvenient situation.

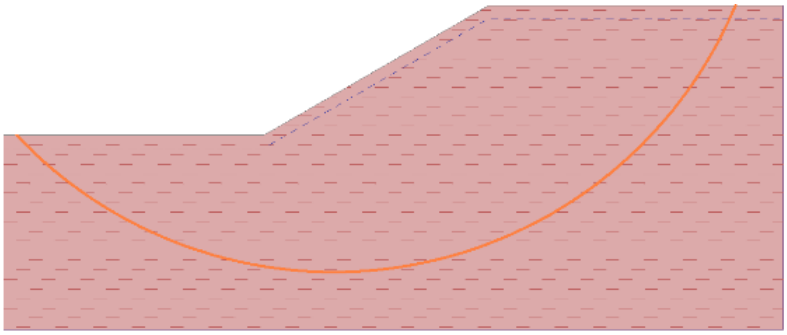

Fig. 2. Circular slip surface for model with 1 m GWL

Table 3. FS values of model with 1 m GWL

Verification method	FS Found	FS Wanted
Bishop	1,57	>1,50
Fellenius / Petterson	1,35	<1,50
Spencer	1,58	>1,50
Janbu	1,58	>1,50
Morgenstern-Price	1,58	>1,50

Table 3 shows the decrease in the safety factor of the slope as the groundwater level approaches the surface. The most unfavorable of the analyzed models is the situation seen in Figure 2. Among the analyses, the Fellenius / Petterson method remained below 1.5, indicating that the slope is unsafe. The Fellenius / Petterson method is an analysis method that is highly affected by the available ground water pressure.

2.3 Analysis of the Model with 3 m Underground Water Level

Next step, the analysis of the model containing the ground water level at 3 m depth was made. Although the safety factor values increase thanks to the underground water level at a depth of 3 m, it is observed that it remains on the unsafe side.

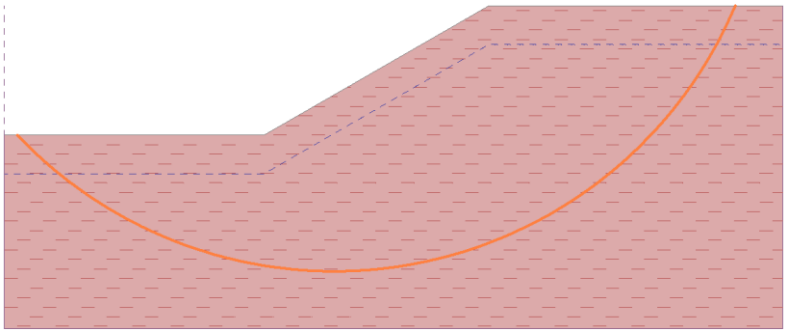

Fig. 3. Circular slip surface for model with 3 m GWL

Table 4. FS values of model with 3 m GWL

Verification method	FS Found	FS Wanted
Bishop	1,71	>1,50
Fellenius / Petterson	1,46	<1,50
Spencer	1,72	>1,50
Janbu	1,72	>1,50
Morgenstern-Price	1,72	>1,50

Table 4 shows that as the depth of the groundwater level increases, the safety factors also increase.

2.4 Analysis of the Model with 5 m Underground Water Level

In the cases examined in the models, it can be said that the most favorable situation in terms of ground is the underground water level at 5 m.

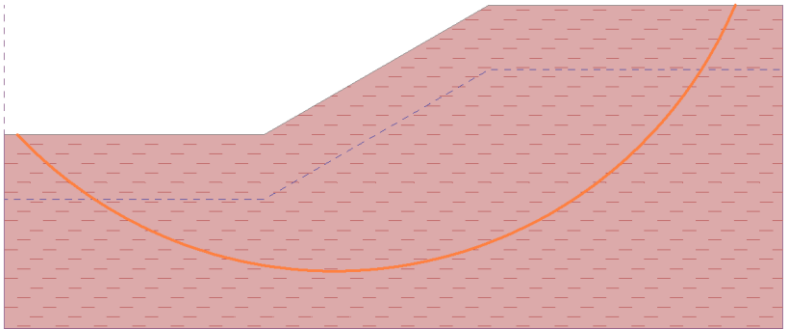

Fig. 4. Circular slip surface for model with 5 m GWL

Table 5. FS values of model with 5 m GWL

Verification method	FS Found	FS Wanted
Bishop	1,84	>1,50
Fellenius / Petterson	1,56	>1,50
Spencer	1,84	>1,50
Janbu	1,84	>1,50
Morgenstern-Price	1,84	>1,50

Table 5 shows that the slope is safe if the groundwater level is 5 m deep. With the increase in safety factors, the situation of being unsafe at previous depths has shifted to the safe side with the underground water level at 5 m depth.

2.5 Analysis of the Model with 10, 20, 50 and 100 kN/m^2 Surcharge Load

The presence of a surcharge load at the top of the slope is one of the most important factors affecting slope stability. In the study, slopes affected by surcharge loads of 10, 20, 50 and 100 kN/m^2, respectively, are seen. The variation of the safety factor according to these surcharge loads was investigated.

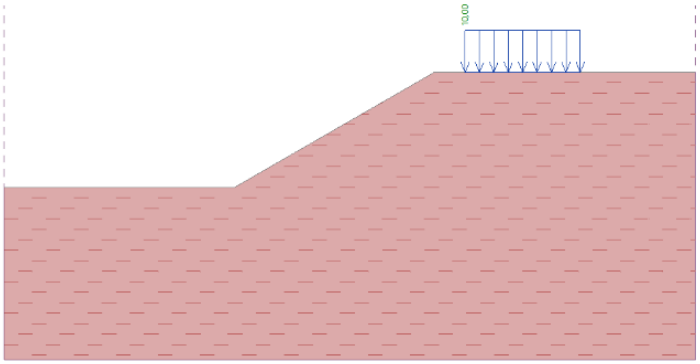

Fig. 5. Slope with 10 kN/m^2 surcharge load

Table 6. FS values of model with surcharge loads of 10, 20, 50 and 100 kN/m^2

Verification method	10 kN/m^2 surcharge load	20 kN/m^2 surcharge load	50 kN/m^2 surcharge load	100 kN/m^2 surcharge load
Bishop	2,31	2,27	2,16	2,00
Fellenius / Petterson	1,98	1,95	1,84	1,70
Spencer	2,31	2,27	2,16	2,00
Janbu	2,31	2,27	2,16	2,00
Morgenstern-Price	2,31	2,27	2,16	2,00

As can be seen in Table 6, an increase in the surcharge load causes a significant decrease in the factor of safety. The constructions planned to be built on the slope should be made by taking this fact into consideration and necessary precautions should be taken.

2.6 FEM Analysis of all Models

It is important to perform finite element analysis for all the models examined in order to see the deformations that may occur.

The FEM analysis started with the creation of the original topography. To create a mesh, mesh edge lengths are taken as 1 m. Finite element network has been successfully created, 5662 nodes and 3069 elements have been determined.

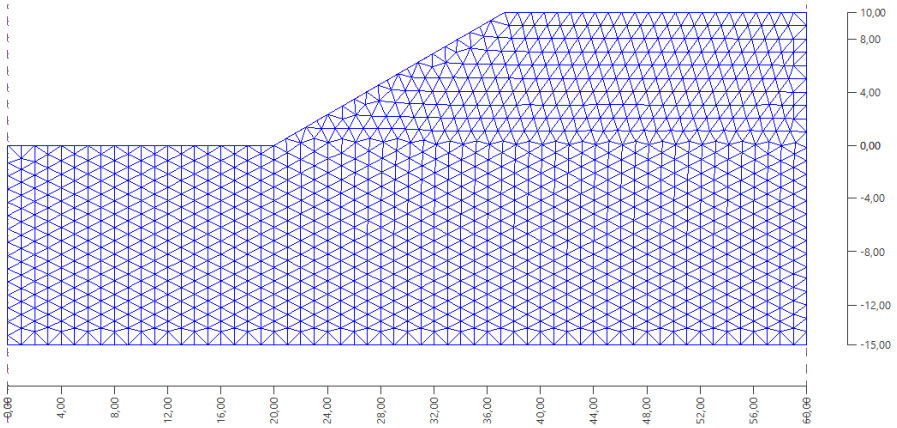

Fig. 6. Creation of the mesh system for the original topography

After the meshing process was completed, FEM analysis was performed for both original topography and for the determined groundwater levels.

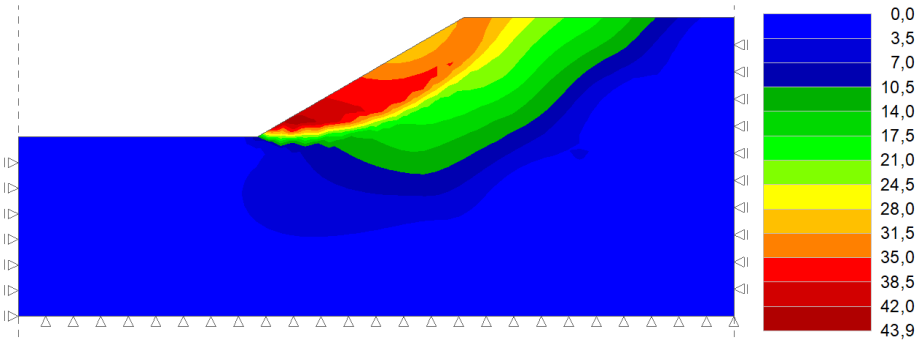

Fig. 7. FEM analysis for original topography

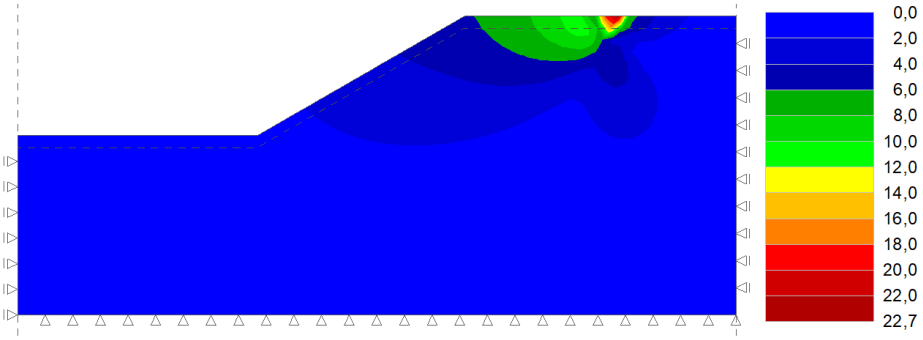

Fig. 8. FEM analysis for model with 1 m GWL

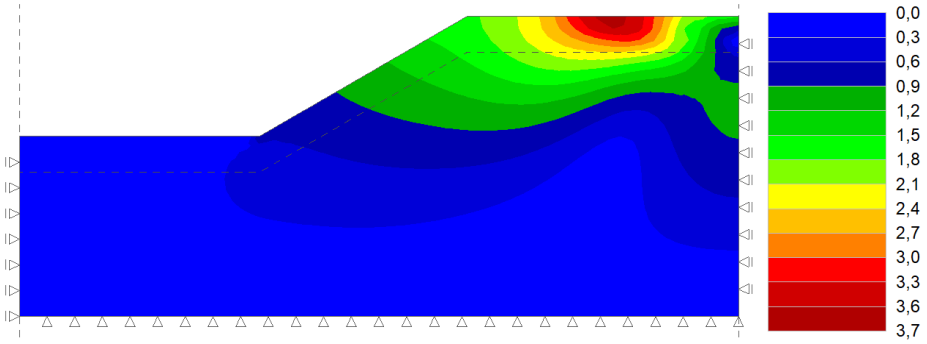

Fig. 9. FEM analysis for model with 3 m GWL

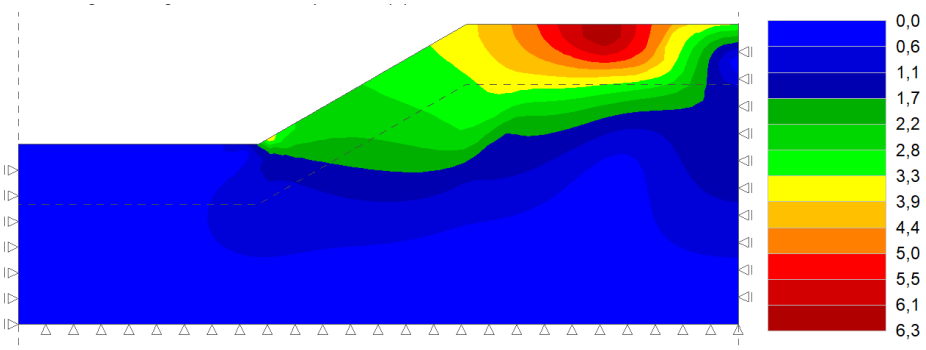

Fig. 10. FEM analysis for model with 5 m GWL

Immediately after the deformations caused by the groundwater level, the deformations caused by the surcharge load placed on the slope were analyzed.

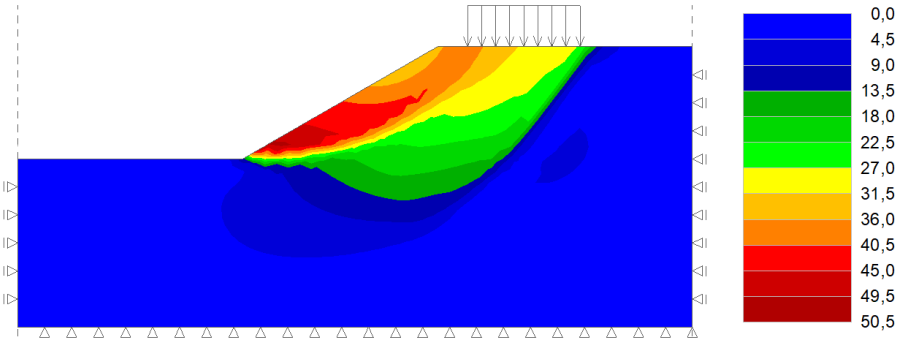

Fig. 11. FEM analysis for slope with 10 kN/m^2 surcharge load

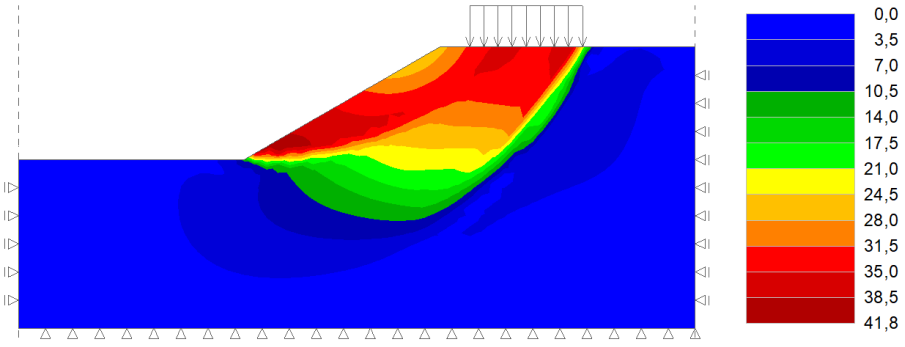

Fig. 12. FEM analysis for slope with 20 kN/m^2 surcharge load

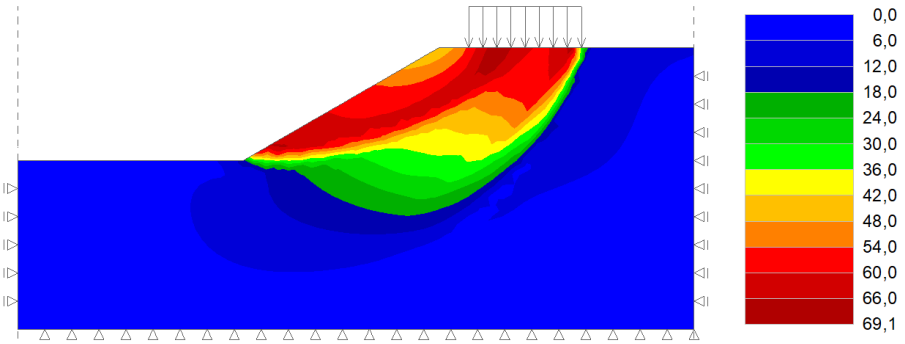

Fig. 13. FEM analysis for slope with 50 kN/m^2 surcharge load

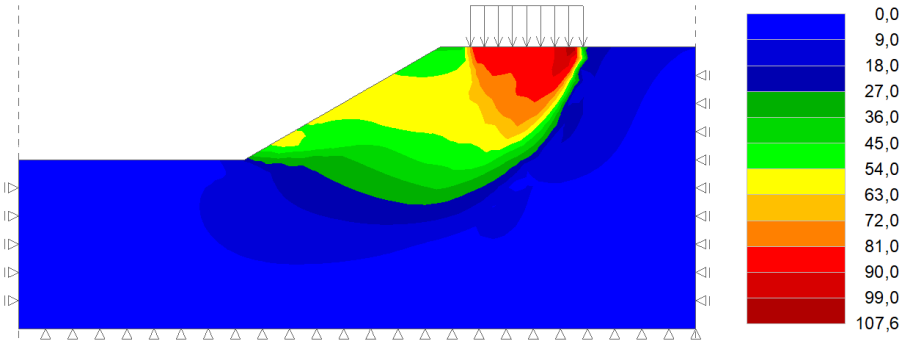

Fig. 14. FEM analysis for slope with 100 kN/m^2 surcharge load

As can be seen in Figures 11, 12, 13 and 14, the deformation of the slope increases as the surcharge load value increases.

3 Conclusion

In this study, the effect of different groundwater levels and surcharge loads on slope stability, along with the resulting deformation on the slope, has been investigated. Firstly, stability analyses were performed on the existing state of the created slope model. The Bishop, Fellenius/Petterson, Spencer, Janbu, and Morgenstern-Price methods were employed in the analyses. Subsequently, the analyses were repeated for different groundwater levels. It was observed that all methods, except for the Fellenius/Petterson method, achieved the required safety factor. This is because the Fellenius/Petterson method is highly influenced by the available groundwater pressure. Furthermore, no issues were encountered in the slope stability analyses conducted for different loadings.

Upon examining the FEM analyses, it was observed that models defined with groundwater level exhibited less deformation compared to the reference model. However, the positive or negative effect of groundwater level variations on deformation increase could not be clearly determined. Additionally, it was determined that as the surcharge load increases, there is an increase in deformation on the slope.

Especially in aquifers with unconfined water tables, groundwater levels rise and approach the surface with increased rainfall. Cyclonic precipitation, commonly observed in our country, saturates the soil, resulting in a greater impact on the water table. The analyses clearly demonstrate that as the water table rises, it adversely affects slope stability, and the distribution of deformation in the soil increases as it approaches the water table. Therefore, conducting studies on slope stability in regions with above-average rainfall and defined soil properties would be beneficial.

Acknowledgments
The Department of Civil Engineering at Kırıkkale University utilizes an educational license of the GEO5 Geotechnical Software Suite provided by the Fine Company.

References

1. Ni, P., Wang, S., Zhang, S., Mei L.: Response of heterogeneous slopes to increased surcharge load. Computers and Geotechnics 78, 99–109 (2016).
2. Chen, J., and Hai, Y.: A φb model for predicting shear strength of unsaturated soils. Advance Materials Research Journal 425–429 (2012).
3. Öztürk, K.: Landslips and the effects of these on Turkey. Gazi Eğitim Fakültesi Dergisi, 22(2), 35–50 (2002).
4. Bishop, A.W.: The use of the slip circle in the stability analysis of slopes. Géotechnique 5(1), 7–17 (1955).
5. Janbu, N.: Slope stability computations. Soil mechanics and foundation engineering report. Trondheim: Technical University of Norway (1968).
6. Morgenstern, N.R., Price, V.E.: The analysis of the stability of general slip surfaces. Géotechnique 15(1), 79–93 (1965).
7. Spencer, E.: A method of analysis of the stability of embankments assuming parallel inter-slice forces. Géotechnique 17(1), 11–26 (1967).
8. Griffiths, D.V., Lane, P.A.: Slope stability analysis by finite elements. Geotechnique 49(3), 387–403 (1999).
9. Chugh, A.K.: On the boundary conditions in slope stability analysis. Int J Numer Anal Meth Geomech 27(11), 905–26 (2003).
10. Wang, C., Tannant, D., Lilly, P.: Numerical analysis of the stability of heavily jointed rock slopes using PFC2D. Int J Rock Mech Min Sci 40(3), 415–24 (2003).
11. Geo5 Homepage, https://www.finesoftware.eu/geotechnical-software/, last accessed 2023/07/10.

Effect Of Stress History on Lateral Earth Pressure Coefficient At Rest Analysis Through Discrete Elements Method

Khellaf Abdelghani [1][0000-0002-7593-4954] and Mansouri Mouloud [2][0000-0002-4179-7488]

[1] Ferhat Abbas University Setif 1, Civil Engineering Department, Setif, Algeria, khellafabdelghani3@gmail.com
[2] Ferhat Abbas University Setif 1, Civil Engineering Department, Setif, Algeria, mansouri_m@yahoo.com

Abstract. This paper investigates the vertical stress history effect on lateral earth pressure at rest of dense sandy soil through a 2D discrete elements modeling of a displacement controlled oedometric test. We used a model based on the molecular dynamics method in which the normal contact forces are calculated by means of the viscoelastic model involving grain deformation and the tangential interaction forces are calculated using a Coulomb-type friction model including stick-slip effect. Circular-shaped elements are employed in this work, a rolling resistance model is integrated in order to take account of natural rolling resistance of the grains. The oedometric tests carried out focused on the estimation of lateral earth pressure coefficient at rest K_0, the effects of over consolidation on K_0. A micromechanical analysis is caried out in order to highlight the effects of the intergranular friction and the anisotropies of contact orientations and normal forces intensity on K_0.

Keywords: Discrete element method, lateral earth pressure coefficient at rest, oedometric test.

1 Introduction

The stress history has a strong effect on the mechanical behavior of a soil. This history is commonly characterized by the over-consolidation ratio (OCR) that is defined as the ratio between the maximal effective pressure to which the soil was subjected during his history and the effective stress at the actual state. This ratio is often used in geotechnical computations such as in settlements calculations and in the estimation of the coefficient of lateral earth pressures at rest (K_0).

Numerous studies dealing with earth pressure theories for normally consolidated soils consider the shearing resistance angle of the soil as the only parameter governing the values of the earth pressure coefficient Terzaghi 1920; [1]. However, more recent studies concluded that the stress history has a significant effect on the lateral earth pressure.

Many experimental researches was focused on the study of the parameters that affect the K_0 values, among these studies: Wanatowski and Chu [2] have measured K_0 for a sand using a plane-strain apparatus; they have concluded that the K_0values does not depend only on the internal friction angle but also on the void ratio and the fabric tensor that characterizes contacts orientations in the soil. Lee et al [3] have investigated experimentally the effect of density and particles shape on the K_0 values using different types of granular materials, they concluded that the effect of material density on K_0 differed depending on the stress history whereas the effect of particle surface roughness, was relatively small.

Massarsch and Fellenius [4] have studied experimentally the effect of deep compaction in granular soils, they concluded that the vibratory compaction causes a permanent over-consolidation effect, which increases the coefficient of lateral earth pressures at rest K_0 because the lateral stress increasing.

On the other hand with the development of computer tools, models taking account of the discontinuous nature of sand have been developed. Discrete element methods (DEM) based on these models form a large family of methods deployed for the study of interacting particle sets [5] and seems to be the best tool for the understanding of granular media behavior.

Lopera Perez et al, [6] have studied the vertical one-dimensional compression of idealized soil through discrete element method using a modified version of the open-source code lammps [7]. They analyzed the effect of the void ratio on the lateral earth pressure coefficient at rest K_0. They showed that the K0 coefficient increases with the sample's compacity decreasing, i.e., with the void ratio increasing. It is an interesting result, but it does not show the determining effect of the overconsolidation state of the material on the lateral earth pressure.

Gu et al [8] have studied the effect of void ratio on K_0 for a granular material using the discrete element methods and they found that the K_0 decreases as the void ratio decreases and the vertical stress increases.

In this paper, the lateral earth pressure coefficient K_0 of a cohesionless dense soil (sand) is investigated numerically through a discrete elements modeling. A 2D simulation of an oedometric test with controlled displacement is carried out. The effect of the vertical stress history on the lateral earth pressures coefficient at rest is analyzed. A micromechanical analysis including directional contact and normal contact forces distributions. The obtained results are compared with that of the previous experimental studies namely, the studies of :[9], [10], [11],[12] and [13].

2 Coefficient of Lateral Earth Pressure At Rest

For a given soil, the ratio between the effective vertical geostatic stress and horizontal stress represents the lateral earth pressure coefficient at rest K_0.

$$K_0 = \frac{\sigma_h}{\sigma_v} \tag{1}$$

Where σ_h is the horizontal effective stress and σ_v the vertical effective stress. These stresses correspond to the state where the lateral deformation is prevented. The empirical formula introduced by Jaky [1] is the most often formula applied to estimate the lateral earth pressure coefficient at rest K_0, which expresses K_0 as a function of internal friction angle φ:

$$K_0 = (1 - sin\varphi) \tag{2}$$

It should be remembered that this formula does not take into account the soil's state parameters and the history of applied stresses, therefore further revisions were introduced. Wroth et al (9) and Mayne and Kulhawy [11] have stated that the lateral earth pressure at rest is greater for over consolidated than for normally consolidated soils. Accordingly, a new expression of the lateral earth pressure coefficient at rest K_0 taking account of the degree of overconsolidation ratio was proposed:

$$K_0 = (1 - sin\varphi)OCR^{\alpha} \tag{3}$$

Where α is the critical parameter that controls the effect of OCR onK_0, having a constant value (α =0.5) according to [10], while [11]and [14] have expressed α as $\alpha = sin\varphi$.

Mayne and Kulhawy [11] have studied the variation of K_0 during loading and unloading cycles for a sandy soil and they suggested the following formula taking account the stress path:

$$\begin{cases} K_{0l} = (1 - sin\varphi) & loading \\ K_{0ul} = (1 - sin\varphi)OCR^{sin\varphi} & unloading \end{cases} \tag{4}$$

Where K_{0l} and K_{0ul} are the lateral earth pressure coefficient at rest during loading and unloading phases, respectively.

Zeng and Ni [12] have studied experimentally the effect of stress history on elastic shear modulus of sandy soil. From this study they proposed an empirical equation expressing K_0 as:

$$\begin{cases} K_{0l} = a(1 - sin\varphi) & loading \\ K_{0ul} = a(1 - sin\varphi)OCR^{b\,sin\varphi} & unloading \end{cases} \tag{5}$$

Where the parameters a and b depend on the soil particles properties.

The lateral earth pressure at rest coefficient K_0 of over-consolidated sandy soil acting on retaining walls was also investigated experimentally by Hanna and Al-Romhein [13].

Consequently, the following empirical formula was proposed:

$$\begin{cases} K_{0l} = (1 - sin\varphi) & loading \\ K_{0ul} = (1 - sin\varphi)OCR^{(sin\varphi - 0.18)} & unloading \end{cases} \tag{6}$$

3 Molecular Dynamics

Molecular dynamics (MD) applied to granular media was initiated by Cundall and Strack [15] successfully used later in the analysis of many phenomena related to the mechanics of granular materials [16]. This method assumes the materials grains as independent elements interacting by contact forces. the overall deformation of the material results from the relative displacement of the elements. The motion of each element is governed by Newton's second law which takes into account contact forces and external forces such as gravity. Thus, for each grain i subjected to its self weigh in contact with n_c neighbor grains these equations are expressed:

$$\begin{cases} m_i \ \ddot{\vec{x}}_i = \sum_{j=1}^{n_c} \overrightarrow{F_{ij}} + m_i \vec{g} & i = 1 \dots n \\ I_i \ \overrightarrow{\ddot{\varphi}_i} = \sum_{j} \vec{M}_{ij} & j = 1 \dots n \end{cases} \tag{7}$$

Where n is the number of elements, m_i and I_i are the mass and the moment of inertia of the grain i , $\ddot{\vec{x}}_i$ and $\overrightarrow{\ddot{\varphi}_i}$ are translational and rotational accelerations of grain i , $\overrightarrow{F_{ij}}$ and $\overrightarrow{M_{ij}}$ are respectively the contact force and momentum applied by a grain j to the grain i,$\vec{g}$ is the acceleration of gravity.

In molecular dynamics, elements are assumed to be slightly deformable, thus contact forces are calculated explicitly in terms of grain deformations. Each contact force ($\overrightarrow{F_{ij}}$) has two components one normal to the contact area and the other tangential. The simplest and commonly used model for the computation of the normal contact force ($\vec{F}_n$) is the viscoelastic model expressed as:

$$F_n = (-\delta_n K_n - v_n V_n) \tag{8}$$

Where:$K_n$is the normal stiffness, $v_n$is the viscous damping coefficient, V_n is the normal velocity of the grain j relative to the grain i .

In this work the tangential contact force is computed through a Coulomb-type friction model that integrates the elastic tangential deformation (Fig.1.). This force is then expressed as:

$$F_s = \min\left(K_s \delta_s + v_s V_s;\ \mu |F_n|\right) \tag{9}$$

Where:$K_s$is the tangential stiffness,$v_s$is the tangential viscous damping coefficient, V_s is the tangential velocity of the grain j relative to the grain i, μ is the friction coefficient and δ_s is the cumulative of elastic displacements.

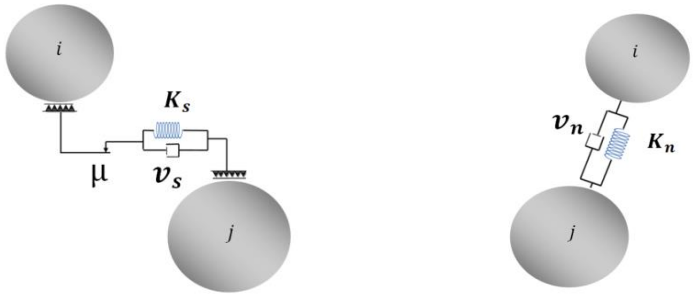

(a) (b)

Fig. 1. Interaction force model grain-grain. (a) Tangential force model, (b) Normal force model.

The interaction forces of grains with external obstacles such as walls could be calculated using models similar to those of grains interaction.

It should be mentioned that the stability of the MD method is conditioned by the correct description of the contact phase [17], therefore the contact duration must be discretized to a sufficiently large number of time steps. In the case where the normal repulsive force is modeled by the viscoelastic model, the contact duration between two colliding grains has the expression:

$$t_c = \frac{\pi}{\sqrt{(k_n/m_{eff}) - (v_n/2m_{eff})^2}} \tag{10}$$

In practice it is common to discretize the contact duration to ten-time steps at least. Then the simulatio1n time step Δt should be:

$$\Delta t \leq \frac{t_c}{10} \tag{11}$$

The shape of the grains is supposed in this work circular. The use of circular elements generates a loss of rolling resistance [18]which has a significant effect on the overall behavior of the material. It is thus common to introduce a rolling resistance to the elements in order to approximate the rolling behavior of actual grains which depends on their shape and on the roughness of their surface.

In our simulations we introduced a simple rolling resistance model that depends on the contact normal force and the grains overlap. In this model it is assumed that the normal contact force is shifted from the contact surface center in the rolling direction (Fig.2.).

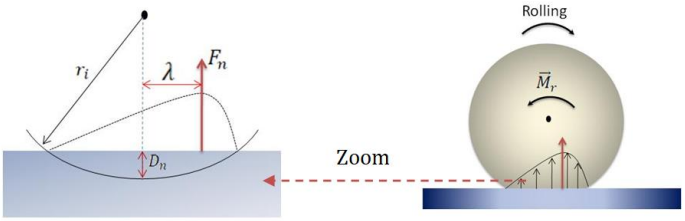

Fig. 2. Illustration of the rolling resistance model

The normal contact force produces therefore a rolling resistance expressed by:

$$\vec{M}_r = -\lambda F_n \frac{\overrightarrow{w_i'}}{\|\overrightarrow{w_i'}\|} \tag{12}$$

Where $\overrightarrow{w_i'}$ is the relative angular velocity of grain i, it is expressed in the general case of rolling of grain i on grain j by: $\overrightarrow{w_i'}=\overrightarrow{w_i}$ - $\overrightarrow{w_j}$.
Where λ is the eccentricity of normal stresses resultant given by:

$$\lambda = \psi \sqrt{r_i^2 - (r_i - \frac{\delta_n}{2})^2} \tag{13}$$

ψ is the coefficient that controls the position of F_n . In all simulations we adopted $\psi = 0.5$.

4 Simulations and Results

4.1 A Description of the Simulated Oedometer

The 2D simulated oedometer cell has the dimensions $L \times H$ (Fig.3.). The left and right walls of the oedometric cell are undeformable (fixed walls) and they are smooth to ensure the K_0 condition during the test. During the tests, the vertical stress (σ_v) is applied through a horizontal undeformable plate placed above the sample inside the cell. This stress is adjusted by a controlled vertical displacement of the plate.

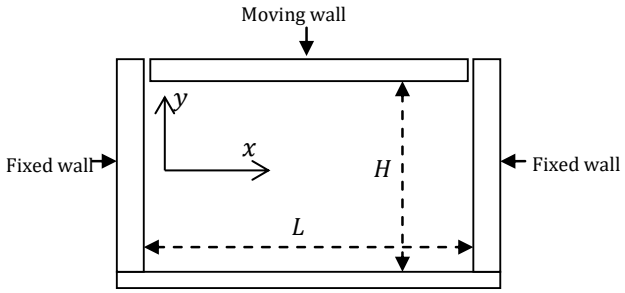

Fig. 3. Diagram of the simulated oedometer

It should be remembered that in laboratory oedometric tests, it is recommended to use cells having a diameter/height ratio greater than 2.5 in order to minimize the effects of soil friction on the side walls [19]. This condition is not necessary in the simulations since the friction on the lateral walls can be eliminated completely in the numerical model.

4.2 Microscopic and Macroscopic Sample Properties

The sample is composed of polydisperse circular shaped particles whose diameters are obtained from the cumulate volume distributions model proposed by Voivret et al [20]. In our simulations, the maximum and minimum diameter values are taken: $dmax = 2dmin = 1mm$. The grain size distribution curve is shown in figure 4. The sample is confined with isotropic pressure of 10 kPa without gravity. In order to obtain a dense specimen, the inter-granular friction is set to zero in the isotropic confining step. During the oedometric compression, the friction coefficient is set to the required value.

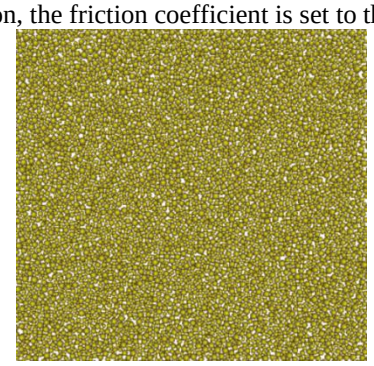

Figure 16: Snapshot of dense sample

As recommended by several researchers [21], the model's grains number is taken greater than 4000 particles in order to respect the representative elementary volume.

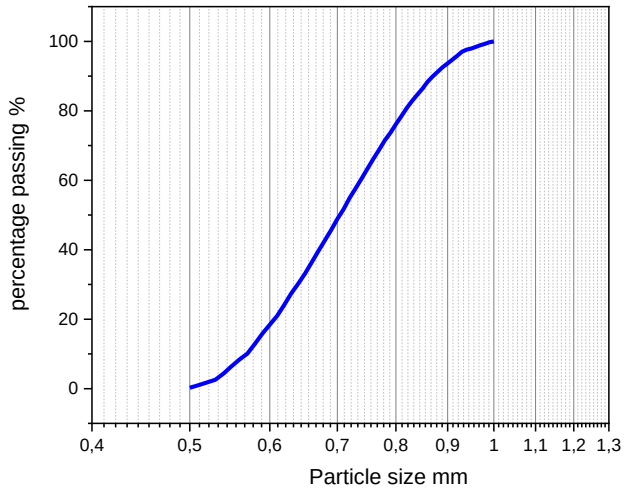

Fig. 4. Grain size distribution

The discrete elements modeling parameters used in the simulations are summarized in table 1:

Table 1**.** Parameters used for oedometric tests

Characteristics	Symbol	Value	Unite
Normal Stiffness	K_n	12000000	N/m^2
Tangential stiffness	K_s	9600000	N/m^2
Normal viscous damping coefficient calculated from a restitution coefficient of 0.1	v_n	41.38	Kg/s^{-1}
Tangential viscous damping coefficient	v_s	33.10	Kg/s^{-1}
Kinetic coefficient of friction	μ_k	0.6	
Static coefficient of friction	μ_s	0.7	
Gravity	G	0	m/s^2
Max radius of grain	$r_i\ max$	0.001	m
Density of grains	ρ	2600	Kg/m^3

As mentioned in this table, it is worth noting that the gravity acceleration is set to zero for all tests that are performed in this work.

The internal friction angle of the numerical specimen is estimated through a biaxial compression test (BC), in order to compare the numerical results to the empirical

formulas based on soil's internal friction angle. The BC tests are applied to samples having a ratio of the height to the width equal to 2 (H / L=2). The sample is first subjected to an isotropic confining stress (σ_1=σ_2) (Fig.5.), then the vertical stress σ_1 is increased through a downward displacement of the upper horizontal plate until the failure. (Fig.6.) shows a simulated test at the failure phase.

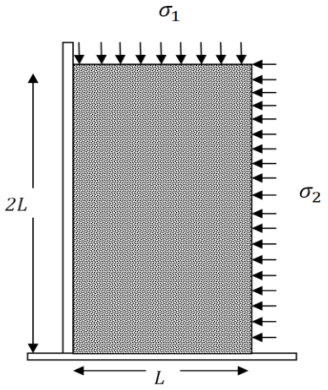

Fig. 5. Principle of the performed biaxial compression shear test

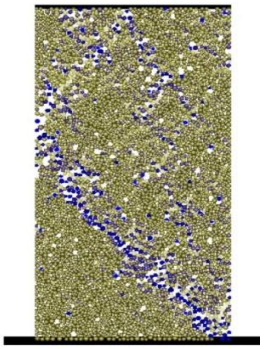

Fig. 6. A simulated sample at failure under the shear test

The blue grains represent the grains with high rolling displacement (shear band)

To evaluate the shear strength parameters, three shear tests are performed with three different confining stresses. The confining stresses and the corresponding deviatoric failure stresses are given in Table 2.

Table 2. Data and results of the performed shear tests

	Specimen 1 (BC-SPC1)	Specimen 2 (BC-SPC2)	Specimen 3 (BC-SPC3)
Confining stress σ_3 (kPa)	50	100	150
Vertical stress at failure σ_1 (kPa)	153	307	452

These stresses are used to plot the Mohr circles and consequently the envelope curve at failure as shown in (Fig.7.).

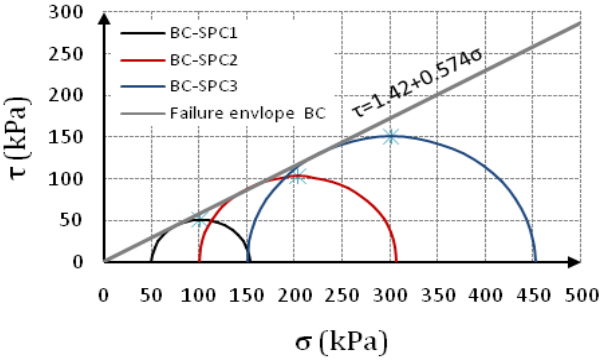

Fig. 7. Mohr circles and envelope curve at failure

The diagram of (Fig.7.) gives an internal friction angle of 29.86° and a negligible cohesion (C). Therefore, the macroscopic shear strength parameters of the simulated granular material are: $\varphi \approx 30°$ and $C \approx 0$.

4.3 Estimation of K_0 from the Modeled Oedometer

The vertical and horizontal stresses involved in the K_0 expression (Eq1) are components of the average intergranular stress tensor. For static or quasi-static problems in granular media, each component of the average stress tensor is expressed by [22]:

$$\sigma_{ij} = \frac{1}{V} \sum_{n_c=1}^{N_c} F_i^{n_c} L_j^{n_c} \tag{14}$$

Where i and j define the computed component of the stress tensor at the center of the volume V, N_c being the total number of contacts in the volume V, $F_i^{n_c}$ is the i component of the interaction force at the contact n_c and $L_j^{n_c}$ is the j component of the vector $\vec{L}$ connecting the centers of the two contacting grains (branch vector). The used stress components to compute K_0 are $\sigma_h = \sigma_{xx}\ (i,j = x,x)$ and $\sigma_v = \sigma_{yy}\ (i,j = y,y)$.

4.4 Evolution of K_0 for One Loading-Unloading Cycle

In order to evaluate the effect of the loading history on the at rest lateral earth pressure coefficient K_0 for a dense sandy soil, an oedometric test with a loading-unloading cycle is simulated. During the loading and unloading phases, the horizontal stress, the vertical stress and the K_0 coefficient are calculated continuously. The evolution of K_0 calculated numerically is plotted in (Fig.8.). For comparison purposes, the empirical equations (3), (4), (5) and (6) relating to the variation of K_0 in terms of the soil's over consolidation ratio are plotted on the same graph.

It could be observed that the stress state in the sample is initially isotropic (K_0=1). When the vertical stress increases, K_0 decreases first sharply, then it stabilizes on a limit value that remains almost constant even for a high vertical stress. This limit compares well with the equation proposed by Zeng and Ni, 1999 for a coefficient $a = 0.9$.

However, during unloading, K_0 increases in a non-linear way. It could be observed that the numerically computed K_0 varies in a similar shape with the empirical formulas (Fig. 8.). This figure shows that the computed K_0 is very close to equations (5) proposed by Zeng and Ni, 1999. It should be noted that the empirical parameters a and b in equation (5) are set to 0.9 and 0.8 respectively, while the critical parameter (α) that controls the effect of stress history in equation (3) is set to 0.5.

As unloading progresses K_0 increases, this demonstrates the increase of this coefficient with increasing the over consolidation ratio.

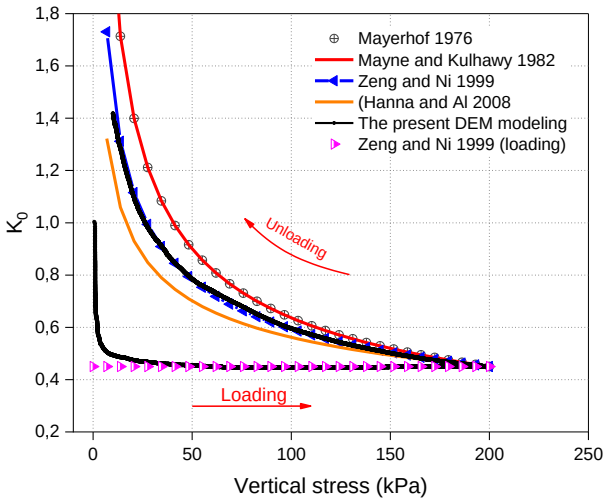

Fig. 8. Evolution of K_0 during loading and unloading, computed and empirical values.

4.5 Highlighting of the Over-Consolidation Ratio Effect on K_0

To highlight the effect of the over consolidation ratio on the at rest lateral earth pressure coefficient K_0 three different tests are carried out.

Test 1:

The aim of this test is to show the effect of consolidation degree on the K_0. For that, three identical samples are subjected to loading-unloading tests with different maximum vertical stresses of 100, 200 and 300kPa. (Fig.9.) shows the evolution of K_0 for the three performed tests. According to this figure, it can be observed that during the loading phases, lateral earth pressure coefficient follows the same path, however during the unloading phases K_0 follows different paths, K_0 is more significant for the

highest over-consolidation loadings. Therefore, the at rest lateral earth pressure coefficient increases when OCR increases.

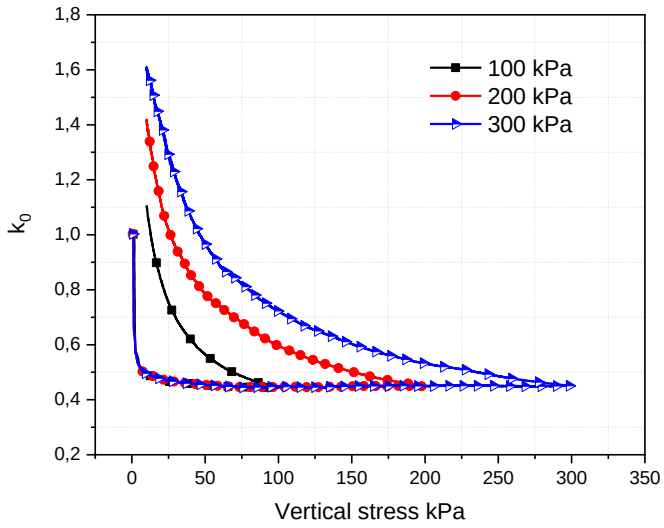

Fig. 9. Evolution of K_0 during loading and unloading phases for three identical samples.

Test 2:

In order to show the effect of cyclic loading on K_0, a same sample is subjected to three loading-unloading cycles, where the maximum vertical stress is set to 200kPa. (Fig.10.) shows the evolution of K_0 during the three loading cycles.

For the first cycle, the behavior of the soil is similar to that described in the section 4.4 where K_0 tends early to have a constant minimum value during the loading phase. For the following cycles, the evolution of K_0, during the loading phases is rather progressive compared to the first cycle and the minimum value is reached at the end of the loading phases, where the sample tends to become normally consolidated. These curves illustrate therefore, the difference between the evolution of K_0, for over-consolidated and normally consolidated soils in loading phases.

For unloading phases, this figure shows again that the at-rest lateral earth pressure coefficient is greater in the unloading phases than in the loading phases. It is worth noting that K_0 in the unloading phases is more significant for third cycle, this could be attributed to the sample densification during cyclic loading.

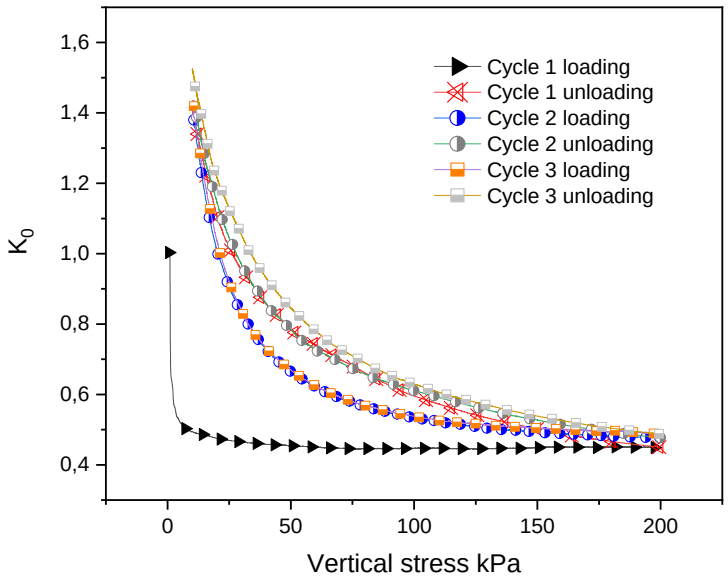

Fig. 10. Evolution of K_0 during three loading and unloading.

Test 3:

In this test, a same sample is subjected to a cyclic loading with variable maximum load for each cycle. The maximum vertical stress in the first, the second and the third cycles are respectively set to 100, 200 and 300kPa.

(Fig. 11.) shows the evolution of K_0 during three cycles. For this test, the relevant remark is that during the reloading phases K_0 reaches its minimum values when the soil becomes normally consolidated and the stress history has no effect on the K_0 final value.

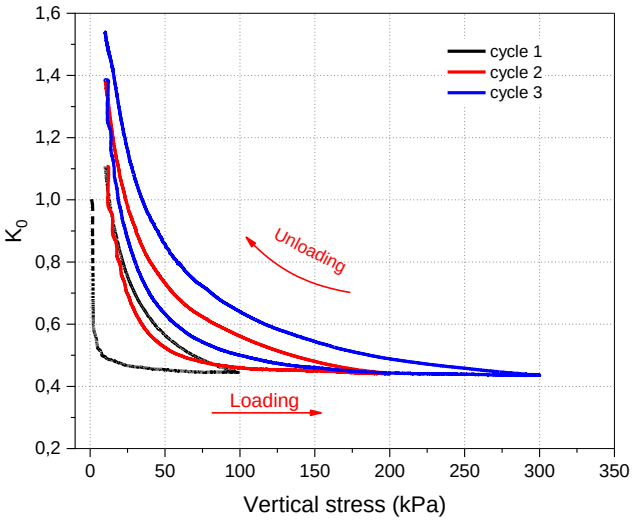

Fig. 11. K_0 evolution Vs vertical stress during three cycles of loading-unloading

5 Micromechanical Analysis

The DEM output parameters offer information on the microscopic structure of the simulated material. The aim of this analysis is to show the effect of some micromechanical parameters on the K_0. We analyze the effects of the number and orientations of the contacts as well as the intergranular friction. This analysis could provide explanations for the macroscopic results presented above.

The contact orientations are described in the discrete element modeling through the fabric tensor (Φ_{ij}) defined by [23][24] and [25]:

$$\Phi_{ij} = \frac{1}{N_c} \sum_{n_c=1}^{N_c} n_i \, n_j \tag{16}$$

Where N_c is the total number of contacts and n_i is the i component of the contact's normal unit vector. The fabric tensor is symmetric, its diagonal components vary between 0 and 1 ($0 \leq \Phi_{ij} \leq 1$, for $i = j$). In 2D case this tensor has three components; Φ_{xx}, Φ_{yy} and Φ_{xy} that define the average orientation of the contacts in the material. in the following, we refer to horizontal contact, when the unit normal vector of the contact is oriented in the horizontal direction. When the contact's normal unit vector is oriented vertically, the contact is referred to vertical contact. In the case where the contacts are rather horizontal (x-direction), Φ_{xx} is greater than Φ_{yy}, the opposite happens when the contacts are rather vertical (y-direction). In all cases the sum of these two components is 1 ($\Phi_{xx} + \Phi_{yy} = 1$).

The ratio $F = \frac{\Phi_{xx}}{\Phi_{yy}}$ describes the structural anisotropy, it will be referred as the degree of anisotropy in the following. For $F = 1$ the fabric state is isotropic.

5.1 A Basic Illustrative Granular Assembly

In order to illustrate the variation of the focused microscopic parameters in a granular material, we consider the example of three grains symmetric assembly subjected to an oedometric loading-unloading cycle. We analyze the variation of K_0 in terms of the fabric tensor, the intergranular friction coefficient and the number of contacts. Two cases are considered; frictionless and rough grains (Fig. 12.).

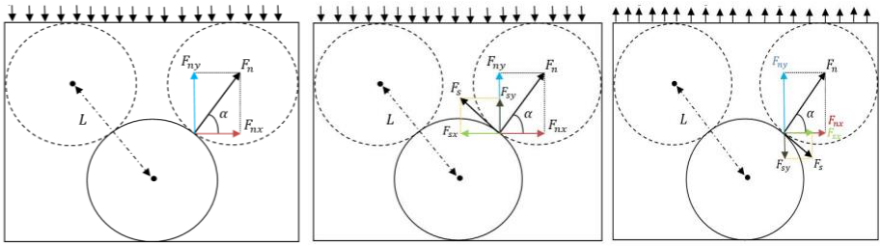

Fig. 11. Force diagrams; (a) Frictionless grains, loading and unloading phases, (b) Rough grains during loading phase, (c) Rough grains during unloading phase.

Analytical Description

Frictionless grains

In this case the friction forces are zero, the interaction force is normal to the contact and its components are $F_{nx} = F_n \cos\alpha$ and $F_{ny} = F_n \sin\alpha$ (Fig. 10 a.).

By using equation 14 and taking account of the problem's symmetry, the at rest lateral earth pressure coefficient K_0 can be expressed:

$$K_0 = \frac{\sigma_{xx}}{\sigma_{yy}} = \frac{N_c F_{nx} L_x}{N_c F_{ny} L_y}$$

With $N_c = 2$ contacts, $L_x = L\cos\alpha$ and $L_y = L\cos\alpha$, it follows therefore:

$$K_0 = \frac{\cos^2\alpha}{\sin^2\alpha}$$

On the other hand, from equation 16 the degree of structural anisotropy is:

$$F = \frac{\Phi_{xx}}{\Phi_{yy}} = \frac{n_x^2}{n_y^2} = \frac{\cos^2\alpha}{\sin^2\alpha}$$

It is clear that in this particular case K_0 and F are similarly expressed in terms of the contact orientation $K_0 = \frac{\cos^2\alpha}{\sin^2\alpha} = F$. Therefore K_0 depends only on the degree of anisotropy F, it does not depend on the contacts number, the applied loading stress and stress path (loading or unloading). It should be noted that when α tends towards zero

K_0 becomes infinite, this is the case of grains forced on the same alignment. On the other hand, when α tends towards 90° K_0 becomes zero, this corresponds to the case of a stack of bricks for example. It should be highlighted that for a granular material the average orientation of the contacts is far from these two extremums, i.e. the degree of anisotropy (F) varies around 1.

Rough grains

The friction forces are tangent to the contact, they change their directions according to the stress path (loading or unloading) (Fig. 10b. and Fig. 10c.). The force diagrams show that in the loading phase the friction force increases the vertical component and decreases the horizontal component of the contact force. The opposite happens in the unloading phase. The ratio $K_0 = \frac{\sigma_{xx}}{\sigma_{yy}}$ is then greater in the unloading phase than in the loading phase. Thus, the force anisotropy depends on the stress path.

Numerical simulations

The three grains example described above is simulated numerically. The sample is first confined with isotropic pressure of 10kPa, then subjected to an oedometric loading-unloading cycle. (Fig. 13) shows snapshots of the simulated example in the two states; the isotropic confining and the oedometric compression states.

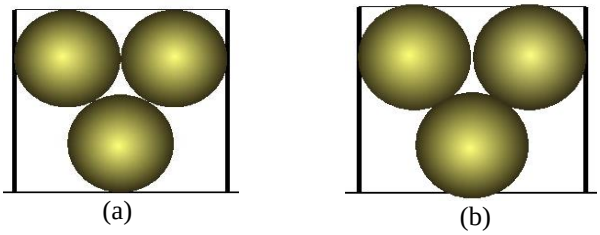

Fig. 13. The simulated example, (a) isotropic confining phase, (b) oedometric compression.

The evolution of K_0 in terms of the degree of structural anisotropy is shown in figure14 for frictionless particles (Fig. 14a.) and rough particles (figure 14b).

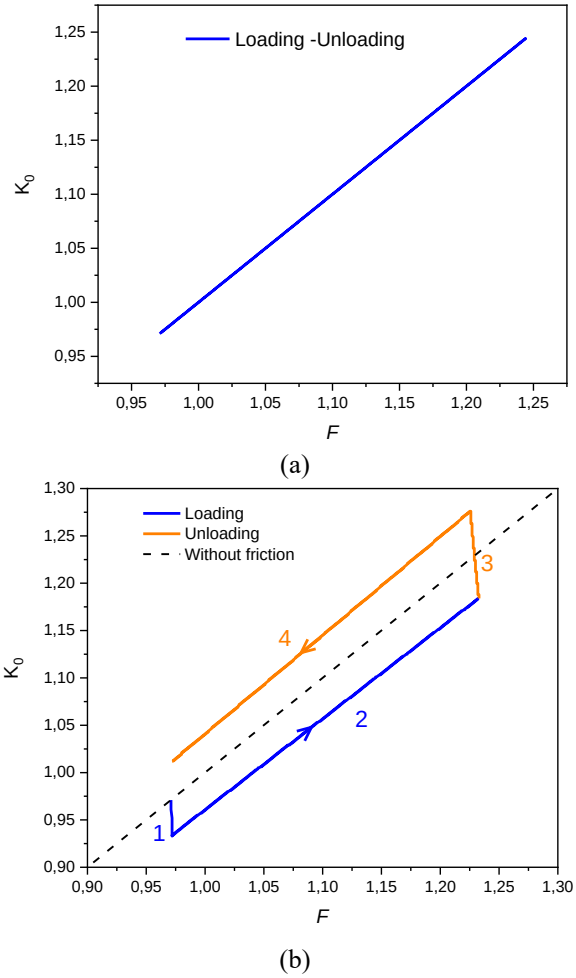

Fig. 14. The at rest lateral earth pressure coefficient vs degree of structural anisotropy, (a) frictionless grains, (b) grains with friction.

This figure shows that for frictionless grains, the at rest earth pressure coefficient is proportional to the degree of structural anisotropy either in loading or unloading paths. However, for rough grains (with friction), the variation of K_0 follows two different paths during the loading and unloading. Thus, the friction forces deviate the evolution of K_0 relative to the proportionality line corresponding to zero friction. As a result, the K_0 variation follows a loop for a loading-unloading cycle. This loop is composed of four branches as indicated in (Fig. 14b.) and described below:

(1) Loading with a frictional force below the coulomb's slip threshold; in this case, there is no sliding, the change in the contact orientation is negligible, F remains

almost constant, K_0 decreases given that the vertical stress increases while the horizontal stress undergoes little variation.

(2) Loading with a frictional force in the neighborhood of the coulomb's slip threshold; the load increasing produces an intergranular slip, F increases since that the contacts orientation tends to the horizontal. K_0 increases proportionally to F.

(3) Unloading with a frictional force less than the coulomb's sliding threshold; in this phase, the frictional force changes direction by passing through zero, the sliding is locked, the change in the contacts orientation is negligible, F remains almost constant, K_0 increases since the vertical stress decreases while the horizontal stress undergoes little variation.

(4) Unloading with a frictional force in the neighborhood of the coulomb's slip threshold; the load decreasing produces an intergranular slip, F decreases since that the contacts orientation tends to the vertical. K_0 decreases proportionally to F.

The loop shape observed in (Fig. 14b.), occurs also for the evolution of K_0 in terms of the vertical stress as shown in (Fig. 15a.). It should be noted that in this application, a low friction coefficient is selected ($\mu = 0.02$) in order to illustrate the contribution of friction forces. When the friction coefficient increases the extents of the different sliding and locking phases change. (Fig. 15b.) shows the variation of K_0 in terms of the applied vertical stress for different coefficients of friction under a loading-unloading cycle.

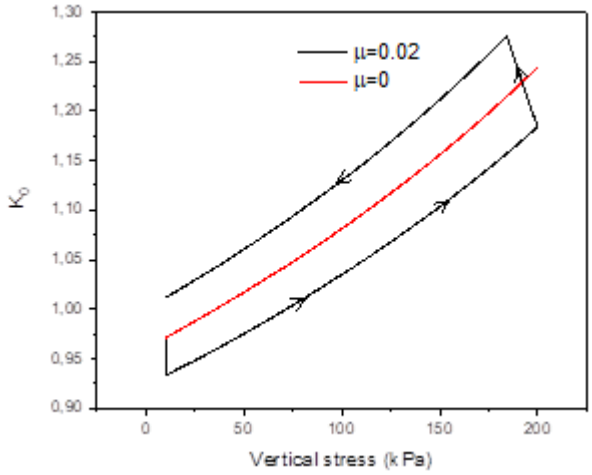

(a)

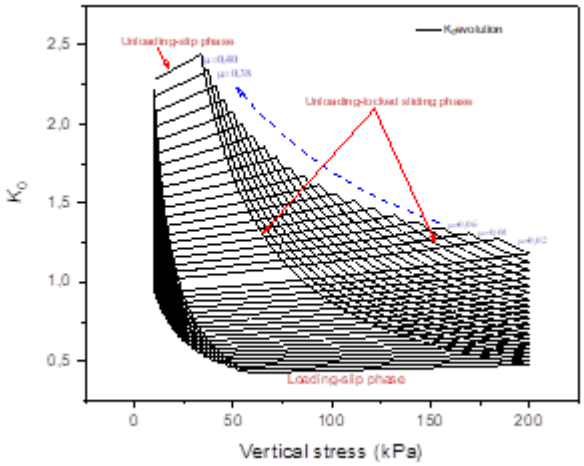

(b)

Fig. 15. K_0 evolution in terms of the applied vertical stress (a) Low friction coefficient, (b) Different friction coefficients.

(Fig. 13b.) indicate that when the friction coefficient increases, the loading sliding phase exhibits little change, the unloading locking phase becomes more significant and the unloading sliding phase decreases, consequently there is a residual slip maintained in the system after unloading. In soil mechanics this effect results in the increase of the over-consolidation ratio. It is worth noting that for practical values of the friction coefficients ($\mu \geq 0.4$), the friction forces become the most predominant parameter on the K_0 (Fig. 15b.). The loops corresponding to the high friction coefficients of figure

15b explain well the effect of stress history on K_0 in the oedometric experiment, plotted in the (Fig. 8.).

Besides, the snapshots of figure 11 show that the number of contacts being 3 initially, switches to 2 during the oedometric compression. This jump is significant for this system since one-third of the contacts number is lost, nevertheless it has no effect on the evolution of K_0. This observation should be valid for samples with a larger number of grains.

5.2 The Large Sample Oedometric Test

In this section, we analyze the results of the oedometric test number 3 carried out in section 4.5 from micromechanical point of view. The choice of this test is perceived as representing all cases of loading and cyclic loading. (Fig. 16.) shows the evolution of the fabric tensor components Φ_{xx} and Φ_{yy} in terms of the applied vertical stress during three loading-unloading cycles having the maximums of 100kPa, 200kPa and 300kPa.

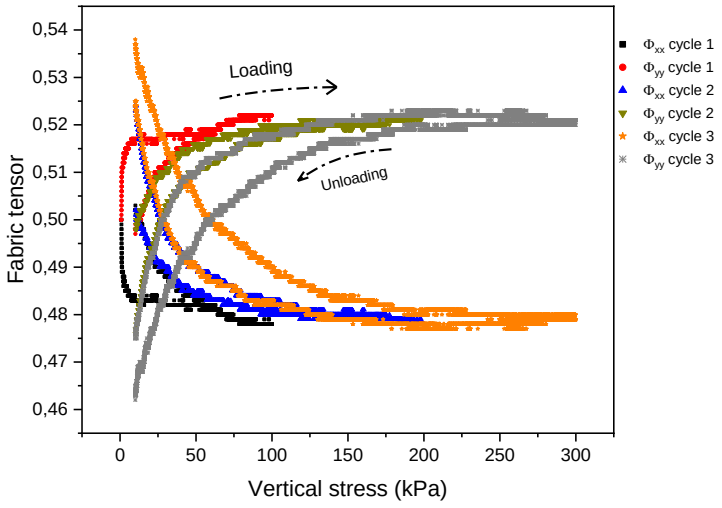

Fig. 16. Fabric tensor components vs vertical stress

Firstly, it should be mentioned that the sample is initially isotropic ($\Phi_{xx} = \Phi_{yy} = 0.5; F = 1$). It can be observed also that for all loading phases Φ_{xx} decreases and Φ_{yy} increases, the opposite occurs in the unloading phases. In addition, Φ_{xx} and Φ_{yy} follow different paths during loading and unloading phases. As seen in the basic example of section (5.1), the gap observed between the loading and unloading curves can be attributed to the intergranular locking related to Coulomb's friction. At the end of each unloading phase Φ_{xx} becomes greater than Φ_{yy}, the degree of structural anisotropy $F = \frac{\Phi_{xx}}{\Phi_{yy}}$ becomes greater than 1. In this example where the maximum load of each cycle is increasing, F increases at the end of each loading-unloading cycle, this means

that the degree of structural anisotropy increases with the rise of the over-consolidation ratio.

Besides, it is observed that during the loading phase of the first cycle Φ_{xx} decreases and Φ_{yy} increases with sharp slopes initially, indeed there are many horizontal contacts that open during the loading phase even for low loads. These contacts do not close after unloading due to intergranular friction, therefore during the subsequent loading phases the components of the fabric tensor change in a softer way.

(Fig. 17a.) and (Fig. 17b.) show the evolution of K_0 in terms of the degree of structural anisotropy. In (Fig. 17a.), only one loading cycle of maximum load 100 kPa is considered, whereas in (Fig. 17b.) three loading cycles of maximum loads 100, 200 and 300 kPa respectively are represented.

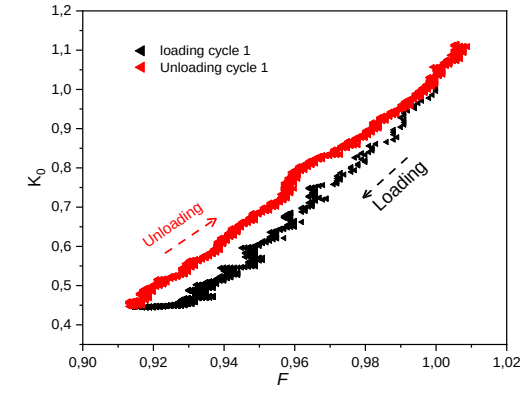

(a)

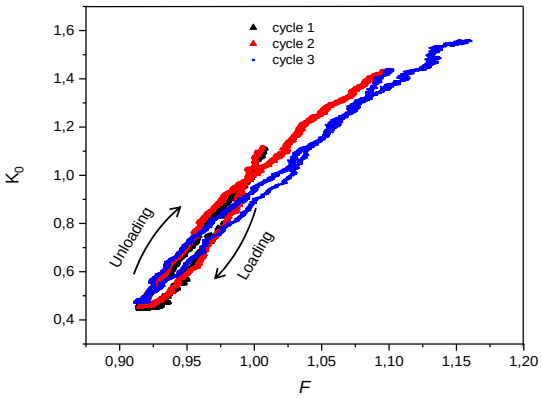

(b)

Fig. 17. K_0 vs degree of structural anisotropy, (a) one loading cycle (b) three loading cycle

Compared to the basic example in Section 5.1, in this experiment many parameters can affect K_0; including intergranular friction, rolling resistance and multiple contact orientations. Again, as shown in (Fig. 17a.), the variation of K_0 in terms of F is nearly

linear with a loop formed by the loading and unloading paths, this shape could be attributed mainly to the intergranular friction. The description of this loop cannot be detailed as for the basic example of section 5.1, given the influence of several parameters. It should be noted in this experiment, that the sliding and locking phases may exist at the same time for different contacts.

For many loading-unloading cycles (Fig. 17b.), the loop shape still presents for each cycle. the loop inclination decreases slightly with the increase of the maximum load, this decrease can be attributed to the deformability of the model's grains.

5.3 Analysis Through Contacts Orientation and Normal Contacts Forces

Rose diagrams showing in Figure 18 and figure 19 respectively represent the contact normal forces intensities and the contacts number according to their orientation for the initial state and after three cycles of loading; each diagram is divided into 18 ranges of 10°. The radial length of each range indicates the contact normal forces intensity (Fig. 19.) and the number of contacts (Fig. 18.) oriented at the angle corresponding to this range.

From (Fig. 18.) it is clear that the number of contacts does not vary significantly before loading or after the three loading cycles, which shows that the number of contacts does not have a great effect on the state of consolidation of the soil. on the other hand, and according to (Fig. 19.), the intensity of the normal contact forces initially (before loading) shows an isotropy but after three loading cycles, the normal contact forces become more horizontal than vertical which explains the increase in K_0.

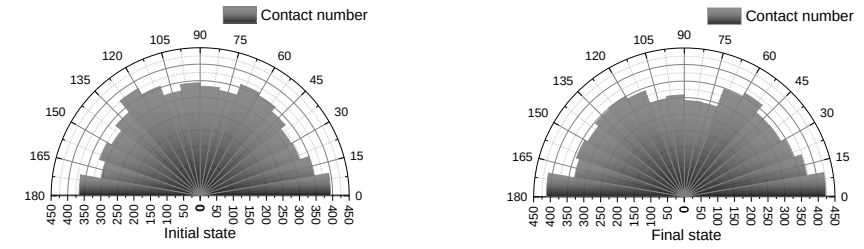

Fig .18. contacts number rose diagram.

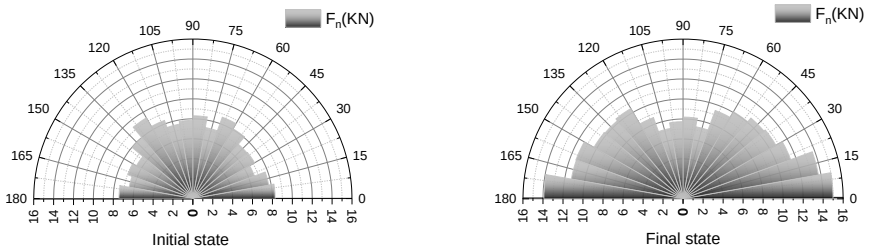

Fig. 19. Normal contact forces rose diagram.

6 Conclusion

The stress history effect on the at rest lateral earth pressure coefficient is investigated through 2D modeling of discrete element method. A dense sample of 4000 grains are subjected to different oedometric tests under K_0 conditions. The numerical results are in very good agreement with empiric formulas. from the macroscopic point of view, the results show the dependence of the at rest lateral earth pressure coefficient on the soil consolidation where the K_0 of the overconsolidated soils is greater than that of the normally consolidated soils, this effect is represented by the introduction of OCR in the empirical formulas which allowed to estimate K_0. To highlighting the effect of OCR on this coefficient three tests are selected, the first one illustrates the effect of consolidation degree on K_0, the second the shows the effect of cyclic loading on K_0 , the third one was a combination between those tests (the first and second), According to these tests we have concluded that the K_0 increases with the increase of OCR and for a normally consolidated soil the stress history has no effect on K_0.

The micromechanical analysis caried out shows that the intergranular friction has an important effect on the fabric tensor and the at rest lateral earth pressure coefficient. Furthermore, the K_0 is less sensitive to the contacts orientation, but rather governed by the intensity of the normal forces acting on these contacts.

References

1. Jaky, J.: The coefficient of earth pressure at-rest. Journal of Society of Hungarian Architects and Engineers. 355–358 (1944).
2. Wanatowski, D., Chu, J.: K 0 of sand measured by a plane-strain apparatus. Journal of Canadian Geotechnical 44(8), 1006–1012 (2007).
3. Lee, Junhwan, Yun, T.S., Lee, D., Lee, Junghwoon,: Assessment of K0 correlation to strength for granular materials. Soils and Foundations. 4(53), 584-595 (2013).
4. Massarsch, K.R., Fellenius, B.H.: Deep Vibratory Compaction of Granular Soils, in: Ground Improvement Case Histories. Ground Improvement Case Histories. Elsevier, 111–135 (2015).
5. Schuhmacher, P.: Rhéologie des écoulements granulaires: variables internes et effets d'échelle (2016).
6. Lopera Perez, J.C., Kwok, C.Y., O'Sullivan, C., Huang, X., Hanley, K.J.: Numerical study of one-dimensional compression in granular materials. Géotechnique Letters.5(3), 96-103 (2015).
7. Khalili, M.H., Roux, J.-N., Pereira, J.-M., Brisard, S., Bornert, M.: Numerical study of one-dimensional compression of granular materials. I. Stress-strain behavior, microstructure, and irreversibility. Physical Review E. 3(95), 032907 (2017).
8. Gu, X., Hu, J., Huang, M., Yang, J.: Discrete Element Analysis of the K 0 of Granular Soil and Its Relation to Small Strain Shear Stiffness. International Journal of Geomechanics. 3(18), 06018003 (2018).
9. Wroth, C. P.: General theories of earth pressure and deformation. Proc., 5th European Conferqnce on Soil Mechanics and Foundation Engineering, pp. 33-52. Madrid, Spain (1973).
10. Mayerhof, G.G.: bearing capacity and settlemtn of pile foundations. Journal of Geotechnical and Geoenvironmental Engineering 102 (1976).

11. Mayne, P., Kulhawy, F.: K0–OCR relationships in soil. Journal of the Geotechnical Engineering Division 108, 851–872 (1982).
12. Zeng, X., Ni, B.: Stress-Induced Anisotropic Gmax of Sands and Its Measurement. Journal of Geotechnical and Geoenvironmental Engineering 125(9), 741–749 (1999).
13. Hanna, A., Al-Romhein, R.: At-Rest Earth Pressure of Overconsolidated Cohesionless Soil. Journal of Geotechnical and Geoenvironmental Engineering. 5(134), 408–412 (2008).
14. Mesri, G., Hayat, T.M.: The coefficient of earth pressure at rest. Journal of Canadian Geotechnical 30(4), 647–666 (1993).
15. Cundall P.A., Strack O.D.L.: A discrete numerical model for granular assemblies. Géotechnique. 29(1), 47-65 (1979).
16. Pöschel, T., Schwager, T.: Computational Granular Dynamics: Models and Algorithms. Springer Science & Business Media (2005).
17. Mansouri, M., El Youssoufi, M.S., Nicot, F.: Numerical simulation of the quicksand phenomenon by a 3D coupled Discrete Element - Lattice Boltzmann hydromechanical model. International Journal for Numerical and Analytical Methods in Geomechanics.41(3), 338-358 (2016).
18. Zhu, H.P., Zhou, Z.Y., Yang, R.Y., Yu, A.B.: Discrete particle simulation of particulate systems: Theoretical developments. Chemical Engineering Science 62(13), 3378-3396 (2007).
19. Mokhtari, M., Shariatmadari, N., Heshmati R, A.A, Salehzadeh, H.: Design and fabrication of a large-scale oedometer. Journal of Central South University 22(3), 931–936 (2015).
20. Voivret, C., Radjaï, F., Delenne, J.-Y., El Youssoufi, M.S.: Space-filling properties of polydisperse granular media. Physical Review E 76(2), 021301 (2007).
21. Scholtes, L., n.d.: Modélisation micromécanique des milieux granulaires partiellement saturés. (2008).
22. B.Andreotti, Y.Forterre O.Pouliquen Granular Media: Between Fluid and Solid, CNRS Edition (2011).
23. Bruno Chareyre : Modélisation du comportement d'ouvrages composites sol-géosynthétique par éléments discrets: application aux ancrages en tranchées en tête de talus. Matériaux. Université Joseph Fourier - Grenoble I, Français (2003).
24. Artigaut, M., Sufian, A., Ding, X., Shire, T., O'Sullivan, C.: Influence of stress anisotropy on stress distributions in gap-graded soils. E3S Web of Conferences 92, 14007 (2019).
25. Jouannot-Chesney, P., Jernot, J.-P., Lantuéjoul, C.: Practical determination of the coordination number in granular media. Image Analysis & Stereology. 1(25), 55-61 (2006).

Use of Recycled Aggregates from Derived Construction and Demolition Waste in the Highway Base Layer

Perihan Biçer[1][0000-0002-4966-4719] and Burak Kılıç[2][0000-0002-3729-2313]

[1] Namık Kemal University, Çorlu Faculty of Engineering, Civil Engineering Department, Tekirdağ, Türkiye, pbicer@nku.edu.tr
[2] Namık Kemal University, Çorlu Faculty of Engineering, Civil Engineering Department, Tekirdağ, Türkiye, muhburakkilic@gmail.com

Abstract. Various construction and demolition wastes are produced worldwide, but these wastes generally consist of concrete, brick, and steel materials. Since these wastes are produced in large quantities, their storage causes serious environmental and economic problems. For this reason, recycling and reusing construction and demolition wastes are very important in reducing the consumption of environmental and natural resources. Within the scope of this study, the highway base usability of waste interlocking concrete paver (ICP) and crushed brick (CB) stored as construction and demolition waste in landfill areas instead of natural aggregate (NA) was investigated. In this study, the granulometry curve of the materials according to the plant-mix base Type 1 specified in the Turkey Highway Technical Specification 2013 (THTS 2013) as the base layer was determined, and the base layer design was made to remain within these gradation limits. ICP and CB materials are to be used as a result of mixing these materials with NA in certain proportions, and for determining the mechanical properties, modified Proctor, California bearing ratio (CBR) and resilient modulus experiments were performed. It investigated whether the materials were suitable for the highway plant-mix base layer by comparing the test result with the specification limits.

Keywords: Construction and demolition waste; Plant-mix base; Waste interlocking concrete paver; Crushed brick

1 Introduction

In recent years, the need for natural aggregates in the construction sector has increased and reached significant levels, so there has been a search for materials that can be alternatives to natural aggregates. Considering the development of the construction sector, construction and demolition wastes are the main materials that will be alternatives to natural aggregates. These wastes generally comprise concrete, asphalt, brick, and various building materials in large volumes and quantities [1]. Since these materials cause environmental impacts and require large storage areas for disposal,

recycling and reusing them in the construction sector is of great importance. For this reason, materials are recycled.

For construction and demolition waste to be utilized, it must be properly extracted, collected, sorted and recycled. By carrying out these processes sustainably, construction and demolition wastes can be expected to reduce the damage to the environment and contribute to the economy.

1.1 Background of the Study

The emphasis has been on investigating the suitability of using materials obtained from construction and demolition waste recycling for road foundations and subbases [2–20]. In previous studies, laboratory studies were conducted to determine whether recycled concrete aggregate (RCA), recycled asphalt pavement (RAP) and crushed brick (CB), which are materials obtained from construction and demolition waste recycling, are generally suitable for use in road foundations and subbases. These materials were used alone or mixed in certain proportions.

Bennett et al. [2] stated that the permanent deformation properties of a mixture of 75% of the natural material used in their region and 25% RCA or a mixture of 75% of the natural material used in their region and 25% RAP captured the natural material and that these wastes would be suitable for use in highway embankments. In their study, Nataatmadja and Tan [3] used four recycled concrete aggregates (RCA) with compressive strength ranging from 15 kPa to 75 kPa. They stated that these aggregates could be used as road base and sub-base backfill material if recycled concrete aggregate can be produced following the standards. Aatheesan et al. [5] reported that crushed brick (CB), a construction and demolition waste material, can safely add up to 30% CB in crushed stone combinations for subbase applications. In their study, Disfani et al. [17] reported that the mechanical and physical properties of construction and demolition waste material containing up to 50% crushed brick improved with 3% cement comply with local highway standards. Edil [20], in his study, showed that the use of RAP and RCA could be a suitable material for highway base course construction.

When previous studies were examined, construction and demolition waste materials were used alone or mixed in different ratios. Some studies stated that it would be possible to use such wastes as foundations or subbases by comparing them with the materials used as natural aggregates in their regions, taking into account some conditions.

This study [21] investigates the suitability of waste interlocking concrete paver and Crushed brick material, stored as construction and demolition waste in landfills, for use in plant-mix foundation layer by comparing with existing natural aggregate and specification limits.

2 Material and Method

In the study [21], basalt aggregate, a volcanic rock, was used as natural aggregate (NA), and waste interlocking concrete paver (ICP) and crushed brick (CB) were used as

construction and demolition waste to investigate its use in the plant-mix foundation layer. Concrete paving stones are building elements produced by machines by mixing cement, aggregate, water and some additives in certain proportions. They are generally used on city roads and sidewalks without heavy vehicle traffic. However, cobblestones exposed to heavy traffic show deformations over time. New cobblestones are placed instead of deformed cobblestones. Waste interlocking concrete pavers are stored in waste storage areas. Since 75% of concrete paving stones are aggregate, reusing this building material is economically and environmentally important. Threshing bricks, also known as firebricks, were used as crushed bricks. Nowadays, during the demolition of old buildings with urban transformation, threshing bricks are frequently encountered. These bricks should be separated from construction and demolition waste and reused.

The natural aggregate used in the study was obtained from Karatepe quarries in the Çorlu district in the form of four sieve groups crushed stone powder (0-5 mm), crushed stone 1 (5-12 mm), crushed stone 2 (12-19 mm), crushed stone 3 (19-37.5 mm) as shown in Figure 1. In the experiments, crushed brick material and waste interlocking concrete paver were crushed and divided into four groups, like natural aggregate. The plant-mix base layer design was made according to the THTS 2013 [22] for the experimental studies. ICP, CB and mixture samples were also carried out according to this design. Figure 2 shows the granulometry curve of the designed plant-mix base layer.

Fig. 1. (a) crushed stone powder (0-5 mm), (b) crushed stone 1 (5-12 mm), (c) crushed stone 2 (12-19 mm), (d) crushed stone 3 (19-37.5 mm) [21]

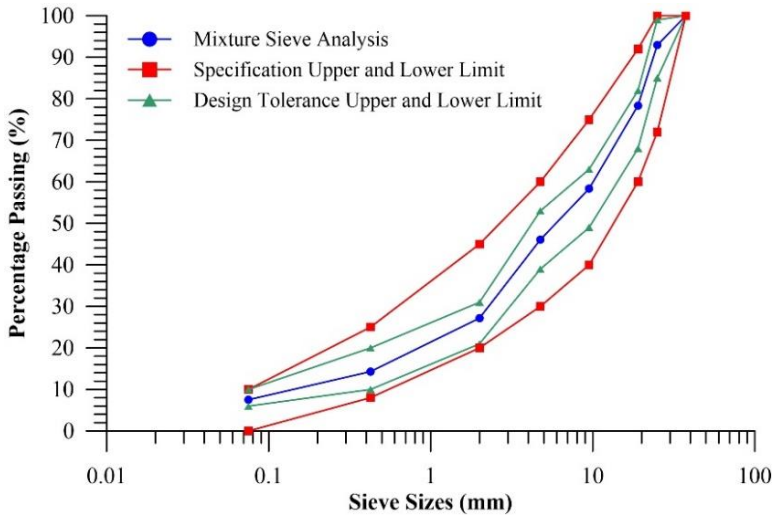

Fig. 2. Plant-mix base layer granulometry curve [21]

2.1 Experiments for Determination of Physical Properties

A series of experimental studies were carried out for NA, ICP and CB to be used in the highway plant-mix base layer. In this study, plant-mix base layer samples were formed using 100% NA, 100% CB and 100% ICP to determine the physical properties of the materials. Water absorption and specific gravity tests, Los Angeles abrasion test, flakiness index test, determination of organic matter content, determination of clay lumps and friable particles in aggregates, resistance to weathering, liquid limit and plastic limit test, methylene blue test were carried out on the samples following the Highway technical specifications.

In the study, the water absorption rates of the mixture samples obtained by mixing natural aggregate, crushed brick and waste interlocking concrete paver in certain ratios were obtained and compared with the specification limits of THTS 2013 [22] and the water absorption values obtained on recycled concrete aggregate (RCA) in the literature.

2.2 Modified Proctor Experiment and California Bearing Ratio Experiment

Following the plant-mix base type-1 gradation design specified in the THTS 2013 and shown in Figure 2, samples were prepared by adding 85%, 75%, 50%, 25%, 15% ICP and 25%, 50% CB to the NA in addition to 100% natural aggregate, 100% waste interlocking concrete paver and 100% crushed brick. Modified Proctor and California Bearing Ratio (CBR) were performed on the samples to determine the mechanical properties of the materials.

3 Results and Discussions

3.1 Physical Characteristic Test Results

The results of the tests carried out to determine the physical properties according to the highway technical specifications were analyzed. Table 1 shows the test results of ICP, CB material and NA. When the results obtained for ICP and CB are compared with those obtained from the THTS 2013 [22] and NA, it is determined that the Los Angeles value of the ICP material is slightly above the specification. The results obtained for the other tests were below the specification limit, and when compared with NA, it was determined that it showed similar performance. It was determined that the CB material did not meet the limits specified in the Highway Technical Specifications 2013 except for the organic matter content test, methylene blue test, and plastic limit test results.

Table 1. Physical characteristics of materials

Test	Material			Specification
	NA	ICP	CB	Limit [22]
Particle Density: Coarse (kN/m^3)	26.9	23.0	20.7	-
Particle Density: Fine (kN/m^3)	25.5	21.8	21.7	-
Los Angeles abrasion %	10.84	35.79	82.84	≤35
Clay lumps and friable particles, %	0.37	0,27	1.22	≤1
Organic content	Negative	Negative	Negative	Negative
Flakiness index, %	21.06	23.22	31.17	≤30
Plastic limit	NP	NP	NP	NP
Methylene blue test, g/kg	4.5	1.5	1.0	≤4.5
Freeze-thaw test, %	11.64	18.75	47.4	≤20

Table 2 shows the laboratory test results obtained for RCA in the literature. According to these test results, it is seen that the specific gravity value, Los Angeles abrasion value and strength value obtained from the weathering test for ICP material are similar to the values obtained for RCA. However, the flatness index value obtained for ICP was found to be higher than the flaxiness index values obtained for RCA in previous studies. It was observed that the specific density value of the CB material was low compared to the studies on RCA in the literature, but the values obtained from other test results were quite high.

Table 3 presents the water absorption values of NA, ICP, and CB and the samples obtained by mixing them with each other in certain ratios and the specification limits. It was determined that the water absorption value of the ICP material was above the limit value in the THTS 2013 [22]. When the mixture samples formed with NA are examined, it is seen that the water absorption value decreases when the ratio of ICP in NA decreases.

Table 2. Test results found in the literature

Reference	Material	Tests and Results			
		Particle density: course (kN/m^3)	Los Angeles abrasion (%)	Flakiness index (%)	Freeze-thaw test (%)
Edil [20]	RCA	22.0-24.00	-	-	-
Arulrajah et al.[16]	RCA	27.1	28.0	-	-
Mohammadina et al.[18]	RCA	26.9	30.8	16.44	-
Cai et al. [23]	RCA	26.06	37.0	-	-
Gabr and Cameron[12]	RCA	26.0-25.5	39.0-37.0	-	19.7
Jimenez et al. [13]	RCA	-	34.0	8.0	-
Haider et al. [24]	RCA	-	-	-	14.3-15.7
Kumar [25]	RCA	-	30.2-33.8	-	16.17
This study [21]	ICP	23.0	35.79	23.22	18.75
This study [21]	CB	20.7	82.84	31.17	47.4

Table 3. Water absorption test results

Material	Absorption (%)	Specification Limit [22]
%100 NA	1.1	≤3
%100 ICP	6.52	≤3
%100 CB	16.98	≤3
%85 DA+%15 ICP	2.58	≤3
%75 DA+%25 ICP	3.04	≤3
%50 DA+%50 ICP	4.11	≤3
%25 DA+%75 ICP	4.75	≤3
%15 DA+%85 ICP	5.34	≤3
%75 DA+%25 CB	4.15	≤3
%50 DA+%50 CB	7.97	≤3
%75 ICP+%25 CB	8.62	≤3
%50 ICP+%50 CB	10.78	≤3
%50 DA+%25 ICP+ %25 CB	4.81	≤3

The water absorption percentage of CB material is above the 3% limit value specified in the Highway Technical Specifications 2013 [22]. CB material also has a higher water absorption percentage than NA. This can be explained by the porous structure of CB material. In addition to these materials, the water absorption percentages obtained from the test performed on the specimens obtained by adding CB at certain ratios to NA were lower than the 100% CB specimen but did not meet the specification limit.

In previous studies, there is a similarity between the water absorption values obtained for RCA material and those obtained for ICP material. Table 4 shows the water absorption laboratory test results obtained for RCA and CB in the literature. When the literature is examined, the variability observed in the water absorption values of CB material is due to the difference in the types of crushed bricks used. Because the

contents of the bricks vary according to different regions, for this reason, if CB material is to be used in the foundation/sub-base layer, the water absorption value should be determined very well.

Table 4. This study and experimental results found in the literature

Reference	Material	Water absorption (%)
Edil [20]	RCA	5.5-6.9
Bozyurt et al. [26]	RCA	5-6.5
Arulrajah et al. [17]	RCA	4.7-9.8
Jayakody et al. [13]	RCA	6.5
Tahmoorian and Samali [27]	RCA	6.3
Tahmoorian and Samali [27]	%25 RCA+%75 NA	2.94
Tahmoorian and Samali [27]	%50 RCA+%50 NA	3.71
Tahmoorian and Samali [27]	%75 RCA+%25 NA	4.62
Mohammadinia et al. [18]	CB	7.02
Arulrajah et al. [6]	CB	6.15-6.87
Zhang et al. [28]	CB	14.61-19.2
Debieb and Kenai [29]	CB	11.5-14.0
This study [21]	ICP	6.52
This study [21]	CB	16.98

3.2 Modified Proctor and California Bearing Ratio Test Results

The maximum dry unit weight and optimum water content values obtained from the modified proctor test on NA, ICP and CB materials and the maximum dry unit weight and optimum water content values obtained for RCA and CB materials in the literature are shown in Table 5. In addition, in this study, when the relationship between the maximum dry unit volume weight and optimum water content obtained according to the ICP content in NA was examined, it was determined that the maximum dry unit volume weight of the samples decreased with increasing ICP content. In contrast, the optimum water content percentage increased. The study has a similarity between the values obtained for ICP and those obtained for RCA material in the literature.

When the results were analyzed, it was determined that the optimum water content value of the 100% CB sample was larger than the 100% NA sample, while the dry unit volume weight was smaller. When the mixture samples were analyzed, it was determined that the optimum water content decreased with the decrease in the CB ratio in NA. At the same time, the maximum dry unit volume weight increased. In previous studies, this situation was suggested to be the lower grain density and higher water absorption capacity of crushed brick material [4]. The optimum water content values obtained for 100% CB sample in this study were lower than those obtained for CB material in previous studies. When the literature results were analyzed, it was determined that the maximum dry unit volume weight of the CB material used in the study was lower. Only the maximum dry unit volume weight value of 75% NA + 25% CB material was close to the maximum dry unit volume weight value determined in previous studies.

Another test performed to determine the mechanical properties of the materials was the CBR test. The wet CBR values of the mixture samples obtained by adding certain ratios of ICP and CB to NA, ICP, CB and NA are given in Table 6.

Table 5. This study and experimental results found in the literature

Reference	Material	w_{opt} (%)	γ_{max} (kN/m^3)
Poon and Chan [4]	RCA	11.8	19.81
Bozyurt et al. [26]	RCA	8.7-11.9	18.9-20.8
Soleimanbeigi and Edil [30]	RCA	8	19.20
Jayakody et al. [31]	RCA	9.4	17.30
Edil [20]	RCA	8.7-11.8	19.4-20.9
Gabr and Cameron [12]	RCA	11-11.5	18.83-19.52
Arulrajah et al. [16]	RCA	12	19.22
Coban et al [32]	RCA	9.5-11.1	19.1-20.2
Arulrajah et al. [6]	CB	10.7	19.81
Mohammadinia et al. [18]	CB	11.38	19.52
This study [21]	NA	4.86	22.50
	ICP	8.79	18.64
	CB	9.9	16.64
	%85NA+%15ICP	5.36	21.48
	%75NA+%25ICP	5.55	20.99
	%50NA+%50ICP	7.65	20.32
	%25NA+%75ICP	8.42	19.25
	%15NA+%85ICP	8.73	19.13
	%50NA+%50CB	9.38	18.98
	%75NA+%25CB	8.45	21.12
	%50ICP+%50CB	9.16	17.34
	%75ICP+%25CB	10.21	17.36

w_{opt}, optimum water content γ_{max}, maximum dry unit volume weight

When the CBR values were analyzed, it was seen that ICP material has a higher CBR value than NA. In addition, the CBR values of the samples formed by adding ICP into NA are higher than NA. When the CBR test results on CB material were analyzed, it was determined that the 100% CB sample had a CBR value lower than the 120% CBR value specified for the plant-mix base layer in the Highway Technical Specifications 2013 [22]. However, the CBR values of the samples formed by adding 50% and 25% CB to NA are above the specification limit.

Table 6. CBR test results of NA, ICP, CB and mixtures

Material	CBR (%)	Specification Limit [22]
%100 NA	164	≥%120
%100 ICP	207	
%100 CB	88	
%85 NA+%15 ICP	175	
%75 NA+%25 ICP	218	
%50 NA+%50 ICP	275	
%25 NA+%75 ICP	199	
%15 NA+%85 ICP	252	
%50 NA+%50 CB	131	
%75 NA+%25 CB	200	
%50 ICP+%50 CB	197	
%75 ICP+%25 CB	192	

4 Conclusions

This study investigated the usability of waste interlocking concrete paver and crushed brick material, which are stored as construction and demolition waste, as an alternative material to natural aggregate (NA) in plant-mix base course. When the results of the experiments carried out on waste interlocking concrete paver material are analyzed, the mixtures formed by adding waste interlocking concrete paver at certain ratios into waste interlocking concrete paver and natural aggregate meet the specification limits specified for the plant-mix base course in the THTS 2013 [22], except that the water absorption values of the mixtures formed by adding waste interlocking concrete paver at certain ratios are high. The Los Angeles abrasion values are at the full limit. If the water absorption value is to be reduced, the proportion of waste interlocking concrete paver in the natural aggregate should be reduced. The waste interlocking concrete paver material used in the study was recycled concrete aggregate used in previous studies.
(RCA), both materials have similarities and differences. RCA obtained from demolition activities is generally heterogeneous and may contain other materials. In addition, since RCA is not obtained from a single source like natural aggregate, there are differences in the strength and quality of RCA collected from different demolition sites. On the other hand, waste interlocking concrete paver material has a certain standard and strength. As a result, it was determined that foundation layers formed by mixing waste interlocking concrete paver material into natural aggregate at certain ratios could be an alternative to foundation layers formed using natural aggregate.

When the physical and mechanical properties of the crushed brick material to be used in the designed plant-mix base layer were examined, it was determined that the Crushed brick material used in the study was insufficient for the plant-mix base layer in terms of both physical and mechanical properties according to the Highway Technical Specifications 2013. However, it was determined that the plant-mix base layers to be formed from mixing the crushed brick material with natural aggregate would perform better. Nevertheless, the physical properties of the mixtures to be

formed by adding certain proportions of crushed brick material into natural aggregate should be determined and evaluated very well.

Acknowledgments
This study was supported by Tekirdağ Namik Kemal University Scientific Research Unit (Project No: NKUBAP.06.YL.19.228).

References

1. Vieira, C.S., Pereira, P.M.: Use of recycled construction and demolition materials in geotechnical applications: A review. Resources, Conservation and Recycling. 103, 192–204 (2015)
2. Bennert, T., Papp Jr, W.J., Maher, A., Gucunski, N.: Utilization of construction and demolition debris under traffic-type loading in base and subbase applications. Transportation research record. 1714, 33–39 (2000)
3. Nataatmadja, A., Tan, Y.L.: Resilient response of recycled concrete road aggregates. Journal of Transportation Engineering. 127, 450–453 (2001)
4. Poon, C.S., Chan, D.: Feasible use of recycled concrete aggregates and crushed clay brick as unbound road sub-base. Construction and building materials. 20, 578–585 (2006)
5. Aatheesan, T., Arulrajah, A., Bo, M.W., Vuong, B., Wilson, J.: Crushed brick blends with crushed rock for pavement systems. In: proceedings of the institution of civil engineers-waste and resource management. pp. 29–35. Thomas Telford Ltd (2010)
6. Arulrajah, A., Piratheepan, J., Aatheesan, T., Bo, M.W.: Geotechnical properties of recycled crushed brick in pavement applications. Journal of Materials in Civil Engineering. 23, 1444–1452 (2011)
7. da Conceição Leite, F., dos Santos Motta, R., Vasconcelos, K.L., Bernucci, L.: Laboratory evaluation of recycled construction and demolition waste for pavements. Construction and building materials. 25, 2972–2979 (2011)
8. Arulrajah, A., Piratheepan, J., Ali, M., Bo, M.: Geotechnical properties of recycled concrete aggregate in pavement sub-base applications. Geotechnical Testing Journal. 35, 743–751 (2012)
9. Arulrajah, A., Piratheepan, J., Bo, M.W., Sivakugan, N.: Geotechnical characteristics of recycled crushed brick blends for pavement sub-base applications. Canadian Geotechnical Journal. 49, 796–811 (2012)
10. Arulrajah, A., Ali, M.M.Y., Piratheepan, J., Bo, M.W.: Geotechnical properties of waste excavation rock in pavement subbase applications. Journal of materials in civil engineering. 24, 924–932 (2012)
11. Cerni, G., Cardone, F., Bocci, M.: Permanent deformation behaviour of unbound recycled mixtures. Construction and Building Materials. 37, 573–580 (2012)
12. Gabr, A.R., Cameron, D.A.: Properties of recycled concrete aggregate for unbound pavement construction. Journal of Materials in Civil Engineering. 24, 754–764 (2012)
13. Jimenez, J.R., Ayuso, J., Agrela, F., López, M., Galvín, A.P.: Utilisation of unbound recycled aggregates from selected CDW in unpaved rural roads. Resources, Conservation and Recycling. 58, 88–97 (2012)
14. Arulrajah, A., Piratheepan, J., Disfani, M.M., Bo, M.W.: Geotechnical and geoenvironmental properties of recycled construction and demolition materials in pavement subbase applications. Journal of Materials in Civil Engineering. 25, 1077–1088 (2013)
15. Arulrajah, A., Piratheepan, J., Disfani, M.M., Bo, M.W.: Resilient moduli response of recycled construction and demolition materials in pavement subbase applications. Journal of materials in civil engineering. 25, 1920–1928 (2013)

16. Arulrajah, A., Disfani, M.M., Horpibulsuk, S., Suksiripattanapong, C., Prongmanee, N.: Physical properties and shear strength responses of recycled construction and demolition materials in unbound pavement base/subbase applications. Construction and Building Materials. 58, 245–257 (2014)
17. Disfani, M.M., Arulrajah, A., Haghighi, H., Mohammadinia, A., Horpibulsuk, S.: Flexural beam fatigue strength evaluation of crushed brick as a supplementary material in cement stabilized recycled concrete aggregates. Construction and Building Materials. 68, 667–676 (2014)
18. Mohammadinia, A., Arulrajah, A., Sanjayan, J., Disfani, M.M., Bo, M.W., Darmawan, S.: Laboratory evaluation of the use of cement-treated construction and demolition materials in pavement base and subbase applications. Journal of materials in civil engineering. 27, 04014186 (2015)
19. Mohammadinia, A., Arulrajah, A., Horpibulsuk, S., Chinkulkijniwat, A.: Effect of fly ash on properties of crushed brick and reclaimed asphalt in pavement base/subbase applications. Journal of hazardous materials. 321, 547–556 (2017)
20. Edil, T.B.: A Review of Recycled Aggregates (RAP and RCA) as Unbound Base Course Material for Sustainable Highway Construction. Proceedings of the 4th Congrès International de Géotechnique-Ouvrages-Structures: CIGOS 2017, 26-27 October, Ho Chi Minh City, Vietnam 4. 3–14 (2018)
21. Kılıç, B.: İnşaat ve yıkıntı atıklarının plent-miks temel tabakasında kullanılabilirliğinin deneysel olarak araştırılması, (2020)
22. Karayolları Teknik Şartnamesi. Karayolları Genel Müdürlüğü, Ankara (2013)
23. Cai, X., Li, X., Wu, K., Huang, W.: Grading design of recycled aggregate cement-stabilized gravel based on rotary compaction. Journal of Highway and Transportation Research and Development (English Edition). 12, 1–6 (2018)
24. Haider, I., Cetin, B., Kaya, Z., Hatipoglu, M., Cetin, A., Ahmet, H.A.: Evaluation of the mechanical performance of recycled concrete aggregates used in highway base layers. In: Geo-Congress 2014: Geo-characterization and Modeling for Sustainability. pp. 3686–3694 (2014)
25. Kumar, R.: Influence of recycled coarse aggregate derived from construction and demolition waste (CDW) on abrasion resistance of pavement concrete. Construction and Building Materials. 142, 248–255 (2017)
26. Bozyurt, O., Tinjum, J.M., Son, Y.-H., Edil, T.B., Benson, C.H.: Resilient modulus of recycled asphalt pavement and recycled concrete aggregate. In: GeoCongress 2012: State of the Art and Practice in Geotechnical Engineering. pp. 3901–3910 (2012)
27. Tahmoorian, F., Samali, B.: Laboratory investigations on the utilization of RCA in asphalt mixtures. International Journal of Pavement Research and Technology. 11, 627–638 (2018)
28. Zhang, J., Li, C., Ding, L., Li, J.: Performance evaluation of cement stabilized recycled mixture with recycled concrete aggregate and crushed brick. Construction and Building Materials. 296, 123596 (2021)
29. Debieb, F., Kenai, S.: The use of coarse and fine crushed bricks as aggregate in concrete. Construction and building materials. 22, 886–893 (2008)
30. Soleimanbeigi, A., Edil, T.B.: Compressibility of recycled materials for use as highway embankment fill. Journal of Geotechnical and Geoenvironmental Engineering. 141, 04015011 (2015)
31. Jayakody, S., Gallage, C., Ramanujam, J.: Effects of reclaimed asphalt materials on geotechnical characteristics of recycled concrete aggregates as a pavement material. Road Materials and Pavement Design. 20, 754–772 (2019)
32. Coban, H.S., Cetin, B., Ceylan, H., Edil, T.B., Likos, W.J.: Evaluation of Engineering Properties of Recycled Aggregates and Preliminary Performance of Recycled Aggregate Base Layers. Journal of Materials in Civil Engineering. 34, 04022053 (2022)

Multiple Regression of Compression Index with Different Soil Parameters

Yeşim Gürtuğ [0000-0001-5498-0620]

[1] Marmara University,Civil Engineering Department, Türkiye
yesim.gurtug@marmara.edu.tr

Abstract. Compressibility is an important factor in soil mechanics. The compression index from one dimensional consolidation tests can be correlated with different soil parameters obtained from the experimental tests will be useful for determining the compressibility behavior of soil in a much simplified and practical way. Therefore this study pertains the relationship between compression index and and other soil parameters such as plastic Limit (P_L), liquid Limit (L_L), initial Void Ratio (e_0), final Void Ratio (ef), percentage of clay, and percentage of silt. With nine different soil parameters the correlations are examined by multiple regression analysis. One parameter correlation, two parameter correlation and three parameter correlations are studied, analyzed and summarized in this regard.

Keywords: Compression index, Atterberg limits, Clay, Silt

1 Introduction

Soil mechanics is a crucial field of study that focuses on investigating the physical and mechanical characteristics of soil. This study aims to examine the relationships of compressibility with different soil parameters, including clay content, plastic limit, liquid limit, sand content, etc. The main aim is to determine the best combination of these parameters to achieve optimal soil mechanics performance.

Multiple regression analysis is an appropriate approach for this study as it enables the identification and quantification of relationships between different variables. By carefully analyzing the experimental data, the study aims to provide insights into the optimized combination of soil parameters that yield the most favorable soil mechanics properties. This contribution will support the development of sustainable and secure infrastructure projects.

Specifically, this study will examine the individual impacts of each soil parameter on soil mechanics, as well as their combined effects on overall performance. Soil mechanics plays a critical role in assessing factors like slope stability, foundation design, and ground settlement. Therefore, comprehending the relationships between these soil parameters is crucial for ensuring reliable and safe infrastructure designs.

2 Materials and Methods

The Atterberg limits, including the Liquid Limit (LL) and Plastic Limit (PL), are soil characteristics used to classify and understand the behavior of fine-grained soils. These limits indicate the moisture content at which the soil undergoes certain state changes. ASTM D4318

The Liquid Limit (L_L) is the moisture content at which a soil changes from a liquid-like state to a plastic state. It reflects the soil's shear strength and its ability to deform under stress. "The liquid limit (L_L) was determined by the Casagrande method as specified by BS: 1377-Part 2, 1990. The liquid limit tests were carried out to obtain a minimum of five points for plotting the curve, the test was conducted on soil samples passing 425μm."

Compressibility, on the other hand, measures how a soil's volume changes under load or pressure. It is determined by parameters like the compression index and coefficient of consolidation, describing the soil's consolidation behavior. These parameters are determined by conducting one dimensional consolidation test. ASTM D 2435.

Multiple regression analysis provides valuable insights into the key factors influencing soil mechanics properties and contributes to the development of predictive models. Engineers and architects can utilize these models to estimate soil performance more accurately and design infrastructure projects accordingly. This promotes the creation of reliable, safe, and sustainable constructions that account for the complexities of soil mechanics properties.

The correlation coefficient denoted as "R" ranges from -1 to +1. A positive value of r indicates a positive correlation, where both variables tend to increase together. A negative value indicates a negative correlation, where one variable tends to increase as the other decreases. A value of zero means there is no linear relationship between the variables. The magnitude of the correlation coefficient indicates the strength of the relationship. Values closer to -1 or +1 represent a stronger correlation, while values closer to zero represent a weaker correlation. A correlation coefficient of +1 or -1 represents a perfect linear relationship where all data points fall on a straight line.

"Hypothesis test for Pearson's population correlation coefficient, R, square root of coefficient of determination, was carried out to determine whether to accept or to reject the null hypothesis, which implies that there is no correlation of plastic limit between standard method and method (a). The test statistic, Calc t, is estimated from the sample and then compared with the standard tabulated test statistic, Tab t. If $|\text{Calc t}| > \text{Tabt t}$, the null hypothesis is rejected and vice versa. The Calc t value can be estimated using the following expression:"

$$Calc\ t = R\sqrt{\frac{N-2}{1-R^2}}$$

In this study 134 collected data form the literature are used. 92 of them are obtained from the Akuyuli [1] and 18 of them from the Vinod et al. [2] and 24 data from Widado [3].The detailed analysis is done by using these datas.

3 Results

Figure 1 and 2 shows the relationship with compression index and the Liquid Limit and plastic limit of Akuyuli paper from 92 data and Figure 3 shows the correlation from Vinod data for 18 data.

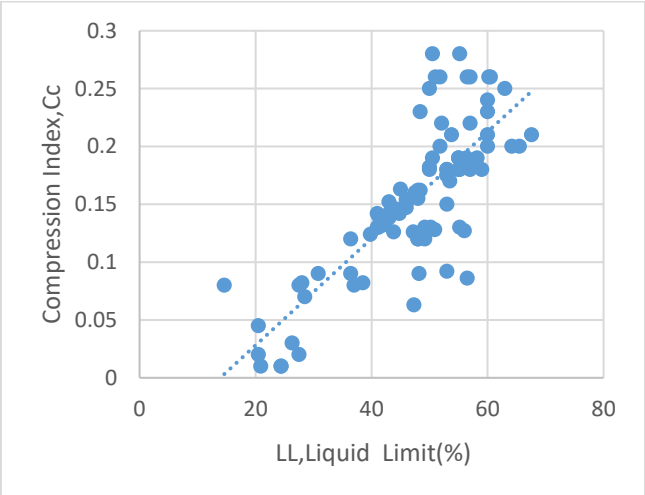

Fig. 1. Relationship between Cc and LL (Akuyuli,2013)

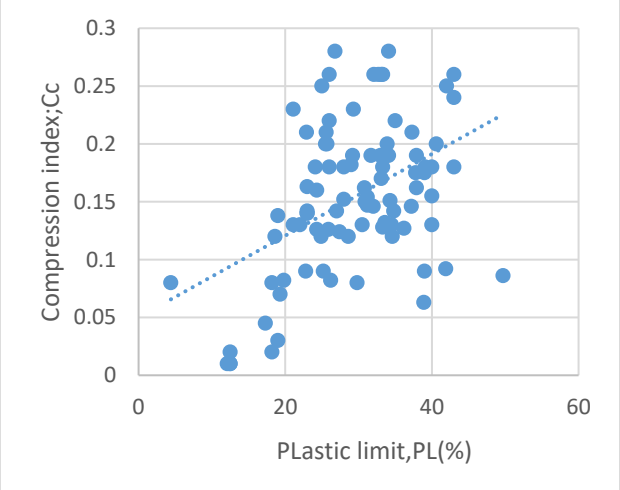

Fig. 2. Relationship between Cc and PL (Akuyuli,2013)

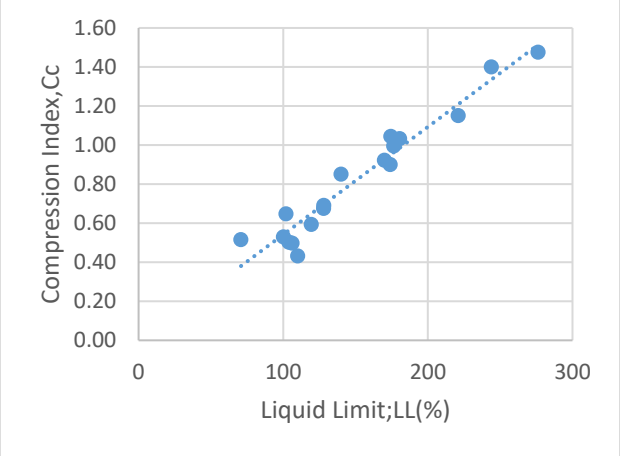

Fig. 3. Relationship between Cc and LL (Vinod, 2010)

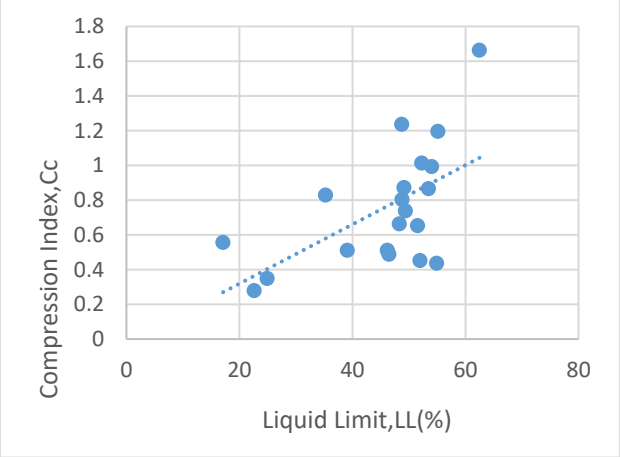

Fig. 4. Relationship between Cc and PL (Widodo,2012)

Regression example of: Cc-LL-Clay

Table 1. Descriptive Statistics

	Mean	Std. Deviation	N
cc	,1535	,06516	90
LL	47,1858	11,20753	90
CLAY	17,9733	13,03383	90

		cc	LL	CLAY
Pearson Correlation	cc	1,000	,793	-,128
	LL	,793	1,000	-,090
	CLAY	-,128	-,090	1,000
Sig. (1-tailed)	cc	.	,000	,115
	LL	,000	.	,199
	CLAY	,115	,199	.
N	cc	90	90	90
	LL	90	90	90
	CLAY	90	90	90

Table 2. Variables Entered/Removed[a]

Model	VariablesEntered	Variables Removed	Method
1	CLAY, LL[b]		Enter

a. Dependent Variable: cc

b. All requested variables entered.

Table 3. Model Summary[b]

Model	R	R Square	Adjusted R Square	Std. Error ofthe Estimate
1	,795[a]	,633	,624	,03995

a. Predictors: (Constant), CLAY, LL

b. Dependent Variable: cc

Table 4. ANOVA[a]

Model		Sum of Squares	df	Mean Square	F	Sig.
1	Regression	,239	2	,120	74,900	,000[b]
	Residual	,139	87	,002		
	Total	,378	89			

a. Dependent Variable: cc

b. Predictors: (Constant), CLAY, LL

Table 5. Coefficients[a]

Model	Unstandardized Coefficients		Standardized Coefficients	t	Sig.
	B	Std. Error	Beta		
1(Constant)	-,058	,020		-2,914	,005
LL	,005	,000	,788	12,081	,000
CLAY	,000	,000	-,057	-,867	,388

Table 6. Coefficients[a]

	95,0% Confidence Interval for B		Correlations			Collinearity Statistics
Model	Lower Bound	Upper Bound	Zero-order	Partial	Part	Tolerance
1 (Constant)	-,097	-,018				
LL	,004	,005	,793	,792	,785	,992
CLAY	-,001	,000	-,128	-,093	-,056	,992

Table 7. Coefficients[a]

Model		Collinearity ...
		VIF
1	(Constant)	
	LL	1,008
	CLAY	1,008

a. Dependent Variable: cc

Table 8. Collinearity Diagnostics[a]

Model	Dimension	Eigenvalue	ConditionIndex	Variance Proportions (Constant)	LL	CLAY
1	1	2,711	1,000	,01	,01	,04
	2	,264	3,203	,02	,04	,89
	3	,025	10,407	,98	,95	,07

a. Dependent Variable: cc

Table 9. Residuals Statistics[a]

	Minimum	Maximum	Mean	Std. Deviation	N
Predicted Value	,0070	,2471	,1535	,05183	90
Std. Predicted Value	-2,827	1,805	,000	1,000	90
Standard Error ofPredicted Value	,004	,015	,007	,002	90
Adjusted Predicted Value	-,0028	,2490	,1535	,05191	90
Residual	-,11247	,11073	,00000	,03950	90
Std. Residual	-2,815	2,772	,000	,989	90
Stud. Residual	-2,847	2,789	,000	1,005	90
Deleted Residual	-,11501	,11211	,00002	,04081	90
Stud. Deleted Residual	-2,972	2,906	,001	1,022	90
Mahal. Distance	,055	11,094	1,978	2,025	90
Cook's Distance	,000	,169	,011	,023	90
Centered Leverage Value	,001	,125	,022	,023	90

a. Dependent Variable: cc

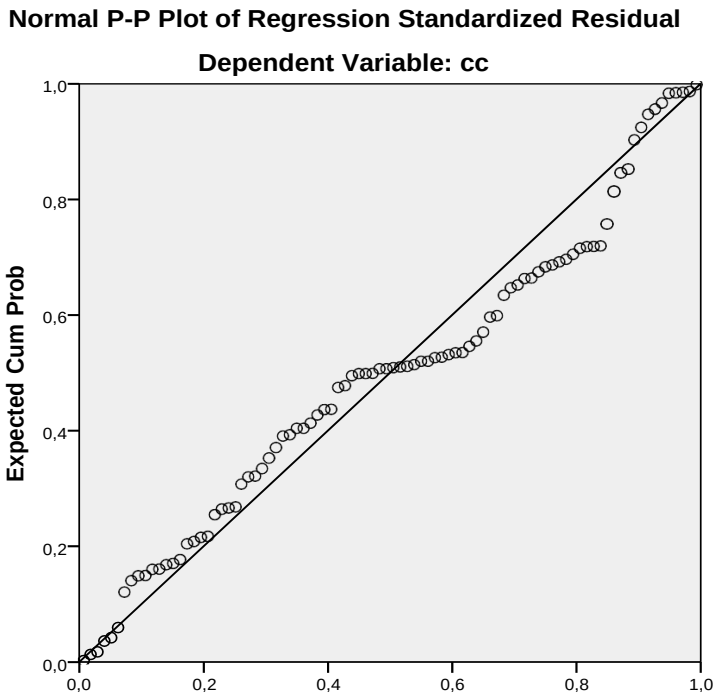

Fig. 5. Normal P-P plot of regression standardized residual dependent variale: cc

4 Conclusion

Parameters	Number of Parameter	R^2
Cc-LL-PL	2	0,66
Cc-LL-PL-Clay	3	0,659
Cc-LL-ef	2	0,632
Cc-LL-Clay	2	0,624
Cc-LL-e0	2	0,622
Cc-LL-Silt	2	0,621
Cc-Clay-LL-Silt-e0	4	0,62
Cc-Clay-PL-Silt	3	0,22
Cc-PL-Clay-e0	3	0,206

The single and two parameters are mostly dependable in the study. Further analysis should be performed.

References

1. Akayuli;2013., Empirical Model for Estimating Compression Index from Physical Properties of Weathered Birimian Phyllites. European Journal of Government and Economics Vol. 18: 6136 - 6144
2. Vinod et al; 2010., Compression index of Highly plastic Clays, Indian Geotechnical Jornal 40(3), 174-180
3. Widado et al; 2012, Estimation of Primary Compression index using physical properties of Pontenak soft clay, International Journal of Research and Application Vol.2 Issue 5 2232-2236

HYDRAULICS

pages: 406 – 525

Trends of Standard Duration Maximum Precipitation Over the Last 30 Years in Kastamonu Province, Northern Turkey

Fatma Akçay[1[0000-0001-8129-3009]], Betül Mete[2[0000-0002-3689-6430]], Murat Kankal[1[0000-0003-0897-4742]] and Adem Bayram[2[0000-0003-4359-9183]]

[1] Bursa Uludag University, Engineering Faculty, Civil Engineering Department, Bursa, Türkiye,
fatmaakcay93@gmail.com
mkankal@uludag.edu.tr
[2] Karadeniz Technical University, Engineering Faculty, Civil Engineering Department, Trabzon, Türkiye,
betulmeteofis@gmail.com
adembayram@gmail.com

Abstract. It is well-known that precipitation events may intensify due to climate change, potentially affecting maximum precipitation values, essential for hydrological design and water resources management applications. For this reason, it is important to determine the changes in the maximum precipitation series. Trend analyses were conducted using the Mann-Kendall (MK), innovative trend analysis (ITA), and improved visualization of innovative trend analysis (IV-ITA) methods to detect changes in maximum precipitation series from five meteorological observation stations operated in Kastamonu Province, northern Turkey, namely: İnebolu, Bozkurt, Devrekani, Kastamonu, and Tosya, being vulnerable to floods. The data cover a period from 1989 to 2020, including 14 standard durations from 5 min to 24 hrs. Considering the MK test results, no significant trend mainly was found. On the other hand, according to innovative methods, increasing/decreasing trends were revealed, with a majority of increases. The station operated in Bozkurt district, which has been very sensitive to floods, showed increasing trends in short durations of precipitation and decreasing trends in medium and long durations of precipitation.

Keywords: Climate change, Innovative trend analysis, Kastamonu Province, Maximum precipitation

1 Introduction

It is known that precipitation is one of the parameters most affected by climate change. According to the Sixth Assessment Report of the Intergovernmental Panel on Climate Change (IPCC), it is estimated that each 1 °C increase in temperature in regions under global climate change will increase extreme precipitation events by 7% [1]. It is also known that the frequency and intensity of extreme precipitation events have increased since the 1950s [2]. This situation brings along drought and flood events. According to this information, knowing the changes in hydrometeorological parameters due to

climate change in water resources management and adaptation studies is extremely important. Trend analysis approaches are frequently used to detect changes in hydrometeorological parameters.

In recent years, innovative approaches have come to the fore in trend analysis [3-7]. The most important feature of these approaches is that they do not contain any assumption [3]. The innovative trend analysis (ITA) method proposed by Sen [3] forms the basis of graphical methods. In this method, data can be divided into low, medium, and high groups, and the trend of each group can be analysed [3-4]. Improved visualization of ITA (IV-ITA), one of the most recent innovative approaches, is a new graphical version of the classical ITA method. This method classifies the subclasses determined as low and high with the Pettitt change point test [7]. With this method, the trends and percentage changes of subcategories can also be calculated.

Maximum precipitation data are widely used to estimate the water stage and maximum discharge at a certain cross-section in hydraulic structures. Therefore, analyzing maximum precipitation is essential for planning, designing, managing, and risk analysis of hydraulic structures [8]. Approaches such as trend analysis are suitable for monitoring long-duration changes in a time series and examining structural changes. In many studies, trend analyses of maximum precipitation have been performed [9-13]. There have been various studies investigating the trend of maximum precipitation heights in Turkey [14-16]. Aksu [8] investigated the spatial and temporal characteristics of maximum precipitation data from 21 meteorological observation stations (MOSs) operated in the Black Sea Region for 14 standard periods ranging from 5 min to 24 hrs. As a result of the trend analyses with the MK test, it was observed that the maximum precipitation heights generally tend to increase in the region.

The Black Sea Region, northern Turkey, is known to be vulnerable to the floods due to its topography, proximity to the Black Sea, and synoptic weather [8]. Kastamonu Province, considered as the study area, is located in the Western Black Sea Region of Turkey. Thirty-seven flood events took place between 1963-2016 in the province [17]. Bozkurt district of Kastamonu Province was the most affected part in the floods after heavy rains on 10-12 August 2021. In these floods, 82 people lost their lives. In addition, the floods damaged shelter areas, transport networks, energy facilities, and access to drinking water in the region. Between 10-12 August, total cumulative precipitations were measured and recorded as 452.5, 389.2, 386.2, and 281.1 mm in Bozkurt Mamatlar Village, Devrekani Kuzköy, Küre, and Abana settlements, repectively, in the province [18].

This study aimed to determine the variations in the past years by applying trend analyses to the annual maximum precipitation height series from five MOSs operated in Kastamonu Province for 14 standard durations ranging from 5 min to 24 hrs. The trend analyses were carried out using the Mann-Kendall (MK) test as a traditional method and the ITA and IV-ITA methods as innovative approaches. The data cover a period between 1989-2020. The change in the high values of these series was revealed by applying the IV-ITA method to the maximum precipitation series. In this way, it was possible to examine in detail the high values of maximum precipitation that pose a flood ris

2 Material and Method

2.1 Study Area and Precipitation Data

Kastamonu Province, the Western Black Sea Region of Turkey, is located between 41° 21' north latitude and 33° 46' east longitude. Its surface area is 13,108 km^2. The province has a generally mountainous terrain and no large plains. It has a coastline of approximately 170 km on the southern Black Sea. According to Thornthwaite climate classification, Kastamonu Province has semi-arid and less humid regions [19]. According to the precipitation records by Turkish State Meteorological Service (TSMS), the average annual precipitation in the province was 483.8 mm between 1930 and 2022 [20]. This study considered maximum precipitation data from five MOSs operated in Kastamonu Province at various standard durations (5, 10, 15, and 30 min and 1, 2, 3, 4, 5, 6, 8, 12, 18, and 24 hrs). The data between 1989 and 2020 were obtained from TSMS. The locations and characteristics of the stations are given in Figure 1.

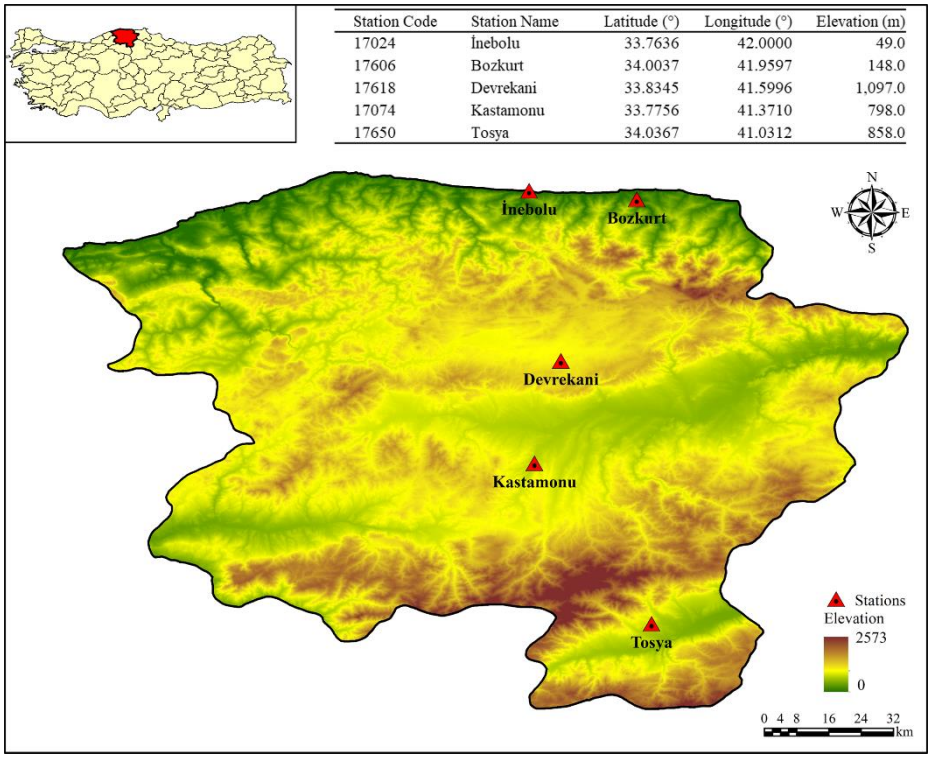

Station Code	Station Name	Latitude (°)	Longitude (°)	Elevation (m)
17024	İnebolu	33.7636	42.0000	49.0
17606	Bozkurt	34.0037	41.9597	148.0
17618	Devrekani	33.8345	41.5996	1,097.0
17074	Kastamonu	33.7756	41.3710	798.0
17650	Tosya	34.0367	41.0312	858.0

Fig. 1. The locations of meteorological observation stations, Kastamonu Province, northern Turkey.

2.2 Mann-Kendall Test

The MK test, a nonparametric test, is widely used in trend analysis studies. The test statistic S is calculated by Eqs. (1-2) [21-22]:

$$S = \sum_{i=1}^{n-1} \sum_{j=i+1}^{n} sgn(x_j - x_i) \tag{1}$$

$$sgn(x_j - x_i) = \begin{cases} 1 & ; \quad x_j > x_i \\ 0 & ; \quad x_j = x_i \\ -1 & ; \quad x_j < x_i \end{cases} \tag{2}$$

When n > 10, the variance of S is calculated by Eq. (3).

$$Var(S) = \frac{\left[n(n-1)(2n+5) - \sum_{i=1}^{p} t_i\,(t_i-1)(2t_i+5)\right]}{18} \tag{3}$$

The number of tied groups is given in Eq. (3). The number of repetitions of data with the same value is denoted by t_i. Finally, Eq. (4) is used to calculate the Z value:

$$Z = \begin{cases} \frac{S-1}{\sqrt{Var(S)}} & , \quad S > 0 \\ 0 & , \quad 0 \\ \frac{S+1}{\sqrt{Var(S)}} & , \quad S < 0 \end{cases} \tag{4}$$

If the absolute value of the calculated Z is greater than the standard z value corresponding to the specified confidence interval (90, 95, and 99%), there is a significant trend. Otherwise, there is no significant trend. The sign of the test statistic determines the direction of the trend. A negative (positive) S value means a decreasing (increasing) trend.

2.3 Innovative Trend Analysis (ITA)

The ITA is a method developed by Sen [3]. The implementation of the method is briefly as follows:

- Time series are first divided into two equal groups,
- Both half series are sorted in ascending order,
- The sorted first (second) half-series values are marked on the x-axis (y-axis),
- A line of 45° is added to the graph.

If the scattered data are in the triangular area above (below) the line of 45°, it can be said that there is an increasing (decreasing) trend. The percentage of relative error (α)

between the averages of the two half-series can be considered an important trend criterion to avoid different visual interpretations (especially for scatter very close to the line of 45°). It is calculated by Eq. (5) [23]:

$$\alpha = 100 \left| \frac{\bar{X}_1 - \bar{X}_2}{\bar{X}_2} \right| \quad (5)$$

In Eq. (5), the arithmetic mean of both half series is expressed as $\overline{X}_1$ ve $\overline{X}_2$, respectively. In practical applications, it is generally accepted that there is no significant trend in the given time series when $\alpha < \pm 5\%$ [23]. If $\overline{X}_1 < \overline{X}_2$ ($\overline{X}_1 > \overline{X}_2$) and $\alpha > 5\%$, there is an increasing (decreasing) trend.

2.4 Improved Visualization of Innovative Trend Analysis (IV-ITA)

The IV-ITA method is a new visualized version of the ITA method [7]. Like the ITA method, the data are divided into two equal groups and sorted in ascending order. The sorted data of both half series are marked on the y-axis. On the x-axis, data numbers from 1 to n/2 are marked, where n is the number of data. The differences between the two half-series are calculated sequentially and added to the graph. No trend is assumed if the difference values fall on the horizontal axis (y = 0) or are insignificantly close to the horizontal axis. Here, the horizontal axis acts as the line of 45° in the classical ITA method. Finally, the Pettitt Test [24] determines the change point using the series of difference values. The values before (after) the change point define the low (high) category. The rates of change of low (high) values are calculated as follows: the average difference values in the low (high) category are divided by the average of the first half series values in this category, and the percentage is calculated. A significant trend is considered if the calculated rates of change are greater than 5% [7].

3 Results and Discussion

3.1 Mann-Kendall (MK) Test Results

According to the MK test results (Table 1), in the analysis of maximum precipitation with standard duration mostly no trend was found. Table 1 shows the trends at a significance level of 0.05. At Bozkurt, Devrekani, and Tosya MOSs, no significant trend was observed in maximum precipitation at any standard duration. The increasing trends were observed in 4, 5, and 8 hrs precipitations at İnebolu MOS and 18 and 24 hrs at Kastamonu MOS.

Table 1. The Mann-Kendall Test Results

Durations	Stations				
	İnebolu	Bozkurt	Devrekani	Kastamonu	Tosya
5 min	−0.89	0.36	−1.14	−0.08	1.05
10 min	−0.42	1.33	0.05	0.73	1.51
15 min	−0.26	1.61	0.00	0.97	1.05
30 min	−0.05	1.09	−0.08	1.52	1.01
1 hr	0.11	0.88	0.58	1.49	1.04
2 hrs	0.81	0.26	0.45	1.38	0.75
3 hrs	1.38	0.02	0.83	1.35	0.99
4 hrs	**2.17**	−0.31	0.57	1.41	0.71
5 hrs	**2.04**	−0.28	0.39	1.36	0.62
6 hrs	1.93	0.13	0.47	1.10	0.49
8 hrs	**2.50**	−0.08	0.45	1.51	0.73
12 hrs	1.77	−0.06	−0.21	1.90	0.41
18 hrs	1.77	−0.23	0.00	**2.48**	0.39
24 hrs	1.35	−0.99	1.27	**2.76**	0.75

Bold expression means significant trend

3.2 Innovative Trend Analysis Results

Table 2 describes the trends in all standard durations of the stations according to the MK and ITA methods. As seen in Table 2, an increasing (decreasing) trend was observed at 50% (37%) of the 70 maximum precipitation series (five stations and 14 standard durations) analyzed according to the ITA method. No significant trend was observed in the nine (13%) precipitation series. Increasing trends were observed at İnebolu and Tosya MOSs for each duration. At Bozkurt station, a decreasing (increasing) trend was observed in most of the medium and long-duration (short) precipitations. At Devrekani and Kastamonu MOSs, decreasing short and medium-durations precipitation trends were noteworthy.

Table 2. Comparison of the trend tests

Stations	Mann-Kendall Test													Innovative Trend Analysis											
	Standard durations													Standard durations											
	5min	10min	15min	30min	1hr	2hrs	3hrs	4hrs	5hrs	6hrs	8hrs	12hrs	18hrs	24hrs	5min	10min	15min	30min	1hr	2hrs	3hrs	4hrs	5hrs	6hrs	8hrs	12hrs	18hrs	24hrs
İnebolu																												
Bozkurt																												
Devrekani																												
Kastamonu																												
Tosya																												

decreasing trend no trend increasing trend

When the trend analyses for the annual maximum precipitation values in Kastamonu Province are evaluated, while there was no trend considering the MK test results, the

ITA method observed a trend in most of the series (Table 2). At İnebolu station, located on the coast, there are increasing trend in three standard durations for the MK test results and while in all standard times for the ITA method. At İnebolu station, located on the coast, there are increasing trend in three standard durations for the MK test and all standard durations for the ITA method.

3.3 Improved Visualization-Innovative Trend Analysis Results

The results of the IV-ITA method for short, medium, and long-duration maximum precipitation series, are shown in Figures 2, 3, and 4, respectively. At İnebolu and Tosya (Devrekani) MOSs, the change in the low values of 5-min maximum precipitation is in the increasing (decreasing) direction by more than 30% (20%). In the 30-min precipitations, each station showed an increasing trend with a rate greater than 5%. In the high values of the short-duration maximum precipitation series, Devrekani and Kastamonu MOSs showed a decreasing trend in all durations. At high values, the increasing trend was more than 20% in precipitation with a duration of 5 min at Tosya MOS and 30 min at İnebolu MOS.

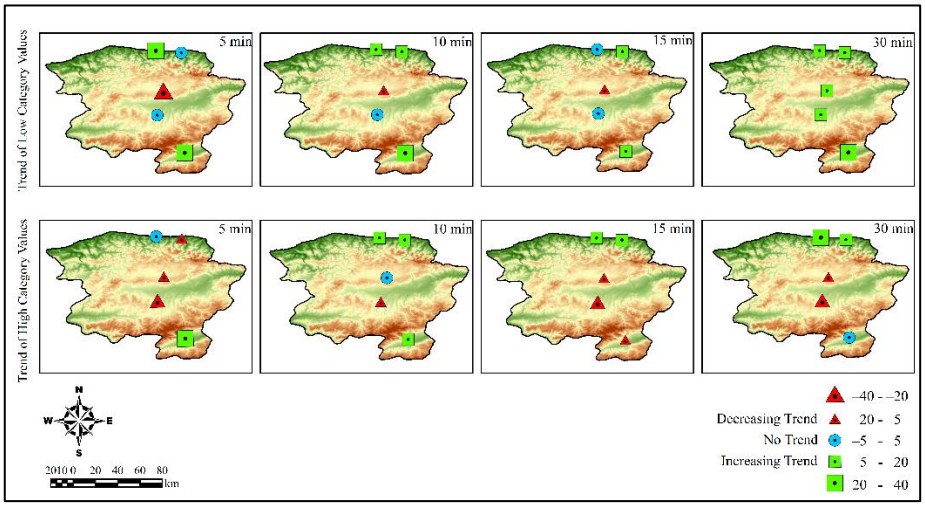

Fig. 2. The IV-ITA results for short-duration precipitations, Kastamonu Province

Figure 3 shows the trends of medium-duration maximum precipitations according to the IV-ITA method. At low values, the stations show an increasing trend in most standard durations, but the percentages of this increase are generally between 5-20%. For 1-hr maximum precipitation, the calculated increasing trend is more than 20% at Bozkurt, Devrekani, and Tosya MOSs. In addition, an increasing trend was observed with a rate of more than 20% in 2 and 3 hrs precipitations at Tosya station. While Bozkurt, Devrekani, and Kastamonu MOSs showed a decreasing trend at the high values of medium duration maximum precipitation, an increasing trend of more than 30% was observed at İnebolu station in all durations. Notably, there was an increasing trend with a rate more than 60% in 4 and 5 hrs precipitations at İnebolu station.

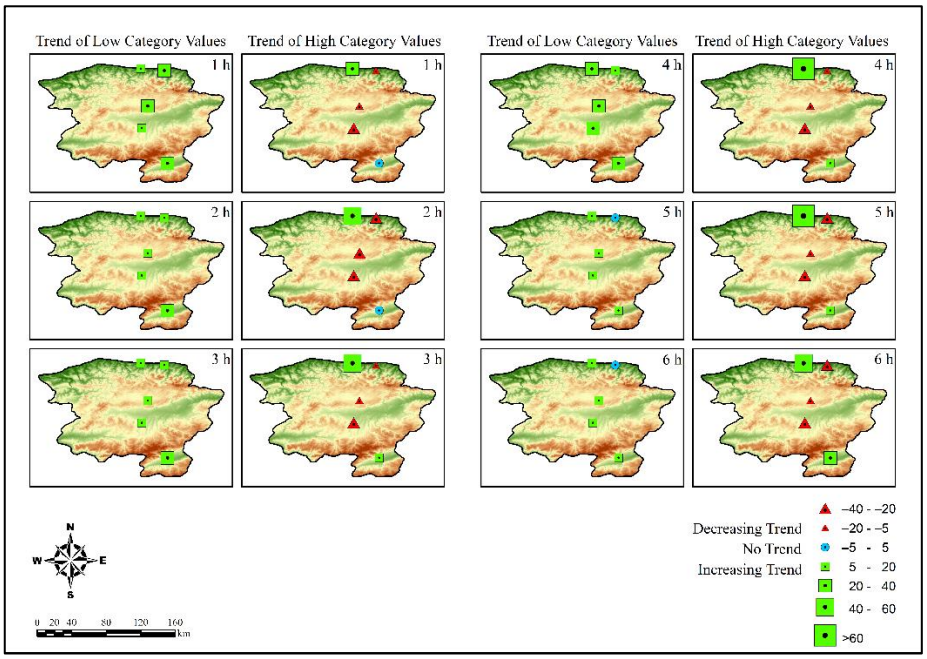

Fig. 3. The IV-ITA results for medium-duration precipitations, Kastamonu Province

The IV-ITA results for long-duration (8, 12, 18, and 24 hrs) maximum precipitation series are shown in Figure 4. Most of the stations showed an increasing trend at low values. At Kastamonu (Devrekani) station, the increasing trend in 12, 18, and 24 hrs (8, 12, and 18 hrs) precipitations was more than 20%. Increasing (decreasing) trends were observed at Inebolu and Tosya (Bozkurt, Devrekani, and Kastamonu) MOSs for most periods with high values. The increasing trend of more than 40% in 8 and 12 hrs precipitations at İnebolu Station was remarkable.

Increasing trends calculated by the ITA method also coincide with the increased percentages of the IV-ITA method at low and high values. At Bozkurt station, the decreasing trends in the medium and long-duration maximum precipitations according to the ITA method coincide with the decreasing trends in the high values of the IV-ITA method. Again, the decreasing trends in short and medium-duration precipitations at Devrekani and Kastamonu MOSs according to the ITA method were observed significantly at the high values of these stations. At Tosya station, the increasing trends observed by the ITA method in all standard durations are consistent with the increasing trends in the low and high values of the IV-ITA method. When a general evaluation is made, the trends alculated by the ITA method mostly increase for İnebolu and Tosya MOSs but decrease for Bozkurt, Devrekani, and Kastamonu MOSs. It was observed that the increasing trends calculated by ITA were largely consistent with the results obtained from the IV-ITA method for low and high values. For decreasing trends, the ITA results were more consistent with the IV-ITA results for high values.

In common with this study, İnebolu and Kastamonu MOSs were included in a study by Aksu et al. (2022) for the Black Sea Region. In their analysis with the MK test, Aksu et al. (2022) identified increasing trends in the medium and long-duration maximum precipitation series between 1959 and 2015 for the İnebolu station. On the other hand, the analysis period in this study was 1989-2020, and increasing trends were observed only in of 4, 5, and 8 hrs precipitations, according to the MK test. In the study by Aksu et al. (2022), no trend was observed in any standard period (1985-2015) for Kastamonu Province. This study observed an increasing trend in 18 and 24 hrs precipitations in Kastamonu Province.

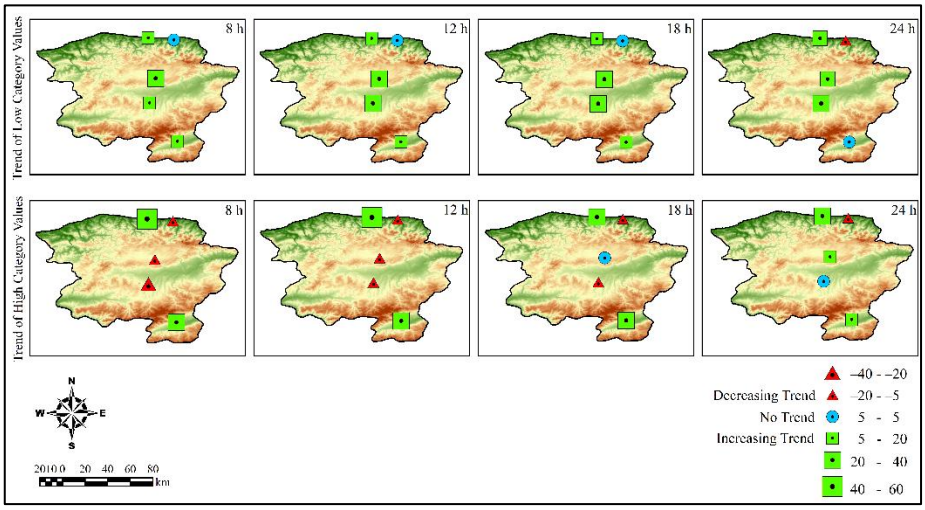

Fig.4. The IV-ITA results for long-duration precipitations, Kastamonu Province

4 Conclusion

In this study, trend analyses of annual maximum precipitation heights of Kastamonu Province were carried out by Mann-Kendall (MK), innovative trend analysis (ITA), and improved visualization-innovative trend analysis (IV-ITA) methods. The data (1989-2020) from five meteorological observation stations were used for the trend analysis. The analyses were performed for 14 standard durations from 5 min to 24 hrs. The analysis results showed that there was generally an increasing trend in the maximum precipitation heights in the province. While the MK test generally did not observed any trend, the innovative methods observed both trends, most of which were increasing. The MK test also observed a few trends observed by the ITA method.

It should be noted that İnebolu station, located on the coast of Kastamonu Province in the Western Black Sea Region sensitive to floods, shows an increasing trend in most standard periods. Again, in the Bozkurt district suffered significant damage to the floods occurred in 2021, increasing trends in short-duration precipitation and decreasing trends in medium and long-duration precipitation are noteworthy.

Acknowledgments
The authors would like to thank the General Directorate of Meteorology provided data used in this study. Also the authors would like to thank the Scientific and Technological Research Council of Turkey (TUBITAK) for 2211-A Domestic Doctoral Scholarship Program and the Council of Higher Education for 100/2000 Doctoral Scholarship Project for the scholarship provided to the first author.

References

1. IPCC, 2021: Summary for Policymakers. In: Climate Change 2021: The Physical Science Basis. Contribution of Working Group I to the Sixth Assessment Report of the Intergovernmental Panel on Climate Change [MassonDelmotte, V., Zhai, P., Pirani, A., Connors, S. L., Pean, C., Berger, S., Caud, N., Chen, Y., Goldfarb, L., Gomis, M. I., Huang, M., Leitzell, K., Lonnoy, E., Matthews, J. B. R., Maycock, T. K., Waterfield, T., Yelekçi, O., Yu, R., and Zhou, B. (eds.)]. Cambridge University Press, Cambridge, United Kingdom and New York, NY, USA, pp. 3-32.
2. Arias, P., Bellouin, N., Coppola, E., Jones, R., Krinner, G., Marotzke, J., Zickfeld, K. (2021). Climate Change 2021: The Physical Science Basis. Contribution of Working Group I to the Sixth Assessment Report of the Intergovernmental Panel on Climate Change; Technical Summary.
3. Sen, Z. (2012). Innovative trend analysis methodology. Journal of Hydrologic Engineering, 17(9), 1042-1046.
4. Sen, Z. (2014). Trend identification simulation and application. Journal of Hydrologic Engineering, 19(3), 635-642.
5. Sen, Z. (2017). Innovative trend significance test and applications. Theoretical and Applied Climatology, 127(3), 939-947.
6. Sen, Z., Sisman, E., Dabanli, I. (2019). Innovative polygon trend analysis (IPTA) and applications. Journal of Hydrology, 575, 202-210.
7. Guclu, Y. S. (2020). Improved visualization for trend analysis by comparing with classical Mann-Kendall test and ITA. Journal of Hydrology, 584, 124674.
8. Aksu, H., Cetin, M., Aksoy, H., Yaldiz, S. G., Yildirim, I., Keklik, G. (2022). Spatial and temporal characterization of standard duration-maximum precipitation over Black Sea Region in Turkey. Natural Hazards, 111(3), 2379-2405.
9. Burn, D. H., Mansour, R., Zhang, K., Whitfield, P. H. (2011). Trends and variability in extreme rainfall events in British Columbia. Canadian Water Resources Journal, 36(1), 67-82.
10. Laz, O. U., Rahman, A., Yilmaz, A., Haddad, K. (2014). Trends in sub-hourly, sub-daily and daily extreme rainfall events in eastern Australia. Journal of Water and Climate Change, 5(4), 667-6.
11. Yilmaz, A. G., Perera, B. J. C. (2015). Spatiotemporal trend analysis of extreme rainfall events in Victoria, Australia. Water Resources Management, 29(12), 4465-4480.
12. Jung, Y., Shin, J. Y., Ahn, H., Heo, J. H. (2017). The spatial and temporal structure of extreme rainfall trends in South Korea. Water, 9(10), 809.
13. Gentilucci, M., Barbieri, M., Lee, H. S., and Zardi, D. (2019). Analysis of rainfall trends and extreme precipitation in the Middle Adriatic Side, Marche Region (Central Italy). Water, 11(9), 1948.
14. Haktanir, T., Citakoglu, H. (2014). Trend, independence, stationarity, and homogeneity tests on maximum rainfall series of standard durations recorded in Turkey. Journal of Hydrologic Engineering, 19(9), 05014009.

15. Sen, K., Aksu, H. (2021). Trend analysis of observed standard duration maximum precipitation for Istanbul. Teknik Dergi, 32(1), 10495-10514.
16. Oruc, S. (2021). Visual and statistical inference of hourly and sub-hourly extreme rainfall trends Central Anatolia, Turkey case. Acta Geophysica, 69(1), 199-216.
17. Kelesoglu, M. K., Temur, R., Gulbaz, S., Memisoglu Apaydin, N., Kazezyilmaz-Alhan, C. M., Bozbey, I. (2023). Site assessment and evaluation of the structural damages after the flood disaster in the Western Black Sea Basin on August 11, 2021. Natural Hazards, 116(1), 587-618.
18. Halis, O., Gonencgil, B., Acar, Z. (2022). An atmospheric approach to the flood disaster in the Western Black Sea region (Turkey) on 10-12 August 2021. Natural Hazards and Earth System Sciences Discussions, 1-26.
19. URL-1. http://taskinyonetimi.tarimorman.gov.tr/_engine/_engine/file.axd?file=/Dokumanlar/Havzalar/bati_karadeniz/bati_karadeniz_typ.pdf (Accessed Date 18.07.2023)
20. URL-2. https://www.mgm.gov.tr/veridegerlendirme/il-ve-ilceler-istatistik.aspx?m=KASTAMONU (Accessed Date 18.07.2023)
21. Mann, H. B. (1945). Nonparametric tests against trend. Econometrica: Journal of the Econometric Society, 245-259
22. Kendall, M. G. (1975). Rank correlation methods. Griffin. London.
23. Sen, Z. (2020). Up-to-date statistical essentials in climate change and hydrology: a review. International Journal of Global Warming, 22(4), 392-431.
24. Pettitt, A. N. (1979). A non-parametric approach to the change-point problem. Journal of the Royal Statistical Society: Series C (Applied Statistics), 28(2), 126-135.

Nonstationary Modelling of Low Flow in Çoruh Basin

Muhammet Yılmaz[1][0000-0002-9844-6654] and Fatih Tosunoğlu[2][0000-0002-8423-1089]

[1] Erzurum Technical University, Civil Engineering Department, Erzurum, Türkiye, muhammet.yilmaz@erzurum.edu.tr
[2] Erzurum Technical University, Civil Engineering Department, Erzurum, Türkiye, ftosunoglu@erzurum.edu.tr

Abstract. Conventional low flow frequency analysis is based on the assumption that low flow time series are stationary. However, this assumption has been challenged in recent years due to the influences of climate variability and human activities. In this study, low flow series from 6 gauging stations in the Çoruh basin are analyzed using both stationary and nonstationary models based on the generalised additive models for location, scale and shape (GAMLSS) technique. Eleven candidate covariates (i.e., Annual, June, July, August, September precipitation and temperature data, and time) are used for the nonstationary models to obtain information on the important drivers of nonstationary in each low flow series. The results revealed that a single distribution cannot be specified as the best fit distribution for low flow series. Inverse gamma distribution (IGAMMA) for 2305, 2315 and 2329 stations, Gamma distribution (GA) for station 2316, Inverse Gaussian distribution (IG) for station 2322, and Lognormal distribution (LOGNO) for station 2325 are chosen as the most suitable. According to the results, using time as an explanatory variable in only one station (station 2316) provided more successful results. However, it was found that the use of physically based covariates in the other five stations provided more suitable models. The generalised Akaike information criterion (GAIC) values indicated that the occurrence rates of low flows are more sensitive to annual precipitation changes compared to the effect of temperature. The results of this study are important for low flow management and development in the study basin.

Keywords: Low flow; Nonstationary; Climatic variables.

1 Introduction

Streamflow is one of the most important elements of the hydrological cycle. In recent years, the effects of global warming on the environment and society have increased rapidly. A warming climate has the potential to change the hydrological cycle at global and continental scales. Observed changes in extreme weather and climate events since the 1950s, such as more heavy rainfall and prolonged drought, have increased the risks of floods and droughts [1; 2, 3]. Increasing drought events in recent years are of great concern. Therefore, more attention should be paid to understanding drought processes that will help reduce the damage caused by droughts.

Many indices have been used to describe drought in the literature. Low flow, which the minimum flow in a river during dry periods of the year, was used for monitoring of hydrological streamflow drought in this study.

Stationarity is a precondition for conventional frequency analysis of hydrological variables; this means that environmental factors such as climate and land cover create or modify the relevant hydrological variable in the same way in the past, present and future [4;5]. However, due to climate change and human interventions, the existing methodology may no longer be valid [6; 7; 8]. To overcome this problem, various approaches have been developed to perform nonstationary hydrological modelling.

In the scope of the study, stationary and non-stationary low flow data were modeled using the Generalized Additive Models in Location, Scale and Shape (GAMLSS) method [9; 10]. GAMLSS has been widely used in nonstationary models of hydrological and meteorological variables.

The aim of the present study is to investigate the main drivers of non -stationarity in low flow frequency and to evaluate their comparative suitability in the study area. The study focuses on the strongest possible combinational effects of different climatic variables on low flows. Low flow series from 6 gauging stations in the Çoruh basin are analyzed using both stationary and nonstationary models based on GAMLSS technique. Eleven candidate covariates (i.e., Annual, June, July, August, September precipitation and temperature data, and time) are used for non-stationary modelling to explore the potential causes for the non-stationarity.

2 Materials and methods

2.1 The Generalised Additive Models for Location, Scale and Shape (GAMLSS) Approach

Under a non-stationary assumption, low flow data were modelled by including explanatory covariates to explain the temporal changes in the statistical parameters for the chosen frequency distribution. The model employed the distribution-based GAMLSS approach that was developed [9] as a common coherent framework for parametric and nonparametric regression models. The GAMLSS method includes several important sub-models relating the distribution parameters to explanatory variables via an additive model or semi-parametric additive model in linear and non-linear form. Eq. (1) provides the semi-parametric additive model formulation.

$$g_k(Q_k) = X_k\beta_k + \sum_{j=1}^{m} h_{jk}(x_{jk}) \quad (1)$$

where Q_k are vectors of length n, X_k represents design matrix (i.e., a matrix of explanatory variables), β_k indicates parameter vector, and h_{jk} denotes unknown

function of explanatory variables representing the functional dependence of the distribution parameters on the explanatory variables x_{jk}.

The GAMLSS package in R software provides a wide variety of probability distributions whose parameters can be expressed as functions of explanatory variables. Eleven candidate covariates (i.e., Annual, June, July, August, September precipitation and temperature data, and time) are used for the nonstationary models The following six distributions were used in this study: (i) log-normal (LOGNO), (ii) gamma (GA), (iii) inverse Gaussian (IG), (iv) Inverse Gamma (IGAMMA), (v) Weibull (WEI), and Generalized Gamma (GG). The corresponding formulas are given in Table 1.

Table 1. Information on distributions used in the study

Code	Name	Probability Density Function
WEI	Weibull	$f_y(y\|\mu,\sigma)=\frac{\sigma y^{\sigma-1}}{\mu^{\sigma}}\ exp\left\{-\left(\frac{y}{\mu}\right)^{\sigma}\right\}$ $y>0,\mu>0,\sigma>0$
IGAMMA	Inverse Gamma	$f_y(y\|\mu,\sigma)=\frac{[\mu(\sigma+1)]^{\sigma}}{\Gamma(\sigma)}y^{-(\sigma+1)}exp\left\{\frac{\mu(\sigma+1)}{y}\right\}$ $y>0,\mu>0,\sigma>0$
LOGNO	Log-Normal	$f_y(y\|\mu,\sigma)=\frac{1}{\sqrt{2\pi\sigma^2}}\frac{1}{y}exp\left\{-\frac{[\log(y)-\mu]^2}{2\sigma^2}\right\}$ $y>0,\mu>0,\sigma>0$
GA	Gamma	$f_y(y\|\mu,\sigma)=\frac{1}{(\sigma^2\mu)^{1/\sigma^2}}\frac{y^{\frac{1}{\sigma^2}-1}e^{-y/(\sigma^2\mu)}}{\Gamma(1/\sigma^2)}$ $y>0,\mu>0,\sigma>0$
IG	Inverse Gaussian	$f_y(y\|\mu,\sigma)=\frac{1}{\sqrt{2\pi\sigma^2y^3}}exp\left\{-\frac{1}{2\mu^2\sigma^2y}(y-\mu)^2\right\}$ $y>0,\mu>0,\sigma>0$
GG	Generalized Gamma	$f_y(y\|\mu,\sigma,\nu)=\frac{\|\mu\|y^{\mu\nu-1}}{\Gamma(\nu)\sigma^{\mu\nu}}exp\{-(y/\sigma)^{\mu}\}$ $y>0,-\infty<\mu<+\infty,\sigma>0,\nu>0$

2.2 Model Selection and Evaluation

The model selection was based on the generalised Akaike information criterion [11]. The Filliben correlation coefficient was used to evaluate the selected models. The fact that the model has a Filliben coefficient greater than 0.97 indicates that it is an acceptable model [12]. In addition, the goodness of fit of the selected models was examined by visual inspection of the diagnostic plots of the residual response or worm plots.

Therefore, three models are assessed in this study: (i) is constant (stationary model, Model 0); (ii) with time (t) as the covariate and changes with t (nonstationary model,

Model 1); (iii) with climate indices as covariates and the climate indices in this study are precipitation and temperature (nonstationary model, Model 2).

3 Study Area and Data

Our study area is Çoruh basin, which is located in the northeast of Turkey. The study area covers an area of 19.748 km^2, which covers approximately 2.53% of Turkey and lying in humid climate. The total length of the Çoruh river is 431 km.

The mean annual rainfall for this basin is about 480 mm and terrain elevations in the basin, with reference to mean sea level, range from 30 to 2200 m [13]. The basin has gained more economic importance for Turkey as a number of the new water resources structures (dams and hydroelectric power plants) have been recently completed, or are already under construction. Therefore, any case study related to investigate changes in river flow is much more important now for water resources planners in the basin. The daily flow records were provided by the General Directorate of State Hydraulic Works for the period 1963–2019. Low flow data from 6 gauging stations across the Çoruh basin were used in the present study. Therefore, four hydrological stations (Fig. 1) were employed from the study area to perform the nonstationary analysis.

Within the scope of the study, temperature and precipitation data were used for annual and dry periods. For this aim, the monthly gridded precipitation and temperature data provided by the CRU TS v4.04 [14] was obtained from the official website (http:// www. cru. uea. ac. uk) and was considered as the reference dataset in this research.

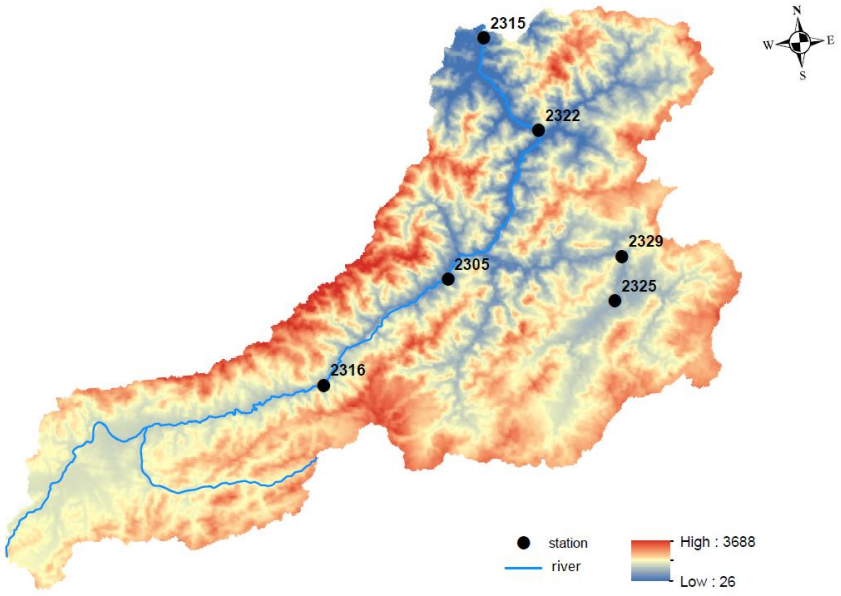

Fig. 1. Study area and spatial distribution of flow gauge stations used in the study.

4 Results

This section examines GAMLSS models for stationary and non-stationary modeling of low flow recordings of six stations. The suitability of the fitted models was evaluated using optimality criteria and diagnostic graphical tools. Hence, we compared the GAIC scores of different models: (1) stationary model 0, in which the parameters of a distribution function remain constant; (2) nonstationary model 1, in which parameter is modelled as a function of time, (3) nonstationary model 2, in which the parameter is modelled as a function of climatic variables. Table 2 lists the GAIC values and Filliben coefficients. Bold numbers indicate that the GAIC values of Model 1 or Model 2 are smaller than those of Model 0. * denote that this GAIC value is the smallest. According to the results, model 2 in 5 stations and model 1 in 1 station showed the most successful results. The stationary model (Model 0) was not successful at any station. The results showed that it is clear that low flows are not stationary in the Çoruh basin. The Filliben coefficients (Table 2) of all the models were higher than 0.97, showing acceptable performance of these models.

Table 2. Comparison of models 0, 1 and 2 for low flow series

Station	Model 0		Model 1		Model 2	
	GAIC	**Filliben**	**GAIC**	**Filliben**	**GAIC**	**Filliben**
2305	264.3	0.99	266.3	0.99	**258.6***	0.99
2315	273.2	0.97	278.11	0.98	**263.7***	0.98
2316	243.4	0.98	**230.2***	0.99	**238.9**	0.99
2322	205.2	0.98	205.6	0.99	**195.9***	0.99
2325	80.5	0.99	83.07	0.99	**67.97***	0.99
2329	135.4	0.99	138.2	0.99	**117.2***	0.99

In addition, Figure 2 shows worm plots for the most successful model. Here, the standard residuals of all the models are seen to be within the 95% confidence interval indicating good statistical performance.

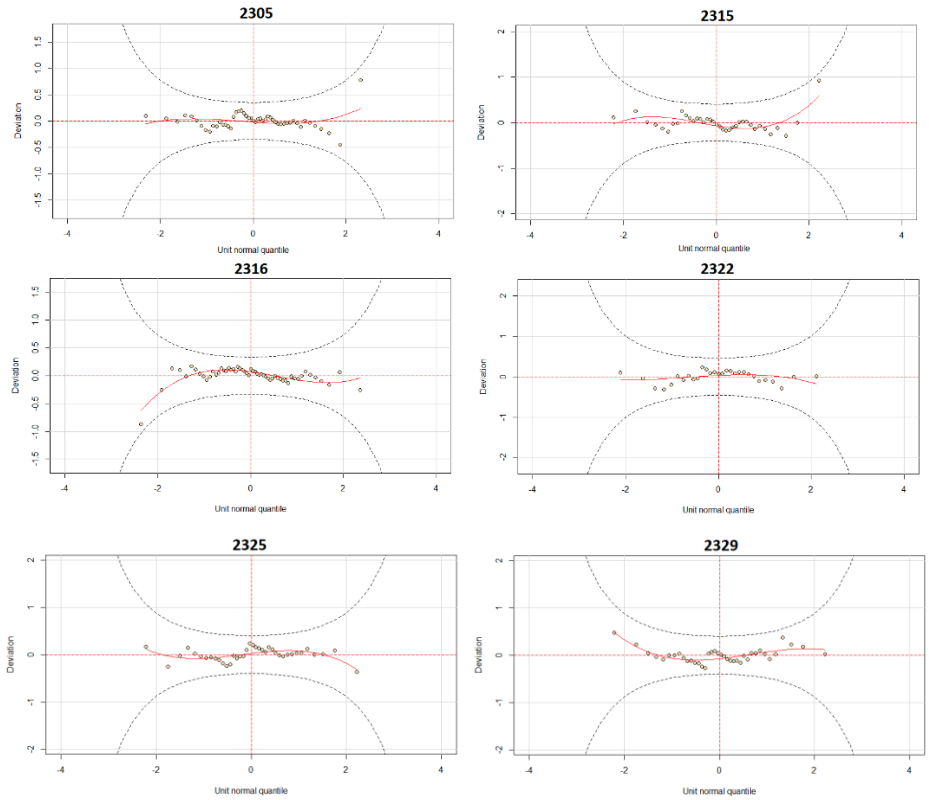

Fig. 2. Worm plots showing the performance of GAMLSS models for the most successful model

The final models obtained are presented in Table 3. IGAMMA, GA, IG and LOGNO distributions showed the best performance at 3, 1, 1 and 1 station, respectively. According to the results, better models were obtained when the sigma parameter was constant. Additionally, low flows are more sensitive to annual precipitation changes compared to the effect of temperature for Çoruh basin.

Table 3. Summaries of best performing models

Station	Distribution	μ	σ
2305	IGAMMA	P_annual	ct
2315	IGAMMA	P_annual	ct
2316	GA	time	ct
2322	IG	T_June + P_annual	ct
2325	LOGNO	P_annual	P_annual
2329	IGAMMA	P_annual	ct

ct denotes that parameter is constant; P indicates precipitation; T refers to temperature.

5 Conclusion

In the present study, low flow series from 6 gauging stations throughout the Çoruh basin were analyzed using both stationary and non-stationary models based on the generalised additive models for location, scale and shape (GAMLSS) framework. Eleven candidate covariates were used for non-stationary models to obtain information on the significant drivers of non-stationarity in each low flow series, leading to the following conclusions:

1) Model 2 in 5 stations and model 1 in 1 station showed the most successful results The stationary model was not successful at any station. This indicates that the stationary model may not always be suitable and that more suitable models can be constructed with physically based covariates.

2) IGAMMA, GA, IG and LOGNO distributions showed the best performance at 3, 1, 1 and 1 station, respectively. The results revealed that a single distribution cannot be specified as the best-fit distribution for the study area.

3) The results of the physically-based models showed that low flows are more sensitive to annual precipitation changes compared to the effect of temperature for Çoruh basin.

The findings of this study contribute to the understanding of the behavior of non-stationary low flows and provide new insights for water resource management.

References

1. Zhang, Q., Xiao, M., Singh, V.P., Chen, X. Copula-based risk evaluation of droughts (2013)
across the Pearl River basin, China. Theor. Appl. Climatol. 111 (1), 119–131.
2. IPCC. Summary for policymakers. In: Stocker, T.F., Qin, D., Plattner, G.-K., Tignor,M.,Allen, S.K., Boschung, J., Nauels, A., Xia, Y., Bex, V., Midgley, P.M. (Eds.), Climate Change : The Physical Science Basis, Contribution of Working Group I to the (2013)
3. Apurv, T., Mehrotra, R., Sharma, A., Goyal, M.K., Dutta, S. Impact of climate change on floods in the Brahmaputra basin using CMIP5 decadal predictions. J. Hydrol. 527, 281–291 (2015).
4. Katz, R.W. Statistical methods for non-stationary extremes. In: AghaKouchak, A., Easterling, D., Hsu, K., Schubert, S., Sorooshian, S. (Eds.), Extremes in a Changing Climate. Springer, Dordrecht, Netherlands. http://dx.doi.org/10.1007/
978-94-007-4479-0_2 (2013).
5. Charles, O., Patrick, W. Uncertainty in calibrating generalised Pareto distribution to rainfall extremes in Lake Victoria basin. Hydrol. Res. http://dx.doi.org/10.2166/nh.2014.052 (2014).
6. Xiong, L.H., Guo, S.L. Trend test and change-point detection for the annual discharge series of the Yangtze River at the Yichang hydrological station. Hydrol. Sci. J. 49 (1), 99–112. http://dx.doi.org/10.1623/hysj.49.1.99.53998 (2004).
7. Milly, P.C.D., Dunne, K.A., Vecchia, A.V. Global pattern of trends in streamflow and water availability in a changing climate. Nature 438 (7066), 347–350.
http://dx.doi.org/10.1038/nature04312 (2005).

8. Milly, P.C.D., Betancourt, J., Falkenmark, M., Hirsch, R.M., Kundzewicz, Z.W., Lettenmaier, D.P., Stouffer, R.J. Stationarity is dead: whiter water management? Science 319 (5863), 573–574. http://dx.doi.org/ 10.1126/science.1151915 (2008).
9. Rigby, R.A., Stasinopoulos, D.M. Generalized additive models for location, scale and shape. J. Roy. Stat. Soc. C – Appl. Stat. 54 (3), 507–554. http:// dx.doi.org/10.1111/j.1467-9876.2005.00510.x (2005).
10. Xiong, L.H., Jiang, C., Du, T. Statistical attribution analysis of the nonstationarity of the annual runoff series of the Weihe River. Water Sci. Technol. 70 (5), 939–946. http://dx.doi.org/10.2166/wst.2014.322 (2014).
11. Akaike, H. Information measures and model selection. Bullet. Int. Stat. Inst. 44, 277–291 (1983).
12. Hao W, Shao Q, Hao Z, Ju Q, Baima W, Zhang D. Non-stationary modelling of extreme precipitation by climate indices during rainy season in Hanjiang River Basin, China. Int J Climatol. 39:4154–4169. DOI: 10.1002/joc.6065 (2019)
13. Yerdelen C, Karimi Y, Kahya E, Frequency Analysis of Mean Monthly Stream Flow in Coruh Basin, Turkey. Fresenius Environmental Bulletin, 19(7): 1300-1311 (2010).
14. Harris, I., Osborn, T.J., Jones, P. et al. Version 4 of the CRU TS monthly high-resolution gridded multivariate climate dataset. Sci Data 7, 109. https://doi.org/10.1038/s41597-020-0453-3 (2020).

Evolution of Low Flows in Çoruh Basin

Muhammet Yılmaz[1][0000-0002-9844-6654] and Fatih Tosunoğlu[2][0000-0002-8423-1089]

[1] Erzurum Technical University, Civil Engineering Department, Erzurum, Türkiye, muhammet.yilmaz@erzurum.edu.tr
[2] Erzurum Technical University, Civil Engineering Department, Erzurum, Türkiye, ftosunoglu@erzurum.edu.tr

Abstract. The Çoruh basin, located in the northeast of Turkey, is one of the important water resources in Turkey. This study investigates the temporal evolution of low-flow regimes of six station and their links with local climate in the Çoruh basin for the 1963–2019 period. The temporal changes for low flow series are explored with The Mann-Kendall (MK) and modified Mann-Kendall test (mMK). According to trend tests, statistically significant decreasing trend was determined in 1 station, while statistically insignificant trends were determined in 5 stations. The study also investigated the relationship between total precipitation and average temperature with the low flow variability for the annual, June, July, August and September period. Simple correlation analysis is used for the relationship between low flows and climatic variables. In general, precipitation correlated positively with low flow patterns, while temperature correlated negatively with low flow series. Significant correlation values between precipitation and low flow series ranged between 0.28-0.63. It reaches its highest value at station 2329 (0.63). Significant correlation values between temperature and low flow series varies from -0.43 to -0.28 and reached its highest value in absolute at station 2322 (-0.43). The results of the correlation analysis show that annual precipitation amount is the dominant control on the magnitude of low flow compared to the temperature. These conclusions may be helpful in long-term decision making regarding low flows in the Çoruh basin.

Keywords: Low flow, trend, temperature, precipitation.

1 Introduction

Water resources are under the influence of population growth, developing industry, agricultural activities and climate change. Greenhouse gases in the atmosphere increase due to fossil fuel use, industrialization phases, environmental pollution, land use change and the reduction of forests, thus increasing global warming. According to studies, an increase of about 0.6 ^{o}C has been determined in global warming in the last century [1]. Due to this increase in global warming, significant changes have been determined in the global climate [2]. As a result of this change in climate, significant changes have been detected in hydro meteorological variables such as groundwater, soil moisture, rain, surface flow, and river flow [3]. Determination of changes and trends in hydro climatological variables due to changes in climate over time has had a great importance in hydrology [4].

Knowing the changes in the frequency and severity of floods and droughts over time will help in more effective planning and management of water resources. In the last few years, a number of studies have been published to identify temporal changes in river flow regimes.

Low flows, which the minimum flow in a river during dry periods of the year, are an important part of the river flow regime, with direct effects on water supply, water quality and ecosystem health [5]. Many indices have been used in the literature to describe low flows. As a result of the research, it was seen that the 7-day low flow index is widely used in the literature for the analysis of extreme events [6; 7]. In this study, the 7-day low flow index was used to define low flow.

There are studies on trend assessment of streamflow in different parts of the world, but the number of studies investigating the relationship between low flows and meteorological variables is very few.

Within the scope of the study, the trends of 7-day low flow data were determined by Mann-Kendall (MK) and Modified Mann-Kendall (mMK) tests. Then, the relationships of the low flow data with precipitation and temperature were investigated.

2 Materials and methods

2.1 Mann Kendall Test

The MK test is a non-parametric test for exploring a trend in a time series without specifying the type of trend (i.e. linear or nonlinear). Mann [8] originally applied this test and Kendall [9] subsequently derived the test-statistic distribution. Under the null hypothesis H0, that a series (x1, ..., x2) comes from a population in which the random variables are independent and identically distributed (clearly, in this case no trend is present), the MK test statistic can be computed as:

$$S = \sum_{i=1}^{n-1} \sum_{j=i+1}^{n} \operatorname{sgn}(x_j - x_i) \tag{1}$$

If the data length in the time series is n> 10, it is assumed that the data are normally distributed and variance is calculated as in equation (2).

$$\operatorname{Var}(S) = \frac{n(n-1)(2n+5) - \sum_{i=1}^{k} t_i(t_i-1)(2t_i+5)}{18} \tag{2}$$

In Equation (1), the z value is calculated according to the value of the MK test statistic. The z value found is compared with the z value read from the normal distribution table at a certain level of significance.

$$z = \begin{cases} \dfrac{S-1}{\sqrt{Var(S)}}; \text{If } S > 0 \\ 0 \qquad\quad ; \text{If } S = 0 \\ \dfrac{S+1}{\sqrt{Var(S)}}; \text{If } S < 0 \end{cases} \tag{3}$$

If the absolute value of the z value calculated as a result of equation (3) is greater than the z value determined at the α significance level, the Ho hypothesis is rejected, that is, there is a significant trend in the time series. If it is small, the Ho hypothesis is accepted, that is, there is no significant trend in the time series. If the MK test statistical value (S) is positive, it is determined that there is an increasing trend, and if it is negative, there is a decreasing trend [10]

2.2 Modified Mann Kendall Test

If there is a significant autocorrelation in the considered time series, the modified Mann-Kendall (mMK) test, which was introduced by [11], is commonly used. In the mMK test, the autocorrelation between the ranks of the observations is first calculated after removing a non-parametric trend estimate, such as the Theil and Senmedian slope, from the data. The variance of the statistic S in Equation (4) is then adjusted to account for the autocorrelation as follows:

$$Var(S) = \frac{n(n-1)(2n+5)}{18}\left[1 + \frac{2}{n(n-1)(n-2)}\sum_{i=1}^{n-1}(n-i)((n-i-2)r_i\right] \tag{4}$$

The MK test statistic is calculated and the z value is calculated according to the limits of the test statistic, the calculated z value is compared with the z value in the normal distribution table, and the presence of significant trends in the time series is determined.

2.3 Correlation analysis

Simple correlation analysis was used for the relationship between low flows and climatic variables. Spearman test was evaluated within the scope of this study as it does not require data to fit normal distribution. The calculated correlations were tested for statistical significance at the 10% level.

3 Study Area and Data

Çoruh basin, which is located in the northeast of Turkey, was selected as study area in this study. The basin covers an area of 19.748 km^2, which covers approximately 2.53% of Turkey. The mean annual rainfall for this basin is about 480 mm and terrain elevations in the basin, with reference to mean sea level, range from 30 to 2200 m [12]. The basin has gained more economic importance for Turkey as a number of the new water resources structures (dams and hydroelectric power plants) have been recently

completed, or are already under construction. Therefore, any case study related to investigate changes in river flow is much more important now for water resources planners in the basin. In this study low flow records of six gauge stations located in the basin were used for trend analyses. The location map of the study area and the stations used are given in Figure 1. The daily flow records were provided by the General Directorate of State Hydraulic Works for the period 1963–2019.

Within the scope of the study, temperature and precipitation data were used for annual and dry periods. For this aim, the monthly gridded precipitation and temperature data provided by the CRU TS v4.04 [13] was obtained from the official website (http:// www. cru. uea. ac. uk) and was considered as the reference dataset in this research.

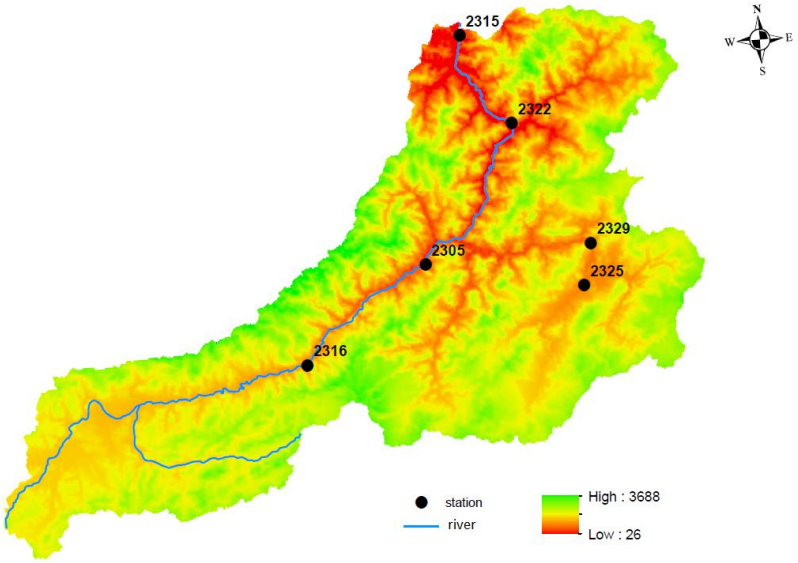

Fig. 1. Study area and spatial distribution of flow gauge stations used in the study.

4 Results

Before applying the MK test to identify trends in the low flow time series, the serial autocorrelation structures of the data need to be checked. According to the results, mMK test was applied to analyze the trends in the low flow data with serial correlation. The trend test results of the stations used in the study are given in Table 1. Figure 2 is presented to visually evaluate the trend results.

Table 1. Trend test results

Station No	z	p
2305	-0.41	0.68
2315	-0.35	0.72
2316	-3.67	0.0002
2322	-1.20	0.23
2325	0.63	0.53
2329	0.53	0.6

As seen in Table 1, while z values are negative at 4 stations, they are positive at 2 stations. However, while statistically significant decreasing trend was determined in 1 station, statistically insignificant trends were determined in 5 stations.

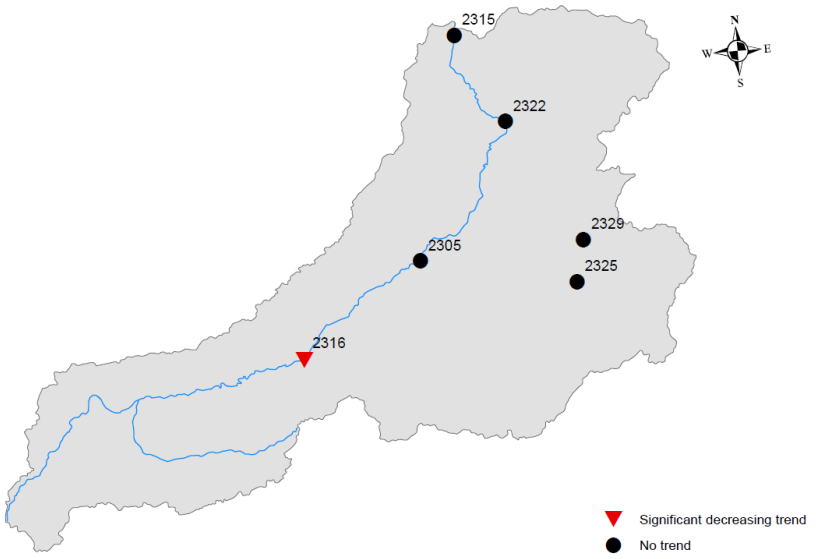

Fig. 2. Spatial presentation of the MK and mMK trend test results with a significance level of 0.05 for the low flow series.

Spearman correlation test was used to investigate the relationship between the low flow data of the stations used in the study and climatic variables. Correlations were evaluated at the 10% significance level. Annual, June, July, August and September period indices are used for the precipitation and temperature.

Correlation values between precipitation and low flows are given in Figure 3. As can be seen in Figure 3, the relationship between September precipitation values and low

flows is quite weak. However, it is seen that annual precipitation values have high correlation values with low flows. Significant correlation values between precipitation and low flow series ranged between 0.28-0.63. It reaches its highest value at station 2329 (0.63). In addition, all significant correlations are positive.

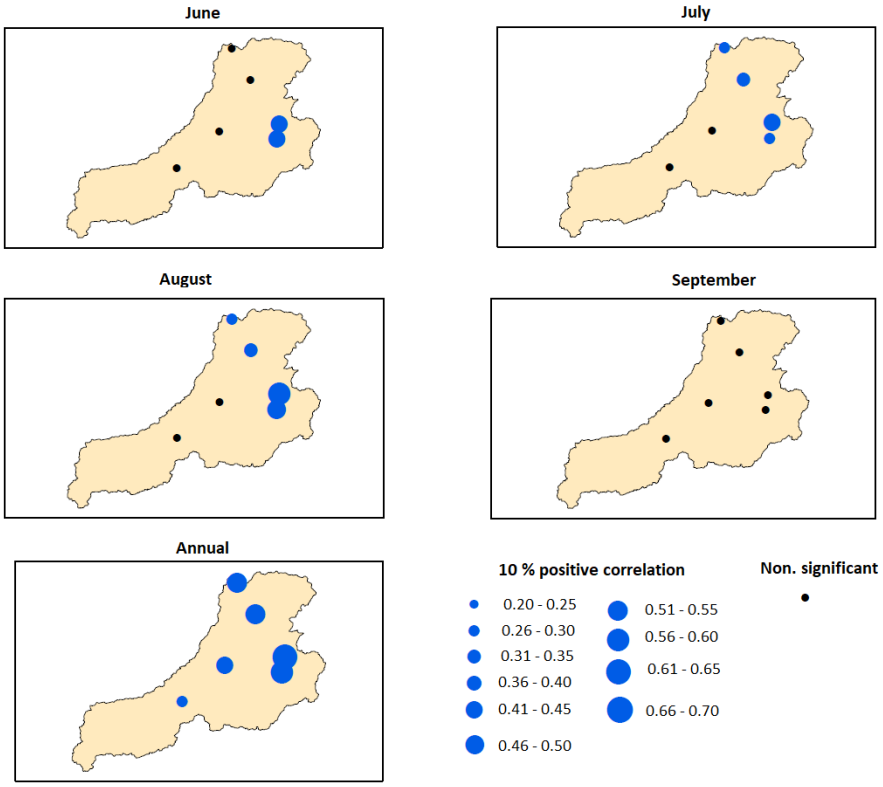

Fig. 3. Spatial and temporal distribution of the correlations between the low flow data and precipitation in annual and dry periods for Çoruh basin

Correlation values between temperature and low flows are given in Figure 4. As can be seen in Figure 4, the relationship between temperature values and low flows is not strong, especially in September. Significant correlation values between temperature and low flow series varies from -0.43 to -0.28 and reached its highest value in absolute at station 2322 (-0.43). In addition, all significant correlations are negative.

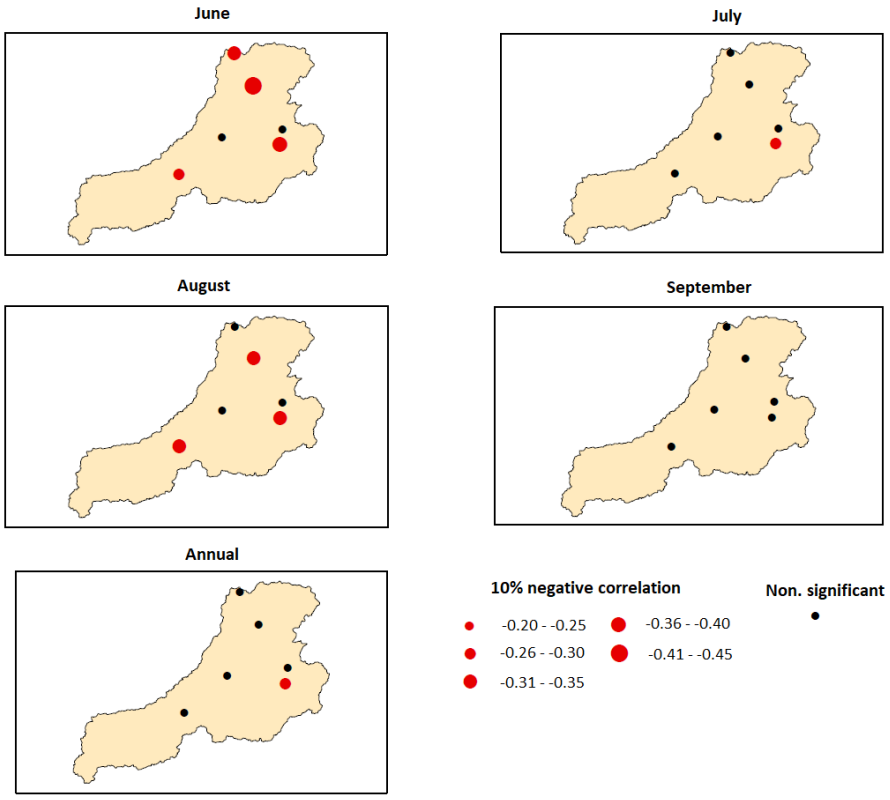

Fig. 4. Spatial and temporal distribution of the correlations between the low flow data and temperature in annual and dry periods for Çoruh basin.

The results of the correlation analysis show that annual precipitation amount for the Çoruh basin is the dominant control on the magnitude of low flow compared to the temperature.

5 Conclusion

In the study, firstly, the autocorrelation structure of low flow data was checked and trend tests were applied according to the results obtained. According to the results, while statistically significant decreasing trend was determined in 1 station, statistically insignificant trends were determined in 5 stations.

In addition, the relationships between low flow data and precipitation and temperature data were investigated in the study. In general, precipitation correlated positively with low flow patterns, while temperature correlated negatively with low flow series. While significant correlation values between precipitation and low flow series ranged between 0.28-0.63, significant correlation values between temperature

and low flow series varies from -0.43 to -0.28. The results of the correlation analysis show that annual precipitation amount is the dominant control on the magnitude of low flow compared to the temperature. The results obtained provide detailed insight into the changing patterns of low flows across Çoruh basin. These conclusions may be helpful in long-term decision making regarding low flows in the Çoruh basin.

References

1. Tabari, H., Nikbakht, J., Talaee, P. Identification of Trend in Reference Evapotranspiration Series with Serial Dependence in Iran. Water Reseour Manage 26, 2219-2232 (2012).
2. Yeh, C., Wang, J., Yeh, H., Lee, C. Spatial and Temporal Streamflow Trends in Northern Taiwan. Water, 7, 634-651 (2015).
3. Goyal, R.. Sensitivity of evapotranspiration to global warming: a case study of arid zone of Rajasthan (India). Agricultural water management, 69,1-11 (2004).
4. Salas, J. Analysis and modeling of hydrologic time series. (Maidment, D.R., Handbook of hydrology), McGraw Hill, 19,1-72, New York (1993).
5. Smakhtin, VU. Low flow hydrology: a review. J. Hydrol 240, 147–186 (2001).
6. WMO. Manual on Low-flow Estimation and Predictions. WMO, Geneva, Switzerlands (2009).
7. Farahani, MA., Khalili, D. Seasonality Characteristics and Spatio-temporal Trends of 7-day Low Flows in a Large, Semi-arid Watershed. Water Resour Manage 27, 4897–4911 DOI 10.1007/s11269-013-0445-6 (2013).
8. Mann, H. Nonparametric tests against trend. Econometrica 13(3), 245-259 (1945).
9. Kendall, M.G. Rank correlation methods. Charles Grifffin: Londan, UK (1975).
10. Yu, Y., Zou, S., Whittemore, D. Non parametric trend analysis of water quality data of rivers in Kansas. Journal of hydrology, 150: 61-80 (1993).
11. Hamed, K.H., Rao, A.R. A modified Mann – Kendall trend test for autocorrelated data. Journal of Hydrology, 204: 182-196 (1998).
12. Yerdelen C, Karimi Y, Kahya E. Frequency Analysis of Mean Monthly Stream Flow in Coruh Basin, Turkey. Fresenius Environmental Bulletin 19(7), 1300-1311 (2010).
13. Harris, I., Osborn, T.J., Jones, P. et al. Version 4 of the CRU TS monthly high-resolution gridded multivariate climate dataset. Sci Data 7, 109 https://doi.org/10.1038/s41597-020-0453-3 (2020).

Possible Effects of Climate Change on Seawater Temperatures: A Case Study for Sarıyer Meteorological Observation Station, Southwestern Black Sea

Sinan Nacar[1][0000-0003-2497-5032], Betül Mete[2][0000-0002-3689-6430], Betül Sezanur Tokgöz[2][0009-0008-4998-4537], and Adem Bayram[2][0000-0003-4359-9183]

[1] Tokat Gaziosmapaşa University, Civil Engineering Department, Tokat, Türkiye, sinannacar@hotmail.com
[2] Karadeniz Technical University, Civil Engineering Department, Trabzon, Türkiye, betulmeteofis@gmail.com
b.sezanur.efiloglu@gmail.com
adembayram@gmail.com

Abstract. An increase in air temperature, one of the parameters most affected by climate change, leads to an increase in seawater temperature (SWT). This situation can have potentially devastating consequences such as thermal expansion, acidification, mucilage formation, and changes in bottom flows. This study investigated the possible effects of climate change on SWT. The Sarıyer meteorological station (southwestern Black Sea, Turkey) was considered for a case study. In this context, a multi-model ensemble was used. It was established with the results of four general circulation models forced under the new shared socioeconomic pathways (SSPs) scenarios in CMIP6. Artificial neural networks (ANNs) and regression-based statistical downscaling methods were used to downscale coarse-resolution data to the regional level. The downscaling performances of the methods were compared using four different statistics. The downscaling performance of the ANNs-based models was higher than that of the regression-based models. Moreover, the SWT values of the Sarıyer station for the future periods (2023-2052 and 2053-2082) under optimistic (SSP2-4.5) and pessimistic (SSP5-8.5) scenarios were compared with the SWT values of the historical period (1985-2014), and their possible changes were determined. The SWT values were estimated to increase by 0.75 and 1.64 °C under SSP2-4.5 scenario and 0.78 and 2.80 °C under SSP5-8.5 scenario during the 2023-2052 and 2053-2082 periods, respectively, compared to the historical period. It has been anticipated that the results of this study will be useful to policymakers and researchers in effectively combating climate change and determining actions that can be taken to address climate change.

Keywords: Black Sea, Climate change, Ensemble model, Seawater temperature.

1 Introduction

Climate change refers to long-term alterations in the Earth's climate and weather patterns. This change is largely caused by human activities, such as burning fossil fuels, deforestation, and industrial processes, which release large amounts of greenhouse gases into the atmosphere and contribute to global warming [1]. Air temperature is considered one of the most significant indicators affected by climate change. It is widely recognized that an increase in air temperature leads to an increase in seawater temperature (SWT). This has significant consequences for both aquatic ecosystems and human societies [2]. Increases in SWTs may cause changes in the distribution and behavior of aquatic species. These changes have the potential to disrupt entire ecosystems and cause cascading effects throughout the food chain. Coral reefs, which serve as critical habitats for numerous aquatic species, are highly susceptible to even slight increases in SWTs, and temperatures above a certain threshold can cause significant damage to these habitats. This damage can lead to a ripple effect that can affect various species that depend on coral reefs for survival [3]. Additionally, increased SWT causes changes in the distribution and behavior (migration patterns or breeding times) of aquatic species [4]. Furthermore, increased SWT can lead to increase severe storms frequent, mucilage formation, changes in bottom flows, and cause sea level rise, which can damage infrastructure and human health, and disrupt economies that depend on fisheries and tourism [5].

According to the Intergovernmental Panel on Climate Change report (IPCC) [6], the effects of climate change on natural systems will continue to worsen in the future, leading to significant deterioration. The devastating effects of climate change on humans and ecosystems have led to growing apprehension on a global scale. For this reason, the effects of climate change on SWTs have recently attracted the attention of researchers. Shaltout and Omstedt [7] examined temporal and spatial SWT variability over the Mediterranean Sea and its surrounding sub-basins using four different scenario (RCP 2.6, RCP 4.6, RCP 6.0, and RCP 8.5) outputs of 24 general circulation models (GCMs) with ensemble model approach. They estimated an annual mean SWT increases of 0.45, 1.15, 1.42, and 2.56 °C for RCP 2.6, RCP 4.6, RCP 6.0, and RCP 8.5, respectively, for the 2020-2029 period. L'Heveder [8] evaluated the seasonal SWT changes by the year 2100 under the RCP 2.6 and RCP 8.5 scenarios of three GCMs using an ensemble model approach in the Western English Channel. It was estimated that the increase in annual mean SWT ranges from 0.5 to 2.5 °C for RCP 2.6 and RCP 8.5. They stated that this increase in SWT may strongly affect marine biology in the Western English Channel. Meier [9] investigated the possible effects of climate change in the Baltic Sea. As a result of the study, they estimated that SWT will increase by 3.5 and 2 °C for the RCP 8.5 and RCP 4.5 scenarios, respectively, in the summer season of the 2069-2098 period compared to the 1976-2005 period. Noori [10] examined the effect of climate change on SWT using a proper orthogonal decomposition model and daily optimum interpolation SWT anomaly data in the Persian Gulf and the Gulf of Oman. They estimated an annual mean increase of 2.2 °C in SWT across the Persian Gulf and the Gulf of Oman for the period 2020-2100. The model indicated that monthly

SWT values in the Persian Gulf may increase by 4.3 °C in August by the end of the century. They estimated that the highest warming will occur during summer for the future period (2020-2100), and the annual mean SWT increase for the Persian Gulf and the Gulf of Oman will be about 2.2 °C by 2100.

There is a lack of research in the existing literature regarding the effects of climate change on SWT. This study aimed to explore the potential effects of climate change on SWT. The study was conducted at the Sarıyer meteorological observation station (MOS) located in the southwestern Black Sea region of Turkey. A multi-model ensemble approach was employed, using the outputs of four GCMs that were forced under the new shared socioeconomic pathways (SSPs) scenarios in CMIP6. To downscale coarse-resolution data to the regional scale, artificial neural networks (ANNs) and regression-based statistical downscaling methods, commonly used in the literature, were utilized. The downscaling performances of the methods were evaluated using four different performance statistics, the root mean squared error (RMSE), mean absolute error (MAE), scatter index (SI), and the Nash-Sutcliffe (NS) efficiency coefficient.

2 Materials and Methods

2.1 Study Area and Seawater Temperature Data

The Black Sea, the largest inland sea, is located between 40° 56' - 46° 33' N latitudes and 27° 27' - 41° 42' E longitudes. It is connected to the Mediterranean Sea through the Bosporus and Dardanelles straits, and to the Sea of Azov through the Kerch Strait [11, 12]. With an area of 461,000 km² and an average depth of 1,300 m, the Black Sea is the largest land-locked sea. The sea has a unique ecosystem and high biodiversity, with many endemic species [13]. However, at depths greater than 180-200 m, the sea is completely covered with hydrogen sulfide gas, resulting anoxic conditions that can support the growth of certain bacteria and other organisms. The Black Sea is a complex and dynamic ecosystem that is highly sensitive to climate change. Therefore, it is important to monitor and understand the effects of climate change on the Black Sea to develop effective strategies for mitigating and adapting to these changes [14].

The Sarıyer MOS is located at 41° 15' 01.80" N - 29° 02' 18.24" E coordinates in the southwest of the Black Sea. The monthly mean SWT data for the period 1963-2014 was obtained from the Turkish State Meteorological Service for the station. It was determined that the lowest, mean, and highest SWT values of the station were 3.33, 14.35, and 26.30 °C, respectively. The standard deviation of the data was calculated as 6.3 °C.

2.2 General Circulation Models and Shared Socioeconomic Pathways Scenarios

The GCMs are complex mathematical models that simulate the Earth's climate system. They work by dividing the Earth's atmosphere and oceans into three-dimensional grids. At each grid cell, the GCMs simulate the exchange of energy, mass, and momentum

between the atmosphere, oceans, land surface, and cryosphere using physical laws [15]. The size of the grid cells can vary from 200 to 600 km, depending on the resolution of the model. In general, the models with higher resolutions have smaller grid cells, which enable them to better capture smaller-scale atmospheric phenomena, such as storms and turbulences [16]. Prediction the accuracy of GCM is impacted by the model's resolution, which can limit the accuracy of local predictions. Statistical downscaling models are commonly used to reduce coarse-resolution GCM outputs to a regional scale. These models include multivariate linear-nonlinear regression types, ANNs algorithms, and correlation analysis [17].

The climate scenarios are projections of future climate conditions based on different assumptions about future greenhouse gas emissions, land use changes, and technological advancements. The IPCC [18] report includes eight different versions of the five key shared socio-economic pathways (SSP1, SSP2, SSP3, SSP4, and SSP5) scenarios. In this study, optimistic (SSP2-4.5) and pessimistic (SSP5-8.5) scenario outputs of four GCMs, CNRM-ESM2-1, MPI-ESM1-2-HR, MRI-ESM2-0, and NORESM2-MM, were used [19]. An ensemble model approach has been employed to evaluate the GCMs collectively, and reduce the uncertainties that arise from their use [20].

2.3 Conventional Regression Analysis

Conventional regression analysis (CRA) is a statistical method used to identify the relationship between a dependent variable and one or more independent variables. The goal of the CRA method is to estimate the values of the unknown parameters of the equation that best fit the observed data [21]. In this study, four functions, linear (LF), power (PF), exponential (EF), and quadratic (QF), were used.

2.4 Artificial neural networks

ANNs are a type of machine-learning algorithm inspired by the structure and function of the human brain [22]. They are used to solve problems such as defining, classifying, predicting, or organizing data [23]. ANN architecture consists of an input layer, one or more hidden layers, and an output layer. ANNs consist of interconnected nodes that can process information and learn from experience, and each node represents an artificial neuron. Each neuron is linked to inputs from neurons in the previous layer, and these connections are defined by weights. Weights are initially random values. During training, the data is given to the input layer of ANNs, and the difference between the output and the actual value is tried to be reduced by updating the weights. This process is repeated until the weights reach the optimum values. ANNs is a system that can predict output values based on training and learning processes with a given set of inputs [24].

2.5 Bias Correction Method

The main approach employed in bias correction methods involves developing a statistical transfer function that connects the model-generated data with the observations obtained in current conditions. This transfer function is subsequently

applied to modify the model's [25]. The quantile delta mapping (QDM) commonly used to adjust climate model outputs to match observations in climate impact studies better, has been employed as bias correction method in this study. The method involves identifying the differences between the cumulative distribution functions of the model outputs and observed data at different quantiles (e.g., 10th, 50th, and 90th percentiles) of the data distribution [26].

3 Model Applications and Evaluations

This study used the data from the Sarıyer MOS for the period 1963-2014 to estimate the SWT for the periods 2023-2052 and 2053-2082 using optimistic and pessimistic scenario outputs of four GCMs from the CMIP6 archive. The CRA and ANNs statistical downscaling methods were used to convert the coarse-scale GCM outputs to a regional scale. The CRA method included four models for LF, PF, EF, and QF, while the ANNs method had five models with 5, 10, 15, 20, and 25 neurons. The models were trained, validated, and tested using 60, 20, and 20% of the data, respectively, and evaluated using performance statistics such as RMSE, MAE, SI, and NS efficiency coefficient. The input variables for the models were monthly mean air temperature from the coarse resolution GCMs and digitized month information of the sampling dates, while the output variable was the monthly mean SWT measured in the Sarıyer MOS.

The models with lower RMSE, MAE, and SI and higher NS efficiency coefficient can be said to be more accurate [27]. Moreover, approaching the NS efficiency coefficient of 1 shows that the model's accuracy increases [28]. Considering these references, the best model was determined. The monthly mean air temperature data in SSP2-4.5 and SSP5-8.5 scenario data sets were introduced as new inputs to the best model and the monthly mean SWT values for the future period were estimated for both scenarios. Then, the QDM bias correction process was applied to the model outputs, and the biases in the downscaling processes were eliminated. Finally, the possible changes in the SWTs were determined by comparing the historical data (1985-2014) of the Sarıyer MOS with the monthly mean SWT data for the future periods estimated under SSP2-4.5 and SSP5-8.5 scenarios.

4 Results and Discussion

This study used the CRA and ANNs statistical downscaling methods to estimate SWT. Firstly, the CRA was performed with the IBM SPSS Statistics 26 software, and the optimum values of the regression coefficients in the used functions were determined. The SWTs were calculated for the validating and testing data sets by the equations created with the determined coefficients. Then ANNs method was applied to the data sets using MATLAB 2020b software. The performance statistics were calculated to determine the ability of the CRA and ANNs methods to estimate the SWTs for the Sarıyer MOS. The performance statistics of training, validating, and testing data sets of ANNs and CRA-based downscaling models are given in Table 1.

Table 1. The comparison of the performance statistics for the CRA and ANNs methods concerning the training, validating, and testing phases for the Sarıyer meteorological observation station, Turkey.

Data sets	Statistics	Functions				Number of neurons				
		LF	PF	EF	QF	5	10	15	20	25
Training	RMSE	1.870	1.849	1.668	1.508	1.485	1.443	1.495	1.430	1.559
	MAE	1.442	1.427	1.316	1.206	1.170	1.140	1.174	1.124	1.233
	SI	0.133	0.132	0.119	0.107	0.106	0.103	0.106	0.102	0.111
	NS	0.909	0.911	0.928	0.941	0.943	0.946	0.942	0.947	0.937
Validating	RMSE	1.965	1.982	1.679	1.623	1.581	1.564	1.603	1.591	1.565
	MAE	1.552	1.573	1.366	1.287	1.237	1.236	1.278	1.246	1.248
	SI	0.135	0.136	0.116	0.112	0.109	0.108	0.110	0.110	0.108
	NS	0.902	0.900	0.928	0.933	0.936	0.938	0.935	0.936	0.938
Testing	RMSE	1.511	1.495	1.474	1.443	1.268	1.233	1.258	1.244	1.244
	MAE	1.180	1.181	1.199	1.142	1.006	0.966	1.002	0.978	0.971
	SI	0.101	0.100	0.099	0.097	0.085	0.082	0.084	0.083	0.083
	NS	0.944	0.945	0.947	0.949	0.960	0.963	0.961	0.962	0.962

It has been determined that the QF from the CRA method had lower values of RMSE, MAE, and SI and higher values of NS efficiency coefficient for all three data sets. On the other hand, lower values of RMSE, MAE, and SI, as well as higher values of NS efficiency coefficient, were obtained from ANN_20 in the training data set and ANN_10 in validating and testing data sets in the ANNs method. It is seen that ANNs-based models generally have better performance values compared to CRA-based models (Table 1). The NS efficiency coefficient values of ANNs-based models varied from 0.937 to 0.947 for the training, 0.935 to 0.938 for the validating, and 0.960 to 0.963 for the testing data sets. According to the classification by Moriasi [28], these values are categorized as “very good”. The results indicate that the models established can accurately estimate the future SWTs. The changes in the models’ future SWT values are considered in determining the best model because the performance statistics of the ANNs-based models are close. The evaluations were carried out on the ANN_5 model, which had the highest variation in SWT.

Air temperature values of SSP2-4.5 and SSP5-8.5 scenarios of GCMs and and digitized month information of the sampling dates were used as input parameters in the established ANNs models, and SWTs for the next periods (2023-2052 and 2053-2082) were estimated. The SWT values for the Sarıyer MOS were compared with the historical (1985-2014) values and determined possible changes in SWTs. The SWT differences (Δt) are visualized by coloring (Tables 2 and 3) to follow the change.

Table 2. Changes of monthly mean seawater temperatures (Δt) of the 2023-2052 period for SSP2-4.5 and SSP5-8.5 scenarios compared to the 1985-2014 period.

Scenarios	Models	Jan	Feb	Mar	Apr	May	Jun	Jul	Aug	Sep	Oct	Nov	Dec	Annual
SSP2-4.5	ANN_5													
	ANN_10													
	ANN_15													
	ANN_20													
	ANN_25													
SSP5-8.5	ANN_5													
	ANN_10													
	ANN_15													
	ANN_20													
	ANN_25													
Δt, °C		–0.97	–0.73	–0.49	–0.25	–0.01	0.23	0.47	0.71	0.94	1.18	1.42	1.66	1.90

Table 3. Changes of monthly mean seawater temperatures (Δt) of the 2053-2082 period for SSP2-4.5 and SSP5-8.5 scenarios compared to the 1985-2014 period.

Scenarios	Models	Jan	Feb	Mar	Apr	May	Jun	Jul	Aug	Sep	Oct	Nov	Dec	Annual
SSP2-4.5	ANN_5													
	ANN_10													
	ANN_15													
	ANN_20													
	ANN_25													
SSP5-8.5	ANN_5													
	ANN_10													
	ANN_15													
	ANN_20													
	ANN_25													
Δt, °C		–1.25	–0.76	–0.28	0.21	0.69	1.18	1.67	2.15	2.64	3.12	3.61	4.10	4.58

For the 2023-2052 period, monthly mean SWT changes were estimated to vary from –0.79 to 1.78 °C in SSP2-4.5 scenario and –0.97 to 1.90 °C in SSP5-8.5 scenario. For both scenarios, it is estimated that there will be some decrease (0.36°C for SSP2-4.5 and 0.55°C for SSP5-8.5) in SWTs for January. It was determined that the highest temperature increase would occur in June (1.78 °C) for SSP2-4.5 and July (1.90 °C) for SSP5-8.5. Seasonally, the highest temperature change will occur in summer at 1.45 and 1.59°C for SSP2-4.5 and SSP5-8.5 scenarios, respectively. The annual mean SWT values are estimated to increase by 0.75 and 0.78 °C for SSP2-4.5 and SSP5-8.5 scenarios, respectively. For the 2053-2082 period, monthly mean SWT changes were estimated to vary from –1.25 to 2.89 °C in SSP2-4.5 scenario and –1.06 to 4.58 °C in SSP5-8.5 scenario. It is seen from Tables 2 and 3 that bigger changes in the SWT values may occur in the future periods. It was determined that the highest temperature increase would occur in May at 2.89 °C for SSP2-4.5 and 4.58 °C for SSP5-8.5. Seasonally, the highest temperature change will occur in summer at 2.40 and 3.65 °C for SSP2-4.5 and SSP5-8.5 scenarios, respectively. The annual mean SWT values are estimated to increase by 1.64 and 2.80 °C for SSP2-4.5 and SSP5-8.5 scenarios, respectively.

5 Conclusions

This study aims to investigate the possible effects of climate change on seawater temperatures (SWTs). The Sarıyer meteorological observation station (MOS), located in the Southwestern Black Sea Region and has 52 years of uninterrupted SWT data, was chosen as the study area. The effects of climate change on mean SWTs were examined with an ensemble model approach using SSP2-4.5 and SSP5-8.5 scenario outputs of four general circulation models (GCMs) selected from the CMIP6 archive. Conventional regression analysis (CRA) and artificial neural networks (ANNs) methods were used for downscaling. Linear, power, exponential, and quadratic functions (LF, PF, EF, and QF) for the CRA method and five models with different neuron numbers for the ANNs method were established. The performances of the methods and models were evaluated by the root mean square error (RMSE), mean absolute error (MAE), scatter index (SI), and Nash-Sutcliffe (NS) efficiency coefficient statistics. The future air temperature scenario outputs of the GCMs and digitized month information of the sampling dates were used as input parameters to obtain the SWTs for the periods 2023-2052 and 2053-2082. Finally, quantile delta mapping bias correction was applied to the model outputs. The results of the study are listed below.

- In estimating SWTs, the ANNs-based models have lower RMSE, MAE, and SI and higher NS efficiency coefficient values than CRA-based models. The model with five neurons (ANN_5) has the highest temperature difference according to the possible SWT change values, which were calculated by comparing estimated values for the future period with observed data for the historical period.
- For the period 2023-2052, seasonal mean SWT values were estimated to vary between 0.10 (winter) and 1.45 °C (summer) for SSP2-4.5 scenario and between –0.08 (winter) and 1.59 °C (summer) for SSP5-8.5 scenario. The maximum increases in the SWT values are estimated to be 1.78 °C in June and 1.90 °C in July for SSP2-4.5 and SSP5-8.5 scenarios, respectively.
- For the period 2053-2082, seasonal mean SWT values are estimated to vary between 0.93 (winter) and 2.41 °C (summer) for SSP2-4.5 scenario and between 1.89 (winter) and 3.65 °C (summer) for SSP5-8.5 scenario. The maximum increases in the SWT values are estimated to be 2.89 and 4.58 °C in May for SSP2-4.5 and SSP5-8.5 scenarios, respectively.
- It has been observed that the SWTs have increased gradually from 2023-2052 to 2053-2082. Therefore, the highest temperature increases are expected to occur at the end of the century. It is thought that this situation may trigger the deterioration of the food chain, fish migration, and the increase of invasive species and cause the local economy to be negatively affected in the Southwestern Black Sea.

It is recommended to use daily data and increase the number of stations to investigate the possible effects of climate change more comprehensively on SWTs. Within the scope of the study, four different GCM outputs were used under two different scenarios and two periods. Conducting a similar study using more GCM will allow a more comprehensive evaluation of possible SWT increases. In addition, regression and

ANNs-based statistical downscaling methods were used in this study. Performing similar analyses using more downscaling methods may be the subject of another study.

References

1 Erdoğan, S.: Energy, environment, and greenhouse gas. Çankırı Karatekin Üniversitesi İktisadi ve İdari Bilimler Fakültesi Dergisi 10(1), 277-303 (2020). (in Turkish with English abstract)
2 Eissa, A.E., Zaki, M.M.: The impact of global climatic changes on the aquatic environment. Procedia Environmental Sciences 4, 251-259 (2011).
3 Munday, P.L., Jones, G.P., Pratchett, M.S., Williams, A.J.: Climate change and the future for coral reef fishes. Fish and Fisheries 9(3), 261-285 (2008).
4 Brierley, A.S., Kingsford, M.J.: Impacts of climate change on marine organisms and ecosystems. Current biology 19(14), R602-R614 (2009).
5 Beardall, J., Stojkovic, S.: Microalgae under global environmental change: implications for growth and productivity, populations and trophic flow. Science Asia 32(1), 1-10 (2006).
6 IPCC: Technical summary. IPCC special report on the ocean and cryosphere in a changing climate [Portner, H.O., Roberts, D.C., Masson Delmotte, V., Zhai, P., Tignor, M., Poloczanska, E., Mintenbeck, K., Alegría, A., Nicolai, M., Okem, A., Petzold, J., Rama, B., Weyer, N.M. (eds.)]. In Press (2019).
7 Shaltout, M., Omstedt, A.: Recent sea surface temperature trends and future scenarios for the Mediterranean Sea. Oceanologia 56(3), 411-443 (2014).
8 L'Heveder, B., Speich, S., Ragueneau, O., Gohin, F., Bryere, P.: Observed and projected sea surface temperature seasonal changes in the Western English Channel from satellite data and CMIP5 multi-model ensemble. International Journal of Climatology 37(6), 2831-2849 (2017).
9 Meier, H.M., Dieterich, C., Eilola, K., Groger, M., Hoglund, A., Radtke, H., Wahlstrom, I.: Future projections of record-breaking sea surface temperature and cyanobacteria bloom events in the Baltic Sea. Ambio 48, 1362-1376 (2019).
10 Noori, R., Tian, F., Berndtsson, R., Abbasi, M.R., Naseh, M.V., Modabberi, A., Klove, B.: Recent and future trends in sea surface temperature across the Persian Gulf and Gulf of Oman. Plos One 14(2), e0212790 (2019).
11 Yuce, H.: Mediterranean water in the Strait of Istanbul (Bosphorus) and the Black Sea exit. Estuarine, Coastal and Shelf Science 43(5), 597-616 (1996).
12 Zavialov, I., Osadchiev, A., Sedakov, R., Barnier, B., Molines, J.M., Belokopytov, V.: Water exchange between the Sea of Azov and the Black Sea through the Kerch Strait. Ocean Science 16(1), 15-30 (2020).
13 Bakan, G., Buyukgungor, H.: The Black Sea. Marine Pollution Bulletin 41(1-6), 24-43 (2000).
14 Tatui, F., Pirvan, M., Popa, M., Aydogan, B., Ayat, B., Gormus, T., Saprykina, Y.: The Black Sea coastline erosion: Index-based sensitivity assessment and management-related issues. Ocean and Coastal Management 182, 104949 (2019).
15 Wilby, R.L., Wigley, T.M.L., Conway, D., Jones, P.D., Hewitson, B.C., Main, J., Wilks, D.S.: Statistical downscaling of general circulation model output: a comparison of methods. Water Resources Research 34(11), 2995-3008 (1998).
16 Nacar, S.: Effect of climate change on temperature and precipitation parameters: a study for the Eastern Black Sea Basin, Turkey. Ph.D. Thesis, Karadeniz Technical University, Graduate School of Natural and Applied Science, Trabzon, Turkey (2020). (in Turkish with English abstract)

17 Shashikanth, K., Madhusoodhanan, C.G., Ghosh, S., Eldho, T.I., Rajendran, K., Murtugudde, R.: Comparing statistically downscaled simulations of Indian monsoon at different spatial resolutions. Journal of Hydrology 519, 3163-3177 (2014).
18 IPCC: Summary for policymakers. The physical science basis. contribution of working group I to the sixth assessment report of the ıntergovernmental panel on climate change [MassonDelmotte, V.P., Zhai, A., Pirani, S.L., Connors, C., Pean, S., Berger, N., Caud, Y., Chen, L., Goldfarb, M.I., Gomis, M., Huang, K., Leitzell, E., Lonnoy, J.B.R., Matthews, T.K., Maycock, T., Waterfield, O., Yelekci, R., Yu, B. (eds.)]. Cambridge University Press. In Press (2021).
19 Zuluaga, C.F., Avila-Diaz, A., Justino, F.B., Martins, F.R., Ceron, W.L.: The climate change perspective of photovoltaic power potential in Brazil. Renewable Energy 193, 1019-1031 (2022).
20 Tebaldi, C. and Knutti, R.: The use of the multi-model ensemble in probabilistic climate projections. Philosophical Transactions of the Royal Society A-Mathematical, Physical and Engineering Sciences 365(1857), 2053-2075 (2007).
21 Bayazıt M.: Hidrolojide İstatistik Yöntemler, İTÜ Matbaası, Gümüşsuyu, İstanbul, Turkey (1981). (in Turkish)
22 Kohonen, T.: An introduction to neural computing. Neural Networks 1(1), 3-16 (1988).
23 Hippert, H.S., Pedreira, C.E., Souza, R.C.: Neural networks for short-term load forecasting: a review and evaluation. IEEE Transactions on Power Systems 16(1), 44-55 (2001).
24 Gupta, N.: Artificial neural network. Network and Complex Systems 3(1), 24-28 (2013).
25 Cannon, A.J., Sobie, S.R., Murdock, T.Q.: Bias correction of GCM precipitation by quantile mapping: how well do methods preserve changes in quantiles and extremes? Journal of Climate, 28(17) 6938-6959 (2015).
26 Nacar, S., Kankal, M., Okkan, U.: A downscaling application for local meteorological variables of Eastern Black Sea Basin and scenario-based predictions. Teknik Dergi, 33(6) 12877 (2022).
27 Uluer, O., Kirmaci, V., Atas, S.: Using the artificial neural network model for modeling the performance of the counter flow vortex tube. Expert Systems with Applications 36(10), 12256-12263 (2009).
28 Moriasi, D.N., Arnold, J.G., Van Liew, M.W., Bingner, R.L., Harmel, R.D., Veith, T.L.: Model evaluation guidelines for systematic quantification of accuracy in watershed simulations. Transactions of the ASABE 50(3), 885-900 (2007).

Examination of the Long-Term Drought Variability of the Continental Climate Regions Using Discrepancy Precipitation Index: The Case of Karaman Station Data, Türkiye

Serin Değerli Şimşek[1][0000-0003-0208-9152] and Evren Turhan[1*][0000-0002-0742-4848]

[1] Department of Civil Engineering, Adana Alparslan Türkeş Science and Technology University, Sarıçam, Adana, Türkiye
eturhan@atu.edu.tr

Abstract. The drought phenomenon is one of the most critical environmental problems of the century. Researchers have been set to work on the quantitative assessment of drought over the years. Drought indices investigations are the most preferred one among these studies. Observed hydrometeorological data are used in the calculation of these indices. Thus, both analyses can be performed in terms of past dry periods, and future forecasting works can be realized. However, many index values can cause discrepancies due to the difference in probability distribution functions. Discrepancy Precipitation Index (DPI), which is newly used in the literature, has been investigated to decrease the disadvantages mentioned. Considering the published literature, it is seen that there are the DPI works regarding arid, semi-arid and Mediterranean climate regions. In this study, Karaman province- where continental climatic conditions are observed and recently adverse drought effects have occurred- has been preferred as a case study. DPI values were calculated using Karaman Precipitation Observation station data between 1970 and 2021. The averages of two distributions, Gamma and Log Normal of Standardized Precipitation Index (SPI), another drought index, were compared with the DPI results. In addition, using the DPI values, some analyses were carried out on the determined drought classifications. According to this study's results, the available data were examined in five different periods, and it was determined that the results of three consecutive periods such as 1981-1990, 1991-2000 and 2001-2010, were realized as Near Normal Drought category. It can be said that the DPI and SPI values are close to each other regarding the number of droughts, and more dry periods are determined in the DPI compared to the SPI. With respect to the DPI, the most common drought class was Moderate Drought with 56%, while according to the SPI values, this occurred in Near Normal Wet with 40%. Extremely Drought was not determined according to both indices in all periods.

Keywords: DPI, SPI, Karaman Precipitation Station, Hydraulics.

1 Introduction

Drought is a concept that has come to the fore frequently since agriculture took place in our lives [1-5]. Drought studies have also gained momentum to ensure the necessary production continuity, mainly due to the increasing population and changing climatic conditions. Although the drought is considered in the category of natural disasters such as earthquakes, floods and forest fires, it differs from others in terms of its specific properties. The main reason for this is that the drought event takes a long time to take place as well as its development, and it is hard to detect the beginning and ending precisely [6,7]. Drought phenomenon may occur when precipitation values fall significantly below the expected average or due to rapid population growth and excessive water use [8]. The drought is examined in four main groups regarding its effect and change over time. These can be referred as meteorological, agricultural, hydrological and socioeconomic drought [9]. This sequencing starts with the fact that the precipitation values are less than 25% of the expected value and then progresses as the agricultural lands are affected by the low precipitation values, respectively. Subsequently, the decreases observed in the surface and sub-surface water resources levels may cause socioeconomic problems [10].

It is only possible to take the necessary measures for drought to be taken with comprehensive research. In this context, drought indices have been developed to quantify drought severity, level and duration. The Palmer Drought Severity Index (PDSI) is one of the first developed drought indices (Palmer, 1965) [11]. Afterwards, the missing aspects of the existing indices were tried to be developed. These indices can be sorted as follows; Van Rooy (1965)- Rainfall Anomaly Index (RAI) [12], Shafer and Dezman (1982)- Surface Water Supply Index (SWSI) [13], McKee et al. (1993)- Standardized Precipitation Index (SPI) [14], Tsakiris et al. (2007)- Reconnaissance Drought Index (RDI) [15], Shukla and Wood (2008)-Standardized Runoff Index (SRI) [16], Vicente-Serrano et al. (2010)- Standardized Precipitation and Evaporation Index (SPEI) [17] and Tayfur (2021)- Discrepancy Precipitation Index (DPI) [18]. Among these indexes, especially the SPI has been generally accepted and applied in many studies in the literature. However, as seen in the study of Tayfur (2021), it is thought that the random precipitation values to the probability distributions in the SPI method cannot produce reliable results. For this reason, it is foreseen that the comparison of the DPI results that do not use probability distribution, with the generally accepted index results like the SPI, would be beneficial with regards to the litareture works.

In this study, the Karaman region, located in the southern part of the Konya Closed Basin, was determined as the study area, and the precipitation values between the years 1970-2021 obtained from the Turkish State Meteorological Service were used. Long-term drought and wet period analyses were carried out by calculating the SPI and DPI values with these data. The DPI method has usually been applied for arid and semi-arid regions. Hence, within the scope of this study, the Karaman region, where continental climate conditions prevail and drought effects have been observed intensely recently, was preferred.

2 Material and Method

Continental climate conditions are generally observed in the Karaman region, located in the Central Anatolia Region and the borders of the Konya Closed Basin. It can be said that the basin has approximately 49.8 km^2 surface area. The region corresponds to 6.4% of Türkiye's surface area, and its also considered the 4th Sub-basin with the largest surface area of the basin [19]. The recorded precipitation data of Karaman Central station used in the study were obtained from the Turkish State Meteorological Service (Figure 1).

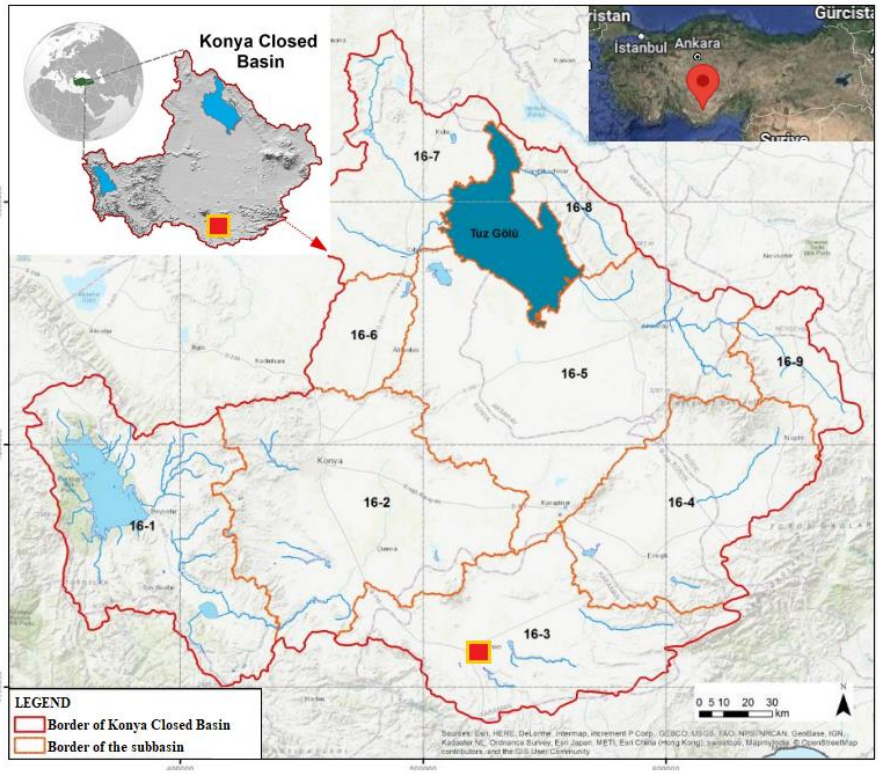

Fig. 1. The study area [19].

With the precipitation data measured between 1970-2021, the determination of dry and wet periods in the long-term was carried out by the SPI and DPI methods. The SPI method was proposed by McKee et al. [14] in 1993 and is still used as one of the most preferred drought indices today. The methodology of the SPI is based on the principle of fitting the precipitation data to probability distributions such as Gamma and Log Normal, which allows calculations in various time scales such as 3, 6, 9, 12, 24 and 48 months.

It is also suitable for using various precipitation data because the index calculation is made by dividing the difference of precipitation data with the average value by the standard deviation. The classifications of the indices calculated according to the SPI method for dry and wet periods are shown in Table 1.

Table 1. SPI Classifications [20]

SPI Values	Classifications
SPI≤-2	Extremely Drought
-2<SPI≤-1.5	Severely Drought
-1.5<SPI≤-1	Moderately Drought
-1<SPI≤0	Near Normal Drought
0<SPI≤1	Near Normal Wet
1<SPI≤1.5	Moderately Wet
1.5<SPI≤2	Severely Wet
SPI>2	Extremely Wet

The Discrepancy Precipitation Index (DPI) method was handled by Tayfur (2021) [18] also to improve the existing indices and eliminate the deficiencies. The DPI method has been developed independently of any probability distribution, considering that fitting the random regular precipitation data to probability distributions in the SPI method may cause poor results. In this method, the logarithm of the ratio of precipitation data to the mean value and index values were calculated and categorized within limits given in Table 2.

Table 2. DPI Classifications [18]

DPI Values	Classifications
DPI≤-0.6	Extreme Drought
-0.4<DPI≤-0.59	Severe Drought
-0.2<DPI≤-0.39	Moderate Drought
0<DPI≤-0.19	Near Normal

3 Results and Discussion

The monthly and annual average precipitation data of MGM Karaman station used in this study are shown in Figure 2. The monthly maximum precipitation value was measured as 180 mm in 2016 and was observed as 43.5 mm in 1976, according to the annual average value. A negative slope was obtained when the change in precipitation values was adjusted to the linear regression graph, indicating that precipitation values have decreased since 1970. Although there is a general decrease in precipitation values, the maximum precipitation value of 52 years of data has occurred in the last five years. While peak values deviated from the average values at certain intervals between 1970

and 2000, the incidence of this situation decreased in recent years; however, its severity increased.

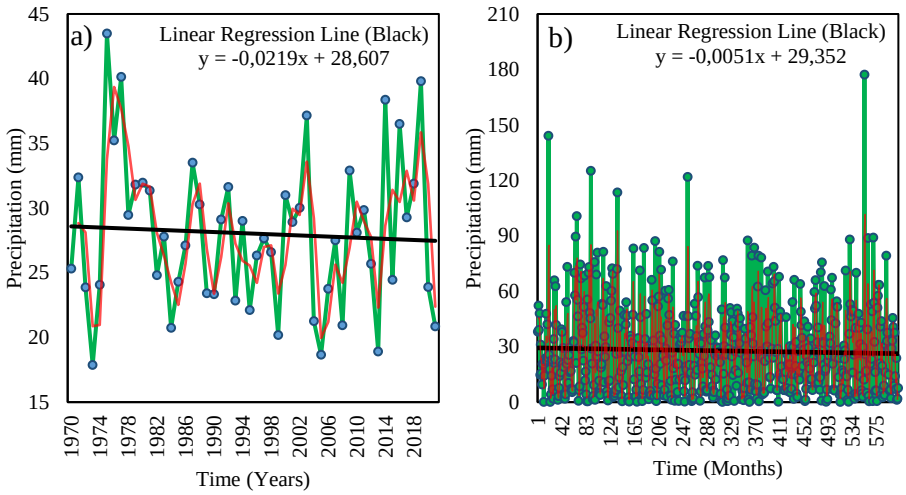

Fig. 2. Precipitation values over time. a) Annual average values, b) Monthly average values

In order to examine the course of drought in the Karaman region, drought indices were calculated according to the SPI and DPI methods (Figure 3). Considering the 12-month index values obtained, while wet periods are frequently encountered in the SPI method, it has been observed that only one wet period occurs according to the DPI method. In addition, three years are seen at the limit of the Extreme Drought period with the SPI method, while only the 1999 period is closest to the Extreme Drought with the DPI. All of the Extremely Drought periods found by the SPI correspond to Moderate Drought in the DPI method, whereas the Extreme Dry period in the DPI method was determined as the Moderate Drought in the SPI method.

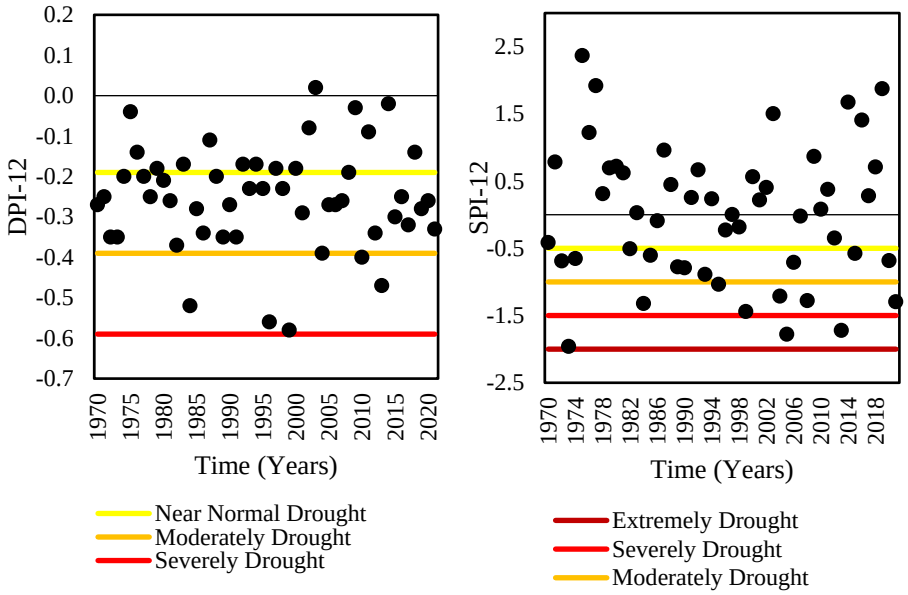

Fig. 3. The DPI and SPI results on 12-months time scale.

In order to examine the 52 years in more detail, the data were divided into five separate groups: 1970-1980, 1981-1990, 1991-2000, 2001-2010 and 2011-2021. In this way, the drought conditions within each 10-year period are discussed. The variation of the SPI and DPI values in five different periods in the Karaman region is given in Figure 4 and Figure 5. In the SPI values, the Near Normal Wet period stands out in 1970-1980 and 2011-2021. In the 1981-1990, 1991-2000 and 2001-2010 periods, it is seen that the Near Normal Drought periods in a row exist in both precipitation index methods. The fact that all five periods determined in the DPI method are Near Normal Drought may mean that the method gives more sensitive results in detecting drought periods.

The comparison of the 10-year averages of SPI and DPI values with each other can be seen in Figure 6. It was thought that index values with different classification ranges should be nondimensionalized to be compared. This process was done by dividing the SPI and DPI values by the average value. It can be stated that the 1981-1990 and 1991-2000 and 2001-2010, and 2011-2021 periods are equal and represent the same drought class. After all, with the SPI value being more significant than the DPI value in the years 1970-1980, it is seen that the SPI value points to the wet period and the DPI value to the drought period.

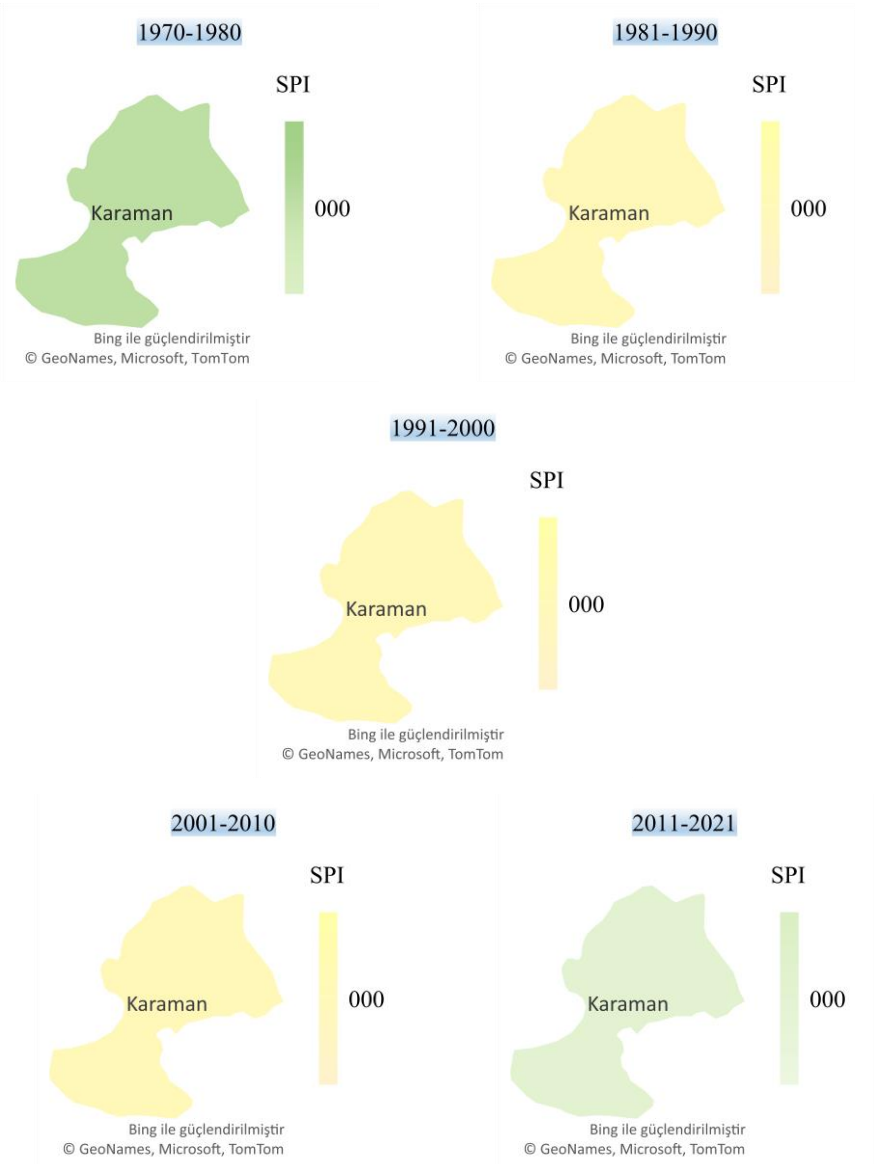

Fig. 4. The SPI values coloured by drought classifications.

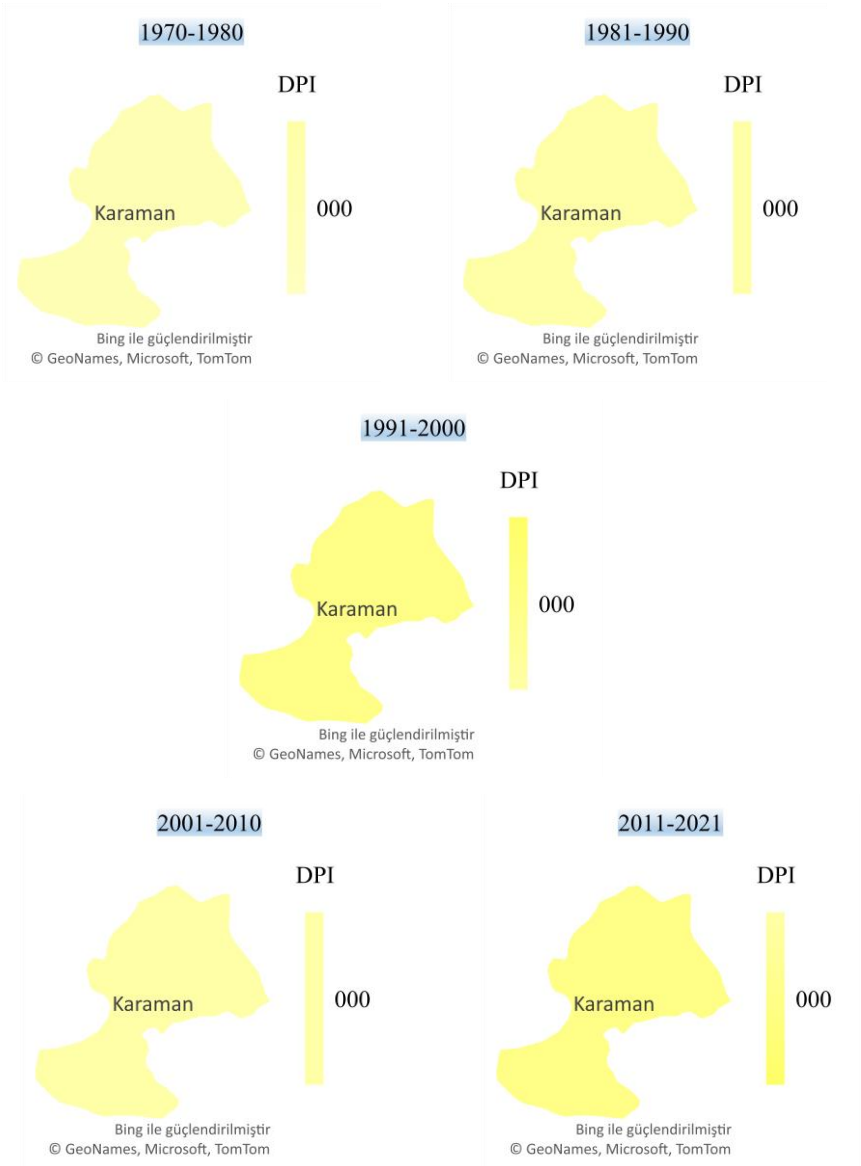

Fig. 5. The DPI values coloured by drought classifications.

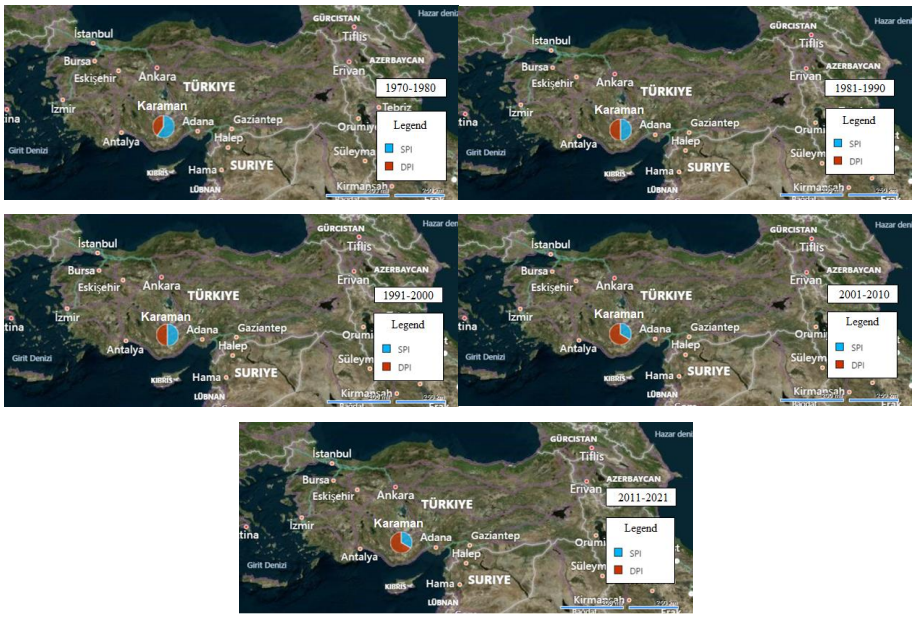

Fig. 6. Comparison of dimensionless SPI and DPI values.

After drought classification was performed according to the SPI and DPI values, the possibilities of occurrence were emphasized (Table 3 and Table 4). Tables 3 and 4 indicate the number of droughts occurring according to the SPI and DPI values, the probability of occurrence of each drought classification, and the expected residence time, respectively. The results showed that the SPI values indicate the Near Normal Wet periods with 40%, while according to the DPI method, the Medium Dry period was determined as 56%.

Table 3. Probability of occurrence of the SPI values

	SPI		
	Number of Drought Classes	Drought class probabilities	Expected Residence Time (Year)
Extremely Drought	0	0%	0
Severely Drought	3	6%	1
Moderately Drought	6	11%	1
Near Normal Drought	16	30%	1
Near Normal Wet	21	40%	2
Moderately Wet	2	4%	1
Severely Wet	4	8%	1
Extremely Wet	1	2%	1

Table 4. Probability of occurrence of the DPI values

	DPI		
	Number of Drought Classes	Drought class probabilities	Expected Residence Time (Year)
Extremely Drought	0	0%	0
Severely Drought	4	8%	1
Moderately Drought	29	56%	2
Near Normal Drought	18	35%	1
Near Normal Wet	1	2%	1

As a result of the study, although there is an impression that the precipitation values in the Karaman region have tended to decrease in the last 20 years, it can be deduced that serious drought effects have not occurred yet. The findings support that the DPI suggested in previous studies gives more sensitive results than the SPI.

4 Conclusions

In this study, the analysis of drought and wet periods investigation was carried out using 52 years of precipitation data from Karaman province central MGM station located in Konya Closed Basin. SPI and DPI drought indices were used to determine the drought and wet periods. In the relevant data, while the maximum precipitation value was seen in 1976 and the minimum precipitation value was observed in 1973, the driest and wettest periods, according to the SPI method, occurred in the specified years, respectively. While the number of determined wet periods was higher in the SPI method, more drought periods were detected than in the DPI method. This situation can be interpreted that the DPI method can provide more sensitive results in drought detection in general.

On the other hand, with the annual averages of both drought indices, the Near Normal Drought period took place between 1981 and 2010. Even though the DPI method is effective in the entire 52-year period, the Near Normal Wet period is observed in the SPI method in the 1970-1981 and 2011-2021 periods. As a result, it is predicted that studies can be done with different drought indices in order to continue the water resources engineering studies that can be done in the region more efficiently and that the results obtained within the scope of this study will contribute to the applications planned to be made in the future.

References

1. Thomas, J. and Prasannakumar, V.: Temporal analysis of rainfall (1871–2012) and drought characteristics over a tropical monsoon-dominated State (Kerala) of India. Journal of Hydrology, 534, 266-280 (2016). https://doi.org/10.1016/j.jhydrol.2016.01.013
2. Yacoub, E., Tayfur, G.: Evaluation and assessment of meteorological drought by different methods in Trarza region, Mauritania. Water Resources Management, 31(3):825–845 (2017). https://doi.org/10.1007/s11269-016-1510-8

3. Danandeh, Mehr, A., Sorman, A.U., Kahya, E., Hesami, Afshar, M.: Climate change impacts on meteorological drought using SPI and SPEI: case study of Ankara Turkey. Hydrol Sci J. (2019) https://doi.org/10. 1080/02626667.2019.1691218
4. Yüce, M., Eşit, M.: Ceyhan Havzası'nın kuraklık risk haritasının SPI ve SPEI metotları ile belirlenmesi. Su Kaynakları, 5 (2), 1-8 (2020). https://dergipark.org.tr/en/pub/su/issue/56995/728965
5. Yüce, M.İ., Aksoy, H., Aytek, A., Eşit, M., Uğur, F., Yaşa, İ., Şimşek, A., Değer İ.H.: Samsun province drought analysis with SPI and SPEI. Kahramanmaras Sutcu Imam University Journal of Engineering Sciences. 256(3),285-295 (2022). https://doi.org/10.17780/ksujes.1108663
6. World Meteorological Organization (WMO): Guidelines on the definition and monitoring of extreme weather and climate events —TT-DEWCE WMO 4/14/2016. World Meteorological Organization, Geneva. (2016).
7. Gümüş, V., Başak, A and Oruç, N.: Drought analysis of Şanlıurfa Station with Standard Precipitation Index (SPI). Harran University Journal of Engineering. 1, 36-44 (2016).
8. Liu, C., Yang, C., Yang, Q., and Wang, J.: Spatiotemporal drought analysis by the standardized precipitation index (SPI) and standardized precipitation evapotranspiration index (SPEI) in Sichuan Province, China. Scientific Reports, 11(1), 1-14 (2021). https://doi.org/10.1038/s41598-020-80527-3
9. Mehr, A.D., Vaheddoost, B.: Identification of the trends associated with the SPI ans SPEI indices accross Ankara, Turkey. Theoretical and Applied Climatology. 139:1531-1542 (2020). https://doi.org/10.1007/s00704-019-03071-9
10. Mukherjee, S, Mishra, A, Trenberth, K.E.: Climate change and drought: a perspective on drought indices. Curr Clim Chang Rep 4:145–163 (2018). https://doi.org/10.1007/s40641-018-0098-x
11. Palmer, W.C.: Meteorological Drought. U.S. Department of Commerce, Weather Bureau. (1965).
12. Van, Rooy, M.P.: A Rainfall Anomaly Index (RAI) independent of time and space. Notos 14:43–48 (1965).
13. Shafer, B. A., Dezman, L. E.: Development of surface water supply index (SWSI) to assess the severity of drought condition in snowpack runoff areas. Proceedıng Of The Western Snow Conference (1982).
14. McKee, T.B, Doesken, N.J., Kleist, J.: The relationship of drought frequency and duration to time scales.8th Conference on Applied Climatology, 17-22 January, Anaheim, CA, 179-184 (1993).
15. Tsakiris, G., Pangalou, D., Vangelis, H.: Regional drought assessment based on the Reconnaissance Drought Index (RDI). Water Resources Management, 21, 821-833 (2007).
16. Shukla, S., Wood, A.W. Use of a standardized runoff index for characterizing hydrologic drought. Geophysical research letters, 35(2) (2008).
17. Vicente-Serrano, S. M., Beguería, S., López-Moreno, J. I.:A multiscalar drought index sensitive to global warming: the standardized precipitation evapotranspiration index. Journal of climate, 23(7), 1696-1718 (2010). https://doi.org/10.1175/2009JCLI2909.1
18. Tayfur, G. Discrepancy precipitation index for monitoring meteorological drought. Journal of Hydrology, 597, 126174 (2021). https://doi.org/10.1016/j.jhydrol.2021.126174
19. Technical Assistance for Conversion of Basin Protection Action Plans to River Basin Management Plans. Konya Closed Basin Management Plan (2018). TR2011/0327.21-05-01-001, Access: 23.03.2023
20. Turhan, E., Değerli, S., Çatal, E.N.: Long-term hydrological drought analysis in agricultural irrigation area: The case of Dörtyol-Erzin Plain, Turkey. Curr. Trends Nat. Sci, 21, 501-512 (2022). doi: https://doi.org/10.47068/ctns.2022.v11i21.054

Tracking Climate Change Impact on Droughts in Northern Cyprus Through Standardized Precipitation Index

Ma'in Ghanem [1], Hasan Zaifoğlu [2][0000-0003-2615-5097]

[1] Sustainable Environment and Energy Systems Department, Faculty of Engineering, Middle East Technical University, Northern Cyprus Campus, Kalkanli, Guzelyurt via Mersin 10, Türkiye
[2] Civil engineering Department, Faculty of Engineering, Middle East Technical University, Northern Cyprus Campus, Kalkanli, Guzelyurt via Mersin 10, Türkiye

Abstract. Understanding the distinct attributes of droughts and their variability assumes critical significance in water resources management, as it aids in the effective mitigation of potential damage. Climate change is anticipated to have significant implications for future droughts with regard to precipitation patterns and temperature. In this context, this study employed the standard precipitation index (SPI) to investigate the drought events in some major cities in Northern Cyprus, utilizing the precipitation stations of Boğaz, Lefkoşa, Güzelyurt, and Mağusa. The drought characteristics were evaluated for two distinct time intervals: 1979-2014, using observed monthly precipitation station data, and 2014-2040, using biased corrected climate model data for moderate (RCP 4.5) and high (RCP 8.5) greenhouse gas emissions scenarios. The SPI was computed for multiple timescales, including 3-, 6-, 9-, and 12-month durations, to examine various drought types. Subsequently, the Mann-Kendall and Sen's slope statistical tests were implemented to assess the trends and their magnitudes. The results indicate that the SPI series based on observed precipitation data from all stations did not exhibit statistically significant trends at the 5% level of significance. However, the SPI3, which is commonly used to indicate meteorological drought, displayed declining trends for the near future period at Boğaz, Mağusa, and Güzelyurt stations, with respective reductions of 0.026, 0.026, and 0.043 per year, respectively. Additionally, a significant downward trend with a rate of 0.038/year was observed for the SPI6 in the future, which represents agricultural drought, at the Güzelyurt station, one of the primary agricultural regions in Northern Cyprus. The study ultimately employs the beneficial precipitation deficit metric to illustrate the distinctive features of both historical and future droughts, with the goal of guiding decision-makers in implementing preventive measures to address the irreversible impacts of droughts.

Keywords: Drought; Standard Precipitation Index; Climate Model; Northern Cyprus.

1 Introduction

Droughts are recognized as one of the most dangerous natural hazards globally. They have a wide spatial impact, initiated by a continuous rainfall deficiency, known as a meteorological drought, if prolonged, it leads to agricultural drought affecting the crop production. Over time, the severity escalates to hydrological droughts affecting river flows and reservoir storages. Finally, these conditions are resulted in socioeconomic droughts leading to severe effects, such as migration [1]. The effects of droughts in Cyprus have been severe as of lately. During the 1976 – 2016 period, the island was considered among the European countries with the highest drought frequencies. Characterized with 40% lower water supply to dams relative to sub-1970's periods, and 1998-2010 period being 20% more dry than the past 900-year droughts [2], [3]. Severe drought events occurred in the 1989-1992, 1995-1998 periods, followed by the 2007-2009 drought, characterized as one of the worst in history, causing water shortages up to 6.8% in major dams, reducing crop production [4].

In the future, climate change will have major effects on the climatic patterns in the Mediterranean region. Giorgi and Lionello [5] showed that a collective 20-25% decrease in precipitation, in addition to 4-5°C increase in temperatures in the Mediterranean region until 2100. Giannakopoulos et al. [6] narrowed the analysis to Cyprus, uncovering similar trends with varying severities.

To date, minor efforts have been spent to quantify climate change effects on drought characteristics in the island of Cyprus. This paper aims to employ the standard precipitation index to analyze droughts for the study area. Particularly, the analysis encompasses the historical interval from 1979 to 2014, as well as the near future span from 2014 to 2040. The characteristics of the major droughts alongside past and projected trends, will be thoroughly investigated. This work will provide a summary for future drought expectations, and work as a baseline for decision making in Northern Cyprus.

2 Study Area and Datasets

The research area selected for this study is located in Northern Cyprus, where the climate is semi-arid, characterized with warm, long summers and mild winters. Specifically, the focus was on drought conditions in the main districts of Boğaz, Güzelyurt, Lefkoşa and Gazimağusa. They were chosen due to their dense population, and coverage of the diverse climatic, topographic, geographic, and hydrologic conditions in Northern Cyprus. Historical precipitation data spanning from 1979 to 2014 was obtained for the stations from the meteorological office of Northern Cyprus [7]. The spatial distribution of the Boğaz, Güzelyurt, Lefkoşa and Gazimağusa stations are presented in Fig. . Table 1 provides information on the longitude, latitude, elevation, and average annual rainfall for each station. Boğaz, located near the Kyrenia Mountains exhibits the highest elevation and annual rainfall among the chosen stations. In contrast, the other stations are located in Mesaoria plain, attributed with lower annual rainfalls and elevations. Future precipitation for the period of 2014-2040 was obtained

from EURO-CORDEX [8]. A collection of future projections was acquired from the 3 different combinations of global climate models (GCM) and regional climate models (RCM), each featuring a grid resolution of 0.11° (approximately 12.5 km). These ensemble members include the pairs of ICHEC-EC-EARTH and GERICS-REMO2015; IPSL-IPSL-CM5A-MR and SMHI-RCA4_v1; and NCC-NorESM1-M and GERICS-REMO2015_v1. The models included two emission scenarios, namely, the moderate emission scenario (RCP4.5) and highest emission scenario (RCP8.5), to simulate drought conditions under both conditions. It is important to note that the climate model data employed in this study comprises bias-corrected datasets.

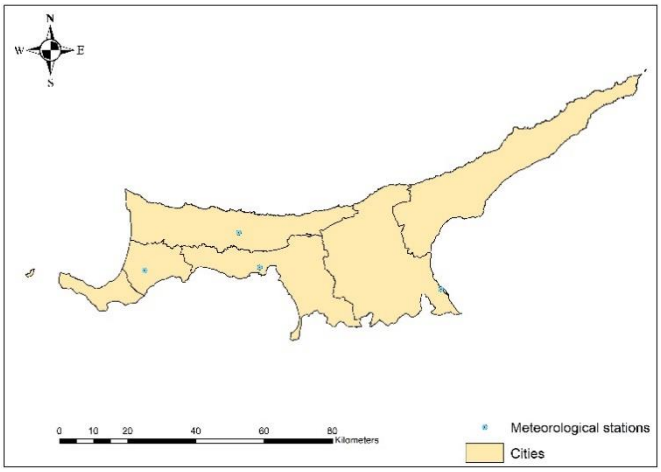

Fig. 1. Location of meteorological stations.

Table 1. Characteristics of meteorological stations.

Station	Latitude (°)	Longitude (°)	Elevation (m)	Average annual rainfall (mm)
Boğaz	35.28825	33.28484	300	401.3
Gazimağusa	35.18889	32.98194	52	284.2
Güzelyurt	35.19639	33.35194	134	306.8
Lefkoşa	35.13639	33.93556	10	332.7

3 Methodology

3.1 Standard Precipitation Index (SPI)

The SPI index is a powerful and commonly used tool for drought detecting and monitoring, utilizing only precipitation data for calculation, providing a level of simplicity. The index can be calculated through fitting long term precipitation data to a

gamma distribution, later transformed to a normal distribution with a mean of zero. The SPI can be calculated with the following equation [9]:

$$SPI = \frac{(X_i - \bar{X})}{\sigma} \tag{1}$$

where X_i is the rainfall value for month i, $\bar{X}$ is the long-term average rainfall, and σ is the standard deviation. Here, i depends upon the monitored drought type. In this study, meteorological droughts were defined using a 3-month time scale, while agricultural droughts were characterized using a 6-month time scale. Additionally, hydrological droughts were delineated based on 9- and 12-month time scales. The calculated SPI values are classified according to Table , as commonly used in the literature. [10]. SPI values were validated through their predictive ability of the 1989-1992, 1995-1998, 2007-2009 drought events.

Table 2. Classification of droughts based on SPI values.

Class	Extremely drought	Severe drought	Moderate drought	Near normal	Moderately wet	Severely wet	Extremely wet
SPI value	SPI ≤ -2	−2.0 < SPI < −1.5	−1.49 < SPI < −1.0	−1.0 ≤ SPI ≤ 1.0	1.49 < SPI < 1.0	2.0 < SPI < 1.5	2.0 ≤ SPI

3.2 Mann- Kendall Trend Test

The Mann-Kendall test was utilized to investigate the statistical trends in the historical and future monthly SPI values. It was chosen due to its ability to measure the monotonic trends without assuming linear trend or normal distribution, and it is especially useful for the long meteorological measurements [11]. The test statistics of Mann-Kendall, S, can be calculated as [12]:

$$S = \sum_{i-1}^{n-1} \sum_{j-1+1}^{n} \text{sgn}\left(x_j - x_i\right) \tag{2}$$

where n is the sample size, x_i and x_j are the time series values ranked from $i = 1, 2 \ldots n-1$ and $j = i+1, 2 \ldots n$, and $\text{sgn}\left(x_j - x_i\right)$ is the sign function depending on:

$$\text{sgn}\left(x_j - x_i\right) = \begin{cases} +1, & \text{if } x_j - x_i > 0 \\ 0, & \text{if } x_j - x_i = 0 \\ -1, & \text{if } x_j - x_i < 0 \end{cases} \tag{3}$$

The variance statistic is given by:

$$\text{Var}\,(S) = \frac{n(n-1)(2n+5) - \sum_{i=1}^{m} t_i(i)(i-1)(2i+5)}{18\ \text{ZS}} \tag{4}$$

where t_i is the number of ties up to the sample value i. Finally, The standardized Z_S statistic is calculated as:

$$Z_S = \begin{cases} \dfrac{S-1}{\sqrt{\sigma^2(S)}}, & \text{if } S > 0 \\ 0, & \text{if } S = 0 \\ \dfrac{S+1}{\sqrt{\sigma^2(S)}}, & \text{if } S < 0 \end{cases} \quad (5)$$

where if $|Z_S| > 1.96$ at $\alpha = 0.05$, the null hypothesis is rejected, and there exists a trend in the data.

3.3 Sen's Slope Estimator

The Sen's slope estimator is a non-parametric test used to quantify the magnitude and the direction of the trends. Positive and negative values of Sen's slope represent increasing and decreasing trends respectively. Furthermore, the highest the absolute value of the slope, the stronger the trend. The magnitude of the trend is computed by [13] :

$$T_i = \frac{x_j - x_k}{j - k} \quad (6)$$

where x_j and x_k are data points in which $j > k$. The median of the T_i values, counted up to N, represents the Sen's slope as follows:

$$Q_i = \begin{cases} T_{\frac{N+1}{2}} N \text{ is odd} \\ 1/2 \left(T_{\frac{N}{2}} + T_{\frac{N+2}{2}} \right) N \text{ is even} \end{cases} \quad (7)$$

4 Results and Discussion

4.1 Historical SPI and Validation (1979-2014)

The study analyzed historical SPI values calculated for the timescales of 3, 6, 9 and 12 months. **Fig.** shows a sample of the calculated SPI values for the Güzelyurt region. The figures reveal that the presence of many drought periods occurring during the studied times. Focusing upon the known droughts of 1989-1992, 1995-1998, 2007-2009, shows that at SPI3, the meteorological droughts occurred especially during the winter and spring months. SPI6 shows the accumulation of the droughts resulting in the agricultural droughts, the most severe of which was in 1989-1992. The SPI9 and SPI12 clearly demonstrated the progression of these droughts to the hydrological droughts, with 1989-1992 and 2007-2009 being most critical. An additional drought was

inspected in the 1981-1985 period, with moderate severity. Interestingly, a start of another drought was found at the end of the series in the year of 2014. The analyses of the Boğaz, Lefkoşa and Gazimağusa showed similar results with Güzelyurt, capturing droughts in the same years. The ability of the calculated SPI values to capture the observed droughts validated the use of the same methodology for future prediction.

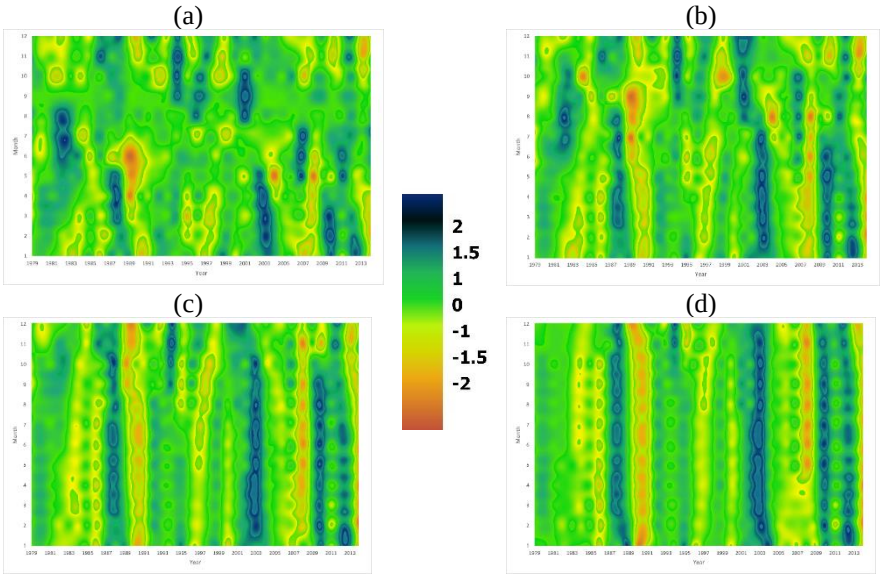

Fig. 2. The SPI for the Güzelyurt station at scales (a) SPI3, (b) SPI6, (c) SPI9, (d) SPI12.

4.2 Historical Trends in SPI

Table presents the calculated Mann-Kendall test statistic values (Z_S) and Sen's slope (Q_i) values found for historical SPI values, examined both annually and monthly. The analysis revealed that when SPI values were aggregated to the annual scale, no statistically significant trends were detected. Similarly, the monthly scale Z_S indicated the absence of significant trends in the SPI3 values, implying no change in meteorological drought occurrence. In contrast, the occurrence of agricultural drought, as represented by SPI6, exhibited positive trends in the Gazimağusa and Lefkoşa stations, with slope values of 0.0008/month and 0.0009/month, respectively. Furthermore, Gazimağusa and Lefkoşa also showed positive trends in SPI9, with slope values of 0.001/month and 0.0008/month, respectively. Moreover, hydrological droughts, represented by SPI12, displayed positive trends in the Boğaz, Gazimağusa and Lefkoşa stations, with slopes of 0.0009, 0.0011 and 0.0008, with Gazimağusa being the most critical. Historically, throughout the observed period, only positive trends were observed, indicating no significant increase in drought occurrence.

Table 3. Mann-Kendall and Sen's slope for historical SPI (1979-2014).

	Z_S (Q_i)							
Stations	SPI3		SPI6		SPI9		SPI12	
Scale	A	M	A	M	A	M	A	M
Boğaz	0.43 ------	1.08 ------	0.74 ------	1.08 ------	0.68 ------	1.80 ------	0.57 ------	**2.34** (0.0009)
Gazimağusa	0.48 ------	1.75 ------	0.68 ------	**2** (0.0008)	0.82 ------	**2.34** (0.001)	0.91 ------	**2.71** (0.0011)
Güzelyurt	0.68 ------	0.78 ------	0.43 ------	1.06 ------	0.51 ------	1.36 ------	0.23 ------	1.45 ------
Lefkoşa	1.39 ------	1.67 `------	1.65 ------	**2.28** (0.0009)	0.94 ------	**2.10** (0.0008)	0.54 ------	**1.97** (0.0008)

Note: Bold values represent statistically significant trends, and A and M represent annual and monthly scales, respectively.

4.3 Near Future SPI Under RCP4.5 and RCP8.5 Climate Scenarios

Fig. illustrates the computed SPI for the Güzelyurt Station under the RCP4.5 conditions. It was observed that four major drought events were anticipated for the RCP4.5 climate scenario. Firstly, the mildest drought was expected in 2019, characterized by minor meteorological droughts, which subsequently led to a hydrological drought, shortly ending in 2020. Furthermore, a severe drought was projected for the 2025-2027 period. The most severe drought was anticipated to transpire in the period of 2031-2033, as presented in the figure. Finally, the year of 2034 was expected to be a very wet year, shortly followed by a drought which persisted in the period of 2035-2037. The mentioned droughts were expected to affect the Boğaz, Gazimağusa and Lefkoşa stations, with varying severity and duration. For instance, the 2025-2026 drought exhibited longer duration and higher severity in Lefkoşa and Boğaz stations, extending until 2028. Conversely, under the RCP8.5 climate scenario, the droughts in Güzelyurt were projected to be prolonged and more severe. The first drought was expected to span from 2017 to 2019, followed by a second highly severe drought for the period of 2027-2030. A third drought took place in the period of 2033-2035. The Lefkoşa and Gazimağusa stations shared similar RCP8.5 patterns to Güzelyurt, with more severe and prolonged. Conversely, the projected Boğaz events varied across different climate scenarios, with certain droughts anticipated to exhibit increased severity and duration, while others demonstrated an opposing trend. This variation can be attributed to discrepancies in elevation and rainfall patterns between the Boğaz station and other stations.

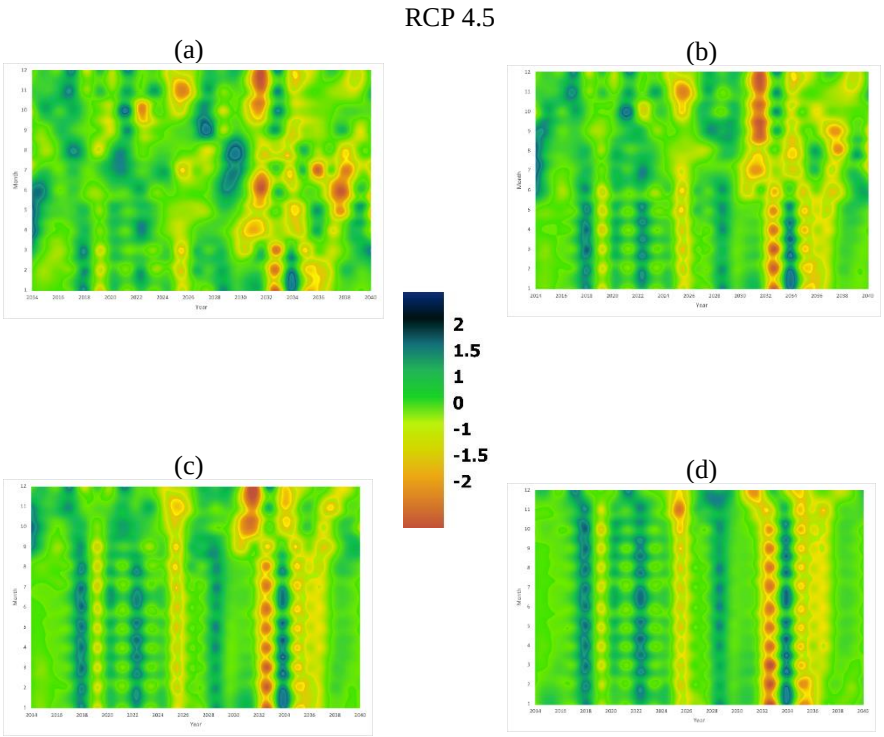

Fig. 3. SPI for the Güzelyurt station at scales (a) SPI3, (b) SPI6, (c) SPI9, (d) SPI12.

4.4 Near Future Trends Under RCP4.5 and RCP8.5

Table presents the results of the Mann-Kendall and Sen's slope test values for the near future SPI, considering both the annual and monthly series under the RCP4.5 and RCP8.5 climate scenarios. For the RCP4.5 scenario, the significant negative trends were found at both annual and monthly scales. On the annual scale, the significant decreasing trends were detected in the SPI3 values for Boğaz, Gazimağusa and Güzelyurt, with the Sen's slopes of -0.026/year, -0.026/year, and -0.043/year, respectively. Güzelyurt was attributed with a major negative trend in SPI6, with a measured slope of -0.038/year. However, no significant trends were detected for the hydrological droughts, represented by annual SPI9 and SPI12 values. When extending SPI to the monthly scales, significant negative trends were observed across all the stations, under all measured SPI's, except the Gazimağusa Station, which showed no trends under SPI12.

On the other hands, the results of the RCP8.5 trend analysis showed no significant trends in the Lefkoşa and Boğaz stations. In Gazimağusa Station, the significant positive trend was observed in SPI12, with a slope of 0.002/month, indicating lower hydrological drought occurrence. The Güzelyurt station on the other hand, displayed

significant negative trends in the SPI6, SPI9 and SPI12, all with measured slopes of -0.001/month.

Table 4. Mann-Kendall and Sen's slope results for the near future SPI (2014 -2040).

RCP 4.5								
	$Z_S\ (Q_i)$							
Stations	SPI3		SPI6		SPI9		SPI12	
Scale	A	M	A	M	A	M	A	M
Boğaz	**-2.29** (-0.026)	**-4.44** (-0.003)	-1.81 ------	**-4.65** (-0.003)	-1.72 ------	**-4.80** (-0.003)	-1.81 ------	**-4.7271** (-0.003)
Gazimağusa	**-2.20** (-0.026)	**-3.85** (-0.002)	-1.72 ------	**-2.89** (-0.002)	-0.93 ------	**-1.87** (-0.001)	-0.22 ------	-1.17 ------
Güzelyurt	**-3.13** (-0.043)	**-4.79** (-0.003)	**-2.47** (-0.038)	**-4.89** (-0.003)	-1.85 ------	**-4.19** (-0.003)	-1.63 ------	**-4.48** (-0.003)
Lefkoşa	-1.59 ------	**-3.21** (-0.002)	-1.59 ------	**-3.41** (-0.002)	-1.28 ------	**-3.89** (-0.003)	-1.06 ------	**-4.33** (-0.003)
RCP 8.5								
	$Z_S\ (Q_i)$							
Stations	SPI3		SPI6		SPI9		SPI12	
Scale	A	M	A	M	A	M	A	M
Boğaz	-0.22 ------	-0.68 ------	0.04 ------	-0.37 ------	0 ------	-0.70 ------	0.31 ------	-0.41 ------
Gazimağusa	0 ------	-0.03 ------	1.01 ------	1.08 ------	1.01 ------	1.81 ------	1.06 ------	**2.19** (0.002)
Güzelyurt	-0.97 ------	-1.85 ------	-0.40 ------	**-2.01** (-0.001)	-0.26 ------	**-1.95** (-0.001)	-0.48 ------	**-2.21** (-0.001)
Lefkoşa	0.66 ------	0.14 ------	0.48 ------	0.87 ------	0.88 ------	1.17 ------	1.01 ------	1.89 ------

Note: Bold values represent statistically significant trends, and A and M represent annual and monthly scales, respectively.

5 Conclusion

Over the past few decades, Northern Cyprus experienced major droughts, causing substantial economic damages. In the future, predicting these droughts before they occur would be an excellent way to assist the management in decision making and preparation. This study aims to achieve this objective by utilizing historical gauge measurements, and bias corrected climate model data, to forecast near future droughts in four major cities. The results presented the meteorological, agricultural, and hydrological droughts, analyzing their past trends and characteristics, and the near future expectations under the RCP4.5 and RCP8.5 scenarios.

The analysis of the historical SPI values (1979-2014) confirmed the occurrence three major droughts: the 1989-1992 drought, the 1995-1998 drought, and the 2007-2009 drought, validating the accuracy of predicted SPI values. Historical trends in SPI values

were tested utilizing the Mann-Kendall and Sen's slope tests, uncovering no trends on the annual scale but significant positive trends at the monthly scale in the Boğaz, Gazimağusa and Lefkoşa stations.

Analysis of the near future (2014-2040) SPI values, specifically the RCP4.5 and RCP8.5 scenarios, predicted the occurrence of two main droughts: one in the 2027-2030 period, followed by a 2033-2035 drought. Moreover, the trend analysis covering both climate models detected significant negative trends in both scenarios, indicating an increased likelihood of drought occurrence in the future across all studied stations. The Güzelyurt station in particular, showed significant negative trends in SPI6, measured in two scales as -0.038/year and -0.003/month, signifying more severe agricultural droughts.

Considering the agricultural and economic importance of Güzelyurt, producing 98% of the Citrus fruits in Northern Cyprus, which form up to 80% of foreign currency exports, agricultural droughts will be detrimental if not adequately prepared for [14]. Therefore, the local authorities are advised to implement a drought management system, considering the importance of future drought prediction and preparation.

References

1. T. A. Awchi and M. M. Kalyana, "Meteorological drought analysis in northern Iraq using SPI and GIS," Sustain Water Resour Manag, vol. 3, no. 4, pp. 451–463, Dec. 2017, doi: 10.1007/s40899-017-0111-x.
2. A. H. Payab and U. Türker, "Comparison of standardized meteorological indices for drought monitoring at northern part of Cyprus," Environ Earth Sci, vol. 78, no. 10, p. 309, May 2019, doi: 10.1007/s12665-019-8309-x.
3. B. I. Cook, K. J. Anchukaitis, R. Touchan, D. M. Meko, and E. R. Cook, "Spatiotemporal drought variability in the Mediterranean over the last 900 years," Journal of Geophysical Research: Atmospheres, vol. 121, no. 5, pp. 2060–2074, Mar. 2016, doi: 10.1002/2015JD023929.
4. D. Myronidis, K. Ioannou, D. Fotakis, and G. Dörflinger, "Streamflow and Hydrological Drought Trend Analysis and Forecasting in Cyprus," Water Resources Management, vol. 32, no. 5, pp. 1759–1776, Mar. 2018, doi: 10.1007/s11269-018-1902-z.
5. F. Giorgi and P. Lionello, "Climate change projections for the Mediterranean region," Glob Planet Change, vol. 63, no. 2–3, pp. 90–104, Sep. 2008, doi: 10.1016/j.gloplacha.2007.09.005.
6. C. Giannakopoulos, P. Hadjinicolaou, E. Kostopoulou, K. V. Varotsos, and C. Zerefos, "Precipitation and temperature regime over Cyprus as a result of global climate change," Advances in Geosciences, vol. 23, pp. 17–24, Feb. 2010, doi: 10.5194/adgeo-23-17-2010.
7. MANC, "Meteorologic Gauge Data," Ankara, 2016.
8. EURO-CORDEX, "Model 1: ICHEC-EC-EARTH (Ireland)-GERICS-REMO2015 (Germany) ", "Model 16: IPSL-IPSL-CM5A-MR (r1i1p1) SMHI-RCA4_v1", "Model 18: NCC-NorESM1-M (r1i1p1) GERICS-REMO2015_v1," 2022.
9. A. S. Tefera, J. O. Ayoade, and N. J. Bello, "Comparative analyses of SPI and SPEI as drought assessment tools in Tigray Region, Northern Ethiopia," SN Appl Sci, vol. 1, no. 10, p. 1265, Oct. 2019, doi: 10.1007/s42452-019-1326-2.

10. A. Mossad and A. A. Alazba, "Determination and prediction of standardized precipitation index (SPI) using TRMM data in arid ecosystems," Arabian Journal of Geosciences, vol. 11, no. 6, p. 132, Mar. 2018, doi: 10.1007/s12517-018-3487-5.
11. Naz, Dars, Ansari, Jamro, and Krakauer, "Drought Trends in Balochistan," Water (Basel), vol. 12, no. 2, p. 470, Feb. 2020, doi: 10.3390/w12020470.
12. W. Kalisa et al., "Spatio-temporal analysis of drought and return periods over the East African region using Standardized Precipitation Index from 1920 to 2016," Agric Water Manag, vol. 237, p. 106195, Jul. 2020, doi: 10.1016/j.agwat.2020.106195.
13. P. K. Sen, "Estimates of the Regression Coefficient Based on Kendall's Tau," J Am Stat Assoc, vol. 63, no. 324, pp. 1379–1389, Dec. 1968, doi: 10.1080/01621459.1968.10480934.
14. M. Ergil, "The salination problem of the Guzelyurt aquifer, Cyprus," Water Res, vol. 34, no. 4, pp. 1201–1214, Mar. 2000, doi: 10.1016/S0043-1354(99)00253-5.

Estimation of Design Rainfalls in Cyprus Under Nonstationary Conditions

Hasan Zaifoglu[1][0000-0003-2615-5097]

[1] Middle East Technical University, Northern Cyprus Campus, Civil Engineering Program, Kalkanli, Guzelyurt via Mersin 10, Türkiye, zhasan@metu.edu.tr

Abstract. The estimation of design rainfalls is a critical aspect of hydrological and hydraulic design in various water resources management applications. However, under changing climatic conditions, the traditional statistical methods that assume stationarity in the data may no longer be appropriate. To investigate nonstationarity, the study employed the Pettitt test, Modified Mann-Kendall test, and simple linear regression analysis. These tests were utilized to determine the breakpoints before and after potential shifts in series means, assess the significance, and quantify the magnitude of trends, respectively. The results indicated a statistically significant upward trend in three out of the five annual maximum rainfall series (AMR) for meteorological stations, which are located in major flood-prone cities in Cyprus. However, Lefkosa and Guzelyurt stations displayed upward trends that were not statistically significant. With the nonstationary frequency analysis carried out in this context, the utilization of stationary models has led to the underestimation of design precipitation, resulting in significant deviations in quantile estimates with return levels of 2, 20, and 100 years reaching up to 31%, 38%, and 26%, respectively. Consequently, it is imperative that engineering designs should take into account the nonstationarity of extreme precipitation to mitigate the risk of increasingly hazardous infrastructures.

Keywords: Design rainfall, Nonstationary frequency analysis, Cyprus.

1 Introduction

In the process of hydraulic structure design, the estimation of design rainfalls holds significant importance, typically achieved through the utilization of frequency analysis based on historical datasets. Traditionally, the assumption of a stationary process has prevailed for numerous years, implying that rainfall time series are independent and identically distributed [1]. However, recently, the stationary assumption has garnered controversy, primarily due to the impacts of climate change on rainfall frequencies and intensities, as well as human activities like land use changes. Particularly, the presence of the variability patterns in extreme rainfalls poses a challenge to the validity of conventional hydraulic engineering designs. Consequently, this raises concerns about the reliability of determined hydrologic risks and infrastructure designs, potentially leading to an increased risk of failure for hydraulic structures [2]. To make contribution to this discussion in the field of hydrology, researchers worldwide have undertaken

numerous investigations and developed new techniques to address the cases where nonstationary exists [3, 4].

The Gumbel distribution, generalized extreme value (GEV) distribution, Log-Pearson Type III distribution, and generalized Pareto distribution (GPD) have been commonly employed in frequency analyses of climatic series [5]. However, in cases where nonstationarity is observed in the extreme value series, the nonstationary GEV models are mostly preferred [6]. Numerous studies have demonstrated the superior performance of nonstationary GEV models in accurately estimating the probabilities of extreme events [7]. Therefore, both stationary and nonstationary GEV models are employed in the present study to comprehensively address the varying characteristics of extreme events.

To address the assumption of nonstationarity, a widely employed technique entails modeling probability distributions in which the distribution parameters are permitted to exhibit temporal variations or respond to other pertinent physical covariates. By adopting this approach, the dynamic nature of hydrological processes is acknowledged, and the influence of changing conditions and factors on rainfall patterns is considered. In the literature, the exploration of nonstationarity has predominantly relied on nonparametric trend tests, such as the Mann-Kendall test or its modified versions. Additionally, the investigation of covariates in explaining the nonstationary behavior has predominantly focused on the temporal aspect, i.e. using time as covariate, with limited systematic incorporation of hydro-meteorological data as covariates [8].

The main aim of this study is to assess the presence of nonstationarity in the selected flood-prone urban centers of Cyprus. This is achieved by employing the homogeneity test of Pettitt and conducting trend analysis using the modified Mann-Kendall (MMK) test and simple linear regression analysis. In addition, a comparison is made between the design rainfall quantiles obtained from stationary and nonstationary models within the frequency analysis framework. The purpose of this comparison is to reveal the importance of employing nonstationary approaches in the design processes, emphasizing the need to consider changing climatic conditions and their potential impact on flood risk assessment and infrastructure design.

2 Study Area and Datasets

2.1 Description of Study Area

The island of Cyprus, situated in the eastern Mediterranean Sea, is subject to the prevailing Mediterranean climate regime. During the winter months, the weather is generally mild, accompanied by limited precipitation, while the summer season brings hot and arid conditions. The island's topography is characterized by a diverse landscape, encompassing the Kyrenia Mountains Range running parallel to the northern coastline, the Mesaoria Plain situated at the island's center, the Karpass Peninsula, and the Troodos Mountains dominating the southwestern region of Southern Cyprus. Consequently, these local geographical variations significantly influence precipitation patterns. In Northern Cyprus, for instance, the mean annual precipitation varies, with

the Western Mesaoria Plain experiencing a minimum of approximately 260 mm, while the Kyrenia Mountains receive a maximum of nearly 550 mm. Thus, to effectively represent different regions, meteorological stations have been carefully selected to cover the diverse characteristics of various regions of the island.

2.2 Annual Maximum Rainfall Series (AMR)

The present study utilized rainfall data in the form of average daily rainfall values obtained from the meteorological stations of the Meteorological Office of Northern Cyprus. Initially, the daily rainfall series from each station were organized and converted into the water year format. Subsequently, these series were manipulated to derive the annual maximum rainfall (AMR) series for each individual station.

Table 1 provides descriptive characteristics of the AMR series from five specific stations that were selected for analysis. Based on the statistical analysis, it is evident that the Girne and Bogaz stations, situated on the north coast and parallel to the Kyrenia mountains, respectively, recorded the highest values for AMR. Conversely, the Lefkosa Station exhibited the minimum AMR value, and Guzelyurt demonstrated the lowest average AMR. Fig. 1 illustrates the locations of the meteorological stations used in this study, named as Bogaz, Lefkosa, Guzelyurt, Magusa, and Girne stations.

Table 1. Characteristics of meteorological stations.

	Meteorological stations				
Characteristic	Bogaz	Lefkosa	Guzelyurt	Magusa	Girne
Observation period	1976-2018	1976-2015	1977-2015	1977-2015	1977-2015
Latitude (◦)	35.28825	35.19639	35.18889	35.13639	35.34194
Longitude (◦)	33.28484	33.35194	32.98194	33.93556	33.33139
Elevation (m)	300	134	52	10	10
Maximum value (mm)	190.0	97.4	100.7	104.7	215.3
Minimum value (mm)	23.5	11.6	16.1	21.5	27.0
Mean Value (mm)	65.0	41.5	35.5	48.0	71.6
Standard deviation (mm)	40.3	16.1	19.2	19.0	42.5
Kurtosis coefficient	2.7	2.6	3.5	1.0	3.0
Skewness coefficient	1.7	1.0	1.8	1.2	1.6

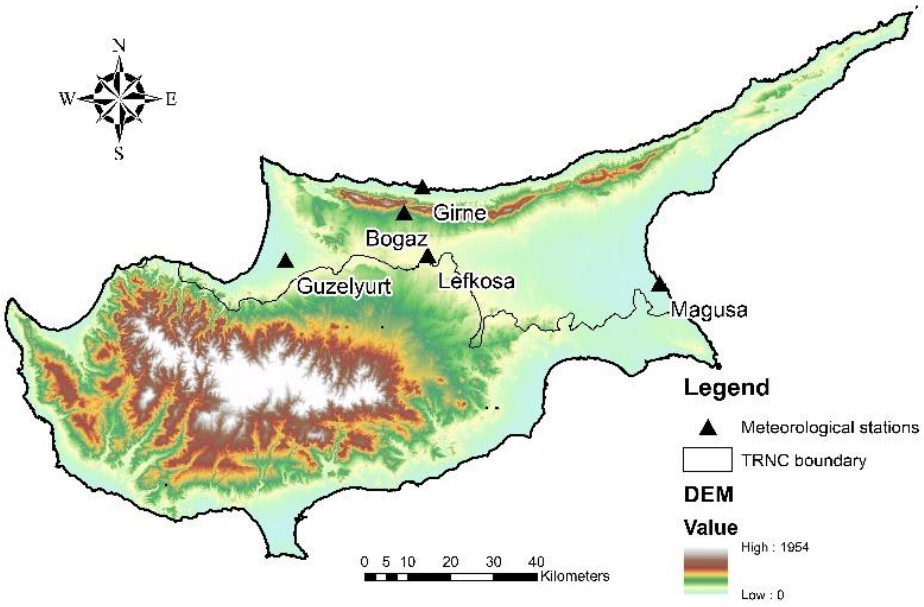

Fig. 1. Locations of meteorological stations.

3 Methodology

3.1 Breakpoint Detection and Trend Tests

The Pettitt's test [9] is an essential statistical method utilized for the identification of abrupt changes in the mean of a time series to detect the breakpoint. As a non-parametric test, it boasts the advantage of not relying on any presumptions concerning the underlying data distribution. The test statistic is computed as follows:

$$S_p = \max_k \left| \sum_{i=1}^{k} \sum_{j=i+1}^{n} \operatorname{sgn}(X_i - X_j) \right| \tag{1}$$

where k varies from 1 to n, n is the sample size, nd S_p exhibits significantly high values in the presence of a data shift. The breakpoint, denoted by k, represents the position where this abrupt change occurs based on the maximum value of S_p. For the purpose of statistical inference, the Pettitt's test provides an approximate p-value as

$$p = 2\exp\left(\frac{-6S_p^2}{n^2 + n^3}\right) \tag{2}$$

The Mann-Kendall test [10, 11] represents a widely adopted nonparametric method employed for the detection of monotonic trends in data. The test statistic (S) used in the test is calculated as:

$$S = \sum_{i=1}^{n-1} \sum_{j=i+1}^{n} \operatorname{sgn}(X_i - X_j) \tag{3}$$

Herein, serial correlation is a prevalent concern encountered in time series data analysis. The modified Mann-Kendall (MMK) test incorporates a variance correction approach [12], which effectively accounts for the presence of serial correlation within the dataset. The proposed modified variance, $V^*(S)$ of the statistic S can be found as:

$$V^*(S) = V(S) \cdot \frac{n}{n^*} \tag{4}$$

where $V(S)$ is the variance of the S in the classic Mann-Kendall test and n^* is the effective sample size.

The least squares linear regression method represents a parametric approach employed for examining the presence of a linear trend within time series data. In the context of this study, the aforementioned method is utilized to ascertain the magnitude of the observed trends. To achieve this objective, a linear regression equation is formulated, establishing a relationship between the time variable and the AMR series:

$$y = \beta x + \beta_0 \tag{5}$$

where y and x variables are dependent and independent variables, respectively, β is the slope of the regression line, and β_0 is the intercept.

3.2 Frequency Analysis of Rainfall

The frequency analysis of annual maximum rainfall involves the application of the generalized extreme value (GEV) distribution. This distribution is employed to construct both stationary (time-invariant) and nonstationary (time-variant) probability distribution models, which aim to describe the nonstationary characteristics inherent in the AMR series. The cumulative distribution of nonstationary GEV can be written as:

$$F(z) = \exp\left\{-\left[1 + \varepsilon\left(\frac{z-\mu}{\sigma}\right)\right]^{-1/\varepsilon}\right\} \tag{6}$$

Herein, μ, σ, and ε are the location, scale, and shape parameters, respectively. In the nonstationary models, the shape parameter is assumed to remain constant due to its high sensitivity to data and associated uncertainty. Conversely, the location and scale parameters are expressed as functions of a time covariate. On the other hand, in the stationary model, all distribution parameters remain constant throughout the time period under consideration. Therefore, the models can be identified as follows: Model

1 (M1) represents the stationary model with constant parameters; Model 2 (M2) denotes the nonstationary model, where the location parameter is expressed as a linear function of time; Model 3 (M3) signifies the nonstationary model, where the scale parameter is expressed as a linear function of time, incorporating a logarithmic function to ensure positive values; and finally, Model 4 (M4) represents the nonstationary model, where both the location and scale parameters are expressed as functions of time. The overview of the evaluated models can be found in Table 2.

Table 2. Characteristics of meteorological stations.

Model	Location parameter (μ)	Scale parameter (σ)	Shape parameter (ε)
M1	constant	constant	constant
M2	$\mu(t) = \mu_0 + \mu_1 t$	constant	constant
M3	constant	$\ln[\sigma(t)] = \varphi(t) = \varphi_0 + \varphi_1 t$	constant
M4	$\mu(t) = \mu_0 + \mu_1 t$	$\ln[\sigma(t)] = \varphi(t) = \varphi_0 + \varphi_1 t$	constant

Furthermore, for the purpose of selecting the most appropriate GEV model in terms of goodness of fit, the Bayesian information criterion (BIC) and the Akaike information criterion (AIC) are employed. In both criteria, lower values indicate a superior fit of the model to the data. Hence, the model with the lowest BIC and AIC scores is considered to provide the best fit among the candidate GEV models. Here, the BIC [13] and AIC [14] are calculated as follows based on the number of parameters (k) and the likelihood function (L):

$$\mathrm{BIC} = k\ln(n) - 2\ln(L) \tag{7}$$

$$\mathrm{AIC} = 2k - 2\ln(L) \tag{8}$$

4 Results and Discussion

4.1 Assessment of Nonstationarity and Trend Analysis

In the investigation of nonstationarity in meteorological stations, a two-step approach was employed. Firstly, the AMR series were partitioned into two subseries at the breakpoints identified using the Pettitt test. Subsequently, the mean and standard deviations of these subseries were computed, and their changes were assessed through the calculation of relative differences. The results presented in Table 3 indicate that the maximum relative differences both in mean and standard deviation for the subseries before and after the breakpoints were observed at Bogaz Station. Specifically, the mean exhibited a substantial increase of 105%, rising from 52.2 mm to 107.2 mm, while the standard deviation increased by 130%, from 23.8 mm to 54.6 mm. On the other hand, the lowest relative change occurred at Lefkosa Station with 21% increase, followed by Guzelyurt Station showing 27% raise. Across all stations, positive relative difference values were found for the means, ranging from 21% to 105%. This suggests an overall increase in the AMR series between the identified subseries.

Similarly, with the exception of Girne Station, which displayed a decrease of 36% in standard deviation, the remaining stations demonstrated an increase in the standard deviations of the subseries, ranging from 36% to 130%. It is worth to note that the observed values at Girne Station were found to be closer to the mean after the breakpoint, displaying the lowest relative difference. Following Girne Station, the Lefkosa series exhibited a relative difference of 45%, which was also significant.

Table 3. Changes in mean and standard deviation before and after the breakpoints in AMR series for each station.

Statistic	Bogaz	Lefkosa	Girne	Magusa	Guzelyurt
μ before breakpoint (mm)	52.2	38.2	63.7	42.9	30.3
μ after breakpoint (mm)	107.2	46.3	83.2	58.7	38.4
Relative difference (%)	105	21	31	37	27
σ before breakpoint (mm)	23.8	13.2	48.0	13.1	14.3
σ after breakpoint (mm)	54.6	19.1	30.7	24.9	21.1
Relative difference (%)	130	45	-36	90	47.2

The locations of breakpoints in the stations, along with the trend test statistics and trend slopes, are provided in Table 4. The analysis reveals a lack of overall consistency in the distribution of breakpoints. However, it is worth noting that Lefkosa and Girne stations exhibited similar breakpoints in the AMR series during the subsequent water years of 1998-1999 and 1999-2000. Despite this observation, it was challenging to establish a clear association between these breakpoints and a common natural or anthropogenic factor. as they exhibited significant differences.

The temporal variations of annual maximum rainfall series were investigated by using the modified Mann-Kendall test at the 5% significance level, and the magnitude of the existing trends were examined utilizing simple linear regression models. Table 4 shows the calculated test statistics and p-value for the MMK test, as well as the slopes of the developed regression models for the AMR series in five meteorological stations.

The results indicate that the MMK test yielded positive test statistic values, indicating increasing trends in all stations. Upon analyzing the p-values, statistically significant upward trends were identified in Bogaz, Girne, and Magusa stations, which would increase the flood risk there. Conversely, in the remaining two stations (Lefkosa and Guzelyurt), the observed trends were not significant at the 5% significance level. These findings align with the previously discussed results based on the relative differences in the AMR series before and after the breakpoints. The stations displaying significant trends also exhibited the highest relative differences in the means of the subseries. Specifically, at Bogaz Station, the average of the AMR subseries increased from 52.2 mm to 107.2 mm; at Girne Station, it increased from 63.7 mm to 83.2 mm; and at Magusa Station, it increased from 42.9 mm to 58.7 mm. These increases in the means could be attributed to the significantly increasing trends observed in those stations.

Furthermore, the slopes of the simple linear regression models ranged from 0.13 mm/year to 1.17 mm/year, indicating the rate of change for the observed upward trends

in the stations. The highest and lowest increasing rates were identified at Bogaz and Lefkosa stations, respectively. Particularly, Bogaz Station exhibited a significant trend with an increasing rate of 1.17 mm/year, Girne Station displayed a significant trend with an increasing rate of 0.5 mm/year, and Magusa Station showed a significant trend with an increasing rate of 0.55 mm/year.

Table 4. Breakpoint and trend analysis test results.

	Pettitt Test	Modified Mann-Kendall Test		Simple Linear Regression
Station	Breakpoint	Test statistic	p-value	Slope
Bogaz	2008-2009	**2.73**	0.006	1.17
Lefkosa	1998-1999	0.45	0.653	0.13
Girne	1999-2000	**3.76**	0.000	0.50
Magusa	2002-2003	**3.99**	0.000	0.55
Guzelyurt	1990-1991	1.16	0.245	0.27

Note: Bold values represent statistically significant trends.

4.2 Design Rainfalls with Stationary and Nonstationary Conditions

The stationary and nonstationary frequency analyses of the AMR series utilizing GEV distribution were carried out, and the best-fitting models were decided by the BIC and AIC criteria. Table 5 presents the estimated parameters of the best-fitting models, along with their corresponding BIC and AIC values.

According to the table, for the stations of Guzelyurt and Lefkosa, where no statistically significant trend was observed, stationary models were found to be the best-fit models. This finding aligns with the results obtained from the trend analysis. Conversely, at Bogaz, Girne, and Magusa stations, where the MMK test identified significant trends at the 5% significance level, nonstationary models were preferred for fitting. Particularly, for Bogaz and Magusa stations, the best-fit models were the nonstationary models with both location and scale parameters varying with time, referred to as M4 models. On the other hand, at Girne Station, the superior model was the nonstationary M2 model, with only the location parameter varying with time.

Table 5. Parameters of stationary and nonstationary best-fitting models.

	μ		$\ln[\sigma(t)]$					
Stations	μ_0	μ_1	φ_0	φ_1	ε	BIC	AIC	Best-fitting model
Bogaz	45.06	6.23	2.94	0.26	0.34	424.55	415.74	Model 4
Lefkosa	34.73	-	2.61	-	-0.07	333.62	328.63	Model 1
Girne	49.83	7.47	3.07	-	0.36	373.44	366.99	Model 2
Magusa	40.49	4.03	2.52	0.39	-0.01	321.94	313.88	Model 4
Guzelyurt	25.55	-	2.28	-	0.37	311.44	306.61	Model 1

In the design process of hydraulic infrastructures such as stormwater sewer systems, dams etc., the selection of return levels for design rainfall is crucial. Commonly used quantiles for design purposes are the 2-, 20-, and 100-year return levels, which correspond to annual exceedance probabilities (AEP) of 50%, 5%, and 1%, respectively. Fig. 2 presents a comparison of estimates obtained from stationary and nonstationary models for all stations.

The results indicate that the design rainfall estimates derived from nonstationary models consistently yielded higher values compared to those obtained from stationary models. Specifically, for the 2-year return level, which represents a common rainfall event, the discrepancies in rainfall estimates ranged from 3% to 31%. The largest difference was observed at Bogaz Station, followed by Magusa and Girne Stations. These findings highlight that the stations where nonstationarity prevailed exhibited higher discrepancies in the estimation process.

In terms of the 20-year return level, the largest disparity in estimates were observed at Magusa Station, with differences ranging from 1% to 38%. Conversely, Guzelyurt Station exhibited the lowest disparity of 1%, as the process was considered stationary. Moving on to the 100-year return level, which represents rare rainfall events, Magusa and Bogaz stations exhibited the highest differences in estimates, 26% and 22% relative differences, respectively. Particularly, the design rainfall estimates increased from 124.7 mm to 157.5 mm at Magusa Station, and from 314.0 mm to 384.4 mm at Bogaz Station. In other words, this suggests that the return level of a design rainfall calculated using the traditional stationary approach significantly decreases when calculated using a nonstationary model.

5 Conclusion

This study aimed to investigate the presence of nonstationarity in the annual maximum rainfall series of five meteorological stations located in flood-prone cities in Cyprus. The research was prompted by the increased frequency of flood events observed in various parts of the island. To comprehend the nonstationarity in the series, comprehensive analyses were conducted, including breakpoint detection, trend analysis, and stationary and nonstationary frequency analysis. The datasets were fitted with the Generalized Extreme Value distribution, and the best-fitting models were determined based on the Bayesian Information Criterion and Akaike Information Criterion.

The results demonstrated that the findings from the trend analysis were consistent with those obtained from the frequency analysis. Stations that exhibited statistically significant trends could be adequately explained using nonstationary models. Additionally, substantial discrepancies were observed, with differences of up to 31% for the 2-year return level, 38% for the 20-year return level, and 26% for the 100-year return level. These discrepancies have the potential to have significant consequences in terms of project cost and the hydrologic risk of failure of hydraulic structures, particularly for the regions of Bogaz, Girne, and Magusa.

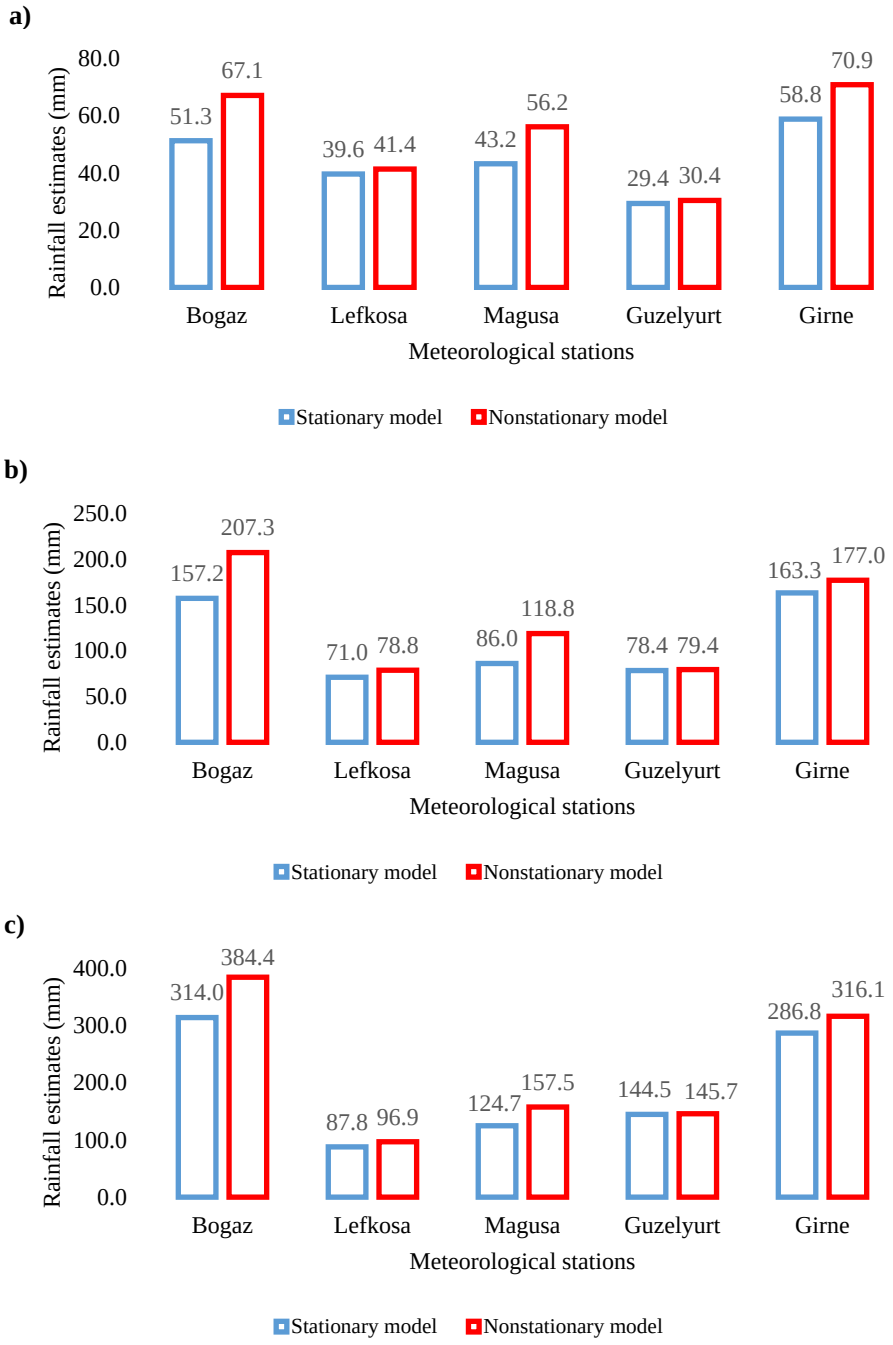

Fig. 2. Stationary and nonstationary model estimates for **a)** 2-year, **b)** 20-year, and **c)** 100-year return levels.

References

1. Nasri, B., Bouezmarni, T., St-Hilaire, A., Ouarda, T. B. Non-stationary hydrologic frequency analysis using B-spline quantile regression. Journal of Hydrology, 554, 532–544 (2017).
2. Jiang, R., Wang, Y., Xie, J., Zhao, Y., Li, F., Wang, X. Assessment of extreme precipitation events and their teleconnections to El Niño Southern Oscillation, a case study in the Wei River Basin of China. Atmospheric research, 218, 372-384 (2019).
3. Salas, J. D., Obeysekera, J. Revisiting the concepts of return period and risk for nonstationary hydrologic extreme events. Journal of hydrologic engineering, 19(3), 554-568 (2014).
4. Salas, J. D., Obeysekera, J., Vogel, R. M. Techniques for assessing water infrastructure for nonstationary extreme events: a review. Hydrological Sciences Journal, 63(3), 325-352 (2018).
5. Ansa Thasneem, S., Chithra, N. R., Thampi, S. G. Assessment of nonstationarity and uncertainty in precipitation extremes of a river basin under climate change. Environmental Modeling and Assessment, 26, 295-312 (2021).
6. Coles, S., Bawa, J., Trenner, L., Dorazio, P.: An introduction to statistical modeling of extreme values (Vol. 208, p. 208). Springer, London (2001).
7. Carney, M., Azencott, R., Nicol, M. Nonstationarity of summer temperature extremes in Texas. International Journal of Climatology, 40(1), 620-640 (2020).
8. Hesarkazzazi, S., Arabzadeh, R., Hajibabaei, M., Rauch, W., Kjeldsen, T. R., Prosdocimi, I., ... Sitzenfrei, R. Stationary vs non-stationary modelling of flood frequency distribution across northwest England. Hydrological Sciences Journal, 66(4), 729-744 (2021).
9. Pettitt, A. N. A non-parametric approach to the change-point problem. Journal of the Royal Statistical Society: Series C (Applied Statistics), 28(2), 126-135 (1979).
10. Mann, H. B. Nonparametric tests against trend. Econometrica: Journal of the econometric society, 245-259 (1945).
11. Kendall, M.G.: Rank correlation methods. Griffin, London, U.K (1975).
12. Yue, S., Wang, C. The Mann-Kendall test modified by effective sample size to detect trend in serially correlated hydrological series. Water resources management, 18(3), 201-218 (2004).
13. Schwarz, G. Estimating the dimension of a model. The annals of statistics, 461-464 (1978).
14. Akaike, H. A new look at the statistical model identification. IEEE transactions on automatic control, 19(6), 716-723 (1974).

Introduction of a Computer Software (S-Hammer) Developed to Analyze Fluid Transients in Pipelines

Saber Habibi Topraghghaleh[1][0000-0003-2989-6528] and Zafer Bozkuş[1][0000-0001-6863-3531]

[1] Middle East Technical University, Civil Engineering Department, Ankara, Türkiye,
saber.topraghghaleh@metu.edu.tr
bozkus@metu.edu.tr

Abstract. A computer program has been developed to address the tedious and time-consuming task of analyzing and simulating fluid transients in hydraulic systems. While there is already sophisticated software available for transient fluid simulations, the purpose of developing this program is to provide a local software solution specifically for teaching and research purposes, thus avoiding high license fees associated with existing software. The newly developed software is implemented using the C sharp programming language and employs the Method of Characteristics to solve the non-linear partial differential equations governing unsteady pipe flow. The primary objective of this software is to rapidly find solutions to a critical issue known as water hammer, which poses significant challenges for hydraulic engineers. Water hammer refers to the generation of pressure waves in a fluid when its flow rate undergoes sudden changes due to boundary conditions. This phenomenon can have severe consequences, even leading to fatal incidents. Consequently, it is crucial to consider water hammer during the design phase of pipelines to ensure safe and reliable operation once the system is operational. Numerous boundary conditions can trigger sudden changes in flow rate, such as valve opening or closing, pump trips, and load rejections or acceptances in turbines, among others. This paper introduces the newly developed software, focusing on a selection of important boundary conditions. Its accuracy is successfully validated through benchmark problems. Future studies aim to enhance the software by incorporating additional boundary conditions to further expand its capabilities.

Keywords: Pipelines, Water hammer, Fluid transients, Software development, Boundary Conditions

1 Introduction

Numerous reasons can cause a disturbance in the steady state of the flow in pipelines. When velocity changes at a fixed point in space, local accelerations or decelerations create supplementary mass forces in a transient flow, and this phenomenon causes corresponding changes in pressure. These can manifest themselves as prominent short-term pressure increases or decreases resulting from the sudden closing of valves, power failure of pumps and turbines, pump trips, or increased pressure losses caused by

pulsating flow. This extreme situation is, in general, called water hammer due to hammering sound in pipes.

Water hammer refers to unsteady hydraulic problems occurring in various systems such as hydropower plants, fluid transmissions, pipelines, and water networks. It creates significant pressure surges and waves, imposing high loads on the system. Neglecting water hammer can lead to catastrophic consequences such as pipe collapse, pump damage, and even loss of life. An example is the Sayano-Shushenskaya hydropower plant accident in Russia on August 17, 2008, where debris-induced turbine closure resulted in the destruction of a hydroelectric generator, severe damage to all generators, and the collapse of the turbine hall. This tragic event claimed 76 lives and caused a financial loss exceeding $310 million [1].

Bozkuş [2] performed a water-hammer analysis using MOC for the Çamlıdere-Ivedik Water Treatment Plant with multiple pipelines with different features. A FORTRAN program is used to simulate the transient event in the system for various conditions. Consequently, for considering the safety in case of a pipe break, to avoid pressure fluctuations in the pipelines, placing protection devices is recommended according to the results obtained. However, he just modified an existing program to perform the task.

A protective measurement has been studied by Çalamak and Bozkuş [3]. Researchers analyzed the reaction of the system caused by water hammer with a computer program using MOC and then ran the code for three different protective measurement scenarios in a case study and compared the results. The cases are instant load rejection with the effect of a flywheel, pressure relief valve, and safety membranes. They did this method on small hydropower plants with a focus on the safety of the system.

Dinçer [4] investigated water hammer problems in the penstocks of pumped-storage power plants. The results were also presented by Dinçer and Bozkuş [5]. They used an available code to solve transient events that are produced by sudden load rejection of the turbine, first with a surge tank and second without it. With the results obtained, they checked and compared the two scenarios to see the effect of protection devices.

Another study has been done by Dalgıç [6], who focused on developing computer-based analyses for pipelines. He developed a computer program by using the method of characteristics, which can solve equations of basic unsteady pipe flows, as mentioned previously. The developed software is named H-Hammer and operates with external help from MS Excel, Visual Basic, and AutoCAD. Numerous boundary conditions are included in the study. For testing the software, he compared his results with those given in the well-known textbooks and concluded that they agreed well. However, his software depended on previous knowledge of AutoCAD, rendering it not so user-friendly.

In the present study of Topraghghaleh [7], the main idea is to develop a brand new software to analyze and simulate the transient pipe flow conditions, which can help engineers to consider essential measures in order to avoid devastating pressure changes while water hammer is happening. In order to do so, Windows-based software is deemed to be appropriate. To make it user-friendly, the software is independent of external programs. The program is presented with a user interface including a designer

canvas, database library, means for producing tables and graphics, wave speed and friction calculators, and other various features. Thoroughly performed simulations can help engineers to design a safer system and find quick and correct solutions, mainly for water hammer problems. This program can guarantee safe control of the system, and engineers can judge genuinely using the knowledge of pressure and discharge information calculated by this software. Furthermore, the program is user-friendly and can be easily used by users whose knowledge about the subject is limited. The ultimate goal of this study is to develop a local computer software that can be used safely for teaching and research purposes.

2 Transient Flow and Method of Characteristics

The condition of flow consists of two states, steady and unsteady. In steady-state flow, the flow conditions at a point, including discharge, pressure, and velocity, do not vary over time. However, in a transient flow, the mentioned properties change at a point in space over time, or in other words, flow is time-dependent. The term "transient" is usually employed to indicate the evolution of the solution over time from an initial steady state until it reaches the new steady-state condition. Between those steady-state conditions, the flow is unsteady. For solving the non-linear partial differential equations, the information of steady-state flow plays an essential role since the initial values are required to deal with the transients along with the boundary conditions. The term, water hammer is used when a transient event occurs in close conduits.

The water hammer analysis aims to determine fluid behavior throughout a transient event in the space and time domain. To achieve this goal, the conservation of mass and momentum principles must be applied. After having applied the conservation of continuity and momentum laws to a control volume in a pipe, the partial differential equations of unsteady flow are obtained.

These partial differential equations can be seen in Equations (1) and (2), in which P and V, pressure and velocity, respectively, are dependent variables.

$$\frac{\partial P}{\partial t} + V\frac{\partial P}{\partial x} + \rho a^2 \frac{\partial V}{\partial x} = 0 \tag{1}$$

$$\frac{\partial V}{\partial t} + V\frac{\partial V}{\partial x} + \frac{1}{\rho}\frac{\partial P}{\partial x} + g\sin\theta + \frac{4\tau_w}{\rho D} = 0 \tag{2}$$

In which,

P = Pressure (N/m^2), ρ = Density of the fluid (kg/m^3), V = Flow velocity (m/s), g = Gravitational acceleration (m/s^2), D = Diameter of the pipe (m), a = Wave speed (m/s), τw = Wall shear stress (N/m^2).

These two equations are non-linear, hyperbolic, partial differential equations in two dependent variables, velocity and pressure, and two independent variables, which are the time and the distance in the flow direction in the pipeline. These two non-linear partial differential equations can be transformed into four ordinary differential

equations using the MOC that Chaudhry [8] or Wylie and Streeter [9] explained in depth and are shown in Eqs. (3) and (4) in terms of the piezometric head (H=P/γ+z) and average flow velocity, V. Eqs. (3) and (4) called C+ and C- equations are written in two pairs. The upper equations are called compatibility equations and they are valid only if the lower equations are valid. The lower equations plot as straight lines in the x-t solution domain and are called the characteristic lines, Fig. 1.

$$C^{+}\begin{cases}\dfrac{g}{a}\dfrac{dH}{dt}+\dfrac{dV}{dt}+\dfrac{fV|V|}{2D}=0\\ \dfrac{dx}{dt}=+a\end{cases} \tag{3}$$

$$C^{-}\begin{cases}-\dfrac{g}{a}\dfrac{dH}{dt}+\dfrac{dV}{dt}+\dfrac{fV|V|}{2D}=0\\ \dfrac{dx}{dt}=-a\end{cases} \tag{4}$$

Where $F=g\sin\theta+f\dfrac{V|V|}{2D}$

The compatibility equations are put into finite difference equations, then, integrated on the characteristic lines to obtain algebraic forms finally to be used for the solution of the two unknowns, Q and H, in the x-t plane, for every node. To do so, a pipeline section is divided into N equal parts that form N+1 nodes to be solved for each time step. The time increment for the calculation scheme can be calculated as $\Delta t = \Delta x/a$, which is called the Courant condition. The x-t solution domain is shown in Fig. 1.

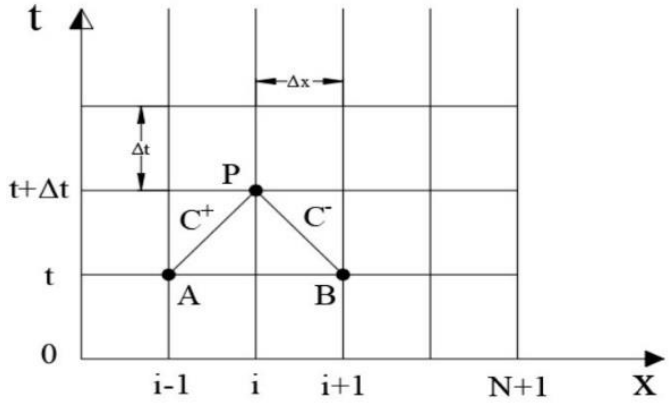

Fig. 1. Characteristics lines for the nodal solution in x-t plane

For any interior intersection point, in other words, at every nodal point, the two compatibility equations are solved simultaneously for the two unknown heads and velocity or discharge at that node. Numerical solutions for C+ and C- characteristic lines are obtained, as seen in Eqs. (5) and (6).

$$C^+ : H_{P_i} = C_P - BQ_{P_i} \tag{5}$$

$$C^- : H_{P_i} = C_M + BQ_{P_i} \tag{6}$$

C_P and C_M are always known, and constant values are obtained by Eq. (7) and (8).

$$C_P = H_{i-1} + BQ_{i-1} - RQ_{i-1}|Q_{i-1}| \tag{7}$$

$$C_M = H_{i+1} - BQ_{i+1} + RQ_{i+1}|Q_{i+1}| \tag{8}$$

Where $B = \frac{a}{gA}$, $R = \frac{f\Delta x}{2gDA^2}$

After obtaining the above equations, the head value at point P can be calculated by eliminating Q from equations (5) and (6). Then

$$H_{P_i} = (C_P + C_M)/2 \tag{9}$$

Discharge at point P can then be calculated from either Eq. (5) or (6). It should be noted that all known values of H and Q are from the preceding time step, either the result of the previous calculation or the initial value given at the beginning of the solution.

The solution scheme requires the knowledge of the boundary values whenever the last and first boundaries of the pipe are reached. Thus, boundary conditions should be defined and handled by special predefined functions.

It should be mentioned that to get the most accurate results and enable convergence, the so-called Courant condition must be satisfied. This condition imposes that

$$\frac{\Delta x}{\Delta t} \le a \tag{10}$$

3 The Developed Software

A computer software named S-Hammer is developed to analyze fluid transients in pipelines. The software was created using the C# programming language in the Visual Studio platform. C# is a modern and object-oriented programming language developed by Microsoft for .NET Technology. The syntax provides a C-like experience. The reason for choosing this software language is that Windows Forms Applications can design programs with a graphical interface that can run on our computer. At the same time, the high speed of the solution is one of our other reasons for preference.

The structure and details of transient equations were described. In order to simulate a transient analysis in terms of head and flow rate, the compatibility equations are calculated in space and time domain across the nodal points throughout the pipeline.

Now, to perform simulations for complex pipeline scenarios, there must be some relevant boundary conditions. The boundaries that are used in the development of the S-Hammer software are introduced and listed below:

- Single Pipe Section
- Series Pipes Connections
- Junction
- Upstream Reservoir with Constant Head
- Upstream Reservoir with Variable Head
- Single Centrifugal Pump
- Downstream Valve
- Downstream Dead End
- Surge Tank

In order to apply the drawings of the elements to the canvas, the component buttons were defined in the "Design" tab of the main form, as seen in Fig. 2.

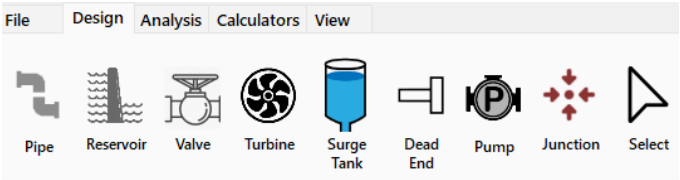

Fig. 2. Hydraulic System Elements Drawing Buttons

3.1 Main User Interface

This part is the main interface where the user works most of the time. All the visual aspects of the software can be found in this part. There are various functions on the main windows form with different menus that are available for the user. Some of the features of the main window are:

- The project tab: This is the first step in which the user starts or loads an available project, and when it started, then the project can be saved.
- The design tab: This tab includes the necessary buttons for design components, protection devices, drawing tools, and engineering libraries.
- View tab: The user can choose a theme for the user interface, and the colors of the background and grid of the canvas can be adjusted.
- Calculators tab: Wave speed and friction factor calculators are available.
- Analysis tab: The user gives the initial transient conditions for the system and can start the analysis. It should be mentioned that after starting the analysis if there is missing data for the solver library, the user will be warned about possible deficiencies. Moreover, table and chart forms are available.
- Canvas: this is where the user draws the hydraulic system.
- Properties: after drawing the system, the user must enter the required information for all the objects here.

Fig. 3 illustrates an image of the main form.

Fig. 3. The main user interface of the software

4 Validation of the Code

The validity of the software is performed by solving various cases and compared with different eminent sources. Hence, in this paper, most commonly encountered three cases are presented to demonstrate the validity of the software.

4.1 Pipes Connected in Series

A simulation is done by comparing the results of S-Hammer with the results of a case study conducted by Wylie and Streeter [9]. Fig. 3 shows the definition of the simulated system and the S-Hammer schematic view of the model. Three pipes are connected in a series configuration. Each pipe has a different length, diameter, and friction. The upstream boundary is a constant head reservoir, whereas the downstream boundary is a valve being closed incrementally in 1.8 s. Consequently, the valve closure is the initiator of the fluid transients. The problem is the determination of the head and discharge values in the pipeline for a duration of 2.1 s. The initial steady-state information needed to start the simulation is provided in Fig. 4. Also, the time interval, Δt for computations is chosen as 0.1 seconds so that the results will be comparable to the case study for numerical values computed at the same time steps. Moreover, the values for the valve closing operation are put as tabular data. This tabular data is presented in the case study.

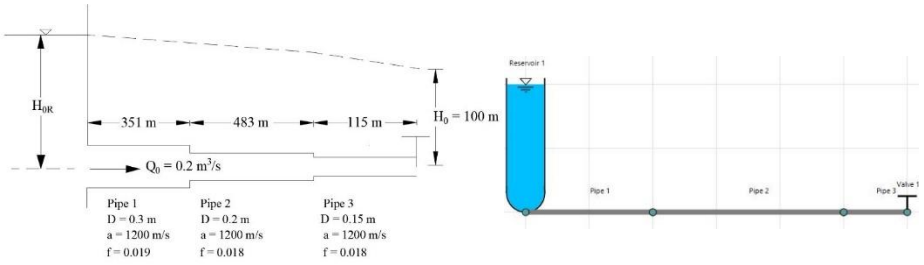

Fig. 4. Series pipes case study, Wylie and Streeter [9] and S-Hammer schematic view of the model

After sketching the system and putting the provided data in the S-Hammer software, the analysis is started, and results are obtained. Fig. 5 illustrates the pipe properties of the S-Hammer software after analysis.

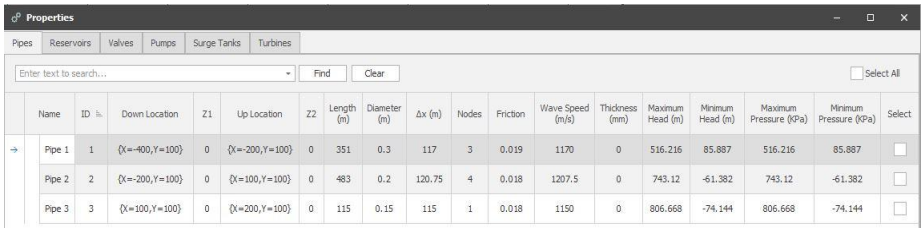

Name	ID	Down Location	Z1	Up Location	Z2	Length (m)	Diameter (m)	Δx (m)	Nodes	Friction	Wave Speed (m/s)	Thickness (mm)	Maximum Head (m)	Minimum Head (m)	Maximum Pressure (kPa)	Minimum Pressure (kPa)	Select
Pipe 1	1	{X=-400,Y=100}	0	{X=-200,Y=100}	0	351	0.3	117	3	0.019	1170	0	516.216	85.887	516.216	85.887	
Pipe 2	2	{X=-200,Y=100}	0	{X=100,Y=100}	0	483	0.2	120.75	4	0.018	1207.5	0	743.12	-61.382	743.12	-61.382	
Pipe 3	3	{X=100,Y=100}	0	{X=200,Y=100}	0	115	0.15	115	1	0.018	1150	0	806.668	-74.144	806.668	-74.144	

Fig. 5. Properties of the pipes of a case study by Wylie & Streeter after analysis

It should be mentioned that the values of the wave speed for all pipes are nominally given as 1200 m/s in the beginning. However, as can be seen in Fig. 4, wave speed values for pipes 1, 2, and 3 are adjusted during computations as 1170, 1207.5, and 1150 m/s, respectively. This is due to the grid-mesh ratio selection of the code so that the stability of the Courant condition is satisfied and does not affect the results considerably. Also, the number of nodes for each pipe is calculated according to the Courant condition. Additionally, various information such as Δx, maximum head, minimum head, maximum pressure, and the minimum pressure for each pipe is provided for the user.

Ultimately, a comparison of the results of S-Hammer software and Wylie and Streeter is made. These values are head and discharge values at the end junctions of the pipes. Fig. 6 shows the graphics of Head vs. Time, and Fig. 7 illustrates Discharge vs. Time at the valve end.

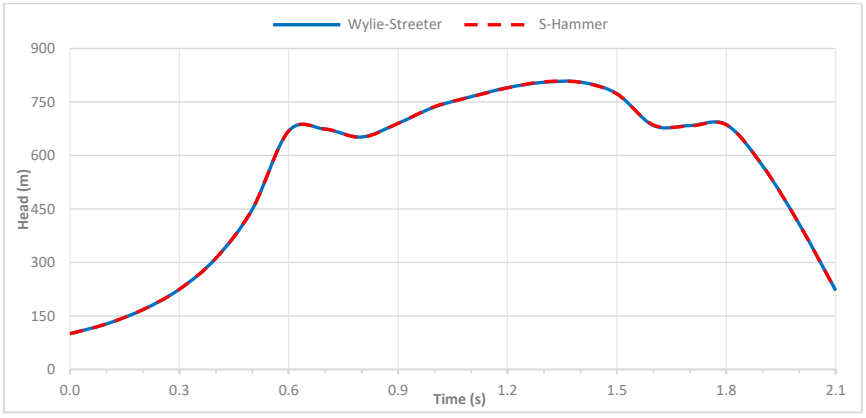

Fig. 6. H vs. Time comparison at the valve end (Wylie-Streeter vs. S-Hammer)

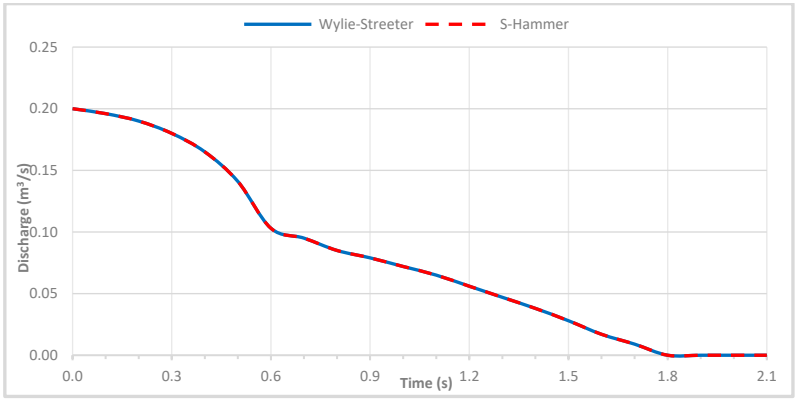

Fig. 7. Q vs. Time comparison at the valve end (Wylie-Streeter vs. S-Hammer)

5 Conclusions and Discussions

In this study, a program was developed to solve and analyze transients in pipelines with a number of user-defined transient scenarios (i.e., boundary conditions). The scenarios were selected carefully as they commonly occur in the engineering practice, and their proper considerations in the problem and measures to be taken if necessary are essential for the safe and reliable operations of such systems. To solve the transient equations, a widely known approach, the method of characteristics, was used in the code. In the previous sections, the theoretical background of this method and the derivation of its equations were briefly explained. Various boundary conditions were used in the code, and these boundaries are single pipe, series pipes, upstream reservoir with constant and variable head, single centrifugal pump, downstream valve closing, downstream dead-end, and a simple surge tank in a power plant. Of which only three cases are presented here.

The developed computer software has a visual user interface with numerous capabilities. The software finishes the analysis quickly and presents tabular and graphical results. Animations showing how the head or discharge varies with time over a pipeline can be performed. Detailed information about the program was explained in the present study by Topraghghaleh [7].

When analyzing a transient event with computer code, numerical stability is essential and critical. As long as the Courant condition is satisfied, no convergence problems are observed in the present study. One must select the properties of the designed system and its grid generation properly by paying great care to this aspect. For instance, the time increment selection plays a crucial role in terms of accuracy. To get more accurate results with a smaller time increment, more accurate and precise results can be obtained at the cost of more CPU time. This would be an important aspect to consider, especially for sophisticated hydraulic systems where there are many numbers of pipes and the boundary conditions are complex. As the newly developed software is planned to be improved and become more advanced in future studies, this aspect will be given more

attention. The time required to solve the case studies used to validate the developed program is presented in Table 1.

Table 1. Simulation time of S-hammer for benchmark studies

Case Studies	Maximum Time (s)	Time Step (s)	Simulation Time (s)
Single Pipe, Wylie & Streeter [9]	4.3	0.1	0.11
Series Pipes, Chaudhry [8]	10	0.5	0.09
Series Pipes, Wylie & Streeter [9]	2.1	0.1	0.08
Simple Surge Tank, Cofcof [10]	1500	0.34	0.82
Surge Tank with a Standpipe, Cofcof [10]	300	0.02	5.6
Pump Failure, Wylie & Streeter [11]	12	0.2	0.11

The validation of the results obtained by the software was done by comparing them with some well-known benchmarks. The comparisons are made graphically and numerically. Results showed that the output of the present study agrees with those of the benchmarks almost perfectly.

The logical structure of the program is user-friendly, and it is independent of any external application. To help users in working with the software, a user manual was prepared to guide them properly. It should be mentioned and emphasized that the program needs to be improved by adding more protection devices as new boundary conditions to compete in this field.

References

1. Seleznev VS, Liseikin A V, Bryksin AA, Gromyko P V. What Caused the Accident at the Sayano–Shushenskaya Hydroelectric Power Plant (SSHPP): A Seismologist's Point of View. Seismological Research Letters. 85(4), 817–824 (2014).
2. Bozkuş Z. Water hammer Analyses of Çamlıdere-Ivedik Water Treatment Plant (IWTP) Pipeline. Teknik Dergi. 19(2), 4409–4422 (2008).
3. Çalamak M, Bozkuş Z. Protective measures against waterhammer in run-of-river hydropower plants. Teknik Dergi. 23(4), 6187–6202 (2012).
4. Dinçer AE. Investigation of waterhammer problems in the penstocks of pumped-storage power plants. (2013).
5. Dinçer AE, Bozkuş Z. Investigation of Waterhammer Problems in Wind-Hydro Hybrid Power Plants. Arab J Sci Eng. 41(12), 4787–4798 (2016).
6. Dalgıç H. Development of a computer code to analyze fluid transients in pressurized pipe systems. (2017).
7. Topraghghaleh S.H. Software development for analyzing fluid transients in pipelines. Master's Thesis, Middle East Technical University, Ankara, Turkey (2020).
8. Chaudhry MH. Applied hydraulic transients. Springer.
9. Wylie EB, Streeter VL. Fluid transients. New York. (1978).
10. Cofcof Ş. Denge bacaları. (2011).
11. Wylie EB, Streeter VL, Suo L. Fluid transients in systems. Prentice Hall Englewood Cliffs, NJ. (1993).

Investigation of Interaction Between Pressure Relief Valve and Turbines During a Transient Flow in a Hydropower Plant

Mehmet Ali Çetintaş[1] [0000-0002-2004-6271], Zafer Bozkuş [2] [0000-0001-6863-3531] and Kutay Çelebioğlu[3] [0000-0001-8845-4928]

[1] Middle East Technical University, Civil Engineering Department, Ankara, Türkiye, mehmetalicetintas@gmail.com
[2] Middle East Technical University, Civil Engineering Department, Ankara, Türkiye, bozkus@metu.edu.tr
[3] TOBB University of Economics and Technology, ETU Hydro, Ankara, Türkiye, kutaycelebioglu@gmail.com

Abstract. The main goal of the present study, Çetintaş (2022), is to investigate the effect of pressure relief valve (PRV) on the hydraulic transients generated by multiple turbine operations. To achieve this goal, a numerical model of KEPEZ-I Hydropower plant (HPP) is constructed in the Bentley HAMMER software, which employs the Method of Characteristics (MoC) for computations. The MoC has been proven worldwide as a versatile and accurate tool for solving non-linear, hyperbolic, partial differential equations in space-time domain for hydraulic transients. The available field data for some specific turbine operations were used to calibrate the numerical model first. The simultaneously measured data from the field such as turbine closure and PRV opening adjustments, and pressure measurements were very useful in establishing and validating the numerical model in the software for the further analyses. Once the confidence was gained for the accuracy of the model a number of numerical simulations were performed for various turbine operations to understand the response of the plant to the transients. Since a pressure relief valve (PRV) is mounted in the hydropower plant already, the study mainly focuses on the effect of PRV on the transients generated by those turbine operations. Different scenarios such as instant load rejection, load acceptance, load variation are applied to the system with and without PRV. The operating conditions of the hydropower plant are analyzed, and the operation limits are determined to prevent any damage to the system by using the computer software. Potentially, most critical operational cases for the penstocks are selected, and the effects of the PRV are observed on the transient flow. It is found that PRV reduces approximately 50% of sudden pressure increase near the turbines. The power plant is protected against the adverse effects of water hammer transients as long as it is operated within the guidelines specified in the study.

Keywords: Waterhammer, PRV, Hydraulic Transients, HAMMER

1 Introduction

Hydropower plants have many advantages over other alternatives for energy production or electric generation. However, it is crucial to design and operate the hydropower plants properly to use them efficiently, which means continuously and reliably producing energy from the water. Some operating conditions may cause destructive results in the water conveying system while operating the hydropower plant to generate electricity. Generally, destructive phenomena occur in transient cases where flow parameters change with respect to time.

The main reason for the transient flow formation is the operational changes that cause sudden variations in the velocity of the flowing water, which in turn create rapid changes in pressures at the hydropower plant while in operation. Routine load acceptance, load variations, power failures, rapid valve closure, operational problems are examples of some of the sources of the changes in the system.

PRV is one of the protective measures that prevents the system from adverse effects of transient flow due to sudden changes in flow velocity. They are opened with the help of a spring or weight according to a set pressure point or they can be controlled by the governor with servomotors and behaves as a throttle control valve in the system. In KEPEZ – I HPP, PRV is controlled by the governor and opened with wicket gate closure operation in order to discharge the pressurized water from the system before excessive pressures are formed.

In this study, the KEPEZ-I Hydropower plant, which was rehabilitated in 2018 with MILHES project, is analyzed with the help of simulations by using computer software named HAMMER. Operational cases are investigated, and since the system has a surge tank and PRV, the effects of these protective measures are discussed by comparing the field data and simulation results. The place of the plant is in Antalya, Turkey. Models are constructed in computer software from the reservoir to the tailwater canal to simulate the transients using the same parameters used in real life. The hydropower plant has three turbine systems, the installed capacity of each turbine is 8.8 MW, and the total capacity of the facility is 26.4 MW. The penstocks convey water from forebay to the powerhouse.

The effects of the PRV are analyzed for different scenarios after computer software model is validated from field data which are collected from the tests for instant load rejection case. The software program uses unsteady pipe flow equations, namely, continuity and momentum. After simulation results obtained from the numerical model the results are validated with the help of measured field data, different scenarios will be undertaken, and results will be analyzed to find the most critical case. The advantages, disadvantages, and effects of the PRV and surge tank will be discussed by comparing the cases and considering the measured field data.

1.1 Literature Review

It is possible to go as far as Allievi (1902) or Joukowsky (1898) in the last quarter of the 19th century in order to summarize the early studies on fluid transients. It is also worth mentioning some researchers who contributed to the field in modern times, such as Streeter and Wylie (1993), Chaudhry(1987), Thorley (2004), and many others.

However, here the focus will be given on the various studies involving valve closure scenarios, HPPs, and protection measures, mainly the effect of PRVs on the transients generated by turbine operations

P.H. Azoury et al. (1986) presented an approach that uses method of characteristics with the help of a computer program to investigate the influences of valve closing behaviors on transients for a basic pipe system.

Hu Peicheng et al. (1989) studied the effect of impulse relief valve and safety membranes in the Libzgengqu Water Power Station in China.

Bozkuş (2008) simulated valve closure scenarios in a FORTRAN program that use method of characteristics to find optimum valve closure times in controlling water hammer.

Dursun (2013) and Dursun et al.(2015) analyzed the effect of the pressure relief valve on the water hammer pressures and turbine speed for Yeşilvadi Hydropower Plant.

Sepetçi et al. (2016) studied the preliminary design of the rehabilitation project of KEPEZ - I Hydropower Plant.

Çelebioğlu (2019) studied the effect of the calcination on the roughness coefficient of the pipeline in the KEPEZ – I Hydropower plant.

2 Transient Flow

Steady flow can be described as a condition where pressure, discharge, and velocity do not change over time at any point in the system. On the other hand, unsteady flow occurs when the mentioned flow parameters are changed with respect to time at a specific location. It can be said that a steady state is a particular instance of unsteady flow. Therefore, equations of the unsteady flow must satisfy steady flow cases. The term “transient flow” is used to describe an intermediate-stage flow that is observed when the flow conditions alternate between two steady states.

2.1 Governing Equations of Transient Flow

The transient flow analysis aims to determine the main parameters such as velocity, V or discharge, Q and pressure, P or piezometric head, H at a specific location and time while water hammer phenomena proceed. In order to find these variables, momentum and continuity equations have an essential role. The Law of mass conservation is used for the derivation of continuity equation, and Newton’s second law of motion is used for the momentum equation derivation. All the variables for the momentum equation are indicated in Figure 1. Pressure is assumed to be distributed uniformly over the

control surfaces, flow is assumed to be slightly compressible and one-dimensional, and pipe walls can be deformed as they are assumed to be elastic.

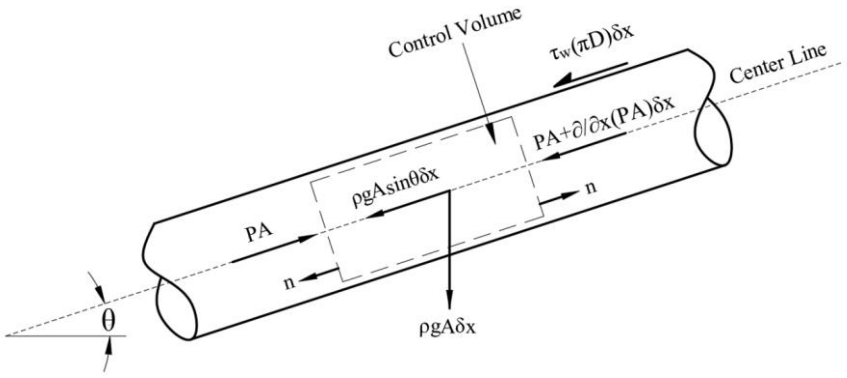

Fig. 1. Control volume that indicates parameters for momentum equation

Applying the conservation law of mass and Newton's second law of motion to the above control volume, continuity and momentum equations of unsteady flow in a pipe in partial differential forms can be obtained as below;

Continuity Equation:
$$\frac{\partial P}{\partial t} + V\frac{\partial P}{\partial x} + \rho a^2 \frac{\partial V}{\partial x} = 0 \quad (1)$$

Momentum Equation:
$$\frac{\partial P}{\partial t} + V\frac{\partial P}{\partial x} + \rho a^2 \frac{\partial V}{\partial x} = 0 \quad (2)$$

where, ρ is mass density of fluid (kg/m^3), P is pressure (N/ m^2), V is the fluid velocity (m/s), a is acoustic speed (m/s), τ_w is wall shear stress (N/m^2), D is pipe diameter (m), g is gravitational acceleration (m/s^2).

The continuity and momentum equations cannot be solved by using a closed-form solution. Next, these equations will be transformed into four ordinary differential equations by the Method of Characteristics.

2.2 Solution of Transient Flow Equations by Method of Characteristics

Method of characteristics transforms partial differential equations into four ordinary differential equations and enables numerical solutions by integrating the equations for two dependent variables: velocity and pressure. (Wylie et al., 1993). These equations are called compatibility equations which are as below;

$$C^+: \quad \frac{1}{\rho}\frac{dP}{dt} + a\frac{dV}{dt} + aF = 0 \quad if \quad \frac{dx}{dt} = +a \quad (3)$$

$$C^-: \quad \frac{1}{\rho}\frac{dP}{dt} - a\frac{dV}{dt} - aF = 0 \quad if \quad \frac{dx}{dt} = -a \quad (4)$$

Figure 2 indicates the characteristics lines in x-t plane. C+ characteristics line has the slope of "+1/a," and C^- characteristics line has the slope of "-1/a" representing Equations 3 and 4. These lines demonstrate the path of the transient flow physically.

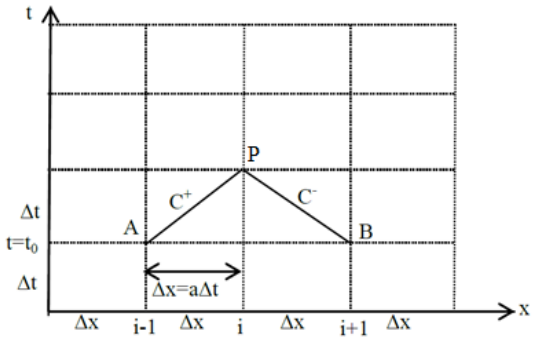

Fig. 2. Characteristics Lines in x-t solution domain

Integration of the compatibility equations along the characteristics lines gives the following equations in terms of H and Q.

$$C^+: \quad H_{Pi} = C_P - BQ_{Pi} \quad and \quad C_P = H_{i-1} + BQ_{i-1} - RQ_{i-1}|Q_{i-1}| \tag{5}$$

$$C^+: \quad H_{Pi} = C_P - BQ_{Pi} \quad and \quad C_P = H_{i-1} + BQ_{i-1} - RQ_{i-1}|Q_{i-1}| \tag{6}$$

were,

$$B = \frac{a}{gA} \qquad and \qquad R = \frac{f\Delta x}{2gDA^2} \tag{7}$$

3 Case Study and Discussion of Results

Input data are gathered for the model from the KEPEZ – I HPP projects and the hydropower plant is modeled in computer software named as Bentley HAMMER. Figure 3 indicates the HAMMER model that includes all the components of the system.

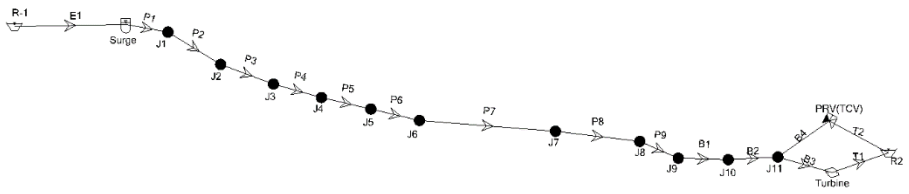

Fig. 3. Hammer model

Flow is conveyed from a reservoir having a water surface elevation of 278.3 m to surge tank by concrete energy tunnel. Corresponding surge tank steady-state water surface elevation is 278.04 m. Then, steel penstock transmits the water to the turbine whose center elevation is 111.05 m, and water reaches the tailwater level with 110.04 m elevation after energy dissipation is completed in the turbine. Table 1 indicates the elevations for the main nodes.

Table 1. Elevations of main nodes in model

Node	Elevation (m)
Reservoir 1	278.3
Surge Tank (bottom)	242.5
Turbine	111.05
PRV	111.05
Reservoir 2	110.04

According to design drawings of the HPP, pipe nodes are determined per bends, expansions, contractions, and branches in the pipeline system. Therefore, the model has 11 junctions between the surge tank and the rehabilitated turbine. All the pipe parameters are collected from the design drawings, and wave speed for each pipe is calculated accordingly. Table 2 shows the pipe parameters. Although there are three turbines with PRV in the facility, simulations are done for only one turbine operation. Since the rehabilitation project is applied on one turbine, tests are held for that turbine, and results are collected.

Table 2. Pipe characteristics of KEPEZ-I HPP

Pipe Name	Length (m)	Diameter (mm)	Thickness(mm)	Wave Speed (m/s)
E1	589.00	2500	200.0	968.63
P1 to P4	294.1	2400	9.0	784.21
P5	100.50	2400	11.0	841.16
P6	103.87	2400	11.5	853.82
P7	206.66	2130	12.0	899.90
P8	62.88	2130	13.0	922.55
P9	34.89	2130	14.0	943.40
B1	3.60	1300	10.0	1161.48
B2	3.60	925	300.0	1300.37
B3	2.00	925	300.0	1300.37
B4	3.90	600	300.0	1356.01
T1	5.00	5000	200.0	772.54
T2	5.00	5000	200.0	772.54

In the study, the model is validated in three steps by comparing with field data. Three different computer models are developed to reach a final model whose results are close to measured data in the field tests.

- Case-1: HAMMER model has surge tank and General Purpose Valve (GPV) simulating the Turbine only but considering the PRV effect in its behavior.
- Case-2: HAMMER model has surge tank, GPV simulating the turbine only, and Throttle Control Valve (TCV) simulating PRV only.
- Case-3: HAMMER model has surge tank, Turbine, and TCV simulating PRV.

After validation of the model, four different scenarios are simulated for 8.5 MW and 9.35 MW turbine power case differently. In this paper, the most severe scenario is taken to discuss the results.

3.1 Instant Load Rejection Scenario

In this scenario, the electrical load which comes from the grid drops to zero instantly. Then, the connection between the generator and the grid breaks, and generator torque is rejected on the turbine. The turbine starts to turn without any resistance. Therefore, the governor closes the wicket gate rapidly to prevent damage to turbine components before reaching runaway speed. Field tests are executed for instant load rejection scenario, and wicket gate closure time 8.55 seconds for the 9.35 MW test. HAMMER models with PRV and without PRV are analyzed and compared to understand the effect of PRV in the HPP.

In the 9.35 MW test, simulations are held for systems with and without PRV for 6.41 m^3/s flow rate and 166.3 m net head at turbine. Then, a comparison for two different systems is investigated to understand the effect of PRV.

From Figure 4, critical points are noted to study on the physical results of numerical values. Maximum pressures are 1830 kPa with a 13.17% increase and 2007 kPa with 24.12% increase for the systems with and without PRV. The pressure rise is reduced 45.40% with the help of PRV.

Pressure is not absorbed by the system after the wicket gate is closed totally for the unprotected system in Figure 4. This phenomenon is being analyzed and being investigated. Although the wave pressures continue to fluctuate in the system, because there is no flow in the pipeline or there is flow with small velocity, friction and minor losses cannot decrease the energy of the waves. In addition, since the surge tank has a 5 m orifice at the entrance of the structure, it is not enough to dissipate the energy of the waves in short times. If the simulations are held for a longer time, it is observed that after approximately 5 minutes, the system absorbs the pressure waves and returns to the steady-state condition. It is understood that since PRV discharges the water after the wicket gate is closed completely, wave pressures are absorbed, and system backs to steady-state condition earlier than the unprotected case. PRV prevents the pipeline system from vibration because of the fluctuation of pressure waves for a long time after the wicket gate is closed.

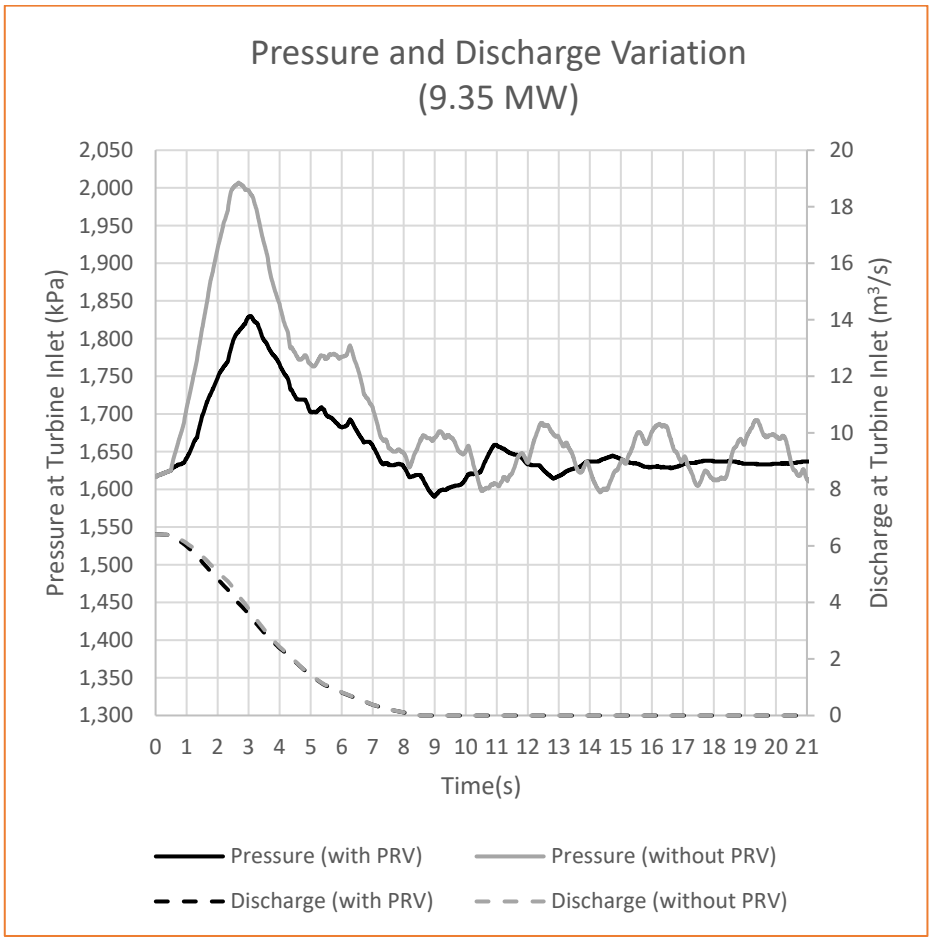

Fig. 4. Pressure and Discharge Variation with and without PRV in 9.35 MW Test

4 Conclusions

In the present study, determination of the effect of the PRV on the transients near a turbine in a power plant is the main concern. The power plant used as a case study is the KEPEZ – I Hydropower Plant in which one of the turbines is rehabilitated. It should be kept in mind that although there is also a surge tank in the system closer to the upstream reservoir than the turbines, the protective response of the PRV has more rapid and direct effect on mitigating the transients since it is is mounted to the turbine spiral case with a by-pass pipe.

- According to the results, transient pressure increase can be prevented before it reaches extreme values by opening PRV at the beginning of the water hammer event. This dual mechanism of closure and opening increases PRV efficiency.

- Unprotected and protected cases are analyzed, and PRV effect is investigated for the system. PRV decreases the pressure rise by approximately 50% in every case. Therefore, mounting a PRV is an efficient way to protect the system from pressure increase with proper operation.
- In the operation stage, transient analysis helps to determine the operation limits of the facility and gives an idea about the effectiveness of the operating method against water hammer. A sudden change in the wicket gates pattern causes a significant rise or reduction of pressure in the system. Therefore, required operation times and allowable pressure limits should be calculated for emergency scenarios with transient analysis.

References

1. Allievi, L. (1902). General theory of the variable motion of water in pressure conduits. Annali della Societa degli Ingegneri ed Architetti Italiani 17(5): 285-325 (in Italian). (French translation by Allievi, in Revue Me' canique, Paris, 1904) (Discussed by Bergant et al., 2006).
2. Azoury, P. H., Baasiri, M., & Najm, H. (1986). Effect of Valve-Closure Schedule on Water Hammer. Journal of Hydraulic Engineering, 112(10), 890-903.
3. Bozkuş Z. (2008). Water Hammer Analyses of Çamlıdere-İvedik Water Treatment Plant (IWTP) Pipeline. Teknik Dergi/Technical Journal of Turkish Chamber of Civil Engineers, April, 4409-4422.
4. Chaudhry, M. H. (1987). Applied Hydraulic Transients. New York: Van Nostrand Reinhold Company Limited.
5. Celebioğlu, K. (2019). Roughness Coefficient of a Highly Calcinated Penstock. Teknik Dergi, 9309–9326. https://doi.org/10.18400/tekderg.447265
6. Çetintaş, M. A. (2022). Investigation of Interaction between PRV and Turbines during a Transient Flow in a Hydropower Plant. Master's Thesis, Middle East Technical University, Ankara, Turkey
7. Dursun, S. (2013). Numerical Investigation of Protection Measures Against Water Hammer in the Yesilvadi Hydropower Plant. Master's Thesis, Middle East Technical University, Ankara, Turkey
8. Dursun, S., Bozkus, Z., & Dincer, A. E. (2015). Effect of pressure relief valves on the fluid transients in the penstocks of a small run-of-river plant. Retrieved From: https://www.researchgate.net/publication/284512453
9. Joukowsky, N. (1898). "Über den hydraulischen Stoss in Wasserleitung-shrohren." [On the hydraulic hammer in water supply pipes.] Mémories de l'Académie Impériale des Sciences de St.-Pétersbourg (1900) Series 8, 9(5), 1-71 (in German).
10. Peicheng, H., Pusheng, Z., Elkouh, A. F. (1989). Relief Valve and Safety Membrane Arrangement in Lieu of Surge Tank. ASCE Journal of Energy Engineering, 78-83.
11. Sepetci et al. (2016). Conceptual Design of a Hydroelectric Power Plant for a Rehabilitation Project. 12th International Conference on Heat Transfer, Fluid Mechanics, and Thermodynamics.
12. Thorley, D. A. R. (2004). Fluid transients in pipeline systems, ASME Press, New York.
13. Wylie, E. B., Streeter, V. L., Suo, L. (1993). Fluid Transients in Systems. New Jersey: Prentice-Hall.

Determination of Sediment Yield of Çoruh River by Field Observation and RUSLE Method

Kutay Yılmaz[1][0000-0001-5529-9239], Saber Habibi Topraghghaleh[2][0000-0003-2989-6528], Yakup Darama[3][0000-0003-0066-2621] and Nazmi Kağnıcıoğlu[4][0009-0005-0633-1147]

[1] ORCAS Engineering & Consultancy, Ankara, Türkiye,
ktyylmz@gmail.com
[2] Middle East Technical University, Civil Engineering Department, Ankara, Türkiye,
saber.topraghghaleh@metu.edu.tr
[3] Atilim University, Civil Engineering Department, Ankara, Türkiye,
yakup.darama@atilim.edu.tr
[4] General Directorate of State Hydraulic Works (DSI), Ankara, Türkiye,
nazmik@dsi.gov.tr

Abstract. The Çoruh River, situated in the northeastern region of Turkey, is a significant watercourse that transports a substantial amount of sediment. To ensure effective management of river systems, it is crucial to determine sediment yield, as it can have a significant impact on various factors such as water quality, aquatic ecosystems, and infrastructure, including dams and bridges. Therefore, the main objective of this study is to determine the sediment yield of the Çoruh River through a combination of field observations and the Revised Universal Soil Loss Equation (RUSLE) method based on Geographic Information Systems (GIS). The research involved conducting field observations to gather data on sediment transport rates and particle size distribution. Additionally, the RUSLE method was employed to estimate soil erosion rates in the watershed. By combining these two approaches, the study aimed to gain a more accurate understanding of the sediment transport of the Çoruh River. The results of the study provided valuable insights into the sediment transport characteristics of the Çoruh River. The findings emphasized the importance of employing a combination of field observations and modeling techniques to accurately estimate sediment transport. The information gathered from this study can help in developing effective management strategies to maintain the health and stability of the Çoruh River and its surrounding ecosystem.

Keywords: Sediment transport, GIS, Erosion, Coruh, RUSLE

1 Introduction

Sedimentation is a major problem for dam reservoirs. The geology of the river basin, slope, climate, drainage density, and drainage pattern, as well as urbanization and deforestation, all contribute to increased sediment yield in the basin. This sediment settles and accumulates in the reservoir area, reducing the storage capacity of the dam.

While long-term sediment and flow measurements have been used to calculate the dead volumes of dams and their economic lifespan, these calculations have been inaccurate due to the variable nature of meteorological, hydrological, and human impact parameters. As a result, reservoirs have filled with sediment more quickly than expected. During short, intense floods, large amounts of sediment can be transported into the reservoir. This sediment can quickly fill the reservoir, reducing its storage capacity and lifespan. This has been a major concern for researchers, as dams provide domestic and agricultural water and hydroelectric power [1]

Determining the amount of sediment carried by rivers is crucial for estimating sediment transport in a watershed. According to Walling [2], there are three methods to obtain sediment yield data: (1) utilizing continuously measured discharge data and applying them to a previously obtained sediment rating curve, (2) combining continuously measured discharge and sediment data, and (3) utilizing reservoir survey data. Among these methods, periodic collection of reservoir survey data is considered a more dependable measure of long-term sediment yield in a basin [1,3,4]. In a study conducted, Munthali et al. [5] using Geographic Information System (GIS) and the Pan-European Soil Erosion Risk Assessment model, the researchers aimed to determine the hydrological potential for sediment, identify areas with high sediment generation in the Songwe River watershed, and assess the likelihood of sedimentation in a proposed reservoir.

Determining the sediment accumulation in dam reservoirs is another important aspect alongside estimating basin sediment yield. Various methodologies and techniques have been employed to assess the sediment volume stored in dam reservoirs. Bilal et al. [6] utilized proxy approaches with spatial and temporal flow data resolution, including river cross-sections and sediment data, to qualitatively simulate bathymetric changes in Japan's Sakuma Dam. They concluded that their study provides conceptual insights into future trends in bathymetric changes. Dadoria et al. [7] employed GIS and remote sensing techniques to compute the loss of storage capacity and sedimentation in the Murrumsilli reservoir located in the Chhattisgarh State of India. Bhavsar & Gohil [8] conducted a review of studies pertaining to reservoir sedimentation and highlighted the applicability and usefulness of remote sensing techniques, particularly in cases where ground data is scarce Patil & Shetkar [9] conducted a study to assess sediment deposition in the Koyna reservoir in Western Maharashtra, India, using analytical methods. They found that the error between the analytical method results and the integrated bathymetric survey measurements was 8.82% and suggested that the analytical method yields better results.

Wulandari et al. [10] conducted a study on the sediment deposition pattern in the Wonogiri Reservoir by monitoring changes in the reservoir's bottom elevation in various years. Measurements were taken in 1980, 1993, 2004, 2005, and 2011. The researchers discovered that 73% of the sediment was deposited in the effective storage zone, while only 27% settled in the dead storage zone of the Wonogiri Reservoir.

Issa et al. [11] investigated the sediment trapping efficiency of the Mosul Dam Reservoir. They employed six different empirical methods based on the residence time principle to determine the trapping efficiency of the reservoir for the period from 1986

to 2011. The results were evaluated using a bathymetric survey conducted in 2011, and the observed error percentage was found to be very small (0.368%).

Godwin et al. [12] highlighted the impact of land use on reservoir sedimentation in Zimbabwe. Through hydrographic surveys and grab sampling methods conducted during rainfall seasons, they determined that the Chesa Causeway Dam in Zimbabwe lost more than half (66%) of its storage capacity over its 19 years of operation.

This study aims to determine the sediment yield for the segment of the Çoruh River in the Northeastern Turkey. By combining field observations and the Revised Universal Soil Loss Equation (RUSLE) method based on Geographic Information Systems (GIS), the research seeks to gain insights into sediment yield and soil erosion rates in the river's watershed. The findings will provide valuable information for effective management strategies to maintain the river's health and stability, as well as preserve the surrounding ecosystem.

2 Study Area

The Çoruh river is located in the northern east of Türkiye. Its length is approximately 438 km and drained into blacked sea. The study area covers the segment of Çoruh river which is located between Deriner and Borçka dams. Only one sediment gauging station exists between the area of aforementioned dams. The watersheds of Çoruh River and its tributriaries between the Deriner and Borçka Dams are constructed in GIS environment. The study area, watersheds as well as gauging stations are presented in Fig. 1.

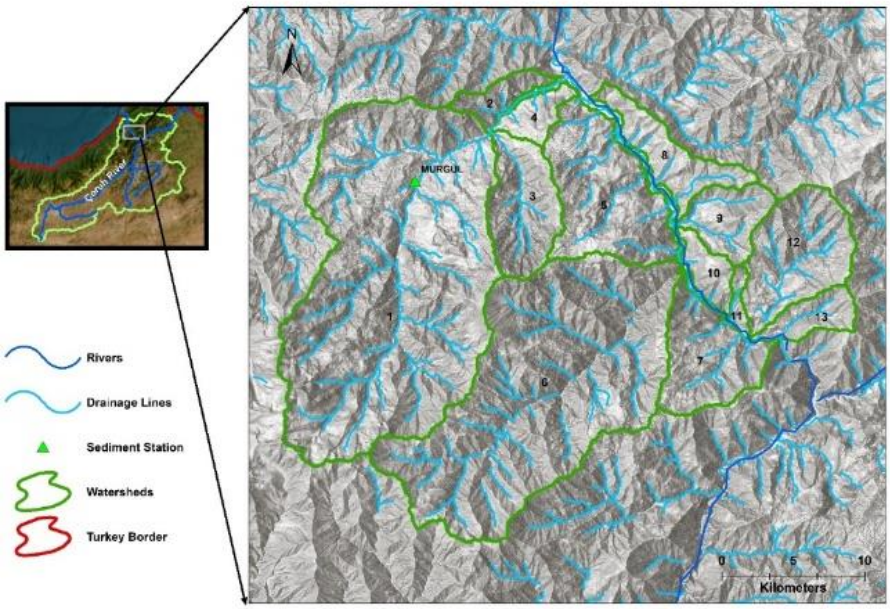

Fig. 1. Study area

3 Methodology

The Çoruh River is one of the most important rivers in Turkey in terms of hydroelectric power potential. In order to utilize this potential several dams were constructed on the main branch of the river. In contrast to hydroelectric potential, this river flows in a supercritical flow regime and carries sediment, which is an important problem for the reservoirs of dams. Several studies were conducted on the sedimentation of reservoirs [1,13]. Sediment accumulation analysis has been calculated on a micro-scale (sub-basin basis) using various methods previously [14]. However, this calculation has not been made on a basin basis.

Determination of sediment transport on a basin basis is a crucial issue for determining the dead volume of dams producing hydroelectric power. Under normal circumstances, the construction of dams on a river should be done from upstream to downstream. However, this process was not done in the Çoruh River Basin case. Due to hydropolitical reasons, the construction of the dams in the Çoruh River Basin started from the downstream to the upstream firstly, a 44 m high clay core rockfill dam was built in the Muratlı district closest to our border and put into operation in 2005. With this project, hydropolitically suitable ground has been prepared for the construction of other energy dams. After the Muratlı Dam, Borcka Dam in 2008, Deriner Dam in 2012, and Artvin Dam in 2015, respectively, were completed and put into operation. For this reason, Muratlı and Borçka dams, which are located downstream on the main branch of the Çoruh River, both stored the sediment naturally carried by the river in the entire basin, and the sediment flowing from the side slopes was transported to the river during the construction of Deriner and Artvin dams. The first sedimentation of the Muratlı dam reservoirs started in 2005, and then sedimentation of the Borçka dam reservoir started in 2008. This situation caused the dead volumes of those two dams to be filled in a shorter time than the dead volumes calculated according to the amount of sediment carried by the river naturally. In order to determine the decrease in dead volumes, bathymetric maps were produced by the field studies of the Borçka dam reservoir in 2017 and the Muratlı dam reservoir in 2020. The analysis of the bathymetric maps showed that the reduction in dead volume in the Muratlı dam reached 48%, while the reduction in dead volume in the Borcka dam reached 28%. The main reason for the decrease in the dead volumes of both dams in a 10-15 year period was during the construction of Deriner and Artvin Dams. After the construction of Deriner, Artvin, Yusufeli, Arkun, Güllübağ, and Laleli dams on the main branch of the river forming a cascade manner, sedimentation of the dam reservoirs has decreased to a certain extent due to the regulation of the river flow, and the sedimentation will be caused by the surface runoff on the slopes of the precipitation that will occur in the basin. In addition, due to the fact that the basin receives a lot of precipitation and accordingly has a high erosion rate, the sediment yield of the basin is calculated using the bathymetric maps taken from the Muratlı and Borcka Dams, analysis of measurements taken from the sediment measurement stations in the main branch and side branches of the Çoruh River without dams.

3.1 Field Studies and Analysis

Before the construction of dams in the Çoruh River Basin, there were 16 sediment measurement stations in the basin. Suspended sediment measurements of those stations' data were analyzed, and sediment rating curves were developed to show the sediment load of the river in relation to discharge. Among those sixteen sediment measurement stations, sediment rating curves of Murgul Creek and Erenkoy station that existed on the main branch of the Coruh River were used and presented as seen in Fig. 2.

After having constructed the sediment rating curve, linear trendline analysis was performed, leading to relate discharge and sediment load. The relation between discharge and sediment load is found as;

$$Q = 2144.9(Q_s)^{0.2752} \quad (1)$$

It should be noted that the correlation coefficient between discharge and sediment load is found as 0.2752 which can be considered as low. Lower correlation coefficient can be related to the mismeasurement.

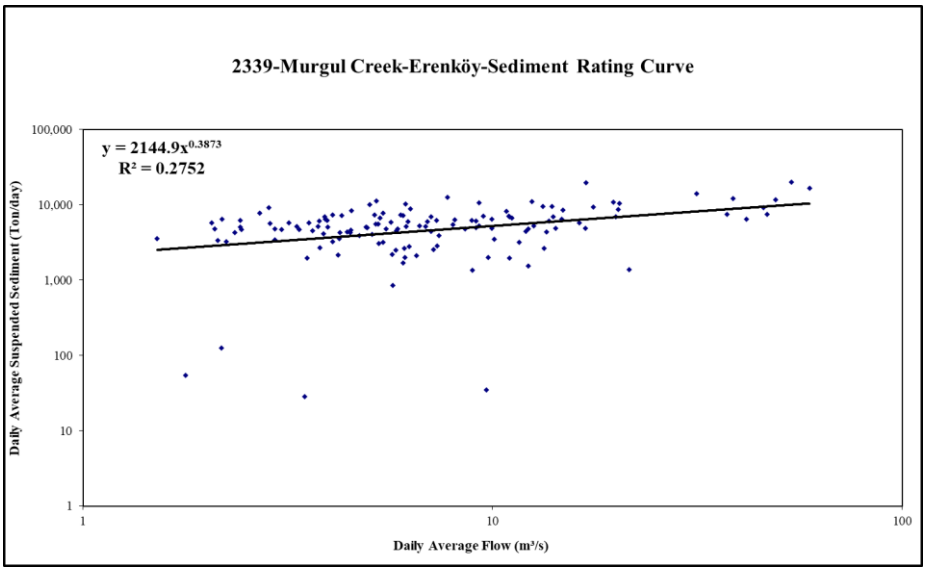

Fig. 2. 2339 Murgul Creek (Tributriary of Çoruh River) –sediment rating curve

3.2 Determination of Annual Soil Loss By RUSLE

Erosion is a natural process taking place naturally. Erosion is caused by both wind and water. According to the State Planning Organization (DPT) of Turkey (2001), water and rainfall account for 99% of erosion in the country, while wind contributes to the remaining 1%.

Various methods have been proposed in the literature to quantify erosion or estimate the annual soil loss caused by water or rainfall. The Universal Soil Loss Equation (USLE) [15] and the Revised Universal Soil Loss Equation (RUSLE) [16] are two widely accepted and used methods. The RUSLE method considers several variables that are the main contributor to erosion, including rainfall-erosivity (R), soil sensitivity to erosion (K), topographic features such as slope length (L) and steepness (S), and crop management (C) and support practices (P). The RUSLE equation is given as follows:

$$A = R \times K \times LS \times C \times P \tag{2}$$

where A is annual soil loss (t/ha/yr), R is rainfall-runoff erosivity factor (MJ/mm/ha/h/yr), K is soil erosion sensitivity factor, L is slope length factor, S is slope steepness factor, C is cover management factor, and P is the support practices factor.

The R and K values of the RUSLE were determined and calibrated throughout Europe, including Turkey [17]. Thus, the R and K values for the study area were obtained from [17]. The LS factor of the study area was calculated based on a 5-meter resampled digital elevation model (DEM) on the GIS environment. To perform the LS calculations, the equation proposed by Moore & Burch [18] was implemented. The cover management and support practices factors were calculated on the GIS environment by taking into account the land use classes and constraints acquired from the literature [19,20]. The spatially varying RUSLE parameters and the corresponding erosion and annual soil losses are presented in Fig. 3.

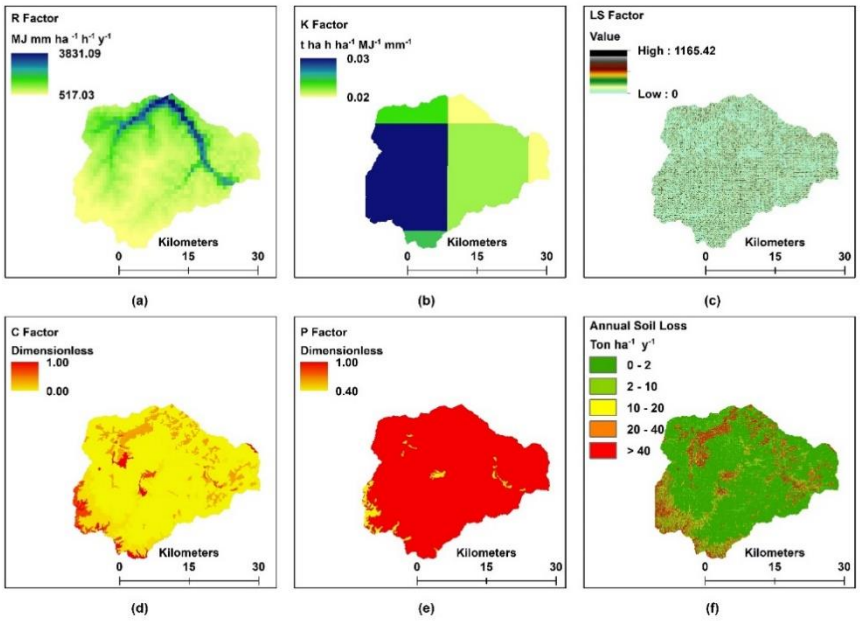

Fig. 3. RUSLE Factors and Annual Soil Loss of the Study Area

After having calculated to yearly soil loss for all the watersheds given in Fig. 1, the data is summarized as flows;

Table 1. Annual soil loss of each watershed and area

Watershed	Area (km^2)	Area (m^2)	Annual Soil Loss (ton/ha)
1	296.14	114.34	22.63
2	12.37	4.77	22.79
3	40.63	15.69	9.84
4	12.24	4.72	39.01
5	69.92	27.00	16.15
6	233.15	90.02	12.05
7	44.38	17.14	15.81
8	29.15	11.25	19.47
9	23.86	9.21	11.80
10	12.46	4.81	22.10
11	4.72	1.82	26.26
12	52.94	20.44	12.72
13	15.45	5.97	13.13

Sediment Delivery Ratio (SDR) is the ratio of sediment yield divided by the total soil loss and expresses the percentage of detached sediment that is transported as surface runoff to a specific location, such as the reservoir. It is a dimensionless parameter, always lower than 1.

$$SDR = \frac{S_{yield}}{A} \tag{3}$$

The sediment delivery ratio is the threshold that each country or region establishes for itself and is defined as a function of area. However, the similarities between regions allow the use of literally available equations for the basins/watersheds that do not have pre-determine SDRs. Literally available SDR equations are listed in Table 2.

Table 2. Literally available SDR equations

Equations	
Vanoni	$SDR = 0.42(A)^{-0.125}$
USDA-SCS	$SDR = 0.51(A)^{-0.11}$
Boyce	$SDR = 0.41(A)^{-0.3}$

The SDR values of each watershed are presented in Table 3 for the literally available SDR equations.

Table 3. Literally available SDR equations

Watershed #	SDR		
	Vanoni	Boyce	USDA - SCS
1	0.30	0.07	0.23
2	0.43	0.19	0.35
3	0.38	0.14	0.30
4	0.43	0.19	0.35
5	0.35	0.12	0.28
6	0.31	0.08	0.24
7	0.37	0.13	0.29
8	0.39	0.15	0.31
9	0.40	0.16	0.32
10	0.43	0.19	0.35
11	0.48	0.26	0.39
12	0.37	0.13	0.29
13	0.42	0.18	0.34

A quick examination of Table 3 reveals that the SDR decreases with increasing watershed area regardless of the equation used. The reason for decreasing SDR is the decreasing accumulation and slope with increasing watershed area.

4 Discussion

Construction of the sediment rating curve for the Murgul Creek, which is the tributary of Çoruh River, provides regression equation given as equation 1. The SDR value of watershed 1 is to be determined by considering equation 1.

According to equation 1, the sediment yield of Murgul Creek is 5208 ton/day by considering the average discharge of 9.88 m^3/sec. On the other hand, the annual soil loss of watershed 1 is 1836.10 ton/day. However, keeping in mind that the SDR should be smaller or equal to 1, the sediment yield of watershed 1 should be smaller than 1836.10 ton/day. Therefore, there exists a significant difference between the station data and the RUSLE. The discrepancy is caused by the lower correlation ratio of equation 1. Furthermore, the lack of sediment gauging stations throughout the study area prevents the determination of SDR from the historical records for the area of interest. However, consideration of the highest SDR value from literally available equations provides a good sight for the sediment yield.

Table 4. Sediment yield of each watershed

Watershed	SDR	Sediment Yield
1	0.30	555.98
2	0.43	33.16
3	0.38	41.27
4	0.43	56.22
5	0.35	109.80
6	0.31	239.29
7	0.37	71.73
8	0.39	60.76
9	0.40	30.81
10	0.43	32.37
11	0.48	16.21
12	0.37	67.52
13	0.42	23.29

Total of 1338.41 tons of sediment would be introduced annually between the Borçka and Deriner dams according to the estimates by RUSLE. Field measurements estimate higher amount of sediment, but the field measurements are neglected due to the low correlation ratio.

5 Conclusions

The evaluation of annual soil loss by RUSLE method on GIS environment can provide useful data. On the other hand, literally available SDR equations can be implemented to determine sediment yield of the area of interest. However, they should be validated by considering the station data with high quality. Lower quality data produce equations with low correlation ratio leads to under/over estimation. The low correlation ratio could produce unreliable estimates. Therefore, the station data should be carefully examined, but consideration of RUSLE with the literally available SDR equations can provide useful information. On the other hand, the SDR values should be developed specifically for the region to obtain reliable results.

References

1. Kokpinar MA, Altan-Sakarya AB, Kumcu SY, Gogus M. Assessment of sediment yield estimations for large watershed areas: a case study for the Seyhan, Demirköprü and Hirfanlı reservoirs in Turkey. Hydrological Sciences Journal. 60(12), 2189–2203 (2015).
2. Walling DE. Measuring sediment yield from river basins. In: Soil erosion research methods, Routledge, 39–80 (1994).
3. Morris GL, Fan J. Reservoir Sedimentation Handbook. New York: McGraw-Hill.
4. Verstraeten G, Poesen J. Using sediment deposits in small ponds to quantify sediment yield from small catchments: Possibilities and limitations. Earth Surf Process Landf. 27, 1425–1439 (2002).

5. Munthali KG, Irvine BJ, Murayama Y. Reservoir sedimentation and flood control: using a geographical information system to estimate sediment yield of the Songwe river watershed in Malawi. Sustainability. 3(1), 254–269 (2011).
6. Bilal A, Dai W, Larson M, Beebo QN, Xie Q. Qualitative simulation of bathymetric changes due to reservoir sedimentation: A Japanese case study. PLoS One. 12(4), e0174931 (2017).
7. Dadoria D, Tiwari HL, Jaiswal RK. Assessment of reservoir sedimentation in Chhattisgarh State using remote sensing and GIS. International Journal of Civil Engineering and Technology. 8(4), 526–534 (2017).
8. Bhavsar MM, Gohil KB. Review of the study of reservoir sedimentation by remote sensing technique. Int J Innov Res Sci Technol. 1(12), 251–254 (2015).
9. Patil RA, Shetkar R V. Prediction of sediment deposition in reservoir using artificial neural networks. Int. J. Civ. Eng. Technol. 7(4), 1–12 (2016).
10. Wulandari DA, D. L, S. D. Evaluation of deposition pattern of Wonogiri Reservoir sedimentation. International Journal of Civil Engineering and Environmental Engineering. 15(02) (2015).
11. Issa IE, Al-Ansari N, Knutsson S, Sherwany G. Monitoring and evaluating the sedimentation process in Mosul Dam Reservoir using trap efficiency approaches. Engineering. 7(4), 190–202 (2015).
12. Godwin MA, Gabriel S, Hodson M, Wellington D. Sedimentation impacts on reservoir as a result of land use on a selected catchment in Zimbabwe. (2011).
13. Darama Y, Selek Z, Selek B, Akgul MA, Dagdeviren M. Determination of sediment deposition of Hasanlar Dam using bathymetric and remote sensing studies. Natural Hazards. 97, 211–227 (2019).
14. Tufekcioglu M, Yavuz M, Vatandaslar C, Musa D, Duman A, Tufekcioglu A. Assessing and Mapping Erosion Risk for Velikoy Sub-watershed within Coruh River Basin in Turkey. Doğal Afetler ve Çevre Dergisi. 4(2), 210–220 (2018).
15. Wischmeier WH, Smith DD. Predicting rainfall erosion losses: a guide to conservation planning. Department of Agriculture, Science and Education Administration.
16. Renard KG. Predicting soil erosion by water: a guide to conservation planning with the Revised Universal Soil Loss Equation (RUSLE). US Department of Agriculture, Agricultural Research Service.
17. Borrelli P, Märker M, Panagos P, Schütt B. Modeling soil erosion and river sediment yield for an intermountain drainage basin of the Central Apennines, Italy. Catena (Amst). 114, 45–58 (2014).
18. Moore ID, Burch GJ. Physical basis of the length-slope factor in the universal soil loss equation. Soil Science Society of America Journal. 50(5), 1294–1298 (1986).
19. Naqvi HR, Mallick J, Devi LM, Siddiqui MA. Multi-temporal annual soil loss risk mapping employing revised universal soil loss equation (RUSLE) model in Nun Nadi Watershed, Uttrakhand (India). Arabian journal of geosciences. 6, 4045–4056 (2013).
20. Pelacani S, Märker M, Rodolfi G. Simulation of soil erosion and deposition in a changing land use: A modelling approach to implement the support practice factor. Geomorphology. 99(1–4), 329–340 (2008).

Flood Risk Mapping with Entropy Based Methods

Filiz Vargün[1*[0009-0006-4454-655X]], Türkay Baran[2[0000-0002-2325-2628]] and Filiz Barbaros[3[0000-0002-2697-911X]]

[1*] Dokuz Eylül University, Civil Engineering Department, İzmir, Türkiye, vargun.filiz@ogr.deu.edu.tr
[2] Dokuz Eylül University, Civil Engineering Department, İzmir, Türkiye, turkay.baran@deu.edu.tr
[3] Dokuz Eylül University, Civil Engineering Department, İzmir, Türkiye, filiz.barbaros@deu.edu.tr

Abstract. The inevitable effects of global warming on meteorological elements are intensely experienced as hydro-meteorological extremes such as floods and drought. While dealing with the destructive consequences of climate change today, accurate evaluation of hydrological data and future forecasts are becoming more vital in making the most efficient decisions for the safety of the environment and living things, as well as the management of water resources. Using long-term precipitation data from 37 meteorological stations in the Gediz Basin, the intensity variability index (IVI), based on intensity entropy (IE), has been used to quantify the variability in observed precipitation. Following the definition of precipitation variations by indices, the regions that could get excessive amounts of precipitation based on probability were determined using index-based maps created according to these indices. The generated entropy-based maps will be an effective tool in the scope of decision-makers' planning in the fight against climate change and flood risk.

Keywords: Gediz Basin, Variability Index, Entropy, Precipitation.

1 Introduction

The most efficient methods for obtaining information about meteorological processes are observation of hydrological processes, which is one of the most significant issues addressed within the context of water resources management. The complexity and stochasticity of water supply systems make it necessary to deal with uncertainty and variability as the key issues. As a result, determining how to assess the measured data is critical.

In order to evaluate potential water resources and analyze environmental changes, it is essential to investigate long-term time series of hydro-meteorological variables [1,2]. Determining the spatial and temporal characteristics of precipitation is essential to assess the regional impacts of climate change and water resources management [3]. The response of the hydrological cycle to climate change and its impact on the variability and availability of water resources on a regional and global scale can be understood by considering spatial and temporal differences in rainfall regimes [4]. The concept of

entropy, which is defined by "information theory" can be defined as the the amount of information gained ≡ reduction of uncertainty through observations [5]. Theory of Information [6] showed us that entropy is a value that can be determined by knowing or calculating the probability distribution function or probability density function of a random variable given in discrete or discrete or continuous form [7]. In the present study, entropy-based methods chosen to evaluate spatial and temporal variability precipitation data by considering the deficiencies in the datasets and Entropy-based indices were used to make the spatial assessment in a major basin as a whole.

2 Study Area

The presented study is carried out in scope of the Gediz basin within the borders of the Aegean Region. The basin is located in between 38° 04' - 39° 13' north latitudes and 26° 42' - 29° 45' east longitudes, constituting 2.17% of Turkey with a total area of 1,703,394 ha [8]. Within the boundaries of the basin, new stations were opened and some of them were relocated under the responsibility of the State Meteorological Service (TSMS). For these and similar reasons, the data recording start dates of the stations vary. As a result, data were collected from 37 stations belonging to the basin by observing between the year when each station started to serve and 2022. In this study, stations with short-term records were excluded in order to more precisely reflect the basin because long-term precipitation data works better in this context.

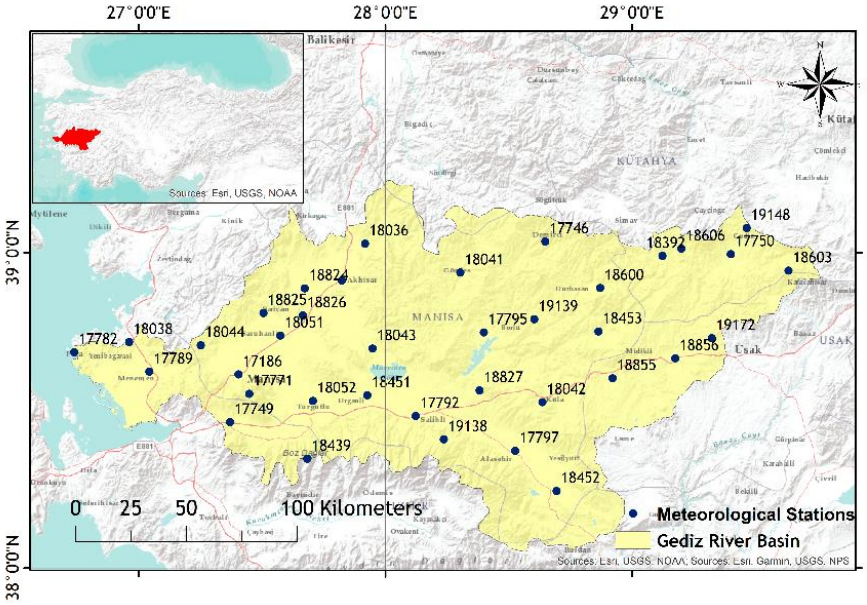

Fig 1. Gediz Basin and the station locations of TSMS.

3 Method

Entropy measures for analysis of precipitation were defined as marginal entropy (ME), intensity entropy (IE), apportionment entropy (AE) and decadal apportionment entropy (DAE) (Mishra et al. 2009). In the presented study, it is aimed to analyze in terms of intensity and the intensity entropy (IE) values are calculated and evaluated by indices.

Index of Variability (IV), calculated by the difference of entropy values from the maximum entropy value, gives information about the variability characteristics of the analyzed time series. The variability will increase as the IV value rises. The variability of a time series is measured using indices based on entropy values computed from annual, seasonal, monthly, or daily time series. Spatial and temporal variability can be compared based on these calculated indices.

The Index of Variability (IV) is defined as the difference between the maximum possible entropy (max H) and the entropy determined from a single time series and is calculated by Equation 1.

$$\mathrm{IV} = (\max H) - H \tag{1}$$

Shannon entropy gets its greatest value when the variable has a uniform distribution. As a result, the range of variation of H is [0, log N]. R is the difference between the random variable's lowest and highest values in the current data set, as represented by Equation 2 [9].

$$maxH = \log(R) \tag{2}$$

It is known as the Intensity Variability Index (IVI) when IV is derived from the intensity entropy, and the higher the IV value (hence the IVI value), the higher the variability is defined.

4 Application

Each station's annual total daily precipitation series is collected and sorted in ascending order. The class range $\Delta x = 3$ was chosen after considering the suggested formulas, and as a result, class number were obtained of minimum 5. The Intensity Entropy method was applied after the frequency analysis of the provided data was finished and the statistical characteristics were obtained considering the temporal and spatial evaluation of the existing long-term precipitation data. IV values were calculated according to equation (1), and maximum entropy values were calculated using equation 2. The intensity entropies and index values calculated on the long-term daily precipitation data of the stations. Table 1 presents the results of the analysis. Figure 2 compares the annual and seasonal IVI values of the basin with each other. Annual analysis of basin shows that the southern part of the basin has high IVI values and therefore high variability. It

is also seen from spring and winter spatial distribution maps that IVI values are at the lowest and therefore uncertainty is higher.

Table 1. Intensity Entropy (IE) and Intensity Variability Indices (IVI) calculated from long-term precipitation data of The Gediz Basin

		Autumn		Winter		Spring		Summer		Annual	
ID	**Station Name**	**IE**	**IVI**	**IE**	**IVI**	**IE**	**IVI**	**IE**	**IVI**	**IE**	**IVI**
17750	Gediz	1.98	4.17	2.36	3.81	2.19	3.36	1.52	4.40	2.10	4.07
18392	Pazarlar	1.42	3.67	1.94	3.78	1.68	3.49	1.35	3.38	1.62	4.09
17184	Akhisar	2.39	3.80	2.93	4.25	2.46	3.99	1.26	4.49	2.50	4.68
18036	Akhisar/Karaköy	1.01	4.92	2.01	4.23	1.50	3.88	0.73	5.40	1.35	4.89
17186	Manisa	2.51	4.33	3.09	4.26	2.55	3.95	1.32	4.47	2.64	4.71
17746	Demirci	1.64	4.21	2.47	3.38	2.12	3.57	1.17	4.48	1.94	3.92
17771	Şehzadeler/Spil	1.45	5.09	2.66	3.90	1.82	4.22	0.79	4.87	1.75	4.81
17792	Salihli	2.06	3.86	2.64	3.51	2.25	3.60	1.26	4.84	2.23	3.93
17795	Köprübaşı	1.25	4.32	1.86	3.96	1.56	3.51	0.96	4.46	1.44	4.38
17797	Alaşehir	1.06	4.84	1.64	3.99	1.39	4.11	0.72	4.73	1.24	4.65
18041	Gördes	1.06	4.82	1.85	4.21	1.55	3.48	0.90	4.80	1.38	4.68
18042	Kula	0.96	4.45	1.80	3.71	1.54	3.49	0.90	4.80	1.35	4.71
18043	Gölmarmara	0.98	4.44	1.83	4.34	1.41	3.91	0.74	5.02	1.28	4.88
18044	Yunusemre/Çakmak	1.10	4.07	2.07	3.98	1.50	3.43	0.66	4.19	1.38	4.67
18052	Turgutlu	1.19	4.28	2.12	4.12	1.49	3.77	0.66	5.38	1.46	4.78
18451	Ahmetli	1.11	4.31	1.83	4.49	1.49	3.34	1.21	3.32	1.45	4.88
18452	Sarıgöl	0.92	5.62	1.66	4.15	1.39	3.19	0.88	4.61	1.25	5.29
18453	Selendi	1.22	4.45	1.84	4.37	1.70	3.65	1.45	4.50	1.58	4.62
17749	Kemalpaşa	1.15	4.78	2.28	4.48	1.50	4.02	0.64	4.78	1.47	5.30
18439	Kemalpasa/Ovacık	1.23	4.90	2.52	4.46	1.73	4.57	0.84	5.03	1.65	5.33
17782	Foça Toprak Su	1.06	5.37	2.12	3.81	1.32	4.45	0.34	3.52	1.30	5.13
17789	Menemen	1.06	5.49	2.05	4.25	1.34	4.38	0.37	5.18	1.28	5.27
18603	Gediz/Murat Dağı	1.28	3.78	1.88	3.81	1.54	3.91	1.21	4.45	1.50	4.19
18606	Şaphane	1.24	3.68	1.82	3.80	1.55	3.48	1.32	3.06	1.51	4.11
19148	Gediz/Yaylaköy	1.02	3.56	1.53	2.68	1.41	3.24	1.29	4.15	1.35	4.08
18855	Eşme/Delibaşlı	0.91	4.45	1.62	3.17	1.48	3.25	0.95	4.05	1.29	4.07
18856	Uşak Tekstil OSB	0.92	4.09	1.68	3.25	1.56	3.05	1.05	3.98	1.36	3.66
19172	Uşak/Selvioğlu	1.01	4.39	1.75	3.31	1.61	3.25	1.08	3.87	1.41	3.99
18824	Akhisar/Mecidiye	0.99	5.08	1.94	4.46	1.31	3.75	0.65	3.85	1.28	5.11
19139	Demirci/İçikler	0.90	3.46	1.70	3.14	1.44	3.24	0.94	3.56	1.29	3.56
18827	Salihli/İğdecik	0.94	4.69	1.77	3.46	1.43	3.28	0.72	4.04	1.27	4.36
19138	Salihli/Çalkadoğanlar	0.93	3.62	1.94	4.37	1.32	3.47	0.77	4.29	1.31	5.00
18051	Saruhanlı	1.06	4.53	2.00	4.35	1.47	3.77	0.71	5.04	1.38	4.97
18825	Saruhanlı/Sarıçam	0.91	4.61	1.98	3.95	1.27	4.43	0.65	3.34	1.27	4.46
18826	Saruhanlı/Tirkeş	1.01	4.72	1.95	4.21	1.32	3.76	0.64	4.42	1.29	4.88
18600	Selendi/Tavak	1.04	4.51	1.70	3.87	1.52	3.53	1.08	3.98	1.37	4.20
18038	Aliağa/Bozköy	1.03	4.90	2.13	3.91	1.35	4.01	0.47	4.48	1.31	4.72

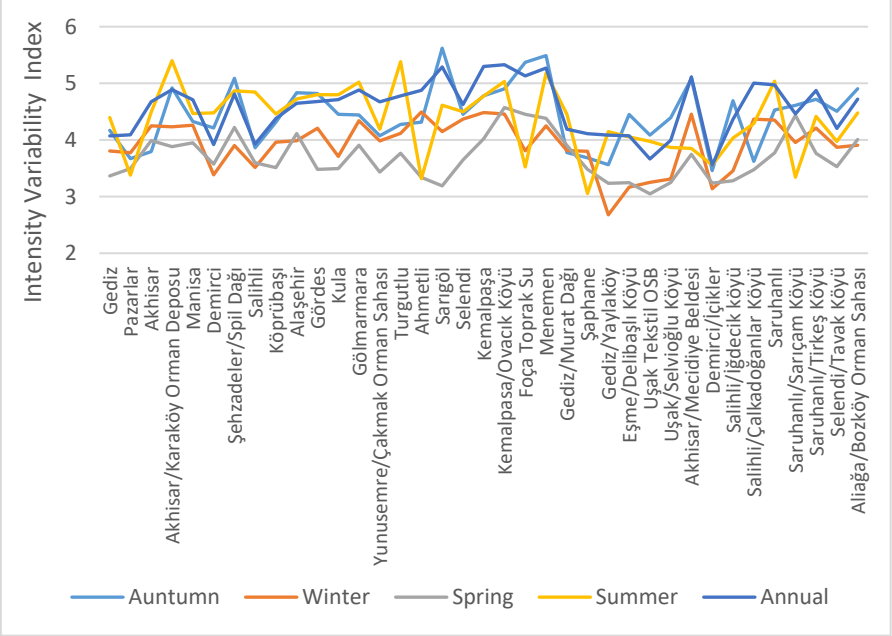

Fig 2. Comparison of Intensity Variability Indices (IVI) between annual and seasonal time series in the Gediz Basin

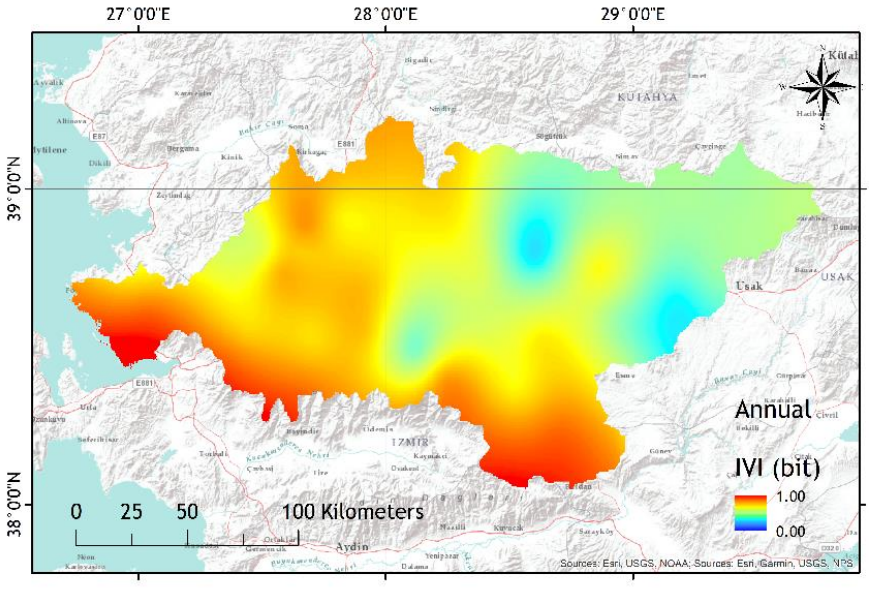

Fig. 3. Spatial distribution of Intensity Variability Indices (IVI) of precipitation time series in the Gediz Basin - Annual

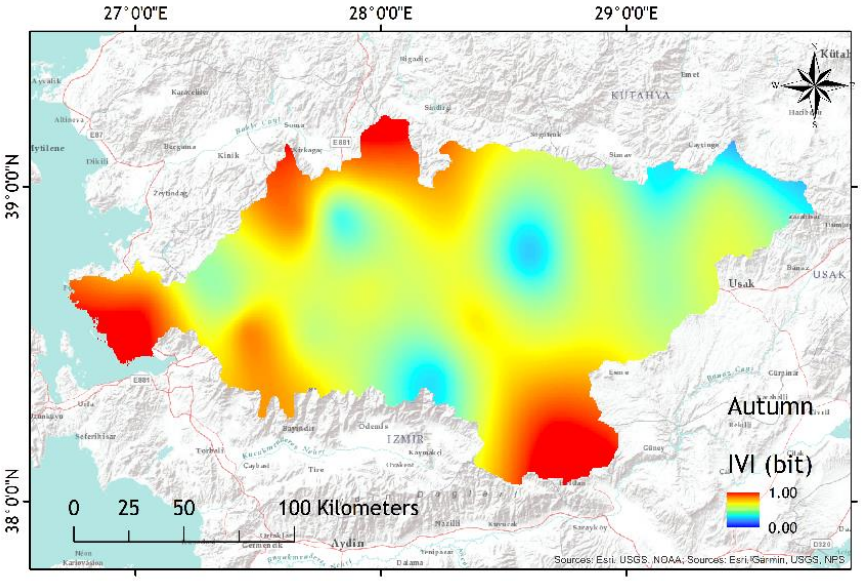

(a)

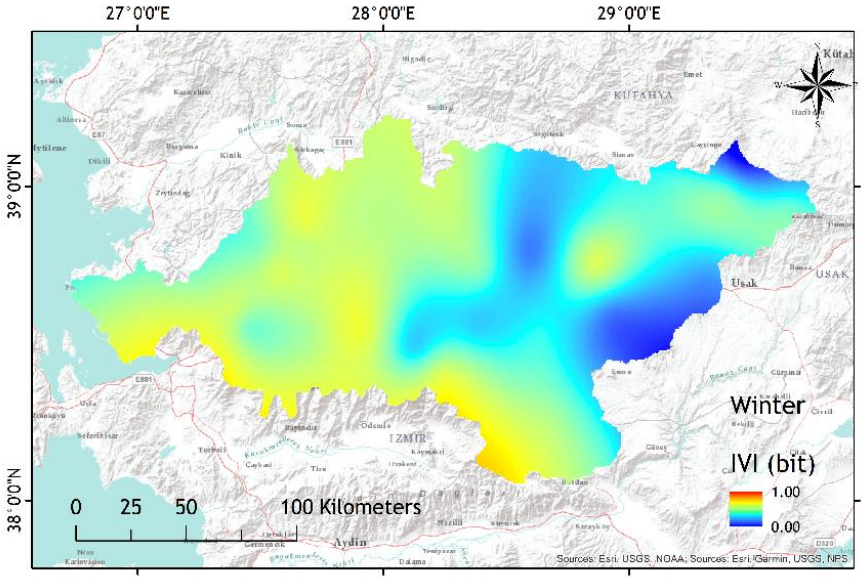

(b)

Fig. 4. Spatial distribution of Intensity Variability Indices (IVI) of precipitation time series in the Gediz Basin; (a) Autumn; (b) Winter

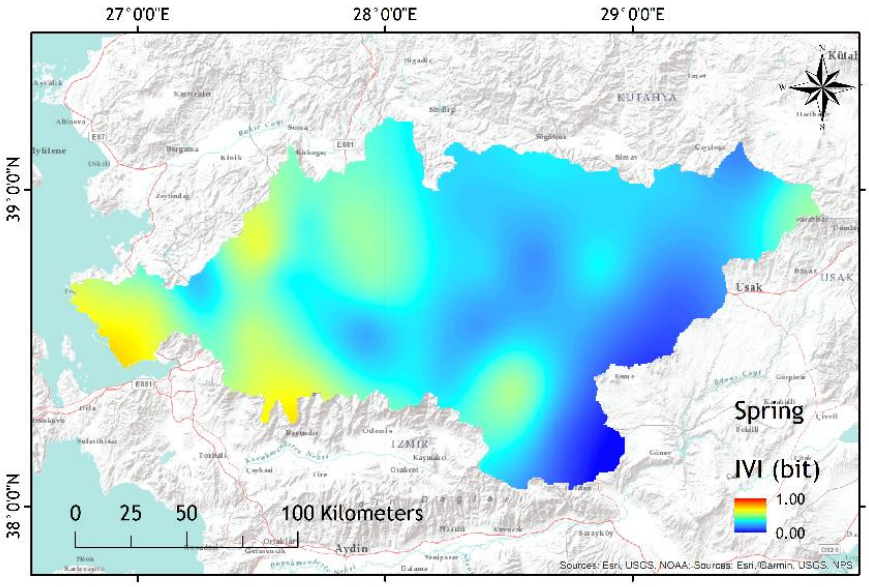

(a)

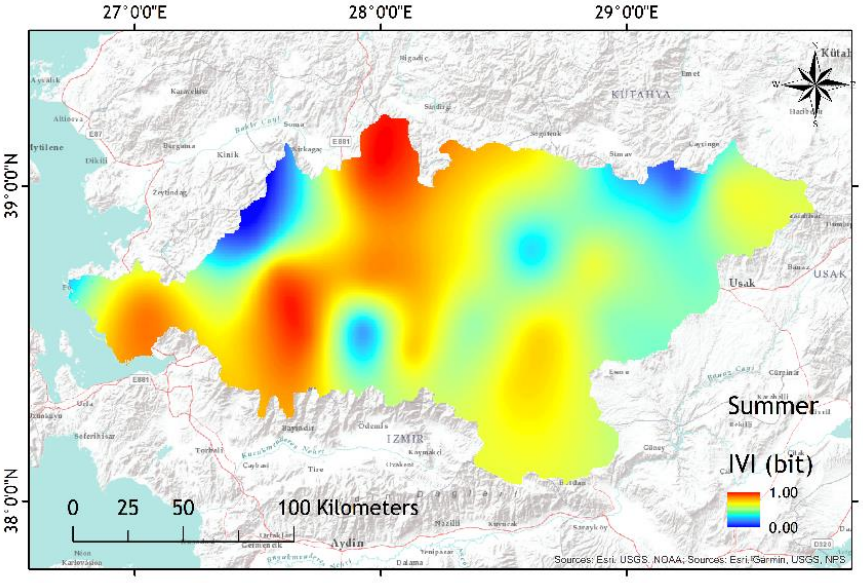

(b)

Fig. 5. Spatial distribution of Intensity Variability Indices (IVI) of precipitation time series in the Gediz Basin; (a) Spring; (b) Summer

5 Results and Concluding Remarks

In scope of the study, the whole basin is analyzed annually and seasonally, and a regional analysis is performed to create risk maps throughout the basin. In regions at risk for hazard, areas with high precipitation variability can be detected, and timely action plans can be developed. The precipitation variability profile in the region will have a significant influence in both present and future river basin management decisions, preventing construction in potentially dangerous locations and managing agricultural processes. The entropy-based maps obtained will be an effective instrument for researchers and policymakers dealing with climate change and flood risk.

Acknowledgments: Authors would like to acknowledge to M.Sc. Mert Can GÜNAÇTI for his great contribution to the mapping process of the manuscript.

References

1. Gu, H., Yu, Z., Li, G., Luo, J., Ju, Q., Huang, Y., & Fu, X. (2020). Entropy-Based Research on Precipitation Variability in the Source Region of China's Yellow River. Water, 12, 2486. https://doi.org/10.3390/w12092486
2. Mishra AK, Özger M, Singh VP (2009) An entropy-based investigation into the variability of precipitation. Journal of Hydrology, 370(1–4):139-154. https://doi.org/10.1016/j.jhydrol.2009.03.006
3. Zhang Q, Zheng Y, Singh VP, Xiao M, Liu L (2016) Entropy-based spatiotemporal patterns of precipitation regimes in the Huai River basin, China, International Journal of Climatology, 36:2335–2344. https://doi.org/10.1002/joc.4498
4. Cleridou N, Benas N, Matsoukas C, Croke B, Vardavas I (2014) Water resources of Cyprus under changing climatic conditions: modelling approach, validation and limitations. Environ. Model. Softw. 60:202–218. https://doi.org/10.1016/j.envsoft.2014.06.008
5. Baran, T., Harmancioglu, N. B., Cetinkaya, C. P., & Barbaros, F. (2017). An Extension to the Revised Approach in the Assessment of Informational Entropy. Entropy, 19(12), 634. https://doi.org/10.3390/e19120634
6. Shannon C.E. (1948). Mathematical Theory of Information. The Mathematical Theory of Information, 27, 170–180, the University of Illinois Press: Urbana, USA
7. Bozoglu, O., Baran, T., & Barbaros, F. (2022). Entropy Based Regional Precipitation Prediction in the Case of Gediz River Basin. Teknik Dergi. https://doi.org/10.18400/tekderg.724164
8. TÜBİTAK MAM (2018) Gediz Havzası Nehir Havzası Yönetim Planlarının Hazırlanması Projesi. TÜBİTAK Marmara Araştırma Merkezi. Çevre ve Temiz Üretim Enstitüsü, Proje Nihai Raporu. URL:https://www.tarimorman.gov.tr/SYGM/Belgeler/NHYP%20DEN%C4%B0Z/GED%C4%B0Z%20NEH%C4%B0R%20HAVZASI%20Y%C3%96NET%C4%B0M%20PLANI.pdf
9. Xiong, F., Guo, S., Chen, L., Chang, F., Zhong, Y., & Liu, P. (2018). Identification of flood seasonality using an entropy-based method. Stochastic Environmental Research and Risk Assessment, 32(1-4). https://doi.org/10.1007/s00477-018-1614-1.

Investigating the Efficacy of Large-Scale Particle Image Velocimetry for Controlled Water Resource Management: An Experimental Approach

Cahit Yerdelen[1[0000-0003-4705-1940]], Mohamed Abdelkader[2[0000-0002-7655-5737]], Ebru Eriş[1[0000-0003-0601-7666]], Ömer Aşıkoğlu[1[0000-0002-2981-5903]], Harun Alp[1[0000-0001-9099-4114]]

[1] Ege University, Civil Eng. Dept., Izmir, Turkey,
[2] Stevens Institute of Technology, Civil Eng. Dept., New York, USA,
*Corresponding Author E-mail: (cahit.yerdelen@ege.edu.tr)

Abstract. This research seeks to improve the controlled management of water resources by reducing the reliance on extensive field measurements through the adoption of cutting-edge 21st-century technologies. The study methodology examines two concurrent strategies: (i) the estimation of average flow velocity using conventional measurement methods, and (ii) the determination of surface velocity via image processing. Velocity measurements were acquired employing Acoustic Doppler Velocimetry (ADV) and Large-Scale Particle Image Velocimetry (LSPIV) techniques.

A series of controlled experiments were conducted in Ege University's Civil Engineering Department's Hydraulic Laboratory, employing an open channel and various channel geometries. Initial experiments investigated the influence of tracers' material type and size on the accuracy of the LSPIV method. Preliminary findings suggest the potential for precise flow rate estimations utilizing image processing-based methodologies.

The results of this study demonstrate that tracer size and material significantly impact the surface flow velocities derived from the LSPIV method. These observations can be attributed to two primary factors: (i) tracer reflectance and proportion in the captured images, and (ii) alterations in surface tension as a function of tracer material. Future research will address the effect of channel bed and geometric features on the accuracy of the LSPIV method.

The findings of this study illuminate the potential role of imaging techniques in fostering the sustainable and efficient management of water resources, a pressing global issue.

Keywords: Open channel; Streamflow velocity; Flow Discharge; LSPIV

1 Introduction

In the last two centuries, rapid population growth, industrial revolution, excessive and uncontrolled water consumption and pollution have caused very difficult conditions for

humanity. These challenges have required a more precise handling of water-related processes with the help of technology. For instance, accurate rainfall runoff modeling is necessary for proper water resources management. The rainfall-runoff models need sufficient and accurate flow data. Flow data measurements, starting using a venturi tube at the end of the 1700s, have reached to satellite image analysis today. The cost of on-site and repeated measurements has pushed scientists to find more feasible methods and devices. The first measuring instruments could measure the velocity, quantity or height of water (Url-1, 2023; Shimizu et al., 2018). However, these instruments are cumbersome or relatively expensive to install and use. Some of them even require the conversion of natural riverbeds into artificial channels in order to operate. However, Acoustic Doppler Velocimetry (ADV) is widely used to measure flow velocity, recently. The working principle of ADV devices is directly related to the sound wave. It has used the principle first described by Doppler in 1842 to measure velocity. ADV measures the frequency of reflected waves due to the particulate structures in water (Das & Mazumdar, 2018; Schugerl et al., 2019). While ADV usage is an effective technique, this method cannot be used in some cases because it is difficult to prepare a suitable setup in-situ measurement for unusual flow conditions such as flooding. Although ADVs are widely used in laboratory and field applications, another measurement technique, Large Scale Particle Imagine Velocimetry (LSPIV), has emerged because of the inability to measure in flood conditions and the possibility of affecting the measurement accuracy of features such as Doppler noise and turbulent velocity fluctuations. The LSPIV is a method that uses imaging to understand the natural water movements on the water surface. LSPIV is an economical and effortless system, which makes it very attractive for modeling. Image recordings are analyzed using a computer and the necessary software, with sufficient light and a suitable tracer for an accurate measurement. In the process, reference points are first determined. Necessary tracers are thrown on the water surface and images records. These image recordings are decomposed into photographs at certain time intervals with the help of a computer. After this stage, the distances between the reference points are entered into the computer. Based on the pixel-meter relationship, the computer correlates the movement of the tracker in the virtual environment with the coordinates defined in the program and the average surface velocity of the water is obtained. Another advantage of this method is that it can be used with unmanned aerial vehicles. Using this measurement technique, it could be easier to make measurements in places where people cannot reach by vehicles or where there is limited access.

The basic steps of LSPIV are similar to those applied for Particle Image Velocimetry (PIV), which is typically used to analyze images obtained with conventional video recordings illuminated with natural or artificial lighting. Based on the PIV method used in small areas, the LSPIV can be used in all free surface flows from a small artificial channel to a large natural river. Although particles are not required in turbulent flows, the use of particles will help to obtain more reliable results. An important aspect of the method is to use suitable material as a 'tracer'. The basic LSPIV data are instantaneous water surface velocity values covering flowing areas up to hundreds of square meters. In LSPIV, sequential images taken at specific time intervals of river surface flow are imaged from a riverbank or a bridge form the survey data and are used to obtain

quantitative flow information. This technique is constantly evolving and undergoing testing in anticipation of various hydraulic applications. The LSPIV technique was developed from the very common PIV, which is used to measure flow velocities in small flow fields to provide velocity fields covering large flow fields in field or laboratory conditions. LSPIV uses a video camera that records the temporal displacement of the floating tracers. This system can also work without floating materials in turbulent flow. However, finding which tracer is more efficient would enable the LSPIV system to be used more effectively.

Based on the aforementioned reasons, this study aimed to investigate the effect of material type and size of tracers on the accuracy of the LSPIV method. The findings of the study illuminate the potential role of imaging techniques in promoting the sustainable and efficient management of water resources.

2 Velocity Measurements

2.1 Acoustic Doppler Velocimetry (ADV)

Acoustic Doppler Velocimeter (ADV) system is based on the Doppler effect. It uses the acoustic frequency difference in the reflection of sound waves from particles traveling at the same speed as the water in the water. It can perform 2- or 3-dimensional measurements for short distances (10 cm away from the transducer in ADVs used in field measurement). The geometry of the ADV probe can be designed so that the transducers diverge from each other. The water passing through the beams is assumed to be homogeneous and the flow velocity is calculated by averaging the velocity calculated by each receiver (Figure 1).

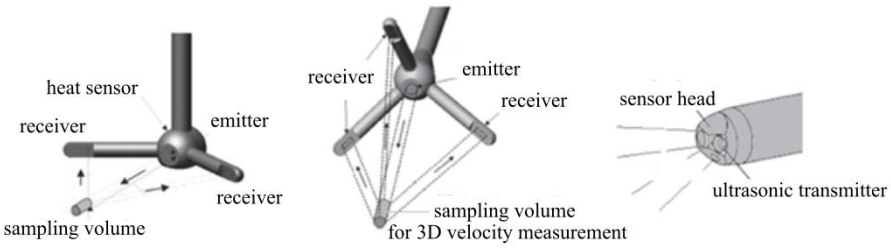

Fig. 1. ADV probe detail

2.2 Large Scale Particle Image Velocimetry (LSPIV)

For uniform flows, the differential equations can be solved for the channel cross-section and the flow rate can be approximately obtained from the integration of the calculated velocity field. As a result of the channel cross-section geometry, bed slope and roughness; a free surface velocity distribution is generated. Among several surface velocity measurement alternatives, cheap, fast and practical imaging techniques can be

preferred. LSPIV is a version of the PIV imaging technique but is often used in larger measurement areas such as riverine environments (Aya et al., 1995; Fujitta and Komura, 1994). The LSPIV algorithm for calculating velocities is the same as that used in conventional high-density imagery PIV, but it requires special arrangement for fluid illumination, fluid tracking and spatial distortion removal. The history of LSPIV goes back to when an image-based technique was proposed as an alternative method for river flow monitoring. The technique used was to combine traditional PIV concepts with pre-processing procedures to eliminate image distortion due to perspective and to correct for distortion introduced by the camera lens. Later, the technique was defined as Large Scale Particle Imaging with Velocimetry (LSPIV), taking into account the large size of the imaged area. LSPIV is a measurement technique that provides instantaneous and average two-dimensional velocity fields on the plane surface and flow rate estimates. The use of tracers to measure flow-surface velocity is based on the imaging technology used for PIV. LSPIV has the advantages of PIV, however it is a more practical method that can be used in large-scale areas such as sea or a river. Furthermore, the cost is low, and the lighting requirements are less than for PIV (no laser light is needed).

Many studies show that the LSPIV method can be successfully and efficiently used for large-scale flows in laboratory or field conditions to measure flow rates. There are four basic steps in conventional LSPIV: flow visualization, lighting, image recording and image processing. Sometimes the reference point is different from the usual free surface position, either it is impossible to mount the camera as you want, or more fluid needs to be included in the analysis. Photos taken from an oblique angle must first be reconstructed for analysis (Aberle et al., 2017). Since LSPIV recording usually involves a large flow field, it requires an additional step of image orthorectification, which aims to reduce the effect of oblique viewing of the flow surface. Furthermore, the LSPIV application requires guidance regarding the necessary size of the interrogation area (IA) to be used. IA is a square area incorporating the tracer particles and suitably large to encompass the scales of interest within the contracted flow field. Relatedly, in these same flow situations, LSPIV lacks guidance on the size of the search area (SA), a rectangle with the same center as the IA but extending beyond the IA to encompass flow directions with designated accuracy (Fahkri et al., 2021). A view of IA and SA in the channel and selection of them using LSPIV software is shown in Figure 2.

There are several application types of LSPIV, such as "mobile LSPIV" (Dramais et al., 2011; Muste et al., 2008), which allows instant in-situ measurements with advanced imaging devices, and "Air-LSPIV", which uses the image transmitted from an airplane or helicopter (Fujita and Hino, 2003; Fujita and Kunita, 2011).

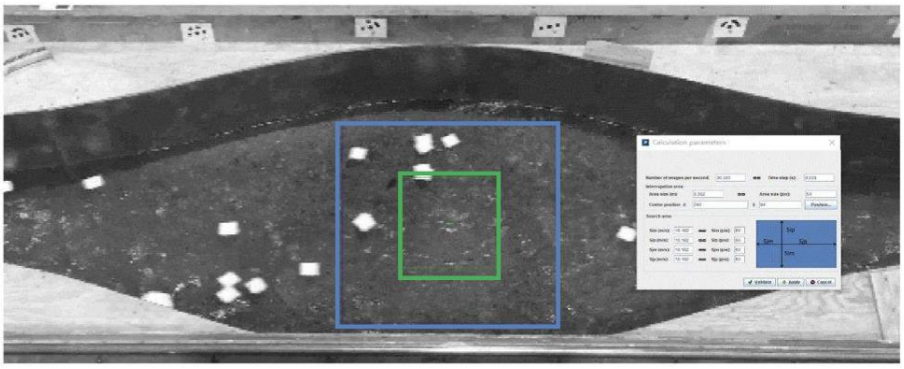

Fig. 2. Selection of IA and SA using LSPIV software

3 Experimental Studies

The experiments were conducted in an 18 m long, 0.5 m deep, 0.7 m wide channel with a slope of 5 ‰ (Figure 3). Data were collected for the ADV and LSPIV methods to determine the velocity of the flow in normal or flood conditions occurring in the streambed.

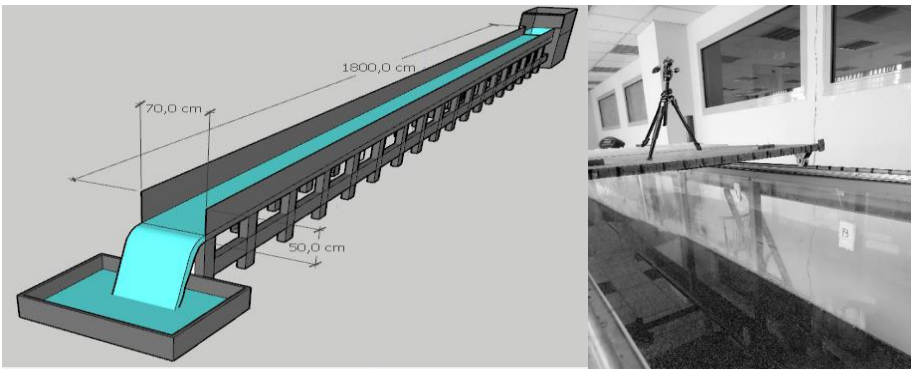

Fig. 3. Experimental channel and view from an experiment

The degree of scour or deposition along the bed of the channel can affect the flow field, resulting in a contraction and expansion. In order to eliminate this effect, it is important to carry out the experiments in a channel with solid and regular surfaces so that measurements can be compared. Since the tracers used will not create geometry-dependent acceleration and deceleration zones in the flow field, these conditions will not be affected by these changes and experiments were carried out only for conditions related to the buoyancy of the tracer material. The tracer particles were selected in sizes that can be used in natural conditions. The measurements were carried out in a 5 m long

area in the center of the channel so that the experiments would not be affected by the channel inlet and outlet conditions. The computer-controlled pump provides a flow rate in the range of 15-70 l/s. The inverter that controls the rotation speed of the pump is operated by computer software and the flow rate is measured by a magnetic flow meter.

3.1 ADV Measurements

ADV device was used for velocity measurements. The probe tip of the ADV was fixed on a system that can be adjusted in depth and can be moved longitudinally or transversely in the open channel in order not to drifted by the effect of the flow velocity. While fixing, it was ensured that the probe tip of the 4-receiver ADV in the x direction was parallel to the flow direction. After the ADV was connected to a computer, software was used to convert the data into a usable format. Measurements were taken in 10 sections at 50 cm intervals in the flow direction, at a distance of 5cm, 15cm, 25cm and 35cm from the side walls of the channel, respectively. For velocity measurement depths within the same cross-section, points were determined from the surface to the bottom in steps of 10% of the water height (Figure 4). This information is included in the technical information of the device.

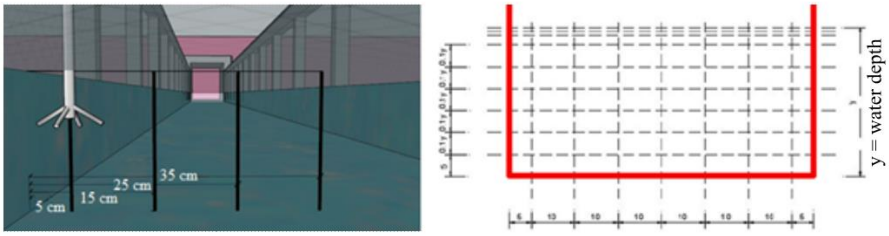

Fig. 4. Schematic representation of the locations of ADV measurements on a cross-section

Both x-direction and resultant ADV values were used. As you know, sampling satisfaction depends on the amount of data. Therefore, ADV-assisted velocity measurements taken at 10 different cross-sections along the flow path were averaged and a final ADV velocity value for the relevant flow rate was determined. However, since it is not yet decided which point velocity value in the cross-section will adequately represent the average velocity (Maghrebi and Givehchi 2009), it is assumed that LSPIV values can be compared with three different ADV velocity measurements. In the first one, the average velocity was calculated at 60% of the flow depth from the surface (V_{ADV-1}), in the second one, the average of the values between 20% and 80% of the flow depth from the surface (V_{ADV-2}), and in the third one, the geometric mean of all measurements (V_{ADV-3}).

3.2 LSPIV Measurements

Computer software was used to convert the motions of the drifting free surface trackers into the free surface flow velocity measurements. With the help of a fixed camera and

reference measurement points, a video image at a specified tracking time was first selected by the software. The critical point in the selection is the image clarity that allows the viewers to be tracked. Moving the camera or changing the reference points will directly affect the result. Orthorectification is then performed with the help of software to prevent perspective errors in the acquired image. Orthorectification is to create an image of the real image for a given plane, free from perspective and scaling effects. For this, reference points must first be defined in the program, then the Ground Reference Points should be marked on the image. LSPIV uses a statistical method based on cross-correlation on orthorectified images to determine the displacement of tracers visible on the surface. The displacement calculation process is used to calculate the velocity from tracer displacements and for this purpose it is necessary to define a number of parameters such as Sampling Area, Tracking Area, etc. The displacements of the tracers relative to the ground reference points are obtained by the digital analysis in the software. The result of all these processes gives the final average surface velocity. Figure 5 shows the eco-friendly trackers of different sizes (large, medium and small styrofoams with 1, 2.5 and 5 cm cubes) used for LSPIV and the velocity vectors obtained with the software.

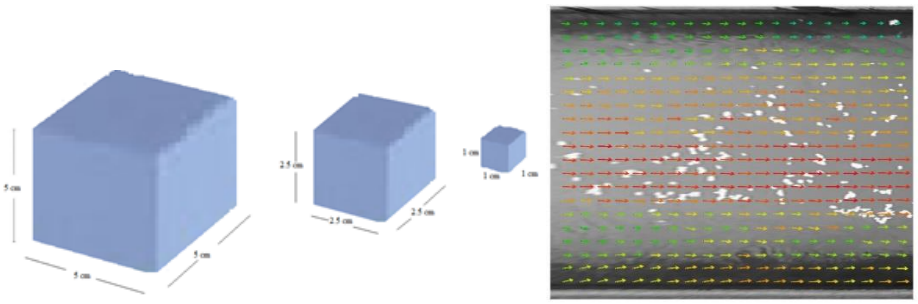

Fig. 5. LSPIV tracer samples (large, medium and small styrofoams) and surface velocity vectors visualization

4 Results and Discussion

The main objective of the study is to determine the flow rate with the help of surface flow velocity in open channels. Accurate calculation of flow rate with the help of surface flow velocities depends on the accuracy of measurement for cross-sectional area and cross-sectional average velocity. The relationship between measured surface velocities and average velocities needs to be verified or proportioned. In order to explain the relationship between the different tracers used and the average velocity, the measurements of the repeated experiments are given in Table 1. Surface flow velocities were determined using the LSPIV method. By using tracer particles of different sizes in the LSPIV application, the effect of interrogation areas (IA) and search areas (SA) on the measurements were examined, where the relationship between tracer motion and velocity values was interpreted. The flow velocities obtained from LSPIV and ADV

were compared with the average flow velocity obtained from the flow rate using continuity. In Table 2, the statistical evaluations for the three different flow rates planned for the study are shown as Set1 Set2 and Set3 groups. Although a constant pump power was determined for each set, both the fluctuations in electrical energy and the variability of the static water level at the intake port of the pump caused the flow rate in each experimental set to move within a small range. As can be seen in Table 2, the mean and standard deviation values of the flow rate oscillations are at acceptable levels.

Table 1. Table captions should be placed above the tables.

	Tracer Type	**Flow rate (l/s)**	**Water depth (cm)**	**LSPIV (m/s)**	**V_{ADV-1} (m/s)**	**V_{ADV-2} (m/s)**	**V_{ADV-3} (m/s)**
SET 1	Large	10.227	14.411	0.120	0.098	0.101	0.113
	Medium	9.918	14.426	0.121	0.103	0.105	0.117
	Small	10.228	14.404	0.121	0.098	0.107	0.118
SET 2	Large	23.225	17.395	0.218	0.190	0.191	0.194
	Medium	23.533	17.364	0.220	0.193	0.189	0.207
	Small	23.225	17.395	0.219	0.194	0.192	0.206
SET 3	Large	34.213	18.359	0.271	0.240	0.250	0.242
	Medium	34.185	18.450	0.274	0.241	0.238	0.263
	Small	34.225	18.361	0.272	0.238	0.245	0.244

The first finding that can be read from the experimental results is that the increase in flow rate values also increases the standard deviation value. The fact that the velocity values do not show any deviation in the experimental sets for different flow rates indicates that the experiments were carried out under similar boundary conditions. Thus, the results can be compared. The standard deviations of the ADV velocities calculated with the help of point velocity measurements are larger than that of all surface velocities made with different sized materials. This indicates that the turbulence conditions inside the flow are higher than at the surface. It is also seen that the LSPIV values determined at the surface are larger than the ADV values. This shows that particles with buoyancy do not encounter air resistance and are less affected by internal flow conditions. It is important to remember that these findings are based only on the velocity values in the mainstream direction. In other words, whether the same conclusions can be reached with vectorial velocity values will be discussed and decided separately in the following.

Table 2. Statistics of velocity measurements

LSPIV	Max	Min	Mean	Std. Dev.	V_{ADV-1}	Max	Min	Mean	Std. Dev.
SET1	0.122	0.116	0.120	0.002	**SET1**	0.103	0.098	0.101	0.002
SET2	0.220	0.211	0.217	0.003	**SET2**	0.198	0.187	0.193	0.003
SET3	0.274	0.263	0.270	0.004	**SET3**	0.247	0.235	0.241	0.010
V_{ADV-2}	**Max**	**Min**	**Mean**	**Std. Dev.**	V_{ADV-3}	**Max**	**Min**	**Mean**	**Std. Dev.**
SET1	0.107	0.101	0.104	0.002	**SET1**	0.120	0.113	0.116	0.002
SET2	0.198	0.189	0.194	0.003	**SET2**	0.208	0.193	0.202	0.006
SET3	0.250	0.238	0.245	0.010	**SET3**	0.270	0.242	0.258	0.010

The first thing that can be clearly seen from Figure 6 is that the velocities increase with flow rate. However, this increase is not instantaneous. Among the reasons for not seeing an increase at the same rate are inertia, conservation of mass and energy etc. Regardless of the materials, ADV measurements are close to each other. Nevertheless, the ADV-3 measurements show slightly larger values than the other two ADV measurements. The large ADV-3 measurements can be partly attributed to the multiple measurement points. Since ADV-1 measures at one point, ADV-2 measures at two points and ADV-3 measures at multiple points in each longitudinal section in terms of depth, it may seem that the ADV-3 value is more accurate, but this requires more experiments to verify. As can be seen from the graphs in Figure 6, large parts also need to be evaluated in more detail in terms of buoyancy and motion. This is because relatively different results are observed with large-scale trackers. Another important issue to be considered while observing the effects of the tracers is the grouping of the tracers or their movement together with the adhesion force.

It is possible to observe two different results from Table 3. The first is which point measurement is more representative whereas the second is which material size is more reliable. The simple statistical indicator "standard deviation" was used to measure both. According to the standard deviation, the value that gives the best surface velocity to cross-sectional velocity ratio is LSPIV-2. It is the cross-sectional average obtained by measurements at 20% and 80% of the depth. LSPIV-3 is expected to give smaller deviations; however, the opposite was observed, this may be due to the lack of measurements close to the bottom. The slight difference between the LSPIV-2 and the LSPIV-3 may be due to the linear variation of the velocity between 0 and 5 cm. This may have also arisen when the velocity in the mainstream direction was analyzed.

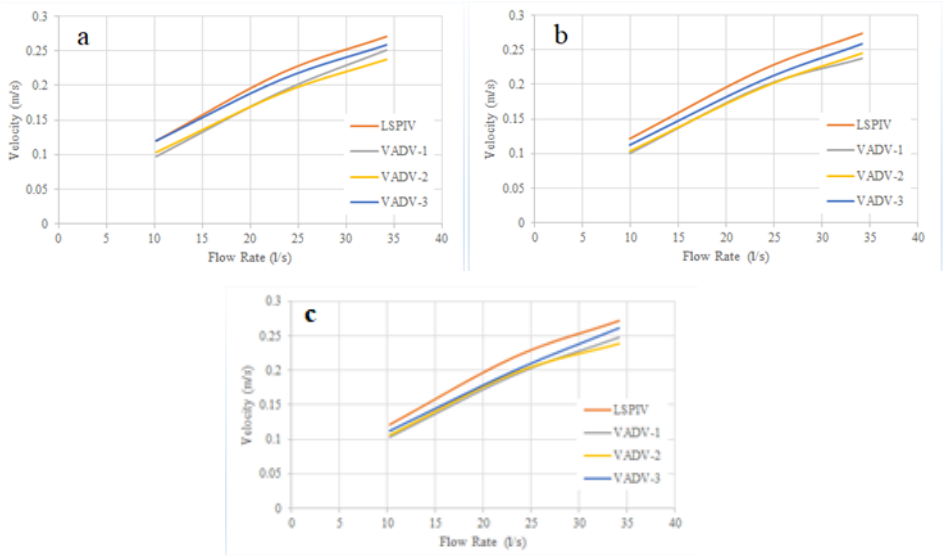

Fig. 6. Relationship between surface velocities as a function of flow rate and cross-sectional average main flow velocities according to tracer sizes and materials: a-Large Styrofoam, b Medium Styrofoam, c-Small Styrofoam

Table 3. Surface and cross-sectional velocity comparisons by tracer types

Tracer	Flow Rate	LSPIV	LSPIV/V_{ADV-1}	LSPIV/V_{ADV-2}	LSPIV/V_{ADV-3}
Large	10.227	0.120	1.224	1.188	1.062
	23.225	0.218	1.147	1.141	1.124
	34.213	0.271	1.129	1.084	1.120
	Stan. deviation		0.051	0.052	0.035
Medium	9.918	0.121	1.175	1.152	1.034
	23.533	0.22	1.140	1.164	1.063
	34.185	0.274	1.137	1.151	1.042
	Stan. deviation		0.021	0.007	0.015
Small	10.228	0.121	1.235	1.131	1.025
	23.225	0.219	1.129	1.141	1.063
	34.225	0.272	1.143	1.110	1.115
	Stan. deviation		0.057	0.016	0.045

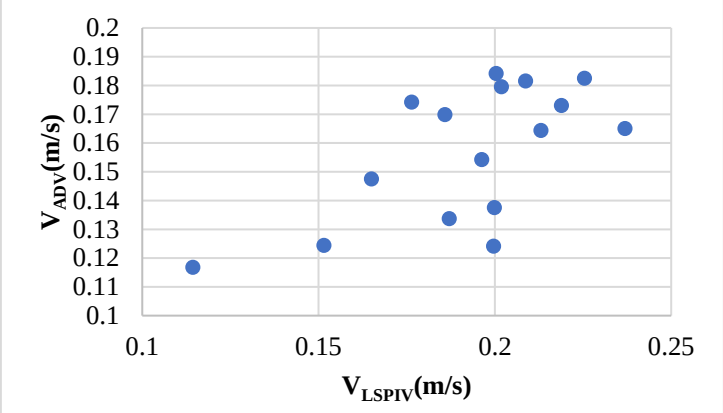

Fig. 7. Relationship between LSPIV and ADV

The scatter plot shown in Figure 7 is obtained for the average surface velocity LSPIV values and average cross-sectional velocity ADV values. In order to observe the effect of the change in flow rate on the velocity, different flow rates were studied and average measurements in 10 different sections were used.

According to the results, the average surface velocity values obtained from PIVLab output for the relevant experimental set vary between 0.1144 m/s and 0.2369 m/s, while the cross-sectional velocities obtained from ADV measurements vary between 0.1168 m/s and 0.1841 m/s. This shows that ADV values were lower than PIVLab values. The ratio between surface velocity and cross-section average velocities was contrary to expectations. According to hydraulic principles, surface velocities are expected to be lower due to friction with air, but possible head losses and turbulence prevented this result.

5 Conclusions

When the developing technology is combined with the challenges of the age, the understanding that is sensitive to environmental conditions and concerned about the living conditions of future generations increases the responsibility of science and pushes academicians to conduct more comprehensive research. With this understanding, as Ege University Department of Civil Engineering, Department of Hydraulics, we aimed to obtain some findings by conducting a series of laboratory experiments. Mainly by using different disciplines such as image analysis, remote sensing, material science, fluid mechanics, hydrology, we tried to obtain some criteria to accurately evaluate natural and unnatural flow conditions.

We can summarize the findings of the study to determine the average flow velocity or flow rate with image analysis as follows.

- Experiments using different sized trackers showed the importance of determining the effective tracker size in LSPIV application.
- It was observed that if the tracer size was too small, the materials could overlap and if it was too large, the flow movement could not be monitored in detail.
- When selecting the effective tracer size, it should be taken into account that if it is too small, it may stick together under the influence of surface tension, and if it is too large, the surface movement cannot be observed in detail.
- It was determined through experimental findings that the optimum size range is approximately 4 - 6% of the channel width. When the tracers are released into the flow, they should be dispersed so that they do not overlap.
- Since the possibility of losing the tracer used during the measurement, environmentally friendly materials that are stable against adhesion and cohesion forces with buoyancy properties should be used.
- When recording the flow velocity, it is important for the measurements that the angle between the camera and the surface flow is as close to vertical as possible.
- The camera should be able to see the reference points and the tracers drifting with the surface flow without interruption. Particular attention should be paid to the importance of light reflections in image analysis in the LSPIV method.
- In addition, the LSPIV method has the advantage that it is possible to make measurements even on an old or amateur video.
- In the experiments, it was observed that the flow velocity results obtained from LSPIV have a strong correlation with the flow velocity results calculated using both the ADV method and the continuity. This proved that the LSPIV technique is accurate for surface flow velocity measurements.
- LSPIV has an advantage over other flow velocity measurement techniques due to the simplicity and practicality of its application. It is also much less risky than the most widely used ADV method in terms of operator safety during measurements. In general, the LSPIV method was found to be an easy-to-use, practical and reliable flow rate measurement method.

Although the results obtained are satisfactory, it is important to examine the subject in depth with non-uniform geometric flow beds and different base roughness materials in the future.

Acknowledgements
We would also like to thank the Ege University Scientific Research Project Office (BAP) for the support on this research with Project No: FGA-2020-21464 and Project Title: Determination of Flow Quantity with the Assistance of Surface Flow Rate in Open Channel Flows

References

1. Aberle, J., Rennie, C. D., & Admiraal, D. M.: Topography and bathymetry. Experimental hydraulics: Methods, Instrumentation, Data Processing and Management International Edition (Vol. 6, Issue 11) (2017).
2. Aya, S., Fujita I., and Yagyu M. : Field observation of flood in a river by video image analysis, Proc. Hydraul. Eng., 39, 447– 452 (1995).
3. Das, S., & Mazumdar, A. : Evaluation of hydrodynamic consequences for horseshoe vortex system developing around two eccentrically arranged identical piers of diverse shapes. KSCE Journal of Civil Engineering, 22(7) (2018).
4. Dramais, G., le Coz, J., Camenen, B., &Hauet, A. : Advantages of a mobile LSPIV methodformeasuringflooddischargesandimprovingstage-dischargecurves. In Journal of Hydro-Environment Research (Vol. 5, Issue 4) (2018).
5. Fakhri A, Ettema R, Aliyari F, Nowroozpour A. : Large-Scale Particle Image Velocimetry for Estimating Vena-Contracta Width for Flow in Contracted Open Channels. Water; 13(1):31. https://doi.org/10.3390/w13010031 (2021).
6. Fujita, I., & Hino, T. : Unseeded and Seeded PIV Measurements of River Flows Video taped from a Helicopter. Journal of Visualization, 6(3) (2003).
7. Fujita, I., & Kunita, Y. : Application of aerial LSPIV to the 2002 flood of the Yodo River using a helicopter mounted high density video camera. Journal of Hydro-Environment Research, 5(4) (2011).
8. Fujıta, I., & Komura, S. : Application of Video Image Analysis for Measurements of River-SurfaceFlows. Proceedıngs of Hydraulıc Engıneerıng, 38 (1994).
9. Maghrebi MF, Givehchi M : Estimation of depth-averaged velocity and boundary shear stress in a triangular open channel. J Water Wastewater 2:71–80 (2009).
10. Muste, M., Fujita, I., &Hauet, A. : Large-scale particle imagevelocimetry for measurements in riverine environments. Water Resources Research, 46(4) (2008).
11. Schugerl, R., Veliskova, Y., & Kimlickova, T. : Comparison of the discharge and flow velocity values determined by ADV device and indicator method. IOP Conference Series: Earth and Environmental Science, 362(1). https://doi.org/10.1088/1755-1315/362/1/012056 (2019).
12. Shimizu, T., Kobayashi, M., Iida, S., & Levia, D. F. : A generalized correction equation for large tipping-bucket flow meters for use in hydrological applications. Journal of Hydrology, 563 (2018).
13. USGS Website, https://www.usgs.gov/special-topics/water-science-school/science/how-streamflow-measured#overview, last accessed 2023/06/10.

STRUCTURES & EARTHQUAKE

pages: 526 – 784

A Computational Model for the Analysis of 2D Beams and Frames Failure Based on Hardening and Softening Behaviors with an Incorporated Damage Model

Mourid Elhoucine[1], Koulli Redhwane[2], and Mamouri Said[3]

[1] TAHRI Mohammed University, Mechanical Engineering Department, L2ME Laboratory, Bechar, Algeria,
mourid.elhoucine@univ-bechar.dz, [orcid ID: 0000-0002-5996-6067]
[2] TAHRI Mohammed University, Mechanical Engineering Department, L2ME Laboratory, Bechar, Algeria,
koulli.redouane@gmail.com, [orcid ID: 0000-0002-5405-1765]
[3] TAHRI Mohammed University, Mechanical Engineering Department, L2ME Laboratory, Bechar, Algeria,
said.mamouri@gmail.com, [orcid ID: 0000-0002-8315-8086]

Abstract. In civil engineering and construction domains, the most widely used materials are perhaps reinforced concrete and steel. Moreover, most of the constructions in civil engineering are based on reinforced concrete (or metal) beams and columns. In order to provide crucial information and knowledge about the lifespan of such constructions, it may be very beneficial to study the behavior of reinforced concrete (or metal) beams and frames up until total failure. Before reaching complete failure, the limit load and the limit ductility constitute important data for such structure. A finite element beam formulation is presented in this paper for the analysis of 2D frame failure. The proposed model is capable of capturing the ductility limit and post-peak structural response of a collapsed structure brought on by a natural disaster like an earthquake or any other unintentional action. The proposed model includes a damage model and is based on hardened-softened behavior. A damage model is combined with a linear geometric analysis that is based on an elastoplastic constitutive law with linear isotropic hardening and a rigid plastic softening law. Such analysis produces plastic hinges and damaged zones in a number of critical areas that cause the redistribution of loads and gravity actions. The structure fails as a result of these plastic hinges and strain localizations, creating a final failure mechanism. In order to illustrate the effectiveness of the suggested model, numerical simulations are examined and concluding remarks are drawn.

Keywords: Hardened-Softened behavior, Damage model, Failure analysis.

1 Introduction

The experimental testes and earthquakes phenomena prove that the localized failure in critical zones is the reason behind the failure of the most stee andl RC frame structures.

The localized failure and yielding in a number of critical cross sections lead to the concept of plastic hinge, which is characterized by keeping constant the limit capacity during the analysis, while other plastic hinges develop. Such procedure does not able to describe the post peak structural response. To compute the post peak response which can be characterized by decreasing load capacity with increasing deformation, the softening of the cross-section has to be taken into account, this leads to the concept of "softening plastic hinge" [1-4].

In the beam finite element analysis, the softening plastic hinge is modeled in classical way by a short finite element with finite length. The localized failure zones can be treated in the context of discontinuity introduced in standard finite element method. The most frequently used method is the so-called Embedded Strong Discontinuity Approach [1-4]. The principal idea is the incorporation of localized energy dissipation in finite element formulation, by introducing a strong discontinuity in kinematics and defining local dissipative mechanism [1-7].

In other hand, the localized failure zones can also be treated as damaged zones appeared within the finite element when the element reaches its ultimate capacity. The response of the concrete is initially elastic up to a certain limit from which the material begins to deteriorate. The damage causes a reduction in the elastic modulus. As results, this leads to decreasing load capacity with increasing deformation which characterized the post peak response [8-11].

In this work, we use a finite element beam model based on curved Timoshenko beam in modelling of failure analysis of 2D RC frames. The main idea is to combine an elastoplastic constitutive law studied by many researchers [1-4] with a simple damage model exist in literature [11] to predict the failure analysis of 2D RC beam and frame. The bending elastoplasticity with linear isotropic hardening is considered when constructing the constitutive law. Such a constitutive relation describes the realistic behavior of RC beam in bending. A concrete damage is considered to describe the response of the beam after the localized failure, such response governed by damage model with linear softening law [1,3,5,11].

2 Failure mechanism creation

A 2D Timoshenko beam is used and the corresponding kinematics and constitutive laws are considered in order to get the beam model that is used in failure analysis and mechanism creation (for more details, see [1,5]).

2.1 Elastoplastic constitutive laws

Response in axial direction is described by the linear elastic law: $N = EA\varepsilon$, where E is the elastic modulus, A is the cross-section area, and ε is the axial strain. Here, we use the elastoplastic law with bi-linear isotropic hardening to describe the bending behavior of the beam (Fig.1) (see [3,5]).

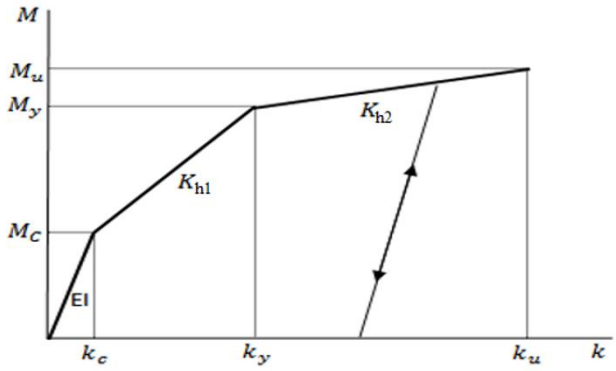

Fig. 1. Elastoplastic constitutive laws.

Before reaching the ultimate moment, the total curvature decomposes into elastic and plastic parts:

$$k = \bar{k}^e + \bar{k}^p \tag{1}$$

The expression of the moment in the plastic phase can be written as:

$$M = \mathrm{EI}(\kappa - \bar{\kappa}^p) \tag{2}$$

To control the plastification process in the bulk, we introduce two yield criteria $\bar{\phi}_c$ *and* $\bar{\phi}_y$ which can be respectively written as:

$$\bar{\phi}_c(M, \bar{q}_c) = |M| - (M_c - \bar{q}_c) \tag{3}$$

$$\bar{\phi}_y(M, \bar{q}_y) = |M| - (M_y - \bar{q}_y) \tag{4}$$

The first criterion controls the cracking of the concrete when reaching the cracking moment value M_c associated with the hardening parameter K_c and the stress-like bending hardening variable $\bar{q}_c = K_{h1}\xi$, where ξ is the strain-like bending hardening variable.

The second criterion controls the yielding of the steel when reaching the yielding moment value M_y associated with the hardening parameter K_y and the stress-like bending hardening variable $\bar{q}_y = K_{h2}\xi$, where ξ is the strain-like bending hardening variable.

2.2 Damage model and softening behavior

In order to describe the softening-damaged behavior (after appearing the damage), we use the damage law characterized by decreasing the moment and increasing the curvature (Fig.2) [11].

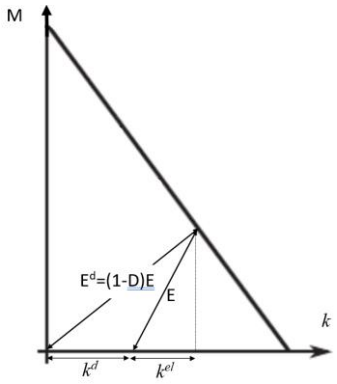

Fig. 2. Softening-damage law.

When the ultimate moment is reached, the total curvature will be enhanced by damaged part in addition to elastic and plastic parts:

$$k = \bar{k}^e + \bar{k}^p + k^d \tag{5}$$

The expression of the moment after reaching the damage criteria can be written as:

$$M = (1 - D)\mathrm{EI}(\kappa - \bar{\kappa}^p) \tag{6}$$

where I is the inertia moment and E is the elastic modulus. D is the damage parameter and its expression can be written as follows:

$$D = 1 - \frac{\bar{k}^e}{\bar{k}^e + k^d} \tag{7}$$

Such choice of damage parameter is made for ensuring that the material is firstly undamaged $(k^d = 0 \Rightarrow D = 0)$, then, with the evolution of damaged part of curvature k^d, the damage parameter grow until reaching its maximal value $(D = 1)$ when k^d reaches important value.

To control the appearance of damage and, consequently, the formation of softening damaged hinge, we introduce the failure function $\bar{\bar{\phi}}$ which can be written as:

$$\bar{\bar{\phi}}(M, \bar{\bar{q}}) = |M| - (M_u - \bar{\bar{q}}) \tag{8}$$

With the particular form of the failure function in (8), it is easy to control the formation of the damaged hinge in the beam from reaching the ultimate moment value M_u at one of the integration points until the total failure of the beam when carrying

capacity drops to zero. The softening of the section characterized by its modulus $K_s < 0$ is exploited here to conduct the failure of the beam, where $\bar{\bar{q}} = -K_s\bar{\bar{\xi}}$ is the stress-like bending softening variable and $\bar{\bar{\xi}}$ is the strain-like bending softening variable.

3 Numerical examples

In this section we illustrate the performance of the proposed model when applying it to RC beam and frame, in order to create the failure mechanisms that leads to the collapse of the structure. The examined numerical tests and necessary data are taken from the previous studies in [1-5,12].

3.1 Cantilever Beam

We consider the cantilever beam of rectangular cross section with length L = 2.5m, two loading cases at the end of the cantilever beam are tested.

The geometric and material proprieties are chosen as: $EI = 77650\ KNm^2$, $M_c = 37.9\ KNm$, $M_y = 268\ KNm$, $K_{h1} = 29400\ KNm^2$, $K_{h2} = 272\ KNm^2$, $M_u = 274\ KNm$, $K_s = -18000\ KNm$.

1. The cantilever beam is loaded at the free end by a moment (Fig.3)

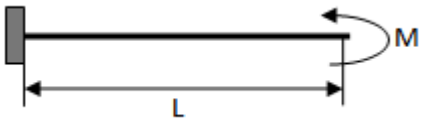

Fig. 3. Cantilever beam with end moment.

The cantilever beam is modelled with 1, 2 ,5 and 10 finite elements. An imposed rotation is applied at the free end in order to get the failure analysis. Fig.4 shows that the four choices of mesh present the same response with same slope softening which illustrates the mesh independency of the model. The homogeneous stress state along the beam axis triggers the localized failure in all elements simultaneously which leads to the simultaneous creation of softening damaged hinges in the beam. However, the real structures are generally characterized by existing defects and heterogeneities of material properties that can be modelled by weakening one of the finite elements by reducing its ultimate moment (see (Fig.5)). As results, the localized failure is appeared only in the weakened element. In such case, the same response with same slope softening, but with different final moment, is remarked between different meshes.

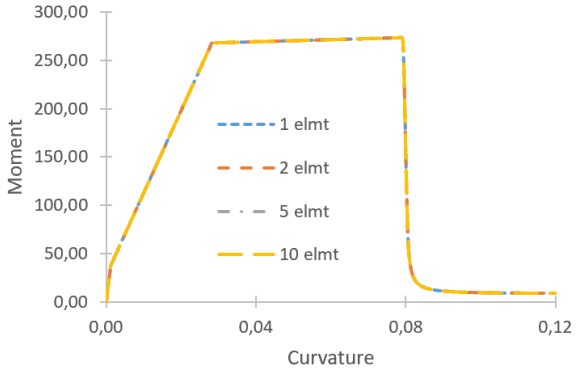

Fig. 4. Response of cantilever beam with end moment: different number of elements with the same properties.

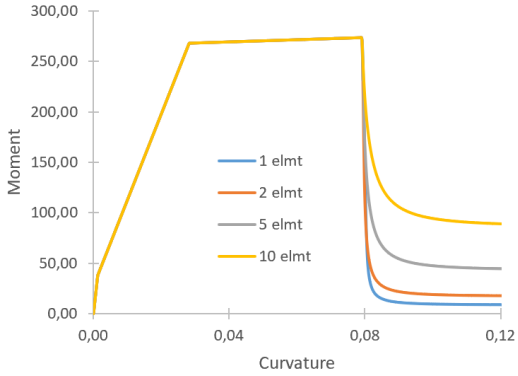

Fig. 5. Response of cantilever beam with end moment: different number of elements with one weakened.

2. Second load case of the cantilever beam concerns the free end vertical force. We use the same geometric and material proprieties as for load case 1, except the ultimate moment value where we use $M_u = 374\ KNm$. (Fig 6)

The cantilever beam is modelled with 10, 25, 50 and 60 finite elements. An imposed vertical displacement is applied at the free end in order to get the failure analysis.

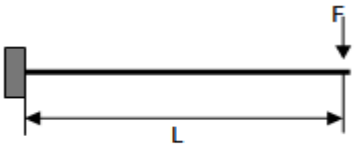

Fig. 6. Cantilever beam under transversal force.

Fig.7 shows that the different mesh grading presents the same slope softening but not the same ultimate load. This difference can appear from the use of only one integration point, which leads to a shift of the softened damaged hinge. In this example, there is no need for weakening one of finite elements, because the nature of problem presents non homogeneous stress state. As results, the localized failure is appeared only in the element with maximal capacity.

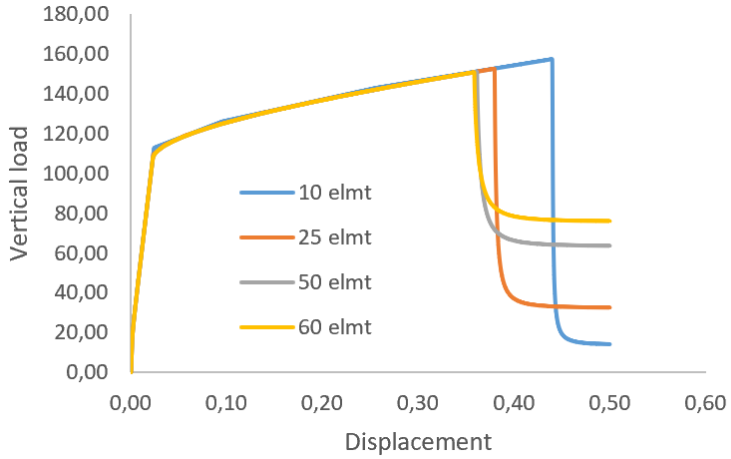

Fig. 7. Response of cantilever beam with vertical load: different number of elements.

3.2 Two-story reinforced concrete frame:

The present example is widely studied either experimentally [12] or numerically [1-5]. We consider two-story reinforced concrete frame with height H =2m and span L =3.5m. Columns and beams have the same rectangular cross section $b \times h = 0.3 \times 0.4\ m^2$. The material proprieties needed for computation are given by (see Dujc *et al.* (2010)):

- for columns:

$$M_c = 100\ KNm;\ \ M_y = 245\ KNm;\ \ M_u = 265\ KNm;$$
$$K_{h1} = 12450\ KNm^2;\ \ K_{h2} = 195\ KNm^2;\ \ \ K_s = -2410\ KNm$$

- for beams:

$$M_c = 30\ KNm;\ \ M_y = 150\ KNm;\ \ M_u = 170\ KNm;$$
$$K_{h1} = 11190\ KNm^2;\ \ K_{h2} = 137\ KNm^2;\ \ \ K_s = -1310\ KNm$$

Columns are clamped at the bottom. The load is applied in two steps. First, constant vertical force act at the top of both columns. Second, we impose horizontal displacement u at the left top of the frame.

The structure is modelled by different finite elements number until ensuring the mesh convergence. Fig.9 shows that our results are in good agreement with experiment [12] and numerical ones [1-5]. The results illustrate that the model is able to predict

the complete failure after creating six softened hinges and damaged zones located in joints beam-column and two bottom clamped support (Fig.10).

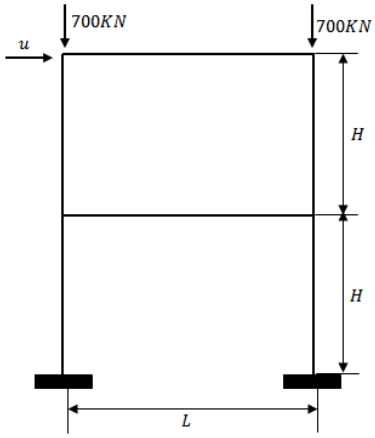

Fig. 8. Two-story frame.

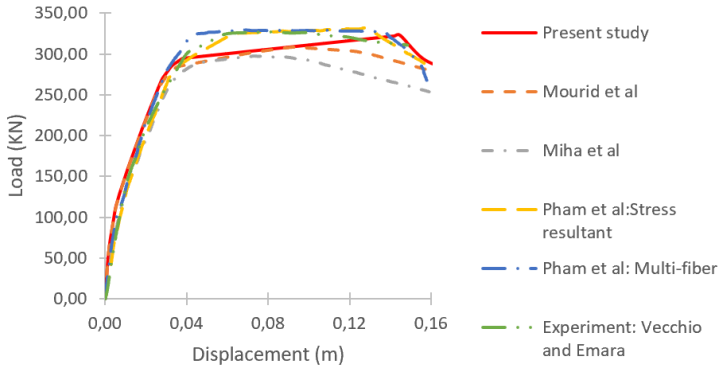

Fig. 9. Response of the frame up to the complete failure: different approaches.

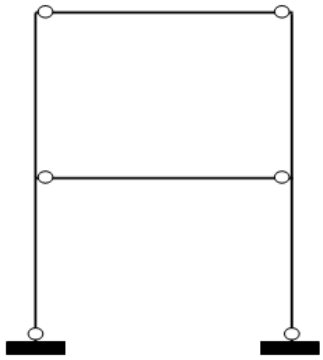

Fig. 10. Localization and damaged zones in the two-story frame.

4 Conclusion

In this work, we present a constitutive law model based on hardening and softening behaviors that can be used for failure mechanism of 2D RC beam and frame. The presented model is able to describe the global characteristics of the RC frame behavior up to its complete failure, such as the concrete cracking, the steel yielding and the localized failure of the beam's cross-section that is associated with formation of the softening damaged hinge. The consideration of the softening of beam cross section and the concrete damage is important for describing the post peak structural response. Our results illustrate that the presented model is able to predict the softening damaged hinges in the structure which leads to the formation of the complete failure mechanism.

References

1. Bui N. N., Ngo M., Nikolic M., Brancherie D., Ibrahimbegovic A., Enriched timoshenko beam finite element for modeling bending and shear failure of reinforced concrete frames, Computers & Structures 143, pp. 9-18 (2014).
2. Dujc J., Brank B., Ibrahimbegovic A., Multi-scale computational model for failure analysis of metal frames that includes softening and local buckling, Computer Methods in Applied Mechanics and Engineering 199 (21-22), pp. 1371-1385 (2010).
3. Jukic M., Brank B., Ibrahimbegovic A., Embedded discontinuity finite element formulation for failure analysis of planar reinforced concrete beams and frames, Engineering Structures 50, pp. 115-125 (2013).
4. Pham B., Brancherie D., Davenne L., Ibrahimbegovic A., Stress-resultant models for ultimate load design of reinforced concrete frames and multi-scale parameter estimates, Computational Mechanics 51 (3) , pp. 347-360 (2013).
5. El Houcine M., Said M., Adnan I., A controlled destruction and progressive collapse of 2d reinforced concrete frames, Coupled Systems Mechanics 7 (2), pp. 111-139 (2018).
6. Ibrahimbegovic A., Brancherie D., Combined hardening and softening constitutive model of plasticity: precursor to shear slip line failure, Computational Mechanics 31 (1-2), pp. 88-100 (2003).

7. Imamovic I., Ibrahimbegovic A., Knopf-Lenoir C., Mesic E., Plasticity-damage model parameters identification for structural connections, Coupled Systems Mechanics 4 (4) , pp. 337-364 (2015).
8. Mazars, J. A description of micro- and macroscale damage of concrete structures. Engineering Fracture Mechanics, 25(5-6) :729–737. (1986).
9. Mazars, J., Hamon, F., and Grange, S. (2014). A new 3D damage model for concrete under monotonic, cyclic and dynamic loadings. Materials and Structures, pages 3779–3793
10. Lemaitre, J. and Chaboche, J.-L. Mechanics of solid materials. Cambridge University Press, Cambridge. (1990).
11. Ibrahimbegović, A. Mécanique non linéaire des solides déformables: Formulation théorique et résolution par éléments finis. Hermes science publ. (2006).
12. Vecchio FJ, Emara MB. Shear deformations in reinforced concrete frames. ACI Struct J;89(1):46–56. (1992).

Calculation Of Seismic Effects in the LIRA 10 Software Complex

Isaak Ievzerov [1][0000-0003-3414-9930], Yurii Heraimovych[2][0000-0002-5605-5276] and Dmytro Marchenko[3][0000-0002-4377-5098]

[1] «LIRA SOFT» LLC, Kyiv, Ukraine, ide@lira.com.ua
[2] «LIRA SOFT» LLC, Kyiv, Ukraine, yury@lira.com.ua
[3] «LIRA SOFT» LLC, Kyiv, Ukraine, mdv@lira.com.ua

Abstract. Earthquakes take a leading place among extraordinary natural phenomena in terms of human casualties and significant material losses. Confirmation, unfortunately, we saw during the recent earthquake in Turkey and Syria. A large part of the territory of Ukraine [1] is seismically dangerous. The magnitude and complexity of the tasks of earthquake-resistant design of civil, industrial and transport construction objects requires appropriate theoretical and programmatic developments. For many years, program complex LIRA 10 (PC LIRA 10) has successfully coped with the tasks of earthquake-resistant design. Calculations for seismic effects according to the building codes of Armenia, Uzbekistan, Ukraine, Turkmenistan, Kazakhstan, Tajikistan, Azerbaijan, Georgia, Kyrgyzstan, USA, Eurocode, Israel, Iran, India, Algeria and Turkey are implemented. Calculations for one-component and three-component accelerograms of earthquakes, calculations based on the reaction spectrum, three-component graphs of dynamics coefficients, direct integration of the equations of motion implemented and Pushover Analysis are also implemented. The article provides an overview of the possibilities and methods of calculating seismic effects implemented in PC LIRA 10.

Keywords: Calculations for seismic effects, PC LIRA 10, accelerogram, seismogram, response spectra, non-reflecting boundary, Pushover Analysis.

1 Equations of Motion

Calculation of dynamic effects is based, as is known [2], on a system of differential equations

$$Mu''(t) + Cu'(t) + Ku(t) + q(t) = 0, \quad (1)$$

where M, C, K – are matrices of masses, damping and stiffness of the system respectively, $u(t)$, $u'(t)$, $u''(t)$, $q(t)$ – vectors of nodal displacements, velocities, accelerations and external loads at a moment in time t.

When calculating for seismic effects, it is assumed that external loads are equal to zero, and the displacements $\gamma \cdot s(t)$, caused by the movement of the earth's surface are added to, $u(t)$, where γ – vector of the guiding cosines of the seismic influence, $s(t)$ – is the given law of the movement of the earth's surface (earthquake seismogram).
The equations of motion than have the form

$$M\big(u(t)+\gamma\cdot s(t)\big)'' + C\big(u(t)+\gamma\cdot s(t)\big)' + K\big(u(t)+\gamma\cdot s(t)\big) = 0, \qquad (2)$$

Let's denote $a(t) = s''(t)$ the given earthquake asselerogram and suppose, that $K\gamma = C\gamma = 0$. We will obtain similar to (1) equations

$$Mu''(t) + Cu'(t) + Ku(t) + M\gamma\cdot a(t) = 0, \qquad (3)$$

external loads are equal to $M\gamma\cdot a(t)$.

To solve system (1), two main methods are used: expansion by the forms of natural oscillations and direct integration of the equations of motion. The method of expansion by forms can be used only for linear calculation, since the principle of superposition does not apply in nonlinear theory. Direct integration methods are general and can be used for all problems of dynamic calculation of structures.

1.1 Expansion by the Forms of Natural Oscillations

A significant part of the methods of dynamic calculation of elastic systems (including those regulated by building regulations) is based on the expansion of the solution by the forms of natural oscillations in the form

$$u(t) = \Phi y(t),\ \Phi = [\varphi_1, \varphi_2, \dots, \varphi_m],\ \varphi_i,\ \ i = 1,2,\dots,m.$$

Forms φ_i and frequencies ω_i of natural oscillations are solutions of the eigenvalue problem

$$K\varphi_i = \omega_i^2 M\varphi_i,$$

and are determined by the method of iterations of subspaces [3] using the modified Jacobi method.
The forms satisfy the conditions of orthogonality

$$\varphi_i^T M\varphi_j = 0,\ \ \varphi_i^T K\varphi_j = 0,\ i \neq j,$$

and are normalized by the mass matrix:

$$\varphi_i^T M\varphi_i = 1,\ \ \varphi_i^T K\varphi_i = \omega_i^2.$$

If the orthogonality conditions are also met for the damping matrix C, then system (1) decomposes into separate equations

$$\ddot{y}_i + 2\xi\omega_i\dot{y}_i + \omega_i^2 y_i = -\varphi_i^T q(t),\ \ i = 1,2,\dots,m. \qquad (4)$$

For impulse, periodic impact, wind, seismicity, further calculations are carried out according to the recommendations of the building regulations.

The modal mass contribution for that form is calculated by the formula

$$m_i^{kpd} = \frac{(\gamma^T M \varphi_i)^2}{(\varphi_i^T M \varphi_i) \cdot (\gamma^T M \gamma)} \cdot 100\%.$$

For summarizing the results obtained for each form, the normative documents suggest a SRSS method (Square Root of the Sum of the Squares) and CQC method (Complete Quadratic Combination). Both methods are implemented in PC LIRA 10.

In the presence of the same frequencies, a single normalized linear combination of forms that have this frequency is calculated from the condition of the maximum contribution to the load. Forms that are orthogonal to the resulting linear combination contribute zero. This avoids possible inaccuracies.

The influence of uncalculated eigenforms in PC LIRA 10 is not taken into account.

1.2 Difference Scheme

When constructing a difference scheme for the system of differential equations (1), acceleration, velocity, and displacement are approximated by difference relations. Let's denote θ a step in time

$$\begin{gathered} t_n = n\theta, u_n = u(t_n), \\ \delta_n u = (u_{n+1} - u_n)/\theta,\ \beta_n u = (u_{n+1} - u_{n-1})/(2\theta) = (\delta_n u + \delta_{n-1} u)/2, \\ \gamma_n u = (u_{n+1} - 2u_n + u_{n-1})/\theta^2,\ \ \alpha_n u = (u_{n+1} + u_{n-1})/2. \end{gathered} \quad (5)$$

By replacing the acceleration, speed and displacement at the instant of time t_n by difference relations (5), we get

$$\begin{gathered} u_n'' = \gamma_n u = (u_{n+1} - 2u_n + u_{n-1})/\theta^2, \\ u_n' = \beta_n u = (u_{n+1} - u_{n-1})/2\theta, \\ u_n = \alpha_n u = (u_{n+1} + u_{n-1})/2. \end{gathered} \quad (6)$$

The error of formulas (6) is of the order of θ^2. Substituting (6) into (1), we get a system of equations

$$M\gamma_n u + C\beta_n u + K\alpha_n u + q_n = 0. \quad (7)$$

Such difference schemes are called implicit because. unknown displacements u_{n+1} are determined by the previously found u_n, u_{n-1}, from the system of linear equations, the matrix of which includes the stiffness matrix K.

Scheme (7) is unconditionally stable [4], therefore it is used in PC LIRA 10 when solving both linear and nonlinear dynamic problems.

It should be noted that, according to building regulations, calculations for a design earthquake can be performed in a linear setting, and for the maximum possible – only

in a physically non-linear one, that is, using the difference scheme. We also note that, as proved in [5], equation (7) coincides with the well-known Newmark scheme [6].

1.3 Diagonal and Consistent Mass Matrix

In the first versions of PC LIRA, a diagonal mass matrix was used for dynamics problems. Starting with version 9.4, a more accurate, consistent mass matrix is used, which is built from the approximating functions used for the stiffness matrix. With this approach, the inertia of rotation is also taken into account – "torque" elements appear in the mass matrix.

Condensation of Masses

A structure may have many forms with near-zero contributions. In order to get rid of such forms, the condensation of masses was implemented. The elements from which the mass must be collected and the nodes into which the collected mass must be distributed are indicated.

1.4 Damping

For expansion by the forms of natural oscillations, a damping coefficient is set, one for all forms, for the difference scheme it can be in the form of concentrated dampers and in the form of Rayleigh – a linear combination of mass and stiffness matrices.

1.5 Physically Nonlinear Bending Finite Elements

In previous versions of PC LIRA, physically nonlinear finite elements of bending rods and plates, based on the nonlinear theory of elasticity, were implemented. These elements are successfully used for static calculations, but are not applicable to dynamic problems. Then two-dimensional and three-dimensional physically nonlinear finite elements based on the theory of elastic-plasticity were developed. These elements are used for both static and dynamic calculations, but do not solve bending problems. New physically nonlinear finite elements of bending rods and plates, based on the theory of elastic-plasticity, are now implemented in PC LIRA 10. These new elements have all the same capabilities as physically nonlinear bending elements – the same set of loads, taking into account shear, the presence of an elastic base, which can be one-sided, the use of hinges for rod finite elements. The new elements can be used for both static and dynamic calculations, in particular, in solving seismic problems.

1.6 New Non-Reflecting Boundary Finite Elements

The calculation model for determining the seismic response of the "soil-building" system consists of the building itself and the foundation area. The base model is a half-space from which a limited area is selected. Additional boundary conditions are required on the part of the boundary of the selected region contained within the half-space. In a static problem, it is enough to choose the dimensions of the soil area so that these boundary conditions do not affect the stresses under the structure.

If this is done for seismic calculations, the waves will reflect from the boundary of the area and return to the building, affecting its oscillations.

That is, the boundaries of the soil area should be moved away so that the reflected waves do not have time to return during the earthquake. But even at the current level of development of computer technology, such a calculation is impossible, because. the calculation scheme will exceed all permissible dimensions.

Finite elements of the non-reflective boundary are implemented in PC LIRA 10. They allow waves to pass through the boundary unhindered and therefore ensure the correct calculation of such problems. For flat calculation schemes, these are two-node FEs, for spatial ones – three- and four-node FEs. Non-reflective boundary conditions have the form [7]

$$\sigma_n = c_n \rho u_n', \sigma_\tau = c_\tau \rho u_\tau', \quad (8)$$

where σ_n, u_n', σ_τ, u_τ' – normal and tangential stresses and velocities, c_n, c_τ – velocities of longitudinal and transverse waves, ρ – soil density.

The library of PC LIRA 10 finite elements includes plane and spatial SE of the soil, which take into account its physical and mechanical properties. The following models have been implemented: Coulomb-Mohr, Drucker-Prager, Botkin, as well as analytical strength theory [8].

The use of these FEs in the MONTAZH system allows you to simulate a wide range of geotechnical tasks: soil excavation, anchoring of sheet pile fences, foundation work in difficult geological conditions, soil subsidence.

2 Calculations

Without pretending to be complete, we will indicate some classes of seismic problems that are solved using PC LIRA 10.

2.1 Calculation by Earthquakes Seismogrames

The equations of motion (2) and the difference scheme are used. The speed of propagation of the seismic wave, which is specified in the initial data, is taken into account. This method of seismic calculation is more natural than using accelerograms. For such structures as bridges and other long-span structures, taking into account the fact that the supporting parts, where the seismogram acts, are included in the work not simultaneously, but as the seismic wave passes, can give significant differences compared to calculations based on accelerograms, a qualitatively different distribution of forces. However, it should be noted that until now there is no generally accepted approach to the determination of seismograms from accelerograms. The results of the calculation based on the seismograms are the total displacements $\big(u(t) + \gamma \cdot s(t)\big)$, therefore, the reference node can be specified in the output data, and the reference node's displacements are subtracted from the displacements of all nodes.

2.2 Calculation by Earthquakes Accelerogrames

In addition to difference schemes, for this calculation it is possible to use expansion by the forms of natural oscillations. Equations (4) have the form

$$\ddot{y}_i(t) + 2\xi\omega_i\dot{y}_i(t) + \omega_i^2 y_i(t) = -p_{i,r}\cdot a_r(t) - p_{i,t}\cdot a_t(t) - p_{i,z}\cdot a_z(t), \qquad (9)$$

where

$$p_{i,r} = \varphi_i^T M\gamma_r,$$
$$p_{i,t} = \varphi_i^T M\gamma_t,$$
$$p_{i,z} = \varphi_i^T M\gamma_z,$$
$$\gamma_r = \{\cos X, \cos Y, 0,0,0,0, \dots, \cos X, \cos Y, 0,0,0,0\}^T,$$
$$\gamma_t = \{\cos Y, \cos X, 0,0,0,0, \dots, \cos Y, \cos X, 0,0,0,0\}^T,$$
$$\gamma_r = \{0,0,1,0,0,0, \dots, 0,0,1,0,0,0\}^T.$$

The formulas are given for the calculation of the three-component accelerogram. When calculating according to the one-component accelerogram, the last two terms in the right-hand side of equation (9) are equal to zero, and the vector γ_r also changes slightly.

The equations are integrated using the Newmark method to obtain maximum displacements y_i^{max}.

Special attention should be paid to the scaling factor for the accelerogram, it is the product of the translation coefficient of the accelerations of the accelerogram in m/s^2 and the scaling factor of the accelerogram. For example, if the acceleration of the seven-point accelerogram are given in fractions of free-fall acceleration g, and the building needs to be calculated on an eight-point platform, the scale factor should be equal to $2g$.

The integration time can be set equal to or greater than the duration of the accelerogram.

Inertia forces are calculated according to the formula

$$S_i = y_i^{max}\omega_i^2 M\varphi_i.$$

The calculation is performed for the first form of natural oscillations and for all other forms of natural oscillations whose modal mass contribution exceeds the minimum modal mass contribution specified by the user (by default 0.01).

2.3 Dynamic calculation of the assembled building

PC LIRA 10 has the ability to perform linear and non-linear dynamic calculation of the assembled structure, including on earthquake accelerograms and seismograms. Calculation results – displacements and forces at the stages of installation and at all moments of time according to dynamic calculation.

2.4 Reaction spectra

For seismic calculation of the equipment installed in the building, the so-called floor accelerograms and floor response spectra are used. After the seismic calculation of the building or structure, the accelerations (floor accelerograms) of the points where the equipment is attached are obtained. They can be directly used to calculate the equipment according to the difference scheme. If a calculation according to the spectral theory of seismic resistance is required, the floor reaction spectra are calculated from these floor accelerograms with the subsequent possibility of their use in the 41 dynamics module.

2.5 Pushover Analysis

Non-linear static calculation Pushover Analysis is used in PC LIRA 10 to assess the behavior of structures under seismic impact beyond the elastic limits, which is a tool for assessing the bearing capacity of the structure. To determine the bearing capacity of the structure, the vertically loaded calculation scheme is subjected to monotonic loading by horizontal seismic forces. The loading is carried out until the user-specified displacements are reached or until the structural failure is reached in order to evaluate the final deformations and load-bearing capacity.

The nonlinear static calculation is performed in two stages:

1. For a non-linear multi-mass spatial calculation scheme of the structure, the distribution of inertial loads for the calculated forms of self-oscillations is determined by the linear-spectral method.
2. A non-linear static calculation of the multi-mass spatial calculation scheme is performed for vertical loads and for the distribution of inertial loads specified by the user, or for the distribution corresponding to the form of natural oscillations with the largest modal mass.

PC LIRA 10 implements several variants of nonlinear static calculation, which differ in the methods of obtaining the spectrum of bearing capacity and further processing of the obtained results, according to:

- EN 1998–1:2004 [9];
- ДБН В.1.1–12:2014 [1];
- Seismic impact according to the one-component accelerogram of an earthquake [1].

3 Example

Podil Bridge, which is being built in the city of Kyiv, is a two-tiered structure, on the upper tier there are six lanes for traffic (three in one direction), and on the lower one there are two tracks of the metro line (Fig. 1). The Podil Bridge is to become the largest arch bridge in Europe.

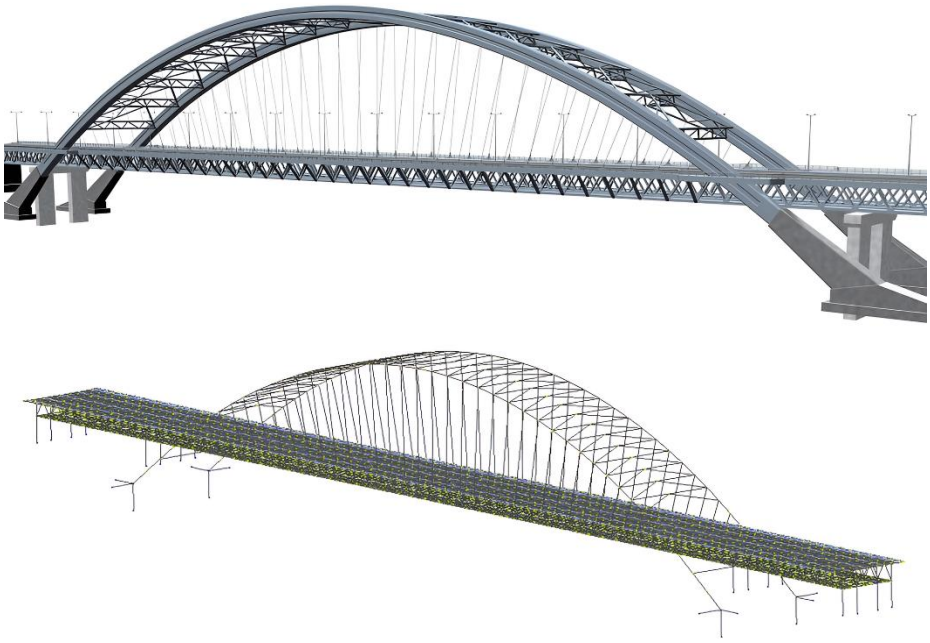

Fig. 1. Layout and calculation scheme of the Podil Bridge.

The city of Kyiv, according to the general seismic zoning map ZSR-2004-C of the territory of Ukraine, is located in the 6-point earthquake intensity zone. The ZSR-2004-C general seismic zoning map was taken because bridges with a span of more than 300 m should, as a rule, be assigned to the responsibility class of CC3 [10].

Figure 2 shows a comparison of the graphs of the longitudinal force in the upper element of the arch during calculations based on the seismogram (black graph) and the accelerogram (white graph). It was considered that the seismic load in the bridge supports comes at the same time.

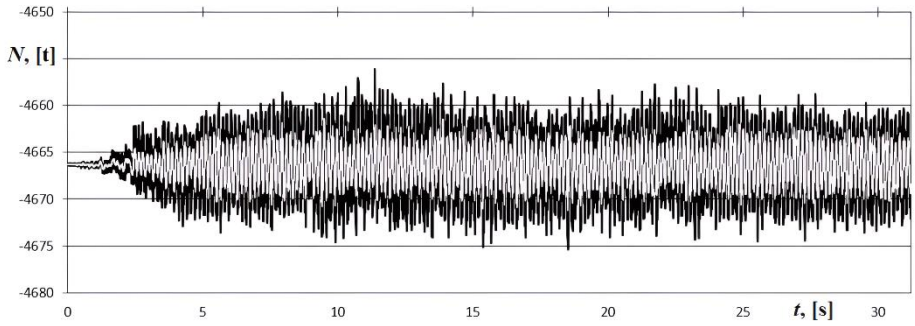

Fig. 2. Graphs of changes in the longitudinal force in the upper element of the arch over time with simultaneous oscillation of the supports.

As can be seen from the graphs, the efforts match up quite well – the maximum difference does not exceed 0.1%.

Figure 3 compares the longitudinal force graphs in the same element as in Figure 2, but in this case seismic wave velocity was taken into account. The distance between the supports of the bridge is 344 m, which can be compared with the speed of seismic wave propagation, which in this case was assumed to be 300 m/s. It can be seen that the forces obtained in the calculations based on the accelerogram (continuous almost straight line) and the seismogram (black dashed line) differ by more than 1.25 times.

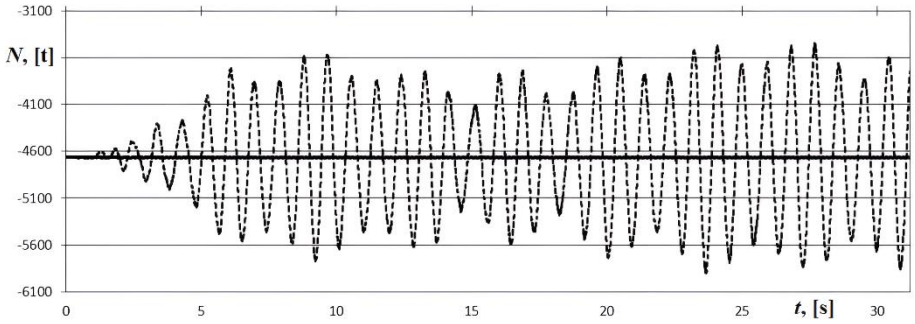

Fig. 3. Graphs of changes in the longitudinal force in the upper element of the arch over time, taking into account the speed of the seismic wave.

That is, as mentioned earlier, significant differences in calculations based on the accelerogram and seismogram, taking into account the speed of the seismic wave, should be expected in long structures.

The developers of PC LIRA 10 hope that the implemented toolkit will facilitate the design of buildings and structures.

References

1. DBN V.1.1–12:2014 Construction in seismic regions of Ukraine. – Kyiv: Ukraine Minregionstroy, 2014. – 110 p.
2. Clough R. Dynamics of structures/ Clough R., Penzien J. – M.: Stroyizdat,1979. – 320 p.
3. Pissanetzky S. Sparse matrix technology/ Pissanetzky S. – M.: Mir,1988. – 411 p.
4. Gorodetsky A.S. Computer models of structures/ Gorodetsky A.S., Ievzerov I.D. – Kiev: Fakt,2007. – 393 p.
5. Maghdid D. Stability and accuracy of Newmark's method. – PhD thesis, Lund University, Denmark, 2002.
6. Newmark N. M. A method of computation for structural dynamics. – A.S.C.E. Journal of engineering, mechanics division. – Vol. 85, 1959, pp. 67 – 94.
7. Dyatlovitsky L.I. Stresses formation in gravity dams/ Dyatlovitsky L.I., Vaynberg A.I. – Kiev: Naukova Dumka, 1975. – 264 p.
8. Litvinsky G. G. Analytical strength theory of rocks and arrays. – Monograph / DonSTU. – Donetsk: Nord-Press, 2008. – 207 p.
9. EN 1998–1:2004 Eurocode 8: Design of structures for earthquake resistance – Part 1: General rules, seismic actions and rules for buildings – Belgium: Brussels, CEN, 2004. – 229 p.
10. DBN V.1.2–14:2018 General principles of ensuring the reliability and structural safety of buildings and structures – Kyiv: Ukraine Minregionstroy, 2018. – 30 p.

Determining the Earthquake Behavior of the Historical Zonguldak Aziziye Mosque Minaret by Considering the 2022 Düzce-Gölyaka (Mw: 5.9) Earthquake

Murat Cavuslu[1][0000-0002-2285-8513]

[1] Zonguldak Bulent Ecevit University, Department of Civil Engineering, Zonguldak, Türkiye, murat.cavusli@beun.edu.tr

Abstract. Historical structures hold great importance in shedding light on the past of civilizations. One of the most significant historical structures in Türkiye is the historical minarets. Due to their elongated geometries, it is essential to study the seismic behavior of these structures. In this study, the seismic behavior of the Aziziye minaret, located in Zonguldak, Türkiye, and constructed in 1871, was investigated using three-dimensional modeling techniques. Firstly, a finite-difference model of the mosque minaret was created. Each stone element of the minaret was individually modeled, and the minaret staircase was intricately placed inside the minaret. Interaction elements were defined between the stone elements. The Burger-Mohr material model was employed for the stone elements, enabling the study of the time-dependent creep behavior of the mosque from 1871 to the present. The minaret foundation was extended downwards and laterally. Boundary conditions that did not reflect the lateral boundaries of the minaret model were defined. The 2022 Düzce-Gölyaka earthquake was used for the seismic analysis of the minaret. The seismic damage performance of the minaret was evaluated based on the earthquake analysis. Additionally, the principal stresses and displacements occurring in the minaret body were assessed as a result of the earthquake analyses. It was observed that the most significant earthquake damage and principal stresses occurred in the upper parts of the minaret balcony.

Keywords: Burger-Mohr Material Model, Düzce-Gölyaka Earthquake, Finite-Difference Method, Mosque Minaret, Seismic Analysis.

1 Introduction

Historical minarets hold profound significance in the preservation of cultural heritage and the understanding of past civilizations. These architectural marvels not only serve as religious symbols but also act as tangible witnesses to the historical and artistic achievements of diverse societies. Minarets, with their towering structures and intricate designs, stand as a testament to the architectural and engineering prowess of their time. They serve as iconic landmarks, visually enriching the urban fabric and serving as beacons of identity for communities. Moreover, historical minarets often showcase the fusion of various artistic styles, reflecting the cultural influences and exchanges that

have shaped their construction. Beyond their aesthetic appeal, historical minarets offer valuable insights into the socio-cultural and religious aspects of their respective periods. They serve as physical embodiments of religious devotion and community unity, having witnessed countless prayers and rituals throughout the ages. The minaret's strategic position within a mosque complex also highlights its role as a call to prayer, establishing a vital connection between the spiritual realm and the daily lives of individuals. From an architectural perspective, studying historical minarets provides valuable knowledge about construction techniques, materials, and structural systems employed in different eras. These insights contribute to the preservation and restoration of not only minarets but also other historical structures, ensuring their longevity and safeguarding their cultural value for future generations. Moreover, historical minarets have a broader significance in terms of cultural dialogue and intercultural exchange. They serve as touchstones for understanding the diverse architectural traditions and influences that have shaped societies across regions and periods. By studying historical minarets, we gain a deeper appreciation for the universal principles of design, craftsmanship, and the enduring human desire to create structures that transcend generations. It is worth mentioning that despite the cultural and historical significance of minarets, there has been a relatively limited amount of research conducted specifically on this subject within the existing literature. While there are numerous studies on seismic behavior and structural analysis of buildings, research specifically focused on minarets is scarce. Işık et al. [1] examined the damages caused by an earthquake in Türkiye, specifically focusing on mosques and minarets. The findings revealed that transition zones between different sections of the minarets were more prone to damage due to stress concentrations. Factors such as suitable ground conditions and the expertise of builders were identified as crucial in determining the extent of damage to buildings. It was seen that changes in minaret cross-sections in transition zones lead to damages, emphasizing the need for well-designed transition segments for load distribution. Moreover, tensile and shear stresses in masonry structures remain low, directly impacting damage levels. It was proposed that the preservation of historical minarets and mosques should be done with sensitivity while ensuring earthquake resistance. Aymelek et al. [2] conducted a detailed dynamic assessment of İskenderpaşa Minaret by utilizing a calibrated finite element (FE) model. The calibration process involved adjusting the model's material properties based on modal test results and considering environmental factors. The calibrated model accurately represented the minaret's structural behavior and demonstrated good agreement with experimental data. The minaret's response to the earthquake and wind loads was evaluated using linear and nonlinear time-history analyses. The calibrated FE model exhibited reduced deformations and lower principal stress values compared to the initial model. The study emphasized the significance of considering the interaction between the minaret and adjacent structures, as well as accurate material characterization in the FE model. These factors played a crucial role in achieving a comprehensive and reliable evaluation of the minaret's structural performance. Kocaman [3] investigated the damages to historical mosques and minarets caused by two earthquakes in Kahramanmaraş. The collapse of spire parts in masonry minarets, the vulnerability of domes, and the inadequacy of structural elements were identified

as key issues. Many masonry minarets were constructed without engineering knowledge, leading to insufficient displacement rigidity and brittle fractures. It was seen that historical mosques with large wall thicknesses are susceptible to damage due to low tensile strength. Nguyen and Livaoğlu [4] presented a damage detection method for slender minarets based on the eigenvalue problem-based inverse solution. Adjustments and modifications were made to adapt the original damage detection method designed for high-rise buildings to minarets. Different combinations of modal modes were used to detect damage in each part of the minaret due to incompletely measured eigenvectors. The numerical investigation demonstrated the robustness of the method, even in the presence of noise in the modal data. Damage detection in the lower parts of the minaret was found to be less sensitive to noise compared to the upper parts. Usta [5] aimed to preserve historical masonry minarets by assessing their earthquake risk levels through finite element modeling and linear dynamic structural analysis. The relative displacement results indicated that the Antalya Kesik minaret had the lowest displacement, likely due to its unique geometry without an upper part. Among the minarets, Yivli Minaret showed the least stress due to its thick body structure. Stress concentrations were observed in certain sections, with the bottom part of the cylindrical body above the transition segment being the most vulnerable under earthquake loads. Calayır et al. [6] employed the Operational Modal Analysis (OMA) method to determine the dynamic characteristics of a masonry minaret. The finite element model (FEM) of the minaret was updated based on the OMA results, considering structure-foundation-soil interaction. Linear elastic assumptions were made for the soil, foundation, and structure domains while ignoring the masses of the foundation and soil. The initial FEM results were compared with the experimental modes using Modal Assurance Criterion (MAC) values. Although the mode shapes showed similarity, the frequency differences were significant, especially for the fourth mode. Yurdakul et al. [7] examined the seismic performance of a 29 m high masonry minaret with various cross-sections. Experimental tests were conducted to determine the mechanical properties of the stone used in the minaret. A 3D finite element model was developed and seismic analyses were performed for three earthquakes. The results showed that the transition region in the minaret body was the most vulnerable area. Different earthquake scenarios resulted in varying stress levels, indicating potential damage in certain sections. The study recommended considering site-response spectra, exploring reinforcement options, and conducting further analyses on different minarets. Bayraktar and Hökelekli [8] proposed cost-effective seismic strengthening techniques for brick-masonry, stone-masonry, and reinforced concrete minarets using the Reinforced Cementitious Matrix (FRCM) composite material. Numerical analysis showed that the proposed techniques effectively reduce the first periods and roof drift ratios of the minarets. The tensile damage parameters decreased significantly after strengthening, and seismic damages in critical regions are eliminated. The results confirmed the reliability and effectiveness of the proposed FRCM strengthening techniques for different types of minarets. Bayraktar and Hökelekli [9] investigated the seismic behaviors of tall and slender brick, stone, and concrete minarets with different foundation types. According to numerical analyses, it was seen that the frequencies of the minarets are influenced by the foundation type, particularly in the higher modes.

Moreover, drift ratios vary depending on the foundation type, with maximum values observed in certain cases. Then, it was concluded that the percentage of damaged elements differs among the foundation types, and considering a massless foundation can lead to an overestimation of minaret responses.

There is a limited body of research in the literature regarding the investigation of the seismic behavior of historical minarets. Furthermore, the finite element method has been predominantly employed for studying the seismic behavior of historical structures, while the application of the finite-difference method to analyze the seismic behavior of historical minarets remains unexplored in the literature. Hence, this study provides significant insights into the seismic behavior of historical minarets, offering valuable contributions to the existing literature. In this study, the stone elements of the Aziziye Minaret were individually modeled, and separate FLAC3D fish codes were developed for each stone element. The Burger-Mohr material model was employed for the stone elements, which has not been utilized in the literature before. Consequently, this study presents a novel perspective in the literature on investigating the seismic behavior of historical minarets. After constructing the foundation of the minaret, appropriate boundary conditions, such as free-field and non-reflecting conditions, were applied to the lateral boundaries and the base of the minaret model. Before the seismic analysis, creep analyses were conducted to understand the deformation and creep behavior of the minaret from 1871 to 2023. The seismic analysis utilized the acceleration records of the 2022 Düzce-Gölyaka earthquake. The findings of the analyses provide significant insights into the seismic behavior of the minaret.

2 General Information About Aziziye Mosque

The Aziziye Mosque in Zonguldak-Kozlu is a historically significant architectural masterpiece that bears witness to the region's rich cultural heritage. The mosque, also known as Aziziye Minaret, was constructed in 1871 during the late Ottoman period, reflecting the architectural style prevalent during that era. Situated in the heart of Zonguldak-Kozlu, the Aziziye Mosque holds great significance for the local community as a place of worship and a symbol of spiritual devotion. Its central location within the town's urban fabric makes it easily accessible to residents and visitors alike, serving as a focal point for religious and social gatherings. The mosque's architectural design showcases the fusion of Ottoman and Islamic architectural elements. It features a prominent minaret that stands tall, commanding attention with its elegant silhouette and intricate ornamentation. The minaret, constructed with meticulous attention to detail, exhibits geometric patterns and delicate calligraphy, showcasing the skill and craftsmanship of the artisans of that period. The Aziziye Mosque's main prayer hall is spacious and well-lit, providing a serene environment for worshippers. The interior design is characterized by intricately decorated walls, adorned with colorful tiles and exquisite plasterwork. The mihrab, indicating the direction of Mecca, is meticulously crafted, further enhancing the mosque's aesthetic appeal. In addition to its architectural splendor, the Aziziye Mosque has played a significant role in the religious and cultural life of Zonguldak-Kozlu. It has served as a place of spiritual guidance, fostering a sense

of community and unity among worshippers. The mosque has witnessed generations of individuals coming together for prayers, religious festivals, and communal activities, reinforcing the mosque's importance as a center for religious and social cohesion. Today, the Aziziye Mosque continues to stand as a testament to the region's historical and cultural legacy. It serves as a living reminder of the architectural heritage of the Ottoman era, captivating visitors with its beauty and providing a tranquil space for prayer and contemplation. In conclusion, the Aziziye Mosque in Zonguldak-Kozlu stands as an architectural gem, embodying the rich history and cultural identity of the region. Its intricate design, historical significance, and religious importance make it a cherished symbol of spiritual devotion and a valuable part of Türkiye's architectural heritage. The height of the minaret of the mosque is 28 meters and the modulus of elasticity of the stone elements used in the minaret is 9000 MPa. General views of the Aziziye mosque minaret were shown in Fig. 1.

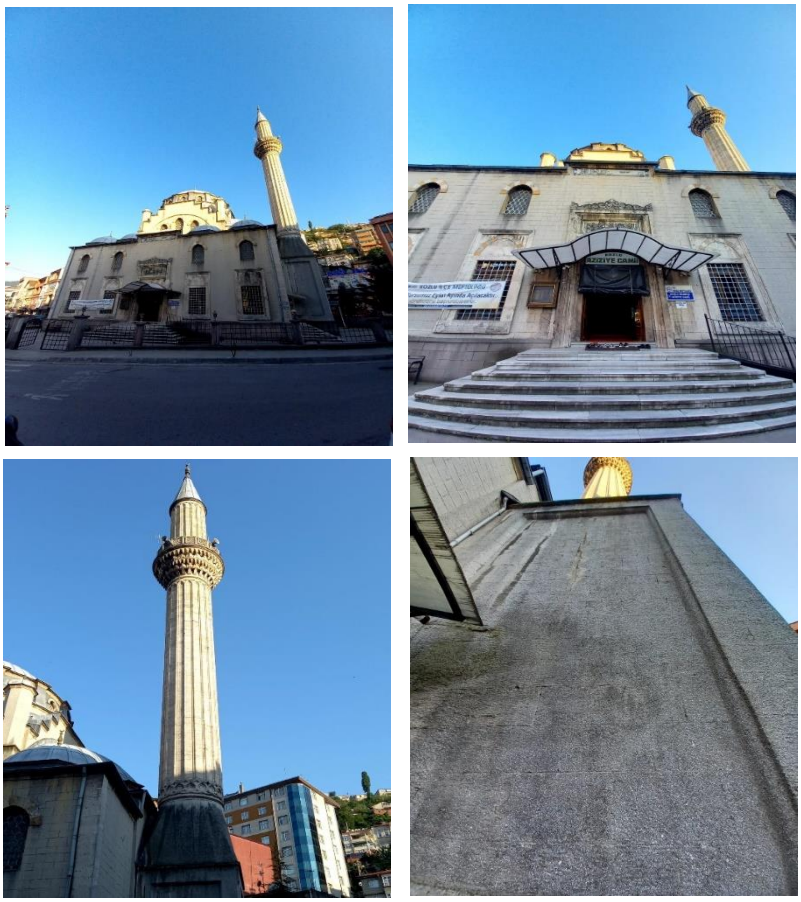

Fig. 1. General views of Historical Aziziye Mosque Minaret.

3 Seismicity of Zonguldak-Türkiye

Türkiye is located in a seismically active region due to its geographical position between the Eurasian and Arabian tectonic plates. It is characterized by the presence of several major fault lines that contribute to its high seismicity. One of the most prominent fault lines is the North Anatolian Fault (NAF), which extends across northern Türkiye and has been associated with numerous large earthquakes throughout history. The NAF is a right-lateral strike-slip fault that accommodates the westward motion of the Anatolian Plate relative to the Eurasian Plate. This fault has produced several significant earthquakes, including the devastating 1999 İzmit earthquake and the 2011 Van earthquake. Another important fault line is the East Anatolian Fault (EAF), which runs through eastern Türkiye and has also been responsible for destructive earthquakes. Türkiye is recognized as one of the most earthquake-prone countries in the world. Its seismic activity is further amplified by the proximity of densely populated areas to active fault lines. Cities such as Istanbul, located near the North Anatolian Fault and the Marmara Sea, are particularly vulnerable to earthquakes. In recent years, Türkiye has experienced several notable earthquakes, such as the, 2023 Kahramanmaraş earthquakes, the 2022 Düzce-Gölyaka earthquake, the 2020 İzmir earthquake, and the 2021 Elazığ earthquake. These events serve as reminders of the ongoing seismic hazard in the region. To mitigate the impact of earthquakes, Türkiye has implemented various measures including the development of seismic building codes, establishment of monitoring networks, and public awareness campaigns. The Disaster and Emergency Management Authority (AFAD) plays a crucial role in coordinating earthquake preparedness and response efforts across the country. Given Türkiye's geographical position and complex tectonic setting, seismicity remains a significant concern. Ongoing monitoring, preparedness measures, and resilient infrastructure are essential to mitigate the risks associated with earthquakes and enhance the safety of the population. Aziziye Mosque is located on the North Anatolian Fault (NAF) line. The NAF is one of the most significant fault lines in Türkiye and plays a crucial role in shaping the country's seismic activity. It is a right-lateral strike-slip fault that extends for approximately 1,500 kilometers across northern Türkiye, running parallel to the Black Sea coast. The NAF accommodates the westward motion of the Anatolian Plate relative to the Eurasian Plate. It has a complex geometry, consisting of multiple segments that have different orientations and slip rates. This fault has been responsible for several major earthquakes throughout history, including the devastating 1999 İzmit earthquake and the 2011 Van earthquake. The NAF exhibits a characteristic behavior known as seismic slip segmentation. It ruptures in distinct earthquake segments, with each segment releasing stress in a major earthquake event. These earthquake sequences propagate along the fault line over time, resulting in a stepwise pattern of seismic activity. The fault exhibits a predominantly right-lateral strike-slip motion, where the blocks on either side of the fault move horizontally past each other. This type of faulting can cause significant ground displacement and can result in destructive earthquakes. The NAF poses a significant seismic hazard, particularly in densely populated areas such as Istanbul, where it traverses the Marmara Sea. Given its historical seismicity and the potential for future earthquakes, ongoing

monitoring and research efforts are essential for understanding the behavior of the fault and assessing the associated seismic risk. Understanding the characteristics of the North Anatolian Fault is crucial for earthquake preparedness and mitigation strategies in Türkiye. It enables scientists and policymakers to develop effective seismic hazard assessments, building codes, and emergency response plans to enhance the resilience of communities located along the fault line (Fig. 2).

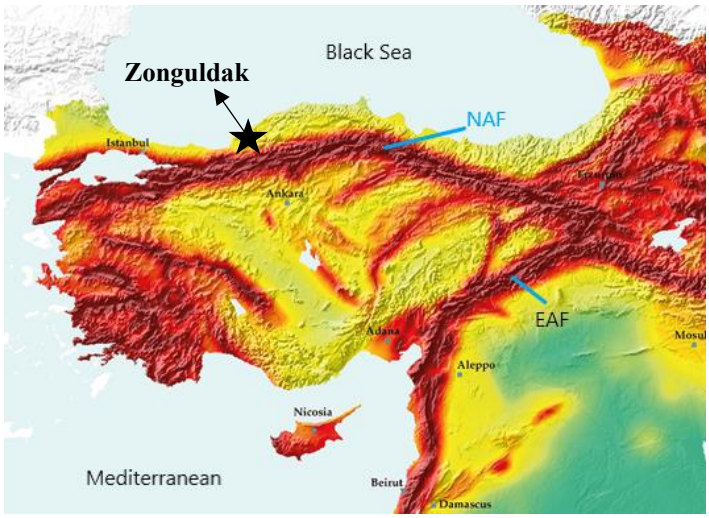

Fig. 2. Seismic fault map of Zonguldak-Türkiye [10].

4 Finite-Difference Modelling of Aziziye Mosque Minaret

In this study, the seismic behavior of the minaret of Aziziye Mosque built in 1871 in the Kozlu district of Zonguldak province, was investigated by considering the finite-difference method. Before the analysis, a finite-difference model of the minaret was created, starting with the selection of stone elements' shapes. The stone elements were constructed using brick and triangular elements available in the FLAC3D program. Each stone element was individually modeled within the minaret model. Fish functions in the FLAC3D program were utilized for the formation of brick and triangular elements. Special interaction functions were defined between the stone elements of the minaret. Interaction stiffness coefficients were calculated using specific formulas provided within the FLAC3D program. The discrete interaction elements defined between the stone elements represent Khorasan mortar, which facilitates interaction between the stone elements in the minarets. The balcony section of the minaret was modeled to match the minaret's geometry. Additionally, the dome section of the minaret was modeled with an approximate height of 1.4 meters. The stairwell section of the minaret was modeled in an oval shape to conform to the minaret's geometry. Oval stone elements were defined in the middle section of the minaret to secure the stairs. The

minaret model consists of three main categories: outer stones, stairs, and middle support stones. A total of 15,875 stone elements were used in the main body of the minaret. Furthermore, 4,746 and 2,487 stone elements were used in the stairwell and middle support sections, respectively. The Burger-Mohr material model was employed for the stone elements. This material model is specific to FLAC3D and designed for the study of the creep and damage behavior of stone element structures. After the construction of the main body of the minaret, the foundation section was created. The foundation of the minaret extends downward or sideways by the length of the minaret. The Burger-Mohr material model was also utilized for the foundation section. Non-reflecting boundary conditions, named free-field and quiet boundary conditions, were defined at the lateral boundaries of the minaret-foundation model to minimize the reflection of seismic waves. Hysteresis damping values were defined in the program before the analysis. These damping values were calculated taking into account the G/Gmax values of each stone element. A time period from 1871 to 2023 was defined in the program for time-dependent creep analyses. Additionally, for seismic analyses, the duration of the 2022 Düzce-Gölyaka earthquake and its acceleration records were provided in the program. The finite-difference model of Aziziye Mosque is illustrated in detail in Fig. 3.

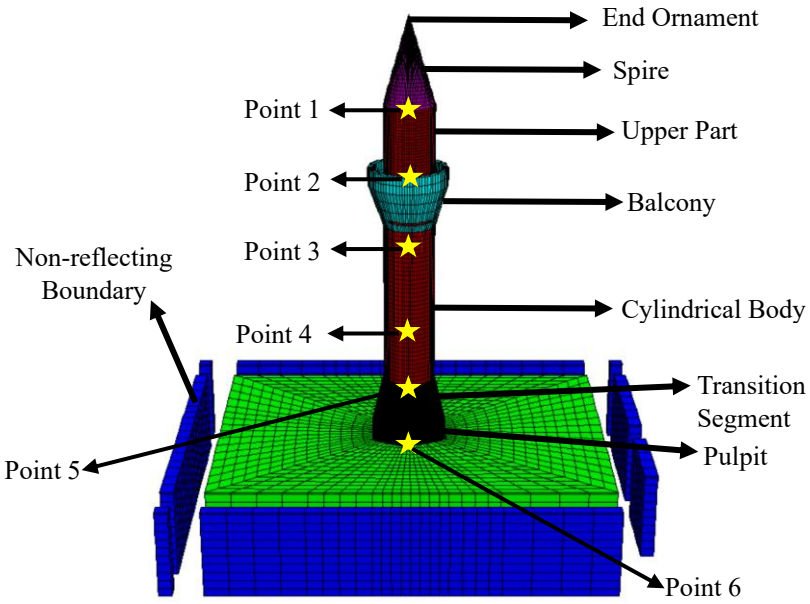

Fig. 3. 3D finite-difference model of Aziziye minaret.

5 Three-Dimensional Numerical Results

In this study, the seismic behavior of the historical stone minaret constructed in 1871 in Zonguldak-Kozlu was evaluated. The seismic analyses were conducted using the FLAC3D program, which is based on the finite-difference timeline method. The finite-

difference method has never been employed in the literature for seismic analysis of historical minarets. Therefore, this study holds significant importance in addressing this gap in the literature. Finite-difference method (FDM) and modeling offer several benefits when it comes to studying the seismic behavior of historical structures. FDM provides a numerical approach to simulate the dynamic response of structures under seismic loads. By discretizing the structure into smaller elements and time steps, FDM allows for a detailed representation of the structural behavior, considering various complexities such as material heterogeneity, irregular geometries, and boundary conditions. This accuracy in representation enables a more comprehensive understanding of how historical structures respond to seismic forces. FDM allows researchers and engineers to model different scenarios and study the seismic behavior of historical structures under various earthquake ground motions. It provides flexibility in considering different input parameters such as material properties, structural dimensions, and seismic characteristics, allowing for a range of analyses to be performed. This adaptability is crucial when dealing with historical structures since they often exhibit unique characteristics that require tailored-modeling approaches. By utilizing FDM, engineers, and researchers can gain valuable insights into the seismic vulnerability and performance of historical structures. Through numerical simulations, FDM can help identify critical areas prone to damage, assess structural integrity, and evaluate the effectiveness of potential retrofit strategies. This information is vital for preserving and safeguarding historical structures, as it aids in making informed decisions regarding their conservation and seismic strengthening. Conducting physical tests on historical structures can be challenging, expensive, and time-consuming. FDM provides a cost-effective and efficient alternative to experimental methods by allowing virtual testing and analysis. The numerical simulations can be conducted in a relatively short time frame, providing quick results and reducing the need for extensive physical testing, which is often not feasible for historical structures due to their delicate nature. FDM, combined with appropriate modeling techniques, can facilitate the optimization of retrofit strategies for historical structures. By simulating the behavior of different retrofit schemes, engineers can assess their effectiveness, evaluate their impact on structural response, and refine them accordingly. This optimization process aids in developing efficient retrofit solutions that minimize structural vulnerability while preserving the historical and architectural value of the structure. In summary, utilizing the finite-difference method and modeling offers accurate representation, flexibility, insightful analysis, cost and time efficiency, as well as design optimization capabilities. These advantages make it a valuable tool for studying the seismic behavior of historical structures and ensuring their long-term preservation. The numerical analysis of the historical Aziziye Minaret was initiated by conducting creep analyses from 1871 to 2022, representing approximately 151 years of deformation behavior. This is because the minaret has been subjected to deformation under specific external loads and its weight for many years. Therefore, in order to understand the seismic behavior of historical structures, it is necessary to first perform time-dependent creep analyses to assess the structure's long-term deformation. After conducting the 151-year creep analyses of the minaret, its modal behavior was investigated. The results of the modal analysis are presented in detail in Fig. 4. Upon examining the modal behavior of the

minaret, it is evident that the first mode is 1.089 Hz. This value is consistent with other studies conducted in the literature [2]. The second mode of the minaret is 1.118 Hz. There are no significant differences observed between the first and second modes. The third mode of the minaret is 5.384 Hz, indicating significant changes between the second and third modes. Furthermore, the fourth mode of the minaret is 5.971 Hz. The modal analysis revealed that the primary and secondary modes corresponded to initial bending phenomena along the north-south and east-west axes, respectively. Similarly, the third and fourth modes exhibited secondary bending characteristics along the north-south and east-west axes, respectively.

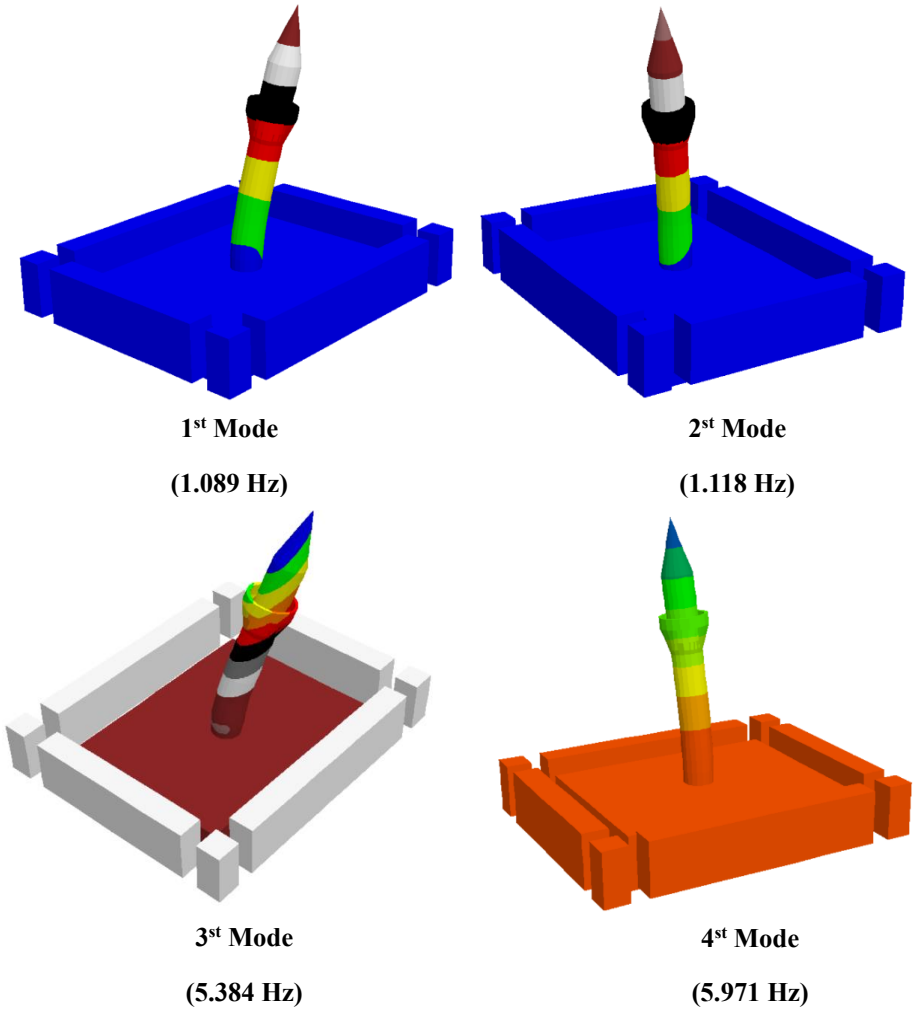

Fig. 4. Mode shapes of the minaret for the first four modes.

The seismic analysis of the minaret was conducted using the earthquake acceleration records from the Gölyaka district of Düzce in 2022. The earthquake acceleration records were obtained from AFAD's website [11]. The Düzce-Gölyaka earthquake lasted approximately 42 seconds and occurred at a latitude of 40.823 and a longitude of 31.025. The depth of the earthquake was approximately 6.81 km, and its magnitude was 5.9. Additionally, the peak ground acceleration (PGA) value of the earthquake was 592.03 cm/s² (TK.8105 EW, Repi: 13.88 km). The peak ground velocity (PGV) value was 73.65 cm/s (TK.8102 EW, Repi: 11.79 km), and the peak ground displacement (PGD) value was 23.39 cm (TK.8102 EW, Repi: 11.79 km). The overall view of the area where the earthquake occurred is presented in detail in Fig. 5.

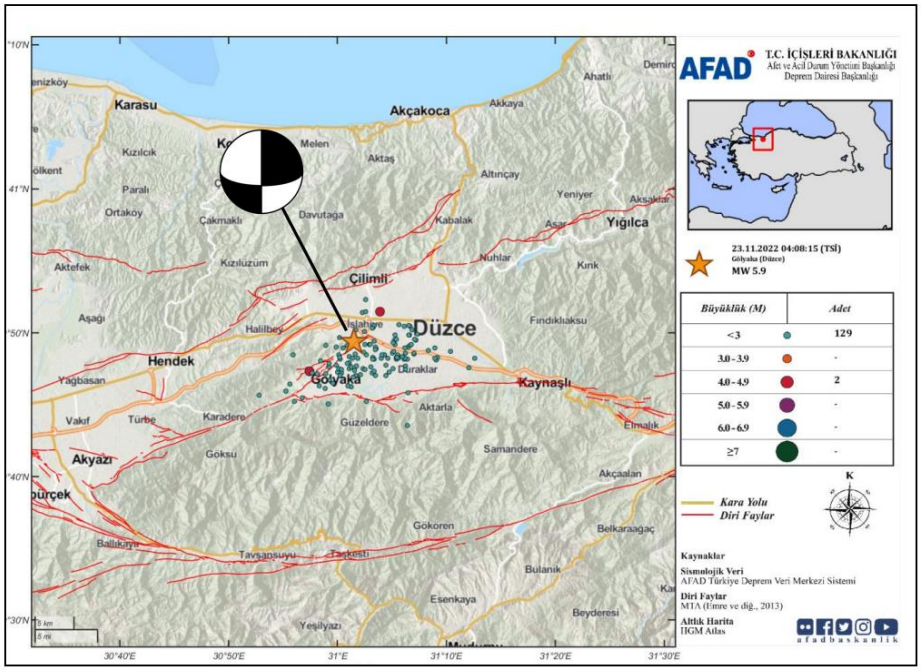

Fig. 5. 23.11.2022 04:08:15 (TSI), Gölyaka (Düzce) M_W 5.9 earthquake [11].

The seismic analysis results of the minaret are presented in detail in Figs. 6-11. Principal stress values occurring at six different points of Aziziye Minaret during the Düzce-Gölyaka earthquake are presented. Point 1 represents the topmost point of the minaret, while Point 6 indicates the bottommost point. Fig. 6 displays the time-dependent principal stress values occurring at the topmost point of the minaret due to the earthquake. According to Fig. 6, the maximum principal stress value that occurred at Point 1 during the earthquake is approximately 14.874 MPa. This value occurred at the 34.8th second of the earthquake. Although high-stress values are observed at Point 1 for 40 seconds, fluctuations in stress values are also observed. Fig. 7 illustrates the principal stress values occurring at Point 2 during the earthquake. According to Fig. 7, the maximum principal stress value occurring at Point 2 during the earthquake is

approximately 10.975 MPa. When comparing Point 1 and Point 2, it can be observed that the principal stress values occurring at Point 1 are relatively greater than those at Point 2. This result demonstrates the influence of height on the principal stress values within the minaret's structure. Fig. 8 presents the time-dependent principal stress values occurring at Point 3 as a result of the Düzce-Gölyaka earthquake. According to Fig. 8, the maximum principal stress value occurring at Point 3 during the earthquake is 10.183 MPa. Although the highest stress values occurring at Point 2 and Point 3 during the earthquake are close to each other, the 40-second principal stress values significantly differ from each other. Fig. 9 presents the time-dependent principal stress values occurring at Point 4 during the earthquake. The maximum principal stress value observed at Point 4 during the Düzce-Gölyaka earthquake is 8.917 MPa. The seismic principal stress values occurring at Point 4 are much smaller compared to Point 1, Point 2, and Point 3. Fig. 10 illustrates the time-dependent seismic principal stress results occurring at Point 5 during the earthquake. According to Fig. 10, the maximum principal stress value occurring at Point 5 during the earthquake is approximately 7.6148 MPa. The maximum principal stress value at Point 5 is smaller compared to the maximum stress values observed at Point 1, Point 2, Point 3, and Point 4. This result indicates that the seismic principal stress values on the minaret increase with an increase in height. The maximum principal stress value occurred at the 24th second of the earthquake, while the minimum principal stress values were obtained at the 7th, 18th, and 29th seconds of the earthquake. Fig. 11 displays the time-dependent seismic principal stress values observed at Point 6. According to Fig. 11, the maximum principal stress value occurring at Point 6 during the earthquake is 6.851 MPa. When comparing all the points, it is evident that the largest seismic principal stress values occurring on the Aziziye Minaret during the Düzce-Gölyaka earthquake are observed at Point 1 and Point 2, which represent the topmost sections of the minaret. The smallest principal stress values observed during the earthquake are obtained at the bottommost section of the minaret. The sections represented by Point 1 and Point 2 do not include stairs, while the sections represented by Point 3, Point 4, Point 5, and Point 6 have stairs. These results indicate that the presence of stairs has a positive impact on the seismic behavior of the minaret. It is concluded that larger seismic principal stress values occur in the sections without stairs, and the presence of stairs contributes to the rigidity of the minaret. In the recent earthquake in Kahramanmaraş, Türkiye, it was observed that the collapse mechanism of historical stone minarets started from sections without stairs. The results obtained from this study are consistent with the observations from the minarets that collapsed during the 2023 Kahramanmaraş earthquake. Therefore, when performing seismic strengthening or restoration of historical minarets, careful examination and reinforcement of the upper sections without balconies are necessary. This finding contributes significantly to the seismic strengthening of historical mosque minarets.

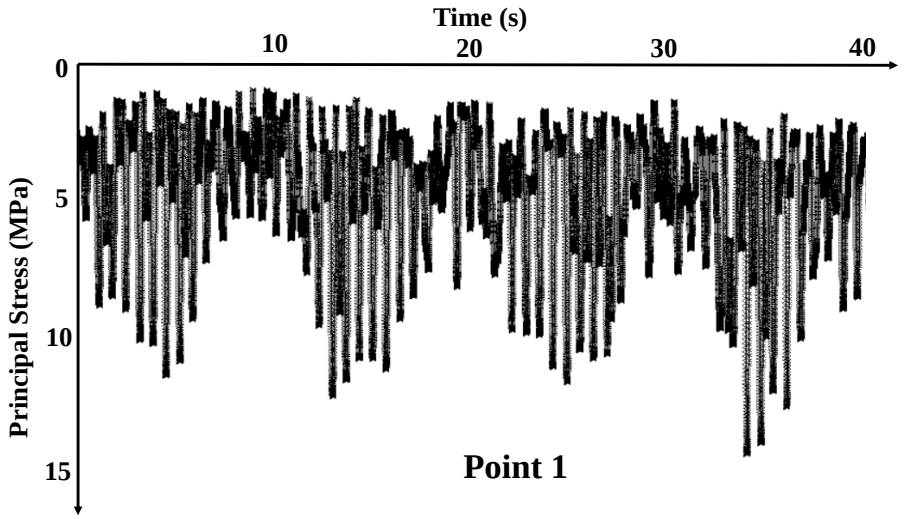

Fig. 6. Time-dependent principal stress results for Point 1.

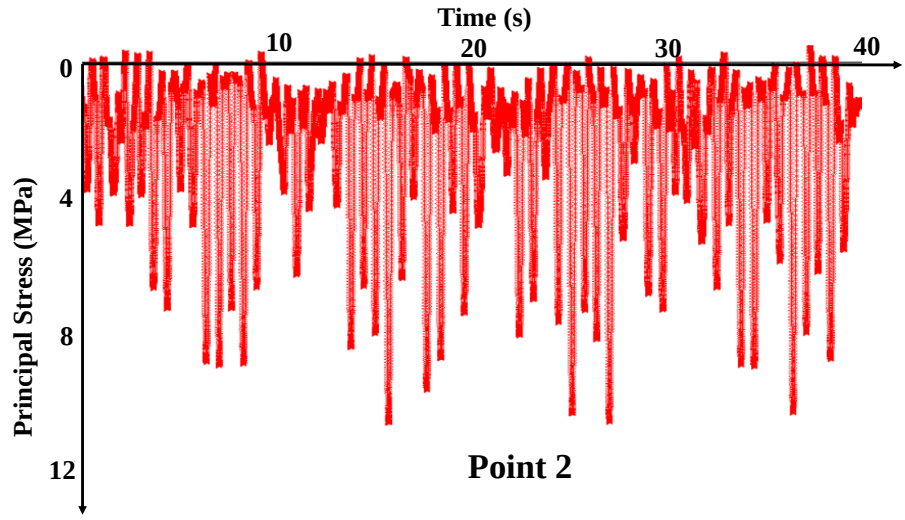

Fig. 7. Time-dependent principal stress results for Point 2.

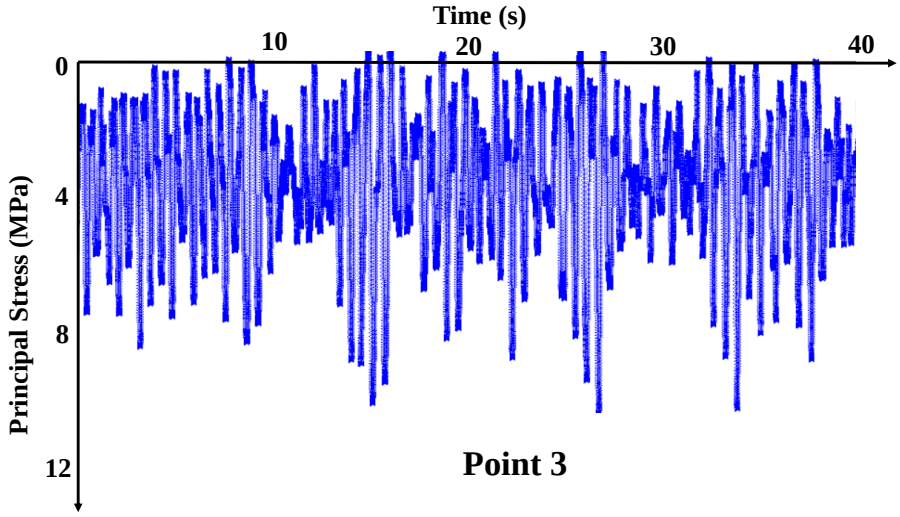

Fig. 8. Time-dependent principal stress results for Point 3.

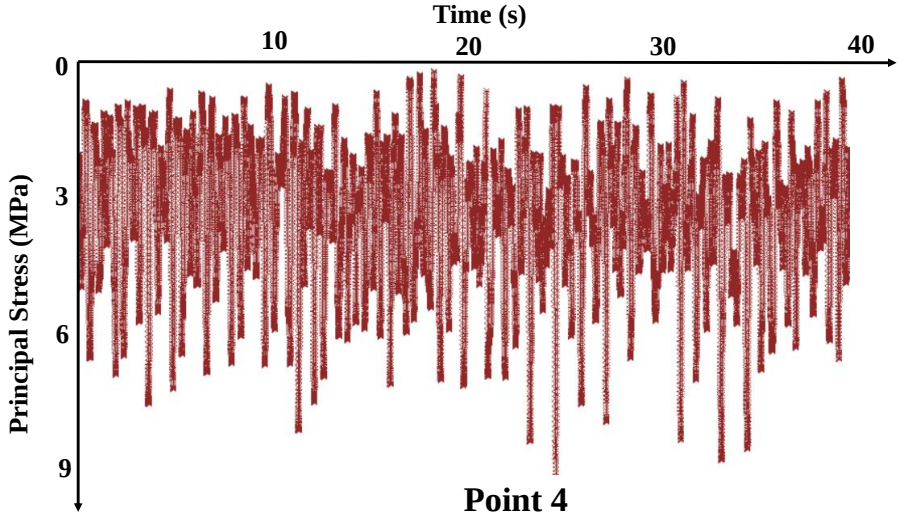

Fig. 9. Time-dependent principal stress results for Point 4.

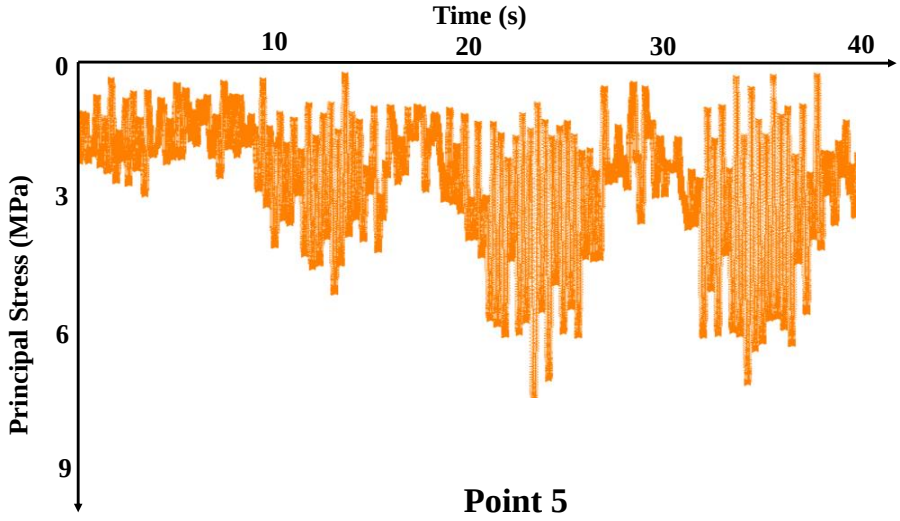

Fig. 10. Time-dependent principal stress results for Point 5.

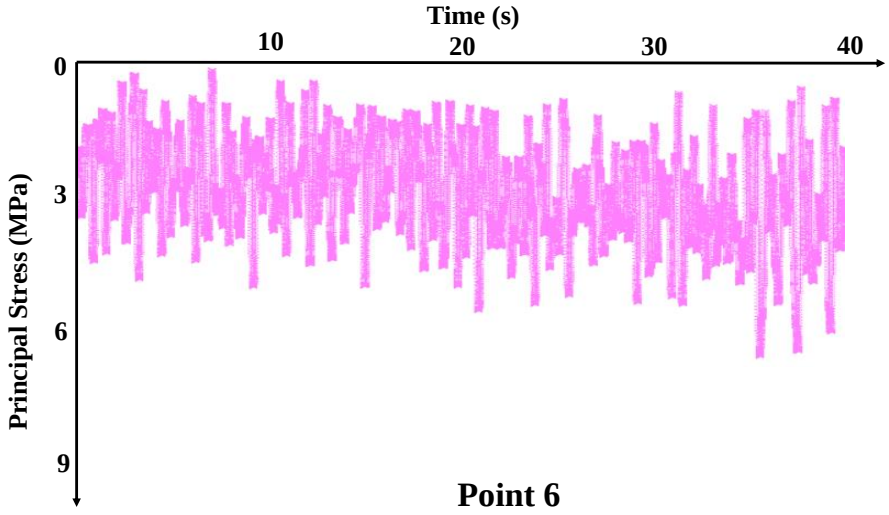

Fig. 11. Time-dependent principal stress results for Point 6.

6 Conclusions

This study conducted seismic analyses of the historical Aziziye Minaret, focusing on its creep behavior over 151 years from 1871 to 2022. 3D numerical analyses were performed using the finite-difference method. Notably, the finite-difference method has not been previously utilized in the literature for investigating the seismic behavior of

historical minarets. Therefore, this study presents original insights into the seismic behavior of historical minarets in the literature.

The Aziziye Minaret experienced deformation over an extended period due to external loads and its weight. To comprehend the seismic response of historical structures, it is crucial to conduct time-dependent creep analyses to assess long-term deformation. Accordingly, the time-dependent creep analyses of the Aziziye Minaret were initially carried out, considering 151 years. Subsequently, modal analyses were performed, revealing that the first mode of the minaret is 1.089 Hz and the second mode is 1.118 Hz. The third mode of the minaret is 5.384 Hz, and the fourth mode exhibits behaviors similar to the third mode. The primary and secondary modes indicate bending along the north-south and east-west axes, respectively.
Seismic analyses were conducted using the 2022 Düzce-Gölyaka earthquake, and the seismic principal stress values were determined at six points on the Aziziye Minaret. Point 1, representing the topmost section, experienced the highest principal stress value of approximately 14.874 MPa at the 34.8th second of the earthquake. Point 2 exhibited a relatively lower principal stress value compared to Point 1. Point 3 displayed a maximum principal stress value of 10.183 MPa. Point 4 had a maximum principal stress value of 8.917 MPa, considerably smaller than those observed at Points 1, 2, and 3. Similarly, Point 5 had a maximum principal stress value of approximately 7.6148 MPa, lower than the values at Points 1, 2, 3, and 4. These findings confirm that the height of the minaret positively influences the seismic principal stress values.

The highest seismic principal stress values on the minaret were observed in the upper regions of the minaret. The absence of stairs in the upper sections of the balcony is the sole reason for this observation. It is believed that the presence of stairs has a positive effect on the rigidity of the minaret. Moreover, it was seen that reinforcement of the upper sections without stairs is crucial for seismic strengthening or restoration of the historical minarets.

References

1. Işık, E., Avcil, F., Arkan, E., Büyüksaraç, A., İzol, R., Topalan, M.: Structural damage evaluation of mosques and minarets in Adıyaman due to the 06 February 2023 Kahramanmaraş earthquakes. Engineering Failure Analysis 151, 107345 (2023).
2. Aymelek, A., Yanik, Y., Demirtaş, B., Yildirim, Ö., Çalik, İ., Türker, T.: Full-scale structural evaluations of İskenderpaşa minaret. Structures 55, 1028-1044 (2023).
3. Kocaman, İ.: The effect of the Kahramanmaraş earthquakes (Mw 7.7 and Mw 7.6) on historical masonry mosques and minarets. Engineering Failure Analysis 149, 107225 (2023).
4. Nguyen, Q.T., Livaoğlu, R.: A health monitoring solution on damage detection of minarets. Engineering Failure Analysis 135, 106154 (2022).
5. Usta, P.: Assessment of seismic behavior of historic masonry minarets in Antalya, Türkiye. Case Studies in Construction Materials 135, 106154 (2022).
6. Calayır, Y., Yetkin, M., Erkek, H.: Finite element model updating of masonry minarets by using operational modal analysis method. Structures 34, 3501-3507 (2021).

7. Yurdakul, M., Yılmaz, F., Artar, M., Can, Ö., Öner, E., Daloğlu, A.T.: Investigation of time-history response of a historical masonry minaret under seismic loads. Structures 30, 265-276 (2021).
8. Bayraktar, A., Hökelekli, E.: A cost-effective FRCM technique for seismic strengthening of minarets. Engineering Structures 229, 111672 (2021).
9. Bayraktar, A., Hökelekli, E.: Influences of earthquake input models on nonlinear seismic performances of minaret-foundation-soil interaction systems. Soil Dynamics and Earthquake Engineering 139, 106368 (2020).
10. Berkeley Seismology Lab: Quake in Türkiye highlights the hazard in the East Bay, (2021).
11. AFAD, Disaster and Emergency Management Presidency, 2023.

The Effect of Masonry Infills on the Performance of Steel Frames

Elif Nazlı Akbas[1][0009-0000-2977-4577], Murude Celikag[2][0000-0002-2751-5528], Ashraf M. L. Milad[3][0009-0003-1090-023X]

[1]Department of Civil Engineering, Faculty of Engineering, Eastern Mediterranean University, Famagusta – North Cyprus, via Mersin 10 Turkey
elif.akbas@emu.edu.tr
[2]Department of Civil Engineering, Faculty of Engineering, Eastern Mediterranean University, Famagusta – North Cyprus, via Mersin 10 Turkey
murude.celikag@emu.edu.tr
[3]Department of Civil Engineering, University of Bani Walied, , Bani Walied City, Libya
ashrafmilad@bwu.edu.ly

Abstract. Infill walls are commonly used to fill steel and concrete frames as interior partitions to divide areas or as exterior claddings for the buildings. However, they are usually ignored in the seismic design process. This paper presents an experimental and analytical study to investigate the behaviour and capacity of masonry infilled steel frames under non-linear static pushover analysis. The experimental test results, including half-scale, single story-single bay, bare and BIMs block masonry infilled steel moment frames, were used to validate the finite element model. The finite element analysis was performed on the validated steel moment resisting frames having variations in number of bays and location of the infill walls. Results of the experimental test on moment frames showed that the presence of infill walls could increase the lateral stiffness of frame and improve the load carrying capacity. Similarly, the results of the analysis of finite element models revealed that infill walls can increase the strength, stiffness and fundamental period of the systems depending on their location in a framing system.

Keywords: Steel frame, moment frame, masonry infill wall

1 Introduction

The reaction of masonry infill walls during an earthquake is complex and unpredictable due to variations in material properties and their brittle force-displacement behaviour. Traditionally infill walls are being ignored during design and analysis of the new structures, and capacity evaluation of the existing buildings.

However, field observations after earthquakes e.g. Adana- Ceyhan (1998), Gölcük-Kocaeli (1999) and L'Aquila (2009), showed that structures with infill walls experience in-plane and out-of-plane wall failures, frame failures and formation of soft and weak story which affects strength, stiffness and ductility of the system. The presence of infill

walls alters the lateral-load transfer mechanism by developing alternative load paths through infills. Studies on reinforced concrete (RC) frames showed that introduction of masonry infill changes the behaviour of structure from frame action to truss action that creates higher axial forces and lower bending moments in the structural members [1]. This can be related to so called equivalent compressive strut actions of infill walls.

The significance of infill walls has been recognized after the results of broad scientific research and in the light of these studies, two earthquake resistant design approaches were suggested [2]. The first one proposed to isolate infill walls from the frame in which they are located to neglect their effects. In the second one, infill walls are considered in the design, detailing and construction by proper introduction of them inside the surrounding frames. Despite the former approach, the second one allows to predict and determine global and local impacts of these stiff and brittle components. These approaches have been adopted by a number of available national codes and design guidelines such as FEMA 306 [3], FEMA 273 [4] and Eurocode 8 [5] which are intended for evaluation and rehabilitation of earthquake prone and damaged buildings to enclose infill walls, but they differ greatly from a seismic performance viewpoint [1].

Thus, infill walls are treated as non-structural elements such as partition, finishing and isolation, in practice. However, they are required to receive more attention for a reliable design.

2 Experimental Program

In the present study, it is aimed to provide information about structural performance of masonry infilled steel framed structures. For this purpose, the experimental test setup, and data of Milad [6] were used to verify the analytical models prepared by using SeismoStruct programme.

The experimental study was conducted with 2D half scale models that were extracted from a full-scale one-story office building having slab plan dimensions of 4m x 3m. Then eight test frames including moment frames and braced frames with and without infill walls were constructed with HEB120 and IPE120 steel sections for column and beam members, respectively. The frame did not have any restraint in the out-of-plane direction.

In this paper, results of only two out of eight experimental specimens were included. These specimens were named as MAJ-1B-1S and MAJ-1B-1S-INF for moment frame and infilled frame respectively. Fig. 1 shows the test set-up of these two specimens.

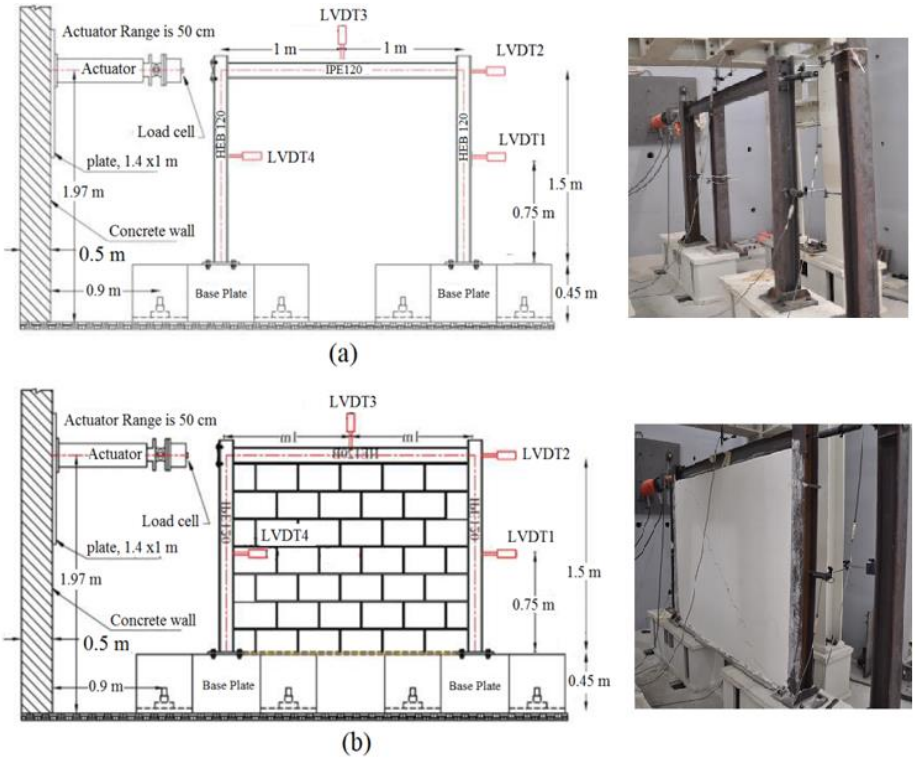

Fig. 1. The experimental test set-up of (a) moment frames without infill wall and (b) moment frames with infill wall.

The cross-sectional dimensions and material properties of the column and beam steel sections are shown in Tables 1 and 2, respectively. The mechanical properties of the column and beam sections were obtained from the coupon tensile tests.

Table 1. Cross-sectional dimensions of the steel sections.

Model No	Column, HEB 120 (mm)				Beam, IPE120 (mm)			
	Thickness		Height	Width	Thickness		Height	Width
	Flange (t_f)	Web (t_w)	(h_c)	(b_c)	Flange (t_f)	Web (t_w)	(h_c)	(b_c)
MAJ-1B	10	6.5	123	121	7.0	5.6	120	64
MAJ-1B-INF	10	6.5	122	121	7.0	5.5	120	64

Table 2. Mechanical characteristics of the steel sections.

Steel Section	Yield Stress (N/mm^2)	Ultimate Stress (N/mm^2)	Ultimate Stain (%)
HEB120	339.70	474.77	26.67
IPE120	318.93	480.37	22.33

3 Finite Element Calibration

The finite element SeismoStruct software version 7.0.6. was employed to verify two basic analytical models (Fig. 3). These analytical models were featuring the same material and geometrical properties, as well as loading conditions with the experimental specimens. The verification of the test results was first done by the investigation of the response of frame with no infill to ensure that infill panel would be left as the only "verification variable" and continued with infilled frame.

Comparison of the experimental and numerical studies is presented in Table 3 and Fig. 2. It is clear from the results of validation procedure that analytical models are highly capable of modelling behaviour of infilled frames.

Table 3. Comparison between the data of experimental test and finite element model.

Specimen ID	Max Top Displacement (mm)		Max Lateral Load (kN)	
	Experimental	Analytical	Experimental	Analytical
MAJ-1B-1S	69.30	67.59	105.69	102.63
MAJ-1B-1S-INF	31.83	41.10	103.69	108.02

After the verification of the finite element models, a new group of models were formed by increasing the number of bays to 2. These models were labelled with 2B (Fig. 4) where the original one bay frame models are labelled with 1B (Fig. 3). They were studied on the bases of lateral load, top displacement, and fundamental period by applying linear pushover analysis. The results of four new models are presented in the following sections. The validation models were also considered as one group for the comparison of all analytical models.

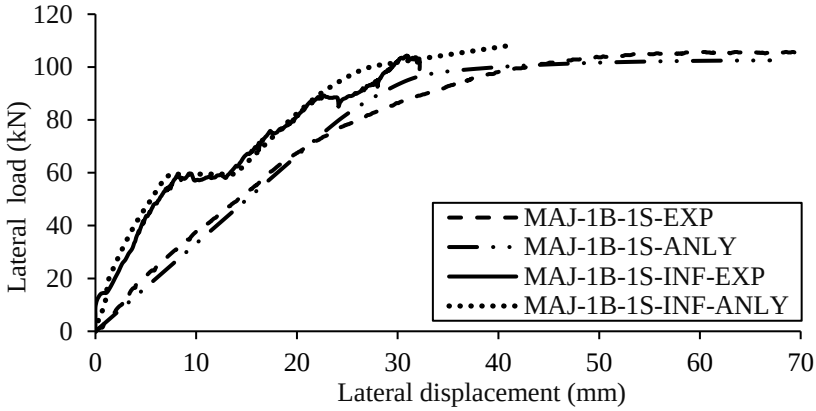

Fig. 2. A graphical comparison of the experimental (denoted with EXP) and analytical results (denoted with ANLY) for the validation procedure.

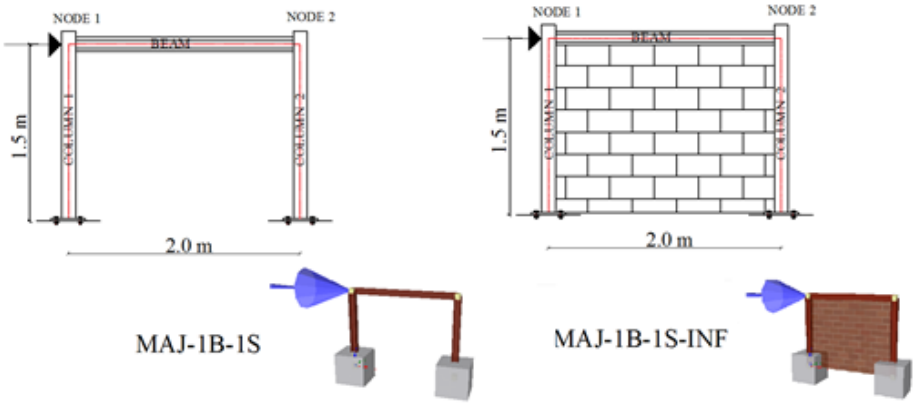

Fig. 3. SeismoStruct models of moment frame without infill, MAJ-1B-1S and moment frame with infill, MAJ-1B-1S-INF.

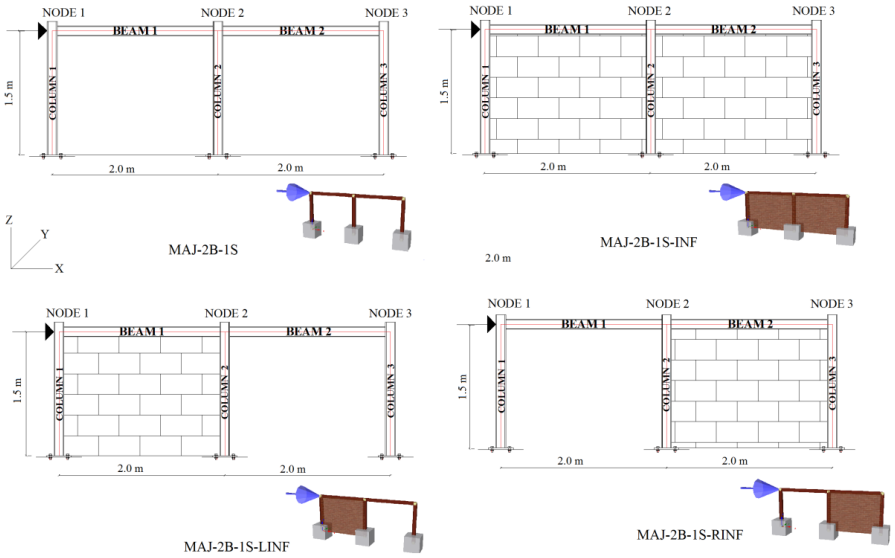

Fig. 4. Details of 1 bay 1 story (1B-1S) models with SeismoStruct illustrations.

4 Results and Discussions

4.1 Lateral Load

The existence of infill walls increased the received lateral load since the bare models received the lowest lateral load. For one story one bay infilled model (1S-1B-INF), the lateral load achieved was increased by about 5% compared to its bare counterpart. Similarly, there is up to 8% increase in the lateral load achieved for one story two bay (1S-2B) infilled frame models. However, this phenomenon is mainly dependent on the location of infill walls, i.e., the results of 2B-1S-INF model did not show considerable difference when compared with the bare steel frame 2B-1S. Additionally, as the number of bays increased the lateral load was also increased (Fig. 5).

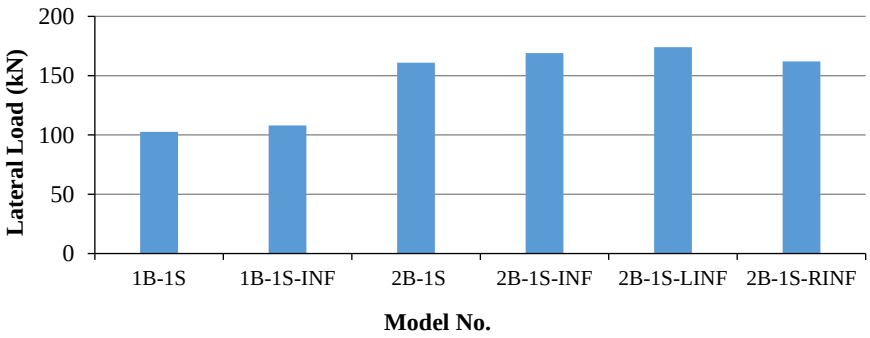

Fig. 5. Lateral load values for 1B-1S and 2B-1S frames with and without infill walls.

4.2 Lateral Displacement

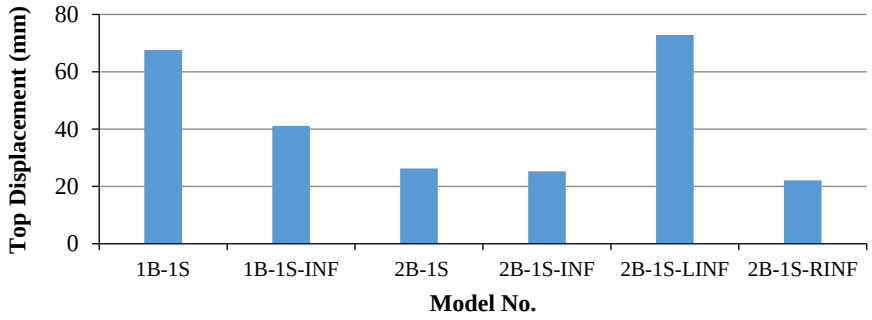

Fig. 6. Top displacement values for 1B-1S and 2B-1S frames with and without infill walls.

All bare frame models experienced higher top displacements when compared to fully infilled frames of the same group. On the other hand, when frames have partial infill walls then the location of infill wall affected the top displacements (Fig. 6). This can be clearly seen by the results of 2B-1S-LINF frame model. Although, bare model, 2B-1S, displaced by 26.3 mm, partially infilled frame, 2B-1S-LINF, displaced by 72.8 mm having 177% difference.

4.3 Fundamental Period

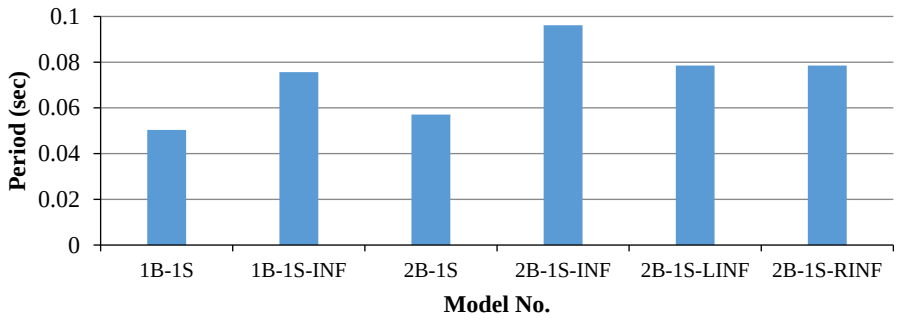

Fig. 7. Fundamental period for 1B-1S and 2B-1S frames with and without infill walls.

The highest fundamental period belongs to fully infilled models whereas the lowest one belongs to the bare frame models (Fig. 7). This conforms with the references [7, 8] that the presence of infill walls increases the natural period due to increased weight. Furthermore, frame models having the same weight, namely 2B-1S-LINF and 2B-1S-RINF, have the same period. This means location of the infill does not affect the period if the number of bays is the same.

5 Conclusion

The analytical study presented in this paper aimed to investigate the structural behaviour of steel moment frames with and without infill walls, when subjected to lateral loads. Once the analytical models were validated with experimental results, then modifications were made to create the new steel frames on SeismoStruct finite element programme. In the light of obtained results, it can be concluded that the presence and location of infill walls have both advantageous and disadvantageous effects on the behaviour of steel framed structures as follows.

- Increased stiffness of fully infilled frames compared to bare and partially infilled frames can be accounted as a positive effect of the presence of infill walls.
- The higher fundamental periods due to increased weight, alterations in top displacements and achieved lateral loads by the changing location of the infill walls are accounted as the negative effects of the presence of infill walls.

References

1. Jain, S., K., Kaushik, H.B., Rai, D.C.: Code approaches to seismic design of masonry-infilled reinforced concrete frames: A state-of-the-art review. Earthquake Engineering Research Institute, Earthquake Spectra 22(4), 961-83 (2006).
2. Bertero, V., Brokken, S.: Infills in seismic resistant building, Journal of Structural Engineering, ASCE, 109(6), 1337–1361 (1983).
3. FEMA (1999) FEMA-306: Evaluation of Earthquake Damaged Concrete and Masonry Wall Buildings—Basic Procedures Manual, Federal Emergency Management Agency, Washington D.C.
4. FEMA (1997) FEMA-273: Guidelines for the Seismic Rehabilitation of Buildings, Federal Emergency Management Agency, Washington, D.C.
5. EUROCODE (1998) EUROCODE-8: Design Provisions for Earthquake Resistance of Structures. European Committee of Standardization, Brussels, Belgium.
6. Milad, A.M.: Effect of infill wall on the seismic behaviour of steel framed structures. Master Thesis, Department of Civil Engineering, Eastern Mediterranean University, Civil Engineering Department, North Cyprus, Turkiye, 116 p (2015).
7. Girgin, S.C., Misir, I.S., Ozcelik, O., Yucel, U.: The behaviour of infill walls in RC frames under combined bidirectional loading. Journal of Earthquake Engineering, 20(4), 559-586 (2016).
8. Arêde, A., Furtado, A., Rodrigues, H.: Modelling of masonry infill walls participation in the seismic behaviour of RC buildings using OpenSees. International Journal of Advanced Structural Engineering, 7, 117-27 (2015).

A Simple Procedure to Approximate Fundamental Mode Period of Vibration

Abdul Hakim Chikho[1]

[1] PhD the University of Sheffield England
Prof of Steel and Structural Eng. Civil Engineering Faculty
Aleppo University
ahchikho@gmail.com

Abstract. Most international codes allow the use of an equivalent lateral method for designing practical buildings to withstand earthquake actions. This method requires calculating an approximation to the fundamental mode period of vibrations of these buildings. Several empirical equations have been suggested to calculate approximations to the fundamental periods of different type of structures. Most of these equations are known to provide only crude approximation to the required fundamental periods and repeating the calculation utilizing more accurate formulas is usually required. In this paper a new formula to calculate a satisfactory approximation of fundamental period of a practical building is proposed. This formula takes in to account the mass and the stiffness of the building therefore; it is more logical than the conventional empirical equations. In order to verify the accuracy of the proposed formula, several examples have been solved. In these examples, calculating the fundamental mode periods of several framed and dual concrete buildings utilizing the proposed formula and the conventional empirical equations has been accomplished. Comparing the obtained results with those obtained from a computer program ROBOT 2020 has shown that the proposed formula provides more accurate estimation of the fundamental periods of practical buildings. Since the proposed method is still simple to use and requires only a minimum computing effort, it is believed to be ideally suited for design purposes.

Keywords: Earthquakes, Fundamental period, Concrete buildings

1 Introduction

Most buildings nowadays are designed to withstand horizontal loading resulted from earthquakes that might strike during the lifetime of the buildings. Calculating an approximate estimation of loading resulted from earthquake actions requires the calculation of fundamental mode period of vibrations, since most design methods recommended by international codes (reference 1,2) allows the use of what's called equivalent lateral forces method. This method takes into consideration only the fundamental mode period of vibration to calculate a set of equivalent horizontal static loads to be applied to the structure. The equivalent lateral forces method is applicable

only to regular buildings that can be analyzed by two planes and whose responses is not highly dependent on higher modes of vibrations. Several empirical equations have been proposed to calculate an estimation to the fundamental mode period of vibrations of practical concrete buildings such as the following equations adopted by the EC8 (see reference 1):

$$T_1 = 0.075\ {h_t}^{0.75} \qquad \text{(for framed concrete buildings)} \qquad (1)$$

h_t is the total building height (taken in m).

$$T_1 = \frac{0.09 h_t}{L^{0.5}} \qquad \text{(for mixed framed and wall concrete buildings)} \qquad (2)$$

h_t, L are building height and width parallel to the applied forces (taken in m).

$$T_1 = 2\pi \left[\frac{1}{g}\frac{\sum w_i\ {\delta_i}^2}{\sum H_i\ \delta_i}\right]^{0.5} \qquad \text{(for all type of structures)} \qquad (3)$$

w_t is the total gravity load of the storey i and δ_i is the lateral displacement of storey i under the effect of
an arbitrary set of horizontal loads Hi applied at each floor level.

Equation (3) is known as Rayleigh equation. Although equations (1 and 2) are simple to use but they usually provide only crude approximation to fundamental periods of practical frames. No mention is given in these equations to the masses and stiffnesses of the buildings despite that they are the most important factors influence the fundamental mode period of vibrations.

Rayleigh equation is known to provide a satisfactory approximation of fundamental periods of buildings, but it requires the use of linear elastic analysis to calculate the building lateral displacements under the effect of a set of horizontal loads H_i applied at each storey level. This requirement might be considered inconvenient since appropriate sub-assemblages might be used to analyze building structures under the effect of either gravity or horizontal loading and complete analysis may never be required during the design of the structures. In this paper a simple equation to calculate the fundamental period of vibration is developed. This equation is simple to use and provides a satisfactory approximation of the fundamental mode period of vibrations for practical buildings.

2 Calculating the fundamental period T_1

It is well known that Rayleigh-Ritz method is the most popular technique for calculating an approximation to the fundamental period T_1 of multi-degree structures.

In this technique an approximation to the lowest eigenvalue of the general eigenvalue problem $[K](\varphi) = \lambda[M](\varphi)$ is given by the well-known Rayleigh quotient

$$\rho(\varphi)a = \frac{(\varphi)_a{}^T[K](\varphi)}{(\varphi)_a{}^T[M](\varphi)} \quad \text{and} \quad \lambda_1 \leq \rho(\varphi)a \leq \lambda_n \tag{4}$$

Where
[K] is the global stiffness matrix of the structure and [M] is the global mass matrix of the structure and

$(\varphi)_a$ is an assumed approximation to the lowest eigenvector of the problem (4).

In equation (4) if the assumed vector $(\varphi)_a$ is chosen identical to the lowest eigenvector of the problem $(\varphi)_1$ then Rayleigh quotient coincides with the lowest eigenvalue $\rho(\varphi)_1 = \lambda_1$. The lowest eigenvector is usually unknown in practical cases and an assumed vector is utilized instead, therefore the Rayleigh quotient will be an upper approximation to the lowest eigenvalue of the problem (see equation 4). The assumed vector $(\varphi)_a$ should be chosen as close as possible to the actual lowest eigenvector of the problem $(\varphi)_1$, in order to obtain good approximation to the lowest eigenvalue of the problem. In a practical analysis the assumed vector $(\varphi)_a$ can be taken as the lateral displacement vector (δ) resulted from applying the structure to a set of lateral load pattern (H), i.e.

$$[K](\delta) = (H); \ (\varphi)_a = (\delta) \tag{5}$$

Where [K] is the global stiffness matrix of the structure. Substituting equation 5 into equation 4 and rearranging gives:

$$\rho(\varphi)_a = \frac{(\delta)^T(H)}{(\delta)^T[M](\delta)} = \frac{\sum_{i=1}^{n} \delta_i H_i}{\sum_{i=1}^{n} m_i {\delta_i}^2} \tag{6}$$

Where δ_i is lateral displacement of storey i, H_i is horizontal load applied at storey i, m_i is lumped mass of storey i and n is number of stories in the structure. Knowing that $\lambda_1 = {\omega_1}^2$ where ω_1 is the lowest circular natural frequency of the structure, hence

$$T_1 = \frac{2\pi}{\omega} = 2\pi\sqrt{\frac{\sum_{i=1}^{n} m_i {\delta_i}^2}{\sum_{i=1}^{n} H_i \delta_i}} = 2\pi\sqrt{\frac{\sum_{i=1}^{n} w_i {\delta_i}^2}{g\sum_{i=1}^{n} H_i \delta_i}} \tag{7}$$

Where g is the gravity acceleration.

In order to facilitate the use of equation 7 and since the assumed vector (δ) is only an approximation to the real lowest eigenvector of the structure. The applied horizontal loads can be assumed to consist of the total storey gravity load applied horizontally at each storey level, i.e. $H_i = w_i$. Hence equation 7 becomes:

$$T_1 = 2\pi \sqrt{\frac{\sum_{i=1}^{n} w_i \ \delta_i^{\,2}}{g \sum_{i=1}^{n} w_i \ \delta_i}} \tag{8}$$

To further simplify equation 8 the following assumptions are adopted

- The storey gravity loads are uniform in the structure, i.e. w_i= cons.
- The storey displacement δ_i is linearly dependent with δ_n the displacement at upper Storey (i.e. $\delta_i = \frac{h_i}{h_t}\ \delta_n$) where δ_n is the horizontal displacement at upper storey of the structure h_i is the storey height taken from ground level and h_t is the total height of the structure.
- Storey heights are uniform and equal to h (i.e. $h = {h_t}/{n}$) Hence equation 8 becomes:

$$T_1 = 2\pi \sqrt{\frac{w_i \times h^2 \times \frac{\delta_n^{\,2}}{h_t^{\,2}}(1^2 + 2^2 + \cdots + n^2)}{g \times w_i \times h \times \frac{\delta_n}{h_t}(1 + 2 + \cdots + n)}} \tag{9}$$

Rearranging equation 9 mathematically gives;

$$T_1 = 2\pi \sqrt{\frac{h \times \frac{\delta_n}{h_t} \times \frac{n \times (n+1)(2n+1)}{6}}{g \times \frac{n}{2} \times (n+1)}} \tag{10}$$

Assuming now that $(2n + 1) \cong 2n$ and rearranging equation 10 gives

$$T_1 = 2\pi \sqrt{\frac{2\delta_n}{3g}} \tag{11}$$

It should be noted here that the assumptions mentioned above should not reduce the ability of equation 11 to handle practical problems since a parametric study conducted by the author, not presented in this paper, has shown that these assumptions have only minimum influence on the fundamental period calculated. Moreover, these assumptions are often satisfied in practical problems.

3 The Proposed Model

In order to calculate an approximation to in equation 11 the model shown in figure 1 is adopted. This model consists of a column connected to upper and lower beams, which for the sake of simplicity, are assumed to be identical. This model has also a linear lateral spring S_i which allows for, if required, the stiffening effects resulted from the

presence of infill panels in storey i in real buildings, i.e. brick walls. Calculating the end moments of the model assuming positive anti-clock wise gives

$$M_{21} = M_{12} = \frac{EI_c}{L_c}\left[6\theta + \frac{6\delta_i}{L_c}\right]; M_{2B} = \frac{EI_b}{L_b}[3\theta] \tag{12}$$

Where, E Young modulus, H horizontal Load, Ic column second moment of area, Lc column height I_b beam second moment of area, L_b beam width θ rotation at upper and lower column ends and δ_i storey drift.
Equilibrium at joint 2 requires that:

$$\sum_2 M_{21} + M_{2B} = 0 \rightarrow \left(\frac{6EI_c}{L_c} + \frac{3EI_b}{L_b}\right)\theta + \frac{6EI_c}{L_c} \times \frac{\delta_i}{L_c} = 0 \rightarrow \theta = \left[\frac{-\frac{6EI_c}{L_c} \times \frac{\delta_i}{L_c}}{\frac{6EI_c}{L_c} + \frac{3EI_b}{L_b}}\right] \tag{13}$$

Considering the equilibrium of the column one gets:

$$\sum_{column} M = 0 \rightarrow M_{12} + M_{12} + (S_i\delta_i - H_i)L_c = 0 \tag{14}$$

Substituting equations (12) and (13) and accomplishing great amount of manipulation gives:

$$\delta = \frac{\frac{HL_c{}^3}{12EI_c}}{G_i + \bar{S}_i} \quad where\ \bar{S}_i = \frac{S_iL_c{}^3}{12EI_c}\ \ and\ G_i = \frac{\frac{3EI_b}{L_b}}{\frac{3EI_b}{L_b} + \frac{6EI_c}{L_c}} \tag{15}$$

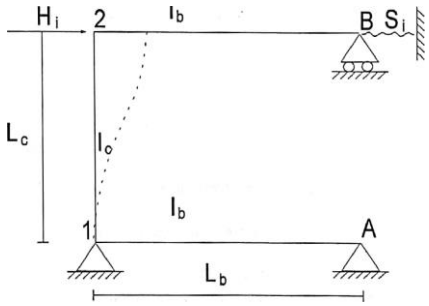

Fig. 1. the model used in the proposed method

In order to use equation 15 for a multistory frame one should consider the following

- In practical sway frames each beam buckles in double curvature. Hence the rotational stiffness of the beam should be multiplied by 2.
- In practical frames each beam restrains two columns, therefore the beam rotational stiffness should be multiplied by 2.

- Finally, each beam in a practical multistory sway frame restrains two columns, i.e. upper and lower columns connected to that beam. Thus, the beam rotational stiffness should approximately be divided by 2.

As a result of above the use of equation (15) for practical multistory frame is permitted providing that the beam rotational stiffnesses is multiplied by 2, or

$$G_i = \frac{\sum_{storey} \frac{6EI_b}{L_b}}{\sum_{storey} \frac{6EI_b}{L_b} + \frac{6EI_c}{L_c}} = \frac{\sum_{storey} \frac{I_b}{L_b}}{\sum_{storey} \frac{I_b}{L_b} + \frac{I_c}{L_c}} \tag{16}$$

It should be noted here that equation 16 underestimates the stiffness of both first storey, where columns might be fully fixed at base, and for upper storey, where no upper columns are present. This underestimation should not affect the accuracy of equation 15 since the second assumption used to derive equation 11 slightly overestimate the frame stiffness; hence the two effects are more likely to be balanced. The factor G_i should be taken as the ratio of the sum of beam rotational stiffnesses of the storey i to the sum of the total storey rotational stiffnesses (beams plus columns).
Corresponding to equation 15 the upper storey drift resulted from subjecting the structure to the total of storey gravity load applied horizontally at each storey level can be calculated as follows:

$$\delta_n = \sum_{i=1}^{n} \delta_i = \sum_{i=1}^{n} \frac{W{L_c}^3}{12EI_c n}\left(\frac{n+1-i}{G_i + \overline{S_\iota}}\right) = \frac{W}{12En}\sum_{i=1}^{n} \frac{{L_{ci}}^3}{I_{ci}}\left(\frac{n+1-i}{G_i + \overline{S_\iota}}\right) \tag{17}$$

Where I_{ci} is the sum of the beam second moment of areas of storey i , L_{ci} is the height of storey i , G_i is the ratio of the storey i (equation 16) and W is the total weight of the structure. Therefore

$$T_1 = 2\pi \sqrt{\frac{W}{18Egn}\sum_{i=1}^{n} \frac{{L_{ci}}^3}{I_{ci}}\left(\frac{n+1-i}{G_i + \overline{S_\iota}}\right)} \tag{18}$$

It should be noted that equation 18 is similar to the equation used to calculate the fundamental period of a single degree of freedom, i.e. $T = 2\pi\sqrt{\frac{m}{k}}$ where m and k are the mass and the stiffness of the corresponding single degree structure.

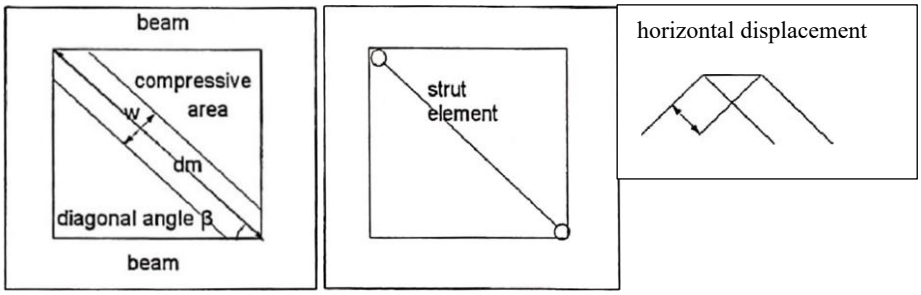

Fig. 2. Modeling of infill panel in concrete structures.

For special case where no infill panels are present ($\bar{S} = 0$) and where beams are very stiff compared to columns (shear buildings G_i =1) equation 18 reduces to

$$T_1 = 2\pi \sqrt{\frac{W}{18Egn}\sum_{i=1}^{n}\frac{{L_{ci}}^3}{I_{ci}}(n+1-i)} \tag{19}$$

4 Calculating the Factor $\overline{S_t}$ for Practical Buildings

The non-dimensional factor $\overline{S_t}$, which allows for the strengthening effect resulted from the presence of infill panels in practical buildings, can be calculated by consider 1cm enforced horizontal displacement at the top of i storey (see figure 2), the corresponding diagonal displacement of the storey equal to (1 cos ß) and the diagonal force on the struts becomes equal to

$$diagonal\ force = \frac{1\cos\beta}{dm}Ewt \tag{20}$$

Where: β is panel diagonal angle (see figure 2), E Young modulus of the panel material, w is the width of the panel, dm is the diagonal length of the panel and t the thickness of the panel. Hence the horizontal force equal to

$$horizontal\ force = \frac{1\cos\beta^2}{dm}Ewt \tag{21}$$

This is equal to the stiffness S since $S = \frac{horizontal\ force}{hporizontal\ displacement}$

The panel width w depends on the diagonal length of the panel dm and can be taken for practical buildings as w = (0.25. dm). Substituting this relation into equation 21 gives:

$$\mathrm{S} = 0.25 \times (\cos\beta^2) \times \mathrm{E} \times \mathrm{t} \tag{22}$$

S_i should be taken as the sum of S for all infill panels of the storey i and $\overline{S_i} = \frac{S_i \times {L_{ci}}^3}{12EI_{ci}}$

Figure 2 shows that accounting for the stiffening effects resulted from the presence of infill panels in practical frames analysis can be accomplished approximately by replacing each infill panel with a diagonal strut element. The cross section of the strut element should be taken as (w. t) with Young modulus equal to the Young modulus of the panel materials.

5 Application of the Proposed Method to Concrete Buildings

When analyzing a concrete frame structure for gravity loads, it is generally accepted to take the gross stiffness of the elements into consideration since cracks are expected to be small enough to be neglected. Under seismic actions, however it is important to take into consideration the uncracked sections of the elements specially when calculating the fundamental period of vibration. It is still impractical to evaluate the uncracked properties of several sections in each element of a multistory frame and a reasonable average value should be utilized instead, i.e. in the analysis of a concrete building I_{eff} the effective second moment of area of the building sections are to be used.

The following table shows recommended values of I_{eff} to be used for beams, columns and walls. In this table I_g represents the gross second moment of area of the section neglecting the reinforcement.

Table 1. Recommended values of I_{eff} for concrete sections.

Section shape	Adopted value I_{eff}
Rectangular beams	0.4 I_g
T and L beams	0.35 I_g
Concrete walls	0.6 I_g
Columns with heavy compression loads	0.8 I_g
Columns with light compression loads	0.6 I_g
Columns with tension loads	0.4 I_g

Concerning the geometric modeling of a framed concrete buildings the beams and the columns are replaced by straight bars coincide with the centroidal axes of their gross concrete sections. This is generally accepted in engineering practice despite the fact that beams and columns in a concrete building are subjected under the effect of earthquake actions to reversal end moments. Hence the uncracked part of the element sections varies along its length and so its neutral axes. This variation is known to have only minor effect on the response of the structure.

The span lengths of member are usually taken as the distance between the intersect points of the reference axes of the beams and columns. No account is considered in the analysis of such structures to the stiffening effects resulted from the joint regions since major cracks might happen in these joints during earthquakes. Finally beams framing into concrete walls in dual buildings can be reasonably modeled as shown in figure 3.

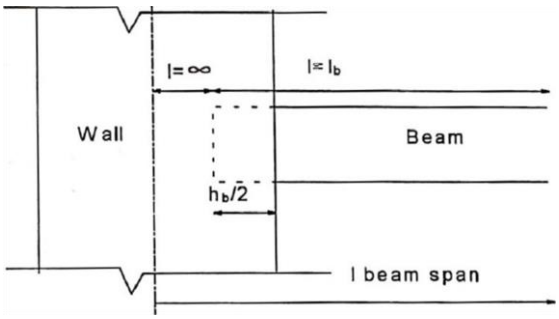

Fig. 3. Modeling of beam framing into concrete wall.

6 Verification of the proposed method

In order to verify the accuracy of the proposed method (equation 18) to calculate a good approximation to the fundamental natural periods of buildings, the following two examples are selected, from many examples solved by the author and not included within.

Example 1

The frame shown in figure (4) which consists of ten multistory two bays concrete frame is utilized in example 1, It is assumed that panels are extended over the full height of bays of the frame with the following properties: $E = 1000\ \text{Mpa}, t = 10\ \text{cm}$ the effective width of the compression region equals to 0.25 of the diagonal length of the corresponding bay. The effective second moment of areas I_{eff} the frame elements are taken for the beams and the columns from table 1 as follows: $Ieff = 0.4\ I_g$ for beam section; $Ieff = 0.8\ I_g$ for column section.

Gravity load for stories (1-9) 0.3 kN/cm and for upper storey 0.2 kN/cm
Dimensions of the cross sections are shown beside each element
E Young modulus for concrete 29000 M pa and for infill panels 1000M pa
Infill panels (not shown) extend over the full heights with thickness 10 cm
All Dimensions are in cm

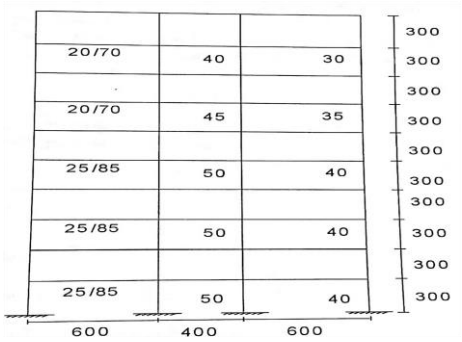

Fig. 4. The frame of example 1.

Table 2 Calculation of example 1.

Storey No.	$I_{ci}\sum_{column} I_c$ cm^4	G_i	$\frac{{L_{ci}}^3}{I_{ci}}(n+1-i)$ l/cm	$\bar{S}_i$	$\frac{{L_{ci}}^3}{I_{ci}}\frac{(n+1-i)}{G_i}$ l/cm	$\frac{{L_{ci}}^3}{I_{ci}}\frac{(n+1-i)}{G_i+\bar{S}_i}$ l/cm
1	1174667	0.43	230	0.36	535	291
2	1174667	0.43	207	0.36	482	262
3	1174667	0.43	184	0.36	428	233
4	1174667	0.43	161	0.36	375	203
5	1174667	0.43	138	0.36	321	175
6	1174667	0.43	115	0.36	268	146
7	746883	0.35	145	0.58	413	156
8	746833	0.35	109	0.58	310	117
9	449333	0.47	120	0.96	254	84
10	449333	0.47	60	0.96	127	42
			$\sum = 1469$		$\sum = 3513$	$\sum = 1709$

Calculating storey properties for the first storey of the frame produces:

$$G_1\frac{2\times\frac{511771}{600}+\frac{511771}{400}}{2\times\frac{511771}{600}+\frac{511771}{400}+\frac{511771}{300}}=0.43$$

$$S_1 = 2(0.25\times0.89^2\times100\times10)+(0.25\times0.8^2\times100\times10)=556\,kN/cm$$

$$\bar{S_1} = \frac{558 \times 300^3}{12 \times 2900 \times 1174667} = 0.36$$

It should be noted here that the effective width of the infill panels w is taken equal to 167 cm and 125 cm for spans 600 cm and 400 cm respectively. Repeating same procedure for all stories of the frame provides table 2. Calculating the fundamental period of the frame utilizing equation (19) and assuming that the frame beams are very stiff (shear building) and infill panels are not present provides the first value of raw 4 in table 3.

Repeating same calculation taking into consideration the flexibility of the frame beams (equation 18 with $\bar{S_i} = 0.0$) gives the second value of raw 4 in table 3. Finally taking into consideration the strengthening effects resulted from the presence of infill panels extended over the full spans of the frame produces the third value of row 4 in table 3. Employing the program ROBOT 2020 to calculate the fundamental period for three cases mentioned above produces row 3 in table 3.

Table 3. The result of example 1.

The Fundamental Period sec.			
	Shear building with no infill panels	Flexible beam building with no infill panels	Flexible beam building with infill panels
Program ROBOT 2020	0.81	1.19	0.84
Proposed method	0.75	1.16	0.81
Conventional method equation 1		0.96	

It is worth noting that, the frame infill panels are modeled as struts (see figure 2) when utilizing the program ROBOT 2020 to calculate the fundamental mode period of vibration of the frame with infill panels (third case). Finally employing the conventional method (equation 1) to calculate the fundamental period of vibration of the frame produces the value tabulated in raw 5 table 3. It can be concluded from table 3 that the prediction of the proposed method is more accurate than the conventional method. Table 3 shows also that, framed concrete buildings with infill panels can be approximated as shear buildings when calculating its fundamental mode period of vibrations.

Example 2

Same procedure used in example 1 is repeated here for the dual frame shown in figure 6 which consists of nine stories and has a continues concrete wall in the middle. For the sake of simplicity, the concrete wall is treated here as a stiff column and the effective

second moment of areas for the frame elements are taking (according to table 1) as follows: E I_{eff} = 0.4EI_g for beam section; E I_{eff} = 0.8 E I_g for column section; E I_{eff} = 0.6 E I_g for wall section, where I_{eff} the effective second moment of area and I_g is the gross second moment of area neglecting the reinforcement. No infill panel is considered in this example $\overline{S_t} = 0$

The geometry model of the concrete wall is shown in figure 6. The rigid element is assumed to have length equal to (150cm — h_b / 2) where h_b is the beam cross section height and second moment of area equal to 10 I_b where I_b is the beam second moment of area. This geometry is included in the analysis of the model frame to calculate its fundamental mode period of vibration employing the program ROBOT 2020. The result is tabulated in row 2 in table 5.

Since the proposed method is intended to be used in hand calculation, only a simple procedure isjustified to allow for the presence of the rigid elements in the model frame shown in figure 6. An approximate second moment of area for each beam and rigid element is calculated as the average after dividing the beam and the rigid element into equivalent segments, i.e. for first storey for example:

I (beam + rigid element) =I_{beam} (1+9 rigid element length/total length= 2,32 I_{beam}

Hence the second moment of areas of all beams of the frame are multiplied by 2.32 to account for, in approximate way, the effects of the presence of the rigid elements in the model frame. Calculating thestory properties of th frame provide Table 4

Table 4. The calculation of example 2.

Storey	G_i	$\frac{L_{ci}^3}{I_{ci}}$	$\frac{L_{ci}^3}{I_{ci}}\frac{(n+1-i)}{G_i}$
1	0.042	30.15	718
2	0.028	7.94	284
3	0.028	6.95	248
4	0.028	5.96	213
5	0.028	4.97	178
6	0.019	3.98	209
7	0.019	2.99	157
8	0.015	2.00	133
9	0.015	0.99	66
			$\sum = 2206$

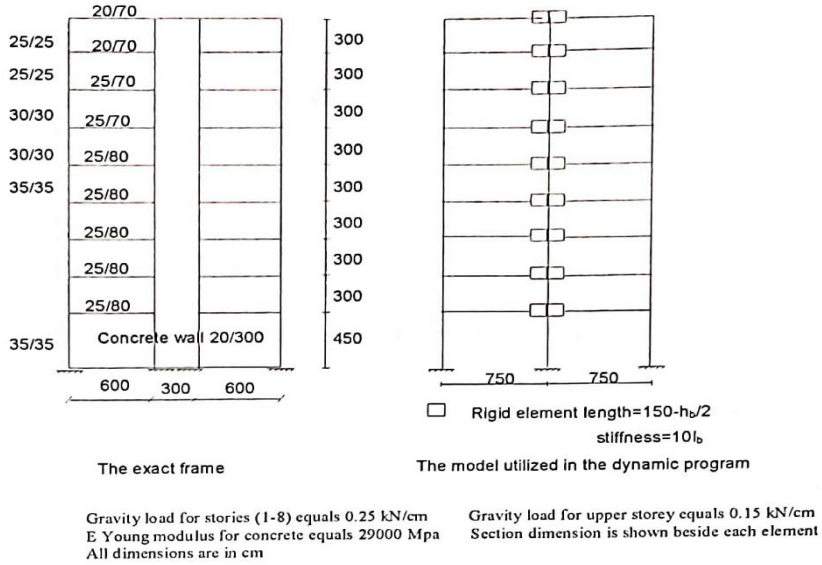

Fig. 5. The frame used in Example 2

Calculating the fundamental period of the structure utilizing the proposed method produces raw 3 in table 5. Employing the conventional method (equation 2) to calculate the fundamental period gives raw 4 in table 5.

Table 5. The result of example 2.

The Fundamental Period sec.	
Program ROBOT 2020	0.82
Proposed Method	0.78
Conventional method equation 2	0.66

Table 5 shows again that the proposed method provided a better approximation to the fundamental period of the structure than the conventional method.

7 Conclusion

A simple design method to calculate the fundamental mode period of vibrations of practical concrete buildings has been proposed. The proposed method is still simple to use and provides more accurate estimation of fundamental period of vibrations of buildings than the conventional methods. It takes into consideration both masses and stiffnesses of practical buildings. Several examples have been solved by the author utilizing the conventional method, the proposed method and the computer program

ROBOT 2020. Comparisons of the results obtained have shown clearly that the proposed method provides satisfactory accurate estimations of fundamental periods of practical buildings. Since the proposed method requires only minimum hand calculation it is believed to be ideal for design office use.

References

1. CEN Tech comm 25/SC8 Eurocod8: Earthquake Resistant Design of Structures-Part1: General Rules and Rules for Building (ENV 1998-1-1/2/3).
2. ICBO (Int. Conf Of Building Officials) Uniform Building Code Edition, Whittier, California, (1994).
3. Chikho, A.H. “Frame behavior with semi-rigid connections.” Ph.D. Thesis, Sheffield University, England. (1990).
4. Chikho, A.H., Kirby, P.A. “An approximate method for the estimation of ultimate column load in steel sway frames.” Nordic Steel Conference'95, Malmo, Sweden, Vol. 2, pp. 711-718. (1995).
5. Chikho, A.H. “An approximate formula for calculating lateral displacements of sway structures” R. J. of Aleppo Univ., Engineering Science Series, No.32, 2002.

Testing of Concrete Masonry Infill Walls Subjected to In-Plane Lateral Load

J. Martin Leal-Graciano[1][0009-0001-6339-7768], Juan J. Pérez-Gavilán[2][0000-0002-4477-6818], A. Reyes Salazar[1][0000-0001-5074-1526] and J. L. Rivera Salas[1][0000-0002-2327-6152]

[1] Autonomous University of Sinaloa, Engineering Faculty, Culiacán Sinaloa, México, jesusleal@uas.edu.mx, reyes@uas.edu.mx, luz@uas.edu.mx
[2] National Autonomous University of México, Institute of Engineering, Mexico City, México, jperezgavilane@iingen.unam.mx

Abstract. The experimental results about the global behavior of four 1:2 scaled reinforced concrete infilled frames subject to in-plane lateral load are presented. The main objective was to generate experimental evidence about the use of steel bars within mortar bed-joints as shear reinforcement on concrete masonry infill walls. To achieve the objective established, four concrete frames infilled with concrete masonry walls were built and tested in pairs, having both specimens in the pair identical characteristics except that one of them included joint reinforcement. The variable between pairs was the aspect ratio of the wall. All cases included tie-columns and tie-beams on the perimeter of the wall to anchor the joint reinforcement. All the specimens were tested in cantilever under reversible cyclic lateral load. To simulate gravity load, constant vertical load was applied on the top of the columns. The results indicate that the joint reinforcement increase lightly the lateral strength of the infilled frames, however, it reduces the deformation capacity of the system. Regarding the effects of joint reinforcement in the performance of confined masonry walls, some facts were confirmed for infill walls: this type of reinforcement produces a more distributed cracking and reduces the width of the cracks.

Keywords: Infill wall, Infilled frame, Masonry wall.

1 Introduction

In the field of Mexican construction based on masonry, two principal structural systems are identified: buildings with load-bearing walls and buildings based on infill walls.

Load-bearing walls are those that support both vertical and lateral loads, since they are the only structural system of the building. Confined masonry walls and masonry walls with interior reinforcement are included in this category. In Mexico, as well as Latin America, East Europe and Indonesia, masonry walls are widely used for low- to mid-raise constructions [1] due to their low cost compared with other structural systems. The use of confined masonry allows a reduction in the cost of both the foundations and the superstructure, because of the required smaller reinforced concrete sections and the better distribution of ground stresses [2].

According to the Mexican code [3], an infill wall is that what is surrounded by beams and columns of a structural frame, to which it provides rigidity against lateral loads. Commonly, buildings based on infilled frames with masonry walls are designed considering the frame as the main resistant element. The contribution of the wall is usually regarded as a resistance reserve. However, this consideration does not always lead to safer designs [4]. Past seismic experiences have indicated that infill walls presence may lead to beneficial or adverse effects on the behavior of the structure, depending on the physical and mechanical characteristics of wall and frame, and their reinforcement conditions.

There is evidence that infill walls have beneficial effects on the seismic behavior of structures when they are uniformly distributed in elevation and in plant of the building [5]. These effects consist on increase the lateral stiffness and strength of the structure, decreasing the deformation demand and improve the system's capacity for energy dissipation. For example, the evidence presented by Hamburger and Meyer [6], and Murty and Jain [7] who noted the better structural behavior of infilled frames with masonry walls compared with others structural systems during the 1906 San Francisco earthquake and moderate earthquakes in India.

On the other hand, because provide greater stiffness to the system, infill walls attract greater seismic load. If the frame has no sufficient lateral load resistance and/or ductility, the strength of the system is drastically reduced after the first cracking of the infill wall. In addition, when the frames are filled with masonry walls located asymmetrically in elevation and in plan of the building, it leads to adverse failure mechanisms that produces premature collapse of the structure. Saatcioglu et al. [8] noted the poor performance of reinforced-concrete-infilled frames, the primary structural system used in Turkey, during the Kocaeli 1999 earthquake. Studies carried out by Ravichandran and Klingner [9] showed that if the resistance of the infill walls exceeds 35% of the total resistance of a story, undesirable effects can be produced in the non-linear behavior of the structure, such as soft floors.

Although in appearance, a confined masonry construction is very similar to that of a reinforced concrete frame filled with masonry walls, these two construction systems are substantially different [1]. When subjected to lateral seismic loads, confined walls act as shear wall and infill walls act as diagonal strut (Figure 1). In the case of infill walls, the masonry wall separates from the surrounding frame due to their different deformation characteristics and to a relative lack of bond. Separation occurs in two diagonally opposite corners while in the other two corners the masonry wall reacts against the frame over a certain length of contact extending from the loaded corners. Consequently, the system behaves approximately as a braced frame. This behavior suggested to researchers [10-17] that a diagonal strut could represent the effect of the infill wall. When the direction of the lateral load is reversed, the braced frame mechanism is developed along the direction of the other diagonal [18].

The significant increase population has led to vertical housing developments. For these mid-rise masonry constructions, seismic loading commonly exceeds the shear strength of the walls. In that case, steel bars within the mortar bed-joints may be provided as shear reinforcement (joint reinforcement). In the Mexican code [3],

equation 1 is included to estimate the contribution of joint reinforcement in the shear resistance of masonry walls.

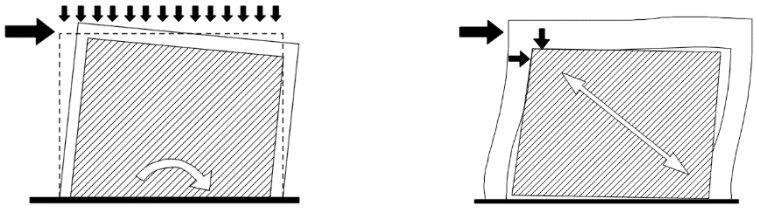

Confined wall Infill wall

Fig. 1. Seismic response of confined walls and infill walls

$$V_{SR} = F_R \, \eta \, \rho_h \, f_{yh} \, A_T \tag{1}$$

In equation 1, F_R is the strength reduction factor, A_T is the cross-section area of the wall, f_{yh} is the yield strength of joint reinforcement, $p_h = A_s/(s \times t)$ is the percent of steel reinforcement, s is the vertical spacing, t is the thickness of the wall and η is an efficiency factor, which depended only on the amount of joint reinforcement given by $\rho_h \, f_{yh}$. Such equation was established as result of some experimental studies about load-bearing walls [19-23].

Few information is found in the existing literature about the effects of joint reinforcement on the seismic behavior of infill masonry walls. Consequently, the Mexican code [3] establishes the same equations to estimate the contribution of joint reinforcement for both confined walls and infill walls. However, the evident differences among confined walls and infill walls (for example, infill walls do not support vertical loads, and when subjected to lateral loads the wall separates from the concrete elements) suggest that the contribution of the joint reinforcement in infill walls is different than in the case of confined walls.

In this manuscript, the effects of the joint reinforcement on the global behavior of reinforced concrete frames infilled with masonry walls are presented. Two aspect ratio (H/L) of the walls are included. Unlike previous studies [24], the infill walls were made with lightweight concrete solid units.

2 Experimental Program

2.1 Specimens

Four concrete frames infilled with concrete masonry walls were built and tested (Figure 2). All cases were scaled 1:2. The specimens are organized in two pairs, having both specimens in the pair identical characteristics except that one of them included joint reinforcement.

The variable between pairs was the aspect ratio of the wall. In the first pair (MD3N_T75 and MD3NRH_T75), the reinforced concrete frames had identical cross section for beams and columns, the height at center of beam was 1.50 m and the length center-to-center of columns was 2.00 m (H/L= 0.75). The second pair of specimens

(MD3N_T41 and MD3NRH_T41) had the same conditions for the concrete frame than the first pair, except that the length center-to-center of columns was 3.50 m (H/L= 0.41).

In all cases, the infill walls were built with lightweight concrete solid units and included tie-columns and tie-beams on the perimeter of the wall to anchor the joint reinforcement. The concrete units, which are widely used on the northwest of Mexico, were manufactured scaled 1:2 especially for this investigation using the same materials and procedure than the real size units. The joint reinforcement consisted on a 4 mm diameter (5/32 inch) steel bars located each four courses. The percent of joint reinforcement correspond to a value of $p_h f_{yh} = 0.7\ MPa$.

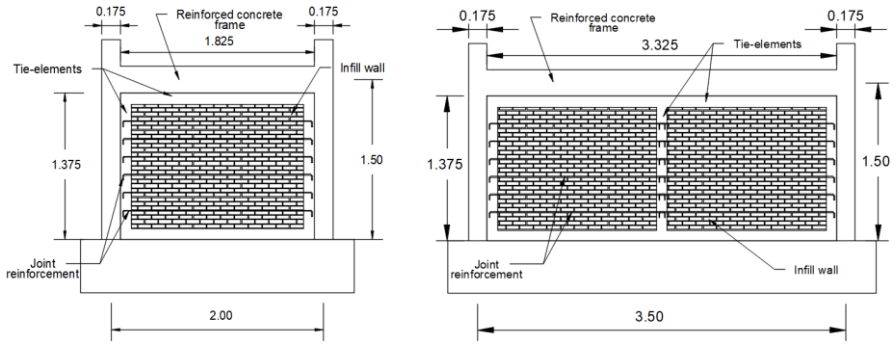

MD3NRH_T75 MD3NRH_T41

Fig. 2. Specimens configuration

Reinforcement Conditions

Figure 3 shows details of reinforcement and dimensions for concrete infilled frames with H/L= 0.41. The longitudinal reinforcement consisted of rebars of 12.7 mm (1/2 inch) and 9.5 mm (3/8 inch) diameter with a nominal yielding stress f_y = 412 MPa. Transverse reinforcement consisted of rebars with 6.3 mm (1/4 inch) diameter stirrups with f_y equal to 230 MPa.

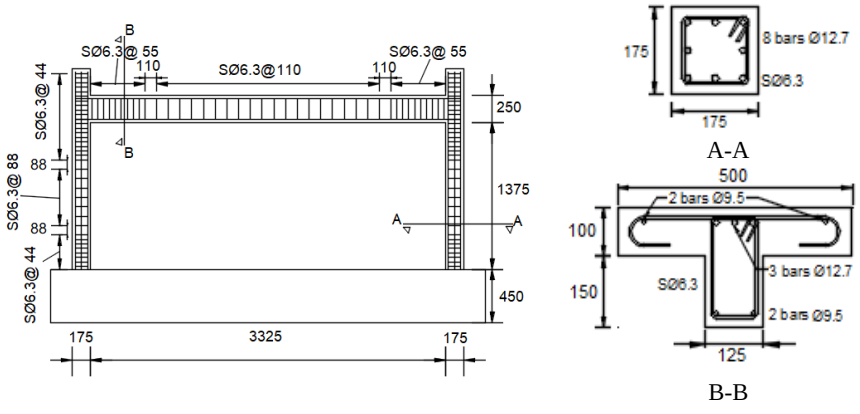

Fig. 3. Reinforcement conditions for concrete infilled frames

Material Properties

The mechanical properties of the material were investigated through the corresponding standard Mexican tests, similar to the ASTM tests. The average values for the compressive strength of masonry units (f_p), compressive strength of mortar (f_j), concrete strength (f_c) and elastic modulus (E_c), compressive strength of masonry (f_m), diagonal compressive strength (v_m) and elastic modulus (E_m) are shown in Table 1.

Table 1. Material properties (MPa).

Specimens	Units	Mortar	Concrete of frame		Concrete of confining elements	Masonry		
	f_p	f_j	f_c	E_c	f_c	f_m	v_m	E_m
MD3N_T75	17.45	19.47	29.06	23378	21.97	9.09	1.82	5422
MD3NRH_T75	17.45	19.47	29.06	23378	21.97	9.09	1.82	5422
MD3N_T41	18.13	22.29	26.29	20038	23.16	10.1	2.03	6857
MD3NRH_T41	18.13	22.29	26.09	20038	26.16	10.1	2.03	6857

2.2 Test Setup and Load Sequence

The test setup used to apply loads to the specimens is shown on Figure 4. The gravity loads were simulated through vertical load applied on the top of the columns. The vertical load equal to 120.17 kN, which was maintained constant during each test, corresponds to the gravity load of a prototype building of three stories. The vertical load leaded to a vertical stress on columns of 3.92 MPa.

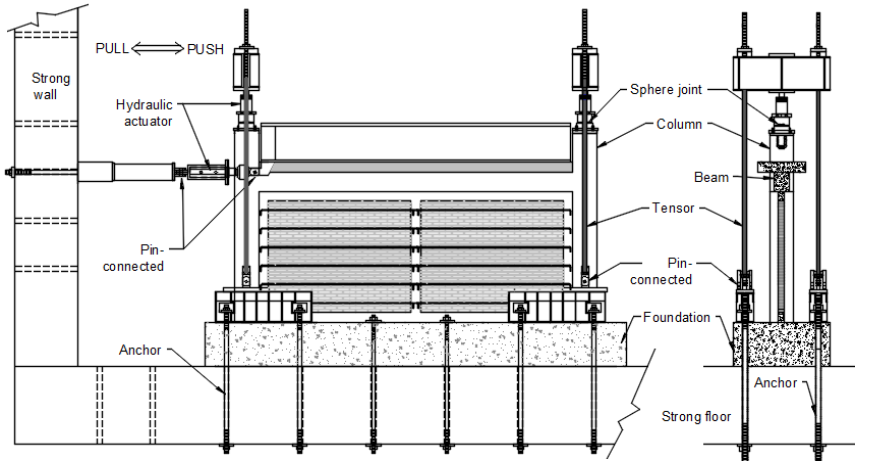

a) Elevation view b) Transverse view

Fig. 4. Test setup

Simultaneously to the vertical load, the specimens were subjected to cycles of quasi-statics alternated lateral load, simulating seismic action. The lateral load was applied following the test procedure described in the Mexican code [3]. So, the lateral load

sequence consisted on cycles applied in pairs, starting with load controlled up to 25% and 50% of the estimated cracking load equal to 58.86 kN. Next, the sequence continued with displacement controlled cycles starting with deformations of 0.001 and 0.002. After that, drifts with increments of 0.002 were applied. When the specimen reached a deformation of 0.02, the drift increment changed to 0.004. The test ended when lateral load decreased to 80% of the maximum strength.

2.3 Instrumentation

Figure 5 shows the instrumentation used to measure displacements in each specimen and strain in the joint reinforcement. Displacement transducers were placed on different locations of the wall to register its deformed configuration. In addition, strain gauges were installed in the joint reinforcement, following a diagonal trajectory on the wall. In the cases of longer infill walls (H/L= 0.41), strain gauges were concentrated in one panel, take in count the symmetry of the wall.

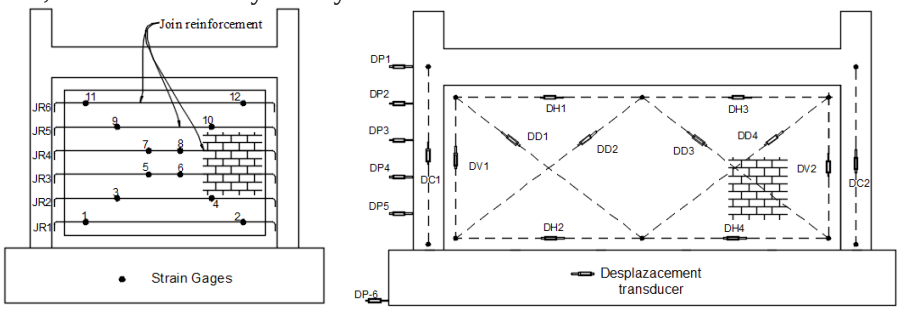

a) Internal instrumentation

a) External instrumentation

Fig. 5. Instrumentation

3 Experimental Results

3.1 Hysteretic curves and cracking

The lateral load – drift hysteretic curves of each specimen are presented in Figure 6. The drift is defined as the lateral displacement divided by the height of the wall. The final cracking patterns are shown in Figure 7. Both hysteretic curves and crack patterns evolution of each infill wall are described below. In the Table 2, the values of lateral load and drift at critical points of the test are summarized.

The specimens MD3N_T75 and MD3N_T41 had a first cracking on the wall significantly different. In the MD3N_T75, the first crack consisted on a horizontal sliding located at half height of the wall. This first cracking occurred in cycle 1 for a lateral load of $V = 17.3$ kN and a drift $\gamma = 0.00017$. In the case of MD3N_T41, the first crack on the wall had diagonal trajectory, and it appeared in cycle 7 for a lateral load $V = 199.3$ kN and a drift level $\gamma = 0.0020$. Commonly, the first cracking is associated to a change on the slope of the hysteretic curve, however, in these specimens the first crack had no an effect on the lateral load – drift curve. In both cases, the first cracking on the concrete frame occurred in cycle 5, corresponding to $\gamma = 0.0010$, at the

ends of the beam. In the specimen MD3N_T75, the first flexural crack appeared at the bottom of a column in cycle 7 for a lateral load of 100.3 kN and drift of 0.0040, whereas in the specimen MD3N_T41 the first flexural crack occurred in cycle 9 for $V = 244.9$ kN and a drift $\gamma = 0.0040$. The specimen MD3N_T75 reached its maximum load $V = 158.38$ kN in cycle 25 for a drift $\gamma = 0.024$; whereas in the MD3N_T41 the maximum strength of the specimen, $V = 272.73$ kN, was reached in cycle 9 for a drift of $\gamma = 0.0060$. In both cases, as the test progressed, the cracking at the beam and the flexural cracking in the columns extended towards the center of the members and diagonal cracks appeared at the beam – column connection. In specimen MD3N_T75, sliding inhibited the production of inclined cracks on the wall, whereas in the specimen MD3N_T41 some new diagonal cracks were appearing according with the sense of the lateral load. In addition, in both cases, crushing at the top corners of the wall occurred, but this fact was more pronounced on the longer wall (MD3N_T41). It was considered that failure of the specimen MD3N_T75 occurred in cycle 28, corresponding to a drift $\gamma = 0.028$, when lateral load was reduced significantly due to the important damage at the beam – column connections. In the case of MD3N_T41, failure occurred to a drift $\gamma = 0.0134$, when lateral load was reduced to 80% of the maximum registered load.

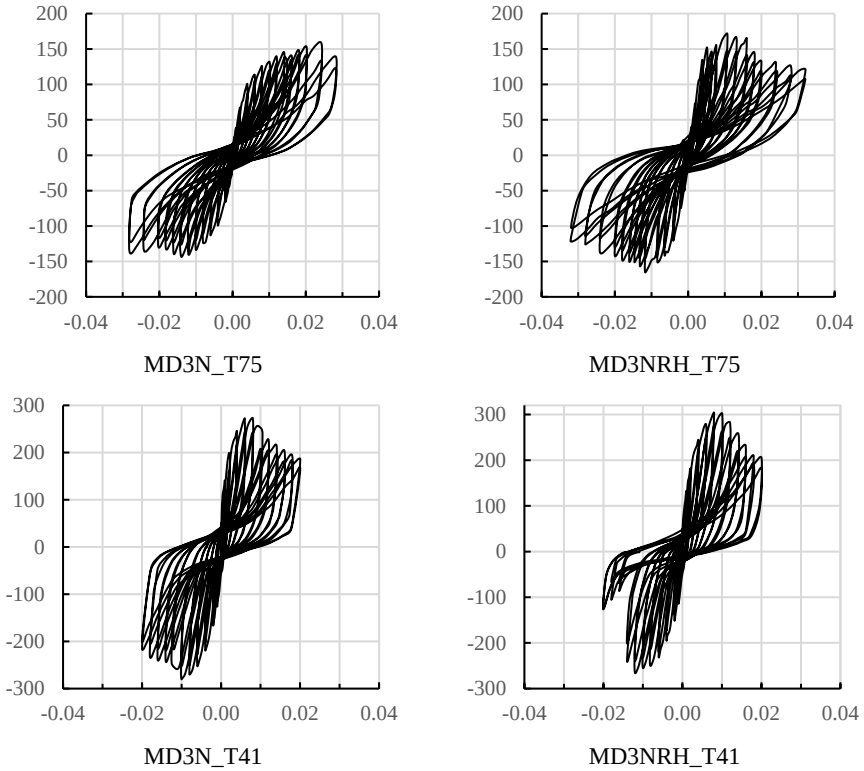

Fig. 6. Lateral load (kN) – drift (mm/mm) hysteretic curves

In the specimens with joint reinforcement (MD3NRH_T75 y MD3NRH_T41), the inclined cracking on the wall was distributed, whereas the cracking on the concrete

frame was similar to that of the specimens without joint reinforcement. In the specimen MD3NRH_T75, the first inclined cracking occurred in cycle 1 for a lateral load $V =$ 15.1 kN and a drift level $\gamma = 0.00015$; whereas in the MD3NRH_T41 the first diagonal crack appeared in cycle 7 for $V = 181.6$ kN and $\gamma = 0.0020$. In both cases, the first cracking in the frame, located at the ends of the beam, occurred in cycle 5, corresponding to $\gamma = 0.0010$. Additionally, the first flexural crack at the bottom of the columns occurred in cycle 9, corresponding to $\gamma = 0.0040$. In both cases, as the test progressed, the cracking at the beam and the columns extended towards the center of the members and diagonal cracks appeared at the beam – column connection. In the specimen MD3NRH_T75, the maximum lateral load $V = 172.11$ kN was registered in cycle 15 for a drift γ = 0.010; whereas in the specimen MD3NRH_T41, the maximum lateral load $V = 302.96$ kN was reached in cycle 13 for a drift γ = 0.008. In both cases, failure was defined when lateral load was reduced to 80% of the maximum lateral load. For MD3NRH_T75 failure occurred to a drift $\gamma = 0.0170$, whereas for MD3NRH_T41 it was to a drift $\gamma = 0.0152$.

MD3N_T75 MD3NRH_T75

MD3N_T41 MD3NRH_T41

Fig. 7. Final crack patterns

Table 2. Drift and shear strength for critical points.

Specimens	First cracking on wall		Maximum strength		Failure	
	γ_{cr}	V_{cr} (kN)	γ_{max}	V_{max} (kN)	γ_u	V_u (kN)
MD3N_T75	0.00017	17.3	0.024	158.4	0.028	139.1
MD3NRH_T75	0.00015	15.1	0.010	172.1	0.0170	137.7
MD3N_T41	0.002	199.3	0.006	272.7	0.0134	218.2
MD3NRH_T41	0.002	181.6	0.008	302.9	0.0152	242.4

4 Conclusions

Four reinforced concrete frames infilled with masonry walls were tested. In two of them, the infill wall included joint reinforcement. The specimens were built with semi-lightweight concrete solid units and scaled 1:2. The study variable were the joint reinforcement and the aspect ratio of the wall. The specimens were tested in cantilever, according with the test procedure established by the Mexican code (2020). Based on the experimental results obtained from the tests, the following conclusions are established.

- The joint reinforcement had no a significant effect on the maximum strength (V_{max}). On average, the specimens with joint reinforcement had a value for V_{max} 10% larger than that of the specimen without reinforcement. In addition, the joint reinforcement decreased lightly the deformation capacity of the system (13% smaller).
- The aspect ratio (H/L) of the wall had an important effect on the maximum strength and the deformation capacity of the system. On average, the longer specimens (H/L= 0.41) had a maximum strength 1.74 times larger than that of the shorter specimens (H/L= 0.75), and the deformation capacity was reduced to 68.5%.
- Similar to confined masonry walls, the joint reinforcement on infill walls produces a more distributed cracking and the width of crack is smaller than in the infill walls without this reinforcement. An important effect of the joint reinforcement is that improve the integrity of the wall for large drifts. This fact is relevant to preserve the out-of-plane stability.

Acknowledgments

This investigation was funded by Consejo Nacional de Humanidades Ciencia y Tecnología (CONAHCYT) under Grant CB 2017-2018/A1-S-36643. The financial support given by the Autonomous University of Sinaloa under Grant PROFAPI 2022 is appreciated. Many thanks are given to the students that participated during construction, instrumenting and testing: Xavier Millán and Samuel Camargo.

References

1. Meli, R., Brzev, S., Astroza, M., Beon, T., Crisafulli, F. J., Farsi, M., Hart, T., Mebarki, A., Moghadam, A., Quiun, D., et al.: Seismic Design Guide for Low-Rise Confined Masonry Buildings. EERI Confined Masonry Network, Oakland, CA, USA (2011).
2. Marques, R., Lourenço, P. B.: Structural behavior and design rules of confined masonry walls: Review and proposals. Constr. Build. Mater. 217, 137–155 (2019).
3. Gaceta Oficial de la Ciudad de México: Normas Técnicas Complementarias para el Diseño y Construcción de Estructuras de Mampostería del Gobierno de la Ciudad de México (In Spanish). Ciudad de México, México (2017).
4. Drysdale, R. G., Hamid, A., Baker, L.: Masonry Structures Behavior and Design. Prentice Hall, U.S.A. (1999).
5. Leal-Graciano, J. M.: Comportamiento ante caga lateral de muros diafragma de mampostería. PhD Thesis, National Autonomous University of Mexico, México (2018).
6. Hamburger, R., Meyer, J. D.: The Performance of Steel Frames building with infill masonry walls in the 1906 San Francisco Earthquake. Earthquake Spectra 22(S2), S43-S67 (2006).
7. Murty, C. V. R., Jain, S. K.: Beneficial influence of masonry infill walls on seismic performance of RC frame buildings. In: 12th World Conference on Earthquake Engineering, Auckland, New Zealand (2000).
8. Saatcioglu, M., Mitchell, D., Tinawi, R., Garnerd, N., Gillies, J., Ghobarh, A., Anderson, D., Lau, D.: The August 17, 1999, Kocaeli (Turkey) earthquake- damage to structures. Canadian Journal of Civil Engineering 28, 715-737 (2001).
9. Ravichandra, S. S., Klinger, R. E.: Seismic Design Factors for Steel Moment Frames with Masonry Infills: Parte 1 y 2. In: 11th North American Masonry Conference, U.S.A. (2011).
10. Polyakov.: Masonry in framed buildings (Godsudarstvenoe Isdatel'stvo Literatury Po Stroidal stvui Architecture. Moscow, 1956). Traduced by G. L. Cairns, 1963. National Lending Library for Science and Technology, Boston (1956).
11. Holmes.: Steel frames with brickwork and concrete infilling. In: Proceedings of the Institution of Civil Engineers 19, 473-478 (1961).
12. Stafford-Smith, B.: Lateral stiffness of infilled frames. ASCE Journal of Structural Division 88(6), 183-199 (1962).
13. Stafford-Smith, B.: Behavior of square infilled frames. Journal of the Structural Division 92 (1), 381–403 (1966).
14. Stafford-Smith, B.: Methods for predicting the lateral stiffness and strength of multi-storey infilled frames. Building Sciense 2, 247-257 (1967).
15. Mainstone, R. J.: Supplementary note on the stiffness and strengths of infilled frames. Building Research Station, Garston, UK (1974).
16. Bazán, Z. T. E.: Muros de Mampostería ante Cargas Laterales, PhD Thesis, National Autonomous University of Mexico, México (1980).
17. Flanagan, R. D., R. M. Bennett.: In plane analysis of masonry infills material. Practice Periodical on Structural Design and Construction 6, 176-182 (2001).
18. Crisafulli, F. J.: Seismic Behavior of Reinforced Concrete Structures with Masonry Infills, PhD Thesis, University of Carterbury. New Zealand (1997).
19. Aguilar, G., Alcocer, S. M.: Efecto del refuerzo horizontal en el comportamiento de muros de mampostería confinada ante cargas laterals. Technical report, Centro Nacional de Prevención de Desastres, México (2001).
20. Pineda, C. J., Alcocer. S. M.: Comportamiento ante cargas laterales de muros de mampostería confinada reforzada con malla electrosoldada. Technical report, Centro Nacional de Prevención de Desastres, México (2004).

21. Zepeda J.A., Alcocer S. M.: Comportamiento ante cargas laterales de muros de ladrillo de arcilla perforado y multiperforado. Technical report, Centro Nacional de Prevención de Desastres, México (2001).
22. Cruz, A. I., Pérez-Gavilan,, J. J., Flores, C. L.: Experimental study of in-plane shear strength of confined concrete masonry walls with joint reinforcement. Engineering Structures 182, 213–226 (2019).
23. Rubio, P. L.: Contribución del refuerzo horizontal a la resistencia a corte de muros confinados de piezas de arcilla extruida. Master degree Thesis, National Autonomous University of Mexico, México (2018).
24. Leal-Graciano, J. M., Pérez-Gavilán, J. J., Reyes-Salazar, A., Valenzuela-Beltrán, F., Bojórquez, E., Bojórquez, J.: Experimental Study of Infill Walls with Joint Reinforcement Subjected to In-Plane Lateral Load. Buildings 12(3):259–259 (2022)

Using Vertical Seismic Isolation by Dividing the Building's Structure into Interactive Parts

Samira Yazdani[1], Mahmood Hosseini[2][0000-0003-3142-4087], Masoud Nekooei[3]

[1] PhD Candidate, Dep. of Civil Eng., Science and Research branch, Islamic Azad University, Tehran, Iran,
Samira.yazdani4@gmail.com
[2] Professor, Dept. of Civil Eng., Eastern Mediterranean University (EMU), Famagusta, North Cyprus,
mahmood.hosseini@emu.edu.tr
[3] Assistant Professor, Dep. of Civil Eng., Science and Research branch, Islamic Azad University, Tehran, Iran,
nekooei@srbiau.ac.ir

Abstract. Among different seismic design methods, the more recent ones are based on improving the energy dissipation potential of the system by using added energy absorbers. One way for increasing the energy dissipation capability of the energy absorbers in a building is dividing its skeleton into some dynamically interactive parts. This partitioning has been studied for 2D structures in past researches. In this paper, a new method is discussed by partitioning the 3D building's structure into four interactive substructures, two stiff and two soft. As the first stage of the study, presented in this paper, a one-story building was designed according to the conventional method, then the structure was divided into four parts with the same mass but different stiffness values, inter connected by linear viscous dampers with different damping coefficients at the roof level. To evaluate the seismic responses of the buildings a set of appropriate two-component records were selected and a series of nonlinear time history analysis (NLTHA) were conducted. The calculated responses include roof absolute acceleration, roof relative displacement, and base shears in both main horizontal directions. Furthermore, the plastic hinges (PHs) formed in the two structures were investigated. Comparison of responses, obtained by NLTHA, shows that partitioning of the skeleton, and using appropriate dampers, provide more desired responses, so that in the partitioned structure the drift values are, on average, 56% less than the single-part structure. Also, based on the formed PHs, the partitioned structure has been observed to have higher seismic performance level than the single-part structure.

Keywords: Linear viscous dampers; Stiff and soft substructures; Nonlinear time history analysis; Plastic hinges formation, seismic performance level.

1 Introduction

In the seismic design of structures based on ductility it is assumed that the structure would present a specified ductile behavior mode subjected to moderate and intensive earthquakes, and would not collapse. As such, ductility-based design is a well-known and acceptable method in most of the seismic design codes for buildings, however, according to some researchers, this method has some shortcomings. In fact, structural ductility, which is based on the concept of plastic behavior of structural materials, is associated with structural damage, and in case of major earthquakes the amount of damage can be so large that makes the building unusable, or even unrepairable after the earthquake. As a result, after a major seismic event, in a large city, particularly in the areas near the fault, we will face a lot of non-repairable structures, which, as stated by Hosseini and Alavi (2014), in addition to the homelessness of thousands of citizens for a long time, will lead to the problematic consequences of demolition, debris management, and finally requiring plenty of time and budget as well as enormous skillful human forces needed for the reconstruction of the new buildings to replace the demolished ones [1].

To overcome the shortcomings of the current ductility-based design methods, there is a need to propose new and practical ideas in the seismic design of structures. Therefore, by using a control approach, energy dissipation and reducing the earthquake input force in structures and maintaining the deformation within the elastic or repairable plastic range are important, so another approach to control or reduce the seismic response is to use new methods, including the use of energy absorbers and active or passive control devices are used in a variety of isolation methods, including base isolation, mass isolation, and vertical mass isolation.

Mass isolation of structures, discussed for the first time by Ziyaeifar (2000), which focuses on the mass of the structure as the main target for seismic isolation and reducing the effects of earthquakes on buildings. In this technique, the structural system usually consists of two subsystems (a mass subsystem and a stiffness subsystem) and energy dissipates between these subsystems. Ziyaeifar and Tavousi (2005), introduced a technique called vertical mass isolation, where the lateral stiffness of the system is not suddenly affected by the isolation. In building structures, a separation technique based on this idea requires that the horizontal component of mass be separated from the lateral stiffness of the structure [2,3]. In other words, in the vertical isolation method, the system is divided into two subsystems, the rigid subsystem that has almost the whole system stiffness and the mass subsystem that carries almost the whole mass of the system, but the minimum lateral stiffness is necessary to keep the mass subsystem stable.

Nekooei and Ziyaeifer (2008), studied the seismic behavior of mass isolated structures with a vertical isolation layer due to an earthquake [4]. The analytical model used for this investigation is a dual mass-spring model which is an extended form of the three element Maxwell model. In this study, the ability of mass isolation techniques in reducing earthquake effects on buildings has been shown with two parametric and numerical approaches. In the parametric approach, by definition an isolation factor for structure and determination the dynamic characteristics of the system, the relative

optimum value of the isolator damping coefficient was obtained. The results provide an insight on role of relative stiffness and mass ratio of the two subsystems. Finally, in the numerical approach, the spectral responses of these structures due to the earthquake have been investigated. The results show a noticeable decrease in earthquake input force to vertical mass isolated structures compared to non-isolated structures.

Increasing the flexibility and ability to absorb energy is one of the characteristics of a number of new methods of seismic design of structures. In these approaches the existence of large energy dissipaters in the system and the structural mechanism that supports the reaction forces of these devices make the current single degree of freedom model inaccurate in analytical investigations on the behavior of such systems. Therefore, a two degrees of freedom model has been proposed to study the behavior of these systems by Ziyaeifar et al., (2012). The model is an extension of the Maxwell three element type model in structural dynamics. Non-classical Eigen analyses on the model reveals the key role of energy-dissipating devices in the determination of main dynamic characteristics of such systems. A large number of dynamic time integration analyses subjected to earthquake motions were carried out on the model [5].

Hosseini and Bozorgzadeh (2013) studied the design of repairable regular steel multistory buildings, by using a 4-cell configuration structure with inclined columns around the central main vertical column of each cell at its base level. The inclined columns, with their bases shifted toward the central column, which cause the building to move basically in rocking mode, are equipped with Double-ADAS (DADAS) devices, and are connected to some strong girders at the first floor of the building. DADAS devices were considered in the inclined columns as well as between the cells along their height. The buildings were designed, once by conventional provisions, and once by using the suggested approach, and then were compared by nonlinear time history analysis using several 3-component accelerograms of selected earthquakes. Results showed that the suggested design approach leads to a more reliable seismic behavior of buildings [6].

Khalkhali et al. (2017), divided building's structure into four interactive rocking parts with a 4-cell configuration to create repairable regular midrise steel multistory buildings. To create more potential of energy dissipation, some dampers can be also used between each pair of the four cells. To show the efficiency of the proposed structural system, a set of 5- and 8-story buildings with similar plans were considered and a series of nonlinear time history analysis (NLTHA) were performed by using a set of 3-component scaled accelerograms of some selected earthquakes, including both far- and near-field events. Numerical results of NLTHA show that the proposed rocking structures can efficiently decrease the seismic damage in the building, so that plastic deformation happens basically in the energy dissipators, and the main structural elements remain elastic, and therefore, the buildings designed and constructed by the proposed technique can be easily repaired even after major earthquakes, and the building can basically keep the IO performance level [7].

Milanchian et al. (2017), investigated the vertical seismic isolation of a building into two substructures with different interaction behavior with viscous and viscoelastic dampers to reduce the seismic response. Response history analyses have been performed by Runge-Kota numerical method in several earthquakes. Damping matrix

in the vertical isolated structure by viscous or viscoelastic dampers is non-classical, and assumption of Rayleigh damping is no longer valid. Therefore, time history analysis by modal method cannot be used [8]. In the analytical model by Milanchian and Hosseini (2020), the original structure is partitioned by vertical planes three-dimensionally into two interactional inner and outer substructures. The results showed that by employing viscous and viscoelastic dampers, torsion in both substructures was properly controlled, although the role of the stiffness of the damper in torsion control was not significant. Also, the investigation of the non-uniform distribution of the damping characteristics, corresponding to the departure from the center of mass in the plan, showed that with the appropriate selection of the distribution parameter, the torsion of the vertical isolated structure has been reduced by about 10 to 15 percent, compared to the uniform distribution, especially for the soft substructure [9].

Taheri et al. (2018), investigated building's structure by dividing it into two inner and outer parts with different dynamic characteristics, and creating dynamic interaction between them by using yielding plate or hysteretic dampers. The results of NLTHA, by using a set of selected earthquakes accelerograms, showed that by using appropriate initial stiffness and yield strength, the inert-story drifts of both inner and outer structures can be significantly reduced. Also, the seismic responses of the two structures were compared, which show that the inter-story drift values of outer and inner substructures decrease on average by 20% and 65%, respectively, comparing to the original structure. This drift reduction leads to decrease of the damage indices of outer and inner substructures by almost 20% and 80%, respectively, comparing to the original structure, making it possible in most cases to have an easily repairable structure [10].

Nekooei and Rahgozar (2021), introduced a vertical seismic isolated rocking-core (VSI-RC) system, in which a controlled rocking-core is separated from the frame using viscous fuses. They presented an analytical solution for estimation of optimal damping constant of damper along with corresponding fundamental frequencies and damping ratio of VSI-RCs, and a parametric study was carried out to quantify non-classical dynamic characteristics. The results demonstrated that the formulas are applicable for rapid Eigen analysis, and proper seismic efficiency of VSI-RCs is observed compared to the non-isolated rocking-core systems [11].

In this paper, a new method of VSI in three-dimensional models have been discussed by partitioning the 3D building's structure into four substructures, two stiff and two soft, having dynamic interaction by viscous dampers. As the first stage of the study, presented in this paper, the one-story building has been considered. Details of the modeling and analyses are presented in the following sections.

2 Analytical 3D Models

2.1 Single-Part Structure

The primary moment frame structure (model M_1), is a single-part (non-partitioned) structure, which is supposed to be designed based on a conventional building code or standard. In this study structure M_1 is a one-story 3D regular frame with two bays in each direction, whose plan and some structural details are presented in Fig. 1, with the

stiffness value (K), indicated in the figure, which is the same for both horizontal main directions because of symmetry of the structure.

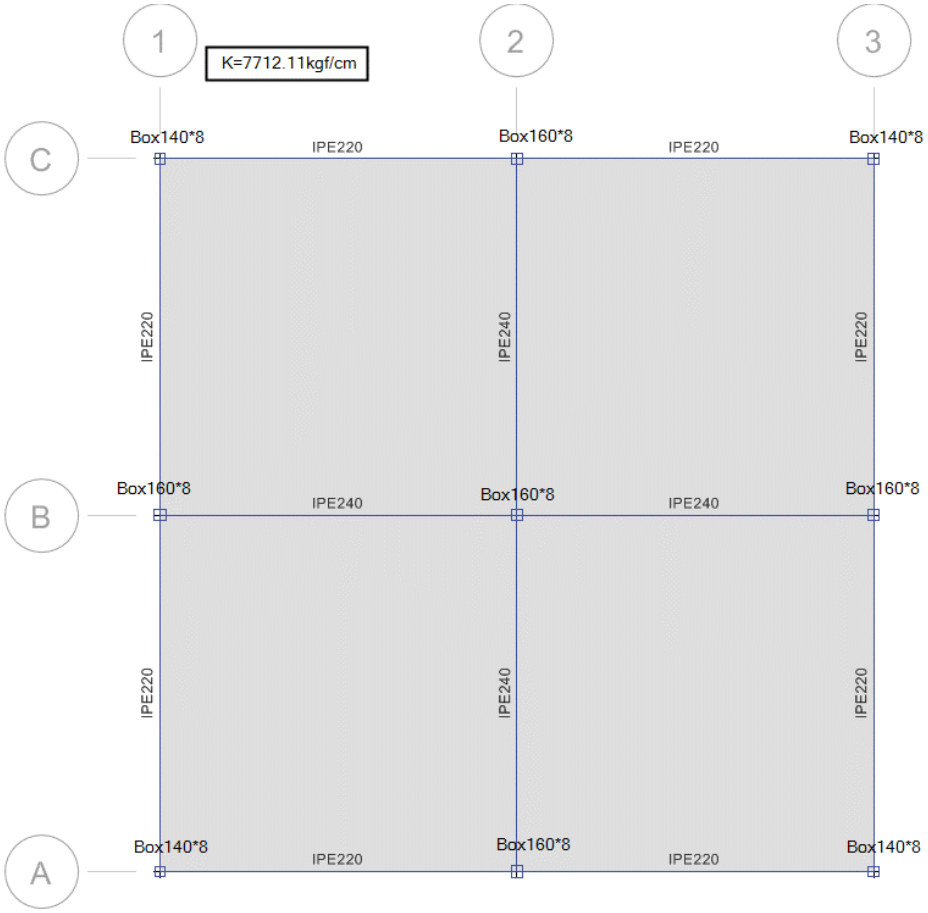

Fig. 1. The primary single-part structure (model M_1), with a mass of 53.11 kgf.s^2/cm.

2.2 Partitioned Structure

In the 3D vertical seismic isolation (VSI), the primary structure is partitioned by dividing the building's skeleton into dynamically interactive parts. This interaction can be created more effectively by dividing the structure into stiff and soft substructures. In this study, the structure is partitioned into four interactive parts, two stiff and two softs with the same area but different stiffness values, in a specific setting so that each stiff part has interaction, through dampers installed in appropriate locations, with two soft parts, and vice versa (model M_2). The linear viscous dampers with different damping coefficients have been considered to investigate the efficiency of this method. In addition, the lateral stiffness value of the single-part structure (model M_1) is equal to the total lateral stiffness values of the four parts of the partitioned structure (M_2).

Assuming K as the stiffness of M_1, the stiffness of each part of M_2 is shown in Fig. 2, which shows the plan and some structural details of the partitioned structure.

Fig. 2. The partitioned structure M_2, with a total mass of 53.77 kgfs^2/cm.

3 Seismic Response of the Structures

3.1 The Earthquake Records Selected for NLTHA

A set of appropriate two-component earthquake records with relatively low frequency content were selected as introduced in Table 1.

Table 1. Specifications of the selected earthquakes for NLTHA

Earthquake	San Fernando	Friuli	Mammoth Lake	Loma Prieta	Bigbear	Northridge	Parkfield
PGA	0.38g	0.26g	0.11g	0.07g	0.07g	0.07g	0.36g
Mag.	6.61	5.91	5.91	6.93	6.46	6.69	6.19
R_{jb}(km)	13.99	14.75	10.31	61.15	70.83	79.83	15.96

The spectral acceleration curves of the earthquake are shown in Fig. 3 with their real peak ground acceleration (PGA) values, however, for NLTHA all of them were scaled to a PGA value of 0.35g, which is the design base acceleration in a very high seismic hazard zone according to the Iranian code of practice (Standard 2800).

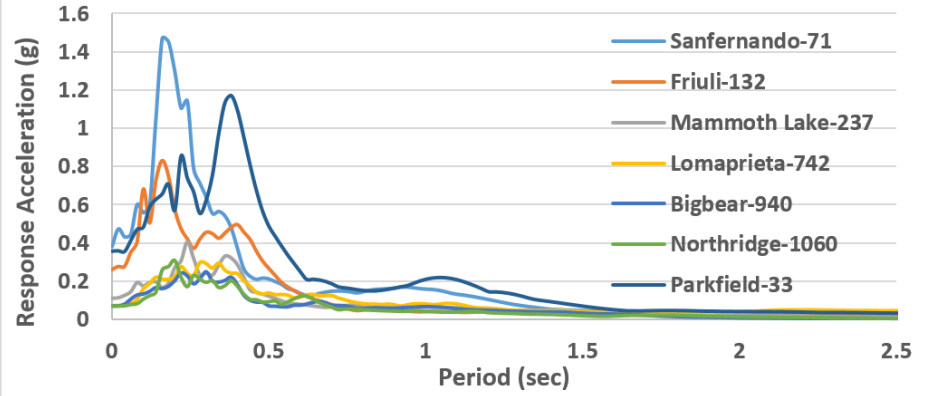

Fig. 3. Spectral accelerations of the selected earthquakes.

3.2 Maximum Drifts Values Obtained by NLTHA

Drift values of the single-part and partitioned buildings were obtained by NLTHA are presented in Table 2.

Table 2. Maximum drift values of single-part structure (M_1) and partitioned structure (M_2) with different values of damping coefficient, c, of the dampers used between the four parts of M_2

Earthquake Name	San Fernando	Parkfield	Friuli	Mammoth Lake	Loma Prieta	Bigbear	Northridge
			Max Drift of M_1 (%)				
	0.69	1.25	1.33	1.16	1.11	1.21	1.24
c (kgf.s/cm)			Max Drift of M_2 (%)				
0	0.87	0.71	0.71	0.82	1.45	1.13	1.30
10	0.63	0.62	0.46	0.43	0.58	0.58	0.77
20	0.51	0.6	0.43	0.38	0.46	0.45	0.61
30	0.47	0.61	0.43	0.41	0.46	0.50	0.52
40	0.46	0.67	0.42	0.46	0.49	0.55	0.46
50	0.47	0.71	0.45	0.51	0.53	0.59	0.42
60	0.47	0.76	0.48	0.56	0.58	0.63	0.39
70	0.48	0.79	0.52	0.60	0.62	0.66	0.38
80	0.49	0.82	0.56	0.63	0.66	0.69	0.34
90	0.50	0.85	0.60	0.66	0.69	0.72	0.36

Table 3 presents the reduction percentage of maximum drift values of M2 building with respect to that of M1 building for various values of c.

Table 3. Reduction of maximum drift value in M_2 building with respect to M_1 building

Earthquake Name	San Fernando	Parkfield	Friuli	Mammoth Lake	Loma Prieta	Bigbear	Northridge	Ave.
c (kgf.s/cm)	[1-(M_2/M_1)] (%)							
10	9	50	65	62	47	52	38	46
20	26	52	67	67	58	62	50	55
30	32	51	68	64	58	58	58	56
40	33	46	68	60	55	54	63	54
50	32	42	66	55	51	51	66	52
60	31	39	64	51	48	48	68	50
70	31	36	61	48	44	45	69	48
80	29	34	58	45	40	43	72	46
90	28	31	55	43	37	40	70	43

According to Table 3, in the partitioned structure the drift values are, on average, 56% less than the single-part structure by using the optimal value of c which was found to be 30 kgf.s/cm.

3.3 Maximum Base Shear Force Values Obtained by NLTHA

Tables 4 and 5 compare the maximum values of base shear for single-part and partitioned structures with optimal c value in X and Y directions respectively.

Table 4. Comparison of maximum values of base shear forces (kgf) in X-direction.

Type of Structure	Earthquake Name						
	San Fernando	Parkfield	Friuli	Mammoth Lake	Loma Prieta	Bigbear	Northridge
M_1	21941	28976	17488	27667	25598	27779	29021
M_2	8398	11325	7819	7971	8833	9964	7731
1-(M_2/M_1) (%)	62	61	55	71	65	64	73

Table 5. Comparison of maximum values of base shear forces (kgf) in Y-direction.

Type of Structure	Earthquake Name						
	San Fernando	Parkfield	Friuli	Mammoth Lake	Loma Prieta	Bigbear	Northridge
M_1	21005	14976	30259	15172	26289	23462	13493
M_2	9561	9513	7107	6774	7612	6731	7519
1-(M_2/M_1) (%)	54	36	77	55	71	71	44

It can be seen in Tables 4 and 5 that the maximum values of base shear in partitioned structure with optimal c is significantly less than single-part structure, with and average ratio of 64% in X-direction and 58% in Y-direction.

3.4 Maximum Absolute Acceleration Values Obtained by NLTHA

Table 6 presents the maximum values of absolute acceleration of single-part structure, as well as stiff and soft substructures of partitioned structure with the optimal c value.

Table 6. Comparison of maximum values of absolute acceleration (m/s^2) in M_1 and M_2 models

Type of the building's structures	Earthquake Name						
	San Fernando	Parkfield	Friuli	Mammoth Lake	Loma Prieta	Bigbear	Northridge
	X-direction						
M_1	4.14	5.45	3.29	5.21	4.82	5.24	5.46
M_2 stiff substruc. & ratio to M_1	2.35 0.56	2.79 0.51	1.95 0.59	2.19 0.42	2.28 0.47	2.40 0.45	1.80 0.33
M_2 soft substruc. & ratio to M_1	1.21 0.29	2.08 0.38	1.41 0.42	1.43 0.27	1.52 0.31	1.70 0.32	1.40 0.25
	Y-direction						
M_1	3.97	2.82	5.69	2.85	4.95	4.41	2.50
M_2 stiff substruc. & ratio to M_1	2.74 0.69	2.44 0.86	2.00 0.35	1.76 0.61	1.76 0.35	1.73 0.39	1.48 0.59
M_2 soft substruc. & ratio to M_1	1.30 0.32	1.52 0.54	1.27 0.22	1.15 0.4	1.41 0.28	1.12 0.25	1.40 0.56

Table 6 shows that, by using the optimal c value of 30 kgf.s/cm, the maximum absolute acceleration in both stiff and soft parts of M_2 structure decreases remarkably, comparing to M_1 structure with average ratios of 52% and 68% respectively in X-direction and 45% and 63% respectively in Y-direction.

3.5 Performance Levels of the Formed Plastic Hinges (PHs)

By using the optimal c value of 30 kgf.s/cm in the M_2 structure the performance level of the formed PHs is mostly IO (with a few cases of LS), while in the M_1 structure PHs are in CP performance level. PH results cannot be shown here due to the lack of space, however they are available in the main report of the study by Yazdani (2023), [12].

4 Conclusions

Based on the results of the conducted NLTHA on single-part and partitioned structures the following conclusions can be made:

- For each structure an optimal damping coefficient can be obtained for dampers of the partitioned structure. In this study the obtained optimal value was 30 kgf.s/cm.
- In the partitioned structure with optimal damping, the maximum values of drift, base shear force, and absolute acceleration in both stiff and soft substructures decreased, on average, to 56%, 58%, 45% and 63% of the single-part structure respectively.

- The plastic hinges (PHs) formed in the single-part structure were in the CP performance level, while in the partitioned structure they were in IO to LS level.
- Based on the above facts, it can be said that partitioning the building's skeleton into stiff and soft interactive substructures can be used as an effective technique for seismic response reduction of building's systems and achieving the goal of creating repairable building structures.

It should be noted that the results presented in this paper are related to only a single-story buildings. For expressing more general conclusions, the results of multi-story buildings should be used. Work on these results is now on progress, and would be hopefully presented in a future paper of the authors.

References

1. Hosseini, M., Alavi, S.: A kind of repairable steel buildings for seismic regions based on building's rocking motion and energy dissipation at base level. International Journal of Civil and Structural Engineering 1(3), 157–163 (2014).
2. Ziyaeifar, M.: Method of Mass Isolation in Seismic Design of Structures. In Proceeding of the 12WCEE, Auckland, New Zealand (2000).
3. Ziyaeifar, M., Tavousi, Sh.: Mass participation in non-classical mass isolated systems. Asian Journal of Civil Engineering 6(4), 273-301 (2005).
4. Nekooei, M., Ziyaeifar, M.: Spectral investigation on the seismic behaviour of vertical mass isolated structures against earthquake. In Proceeding of the 14WCEE, Beijing, (2008).
5. Ziyaeifar, M., Gidfar, S., Nekooei, M.: A model for mass isolation study in seismic design of structures. Structural Control and Health Monitoring 19(6), 627-645 (2012).
6. Hosseini, M., Bozorgzadeh, S.: An Innovative Design for Repairable Regular Steel Buildings by Using a 4-Cell Configuration Structure with Some Inclined Columns at Base Level, Equipped with Double-ADAS Devices, and Security Cables at Corners. Proceedings of EASEC-13, Sapporo University, Japan, (2013).
7. Khalkhali, S.M.H., Hosseini, M., Aziminejad, A.: Dividing Building's Structure into 4 Interactive Rocking Parts to Make It Repairable after Major Earthquakes. In Proceedings of the 16WCEE, Santiago, Chile, (2017).
8. Milanchian, R., Hosseini, M., Nekooei, M.: Vertical isolation of a structure based on different states of seismic performance. J. of Earthq. and Struc., 13(2), 103-118 (2017).
9. Milanchian, R., Hosseini, M.: Torsional response reduction of plan-asymmetric vertical seismic isolation by appropriate distribution of viscous and viscoelastic dampers. Journal of Structures (27), 962-974 (2020).
10. Taheri, A., Hosseini, M., Moghadam, A.S.: Creation of innovative earthquake resistant steel buildings by dividing the structure into inner and outer parts having interaction by hysteretic dampers. Journal of Vibroengineering 20(1), (2018).
11. Nekooei, M., Rahgozar, N.: Vertical seismic isolated rocking-core system. Proceedings of the Institution of Civil Engineers-Structures and Buildings 174(8), 627-636 (2021).
12. Yazdani, S: Introducing the new method of four-part vertical isolation to improve the seismic behavior of low to medium-rise steel buildings. PhD dissertation on Structural Eng., Science and Research Branch of the Islamic Azad University, Tehran, Iran, (2023).

Comparison of the Seismic Behavior of RC Frame with Wide Beam and Deep Beam Non-linear Time History

Mahmoud Eissa[1][0000-0001-5734-5411] and Murude Celikag[2][0000-0002-2751-5528]

[1] Eastern Mediterranean University, Civil Engineering Department, North Cyprus, Türkiye, mahmoud6cyprus@gmail.com
[2] Eastern Mediterranean University, Civil Engineering Department, North Cyprus, Türkiye, murude.celikag@emu.edu.tr

Abstract. A reinforced concrete frame with wide beams and a one-way slab is a structural system in which the slab is built with joists that transfer the load to shallow beams. These beams are long and narrow in comparison to their height and depth. If the whole depth of the beam is embedded into the thickness of the slab, then we have a so-called thick plate, plate which stands directly on top of the column. Experimental and analytical evidence suggests that wide beam may have disadvantages in comparison to deep beam, including inadequate stress transfer between connections, reduced lateral stiffness, and inferior energy dissipation in beams. However, recent scholarly research indicates that design elements in modern earthquake codes may directly or indirectly mitigate such shortcomings. Experimental and analytical investigations concentrating on regional structural behavior constitute majority of the wide beam literature. Still, there is lack of systematic studies addressing global performances of wide beam against equivalent deep beam. Herein, a comparison of seismic performance of both structural types is carried out by non-linear time history analysis with 51 different ground motions. The results are assessed in terms of natural period, story shear, base shear, story displacement, roof displacement, and inter-story drift for both cases, which prove that deep beam behaved better than wide beam in terms of seismic performance.

Keywords: Wide Beam; Deep Beam; NTHA; Seismic Performance

1 Introduction

Wide beam-column joints in buildings and composite structural systems have gained significant popularity as load-resisting frames in regions with low seismicity (1-3). Initially, the potential advantages and applications of wide beam systems in lateral load-resisting structures were overlooked due to a lack of understanding regarding their seismic performance. Consequently, certain design guidelines strictly limited the use of wide beam-column joints for earthquake resistance. To address this knowledge gap, extensive testing was conducted in both laboratory and field settings to investigate the moment resisting capacity and energy dissipation capabilities of wide beam-column joints subjected to cyclic horizontal loading. The scientific research conducted on these

joints revealed valuable insights into their structural behavior. Consequently, structural engineers now employ reinforced concrete moment resisting frames (RCMRF) with wide beams (WBF) in regions characterized by low seismic activity (4). This growing body of research has provided a deeper understanding of the seismic performance of wide beam-column joints, allowing for their safe and effective utilization in non-seismicity regions. By incorporating wide beams into the design of load-resisting structures, engineers can capitalize on the benefits offered by these systems, thereby enhancing the overall structural integrity and resilience of buildings.

In regions characterized by moderate seismicity, such as the Mediterranean area encompassing Spain, Italy, and Portugal, reinforced concrete moment resisting frames (RCMRF) with wide beam-column connections featuring one-way joists have been widely adopted (5). However, recent developments in seismic design have led to the increased utilization of RCMRF with two-way joists instead of one-way joists. Furthermore, in high seismicity areas, engineers often opt for a dual system approach to enhance structural performance. When designing buildings for regions with medium to high seismicity, the use of wide beams is deemed appropriate, provided that the necessary design checks have been conducted to address specific concerns. For exterior connections, careful consideration should be given to torsional cracking, while for interior connections where bar debonding may occur, additional assessments are required. These assessments encompass P-Delta stability, concrete crushing capacity, and serviceability deflections (5). By incorporating wide beams into the structural design, engineers can effectively mitigate the effects of seismic activity in regions prone to earthquakes. The utilization of two-way joists and the consideration of a dual system further contribute to the overall seismic resilience of buildings. Through meticulous design checks and comprehensive evaluations, the structural integrity and performance of RCMRF with wide beam-column connections can be optimized to withstand seismic forces, ensuring the safety and durability of the constructed environment (5).

Extensive experimental and analytical research has indicated that Wide Beam-Column Joints (WBF) may exhibit certain drawbacks in comparison to Dual Beam-Column Joints (DBF). These drawbacks include deficient stress transfer within connections, lower lateral stiffness, and poorer energy dissipation in beams. However, recent studies in the literature (6) have provided evidence that modern seismic design provisions, either directly or indirectly, can effectively address and overcome these deficiencies. The existing body of literature on WBF primarily consists of experimental and analytical investigations focusing on the local structural behavior (7-9). However, there is a noticeable absence of systematic studies that comprehensively address the global performance of WBF relative to equivalent DBF, while meeting the requirements of different design standards.

In this study, we aim to bridge this research gap by conducting a comparative seismic assessment of both structural types, employing non-linear time history analyses and utilizing 51 distinct earthquake records. The primary objective is to investigate whether the comprehensive framework of modern performance-based codes can effectively balance the behavior of WBF and DBF. By subjecting both structural configurations to rigorous analysis, considering various real earthquake scenarios, we seek to provide valuable insights into the seismic performance of WBF and its equivalence to DBF in terms of meeting performance objectives as stipulated by contemporary design standards. This research endeavors to contribute to the advancement of knowledge in the field, informing structural engineers and practitioners

about the viability and effectiveness of WBF within the context of modern performance-based seismic design codes.

2 Methodology

2.1 Case Study

The present study focuses on a case study involving a building configuration consisting of three and five stories, as depicted in Figure 1 where all dimensions in cm. To evaluate the seismic performance of reinforced concrete (RC) moment resisting frames with different slab types, the typical floor configuration of the selected building is shown in Figure 2. Each building, designed as a three-dimensional structure using ETABS 16, has been subjected to gravity load and lateral load analysis employing the equivalent static method. The design process adheres to the requirements specified in EN4 and ASCE/SEI 7-16 (10). Considered as a residential building, the structure is designed to withstand an additional dead load of 1.2 kN/m² and an imposed load of 3 kN/m². Seismic parameters utilized in this investigation are obtained from (11). Detailed information regarding the cross-section and reinforcement of the structural members is provided in Table 1.

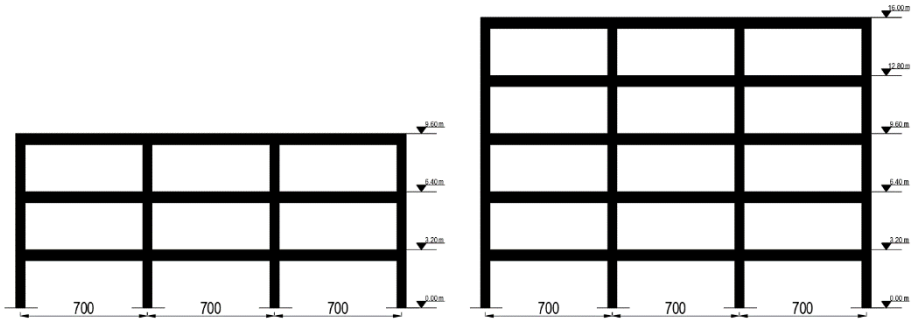

Fig. 1. Case study buildings elevation.

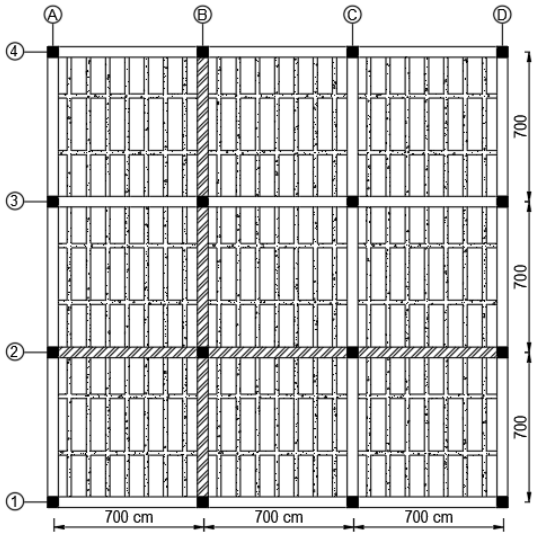

Fig. 2. Top view of the selected case study building with different slab type.

Table 1. Cross-section dimension and rebar area for all analyzed frames.

Slab type	Thickness (cm)	Beams (cm)	Columns (cm)	Column rebar	Beam rebar B	Beam rebar T
JOIST D	28	25/50	50/50	8Ø20	5Ø20	6Ø20
JOIST W2	28	50/28	50/50	8Ø20	4Ø20	6Ø20
JOIST WB	28	50/28	50/50	8Ø20	3Ø20	4Ø20

Table 2. Selected ground motions with their properties.

Result ID	RSN	MSE	Scale Factor	Tp (s)	Event	Year	Mag	Rjb (km)	Vs30 (m/s)
					NF NP				
1	130	0.6	10.5	-	Friuli, Italy-02	1976	5.9	11.0	310.7
2	187	0.1	5.6	-	Imperial Valley-06	1979	6.5	12.7	348.7
3	236	0.5	5.7	-	Mammoth Lakes-03	1980	5.9	2.7	382.1
4	313	0.4	4.5	-	Corinth, Greece	1981	6.6	10.3	361.4
5	320	0.8	9.4	-	Mammoth Lakes-10	1983	5.3	6.5	382.1
6	391	0.6	10.0	-	Coalinga-03	1983	5.4	12.9	352.2
7	445	0.3	13.3	-	New Zealand-01	1984	5.5	3.8	356.4
8	457	0.5	7.6	-	Morgan Hill	1984	6.2	13.0	349.9
9	517	0.6	3.7	-	N. Palm Springs	1986	6.1	1.0	359.0
10	547	0.5	5.7	-	Chalfant Valley-01	1986	5.8	6.1	316.2
11	564	0.3	4.0	-	Kalamata, Greece-01	1986	6.2	6.5	382.2
12	613	0.7	12.6	-	Whittier Narrows-01	1987	6.0	9.5	324.8
13	725	0.4	3.2	-	Superstition Hills-02	1987	6.5	11.2	316.6
14	821	0.3	1.8	-	Erzican, Turkey	1992	6.7	0.0	352.1
15	864	0.3	3.7	-	Landers	1992	7.3	11.0	379.3
16	953	0.4	2.2	-	Northridge-01	1994	6.7	9.4	355.8
17	1615	0.1	8.7	-	Duzce, Turkey	1999	7.1	9.1	338.0
18	2628	0.4	4.5	-	Chi-Chi, Taiwan-03	1999	6.2	0.0	443.0
19	4130	0.3	4.0	-	Parkfield-02, CA	2004	6.0	1.6	381.3
20	4337	0.8	5.7	-	Umbria Marche (foreshock), Italy	1997	5.7	0.6	317.0
21	4349	0.6	7.3	-	Umbria Marche, Italy	1997	6.0	0.8	317.0
22	4457	0.2	4.6	-	Montenegro, Yugoslavia	1979	7.1	1.5	410.4
23	8157	0.7	1.3	-	Christchurch, New Zealand	2011	6.2	0.0	422.0
					NF P				
1	148	0.6	5.4	1.2	Coyote Lake	1979	5.7	6.8	349.9
2	292	0.1	2.9	3.3	Irpinia, Italy-01	1980	6.9	6.8	382.0
3	566	1.2	13.0	0.8	Kalamata, Greece-02	1986	5.4	4.0	382.2
4	723	0.3	1.3	2.4	Superstition Hills-02	1987	6.5	1.0	348.7
5	802	0.2	2.5	4.6	Loma Prieta	1989	6.9	7.6	380.9
6	828	0.3	2.3	3.0	Cape Mendocino	1992	7.0	0.0	422.2
7	1004	0.6	1.8	0.9	Northridge-01	1994	6.7	0.0	380.1
8	1119	0.3	1.5	1.8	Kobe, Japan	1995	6.9	0.0	312.0
9	4065	0.4	4.7	1.2	Parkfield-02, CA	2004	6.0	1.4	383.9
10	4458	0.2	3.0	2.0	Montenegro, Yugoslavia	1979	7.1	4.0	318.7
11	4847	0.1	2.3	1.4	Chuetsu-oki, Japan	2007	6.8	9.4	383.4
12	6911	0.1	1.3	9.9	Darfield, New Zealand	2010	7.0	7.3	326.0
					FF				
1	103	1.3	12.5	-	Northern Calif-07	1975	5.2	28.5	368.7
2	138	0.1	6.6	-	Tabas, Iran	1978	7.4	24.1	324.6
3	154	0.5	13.1	-	Coyote Lake	1979	5.7	19.5	335.5
4	214	0.3	6.5	-	Livermore-01	1980	5.8	15.2	377.5
5	290	1.1	13.7	-	Irpinia, Italy-01	1980	6.9	29.8	428.6
6	310	1.0	14.8	-	Taiwan SMART1(5)	1981	5.9	24.7	327.6
7	339	0.4	5.5	-	Coalinga-01	1983	6.4	28.0	307.6
8	534	1.4	11.6	-	N. Palm Springs	1986	6.1	23.0	447.2
9	544	0.4	9.8	-	Chalfant Valley-01	1986	5.8	23.4	303.5
10	562	0.8	9.8	-	Chalfant Valley-04	1986	5.4	24.0	303.5
11	626	1.1	7.5	-	Whittier Narrows-01	1987	6.0	18.2	301.0
12	730	0.1	4.6	-	Spitak, Armenia	1988	6.8	24.0	343.5
13	770	0.8	6.4	-	Loma Prieta	1989	6.9	22.4	333.9
14	850	0.2	5.7	-	Landers	1992	7.3	21.8	359.0
15	991	0.7	7.0	-	Northridge-01	1994	6.7	29.0	366.7
16	1107	0.4	4.3	-	Kobe, Japan	1995	6.9	22.5	312.0

2.2 Record Selection and Scaling Method

In this study, a total of 51 real ground motion data samples were carefully chosen from the PEER website. These samples were then categorized into three distinct groups based on their characteristics: NFNP (near fault non-pulse), NFP (near fault pulse-like),

and FF (far fault). The selection of the ground motion data was primarily based on two parameters: magnitude and soil type, as indicated in Table 2. To ensure consistency and comparability, the MSE scaling method was employed to scale the selected ground motions. The main objective of this scaling process was to attain an average spectrum for the resulting scaled earthquake records that closely aligns with the target spectrum within the desired period of interest.

2.3 Modeling Technology and Material Used

The The present study adopts a rigorous fiber section approach, incorporating fully distributed plasticity element models in conjunction with non-linear beam-column elements. The Gauss-Lobatto integration method, coupled with Geo-transfer of P-delta for columns, is employed, while the beams are modeled linearly. Careful consideration is given to the selection of fiber-section locations and integration weights to ensure the utilization of optimal integration algorithms. The computational platform used for this purpose is OpenSees, which enables the precise specification of the fiber section's location within the plastic hinge length (12).

It should be emphasized that the fiber-section elements primarily account for flexural deformations by integrating moment-curvature relationships along the length of the member. Consequently, the inclusion of bar-slip and shear flexibilities becomes imperative for fiber-section frame elements (12). In order to incorporate the effects of the slab, a distributed mass extending from the floor to the adjusted beams is taken into consideration.

Moreover, the efficacy of the aforementioned modeling approach has been validated by (13), and it has been recommended by (14) based on a comparative analysis conducted among various non-linear modeling techniques. However, in order to account for shear deformation effects and bar-slip, these elements have been added to the model as zero-length elements.

.

3 Result and Discussion

3.1 Story Shear

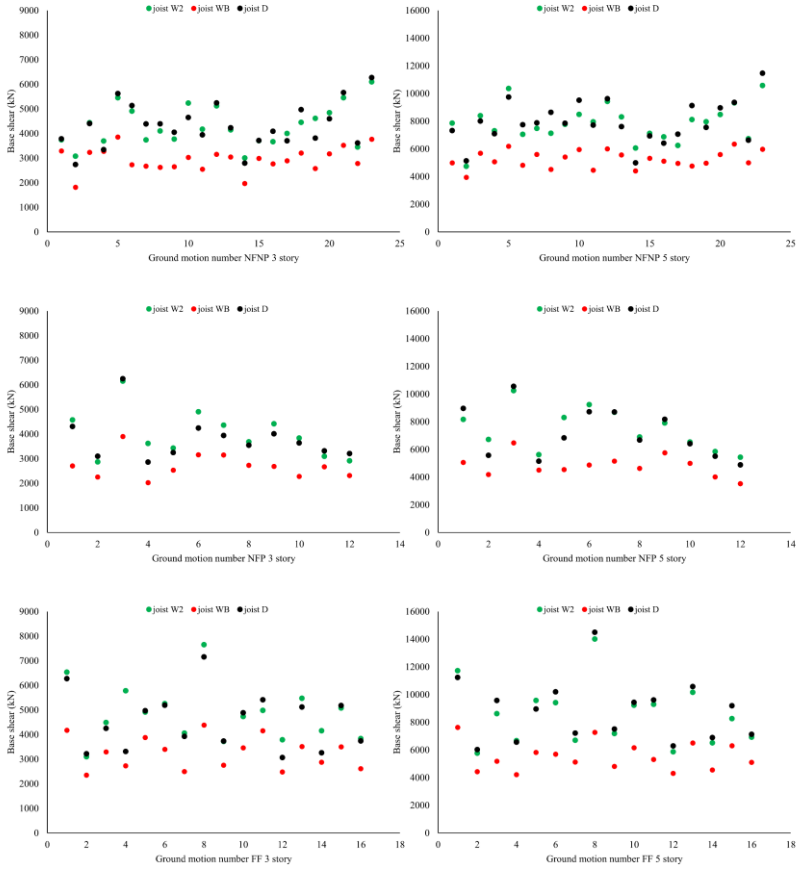

Fig. 3. Base shear data distribution for both three and five story buildings.

The distribution of base shear data for the analyzed building frames, comprising joist floors with deep and wide beams, is illustrated in Figure 3. The data considers two different axes, namely 2 and B, along with varying numbers of stories. Observing the figure, it becomes apparent that the joist floor with a flexible axis B exhibits a lower transfer of mass to axes B, while a greater transfer of mass occurs to axes 2. This can be attributed to the one-way slab nature of the joist floor. Furthermore, in comparison to the other two cases and across all building heights, the configuration featuring a wide beam displayed a lower base shear. In addition, the difference in base shear between Joist D and Joist W2 was found to be minimal when compared to Joist B and the other cases. This observation provides substantial evidence supporting the proposition that

the base shear value primarily depends on the building's mass rather than its stiffness. Notably, Joist D and Joist W2 possess identical mass but differ in stiffness.

3.2 Story Displacement

The diagram depicted in Figure 4 illustrates the roof displacement for all analyzed cases across varying building heights. The presented data unambiguously indicates that the Joist D configuration consistently exhibits significantly lower roof displacement when compared to the other frame variations, irrespective of the building height. In both the Non-Flexural Performance (NFP) and Non-Flexural Non-Performance (NFNP) records group, Joist D outperforms the other two cases, while in the Flexural-Flexural (FF) record case, Joist D and Joist W2 demonstrate similar levels of roof displacement. Moreover, it is worth noting that in the case of five-story buildings, the disparity in roof displacement becomes more pronounced among the analyzed frames. This observation highlights the dependence of building roof displacement on the stiffness characteristics of the structure. Therefore, it can be concluded that building roof displacement is a parameter that relies on the stiffness properties of the structure.

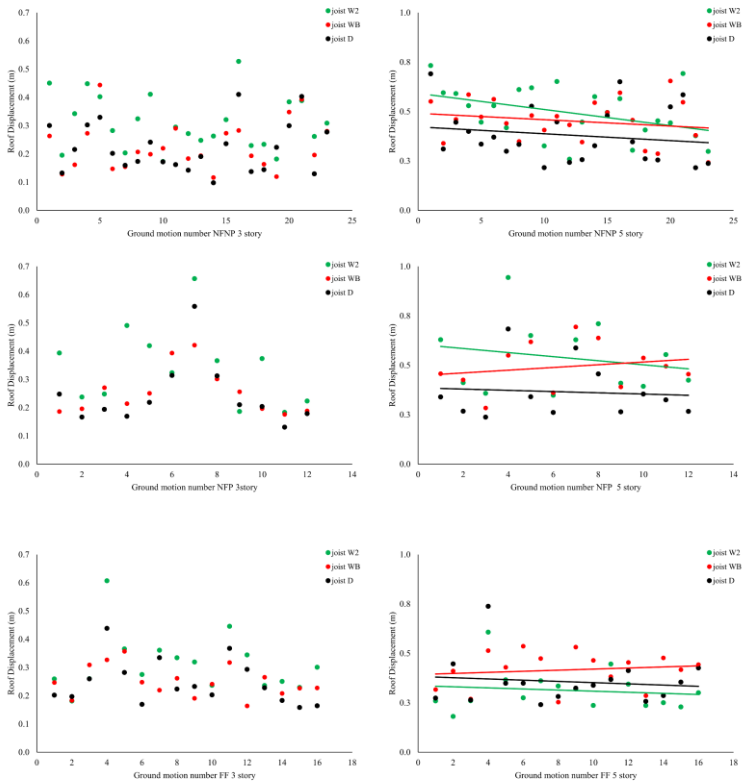

Fig. 4. Roof displacement data distribution for three and five story buildings.

3.3 Max Inter-Story Drift Ratio

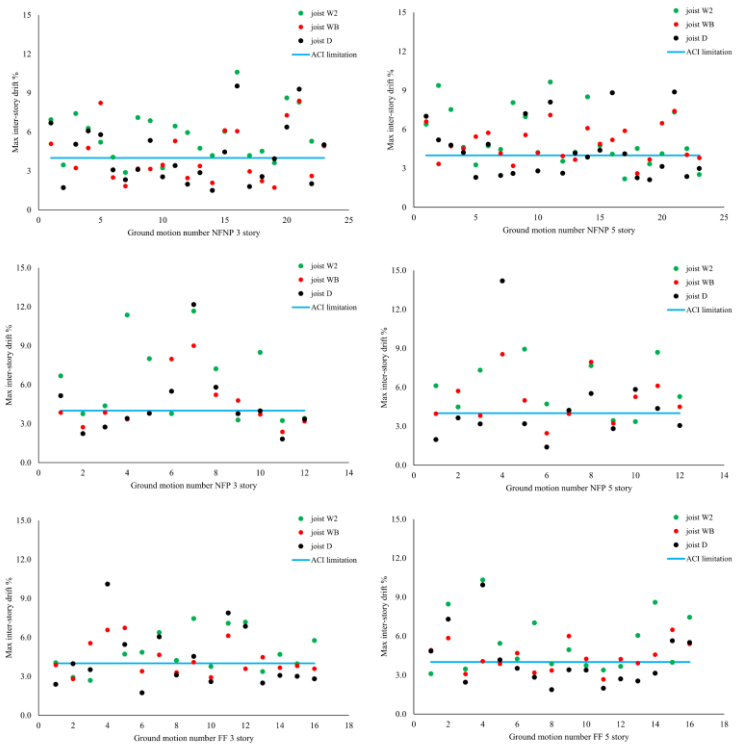

Fig. 5. Max inter-story drift ratio for all analyzed frames.

Inter-story drift plays a pivotal role in determining the seismic performance of a structure. It is considered one of the primary parameters assessed by national standards to evaluate buildings. Figure 5 presents the maximum inter-story drift of all analyzed cases in comparison to the limitations set by the American Concrete Institute (ACI). Remarkably, Joist D consistently outperforms the other two cases in terms of inter-story drift. This finding clearly demonstrates that the wide beam configuration possesses inherent limitations when it comes to inter-story drift. Additionally, the reduced stiffness associated with wide beams contributes to an overall decrease in the performance of the structural frame. It should be noted that a slight decrease in inter-story drift can be observed by reducing the mass of wide beam frames, as evidenced by the difference between Joist W2 and Joist WB.

4 Conclusion

The seismic behavior of RC frame with joist floor and deep and wide beam has been evaluated through a vary detailed non-linear time history analysis using 51 different real earthquake records the following are the conclusion

- The configuration with wide beams consistently displayed lower base shear across all building heights, indicating its potential advantage in reducing the base shear response.
- Joist D configuration consistently demonstrated significantly lower roof displacement compared to the other frame variations, regardless of building height. This superior performance was observed in both (NFP) and (NFNP) records, while the Joist D and Joist W2 cases exhibited similar roof displacement in the (FF) record.
- Moreover, the assessment of inter-story drift in Figure 5 revealed that Joist D consistently outperformed the other cases, indicating its superior performance in mitigating inter-story drift. The wide beam configuration was found to have inherent limitations in inter-story drift, attributed to its reduced stiffness.

Overall, these findings highlight the importance of considering mass-stiffness relationships in understanding and evaluating the seismic performance of building structures. Further research in this area could enhance our understanding of structural behavior and aid in the design of more resilient and efficient buildings.

References

1. Benavent-Climent A. Seismic behavior of RC wide beam-column connections under dynamic loading. Journal of earthquake engineering. 2007;11(4):493-511.
2. Benavent-Climent A, Cahís X, Vico J. Interior wide beam-column connections in existing RC frames subjected to lateral earthquake loading. Bulletin of Earthquake Engineering. 2010;8(2):401-20.
3. Benavent-Climent A, Donaire-Ávila J. Moment transfer and influence of transverse beams in interior waffle flat plate–column connections under lateral loading. Engineering Structures. 2013;49:146-55.
4. Toader N, Kiss Z. The seismic performance of reinforced concrete frame structures using wide beams. Acta Technica Napocensis: Civil Engineering and Architecture. 2013;56(1):90-9.
5. Stehle JS, Abdouka K, Goldsworthy H, Mendis P, editors. The seismic performance of reinforced concrete wide band beam construction. Twelfth World Conference on Earthquake Engineering; 2000.
6. Gómez-Martínez F, Alonso-Durá A, De Luca F, Verderame GM. Ductility of wide-beam RC frames as lateral resisting system. Bulletin of Earthquake Engineering. 2016;14:1545-69.
7. Li B, Kulkarni SA. Seismic behavior of reinforced concrete exterior wide beam-column joints. Journal of structural engineering. 2010;136(1):26-36.
8. Masi A, Santarsiero G, Nigro D. Cyclic tests on external RC beam-column joints: role of seismic design level and axial load value on the ultimate capacity. Journal of Earthquake Engineering. 2013;17(1):110-36.
9. Siah W, Stehle J, Mendis P, Goldsworthy H. Interior wide beam connections subjected to lateral earthquake loading. Engineering structures. 2003;25(3):281-91.
10. Engineers ASoC, editor Minimum design loads and associated criteria for buildings and other structures2017: American Society of Civil Engineers.

11. Kitayama S, Constantinou MC. Seismic performance of buildings with viscous damping systems designed by the procedures of ASCE/SEI 7-16. Journal of Structural Engineering. 2018;144(6):04018050.
12. ATC, editor Guidelines for Nonlinear Structural Analysis for Design of Buildings. Part IIb–Reinforced Concrete Moment Frames (NIST GCR 17-917-46v3)2017: ATC Redwood City, CA, USA.
13. Oinam RM, Sahoo DR. Numerical evaluation of seismic response of soft-story RC frames retrofitted with passive devices. Bulletin of earthquake engineering. 2018;16(2):983-1006.
14. Huang X, Kwon OS. Numerical models of RC elements and their impacts on seismic performance assessment. Earthquake Engineering & Structural Dynamics. 2015;44(2):283-98.

A Nonlinear Study of The Influence of Strong Earthquake Ground Motion from The February 2023 Turkey Sequence (M = 7,8)

Filip Pachla[1][0000-0003-1751-2339], Tadeusz Tatara[2][0000-0002-4071-2358], Waseem Aldabbik[3][0000-0002-7705-9399]

[1] Faculty of Civil Engineering, Cracow University of Technology, ul. Warszawska 24, Kraków, Poland
filip.pachla@pk.edu.pl
[2] Faculty of Civil Engineering, Cracow University of Technology, ul. Warszawska 24, Kraków, Poland
tadeusz.tatara@pk.edu.pl
[3] Faculty of Civil Engineering, Cracow University of Technology, ul. Warszawska 24, Kraków, Poland
waseem.aldabbik@doktorant.pk.edu.pl

Abstract. On Monday, February 6, 2023, the largest natural disaster in the history of Turkey and Syria took place, because an earthquake with a magnitude of 7.8 occurred in the morning at 4:17 local time near Gaziantep. Many people were buried under the rubble of buildings. During the next hours and days, this area was hit by a series of over 100 powerful aftershocks (the most intensive quake of 7.7-magnitude occurred several dozen kilometres to the north). Unfortunately, the scale of the damage is huge and more aftershocks threaten. The total death toll from the earthquake in Turkey and Syria now stands at 50,000. According to data from mid-February 2023 more than 25,000 buildings have been destroyed in Turkey and the state of 170 thousand must be examined. Two phenomena of similar intensity, but registered at seismic stations located on two site classifications (A and B) according to EC-8, were selected for detailed analyses. The most precise way to estimate the dynamic response of irregular structures subjected to earthquakes is to create a 3D model and conduct a nonlinear response time history analysis. The building was measured to find its dynamic properties using different ways of excitation. The model was influenced by two chosen far-field representative events originating from strong ground motion caused by the last earthquake in Turkey. The results of the analysis indicated locations of structural damages and permit assessing the dynamic resistance of the structure.

Keywords: Earthquakes, RC irregular structures, Nonlinear analysis, Time history analysis.

1 Introduction

On Monday, February 6, 2023, the largest natural disaster in the history of Turkey and Syria took place, because an earthquake with a magnitude of 7.8 occurred in the morning at 4:17 local time near Gaziantep. Many people were buried under the rubble of buildings. During the next hours and days, this area was hit by a series of over 100 powerful aftershocks (the most intensive quake of 7.7-magnitude occurred several dozen kilometres to the north). Unfortunately, the scale of the damage is huge and more aftershocks threaten. The total death toll from the earthquake in Turkey and Syria now stands at 50,000. According to data from mid-February 2023 more than 25,000 buildings have been destroyed in Turkey and the state of 170 thousand must be examined.

Despite massive damage in over 130,000 buildings completed by the Turkish Housing Development Administration (TOKI), built in the earthquake zone in 10 provinces centred in Kahramanmaras did not suffer any structural damage. TOKI buildings were not damaged thanks to its earthquake-resistant structures applied in buildings such as "raft foundation", "tunnel formwork carrier system" and "high concrete strength". TOKI has performed project design studies by all applicable laws and regulations, especially the Earthquake Regulation. There have been many strong earthquakes throughout history, and some of the most devastating ones include the 2004 Indian Ocean earthquake, which had a magnitude of 9.1 and caused a tsunami that killed over 230,000 people, and the 2011 Tohoku earthquake in Japan, which had a magnitude of 9.0 and caused a massive tsunami that killed over 15,000 people.

The recorded waveforms of surface vibrations, which were made available in databases [1, 2, 3], were analysed. The authors of the report examined data concerning ground motion at a regional scale and near-source ground motion [4].

Two phenomena of similar intensity, but registered at seismic stations located on two site classifications (A and B) according to EC-8 [5], were selected for detailed analyses. The most precise way to estimate the dynamic response of irregular structures subjected to earthquakes is to create a 3D model and conduct a nonlinear response history analysis. Numerical models are also very useful for studying the dependence between strong motion duration and structural damage [6, 7]; this is due to providing the opportunity to separate different components of ground motion and investigate interesting aspects of the dynamic response of the structure in question.

The article presents numerical studies of the nonlinear MES model of the experimentally verified model of the selected RC building with irregularities. The building was under the previous investigation in [8]. The building was measured to find its dynamic properties using different ways of excitation. The model was influenced by two chosen far-field representative events originating from strong ground motion caused by the last earthquake in Turkey. Time history non-linear analysis is used in the study. The nonlinear concrete model was adopted in the analysis. The results of the calculations permit to assessment seismic behaviour of the studied structure and the estimated influence parameters of earthquakes on the dynamic response of the analysed structural model. The results of the analysis indicated locations of structural damages and permit assessing the dynamic resistance of the structure.

2 Ground Motion Parameters

Dynamic analysis is essential in understanding how structures respond to dynamic loading conditions such as ground vibrations caused by earthquakes or mining-related activities. To accurately assess the impact of these vibrations on structures, detailed records of the horizontal components of ground acceleration are required.
In Turkey, where earthquakes are prevalent, these records have been utilized to study the response of structures to seismic activity. Two stations were chosen in Turkey, and the horizontal components of ground acceleration vibrations were recorded. The earthquake records from the districts of stations No. 2703 and No. 3134 are presented in Figures 1 and 2, respectively.

Furthermore, the maximum values of the horizontal components' 'x' and 'y' (PGAx, PGAy) of acceleration records in station No. 3134 were found to be higher than the corresponding components of vibrations in station No. 2703 - comp. Figs. 1, 2, and Table 4.

Figures 1 and 2 illustrate the content of the dominant frequencies in analysed records from stations No. 2703 and No. 3134. The results of the FFT analysis on the vibration records from these figures reveal that the primary frequencies of ground acceleration vibrations are consistently below 5Hz.

The duration of intensive phase of vibrations is long and lasts for over 40 s. In the case of earthquakes, this duration is much longer and amounts to several dozen seconds. According to Table 4, the duration of the intensive phase of vibration records in station No. 2703 is higher than in station No. 3134.

To conduct a dynamic numerical analysis, a nonlinear time history analysis (THA) was carried out using earthquake records as the ground excitation by using the DIANA FEA program (DIANA user manual release 10.6).

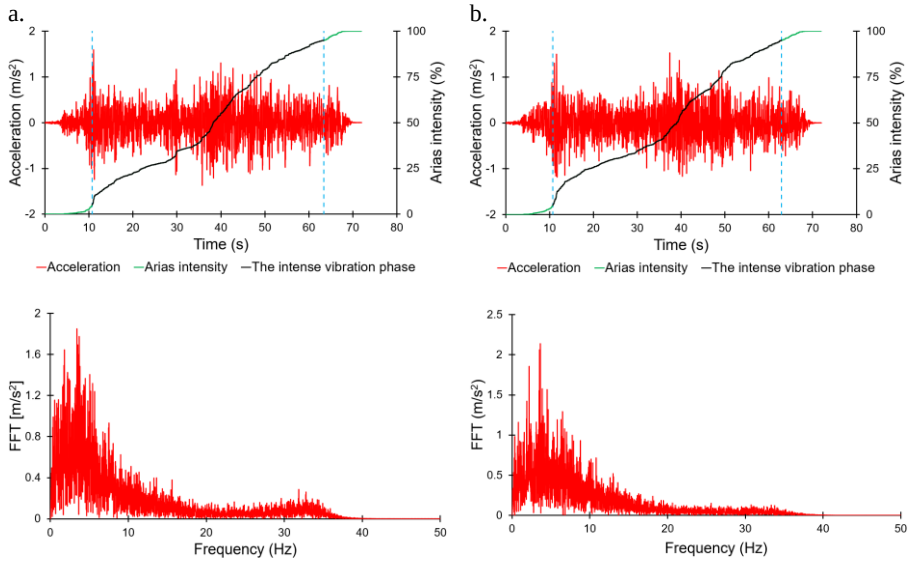

Fig. 1. Earthquake station No. 2703 a. EW direction, b. NS direction.

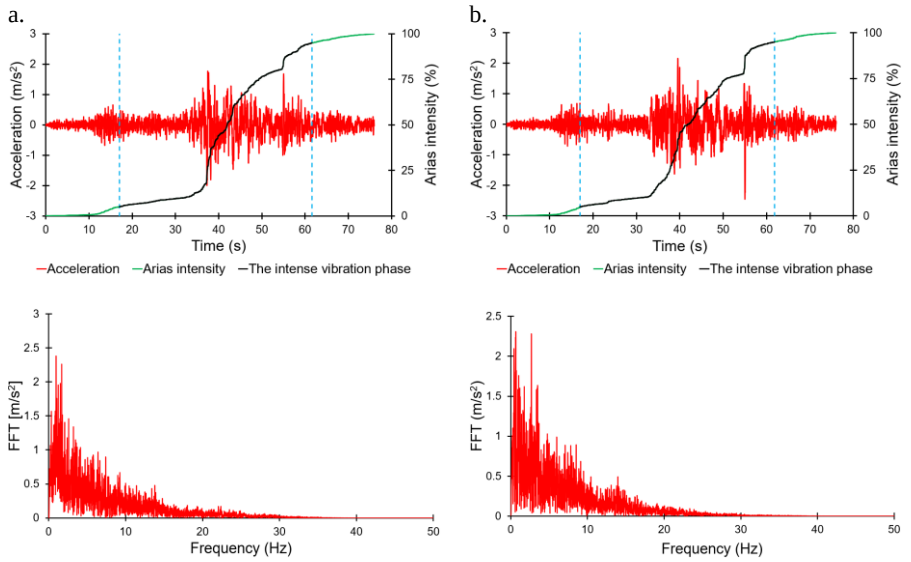

Fig. 2. Earthquake station No. 3134 a. EW direction, b. NS direction.

Table 1. Characteristics of the analysed components of vibrations.

		Station No. 2703	Station No. 3131
PGA (mm/s^2)	X	1650.64	2039.09
	Y	1566.34	2461.07
PGV (mm/s^2)	X	165.29	396.42
	Y	130.67	391.53
PGA/PGV (1/s)	X	9.986	5.144
	Y	11.987	6.286
t * (s)	X	52.68	44.56
	Y	52.16	44.83

* Duration of the intensive phase of acceleration.

3 FEA Model

The structure selected for analysis is a five-storey building consisting of reinforced concrete walls and columns with masonry infill walls. It features a system of columns and floors that are typical for this type of structure, with dimensions of 17.6 x17.9 m and a height of 23.2 m.

The columns in the building are 25 x 25 cm to 35 x 35 cm, while the floor slabs are 25 cm thick. This is an irregular building, and the concrete staircases are located on the northern side of the building. Figure 2 shows the building plans and the cross-section of the building.

To conduct a dynamic analysis of the building, a spatial model needs to be constructed using methods such as the finite element method (FEM). The decision to use a spatial model was made due to the irregularity of the load-bearing element positions, making it impossible to apply simplifications to the model's construction.
The building model encompasses all the essential elements that influence stiffness and mass distribution and determine the dynamic properties of the model. At the foundation level, the model is supported by fixed translation and rotational degrees of freedom. Figure 4 depicts the structural model that was analysed. The model was precisely described in the paper [8].

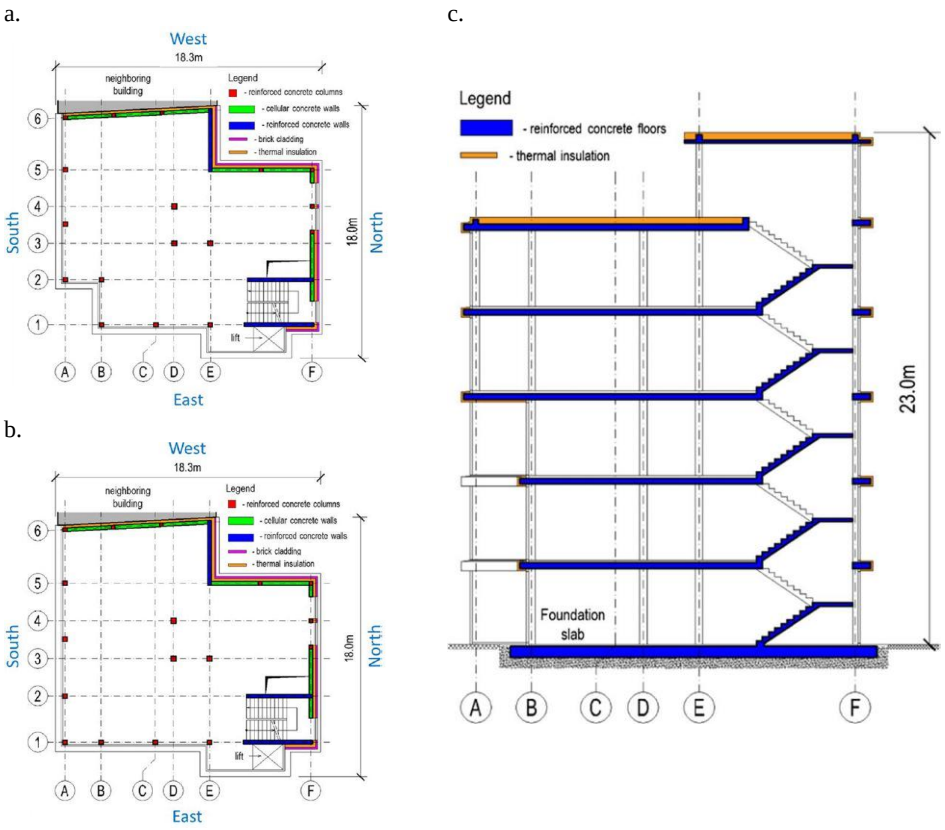

Fig. 3. View of the building: a. plan of the ground floor, b. plan of 4th floor, c. cross-section of the building [8].

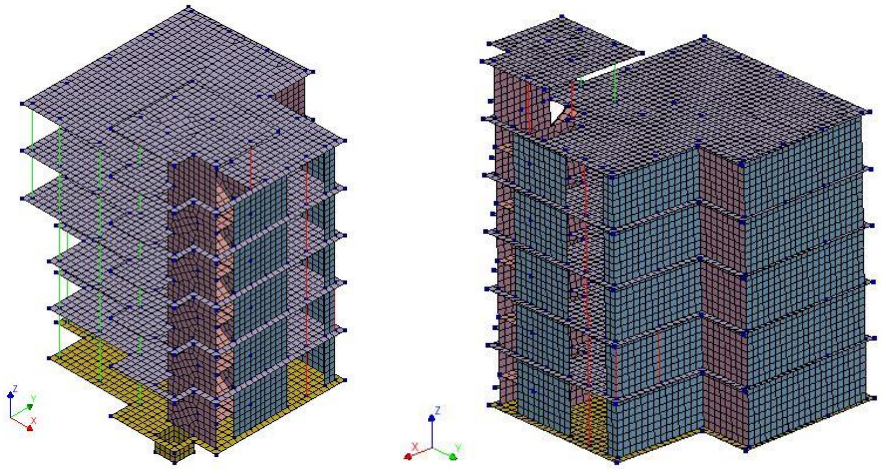

Fig. 4. FEA model of the building.

4 Time History Analysis

Figure 5 displays the maximum horizontal force (base shear) calculated through the Time history method for the analysed models, following a nonlinear analysis. The calculated displacements due to excitation from station No. 3134 are observed to be higher than for load from station No. 2703.

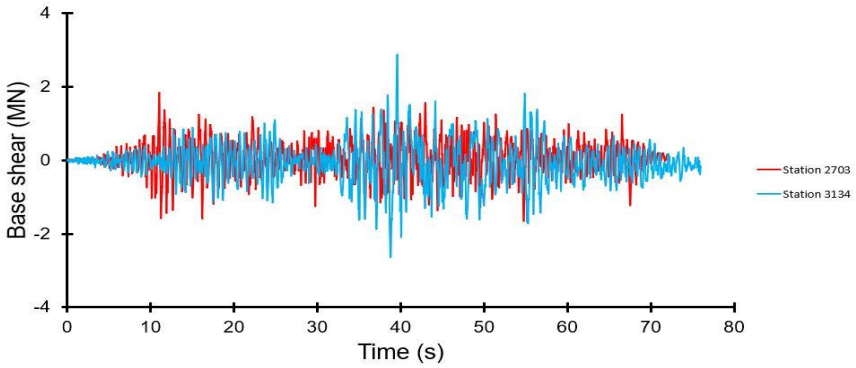

Fig. 5. Maximum horizontal force (base shear) for stations No. 2703 and No. 3134.

For a specific point, Figure 6 presents the displacement of the entire building from the roof of the last floor to the foundations. This is the highest value for displacement in the building.

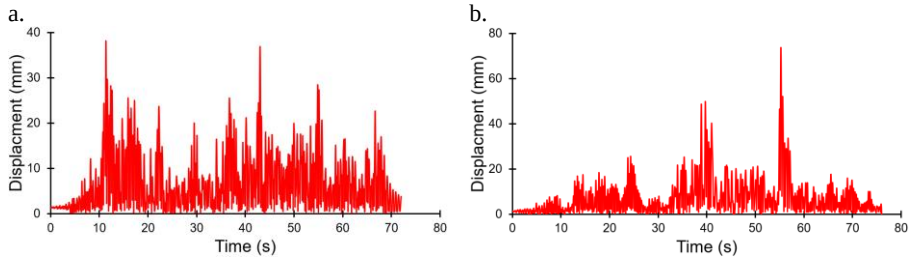

Fig. 6. Maximum displacements for excitation from station a. No. 2703, b. No. 3134.

Table 2. Selected results.

Selected results	Excitations from the station	
	No. 2703	**No. 3134**
Max of Base Shear (MN)	1.84	2.88
Max of drift (mm)	38.18	73.82

The failure modes and crack patterns are illustrated in Figures 7 and 8. The crack patterns, represented using normal principal strains, are concentrated in the staircase core, which transfers the seismic horizontal forces along with the external columns. Major cracks diffused at the last floor, where the weak and soft closing of the staircase core is located, as well as around the connection with the foundation slab. The summary of the damage is presented in Table 3. Table 3 also compares the damage to mining tremors and natural earthquakes from California and Alaska following the paper [8].

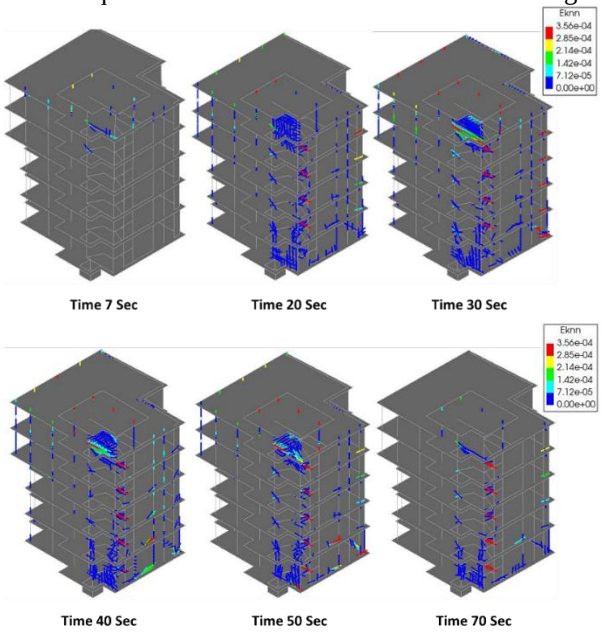

Fig. 7. Maximum Crack strains - station 2703.

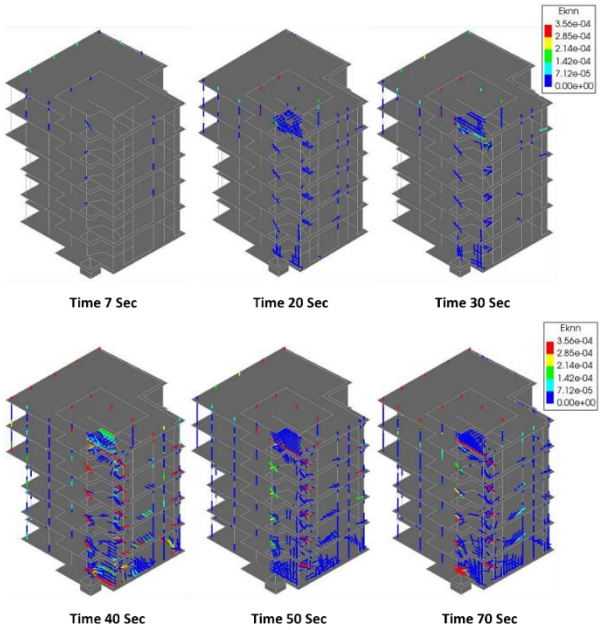

Fig. 8. Maximum Crack strains - station No. 3134.

Table 3. Summary of damage.

Type of excitation	Type of damage
Mining tremor no. 1 – [8]	Small, local cracks
Mining tremor no. 2 – [8]	Small, local cracks
Mining tremor no. 3 – [8]	Cracks in structural elements
Sitka earthquake – [8]	Cracks in structural elements
El Centro earthquake – [8]	Damages in structural elements
Turkey earthquake from station No. 2703	Damages in structural elements
Turkey earthquake from station No. 3134	Damages in structural elements

5 Conclusions

The article presents the results of dynamic analyses of an irregular reinforced concrete building subjected to seismic shocks on February 6, 2023. A building with an irregular structure was selected for the calculations and the level of damage after the earthquake was verified. The results were compared with selected earthquakes in California and Alaska. Differences in seismic characteristics have a significant impact on the dynamic response of a building.

References

1. Ground motion records AFAD: https://tadas.afad.gov.tr/list-waveform (last accessed 14/03/2023 01:20 UTC).
2. EPOS earthquake data: https://seismicportal.eu/ (last accessed 14/03/2023 7:00 UTC).
3. ESM Ground motion records: https://esm-db.eu/ (last accessed 14/03/2023).
4. Baltzopoulos G., Baraschino R., Chioccarelli E., Cito P., Iervolino I. (2023) Preliminary engineering report on ground motion data of the Feb. 2023 Turkey seismic sequence V2.5 – 25/02/2023.
5. EN 1998-1 Eurocode 8 (1998) Design of structures for earthquake resistance—part 1: general rules, seismic actions and rules for buildings (European standard EN 1998, December 2004).
6. Barbosa A.R., Ribeiro F.L.A., Neves L.A.C. (2017) Influence of earthquake ground-motion duration on damage estimation: application to steel moment resisting frames. Earthquake Engineering and Structural Dynamics, 46:27–49. https://doi.org/10.1002/eqe.2769
7. Chandramohan R., Baker J.W., Deierlein G.G. (2016) Quantifying the influence of ground motion duration on structural collapse capacity using spectrally equivalent records. Earthquake Spectra, 32(2):927–950. https://doi.org/10.1193/122813EQS298MR2
8. Pachla F., Kowalska-Koczwara A., Tatara T., Stypuła K. (2019) The influence of vibration duration on the structure of irregular RC buildings. Bullettin of Earthquake Engineering, 17: 3119. https://doi.org/10.1007/s10518-018-00546-4

Adaptive Sliding Mode for A Semi Active Vibration Control

Khaled Zizouni[1][0000-0001-6575-9067], Abdelkrim Saidi[2][0000-0002-1560-6596], Leyla Fali[3][0000-0003-2033-1133], and Bousserhane Ismail Khalil[4][0000-0002-8037-1770]

[1] Tahri Mohamed University, Civil Engineering Department, ArchiPEL Lab, Bechar, Algeria, zizouni.khaled@univ-bechar.dz
[2] Tahri Mohamed University, Civil Engineering Department, ArchiPEL Lab, Bechar, Algeria, saidi.abdelkrim@univ-bechar.dz
[3] Tahri Mohamed University, Civil Engineering Department, FIMAS Lab, Bechar, Algeria, fali.leyla@univ-bechar.dz
[4] Tahri Mohamed University, Electrical Engineering Department, ArchiPEL Lab, Bechar, Algeria, ismail.bousserhane@univ-bechar.dz

Abstract. The paper provides a numerical study of a semi-active control of structural vibrations caused by earthquake or wind excitations. A Magneto-Rheological damper is proposed and integrated to the structure to assure the control. A nonlinear controller was designed and coupled to a Clipped optimal algorithm current driver. The Sliding mode controller is reinforced by adaptive adjusted gain law to overcome the chattering problem and perform the stability of the controller. The numerical simulation results of a scaled steel structure have shown the performance of the proposed semi-active control. Where the structure was a subject of an earthquake records and the results of the controlled and uncontrolled structure responses are compared and discussed.

Keywords: Sliding mode, Semi-active control, Vibration control, Adaptive law.

1 Introduction

In civil engineering, all structures are calculated to resist earthquake loads. The building design, structural element dimensions, or construction materials and technics are linked to the capability of resistance and safety. In practical cases, earthquakes are the origin of the almost disaster and economic losses. For example, a magnitude 7.8 earthquake struck the Gaziantep province in southern Turkey on February 6th, 2023[1]. As a result, several Turkish and Syrian cities were destroyed as shown in Figure 1, and more than 51.000 people have died, according to local media reports.

Several decades ago, active control strategies were the subject of various research works. These strategies offered the possibility of structural safety increase using additional active dampers installed on the main structure [2]. Therefore, semi-active dampers are widely used in structural vibration control. The advantages offered by these devices make them the frequently proposed dampers for structural safety against

earthquakes. Magnetorheological dampers are semi-active devices combining the advantages of both active and passive devices. For numerical simulation studies, various mathematical models are proposed to describe the nonlinear behavior of the device [3]. All these mathematical models are generally presented with second-order differential/derivative of arbitrary-order equations based on the earlier mathematical works of Euler, Fourier, Laurent, Caputo, and Podlubny [4-5] and others.

Fig. 1. Kahramanmaras, Turkey on February 10, 2023.

In the 1950s, a nonlinear controller was proposed for dynamic systems control. This controller provides a practical and robust tool for nonlinear dynamic systems stability in the presence of uncertainties and external condition variations. Since then, the sliding mode controller has been widely used in industrial areas, offering performance tracking and quick responses for most dynamic industry problems. Unfortunately, the discontinuous switching function is a downside of sliding mode technics in which the system response switches between two opposite values for a while.

The structural vibration control of earthquake-excited systems was the subject of various numerical and experimental studies. Therefore, the literature is full of encouraging results in structural vibration control in civil engineering. Saidi et al. proposed a passive control strategy using the tuned mass damper to control de vibration of the bridge-vehicle system. The system interaction system is investigated based on Euler-Bernoulli's beam model and the quart vehicle model [6]. However, an Artificial Neural Network (ANN) is proposed to control the magnetorheological damper to suppress the structural vibration of an earthquake-excited structure. The numerical simulation results prove the effectiveness of the proposed intelligent control of the semi-active strategy, comparing the floor displacement responses of the controlled structure to these of the uncontrolled structure [7]. In addition, an active mass damper is proposed to reduce the vibration of a three-scaled structure. A classical sliding mode

controller controls the damper, and the structure is excited using the 2003 Boumerdès earthquake. As a result, the numerical simulations prove the robustness of the active strategy to control de structural vibrations and the stability of the nonlinear classical sliding mode controller [8].

The present paper proposes a semi-active damper to reduce the structural vibration induced by the excitation of earthquake loads. The current driver of the damper switches using the Bang-Bang algorithm, while the damper is controlled using a sliding mode controller. An adaptive law reinforces the stability of the nonlinear controller. The numerical simulation results and the calculated peak reduction ratios prove the robustness of the control strategy.

2 Damper Modeling

The electrorheological and magnetorheological fluids took considerable places in many industrial, electrical, and mechanical fields. The magnetorheological fluid success attracted several studies to push its nonlinear behavior knowledge. The mathematical modeling of the mass-spring-magnetorheological damper was the subject of numerical study [9]. The study investigated the dependence of the fractional ratio on the viscosity-damping variation in the mechanical system. Wang proposed an inverse magnetorheological damper nonlinear behavior model based on an adaptive neuro-fuzzy. The numerical simulation results demonstrate the efficiency of the proposed intelligent model to approximate the experimental results of the magnetorheological damper behavior [10]. In [11], Kallio investigated the magnetic particle alignment effect on the magnetorheological damper proprieties in magnetic field presence. The study results prove that the stiffness and damping of the damper are affected by the magnetic field presence if this surpasses 15%. The damping rises with the volume iron percentage at 27%. Additionally, it was discovered that by enhancing particle density and alignment, the stiffness and damping of the damper are improved in magnetic field application.

The most used mathematical model is that proposed by Spencer et al. [12], presented in Figure 1, based on the Bouc-Wen hysteresis model in which the equations governing the model are

$$f_{MRD} = c_1\dot{y} + k_1(x - x_0) \tag{1}$$

$$c_1\dot{y} = c_0(\dot{x} - \dot{y}) + k_0(x - y) + \alpha z \tag{2}$$

$$\dot{z} = -\gamma|\dot{x} - \dot{y}|z|z|^{n-1} - \beta(\dot{x} - \dot{y})|z|^n + A(\dot{x} - \dot{y}) \tag{3}$$

$$\alpha = \alpha_a + \alpha_b u \;;\; c_0 = c_{0a} + c_{0b}u \;;\; c_1 = c_{1a} + c_{1b}u \tag{4}$$

$$\dot{u} = -\eta(u - v) \tag{5}$$

Where x and $\dot{x}$ are the damper across displacement and velocity, f_{MRD} is the generated force of the device, γ, β, z, n, α and A are the hysteresis parameters, c_0, c_1, k_0 and k_1 are the fluid characteristics in low and high velocity, v is the current voltage, u is dynamic variable and η is a time factor.

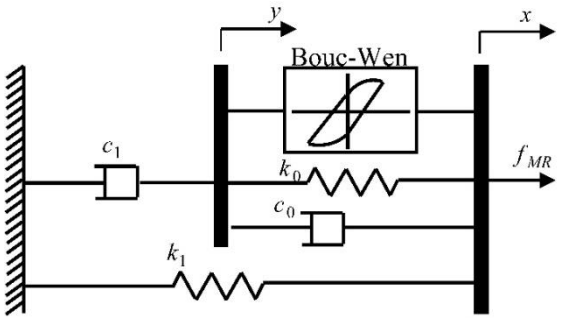

Fig. 2. Magnetorheological damper model

The used optimized model parameters by [13] are defined in Table 1. The damper's nonlinear behavior is depicted under a sinusoidal displacement with amplitude of 1.5*cm*, frequency of 2.5*Hz*, and voltage level of 1.25*V*. Figures 3, 4, and 5 illustrate the damper force function of time, displacement, and velocity.

Table 1. Magnetorheological model parameters.

α (N/cm)	β (cm^{-2})	γ (cm^{-2})	k_0 (N/cm)	c_0 (N·s/m)	k_1 (N/cm)	c_1 (N·s/m)	A	x_0 (cm)
716.77	11.26	25.13	1.63	22.53	2.05	259.55	33.63	-1.93

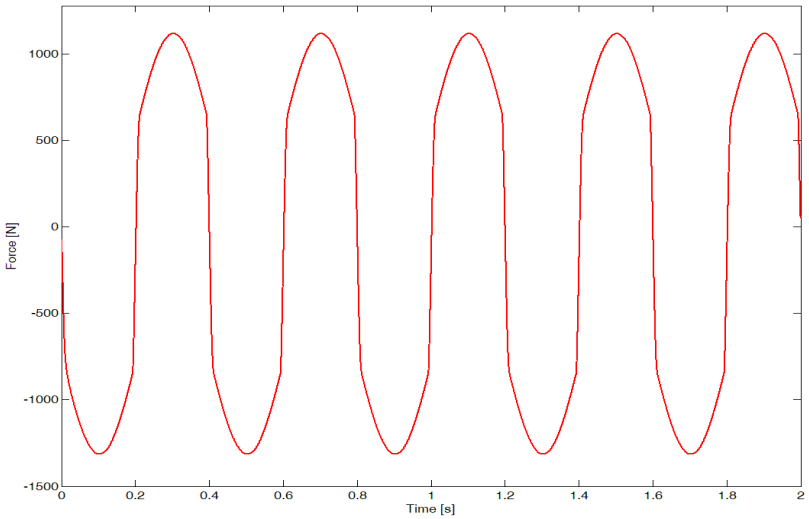

Fig. 3. The damper force function of time of optimized model

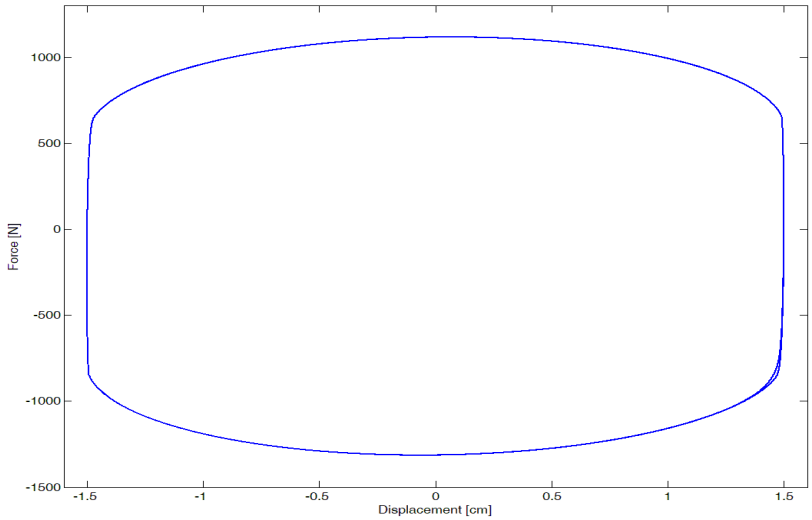

Fig. 4. The damper force function of displacement of optimized model

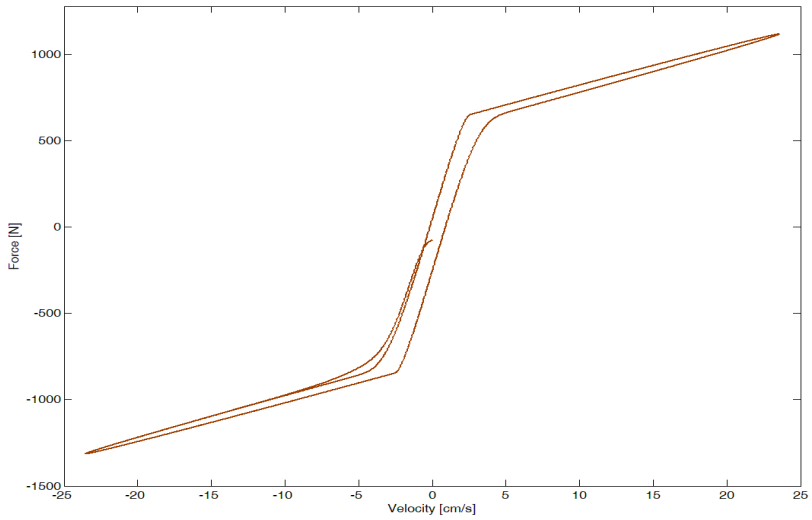

Fig. 5. The damper force function of velocity of optimized model

3 Control Design

3.1 Adaptive Sliding Mode Controller Design

This section uses an adaptive law control to reinforce the sliding mode controller stability. As presented in the first section, the switching process of the sliding mode controller causes instability called chattering phenomena. Nevertheless, it should be pointed out that the literature is still full of chattering problem solutions that should be

thoroughly examined in terms of robustness and phase elimination. The chattering problem of the sliding mode controller is overcome using an adaptive fast terminal sliding mode control technique reinforced by the global sliding mode control strategy [14]. Therefore, in [15], a low pass filter is proposed using an integrator positioned in the front of the classical sliding mode approach is proposed to suppress the undesirable chattering problem in a dynamical system. Moreover, chattering suppression using an adaptive control law is widely investigated. [16-17] proposed and investigated the robustness of using an adaptive sliding mode controller in structural vibration mitigation under earthquake loads. However, Zizouni et al. proposed in [18] a hybrid fuzzy sliding mode controller to overcome the chattering problem by switching term fuzzification. The numerical investigation shows the effectiveness and stability of the proposed controller in structural vibration reduction under earthquake excitation.

Let's consider the dynamic problem as follow

$$\dot{x} = f(x,t) + g(x,t)u \tag{6}$$

Where x, t and u are the state vector, time and the output problem, f and g are two smooth function of the sliding surface presented by

$$s \cdot \dot{s} < 0 \tag{7}$$

Hereby the sliding surface derivative is given by

$$\dot{s} = \frac{\partial s}{\partial x} \cdot \frac{\partial x}{\partial t} = \frac{\partial s}{\partial x}\left(f(x,t) + g(x,t)u \right) = 0 \tag{8}$$

In the sliding technic the solution of Eq. (8) is called the equivalent solution given as

$$u_{eq}(x,t) = -\left(s(x)g(x,t) \right)^{-1} s(x) f(x,t) \tag{9}$$

From Eqs. (6) and (9)

$$\frac{\partial s}{\partial x}\left(f(x,t) + g(x,t)u \right) \cdot s(x) < 0 \tag{10}$$

Therefore, the solution of Eq. (10) is given by [20] as

$$u_s = K \cdot \mathrm{sgn}(s) \tag{11}$$

K is a positive gain and sgn is the signum function [16]. However, to overcome the infinite frequency oscillation caused by the signum function, the switching solution of Eq. (11) is adapted as follow

$$u_{as} = \hat{K} \cdot \mathrm{sat}(s) \tag{12}$$

Where $\widehat{K}$ is the adapted switching gain and sat is the saturation function given by [16]. Whereof, the adapted gain is proposed as

$$\dot{\hat{K}} = \chi |s| \tag{13}$$

Where χ is the bounded adaptation gain and $\dot{\hat{K}}$ is the adaptation speed.

3.2 Stability Analysis

In this subsection, the theoretical stability of the proposed adaptation is analyzed using the Lyapunov candidate written as

$$V = \frac{1}{2}s^2 + \frac{1}{2}\chi\hat{e}^2 \tag{14}$$

$$\hat{e} = \hat{K} - K_d \tag{15}$$

$$\dot{V} = s\dot{s} + \chi\hat{e}\dot{\hat{e}} \tag{16}$$

$$\dot{V} = s\left(d - \hat{K}\cdot\mathrm{sgn}(s)\right) + \chi\left(\hat{K} - K_d\right)s\cdot\mathrm{sgn}(s) \tag{17}$$

$$\dot{V} = d\cdot s - K_d\cdot|s| \tag{18}$$

Noting that, e is the tracking error, K_d is the limit value of switch and d is the roll motion value. In contrast, the term in Eq. (16) is absolutely positive and to ensure the Lyapunov stability given by $V\cdot\dot{V} < 0$ the term of Eq. (18) must always been negative so the condition is that $K_d > d$

4 Simulation Example

In this section, the stability and robustness of the adaptive sliding mode controller is proven by numerical simulation of the schematic block presented in the Figure 6.

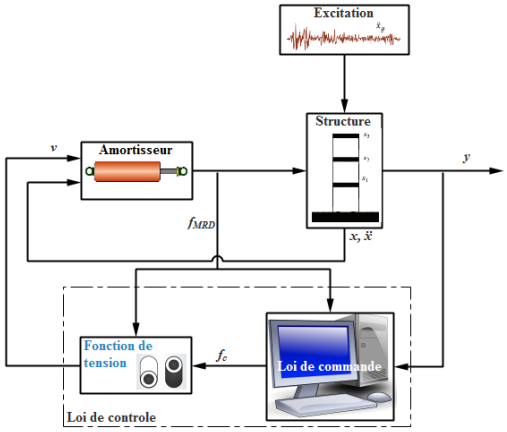

Fig. 6. Schematic block of the proposed semi-active adaptive sliding mode control

The tasted structure is a three-scaled steel structure with the characteristics given by [16]. Although, the system is excited using the 2003 Boumerdès earthquake records given by [18] and represented in Figure 7. Thus, the function of tension is given as

$$v = v_{max} H\left(f_c - f_{MRD} \right) \tag{19}$$

$$f_c = u_{eq} + u_{as} \tag{20}$$

Where v_{max} is the maximum voltage level, $H\{.\}$ is a Heaviside step function, f_c is the required force of control, f_{MRD} is the generated force by the damper.

Although, the numerical simulation responses of the structure floor's displacement are presented in Figure 8.

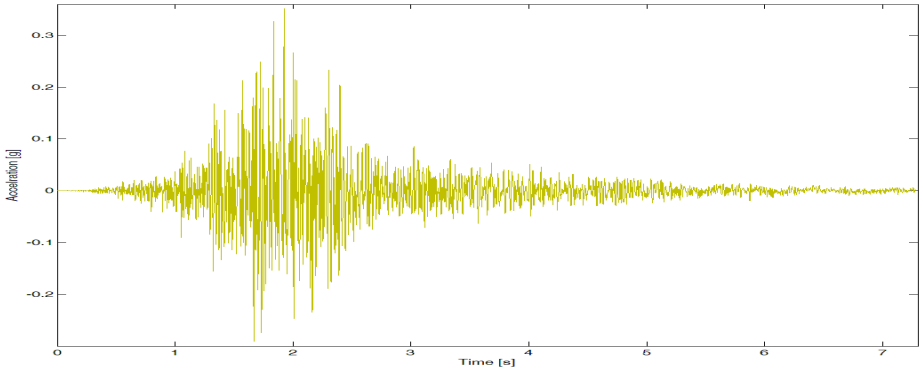

Fig. 7. The 2003 Boumerdès earthquake time-scaled record

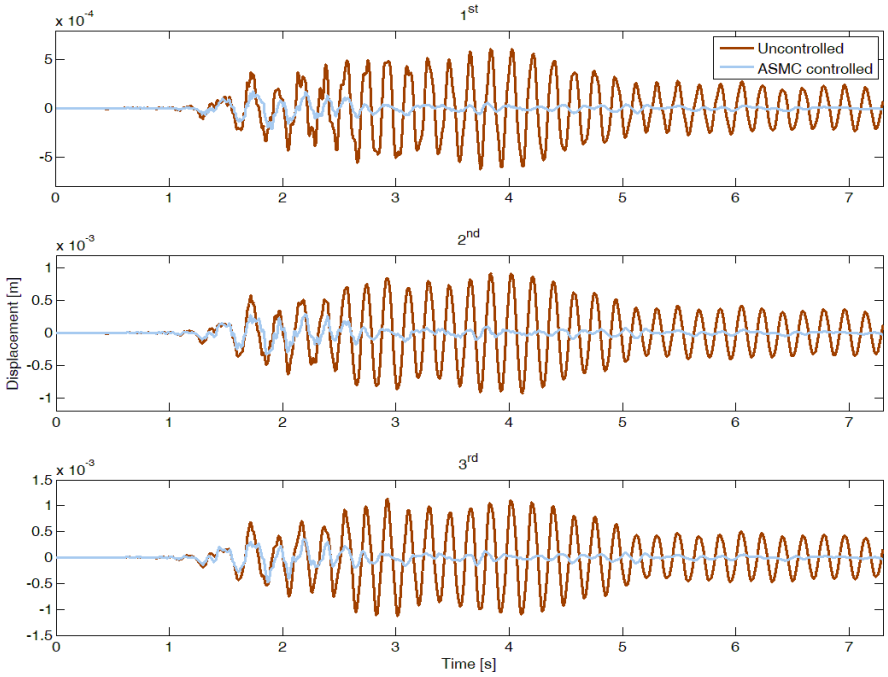

Fig. 8. The floor displacement responses of the structure under the 2003 earthquake excitation

Therefore, the superimposed responses of the adaptive semi-active controlled and uncontrolled in Figure 8 show the effectiveness of the proposed control strategy. As shown, the displacement responses of each floor are clearly reduced using the semi-active damper controlled by the adaptive sliding mode controller. On the third floor, the reduction of the peak displacement is esteemed at about 60%.

5 Conclusion

This study proposes a semi-active control strategy using a magnetorheological damper controlled by an adaptive sliding mode controller. The semi-active approach proves a robust control by the remarkable structural vibration mitigation of structures subjected to earthquake excitations. In addition, the tested three-scaled structure with one damper installed on the bottom floor excited with the 2003 Boumerdès historical earthquake records. It has been observed that the designed adaptive controller effectively reduces the peak displacement of each structure floor.

References

1. Baltzopoulos, G., Baraschino, R., Chioccarelli, E., Cito, P., Vitale, A., Iervolino I.: Preliminary engineering report on ground motion data of the Feb. 2023 Turkey seismic sequence. Technical report V3 – 17/03/2023 (2023).

2. Zizouni, K., Fali, L., Bousserhane I.K., Sadek, Y.: Active Mass Damper Vibrations Control under Earthquake Loads. In: 72nd International Conference of Civil Engineering and Environmental, pp. 1-5, Istanbul, Turkey, Dec 6-7 (2019).
3. Zizouni, K., Fali, L., Sadek, Y., Bousserhane, I.K.: Linear Semi Active Controller of Magneto-Rheological Damper for Seismic Vibration Attenuation. In: International Conference Proceedings of Multi-Storey Buildings and Structural Analysis, Part VII, pp. 739-744, Dubai UAE Mar 21-22 (2019).
4. Euler, L.: Methodus generalis summandi progressiones. In: Commentarii academiae scientiarum Petropolitanae 6, pp. 68-97 (1738).
5. Podlubny, I.: Fractional Differential Equations: An Introduction to Fractional Derivatives, Fractional Differential Equations, to Methods of Their Solution and Some of Their Applications. 1st edn. Academic Press, San Diego (1999).
6. Saidi, A., Fali, L., Bousserhane, I.K., Hamouine, A.: Passive control application using TMD in bridge-vehicle interaction. In: Proceedings of IASTEM International Conference, Colombo, Sri Lanka, pp. 7-10 (2018).
7. Zizouni, K., Fali, L., Sadek, Y., Bousserhane, I.K.: Neural Network Control for Earthquake Structural Vibration Reduction using MRD. Frontiers of Structural and Civil Engineering 13(5), pp. 1171-1182 (2019).
8. Zizouni, K., Fali, L., Bousserhane, I.K., Sadek, Y.: Active Mass Damper Vibrations Control under Earthquake Loads. International Journal of Advances in Mechanical and Civil Engineering 7(2), pp. 26-30 (2020).
9. Escalante-Martínez, J.E., Morales-Mendoza, L.J., Cruz-Orduña, M.I., Rodriguez-Achach M., Behera, D., Laguna-Camacho, J.R., López-Calderón, H.D., López-Cruz, V.M.: Fractional differential equation modeling of viscoelastic fluid in mass-spring-magnetorheological damper mechanical system. The European Physical Journal Plus 135, 847 (2020).
10. Rozaina, I., Azmi, I., Hanizah, A.: A Review of Magnetorheological Elastomers: Characterization Properties for Seismic Protection. In: Rohana, H., Marina, Y., Zulhabri, I., Norliyati, M.A., Mohd, A.F., (eds) InCIEC 2013. Springer, Singapore (2014).
11. Kallio, M.: The elastic and damping properties of magnetorheological elastomers. Doctor of Technology Thesis, Tampere University of Technology, Finland, vol. 565 VTT publications (2005).
12. Spencer, B.F., Dyke, S.J., Sain, M.K., Carlson, J.D.: Phenomenological model for Magnetorheological Dampers. Journal of Engineering Mechanics, 123(3), pp. 230-238 (1997).
13. Zizouni, K., Saidi, A., Fali, L., Bousserhane, I.K.: Bouc-Wen Model Parameters Optimization using a Naturally Inspired Meta-Heurisics Algorithm. In: 1st International Conference on Materials Sciences and Technology (MatScience-2022), Khenchela, Algeria, Dec 13-15 (2022).
14. Mobayen, S.: An adaptive fast terminal sliding mode control combined with global sliding mode scheme for tracking control of uncertain nonlinear third-order systems. Nonlinear Dynamics, 82, pp. 599-610 (2015).
15. Karami-Mollaee, A.: A new structure of sliding mode observer in dynamic sliding mode control of generator torque wind turbine. Journal of Mechanical Science and Technology, 35(12), pp. 5681-5687 (2021).
16. Fali, L., Djermane, M., Zizouni, K., Sadek, Y.: Adaptive sliding mode vibrations control for civil engineering earthquake excited structures. International Journal of Dynamics and Control, 7, pp. 955–965 (2019).
17. Zizouni, K., Saidi, A., Fali, L., Bousserhane, I.K., Djermane, M.: Adaptive sliding-mode control for improved vibration mitigation in civil engineering structures. Mechanical Sciences Journal, 13(2), pp. 899-908 (2022).

18. Zizouni, K., Saidi, A., Fali, L., Bousserhane I.K., Djermane, M.: Semi-active structural vibrations control with magneto-rheological damper based on the hybrid fuzzy sliding mode controller. Revista De La Construcción. Journal of Construction, 22(1), pp. 36–50 (2023).
19. Yan, X.G., Spurgeon, S.K., Edwards, C.: Variable Structure Control of Complex Systems: Analysis and Design. Communications and Control Engineering, Springer International Publishing AG, Switzerland (2017).

Corroboration of the Pre- and Post-Earthquake Assessment of the Buildings in 2023 Kahramanmaraş Earthquake Using Field Inspections and Street-Level Imagery

Ayşe Elif Özsoy Özbay[1][0000-0001-5397-398X], Işıl Sanrı Karapınar[2][0000-0002-3695-5867] and Hüseyin Can Ünen[3][0000-0001-9489-9798]

[1] Maltepe University, Civil Engineering Department, İstanbul, Türkiye, ayseelifozsoyozbay@maltepe.edu.tr
[2] Maltepe University, Civil Engineering Department, İstanbul, Türkiye, isilkarapinar@maltepe.edu.tr
[3] Yer Çizenler Mapping for Everyone Association, İstanbul, Türkiye, can.unen@yercizenler.org

Abstract. Two major earthquakes with a magnitude of Mw=7.7 and Mw=7.6, which occurred in Kahramanmaraş, Turkey on February 6, 2023, caused thousands of deaths and great economic losses in the region. After this devastating seismic event, the extent of the observed damage to the existing building stock was determined with the post-earthquake inspections organized by the Ministry of Environment, Urbanization and Climate Change. In this study, by the use of these field assessment studies, building clusters along the main roads of Kahramanmaraş were selected from the geo-located building damage data and with the use of street-level images, the pre-earthquake assessment of the georeferenced damage database was performed by using rapid visual screening method. Also, in order to facilitate cross-referencing and communication between users, an online map to follow the process was created using online maps. As a result of this study, the corroboration of the pre- and post-earthquake evaluation of the damaged buildings were achieved by comparing the seismic risk prioritization distribution of the inspected buildings and the actual damage states observed through post-earthquake field inspections. In conclusion, this study is believed to contribute to the joint management of pre- and post-earthquake assessment efforts with the generation of spatial distribution of the existing database.

Keywords: Pre-Earthquake Assessment, Post-Earthquake Data, Spatial Distribution, Rapid Visual Screening.

1 Introduction

It is well known that severe earthquakes induce enormous socioeconomic consequences. Due to the effects of devastating earthquakes, irreversible losses are

caused especially in countries under seismic risk. Unfortunately, if the actions for the pre- and post-earthquake disaster preparation are not well taken, earthquakes lead to grave consequences regarding widespread structural damage, fatalities, injuries and economic loss. Thus, especially in countries exposed to high seismic risk, the pre-and post-earthquake assessment methodologies to be employed in the built environment have a crucial role in disaster management strategies. For local and central governments, seismic risk mitigation and strengthening strategies in earthquake-prone cities are of great importance. Therefore, the implementation of pre- and post-earthquake assessment methodologies is gaining more importance and attracting increasing interest.

Many studies have been published on the pre-earthquake assessment of the existing building stocks focusing to rank the buildings with respect to their seismic safety level for the prioritization of the most vulnerable buildings by using the rapid visual screening (RVS) methods [1-4]. The case studies in these research into structural vulnerability assessment in literature have used various RVS methodologies proposed by many countries. The RVS methods developed by the United States (FEMA), the New Zealand Society of Earthquake Engineering (NZSEE), the National Research Council (NRC) of Canada, the Japanese Building Disaster Prevention Association (JBDPA), Ministry of Environment, Urbanization and Climate Change of Turkey, and the National Earthquake Defense Group (GNDT) of Italy have been the most common methods applied to the existing building stocks [5-10]. Also, there are studies based on the post-earthquake survey of buildings that evaluate the seismic effects by specifying their damage levels after major earthquakes [11, 12]. In these studies, considerable insight has been exposed for the statistical distribution of the damage extent after the seismic actions by assembling the damage data.

On the other hand, unfortunately there is no data flow from the pre-earthquake assessment procedure to the post-earthquake procedure. In literature, there is so limited work focusing on the schemes aiming to provide the data flow and integrate the pre- and post-earthquake information [13-15]. With this motivation, this study aims to conduct a joint pre- and post-earthquake assessment of buildings affected by the devastating earthquake with a magnitude of Mw=7.7 occurred on February 6, 2023, in Kahramanmaraş in the southern region of Turkey. This earthquake was also followed by another major earthquake on a different fault line having a magnitude of Mw=7.6. As a result, other than Kahramanmaraş, also ten other neighboring provinces in the same region (Adana, Adıyaman, Diyarbakır, Elazığ, Gaziantep, Hatay, Kilis, Malatya, Osmaniye, Şanlıurfa) were seriously affected by the devastating impacts of the earthquake sequence. As a post-earthquake action, the Ministry of Environment, Urbanization and Climate Change has reported the extent of the observed damage to the existing building stock. In this study, with the use of this data, a number of reinforced concrete buildings in Kahramanmaraş (Fig.1) were assessed for the case study that enables the corroboration of the pre- and post-earthquake analyses of the damaged buildings. Pre-earthquake assessment was performed by the implementation of the vulnerability assessment methodology presented in the Specifications for Determination of Seismically Vulnerable Buildings (SDSVB) that is proposed for the determination of the regional seismic risk prioritization [9]. With the use of street-level

images, the seismic risk prioritization distribution of the selected building stock was obtained and then, the results were compared with the actual damage states observed through the post-earthquake field survey results. Also, online collaborative mapping tools and methods were used for the comparison of the spatial distributions of the pre- and post-earthquake assessment results.

Fig. 1. Study area within Kahramanmaraş.

2 Methodology

This section is organized as the pre- and post-earthquake assessment procedures followed in this study. The first section briefly describes application of the RVS method, and the second section details the generation of spatial datasets concerning the actual damage states of the buildings observed after the earthquake.

2.1 Pre-Earthquake Assessment

The pre-earthquake evaluation of the inspected buildings is performed by the first tier procedure given in SDSVB proposed for the regional assessment of the seismic vulnerability of reinforced concrete buildings [9].

In the preliminary stage of the procedure, the hazard zone is identified for the soil condition and the seismicity of the studied region using the online calculation software provided by National Disaster and Emergency Management Authority (AFAD 2018) [16]. For the specified soil class in the survey area, the site-specific the short-period spectral acceleration coefficient (SDS) obtained for the geographic location of each inspected building is utilized to determine the hazard zone of the study region as illustrated in Table 1.

Table 1. Determination of the hazard zones in the pre-earthquake assessment procedure.

Hazard zone	S_{DS}	Soil class
I	$S_{DS} \geq 1.0$	ZC, ZD, ZE
II	$S_{DS} \geq 1.0$	ZA, ZB
	$0.75 \leq S_{DS} \leq 1.0$	ZC, ZD, ZE
III	$0.75 \leq S_{DS} \leq 1.0$	ZA, ZB
	$0.50 \leq S_{DS} \leq 0.75$	ZC, ZD, ZE
IV	$0.50 \leq S_{DS} \leq 0.75$	ZA, ZB
	$S_{DS} \leq 0.50$	All site classes

In the second stage of the assessment procedure, the structural parameters that are required for the calculation of performance scores of the buildings are specified by visual inspections conducted during the walk-down survey in the study region. The building-specific parameters considered in the methodology are the number of stories above the ground, the apparent quality of the building classified as good, moderate and poor according to the observed quality of the construction material, topographic effect for the buildings constructed on slope sites, the effect of pounding categorized as edge/middle regarding the location of the building within the adjacent structural units; and aligned/not aligned according to the floor levels of the buildings and the existence of soft story, heavy overhang, short columns and structural irregularities in plan and elevation of the building. Based on these visually inspected parameters on site, performance scores (PS) are obtained from the following equation:

$$PS = BS + \sum[(VSM) \times (VS)] \quad (1)$$

In Equation 1, the base score (BS) changes according to the number of stories of the building. The vulnerability score (VS) represents the effect of each vulnerability parameter determined to exist on the inspected building as given in Table 1. The vulnerability score modifier (VSM) in Equation 1 defines the presence of the vulnerability parameters for the surveyed building. The value of the modifier is taken as 1 or 0 for each vulnerability parameter that is determined to exist or not to exist during the site survey, respectively. For the apparent quality, VSM is regarded as 0, 1 and 2, depending on three different observations identified as *good*, *moderate* or *poor* condition of the building, respectively.

Table 2. Base scores and vulnerability scores for reinforced concrete buildings.

No. of stories	Base Scores (BS)				Vulnerability Scores (VS)										
	Seismic hazard zones				Soft story	Apparent quality	Heavy overhang	Pounding effect				Structural irregularities		Short column	Topog. effects
								aligned		not aligned					
	I	II	III	IV				mid	edge	mid	edge	in elev.	in plan		
1,2	90	120	160	195	-10	-10	-10	0	-10	-5	-15	-5	-5	-5	-3
3	80	100	140	170	-20	-10	-20	0	-10	-5	-15	-10	-10	-5	-3
4	70	90	130	160	-30	-15	-30	0	-10	-5	-15	-15	-10	-5	-3
5	60	80	110	135	-30	-25	-30	0	-10	-5	-15	-15	-10	-5	-3
6,7	50	65	90	110	-30	-30	-30	0	-10	-5	-15	-15	-10	-5	-3

With the implementation of the pre-earthquake assessment methodology, PS of each individual building is calculated and ranked from higher to lower to categorize the prioritization of the seismically vulnerable buildings in the selected region.

2.2 Post-Earthquake Assessment by the Generation of GIS-Database

The process of obtaining government data in tabular format through the contributions of volunteers and subsequently converting it into spatial datasets via geocoding based on address information represents an innovative approach to data collection. The geocoded datasets were then made available to the public through third-party online map services [17] as seen on Fig.2, facilitating access to spatial information for a wide range of users.

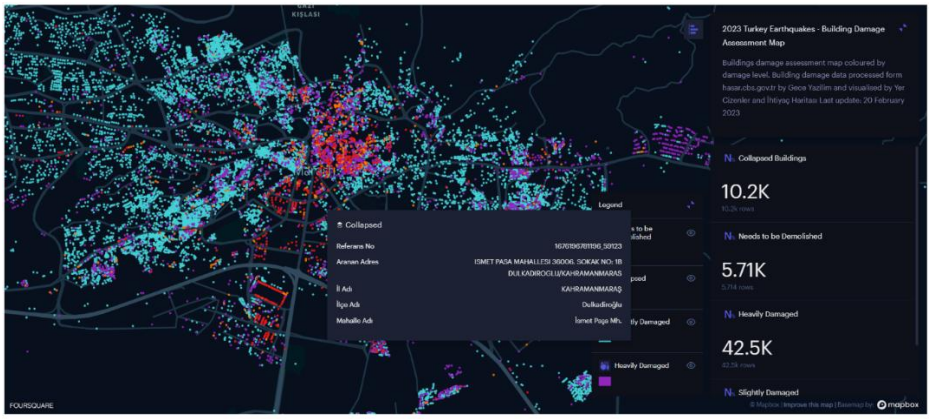

Fig. 2. Visualization of the country-wide earthquake damage dataset.

Once the analysis area of interest is determined, relevant data is filtered and downloaded from the available datasets. Google MyMaps is utilized to establish a collaborative map, promoting collaboration among experts. This platform enables the integration of various data sources, including address information, post-earthquake

damage assessment results, and additional notes from the authors. Furthermore, the integration of Google Maps and Google StreetView within MyMaps enriches the analysis by granting access to pre-earthquake street-level images of the analyzed buildings. This integration allows researchers to visually examine the buildings' conditions before the earthquake, providing valuable context for their assessments.

The adoption of this integrated data management approach provides significant benefits for coordinating multiple experts. Asynchronous collaboration becomes feasible, as researchers can conveniently access and contribute to the collaborative map. This flexibility enables experts to work independently on different aspects of the analysis while still leveraging the collective insights of the team. Additionally, the collaborative map serves as a centralized repository of information, ensuring that all experts have access to the same dataset and minimizing the potential for data duplication or inconsistencies. Overall, this approach improves the efficiency and effectiveness of data analysis and fosters interdisciplinary collaboration by harnessing the capabilities of modern mapping and visualization technologies.

3 Results and Discussion

Herein, 70 damaged buildings located in Kahramanmaraş were evaluated for the pre- and post-earthquake assessment studies. The damage dataset consists of mid-rise reinforced concrete buildings which are constructed adjacently and have number of stories ranging between 2 to 7. According to the post-earthquake data, the inspected damage states were categorized with respect to the number of stories of the selected buildings as presented in Table 3. As detailed in the table, 37.14, 34.29 and 28.57% of the buildings were classified as collapsed; highly damaged and to be demolished; and slightly damaged, respectively. Among the group of collapsed buildings, 50% was found to be 7-story buildings. Also, a closer inspection of the damage data in Table 3 revealed that the buildings having 5 to 7 stories were severely affected whereas the ones having up to 4 stories were slightly damaged.

Table 3. Distribution of damage states with respect to number of stories of the buildings.

# of Stories	# of Buildings		
	Collapsed	Highly damaged and to be demolished	Slightly damaged
2	0	2	0
3	2	1	2
4	6	7	5
5	4	9	4
6	1	2	7
7	13	3	2
Total	26	24	20
%	37.14	34.29	28.57

Using the street-level images, pre-earthquake assessment of the geo-referenced damage database was performed by rapid visual screening. First, 8 vulnerability parameters representing the structural characteristics were identified and classified with respect to the number of stories of the buildings as demonstrated in Table 4. The number of stories was found to be the key parameter changing the seismic risk level of the buildings. As can be seen from the table, the majority of the buildings was identified to suffer from soft story, short column and irregularity in elevation in common.

Table 4. Classification of vulnerability parameters due to the number of stories for the inspected RC buildings.

# of Stories	# of Build.	Soft Story	Apparent Quality (Poor/Mod.)	Heavy Overhang	Pounding Effect (edge)	Pounding Effect (middle)	Irregularities in Elevation	Irregularities in Plan	Short Column	Topog. effect
2	2	2	2	2	2	0	2	2	2	2
3	5	4	5	4	3	2	5	1	2	1
4	18	17	18	9	4	12	14	2	7	4
5	17	15	16	2	8	9	10	6	9	5
6	10	10	9	2	6	3	2	0	5	2
7	18	17	17	4	11	0	10	4	10	6
Total	70	65	67	23	34	26	43	15	35	20
%		92.86	95.71	32.86	48.57	37.14	61.43	21.43	50.00	28.57

The street-level imagery of the geo-referenced buildings was utilized to calculate the performance score (PS) of each individual building by cross-referencing the generated online map of the post-earthquake damage database. As a result, the seismic priority levels of buildings were ranked as high, moderately high, very high and extremely high according to the ranges of PS distribution.

Fig. 3 illustrates the distribution of buildings due to the PS ranges for which $10<PS\leq25$, $-15<PS\leq10$, $-40<PS\leq-15$ and $-40<PS\leq-65$ correspond to high, moderately high, very high and extremely high levels, respectively. As observed from the distribution given in Fig. 3, 30.00, 32.86, 27.10 and 10% of the buildings were categorized as extremely high, very high, moderately high and high priority levels among the whole building stock.

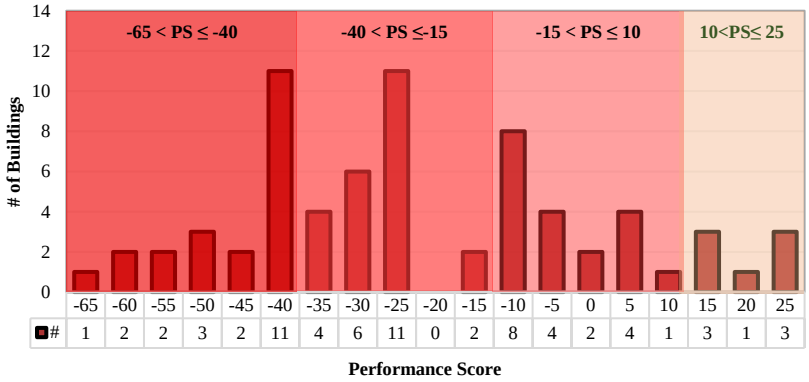

	-65	-60	-55	-50	-45	-40	-35	-30	-25	-20	-15	-10	-5	0	5	10	15	20	25
#	1	2	2	3	2	11	4	6	11	0	2	8	4	2	4	1	3	1	3

Fig. 3. Distribution of the buildings with respect to performance scores.

In order to reveal the main structural deficiencies that commonly exist in the surveyed group of buildings, post-earthquake damage states were also examined regarding the vulnerability parameters in Fig. 4. In the set of collapsed buildings, it was clearly observed that, apart from the heavy overhang, plan irregularity and topographic effect, all the other vulnerability parameters were found to exist.

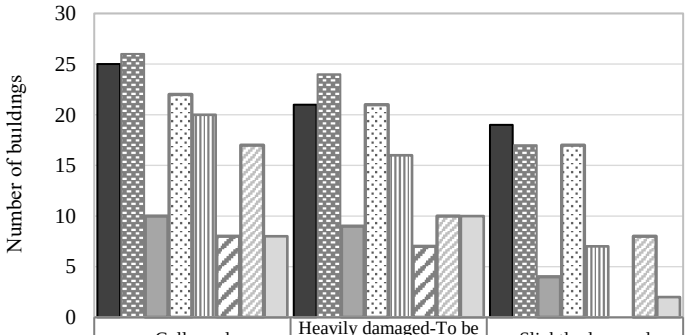

	Collapsed	Heavily damaged-To be demolished	Slightly damaged
Soft story	25	21	19
Apparent quality	26	24	17
Heavy overhang	10	9	4
Pounding effect	22	21	17
Irreg.in elevation	20	16	7
Irreg.in plan	8	7	0
Short column	17	10	8
Topog. effect	8	10	2

Fig. 4. Distribution of post-earthquake damage states with respect to vulnerability parameters.

In order to corroborate the pre and post-earthquake results, Fig. 5 presents the correlation between the observed damage states and the corresponding ranges of PSs

of the building dataset. In Fig. 5a, the box and whisker plot of the data shows that as the damage states differ from slightly damaged to collapsed, the second and third quartile of PS distribution of each state also tend to decrease. The same trend was also observed for the mean PS values. Besides, Fig. 5b proves that the majority of the collapsed buildings in the post-earthquake assessment correspond to the buildings which were prioritized as extremely high and very high in the pre-earthquake assessment stage.

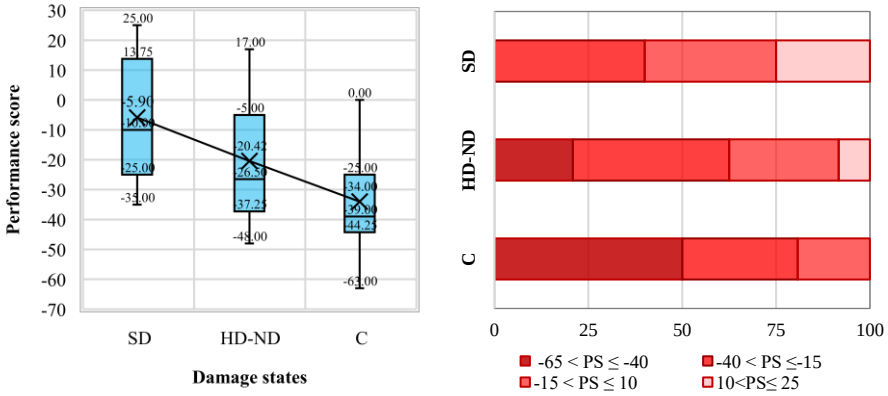

(a) (b)

Fig. 5. Comparison of the pre and post-earthquake results.

3.1 GIS-Database Implementation

The assessment of the validity, reliability, and applicability of visual rapid assessment methods involves a comparison between the pre-earthquake assessment of individual buildings using street-level imagery and the subsequent observation of structural damage following an earthquake event. This comparison can be visually inspected via Fig. 6. Fig.6a portrays the observed structural damage on a selected set of buildings, visually representing their post-earthquake condition. Fig.6b illustrates the visual assessment of the same buildings based on their street-level imagery captured prior to the earthquake.

By juxtaposing these two visualizations, experts are provided with the opportunity to evaluate the validity, reliability, and applicability of visual rapid assessment methods. The comparison enables a direct examination of the consistency between the pre-earthquake visual assessment and the subsequent observed damage. Discrepancies between the two visualizations offer valuable insights into the limitations and strengths of the employed visual rapid assessment techniques.

Moreover, this comparative approach fosters a deeper understanding of the relationship between pre-earthquake building conditions and post-earthquake damage. By analyzing the correlation between the observed damage and the visual assessment, experts can identify discernible patterns, trends, or indicators that contribute to the accuracy of rapid assessment methods.

(a) (b)

Fig. 6. Spatial distribution of the buildings with respect to (a) the observed damage states and (b) the pre-earthquake risk categories based on the performance scores.

4 Conclusion

Integration of the pre- and post-earthquake information is critical in earthquake-prone cities for earthquake preparedness and disaster management. In order to mitigate the seismic risk, thorough planning that enables the data flow between the pre- and post-assessment procedures needs to be developed.

The utilization of street-level imagery as a predictive or vulnerability identification tool is facilitated through this comparative analysis, thereby contributing to the enhancement of disaster preparedness and response strategies. The insights gained from this analysis inform the refinement and optimization of visual assessment protocols, facilitating more effective and efficient pre-disaster evaluations of building conditions. Ultimately, the integration of street-level imagery and post-earthquake observations advances the field of disaster risk reduction, bolstering the reliability and applicability of visual rapid assessment methods. One hindrance to this process might be limited availability or datedness of the street-level imagery at hand. However, with organized field data collection efforts during the preparedness phase before earthquakes, one can collect up-to-date street-level imagery by utilizing community-driven open data tools such as Mapillary or KartaView for this purpose.

With this motivation, this study underlined the importance of the need for a unified structure integrating pre- and post-earthquake assessment of buildings with a case study based on the Kahramanmaraş earthquake comparing the seismic risk prioritization distribution of the buildings and the actual damage states observed through post-earthquake field inspections. In conclusion, in this study, the corroboration of the pre- and post-earthquake evaluation of the buildings was achieved which contributes to the joint management of pre- and post-earthquake assessment efforts.

References

1. Sucuoğlu, H., Yazgan, U.: Simple survey procedures for seismic risk assessment in urban building stocks. In: Wasti, S.T., Özcebe, G. (eds.) Seismic Assessment and Rehabilitation of Existing Buildings, Earth and Environmental Sciences, pp. 97-118 Vol.29 Kluwer Academic Publishers, London (2003).
2. Sadat, M.R., Huq, M.S., Ansary, M.A.: Seismic vulnerability assessment of buildings of Dhaka City. Journal of Civil Engineering (IEB) 38(2), 159-172 (2010).
3. Özcebe, G., Sucuoğlu, H., Yücemen, M., Yakut, A., Kubin, J.: Seismic risk assessment of existing building stock in Istanbul - A pilot application in Zeytinburnu District. In: 8th National Conference on Earthquake Engineering, Earthquake Engineering Research Institute, San Francisco (2006).
4. Albayrak, U., Canbaz, M., Albayrak, G.: Rapid seismic risk assessment method for existing building stock in urban areas. International Conference on Sustainable Design, Engineering and Construction, Procedia Eng 118, 1242-1249 (2015).
5. American Standard FEMA P-154. Rapid visual screening of buildings for potential seismic hazard: A handbook (2015).
6. NZSEE. Assessment and improvement of the structural performance of buildings in earthquakes, New Zealand Society for Earthquake Engineering, Wellington, New Zealand (2006).
7. Canadian Standard NRC/IRC. Manual for screening of buildings for seismic investigation (1992).
8. Japan International Cooperation Agency (JICA). Istanbul Metropolitan Municipality (IMM) 2002. The study on a disaster prevention/mitigation basic plan in İstanbul including seismic microzonation in the Republic of Turkey. Final Report (2002).
9. SDSVB 2019. Riskli Yapıların Tespit Edilmesine İlişkin Esaslar. Çevre, Şehircilik ve İklim Değişikliği Bakanlığı.
10. Grünthal, G.: European Macroseismic Scale EMS-98. Centre Europeen de Geodynamique et de Seismologie, Luxembourg (1998).
11. Dolce, M., Speranza, E., Giordano, F., Borzi, B., Bocchi, F.: Da.DO - A web-based tool for analyzing and comparing post-earthquake damage database relevant to national seismic events since 1976. In: Atti Del XVII Convegno ANIDIS L'ingegneria Sismica in Italia. pp. 347–57 Pisa University Press (2017).
12. Yücemen, M.S., Özcebe, G., Pay, A.C.: Prediction of potential damage due to severe earthquakes. Structural Safety 26(3), 349–366 (2004).
13. Sextos, A.G.: Computer-aided pre- and post-earthquake assessment of buildings involving database compilation, GIS visualization, and mobile data transmission. Comput-Aided Civ Inf 23, 59-73 (2008).
14. Özsoy Özbay, A.E., Sanrı Karapınar, I., Ünen, H.C.: Visualization of seismic vulnerability of buildings with the use of a mobile data transmission and an automated GIS-based tool. Structures 24, 50–58 (2020).

15. Sanrı Karapınar, I., Özsoy Özbay, A.E., Ünen, H.C.: GIS-based assessment of seismic vulnerability information of old masonry buildings using a mobile data validation system. Journal of Performance of Constructed Facilities, 35(3), 04021009 (2021).
16. AFAD. Türkiye deprem haritaları interaktif web uygulaması. Available from https://tdth.afad.gov.tr/ Accessed date: 7 November 2019 [Online].
17. Yer Çizenler. 2023 Turkey Earthquakes - Building Damage Assessment Map. Available from https://hasar.6subatdepremi.org/ Accessed date: 28 May 2023 [Online].

Effect of Mass Irregularity on Seismic Performance of a Base-Isolated RC Building

Gökhan Özdemir[1][0000-0002-2962-2327], Fatmagül Ağlan[2], Anıl Gelmez[2], Barış Dilek[2], Esengül Çavdar[3*][0000-0003-1497-0908]

[1]Prof. Dr., ESQUAKE Seismic Isolator Test Laboratory, Eskisehir Technical University, Eskisehir, Turkey
[2]Undergraduate Student, Civil Engineering Department, Eskişehir Technical University, İki Eylül Campus, Eskişehir, Turkey
[3]Lecturer, ESQUAKE Seismic Isolator Test Laboratory, Eskisehir Technical University, Eskisehir, Turkey
*Corresponding Author E-mail: esengulcavdar@eskisehir.edu.tr

Abstract. This study investigates the change in seismic performance of a base-isolated reinforced concrete (RC) building due to mass irregularity in the superstructure. Accordingly, several Nonlinear Response History Analyses (NRHA) were performed considering 3-story RC building models with different combinations of story masses. Seismic isolation system of the analyzed building is assumed to be composed of Lead Rubber Bearings (LRBs). In the analyses, LRBs were modeled by deteriorating nonlinear force-displacement curves in order to consider the variation in strength of LRBs as a function of lead core heating during cyclic motion. Ground motion pairs used in the analyses were selected and scaled to represent a target spectrum as per seismic code specifications. Then, orthogonal horizontal components of each ground motion pair were subjected to structural model, simultaneously. Maximum drift ratios at story levels were recorded in the analyses and presented in a comparative manner to underline the effect of mass irregularity in the superstructure. Results were also used to discuss the effectiveness of seismic isolation to limit the drift ratios by %0.5 in case of mass irregularity.

Keywords: Mass Irregularity, Seismic Isolation, Lead Rubber Bearing, Nonlinear Response History Analyses

1 Introduction

Nowadays, many countries build structures for both commercial (e.g., shopping malls, parking, and data centers) and residential purposes. Aesthetic considerations in urban design can result in irregularities in the design of new structures. Nevertheless, it is known that numerous buildings destroyed or damaged by past earthquakes had irregularities [1]. Consequently, to ensure that these structures can be used in the long term, their seismic resistance should be thoroughly evaluated by means of dynamic analysis. It is crucial for engineers to conduct necessary checks for the variables

specified in the design stage. In Turkey, the Turkish Building Earthquake Code [2] divides irregularities into two categories: plan and vertical. Plan irregularities include torsional irregularities, floor discontinuities, and re-entrant corner irregularities. Vertical irregularities can arise in cases of soft stories, weak stories, and discontinuities in the vertical elements of the structural system. Nonetheless, considering international codes, "mass irregularity" must also be considered when designing buildings, in addition to the previously mentioned irregularities. Therefore, mass irregularity occurs when the effective mass of any floor is more than 150% that of the next [3].

Numerous studies in the literature have been devoted to investigate vertical mass irregularity. Magliulo [4], investigated the definition of mass irregularity, as outlined in international codes, and its influence on nonlinear response of structures. The authors showed that varying the mass ratios between floors did not have a major impact on linear demands. Choi [5] noted that mass irregularities affect structural responses during earthquakes. On the other hand, Tremblay and Poncet [6] questioned the need for dynamic analysis techniques for structures with vertical-mass irregularities. They evaluated the seismic performance of eight-story buildings with mass irregularities through both static and dynamic calculations and tested a variety of combinations. The researchers showed the differences in the maximum story drift ratios and concluded that the static and dynamic analysis techniques did not differ significantly in terms of the examined structural parameters. Michalis et al. [7] conducted an incremental dynamic analysis by gradually increasing the mass of certain floors in a building under consideration. This study highlighted that vertical mass irregularity has a considerable influence on the relative story drift ratio. Based on their probabilistic analysis, Pirizadeh and Shakib [8] found that mass irregularity can have a considerable impact on the seismic performance of structures. The findings of this study indicate that placing heavier stories at the bottom of the vertical direction significantly diminishes the global stability performance levels of the structure in comparison to regular structures. Mohsenian and Nikkhoo [9] studied the vulnerability level of vertical mass irregularities in reinforced concrete structures. The research revealed that the uneven distribution of mass along the building's height affects the period of the building and mass participation rates in the modal analysis. Amiri and Yakhchalian [10] studied the influence of earthquake intensity measurements on the collapse strength of steel frame members with vertical mass irregularities.

The aforementioned studies examined the influence of vertical mass irregularity on structural performance, particularly in the context of fixed-base structures. Few studies have assessed the effects of this irregularity on seismically isolated structures. Doudoumis [11] investigated the accuracy of the linear static method, which is typically used to calculate the seismic response of structures classified as regular when irregularities are present in the plan or vertical direction. The findings indicated that the linear static approach overestimates the inter-story shear force by approximately 40% in seismic isolated structures. In contrast, Wasey et al. [12] investigated the effectiveness of seismic isolation, dampers, and shear walls in structures with vertical mass irregularities. It is stated that seismic isolation system and dampers are more effective in reducing earthquake effects and shear walls are more effective in reducing story drift rates in buildings with vertical mass irregularities.

In the literature, numerous studies have examined the impact of vertical mass irregularity on the structural responses of both low-rise and high-rise fixed-base frame structures. The summarized studies indicate that vertical mass irregularity either has no significant effect on the considered structural responses or has a major impact on the drift ratios under ground motion effects. The contrasts in the literature are mainly due to the different modeling techniques and assumptions employed in the investigations. Additionally, the location of the heavy floor can influence the seismic performance of the structure. Furthermore, few studies have been conducted to analyze the effects of vertical mass irregularities on seismically isolated structures. The objective of this study was to investigate the influence of vertical mass irregularities in seismically isolated structures through a series of dynamic analyses. To reflect the actual behavior of the isolators, a deteriorating hysteretic model approach was considered in the structural model.

2 Seismic Isolation System

The seismic isolation system employed in this study was composed of lead-rubber bearings. The isolation period was 3.00 seconds and characteristic strength was calculated as 0.075. These values were established by considering design values typically used for seismically isolated structures. The analytical model approach developed by Kalpakidis and Constantinou [13,14] was used to model the strength degradation in lead rubber bearing due to temperature increase in the lead core. In this model, the authors defined the shear stress of lead, which determines the strength of the isolator in the horizontal direction, as a function of temperature. In the mathematical model presented in Equation (1), $\sigma_{YL}(T_L)$ represents the temperature-dependent shear stress of lead, σ_{YL0} represents the initial shear stress of lead, T_L represents the total temperature in the lead core and E_2 is a constant value. This model, which takes into account the strength degradation in the lead core, was later developed in a study by Kumar et al. [15] and made available in the OpenSees library as the LeadRubberX element model.

$$\sigma_{YL}(T_L) = \sigma_{YL0} \cdot \exp(-E_2 T_L) \tag{1}$$

Figure 1 provides an example of the force-displacement curve of a lead rubber bearing isolator that takes into account the strength reduction caused by the temperature rise in the lead core of isolator.

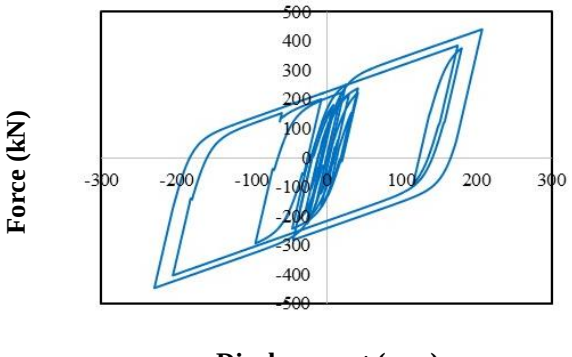

Fig. 1. A representative force-displacement curve of a typical lead rubber bearing.

3 Structural Model

The building model to be analyzed consists of 3-storey reinforced concrete building (Figure 2). The building is designed with three axes spanning 8m in the short direction and five axes spanning 6m in the long direction. The slab height was selected as 18 cm to demonstrate the rigid diaphragm behavior. The columns are 60 × 60 cm and the beams are 40 × 70 cm in dimension. Tree-dimensional and plan views of the analyzed structure are given in Figure 2. Three different mass combinations in the superstructure were considered as shown in Figure 3. Accordingly, the mass of the strong floor above the isolation level subject to change while the masses of the above floor remain the same. It is to be noted that the lateral stiffnesses of the isolation systems modeled for all structural systems were defined so that their isolation periods are identical.

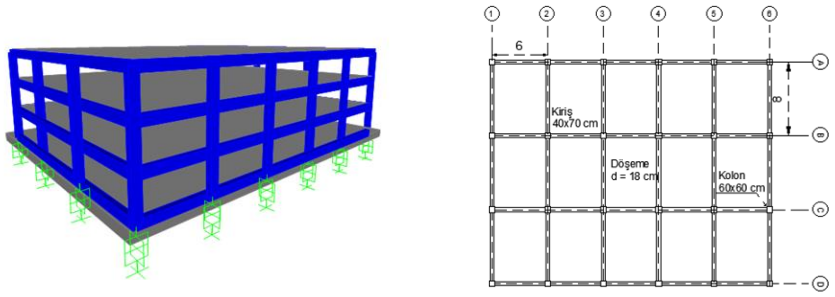

(a) (b)

Fig. 2. (a) Three-dimensional view of reinforced concrete building model and (b) plan dimensions of structural model.

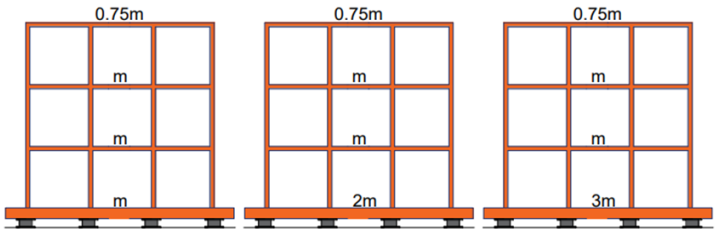

Fig. 3. The considered mass distribution scenarios for isolated structure.

4 Selection and Scaling of Ground Motion

In this study, three distinct ground motion sets, each containing 11 pairs of records. The earthquakes were selected from near-field records having a closest distance to fault rupture less than 20 km [16] and downloaded from PEER database. The scaling approach used in this study involves two stages. These are referred to as geometric mean scaling (geomean scaling) and SRSS scaling (square root of sum of squares). First, the error between individual response spectra and the design spectrum is minimized within a period range defined as $0.5T_{iso}$ and $1.25T_{iso}$. In the second stage, code specifications [2] are fulfilled. Accordingly, the average of the square root of the sum of squares (SRSS) of the spectral ordinates in the relevant period range should not be less than 1.3 times the target spectrum values. The coefficients obtained from the two-phase scaling process were multiplied to calculate the final scale factors to be applied to ground motions. Figure 4 presents the compatibility of the scaled ground motions with the selected target spectrum for all ground motion groups. Detailed information about the records and final scale factors are given in Table 1.

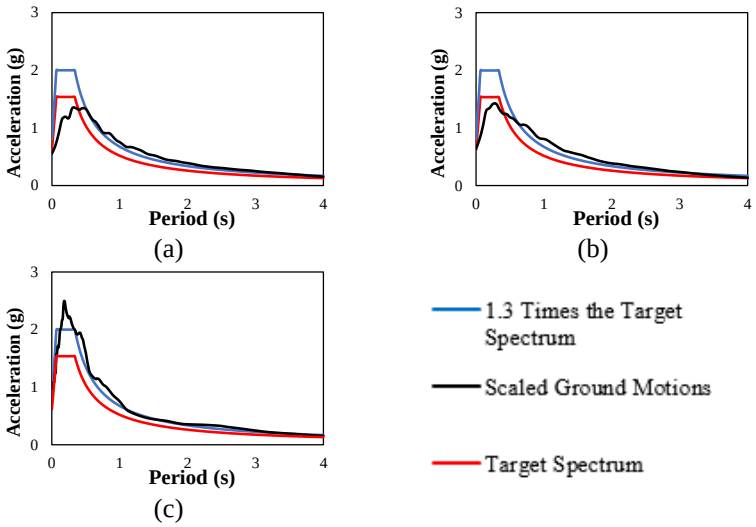

Fig. 4. Compatibility of considered target spectrum and scaled ground motions for ground motion groups (a) 1, (b) 2 and (c) 3.

Table 1. Characteristics of the selected ground motions and computed scale factors.

Group 1			
Name	**Station**	**M_w**	**Scale Factor**
Chi-Cgi, Thaiwan	TCU039	7.6	2.02
Irpinia, Italy-01	Sturno (STN)	6.9	1.96
Aloha Ave-Loma Prieta	Saratoga	6.9	1.94
Northridge-01	Pacoima Kagel Canyon	6.7	2.13
Chi-Cgi, Thaiwan	CHY006	7.6	1.51
Cape Mendocino	Centerville Beach, Naval Fac	7.0	1.45
Northridge-01	Sylmar-Olive View Med FF	6.7	0.97
Cape Mendocino	Bunker Hill FAA	7.0	1.90
Loma Prieta	BRAN	6.9	2.46
Chuetsu-oki, Japan	Joetsu Kakizakiku	6.8	1.32
Chi-Cgi, Thaiwan	TCU076	7.6	2.01

Group 2			
Name	**Station**	**Mw**	**Scale Factor**
Northridge-01	Sylmar - Olive View Med FF	6.69	1.04
Loma Prieta	LGPC	6.93	1.21
Northridge-01	Jensen Filter Plant Generator Building	6.69	0.99
Chi-Chi, Taiwan	TCU103	7.62	2.66
Cape Mendocino	Petrolia	7.01	1.18
Chuetsu-oki, Japan	Joetsu Kakizakiku Kakizaki	6.8	1.36
Bam, Iran	Bam	6.6	1.00
Northridge-01	Jensen Filter Plant Administrative Building	6.69	0.64
Cape Mendocino	Centerville Beach, Naval Fac	7.01	1.77
Chi-Chi, Taiwan	TCU129	7.62	1.58
Chi-Chi, Taiwan	TCU071	7.62	1.28

Group 3			
Name	**Station**	**Mw**	**Scale Factor**
Chi-Chi,Taiwan	TCU106	7.6	2.16
Cape Mendocino	Ferndale Fire Station	7	1.43
Irpinia Italy-01	Sturno (STN)	6.9	2.06
Loma Prieta	WAHO	6.9	1.67
Manjil Iran	Abbar	7.4	1.89
Kobe-Japan	Nishi-Akashi	6.9	2.90
Chi-Chi,Taiwan	CHY024	7.6	1.86
Corinth, Greece	Corinth	6.6	3.22
Loma Prieta	Anderson Dam (Downstream)	6.9	3.80
Tottori, Japan	MNH01	6.6	3.89
Nahanni, Canada	Site 1	6.8	2.11

5 Analysis Results

This section presents the results of NRHA conducted by three different set of ground motions scaled to represent a target spectrum in accordance with the code specifications. In the analyses, drift ratios at story levels are recorded in both orthogonal horizontal directions x and z. Figure 5 presents the variation of drift ratios through the height of the analyzed structural models. Figure 5.a shows the drift ratios computed in x-direction whereas Figure 5.b depicts the drift ratios in z-direction. The first earthquake set is represented by a solid line, the second earthquake set is represented by a dashed line, and the third earthquake set is represented by a dotted line.

Figure 5 clearly demonstrates that, in all of the cases, drift ratios are less than 0.5% limit defined for continuous functionality of seismically isolated structures after an earthquake. It is also seen that drift ratios tend to increase with an increase in strong floor mass. However, the amount of increase in drift ratios is found to be dependent of the characteristics of the ground motions used in the analyses. For instance, the effect of strong-floor mass on inter story drift ratios is only marginal based on the analyses performed with ground motion group 2. On the other hand, for analyses conducted with ground motion group 3, the amount of increase in maximum inter story drift ratio is about 20%.

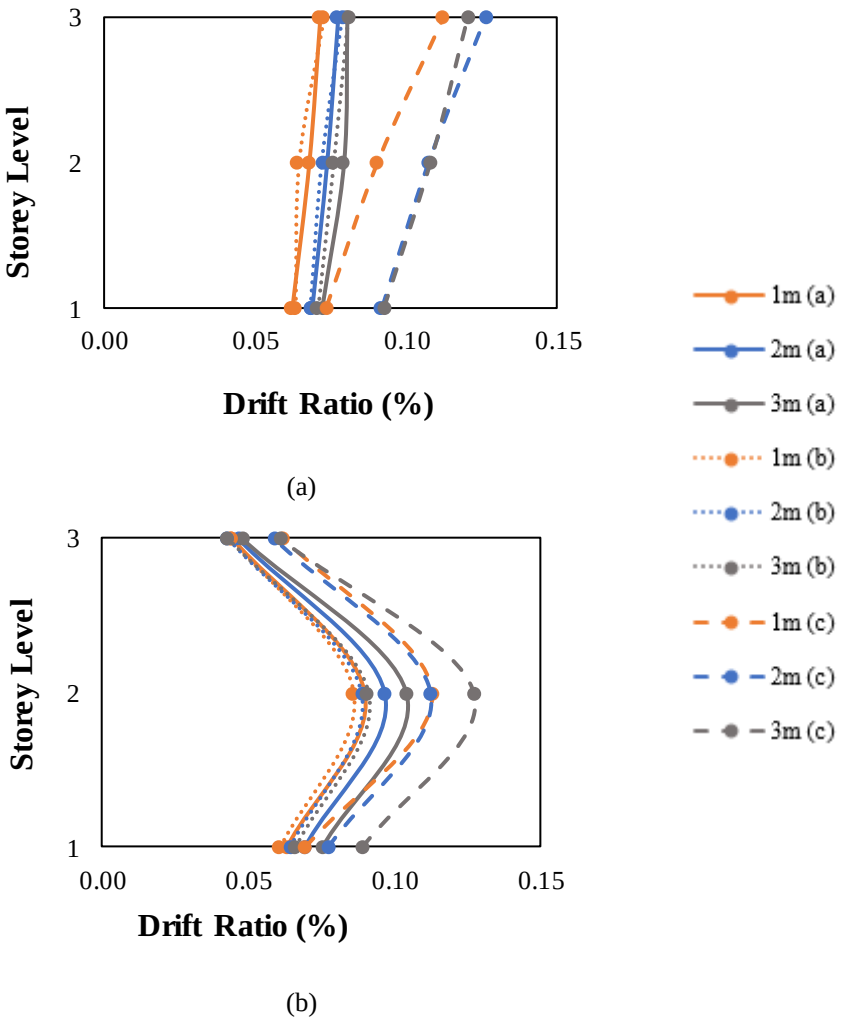

(a)

(b)

Fig. 5. Inter story drift ratios for each story level computed for

6 Conclusion

Inter story drift ratio is one of the response quantities used to assess the level of damage in a reinforced-concrete structure. And, in order to satisfy the continuous functionality of a seismically isolated structure, the code specified limitation for maximum inter story drift ratio is 0.5%. This study assesses the change in inter story drift ratios of a seismically isolated structure as a function of strong floor mass. The isolation units are composed of LRBs and modeled by deteriorating hysteretic representations. Bi-directional nonlinear response history analyses were performed with structural models having different strong floor masses. In the analyses, three distinct ground motion sets were clustered and scaled as per code specifications. It is revealed that increasing the

strong floor mass leads to an increase in maximum drift ratios. And, level of increase is found to be sensitive to ground motion characteristics used in the analyses.

References

1. Karami, A., Shahbazi, S., Kioumarsi, M.: A Study on the Effects of Vertical Mass Irregularity on Seismic Behavior of BRBFs and CBFs. Applied Sciences 10(23), 8314 (2020).
2. Turkish Building Earthquake Code (2018)
3. American Society of Civil Engineers, Structural Engineering Institute (ASCE/SEI). 2016. "Minimum Design Loads and Associated Criteria for Buildings and Other Structures." ASCE 7-16.
4. Magliulo, G., Ramasco, R., Realfonzo, R.: A Critical Review of Seismic Codes Provisions for Vertically Irregular Frames. In Proceedings of the 3rd European Workshop on the Seismic Behavior of Irregular and Complex Structures, Florence, September (2002).
5. Choi, B.J.: Hysteretic Energy Response of Steel Moment Resisting Frames with Vertical Mass Irregularities. The Structural Design of Tall and Special Buildings 13(2), 123–144 (2004).
6. Tremblay, R., Poncet, L.: Seismic Performance of Concentrically Braced Steel Frames in Multistory Buildings with Mass Irregularity. Journal of Structural Engineering 131(9), 1363-1375 (2005).
7. Michalis, F., Dimitrios, V., Manolis, P.: Evaluation of The Influence of Vertical Irregularities on The Seismic Performance of a Nine-Storey Steel Frame. Earthquake Engineering and Structural Dynamics 35(12), 1489-1509 (2006).
8. Pirizadeh, M., Shakib, H.: Probabilistic Seismic Performance Evaluation of Non-Geometric Vertically Irregular Steel Buildings. Journal of Constructional Steel Research 82, 88–98 (2013).
9. Mohsenian, V., Nikkhoo, A.: A Study on The Effects of Vertical Mass Irregularity on Seismic Performance of Tunnel-Form Structural System. Advances in Concrete Construction 7(3), 131-141 (2019).
10. Amiri, M., Yakhchalian, M.: Performance of Intensity Measures for Seismic Collapse Assessment of Structures with Vertical Mass Irregularity. Structures 24, 728-741 (2020).
11. Doudoumis, N.I., Doudoumis, I.N., Gravalas, F.: Effects of Vertical Irregularities on The Seismic Behaviour of Multi-Storey Buildings with Base Isolation. 4th European Workshop on Irregular and Complex Structures (2005).
12. Wasey, M.A., Siddiqui, M.M., Azeem M.A.: Optimum Seismic Control Systems for Vertically Irregular Buildings. Materials Today: Proceedings 65, 1674-1689 (2022).
13. Kalpakidis, I.V., Constantinou, M.C.: Effects of Heating on The Behavior of Lead-Rubber Bearing. I:Theory. Journal of Structural Engineering 135(12), 1440-1449 (2009a).
14. Kalpakidis, I.V., Constantinou, M.C.: Effects of Heating on The Behavior of Lead-Rubber Bearing. II:Verification of Theory. Journal of Structural Engineering 135(12), 1450-1461 (2009b).
15. Kumar, M., Whittaker, A.S., Constantinou, M.C.: An Advanced Numerical Model of Elastomeric Seismic Isolation Bearings. Earthquake Engineering and Structural Dynamics 43(13), 1955–1974 (2014).
16. Somerville, P.G., Smith, N.F., Graves, R.W., Abrahamson, N.A.: Modification of Empirical Strong Ground Motion Attenuation Relations to Include the Amplitude and Duration Effects of Rupture Directivity. Seismological Research Letters, 68(1), 199-222 (1997).

Effects of Configuration Changes on Live Load Carrying Capacity of Steel Railway Bridges with Same Span Length

Fatih Yilmaz[1][0000-0001-6913-5067], Mehmet Fatih Yilmaz[2][0000-0002-2746-7589], Kadir Ozakgul[3][0000-0002-2666-3836] and Barlas Ozden Caglayan[4][0000-0002-8986-9188]

[1] Recep Tayyip Erdoğan University, Civil Engineering Department, Rize, Türkiye, f.yilmaz@erdogan.edu.tr
[2] Ondokuz Mayıs University, Civil Engineering Department, Samsun, Türkiye, mehmetfatih.yilmaz@omu.edu.tr
[3] Istanbul Technical University, Civil Engineering Department, Istanbul, Türkiye, ozakgulk@itu.edu.tr
[4] Istanbul Technical University, Civil Engineering Department, Istanbul, Türkiye, caglayan@itu.edu.tr

Abstract. This study examines the impact of configuration changes on the live load carrying capacity of steel railway bridges with the same span length. Open-deck steel truss railway bridges with a span length of 60 m, currently in use on Turkish railway lines, were studied. A three-dimensional finite element model of these bridges were generated based on their original constructional drawings using a commercial structural analysis and design software. Free vibration tests were conducted using strong motion accelerometers and a test train as the excitation mechanism to assess the current condition of the bridges. The initial finite element model was updated using data from the in-situ dynamic tests and modal analyses. Subsequently, live load rating factors and safety indices were then calculated for each bridge's structural components and system under the desired loading conditions. The study concludes by determining the effects of bridge configuration differences on the live load carrying capacity of these bridges with the same span length, based on the calculated rating factors and safety indices.

Keywords: Railway Bridge, Dynamic Test, Rating Factor, Safety index.

1 Introduction

The majority of railway bridges in Turkey were built in the 19th century and are still in service for over 100 years. Since existing railway bridges are used not only for freight transport but also, for passenger transportation, changes in axle and traffic loads from the time these bridges had been built to now, decrease the safety of these bridges and thereby railways. Therefore their live load carrying capacity and safety should be checked and strengthened if necessary. Currently, to measure the load bearing capacity and structural safety of existing bridges, live load rating factors and safety (reliability)

indexes (or probability of failure) of elements and system are generally (widely) used [1-7].

Wang et al. [8] recommended some improvements to current bridge rating methods consistent with the load and resistance factor rating (LRFR) using structural reliability methods and load testing for bridges. Casas and Gomez [9] presented the calculation of load rating through proof load testing to evaluate load carrying capacity of existing highway bridges. Sayed et al. [10] proposed a evaluating methodology considering the substructure load rating for scour-prone bridges over waterways, where the substructure load rating is reviewed and reevaluated if scour occurs then the substructure load rating is compared with the superstructure rating and the lower value is assigned to the bridge. Sanayei et al. [11] presented a comparison of load ratings achieved by the LRFR method using three different approaches for a fully instrumented bridge. Bagheri et al. [12] proposed a nondestructive method for load rating of reinforced concrete (RC) slab bridges without structural plans or insufficient structural details available. Sherman et al. [13] used diagnostic load testing to improve traditional load rating procedures and obtained the positive results. Dong et al. [14] conducted static and dynamic load tests to determine the live load distribution factor (DF) and rating factor (RF) as well as serviceability and modal characteristics of an existing in-service concrete pre-stressed girder bridge. Kaloop et al. [15] investigated the use of output-only structural health monitoring (SHM) to assess the reliability and safety of a highway steel plate girder bridge.

In this study, impact of configuration changes on the live load carrying capacity for two type of open-deck steel truss railway bridges with a span length of 60 m and different configurations currently in use on Turkish railway lines was examined by using load rating and reliability procedures. 3-D finite element (FE) model of the bridges were created using a commercial structural analysis and design software SAP2000 [16] according to original constructional drawings. In-situ field dynamic tests were performed by using a special test train on these bridges to obtain the dynamic parameters of the bridges and to calibrate their FE models. Test train was used as the excitation mechanism for the bridges. Each recorded data is the data corresponding to the free vibration of the bridges, which is measured and collected after the train crosses the bridge and leaves the bridge completely. The calibration of the FE models was obtained by comparing the dynamic parameters obtained from the dynamic tests with those from the modal analysis of the models. Finally, the rating factors (RFs) and safety indexes (β) of each bridge were calculated using the calibrated 3D FE bridge models.

2 Description and FE Models of the Steel Truss Railway Bridges

The spans of the two steel railway bridges considered in this study are the same i.e., 60 m long, as well as their cross-section geometries are also similar but their truss girder geometries are different. Elevation and cross-section views of the bridges are given in Figs. 1 and 2. The bridges are about 80-85 years old and still continue to service. These simply supported bridges have a single-track railway line and comprise of two parallel main truss girders rigidly connected to the floor beams at both sides of the open-deck

consisted of floor beams and stringers. The truss girders constituted by upper and lower chords connected by verticals and diagonals are supported by steel rocker bearings as a fixed bearing and roller-rocker bearings as a sliding bearing at the seat-type abutments. The bridges are transversely stiffened with horizontal lateral bracing at both chords levels. All the members are built-up riveted sections produced by connecting various plates, angles and channel sections through rivets. All connections are manufactured using rivets. A general view of the bridges is given in Figs. 3 and 4.

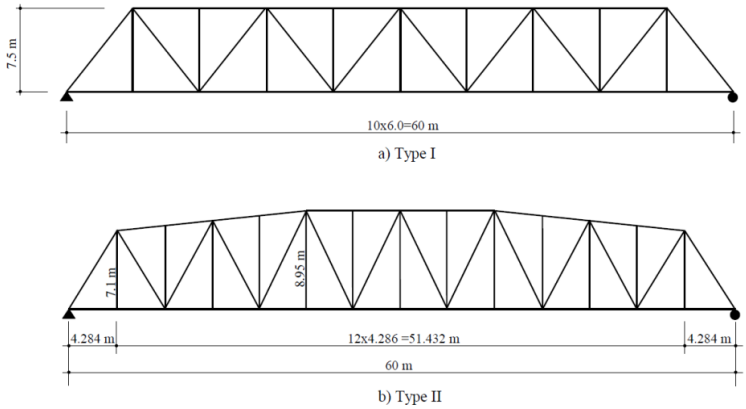

Fig. 1. Elevation view of the bridges.

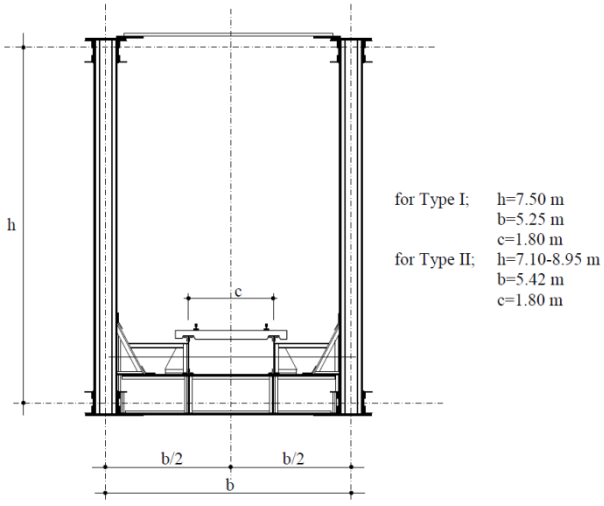

Fig. 2. Cross-section view of the bridges.

Fig. 3. General view of the Bridge I.

Fig. 4. General view of the Bridge II.

3D FE models of these steel bridges were created with the SAP2000 [16] software using original construction drawings (see Fig. 5). All the members were modeled using 3D beam-column element with two nodes. The railway track consisted of the rails, guard rails and sleepers on the bridges was modeled as lumped masses along the stringers. Additionally, the riveted gusset plate connections and the bearings were simulated by using linear link and translational spring elements, respectively. The grade of the steel material used to manufacture the bridges, as indicated in the original constructional drawings, is taken as St 37 (S235).

3 In-Situ Dynamic Tests of the Bridges

To obtain the experimental dynamic properties of the bridges and to verify and to calibrate the FE models, in-situ dynamic tests were conducted using SA-102 model

accelerometers placed at mid and quarter points of the span on both side of the bridges. A 16-channel data acquisition system was used to record and collect the free vibration data at a sampling rate of 100 Hz after the test train, consisting of a DE24000 class diesel locomotive and four passenger cars, had completely left the bridge. After processing the collected raw acceleration data, the acceleration spectra of the bridges were derived from the processed data using Fast Fourier Transform (FFT) technique (see Fig. 6). The initial FE models were updated by adjusting the rigidities of the spring elements to minimum the difference between the experimentally obtained natural frequencies and those from the modal analysis (see Table 1).

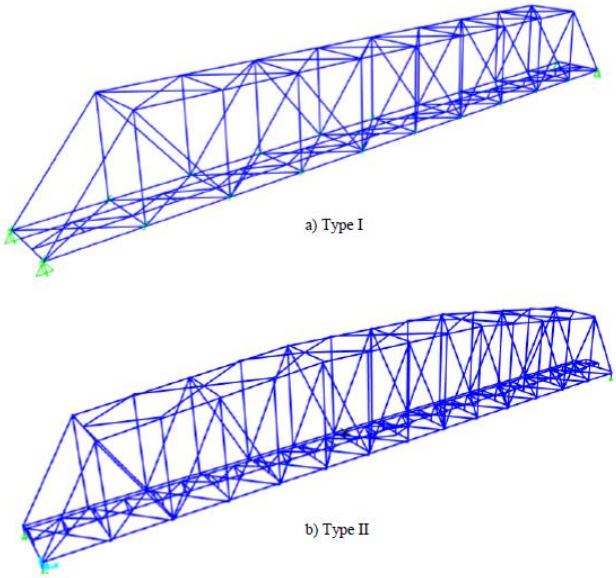

Fig. 5. 3D FE models of the bridges.

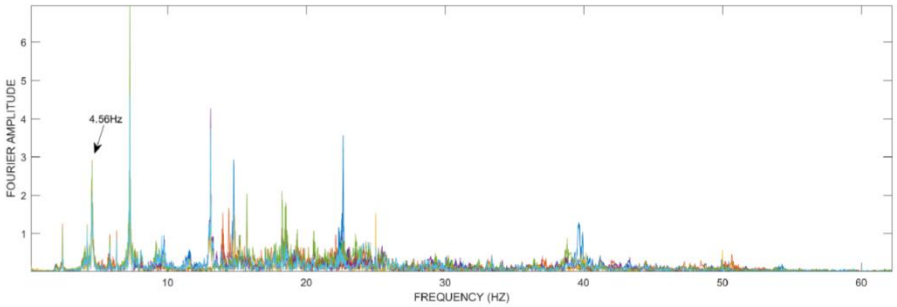

Fig. 6. Fourier spectra obtained from dynamic measurements of Bridge II.

Table 1. Natural frequencies of the bridges.

	Experimental frequency (Hz) for 1st vertical bending mode	Numerical frequency (Hz) for 1st vertical bending mode	Relative Difference (%)
Bridge I	4.10	4.19	2.20
Bridge II	4.56	4.69	2.85
Relative Difference (%)	11.22	11.93	

4 Load Rating Factors (RF) and Safety Indexes (β) of the Bridges

To evaluate and compare live load carrying capacity of the bridges, the RFs of each bridge member were calculated using the updated FE models for the UIC-71 European train load model [17] (see Fig. 7). The RF is defined as the ratio of the element capacity minus the dead load effect to the live load effect including the impact effect. In this study, the RF formulation based on Allowable Stress Rating (ASR) method was used [18]. A RF value greater than 1.0 for a desired load pattern indicates that the bridge can safely carry that live load. The RF values obtained for the bridges are presented in Table 2.

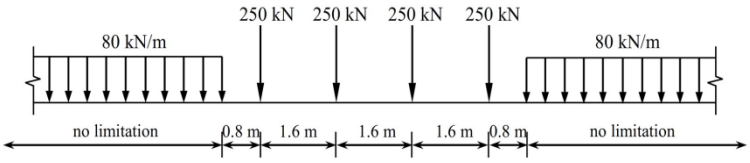

Fig. 7. UIC load model 71 [17].

Structural safety margin (g=R-Q) can be defined as the difference between the structural resistance R (capacity) and the load effect Q (demand). It can be inferred that the structure fails when g is less than 0, while the structure is safe with g values greater than 0. Safety (reliability) index (β) is expressed as the ratio of mean value of the safety margin (g) to its standard deviation. A high safety index (β) indicates a safer structure. According to the regulations of the Turkish Railways Administration, a safety index (β) for railway bridges must exceed the target safety index value (β_{target}=3.0) for UIC 71 loading. The obtained β values of the bridges are given in Table 2.

As can be seen from the Table 2, it was found out that the increases in the rating factors and safety indexes of structural elements in Bridge II were approximately up to 122% and 80%, respectively.

Table 2. Rating Factors (RFs) and safety indexes (βs) of the bridges.

Structural elements	Bridge I		Bridge II		Relative Difference (%)	
	RF	β	RF	β	RF	β
Upper chord	1.99	4.55	1.75	4.11	12,06	9.67
Lower chord	2.32	5.04	2.68	5.46	-15.52	-8.33
Diagonal	2.31	5.02	2.11	4.74	8.66	5.58
Vertical	1.40	3.26	3.11	5.85	-122,14	-79.45
Floor beam	1.32	3.00	1.95	4.48	-47.73	-49.33
Stringer	1.32	3.00	2.17	4.84	-64.39	-61.33
Upper wind braces	3.63	6.22	5.99	7.15	-65.01	-14.95
Lower wind braces	2.96	5.73	3.23	5.95	-9.12	-3.84

5 Conclusions

In this study, the changes in the load rating factors (RFs) and safety indexes (βs) of steel railway bridges with the same span length but different configuration were investigated. For this, two types of open-floor steel truss railway bridges with a span of 60 m, which are still in service on Turkish railway lines, were considered. 3D FE model of the bridges were produced using the structural analysis and design software according to the original constructional drawings. To obtain the dynamic properties and to update the initial FE models of the bridges, in-situ dynamic tests were performed using accelerometers placed on the bridges, a data acquisition system, and a test train as excitation mechanism. The RFs and βs for each bridge member were calculated using the updated FE models for the UIC-71 European train load pattern. Upon comparing the results, it was observed that the Bridge II has a greater advantage in terms of live load bearing and structural safety. These results may be useful in informing future bridge manufacturing choices.

References

1. Akgül, F., Frangopol, D.M.: Time-dependent interaction between load rating and reliability of deteriorating bridges. Engineering Structures 26(12), 1751-1765 (2004).
2. Bell, E.S., Lefebvre, P.J, Sanayei, M., Brenner, B., Sipple, J.D., Peddle, J.: Objective load rating of a steel-girder bridge using structural modeling and health monitoring. Journal of Structural Engineering 139, 1771-1779 (2013).
3. Lalthlamuana, R., Talukdar, S.: Rating of steel bridges considering fatigue and corrosion. Structural Engineering and Mechanics 47(5), 643-660 (2013).

4. Tohme, R., Yarnold, M.: Steel bridge load rating impacts owing to autonomous truck platoons. Transportation Research Record: Journal of the Transportation Research Board 2674(2), 57-67 (2020).
5. Baisthakur, S., Chakraborty, A.: Experimental verification for load rating of steel truss bridge using an improved Hamiltonian Monte Carlo-based Bayesian model updating. Journal of Civil Structural Health Monitoring 11, 1093-1112 (2021).
6. Bouzas, O., Conde, B., Cabaleiro, M., Riveiro,B.: A holistic methodology for the non-destructive experimental characterization and reliability-based structural assessment of historical steel bridges. Engineering Structures 270, 114867 (2022).
7. Hou, R., Jeong, S., Lynch, J.P., Ettouney, M.M., Law, K.H.: Data-driven analytical load rating method of bridges using integrated bridge structural response and weigh-in-motion truck data. Mechanical Systems and Signal Processing 163, 108128 (2022).
8. Wang, N., O'Malley, C., Ellingwood, B.R., Zureick, A.H.: Bridge rating using system reliability assessment. I: Assessment and verification by load testing. Journal of Bridge Engineering 16(6), 854-862 (2011).
9. Casas, J.R., Gomez, J.D.: Load rating of highway bridges by proof-loading. KSCE Journal of Civil Engineering 17(3), 556-567 (2013).
10. Sayed, S.M., Sunna, H.N., Moore, P.R.: Load rating of pile-supported bridges susceptible to scour. Journal of Bridge Engineering 18(5), 439-449 (2013).
11. Sanayei, M., Reiff, A.J., Brenner, B.R., Imbaro, G.R.: Load rating of a fully instrumented bridge: Comparison of LRFR approaches. Journal of Performance of Constructed Facilities 30(2), (2015).
12. Bagheri, A., Alipour, M., Ozbulut, O.E., Harris, D.K.: A nondestructive method for load rating of bridges without structural properties and plans. Engineering Structures 171, 545-556 (2018).
13. Sherman, R.J., Hebdon, M.H., Lloyd, J.B.: Diagnostic load testing for improved accuracy of bridge load rating. Journal of Performance of Constructed Facilities 34(5), (2020).
14. Dong, C., Bas, S., Debees, M., Alver, N., Catbas, F.N.: Bridge load testing for identifying live load distribution, load rating, serviceability and dynamic response. Frontiers in Built Environment 6, 1-14 (2020).
15. Kaloop, M.R., Eldiasty, M., Hu, J.W.: Safety and reliability evaluations of bridge behaviors under ambient truck loads through structural health monitoring and identification model approaches. Measurement 187, 110234 (2022).
16. SAP2000. Structural analysis program. Computers and Structures Inc., Berkeley, California, USA, 2020.
17. UIC 776-1. Loads to be considered in railway bridge design. 5th Edition, International Union of Railways, Paris, 2006.
18. Caglayan, O., Ozakgul, K., Tezer, O.: Assessment of existing steel railway bridges. Journal of Constructional Steel Research 69(1) , 54-63 (2012).

Finite Element Analysis on Axial Compressive Performance of RHHCFST Short Columns with Longitudinal Stiffeners

Zhijian Yang*, Wenzhi Zuo

School of Civil Engineering, Shenyang Jianzhu University, No.25 Hunnan Middle Road, Shenyang, China
faemail@163.com

Abstract. To study the axial compressive performance of reinforced hollow high concrete filled square steel tubular (RHHCFST) short columns with longitudinal stiffener, twelve members were simulated and analyzed by finite element method. The finite element analysis results showed that the bearing capacity of RHHCFST short columns is significantly increased by using stiffener, while the bearing capacity of the double-stiffeners members is slightly higher than the single-stiffener members. The whole process of loading can be divided into elastic stage, elastoplastic stage, plastic strengthening stage and descending stage. For the RHHCFST members with stiffener, the internal force shared by the steel tube and the concrete reached the peak value at the same time, and the internal force shared by the steel tube did not decrease significantly after reaching the peak value. When the peak load was reached, the proportion of internal force shared by the steel tube section of the RHHCFST members is 18%~24%, and that of the RHHCFST members with longitudinal stiffener is 32%~34%. It can be concluded that the stiffeners can inhibit the buckling of steel tube, enhance the restraint effect on concrete, enable the steel tube section to share more internal force by making full use of compressive performance of the steel. Compared with increasing the thickness of steel tube, adding stiffeners inside of the steel tube can more effectively improve the axial compressive performance of the RHHCFST member, and can also reduce the cost by reducing the amount of steel consumption.

Keywords: First Keyword, Second Keyword, Third Keyword.

1 Introduction

With the development of concrete filled steel tube (CFST) structures, scholars have proposed different forms of concrete filled steel tube members and conducted a large number of experiments and finite element studies. Hollow concrete-filled steel tube is a type of CFST made by filling concrete in the steel tube using centrifugal method, which reduces the dead weight of the concrete, and can lay pipelines in the hollow area, which can save building space. In 1986, Cai et al.[1-2]first conducted axial compression

tests on hollow concrete filled steel tubular columns, studying the effects of void ratio and slenderness ratio on the axial compressive performance of members, and deriving the ultimate bearing capacity formulas for short and long columns under axial compression. In 2019, Zhao et al. [3] conducted tests on centrifugal concrete filled steel tubular short columns under axial compression, and derived a formula for calculating the ultimate compressive strength of CFST members considering the effect of confinement, which can be used to estimate the ultimate compressive strength of concrete filled steel tubular members.

Reinforced hollow concrete-filled steel tube is a new type of composite member made by placing prefabricated PHC tube columns into steel tube and pouring sandwich concrete afterwards. Research shows [4-5] that spiral stirrups can enhance the constraint on the concrete of tubular columns. Compared to the constraint of square steel tube on the core concrete, the constraint of spiral stirrups is more uniform, which has certain limitations on the local buckling of members during the late loading period. This effectively solves the problems of poor ductility and low stability of hollow square steel tube concrete.

The traditional CFST members are prone to buckling. When the members are damaged, the steel tube only yields at the buckling point, which cannot fully exert the performance of the steel. In response, some scholars have proposed adding stiffeners to the square steel tube wall, and have conducted a large number of experiments and finite element studies [6-7] on stiffener members. It has been found that stiffener can enhance the restraint effect of concrete at the corners of the steel tube and at the stiffeners, and can significantly delay the local buckling of the steel tube. Different stiffening measures have different effects on the mechanical properties of concrete filled steel tubular members. In 2021, Yang [8] investigated the effects of the yield strength of steel tube and the type of stiffening measures on the failure pattern, load-displacement curve, bearing capacity, combined elastic modulus, ductility coefficient, and other mechanical indicators of the specimen. The research results show that the stiffening measures of cable-stayed steel plate stiffener with circular holes are more effective in improving the bearing capacity and ductility, while the stiffening measures of double row steel plate ribs are more effective in improving the combined elastic modulus.

In 2021, Li [9] conducted a study on the behavior of reinforced hollow square steel tube high-strength concrete (RHHCFST) short columns under axial compression, and found that the wall thickness of the steel tube had the greatest impact on the axial compression performance of the members. To improve the axial compression bearing capacity of RHHCFST members, this paper proposes to weld longitudinal stiffeners in the middle of the steel tube section. A total of 12 members, including non-stiffener, single-stiffener and double-stiffener members were simulated by finite element method, and the axial compression performance of the three types of members was compared and analyzed. Figure (1) is a cross-sectional diagram of three types of members.

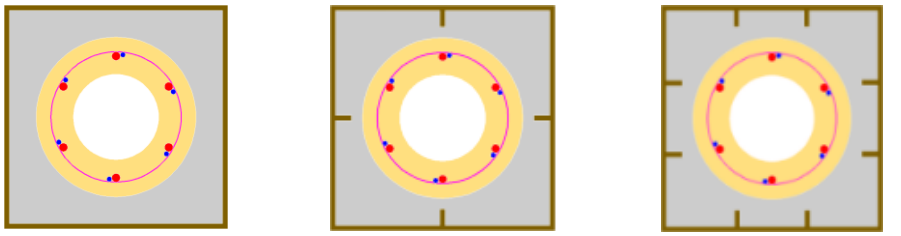

Non-stiffener member Single-stiffener member Double-stiffeners member

Fig. 1. Schematic Diagram of Section

2 Finite Element Model

2.1 Model Establishment

Concrete, end plates, end stiffeners, and longitudinal stiffeners used solid elements (C3D8R), steel tube used shell elements (S4R), and steel bars used truss elements (T3D2). The interaction between steel tube and stiffener, between end plate and stiffener was binding. The sandwich concrete was set in hard contact with steel tube and stiffener. The tangential contact between steel tube and sandwich concrete adopted a penalty function, with a friction coefficient of 0.4. The contact mode between sandwich concrete, PHC column concrete, and end plate was hard contact.

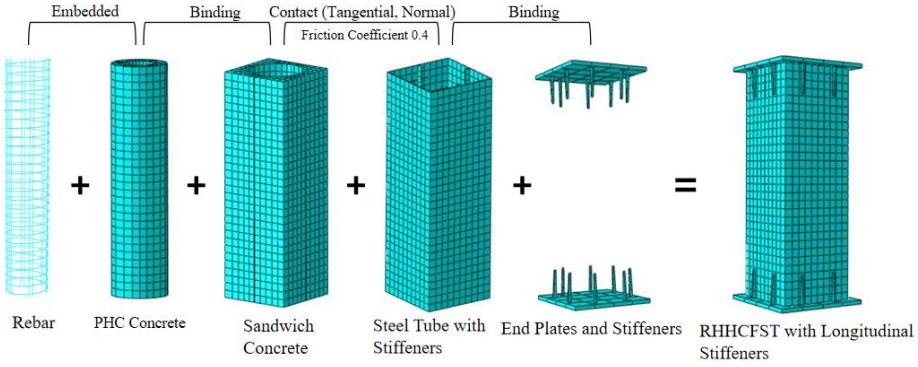

Fig. 2. Model diagram.

2.2 Constitutive Relation

The stress-strain relationship model of core concrete under compression modified by Liu[10] was adopted for the constitutive relationship of concrete. The finite element analysis is in a completely ideal situation, but due to the large cross-sectional dimensions of members, size effects should also be considered in practical situations. The formula for calculating the peak stress and peak strain size effect of confined concrete proposed by Chen[11] was used, as shown in Formula (1). Eventually, the σ_0 and ε_0 were replaced with $\sigma_0\gamma_\sigma$ and $\varepsilon_0\gamma_\varepsilon$.

$$\gamma_\sigma = \frac{0.7 - 0.99\mathrm{p}f_c'^{-1}}{\sqrt{1 + 0.34\sqrt{\mathrm{A_c}\left[\pi\left(1 - 3\mathrm{p}f_c'^{-1}\right)\right]^{-1}}}} + 0.63 \quad \gamma_\varepsilon = 1.4\gamma_\sigma - 0.4 \tag{1}$$

Where, γ_σ, γ_ε, A_c, p are the size effect coefficients of the peak axial stress and peak axial strain, the cross-sectional area of the concrete, and the confining pressure, respectively.

The tensile stress-strain relationship of concrete is expressed by the fracture energy GF and calculated according to American standard[12].

$$G_F = \left(0.0469\mathrm{d_{max}}^2 - 0.5\mathrm{d_{max}} + 26\right)(0.1f_c)^{0.7} \tag{2}$$

The yield strength of steel tube and longitudinal stiffeners f_y=355MPa ≤ 460MPa, so the five-fold model is used for the constitutive relationship. The yield strength of ordinary steel bars, prestressed steel bars, and spiral stirrups are greater than or equal to 460MPa, and they are high-strength steel. Therefore, the two-fold model is used for the constitutive relationship.

2.3 Model Parameter

The cross-sectional dimension of the model concrete is 400mm×400mm, the wall thickness of steel tube is 5mm, 6mm, 7mm, 8mm. The strength grade of sandwich concrete is C80, and the elastic modulus of concrete is defined as 4733√(f_c), with a Poisson's ratio of 0.2. The yield strength of steel tube is 355MPa, elasticity modulus 206000MPa, and Poisson's ratio 0.3. Specific parameters of members are shown in Table 1. PHC column has an outer diameter of 300mm, an inner diameter of 160mm, and a spiral stirrup coil diameter of 230mm. The concrete strength grade is C80. The specific parameters are shown in Table 2.

Table 1. Parameter of members

Specimen label	B/mm	L/mm	t/mm	t_s/mm	h_s/mm	f_{cu}/MPa	Notes
N5-80	400	1200	5	5	30	80	Non-stiffener
S5-80	400	1200	5	5	30	80	Single-stiffener
DS5-80	400	1200	5	5	30	80	Double-stiffeners
N6-80	400	1200	6	6	30	80	Non-stiffener
S6-80	400	1200	6	6	30	80	Single-stiffener
DS6-80	400	1200	6	6	30	80	Double-stiffeners
N7-80	400	1200	7	7	30	80	Non-stiffener
S7-80	400	1200	7	7	30	80	Single-stiffener
DS7-80	400	1200	7	7	30	80	Double-stiffeners
N8-80	400	1200	8	8	30	80	Non-stiffener
S8-80	400	1200	8	8	30	80	Single-stiffener
DS8-80	400	1200	8	8	30	80	Double-stiffeners

Note: B is the section width dimension of tube, L is the height of member, t is the wall thickness of steel tube, t_s is the thickness of Stiffene, h_s is the height of stiffener, f_{cu} is the compressive strength of concrete cube.

Table 2. Material Property of Steel

Steel products	Diameter (Thickness)/mm	Yield strength /MPa	Elastic modulus /MPa
Prestressed steel bar	7.1	1470	206000
Ordinary steel bar	16	460	206000
Spiral stirrup	4	635	206000
Steel tube	5~8	355	206000
Stiffener	5~8	355	206000

3 Finite Element Analysis

3.1 Whole Process Analysis

Figure (3) shows the internal force displacement curve shared by each component in the middle section of a typical member N5-80. Four characteristic points are defined

for the entire process of loading a typical member and divided into four stages, namely, OA (elastic stage), AB (elastoplastic stage), BC (plastic strengthening stage), and CD (falling stage).

In the OA stage, the load increases linearly, and both steel tube and concrete are in the elastic working stage, with consistent deformation and almost no interaction. In the AB stage, the Poisson's ratio of concrete gradually exceeds the Poisson's ratio of steel tube. Steel tube has a confinement effect on concrete, leaving the concrete in a three-dimensional compression state. When reaching point B, the steel tube partially appears slightly buckling, and the curve begins to exhibit nonlinear growth. During the BC stage, the steel tube yields in a large area, and some of the steel bars have also yielded. The prestressed steel bars change from a tensile state to a compressive state. During the CD stage, the bearing capacity of the member significantly decreases, both the sandwich concrete and the PHC column concrete reach the ultimate compressive strain, and damage occurs. When reaching point D, the prestressed steel bars reaches its yield strength.

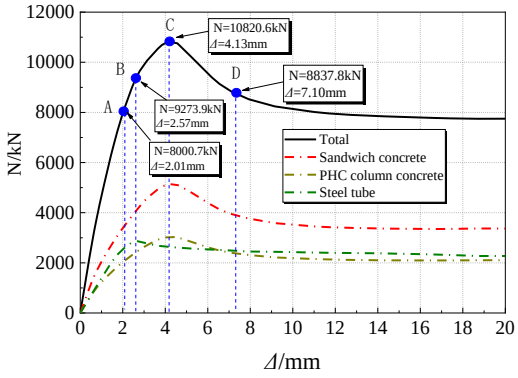

Fig. 3. Shared internal force-displacement curve of N5-80

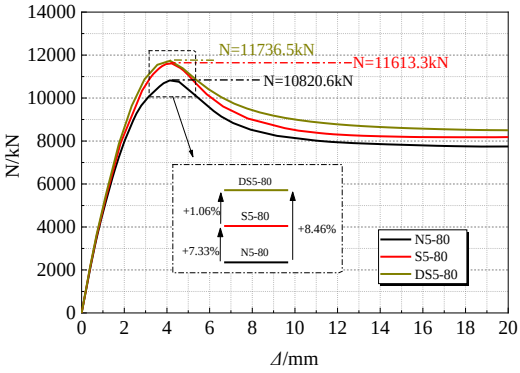

Fig. 4. Load-displacement curves for three types of members

3.2 Load-Displacement Curve

When the wall thickness of the steel tube is 5mm, the load-displacement curves of the non-stiffener, single-stiffener and double-stiffeners members are shown in Figure (4).

The initial stiffness of the three types of member is relatively close, and the bearing capacity of the single-stiffener and double-stiffeners members have increased by 7.33% and 8.46% compared to the non-stiffener member, while the bearing capacity of the double-stiffeners member has only increased by 1.06% compared to the single-stiffener member.

3.3 Section Sharing Internal Force

Figure (5) shows the shared internal force-displacement curve with a steel tube wall thickness of 5mm. Before reaching the peak load, the steel tube of a non-stiffener member has reached its ultimate bearing capacity and entered a declining stage. The steel tube of a single-stiffener member reached its ultimate bearing capacity before the peak load, and then tended to stabilize, with a slow decline in the curve. After reaching the ultimate bearing capacity, the steel tube of the double stiffeners member had no obvious downward section, and even had an upward trend. The above phenomenon indicates that stiffener can enable the steel tube section to share more internal forces, thereby improving the bearing capacity and ductility of the member.

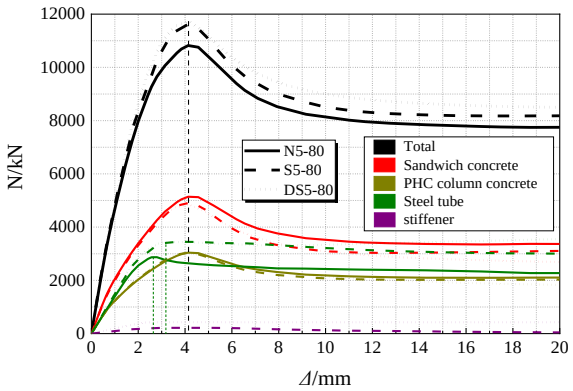

Fig. 5. Shared internal force-displacement curve for three types of members

Figure (6) shows the sectional height shared internal force curve of members N5-80, S5-80, and DS5-80. When loaded to the characteristic point C, the internal forces shared by the steel tube at the heights of 1/6 and 5/6 columns of the stiffener member become significantly smaller, and the sandwich concrete shared a larger internal force, but the stresses shared by the steel tube at other locations are also less. Steel tube with stiffener members can share more axial internal forces due to their small deformation; Accordingly, the internal force shared by the sandwich concrete is relatively small. When loaded to characteristic point D, although the concrete of the stiffener member had retired from its compressive work, the steel tube had not yet significantly buckled and can continue to bear the axial load, so the proportion of the internal force shared by the steel tube increases sharply. At this moment, the concrete and steel tube of the stiffener member almost all quit working, so the stiffener member exhibits better ductility.

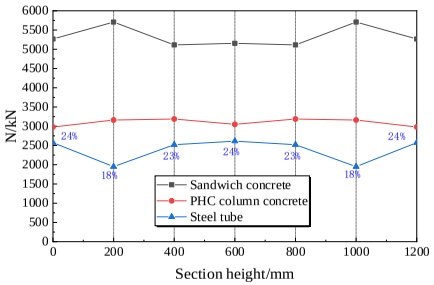

N5-80

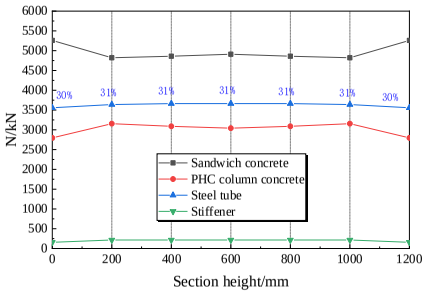

S5-80

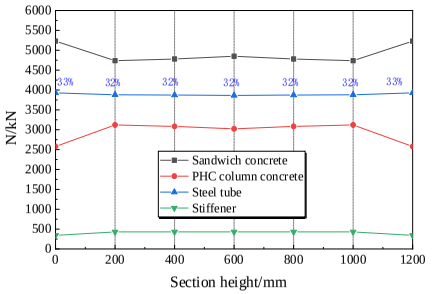

DS5-80

Characteristic point C

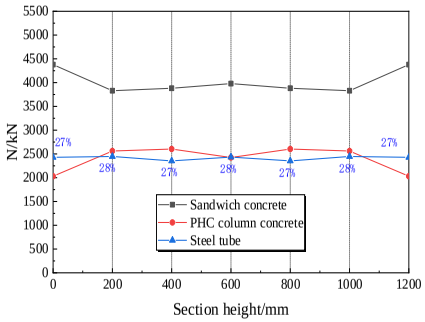

N5-80

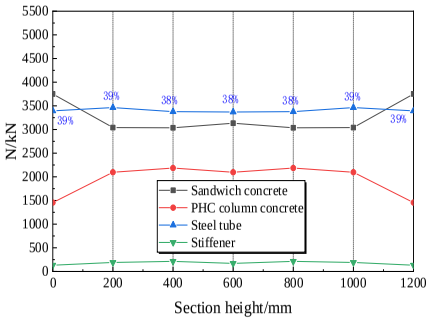

S5-80

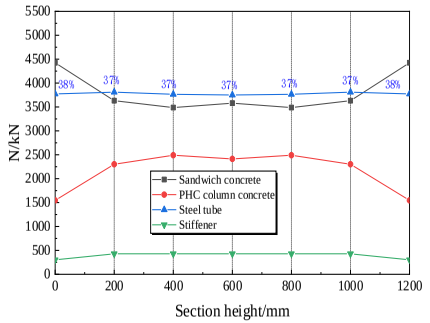

DS5-80

Characteristic point D

Fig. 6. Shared internal force - section height curve

3.4 Comparison of Section Forms

As shown in Figure (7), the finite element calculation results show that the ultimate bearing capacity does not increase linearly with the increase in steel consumption.

Table (3) is a comparison table of sectional forms. Through three control groups, it is found that the bearing capacity of single-stiffener members with low steel content and non-stiffener members with high steel content are close to or even higher.

Taking the first group of control groups as an example, Figure (8) shows a comparison diagram of the internal force displacement curves shared by each component in the middle sections of S5-80 and N6-80. The load-displacement curves of the two members almost coincide. Before the peak load, the axial load borne by the steel tube is almost the same. After the peak load, the bearing capacity of the steel tube of the member S5-80 hardly decreases. Compared to the single-stiffener member N6-80, the steel tube shares more internal forces. After the steel tube of N6-80 reaches its ultimate bearing capacity, it begins to enter the descending section.

Table 3. Comparison table of sectional forms

Control group	Specimen label	Steel tube wall thickness/mm	Stiffener wall thickness/mm	Stiffener height/mm	B/t	Bearing capacity/kN	α
1	S5-80	5	5	30	80	11613.3	6.08%
	N6-80	6	6	30	66.7	11500.4	6.76%
2	S6-80	6	6	30	66.7	12116.3	7.27%
	N7-80	7	7	30	57.1	12281.8	7.87%
3	S7-80	7	7	30	57.1	12719.0	8.47%
	N8-80	8	8	30	50	12697.8	8.97%

α is the Steel content $\alpha=A_S/A$

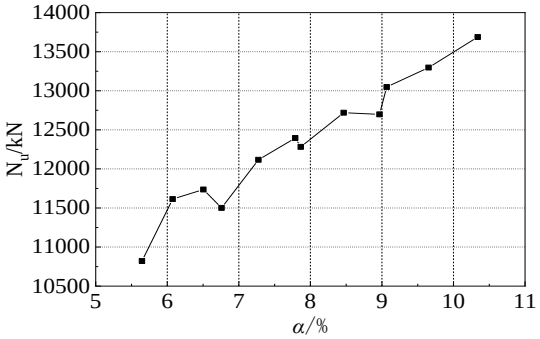

Fig. 7. Bearing capacity-steel ratio curve

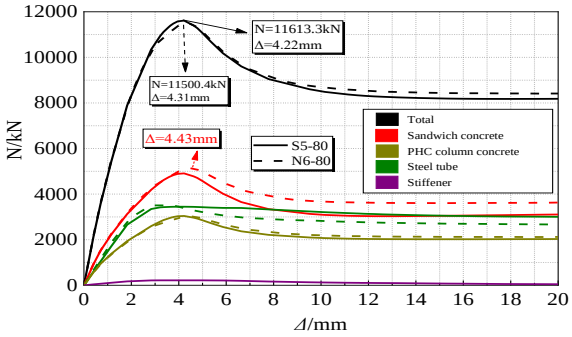

Fig. 8. Shared internal force-displacement curve for S5-80 and N6-80

4 Conclusion

This article conducted finite element simulation on 12 members, studied the influence of stiffeners on the mechanical properties and mechanism of axial compressive performance of RHHCFST short columns, and obtained the following conclusions.

Stiffeners suppress the bulging of steel tube, allowing them to bear more axial loads, fully utilizing the axial compression performance of the steel, and the stiffeners themselves can also bear a small portion of the axial load. Stiffeners can also enhance the restraining effect of steel tube on concrete, enabling the concrete to be better placed in a three-dimensional compression state, improving the compressive strength of sandwich concrete, and thus enhancing the bearing capacity of components.

When the yield strength of the steel tube is 355MPa, the bearing capacity of RHHCFST short columns is significantly increased by using stiffener, while the bearing capacity of the double-stiffeners members is slightly higher than the single-stiffener members. Therefore, the stiffeners should be installed in the middle of the steel tube wall section to achieve the effect of low cost and high performance.

Compared to increasing the wall thickness of reinforced hollow concrete filled steel tubular members, adding ribs in the middle of the steel tube wall can more effectively improve the axial compression performance of the member, and can also reduce the amount of steel used to reduce costs.

Acknowledgements
This research was supported by National Natural Science Foundation of China (52178148, 51938009), Excellent Youth Fund of Liaoning Province (2021-YQ-10), Fundamental scientific research project of Liaoning Provincial Department of Education (LJKZ0598).

References

1. Cai S H, Gu W P. Behaviour and Ultimate Strength of Short Concrete-Filled Steel Tubular Hollow Columns[J]. Building Science, 4(4): 23-31(1986).
2. Cai S H, Gu W P. Behaviour and Load-Carrying Capacity of Long Concrete-Filled Steel Tubular Hollow Columns[J]. Building Science, 2(4): 11-21(1987).
3. Zhao Y G, Yan X F, Lin S Q. Compressive Strength of Axially Loaded Circular Hollow Centrifugal Concrete-Filled Steel Tubular Short Columns[J]. Engineering Structures, 201(15):109828.1-109828.15(2019).
4. Chen Z P, Jing C G, Xu J J, et al. Mechanism and Load-Bearing Capacity of Square Steel Tubular and Spiral Stirrup Composite Confined-Concrete Stub Columns Under Axial Compression[J]. China Civil Engineering Journal, 50(5): 47-56(2017).
5. Chen Z P, Jing C G, Zhou S W, et al. Experimental Study on Failure Mechanism of Square Steel Tube and Spiral Reinforcement Multiple Confined Concrete Stub Columns Under Axial Compression[J]. Journal of Building Structures, 39(3): 93-102(2018).
6. Huang H, Zhang A G, Li Y, et al. Experimental Research and Finite Element Analysis on Mechanical Performance of Concrete-Filled Stiffened Square Steel Tubular Stub Columns Subjected to Axial Compression[J]. Journal of Building Structures, 32(2):75-82(2011).
7. Li B, Guo S Z, Gao Y C. Experimental Research on Mechanical Behavior of Concrete-Filled Thin-Walled Stiffened Square Steel Tubular Short Column Under Axial Load[J]. Journal of Building Structures, 38(1):218-225(2017).
8. Yang Y F, Guo H X. Axial Compression Behavior of The Stiffened Concrete-Filled Thin-Walled High-Strength Square Steel Tube Stub Columns[J].Journal of South China University of Technology(Natural Science Edition), 49(8):43-52(2021).
9. Li X. Behavior of Reinforced Hollow High Strength Concrete Filled Square Steel Tube Short Columns under Axial Compression[D]. Shenyang: Shenyang Jianzhu University(2021).
10. Liu W. Research on Mechanism of Concrete-Filled Steel Tube Subjected to Local Compression[D]. Fuzhou: Fuzhou University(2005).
11. Chen P. Research on Size Effect of Axially Loaded Circular Concrete-Filled Steel Tubular Stub Column[D]. Harbin: Harbin Institute of Technology(2018).
12. ACI 318-14, Building Code Requirements for Structural Concrete and Commentary, Farmington Hills, Michigan, USA(2014).

Indicators Affecting the Design of Subway Stations to be More Responsive in Emergencies

Mahshid Doostmohamadian [1], Mahmood Hosseini[2*[0000-0003-3142-4087]]

[1] Azad University, Department of Architecture, Science and Research Branch of the Islamic, Tehran, Iran,
doostmohamadian@gmail.com
[2] Eastern Mediterranean University, Department of Civil Engineering, , North Cyprus,Türkiye,
mahmood.hosseini@emu.edu.tr
*Corresponding Author

Abstract. Regarding the importance of subway stations as the potential shelters after major earthquakes in populated cities, in this study, after reviewing and classifying the previous related publications, three assumptions with regard to design flexibility of these spaces are made and discussed as follow. 1) a flexible design for these spaces would allow for a consistent space in normal and emergency situations, 2) factors, such as favorable geotechnical quality of the underground structure and distance from the seismic faults in the area, have a great influence on the flexibility of the stations design, and 3) factors such as the maximum distance to existing routes and the use of maximum slope to shorten the length of access spaces have a great impact on station architecture as a temporary shelter. The research methodology for this paper has been a descriptive (Delphi) method, by using questionnaires. For this purpose, after identifying the flexible environment, the factors influencing flexibility were identified according to the abovementioned assumptions and formulated in a questionnaire. After scoring, the results were analyzed by using SPSS program, and the correlation tables were obtained. After analyzing the SPSS outputs, the degree of internal consistency between the questions was found. Then, the mean and standard deviation were determined for each component indicating the factors influencing future research. By using the results of this study it would be possible to find a way to fit into different functions as a multipurpose space with a structure adaptable to environmental change over time for different activities.

Keywords: subway stations; underground structures; potential vulnerabilities; flexible design

1 Introduction

As most subway stations have underground structures, their safety is of paramount importance. Indicators affecting the design of these underground spaces with a high level of safety include architectural indicators such as passive defense features, as well as technical and economic protection. Following the development of transportation

industry and services, many countries have used the subway station as a temporary accommodation to address concerns in critical situations.

In this research an analytical method for designing multipurpose architectural spaces is presented based on architectural flexibility, which is a great factor to help for creation of a multi-purpose space that provides three functions including a transit station, a commercial-cultural complex and finally a temporary accommodation space.

The urban transport industry has the task of facilitating emergency management and reducing potential vulnerabilities and providing satisfaction in critical situations. In this research, there is an analytical approach for designing multi-purpose spaces.

Underground spaces play a fundamental role in the physical conservation of national capitals. These spaces are highly efficient due to being enclosed in the basement and as a result of high security, less energy consumption, under control and exposure to environment. One of the shortcomings that exist in their architecture today is that they are not planned to make the best and most possible use of the space. In other words, we can take advantage of the facilities and equipment of stations to use space for short-term settlement of individuals. The purpose of this study is to answer these questions:

1- Which factors are effective for multi-purpose use of complex stations?

2- Which architectural components have more impact on the flexibility of the stations?

Based on previous research and background studies, three research hypotheses can be proposed:

1- Flexible design for these spaces can be exploited for a fixed space in normal and emergency situations.

2- Factors such as the optimal geotechnical quality of the underground structure have a great impact on the stations' flexibility.

3- Factors such as maximum distance to existing routes and use of maximum slope to shorten the length of access space have a great impact on station architecture as a temporary haven.

2 Literature review and Theoretical Framework

2.1 Research Background

Given the extensive research on subway stations, the main objectives are divided into these three segments:

- Architectural art in the form of design style, form and appropriate use of materials, good and accurate harmony with the environment, beauty and inducing a sense of mental and security and flexibility.
- Observing safety and security points through passive defense and its impact on the continuity of activities and services.
- Considering the role of undeniable in physical protection of human and national capitals

Regarding that the main function of subway is the creation of an appropriate relationship between travelers and transportation system, the literature on design of flexible and multi-function spaces can be divided into two sections as well:

- Functional objectives of subway including main function, side function, and function for time of emergencies
- Creation of a variety of usages, which will increase the travel intentions and attract more audiences, which will improve the transport system.

In its side function, the relationship is based on providing the needs of travelers to commercial, cultural and health services, and ultimately the operation of the subway at the time of crisis, which is defined based on the relationship between the basic needs of human, including water, medicine, food and temporary settlement in emergency conditions, as discussed in 2013 by Doostmohammadian [1]. One of the side functions of subway, especially the stations that has been considered less in Iran, is the emergency shelter. However, from the emergency management point of view in design and usage of a double-purpose subway station the following points should be taken into consideration:

- Estimating the required emergency management center
- Secure communication with outside
- Estimating the required relief space
- Preparing special training programs for emergency conditions

The benefits of creating secure subway stations as emergency or temporary settlement include:

- Expansion of the refuge areas throughout the country
- Increasing human capital safety and reducing adverse damages
- Increasing the mood of citizens preparedness against crisis
- Increasing the possibility of continuing the necessary activities of the city even in the conditions of enemy invasion
- Increasing the costs of enemy military raid in crisis conditions
- Defensive enhancement against enemy in critical conditions during passive defense, as discussed by Massey et al. (2006) [2] and also Shakibamanesh et al. (2014) [3].

The functional concepts of attention to this kind of coherent design include fluidity, security and variety to attract people. The morphing of the city location, while the user diversity and improvement of the social behavior of travelers in emergency situations, can also increase the security and protect human wonders of individuals. Flexible and design of the space for human actualization, creating a sense of security and tranquility through the transparency and readability of spaces for the main and extra functions of the subway and the operation in emergency situations are among design concerns as well, as discussed by Khan and Wurman (1986) [4], Malofiy (1998) [5], Hosseini (2003) [6], and Habraken (2008) [7].

With regard to architectural indicators of underground spaces in general there are three categories of factors, including technical, passive defense, and economic as follows. Technical factors consist of:

- Being away from active zone faults

- Optimal quality of geotechnical space site
- Maximum distance to existing routing
- The use of maximum pitch slope to reduce the length of access space
- Choosing the right place to dig properly according to the slope direction of the layers

Passive defense factors include:

- Reducing the direct vision of the enemy and his internal factors relative to the inputs
- Creating the maximum useful slag in the areas required by underground ….
- Minimum change in vegetation with access road and inputs
- Reduce the minimum of rock loss to place inputs at probable time
- Ability to run deception structure at the beginning of the entrance for the lack of drilling detection for underground spaces.

Finally, economic factors comprise:

- The shortest length to access the original inputs and spaces
- The possibility of using natural effects in order to target
- Possibility of construction and use of spaces
- Appropriate and less spacing for the transmission of infrastructure services [1].

Table 1 summarizes the factors affecting flexibility, and relates them to the main independent elements in spaces, based on the available literature.

Table 1. Factors affecting flexibility in spaces from the literature review

Independent elements	Flexibility components
Location components	Spatial fluidity and flexibility [10]
	Providing freedom, system and mental security of individuals [7]
Physical components	Flexibility [11]
	Performance
	Readability (ability to understand and orientation)
	Runtime restrictions [10]
	Development capability [9]
Physical and functional components	Variety [12]
	Dynamics
	Meet the needs of individuals [7]
	Optimal geotechnical quality of underground structure [10]

2.2 Theoretical Framework

With an overview of the existing knowledge, shortage of concepts was turned on to understand multi-purpose architecture for underground spaces and the required research to fill the existing gap. After classifying the components based on their influence, the categories were given to experts, in the form of a questionnaire, and as a result of the expert views, the flexibility components were prioritized. Turns is another flexible space to meet the needs of travelers and transport, facilities, emergency

management, reduction of vulnerability and satisfaction at the same time, while contributing to temporary shelter. By using this theoretical framework the main research work was carried out as explained in the next section of the paper along with the obtained results.

3 Materials and Methods and Analysis Results

The research method in this study is a descriptive survey by using Delphi Technique, used in emergency management by O'Connor in 2008 [14] and Kim and Huang (2014) [14]. The type of descriptive research, used in this study, includes classification through questions to examine the nature and situation of existing conditions or the relationship between the phenomena of a field. Having the factors identified, among them the most important factors that affect the versatility of stations, and their related elements were identified and presented in the form of a questionnaire to be sent to some experts to give their views. According to the present approach, the method of descriptive Delphi research, the developed questionnaires were given to experts. At the end, a new prioritization was provided based on their answers. Flexibility components and elements was created in the form of a table, then each component was accompanied by a short description and a sample, and then its impact on subway stations was investigated. In total 25 experts were considered for the survey, out of them, 15 experts replied to our request and filled the questionnaires after one week. Then, the responses were analyzed by using SPSS software, which revealed that two factors of flexibility and efficiency had the most impact on the multifunctional design.

3.1 Analysis of Obtained Data

Two subway stations, one in east and another in west of Tehran were studied as case samples. Based on observations and assumptions, eleven factors were selected and the impact of each factor on flexibility was investigated. By using SPSS software for analyzing the data, internal consistency coefficient of the questions, obtained as 0.79 and proximity of this value to 1, we can conclude the degree of internal stability and the homogeneity between the questions are satisfactory. Table 2 presents mean and standard deviation, and the minimum and maximum values for each component, and their ranks among the eleven variables, showed that the flexibility and efficiency of the architecture plan are the most important elements of flexibility in the station.

Table 2. Comparison of mean and flexibility of the ranking

Variable	Symbol	min	Mean	SD	Max
Spatial fluidity	Q1	3	3.67	0.49	4
Providing freedom, system and mental security of individuals	Q2	2	3.00	0.66	4
Flexibility	Q3	3	3.87	0.35	4
Performance	Q4	3	3.73	0.46	4
Readability (to be understood and oriented)	Q5	2	3.13	0.74	4
Runtime restrictions	Q6	2	2.87	0.64	4
Development capability	Q7	1	2.93	0.80	4
Variety	Q8	2	3.47	0.64	4
Dynamics	Q9	2	3.47	0.64	4
Meet the needs of individuals	Q10	2	3.20	0.65	4
Optimal geotechnical quality of underground structure	Q11	3	3.60	0.51	4

3.2 Interpretation of the Results

In this section, the mean statistical indices, standard deviation and error percentage (independent and dependent variable) have been reported. In fact, these indicators can help to understand more research variables. The average of the most common criteria is tendency to center.

A study of distribution of a statistical society called the amount of representative that the sizes are distributed around and any numeric criteria that represent the center of the data set. The criteria are called trends. One of the dispersion indicators is the standard deviation that indicates how much data the average value of the interval is. If the standard deviation is a series of data close to zero, it is a sign that the data is close to average and the scatter is a little. While large deviations are indicative of significant data dispersion. In fact, standard deviation is used to determine the reliability coefficient in statistical analysis. In scientific studies, usually, the data with standard deviation is considered more than two as the Perth data and are excluded from the analysis.

Flexibility and performance are factors that, due to the type of layout and arrangement of surfaces in the design can be coordinated with the needs change, such as the commercial and cultural spaces within the subway stations, which can turn themselves into spaces for accommodation in the necessary situations. The value of this component is also higher than the average index. Providing freedom, system and mental security of individuals, including location components, is related to the physical characteristics of the location, the function and activity of citizens in the place and have an effective role in the quality improvement of the location and also associated with the platform of location.

Readability components, time constraints and development capabilities of physical components are more attention to highlighting the physical signs of the plot, internal and external dependence which includes the design, the appropriate motor system plan in the station and the prevention of motor disturbance and transparency, creation of

comfort and security. In response to travel demand, architectural and design form of station space.

Diversity factors, dynamism, supply needs of people and geotechnical quality in the underground structure are functional physical components, including focusing and planning on public transportation system and increasing the audience of this system, security and comfort in the field influenced by the station, improving the quality of daily trips of citizens, Creating a suitable urban environment for pedestrians, building a variety of audience travel and attracting more passengers, upgrading the transport system.

According to the interpretations of the above and the figures obtained from table 2 and stating that the average index alone does not describe the full status of the data distribution, and in addition to recognizing the criteria of the center, the criterion for recognizing their dispersion. Factors such as spatial fluidity, flexibility, efficiency and performance and geotechnical quality of the underground structure with the average indices (3.66), (3.86), (3.73) and (3.60) have a higher centrality than the average index, In other words, the standard deviation or variable dispersion index is flexibility (0.35), which is much lower than the rest of the variables and this means that more experts have given this variable priority.

Efficiency variables with dispersion index (0.35) and spatial fluidity with dispersion index (0.49), geotechnical quality of underground structure with index (3.47) are introduced as appropriate criterion for the level of centrality. This component has SD (0.64). Other elements, including the needs of people, supply of freedom, readability, and development capabilities with figures (3.20), (3.00), (3.13) and (2.93) of the average criteria are lower and can be said on this basis due to the coefficient of change, the development capability element is ranked with high changes in the 11th row, and flexibility, performance, efficiency and fluidity are ranked with the lowest changes in the first to third ranks. With a review of the ranking table obtained from the results, a different prioritization of the primary prioritization assumed in the questions is achieved, in Table 3.

Table 3. Priority of the results

Component	Rank
Spatial fluidity	7.27
Providing freedom, system and mental security of individuals	4.30
Flexibility	8.33
Performance	7.63
Readability (to be understood and oriented)	5.20
Runtime restrictions	3.77
Development capability	4.30
Variety	6.60
Dynamics	6.47
Meet the needs of individuals	5.13
Optimal geotechnical quality of underground structure	7.00

Friedman test results are used to rank components. If the average score of the variable has the highest value, as the most important variable as the least is the most important variable. According to Table 3 and after the evaluation, a new ranking is achieved where the flexibility component is in the first place, Performance variable and performance with lower dispersion rate compared to other variables in the second rank, spatial fluidity, geotechnical quality of underground structure and spatial diversity are in subsequent ranks. The dynamics element comes with a 3-degree climb towards the initial prioritization to the 6th grade. The execution component of the runtime will sink to the last rank. In order to achieve the research goals, observing the flexibility, efficiency and spatial fluidity as the most important elements are important. In continuation, the correlation chart of the research variables, which can be achieved between different components and evaluated the highest and lowest of this communication.

Table 3. Correlation between variables

	Q1	**Q2**	**Q3**	**Q4**	**Q5**	**Q6**	**Q7**	**Q8**	**Q9**	**Q10**	**Q11**
Q1	1										
Q2	0.224	1									
Q3	0.139	0	1								
Q4	0.853	0.24	0.207	1							
Q5	-0.263	0.44	0.346	-0.098	1						
Q6	0.305	0.51	-0.085	0.358	0.49	1					
Q7	0.122	0.27	0.22	0.339	0.5	0.68	1				
Q8	-0.152	0.51	0.296	-0.033	0.61	0.34	0.07	1			
Q9	-0.076	0.51	0.613	0.211	0.46	0.16	0.48	0.48	1		
Q10	0.217	0.65	0.42	0.415	0.51	0.4	0.56	0.26	0.76	1	
Q11	0.289	0.22	0.08	0.431	0.31	0.48	0.46	0.04	0.18	0.46	1

The above table shows the results of the correlation between variables. If the value of the numeric correlation coefficient is negative, there is an inverse relationship between them, otherwise there is a direct relationship between them. By examining the table of priorities obtained and the correlation between them can be said, although there is no significant relationship between flexibility with concepts such as runtime limitations, geotechnical quality, there is a significant correlation between flexibility and other components such as dynamism and supply needs of people with cultivars (0.613) and (0.420). Their dynamic factors and the needs of people are highly coordinated and very high correlation (0.759). However, there is no significant relationship between flexibility concepts and runtime constraints. Between the component of performance and performance with a variety, coordination is much more difficult than creating the difference and according to the numerical level (0.033), the two have no significant relationship with each other. Because of the correlation, I have been evaluated below zero. Also, in relation to flexibility, we can say that, among the factors, has a relationship with efficiency and dynamism and has a high correlation. According to the results of the study, the highest correlation between fluidity and efficiency factors, and

according to the amount of relationships between components, can be said that a cohesive space can be easily changed and transformed through internal and external communication. This space is also dynamic and efficient, and enables the reallocation of spaces and provides a good connection between the inside and outside spaces.

4 Conclusions

Studies have shown that spatial resilience is one of the most important factors influencing the flexibility and multitasking of spaces, so that most experts emphasize this component. The descriptive achievements of the research indicate the following two main outcomes:

- According to the ratings, the flexibility component with the lowest dispersion around the average index, and with the most effect on the application, is in the first place, and operating performance and performance in the second place, but in the amount of correlations can be used to provide this compromise, flexible and integrated spaces are designed to enhance the dynamism of the time in them and the runtime constraints with the mean index digits (2.86) and with high dispersion, factor is introduced, which is very trickier to coordinate with other factors, particularly flexibility on the quality of geotechnical underground structure.
- Flexibility, efficiency and spatial flexibility are the most important factors that should be considered for the architectural efficiency of the subway stations. The study, stating that a subway station with respect to these features can have two functions at the same time. In other words, the spaces of underground stations are designed to be integrated and legible, while presenting varied activities can be transformed into spaces with a new usage and can be used through previous forecasts to provide a variety of activities for new users, so that all three of the desired functions including transportation, providing travelers' needs and facilitating temporary shelters in emergencies.

References

1. Doostmohammadian, Mahshid. Design of subway station complex by the crisis management approach in Shahrak-e Gharb in Tehran (in Persian), Master's thesis in architecture, School of Architecture, Science and Research Branch of the Islamic Azad University, Tehran, Iran, (2013).
2. Massey, Joseph Eric, and John P. Larsen. "Crisis management in real time: How to successfully plan for and respond to a crisis." Journal of Promotion Management 12, no. 3-4 (2006): 63-97.
3. Shakibamanesh, Amir, Mahshid Ghorbanian, and Selda Nazari. "Railway and Subway Design Considerations towards Secure Urban Design in Terms of Passive Defense." International Journal of Academic Research 6, no. 1 (2014).
4. Kahn, Louis I., and Richard Saul Wurman. "What will be has always been: the words of Louis I. Kahn." (No Title) (1986).
5. Malofiy, Michael. "Order and flexibility: their coexistence as architectural principle." PhD diss., Virginia Tech, 1998.

6. Hosseini, M. "Seismic considerations in architectural design of special buildings." In Proceedings of the 6th international congress on civil engineering, IUST, Tehran, Iran, 2003.
7. Habraken N John. (2008): Design for flexibility, in Tatjana Schneider and Jeremy Till, Architectural Press. UK, ISBN 9780750682022.
8. Dittoe W and N Porter (2007): Appealing Spaces. American School & University, vol: 80, no. 2.
9. Ehrenkrant E and E Eckstut and Kuhn Architect (1999): Planning for Flexibility, Not Obsolescence
10. Govoroff-Regnault, V. "Station de Metro Saint-Martin: A Parisian subway stop that converts into a shelter for the homeless." ARCHITECTURE D AUJOURD HUI 327 (2000): 2-22.
11. Correal, Annie, and Benjamin Norman. "In deepest cold, a subway car becomes the shelter of last resort." New York Times, January 8 (2018).
12. Gilbey, M. J., and S. J. Kemp. "Comfort indices used for subway design." In Proceedings of the 13th International Symposium on Aerodynamics and Ventilation of Vehicle Tunnels, New Jersey, 13–15 May 2009, pp. 707-720. 2009.
13. O'Connor Jr, Ed D, Michael J. "A study utilizing the Delphi technique to develop a consensus on the importance of certain curricular goals for emergency management associate, bachelor's and master's-level programs in the United States." Journal of Applied Security Research 3, no. 2 (2008): 231-240.
14. Kim, Eun Young, and Eun Kyoung Hwang. "The Classification and Development of a Selection Support Program of a Subway Station as a Temporary Shelter." Applied Mechanics and Materials 638 (2014): 2060-2064.

Reviewing Prestress Losses in An Aged Spanish Concrete Bridge

Juan Antonio Mateu-Sánchez[1*][0000-0001-6351-5886], José Rocío Martí-Vargas[2][0000-0003-1665-2348] and Juan Navarro-Gregori[3][0000-0002-6319-7029].

[1]Institute of Concrete Science and Technology (ICITECH), Universitat Politècnica de València, Camí de Vera, s/n, 46022 Valencia, Spain. juamasa8@cam.upv.es
[2] Institute of Concrete Science and Technology (ICITECH), Universitat Politècnica de València, Camí de Vera, s/n, 46022 Valencia, Spain. jrmarti@cst.upv.es
3 Institute of Concrete Science and Technology (ICITECH), Universitat Politècnica de València, Camí de Vera, s/n, 46022 Valencia, Spain. juanagre@cst.upv.es

Abstract. Prestressed concrete structures have been widely used in Europe since the 1960s for their ability to support long spans. However, as these structures approach the end of their service life, it is crucial to assess their current stress state. Errors in prestressing force calculations and execution mistakes have resulted in the collapse of prestressed concrete bridges. In Spain, bridges built during the 1980s with similar designs are now facing time-dependent prestress losses that affect their prestressing state. Methods for calculating time-dependent prestress losses have evolved to enhance durability. An analysis comparing different regulations, including EP-77, Eurocode 2, and ASSTHO-2020, is proposed to validate calculations. The study focuses on a typical Spanish bridge, considering adjusted loads, time-dependent prestress losses, and current durability regulations. Project calculations and a comparative finite element model using Eurocode 2 parameters are presented. The objective is to identify deviations and errors in predicting short- and long-term prestress losses and meeting serviceability requirements. Advanced age analyses of prestressed concrete infrastructures are vital for ensuring future durability and functionality.

Keywords: Bridge, Concrete, Prestress, Losses, Code.

1 Introduction

A significant portion of the current prestressed concrete infrastructure in continental Europe and the United States has aged since its construction in the 1950s-1960s and is nearing the end of its service life [1]. It is crucial to adequately study the current condition of these elements. Most prestressed concrete structures (PCES) were designed according to outdated codes that did not consider certain considerations related to time-dependent prestress losses occurring in prestressed concrete elements. Additionally, various loading effects on the bridge and aspects of premature degradation of the elements must be taken into account. Therefore, due to the rapid

aging and functional deterioration of the structures, this is a significant problem that needs to be addressed promptly.

Hence, accurate determination of residual prestress is essential for the assessment of prestressed concrete structures (PCES) since the prestressing effect has a significant impact on the stress-strain response and capacity in this type of structure. In the design process, the designer must determine the prestressing force and estimate the prestress loss of prestressing force for the structure to meet its requirements during its service life. That is why it is important to obtain an approximation of the theoretical condition of such structures. Therefore, this text proposes, for a specific case, the calculation based on the applicable regulations in force at the time of the bridge's construction, such as the Instruction for the Design and Execution of Prestressed Concrete Works (EP-77) [4], and how it would be if the most commonly used calculation techniques for bridge design in Europe, such as Eurocode 2 (EC2) [5], and the American Association of State Highway and Transportation Officials (AASHTO 2020) [6], were used.

Hence, due to the aging of infrastructure composed of PCES, there is a growing trend in the capacity to detect, quantify, and predict damages by bridge owners, allowing for an effective and safe assessment of structural condition. Traditionally, periodic visual inspections have dominated maintenance programs worldwide [2]. However, it is important to have knowledge of quantifying prestress losses provided by outdated codes and compare them with those offered by more current codes.

Therefore, this study aims to analyze a bridge built in the 1980s located in Spain, initially designed according to the applicable code at that time for prestressed concrete elements, EP-77, and compare the values with those obtained using current codes in Europe and the United States. The main objective is to determine the prestress losses obtained from each of the codes and thus identify the variations between them.

2 Description of Structures

2.1 Geometry

The specimen studied in this paper corresponds to a bridge with a span of 30 meters and a platform width of 12 meters. The bridge section consists of a semi-rigid reinforced concrete barrier and parapet, a 7-centimeter thick bituminous wearing course, and a 25-centimeter thick reinforced concrete slab supported by 6 double T-section beams (see Fig. 1) [3].

Regarding the beams that make up the support of the deck, we have beams with a depth of 2.1 meters and a width of 0.8 meters. The geometric characteristics of the beam can be observed in the left part of Figure 2. There are 5 tendons, all of the same cross-section, with different alignments in both plan and elevation.

As for the arrangement of passive reinforcement, it can be observed in the right part of Figure 2.

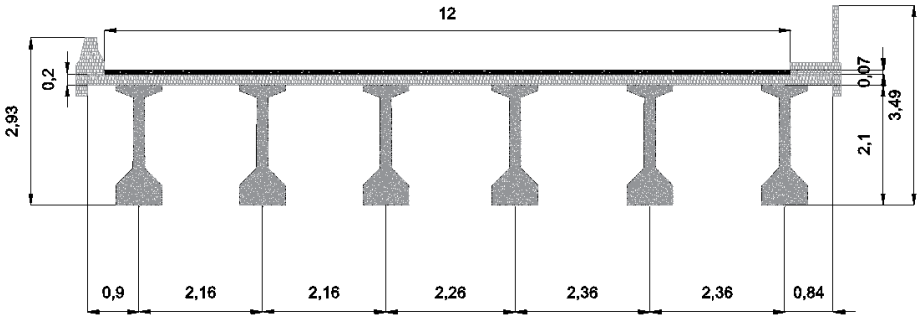

Fig. 1. Cross-section deck.

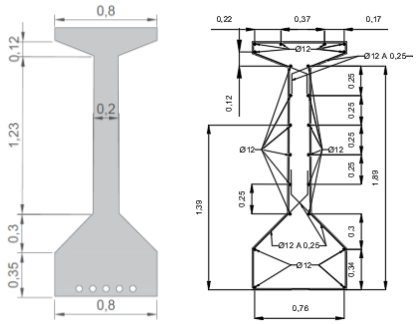

Fig. 2. Cross-section beam.

2.2 Materials Properties

The beams are made of concrete with a strength of 35 MPa, while the modulus of elasticity has been calculated for each of the different codes, resulting in a value of 35545,75 MPa for the design code (EP-77). For Eurocode 2, a value of 34000 MPa was obtained, and for the AASHTO 2020 code, a value of 29437 MPa was obtained.
The steel used for the passive reinforcement in the prestressed concrete elements is of type AEH-400N, with a modulus of elasticity of 210000 MPa and a yield strength of 400 MPa, which is currently referred to as B 400 S.

For the calculation of the layout and dimensioning of the steel cables that make up the active reinforcement, the following characteristics have been considered: a longitudinal deformation modulus of 190000 MPa, relaxation testing at 120 hours, at a temperature of 20°C, and a stress equivalent to 70% of the rupture of 1,35%, and relaxation testing at 1000 hours, at a temperature of 20°C, and a stress equivalent to 70% of the rupture of 2%. As for the cables used as active reinforcement, they have a net tendon area of 11,84 cm^2, a guaranteed breaking load of 1910 N/mm^2, and a load corresponding to the characteristic yield strength of 1718 N/mm^2.

2.3 Loads Pattern

The actions that affect the structure have been limited to permanent actions for the calculation of prestress losses and dimensioning of prestressing force. The permanent actions include the self-weight of the beam, the load of the slab, the wearing course, and the barriers at the ends, with the latter represented as linear loads. On the other hand, variable actions refer to the live load, which is considered as a surface load. In frequent use situations, 40% of the total maximum live load is taken as an additional load.

Considering all these factors, the beam with the highest load demand is chosen as the object of study, and therefore, the calculation of prestress losses is performed.

3 Prestress Losses

According to the initial design, each tendon was prestressed with a prestressing force of 1675 kN (1404 MPa), with the stress level in each tendon being 75% of the ultimate tensile strength (1980 MPa).

For the prestress losses due to friction and wedges' penetration, the same methodology was employed for the different codes, as the calculation for these prestress losses is similar. Based on this approach, the obtained results along the tendon for each of the mentioned codes are presented below.

3.1 Code-Based Analysis

In this section, graphs are presented for tendons 1, 2, and 5, as well as the current stress state, which significantly represent the behavior of the beam. Tendons 1 and 2 are most affected by elastic shortening as they are the first to be tensioned, while tendon 5, being the last in the tensioning sequence, does not experience any effect of elastic shortening. The graphs show the variations obtained according to the type of normative used.The graphs include instantaneous prestress losses, which take into account the elastic shortening, as well as total prestress losses, which reflect all the prestress losses in the tendon. In the calculation of instantaneous prestress losses, prior to elastic shortening, all the normatives used in this analysis share the calculation of prestress losses due to friction and wedging. Therefore, the variation in instantaneous prestress losses is solely due to elastic shortening.

Regarding tendon 5 (see Fig. 5), it can be observed that there is no difference between the different instantaneous prestress losses. This is because, due to the tensioning procedure, tendon 5 is the last one to be tensioned, and therefore it is not affected by prestress losses due to elastic shortening. As a result, the instantaneous prestress losses only take into account prestress losses due to friction and to wedge penetration.

In the graph corresponding to total stresses (see Fig. 6), it can be observed that the upper fiber ($\sigma 1$) is less compressed, while the lower fiber ($\sigma 2$) corresponds to the most compressed fiber in the beam for each of the different normatives used in the calculation.

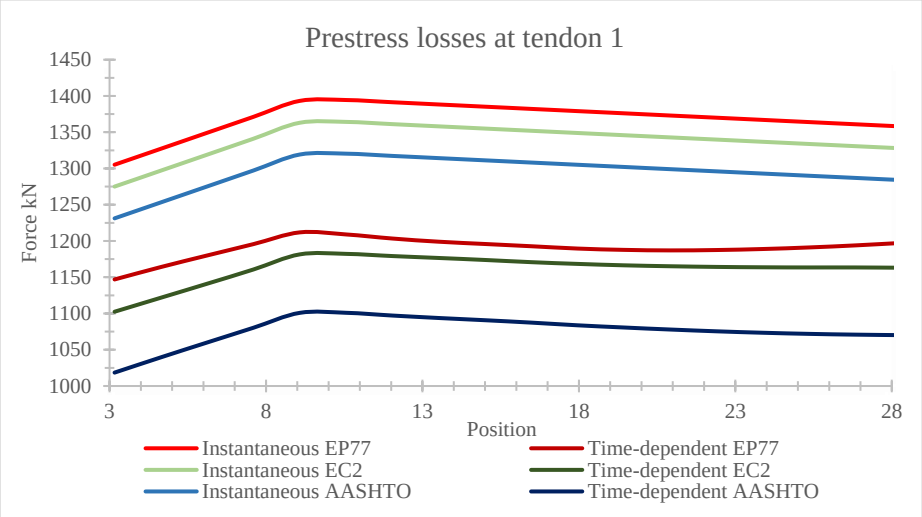

Fig. 3. Pretress losses at tendon 1.

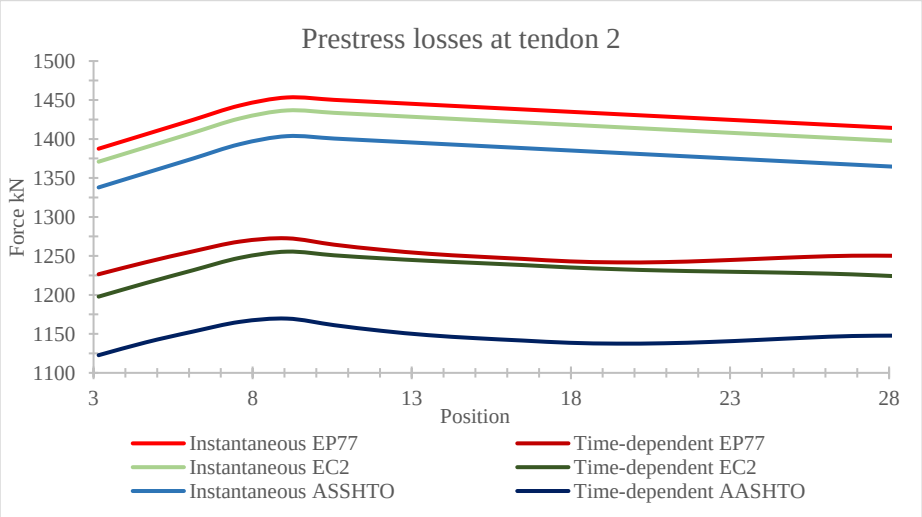

Fig. 4. Pretress losses at tendon 2.

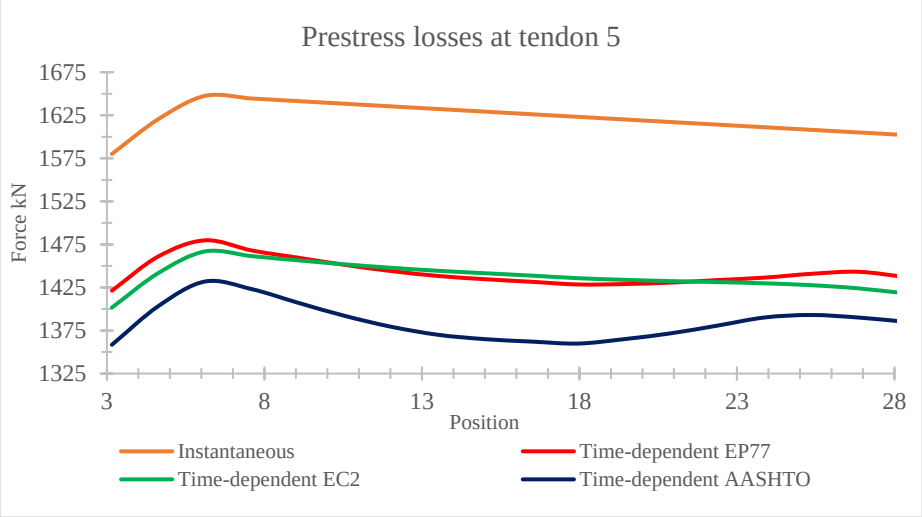

Fig. 5. Pretress losses at tendon 5.

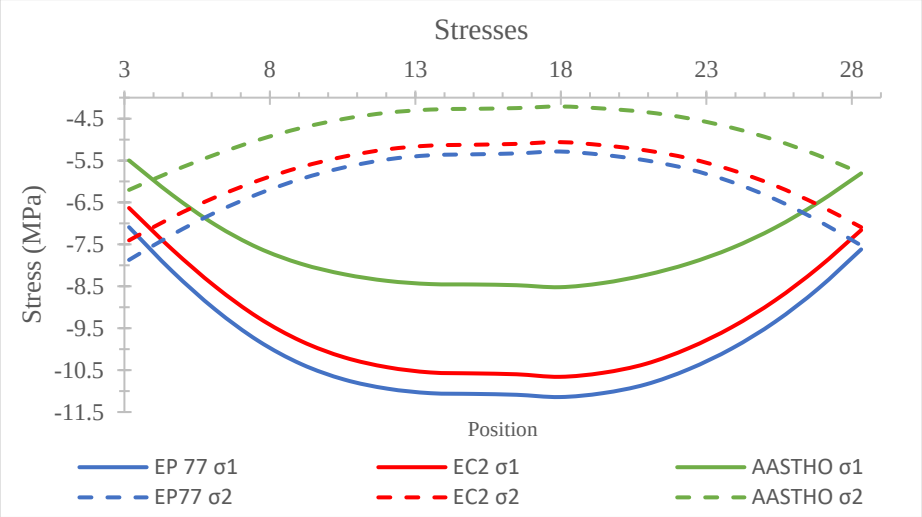

Fig. 6. Maximum and minimum stresses at beam.

3.2 Numerical Analysis

For the numerical analysis, the commercial structural analysis software SAP2000 was used. The staged construction analysis method was employed, which allows for long-term analysis of structural elements, as well as the sequencing of tendon stressing and consideration of loads introduced over the structure's service life [7].

To create the model, the elements were defined as tendon type, and the different tendon layouts were inputted. The calculation procedure followed the guidelines of the

Eurocode 2 (EC2) design code. As can be seen, a comparison was made between the results obtained from the EC2 calculation method and those provided by the finite element model (see Fig. 8).

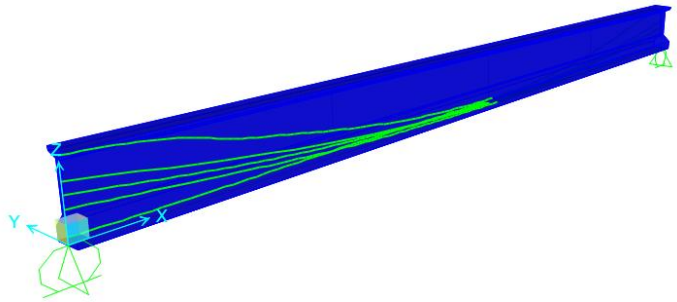

Fig. 7. Beam model from SAP2000.

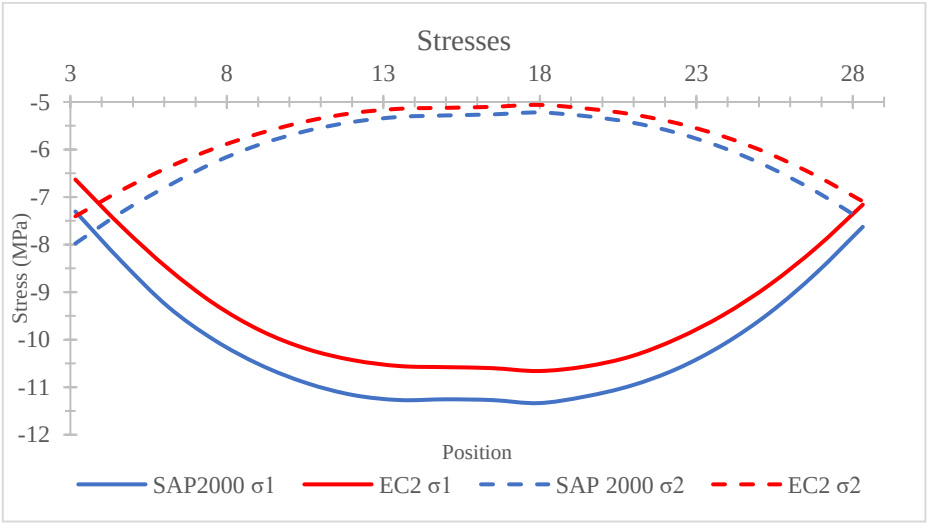

Fig. 8. Maximum and minimum stresses at beam.

4 Discussion

Regarding tendon 1, it can be observed that EP-77 predicts the lowest prestress losses, making it the least conservative option. It has an average prestress loss of 18%, with a maximum prestress loss of 22% in the beam. On the other hand, the EC2 accumulates average instantaneous prestress losses of 20%, with a maximum of 24%. As for the prestress losses calculated according to the AASTHO formulation, they are 23% on average and 26% at maximum. It is important to note that prestress losses due to wedge slip and friction were calculated using the same methodology and parameters provided by the project. The difference lies in the prestress losses due to elastic shortening.

Regarding time-dependent prestress losses in the concrete, EP-77 and EC2 show very similar total values of time-dependent prestress losses. However, it is worth noting that prestress losses due to shrinkage are much higher in EC2, while in EP-77, creep plays a more significant role. This is mainly due to the formulation used to calculate these prestress losses. EC2 takes into account the interaction between shrinkage, creep, and relaxation to obtain the total prestress losses, while EP-77 does not.

A similar pattern can be observed for tendon 2, where EP-77 is the least conservative in terms of instantaneous prestress losses, with an average prestress loss of 15% and a maximum of 17%. On the other hand, EC2 and AASTHO formulations have average prestress losses of 16% and 18%, respectively, with maximum prestress losses of 18% and 20%. The difference lies in the prestress losses due to elastic shortening.

Regarding time-dependent prestress losses in the concrete, EP-77 and EC2 show similar total values. However, EC2 (20%) has higher prestress losses due to shrinkage compared to EP-77 (17%). Additionally, the AASTHO code (23%) shows even higher prestress losses compared to the calculations made using the EC2 code.

For tendon 5, there is a greater difference in the calculation methods for time-dependent prestress losses. It can be observed that the highest time-dependent prestress losses, both in concrete and steel, occur according to the AASHTO code. On the other hand, EP-77 and EC2 yield quite similar results, with an average prestress loss of 14% for both and a maximum prestress loss of 15% and 17%, respectively. In contrast, the AASHTO code has an average prestress loss of 17% and a maximum prestress loss of 19%.

Regarding the time-dependent prestress losses, as previously observed in each of the tendons, the code that contributes the highest tension loss in the structure for each tendon can be seen in Figure 6. It is evident that the AASTHO code provides the highest tension loss. Consequently, after analyzing the stresses starting from the middle tendon, the AASTHO code again indicates a global state in the structure with less compression. In terms of comparing the ESP77 and EC2 codes, they provide very similar tension values. This similarity arises from the resemblance in calculating the time-dependent parameters among the different codes. However, the EC2 code is slightly more conservative due to modifications in obtaining parameters, leading to more conservative results than those obtained from the ESP77 code.

Regarding the comparison with the finite element model, the results obtained using the prestress loss formulation provided by the EC2 code reveal prestress losses around 11% compared to instantaneous prestress losses. On the other hand, the finite element method (FEM) yields a slightly higher value, with prestress losses of 13%. This is mainly because the values provided by the EC2 code are calculated based on approximate data regarding concrete elastic shortening values, while the FEM performs a more accurate calculation of elastic shortening.

As for time-dependent prestress losses in the concrete, the finite element method shows average total prestress loss values close to 27% of the initial prestress force. On the other hand, the calculation performed using the EC2 code provides values around 25%. This indicates that the finite element method offers very similar results to EC2 in terms of time-dependent prestress losses in the concrete, as the creep, shrinkage, and relaxation parameters of the concrete used are those provided by the EC2 code. Finally

in figure 8, it can be observed that the tension values existing in the beam for the Eurocode 2 case, the compressive stresses in the beam are lower than those provided by the finite element model, specifically in the upper fiber (less tensile zone), the value is 6.8% lower than the calculated model, while for the most compressed fiber, it is 4.4% lower.

5 Conclusions and Future Lines of Research

This article has presented a specific case study on the evaluation of prestressing in a concrete beam. Three different design codes have been used to assess the prestressed state of the bridge based on the applicable regulations. It has been possible to verify the differences between modern regulations and those used during the bridge design, as well as the deviations from the calculation codes based on the age of these elements. Therefore, the conclusions drawn are as follows:

- During the 1980s, the design methods used in Spain for most structures tended to underestimate the prestress losses of prestressing compared to current codes, particularly in terms of time-dependent prestress losses.
- The American code method presents significant advantages, especially in terms of time-dependent parameters, as the prestress losses at this stage are higher than those provided by the EC2 code.
- In this particular case, a consistent trend is observed where the prestress losses according to the EC2 code tend to be approximately 4% lower compared to the AASHTO code. This suggests that the AASHTO code aligns more closely with the calculation obtained by the finite element method (FEM).
- Regarding the EP-77 code, the prestress losses obtained during the study were 10% for instantaneous prestress losses and 21% for time-dependent prestress losses. These values are lower than those obtained with other codes, indicating that this code may be indicating higher prestressing values than what actually exists in the structure. This could be potentially dangerous in some cases, as having less acting prestressing force increases the risk of failures if these parameters are not adequately considered.
- It is unclear whether the values provided by different codes are sufficient to adequately evaluate the condition of current bridges, as there are numerous variables that cannot be solely considered based on the codes.

The uncertainty of not knowing the actual prestressing force in the cables is a significant problem. If it were possible to accurately determine the current prestressing force through periodic inspections of prestressed beams, it would be much easier to develop maintenance and repair plans.

The future of this field lies in seeking techniques that can accurately assess the current prestressing force in structures. There is already a considerable amount of research that has made progress in this area, successfully obtaining tension measurements in the active reinforcement. In modern structures, there are sensor devices and monitoring systems that track the variation of prestressing force over time.

However, it is essential to have initial data on the structures and their evolution throughout their service life.

Other research avenues are focused on obtaining residual prestressing in structures through indirect measurement techniques [8]. These methods involve measuring the prestressing force at a specific moment. Techniques like Crack Opening [9,10] or Tendon Cutting [11,12] have shown promising results, but they are destructive and render the structure unusable.

Therefore, it would be valuable to develop non-destructive indirect measurement techniques for assessing prestressing force. Currently, numerous research groups are dedicated to interpreting results and parameterizing the current state of prestressed concrete elements based on experimental methods. This line of research appears to be appropriate for further investigation in order to accurately determine the tensional state of these structures.

Acknowledgments
This work forms part of the Project "Looking for the lost prestress: multi-level strategy and non-destructive method for diagnosis of existing concrete structures" funded by the Agencia Estatal de Investigación (State Research Agency) of Spain (competitive research project PID2020-118495RB-I00 / AEI / 10.13039/501100011033 and human resources funding PRE2021-098777 / AEI / 10.13039/501100011033).

References

1. FIB: Partial factor methods for existing concrete structures. Bulletin nº 80. Federation Internationale du Beton, Lausanne (2016).
2. Li J, Mechitov KA, Kim RE: Efficient time synchronization for structural health monitoring using wireless smart sensor networks. Struct Contr Health Monitor 23:470–486. (2016)
3. Ministry of Public Works and Transport: Collection of Pretensioned Beam Bridges IIC. Road Crossing Works (1986).
4. Ministry of Development of Spain :Instruction for the Design and Execution of Prestressed Concrete Works EP-77 (1977).
5. National Annex AN/UNE-EN 1992-2: Eurocode 2: Design of Concrete Structures. Part 2: Concrete Bridges. Calculation and Construction Provisions (2013).
6. AASTHO. American Association of State Highway and Transportation Officials.. LRFD Bridge design specifications. (2020).
7. Manual SAP2000 v23: Integrated Software for Structural Analysis & Design (2022).
8. Mateu-Sánchez J. A, Serna P, Giménez-Carbó E, Castro-Bugallo M C, Navarro-Gregori J. and Martí-Vargas J. R: 'Analysis of prestressing in old full-scale concrete members', Materials Today Proc. (2023).
9. Rabbat B: 25-Year-Old Prestressed Concrete Bridge Girders Tested. PCI J 29(1):177–179 (1984).
10. Shenoy C, Frantz G: Structural Tests of 27-year-Old Prestressed Concrete Bridge Beams. PCI J 36(5):80–90 (1991).
11. Halsey JT, Miller R: Destructive testing of two forty-year-old prestressed concrete bridge beams. PCI J 41(5):84–91 (1996).
12. Czaderski C, Motavalli M: Determining the remaining tendon force of a large-scale, 38-year-old prestressed concrete bridge girder. PCI J 51(4):56–68 (2006)

Seismic Assessment of Bridges Under Aftershock Affects

M. Fatih Yilmaz[1[0000-0002-2746-7589]], Fatih Yilmaz[2[0000-0001-6913-5067]], Kadir Ozakgul[3[0000-0002-2666-3836]], B. Ozden Caglayan[4[0000-0002-8986-9188]]

[1] Department of Civil Engineering, Ondokuz Mayıs University, Kurupelit 55220, Samsun, Turkey, mehmetfatih.yilmaz@omu.edu.tr
[2]Department of Civil Engineering, Recep Tayyip Erdoğan University, Merkez 53100, Rize, Turkey, f.yilmaz@erdogan.edu.tr
[3]Department of Civil Engineering, Istanbul Technical University, Maslak 34469, Istanbul, Turkey, ozakgulk@itu.edu.tr
[4]Department of Civil Engineering, Istanbul Technical University, Maslak 34469, Istanbul, Turkey, caglayan@itu.edu.tr

Abstract. Earthquakes and their aftermaths result in increasing loss of life and economic damage. Recent earthquakes have demonstrated that buildings can collapse or be severely damaged by aftershocks, even if they suffered only minor damage during the main earthquake. This was painfully illustrated in Turkey during the 2011 Van earthquake and the 2023 Kahramanmaraş earthquakes. Structural designs only consider the main earthquake loads and fail to account for the behavior of damaged buildings during aftershocks. Therefore, it is crucial to determine the extent of damage caused by aftershocks. Transportation systems must remain operational to quickly and safely provide post-earthquake aid and transfer victims to safer areas. Bridges are particularly critical in this regard. This study investigated the behavior of bridges exposed to different levels of damage during aftershocks. Static pushover analyses were conducted to determine the extent of damage, and different earthquake records were used to simulate aftershocks. Bridges that suffered only minor damage performed well during aftershocks, while those that had sustained severe damage collapsed or suffered permanent deformation.

Keywords: Aftershock; Bridge; Earthquake Damage.

1 Introduction

Earthquakes emerge as one of the most significant natural disasters causing considerable loss of life and property in many parts of the world. Furthermore, recent earthquakes in our country have resulted in substantial human and economic losses, highlighting the necessity to reevaluate our current earthquake preparedness. Moreover, following these earthquakes, the occurrence of aftershocks has been noted, causing already damaged structures to collapse due to the subsequent shaking, thereby leading to additional loss of life[1]. This underscores the critical importance of assessing the earthquake resilience of structures.

An earthquake is a seismic event caused by the fracturing of the Earth's crust and typically occurs in two stages: the main shock and aftershocks. The main shock represents the largest and most destructive shaking during the earthquake, followed by aftershocks. Despite being of lesser intensity than the main shock, aftershocks have the potential to generate destructive effects.

Indeed, bridges serve as the most critical structural elements within transportation systems, simultaneously representing the most susceptible components. Therefore, to ensure the continued use of transportation systems after natural disasters like earthquakes, it is essential to determine the behavior of bridges under seismic effects and design earthquake-resistant bridges. The resilience of structures in the face of earthquakes and subsequent seismic events is studied through the concept of structural durability[2]. The ability of a structure to undergo additional displacements and carry loads after experiencing damage enhances its safety against aftershocks. In this regard, the design of the structure, material selection, construction processes, and details play a significant role. Designing structures with ductility and substantial displacement capacity contributes significantly to their behavior under aftershocks.

Furthermore, various improvement and strengthening applications are undertaken to enhance the seismic performance of bridges and address the resilience losses incurred after earthquakes. These actions can be examined under two primary principles. Firstly, element-based maintenance aims to increase structural components' deformation capacity and strength through strengthening techniques. Fiber-reinforced polymer systems and jacketing methods are frequently utilized in this context[3]. Additionally, there may arise a need for systemic improvements within the structure. In such cases, seismic isolators are employed to restrict the seismic loads on the structure. For added damping and increased rigidity, supplemental structural elements like additional steel cross-bracings, buckling-restrained bracings, and reinforced concrete walls can be incorporated to elevate the lateral rigidity of the structure and limit its displacements. Fiber-reinforced polymer systems and seismic isolators emerge as two significant methods extensively employed in bridge-strengthening endeavors[4].

The determination of bridge behavior under aftershock effects heavily relies on field observations, which are of significant importance. However, due to limited access to a sufficient amount of data, these observations cannot be widely utilized. Consequently, numerical analyses based on mathematical models of bridges are employed to investigate their behavior under aftershock conditions[5]. Through the utilization of real earthquake records in these analyses, weak points and potential areas of damage in bridges can be identified. By modeling the behavior of bridges under aftershock effects, potential damages that may occur under such conditions can be detected for bridges that have already sustained certain levels of damage during the main shock. As a result, the durability of bridges can be determined, enabling transportation systems to operate in a safer and more sustainable manner while minimizing potential risks.

In this study, an ordinary highway bridge was considered, and its nonlinear behavior was investigated through incremental pushover analyses. Subsequently, peak displacements were correlated with damage states in the bridge to determine damage limit states. A bridge model, including plastic deformations resulting from certain levels of damage, was then subjected to 25 real earthquake records from distant faults,

and the bridge's time-domain behavior was assessed. This allowed for a comparison of the seismic responses of bridges with different levels of damaged and undamaged bridges.

2 Description of the Bridge and Finite Element Model

In the context of ordinary highway bridges in Turkey, the essential components of these bridges were constructed predominantly after the 1990s. These bridges are categorized into four distinct classes based on their structural attributes [6]. Caltrans (2006) defines ordinary standard roadway bridges, where the bridge superstructure is supported by steel shim elastomeric bearings located on the abutments and bending cap beams. Base isolators in the form of elastomeric bearings are commonly employed to mitigate seismic loads, comprising steel plates, rubber pads, and steel core materials. The connection between the abutment-elastomeric bearing and the superstructure-elastomeric bearings relies solely on friction force, with no interconnecting devices present. In the event of a severe earthquake, the friction force may be surpassed, leading to the superstructure sliding on the elastomeric bearing, resulting in unseating. To safeguard the superstructure, piers, and abutments, a shear key was incorporated as a fuse element, designed to prevent the superstructure from descending below the piers and sacrificially absorbing the seismic forces.

Ordinary highway bridges in Turkey are characterized by multi-span composite structures, incorporating pre-stressed concrete girders and continuous cast-in-place reinforced concrete decks (see Fig.). The girders were constructed using C40 concrete material, while the deck was made of C25 concrete material. For all reinforced elements, S420 reinforcement steel was utilized. Additionally, Fig. illustrates a typical single-column pier view of the ordinary roadway bridge in Turkey.

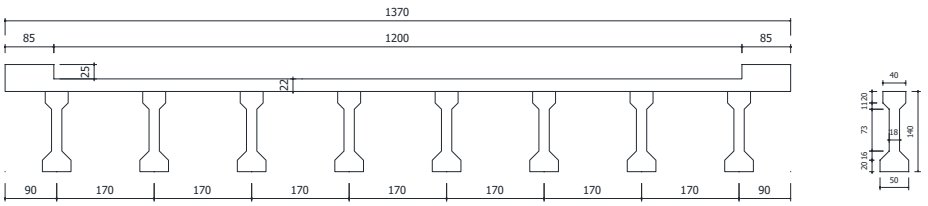

Fig. 1. Typical shape of the superstructure of the ordinary bridges (All dimensions are in cm).

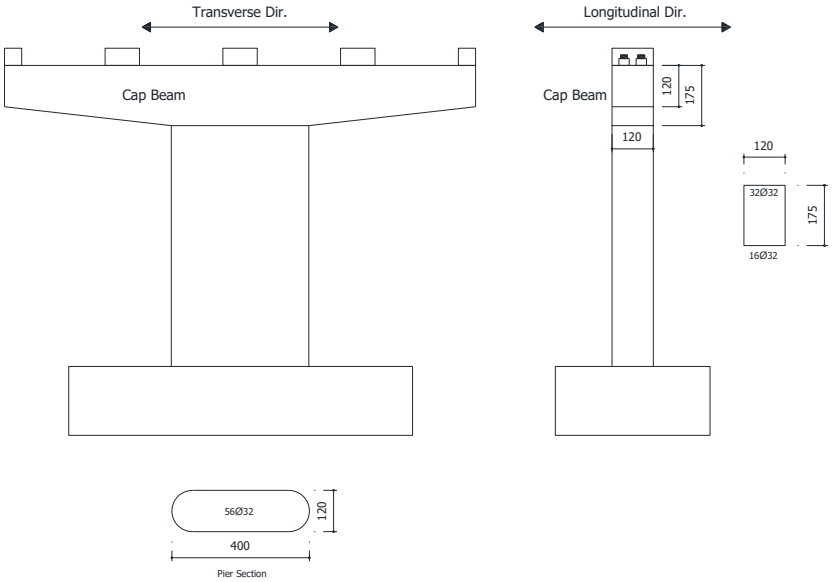

Fig. 2. Typical view of the single column pier of the ordinary bridges.

A 3-D finite element model of the bridge was developed using Sap2000 software [7] (see Fig. 3). The model took into account P-Δ with large displacements to determine the second-order effects on the piers. The concrete grade was modeled as C25, and the reinforcement class as S420. It was assumed that the bridge superstructure exhibits linear behavior. However, to characterize the nonlinear behavior of the bridge piers, The section-designer was utilized to model the bridge piers and the moment-curvature relationship was determined.

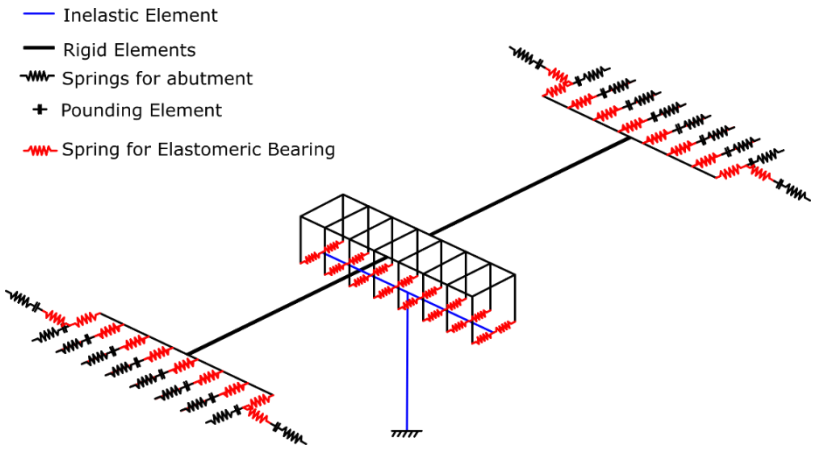

Fig. 3. 3-D analytical model of the bridges.

The lateral load transfer between the superstructure and the abutments in the elastomeric bearing is accomplished through friction. Given the absence of connecting devices, the lateral load-carrying capacities are influenced by both the dynamic friction coefficient and the axial load acting on the systems. Once the friction load surpasses the lateral load capacity, it remains constant. According to Caltrans (2006), the friction coefficient is defined as 0.4. Elastomeric bearings were modeled using the multilinear spring elements modeling approach. The initial rigidity of the elastomeric bearing was calculated using the formula: $K_{bearing} = \frac{G * A}{h_{nt}}$, where G is the shear modulus of the rubber pads, A is the area of the elastomeric bearing, and h_{nt} is the total thickness of the rubber.

The bridge's superstructure and substructure exhibit non-continuous behavior in both horizontal and vertical directions. This disparity in behavior results in the expansion joint undergoing opening and closing movements, inducing a nonlinear and discontinuous effect on the bridge. The collision between adjacent bridge components during joint closure is simulated using pounding elements. Longitudinal and transverse gaps of 50mm and 25mm, respectively, are modeled, considering their initial stiffness and shear yielding capacity. The multilinear spring elements were utilized to model the pounding elements accurately. Additionally, the abutment and backfill soil models were developed based on the models [8].

3 Determination Damage Limits of the Bridge

Excessive plastic stresses and accumulation of plastic strain in structural elements are utilized to determine the deterioration conditions of these elements. In girder bridges, the critical region can be determined as the end regions of the bridge piers and possible damage is expected to occur in this region. Therefore, inelastic displacements can be used to determine performance levels in bridges. The greatest horizontal displacement occurring at the top of the bridge pier was used in this study to determine the damage state. In addition, other critical parts of the structure that are likely to be damaged can also be identified and easily included in the calculations in determining the structural damage [9]. Thus, multiple damage cases can be examined at the same time. Damage conditions determined due to displacement are taken as seen in Table .

Table 1. Displacement limits corresponded to the different structural performance levels. [10]

Performance Level	Description	Limits
PL-1	No Damage	$\Delta_y + 0.3\Delta_p\ \Delta_y$
PL-2	Slight Damage	$\Delta_y + 0.3\Delta_p$
PL-3	Moderate Damage	$\Delta_y + 0.6\Delta_p$
PL-4	Extensive Damage	$\Delta_y + 0.8\Delta_p$
PL-5	Collapse	$\Delta_y + \Delta_p$

In order to determine the displacement limits, a nonlinear pushover analysis was performed. The maximum displacement and base shear force values of the bridge to be pushed from the initial state were recorded. The loads are increased until a significant decrease in the bridge strength is performed. While performing the incremental pushover analysis, nonlinear behaviors in terms of geometry and material were also taken into account. In the pushover curve obtained (see Fig. 4), the displacement limits corresponding to the slight damage, the moderate damage, the extensive damage and the collapse prevention damage conditions are colored green, yellow, orange and red, respectively.

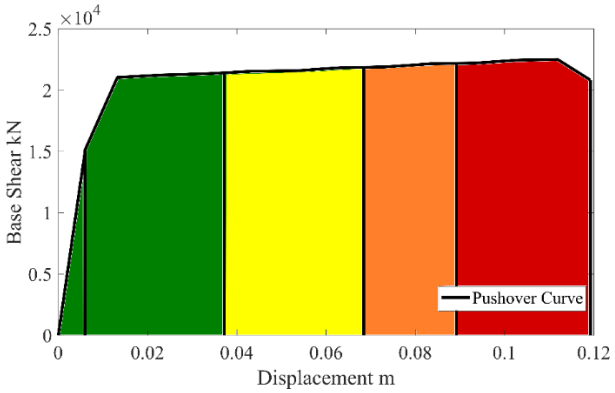

Fig. 4. Pushover curve of the bridge.

4 Nonlinear Time History Analysis of the Damaged Bridge

In order to determine the behaviour of bridges under the influence of aftershocks, first of all, the expected damages on the bridge should be determined at different damage limit values. In the study carried out in Chapter 3, incremental thrust analyses were performed on the bridge, and the peak displacements corresponding to different damage conditions were determined. Twenty-five real earthquake records were selected to analyze the time history, and these records were proportioned to the DD1 earthquake

hazard level according to TBEC 2018 [11]. The spectrum curve used in the ratio of earthquake records was produced according to TBEC 2018 [11] by selecting a region in Istanbul. Earthquake records were randomly selected to include different moment sizes, focal lengths, and acceleration values determined as records under the effect of distant faults.

Before conducting analyses in the time domain, vertical loads were applied to the structure, and incremental pushover analyses were performed with the consideration of vertical loads, and lateral loads were applied to the structure with displacement control. In order to obtain the conditions of specified damages in the structure and to perform time domain analyses on these damaged structures, incremental pushover analyses were first conducted until the corresponding peak displacement for the damage state was reached. Subsequently, the base shear forces on the bridge were reset to zero, and the resulting permanent plastic deformations were obtained. Time history analyses were then performed with these permanent plastic deformations, thus considering the anticipated initial damages in the structure.

In Fig. , differences between the deformations caused by the earthquake record on the slightly damaged bridge after the initial permanent plastic deformations are observed. Despite a slight reduction in permanent plastic deformations, as seen in the analysis results, significant displacements are evident under the earthquake effect, starting from the third second of the earthquake. Similarly, variations in the initial permanent shape deformations are observed for a moderately damaged bridge under the ANZA AZF earthquake record.

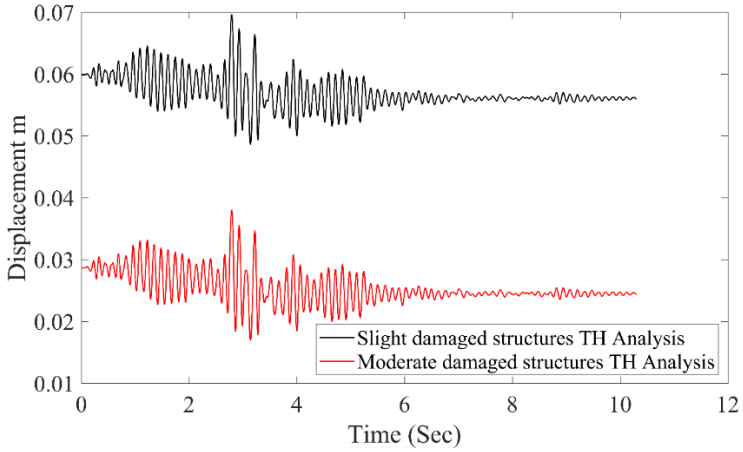

Fig. 5. Nonlinear time history analysis of damaged structure.

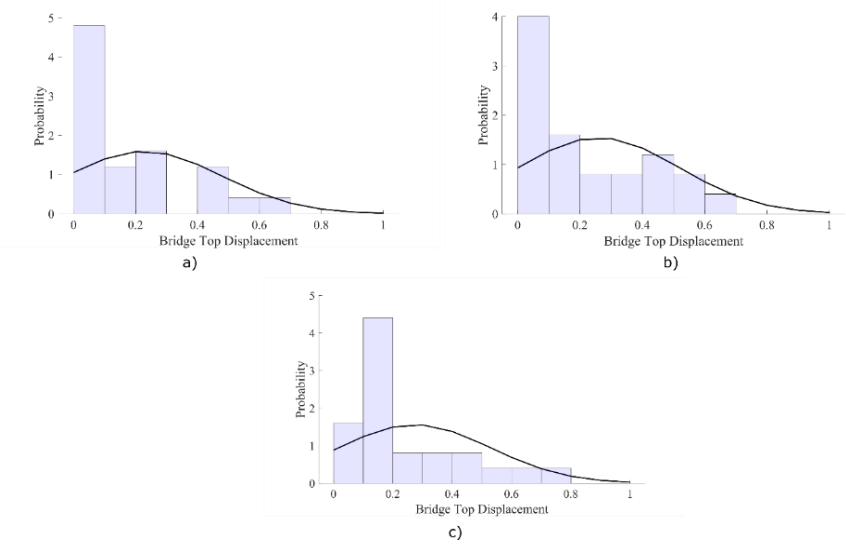

Fig. 6. Top displacement distribution of a) no damaged, b) slight damaged, c) large damaged bridge.

Analysis was conducted for three types of bridges: undamaged bridges, slightly damaged bridges, and moderately damaged bridges, using 25 real earthquake records. The results of the analyses showed that for undamaged bridges, the average displacement demand under earthquake records was found to be 0.2279m, with a standard deviation of 0.2504m. As expected, for slightly damaged bridges, the displacement demands increased, with the average reaching 0.2504m. Additionally, the standard deviation of displacement demands was determined to be 0.2582m. In the case of moderately damaged bridges, the analysis revealed an average displacement demand of 0.27m and a standard deviation of 0.25. The corresponding histograms of these displacement demands are shown in Fig. . To focus on the safety of bridge usage after earthquakes, the analyses only considered the scenarios where the bridges sustained either slight or moderate damage, omitting the cases with severe damage or collapse.

5 Conclusions

In this study, a standard highway bridge was examined, and by using incremental pushover analysis, damage threshold conditions against the damage levels that would occur on the bridge were determined. The bridge was pushed until a certain peak displacement was achieved to induce slight and moderate damage. Subsequently, selected seismic records were applied to the damaged bridge, and the differences in peak displacement and damages on the bridge were investigated.

As a result of time-history analyses conducted on the undamaged bridge, the average peak displacement value was determined to be 0.227 m. When the identical seismic

records were applied to the slightly damaged bridge, the average peak displacement was found to be 0.25 m, and for moderately damaged bridges, it reached 0.27 m.

As the damage level increases, the permanent deformations on the bridge increase, and the probability of damage under earthquake effects also rises. Despite the increase in peak displacements, no significant difference was observed in the standard deviation values, which were calculated as 0.25 m for all three cases. In conclusion, bridges that have experienced primary earthquake effects are more affected by aftershocks, and as the damage level increases, the destructive characteristics of aftershocks also increase.

References

1. E. Omranian, A. E. Abdelnaby, and G. Abdollahzadeh, "Seismic vulnerability assessment of RC skew bridges subjected to mainshock-aftershock sequences," Soil Dynamics and Earthquake Engineering, vol. 114, pp. 186–197, Nov. 2018, doi: 10.1016/j.soildyn.2018.07.007.
2. P. Franchin and P. E. Pinto, "Allowing traffic over mainshock-damaged bridges," Journal of Earthquake Engineering, vol. 13, no. 5, pp. 585–599, Jun. 2009, doi: 10.1080/13632460802421326.
3. J. S. Jeon, R. Desroches, and D. H. Lee, "Post-repair effect of column jackets on aftershock fragilities of damaged RC bridges subjected to successive earthquakes," Earthq Eng Struct Dyn, vol. 45, no. 7, pp. 1149–1168, Jun. 2016, doi: 10.1002/eqe.2700.
4. M. Fakharifar, G. Chen, L. Sneed, and A. Dalvand, "Seismic performance of post-mainshock FRP/steel repaired RC bridge columns subjected to aftershocks," Compos B Eng, vol. 72, pp. 183–198, 2015, doi: 10.1016/j.compositesb.2014.12.010.
5. M. Kumar, A. S. Whittaker, and M. C. Constantinou, "An advanced numerical model of elastomeric seismic isolation bearings," Earthq Eng Struct Dyn, vol. 43, no. 13, pp. 1955–1974, Oct. 2014, doi: 10.1002/eqe.2431.
6. Ö. Avşar, A. Yakut, and A. Caner, "Analytical Fragility Curves for Ordinary Highway Bridges in Turkey," Earthquake Spectra, vol. 27, no. 4, pp. 971–996, 2011, doi: 10.1193/1.3651349.
7. Computers and Structures., "SAP2000. (2015). Structural analysis program." Berkeley, California.
8. Caltrans, Seismic Design Criteria. Sacramento, CA., 2006.
9. L. Capacci, F. Biondini, and A. Titi, "Lifetime seismic resilience of aging bridges and road networks," Structure and Infrastructure Engineering, vol. 16, no. 2, pp. 266–286, Feb. 2020, doi: 10.1080/15732479.2019.1653937.
10. F. Biondini, E. Camnasio, and A. Palermo, "Lifetime seismic performance of concrete bridges exposed to corrosion," Structure and Infrastructure Engineering, vol. 10, no. 7, pp. 880–900, 2014, doi: 10.1080/15732479.2012.761248.
11. TBEC. (2018). Turkish Building Earthquake Code. Ankara, Turkey, T.C. Resmi Gazete.

The Effect of Foundations Uplift on The Seismic Behavior of Multi-Story Moment Frames Regular RC Buildings

Amir Amirbeygloo [0009-0007-0464-1234] and Mahmood Hosseini[2*] [0000-0003-3142-4087]

[1]Graduate Student, Dept. of Civil Eng., Eastern Mediterranean University (EMU), 99628 Famagusta, North Cyprus via Mersin 10, Türkiye
22500295@emu.edu.tr
[2] Professor, Dept. of Civil Eng., Eastern Mediterranean University (EMU), 99628 Famagusta, North Cyprus via Mersin 10, Türkiye
mahmood.hosseini@emu.edu.tr
*Corresponding Author

Abstract. Routinely in the seismic design of buildings, it is assumed that the structure's foundation is fixed inside the ground; while at least for moving in the vertical direction, this is not actually true, and uplift of foundations may happen during an earthquake, and therefore, the assumption of fixed foundations may lead to some miscalculations in design, particularly on soft soils. Foundation uplift corresponds to the upward movement of foundations of columns or other load-bearing elements during earthquakes. In this article, the effect of foundation uplifting on regular multi-story concrete structures with moment frames is investigated. The study considers characteristics like foundation geometry, number of stories, and number of bays. As the first part of the study, three buildings of 4, 7, and 12 floors with concrete frames have been considered. The structural response of the building has been obtained by using the non-linear time history analysis method (NLTHA) employing the SAP2000 software. The results of the NLTHA, conducted by applying a set of selected earthquake accelerograms, have shown that the tendency of foundations' uplift depends on the number of the building's stories, and that the amount of uplift can affect the seismic behavior of the building to a great extent. In some cases, the possibility of the foundation rising reduces the base shear force, roof absolute acceleration, and inter-story drift values. So, in some cases foundation uplift may be used as a means for decreasing of the seismic responses, however, more research is necessary for getting more confident conclusion.

Keywords: RC building, Uplift, Fixed base, Nonlinear time history analysis, Seismic response

1 Introduction

In the conventional seismic design of buildings the foundations are assumed to be fully fixed inside the ground as a rigid media, however certain observations have revealed that the foundation can, in fact, elevate slightly during the earthquake, albeit only -

a little. Although scholars have noticed this phenomenon since early 60s, majority of pervious studies on this phenomenon have been conducted by considering a very simplified model of the building's structure, mainly due to the deficiency in computer programs for realistic modeling of the intricate behavior of the soil under and around the foundations. For example, after investigating the behavior of buildings in the Chilean earthquake of May 1960, Housner (1963) noticed that a number of tall, slender structures survived the ground shaking whereas more stable appearing structures were severely damaged. By using the inverted pendulum concept, he tried to show that that there is a scale effect which makes tall slender structures more stable against overturning than might have been expected [1]. Years later, Yim and Chopra (1984) investigated the effects of transient foundation uplift on the earthquake response of flexible structures by modeling the structure as a single-degree-of-freedom system attached to a rigid foundation mat which is flexibly supported. The flexibility and damping of the supporting soil were represented by a Winkler foundation with spring-damper elements distributed over the entire width of the foundation [2]. Based on the response spectra presented for several sets of system parameters, they identified the effects of foundation-mat uplift on the maximum response of structures. They also investigated the influence of earthquake intensity, structural slenderness ratio, ratio of foundation mass to structural mass, foundation flexibility and p-δ effects on the response of uplifting structures. However, their result are only applicable to slender buildings on relatively rigid mat foundation.

Iwashita et al. (2003), mentioning the slight damaged office building, designed before establishing the new seismic design code, in seismic intensity VII area at the 1995 Hyogo-Ken Nanbu earthquake, expressed that uplift of base may reduce the structural damage [3]. They studied the effect of uplift on earthquake response of buildings by nonlinear analysis considering several types of structural characteristics. Their analytical models consisted of one span and eleven stories frame and the frame with shear wall. As a result of nonlinear earthquake response analysis considering uplift, the frame with wall tended to cause uplift more than pure frame. Maximum shear force of the frame with wall was about half compare to that of the pure frame. They also examined the effects of structural characteristics, including distance between supports, support stiffness, and building stiffness. However, their study was limited to the single-bay frames with rigid foundation, and the soil modeled by linear springs.

In a more recent study, Jafarieh and Ghannad (2020), mentioning that in most of researches on soil-structure systems, it is assumed that the foundation is bonded to the ground where no foundation uplift is allowed, have investigated parametrically the effect of uplift on soil-structure-interaction (SSI) through time history analysis for a wide range of systems subjected to harmonic excitation and also ground motions recorded on soft soil with predominant period [4]. They have observed that the ratio of the soil-structure system period to the predominant period of ground motion has an important rule on the response of uplifting systems. While this period ratio is greater than one, the total displacement of uplifting soil structure systems almost equals to elastic soil-structure system when uplifting is prevented but the drift of the structure as a part of soil-structure system while uplifting is permitted decreases in comparison with corresponding systems which foundation uplift is prevented. If the period ratio becomes smaller than one, systems which are allowed to uplift experience larger displacements in comparisons with corresponding case which foundation uplift is prevented. They

have shown that neglecting the influence of foundation uplift on seismic performance assessment procedure of stiff and squat structures located on soft soil is not conservative, because in this situation structures can experience larger drift due to foundation uplift in comparison with the case that uplifting is prevented while subjected to excitation with long predominant period. It should be noted that although they have discussed various conditions of the structure from period point of view, their model is still the inverted pendulum, which is not realistic for most of buildings' structures.

This study has examined the impact of uplift on RC buildings' structures with various spans and heights, by using their actual model in SAP2000-24 software, in which the infill walls are also modeled for greater realism. Building code requirements for structural concrete, ACI 318-19, [5], and minimum design loads, and associated criteria for buildings and other structures NEHRP, [6], have used for the analysis and design of the structures in this work. In order to perform response history analyses, three ground motions have been chosen and scaled based on NIST guidelines for selecting and scaling earthquake ground motions [7]. Two groups of structures, those that are firmed to the soil, and those that are permitted to uplift have been modeled, and the maximum values of their seismic responses, including roof relative displacement, roof absolute acceleration, inter-story drifts and base shear, as well as performance levels of plastic hinges (PHs), have been compared. Details of modeling and analyses and the obtained results are presented in the following sections.

2 The Considered Buildings and Their Seismic Analyses

Two groups of regular RC buildings for residential usage, having 4, 7, 12 stories, with 3 meters height, and 3, 5, 7 bays with 5 meters span size, were considered, one group with fixed foundations, and another group with foundations allowed to uplift. Buildings were designed according to ACI 318-19, [5], by using SAP2000-24 software and considering the material properties given in Table 1, and applying the NEHRP recommended Minimum Design Loads and Associated Criteria for Buildings and Other Structures [6], and using the design response spectrum shown in Fig. 1.

Table 1. Specifications of materials used in design of the considered buildings

Materials	Grade
Concrete	5000 psi (34470 kN/m^2)
Longitude Steel Bars	A615GR40
Confinement Steel Bars	A615GR60
Infills Load	8500 kN/m

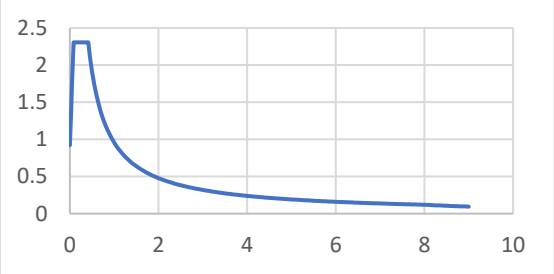

Fig. 1. MCE Response Spectrum

Modal periods of the designed fixed base structures, as the first group of the considered buildings are presented in Tables 2 to 4 for buildings with three, five and seven bays, respectively.

Table 2. Modal periods of building with three bays

Mode	4-Story	7-Story	12-Story
1-Lateral	0.70	1.01	1.61
2-Lateral	0.70	1.01	1.61
3-Tortional	0.55	0.82	1.27

Table 3. Modal periods of building with seven bays

Mode	4-Story	7-Story	12-Story
1-Lateral	0.75	1.16	1.72
2-Lateral	0.75	1.16	1.72
3-Tortional	0.66	1.03	1.53

Table 4. Modal periods of building with five bays

Mode	4-Story	7-Story	12-Story
1-Lateral	0.82	1.22	1.78
2-Lateral	0.82	1.22	1.78
3-Tortional	0.61	0.95	1.43

For the second group of buildings, namely those which have the possibility of foundations' uplift, a zero-length GAP element, working only in compression, were considered at the bottom of each column, with a stiffness values of 600000 kN/m. In this group of buildings, in addition to the normal beams and columns, the tie beams were also considered at the foundation level to make the model more realistic.

For nonlinear time history analysis (NLTH) ground motion records of three well-known earthquakes, Chi-Chi, Coalinga, and Darfield were chosen and scaled based on Selecting and Scaling Earthquake Ground Motions for Conducting Response-History Analyses [7]. Characteristics of the selected earthquakes are given in Table 5, and the spectral acceleration curves of their major horizontal components are shown in Fig. 2.

Table 5. Character of ground motion

Earthquake Name	Year	Magnitude	Mechanism	Vs30 (m/sec)
Chi-Chi, Taiwan	1999	7.62	Reverse Oblique	438
Coalinga-05, USA	1983	5.77	Reverse	352
Darfield, New Zealand	2010	7.00	Strike Slip	326

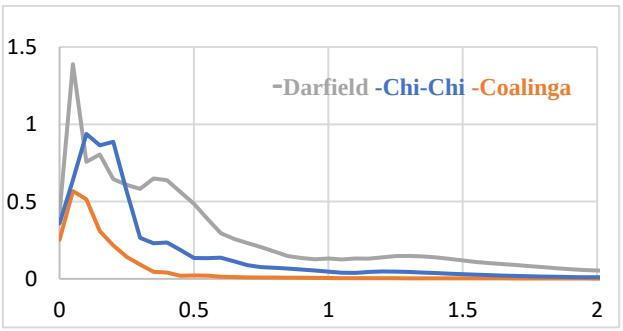

Fig. 2. Spectral acceleration curves of the main components of the selected earthquakes

It is seen in Fig. 2 that the PGA values of selected earthquakes are between 0.25g to 0.45g. For scaling the selected earthquakes' records, according to the fundamental period of buildings, to be used in their NLTHA, the amplification factors, given in Table 6, had to be applied.

Table 6. Amplification for 4 and 7 stories

	Earthquake		
No. of Stories	Chi-Chi	Coalinga	Darfield
4 and 7	1.56	2.83	1.90
12	1.20	1.72	1.64

The NLTHA cases were performed for both groups of buildings, using the scaled three-component records, and their responses, including roof relative displacement, roof absolute acceleration, inter-story drifts, and base shear, as well as performance levels of PHs were obtained for comparison, as presented in the next section.

3 Results and Discussion

Three structural dynamic seismic responses, including roof relative displacement, roof absolute acceleration, inter-story drifts, and base shear, were investigated and their maximum values were compared to see how much the uplift affects the seismic response of each building. Fig. 3 shows the vertical and horizontal displacement histories of a corner point of the roof of 3-bay 4-storys building with uplift possibility, subjected to Chi-Chi earthquake, as samples of seismic responses of this building.

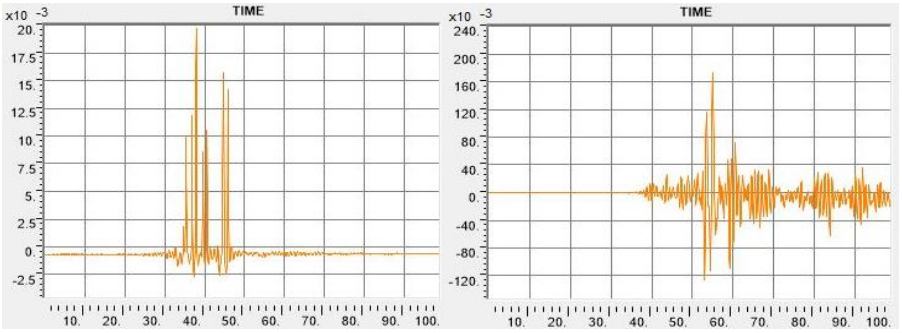

Fig. 3. Vertical and horizontal displacement histories (in meters) of a corner point of the roof of 3-bay 4-storys building with uplift possibility, subjected to Chi-Chi earthquake.

In Fig. 3 the nonzero value of vertical displacement at start and end of earthquake is due to the gravity loads. Also it can be seen in this figure that the horizontal displacement in zero at start, but it is not at the end, and that is because of plastic deformations in the body of the structure. The maximum responses of 3-bay 4-storys building with uplift possibility, subjected to the three applied earthquakes, are presented in Table 8 in comparison with those of its fixed base counterpart, and Table 9 presents the maximum inter-story drifts of 3-bay 4-storys buildings subjected to the three applied earthquakes are presented.

Table 8. Maximum responses of 3-bay 4-storys buildings subjected to the three applied earthquakes

	Response type					
	Base shear (kN)		Acceleration (m/s^2)		Displacement (mm)	
Earthquake	Fixed base	With uplift	Fixed base	With uplift	Fixed base	With uplift
Chi-Chi	3770	3770	8.366	7.90	174	172
Coalinga	4563	4440	7.65	7.33	181	175
Darfield	5363	5390	8.53	8.65	195	200

Table 9. Maximum drifts (in mm) of 3-bay 4-storys buildings subjected to Chi-Chi earthquake

Floor No.	1	2	3	4
Fixed based	53	50	39	32
With uplift	51	51	38	32

It is seen in Tables 8 and 9 that there is not any significant difference between the maximum responses of the two groups of buildings. As samples of responses of 5-bay 7-story building with uplift possibility Fig. 1 shows the roof absolute acceleration and roof relative displacement histories of this building subjected to Coalinga earthquake.

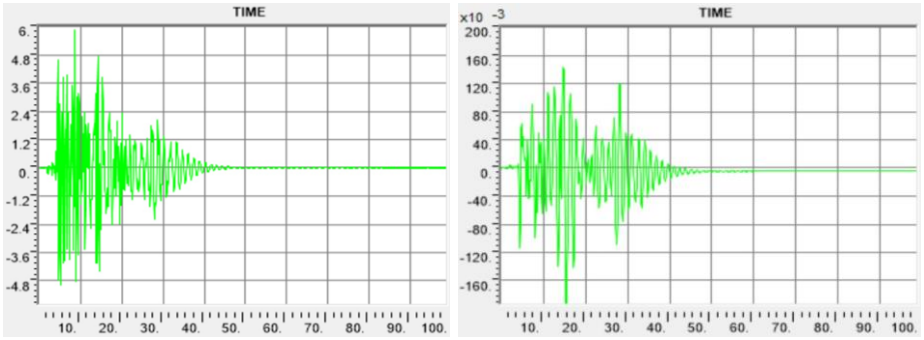

Fig. 4. Roof absolute acceleration (left) and roof relative displacement (right) histories of 5-bay 7-story building with uplift possibility subjected to Coalinga earthquake

In table 10, the maximum responses of both 5-bay 7-storys buildings subjected to the three applied earthquakes are shown, and Table 11 displays the maximum inter-story drifts of these buildings subjected to Coalinga earthquake.

Table 10. Maximum responses of 5-bay 7-storys buildings subjected to the three applied earthquakes

	Response type					
	Base shear (kN)		Acceleration (m/s^2)		Displacement (mm)	
Earthquake	Fixed base	With uplift	Fixed base	With uplift	Fixed base	With uplift
Chi-Chi	8850	8590	4.30	4.48	341	349
Coalinga	7350	7320	5.83	5.85	1984	1972
Darfield	18100	17800	9.43	9.10	809	824

Table 11. Maximum drifts (in mm) of 5-bay 7-storys buildings subjected to Coalinga earthquake

Floor No.	1	2	3	4	5	6	7
Fixed base	18	30	35	35	36	27	17
With uplift	15	31	34	38	36	26	17

By looking at Tables 10 and 11 it can be again seen that there is no significant difference in the maximum response values of the two groups of buildings. As samples of responses of 7-bay 12-story building with uplift possibility Fig. 5 shows the time histories of base shear and roof displacement of the building subjected to Darfield earthquake.

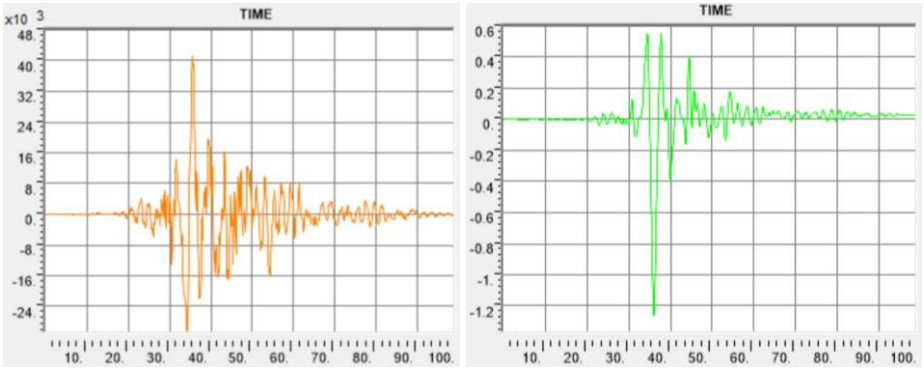

Fig. 5. Time histories of base shear (kN) (left) and roof displacement (m) (right) of the 7-bay 12-story building with uplift possibility subjected to Darfield earthquake

Table 12 presents the maximum values of the seismic responses of both 7-bay 12- story buildings subjected to the three applied earthquakes, and Table 13 display the maximum inter-story drifts of the two building subjected to Darfield earthquake.

Table 12. Maximum responses of 7-bay 12-storys buildings subjected to the three applied earthquakes

	Response type					
	Base shear (kN)		Acceleration (m/s^2)		Displacement (mm)	
Earthquake	Fixed base	With uplift	Fixed base	With uplift	Fixed base	With uplift
Chi-Chi	22300	19700	3.95	3.61	314	292
Coalinga	19400	17900	3.95	3.89	207	195
Darfield	44700	41100	5.86	5.77	1260	1260

Table 13. Maximum drifts (in mm) of 7-bay 12-storys buildings subjected to Darfield earthquake

Floor No.	1	2	3	4	5	6	7	8	9	10	11	12
Fixed base	145	158	159	154	140	122	102	97	78	57	33	16
With uplift	130	159	158	155	141	123	103	97	79	60	35	19

By looking at Tables 12 and 13 it can be seen that almost all maximum responses of the building with uplift possibility are less than those of the fixed base building, however, the maximum drift values are not so much different in the two buildings. On this basis, it can be said that by increase in the building's height the effect of uplift in reduction of seismic responses increase as well.

Regarding that the infill masonry walls were also considered in the buildings' modeling as struts or only-compression elements, it is good to have a look at the seismic response of these elements as well. Fig. 6 shows the force – deformation behavior of

one of these elements as a sample, in which it is seen that the element has worked only in compression.

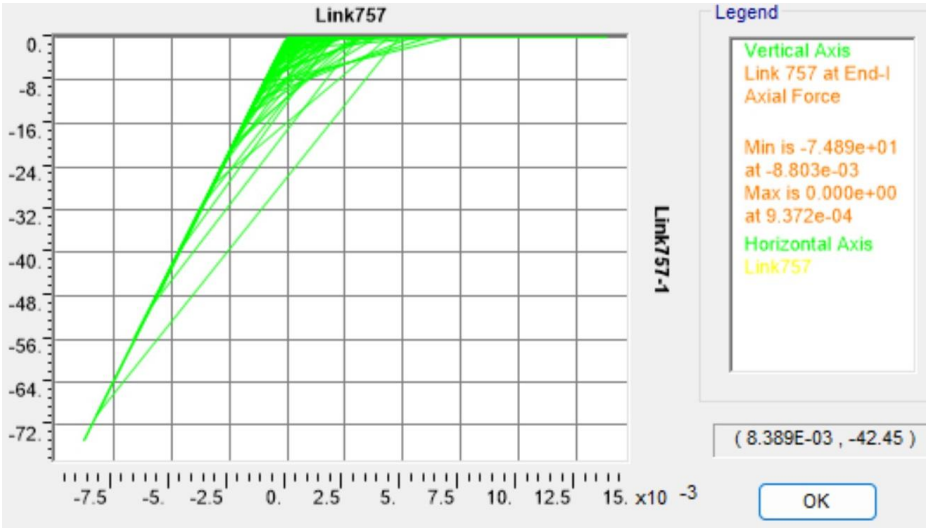

Fig. 6. Force (kN) – deformation (m) behavior of one of infills subjected to Darfield earthquake

As the last set of sample results, Fig. 7 compares the PHs formed in the two 7-bay 12–story buildings subjected to Darfield earthquake.

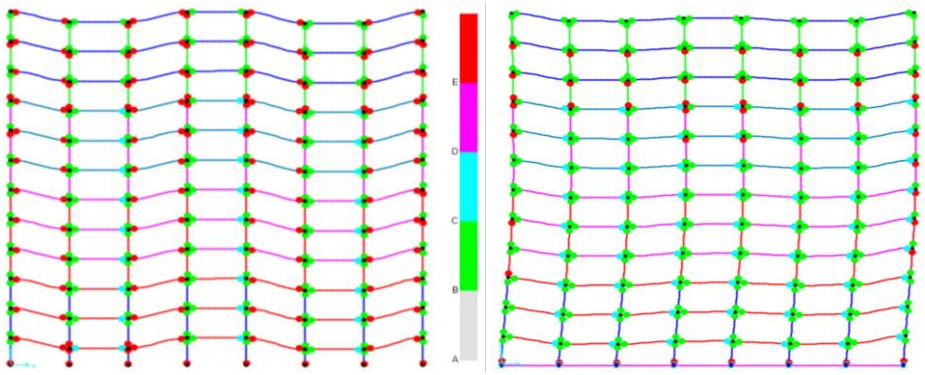

Fig. 7. PHs formed in 7-bay 12-story buildings in fixed base (left) and uplift possibility state (right), subjected to Darfield earthquake

It is seen in Fig. 7 that the number of PHs in the Collapse Prevention (CP) performance level, formed in the building with uplift possibility is much lower than those in the fixed base building. This apparently means that the seismic behavior of the building with possibility of uplift of foundations is much better the fixed base building. Better behavior of building with possibility of uplift can be confirmed by the moment – rotation hysteresis of PHs in the frames elements. Figs. 8 and 9 show the hysteretic

loops of PH is beam and a column, respectively, in the building with possibility of uplift in comparison with those of the same PHs in the fixed base building.

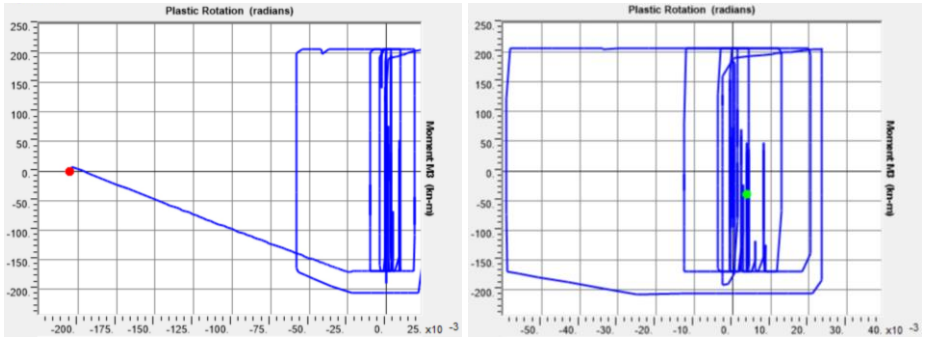

Fig. 8. Moment – rotation hysteretic curves of the PH in a beam element of the fixed base building (left) and building with possibility of uplift (right)

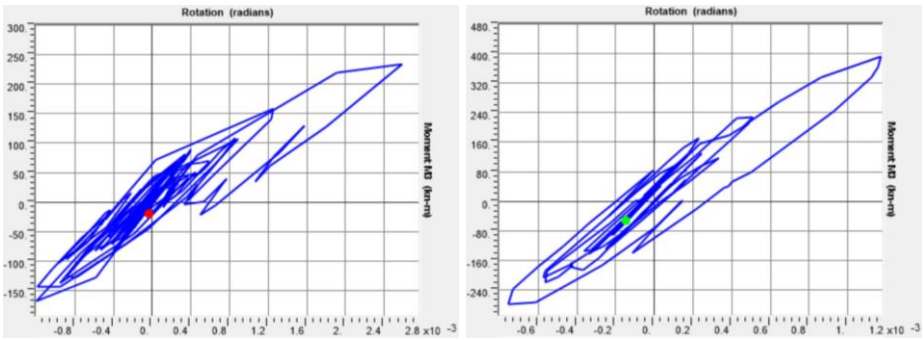

Fig. 9. Moment – rotation hysteretic curves of the PH in a column element of the fixed base building (left) and building with possibility of uplift (right)

It is seen in Figs 8 and 9 that the PHs in the fixed base building has reached the CP performance level, indicated by the red dots in the figures, while in the building with possibility of uplift their performance level is still in Life Safety condition, indicated by the green dots in the figures.

4 Conclusion

Based on the results of the series of NLTHA, conducted by applying a set of selected earthquake accelerograms, for nine multi-bay multi-story buildings in two states of fixed base and with possibility of uplift the following concluding remarks ca be stated:

- Tendency of foundations' uplift depends on the number of the building's aspect ratio (height over plan dimension).
- For buildings with the same aspect ratio the differences between responses of the two states are almost the same.

- In some cases the building with possibility of uplift show a better seismic performance, and sometime vice versa. Therefore, design of buildings by assuming fixed base columns can be either conservative or non-conservative. Therefore, to make sure, it is recommended that the condition with possibility of uplift is used for checking the design.
- Finally, it should be noted that in this study only regular buildings with moment frames were considered, and to complete the study, other types of buildings, including those with shear wall, as well as buildings with irregularities should be taken into consideration.

References

1. Housner G.W., "The behavior of inverted pendulum structures during earthquakes," Bulletin of the Seismological Society of America, vol. 53, pp. 403-417, 1963.
2. Yim, Chik-Sing, and Anil K. Chopra. "Earthquake response of structures with partial uplift on Winkler foundation." Earthquake engineering & structural dynamics 12, no. 2: pp. 263-281, 1984.
3. Iwashita, Keizo, Hajime Taniguchi, H. Kimura, and Y. Kasuga. "Effect of uplift on earthquake response of building." Journal of Structural and Construction Engineering 567 (2003): 33-40.
4. Jafarieh, Amir Hossein, and Mohammad Ali Ghannad. "Seismic performance of nonlinear soil-structure systems located on soft soil considering foundation uplifting and soil yielding." Structures, vol. 28, pp. 973-982. Elsevier, 2020.
5. ACI, Building code requirements for structural concrete (ACI 318-19), American Concrete Institute, 2019.
6. NEHRP, Guidlines for the seismic rehabilitation of buildings (FEMA publication 273), Applied Technology Council, 1997.
7. NIST, Selecting and scaling earthquake ground motions for performing response-history analyses, National Institute of Standards and Technology, 2011.

Vision-Based Identification of Dynamic Characteristics Using Cameras: A Case Study on One of Tehran's Bridges

Maryam Abazarsa[1*] and Mahmood Hosseini[2] [ORCID: 0000-0003-3142-4087]

[1] Graduate Student, Department of Civil Engineering, South Tehran Branch of the Islamic Azad University (IAU), Deh Haghi Avenue, Tehran, Iran
m.abazarsa@gmail.com
[2] Professor, Department of Civil Engineering, Eastern Mediterranean University (EMU), Famagusta 99628, North Cyprus via Mersin 10, Türkiye
mahmood.hosseini@emu.edu.tr
*Corresponding Author

Abstract. Vibration-based Structural Health Monitoring (SHM) is a promising approach for operation and post-event assessment of important civil structures, like bridge, and in this regard system identification is the key factor. In traditional SHM solutions, the response of structural systems is measured by measuring their acceleration, velocity, displacement, and strains through contact sensors like accelerometers at sparse locations. However, the installation, maintenance, and operation of these sensors are laborious and time-consuming, limiting the application of SHM solutions. As a remedy to these problems, vision-based measurement methods have emerged in recent years thanks to the development in computer science and camera technology. But, using high-resolution, high frame-rate cameras could defeat the purpose of the vision-based solutions. In this study, ordinary cameras or smartphones were used for this purpose. Also, it was tried to use a target-less approach and measure the vibration signals by tracking structural features. First, a video of the bridge's swing was produced for 60 seconds, gotten from the front view of the bridge. Then, the vertical displacement in the middle of the bridge was extracted from the produced video and compared with the actual values of the displacement signals obtained (by integration) from the accelerometer installed on the bridge. To select the tracked points to extract the displacement signal, Kanade-Lucas-Tomasi algorithm was used. Also, frequency domain decomposition algorithm was used to detect the dynamic characteristics of the structure from the extracted signals. The results show the desirable ability of the proposed image-based method to identify the characteristics of structures.

Keywords: Structural Health Monitoring, Dynamic Characteristics, KLT algorithm, FDD algorithm.

1 Introduction

Civil engineering structures, including buildings and bridges, are exposed to various external loads during the operational lifetime, and monitoring structures is necessary

for providing quantitative information for their safety evaluation. However, obtaining these data is expensive and time-consuming. Sensors that are currently used to measure structural displacements are divided into two categories: contact-type such as LVDT[1] that require a fixed reference point for installation as well as direct access to the structure which is often difficult or even impossible to locate, and noncontact-type like GPS[2] that have the limitation of measurement accuracy and usually with errors between 5 and 10 mm.

To cope with these problems, Structural Health Monitoring (SHM) method have been developed recently and it is aimed at providing useful information for structural assessment and maintenance through relevant measures of structural response. Recently, vision-based methods provide an opportunity to measure the dynamic characteristics of structures with little effort that is economical, convenient and reliable. SHM have shown good capabilities, including simple installation and the capacity to measure the displacement of several points using only one camera. Of course, vision-based methods have been used before to monitor the deformation of tall structures [1], short-span [2-5] and large-span bridges [6-8] and they have a significant ability to assess the state of the structure, especially in the field of determining the characteristics of the structures [9-11], and participating by traffic monitoring systems [4].

Some authors have recently worked on identification system through image processing that show these methods are acceptable tools and multiple approaches exist to identify modal characteristics such as natural frequencies. In this paper, we have tried to use a cellphone and an ordinary camera for tracking feature of the structure to extract displacement signals, and use it to find the natural frequencies and modal shapes.

2 The Approach Steps

To obtain structural dynamic characteristics of any structure three steps are required as follow:

-Feature tracking to extract displacement signal
-Processing extraction signal
-Test in three phase to determine natural frequency and mode shape of structure

2.1 Feature Selection

In previous studies, several definitions for good feature selection have been presented, for example, some researchers worked on a using windows with high standard deviation in spatial intensity [12, 13], Laplacian zeros of the image intensity [14] and the corner features based on the first and second derivatives of the image intensity function [15, 16]. The important thing is that a single pixel cannot be tracked unless it has a very distinct brightness from all its neighbors. As a result, it is often difficult or impossible to determine where a pixel has gone in the next image based on its local information alone. Because of these problems, we do not track a single pixel, actually, we rather a

[1] Linear Variable Differential Transformer
[2] Global Positioning System

window of pixels that contain sufficient information and features. Researchers have suggested that corners be tracked, windows with high spatial frequency content or ranges where the mixture of second-order derivatives is sufficiently high. Definitely, all these definitions usually lead to find traceable features. An ideal window based on previous studies for tracking is a window which has the following condition.

$$\min(\lambda_1, \lambda_2) > \lambda \tag{1}$$

λ_1 , λ_2 are eigenvalue of matrix G, and G is an image gradient and λ is a predefined limit. To determine λ we first calculate the eigenvalues for a range that has approximately the same brightness for photos taken. This gives a lower bound for λ. Then we select a set of various types of features, including corners and boundaries to obtain an upper bound for λ. Actually, we find out that these two limits are well separated from each other and the value of λ will not be a problem if the middle limit is chosen between these two limits.

2.2 Kanade-Lucas-Tomasi (KLT) Algorithm

Tracking algorithms provide the ability to predict future position of multiple moving objects based on the history of the individual positions and there are various algorithms for feature tracking that have different approaches. In this paper, we decided to use KLT algorithm [17] that is an approach to feature extraction. It is proposed mainly for the purpose of dealing with the problem that traditional image registration techniques are generally costly. KLT makes use of spatial intensity information to direct the search for the position that yields the best match. It is faster than traditional techniques for examining far fewer potential matches between the images. Therefore, the image intensities in the transferred window can be written as the values of the original window plus an additional term that is almost linearly dependent on the transfer vector.

As a result of these estimates, we can write a 2×2 linear system which is the displacement vector between two windows. The fundamentals of tracking can be explained by looking at two images in an image sequence. Let us assume that the first image was captured at time t and the second image at time t + τ. It is important to keep in mind that the incremental time τ depends on the frame rate (capture rate) of the video camera and should be as small as possible. An image can be represented as function of variables x and y. We add the variable t as the time the image was captured. Thus, any section of an image can be defined by an intensity function $I(x, y, t + \tau)$. The basic assumption of the KLT tracking algorithm is:

$$I(x, y, t + \tau) = I(x - \xi, y - \eta, t) \tag{2}$$

It is clear that every point in the second window can obtained by shifting every point in the first window by an amount (ξ, η). This amount can be defined as the displacement $d = (\xi, \eta)$ and the main goal of tracking is to calculate d. The basic information has now been established to solve the displacement d of a feature from one window to the next. Any differences between subsequent windows that cannot be

explained by the transfer are considered errors, and the transfer vector is determined in such a way as to minimize this error. Therefore, if

$$J(x) = (x, y, t + \tau) \tag{3}$$

$$I(x - d) = I(x - \xi, y - \eta, t) \tag{4}$$

the image model is expressed as

$$J(x) = I(x - d) + n(x) \tag{5}$$

where n is the noise, the displacement vector d is chosen to minimize the residual error by the double integral over the window w.

$$\epsilon = \int_{w}^{\infty} [I(x - d) - J(x)]^2 \, w \, dx \tag{6}$$

W is a function of weight. In a simple case, W can be assumed equal to 1. W can be a Gaussian function that emphasizes the middle region of the window.

3 Signal Processing in Frequency Domain

After extracting the displacement signal from the recorded videos, it is time to process the signal. In order to be able to extract the information hidden in the signal, we must use the existing methods to determine the characteristics of the structures using their response signals. There are many ways such as OKID[3] [18], ERA[4] [19], SSI[5] [20, 21], frequency domain decomposition (FDD) [22, 23], and so on. FDD is a method which is based on a frequency analysis and it is clear that frequency representation is one of the most important and powerful tools for investigating signals. The FDD method is a method of determining the characteristics of the structure using only the response of the structure. It is especially used for the analysis of large structures such as bridges and buildings. This method makes it possible to extract the mode parameters (mode shape and damping ratio frequency) under environmental vibration excitation. The main advantage of the FDD method is the possibility of distinguishing close modes and its ability to analyze signals with a high noise-to-signal ratio. The FDD method uses the PSD[6] of the signals instead of the Fourier transform of the impulse response function. The relationship between the uncertain input signal vector x(t) and the measured response signal vector y(t) is described as follows.

$$G_{yy}(jw) = \bar{H}(jw) G_{xx}(jw) H^T(jw) \tag{7}$$

[3] Observer/Kalman Identification Algorithm
[4] Eigensystem Realization Algorithm
[5] Spectral segmentation and Identification
[6] Power Spectral Density

Matrix $G_{xx}(jw)$ with size (r, x, r) is the density spectral matrix PSD of the input signals, r is the number of input signals. Matrix $G_{yy}(jw)$ with dimensions (m, x, m) is the matrix PSD of the system response, m the number of response signals. H(jw) with dimensions (m, x, r) is a FRF[7] of the system.

4 Obtaining Structural Dynamic Characteristics

In evaluating phase for measuring the performance of the presented process for extracting the displacement signal and thus determining the characteristics of the structure from the extracted record, first of all, a video generated from a computer model has been used. The proposed method was verified using a video generated from a numerical model of a bridge under a realistic traffic load. A traffic scenario by 16 vehicles with different weights and speeds is considered as the traffic load applied to the model. For this study, a video of the bridge swing was produced for 60 seconds and was prepared from the front view of the bridge, so the vertical displacement in the middle of the bridge was extracted from the produced video and compared with the actual values.

To apply the method, first, the desired window is selected to determine the points with special features for tracking. Since we are looking for the vertical displacement of the middle of the span of the bridge, we choose the window that is in the middle of the span and not so small that there are few points inside it, and not so large that the points with different displacements are placed in it because increasing the calculation time and the possibility of errors and outliers. Then the selected window was tracked by the KLT algorithm to extract the displacements of points with special features.

In order to extract the characteristics of the structure from the extracted displacement signal, first, it is converted into an acceleration signal by derivation twice. The reason for this is that the displacement signal contains low frequencies that are related to the traffic load applied to the bridge. Therefore, it makes it very difficult to detect the frequency of the structure. Now, derivation filters low frequencies. But since taking the derivative twice to convert the displacement signal into acceleration amplifies the high frequencies, so the possible noises in the signal are amplified, using a low-pass filter is effective in removing the high frequencies related to the noise.

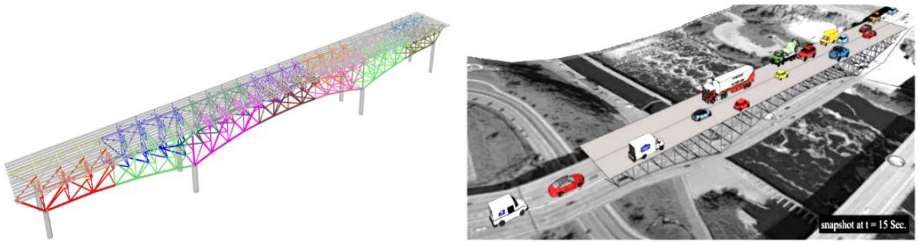

Fig. 1. Finite element model of the bridge (left), and a view of traffic load applied to stimulate its structural response (right)

[7] Frequency Response Function

To check the performance of this method, the displacement is magnified with a different magnification factor to assess the level of vibration impact on results. On the other hand, in order to improve the results, it has been decided to make a zoomed video on the middle part of bridge, this can be done in reality by lens and optical zoom. The results are better than before and zooming on the desired location, of course, optical zoom can help a lot to improve the results. Fig. 2 shows a bird view of the considered bridge and a close-up of the position of the video shooting. Also Fig. 3 shows the selected window for tracking, and selected points for tracking in the window, and Figs. 5 to 8 shows the average displacements of successful points tracked by various magnification factors with or without zooming.

Fig. 2. A bird view of the considered bridge (left) and a close-up of the target area of the video shooting (right)

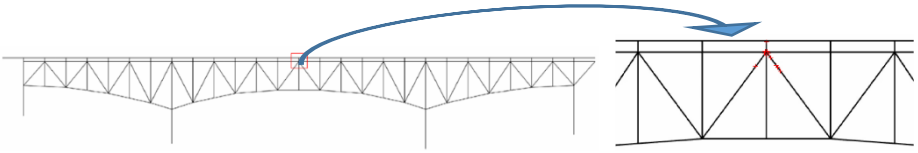

Fig. 3. Selected window for tracking (left), and selected points for tracking in the window

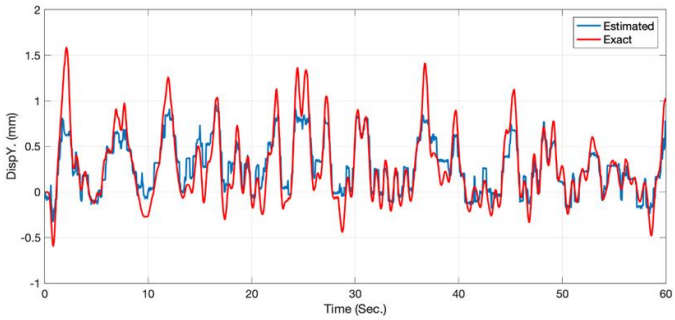

Fig. 4. Average displacements of successful points tracked by no magnification and zooming

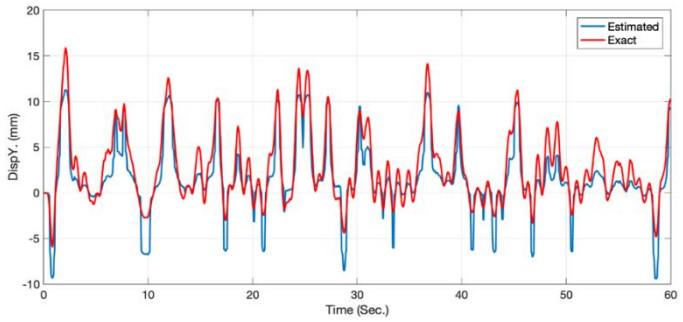

Fig. 5. Average displacements of successful points tracked by magnification factor of 10

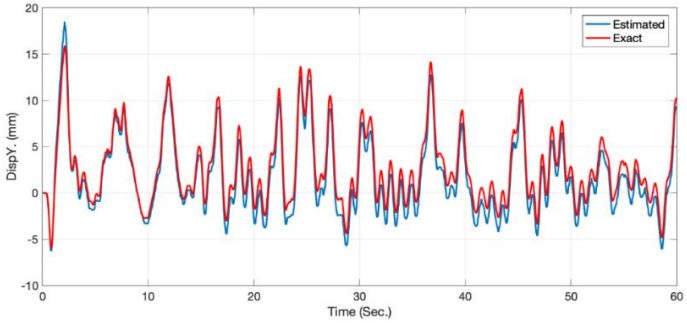

Fig. 6. Average displacements of successful points tracked by magnification factor of 10 and zooming

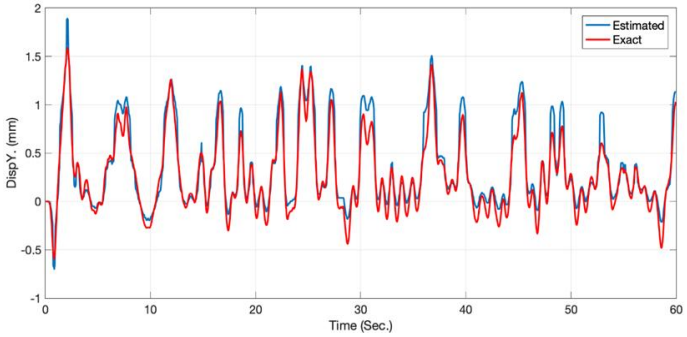

Fig. 7. Average displacements of successful points tracked just by zooming

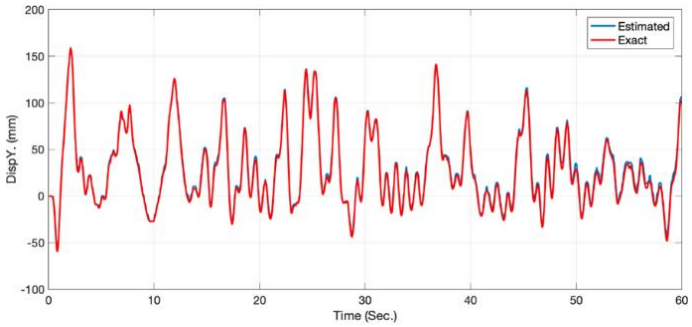

Fig. 8. Average displacements of successful points tracked by magnification factor of 100

The amount of error in the results obtained from the examination of the above cases, and presented in Table 1, was calculated by using the following formula.

$$e = \frac{|x_1 - x_2|}{|x_1||x_2|} \tag{8}$$

x_1: accurate displacement signal at the target point.
x_2: the estimated displacement signal at the target point.

Table 1. Calculated errors for different tracking procedures

Tracking Procedure	Error
Without magnification and without zooming	0.1835
Magnification 10	0.1604
Magnification 10, with zooming	0.0704
Just zooming	0.0629
Magnification 100	0.0033

It is seen in Table 1 that the best result is obtained by using a magnification factor of 100, with no zooming, although by just zooming the result is also satisfactory. Similar results for the acceleration signals cannot be presented here because of lack of space, however, they can be found in the main report of the study (Abazarsa 2020) [24]. Fig. 9 shows the Fourier Transform of the acceleration signals in both original and filtered cases.

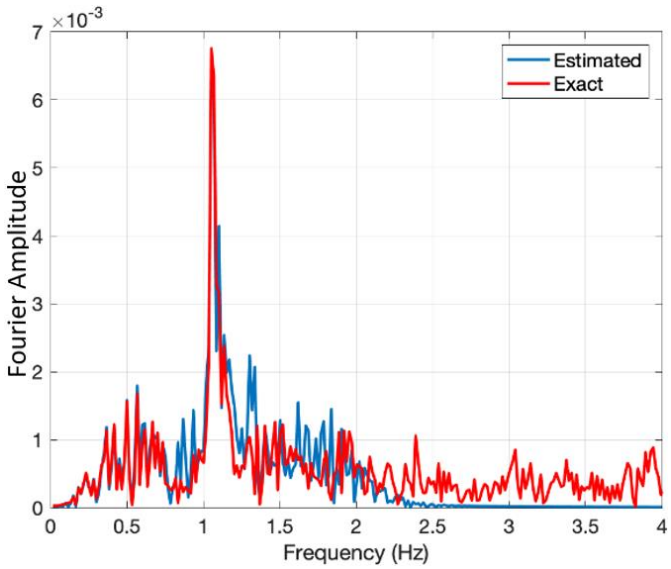

Fig. 9. Fourier Transform of the extracted acceleration and filtered signals

It can be seen in Fig. 9 that in both original and filtered acceleration signals the peak frequency is the same, and equal to 1.2 Hz.

5 Conclusion

A vision-based method was presented without artificial target to determine dynamic characteristic of structure using conventional cameras. Based on the obtained results it can be concluded that the proposed method, which is based on the KLT algorithm, create acceptable results a precision of more than 99%. However, there are still some issues to be discussed for more reliable use of the proposed method, as follow:

- Selecting the desired window is the only part where the user can intervene. How to choose a window can affect the results obtained. The first point is that the window should not be chosen too big or too small. If it is too large, the displacements of different feature that fall inside the window will not be the same, and getting average of them will not be correct in the future, and if it is too small, the number of trackable features found inside the window will be small, so the obtained signals will have a lot of noise. Therefore, it is better to try to track three points, which will eliminate noise and many errors.
- Since ordinary cameras and mobile phones are cheap and accessible, they were used in this research, but it should be kept in mind that these cameras suffer from the aliasing phenomenon. Actually, these cameras have a small number of frames per second (for example, 24 to 60 frames per second), if the structure has frequencies higher than half the number of frames per second, the measured displacement will be distorted. It mean that the information related to those higher frequencies that are not possible to be measured can contaminate the

information of lower frequencies. Aliasing in sensors can be eliminated by using an anti-aliasing filter, but aliasing cannot be eliminated in vision-based systems. Therefore, to obtain the correct measurement, the highest frequency of the structure must be less than half of the frame rate, otherwise the results will not be reliable. Another problem with ordinary cameras is that the speed of capture an image may not be accurate. If the speed is not same as mentioned, it causes an error in the frequency value. Also, it should be noted that the proposed method, and all the studies and analyzes carried out, are based on the assumption that the intended vibrations of the structure are perpendicular to the axis of the camera, in some cases, due to existing obstacles, it may not be possible to simply adjust the axis of the camera in this way.

In spite of all the mentioned issues, the vision-based structure identification method using ordinary cameras and without the need to install a target on the structure is able to detect the frequency of the first mode of the structure, and also if the video includes the entire structure, it is able to identify mode shape of structure.

References

1. Liao WY, Chen WH, Ni YQ, Xia Y (2010) Development of a vision-based real-time displacement measurement system for Guangzhou New TV Tower.
2. Feng D, Feng M, Ozer E, Fukuda Y (2015) A vision-based sensor for noncontact structural displacement measurement.
3. Kim S-W, Kim N-S (2011) Multi-point displacement response measurement of civil infrastructures using digital image processing.
4. Ribeiro D, Calc¸ada R, Ferreira J, Martins T (2014) Non-contact measurement of the dynamic displacement of railway bridges using an advanced video-based system.
5. Chang CC, Xiao XH (2010) Three-dimensional structural translation and rotation measurement using monocular Video grammetry
6. Wahbeh AM, Caffrey JP, Masri SF (2003) A vision-based approach for the direct measurement of displacements in vibrating systems.
7. Ye XW, Ni YQ, Wai TT et al (2013) a vision-based system for dynamic displacement measurement of long-span bridges: algorithm and verification.
8. Martins LL, Rebordaˇo JM, Ribeiro AS (2015) Structural observation of long-span suspension bridges for safety assessment: implementation of an optical displacement measurement system.
9. Yoon H, Elanwar H, Choi H et al (2016) Target-free approach for vision-based structural system identification using consumergrade cameras.
10. Caetano E, Silva S, Bateira J (2007) Application of a vision system to the monitoring of cable structures. In: Seventh international symposium on cable dynamics.
11. Oh BK, Hwang JW, Kim Y et al (2015) Vision-based system identification technique for building structures using a motion capture system.
12. Hans Moravec. Obstacle avoidance and navigation in the real world by a seeing robot rover. PhD thesis, Stanford University.
13. Chuck E. Thorpe. Vision and navigation for a robot rover. PhD thesis, Carnegie Mellon University, December 1984.
14. David Marr, Tomaso Poggio, and Shimon Ullman. Bandpass channels, zero-crossings, and early visual information processing.
15. Kitchen L and A. Rosenfeld. Gray-level corner detection. Computer Science Center 887, University of Maryland, College Park, April 1980.

16. B.K.P. Horn and B.G. Schunck. Determining optical flow.
17. B. D. Lucas and T. Kanade. An iterative image registration technique with an application to stereo vision.
18. JN Juang, JE Cooper, and JR Wright, "An Eigensystem Realization Algorithm using Data Correlation (ERA/DC) for modal parameter identification.
19. JN Juang and RS Pappa, "An Eigensystem Realization Algorithm for modal parameter identification and model reduction," Journal of Guidance, Control, and Dynamics.
20. GH James, TG Carne, and JP Lauffer, "The Natural Excitation Technique (NExT) for modal parameter extraction from operating structures.
21. JL Beck, BS May, and DC Polidori, "Determination of modal parameters from ambient vibration data for structural health monitoring," in in Proceedings of the 1st World Conference on Structural Control, Los Angeles, California, 1994.
22. Brincker R, Zhang L and Andersen P 2001 Modal identification of output-only systems using Frequency domain decomposition Smart Mater.
23. Tarinejad R and Damadipour M 2014 Modal identification of structures by a novel approach based on FDD-wavelet method Journal of Sound and Vibration.
24. Abazarsa Maryam, Vision-based Identification of Dynamic Characteristics Using Cameras: A Case Study one of Tehran's Overpass Bridges, MSc Thesis, under supervision of Prof. Mahmood Hosseini, submitted to Dept. of Civil Eng., South Tehran Branch of the Islamic Azad University, Tehran, Iran, 2020.

Shear Buckling of Corrugated Web Beams with Openings

Hartmut Pasternak[1][0000-0003-473-0302] and Zheng Li[2]

[1] Brandenburg University of Technology, Cottbus, Germany
hartmut.pasternak@b-tu.de
[2] Technical University of Berlin, Berlin, Germany
Zheng.li@tu-berlin.de

Abstract. The sinusoidal corrugated web girder represents a relatively novel structural form that finds diverse applications in steel structures. These beams offer a substantial reduction in weight compared to hot rolled profiles or welded I-sections due to their thin web. By utilizing corrugations, they enhance out-of-plane stiffness, effectively preventing web buckling. Incorporating openings for pipes in corrugated steel girders presents an economical solution without requiring increased building height. However, such openings inevitably compromise the overall stiffness and strength of the steel beam. To investigate the mechanical behavior of corrugated web girders with circular openings and accompanying opening rings, we conducted shear bearing capacity tests on three specimens. The finite element analysis, conducted using Abaqus®, yielded simulation results that closely aligned with the experimental findings, accounting for geometric imperfections. Our research demonstrates that the inclusion of an opening ring significantly enhances the bearing capacity of corrugated web girders with openings. Furthermore, a parameter study revealed that increasing the thickness of the opening ring amplifies the influence of geometric imperfections on corrugated web girders. Besides, the shear load bearing capacity of the corrugated web girder with circular opening ring can be estimated using a simplified hand calculation model.

Keywords: Corrugated web beam, opening, shear buckling.

1 Introduction

Corrugated web beams are welded beams with a thin-walled web and wide flanges. Due to its profiled shape, the corrugated web has an improved shear force carrying capacity, so that transverse stiffeners or thicker webs are no longer necessary. For more than 20 years, corrugated web girders have been used particularly frequently in single-story buildings with large spans. Compared with rolled and welded beams, the corrugated web beam has the advantages of low dead weight and excellent web buckling resistance. The load-bearing capacity of the corrugated web girder with a web thickness of 3 mm can reach the level of the traditional steel girder with the same cross-section size with a web of approx. 7 mm. A corrugated web of 6 mm replaces a thick

web of 10 mm [1]. Another competitive advantage of corrugated web beams is the fully automatic production [1],[2] developed by the Austrian company ZEMAN.
The advantages of corrugated web beams have garnered significant attention in the field of steel construction. As a result, extensive theoretical and experimental investigations have been conducted to explore their load-bearing capacity. These studies primarily focus on web buckling, elastic shear resistance of the entire beam under shear loading [3-7] local force application [8], interaction of bending moment and shear force [9], flange behavior, dynamic stress response [12], influence of one-sided welded corrugated web [13], and their application in steel composite construction [14-15]. The advent of computer technology has facilitated the use of numerical methods for analyzing corrugated web beams, which has become a standard practice in research. Additionally, Annex D of DIN EN 1993-1-5 [16] provides verification methods and simplified formulas for local web buckling reduction factors, enabling the practical implementation of corrugated web beams.
The reduced web thickness in corrugated web beams may lead to a decrease in shear resistance compared to conventional rolled sections or welded beams with a flat web. Research by Pasternak and Piekarczyk [17], as well as Kizmaz et al. [18], through experimental and numerical investigations, confirmed that web openings without an opening crown significantly diminish the load-bearing capacity. Additionally, Kizmaz et al. [18] studied the optimal placement of web openings based on numerical analysis. A recent development by Robra and Krasotina [19] introduced a simplified calculation model that enables estimating the shear force carrying capacity of a corrugated web girder with an opening ring through hand calculations. The primary purpose of the opening ring is to absorb the forces exerted by the web, which are released through the opening. Unlike web openings without ring, the position of the opening within the web panel does not affect the transverse load-bearing capacity, nor does the aspect ratio of the web panel's length to height. Only the opening diameter, dimensions, and material quality of the opening ring have an influence.

2 Tests

Three corrugated web beams with an opening ring were manufactured by ZEMAN company using fully automated processes in a factory setting. The beams had flanges measuring 250×12 mm. The corrugated web had sinusoidal profiling with a nominal thickness of 2 mm, a period length of 155 mm, and an amplitude of 40 mm, featuring one-sided welding. To prevent local buckling failure, vertical load introduction stiffeners were welded in the middle and at both ends of the beam. The placement of the central transverse stiffeners divided the profiled corrugated web into two equal sections. At the midpoint of each subfield, an opening was created automatically using a cutting robot, with variable radii of 108 mm and 305 mm. On both sides of the openings, three opening rings with different thicknesses were welded using a 3 mm wide weld seam. The dimensions of the test specimens can be seen in Figure 1 and Table 1.

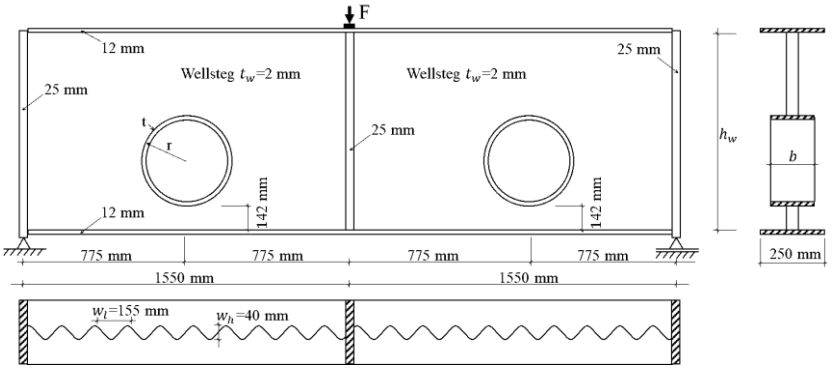

Fig. 1. Schematic illustration of corrugated web beam specimen

Table 1. Geometric dimensions of test specimen

Tests	h_w [mm]	b [mm]	r [mm]	t [mm]
Nr.1	500	150	108	8
Nr.2	500	150	108	12
Nr.3	1250	165	305	25

The test specimens are made of steel with different steel grades. The corrugated webs are made of cold-rolled strip St37-2G according to DIN 1623-2, the opening ring is made of S355 J2 and everything else is made of S235 JR. To ensure more precise calculation results using numerical methods, the material properties of the steel are determined through tensile tests using round specimens. Given the thinness of the corrugated web (2 mm), the H-shaped flat sample specified in DIN EN 50125 [20] is chosen. Three tensile specimens are tested for each steel grade, and the average values are used as the test results. Typically, numerical programs require material properties to be set with characteristic values. Based on the experimental findings, the moduli of elasticity for the three mentioned steel grades are assumed to be 208 GPa, 206 GPa, and 208 GPa for the finite element calculations, and the yield stresses are 300 MPa, 358 MPa and 329 MPa, respectively.

The test girders were examined at the laboratory of BTU. The vertical loading of the girders occurred at the center above the load introduction stiffener, allowing for central load transfer in the middle of the girder. In all three tests, the centric load was applied using a 30 mm thick steel plate with a load application area of 250×50 mm. The test beam was supported by a loose and a fixed roller bearing, and the bearing loads were transmitted through the two bearing stiffeners on the corrugated web girder. Magnetic displacement transducers were positioned on both sides of the load introduction stiffener on the lower chord to measure the deformation of the test specimen.

The load tests were path-controlled, carried out with a load speed of 0.5 mm/min and a 10 Hz sampling rate. During the test, the force was first loaded to half of the estimated load capacity to verify the measuring system and the loading system. The test

specimen was then reloaded until web buckling occurred during the test and the load-deformation curve dropped again.

Figures 2 and 3 depict the test specimen before and after loading. It is evident that the failure modes of the three beams exhibit similarities, with shear buckling observed on the corrugated web. The testing process can be divided into three phases: 1: Initial loading results in a linear increase in vertical deflection at the beam's center, with no significant out-of-plane deformation of the corrugated web. 2: The load-deformation curve gradually exhibits non-linear behavior. Concurrently, the corrugated web displays evident buckling and deformation adjacent to the circular ring of openings. 3: In the final phase, the vertical deformation of the test specimen rapidly increases, accompanied by a continuous decrease in load-bearing capacity. Eventually, buckling occurs across multiple waves, demonstrating post-buckling behavior.

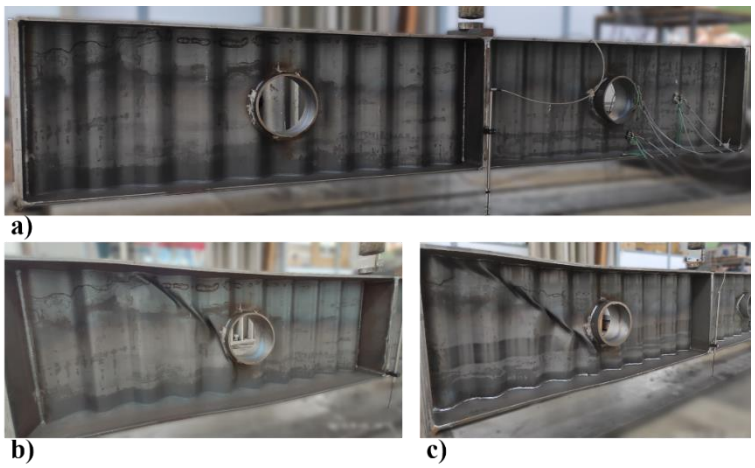

Fig. 2. a) Test setup, b) Failure mode of the experiment specimens No. 1, c) Failure mode of specimens No. 2

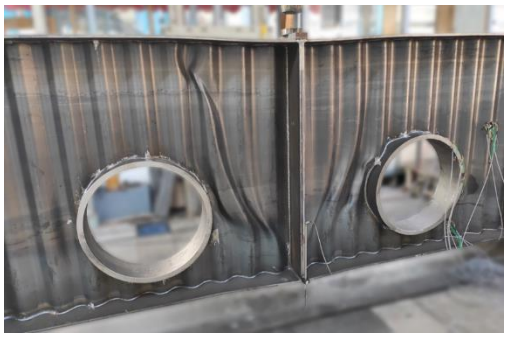

Fig. 3. Failure mode of the experiment specimens No. 3

3 Numerical Simulation

The numerical investigation of the corrugated web beam was carried out using the finite element method using the commercial program Abaqus®. The test vehicles are simulated in the numerical program with their geometric dimensions according to Figure 2 and Table 1. The material properties of the FE model are based on the measured material properties. Four-node S4R and three-cornered S3 shell elements are used to mesh the created numerical geometry. The element size was defined by sensitivity studies as 10 mm.

If the experimental results are to be simulated as precisely as possible, it is necessary to take the imperfection into account in the FE calculation. In this paper, the equivalent imperfections based on equivalent deformations affine to the first mode shape are considered in numerical calculations. According to EC3 part 1-5, it is assumed that the amplitude rise for this sinusoidal corrugated web support is $h_w/200$.

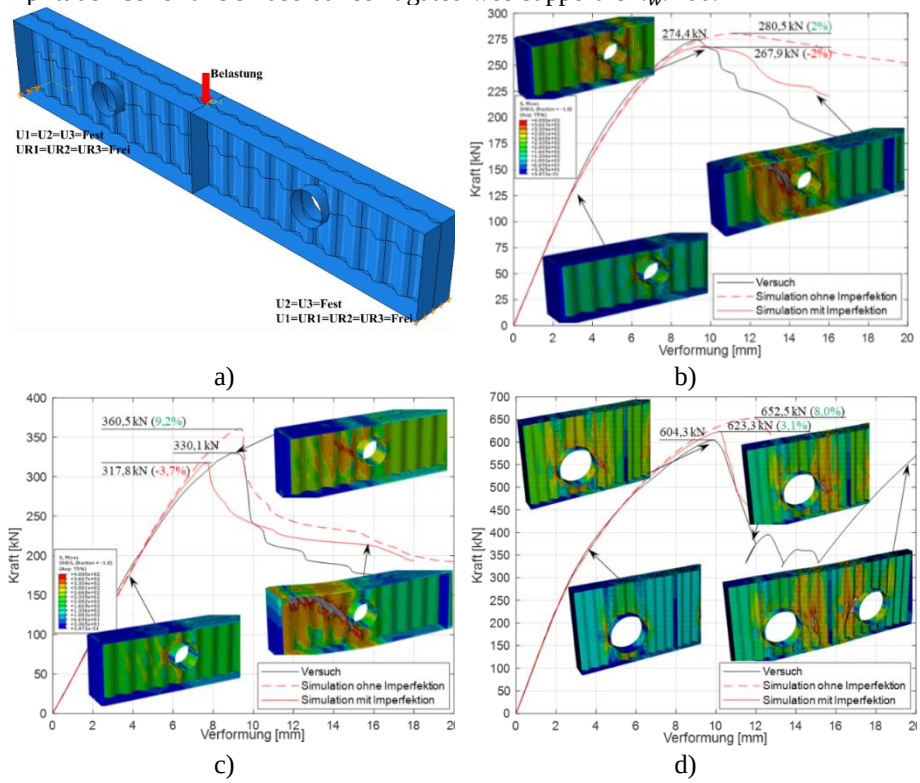

Fig. 4. a) Finite element model of specimen No. 1, Experimental and numerical load-deformation curve b) test No. 1, c) test No. 2, d) test No. 3

Figure 4 illustrates the load-deformation curves obtained from both experimental and numerical analyses for the three test specimens. It is evident that within the deformation range of 0 to 20 mm, the elastic strain phase of the test specimens aligns closely with the numerical model. Comparing the ultimate loads between the tests and FE

calculations without considering imperfections reveals a difference ranging from 2% to 9%. However, when accounting for the adverse effects of imperfections, the maximum loads deviate by less than 4% for all test beams. These findings emphasize the importance of considering geometric imperfections when using numerical methods to calculate corrugated web beams with circular aperture crowns. Neglecting imperfections in the numerical model can result in an overestimation of the actual load-bearing capacity by 10% or more.

Beam 1 and Beam 2, which are similar test specimens differing only in the thickness of the circular opening ring, exhibit significant differences in the sensitivity to geometric imperfections. When considering imperfections of the same size in the numerical model, the load-bearing capacity of Beam 2 decreases by over 10% compared to the perfect corrugated web beam. However, the reduction in load-bearing capacity for Beam 1 is less than 5%. It is noteworthy that even when imperfections are considered, the simulated load-bearing capacity of Beam 3 surpasses the experimental value. This discrepancy may be attributed to the fact that the first eigenmode may not represent the most critical pre-deformation for corrugated web beams with a relatively large web height. Deformations or residual stresses during the "flange-web" and/or "web-opening ring" welding process could then dominate the eigenmode.

Figure 4 c) and d) illustrates the deformation pattern and von Mises stresses of the entire specimen, showing that the post-buckling behavior in the FE model aligns precisely with the experimental results. The calculations demonstrate local shear buckling failure in the sinusoidal corrugated web at the ultimate load, which progresses towards global buckling in the post-buckling region until the load-bearing capacity is completely lost. Notably, the global buckling of test beams 1 and 2 does not extend over the entire height of the web. In Figure 4 d), it is evident that the buckling occurs on one side of the opening ring and diagonally extends towards the upper portion. This indicates an interaction of bulge shapes, referred to as zonal buckling or a mixed form of local and global buckling. In this case, the shear buckling extends over multiple waves, but the buckling forms do not encompass the full height of the web. In contrast, test beam 3 initially displays minor local buckling between the load introduction area and the opening ring, followed by clear global buckling spanning the entire height. Additionally, a second shear buckling occurs in another subfield of the test during the post-buckling phase, resulting in a vertical deformation of approximately 20 mm.

4 Parametric Studies

To assess the impact of circular openings and corresponding ring thickness on the load-bearing capacity of corrugated web beams, an analysis of influencing parameters is conducted. The parameter study considers corrugated web beams with and without circular openings, varying ring thicknesses for different test beam dimensions (No. 1/2 and No. 3). The study specifically examines the shear force carrying capacity of corrugated web girders with opening rings and the sensitivity of geometric imperfections. Constant parameters include the geometry of the test specimen and the dimensions and position of the opening. The ring thickness is varied, with values of

t={2;4;6;8;10;12;14} mm for test specimen No. 1/2 and t={10;15;20;25;30;35} mm for test specimen No. 3. All calculations are performed using geometric and material nonlinear analysis with imperfections accounted for (GMNIA) in the Abaqus®. The structural behavior is investigated through eigenanalysis for pre-deformation and nonlinear analysis using the Riks method for ultimate loads.

Figure 5 presents the influence of circular openings and corresponding rings on shear force resistance. The numerical results indicate that the presence of openings in the corrugated web not only reduces the load-bearing capacity but also diminishes the overall stiffness of the beam. For test specimens No. 1/2, the load capacity without openings reaches approximately 330 kN. However, with the opening (radius r=108 mm), the load capacity decreases to only 120 kN, as depicted in Figure 5 a). In the case of test specimen No. 3, which features a relatively large opening, the presence of the opening reduces the shear force carrying capacity to approximately 1/10 of that of an unopened corrugated web girder. Nevertheless, it is evident that the opening rim can significantly enhance both the shear force carrying capacity and overall rigidity of the corrugated web girder. Moreover, both of these values steadily increase with increasing ring thickness. However, when the ring thickness is sufficiently large (e.g., over 14 mm for test specimen No. 1/2), a thicker opening ring has no effect on improving the load-bearing capacity.

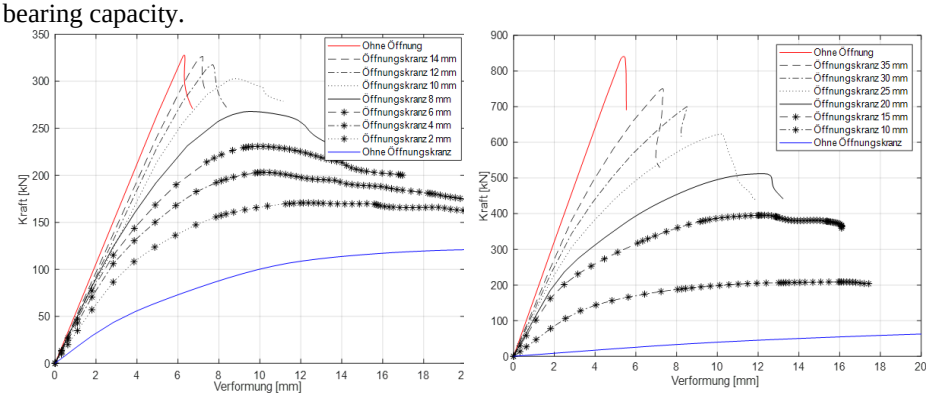

a) b)

Fig. 5. Influence of the opening wall on the load-bearing capacity a) specimen No. 1/2, b) specimen No. 3

To evaluate the impact of geometric imperfections on the load-bearing capacity of corrugated web girders with varying ring thicknesses, the test specimens are computed as reference values without considering pre-deformation. An influencing factor α is defined to account for the imperfections, and is given by the following equation:

$$\alpha = \frac{F_{without} - F_{with}}{F_{with}} \tag{1}$$

where $F_{without}$ represents the load capacity without geometric imperfection and F_{with} with represents the load capacity with imperfection considered. Figure 6 illustrates the relationship between the influencing factor α and the ring thickness.

When the opening does not have a ring (i.e., ring thickness is 0 mm), the geometric imperfection has minimal to no effect on the load-bearing capacity of the test beams. However, as the ring thickness increases, the influence of imperfection becomes more significant. For example, considering the imperfection reduces the calculated load-bearing capacity of test beam 1/2 with an 8 mm ring thickness by approximately 5%. With a 12 mm ring thickness, the reduction increases to 12%. Therefore, it is crucial to account for geometric imperfections when analyzing corrugated web beams with a circular ring of openings. Failure to consider imperfections overestimates the actual load-bearing capacity, making the component potentially unsafe. The influencing factor remains below 5% for ring thicknesses below 8 mm for test beam 1/2 and 25 mm for test beam 3. Moreover, the critical values for the thickness of the opening crown and corresponding values between corrugated web failure and opening ring failure, as shown in Figure 6, follow a similar trend according to Equation (8) in [19]. This suggests that the imperfection of the corrugated web has minimal impact on the shear resistance of the corrugated web girder with opening ring failure. Aperture failure occurs primarily due to stress-related flexing in the wall, rather than stability concerns.

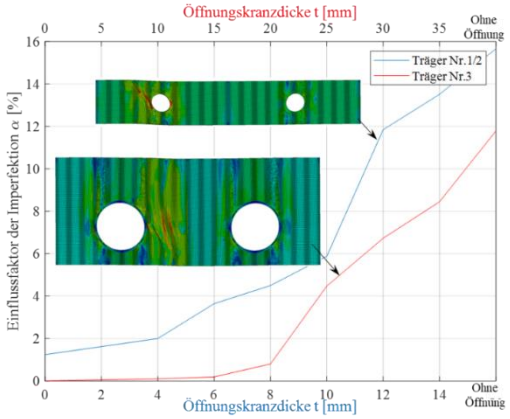

Fig. 6. Relationship between the influencing factor of geometrical imperfection and opening ring thickness

Figure 7 presents the relationship between the shear force resistance of the corrugated web beam and the thickness of the opening ring, showcasing both the test and simulation results. Additionally, reference values are included for the unperforated corrugated web support according to DIN EN 1993-1-5, as well as the manual calculation methods based on [19] for the corrugated web with a circular opening ring. The experimental and numerical results demonstrate that the model employed in DIN EN 1993-1-5 is no longer applicable to corrugated web beams with an opening ring. Particularly, when the opening ring thickness is very small, the opening significantly reduces the shear resistance of the beam, sometimes by as much as 50%. However, the manual calculation method [19] offers reliable results for determining the load-bearing capacity. According to the FE results, it can be concluded that the error in the manually calculated shear force resistance increases as the thickness of the opening ring

decreases. This is due to the corrugated web acting as a bedding on the opening ring in certain areas, and the flanges of the beam contributing to the transfer of shear forces through flange bending [19]. Moreover, it is evident that perforated corrugated web beams with sufficient thickness in the opening ring can attain the full shear load capacity of an unperforated web. The minimum required thickness for the opening ring can be determined and calculated using Equation (8) as provided in [19].

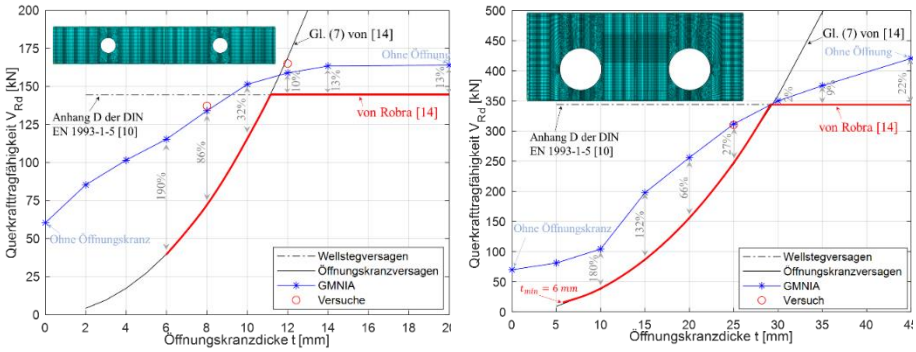

a) b)

Fig. 7. Shear load capacity depending on the opening wall thickness

5 Conclusion

In the present work, an investigation of the behavior of sinusoidal corrugated web beams with circular openings and different opening rings was carried out. First, the shear load capacities of three corrugated web beams with different geometries were tested and the corresponding buckling behavior was analyzed. The FE program Abaqus® was used to simulate the experimental results of the corrugated web beam with opening crown. In addition, the parameter studies on the influence of the opening ring thickness on the load-bearing capacity of the corrugated web beam were carried out and the sensitivity of the geometric imperfection for the corrugated web beams with different opening ring thicknesses was examined. Based on the theoretical and experimental results of the corrugated web beam, the following conclusions can be derived.

1. The numerical method can simulate the load-bearing behavior of corrugated web beams with an opening ring relatively precisely if the geometric imperfections are considered.
2. Openings in the corrugated web (without an opening ring) reduce the load-bearing capacity and overall rigidity of the beam. In contrast, the opening ring can significantly improve the shear force carrying capacity and rigidity of the corrugated web beam with circular openings.
3. In the corrugated web beam without an opening ring, the geometric imperfection has only a negligible influence on the load-bearing capacity. However, the influence of the pre-deformation increases with increasing thickness of the rim.

4. The model developed in [19], based on the frame load-bearing capacity of the opening ring, offers a simplified verification method for the corrugated web beam with circular opening ring that is on the safe side.

References

1. Pasternak, H.; Robra, J.; Bachmann, V.: Corrugated web beams with increased web thickness. In: Eurosteel 2008 Vol. B, Graz, 2008, pp. 1161-1166.
2. Siokola, W.: Wellstegträger. Herstellung und Anwendung von Trägern mit profiliertem Steg. In: Stahlbau 66 (1997), Heft 9, S. 595-605.
3. Pasternak, H.; Branka, P.: Zum Tragverhalten von Wellstegträgern, In: Bauingenieur 73 (1998), Heft 10, S. 437–444.
4. Pasternak, H.; Hannebauer, D.: Träger mit profilierten Stegen, In: Stahlbau-Kalender 2004, S.449-492.
5. Pasternak, H.; Robra, J.; Bachmann, V.: Wellstegträger mit größeren Stegblechdicken. Fertigungstechnologie und Tragverhalten, In: Bauingenieur. 84 (2009), Heft 10, S. 415–419.
6. Pasternak, H.; Kubieniec, G.: Plate girders with corrugated webs, In: J. Civ. Eng. Manag. 16 (2010), pp. 166–171.
7. Nikoomanesh M.R.; Goudarzi M.A.: Experimental and numerical evaluation od shear load capacity for sinusoidal corrugated web girders. In: Thin-Walled Structures Vol. 153 (2020), pp. 1-12.
8. Pasternak H.; Branka, P.: Tragverhalten von Wellstegträgern unter lokaler Lasteinleitung. In: Bauingenieur 74 (1999), Heft 5, S. 219-244.
9. Kuchta, K.: Zum Einfluss der Interaktion von Biegemoment und Querkraft auf das Tragverhalten von Wellstegträgern. In: Stahlbau 75(2006), Heft 7, S. 573-577.
10. Guo, Y.; Zhang, Q.; Siokola, W.; Hofer, A.: Flange buckling behavior of H-shaped member with sinusoidal webs. In: 5th Intern. Conference on Thin -Walled Structures, Brisbane, Australia 2008.
11. Pasternak, H.; Kubieniec G.: Flange buckling of sinusoidal corrugated girders. In: 6th Intern. Conference on Thin-Walled Structures Vol. 2, Timisoara, 2011, pp. 625-632
12. Machacek, J.; Tuma, M. : Fatigue life of girders with undulating webs. In: Journal of Civil Engineering and Management 10 (2004), Iss. 1, pp. 45-49.
13. Dilger K.; Pasternak H.; u.a.: Einsatz der Schweißsimulation zur systematischen Entwicklung verbesserter Modelle für die Berechnung der Tragfähigkeit komplexer Stahlleichtbaustrukturen. (P 785/08/2008 / IGF- Nr. 287 ZBG). Report 2011.
14. Motak, J.; Machacek, J.: Experimental behaviour of composite girders with steel undulating web and thin-walled shear connectors Hilti Stripcon. In: Journal of Civil Engineering and Management 10 (2004), Iss. 1, pp. 45-49.
15. Śledziewski, K.; Górecki, M.: Finite element analysis of the stability of a sinusoidal web in steel and composite steel-concrete girders, In: Materials (Basel) 13 (2020). Iss. 5. Pp. 1-15.
16. DIN EN 1993-1-5, Bemessung und Konstruktion von Stahlbauten – Teil 1-5: Plattenförmige Bauteile, Europ. Comm. Stand. Deutsche Fassung, Ausgabe Oktober 2019.
17. Pasternak, H.; Piekarczyk, M.: Tests and FE Simulations of beams with corrugated web with openings (in Polish). In: Konstrukcje Stalowe. 5 (2006), pp. 37–39.
18. Kiymaz, G.; Coskun E., et al..: Transverse load carrying capacity of sinusoidally corrugated steel web beams with web openings, In: Int. Symp. “Steel Structures: Culture & Sustainability 2010”, Istanbul, 2010, pp. 69–85.

19. Robra, J.; Krasotina, L.: Querkrafttragfähigkeit von sinusförmig profilierten Stahlträgerstegen mit runden und quadratischen Öffnungen, In: Bauingenieur 94 (2019), Heft 7, S. 285–291.
20. DIN 50125: Prüfung metallischer Werkstoffe – Zugproben, Ausgabe Dezember 2016.

Systems for Monitoring a Bridge Using Wireless Sensor Networks

Gokhan Kilic[1*[0000-0001-6928-226X]], Gokhan Altindas[2[0000-0003-2334-7704]], Zafer Kutug[3[0000-0002-9147-8135]], and Dila Çiğdem[4 [0000-0002-8818-120X]]

[1*] Izmir University of Economics, Civil Engineering Department, Izmir, Türkiye, gokhan.kilic@ieu.edu.tr
[2] Celal Bayar University, Civil Engineering Department, Manisa, Türkiye, Gokhan.altintas@mcbu.edu.tr
[3] Yildiz Technical University, Civil Engineering Department, Istanbul, Türkiye, kutug@yildiz.edu.tr
[4] Izmir University of Economics, Civil Engineering Department, Izmir, Türkiye, dilacigdem2003@gmail.com

Abstract. Assessing the health and condition of structures like bridges involves frequently using structural health monitoring (SHM). In the past, wire sensors had to be installed on bridge structures as part of the SHM process so that data could be collected and sent to a data gathering unit there. However, this study suggests switching out the conventional wire sensors with wireless ones to create a Bridge Health Monitoring System (BHMS) that is affordable, practical, and simple to install. A software translation program attached to the monitoring server is used by each wireless sensor. In a GSM LAN (Global System for Mobile Communications) environment, this monitoring server system has the ability to link and interact with other similar systems of that type. The evaluation approach provided by the BHMS is thorough, secure, and portable.

Keywords: Bridge, Structural Health Monitoring, wireless sensor.

1 Introduction

With the key role bridges play in a society's economic and environmental wellbeing, it is of the utmost importance to ensure their continued integrity. There exist many thousands of bridges and the nature of the construction of these structures varies, depending on such parameters as location and their initial perceived purpose. The structural integrity of a bridge is compromised on a daily basis from many directions, including flooding, certain weather conditions, the natural ageing process and traffic loads. However, the scarcity of knowledge in relation to the effects of traffic loads on bridge structures is in part due to the difficulties involved in synchronizing the monitoring of both the bridge dynamics and a moving vehicle.

A clear sign of degeneration in a bridge structure is the appearance of cracks. Not all cracks are obvious from visual inspection, as some may be internal (e.g. related to water

ingress) and others may be occur below the ground, but all can conceivably weaken bridge decks and supports, potentially to the point of collapse. A vigorous health monitoring and assessment plan must therefore be considered to be of the utmost importance for bridge owners, in terms of avoiding the disruption caused by an inoperative bridge, the high cost of bridge repairs and potential human safety issues.

There are various techniques of bridge inspection available, such as initial inspection, routine inspection, detailed inspection and structural assessment, with both destructive and non-destructive testing (NDT) methods being commonly used. However, with increasingly complex bridges being constructed, improved systems of assessment and monitoring are imperative because traditional methods are not adequate enough for this purpose.

We turn now to examine some of the typical systems of bridge assessment currently available to bridge engineers. The IBIS-S interferometric radar system offers an advanced NDT method of assessment which can accurately (up to a hundredth of a millimeter) measure the dynamic or static displacement and vibration of bridge (and other) structures. The system is capable of monitoring these structural movements [1] insofar as vertical bending movements dominate torsional movements. The interferometric sensor module transmits, receives and operates electromagnetic waves based on the precept of electromagnetic conflict between controlled waves.

It should be noted that obstructions located between the radar and reflectors will lead to inaccurate data collection by IBIS S. In addition, structural defects will not register on the system. Whilst the system clearly has the capacity to monitor the structural behavior of a bridge under load, it must be used in combination with other testing methods in order to offer full structural health assessment [2] can provide further information in this regard.

Another NDT technique commonly used within the field of bridge engineering is the quick and economical accelerometer method. There are many designs of accelerometer available, with various capability ranges in terms of measurement, range and resolution, the choice of which should depend on the ultimate use to which the system will be put, and the particular structure it will be monitoring [3]. Accelerometers have the capacity to be integrated with handheld data collectors for permanent mount and routed applications [4]. The accelerometer method of assessment enables bridge engineers to analyses and determine resolution time histories of acceleration and, according to [5], the system has useful application in analyzing the displacement and stress levels a bridge structure comes under. It can detect and measure vibrations caused by objects such as hanger cables, pylons and stiffening trusses. It is also widely used within the industry to evaluate load capacity and is especially useful for testing on reinforced concrete bridges. The system can detect the presence of cracks, monitor beam behavior and follow dynamic interactions between vehicle and bridge upon that vehicle passing over the structure [6]. By assimilating the collected acceleration data, knowledge can be gained on the deflection and rotation of the structure in question.

First, the system has advantages; however, there are three points that need consideration. Although installation of accelerometers is a straightforward procedure, caution should be exercised in the actual placing of the accelerometers, since the effect of dynamic interaction in the presence of existing cracks needs to be analyzed. In

addition, a large amount of power is required to transmit the mass of information from the main station by cellular modem [7]. Finally, resolution can be problematic for the accelerometer method of assessment as, due to resistive noise, their suitability is limited to low and medium frequencies.

Despite the successes of the above two methods of inspection, recent technological progressions have seen much growth in the popularity of the Wireless Sensor Network (WSN) method of inspection, partly due to its mobility, ease of use and low level maintenance. In addition, it is reality inexpensive and quick to install the system on major structures. WSN offers a highly accurate means of collecting data in relation to dynamic and static displacement monitoring from various locations on the bridge structure. In addition, [8,9] describe the system's suitability for the remote measurement of structural displacements under such loads as micro-tremors, traffic and wind. Major bridges to have had the WSN installed include the Alamosa Canyon Bridge in New Mexico, Geumdang Bridge in South Korea, WuYuan Bridge in China, and Voigt Bridge in California [3]. Research by [10] provides additional information on WSN in relation to bridge assessment.

The number of sensors in a complete WSN system can range from a few to many thousands. There is flexibility in terms of placement and reorganization of the sensors in order to offer the particular formation required [11]. A small number of sensors will be placed strategically in order to gain information for system operatives on environmental parameters. A fully networked system requires an information gathering system, transmission system, processing system, analysis system, system control and feedback [12]. Individual wireless sensors interact and transmit data either to the data acquisition hardware or via neighboring sensors.

Despite its benefits to the world of bridge engineering, there are restrictions to the use WSN in terms of its detection of damage, limitations in the range and speed of data communication, and the fact that radio wave reflection and absorption can arise in the presence of concrete and steel. In addition, there is a necessity for wireless models and computer compatibility.

2 Design and Methodology-

2.1 Site Description

HMS Chatham Bridge is located in Chatham, Kent and was constructed in 1996 (Fig. 1) [13].

Fig. 1. Location of the HMS Chatham Bridge [13].

In 1994 St Marys Island Lifting Bridge (see Fig. 2) project involved the removal of an existing bridge structure and construction of a new access bridge to St Marys (Fig. 3) and its approach embankments [13].

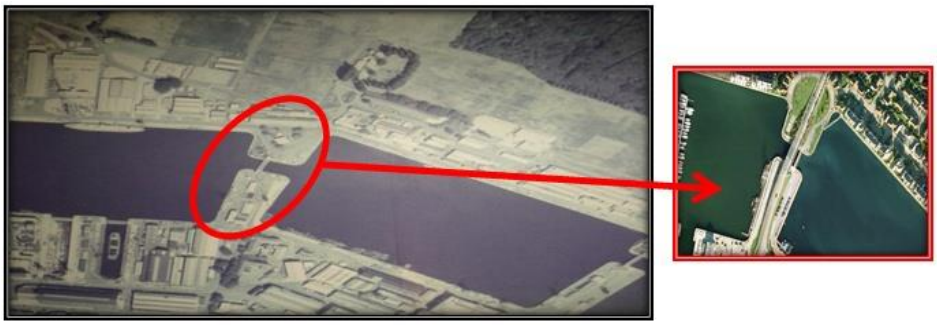

Fig. 2. The St Marys Island Bridge previous (left) and recent view (right) [13]

The bridge consists of two concrete approach spans and a single leaf lifting bridge centre span. The carriageway measures 6.75m. In addition, a footpath/cycle path on the west side of the bridge measures 3.0m and a footpath on the east side measures 1.8m. Two internal piers connect to pile caps, which in turn are supported by bored piles.

On 10 June 2012, the author conducted a visual inspection of HMS Chatham Bridge, which revealed no obvious structural defects. The conditions on the day were bright and dry and a temperature of 16 ˚C was recorded.

Fig. 3. HMS Chatham Bridge [14]

2.2 WSN for Bridge and Vehicle Monitoring

Whilst the WSN method of inspection provides reliable data within the context of SHM, the large volume of data gathered during an inspection of a bridge structure can lead to certain constraints in terms of resources [15].

WSN works by collecting and assessing data from a structure in relation to its behaviour under static or dynamic loading. This information is collected at an individual node before being processed centrally. This method of inspection is economical, includes the necessary technological requirements for the processing of data, and is simple to install [10, 11, 12].

In order to ascertain the load bearing capacity of a bridge, it is necessary to conduct vehicle loading tests, using a vehicle of a specific known weight, to evaluate the quasi-static response of the structure in such areas as neutral axis locations and load shedding paths. Since the bridge must remain out of commission for the duration of the test, it is not practical to carry out continuous monitoring, and so inspection needs to be conducted on a periodic basis [16].

2.3 Monitoring Strategy of HMS Chatham Bridge

Following the visual inspection carried out on HMS Chatham Bridge on 10 June 2012, WSN testing was conducted the following day. Conditions were broadly similar, i.e. bright and dry with a temperature of 16 ˚C. As already explained, structures undergoing this method of inspection are required to be closed to all traffic.

The inspection involved the driving of an 8 tonne vehicle across the bridge 16 times, simultaneous to the electronic acquisition of data. The speed of the vehicle was strictly limited to 25 miles per hour to ensure that the test could be reproduced (see Fig. 4).

Fig. 4**.** The vehicle passing the bridge during data acquisition [14]

Approximate crossing durations are listed in Table 1.

Table 1. Moving vehicle crossing durations (seconds)

Crossing	Time (second)
1	6.16
2	6.53
3	6.43
4	6.17
5	6.25
6	6.28
7	6.57
8	6.53
9	6.12
10	6.23
11	6.54
12	6.29
13	6.35
14	6.29
15	6.10
16	6.48
Average	6.33

2.4 Development of Software

The particular node used for the inspection on HMS Chatham Bridge was an Oracle SunSPOT wireless sensor node, as shown in Fig. 5.

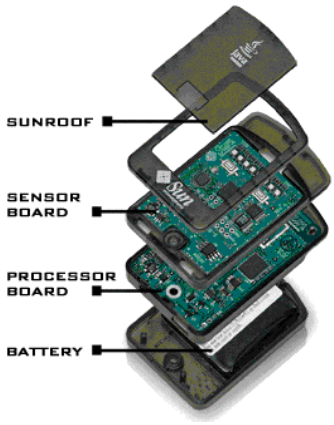

Fig. 5. Oracle SunSPOT wireless sensor [14]

The system (see Fig. 5) requires a base station (connected to a laptop) and eight SunSPOT sensor nodes located 10m apart. Each node is designed to communication with its neighbouring node. Specifications of the WSN system for both the hardware and software used from the litreture shown in Table 2 [15].

Table 2. The hardware specifications and software versions used to evaluate the algorithms [15].

Name	Alix	Back-End
RAM	256 MB	512 MB
CPU	Geode (TM) Integrated	AMD Athlon (tm) 64 3000+
CPU Speed	500 MHz	2 GHz
Java version	1.6.0u21	1.6.0u21
Application container	Tomcat 6.0.18	Glassfish 2.1.1
Reasoner	Pellet 2.2.2	none
Metamodel service	none	Joseki 3.4.1

Fig. 6 demonstrates how this works in principle – sensor 5 transmits its own data, along with the data received from sensor 4, to sensor 6, and so on. Ultimately, sensor 8 transmits a full set of data to the base station for analysis by Global System for Mobile Applications (GSMA) software.

Fig. 6. Diagram of the system [14]

The Oracle SunSPOT wireless sensor node is controlled by Java embedded software and needs no operating system [17]. The main processor used in this research is an Atmel AT91RM9200 system on a chip, which is based on an ARM (Acorn Reduced instruction set computer Machine) processor, which has 512 K of RAM and 4 MB of flash memory. The design of the sensor communication board is based on the IEEE 802.15.4 radio over the 2.4 GHz frequency band [18].

3 Results

As explained, by initiating deck deflection tests utilising both a loaded and unloaded bridge deck, it is possible to compare results in order to understand the behaviour of the structure under dynamic, live and static loads.

The WSN method of assessment is ideal for testing of this nature, since the wireless sensor nodes are powered by battery and can be recharged by connecting to a laptop. With this particular test necessitating many sets of 16 vehicle crossings, this recharging facility was of key importance. A further solution involved simply powering down the nodes when not in use. Schematic view on measurement system of transmission is further demonstrated in Fig. 7.

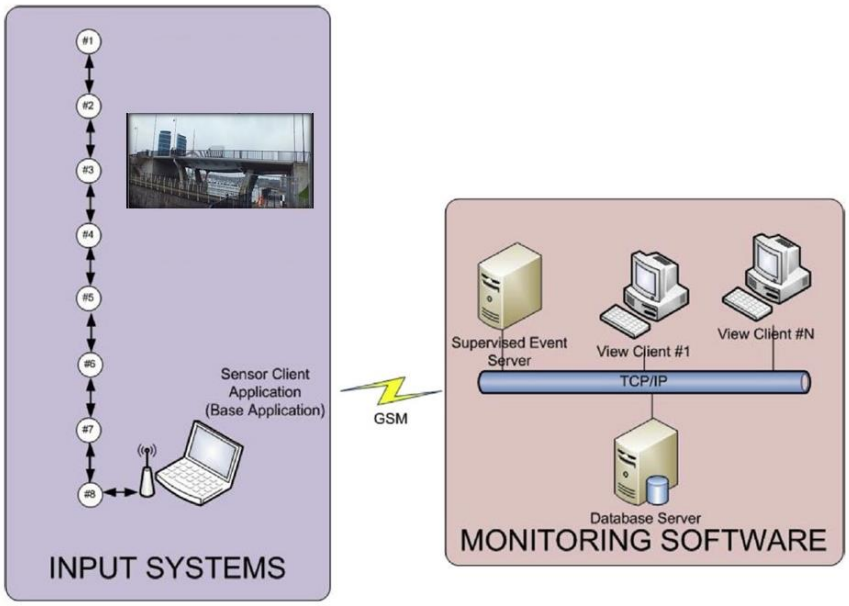

Fig. 7. Schematic view on measurement system

The deflection time history (Frequency/Hz – Time) taken from the initial four crossings of the vehicle can be viewed in Fig. 8. This diagram demonstrates that there are four district points on the bridge deck where heightened deflection occurs. These results are considered highly reliable because the timing of the survey was recorded and the vehicle location on the bridge at any specific time was visual recorded.

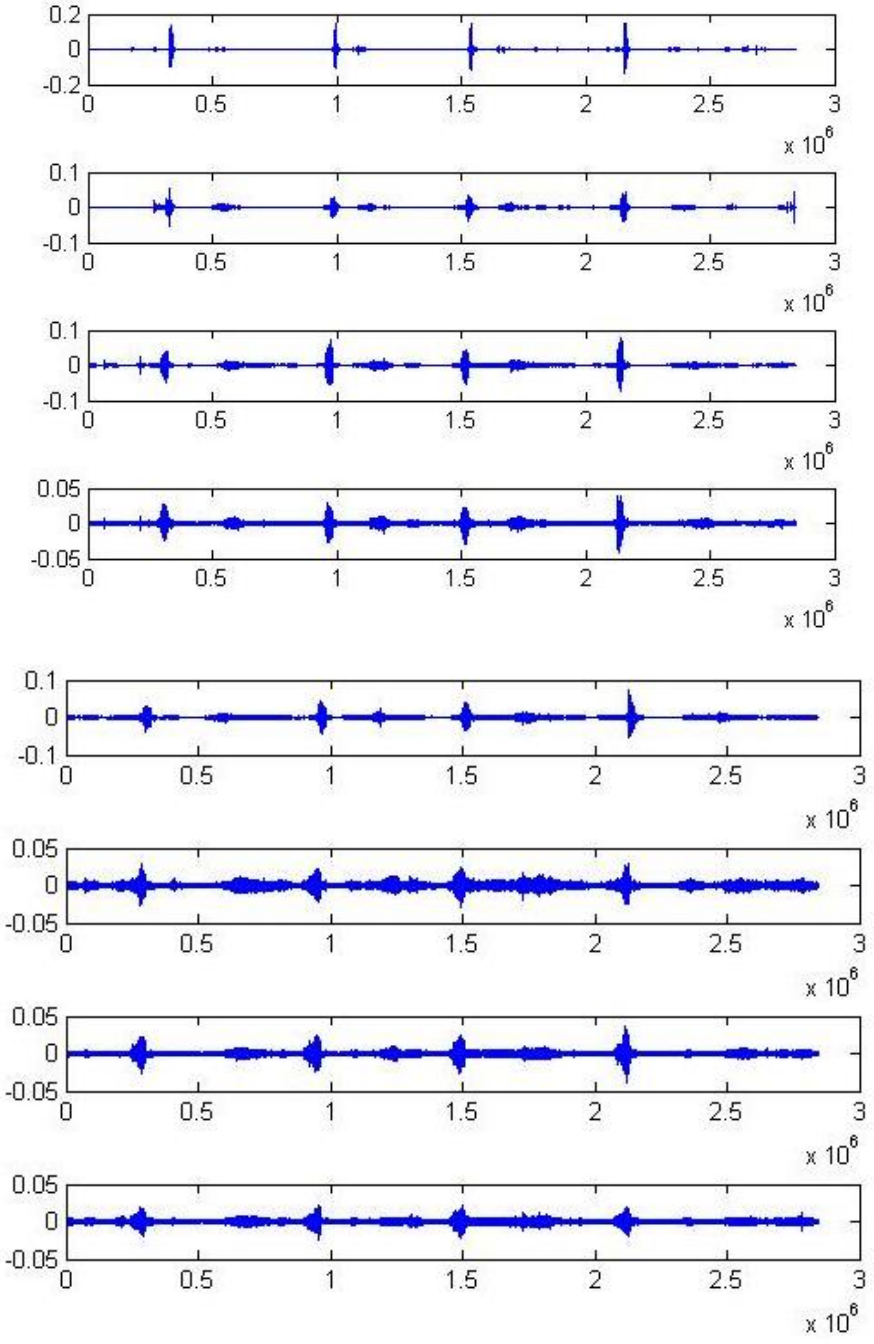

Fig. 8. Deflection time history diagram at the WSN node 1-8 (Frequency/Hz – Time)

4 Discussion

In considering the BHMS network presented in this work, the monitoring server is the thin server and clients are the thick clients. The flexibility of the monitoring server allows clients to interact with the relevant hardware, with the monitoring server only distributing messages to relevant clients. It is then for the client to process those received messages.

A crucial benefit of the monitoring server utilised in this BHMS system relates to the fact that all hardware, even if out-of-date, can be linked with the system, so long as there is a compatible software client. There is no requirement for the system's processes to be comprehended by the developer since the client control takes on this function. The software allows for the rapid development of new client applications.

As we have seen, an important consideration of bridge health monitoring is the minimization disruption of to the operation of bridge structures. It is therefore worthwhile installing a permanent sensor system on each structure. Discussions above have outlined the power consumption needs of the system, and therefore the use of solar power would be of great benefit, potentially in terms of a system fully customised for bridge health monitoring. In particular, this is a great potential benefit for developing countries, where poor construction procedures and ineffective maintenance schemes lead to a much more frequent occurrence of bridge collapses than in countries such as the UK [19-25].

5 Conclusions and Future Work

The research presented combines different monitoring systems in a GSM and LAN based environment. Each sensor device is inter-connected to the monitoring server (Fig. 3) by a software translator application. This allows findings to be correlated alongside actual measurements taken from the eight wireless sensor nodes.

The monitoring server has the capacity to present a highly distributed GSM-LAN based system, offering security, flexibility of use and mobility. The software allows a client to transmit messages to the monitoring server, which in turn transmits those messages immediately to other interested clients, thus facilitating the mobility of all clients, as well as improving the GSM-LAN system.

The reliability of communication is the most critical function of the BHMS. By investigating various network environments, reliability can be further enhanced. The workings of the system allow various data pathways to be taken, thus a failed sensor node will not jeopardise the effective functioning of the system. The system discussed in this research transfers all information from all sensor nodes onto sensor node 8, from which the complete data set is transmitted to the base unit (Fig. 7). However, the new topology allows for the transmission of data to the base unit from the various sensor nodes, thus further accelerating the process.

Whilst SunSPOT sensor nodes were implemented in the study on HMS Chatham Bridge, these are unsuitable for long term bridge health monitoring because of their short battery life. Future technological advancements, however, may allow WSN to be

combined with a BHMS in which power supply has been optimised. For example, the introduction of solar power as an element of this system could allow a more economical means of bridge assessment in comparison to other methods. This in turn could facilitate an increase in the amount of bridge assessment conducted, leading to increased data collection and, ultimately, to a significant increase in overall knowledge in this area.

References

1. Dei, D., Pieraccini, M., Fratini, M., Atzeni, C. & Bartoli, G. 2009. Detection of vertical bending and torsional movements of a bridge using a coherent radar. NDT & E International, 42, 741-747.
2. Ids Manual, 2010, access: www.idscompany.it (http :// www .idscompany .it/upload4 / File / BRO _GEO_ IBIS_FS_12_REV1.0_LR . pdf)
3. Chae, M. J., Yoo, H. S., Kim, J. Y. & Cho, M. Y. 2012. Development of a wireless sensor network system for suspension bridge health monitoring. Automation in Construction, 21, 237-252.
4. PCB Group, 2012 URL: http://www.pcb.com/
5. Gastineau, A., Johnson, T. & Schultz, A. 2009. Bridge Health Monitoring and Inspections – A Survey of Methods In: TRANSPORTATION, M. D. O. (ed.). University of Minnesota.
6. Chowdhury, M. R. & Ray, J. C. 2003. Accelerometers for bridge load testing. NDT & E International, 36, 237-244.
7. Briaud, J.-L., Hurlebaus, S., Chang, K.-A., Yao, C., Sharma, H., Yu, O.-Y., Darby, C., Hunt, B. E. & Price, G. R. 2011. Realtime monitoring of bridge scour using remote monitoring technology. February 2011, UNT Libraries Government Documents Department.
8. Farhey, D. (2006). Integrated virtual instrumentation and wireless monitoring for infrastructure diagnostics., Structural Health Monitoring, 5, 29. (DOI: 10.1177/1475921706057980)
9. Kamel G., Energy Efficient Structural Health Monitoring of the Cutty Sark using Wireless Sensors, 2010. Wireless Sensor & Actuator Networks
10. Kim J., Lynch J.P.,2011, Experimental analysis of vehicle bridge interaction using a wireless monitoring system and a two stage system identification technique, Mech. Syst. Signal Process. (2012), doi:10.1016/ j.ymssp. 2011.12.008.
11. Lee, R.-G., Chen, K.-C., Lai, C.-C., Chiang, S.-S., Liu, H.-S. & Wei, M.-S. 2007. A backup routing with wireless sensor network for bridge monitoring system. Measurement, 40, 55-63.
12. Guoa. 2011. Optimal sensor placement in structural health monitoring (shm) with a field application on arc bridge, University of New Mexico. Dept. of Civil Engineering
13. Chatham Maritime House, Performance comparison of multi-path aodv and dsr protocols in hybrid mesh networks. 2010 URL: http://www.cmtrust.co.uk/ A. A. Pirzada, M. Portmann, and J. Indulska, 2006.
14. Kilic, Gokhan, 2014, Wireless Sensor Network Protocol Comparison for Bridge Health Assessment, Structural Engineering and Mechanics, 2014, ISSN 1225-4568
15. Verstichel S, Volckaert B, Dhoedt B, Demeester P, De Turck F. Context-Aware Scheduling of Distributed DL-Reasoning Tasks in Wireless Sensor Networks. International Journal of Distributed Sensor Networks. 2011;7(1). doi:10.1155/2011/521810
16. Basharat, A., CATBAS, N. & SHAH, M. A framework for intelligent sensor network with video camera for structural health monitoring of bridges. Pervasive Computing and

Communications Workshops, 2005. PerCom 2005 Workshops. Third IEEE International Conference on, 8-12 March 2005 2005. 385-389.
17. Whelan, M. J., Gangone, M. V. & Janoyan, K. D. 2009. Highway Bridge Assessment Using an Adaptive Real-Time Wireless Sensor Network. Sensors Journal, IEEE, 9, 1405-1413.
18. Randall P. Smith, SPOT World and the Sun SPOT. Proceedings of the 6th international conference on Information processing in sensor networks, Cambridge, MA, USA, 2007.
19. Oracle Corporation, 2012, Sun Spot LIMITED URL: http://www.sunspotworld.com Sun ; Oracle, "Documentation," November 2010. [Online]. Available: http://www.sunspotworld.com /docs/Yellow/SunSPOT-Programmers-Manual.pdf. [Accessed 28 July 2011].
20. Zhu, Z., German, S. & Brilakis, I. 2010. Detection of large-scale concrete columns for automated bridge inspection. Automation in Construction, 19, 1047-1055.
21. Abdelkrim Hadjidj, Marion Souil, Abdelmadjid Bouabdallah, Yacine Challal, Henry Owen, Wireless sensor networks for rehabilitation applications: Challenges and opportunities, Journal of Network and Computer Applications, Volume 36, Issue 1, January 2013, Pages 1-15, ISSN 1084-8045
22. Bacon J., Bates J., Richard H., and Moody K., 1995, Using Events to Build Distributed Applications, 2nd International Workshop on Services in Distributed and Network Environments, Whistler, British Colombia, 1995.
23. Gonzalez-Ortega D., F. Diaz-Pernas, M. Martinez-Zarzuela, M. Anton-Rodriguez, J. Diez-Higuera, D. Boto-Giralda, 2010, Real-time hands, face and facial features detection and tracking: application to cognitive rehabilitation tests monitoring, Journal of Network and Computer Applications, 33 (4) (2010), pp. 447–466
24. Jones T. C.,1984, "Reusability in Programming: A Survey of the State of the Art", IEEE Transactions on Software Engineering, vol. SE-10, no. 5, pp. 488-493, 1984.
25. J.M.W. Brownjohn, Filipe Magalhaes, Elsa Caetano, Alvaro Cunha, Ambient vibration re-testing and operational modal analysis of the Humber Bridge, Engineering Structures, Volume 32, Issue 8, 2010, Pages 2003-2018, ISSN 0141-0296, https://doi.org/10.1016/j.engstruct.2010.02.034.

Utilizing Shear Walls Constructed with a Blend of Crushed Waste Tire Rubber for Seismic Assessment and Retrofitting of an Existing RC Building

Abdullah R. M. Alariyan[1][0009-0005-0907-5249] and Mehmet C. Genes[2][0000-0002-9052-7361]

[1] Eastern Mediterranean University, Civil Engineering Department, North Cyprus, Türkiye, 20600065@emu.edu.tr
[2] Eastern Mediterranean University, Civil Engineering Department, North Cyprus, Türkiye cemal.genes@emu.edu.tr

Abstract. The seismic events occurring in Turkey and neighboring countries pose a significant threat to the region. This research paper presents a case study focusing on enhancing the structural integrity of a five-storey reinforced concrete building in Antakya, Turkey. The building, constructed in 1988, incorporates RC shear walls composed of waste crushed rubber. The study is comprised of three main stages. Firstly, data collection is conducted. Secondly, the structure is modeled, and a nonlinear static pushover analysis is performed to assess its seismic performance. In the third stage, the model is reinforced by incorporating shear walls constructed with waste crushed rubber. Various locations for the shear walls are explored to determine the most suitable configuration. The shear walls are strategically placed on both sides of the building in the Y-direction, targeting areas with subpar performance. The study highlights that this strengthening technique is appropriate based on performance.

Keywords: Earthquake Evaluation, Pushover analysis, Retrofitting, Shear walls.

1 Introduction

1.1 Literature Review

Turkey is located in the high active earthquake zone. This requires the buildings to adhere to the Turkish Earthquake Code (TEC) 2007 [1]. Moreover, Turkish Earthquake Code (TEC) 2018 [2] is published. This code ensures the safety of structures. However, it has been noted that most of residential structures, which are constructed before 1998 are designed without adequate details and reinforcement for seismic performance. Thus, there is a need for fast and cost-effective way to evaluate and retrofit the current structure of residential buildings.

In Turkey, the majority of multi-story buildings feature reinforced concrete structural frames. Unfortunately, during earthquakes, this particular type of building has suffered the highest amount of damage and casualties. Numerous researchers have

extensively investigated the reasons behind these collapses and damages, and their findings can be found in various literature sources ([3], [4], [5], [6], [7], and [8]).

The primary objective of any strengthening method is to provide support to a building and prevent its displacement from surpassing its capacity (Kaplan [9]). Reinforced concrete jacketing involves three main methods: beam jacketing, column jacketing, and beam-column joint jacketing. In their research, Karayannis and Sirkelis [10] experimentally examined a novel type of reinforced concrete jacket designed for external beam-column joints damaged by seismic activity. The experimental procedure involved subjecting the joints to continuously increasing cyclic loads, retrofitting them with the proposed reinforced concrete jackets, and subsequently retesting them under the same loading conditions. Another commonly used retrofitting technique is infill wall strengthening, which was investigated by Kahn and Hanson [11] . They conducted experiments on five one-story, one-bay reinforced concrete frames, with two of the specimens serving as references: one being a bare frame and the other incorporating a monolithically cast shear wall [12]. Mosalam and Naito [13] conducted a study to evaluate the retrofit of an existing reinforced concrete building without seismic activity. The study analyzed the structural characteristics before and after the incorporation of masonry infilled frames.

Previous research studies have primarily focused on the application of tire rubber particles in cement-based materials and their use as coarse aggregate in concrete. These studies predominantly examine the mechanical properties of such materials. The findings generally indicate a decrease in density, an increase in ductility and toughness, a reduction in splitting tensile strength and compressive strength, and an improvement in insulation properties. The utilization of waste tire rubber as aggregate in concrete has experienced significant growth in recent decades. It is used either as a substitute for or a complete replacement of traditional aggregates in concrete mixtures ([14] and [15]). Concrete incorporating rubber particles is known to have reduced workability compared to traditional concrete mixtures ([16] and [17]). The accumulation of used tires poses both environmental and economic risks due to their high volume.

Researchers have found that the combination of rubber and concrete decrees the compressive strength of concrete ([18] and [19]). In concrete has mixture of waste tire rubber, A 50% decrease in cube and cylinder compressive strength was reported by Topu [19]. In addition, tensile strength showed a 64% increase with fine rubber particles. About 60% and 80% decrease in cube and cylindrical compressive strength was reported when coarse rubber particles were introduced, and also the tensile strength showed a decrease of about 74%.

1.2 Building Under Study

This research focuses on assessing the seismic vulnerability of a pre-existing 5-story apartment building located in the outskirts of Antakya, Turkey. The building was constructed in 1988 and is situated at coordinates 36°12'17.78"N 36°8'39.67"E according to Google Earth Map records from 2019. Antakya is classified as being in seismic zone I. The building itself is a reinforced concrete (RC) structure with dimensions of 23 meters in length, 14.4 meters in width, and 3 meters in height for each

floor. The study also explores retrofitting options to enhance the building's seismic resistance.

2 Methodology

2.1 Pushover Analysis Applications in SAP2000

To apply the building model in SAP2000, it is necessary to gather properties and parameters. The concrete's modulus of elasticity (Ec) is calculated using the equation Ec = 3250√f_c' + 14000(MPa), where fc' represents the cylinder characteristic strength of the concrete during model calibration. The compressive strength of the existing concrete is determined according to the formula provided in TS500, while the tensile strength of the existing steel reinforcement is obtained from the building project.

Additionally, seismic parameters such as seismic zone, factors, and building & soil conditions are collected and presented in Table 1. [20]. The initial 3D model of the building is generated based on the original plan, as depicted in Fig. 1.

Table 1. Existing properties and code parameters of the building

Existing Building Properties	
Knowledge level	Moderate
Modulus of Elasticity	30000 MPa
Knowledge level factor	0.9
Existing concrete compressive strength	25 MPa
Existing steel reinforcement tensile strength	220 MPa
Earthquake Code Parameters	
Seismic Zone	1
Seismic Zone Factor (***Ao***)	0.1
Building Importance Factor (***I***)	1.0
Soil Class	Z4
Live Load Participation Factor	0.3

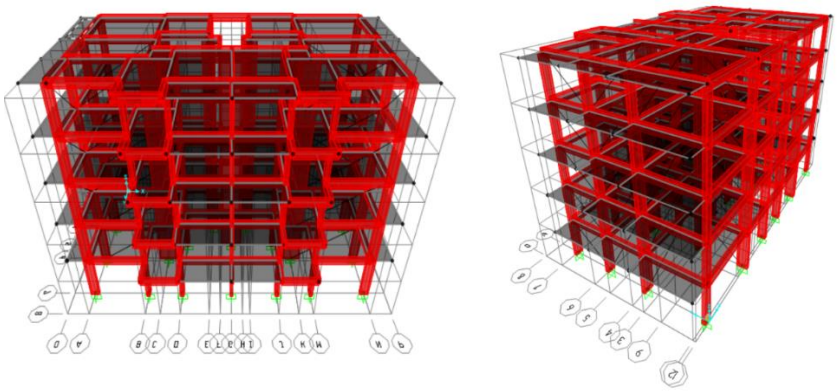

Fig. 1. Three-dimensional model of the building.

2.2 Retrofit the Building Using Shear Wall with Crushed Waste Tires

Utilizing a shear wall system to reinforce the deficient RC building proves to be an effective solution for enhancing both its strength and stiffness to withstand lateral forces. The retrofitting objectives, spanning from controlling drift to preventing collapse, are achieved through the implementation of a shear wall specifically designed for this purpose. To meet these goals, four different mix proportions have been employed for retrofitting the existing building, as outlined in Table 2 and Table 3 [21], [22] and [23].

Table 2. Mix identifications and proportions of materials

Mix ID	Cement (kg/m3)	Course aggregate	Fine aggregate	Rubber Powder (kg/m3)	Tire chips	Fine crumb rubber	Rubber chipped (kg/m3)	Silica Fume (kg)	Steel Fiber (kg)
5TC5FCR [21]	450	1434.6	0	0	29.9	14.1	-	-	-
10% Powder rubber [22]	42	927	858	38	-	-	-	-	-
10% aggregate rubber [22]	380	839	858	-	-	-	93	-	-
High performance 25RBC [23]	1000	504	336	-	-	-	-	117	78

Table 3. Mechanical properties of concrete replaced with waste rubber

Mix ID	Compressive strength (MPa)	Splitting tensile strength (MPa)	Flexural tensile strength (MPa)	Elasticity moduli (GPa)
5TC5FCR [21]	13.20	0.81	-	8.2
10% Powder rubber [22]	20	1.7	3.9	19
10% aggregate rubber [22]	25	1.5	3.4	20
High performance 25RBC [23]	55.07	4.88	4.39	36.6

3 Results and Discussion

3.1 Performance of The Building Before Retrofitting

The building's performance is assessed in both the X and Y directions without any retrofitting, using the ATC-40 CSM [25] method. This approach considers various factors, such as the expected seismic activity in Antakya, soil properties at the site, effective mass in the first mode, and the existing building's viscous damping capacity. By transforming shear force into spectral acceleration and displacement into spectral displacement, the method generates a target displacement and shear force curve, which can be compared with the demand curve.

In the X-direction, the performance point is obtained as a shear force of 2262.642 kN and a displacement of 0.074 m, while in the Y-direction, it is a shear force of 2240.436 kN and a displacement of 0.134 m, as shown in Fig. 2. Next, the performance point is compared with the base shear force from Table 4., and it falls between step 5 and 6. The more conservative choice is step 6, corresponding to the immediate occupancy level. Similarly, the procedure is applied to the Y-direction, and step 19 is identified as the critical point, representing the collapse prevention level, as shown in Table 5. Detailed hinge level information at the final step of pushover analysis in both directions is illustrated in Fig. 3.

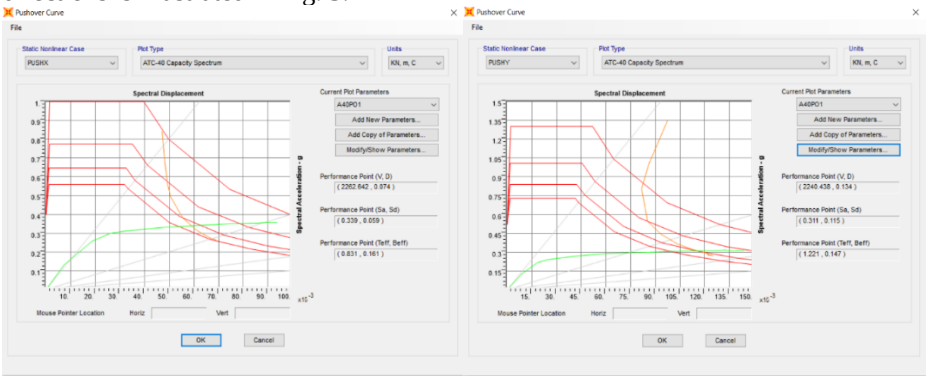

(A) (B)

Fig. 2. Demand and capacity spectrum in X-direction(A) and Y-direction(B) before retrofitting

Table 4. Plastic hinges state in X-direction before retrofitting

LoadCase	Displacement	BaseForce	AtoB	BtoIO	IOtoLS	Total
Text	m	KN	Unitless	Unitless	Unitless	Unitless
PUSHX	0.000044	0	750	0	0	750
PUSHX	0.010213	831.112	749	1	0	750
PUSHX	0.024377	1641.90	688	62	0	750
PUSHX	0.033322	1924.73	647	103	0	750
PUSHX	0.040241	2035.12	616	134	0	750
PUSHX	0.060406	2202.26	581	169	0	750
PUSHX	0.081431	2299.05	550	190	10	750
PUSHX	0.093447	2344.76	529	193	28	750
PUSHX	0.107107	2382.17	513	204	33	750
PUSHX	0.107136	2382.08	513	204	33	750
PUSHX	0.107524	2383.22	513	204	33	750
PUSHX	0.111363	2389.80	508	208	34	750
PUSHX	0.115919	2401.20	502	212	36	750
PUSHX	0.116082	2401.44	502	212	36	750
PUSHX	0.116834	2403.22	502	212	36	750
PUSHX	0.116916	2403.23	502	212	36	750
PUSHX	0.118347	2406.23	501	213	36	750

Table 5. Plastic hinges state in Y-direction before retrofitting

LoadCase	Displacement	BaseForce	AtoB	BtoIO	IOtoLS	DtoE
Text	m	KN	Unitless	Unitless	Unitless	Unitless
PUSHY	0.000237	0	750	0	0	0
PUSHY	0.011876	816.587	748	2	0	0
PUSHY	0.023481	1440.12	693	57	0	0
PUSHY	0.030631	1633.51	651	99	0	0
PUSHY	0.05124	1888.74	609	141	0	0
PUSHY	0.072434	2034.79	575	152	23	0
PUSHY	0.099001	2147.30	557	140	53	0
PUSHY	0.124186	2217.39	536	135	79	0
PUSHY	0.146882	2268.34	517	129	104	0
PUSHY	0.150685	2273.79	515	129	105	0
PUSHY	0.15069	2271.74	511	133	105	0
PUSHY	0.154039	2285.08	509	130	110	0
PUSHY	0.154059	224.856	509	130	110	1
PUSHY	0.154368	2251.53	509	128	112	1
PUSHY	0.1548	2254.01	509	128	112	1
PUSHY	0.157957	2263.43	508	126	113	1
PUSHY	0.157977	2251.69	508	126	113	1
PUSHY	0.158349	2255.69	508	126	113	1
PUSHY	0.158369	2228.52	508	126	113	3
PUSHY	0.159423	2241.25	504	126	113	7
PUSHY	0.16084	2251.78	504	126	113	7
PUSHY	0.163998	2262.18	503	125	115	7
PUSHY	0.166047	2266.00	501	124	117	8
PUSHY	0.166047	2266.00	501	124	117	8

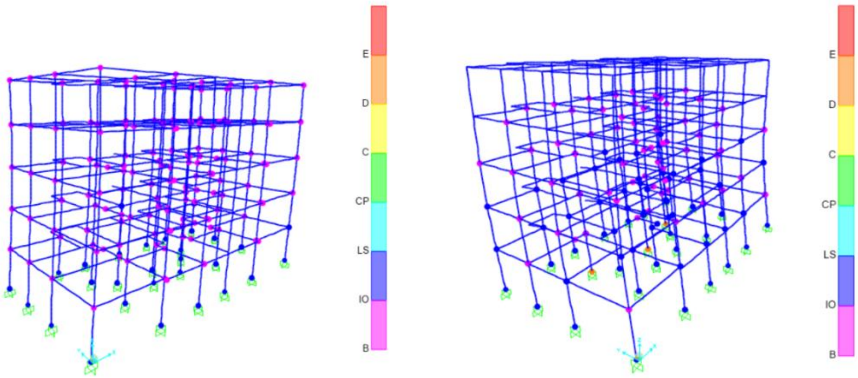

(A) (B)

Fig. 3. Hinges state in step 16 in X-direction (A) and Hinges states in step 23 Y-direction (B).

3.2 Performance of The Building After Retrofitting

To achieve an optimized shear wall with improved ductility, three distinct shear wall configurations are employed. The deficient Y-direction of the existing RC building has been retrofitted by utilizing five different concrete mix proportions specifically designed for shear walls constructed with crushed rubber.

The first configuration comprises three shear walls: Shear wall-I, Shear wall-II, and Shear wall-III, as depicted in Fig. 4. These shear walls are constructed within the building's frame core and are modeled using mid-pier frames with plastic hinges.

Following the retrofitting process in the X-direction, the capacity spectrum curve shows an increase in load from 2202.64 kN to 2363.18 kN, and a decrease in displacement from 0.074 m to 0.051 m when employing a normal shear wall. Shear wall-III demonstrates superior capacity in handling higher shear force and displacement compared to Shear wall-I and Shear wall-II. The building's performance in the X-direction slightly improves, as the shear wall was installed in the Y-direction.

Upon retrofitting in the Y-direction, the capacity spectrum curve shows a significant performance improvement, with the load increasing from 2240.436 kN to 2873.19 kN and the displacement decreasing from 0.134 to 0.082 with the implementation of a normal shear wall. As expected, this direction experiences a notable increase in the performance point. The performance points before and after retrofitting are shown in Table 6.

The condition of the hinges for each member of the frame, when using normal Shear wall-III, is presented in Fig. 5. In both the X and Y directions, the hinge states fulfill the requirements for immediate occupancy, as indicated in Table 7. Consequently, the placement of Shear wall-III proves to be the most effective compared to Shear wall configurations I and II.

Additionally, the retrofitting of the residential building resulted in an immediate occupancy level of strengthening, which signifies a significant enhancement for a

residential structure. However, this outcome is attributed to the building's pre-existing state, where the installation of a shear wall between two columns was necessary. Building it in a short distance between these columns was not feasible due to the risk of creating a short beam, which is not designed to handle such a configuration.

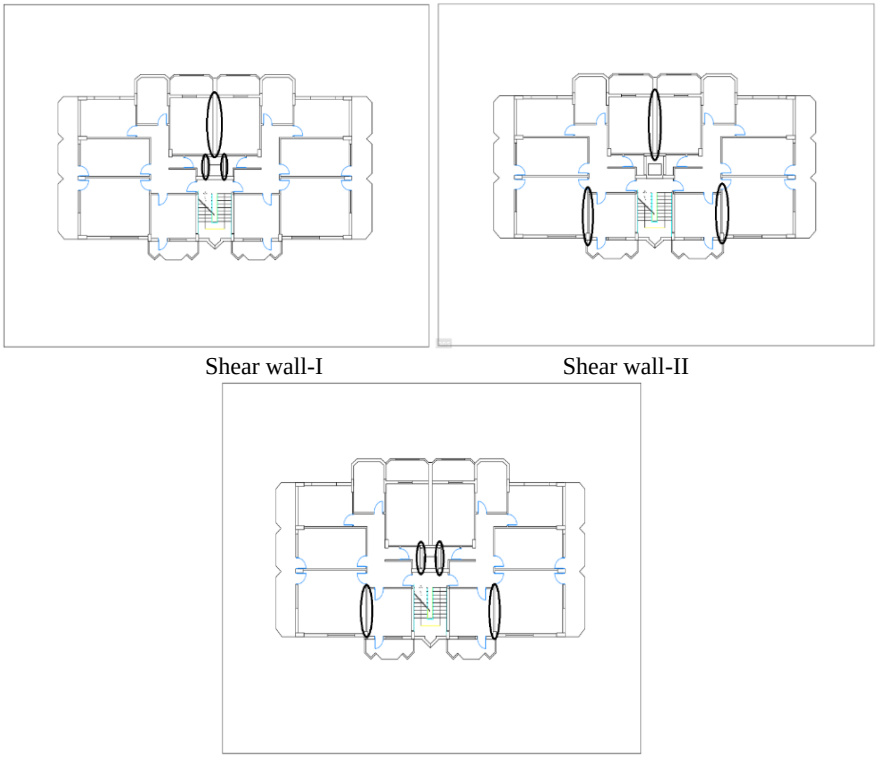

Fig. 4. Shear wall configuration used for retrofitting

Table 6. Performance points for both of frames with and without shear wall (Y-Direction)

	Configuration	Shear Force (kN)	Displacement (m)
Without shear wall		2240.43	0.134
Normal shear wall	Shear wall-I	2789.47	0.09
	Shear wall-II	2843.72	0.086
	Shear wall-III	2873.19	0.082
Shear wall with 5TC5FCR [21]	Shear wall-I	2472.65	0.113
	Shear wall-II	2523.41	0.109
	Shear wall-III	2595.77	0.102
Shear wall with 10% Powder rubber [22]	Shear wall-I	2657.24	0.109
	Shear wall-II	2679.73	0.098
	Shear wall-III	2698.74	0.094
Shear wall with 10% aggregate rubber [22]	Shear wall-I	2683.27	0.099
	Shear wall-II	2697.18	0.097
	Shear wall-III	2734.84	0.091
High performance shear wall 25RBC [23]	Shear wall-I	3047.84	0.077
	Shear wall-II	3101.05	0.073
	Shear wall-III	3143.72	0.068

Table 7. Hinges states in Y direction

	Configuration	IO	LC	CP
Without shear wall		113	21	7
Normal shear wall	Shear wall-I	156	11	0
	Shear wall-II	153	9	0
	Shear wall-III	143	6	0
Shear wall with 5TC5FCR [21]	Shear wall-I	140	18	0
	Shear wall-II	138	16	0
	Shear wall-III	130	12	0
Shear wall with 10% Powder rubber [22]	Shear wall-I	139	13	0
	Shear wall-II	134	10	0
	Shear wall-III	128	9	0
Shear wall with 10% aggregate rubber [22]	Shear wall-I	140	10	0
	Shear wall-II	136	9	0
	Shear wall-III	132	8	0
High performance shear wall 25RBC [23]	Shear wall-I	121	9	0
	Shear wall-II	119	7	0
	Shear wall-III	117	6	0

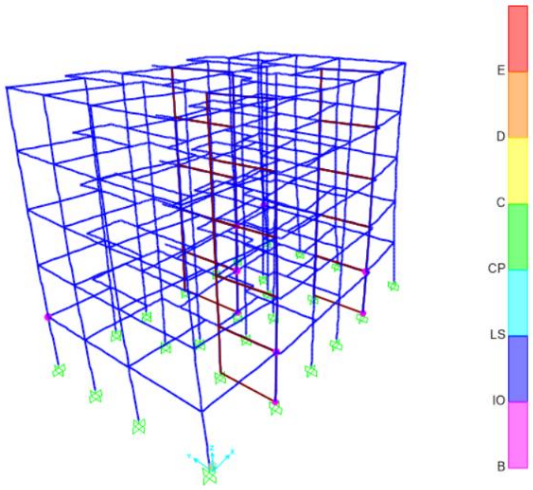

Fig. 5. Hinges states step 12 in Y-direction (Normal shear wall- Shear wall-III)

4 Conclusion

This research aims to establish a fast and dependable procedure for assessing and reinforcing existing buildings. The key findings are as follows:

Prior to retrofitting, the structural evaluation indicated that the building was on the verge of collapse, according to the Turkish Earthquake Code (TEC2007). In the X-Direction, the performance level reached immediate occupancy, while in the Y-Direction, seven hinges were at the collapse level. As a result, retrofitting was recommended.

Three infill shear walls were constructed using a mixture of crushed waste rubber as a replacement material. The significant advantage of employing infill shear walls lies in their minimal impact on building residents and limited damage to the building.

The same evaluation method was applied after the retrofitting process. The results demonstrated that all plastic hinges' performance in the Y-direction improved to the immediate occupancy level, in compliance with the Turkish Earthquake Code (TEC 2007). Moreover, the study concluded that infill shear walls were unnecessary for the X-direction of the building's framework since the building was sufficiently rigid, and there was no risk of collapse in this direction.

Acknowledgment
The authors extend their heartfelt gratitude for the support received from Eastern Mediterranean University. They also assume complete responsibility for all opinions, findings, outcomes, or suggestions presented in this material, which may not necessarily align with the perspectives of Eastern Mediterranean University.

References

1. TEC 2007, (2007). Turkish Earthquake Code: Regulation on Structures Constructed in Disasters Region., Ankara, Turkey.
2. TEC 2018. Turkish Earthquake Code: Regulation on Structures Constructed in Disasters Region., Ankaraa, Turkey, 2018.
3. H. Binici , "Bingol-Karliova earthquakes and the damages caused by the material quality and low workmanship in the recent earthquakes.”," Eng. Fail. Anal, vol. 14, no. 1, pp. 233-238, 2007.
4. Y. S. Tama, "“Structural damages observed in state buildings after Simav/Turkey earthquake occurred on 19 May 2011," Nat. Hazard Earth Syst, vol. 12, no. 8, pp. 2709-2718, 2012.
5. Y. S. Tama, A. Solak, N. Cetinkaya, G. Sen, S. Yılmaz and H. Kaplan, "Damages to unreinforced masonry buildings by the Van earthquakes of 23 October and 9 November 2011," Nat. Hazard Earth Syst, vol. 13, no. 2, pp. 329-337, 2013.
6. F. Kilci, B. Y. Kara and B. Bozkaya, "“Locating temporary shelter areas after an earthquake A case for Turkey," Eur. J. Oper. Res, vol. 243, no. 1, pp. 323-332, 2015.
7. F. Cakir, Uckan, J. Uckan, B. S. Seker and B. Akbas, "Seismic damage evaluation of historical structures during Van earthquake, October 23, 2011," Eng. Fail. Anal., vol. 58, no. 1, p. 249*266, 2015.
8. O. Murat , "Field reconnaissance of the October 23, 2011, Van,Turkey, earthquake: Lessons from structural damages," J. Perform Constr. Facil, 2015.
9. H. Kaplan, S. Yilmaz, N. Cetinkaya and E. Atimtay, "Seismic strengthening of performance evaluation methodologies for civil engineering structures," in Indian RC structures with exterior shear walls, Sadhana, 2011.
10. C. Karayannis and G. Sirkelis, "Strengthening and rehabilitation of RC beam–column joints using carbon-FRP jacketing and epoxy resin injection," Earthquake Engineering & Structural Dynamics, vol. 37, no. 5, pp. 769-790, 2008.
11. L. Kahn and R. Hanson, "Infilled walls for earthquake strengthening," Journal of the Structural Division, vol. 105, no. 2, pp. 283-296, 1979.
12. M. Baran, "Precast concrete panel reinforced infill walls for seismic Technology strengthening of reinforced concrete framed structures," A Doctor of Philosophy Thesis in Civil Engineering Middle East Technical University, Ankara, 2005.
13. K. Mosalam and C. Naito, "Seismic evaluation of gravity-load-designed column-grid system," Journal of Structural Engineering, vol. 128, no. 2, pp. 160-168, 2002.
14. I. Marie and H. Quiasrawi, "Closed-loop recycling of recycled concrete Institute aggregates," Journal of Cleaner Production, vol. 37, pp. , 243-248, 2012.
15. H. Su, J. Yang, T. Ling, G. Ghataora and S. Dirar, "Properties of concrete prepared with waste tyre rubber particles of uniform and varying sizes," Journal of Cleaner Production, vol. 91, pp. 288-296, 2015.
16. K. Khatib and F. Bayomy, "Rubberized Portland cement concrete," Journal of materials in civil engineering, vol. 11, no. 3, pp. 206-213, 1999.
17. N. Oikonomou and S. Mavridou, "The use of waste tyre rubber in civil engineering works," in In Sustainability of construction materials, Woodhead Publishing, 2009.
18. N. Eldin and A. Senouci, "Rubber-tire particles as concrete Steel Structures aggregate," Journal of materials in civil engineering, vol. 5, no. 4, pp. 478-496, 1993.
19. I. Topçu, "Assessment of the brittleness index of rubberized concretes," Cement and Concrete Research, vol. 27, pp. 177-183, 1997.
20. E. Özşahin and M. Değerliyurt, "Modeling of Seismic Hazard Risk Analysis in Antakya (Hatay, South Turkey) by Using GIS.," International Journal of Innovative Environmental Studies Research, vol. 1, no. 3, pp. 31-54., 2013.

21. M. Gesoğlu, E. Güneyisi, G. Khoshnaw and S. İpek, "Investigating properties of pervious concretes containing waste tire rubberss," Construction and Building Materials, vol. 63, pp. 206-213, 2014.
22. B. Jaivignesh and A. Sofi, "Study on mechanical properties of concrete using plastic waste as an aggregate. In IOP Conference Series," Earth and Environmental Science, vol. 80, no. 1, p. 012016, 2017.
23. " Experimental and Analytical Study on the Structural Performance of RC Frame," A Master Thesis in Civil Engineering, , Famagusta, Cyprus, 2019.
24. Genes, M, C Murat B, Sahin B, "Full-Scale Dynamic Testing Of A RC Frame Building By Investigation The Effect Of Brick-Infilled Frames.," International Civil Engineering & Architecture Symposium for Academicians., 2011.
25. ATC-40 . Seismic Analysis Retrofit of Concrete Buildings, Redwood City, CA, USA.: Vol. I, Applied Technology Council, , 1996.

Seismic Response and Reliability Analysis of A High-Pier Rigid Frame Bridge

Liu Zixin[1][0000-0003-3550-9547]

[1] Key Laboratory of Building Collapse Mechanism and Disaster Prevention, Institute of Disaster Prevention, China Earthquake Administration, Sanhe, China
liuzixin@cidp.edu.cn

Abstract. In recent years, the probability density evolution method for structural random dynamic analysis can capture the refined probability density function and its evolution process with regard to both linear and nonlinear, single degree of freedom and multi-degree of freedom structural systems, which provides the satisfactory requirements of accurate structural design and analysis. In this study, firstly, the dimension-reduction simulation method of fully non-stationary mD-nV stochastic vector processes is applied to generate multi-component non-uniform seismic excitation for long-span bridge structures. Secondly, the finite element model of a long-span and high-pier rigid frame bridge with practical engineering background is established. And the representative time-histories of multi-component non-uniform and non-stationary ground motion realized by the dimension-reduction representation are used as random external excitation of the target bridge structure. Then, the probability density evolution method is employed to analyse the refined dynamic response of bridge structure subjected to different seismic excitation conditions. Finally, combined with the equivalent extreme events, the seismic reliability of bridge structure under multi-dimensional non-uniform seismic excitation is investigated. This study verifies the effectiveness of the dimension-reduction representation for simulation realization of multi-support non-uniform ground motion. Meanwhile, the influence of multi-component non-uniform random ground motion on the seismic response and dynamic reliability of long-span and high-pier rigid frame bridge is thoroughly scrutinized, which can provide the basis for the seismic design and analysis of bridge structures.

Keywords: Seismic Dimension-reduction Simulation; High-pier Rigid Frame Bridge; Probability Density Evolution Method; Seismic Response; Dynamic Reliability

1 Introduction

Studies show that, due to the significant spatial variability of ground motion, the spectrum, amplitude and phase of ground motion suffered by different supports of long-span structures are different under the action of earthquake, which is the main factor causing the seismic damage of long-span structures. At the same time, the seismicity is

multi-dimensional, that is, three-dimensional translational components including two horizontal components and one vertical component can be observed in one ground motion event. The spatial variability and multi dimension of ground motion have great influence on the seismic response and damage mechanism of large spatial structures. Therefore, for the seismic analysis of large and complex spatial structures, the spatial correlation multi-support and multi-dimensional ground motion input is used, so as to make the structural design safe and reasonable [1].

In recent years, with the rapid development of China's social economy and transportation, the number of new bridges has increased significantly. Among them, the high-pier and long-span rigid frame bridges are widely used in Western China because of their reasonable internal force distribution, strong crossing capacity and beautiful appearance. At the same time, most of the above regions belong to the areas with frequent seismic activities, thus the seismic analysis and design of high-pier and long-span rigid frame bridges have gradually become a research hotspot in the engineering field. For the dynamic response analysis of high-pier and long-span rigid frame bridge under multi-support non-uniform seismic excitation, Li and Shi used a group of different ground motion time-histories as inputs of a four-span continuous rigid frame bridge considering the traveling wave effect. The analysis showed that the dynamic response of the bridge girder became larger under the influence of the traveling wave effect [2]. Pan et al. analyzed the influence of traveling wave effect on the difference between high and low piers of continuous rigid frame bridge under multi-support non-uniform excitation. The research showed that the greater the difference between high and low piers, the greater the influence of traveling wave effect on the structure [3]. Li et al. analyzed the vulnerability of a long-span continuous rigid frame bridge under multi-point excitation, and gave the failure probability of this kind of structure under earthquake action [4]. Based on the probability density evolution method, Liu et al. studied the random seismic response of the double track bridge of Shibanpo Yangtze River Bridge in Chongqing, and realized the evaluation of the seismic reliability of the bridge combined with the principle of equivalent extremum [5].

Based on the above research status, it can be concluded that the main challenges of seismic response analysis of high-pier and long-span rigid frame bridges are as follows: 1) At present, inconsistent seismic excitation is often used, and the influence of multi-dimensional effect of ground motion on structural dynamic response is seldom considered; 2) Generally, the measured records or a few synthetic seismic time-histories are usually selected for the seismic response analysis of the above-mentioned bridge structures as the input, which does not fully consider the randomness of the ground motion and the structural parameters, and fails to obtain a more refined seismic response and reliability assessment of the structure. Therefore, in this study, the idea of dimension-reduction of random function is introduced to establish the dimension reduction model of multi-support and multi-dimensional (mD-nV) fully non-stationary seismic random field, that is, just two elementary random variables can be used to accurately express the non-stationary mD-nV random field on the probability density level. Furthermore, the finite element analysis model of high-pier and long-span continuous rigid frame bridge considering pile-soil effect is established based on the ANSYS general finite element analysis platform according to an actual project.

Combined with the probability density evolution theory, detailed dynamic response analysis of the bridge structure under four multi-support and multi-dimensional seismic working conditions are implemented. This study can lay a foundation for the accurate dynamic response analysis and dynamic assessment of large and complex engineering structures under random earthquake excitation, and provide a theoretical basis for the seismic analysis and design of high-pier and long-span bridges.

2 The Spectral Decomposition Expression of Multi-support and Multi-dimensional Seismic Random Field

Suppose that $\boldsymbol{X}(t)=\left[\boldsymbol{X}_1(t),\boldsymbol{X}_2(t),\mathrm{L}\ ,\boldsymbol{X}_n(t)\right]^{\mathrm{T}}$ is a 3D-*n*V random vector process, in which each component process is $\boldsymbol{X}_i(t)=\left[X_{ix}(t),X_{iy}(t),X_{iz}(t)\right]^{\mathrm{T}}$. Generally, the probability information of the random vector process can be completely determined by the evolutionary power spectral density (EPSD)matrix:

$$\boldsymbol{S}(t,\omega)=\begin{bmatrix}\boldsymbol{S}_{11}(t,\omega) & \boldsymbol{S}_{12}(t,\omega) & \mathrm{L} & \boldsymbol{S}_{1n}(t,\omega)\\ \boldsymbol{S}_{21}(t,\omega) & \boldsymbol{S}_{22}(t,\omega) & \mathrm{L} & \boldsymbol{S}_{2n}(t,\omega)\\ \mathrm{M} & \mathrm{M} & \mathrm{O} & \mathrm{M}\\ \boldsymbol{S}_{n1}(t,\omega) & \boldsymbol{S}_{n2}(t,\omega) & \mathrm{L} & \boldsymbol{S}_{nn}(t,\omega)\end{bmatrix} \tag{1}$$

where *n* is the number of support nodes at the seismic action; $\boldsymbol{S}_{ii}(t,\omega)$ is the EPSD matrix of three directional ground motion components at the same point; $\boldsymbol{S}_{ij}(t,\omega)$ $(j\neq i)$ is the mutual EPSD matrix of three directional ground motion components at different points, respectively.

Further, $\boldsymbol{S}_{ii}(t,\omega)$ and $\boldsymbol{S}_{ij}(t,\omega)$ can be unified in the following form:

$$\boldsymbol{S}_{ij}(t,\omega)=\begin{bmatrix}S_{ix,jx}(t,\omega) & S_{ix,jy}(t,\omega) & S_{ix,jz}(t,\omega)\\ S_{iy,jx}(t,\omega) & S_{iy,jy}(t,\omega) & S_{iy,jz}(t,\omega)\\ S_{iz,jx}(t,\omega) & S_{iz,jy}(t,\omega) & S_{iz,jz}(t,\omega)\end{bmatrix},\ i,j=1,2,\mathrm{L}\ ,n \tag{2}$$

where $S_{ix}(t,\omega)$, $S_{iy}(t,\omega)$ and $S_{iz}(t,\omega)$ denote the EPSD of the three-directional seismic component of the *i*-th point; γ_{ij} is the coherence function of the *i*-th point and the j-th point (if $j=i$, then $\gamma_{ij}=1$), respectively.

Furthermore, the EPSD matrix $\boldsymbol{S}(t,\omega)$ of multi-support and multi-dimensional fully non-stationary random seismic field can be decomposed into the following form [6]:

$$\boldsymbol{S}(t,\omega)=\boldsymbol{D}(t,\omega)\boldsymbol{\gamma}(\omega)\boldsymbol{D}^{\mathrm{T}}(t,\omega) \tag{3}$$

where "T" denotes matrix transpose; $\boldsymbol{D}(t,\omega)=\mathrm{diag}\left[\boldsymbol{D}_1(t,\omega),\boldsymbol{D}_2(t,\omega),\mathrm{L}\ ,\boldsymbol{D}_n(t,\omega)\right]$ denotes diagonal matrix, in which $\boldsymbol{D}_i(t,\omega)=\mathrm{diag}\left[\sqrt{S_{ix}(t,\omega)},\sqrt{S_{iy}(t,\omega)},\sqrt{S_{iz}(t,\omega)}\right]$.

In Eq. (3), $\boldsymbol{\gamma}(\omega)$ is the coherence function, which can be defined as:

$$\boldsymbol{\gamma}(\omega)=\begin{bmatrix}\gamma_{11}(\omega) & \gamma_{12}(\omega) & \mathrm{L} & \gamma_{1n}(\omega)\\ \gamma_{21}(\omega) & \gamma_{22}(\omega) & \mathrm{L} & \gamma_{2n}(\omega)\\ \mathrm{M} & \mathrm{M} & \mathrm{O} & \mathrm{M}\\ \gamma_{n1}(\omega) & \gamma_{n2}(\omega) & \mathrm{L} & \gamma_{nn}(\omega)\end{bmatrix} \tag{4}$$

where $\boldsymbol{\gamma}_{ij}(\omega)$ can be expressed as:

$$\boldsymbol{\gamma}_{ij}(\omega)=\begin{bmatrix}\gamma_{ix,jx}(\omega) & \gamma_{ix,jy}(\omega) & \gamma_{ix,jz}(\omega)\\ \gamma_{iy,jx}(\omega) & \gamma_{iy,jy}(\omega) & \gamma_{iy,jz}(\omega)\\ \gamma_{iz,jx}(\omega) & \gamma_{iz,jy}(\omega) & \gamma_{iz,jz}(\omega)\end{bmatrix},\ i,j=1,2,\mathrm{L}\ ,n \tag{5}$$

Generally, the coherence function matrix $\boldsymbol{\gamma}(\omega)$ is a nonnegative definite Hermitian matrix, which can be decomposed by eigen orthogonal decomposition (POD). If it is a positive definite Hermitian matrix, it can be represented by Cholesky decomposition, i.e. spectral representation. From the above, the spectral decomposition expression of multi-support and multi-dimensional seismic random field can be obtained:

$$\begin{aligned}X_{iv}(t)=2\sum_{r=1}^{M}\sum_{k=1}^{N}\sqrt{S_{iv}(t,\omega_k)\Delta\omega}G_r(\omega_k)\times\big[&C_{mr}(\omega_k)\left(R_{rk}\cos\omega_k t-I_{rk}\sin\omega_k t\right)\\ &-D_{mr}(\omega_k)\left(R_{rk}\sin\omega_k t+I_{rk}\cos\omega_k t\right)\big]\end{aligned} \tag{6}$$

where $X_{iv}(t)$ and $S_{iv}(t,\omega_k)$ denote the acceleration component and the EPSD function in the *v*-th direction at the *i*-th point, respectively.

In Eq. (6), R_{rk} and I_{rk} are orthogonal random variables with zero mean, which satisfy the following basic conditions:

$$E\left[R_{rk}\right]=E\left[I_{rk}\right]=0,\ E\left[R_{rk}I_{sl}\right]=0,\ E\left[R_{rk}R_{sl}\right]=E\left[I_{rk}I_{sl}\right]=\frac{1}{2}\delta_{rs}\delta_{kl} \tag{7}$$

3 Dimension-Reduction Simulation of Multi-Support and Multi Dimensional Seismic Random Field

In general, the simulation of multi-support and multi-dimensional fully non-stationary seismic random field, whether using spectral representation or POD, belongs to the traditional Monte Carlo simulation method, which requires a large number of random variables (up to millions), and the probability information of the generated sample set is incomplete, which brings great challenges to the refined dynamic response analysis of engineering structures. Therefore, this paper introduces the idea of dimension-reduction of random function [6], that is, the orthogonal random variable is defined as the following random function form:

$$\begin{cases} \bar{R}_{sl} = \cos(s \times \Theta_1 + l \times \Theta_2) \\ \bar{I}_{sl} = \sqrt{2}\sin(s \times \Theta_1) \times \cos(l \times \Theta_2) \end{cases}, \; s = 1,2,\mathrm{L}\ ,M\ ,\ l = 1,2,\mathrm{L}\ ,N \tag{8}$$

where the elementary random variables Θ_1 and Θ_2 are uniformly distributed over the interval $(0, 2\pi)$. It can be proved that the orthogonal random variables defined by Eq. (8) can completely satisfy the basic conditions defined in Eq. (7). In this way, the high-dimensional random variable is reduced to 2, and the dimension-reduction simulation of multi-support and multi-dimensional seismic random field is realized.

Four observation points (representing soil sites of I_0, I_1, II and III) with a distance of 50m between two adjacent points are selected on the ground along the X direction to simulate the acceleration process of multi-dimensional ground motion at the four selected points respectively. Then the multi-support and multi-dimensional non-stationary seismic random field can be regarded as a 1D-12V non-stationary seismic random vector process. Considering the hysteresis coherence effect and traveling wave effect of spatial variability of ground motion, the representative time-histories of ground motion generated are shown in Fig. 1. For each soil site, it can be observed that the shape of the time-history curves of the ground motion in the two horizontal directions are relatively close, because the time-varying power spectrum model used in the modeling of the ground motion components in the two horizontal directions is exactly the same, but due to the different parameters of the intensity modulation function, it can be observed that the peak arrival time in the two horizontal directions is not exactly the same. In addition, there is a significant difference between the vertical acceleration time-history curve and the horizontal acceleration time-history curve, because the difference between the vertical component and the horizontal component is fully considered. Numerical examples show the effectiveness of the proposed method.

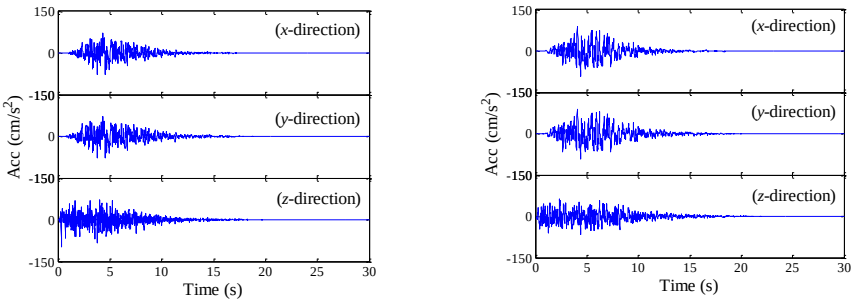

(a) Soil site I_0 (b) Soil site II

Fig. 1. Representative time-histories of multi-support and multi-dimensional seismic random field

4 Engineering Background and Finite Element Modelling of High-Pier and Long-Span Rigid Frame Bridge Structure

In this study, the finite element model of high pier long-span rigid frame bridge is based on the actual project The bridge is a highway bridge, and its seismic fortification category is class B. According to the seismic parameter zoning map of China (GB 18306-2015), the soil site is classified as Type I (moderately weathered basalt), the characteristic period of the bridge site is 0.45s, and the seismic peak acceleration is 0.17g. The seismic fortification level of bridge is 8-degree. The superstructure of the main bridge is a continuous rigid frame with variable cross-section prestressed concrete, of which the total length is 281m. The height of No.2 and No.3 main piers are 123m, and the height of transition piers are 69.5m (No.1) and 62.2m (No.4) respectively. The finite element model of the bridge structure is shown in Fig. 2.

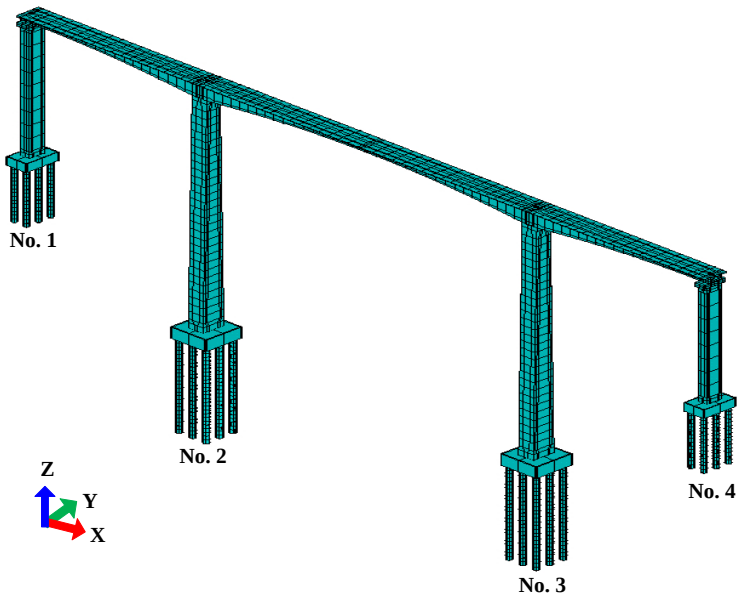

Fig. 2. The finite element model of the bridge structure

5 Seismic Response and Reliability Analysis of Long-Span and High-Pier Bridge

In order to study the influence of multi-dimensional ground motion on the seismic response of long-span and high-pier rigid frame bridge, four loading conditions are set in this study, and the random seismic response of long-span rigid frame bridge with high piers is investigated in detail under the condition of the combination of different directions of ground motion components along the bridge direction (x-direction), transverse bridge direction (y-direction) and vertical bridge direction (z-direction), that is x-direction excitation (Condition 1), x+y-direction excitation (Condition 2), x+z-direction excitation (Condition 3) and x+y+z-direction excitation (Condition 4), respectively.

Fig. 3 shows the mean and standard deviation (Std. D) of the displacement time-histories along the bridge direction at the top of No.2 main pier under the action of multi-support and multi-dimensional random earthquake of the four different conditions. The average displacement of the pier along bridge direction is larger under condition 1 and 4, and the peak values of both are close. The average displacement of pier top along bridge direction is the smallest under condition 3. At the same time, the Std. D time-history of pier top displacement along the bridge direction has little difference. In fact, in addition to the displacement along the bridge direction, the seismic excitation in other directions will cause the displacement response along the

corresponding direction. Therefore, in order to ensure the safety of the high-pier and long-span bridge structure, the influence of multi-support and multi-dimensional seismic input on the structural dynamic response should be fully considered in the structural seismic analysis.

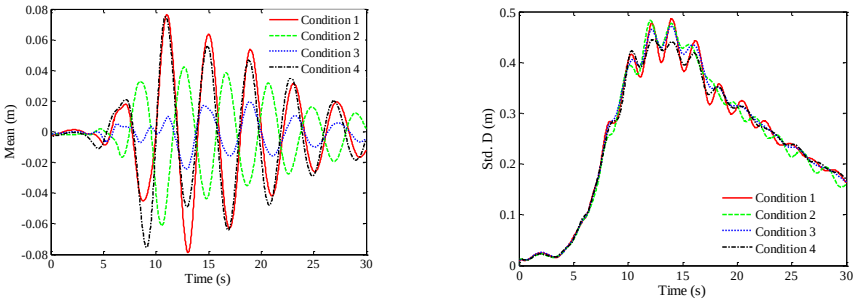

(a) Mean (b) Std. D

Fig. 3. Mean and Std. D of displacement of time-histories along the bridge direction at the top of No.2 main pier

The proposed dimension-reduction representation of the multi-support and multi-dimensional stochastic ground motion filed is consistent with the probability density evolutionary method in essence, thus the accurate dynamic response analysis of the earthquake-excited bridge structure can be performed. Furthermore, the dynamic reliability evaluation of the structural system can be calculated combing with the equivalent extreme events. In this study, the inter-story drift is introduced to assessment the dynamic reliability of the rigid frame bridge structure. Table 1 shows the dynamic reliability of each pier and the overall dynamic reliability of the bridge structure with the inter-story drift of the pier as the failure criterion. From the table, it can be seen that the dynamic reliabilities of the two transition piers are close, correspondingly, the dynamic reliabilities of the two main piers are close. At the same time, the dynamic reliabilities of the main piers are higher than those of the transition piers, which is due to the strengthening of the main piers in the design to improve the seismic capacity of the main piers and the whole bridge structure.

Table 1. Dynamic reliability of the high-pier and long-span rigid frame bridge

Inter-story drift	Dynamic reliability					
	0.005	0.010	0.015	0.020	0.025	0.030
No. 1 pier	0.03	0.49	0.93	0.99	1	1
No. 2 pier	0.17	0.83	0.99	1	1	1
No. 3 pier	0.20	0.88	1	1	1	1
No. 4 pier	0.02	0.51	1	1	1	1
Global reliability	0.95	0.38	0.88	0.99	1	1

6 Conclusions

By introducing the idea of random function, the dimension-reduction simulation of multi-support and multi-dimensional nonstationary seismic random field is realized. Furthermore, combined with probability density evolution method, the refined dynamic response and reliability analysis of high-pier and long-span continuous rigid frame bridge under multi-support and multi-dimensional random earthquake is conducted. Numerical analysis verifies the effectiveness of the dimension-reduction simulation method.

References

1. Zerva, A., Zervas, V.: Spatial variation of seismic ground motions: An overview. Applied Mechanics Reviews 55(3), 271-296 (2002).
2. Li, Z.X., Shi, Z.L.: Seismic response analysis for long-span continuous rigid-framed bridges under excitation of traveling waves. Earthquake Engineering and Engineering Vibration 23(2), 68-76 (2003). (in Chinese)
3. Pan, Q., Fang, S.S., Cheng, X.D.: The traveling wave effect of seismic response of high-pier-span continuous rigid frame bridge. Journal of Hunan Institute of Engineering 20(2), 82-85 (2010). (in Chinese)
4. Li, J.T., Yang, Q.S., Liu, Y.B.: Fragility analysis of long span continuous rigid frame bridge under multi-support excitations. Journal of Vibration and Shock 32(5), 75-80 (2013). (in Chinese)
5. Liu, Z.J., Xiong, M., Wan, Y.: Seismic Reliability analysis of continuous rigid frame bridge using probability density evolution method. Journal of Southwest Jiaotong University 49(1), 39-44 (2014). (in Chinese)
6. Liu, Z.X., Liu, Z.J., Ruan, X.X., et al: Spectral representation-based dimension reduction for simulating multivariate non-stationary ground motions. Soil Dynamics and Earthquake Engineering 114,3 13-325 (2018).

TRANSPORTATION

pages: 785 – 913

Financial and Structural Innovations in Mega Transportation Projects in Turkiye

Efecan Ünal [0009-0007-1666-3959]

Civil Engineering Faculty, Eastern Mediterranean University, Mağusa, North Cyprus,
efecan.unal@emu.edu.tr

Abstract. Public Private Partnership Financing method was used for the first time Gebze Orhangazi İzmir Motorway Project in the Turkish transportation sector. In addition, Osmangazi Bridge, which was Turkiye's longest suspension bridge at the time of its construction, was built in this project and innovations were carried out for suspension bridges.The construction of the first suspension bridge in Turkiye started in 1970. So far, 5 suspension bridges have been opened to traffic. Turkish Suspension Bridges have left their mark on the 21st Century World Suspension Bridge Literature with their new financing method, design, and innovations in the construction, maintenance, and operation phases. Osmangazi Bridge is the first suspension bridge in Turkiye with caisson construction and its towers on the sea, it is also the first tower made of steel segments. Since Osmangazi Bridge passes through a seismically active fault line, the seismic measures taken are an innovation for suspension bridges. The dehumidification system applied for the first time in Turkiye was applied for the steel elements in this bridge. While the steel and concrete production in the first 2 suspension bridges was considered as a 50-year design projection according to the Highways Technical Specifications, the steel and concrete productions with this bridge were designed for 100 years projection. In addition, the latest technological products were used in the paints made for the protective coating of steel fabrications. It is thought that the protective coating will provide optimum benefit both economically and in terms of time during the maintenance phase. Another feature of the Osmangazi Bridge is that it takes 1 hour 30 minutes by car to use the existing State Road, 45-60 minutes by ferry to the gulf crossing, and 6 minutes to use Osmangazi Bridge. Gebze Orhangazi İzmir Motorway shortens the existing state road by approximately 97 km and this bridge provides 78 km of it. Yavuz Sultan Selim Bridge, with its deck area, 8-lane highway crossing, 2-lane railway and 59 meters in size, is the world's widest suspension bridge with a deck crossing. Another innovative feature is that it is a hybrid bridge. It is the longest hybrid bridge in the world with a main span of 1408 meters. In addition, the 322-meter reinforced concrete tower is the tallest tower in the world. Canakkale Bridge is the last suspension bridge opened to traffic and is the longest main-span bridge in the world. Structural Health Monitoring System (SHMS) and Intelligent Transportation Systems (ITS), which are applied during the Maintenance and Operation phase, are also applied in the newly constructed Suspension Bridges. All 3 suspension bridges have been opened to traffic with a team effort that requires professional engineering and advanced technology. The suspension bridges of Turkiye have left their mark on the World Suspension Bridge literature in recent years, both with their aesthetics and their construction methods and features. This process continues with the opening of the world's longest main span Canakkale Bridge to traffic.

Keywords: MEGA Project, Suspension Bridge, Public Private Partnership, Transportation

1 Introduction

1.1 PPP Methods Applied in Turkiye

The Transportation Sector in Turkiye has employed the Build-Operate-Transfer (BOT) method for infrastructure investments, particularly those demanding advanced technology and substantial resources. The BOT model involves granting the private sector the right to construct a facility on public land, with risks shared between the private sector and the public. During a specified period, the private sector assumes the responsibility of operating, maintaining, and repairing the facility before transferring it back to the public at the end of the agreed-upon term. This model finds application in various domains, including highway, airport, port, bridge, tunnel construction, as well as nature park and wholesale market development. The BOT approach is particularly suitable for infrastructure projects that necessitate advanced technology and significant financial resources. [1]

The Build-Operate method was implemented in the Energy Sector, specifically in electricity generation. Under this model, the private sector is granted permission to establish and operate thermal power plants under their ownership, with the state purchasing the electricity generated. At the conclusion of the contract, the facility remains in the possession of the private sector.[2] In the context of Turkiye, five power generation projects with a combined capacity of 4,271 MW were executed using this model.

The Build-Lease-Transfer method was utilized in the Health and Education Sector. In this model, the private sector assumes the responsibility of constructing the facility, providing the necessary physical equipment, and operating the designated areas for a specified period. Eventually, the facility is transferred to the public sector. During the contract period, the public sector pays rent to the private sector.[3] This model has been adopted in Turkiye for the establishment of City Hospitals and Health Campuses in the healthcare sector.

The Transfer of Operating Rights method was employed to transfer the operating rights of airports to the private sector for a fixed duration. In this model, the private sector assumes the operating rights of existing state-owned airports for a specified period, without involving ownership transfer. Unlike other models, the Transfer of Operating Rights model does not entail a complete customization process, as the ownership of the facility remains with the public sector [4].

2 Completed BOT Projects

2.1 Gebze-Orhangazi-İzmir Motorway

The Gebze-Orhangazi-Izmir Motorway, which includes the Izmit Bay Crossing and Access Roads, is a Build-Operate-Transfer (BOT) project with a total length of 433 km. The motorway itself spans 384 km, while the remaining 49 km comprises connection roads.

The project carries an investment cost of 6.3 billion USD and has a duration of 22 years and 4 months as per the contractual agreement.

Prior to the construction of the motorway, the journey across the gulf took approximately 1 hour and 20 minutes by car or 45-60 minutes by ferry using the existing State road. With the completion of the motorway, the travel time has significantly reduced. It now takes just 6 minutes to crossing the gulf and has decreased the travel time from Istanbul to Izmir from 8-10 hours to 3.5-4 hours. This notable reduction in travel time has greatly improved transportation efficiency in the region.[5]

Special Structures Located on Gebze-Orhangazi-İzmir Motorway

Osmangazi Suspension Bridge

The suspension bridge in question features steel towers reaching a height of 252 meters, positioning it as the second tallest suspension bridge worldwide based on this measurement.

Upon its inauguration on July 1, 2016, the suspension bridge boasted a main span of 1,550 meters, securing its place as the fourth-largest suspended bridge globally at that time [6].

South Approach Viaduct

The South Approach Viaduct is 1.380 m., starting from the reinforced concrete approach foot of the Suspension Bridge at Km: 7+082, ending at Km: 8+460 and connecting with the motorway body to long steel structure.
It is the only steel viaduct constructed in the world with its four features.

Push-Slide Operation

The viaduct's deck, measuring 1,123 meters in length and 36 meters in width, with a height ranging from 13.5 meters to 57 meters, was constructed as a single piece by utilizing the push-slide method. This technique involved pushing the deck into place, ensuring a slope of 3.5% and a radius of 2,000 meters. With a total weight of 22,500 tons, this approach showcased its uniqueness within the construction industry.

Heavy Lift Operation

The South Approach Viaduct also achieved a country record by employing the heavy lift technique. A single-piece viaduct structure, measuring 128 meters in length and 36 meters in width, and weighing 2,600 tons, was successfully lifted to a height of 57 meters. This impressive feat showcased the innovative construction methods employed during its development.

Maintenance-Free Exterior Surface Protection

The viaduct incorporates a specialized exterior surface protection coating that ensures maintenance-free performance for 35 years, even under the most corrosive environmental conditions. This coating demonstrates its longevity and durability, providing an effective shield against environmental factors.

Horizontal Continuously Reinforced Diaphragm Wall Foundation

The construction of the South Approach Viaduct implemented a groundbreaking foundation method known as the Horizontal Continuously Reinforced Diaphragm Wall Foundation. This foundation type, utilized for the first time in Turkiye, showcases its pioneering nature and further contributes to the viaduct's exceptional design and construction techniques.

Orhangazi Tunnel

The Orhangazi Tunnel holds the prestigious title of being the longest motorway tunnel in Turkiye, stretching an impressive length of 3,591 meters. This tunnel, opened to traffic on April 21, 2016, stands as a remarkable engineering achievement in the country.[7]

Bornova Viaduct

The Bornova Viaduct, with a remarkable length of 2,200 meters, claims the distinction of being Turkiye's longest highway viaduct. This impressive structure showcases the country's commitment to developing extensive and advanced infrastructure to enhance transportation networks and connectivity [8].

2.2 Northern Marmara Motorway

The Project consists of 7 sections. Total length of the project is 352 kilometers. It was opened to traffic on August 26, 2016.[9]

- It is 95 km long including Yavuz Sultan Selim Bridge,
- Investment cost is 2.5 billion USD,
- Construction and Operation period is 10 years 2 months 20 days,
- It consists of the Çamlık and Riva Tunnels, which are the largest tunnels in Turkey and Europe, with a diameter of 22 meters and an excavation area of 236 square meters. [10,11]
- Comparing the deck area on the main span it is the widest bridge of the world. It is the only Hybrid Bridge project where suspension ropes and inclined suspension ropes are used.

2.3 Kınalı-Tekirdağ-Çanakkale Motorway (including 1915 Canakkale Suspension Bridge)

101 km. Motorway, Tender date: January 26, 2017, Investment amount: 2,722 billion US$, Construction and Operation period: 16 years 2 months 12 days.

2.4 Menemen - Aliağa - Çandarlı Otoyolu

- Tender date: 15 February 2017,
- Investment amount: 394 Milyon US $,
- Construction and Operation period: 9 years 10 months 11 days,

- The motorway will pass through the West of Aliağa Organized Industrial Zone and end in Çandarlı Port area.

2.5 Ankara - Niğde - Otoyolu

- Tender date: 17 April 2017,
- Investment amount: 1,102 billion US Dolar
- Construction and Operation period: 11 years 10 months 17 days
- With the construction of the 330-kilometer Ankara Niğde Motorway, uninterrupted transportation from Edirne to Sanliurfa was provided.

3 The Main Purpose of Bot Projects on The Motorways of Turkiye

- It is the combination of the interest of the Contractor making the investment to ensure the return of the Loan and the benefit of the Investment Owner Administration to reach the investment without incurring a financial burden.
- Consultancy Control Organization: It ensures that the BOT Project, which is under the commitment of the Company in Charge, is carried out on behalf of the Administration in accordance with the procedures, principles and specifications included in the BOT contract and its annexes.[12]

Contractor

- The construction and operation period is specified in the contract.
- Contractor will consider making use of all the possibilities of technology, bringing the construction period forward, adding it to the operation phase and generating more income.
- Contractor will act in accordance with the national and international standards, Technical specifications and requirements, Maintenance-Repair-Operation Standards and Quality Plan accepted by the Administration in the performance of the works subject to the Contract.Incumbent Company,
- Administration
- It will want to buy the highway and its outbuildings at the end of the operation period, free from all kinds of debts, well-maintained and in working condition with all its functions.
- Consultant
- In line with the organization chart determined by the Administration, it establishes the Control Organization with experts with the knowledge, skills and experience specified in the Specification.
- It creates a full Supervision mechanism on behalf of the Administration at every stage of the works carried out in the field.

- Brings the suggestions that will provide advantages in terms of time and cost to the attention of the Administration and Contractor.
- Its main task is to make it in the quality defined in the Contract and its annexed Specifications, as in the approved project of the Work.

3.1 Results

The Consultant, who is strong, experienced, reliable and works shoulder to shoulder with the Administration in Public-Private Sector Partnership BOT Projects, is the guarantee of the Project's success and plays an important role in the overall quality of the Project. [13]

The most successful Projects occur when there is a professional relationship based on absolute trust between the Administration and the Consultant. [14]

A successful PPP Suspension Bridges Example (Osmangazi Bridge)

Project Description:

Provision of financing, design, construction, operation, maintenance and repair of the Gebze-Orhangazi-İzmir Motorway (including İzmit Bay Crossing and Access Roads) in accordance with the contract and transfer of it to the Client free of charge at the end of operation period free from any kind of liabilities, in good repair, operating and usable condition. Project Description

Project Model: Build-Operate-Transfer (BOT)
Ministry: Ministry of Transport and Infrastructure
Client: General Directorate of Highways (KGM)
Client Consultant (workplace): Public Private Partnership Division Directorate (KÖSOB)
Consultant (Construction) : Yüksel Project-Emay-Chodai Joint Venture
Appointed Company: Otoyol Yatırım ve İşletme A.Ş. (OYİAŞ)
EPC Contactor: Nurol-Özaltın-Makyol-Astaldi-Yüksel-Göçay Joint Venture (NÖMAYG)
Contracts
Tender Announcement : 07.04.2008
Tender Date : 09.04.2009
Contract Date : 27.09.2010
Contract Effective Date : 15.03.2013
Duration of the Contract : 22 Years 4 months (Construction + Operation)
Beginning of Works: 05.04.2013
Construction Period: 7 Years (15.03.2020)
Completion of Works: 15.07.2013

3.2 General Information (Km. 4+175 – 7+084)

İzmit Bay Suspension Bridge, is the 4 th longest main span suspension bridge in the world with the 1550 m. main span lenght. It is also 2nd highest steel tower with the height of 252 meters.

İzmit Bay Bridge technical information as follows:

- Structure Type : Steel Suspension Bridge
- Contract Type : Engineering + Procurement + Construction
- Client : Karayolları Genel Müdürlüğü
- Appointed Company : OTOYOL A.Ş.
- EPC Contactor : NÖMAYG A.O.
- Suspension Bridge Subcontractor : IHI-ITOCHU Consortia
- Suspension Bridge Design : COWI
- Ground Investigation : Fugro
- Suspension Bridge Design Verification : Halcrow ve Ty-Lin
- Infrastructure Works : STFA
- Steel Tower and Deck Fabrication : ÇİMTAŞ
- Main Span: 1550 m, Side Spans : 566 m
- North Transition Length : 120 m
- South Transition Length : 105 m
- Tower Height :252 meters from sea level.
- Carriage of Way : 2 X 3
- Lane Width : 3,65 m
- Deck Width : 35,93 m
- Navigational Clearance (H X W) : 64,30 m X 1000 m

3.3 Design Base

İzmit Bay Bridge first level design bases are determined and detailed design works are completed as following fundamental concepts:

- Maximum Quality
- Safe Structure
- Durable and enabling easy maintenance.
- Esthetic
- Short construction time
- Cost Effective

In relation to the abovementioned data, the structure of the bridge is determined as a suspension bridge design. At the design stage KGM and Eurocode (EN 1991-2 Traffic Loads on Bridges) standards and regulations were taken into consideration.

The load descriptions are considered as:

- Permanent/Temporary, Traffic Loads, Wind, Temperature etc.
- Seismic and Ship Crash (according to AASHTO)
- Unfavorable load combinations

After the general concept is determined, the structure is determined and finalized. The suspension bridge design includes:

- Concrete anchor blocks and tower foundations
- Tower foundations approximately 40 m deep, seismically isolated by a gravel layer

- Steel Towers
- Continous deck not supported vertically at the tower locations.
- South Piers supported on south anchor block (integrated structure)

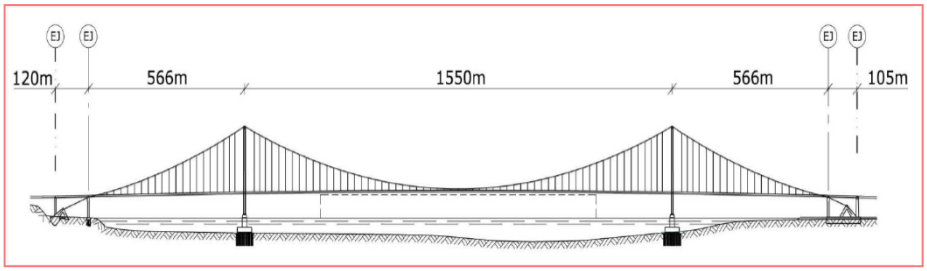

Fig. 1. Design of Suspension Bridge

As requirement of design, seismic performance criterias are determined. Fugro performed site investigation designed to address the following issues:

Regional fault setting with a focus on understanding the location of the North Anatolian Fault in the project vicinity.

Alignment area geology and site conditions, with a focus on evaluating variations in near-surface site conditions within a few hundred meters of the proposed bridge alignment, and potential shallow geohazards that may impact the proposed bridge.

Foundation stratigraphy in an area within approximately 100 to 200 meters around the proposed bridge foundations.

A detailed study is conducted on earthquakes happened in North Anatolian Fault Zone in 20th century. Locations of active and secondary fault zones are also determined during these site investigations. After modelling of the soil, it is founded that the according to original design, the soil under the south tower of the suspension bridge have possibility for slope sliding. Maximum displacements of the soil is calculated as 5m-6m. Therefore, south tower of the bridge is moved to the north for 60 meters and located on a stable soil to avoid unstable conditions caused by slope stability.[15] [16]

Table 1. Seismic Event Performance

Seismic Event	Ground Motion Return Period	Service Performance Level	Damage Performance Level
Functional Evaluation Earthquake (FEE)	150 years (50% in 100 years)	Immediate Access	NoDamage
Safety Evaluation Earthquake (SEE)	1000 years (10% in 100 years)	Limited Access	Repairable Damage
No Collapse Earthquake (NCE)	2475 years (4% in 1000 years)		No collapse, no casualties Significant damage

The primary design of the Osmangazi Bridge adhered to the safety evaluation earthquake conditions set forth by the General Directorate of Highways (KGM). Based

on these requirements and regulations, the design considered the possibility of a safety evaluation earthquake with a 10% probability of occurrence within a 1000-year period.

To improve the ground conditions at the locations where the south and north towers were to be situated, dredging was carried out at an elevation of -43.00 meters below the surface. Following the dredging process, pipe works were implemented, and 195 steel piles with a diameter of 2 meters were driven into the ground for ground improvement purposes. [12]

To allow the foundations to move during earthquakes without causing damage to the bridge structure, a unique engineering solution was employed. A 3-meter-thick layer of gravel was spread over the piles, enabling the concrete foundation block to move freely. This engineering approach, known as seismic isolation of the foundations, provided enhanced seismic performance and protection.

Regarding wind force criteria, the wind design criteria were identified based on EN 1991-01-04, which specifies actions on structures, particularly wind actions. The basic wind velocity, defined as the characteristic 10-minute mean wind velocity at 10 meters above ground level in open country terrain with low vegetation and isolated obstacles, was calculated to be 25.4 m/s (94 km/h).

At the deck level (+70m elevation), the wind design speed was determined to be 38 m/s in a specific direction (137 km/h). The critical wind speed, denoted as the maximum wind speed that the structure can withstand, was identified as 58 m/s (209 km/h).

To ensure the design's accuracy and reliability, wind tunnel tests were conducted in Denmark, Canada, and Italy. These tests provided valuable data and insights for the wind design of the Osmangazi Bridge, contributing to its structural integrity and resilience against wind forces.[12]

The wind tunnel tests conducted for the Osmangazi Bridge project yielded important findings and recommendations regarding wind effects and structural stability. The key findings from the wind tunnel tests are as follows:

- Flutter Effect and Wind Panels: The usage of wind panels across the entire bridge resulted in flutter on the deck section. As a result, it was recommended that wind panels should only be used at the tower areas to mitigate flutter and ensure the structural stability of the bridge. Flutter refers to self-excited vibrations caused by the interaction between aerodynamic forces and structural dynamics.[17]
- Absence of Vortex Shedding: Vortex shedding, which refers to the formation and shedding of vortices as wind passes around structures, was not measured during the wind tunnel tests.[18] This suggests that the bridge design effectively minimized vortex shedding effects, contributing to the overall stability of the structure.
- Measurement of Static Wind Load Coefficients and Aerodynamic Derivatives: The wind tunnel tests allowed for the measurement of static wind load coefficients and their associated aerodynamic derivatives.[19] These measurements provide crucial data for accurately determining the wind-induced forces acting on the bridge and optimizing its design.

To address tower vibrations during both the construction and service life periods, active mass dampers (AMD) will be employed. Active mass dampers are devices used to mitigate vibrations by introducing controlled counteracting forces. In this case, small-sized AMDs will be installed at the elevation of 170 meters on each tower. These active mass dampers will effectively reduce tower vibrations, enhancing the structural performance and safety of the bridge. (Fig.3, Fig.4)

Overall, the wind tunnel tests played a vital role in assessing wind effects, optimizing the bridge design, and ensuring the structural integrity and stability of the Osmangazi Bridge. The findings and recommendations from these tests allowed for the implementation of appropriate measures, such as the use of wind panels and active mass dampers, to mitigate wind-induced vibrations and enhance the overall performance of the bridge [20].

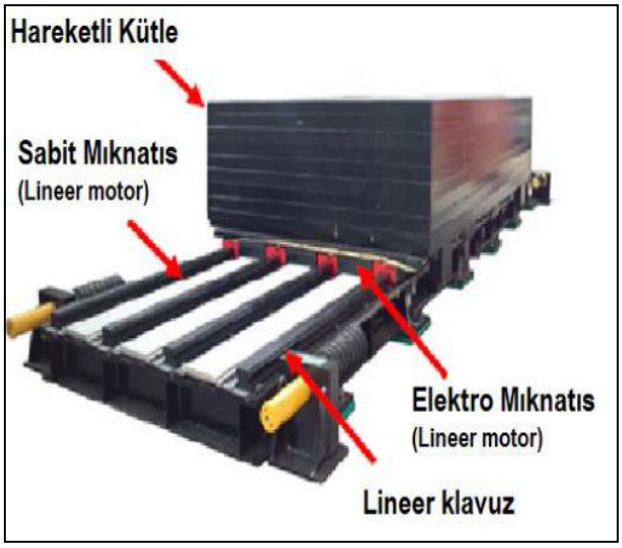

Fig. 2. Active Mass Dampers

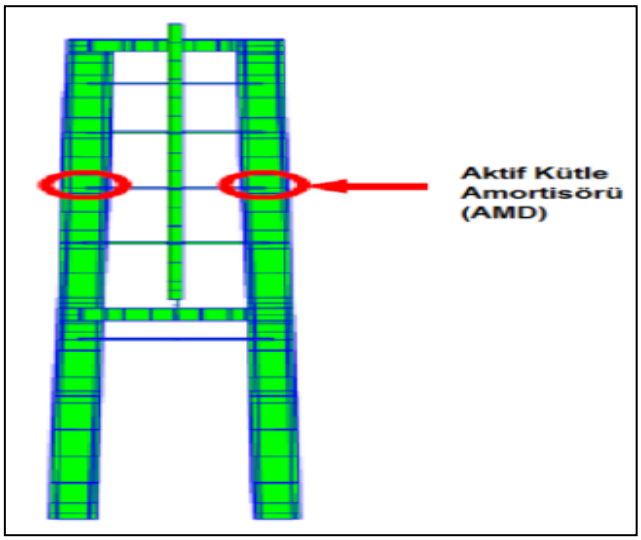

Fig. 3. Active Mass Dampers Location

4 Dehumidification System

To protect against corrosion and ensure the longevity of the suspension bridge, a classical dehumidification system is applied. The process involves the following steps:
1. Zinc Paste Application: Before wrapping the cables, a layer of zinc paste is applied to the main wires. Zinc paste provides a protective barrier against corrosion, acting as a sacrificial layer that prevents the underlying steel from oxidizing. [21]
2. Cable Wrapping: After the zinc paste application, the cables are wrapped using appropriate materials. This wrapping helps to secure and protect the cables, preventing moisture and external elements from reaching the underlying steel structure. [22]
3. Rubber-Based Paint Application: Once the cable wrapping is complete, a rubber-based paint is applied to further safeguard against corrosive effects. This paint serves as an additional protective coating, enhancing the resistance of the cables to environmental factors, such as moisture and atmospheric pollutants. [23]

By implementing the dehumidification system, the suspension bridge aims to minimize the impact of corrosion on the cables and ensure their long-term durability.[24] The combination of zinc paste, cable wrapping, and rubber-based paint provides a comprehensive protective layering system that helps to preserve the integrity and performance of the bridge's cables.

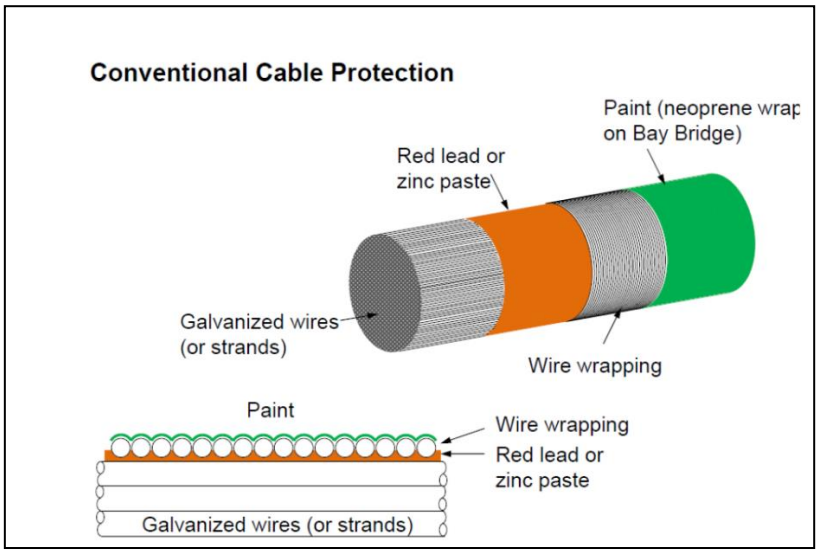

Fig. 4. Conventional dehumidification method on bridge cables

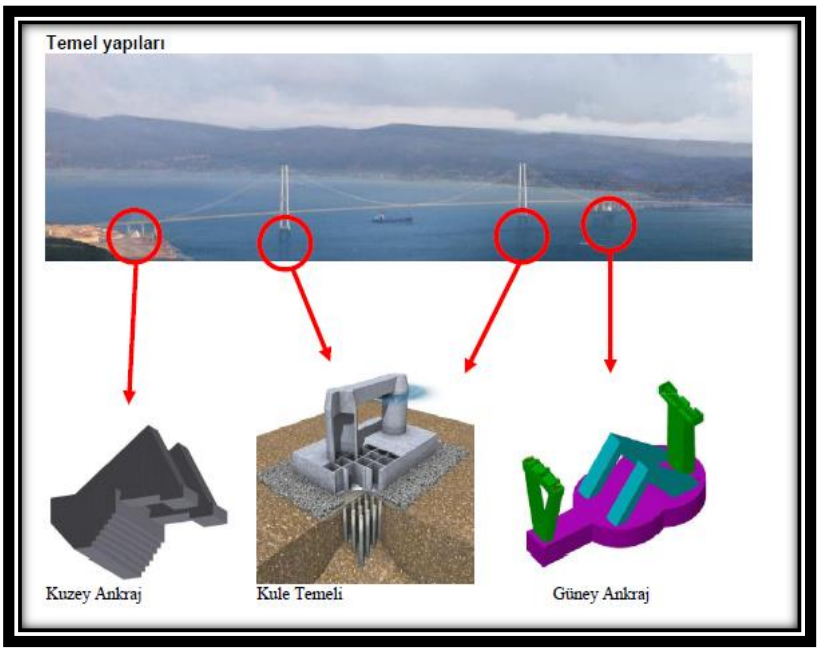

Fig. 5. Izmit Bay Crossing Suspension Bridge Main Structures

- The north anchor block of the bridge is designed as a classical massive gravity type anchor block. The tensions from the cables are transferred over saddles

to the anchor block. This design ensures the stability and proper distribution of forces within the anchor block structure.

- The south anchor block is a unique and integrated structure that includes hollow splay saddle legs, a massif concrete block embedded in the soil, a transition pier, and a side span pier. This design provides stability and supports the overall structural integrity of the bridge.
- Tower Foundations:
  - Reinforced soil with steel inclusion piles (195 piles with a diameter of 2 meters per foundation) is used for the tower foundations.
  - A gravel bed with a thickness of 3 meters is incorporated to allow the caisson to slide during earthquakes, reducing the impact on the foundation.
  - Prefabricated caissons (54x67x15 meters) are utilized for the foundation construction.
  - Composite steel/concrete shafts with a diameter of 16 meters and a thickness of 1.2 meters are employed, ensuring high robustness against ship impact.
  - Solid plinths with anchor bolts are utilized to fix the steel tower to the foundation.
- Towers:
  The bridge towers are designed as steel towers to provide a lightweight structure, facilitate fast construction, and enable more elastic behavior during earthquakes. Each tower is constructed by connecting 22 steel blocks, which are welded and connected by bolts. The tower height is 252 meters, making the İzmit Bay Bridge the second-highest steel tower in the world. The steel tower blocks are manufactured in the Çimtaş Gemlik factory and transported to the site by buoys.
- Main Cable:
  The main cable transfers the deck loads to the towers, side piers, and anchor blocks. The main cable wires and galvanizing process are carried out in the China Tokyo Rope factory. The main cable is transported to the site in three separate sections. Hanger manufacturing works are conducted in the South Korea Sam Young factory. A prefabricated parallel wire strand system is applied in the main cable, consisting of 110 strands, each with 127 wires with a diameter of 5.91 mm. When compacted, the main cable has a diameter of 0.781 meters in the main span and 0.788 meters in the side spans. The total length of the cable structure is approximately 84.518 kilometres.[12]
- Bridge Deck:
  The bridge deck is constructed as a closed steel box girder with a depth of 4.75 meters. Truss diaphragms are installed at 5-meter spacing to enhance structural stability. The deck plate has a thickness of 14 mm, and a 360 mm depth extends through the deck, with a 60 mm roadway surfacing on top. The interior of the box girder is protected from corrosion through dehumidification methods, ensuring the long-term durability of the deck structure.[16]

Table 2. Bridge Parameters

Bridge Deck Technical Details		
Width	meter	36
Length	meter	25
Height	meter	4.75
Weight	ton/block	302 Ton/Block
Total Weight	ton	33,506 Ton/ Bridge
Total Deck Segment	Nos	113 Nos

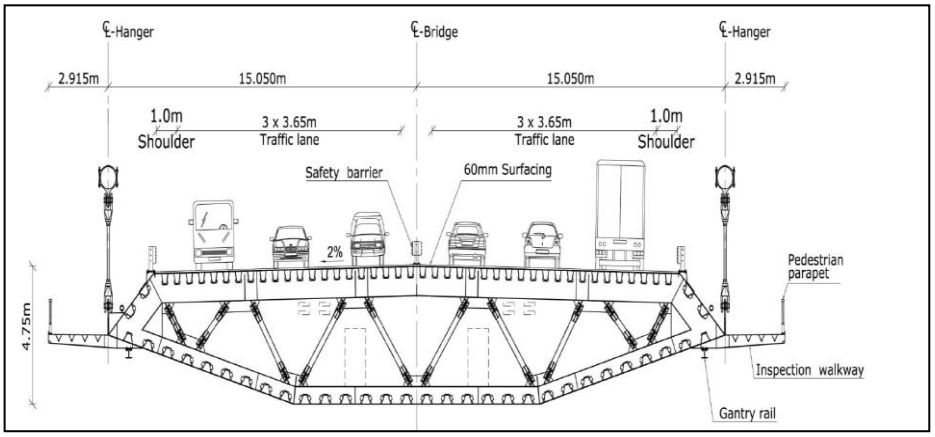

Fig. 6. Deck Panels Cross Section (Deck panels are manufactured in Çimtaş Gemlik factory and welded in Gölcük factory.)

5 Conclusion

The Gebze-Orhangazi-İzmir Motorway project, including the İzmit Bay Crossing, is a significant infrastructure development in Turkey. Some key points can be highlighted:

- Cost and Scale: The project's total construction cost is approximately 6.3 billion US dollars, making it one of the largest and most expensive Built Operate and Transfer projects in the world. When considering financing costs, the investment reaches around 8 billion US dollars. This scale of investment surpasses the annual budgets of many medium-sized countries.
- Connectivity and Economic Impact: The project connects the Edirne-İstanbul-Ankara Motorway to the İzmir-Aydın and İzmir-Çeşme Motorways, creating a fully-accessible motorway network that links the Marmara and Aegean Regions. These regions are vital to the Turkish economy, and the improved connectivity will facilitate industrial, trade, and touristic traffic between cities such as İstanbul, Kocaeli, Yalova, Bursa, Balıkesir, Manisa, and İzmir. This enhanced connectivity will lead to significant benefits, including time and cost savings for both business and leisure travel, reduced traffic congestion in urban areas, and improved safety and economic efficiency.

- Journey Time Reduction: The Gebze-İzmir Motorway significantly reduces the travel distance by about 95 kilometers compared to the state road alternative. As a result, the journey time between the cities of İstanbul and İzmir is reduced to approximately 3-3.5 hours, as opposed to the previous 8-10 hours. This time-saving measure is estimated to result in annual savings of around 650 million US dollars.
- Overall, the Gebze-Orhangazi-İzmir Motorway project brings immense economic, social, and logistical benefits to the regions it connects. It enhances regional connectivity, reduces travel times, improves traffic flow, and contributes to the overall development and prosperity of the areas it serves.[12]

References

1. M. Top and C. Sungur, "Opinions and evaluations of stakeholders in the implementation of the public-private partnership (PPP) model in integrated health campuses (city hospitals) in Turkey," The International journal of health planning and management, vol. 34, no. 1, pp. e241-e263, 2019.
2. M. Li, P. Tang, X. Lin, and F. He, "Multistage planning of electric transit charging facilities under build-operate-transfer model," Transportation Research Part D: Transport and Environment, vol. 102, p. 103118, 2022.
3. L. A. qizi Urokova, "PUBLIC-PRIVATE PARTNERSHIP AND ITS ROLE IN THE ECONOMY OF A COUNTRY," Educational Research in Universal Sciences, vol. 2, no. 5, pp. 759-766, 2023.
4. A. K. Sinha and K. N. Jha, "Dispute resolution and litigation in PPP road projects: Evidence from select cases," Journal of Legal Affairs and Dispute Resolution in Engineering and Construction, vol. 12, no. 1, p. 05019007, 2020.
5. O. Solak, "Toll roads in Turkey: Private versus public," Case Studies on Transport Policy, vol. 10, no. 2, pp. 1110-1117, 2022.
6. Ö. Güzel, "1915 Çanakkale Bridge–Dream to Reality," 2023: Springer, pp. 27-46.
7. S. Gundes and N. Atakul, "The Eurasia Tunnel Project," Network Industries Quarterly, vol. 23, no. 3, pp. 13-16, 2021.
8. N. Erdem and E. Timur, "Analysis of Traffic-Induced Ground Vibration in Highway Viaducts," Türk deprem araştırma dergisi (Online), vol. 4, no. 2, 2022.
9. M. Çakıner and E. Bozkurtoğlu, "Importance of engineering geology on slope stability analysis applied in Northern Marmara Motorway (Section-5), İzmit, Turkey," 2022.
10. E. Aysev, "Urbanization Processes of Northern Istanbul in the 2000's: Yavuz Sultan Selim Bridge and the Northern Marmara Highway," 2022.
11. M. Ambor et al., "Design of Ihsaniye Viaduct of Northern Marmara Motorway, Turkey."
12. K. G. M. E. B. YÜKSEL PROJE-EMAY-CHODAİ "Karayolu Temel Kursu Saha Ziyaretleri," ed. Bursa, 2014-2019.
13. P. T. Nguyen, V. Likhitruangsilp, and M. Onishi, "Success factors for public-private partnership infrastructure projects in Vietnam," International Journal on Advanced Science, Engineering and Information Technology, vol. 10, no. 2, pp. 858-865, 2020.
14. F. D. Cherkos, K. N. Jha, and A. Singh, "Framework to select public–private partnership modalities," Journal of Legal Affairs and Dispute Resolution in Engineering and Construction, vol. 12, no. 4, p. 04520034, 2020.
15. (2014-2019). Karayolu Temel Kursu Saha Ziyaretleri.
16. YÜKSEL and PROJE-EMAY-CHODAİ, "Gebze-Orhangazi-İzmir Otoyolu (İzmir Körfez Geçişi ve Bağlantı Yolları Dahil) Aylık Faaliyet Raporları," Bursa, 2014-2016.

17. W. Yuan, S. Laima, W.-L. Chen, and H. Li, "External excitation effects on the flutter characteristics of a 2-DOF rigid rectangular panel," Journal of Wind Engineering and Industrial Aerodynamics, vol. 209, p. 104486, 2021.
18. M. M. Rai, "Wakes of thin flat plates: Intermittency, cessation of vortex shedding and the emergence of an intermediate-wake instability," International Journal of Heat and Fluid Flow, vol. 89, p. 108814, 2021.
19. M. S. Thordal, J. C. Bennetsen, S. Capra, and H. H. H. Koss, "Towards a standard CFD setup for wind load assessment of high-rise buildings: Part 1–Benchmark of the CAARC building," Journal of Wind Engineering and Industrial Aerodynamics, vol. 205, p. 104283, 2020.
20. (2014-2019). İnşaat Mühendisleri odaları, Üniversiteler, Uluslararası Organizasyonlar, Sivil Toplum Örgütleri ve Kamu Kurum Kuruluşlarına Bağlı Gruplara Yapılan Sunumlar.
21. M. Zhang, S. Huang, P. Li, K. W. Shah, and X. Zhang, "Application of dehumidification as anti-corrosion technology on suspension bridges: A review," Applied Thermal Engineering, vol. 199, p. 117549, 2021.
22. W. Chen, R. Shen, M. Que, M. Gong, and R. Miao, "New dehumidification system design and dehumidification test for the main cable of suspension bridge," Journal of Civil Structural Health Monitoring, vol. 11, no. 5, pp. 1321-1335, 2021.
23. A. Downey et al., "Durability and weatherability of a styrene-ethylene-butylene-styrene (SEBS) block copolymer-based sensing skin for civil infrastructure applications," Sensors and Actuators A: Physical, vol. 293, pp. 269-280, 2019.
24. J. L. Jensen, H. Narasimhan, L. Giuliani, and G. Jomaas, "Development of fire protection for bridge cable systems," ce/papers, vol. 3, no. 3-4, pp. 671-676, 2019.

Optimal Pavement Design and Maintenance Approach Using HDM-4

Amarendra Kumar Sandra[1], Pattabhiram Yegulla[2], J Janardhan[3]

[1]Corresponding Author
[1]Professor, Civil Engineering Department, Rajiv Gandhi University of Knowledge Technologies (RGUKT), RK Valley, Andhra Pradesh, India – 516330
Email: aksandra@rguktrkv.ac.in
[2]Highway Design Engineer, Druta Designs, Hyderabad
Email: Pattabhi@drutadesigns.in
[3]Pavement Design Engineer, Druta Designs, Hyderabad
Email: Janardhana.j@drutadesigns.in

Abstract. The basic principle of pavement design and maintenance is that the pavement's functional and structural condition should remain below an acceptable level under the expected traffic during its design life. Considering this, a new pavement design and maintenance approach is suggested in this paper based on the life cycle cost analysis using HDM-4. This involves designing pavement compositions for various traffic levels, estimated for selected design periods as an alternative to designing a pavement composition for design traffic obtained over the entire design life and maintaining the pavement by providing an overlay whenever the performance indicator, surface roughness, reaches the trigger limit. The process shall be continued until the pavement reaches its concession period. In addition, the widening proposal was also considered when the volume/capacity ratio was greater than 0.8 during the concession period, and its impact on pavement deterioration was studied. The proposed 6-lane (3-lane on either side) greenfield bituminous concrete road project is considered a case study to demonstrate the proposed approach. On the proposed road, the expected design traffic in terms of million standard axles (MSA) was estimated for the different design periods of 10, 15, and 20 years starting from the base year 2024 and found to be 45 MSA, 80 MSA, and 130 MSA, respectively. Conventional pavement compositions were designed using elastic layer theory for all design traffic levels. Inputting parameters such as traffic pattern, design traffic, pavement composition, and other relevant data into the HDM-4 project analysis framework, the year-wise change in surface roughness values in terms of the International Roughness Index (IRI) was estimated. Assuming the mostly accepted pavement functional performance triggering value, IRI of 3.30 m/km, a functional overlay was recommended. Analysis was carried out with three different practical overlay thicknesses of 30mm, 40mm, and 50mm. Continuing the same procedure up to the end of concession period, economic analysis was carried out using HDM-4 to identify the best/ optimum pavement composition and maintenance approach, which gives the highest NPV/cost ratio. In the present case, the best alternative is the pavement with 80 MSA design traffic and a 40mm overlay when roughness reaches 3.30 IRI.

Keywords: Pavement Surface Roughness, Pavement Deflection, Economic Analysis, Life Cycle Cost Analysis

1 Introduction

Bituminous Pavement is a structure comprising different layers, such as subgrade, granular subbase, granular base, bituminous base, and surface courses. These layers are designed to be stronger than the natural ground (natural subgrade) and protect it from being overstressed due to vehicle loads. The thickness of the pavement structure and its layers is of utmost importance, as it needs to be adequate to receive the stresses caused by loads and distribute them on the natural ground safely without any deformation. Several organizations and institutes have developed guidelines for designing pavement structures using different methods. These methods include Group Index, CBR, Empirical, Mechanistic, and Mechanistic-Empirical (ME) methods [1-5]. Currently, many pavement design guidelines are based on the ME approach, which employs the theory of mechanics for computing traffic and environmentally induced strains at critical locations in the pavement structure [6,7]. These strains are incorporated in to the empirical equations to predict allowable traffic in the design period. While the ME approach is more scientific than other methods, it has a few limitations. Specifically, it only determines the thickness of the pavement structure for given loading conditions and material properties and does not predict the performance of the pavement during its design period.

Regarding pavement design, it is not just about the pavement thickness; the pavement functional condition or riding quality (expressed in roughness) must also be within acceptable limits throughout the design period, despite the impact of traffic and environmental factors [8-10]. Over time, the pavement is exposed to various vehicle loads, temperature changes, and moisture conditions. All of which can affect the pavement roughness. To ensure that the roughness stays within acceptable levels, the pavement must be timely maintained [11,12]. This may involve resurfacing if the roughness is still low or an overlay if the roughness has increased. If the pavement is not properly maintained, it will deteriorate over time and eventually reach a point where it requires rehabilitation or even reconstruction [13,14]. Therefore, keeping roads in good condition is important, as neglecting maintenance can lead to much higher transportation costs. Studies reported that it can cost up to three to five times more to rejuvenate a road in poor condition than it would to maintain and keep it in good condition. So, investing in regular maintenance is financially wise and helps keep the roads safe and functional.

Considering the above fact, it is important to include pavement maintenance in the pavement design process to maintain acceptable roughness levels. Various maintenance types are discussed in the literature, but the authors focused on two specific types. The first type is routine maintenance, which involves making local repairs on the pavement, repairing road furniture, and horticulture maintenance. The second type is performance-based maintenance, which consists of laying a renewal course on the pavement if the pavement roughness, expressed in the International Roughness Index (IRI) reaches the most acceptable trigger value of 3.30 m/km [15]. To effectively forecast the pavement condition over time and determine when maintenance is needed based on certain trigger levels, it is essential to have an interface that contains pavement performance prediction models as well as a system for assigning maintenance standards based on condition. To

achieve this, it is decided to utilize the Highway Development and Management (HDM-4) package developed by the Word Bank [16] as this tool can handle all the tasks above, including estimating lifecycle costs based on various types of maintenance performed throughout the design period [17-20].

A 6-lane (3-lane on either side) divided greenfield bituminous concrete road project (Vijayawada Bypass in the state of Andhra Pradesh, India) is considered a case study to demonstrate the proposed approach, which emphasizes pavement design and maintenance as an integral part. On this road, the expected design traffic in terms of Million Standard Axles (MSA) for the design periods of 10, 15, and 20 years have been determined based on the base year 2024 commercial traffic. The values are 45 MSA, 80 MSA, and 130 MSA, respectively. For all three-design traffic, the conventional pavement compositions consist of a Bitumen Concrete Surface Course, Bitumen Concrete Base Course, Granular base course, and Granular Subbase courses on top of the subgrade were designed using elastic-layered theory.

After inputting various parameters such as traffic patterns, design traffic, pavement composition, and other relevant data into the HDM-4 project analysis framework, the year-wise pavement surface condition and change in surface roughness values (as measured by IRI) were estimated. Two maintenance options were chosen when the performance indicators reached the trigger levels to maintain the pavement in acceptable condition. The first option involves implementing a functional Overlay when the IRI value reaches 3.30m/km without routine maintenance. In this option, three different functional overlays with thicknesses of 30mm, 40mm, and 50mm were studied to examine the impact of overlay thickness. On the other hand, the second option includes routine maintenance in addition to the activities suggested in the first option. The same procedure was followed until the concession period. An economic analysis using HDM-4 to identify the best pavement composition and maintenance approach that would give us the highest NPV/cost. After a thorough investigation, it was found that a pavement composition designed for 45 MSA traffic and a 30mm overlay when roughness reaches 3.30 m/km (IRI) is the most viable alternative. Furthermore, it was noticed that the volume/capacity ratio reaches 0.8 in 2040, which suggests widening the pavement to 8 lanes.

2 Objective of the Work

The objective of this study was to ensure that the pavement design process incorporates pavement maintenance so that the riding quality remains consistent throughout the design period. This would be achieved by applying appropriate maintenance standards whenever required while minimizing the life cycle cost. The study involved several stages, including the estimation of design traffic based on the base year traffic; the design of pavement crust composition for the estimated design traffic; inputting pavement crust, traffic, and environmental data into the HDM-4 framework; predicting the year-wise pavement condition and roughness changes, and assigning maintenance standards when performance indicators or roughness reaches the triggered values.

Finally, the study would conduct a life cycle cost analysis using HDM-4 for all pavement alternatives and recommended maintenance standards. The best pavement composition with the highest NPV/cost would then be identified.

3 Pavement Design and Maintenance Approach

To showcase the proposed approach, a step-by-step method was employed.

3.1 Traffic Projections and Estimation of Design Traffic

A network-level traffic volume count survey was carried out and determined the amount of divertible traffic that is expected to utilize the greenfield project section (as shown in Table 1). Additionally, Origin-Destination and Axle Load surveys were conducted to estimate growth rates and Vehicle Damage Factors (VDF). The results of our analysis are presented in Table 2, which includes the growth rates and VDF values.

Table 1. Base Year Traffic on the Project Road

Direction	Annual Average Daily Traffic (AADT)					
	CAR	BUS	Light Commercial Vehicle (LCV)	2 – Axle Truck	3 – Axle Truck	Multi Axle Vehicle (MAV)
Downward	5499	404	582	658	892	1259
Upward	4691	462	730	592	928	1288

Table 2. Traffic Growth Rates and Vehicle Damage Factors

Description	Type of Vehicle					
	CAR	BUS	LCV	2 – Axle Truck	3 – Axle Truck	MAV
Growth Rates (%)	5.70	5.00	7.05	5.00	6.42	5.16
Vehicle Damage Factors	-	1.19	0.76	3.38	5.40	6.59

Based on the data presented in Tables 1 and 2, traffic was forecasted over the concession period of 25 years; it is to study the Volume by Capacity ratio (v/c). Also, the design traffic was estimated for designing pavement compositions for three different design periods. Specifically, the estimated design traffic for 10 years is 45MSA, while for 15 years, it is 80MSA, and for 20 years, it is 130MSA. Typically, bituminous pavements are designed for 20 years of design life. However, to optimize life cycle cost, design traffic was estimated for three different design periods; accordingly, three different pavement compositions were considered in the study.

3.2 Design of Pavement Crust Composition

Following IRC 37-2018 guidelines [5], the conventional pavement compositions were designed for different design traffic and subgrade CBR value of 15%. The proposed pavement crust details are furnished in Table 3.

Table 3. Design of New Flexible Pavement

Design Parameters			
Design Traffic	45 MSA	80MSA	130MSA
Design Life	10-Year	15-Year	20-Year
Design CBR	15%	15%	15%
Layer Description	**Proposed Composition**	**Proposed Composition**	**Proposed Composition**
Bituminous Surface Course	50 mm	50 mm	50 mm
Bituminous Base Course	80 mm	95 mm	120 mm
Granular Base Course	250 mm	250 mm	250 mm
Granular Subbase (GSB)	200 mm	200 mm	200 mm
Subgrade with CBR 15%	500 mm	500 mm	500 mm

Maintenance Standards

The Maintenance Standards ensure the road network is always at its desired level. These standards comprise various work items, each defined in terms of the road surface class, intervention level, operation type (Functional Overlay, Routine Maintenance, etc.,) and resultant effect on the pavement. Each treatment standard has a trigger called the treatment assigning criteria, which indicates when the treatment should be applied. Some treatments, like routine maintenance, are carried out annually, while others, such as functional overlay, are only applied when the road condition deteriorates to a certain level.

Maintenance Standards include Routine Maintenance, Performance-based Maintenance, and Improvements. Routine Maintenance involves addressing cracking and raveling; two distresses that can lead to other issues, as shown in Figure 1 [21]. Performance-Based Maintenance consists of assessing the road's roughness and considering a different functional overlay of 30mm BC, 40mm BC, or 50mm BC if the roughness reaches 3.30m/km. Finally, Improvement Standards entail considering lane addition when the Volume by Capacity ratio (V/C) reaches 0.8 within the analysis period.

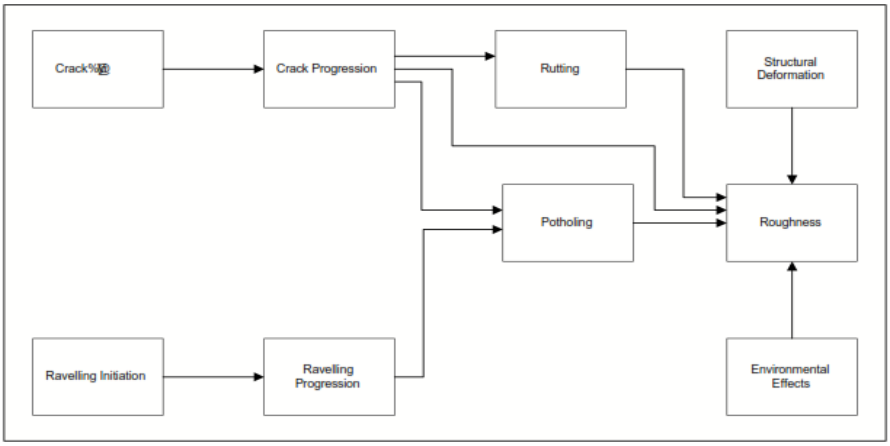

Fig. 1. Distress Progression Process

Six maintenance standards were assigned to each of the three pavement compositions under consideration to determine the optimal pavement composition. These include with routine maintenance, lane addition, and functional overlay thicknesses of 30mm, 40mm, and 50mm, as well as without routine maintenance, while the rest of the factors remains the same. In addition, a base alternative option under this a Routine Maintenance (Cracking, Reveling) without providing any overlay and suggested reconstruction when the IRI reaches 7.0m/km [15]. Depends on the trigger values these maintenance standards will be assigned automatically. Assigned maintenance standards are given in the Table 4. Type of maintenance, criteria / trigger values, and the costs required for routine maintenance, strengthening, and lane addition works are furnished in Table 5 and Table 6.

Table 4. List of Maintenance Assigned (Base Alternative)

Sl. No.	Base Practice	45MSA	80MSA	130MSA
Case-1: With Routine Maintenance				
1	Base Alternative	1.Functional Overlay (30mm BC) Routine Maintenance Improvement Standards 2.Functional Overlay (40mm BC) Routine Maintenance Improvement Standards 3.Functional Overlay (50mm BC) Routine Maintenance Improvement Standards	1.Functional Overlay (30mm BC) Routine Maintenance Improvement Standards 2.Functional Overlay (40mm BC) Routine Maintenance Improvement Standards 3.Functional Overlay (50mm BC) Routine Maintenance Improvement Standards	1.Functional Overlay (30mm BC) Routine Maintenance Improvement Standards 2.Functional Overlay (40mm BC) Routine Maintenance Improvement Standards 3.Functional Overlay (50mm BC) Routine Maintenance Improvement Standards
Case-2: Without Routine Maintenance				
2	Base Alternative	1.Functional Overlay (30mm BC) Improvement Standards 2.Functional Overlay (40mm BC) Improvement Standards 3.Functional Overlay (50mm BC) Improvement Standards	1.Functional Overlay (30mm BC) Improvement Standards 2.Functional Overlay (40mm BC) Improvement Standards 3.Functional Overlay (50mm BC) Improvement Standards	1.Functional Overlay (30mm BC) Improvement Standards 2.Functional Overlay (40mm BC) Improvement Standards 3.Functional Overlay (50mm BC) Improvement Standards

Table 5. Maintenance Standards and Costs (With Routine Maintenance)

Alternative	Type of Maintenance	Item Name	Criteria / Trigger value	Economic Cost (INR)	Financial Cost (INR)
1. Base Alternative	(i) Routine Maintenance	Ravelling	Ravelling >=10%	201.0/Sq m	241.0/Sq m
		Crack Sealing	All Structural Cracking >=10%	63.0/Sqm	76.0/Sqm
	(ii) Periodic Maintenance	Pavement Reconstruction	Roughness IRI >=7.0m/km	8,34,00,000/km	10,00,80,000/km
2. Functional Overlay (30mm BC)	(i) Performance Based Maintenance	Functional Overlay	Roughness IRI >=3.30m/km	360.0/ Sqm	432/ Sqm
	(ii) Routine Maintenance	Ravelling	Ravelling >=10%	72.0/ Sqm	87/ Sqm
		Crack Sealing	All Structural Cracking >=5%	63.0/ Sqm	76.0/ Sqm
	(iii) Improvement Standards	Lane Addition	Daily Avg. Volume Capacity >=0.8	C1: 2,11,43,731/km	C1: 2,53,72,477/km
				C2: 2,34,87,984/km	C2: 2,81,85,581/km
				C3: 2,23,15,857/km	C3: 2,67,79,028/km
3. Functional Overlay (40mm BC)	(i) Performance Based Maintenance	Functional Overlay	Roughness IRI >=3.30m/km	480.0/ Sqm	576/ Sqm
	(ii) Routine Maintenance	Ravelling	Ravelling >=10%	72.0/ Sqm	87/ Sqm
		Crack Sealing	All Structural Cracking >=5%	63.0/ Sqm	76.0/ Sqm
	(iii) Improvement Standards	Lane Addition	Daily Avg. Volume Capacity >=0.8	C1: 2,20,22,826/km	C1: 2,64,27,391/km
				C2: 2,20,22,826/km	C2: 2,64,27,391/km
				C3: 2,36,02,031/km	C3: 2,83,22,437/km
4. Functional Overlay (50mm BC)	(i) Performance Based Maintenance	Functional Overlay	Roughness IRI >=3.30m/km	360.0/ Sqm	432/ Sqm
	(ii) Routine Maintenance	Ravelling	Ravelling >=10%	72.0/ Sqm	87/ Sqm
		Crack Sealing	All Structural Cracking >=5%	63.0/ Sqm	76.0/ Sqm

Alternative	Type of Maintenance	Item Name	Criteria / Trigger value	Economic Cost (INR)	Financial Cost (INR)
4. Functional Overlay (50mm BC)	(iii) Improvement Standards	Lane Addition	Daily Avg. Volume Capacity >=0.8	C1: 2,36,02,031/km	C1: 2,83,22,437/km
				C2: 2,59,46,285/km	C2: 3,11,35,542/km
				C3: 2,47,74,158/km	C3: 2,97,28,990/km

Table 6. Maintenance Standards (Without Routine Maintenance)

Alternative	Type of Maintenance	Item Name	Criteria	Economic Cost (INR)	Financial Cost (INR)
1. Base Alternative	(i) Routine Maintenance	Ravelling	Ravelling >=10%	201.0/Sqm	241.0/Sqm
		Crack Sealing	All Structural Cracking >=10%	63.0/Sqm	76.0/Sqm
	(ii) Periodical Maintenance	Pavement Reconstruction	Roughness IRI >=7.0m/km	8,34,00,000/km	10,00,80,000/km
2. Functional Overlay (30mm BC)	(i) Periodical Maintenance	Functional Overlay	Roughness IRI >=3.30m/km	360.0/ Sqm	432/ Sqm
	(ii) Improvement Standards	Lane Addition	Daily Avg. Volume Capacity >=0.8	C1: 2,11,43,731/km	C1: 2,53,72,477/km
				C2: 2,34,87,984/km	C2: 2,81,85,581/km
				C3: 2,23,15,857/km	C3: 2,67,79,028/km
3. Functional Overlay (40mm BC)	(i) Periodical Maintenance	Functional Overlay	Roughness IRI >=3.30m/km	480.0/ Sqm	576/ Sqm
	(ii) Improvement Standards	Lane Addition	Daily Avg. Volume Capacity >=0.8	C1: 2,20,22,826/km	C1: 2,64,27,391/km
				C2: 2,20,22,826/km	C2: 2,64,27,391/km
				C3: 2,36,02,031/km	C3: 2,83,22,437/km
4. Functional Overlay (50mm BC)	(i) Periodical Maintenance	Functional Overlay	Roughness IRI >=3.30m/km	360.0/ Sqm	432/ Sqm
	(ii) Improvement Standards	Lane Addition	Daily Avg. Volume Capacity >=0.8	C1: 2,36,02,031/km	C1: 2,83,22,437/km
				C2: 2,59,46,285/km	C2: 3,11,35,542/km

Alternative	Type of Maintenance	Item Name	Criteria	Economic Cost (INR)	Financial Cost (INR)
				C3: 2,47,74,158 /km	C3: 2,97,28,990/km

Inputting Data into the HDM-4 Framework

Inputted various data included the initial pavement composition, the type of vehicles expected on the project road and their characteristics, environmental conditions, maintenance standards, and calibration factors [22] in to the HDM-4 framework.

Predicting Pavement Roughness using HDM-4 for Various Pavement Compositions

Using the roughness deterioration model in the HDM-4 framework, the roughness was estimated for three different pavement compositions every year, starting from the base year of 2024, by considering with and without routine maintenance. For the base alternative, the roughness was allowed to progress until it reached 7.0m/km, at which point full reconstruction was suggested. However, for the other cases, a functional overlay of 30mm, 40mm, and 50mm was presented independently when the roughness reached the trigger value of 3.30m/km. Through this exercise, the pavement condition improves, resulting in a decrease in the roughness value. Again, the roughness value will increase with the passage of traffic and environmental conditions, but the overlay lays will continue when the roughness declines to 3.30m/km. This exercise continued until the end of the concession period, and as a result, the pavement roughness level remained within the acceptable limit.

Progression of Roughness for Base Alternative

Table 7 provide the roughness progression for the base alternative (routine maintenance and reconstruction at 7 IRI) for different pavement compositions. Table 7 also gives the V/C ratio over a concession period of 25 years.

Table 7. Roughness Progression for the Base Alternative (reconstruction at 7 IRI)

Year	Progress of Roughness in terms of IRI for the Pavement Composition designed for			V/C Ratio for the lane addition
	45 MSA	80MSA	130MSA	
2024	2.83	2.83	2.82	0.36
2025	3.03	3.02	3.01	0.38
2026	3.34	3.33	3.31	0.40
2027	3.57	3.56	3.53	0.42
2028	3.84	3.81	3.77	0.44
2029	4.13	4.09	4.04	0.47
2030	4.46	4.41	4.34	0.49

Year	Progress of Roughness in terms of IRI for the Pavement Composition designed for			V/C Ratio for the lane addition
	45 MSA	80MSA	130MSA	
2031	4.80	4.78	4.68	0.52
2032	5.17	5.15	5.02	0.55
2033	5.59	5.57	5.40	0.58
2034	6.05	6.03	5.81	0.61
2035	6.57	6.56	6.28	0.64
2036	7.17	7.17	6.80	0.68
2037	2.30	2.30	7.50	0.71
2038	2.49	2.49	2.31	0.75
2039	2.70	2.70	2.50	0.79
2040 (Lane Addition + Overlay)	2.95	2.95	2.72	0.84
2041	3.21	3.21	2.97	0.51
2042	3.50	3.50	3.24	0.54
2043	3.84	3.84	3.54	0.57
2044	4.23	4.23	3.88	0.60
2045	4.68	4.68	4.28	0.63
2046	5.22	5.22	4.73	0.66
2047	5.87	5.87	5.28	0.70
2048	6.66	6.66	5.94	0.74

It can be observed from the table that with routine maintenance, the road roughness reached 7.0m/km by the year 2036, which is 12 years after the initial construction. At this point, it is necessary to undergo reconstruction to ensure the road remains safe and functional. Also, in 2040, the Volume by Capacity (V/C) ratio is projected to reach 0.8, which means that an additional lane requirement is necessary. Therefore, a lane addition was proposed in that year, followed by a 40mm BC overlay for the entire width and length of the existing pavement to ensure that the same cross slope is maintained. This lane addition in the year 2040 is applicable for all cases.

Progression of Roughness for Different Overlay Thickness Combined with or without Routine Maintenance

Tables 9 to Table 10 show the progress of roughness for overlay thicknesses of 30mm, 40mm, and 50mm, with and without routine maintenance when it reaches 3.30m/km (IRI). The data in these tables can help to understand how different overlay thicknesses and maintenance strategies can impact road roughness over time.

Table 8. Roughness Progression with 30mm BC Overlay Proposal at 3.30 IRI

Year	Progress of Roughness in terms of IRI for the Pavement Composition designed for (With routine maintenance)			Progress of Roughness in terms of IRI for the Pavement Composition designed for (Without routine maintenance)		
	45 MSA	80MSA	130MSA	45 MSA	80MSA	130MSA
2024	2.83	2.83	2.82	2.83	2.83	2.82
2025	3.03	3.02	3.01	3.03	3.02	3.01
2026	3.24	3.22	3.21	3.24	3.22	3.21
2027	3.46	3.44	3.42	3.46	3.44	3.42
2028	2.55	2.54	2.54	2.55	2.54	2.54
2029	2.72	2.72	2.71	2.73	2.72	2.71
2030	2.91	2.90	2.89	2.92	2.91	2.89
2031	3.12	3.10	3.09	3.13	3.11	3.09
2032	3.34	3.32	3.30	3.35	3.33	3.31
2033	2.53	2.53	3.53	2.54	2.53	2.52
2034	2.71	2.70	2.55	2.71	2.70	2.69
2035	2.90	2.89	2.72	2.90	2.89	2.88
2036	3.11	3.09	2.90	3.11	3.09	3.07
2037	3.33	3.31	3.10	3.34	3.31	3.28
2038	2.53	2.53	3.31	2.53	2.53	3.51
2039	2.71	2.70	2.53	2.71	2.70	2.55
2040 (Lane Addition + Overlay)	2.90	2.89	2.70	2.90	2.89	2.72
2041	2.15	2.15	2.15	2.15	2.15	2.15
2042	2.31	2.31	2.30	2.31	2.31	2.30
2043	2.48	2.48	2.48	2.48	2.48	2.48
2044	2.68	2.68	2.67	2.68	2.68	2.67
2045	2.90	2.90	2.89	2.90	2.90	2.89
2046	3.15	3.15	3.14	3.15	3.15	3.14
2047	3.40	3.39	3.39	3.44	3.44	3.43
2048	2.53	2.53	2.52	2.54	2.54	2.54

Table 9. Roughness Progression with 40mm BC Overlay Proposal at 3.30 IRI

Year	Progress of Roughness in terms of IRI for the Pavement Composition designed for (With routine maintenance)			Progress of Roughness in terms of IRI for the Pavement Composition designed for (Without routine maintenance)		
	45 MSA	80MSA	130MSA	45 MSA	80MSA	130MSA
2024	2.83	2.83	2.82	2.83	2.83	2.82
2025	3.03	3.02	3.01	3.03	3.02	3.01
2026	3.24	3.22	3.21	3.24	3.22	3.21
2027	3.46	3.44	3.42	3.46	3.44	3.42
2028	2.37	2.37	2.36	2.37	2.37	2.36
2029	2.54	2.53	2.52	2.54	2.53	2.52
2030	2.72	2.71	2.69	2.72	2.71	2.69
2031	2.91	2.89	2.88	2.91	2.90	2.88
2032	3.12	3.10	3.07	3.12	3.10	3.07
2033	3.34	3.32	3.28	3.35	3.32	3.29
2034	2.36	2.35	3.52	2.36	2.36	3.52
2035	2.52	2.52	2.37	2.53	2.52	2.37
2036	2.70	2.69	2.53	2.70	2.69	2.54
2037	2.89	2.87	2.71	2.89	2.88	2.71
2038	3.09	3.07	2.89	3.10	3.08	2.89
2039	3.32	3.29	3.09	3.33	3.31	3.09
2040 (Lane Addition + Overlay)	2.36	3.54	3.30	2.36	2.35	3.31
2041	2.12	2.12	2.16	2.12	2.12	2.16
2042	2.26	2.26	2.33	2.26	2.25	2.33
2043	2.40	2.41	2.52	2.40	2.40	2.52
2044	2.56	2.57	2.73	2.56	2.56	2.73
2045	2.74	2.74	2.97	2.74	2.74	2.97
2046	2.94	2.95	3.24	2.94	2.94	3.24
2047	3.13	3.14	3.51	3.17	3.17	3.55
2048	3.34	3.34	2.37	3.45	3.44	2.38

Table 10. Roughness Progression with 50mm BC Overlay Proposal at 3.30 IRI

Year	Progress of Roughness in terms of IRI for the Pavement Composition designed for (With routine maintenance)			Progress of Roughness in terms of IRI for the Pavement Composition designed for (Without routine maintenance)		
	45 MSA	80MSA	130MSA	45 MSA	80MSA	130MSA
2024	2.83	2.83	2.82	2.83	2.83	2.82
2025	3.03	3.02	3.01	3.03	3.02	3.01
2026	3.24	3.22	3.21	3.24	3.22	3.21
2027	3.46	3.44	3.42	3.46	3.44	3.42
2028	2.20	2.20	2.19	2.20	2.20	2.19
2029	2.35	2.35	2.34	2.35	2.35	2.34
2030	2.52	2.51	2.50	2.52	2.51	2.50
2031	2.69	2.68	2.67	2.70	2.68	2.67
2032	2.89	2.87	2.85	2.89	2.87	2.85
2033	3.10	3.08	3.04	3.10	3.08	3.05
2034	3.33	3.31	3.26	3.34	3.31	3.27
2035	2.18	2.18	3.50	2.19	2.18	3.51
2036	2.34	2.33	2.20	2.34	2.33	2.20
2037	2.50	2.49	2.35	2.50	2.49	2.35
2038	2.67	2.66	2.51	2.67	2.66	2.51
2039	2.86	2.84	2.67	2.87	2.85	2.68
2040 (Lane Addition + Overlay)	3.07	3.05	2.86	3.08	3.05	2.86
2041	2.14	2.14	2.14	2.14	2.14	2.14
2042	2.29	2.29	2.29	2.29	2.29	2.29
2043	2.45	2.45	2.45	2.45	2.45	2.45
2044	2.64	2.63	2.63	2.64	2.63	2.63
2045	2.84	2.84	2.83	2.84	2.84	2.83
2046	3.07	3.07	3.06	3.07	3.07	3.06
2047	3.31	3.29	3.29	3.35	3.34	3.34
2048	2.83	2.83	2.82	2.17	2.17	2.17

The table shows that the roughness of pavement compositions remained relatively stable during the first four years, likely due to passage of lower traffic volume. However, once overlay was initiated, a change in roughness was observed. As expected, those pavements with 50mm of functional overlay experienced delayed roughness compared to those with 30mm and 40mm. Slight variation in roughness progression observed due to routine maintenance.

Figures 2 to 7 illustrate the comparison between the with and without Routine Maintenance options, as well as the base alternative, for the cases listed below.

- Pavement composition for the Design Traffic of 45MSA followed by 30mm BC, 40mm BC and 50mm BC when IRI>=3.30m/km
- Pavement composition for the Design Traffic of 80MSA followed by 30mm BC, 40mm BC and 50mm BC when IRI>=3.30m/km
- Pavement composition for the Design Traffic of 135MSA followed by 30mm BC, 40mm BC and 50mm BC when IRI>=3.30m/km

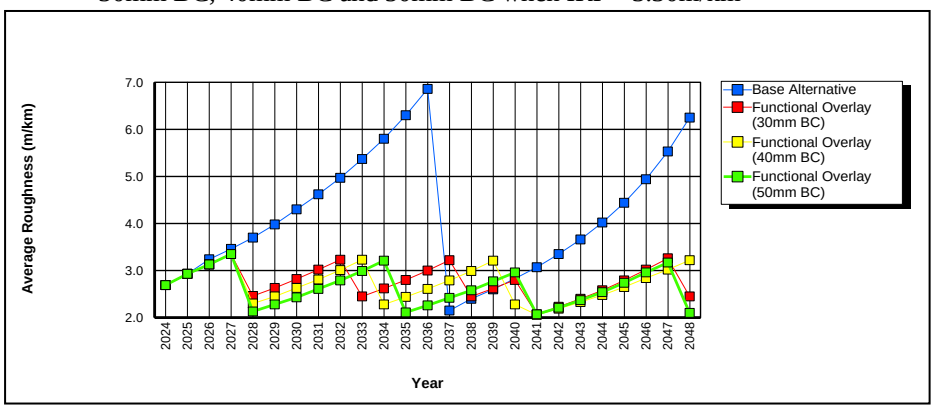

Fig 2. Roughness Progression Graph for 45 MSA Pavement Composition with routine maintenance

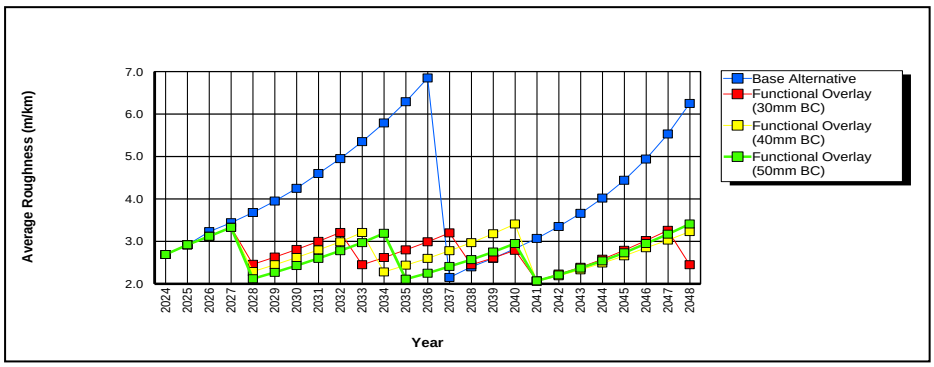

Fig 3. Roughness Progression Graph for 80 MSA Pavement Composition with routine maintenance

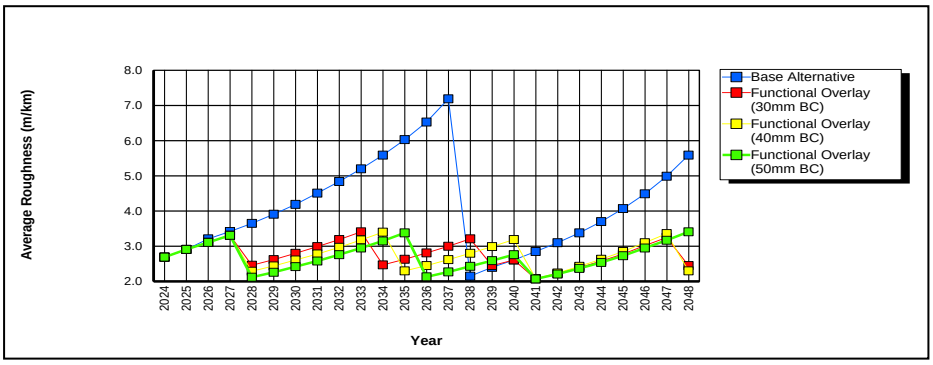

Fig 4. Roughness Progression Graph for 135 MSA Pavement Composition with routine maintenance

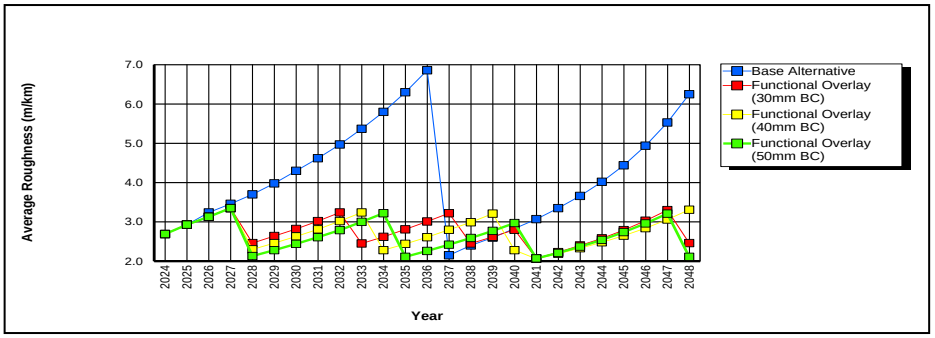

Fig 5. Roughness Progression Graph for 45 MSA Pavement Composition without routine maintenance

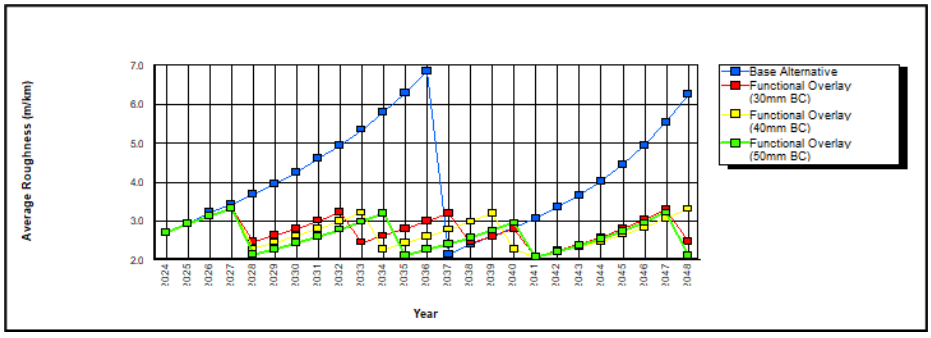

Fig 6. Roughness Progression Graph for 80 MSA Pavement Composition without routine maintenance

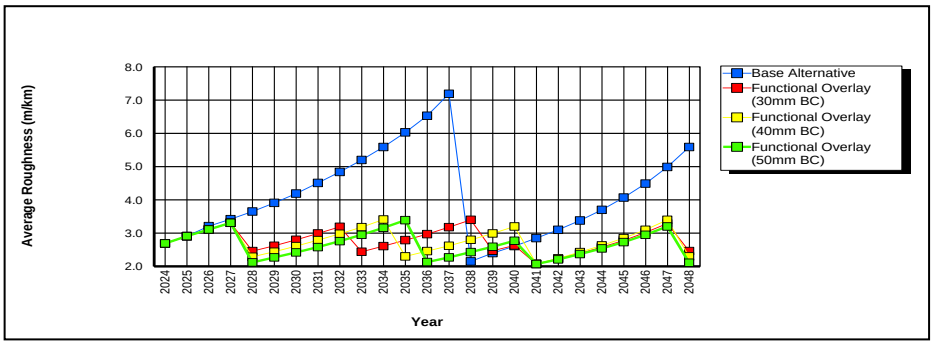

Fig 7. Roughness Progression Graph for 135MSA Pavement Composition without routine maintenance

Figures 2 to 7 show that the roughness progress is highly influenced by the provision of overlay and its thickness. The absence of overlay in the base alternative leads to a steady roughness progression. However, in the overlay section, the thickness of the overlay plays a crucial role in determining the roughness progression. More thickness leads to less progression and vice versa.

Life Cycle Cost Analysis

To keep the project section under the serviceable limit of IRI 3.30m/km, it is necessary for the agency to invest funds in routine maintenance, periodical/performance-based maintenance, and capital works throughout the pavement concession period. In order to ensure that costs are being spent effectively, it is important to conduct a cost-benefit analysis and compare various alternative options. The HDM-4 module estimated the increased road agency costs due to routine maintenance and strengthening, as well as the decreased road user costs due to good pavement condition, to compute the net benefit costs. These net benefits are then reduced to net present value (NPV), based on user-defined discount factors. A positive NPV/CAP ratio indicates a viable pavement alternative that is better than the base alternative. The alternative with the highest NPV/CAP ratio is the best alternative on economic considerations, which minimizes total transport costs. On the other hand, a negative NPV/CAP ratio means that the project is not viable and should not be chosen for construction or maintenance. Therefore, the optimum section alternative is selected based on the NPV/CAP ratio, which should be more than 1, and the Economic Internal Rate of Return (EIRR), which should be more than 12%. Economic indicators and lifecycle cost summary for various maintenance alternatives are presented through Table 11 to 14.

Table 11. Economic Indicators Summary (With Routine Maintenance)

Sl. No.	Section	Alternative	Present Value of Total Agency Costs (RAC)	Present Value of Agency Capital Costs (CAP)	Increase in Agency Costs (C)	Decrease in User Costs (B)	Net Exogenous Benefits (E)	Net Present Value (NPV = B+E-C)	NPV/Cost Ratio (NPV/RAC) (F)	NPV/Cost Ratio (NPV/CAP) (G)	Economic Internal Rate of Return (EIRR)	Ranking (in consideration of (F))	Ranking (in consideration of EIRR)
1	Pavement Construction for 45MSA followed by 30, 40 and 50mm BC Overlay	Base Alternative	394.2	382.8	0	0	0	0	0	0	0	-	-
		Overlay (30mm BC)	343.7	282.4	-50.47	391.63	0	442.1	1.286	1.565	37.4	***1**	***1**
		Overlay (40mm BC)	404.0	342.6	9.81	401.46	0	391.6	0.969	1.143	33.1	-	-
		Overlay (50mm BC)	414.9	353.7	20.79	415.15	0	394.4	0.950	1.115	30.5	-	-
2	Pavement Construction for 80MSA followed by 30, 40 and 50mm BC Overlay	Base Alternative	393.6	382.8	0	0	0	0	0	0	0	-	-
		Overlay (30mm BC)	346.2	284.9	-47.40	389.31	0	436.7	1.261	1.533	37.1	**2**	**2**
		Overlay (40mm BC)	362.2	300.8	-31.46	390.93	0	422.4	1.166	1.404	33.4	**4**	**4**
		Overlay (50mm BC)	415.1	353.7	21.40	408.51	0	387.1	0.933	1.095	30.3	-	-

Sl. No.	Section	Alternative	Present Value of Total Agency Costs (RAC)	Present Value of Agency Capital Costs (CAP)	Increase in Agency Costs (C)	Decrease in User Costs (B)	Net Exogenous Benefits (E)	Net Present Value (NPV = B+E-C)	NPV/Cost Ratio (NPV/RAC) (F)	NPV/Cost Ratio (NPV/CAP) (G)	Economic Internal Rate of Return (EIRR)	Ranking (in consideration of (F))	Ranking (in consideration of EIRR)
3	Pavement Construction for 135MSA followed by 30, 40 and 50mm BC Overlay	Base Alternative	355.3	341.7	0	0	0	0	0	0	0	-	-
		Overlay (30mm BC)	340.3	278.9	-15.03	397.03	0	412.1	1.211	1.477	35.5	**3**	**3**
		Overlay (40mm BC)	360.7	299.4	5.38	402.57	0	397.2	1.101	1.327	31.9	**5**	**5**
		Overlay (50mm BC)	410.7	349.3	55.38	418.68	0	363.3	0.885	1.040	28.8	-	-

Table 12. Life Cycle Cost Summary (With Routine Maintenance)

Sl. No.	Pavement Option Details	Cost Ratio/ Returns		Ranking		IRI at the end of Year	Budget Estimate (Financial Cost)			Priority Order
		NPV/Cost Ratio (NPV/RAC)	Economic Internal Rate of Return (EIRR)	Ranking (Based on NPV/RAC)	Ranking (Based on EIRR)		Routine Maintenance Cost (Cr. Rs.)	Periodic Maintenance Cost (Cr. Rs.)	Total Maintenance Cost (Cr. Rs.)	
1	Pavement New Construction (45MSA) followed by Strengthening (30mm BC)	1.286	37.40	*1	*1	2.53	3.86	148.9	152.73	**Priority-1**
2	Pavement New Construction (80MSA) followed by Strengthening (30mm BC)	1.261	37.10	2	2	2.53	3.86	150.8	154.62	**Priority-2**
3	Pavement New Construction (130MSA) followed by Strengthening (30mm BC)	1.211	35.50	3	3	2.52	3.86	154.2	158.01	**Priority-3**
4	Pavement New Construction (130MSA) followed by Strengthening (40mm BC)	1.166	33.40	4	4	3.34	4.00	152.3	156.31	**Terminated**
5	Pavement New Construction (80MSA) followed by Strengthening (40mm BC)	1.101	31.90	5	5	2.37	3.86	155.7	159.55	**Priority-4**
6	Pavement New Construction (45MSA) followed by Strengthening (40mm BC)	0.969	33.10	-	-	3.34	4.00	180.2	184.18	**Terminated**
7	Pavement New Construction (45MSA) followed by Strengthening (50mm BC)	0.950	30.50	-	-	2.16	3.86	173.0	176.88	**Terminated**

Sl. No.	Pavement Option Details	Cost Ratio/ Returns		Ranking		IRI at the end of Year	Budget Estimate (Financial Cost)			Priority Order
		NPV/Cost Ratio (NPV/RAC)	Economic Internal Rate of Return (EIRR)	Ranking (Based on NPV/RAC)	Ranking (Based on EIRR)		Routine Maintenance Cost (Cr. Rs.)	Periodic Maintenance Cost (Cr. Rs.)	Total Maintenance Cost (Cr. Rs.)	
8	Pavement New Construction (80MSA) followed by Strengthening (50mm BC)	0.933	30.30	-	-	3.55	4.00	174.9	178.91	**Terminated**
9	Pavement New Construction (130MSA) followed by Strengthening (50mm BC)	0.885	28.80	-	-	3.54	4.00	178.3	182.30	**Terminated**

Table 13. Economic Indicators Summary (Without Routine Maintenance)

Sl. No.	Section	Alternative	Present Value of Total Agency Costs (RAC)	Present Value of Agency Capital Costs (CAP)	Increase in Agency Costs (C)	Decrease in User Costs (B)	Net Exogenous Benefits (E)	Net Present Value (NPV = B+E-C)	NPV/Cost Ratio (NPV/RAC) (F)	NPV/Cost Ratio (NPV/CAP) (G)	Economic Internal Rate of Return (EIRR)	Ranking (in consideration of (F))	Ranking (in consideration of EIRR)
1	Pavement Construction for 45MSA followed by 30, 40 and 50mm BC Overlay	Base Alternative	394.2	382.8	0	0	0	0	0	0	0	-	-
		Overlay (30mm BC)	316.0	282.4	-78.16	391.01	0	469.2	1.484	1.661	47.1	***1**	***1**
		Overlay (40mm BC)	376.2	342.6	-17.97	400.47	0	418.4	1.112	1.221	39.5	**6**	**4**
		Overlay (50mm BC)	387.3	353.7	-6.89	414.57	0	421.5	1.088	1.192	35.0	**7**	**7**
2	Pavement Construction for 80MSA followed by 30, 40 and 50mm BC Overlay	Base Alternative	393.7	382.8	0	0	0	0	0	0	0	-	-
		Overlay (30mm BC)	318.6	284.9	-75.09	388.84	0	463.9	1.456	1.628	46.7	**2**	**2**
		Overlay (40mm BC)	372.0	338.4	-21.61	398.45	0	420.1	1.129	1.241	39.2	**5**	**5**
		Overlay (50mm BC)	389.8	356.2	-3.83	412.44	0	416.3	1.068	1.169	34.8	**8**	**8**
3	Pavement Construction for 135MSA	Base Alternative	355.3	341.7	0	0	0	0	0	0	0	-	-
		Overlay (30mm BC)	319.3	285.6	-36.03	399.30	0	435.3	1.363	1.524	43.3	**3**	**3**
		Overlay (40mm BC)	332.9	299.4	-22.31	402.09	0	424.4	1.275	1.418	37.6	**4**	**6**

Sl. No.	Section	Alternative	Present Value of Total Agency Costs (RAC)	Present Value of Agency Capital Costs (CAP)	Increase in Agency Costs (C)	Decrease in User Costs (B)	Net Exogenous Benefits (E)	Net Present Value (NPV = B+E-C)	NPV/Cost Ratio (NPV/RAC) (F)	NPV/Cost Ratio (NPV/CAP) (G)	Economic Internal Rate of Return (EIRR)	Ranking (in consideration of (F))	Ranking (in consideration of EIRR)
	followed by 30, 40 and 50mm BC Overlay	Overlay (50mm BC)	385.4	351.9	30.14	422.53	0	392.4	1.018	1.115	33.0	**9**	**9**

Table 14. Life Cycle Cost Summary (Without Routine Maintenance)

Sl. No.	Pavement Option Details	Cost Ratio/ Returns		Ranking			Budget Estimate (Financial Cost)			Priority Order
		NPV/Cost Ratio (NPV/RAC)	Economic Internal Rate of Return (EIRR)	Ranking (Based on NPV/RAC)	Ranking (Based on EIRR)	IRI at the end of Year	Routine Maintenance Cost (Cr. Rs.)	Periodic Maintenance Cost (Cr. Rs.)	Total Maintenance Cost (Cr. Rs.)	
1	Pavement New Construction (45MSA) followed by Strengthening (30mm BC)	1.484	47.1	*1	*1	2.54	-	148.9	148.9	**Priority-1**
2	Pavement New Construction (80MSA) followed by Strengthening (30mm BC)	1.456	46.7	2	2	2.54	-	150.8	150.8	**Priority-2**
3	Pavement New Construction (130MSA) followed by Strengthening (30mm BC)	1.363	43.3	3	3	2.54	-	154.2	154.2	**Priority-3**
4	Pavement New Construction (130MSA) followed by Strengthening (40mm BC)	1.275	37.6	4	6	2.38	-	155.7	155.7	**Priority-4**
5	Pavement New Construction (80MSA) followed by Strengthening (40mm BC)	1.129	39.2	5	5	3.44	-	177.0	177.0	**Terminated**
6	Pavement New Construction (45MSA) followed by Strengthening (40mm BC)	1.112	39.5	6	4	3.45	-	180.2	180.2	**Terminated**
7	Pavement New Construction (45MSA) followed by Strengthening (50mm BC)	1.088	35	7	7	2.17	-	173.0	173.0	**Priority-5**
8	Pavement New Construction (80MSA) followed by Strengthening (50mm BC)	1.068	34.8	8	8	2.17	-	174.9	174.9	**Priority-6**
9	Pavement New Construction (130MSA) followed by Strengthening (50mm BC)	1.018	33	9	9	2.17	-	178.3	178.3	**Priority-7**

In Tables 11 to 14, a few project alternatives were terminated due to non-viability. Specifically, the NPV/CAP ratio has fallen below 1, indicating that these alternatives are unsustainable. Additionally, the International Roughness Index (m/km) value has exceeded the serviceability limit of 3.30m/km, resulting in poor conditions for the project section at the end of the analysis year. The benefit ratios and Economic Internal Rate of Returns have also been presented in the tables to provide further insight into the ranking of each section alternative.

Identification of Best Pavement Alternative

The non-viable alternatives terminated in Tables 11 to 14, and the prioritized alternatives have been presented in Tables 15 and Table 16.

Table 15. Prioritization of Alternatives (with maintenance)

Sl. No.	Pavement Option Details	Cost Ratio/ Returns		Priority
		NPV/RAC	EIRR	
1	Pavement composition for 45MSA traffic and overlay of 30mm BC @ 3.3IRI	1.286	37.400	**Priority-1**
2	Pavement composition for 80MSA traffic and overlay of 30mm BC @ 3.3IRI	1.261	37.100	**Priority-2**
3	Pavement composition for 135MSA traffic and overlay of 30mm BC @ 3.3IRI	1.211	35.500	**Priority-3**
5	Pavement composition for 135MSA traffic and overlay of 40mm BC @ 3.3IRI	1.101	31.900	**Priority-4**

Table 16. Prioritization of Alternatives (without maintenance)

Sl. No.	Pavement Option Details	Cost Ratio/ Returns		Priority
		NPV/RAC	EIRR	
1	Pavement composition for 45MSA traffic and overlay of 30mm BC @ 3.3IRI	1.484	47.100	**Priority-1**
2	Pavement composition for 80MSA traffic and overlay of 30mm BC @ 3.3IRI	1.456	46.700	**Priority-2**
3	Pavement composition for 135MSA traffic and overlay of 30mm BC @ 3.3IRI	1.363	43.300	**Priority-3**
4	Pavement composition for 135MSA traffic and overlay of 40mm BC @ 3.3IRI	1.275	37.600	**Priority-4**
7	Pavement composition for 45MSA traffic and overlay of 50mm BC @ 3.3IRI	1.088	35.000	**Priority-5**
8	Pavement composition for 80MSA traffic and overlay of 50mm BC @ 3.3IRI	1.068	34.800	**Priority-6**
9	Pavement composition for 135MSA traffic and overlay of 50mm BC @ 3.3IRI	1.018	33.000	**Priority-7**

As per the Tables 15 and 16, pavement composition designed for 45 MSA traffic followed by a 30mm functional overlay at 3.30m/km (IRI) is the first best/ optimum alternative. However, the authors suggest that the second-best option should be implemented due to the potential for changes in traffic patterns and loading characteristics. This alternative consists of a pavement composition designed for 80MSA traffic and followed by a 30mm functional overlay at 3.30m/km (IRI).

4 Conclusions

The major objective of this work is to investigate the importance of integrating performance-based maintenance into the pavement design process. Additionally, identifying the most cost-effective pavement compositions among the different alternatives that are tailored to different traffic levels during varied design periods.

Based on the Economic Indicators and Life Cycle Cost summary, it was observed that out of the three pavement compositions designed for traffic levels of 45 MSA, 80 MSA, and 130 MSA, the optimal choice is the pavement composition intended for 45 MSA traffic with a 30mm functional overlay at 3.30m/km (IRI). This alternative is ranked the highest for both with and without routine maintenance. Although there was a slight decrease in roughness values with routine maintenance, it was not considered significant since the criteria selected for the routine maintenance were cracking and raveling. Their impact on roughness appears minimal even if those distresses are not maintained. Finally, the authors suggest that the second-best option should be implemented that is a pavement composition designed for 80MSA traffic and followed by a 30mm functional overlay at 3.30m/km (IRI). It is due to the potential for changes in traffic patterns and loading characteristics.

If standard routine maintenance is assigned, the roughness levels gradually increase over time and reach the 7.0m/km (IRI) mark after 12 years of construction, that is, in 2036. At this point, it is required to reconstruct the pavement. According to the analysis, the V/C ratio is projected to reach 0.8 by 2040. Therefore, it has been recommended that an additional lane be added at this point. It is important to note that if the extra lane is to be constructed, an overlay must be laid on the existing pavement. It is crucial to carefully analyze this process, as the overlay on the existing pavement may be delayed if it is to be provided within a short timeframe.

References

1. Monismith CL (2004), Evolution of Long-Lasting Asphalt Pavement Design Methodology: A Perspective, International Symposium on Design and Construction of Long-Lasting Asphalt Pavements, Auburn University. https://asphalt.org/downloads/Monismith_lecture.pdf

2. Maram Saudy, Tamer Breakah, Mosbeh R. Kaloop, Sherif El-Badawy, Regional implementation of the mechanistic empirical pavement design and analysis approach: Egyptian case study, Case Studies in Construction Materials, Volume 18, 2023, e01863, ISSN 2214-5095, https://doi.org/10.1016/j.cscm.2023.e01863.

3. Brown SF (1997), Achievements and Challenges in Asphalt Pavement Engineering, ISAP - 8th International Conference on Asphalt Pavements, University of Nottingham Nottingham. https://asphalt.org/downloads/Browns_lecture.pdf
4. American Association of State Highway and Transportation Officials (2008), AASHTO mechanistic-empirical pavement design guide: a manual of practice, interim edition. American Association of State Highway and Transportation Officials, Washington, DC
5. Indian Roads Congress (IRC) (2018), Guidelines for the design of flexible pavements IRC: 37-2018, 4th Revision, Indian Road Congress, New Delhi.
6. Colorado Department of Transportation (CDoT) (2021), M-E Pavement Design Manual, CDoT, Durango.
https://www.codot.gov/business/designsupport/materials-and-geotechnical/manuals/2021-m-e-pave-design-manual
7. Austroads (2017), Guide to Pavement Technology Part 2: Pavement Structural Design, AGPT02-17, Austroads Ltd., Sydney.
8. Chen, D., Hildreth, J., & Mastin, N. (2019). Determination of IRI Limits and Thresholds for Flexible Pavements. Journal of Transportation Engineering, Part B: Pavements, 145(2), 04019013. doi:10.1061/jpeodx.0000113
9. Sayers, M. W., T. D. Gillespie, and C. A. V. Queiroz. 1986. The International road roughness experiment: Establishing correlation and a calibration standard for measurements. Washington, DC: World Bank
10. Titi, H. H., and M. Rasoulian. 2008. “Evaluation of smoothness of Louisiana pavements based on international roughness index and ride number.” Jordan J. Civ. Eng. 2 (3): 238–249.
11. Georgiou, P., Plati, C., & Loizos, A. (2018). Soft Computing Models to Predict Pavement Roughness: A Comparative Study. Advances in Civil Engineering, , 1–8. doi:10.1155/2018/5939806.
12. Khattak, M. J., Nur, M. A., Bhuyan, M. R.-U.-K., & Gaspard, K. (2013). International roughness index models for HMA overlay treatment of flexible and composite pavements. International Journal of Pavement Engineering, 15(4), 334–344. doi:10.1080/10298436.2013.842237
13. Sandra, Amarendra & Sarkar, Ashoke. (2012). Development of a model for estimating International Roughness Index from pavement distresses. International Journal of Pavement Engineering - INT J PAVEMENT ENG. 14. 1-10. 10.1080/10298436.2012.703322.
14. Chandra, S., 2004. Effect of road roughness on capacity of two-lane roads. Journal of Transportation Engineering, ASCE, 130 (3), 360– 364.
15. Indian Roads Congress (IRC) (2019), Guidelines on Measuring Road Roughness and Norms, IRC: SP:16-2019, 2nd Revision, Indian Road Congress, New Delhi.
16. HDM-4. (2003) Highway Development and Management Model, Version 1.3. World RoadAssociation, ISOHDM, PIARC, Paris, France
17. Tsunokawa, K. and R. Ul-Islam (2003). Optimal Pavement Design and Maintenance Strategy for Developing Countries: An Analysis Using HDM-4. International Journal of Pavement Engineering, Vol. 4, pp.193-208
18. Dinh Van HIEP and Koji T. (2005), Optimal Maintenance Strategies for Bituminous Pavements: A case Study in Vietnam using HDM-4 with gradient methods, Journal of the Eastern Asia Society for Transportation Studies, Vol 6, pp. 1123-1136.
19. Bannour, A., El Omari, M., Khadir Lakhal, E., Afechkar, M., & Joubert, P. (2021). Highway pavement maintenance optimisation using HDM-4: a case study of Morocco’s arterial network. International Journal of Pavement Engineering, 1–14. doi:10.1080/10298436.2021.1892106
20. Jorge, D., and Ferreira, A., 2012. Road network pavement maintenance optimisation using the HDM-4 pavement performance prediction models. The International Journal of Pavement Engineering, 13 (1), 39– 51

21. Rohde, G. T.; Fritz, Z.; Elzbieta, S. and Theunis, H. (1998); "The Calibration and Use of HDM–4 Performance Models in Pavement Management system", Proceedings, 4th International Conference on Managing Pavements, Durban, South Africa. pp 1312–1332.
22. Jain, S. S., Aggarwal, S., & Parida, M. (2005). HDM-4 Pavement Deterioration Models for Indian National Highway Network. Journal of Transportation Engineering, 131(8), 623–631. doi:10.1061/(asce)0733-947x(2005)131:8(623)

Investigation of the Effect of Bio-char and Activated Carbon on the Physical Properties of Asphalt Binder

Mehmet Saltan[1][0000-0001-6221-4918] Öznur Karadag[2][0000-0003-0755-5626] and Gizem Kacaroglu[3][0000-0002-5734-7131]

[1] Süleyman Demirel University, Civil Engineering Department, Isparta, Türkiye, mehmetsaltan@sdu.edu.tr
[2] Süleyman Demirel University, Civil Engineering Department, Isparta, Türkiye, oznurkaradag92@gmail.com
[3] Süleyman Demirel University, Civil Engineering Department, Isparta, Türkiye, gizemkacaroglu@sdu.edu.tr

Abstract. The aim of this study is to investigate the suitability of bio-char and activated carbon as potential modifiers in order to improve the physical properties of asphalt binder. In this study, the performance of bio-char obtained from the pyrolysis of brewed waste tea in asphalt binder were examined for the first time. Bio-char which is used as a modifier, is the material obtained from the pyrolysis of brewed waste tea by using nitrogen gas for approximately 1 hour at 550 ˚C temperature. Activated carbon which has a size less than 75 microns and large surface area was also used as a modifier to compare the properties of asphalt binders modified with bio-char. Asphalt binder which has 50/70 penetration grade was modified with bio-char and activated carbon at the ratios of 0.5, 1, 2, 3 and 4% with the help of a high-speed mixer for 1 hour at 2000 rpm and 150˚C. In order to evaluate the performance of asphalt binder, penetration, softening point, penetration index (PI), rotational viscometer and storage stability tests were carried out all modified binders. According to the obtained results, the use of commercially activated carbon and bio-char obtained from pyrolysis of brewed waste tea as a modifier on asphalt binder showed that the stiffness of the modified asphalt binders increased and their storage at high temperature. In addition, the viscometer test results of asphalt binders modified with bio-char show that the bio-char material is agglomerated in the asphalt binder.

Keywords: Bio-char, Activated Carbon, Pyrolsis Process, Bitumen Modification.

1 Introduction

The increase in the world population causes an increase in waste materials which are generated in agriculture, construction and industrial sectors. Waste materials which fill landfills and cause a decrease in habitable areas cause environmental pollution. Waste

materials which are recycled by conventional incineration release toxic gases into the atmosphere. Thus, sustainable methods are researched in order to reuse and recycle waste materials. The use of waste materials in asphalt binder and asphalt mixtures is considered as one of the sustainable methods to evaluate waste materials. Waste materials which are sustainable, have low maintenance cost, are easy to produce, have a large surface area and can be used as a modifier in asphalt binder are used in the pavement. Different waste materials (polymers and plastics, tire rubber powder, building construction waste, waste glass, bricks, fly ash and ceramics) are used to improve the physical and mechanical properties of asphalt mixtures under traffic load and environmental conditions [1,2]. Bio-oil and bio-char materials obtained as a result of the pyrolysis process which allows the reuse of organic waste materials and reduces the negative effects of waste materials on the environment are used in asphalt binders and asphalt mixtures [3]. Due to the carbon origin of bio-char obtained from different biomass materials are investigated using as an asphalt modifier. The effects of bio-chars obtained from the pyrolysis process of walnut crust and apricot seed shell [4], Mesue ferrea seed cover waste [5], waste wood [6], cypress waste wood (sawdust) [7], straw stalk [8], switchgrass [9] and oat hulls [10] on asphalt binder were investigated. The decrease in penetration value, increase in softening point and viscosity values of asphalt binders modified with bio-char show that bio-char materials improve high temperature performance [7,8,10-13]. However, bio-char material didn't have a positive effect on the low temperature performance of modified asphalt binders [9, 14-15]. Commercially activated carbon is used to compare the performance of bio-char obtained from different raw materials in asphalt binder [11].

In this study, bio-char (BC) material was obtained from the pyrolysis of brewed waste tea which is an agricultural waste biomass material and has a great potential on our country for the first time. Commercially activated carbon (AC) was used to compare the effect of bio-char obtained from the pyrolysis of brewed waste tea which are collected from homes and restaurants on asphalt binder. Penetration, softening point, rotational viscometer and storage stability tests were performed on asphalt binders modified with bio-char and commercially activated carbon. In addition, penetration index values were calculated by using softening point and penetration values of modified asphalt binders.

2 Materials

2.1 Asphalt Binder

50/70 asphalt binder which is supplied from Isparta Municipality was used in this study. The properties of 50/70 asphalt binder are shown in Table 1.

2.2 Bio-char and Commercially Activated Carbon

In the present study, pyrolysis process was carried out in order to eliminate the organic property of the brewed waste tea which is collected from homes and restaurants. The brewed waste tea burned with nitrogen gas for approximately 1 hour at 550 ˚C

temperature, after it was placed in the reactor. Then, the bio-char which is obtained from the pyrolysis process was sieved through the No.200 sieve in order to ensure homogeneous dispersion in asphalt binder. It is thought that the use of activated carbon which is obtained by applying different processes to bio-char obtained from different materials on asphalt binder may be beneficial in terms of environment, economy and performance [12]. Therefore, activated carbon which has high surface energy, specifically large surface area and porous structure was used in the study. It was sieved through a No.200 sieve to ensure a homogeneous dispersion of commercially activated carbon in the asphalt binder.

Table 1. Properties of 50/70 asphalt binder.

Properties	50/70 Asphalt Binder		Standard
Specific gravity	1.017		TS EN 15326+A1
Penetration (25˚C)	54		TS EN 1426
Softening point, (˚C)	49.3		TS EN 1427
Ductility (5 cm/min)	>100		TS EN 13589
Rotational viscometer (cP)	135˚C 470	165˚C 129	ASTM D4402

3 Materials

3.1 Asphalt Binder Modification Procedure

The mixing parameters (mixing temperature, time and speed) [5-8, 16] used in the modification of asphalt binder with bio-char obtained from the pyrolysis of brewed waste tea were determined taking into account the previous studies. Asphalt binder which has 50/70 penetration grade was modified with BC and AC at the ratios of 0.5, 1, 2, 3 and 4% with the help of a high-speed mixer for 1 hour at 2000 rpm and 150 ˚C.

3.2 Conventional Tests

Conventional tests such as penetration (TS EN 1426), softening point (TS EN 1427) and rotational viscometer (ASTM D4402) were performed to determine the properties of asphalt binders which are modified with bio-char and activated carbon. In addition, the penetration index (PI) was calculated by using the penetration and softening point values of the modified asphalt binders. Seyrek et al. (2020) [12] stated that the storage stability test of asphalt binders modified with activated carbon should be determined.

Therefore, storage stability test (TS EN 13399) was performed to determine the compatibility of asphalt binder modified with BC and AC. The asphalt binders which were modified with 0.5, 1, 2, 3 and 4% bio-char and activated carbon were poured into an aluminum tube with 160 mm in height and 25-40 mm in diameter. After place the tubes vertically in an oven at 180˚C for 72 hours, they were cooled in the freezer at -20 ˚C for 30 minutes. The tubes which are removed from the freezer were divided into

three equal parts and the softening point test on the modified asphalt binders on top side and underside of tubes were performed.

4 Results

The penetration test results of asphalt binders modified with bio-char obtained from the pyrolysis of brewed waste tea and commercially activated carbon are given in Fig. 1. According to the obtained results, it is seen that the modified asphalt binders harden as the amount of bio-char and commercially activated carbon which were added to the asphalt binder increases.

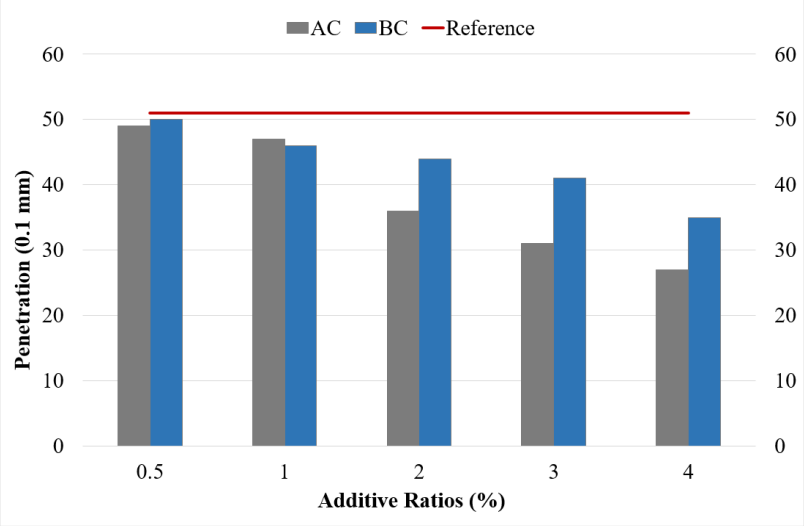

Fig. 1. Results of penetration test of modified asphalt binders.

It was observed that the softening point values of the modified asphalt binders increased as the amount of bio-char and commercially activated carbon which were added to the asphalt binder increased according to the reference asphalt binder (Fig. 2).

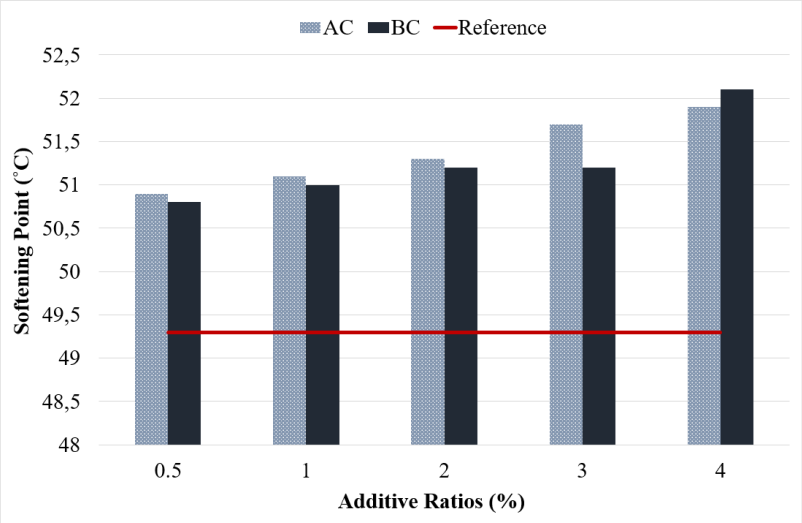

Fig. 2. Results of softening point of modified asphalt binders.

The penetration index (PI) was calculated in order to examine the effect of bio-char obtained from the pyrolysis of brewed waste tea and commercially activated carbon on the temperature sensitivity of the asphalt binder. When Fig. 3 is examined, while the PI values of asphalt binders modified with 0.5 and 1% AC increased, the penetration index values of asphalt binders modified with 2, 3 and 4% AC decreased according to reference asphalt binder. While the temperature sensitivity of asphalt binders modified with 0.5 and 1% AC decreased according to reference asphalt binder, the temperature sensitivity of asphalt binders modified with 2, 3 and 4% AC increased.

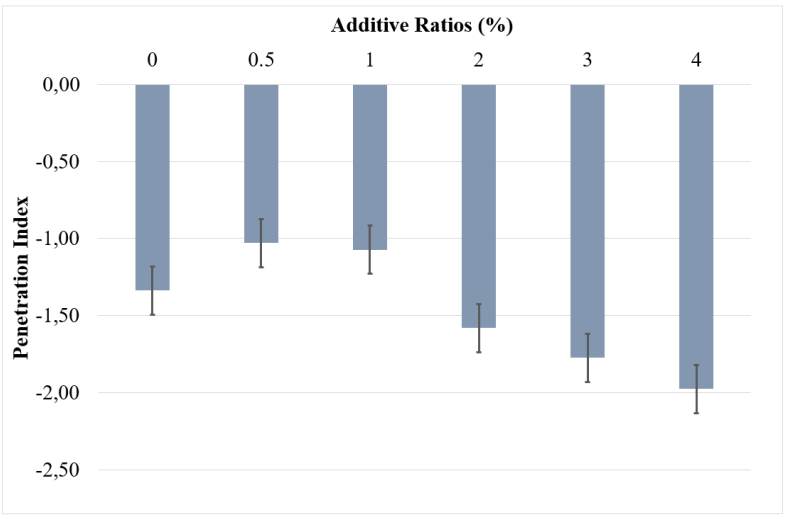

Fig. 3. Penetration index values of asphalt binders modified with activated carbon.

The PI values of the asphalt binders modified with 0.5, 1 and 2% BC increased, the PI value of the asphalt binder modified with 3% BC was the same and the PI value of the asphalt binder modified with 4% BC decreased according to reference asphalt binder (Fig. 4). Temperature sensitivity of only 4% BC modified asphalt binder among the asphalt binders modified with BC at different ratios increased.

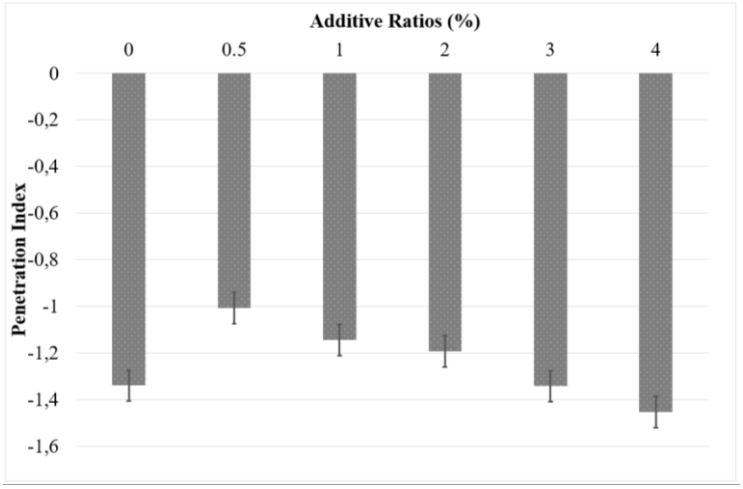

Fig. 4. Penetration index values of asphalt binders modified with bio-char.

The results of the storage stability tests carried out to determine the storage properties of asphalt binders modified with commercially activated carbon and bio-char at high temperatures are shown in Table 2. Since the difference between the softening point values of top side and underside of samples is less than 5 ˚C, the obtained results show that asphalt binders modified with these materials (AC and BC) are storable at high temperature.

Table 2. Softening point test results of reference and asphalt binders modified with AC.

Name of Samples	Softening Point (˚C)		Difference
	Top Side (T)	Underside (U)	
Reference	49.3	49	0.3
0.5% AC	50.6	50.7	0.1
1% AC	51.1	50.4	0.7
2% AC	50.5	50.7	0.2
3% AC	50.8	51.2	0.4
4% AC	51.6	50.7	0.9
0.5% BC	51.2	51.3	0.1
1% BC	52.2	52	0.2
2% BC	52.3	53.2	0.9
3% BC	51.2	50.6	0.6
4% BC	51.5	51.7	0.2

The viscometer test results of asphalt binders modified with AC are shown in Fig. 5. According to the obtained results, as the amount of activated carbon added to the asphalt binder increased, the mixing and compaction temperatures of the modified asphalt binders increased.

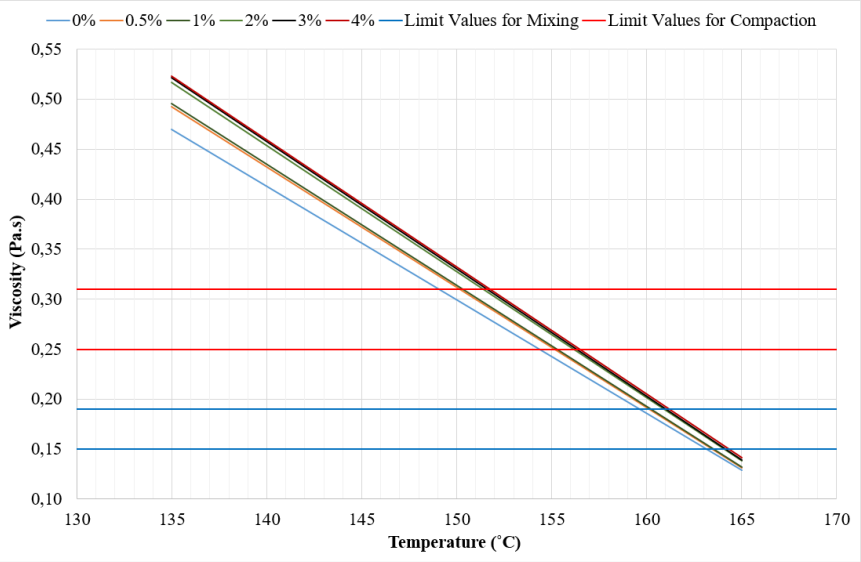

Fig. 5. Viscometer test results of asphalt binder modified with AC.

The viscometer test results of asphalt binders modified with BC are shown in Fig. 6. According to the obtained results, it is thought that the bio-char material is not homogeneously dispersed and is agglomerated in asphalt binders modified with 2, 3 and 4 % BC. Agglomeration occurred due to chemical interaction between small sized materials such as bio-char and asphalt binder is considered as a possible situation [17]. It was observed that the mixing and compaction temperatures of asphalt binders modified with 0.5 and 1% BC were increased in comparison with reference asphalt binder.

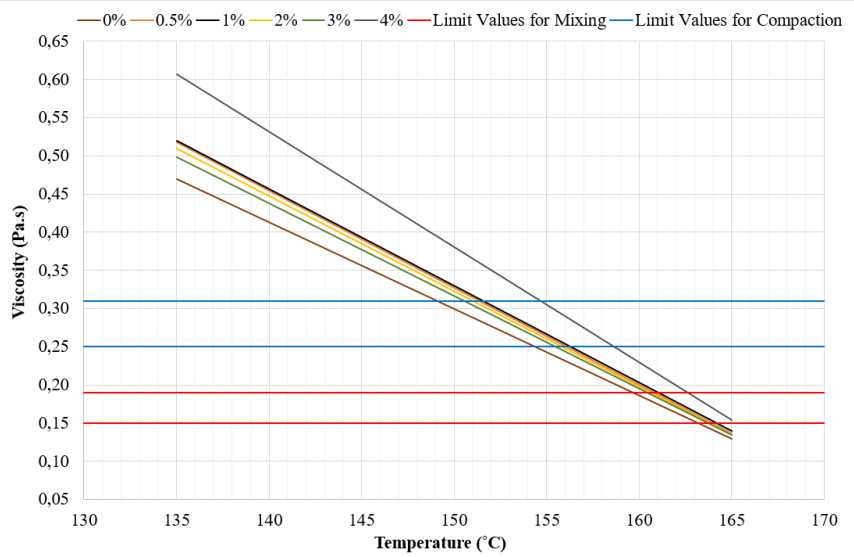

Fig. 6. Viscometer test results of asphalt binder modified with BC.

The mixing and compaction temperatures of asphalt binders modified with AC and BC are given Table 4.

Table 4. The mixing and compaction temperatures of modified asphalt binder.

Name of Samples	Viscometer (cP)		Mixing Temperatures Range (˚C)	Compaction Temperatures Range (˚C)
	135 ˚C	165 ˚C		
0%	470	129	159.6 – 161.4	149.1 – 151.7
0.5% AC	492.5	131.5	160.1 – 161.8	150.2 – 152.7
1% AC	495.8	132.5	160.3 – 161.9	150.3 – 152.8
2% AC	516.9	138.1	160.9 – 162.5	151.4 – 153.8
3% AC	521.9	139	161.0 – 162.6	151.6 – 153.9
4% AC	523.1	141.3	161.2 – 162.7	151.7 – 154.1
0.5% BC	517.9	136.9	160.8 – 162.4	151.4 – 153.7
1% BC	519.8	139.4	161.0 – 162.6	151.5 – 153.9
2% BC	510.0	135.6	160.6 – 162.2	151.0 – 153.4
3% BC	498.8	134.2	160.4 – 162.1	150.5 – 153.0
4% BC	606.9	154.4	162.6 – 164.0	154.7– 156.7

5 Conclusions

In this study, the effect on asphalt binder of bio-char obtained from the pyrolysis of brewed waste tea which are collected from homes and restaurants was evaluated for first time. Commercially activated carbon was used to compare the effect of bio-char on asphalt binder. While the penetration values of asphalt binders modified with 0.5, 1, 2, 3 and 4% bio-char and commercially activated carbon in comparison with the reference asphalt binder decreased, the softening point values increased. According to the results of storage stability test, storable of asphalt binders modified with the bio-char and commercially activated carbon at high temperature was determined. The temperature sensitivity of asphalt binders modified with 2, 3, 4% AC and 4% BC increased according to reference asphalt binder. The mixing and compaction temperatures of asphalt binders modified with commercially activated carbon were increased in comparison with reference asphalt binders. According to the viscometer test results, it is thought that the bio-char material is not homogeneously dispersed and is agglomerated in asphalt binders modified with 2, 3 and 4 % BC. Therefore, it is thought that the usability of bio-char obtained from the pyrolysis of brewed waste tea in certain ratios in asphalt binder is appropriate. In future studies, both the mixing performance of asphalt binders modified with bio-char and the usability of bio-char as filler at different ratios in asphalt mixtures will be examined.

References

1. Rahman, M. T., Mohajerani, A., and Giustozzi, F.: Recycling of waste materials for asphalt concrete and bitumen: A review. Materials 13(7), 1495 (2020).
2. Milad, A. A., Ali, A. S. B., and Yusoff, N. I. M.: A review of the utilization of recycled waste material as an alternative modifier in asphalt mixtures. Civil Engineering Journal, 6, 42-60 (2020).
3. Rondón-Quintana, H. A., Reyes-Lizcano, F. A., Chaves-Pabón, S. B., Bastidas-Martínez, J. G., and Zafra-Mejía, C. A.: Use of biochar in asphalts. Sustainability, 14(8), 4745 (2022).
4. Çeloğlu, M. E., Mehmet, Y., Kök, B. V., and Yalcin, E.: Effects of various biochars on the high temperature performance of bituminous binder. In Proceedings of the 6th Euraphalt & Eurobitume Congress, Czech Republic, European Asphalt Pavement Association (EAPA) and Eurobitumen (2016).
5. Kumar, A., Choudhary, R., Narzari, R., Kataki, R., and Shukla, S. K.: Evaluation of bio-asphalt binders modified with biochar: a pyrolysis by-product of Mesua ferrea seed cover waste. Cogent Engineering, 5(1), 1548534 (2018).
6. Zhang, R., Wang, H., Ji, J., and Wang, H.: Viscoelastic properties, rutting resistance, and fatigue resistance of waste wood-based biochar-modified asphalt. Coatings, 12(1), 89 (2022).
7. Zhou, X., Zhao, G., Wu, S., Tighe, S., Pickel, D., Chen, M., Adhikari, S., and Gao, Y.: Effects of biochar on the chemical changes and phase separation of bio-asphalt under different aging conditions. Journal of Cleaner Production, 263, 121532 (2020).
8. Ma, F., Dai, J., Fu, Z., Li, C., Wen, Y., Jia, M., Wang, Y., and Shi, K.: Biochar for asphalt modification: A case of high-temperature properties improvement. Science of the Total Environment, 804, 150194 (2022).

9. Zhao, S., Huang, B., and Ye, P.: Laboratory evaluation of asphalt cement and mixture modified by bio-char produced through fast pyrolysis. In Pavement Materials, Structures and Performance, 140-149 (2014).
10. Martínez-Toledo, C., Valdés-Vidal, G., Calabi-Floody, A., González, M. E., and Reyes-Ortiz, O.: Effect of biochar from oat hulls on the physical properties of asphalt binder. Materials, 15(19), 7000 (2022).
11. Zhao, S., Huang, B., Ye, X. P., Shu, X., and Jia, X.: Utilizing bio-char as a bio-modifier for asphalt cement: A sustainable application of bio-fuel by-product. Fuel, 133, 52-62 (2014).
12. Seyrek, E. Ş., Yalcin, E., Yilmaz, M., Kök, B. V., and Arslanoğlu, H.: Effect of activated carbon obtained from vinasse and marc on the rheological and mechanical characteristics of the bitumen binders and hot mix asphalts. Construction and Building Materials, 240, 117921 (2020).
13. Bostancioğlu, M., and Oruç, Ş.: Optimizing activated carbon size and ratio in bitumen modification. Gradevinar, 69(3) (2017).
14. Dong, W., Ma, F., Li, C., Fu, Z., Huang, Y., and Liu, J.: Evaluation of anti-aging performance of biochar modified asphalt binder. Coatings, 10(11), 1037 (2020).
15. Gan, X., and Zhang, W.: Application of biochar from crop straw in asphalt modification. Plos One, 16(2), e0247390 (2021).
16. Zhang, R., Dai, Q., You, Z., Wang, H., and Peng, C.: Rheological performance of bio-char modified asphalt with different particle sizes. Applied Sciences, 8(9), 1665 (2018).
17. Yılmaz, B., & Gürbüz, H. E.: Rheological and morphological evaluation of nanoclay modified asphalt binder. Construction and Building Materials, 313, 125479 (2021).

The Effects of Nano Expanded Vermiculite on Asphalt Binder Properties

Mehmet Saltan[1][0000-0001-6221-4918], Gizem Kaçaroğlu[2][0000-0002-5734-7131] and Öznur Karadağ[3][0000-0003-0755-5626]

[1] Süleyman Demirel University, Engineering Faculty, Civil Engineering Department, Isparta, Türkiye, mehmetsaltan@sdu.edu.tr
[2] Süleyman Demirel University, Engineering Faculty, Civil Engineering Department, Isparta, Türkiye, gizemkacaroglu@sdu.edu.tr
[3] Süleyman Demirel University, Engineering Faculty, Civil Engineering Department, Isparta, Türkiye, oznurkaradag92@gmail.com

Abstract. Nanomaterials are preferred in pavement construction due to their properties such as having small sizes and large surface areas. As a type of nanomaterial, nano clays are just one of the materials which can enhance the properties and performances of bituminous binder and consequently various asphalt mixtures. So, this study investigates the effects of nano expanded vermiculite which is a clay mineral on physical properties of bituminous binder. Nano expanded vermiculite was used to modify reference bitumen (50/70) in the ratios of 1, 2 and 3%. Physical properties such as penetration, softening point, temperature susceptibility, ductility and viscosity of reference and modified binders were determined and compared. The storability of modified binders was investigated with storage stability test. In addition, Vialit, Nicholson Stripping and California Stripping tests were performed to evaluate adhesion performances and stripping resistances of samples. Results of tests showed that the usage of nano expanded vermiculite decreases penetration and increases softening point, temperature-dependent susceptibility and viscosity. In addition, it was seen that nano expanded vermiculite additive used in the modification is suitable in terms of storability. The rise in additive ratio in bitumen decreased slightly adhesion performance. However, it can be said that mixtures containing nano expanded vermiculite modified binders can perform better in terms of stripping resistance in the presence of water and under the influence of traffic loads. According to the obtained results, it has been seen that modification of bitumen with nano expanded vermiculite can increase the resistance of asphalt binders to hot climate conditions.

Keywords: Expanded Vermiculite, Nanomaterials, Bitumen Properties, Adhesion and Stripping.

1 Introduction

Increasing the resistance of the pavement to permanent deformation, low-temperature cracking, etc., usually caused by temperature susceptibility, will ensure that the life cycle of the pavement is kept at a certain level [1]. It is desired that flexible pavements show enough strength during their service life, enough stability at hot weather conditions, and enough flexibility at cold weather conditions; but the usage of bituminous binders with high-temperature susceptibility often does not make it possible. In addition, the failure of the bond between bitumen and aggregates due to the effects of water, temperature and traffic is another problem for asphalt mixtures [2]. The way to eliminate these problems is usually the modification of the bituminous binder or mixture. Up to the present, different types of additives such as polymers [3-5], fillers [6, 7], waste and recycled materials [8-10], fibers [11-13] and chemicals [14, 15] have been used for improvement of the bituminous binder or mixture performance. In addition to these materials, one of the most preferred additives to use recently is nanomaterials [16-19].

Nanomaterials are defined as materials with at least one or more external dimensions between 1 and 100 nm [1, 20]. Nanomaterials have some extraordinary properties, such as having small size and large surface area, which can considerably change the characteristics of bituminous binders and mixtures. As a result of the interaction between bituminous binders and nanomaterials, high and low temperature behaviors of binders can be improved [1].

As a type of nanomaterial, nano clays are just one of the materials which can enhance the properties and performances of bituminous binder and consequently various asphalt mixtures. Even if the amount of nano clay added to the bituminous binder is small, fundamental changes in physical and rheological properties can be observed [21]. These materials generally affect the consistency properties of bituminous binders by increasing the softening point and viscosity while decreasing the penetration [22-24]. Because they can increase the binder stiffness, it is stated in different studies that nano clays enable bituminous binders to have a tendency to show higher resistance, especially against hot climatic conditions [25, 26]. In addition, these additives have positive effects in terms of fatigue life, permanent deformation, fracture, stripping and aging resistances of bituminous binders or mixtures [20, 27, 28]. It has also been found that addition of nano clays into bituminous binders can improve their storability [20, 29].

As well as the nano clays used in the pavement and creating the above-mentioned effects are very diverse, the most widely used type among these in the studies is montmorillonite [1]. Vermiculite is also a member of the montmorillonite clay mineral group, because it is similar to montmorillonite in terms of structure and composition. Although there is limited availability of studies in the literature that examine the effects of expanded vermiculite which is a clay mineral and subjected to different treatments, on bituminous binder [30-35], the effects of the nano-sized state of this material have never been investigated. So, this study investigates the effects of nano expanded vermiculite (NEV) on physical properties, adhesion performance and stripping

resistances of bituminous binder. NEV was used to modify reference bitumen (50/70) in the ratios of 1, 2 and 3%.

2 Materials and Method

2.1 Materials

Bituminous Binder. 50/70 penetration graded bituminous binder was used in this study. Table 1 shows the properties of reference bituminous binder.

Table 1. Physical properties of bituminous binder.

Test	50/70 bituminous binder	
Penetration (0,1 mm)	51	
Softening Point (˚C)	49,3	
Ductility (cm)	>100	
Specific Gravity (g/cm^3)	1,017	
Viscosity (cP)	135˚C / 100 rpm	165˚C / 100 rpm
	444,8	121,3

Nano Expanded Vermiculite (NEV). Vermiculite is a clay mineral with a 2:1 layered, hydrated magnesium – aluminum – iron silicate composition. Specific gravity is in the range of 2.0 – 2.8 gr/cm^3 of translucent vermiculite. A vermiculite layer which is similar in structure to mica consists of an octahedral layer and two tetrahedral layers.

Vermiculite mineral has the ability to expansion. As a result of the expansion, the bulk density of the material decreases approximately 10 times, from 0.8 gr/cm^3 to 0.08 gr/cm^3. Vermiculites with low bulk density obtained by the expansion process are mostly used in the construction/building and agriculture/horticulture sectors [36-38]. Physical properties of expanded vermiculite are given in Table 2.

Table 2. Physical properties of expanded vermiculite [38].

Physical Property	Expanded Vermiculite
Color	Yellowish Brown/Brown/Bronze
Shape	Accordion-grain shaped
Density (kg/m^3)	64-160
Loss in moisture at 110 °C (%)	4-10
pH (aqueously)	6-9
Mohs hardness	1,5-2,8
Sintering temperature (°C)	1150-1250
Melting temperature (°C)	1200-1320
Water-holding capacity by volume (%)	20-50
Crystal class	Prismatic (2/m)

In this study, the expanded vermiculite used for the modification of the bituminous binder was purchased from a commercial production company. The material was ground to nano size (38,08 nm) in order to be suitable for use in modification and then sieved through No. 200 sieve. Expanded vermiculite and NEV can be seen in Fig. 1.

Fig. 1. Expanded vermiculite and NEV.

2.2 Method

Bitumen Modification. In the study, bitumen was modified to examine the effects of NEV on the 50/70 bituminous binder. NEV was added to bituminous binder at the ratios of 1%, 3% and 5% by weight. Modifications were carried out with the help of a temperature-controlled high shear mixer at 160 °C and 2000 rpm for an hour.
Bitumen Tests and Storage Stability. Penetration, softening point, ductility, rotational viscometer and storage stability tests were carried out to determine the properties of reference and modified bituminous binders. In addition, the penetration index (PI) values were calculated to determine the effect of NEV on the temperature susceptibility of the bituminous binders.

Adhesion and Stripping Tests. The Vialit test was performed to evaluate the adhesion between the reference and NEV modified bituminous binders and the aggregate. In addition, Nicholson and California stripping tests were carried out to examine the effect of modification in terms of moisture-induced damage can be observed with the help of loose mixes. While the Nicholson stripping test evaluates the resistance of loose aggregate-binder mixtures against moisture resulting from the simultaneous presence of water and heat, the California stripping test presents the resistance of loose mixtures against water and traffic effects.

3 Results and Discussion

3.1 Results of Bitumen Tests and Storage Stability

To determine the consistency of samples, penetration, softening point, ductility and rotational viscometer tests have been applied on the reference bituminous binder and all modified samples. The temperature susceptibilities of the samples were determined by using the penetration and softening point values. In addition, the effects of

modification with NEV on the storability of the samples were also investigated. In this section, the results of these tests are given.

The effect of NEV modification on the penetration and softening point of bituminous binder can be seen in Fig. 2. As can be seen from the graph, the softening point temperatures increased while the penetration values decreased according to the reference binder as the NEV ratio increased. In similar studies in the literature, nano clay modification showed similar effects on the bituminous binder [21-24]. These results show that modification with NEV stiffens the bituminous binder. It is thought that this situation can decimate the potential of rutting occurrence that can be seen on the pavement in hot weather.

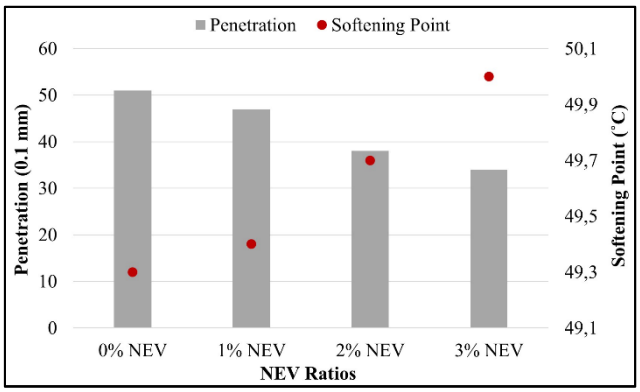

Fig. 2. Penetration and softening point test results of NEV modified binders.

According to the results of ductility tests, the reference bituminous binder and all modified samples have indicated elongation without breakage by exceeding the specification limit value of 100 cm at 25 °C. This means that the reference bitumen and all modified samples can indicate durability under the tensile effects caused by traffic on the pavement.

It is stated that in the literature, evaluation of results of penetration and softening point tests simultaneously is more reasonable in terms of interpretation of temperature susceptibilities of bituminous binders [2]. Therefore, the temperature sensitivities of the samples were evaluated using the penetration and softening point test results. The PI results obtained with the calculation are given in Fig. 3.

According to Fig. 3, the PI values decrease as the NEV ratio added to the bituminous binder increases. In another study, the usage of a similar nano clay resulted in a similar effect at certain rates [22]. The present case can be interpreted as the increase in the additive ratio increases the temperature-dependent susceptibility of the samples. To this respect, it is considered that the performance expectation at low and high temperatures can be low for the asphalt mixtures which will be prepared with bituminous binders modified with NEV.

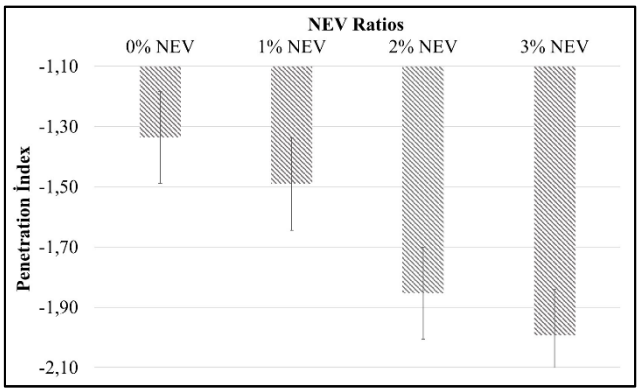

Fig. 3. PI results of NEV modified binders.

In rotational viscometer test, two temperature values, 135 and 165 °C, have been used as test temperatures. According to the reference binder, the changes in viscosity of the samples modified with NEV can be seen in Fig. 4. As can be seen from the graph, both the mixing/compaction temperatures and the temperature ranges increased slightly with the increasing of additive ratio. A similar trend for viscosity was observed in some studies using nano clays with different properties [22-24, 39]. The maximum increase in the mixing/compaction temperature was seen at the 3% additive ratio. Although there is an increase in the viscosity, the workability of binders was not affected negatively by rising of additive ratio.

The homogeneities and storability properties of reference and modified bituminous binders were examined by subjecting them to the storage stability procedure. According to this procedure, after holding the bituminous binders in standard aluminum tubes at 180 °C for 72 hours, the softening point tests were applied to the samples taken from the top and bottom of the tubes. Softening point values of binders after storage stability test are given in Table 3.

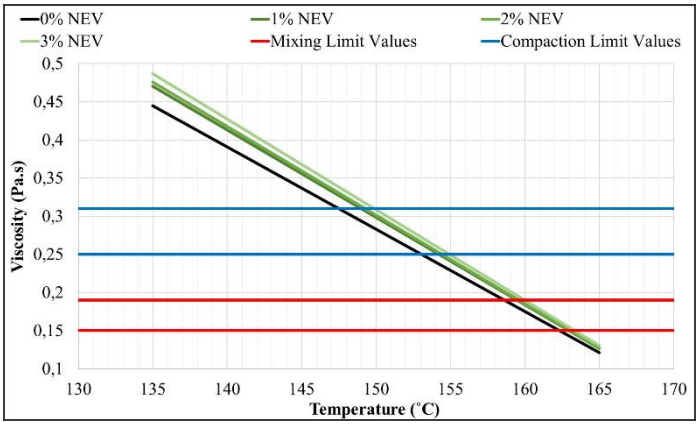

Fig. 4. Rotational viscometer test results of NEV modified binders.

According to the results obtained from the softening point tests carried out after storage stability test, the nanomaterial used in three different ratios accumulated in the top part of the tubes, and as a result, the softening point values of the top parts show an increase compared to the bottom parts. However, the fact that the temperature differences between the top and bottom parts are not much indicates that no significant phase separation has occurred. Accordingly, it can be said that the NEV additive used in the modification is suitable in terms of storability. When the storage stability test results in different studies are examined, the existence of the same situation can be seen [20, 29].

Table 3. Softening point values of binders after storage stability test.

Sample	Bottom (˚C)	Top (˚C)	Difference (˚C)	Original (˚C)
0% NEV	49,4	49,7	0,3	49,3
1% NEV	49,7	50,2	0,5	49,4
2% NEV	50,9	51,7	0,8	49,7
3% NEV	51,3	52,1	0,8	50

3.2 Results of Adhesion and Stripping Tests

To determine the adhesion performances and stripping resistances of reference and NEV modified bituminous binders Vialit test and Nicholson and California stripping tests were performed, respectively. In this section, the results of these tests are given.

Vialit test was carried out to determine how the adhesion between the aggregates and the bituminous binder is affected by the presence of water. The results of Vialit test showed that the usage of 1% NEV did not affect the adhesion performance compared to the reference binder. However, it was seen that the adhesion between the bituminous binder and the aggregates decreases a little as the amount of NEV added to the bituminous binder increases.

Sometimes deformations can occur in asphalt mixtures as a result of breaking the bonds between the aggregates and bituminous binder with the effect of water. Nicholson and California tests employed in this study are the stripping tests which measure the resistance of loose mixtures against water and traffic effects. Results of these tests were given in Fig. 5.

According to the results, when Nicholson stripping test was judged, although a slight increase in the percentage of aggregates without stripping for NEV modified binders has been observed, values are pretty close to reference binder. However, in the California stripping test, a more apparent increase in the percentage of aggregates remaining without stripping was seen. So, it can be said that mixtures containing NEV modified binders can perform better in terms of stripping resistance in the presence of water and under the influence of traffic loads.

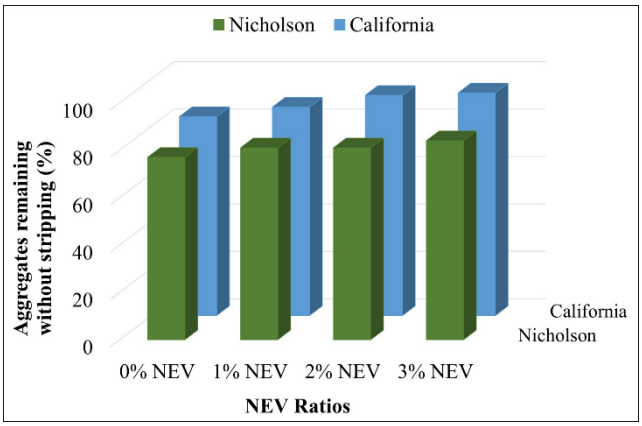

Fig. 5. Results of Nicholson and California tests.

4 Conclusions

In this study, physical properties, adhesion properties, stripping resistances and storability properties of reference and NEV modified binders were investigated and compared. Results of tests showed that the usage of NEV decreases penetration and increases softening point. The increase in the additive ratio increased the temperature-dependent susceptibility of the samples. According to the rotational viscometer test, both the mixing/compaction temperatures and the temperature ranges increased slightly with the increasing of additive ratio. In addition, it was seen that the NEV additive used in the modification is suitable in terms of storability. Rising of NEV ratio in bitumen decreased slightly adhesion performance. However, it can be said that mixtures containing NEV modified binders can perform better in terms of stripping resistance in the presence of water and under the influence of traffic loads. According to the obtained results, it has been seen that modification of bitumen with NEV can increase the resistance of asphalt binders to hot climate conditions.

References

1. Yao, H., You, Z.: Innovative Developments of Advanced Multifunctional Nanocomposites in Civil and Structural Engineering. 1st edn. Woodhead Publishing, U.K. (2016).
2. Yener, E., Yadollahi, M.M.: The Effect of Olive Pomace on Asphalt Binder Properties. In: International Conference on Civil Eng., Archit. & Urban Sustainable Develop., Iran (2013).
3. Wang, C., Song, L., Sun, G.: Comparison and correlation between polymer modified asphalt binders and mastics in high-and intermediate-temperature rheological behaviors. Construction and Building Materials 364, 129963 (2023).
4. Hawesah, H.A., Sadique, M., Harris, C., Nageim, H.A., Stopp, K., Pearl, H.: Polymer modified asphalt binder–an approach for enhancing temperature sensitivity for emergency pavement repair. International Journal of Pavement Engineering 23(13), 4760-4774 (2022).

5. Xia, T., Zhang, A., Xu, J., Chen, X., Xia, X., Zhu, H., Li, Y.: Rheological behavior of bitumen modified by reclaimed polyethylene and polypropylene from different recycling sources. Journal of Applied Polymer Science 138(20), 50435 (2021).
6. Deng, Y., Hu, M., Xu, L., Ling, S., Ni, H., Sun, D.: Dual roles played by manganese dioxide filler in asphalt pavement material: Chemical modification and healing improvement. Construction and Building Materials 345, 128371 (2022).
7. Aboutalebi Esfahani, M.: Influence of herbal and mineral fillers on physical and rheological properties of bitumen. Australian Journal of Civil Engineering 19(1), 35-45 (2021).
8. Li, H., Zhou, L., Sun, J., Wang, S., Zhang, M., Hu, Y., Temitope, A.A.: Analysis of the Influence of Production Method, Plastic Content on the Basic Performance of Waste Plastic Modified Asphalt. Polymers 14(20), 4350 (2022).
9. Yan, K., Wang, S., Ge, D., Chen, J., Tian, S., Sun, H.: Laboratory performance of asphalt mixture with waste tyre rubber and APAO modified asphalt binder. International Journal of Pavement Engineering 23(1), 59-69 (2022).
10. Huang, J., Li, X., Kumar, G.S., Deng, Y., Gong, M., Dong, N.: Rheological properties of bituminous binder modified with recycled waste toner. Journal of Cleaner Production 317, 128415 (2021).
11. Gu, Q., Kang, A., Li, B., Xiao, P., Ding, H.: Effect of fiber characteristic parameters on the high and low temperature rheological properties of basalt fiber modified asphalt mortar. Case Studies in Construction Materials 17, e01247 (2022).
12. Cui, S., Sheng, Y., Wang, Z., Jia, H., Qiu, W., Temitope, A.A., Xu, Z.: Effect of the fiber surface treatment on the mechanical performance of bamboo fiber modified asphalt binder. Construction and Building Materials 347, 128453 (2022).
13. Zhang, Z., Zhang, H., Gao, Y., Kang, H.: Laboratory evaluation of the effect of kapok fibers on the rheological and fatigue properties of bitumen. Construction and Building Materials 272, 121819 (2021).
14. Gómez, N.H.C., Oeser, M., Fleischel, O.: Chemical modification of bitumen with novel isocyanate-based additive to enhance asphalt performance. Construction and Building Materials 301, 124128 (2021).
15. Jailani, N., Ibrahim, A.N.H., Rahim, A., Hassan, N.A., Yusoff, N.I.M.: Chemical and physical properties of poly (lactic) acid modified bitumen. Ain Shams Engineering Journal 12(3), 2631-2642 (2021).
16. Ezzat, H., El-Badawy, S., Gabr, A., Zaki, S., Breakah, T., Arab, M., Zeiada, W.: Nanomodified Asphalt Binders Aging Study and Predicted Performance under Different Climatic Conditions Using AASHTOWare. Journal of Materials in Civil Engineering 35(6), 04023146 (2023).
17. Mamuye, Y., Liao, M.C., Do, N.D.: Nano-Al2O3 composite on intermediate and high temperature properties of neat and modified asphalt binders and their effect on hot mix asphalt mixtures. Construction and Building Materials 331, 127304 (2022).
18. Nisar, M.A., Zaidi, S.B.A., Fareed, A., Carvajal-Munoz, J.S., Ahmed, I.: Performance evaluation of Nano wood ashes in asphalt binder and mixture. International Journal of Pavement Engineering 23(10), 3318-3332 (2022).
19. Hussein, A.A., Putra Jaya, R., Yaacob, H., Abdul Hassan, N., Oleiwi Aletba, S.R., Huseien, G.F., ..., Mohd Hasan, M.R.: Physical, chemical and morphology characterisation of nano ceramic powder as bitumen modification. International Journal of Pavement Engineering 22(7), 858-871 (2021).
20. Martinho, F.C., Farinha, J.P.S.: An overview of the use of nanoclay modified bitumen in asphalt mixtures for enhanced flexible pavement performances. Road Materials and Pavement Design 20(3), 671-701 (2019).
21. Jahromi, S.G., Khodaii, A.: Effects of nanoclay on rheological properties of bitumen binder. Construction and Building Materials 23(8), 2894-2904 (2009).

22. Yılmaz, B., Gürbüz, H.E.: Rheological and morphological evaluation of nanoclay modified asphalt binder. Construction and Building Materials 313, 125479 (2021).
23. Vargas, M.A., Moreno, L., Montiel, R., Manero, O., Vázquez, H.: Effects of montmorillonite (Mt) and two different organo-Mt additives on the performance of asphalt. Applied Clay Science 139, 20-27 (2017).
24. El-Shafie, M., Ibrahim, I.M., Abd El Rahman, A.M.M.: The addition effects of macro and nano clay on the performance of asphalt binder. Egyptian Journal of Petroleum 21(2), 149-154 (2012).
25. Yilmaz, B., Özdemir, A.M., Gürbüz, H.E.: Assessment of Thermal Properties of Nanoclay-Modified Bitumen. Arabian Journal for Science and Engineering 1-13 (2022).
26. Ezzat, H., El-Badawy, S., Gabr, A., Zaki, E.S.I., Breakah, T.: Evaluation of asphalt binders modified with nanoclay and nanosilica. Procedia engineering 143, 1260-1267 (2016).
27. Iskender, E.: Evaluation of mechanical properties of nano-clay modified asphalt mixtures. Measurement 93, 359-371 (2016).
28. Ashish, P.K., Singh, D., Bohm, S.: Evaluation of rutting, fatigue and moisture damage performance of nanoclay modified asphalt binder. Construction and Building Materials 113, 341-350 (2016).
29. Golestani, B., Nam, B.H., Nejad, F.M., Fallah, S.: Nanoclay application to asphalt concrete: Characterization of polymer and linear nanocomposite-modified asphalt binder and mixture. Construction and Building Materials 91, 32-38 (2015).
30. Zhang, H., Duan, H., Luo, H., Shi, C.: Synthesis, characterization and utilization of zinc oxide/expanded vermiculite composite for bitumen modification. Fuel 306, 121731 (2021).
31. Wang, J., Zhang, H., Zhu, C.: Effect of multi-scale nanocomposites on performance of asphalt binder and mixture. Construction and Building Materials 243, 118307 (2020).
32. Zhu, C., Zhang, H., Shi, C., Li, S.: Effect of nano-zinc oxide and organic expanded vermiculite on rheological properties of different bitumens before and after aging. Construction and Building Materials 146, 30-37 (2017).
33. Zhang, H., Chen, Z., Li, L.: Effect of nanozinc oxide and organic expanded vermiculite compound on antiaging properties of SBR modified bitumen. Journal of Materials in Civil Engineering 29(11), 04017204 (2017).
34. Liu, J., Yan, K., Zhao, X.: Rheological and aging properties of warm mix asphalt binders containing expanded vermiculite. Petroleum Science and Technology 34(11-12), 1042-1047 (2016).
35. Zhang, H., Jia, X., Yu, J., Xue, L.: Effect of expanded vermiculite on microstructures and aging properties of styrene–butadiene–styrene copolymer modified bitumen. Construction and Building Materials 40, 224-230 (2013).
36. Ehsani, İ.: Effects of Sulphuric Acid Leaching on The Physical, Chemical and Thermal Properties of a Vermiculite. Hacettepe University, Institute of Science and Technology, Master of Science Thesis, Ankara (2015).
37. Saltan, M., Uysal, F.: Research of Vermiculite Usability Hot Mix Asphalt by Marshall Stability Test Method. Süleyman Demirel University Journal of Natural and Applied Sciences 22(1), 253-257 (2018).
38. Arıkan, F.: Vermiculite in the World and Turkey, Department of Feasibility Studies. General Directorate of Mineral Research and Exploration, Ankara (2021).
39. You, Z., Mills-Beale, J., Foley, J.M., Roy, S., Odegard, G.M., Dai, Q., Goh, S.W.: Nanoclay-modified asphalt materials: Preparation and characterization. Construction and Building Materials 25(2), 1072-1078 (2011).

Modelling Shared Bicycle Demand Using Artificial Neural Networks

Selim Dündar[1][0000-0003-4433-1998], Pelin Alcan Gezginci[2][0000-0001-7155-7621], Gürkan Günay[3][0000-0003-0597-1511], Elçin Mert[4][0000-0002-7539-6666] and Ersoy Soyer[5][0000-0002-6299-5846]

[1] Istanbul Okan University, Civil Engineering Department, Istanbul, Türkiye, selim.dundar@okan.edu.tr
[2] Istanbul Okan University, Industrial Engineering Department, Istanbul, Türkiye, pelin.alcan@okan.edu.tr
[3] Istanbul Bilgi University, Civil Engineering Department, Istanbul, Türkiye, gurkan.gunay@bilgi.edu.tr
[4] Yapıdrom Technology, Istanbul, Türkiye, elcin.mert@yapidrom.com.tr
[5] Yapıdrom Technology, Istanbul, Türkiye, ersoy.soyer@yapidrom.com.tr

Abstract. Since bicycles are based entirely on muscle power, they are the transportation vehicles with the lowest negative impact on the environment. In addition, since they are an active mode of transportation, they are also named among the leading modes in terms of sustainability. They are also the leading vehicle type among the micro mobility systems, which can be considered as small-sized and individual transportation modes, in terms of their historical background as well as purchasing and operating costs. Today, bicycle ridership rates are increasing thanks to the bike-sharing or rental services provided by both local governments and companies in the private sector. Traveling by bicycle, rather than using a motor vehicle, has a positive effect on the natural environment as it does not cause pollutant gas emissions and affects the traffic jams minimally. It is crucial to investigate the periodic changes in the use of shared bicycle systems, especially in order to define the factors that affect this modal shift and to predict the demand for bicycle use in the future. Within the scope of the developed study, the changes in bicycle use and various factors affecting it were investigated in 4 of the cities in which one of Turkey's leading companies in micro mobility provides bicycle sharing services. The values regarding bicycle use were then modelled using artificial neural networks. Thanks to the developed model, it will be possible to predict the number of future trips in the cities where bike sharing service is provided and the periodic changes of these trips, as well as to make estimations about the passenger demand that will arise in a city where the new service will be provided.

Keywords: Bicycle, Micro mobility, Traffic demand, Artificial Neural Networks.

1 Introduction

The concept of micromobility, which refers to small-sized and individual transportation, which is generally operated at speeds of less than 25 km/h, is a popular concept that has emerged in recent years. Especially with the effect of the COVID-19 pandemic, people tried to avoid using public transportation and this has led to an increase in the use of micromobility systems such as bicycles and e-scooters. Although micromobility is a new concept, some micromobility vehicles, especially bicycles, have actually existed in our lives for many years as a mode of transportation. The modern form of the bicycle, whose very primitive models were seen in 12th century China, was developed by Conte de Sivac in France in 1791 [1]. Since then, the bicycle, which has been developed in different models, has maintained its popularity and has become an important mode of transportation.

Since bicycles are a type of transportation based entirely on muscle power, they are the means of transportation with the lowest negative impact on the environment. Unlike vehicles with internal combustion engines, they do not emit any polluting gases during their use. Unlike electrically powered vehicles, they do not have a battery containing chemicals. However, nowadays, electric bicycles (e-bikes) have also started to be used in order to eliminate the factors that may create adverse conditions during bicycle use, such as high gradients. Fully muscle-powered bicycles, which can be defined as classic bicycles, are among the leading transportation modes in terms of sustainability, as they are an active mode of transportation. Among the micromobility systems, which can be considered as small-sized and individual transportation, bicycle is the leading transportation vehicle due to both its historical background and its purchasing and operating costs. On the other hand, it is not possible to claim that they don't have any negative impact on the environment due to the various metal alloys, plastic parts and processes used in their production. However, since it is the transportation mode that has the least damage to the environment after walking, it is preferred especially by the young people with higher environmental awareness.

Today, it is aimed to increase the rate of bicycle usage thanks to the vehicle sharing or rental services provided by both local governments and companies in the private sector. The increase in the use of bicycles shows that the journeys made with different transportation modes cause a shift towards the use of bicycles. From which transportation modes do this modal shift occur is among the subjects that researchers are currently working on. According to a study e-scooter and e-bike vehicles have the opportunity to replace other types on journeys less than 8 km [2]. These mentioned trips in the EU, USA and China have a share of approximately 50-60% of the total trips. For bicycle sharing systems, an online survey was conducted on bicycle and public transport integration within the scope of the study carried out in Montreal, Canada in the summer of 2010 [3]. The questionnaire consists of six parts: general travel habits, public transport questions, cycling/transfer questions, priorities for improving cycling and its integration with public transport, general demographics and comments section. In the study, 1432 questionnaires were collected, and a binary logit model was developed to determine the factors that encourage the use of the bike sharing system

called BIXI (bike taxi). The dependent variable is whether BIXI was used before (yes-no). A linear regression was then applied to a subsample of BIXI users to identify factors affecting the frequency of use of shared bikes. The dependent variable in this second model is the number of BIXI uses for 2010. The first model tests various variables (age, gender, income level) based on the results of previous studies examining the motivation to cycle in general or the use of shared bicycle systems. As a result of the research, the factors that motivate the use of BIXI are using BIXI for transfer (bus-train), proximity to the station, living close to the city center, low security of personal bicycles in Montreal (bicycle theft is high), users not paying for the first half hour in BIXI, no need for maintenance and popularity of BIXI. The factors that reduce usage are having a driver's license and riding a bicycle for recreational purposes only. The variable with the strongest effect was found to be the presence of a BIXI station less than 500 m from the house, in which case individuals were 3 times more likely to use a shared bicycle. It was stated that the proximity of a BIXI station to the route that the participant regularly travels will increase the probability of using BIXI. Recreational cyclists and women were less likely to use BIXI, while integrating bicycle and public transport for trips and holding a driver's license increased a person's likelihood of using BIXI.

Traveling by bicycle, rather than using a motor vehicle, has a positive impact on the natural environment as it does not cause pollutant gas emissions and does not contribute to traffic jams. With the increase in environmental awareness recently, the demand for the use of micromobility systems, especially bicycles and e-scooters, has increased, particularly among young people. Another reason for the increase in demand for micromobility systems is that it is used as a complementary mode to public transportation, especially in trips defined as the last kilometer.

It is necessary to examine the periodic changes in the use of shared bicycle systems, in order to examine the factors that affect the modal shift from other modes of transportation to bicycles, and to predict the demand for bicycle use in the future. Within the scope of the developed study, the number of periodic bicycle use and various factors affecting this in 4 of the cities where Yapıdrom Technology JSC, one of Turkey's leading organizations in the field of micromobility provides bicycle sharing services, were examined and modeled by artificial neural networks (ANN) method.

2 Methodology

Yapıdrom Technology JSC, which was founded by Yavuz Salih Şahin in 2012, while the subject of micromobility is not talked about much in the world, is Turkey's first micromobility company. The infrastructures established for shared bicycles operating in dozens of cities and districts of Turkey today serve the transportation of more than five million people using electric bicycles and scooters in the cities. Thanks to this system initiated by Yapıdrom, environmental awareness has provided great benefits in reducing carbon emissions and developing alternative transportation systems in the Turkey today.

While the “Baksi” brand within Yapıdrom refers to sustainable smart bike sharing systems; mainly in Istanbul (Isbike), Izmir (Bisim), Antalya (Antbis), Bursa (Nilespit) etc. continues to serve the public together with public institutions in nearly thirty cities. In 2019, Yapıdrom launched their first e-scooter operation, the “Tazı” brand. In addition, in 2022, they launched Turkey's first e-bike operation with Jant-i e-bikes in Bursa. Tazı, which aims to provide access to alternative transportation systems in Turkey, especially in Anatolian provinces, offers a safe and enjoyable transportation service for everyone with electric bicycles and e-scooters in eight provinces.

Within the scope of the study, bicycle usage data of Yapıdrom were obtained for four cities with different characteristics, where bicycle rental services are provided by the company. These four cities are Çanakkale and Nilüfer District of Bursa in the Marmara Region, Çorum in the Central Black Sea Region and Marmaris District of Muğla in the Mediterranean Region.

2.1 Çanakkale

Çanakkale, located in the Marmara Region in the northwest of Turkey, has a population of 559,383 people [4]. The city, which is divided into two by the Dardanelles Strait, is one of our two cities with lands in both Europe and Asia, together with Istanbul. Since the city hosts Çanakkale Onsekiz Mart University, it also attracts a significant number of students from different cities. Yapıdrom started shared bicycle services in Çanakkale in August 2016. Shared bicycle services still continue in Çanakkale.

2.2 Bursa-Nilüfer Municipality

Bursa, located in the Marmara Region in the northwest of Turkey, is the fourth most populous city with a population of 3,194,720 people. The population of Nilüfer Municipality is 536,365 [4]. The city hosts Bursa Uludağ University, Bursa Technical University an, Mudanya University. Bursa Orhangazi University, which was opened in 2011, was closed in 2016. As it hosts three different universities, the city also has a significant student population. Yapıdrom started shared bicycle services in Nilüfer Municipality of Bursa in April 2016. Shared bicycle services still continue within the borders of Nilüfer Municipality.

2.3 Çorum

Located in the Inner Central Black Sea Region of northern Turkey, Çorum has a population of 524,130 [4]. Hittit University, founded in 2006, is located in the city. Yapıdrom started shared bicycle services in Çorum in August 2020. Shared bicycle services still continue in Çorum.

2.4 Muğla-Marmaris Municipality

Muğla, which is located in the Aegean Region in the west of Turkey and the Mediterranean Region in the south, has a population of 1,048,185 people. The population of Marmaris Municipality, located in the Mediterranean Region, is 97,818 [4]. However, since Marmaris is one of the important summer tourism centers, it attracts

a significant number of tourists between May and October. Due to Muğla Sıtkı Koçman University, it also has a significant student population. Yapıdrom started sharing bicycle services in Çorum in April 2019. Shared bicycle services still continue in Marmaris.

2.5 Data Collection

In order to examine the demand for shared bicycle use, first of all, for each of the four cities, the total rental numbers, total usage times and average usage times of bicycles were obtained on a monthly basis from the date Yapıdrom started to serve in the city until the end of 2021. Then, the factors that may affect the usage were investigated and for each city, the total population, female and male population [4], gross domestic product (GDP) in TL and USD, population between 16-35 years of age [5], population with university students (compiled from the websites of universities), length of the urban road network [6], average air temperatures on a monthly basis, average number of rainy days [7], whether it is COVID-19 pandemic period, whether full closure was implemented, and how long shared bicycle service was provided in that city were collected. While all the collected data had real values, only the pandemic and closure variables were shown with a dummy variable of 0 when they were applied and 1 when they were not. Since 2022 GDP values were not disclosed during the research, all data were obtained for the time intervals until the end of 2021.

2.6 Artificial Neural Networks Model

Artificial Neural Networks (ANN) is a machine learning method developed based on the basic working principles of the human brain such as learning, generalizing, remembering and memorizing. It is called a black box modeling technique because it aims to produce appropriate output values from the input values, rather than creating a mathematical relationship between them.

Within the scope of this study, using the collected data, ANNs have been developed that try to predict the shared bike usage demand. First of all, for each city, 3 different models were developed that estimate the total number of rentals, the total usage time in minutes and the average usage time in minutes. Finally, by evaluating the data collected for all cities together, 3 different models have been developed that can be used to predict output values for any city. Thus, a total of 15 different ANN models were created. An example of the models created is shown in Figure 1.

The hyper parameters of each ANN model were determined by trial-and-error method proposed by [8], due to its simplicity. For the rapid convergence of the ANN model, all input and output values are normalized to the range of 0 and 1 as seen in Equation 1.

$$x_{normalized} = \frac{x_i - x_{min}}{x_{max} - x_{min}} \quad (1)$$

Here, xnormalized, xi, xmin, xmax represent the normalized value of the input or output, the actual value, the smallest and largest value that variable can take,

respectively. The sigmoid function was chosen as the activation function in the hidden layer, and the linear function in the output layer. Levenberg Marquardt (LM) algorithm was preferred in ANN training because it converges rapidly and requires less iteration. MATLAB®'s default values are used for the parameters of the LM algorithm; where initial mu is 0.001, mu reduction factor is 0.1, mu increase factor is 10, and maximum mu is 100000000000. 70%, 15%, and 15% of the data is selected randomly as training, test, and validation sets, respectively. The output values of the developed ANN model are denormalized by using Equation 2.

$$x_i = x_{normalized} \times (x_{max} - x_{min}) + x_{min} \quad (2)$$

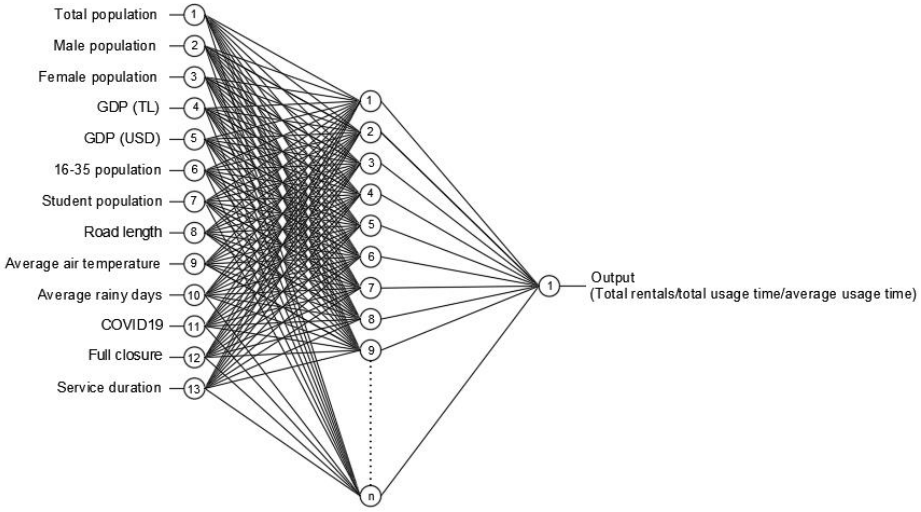

Fig. 1. Developed ANN model.

3 Results

In order to evaluate the success of the developed ANN models, a scatter diagram was drawn between the measured values and the model result, and the coefficient of determination, r2 was measured. In addition, observed and modeled values are plotted as time series. The scatter diagrams and the time series drawn for Çanakkale are given in Figure 2 and 3, respectively. The scatter diagrams and the time series drawn for all the cities are evaluated together and are given in Figure 4 and 5, respectively. The r2 coefficients of ANN models developed for each city are shown in Table 1.

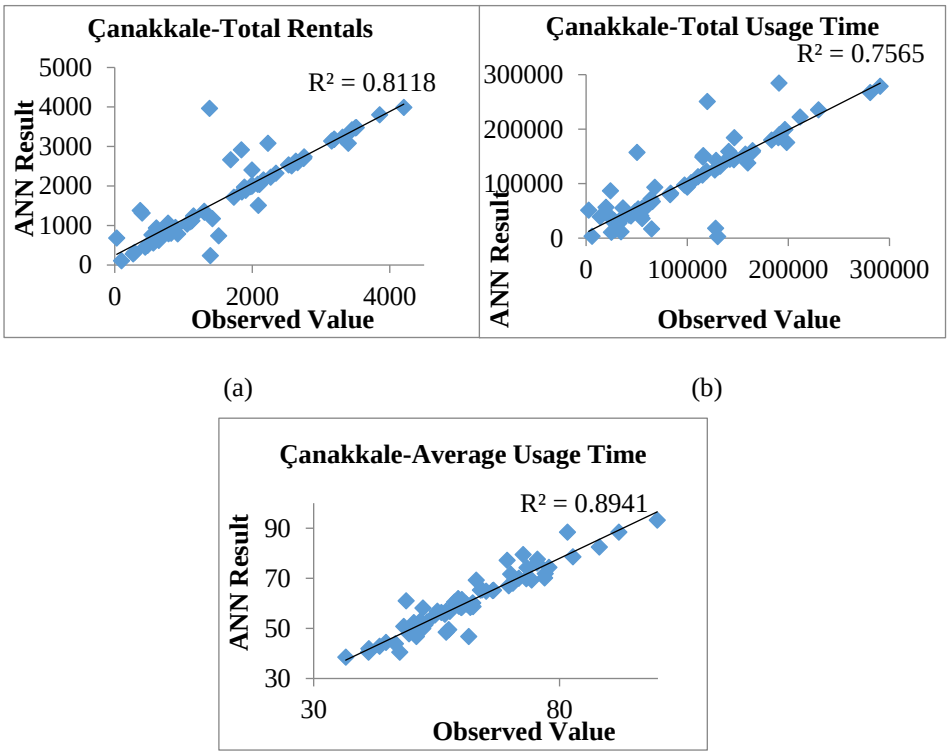

Fig. 2. Scatter plot for Çanakkale (a) total rentals, (b) total usage time, (c) average usage time

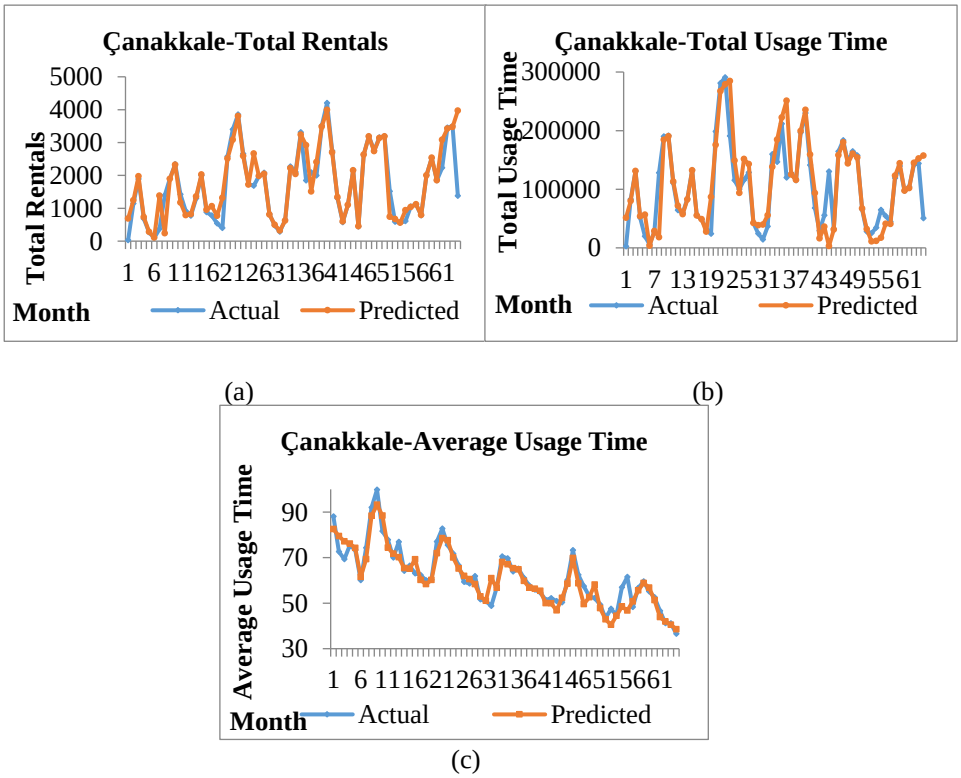

Fig. 3. Time series for Çanakkale (a) total rentals, (b) total usage time, (c) average usage time

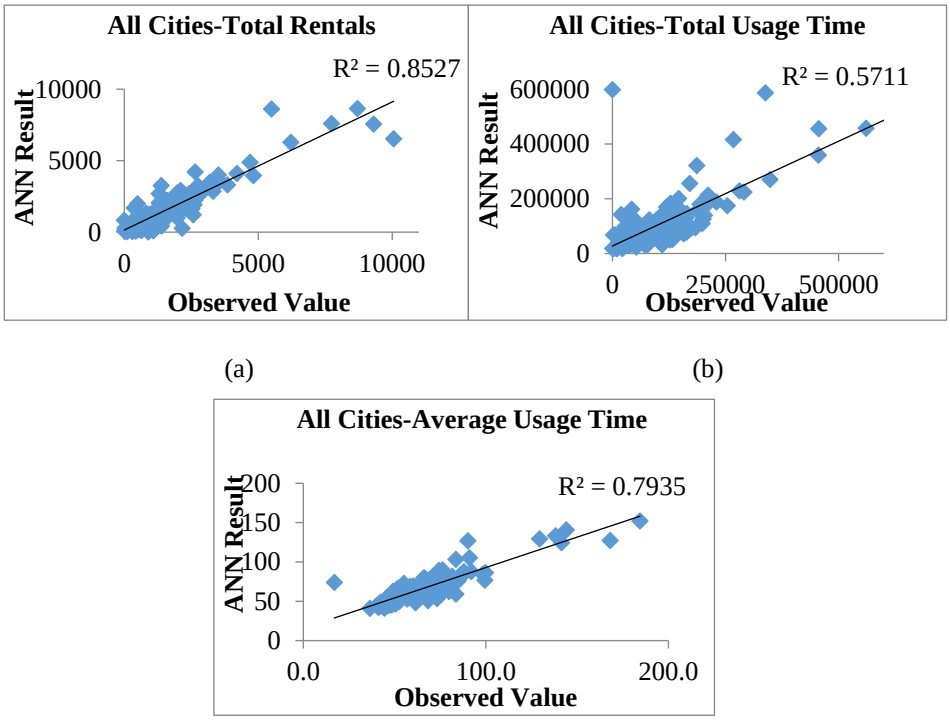

Fig. 4. Scatter plot for all cities evaluated together (a) total rentals, (b) total usage time, (c) average usage time

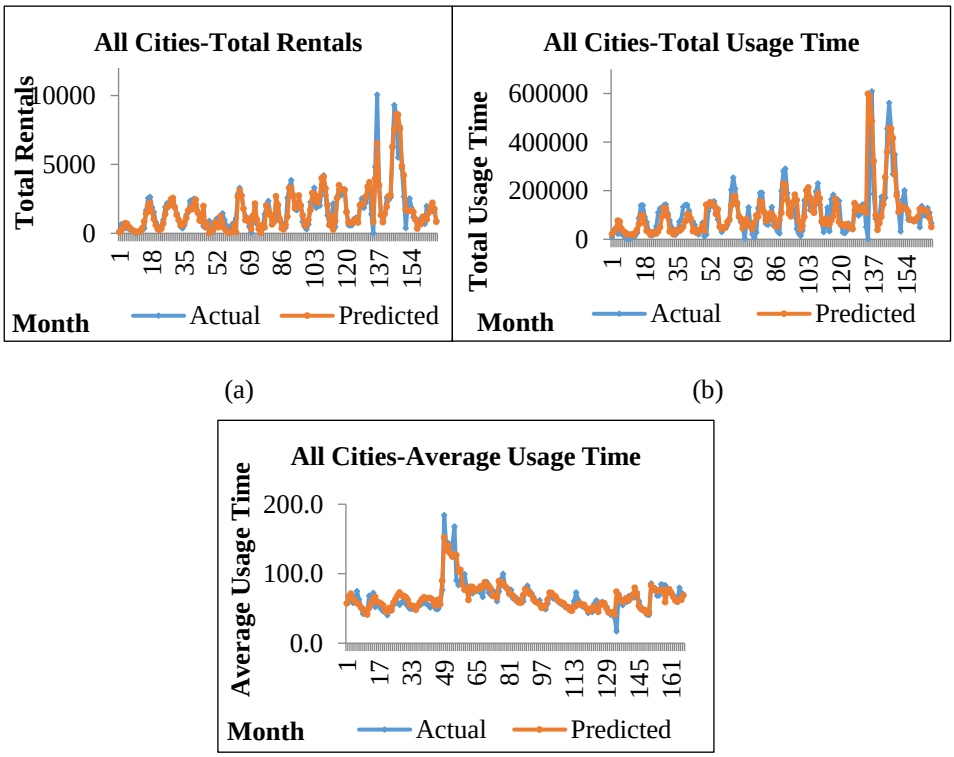

Fig. 5. Time series for all cities evaluated together (a) total rentals, (b) total usage time, (c) average usage time

Table 1. Performance of ANN models.

City/r^2	Total rentals	Total usage time (min)	Average usage time (min)
Çanakkale	0,8118	0,7565	0,8941
Nilüfer	0,9038	0,8624	0,6557
Çorum	0,4354	0,1512	0,8671
Marmaris	0,6364	0,1621	0,3722
All	0,8527	0,5711	0,7935

4 Discussions

The performance of the ANN models developed for Çanakkale and Nilüfer Municipality, two cities where Yapıdrom has been serving for a longer period, are higher than Çorum and Marmaris, which have been in service for a shorter period and therefore have less data. With the acquisition of new data, more successful ANN models can be obtained for these two cities. The model, in which data for all cities were evaluated together, was more successful in estimating changes in bicycle usage demand than the models developed for Çorum and Marmaris, which had less data. It was more

successful in estimating the total number of rentals for Çanakkale and the average usage time for Nilüfer Municipality, with more data obtained. This shows that when enough data is obtained and a separate model is established for each city, higher performance will be achieved. On the other hand, when a single model can be developed for all cities, it can be used to predict the demand, or in other words, the number and usage time for a completely different city. This can be a guide for investments to be made in a new city.

When the time series obtained from the results of the ANN models are examined, it is seen that the models generally catch the trend of increase or decrease in the number or duration of use. Thus, it can be said that it can be usefully used in the prediction of future change trends. For this reason, it can be used as a useful method in making decisions regarding maintenance/repair needs that may arise especially for vehicles and/or infrastructure and, if necessary, expansion or contraction of the vehicle fleet.

Acknowledgements
This study has been prepared with the contribution of Yapidrom Technology JSC and with the support from the European Union's H2020 research and innovation programm under the RECIPROCITY Project (Grant NO 101006576). The authors would like to thank the European Union and Yapıdrom for their support.

References

1. Sığırcı, M.: Bisiklet: Kim, Ne Zaman İcat Etti?, https://bilimgenc.tubitak.gov.tr/makale/bisiklet-kim-nezaman-icat-etti Last accessed 2023/05/12.
2. Şengül, B., Mostofi, H.: Impacts of e-micromobility on the sustainability of urban transportation - a systematic review. Applied Sciences, 11(13), 5851 (2021). https://doi.org/10.3390/app11135851
3. Bachand-Marleau, J., Lee, B.H.Y., El-Geneidy, A.: Better Understanding of Factors Influencing Likelihood of Using Shared Bicycle Systems and Frequency of Use. Transportation Research Record: Journal of the Transportation Research Board, 2314, 66–71, (2012). https://doi.org/10.3141/2314-09
4. Turkish Statistical Institute (Türkiye İstatistik Kurumu - TÜİK): Adrese Dayalı Nüfus Kayıt Sistemi Sonuçları 2022, https://data.tuik.gov.tr/Bulten/Index?p=Adrese-Dayali-Nufus-Kayit-Sistemi-Sonuclari-2022-49685, last accessed 2023/05/12.
5. Turkish Statistical Institute (Türkiye İstatistik Kurumu - TÜİK): İl Bazında Gayrisafi Yurt İçi Hasıla, 2021, https://data.tuik.gov.tr/Bulten/Index?p=Il-Bazinda-Gayrisafi-Yurt-Ici-Hasila-2021-45619, last accessed 2023/05/12.
6. Ulaştırma ve Altyapı Bakanlığı, Karayolları Genel Müdürlüğü (KGM): İstatistikler, https://www.kgm.gov.tr/sayfalar/kgm/sitetr/istatistikler/devletveilyolenvanteri.aspx, last accessed 2023/05/12
7. Turkish State Meteorological Service (T.C. Çevre, Şehircilik ve İklim Değişikliği Bakanlığı Meteoroloji Genel Müdürlüğü) Resmi İstatistikler, https://www.mgm.gov.tr/veridegerlendirme/il-ve-ilceler-istatistik.aspx, last accessed 2023/05/12
8. Murat, Y.Ş., Başkan, Ö.: Modelling vehicle delays at signalized junctions: Artificial neural networks approach. Journal of Scientific & Industrial Research, Vol. 65(1), 558-564 (2006).

Development of Pavement Condition Prediction Models in Urban Areas Using Micro PAVER

Turki I. Al-Suleiman (Obaidat)[1][0000-0001-3460-3275] and Linda Zaid Abu Ghazaleh[2][0000-0001-7860-5390]

[1] Professor of Civil Engineering, Civil Engineering Department, Jordan University of Science and Technology, Irbid, Jordan.
turk957@just.edu.jo
[2] Graduate Research Assistant, Civil Engineering Department, Jordan University of Science and Technology, Irbid, Jordan.
abugazllehlinda@gmail.com

Abstract. This study presents a pavement condition evaluation for the street network in Jerash city, Jordan. The Micro PAVER 5.2.3 Pavement Management System (PMS) developed by the US Army Corps of Engineers was used for the first time in Jordan to evaluate the pavement condition and develop sound pavement performance models. An integrated database was developed for the inspected pavement sections including information on pavement identification, construction and Maintenance and Rehabilitation (M& R) history, and pavement condition. The database consisted of 158 pavement sections representing three street classes (arterial, collector, and local) and ten administrative zones. The Pavement Condition Index (PCI) was used to represent the structural integrity and operational surface condition of the inspected pavement sections. It is a numerical index from 0 for failed pavement to 100 for a perfect pavement. The results of the pavement evaluation showed that the average pavement condition was fair with a mean age of 10.70 years. The Fourth polynomial function using Micro PAVER was applied to develop the most suitable models. The R^2 values for the polynomial models were found 0.718, 0.796 and 0.776 for the arterial, collector, and local streets, respectively. The results showed that the Micro PAVER prediction models can be used accurately to estimate the current and future pavement condition of the street network in urban areas.

Keywords: Micro PAVER, Pavement Condition, Prediction models, Urban Areas.

1 Introduction

Pavements are the major component in urban street networks. The major functions of pavements are to ensure comfortable and safely riding, water drainage and protection of subgrade soil. The performance of pavement is mainly affected by traffic loads and environmental conditions (Mfinanga et al. 1996), in addition to the quality of construction materials and Maintenance and Repair (M&R) practices (Adlinge and

Gupta, 2013). Keeping the pavement in good condition is one of the challenges facing governments and transportation agencies. This requires systematic methods to evaluate pavement conditions, estimate M&R needs, and set priorities.

Pavement condition evaluation is an important component of any Pavement Management System (PMS) because it provides the required database for developing pavement performance models. Pavement condition evaluation methods can be classified as subjective and objective. Subjective methods are used to assess the serviceability and consequently estimate the maintenance needs, and these are usually based upon the experience of the raters and reflect only the riding comfort of the road users. While objective methods depend on many factors such as the type, quantity and severity of pavement distresses. Also, destructive and non-destructive testing are considered objective procedures of pavement evaluation.

The most common and objective method of pavement condition evaluation is the PAVER system which was developed by U.S Army Crops Engineering (Shahin, 1994). This system used the pavement condition index (PCI). The PCI is a numerical index from 0 to 100 and depends mainly on the type, severity, and quantity of pavement distresses. The standard PCI is divided into seven different categories vary from failed too excellent.

The U. S Army Corps of Engineers developed the Micro PAVER as a computerized PMS to manage roads, streets, parking lots, and airfield pavements (Shahin, 1994). It provides many capabilities including pavement network inventory, pavement condition rating, development of pavement condition models, determining M&R alternatives, and performing life-cycle cost analysis to choose the best alternative (ERDC-CERL 2004).

Hosseini and Smadi, 2021) stated that the main element of any PMS is the development of pavement condition prediction models that can be employed to predict future pavement condition and consequently estimate the M&R needs. The aim of pavement condition prediction models is to investigate the effect of different factors on pavement deterioration. Pavement condition prediction models are mainly used to determine the required M&R activities, setting M&R priorities, and optimize the available budget.

(Kareem and Shubber, 2021) evaluated pavement condition by using the Micro PAVER version 5.2 for 4 collector roads in Najaf city, Iraq. (AL-neami et. al. 2017) developed a database for 10 roads in al-Cut city in Iraq include 8 internal and 2 external roads. The results showed that 48% of the evaluated sections were in good condition, 27% in poor condition, and 25% in fair condition. Based on these results, it was concluded that using the Micro PAVER will reduce the expected errors related to conventional method.

(Ahmad, 2014) used the Micro PAVER to develop pavement condition models. He studied the effects of different factors on pavement conditions. The results of his study showed that 59% of the distresses observed were due to other causes, while the percentages of load and environment related distresses were found 22% and 19%, respectively. He suggested using the developed pavement condition models in estimating the M & R needs. (Ali et. al. 2016) evaluated roads in central and eastern regions of Sudan by using the Micro PAVER. The results indicated that environmental conditions contributed to about 52.3% of the pavement distresses, 21.7% related to

traffic loading and 26% due to other causes. They concluded that the current maintenance practices are not based on scientific procedures and a computerized maintenance management system should be developed. (Moazami et al. 2010) used the Micro Paver to investigate the pavement condition of main streets in Tehran. The results showed that approximately 57% of sections surveyed were in very good and excellent condition.

2 Research Significance and Objectives

Jerash city is the center of Jerash governorate, has witnessed noticeable growth over the past decades due to the development of commercial and tourism activities. The city is the second tourist destination in Jordan behind the ruins of Petra. Jerash is one of the most important roman ancient cities, which makes it a place to attract tourists from all over the world.

Jerash city faces many challenges related to improper methods of pavement design, poor quality of construction, deterioration of pavements due to aging of the surface layer, and lack of regular maintenance plans because of limited financial resources. Most maintenance work depends mainly on complaints submitted by citizens. Moreover, utility cut patching due to excavations and installation of utilities are spread widely on the street network.

This study is considered significant because of two reasons. First, using the Micro PAVER 5.2.3 management system to evaluate pavement condition for the first time in Jordan. So, using this software will save time, and reduce the cost of data collection. Second, developing pavement performance models to be used in the future predictions of pavement condition and consequently estimate the timing and needs of M&R.

The following specific objectives were accomplished in this research effort:

1. Evaluating the pavement condition of the arterial, collector, and local streets using the Micro PAVER management system.
2. Development of pavement condition prediction models (polynomial regression models) for the three street classes using the Micro PAVER software.

3 Methodology and Database

An effective and successful pavement management system depends mainly on an accurate, reliable, and comprehensive database. To accomplish the objectives of this study, an integrated database of 158 pavement sections representing the street network in Jerash city was developed. The database included mainly information on pavement section identification, pavement construction and rehabilitation history, and pavement condition of the selected pavement sections.

Jerash city was divided into 12 administrative zones according to the Department of Engineering Affairs (DEA) in the Municipality of Greater Jerash (MGJ). Two zones were excluded because they are located in the ancient city and inspection activities are not allowed. According to the records of the MGJ, the total length of the street network

is about 683 km and the area of paved streets is equivalent to approximately 70% of the total city's street network (DEA, 2021). The streets of the city are classified into three classes: arterial, collector, and local streets.

The fundamental component of the database is the pavement section. A pavement section can be defined as a homogeneous stretch that has the same structure, traffic volume, rank and age. The pavement sections in this research were selected to cover most of the administrative zones and they should have considerable variations in pavement age, pavement condition, and traffic volume. This was assured during preliminary inspection before the development of the database. Table I shows the distribution of the selected pavement sections classified by zone and street class.

Table 1. Distribution of the selected pavement sections classified by zone and street class.

No.	Zone Name	No. of Pavement Sections			Total No. of Sections	Total Length (m)
		Arterial	Collector	Local		
1	Downtown	8	10	3	21	3164
2	Al-Kaerwan	3	1	4	8	982
3	As-Shaikh Mesleh	7	2	4	13	2028
4	Jabal Al-Atmat	3	8	9	20	2077
5	The Prince Hamzah bin Al-Hussain	2	2	7	11	1213
6	Dahr As-Sarou	7	10	11	28	4130
7	Al-Jabal Al-Akhdar	6	4	3	13	1920
8	The prince Ali Bin Al-Hussain	2	5	6	13	1526
9	Ad-Deir	10	3	5	18	2807
10	Al-Madinah Arryadeah	6	4	3	13	1770
	Total	54	49	55	158	21617

The database was developed from the following sources:

a. **Municipality of Greater Jerash (MGJ)**: the information of zone identification, street name and class, Street length and width, and Pavement age (year of construction or last major maintenance) about the selected pavement sections were collected from the available documents in the Department of Engineering and Technical Affairs in MGJ.

b. **Field Survey:** the division and definition of the street network to be inspected is the first step in the PMS, the network is usually divided into branches, sections, and sample units, which is the smallest component of the pavement network. It is used for inspection purposes with an area of about 233 ± 93 m². Each pavement section is divided into several sample units based on the length and width of pavement section.

The pavement inspection is a process in which distresses are determined, quantified, and recorded from the field following ASTM (D6433). It is accomplished by a team of at least two inspectors. The PAVER distresses identification manual (Shahin 1994) was used in the field to identify the existing distresses and their severities and quantities.

The application of Micro PAVER includes the following steps:

a. Select the unit of measurement: the quantities of distresses may by measured in square feet (square meters), linear feet (linear meters), or number of occurrences, depending on the distress type. In this study the distresses were measured using metric units.
b. Network Inventory Process: the inventory module provides an interface that enables the user to store all information about branches, and sections by code and name.
c. Calculation of Pavement Condition Index (PCI): PCI module provides the user with an interface to determine the number and size of inspected samples in each section, enter the distress information obtained from survey sheet for each sample unit, calculate the PCI and condition rating, extrapolate quantities of distresses, and determine the percentage of deduct values based on distress mechanism.

4 Results of Pavement Condition Evaluation

The main variables in this study are the Pavement Condition Index (PCI) and pavement age since construction or last major maintenance. Table 2 shows the statistical characteristics of the variables included for arterial, collector, and local streets. As shown in this table, the arterial streets had the lowest mean pavement age 8.17 years, with a standard deviation of 3.54 years. While the collector and local streets had mean pavement age of 11.33, and 12.62 years, with a standard deviation of 3.96, and 3.49 years, respectively. This indicates that the arterial streets receive most of the major maintenance work. This finding reflects a general policy in which the arterial streets had priority for M&R over collector and local streets. This trend seems to be practical and acceptable since arterial streets serve higher traffic volumes than other street classes. As shown in Table 2, the mean PCI for arterial, collector, and local streets were found equal to 56.68., 54.29, and 54.70, respectively. These results indicated that the collector and local streets have approximately the same mean PCI values and standard deviations. The average condition of arterial streets was rated fair, while the average conditions of collector and local streets were rated poor.

Table 2. The statistical characteristics of the analyzed variables for the evaluated pavement sections.

Variable		Arterial	Collector	Local
Age (years)	Min.	4.00	3.00	4.00
	Mean	8.17	11.33	12.62
	Max.	15.00	17.00	19.00
	Std. dev	3.54	3.96	3.49
PCI	Min.	25.00	19.00	17.00
	Mean	56.68	54.29	54.70
	Max.	83.00	92.00	90.00
	Std. dev	15.02	17.07	17.34

For arterial streets, it was found that 18.52% of the inspected sections were in satisfactory condition, 33.33% in fair condition, 29.63% in poor condition, 16.67% in very poor condition, and 1.27% were classified as being in a serious condition. For collector streets, 2.04% of the inspected sections were found in good condition, while 12.24, 36.73%, 26.53%, 16.33%, and 6.12% were found in satisfactory, fair, poor, very poor, and serious conditions, respectively. Where, 1.82% of local streets were in good condition, 21.82% in satisfactory condition, 25.45% in fair condition, 27.27% in poor condition, 18.18% in very poor condition, and 5.45% in serious condition. Most of the inspected sections of arterial and collector streets were in fair condition. While most of the inspected sections of local streets were in poor condition.

5 Development of Pavement Condition Models

Modeling of pavement condition can be conducted easily by using the Micro PAVER software. This software allows the user to define a family based on several factors including use, rank, surface type, zone, section category, last construction and rehabilitation date, and PCI. As mentioned variously, in this study pavement sections were grouped into three families with the same surface type, pavement use, and pavement rank.

The results of previous studies showed that PCI is strongly related to pavement age for a given pavement family. So, the prediction modeling tool in Micro PAVER was used to develop the PCI models for the three street classes with age as independent variable. Data filtering analysis was conducted to filter out doubtful data points at 95% (1.960) outlier boundary. The resulted polynomial models for arterial, collector, and local streets are presented in Equations 1, 2, and 3, respectively:

$$PCI = 100 - 3.03435Age - 1.56294Age^2 + 0.21218\,Age^3 - 0.00769Age^4 \quad (1)$$

$$PCI = 100 - 8.48029Age + 0.77724\,Age^2 - 0.03168\,Age^3 \quad (2)$$

$$PCI = 100 - 0.00001Age - 2.156Age^2 + 0.37Age^3 - 0.024Age^4 + 0.0005Age^5 \quad (3)$$

The fourth order polynomial function was resulted to predict the pavement condition for arterial street family, third order function for the collector street family, and fifth order for local street family. Table 3 summarizes the statistical characteristics of these models. As shown in this Table, the models were found highly significant with R^2 values equal to 0.718, 0.796, and 0.776 for arterial, collector, and local streets, respectively. This means that about 70% of PCI variation of arterial streets can be explained by pavement age. While approximately 80% of PCI of collector and local streets can be explained by pavement age. The remaining percentage of variation can be related to other factors such as traffic volume and loading, climate, and construction material and practices.

Table 3. Statistical Analysis of polynomial models in Equations 1-3.

Model in Equation	Coefficient of Correlation (R)	Approximate (R^2)	Standard Deviation of Error	Absolute Mean of Error	Arithmetic Mean of Error
1	0.847	0.718	8.47	6.701	0.012
2	0.892	0.796	8.234	6.525	0.084
3	0.881	0.776	8.741	6.603	0.059

Figures 1-3 show the pavement life prediction curves for arterial, collector, and local streets, respectively. As shown in these figures, one section was found out of bound state for each prediction model. These figures show an envelope containing most of the data (95% confidence limits). Pavement sections located within that envelope are classified as deteriorating at a normal rate; the points above the envelope is classified as having low deterioration rate, and those below the envelope as having a high deterioration rate. It was observed that the deterioration of arterial streets was faster than that of local and collector streets. This can be explained by the fact that arterial streets receive higher traffic volumes and loading than collector and local streets. Although the arterial streets receive more maintenance works,this practice is not sufficient. The deterioration rate of collector streets was found faster than that of local streets. Also, a high deterioration rate for arterial streets was found during the first 4 to 6 years. While, for collector and local streets, the high deterioration occurred after 8 years.

Pavement life prediction curves can be used effectively to estimate the critical PCI. Critical PCI is defined as the value at which the pavement deterioration starts increasing rapidly, or the cost of conducting localized pavement maintenance increases significantly. Usually, critical PCI values range from 55 to 70 (Shahin 1994). In this study, as shown in Figures 1-3, the critical PCI values for arterial, collector, and local streets were found equal to 60, 55, and 50, respectively. The application of major M&R activities depends mainly on the critical PCI value and funds availability. For example, if the PCI value for any arterial street in Jerash city is below 60, major M&R should be applied according to funds availability.

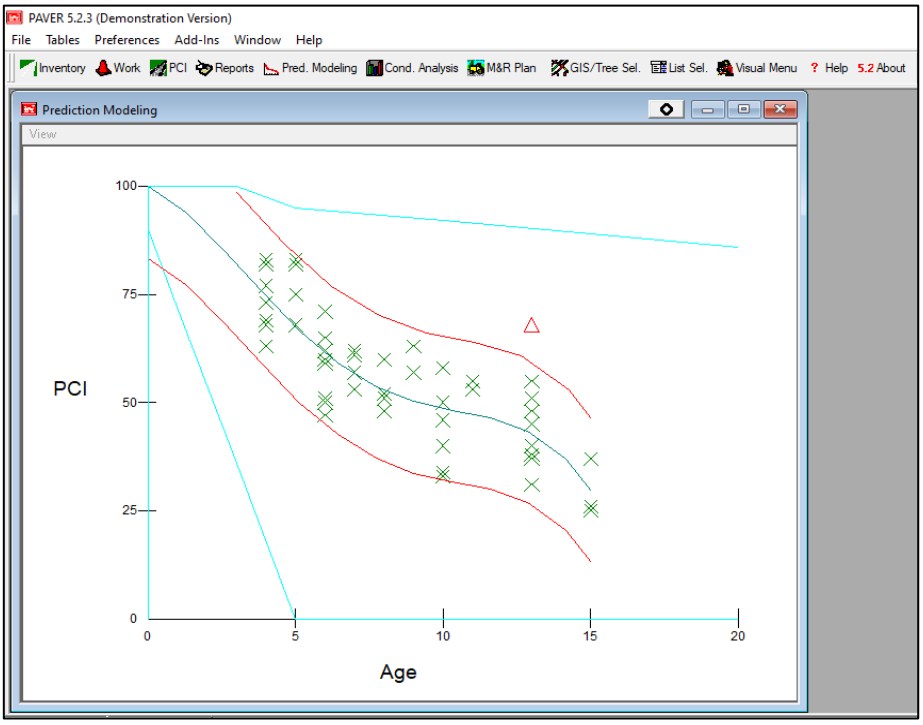

Fig. 1. Pavement condition prediction curve using Micro PAVER for arterial streets.

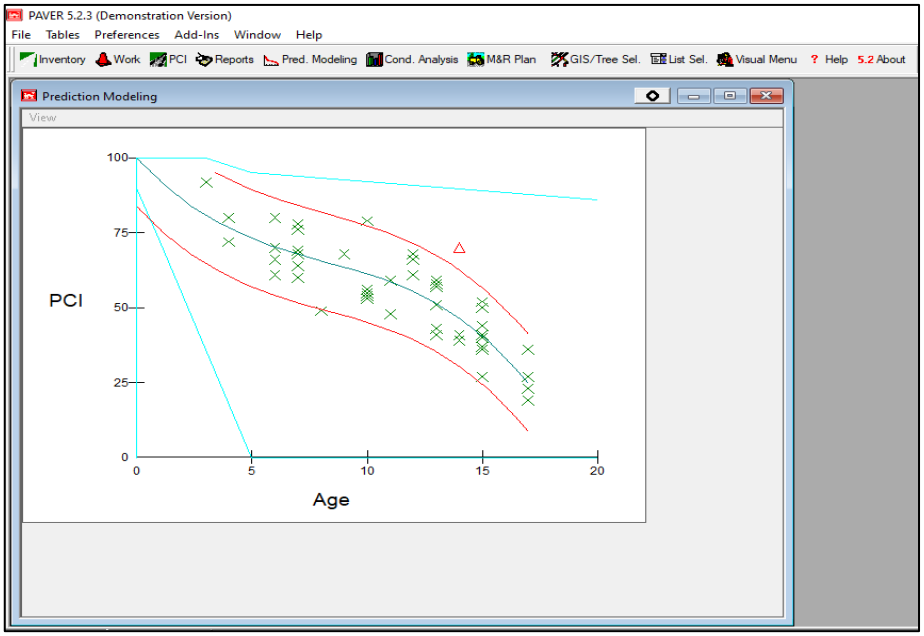

Fig. 2. Pavement condition prediction curve using Micro PAVER for collector streets.

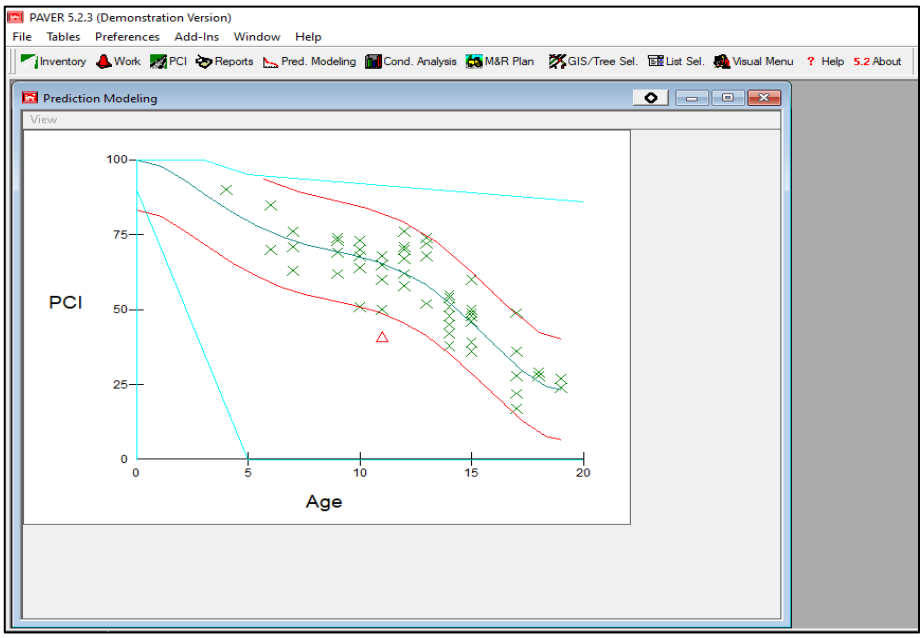

Fig. 3. Pavement condition prediction curve using Micro PAVER for local streets.

6 Conclusions and Recommendations

This study was conducted to evaluate pavement condition and pavement deterioration of the street network in Jerash city, Jordan. A database covering 158 pavement sections was developed. It represented three street classes and ten administrative zones. The pavement sections were evaluated by visual inspection and using the Micro PAVER software. The database was used to develop pavement condition prediction models. Based on the finding presented in this study, the Micro PAVER was found to be a suitable tool to develop pavement condition prediction models and estimate M&R needs. The results showed that the Micro PAVER prediction models can be used to estimate the current and future pavement condition of the street network in the Municipality of Greater Jerash (MGJ). Based on the analysis presented in this research, the following conclusions can be drawn:

1. The average pavement age of the street network in Jerash city was found to be equal to 10.70 years, with average Pavement Condition Index (PCI) of 55.24 indicating that the average pavement condition rating was Fair.
2. The lowest average pavement age was found for arterial streets, with average condition index (PCI) equal to 56.68 indicating that the average pavement condition was Fair. Where, the average condition of collector and local streets were rated poor.

3. It was found that 16.67%, 16.33%, and 18.18% of the inspected pavement sections were found in very poor condition for arterial, collector, and local streets, respectively.
4. The developed pavement condition prediction models (polynomial models) using Micro PAVER were found highly significant with relatively high R^2 values (0.718 for arterial streets, 0.796 for collector streets, and 0.776 for local streets).

Based on the findings of this study, the following recommendations should be taken into consideration:

1. A database for the street network in Jerash city should be developed to include all historical and geometrical data in order to develop a comprehensive and integrated pavement management system which will help the decision makers to evaluate pavement condition and estimate M&R needs and priorities.
2. Using the Micro PAVER software will simplify the computation of pavement condition index (PCI) and development of pavement condition prediction models.

References

1. Adlinge S, Gupta K.: Pavement deterioration and its causes. International Journal of Innovative Research and Development, 2 (4), 437-450 (2013).
2. Ahmed N, Awda G, Saleh S.: Development of pavement condition index model for flexible pavement in Baghdad City", Journal of Engineering, 14 (1). 2120-2135(2008).
3. Ali A, Eisa M, Suleiman E.: Use of Micro Paver Program for Pavement Maintenance Management System (PMMS) of Roads in Central and Eastern Sudan", Journal of Building and Road Research, 12(1) (2016).
4. Al-Neami M, Al-Rubaee, R. H., Kareem, Z. J.: Evaluation of Pavement Condition Index for Roads of Al-Kut City. International Journal of Current Engineering and Technology, Vol. 7 No. 4, pp. 1461-1467(2017).
5. Department of Engineering Affairs (DEA) (2021), Jerash Municipality Records. Municipality of Greater Jerash.
6. Hosseini S, Smadi O.: How prediction accuracy can affect the decision-making process in pavement management system. Infrastructure. 6(2), 28 (2021).
7. Kareem S, Shubber, K.: Pavement condition index (PCI) for some highways collector selected in Najaf city implemented with PAVER software. Journal of Physics: Conference Series, 1895(1),012021(2021).
8. Mfinanga, D. A, Ochiai, H., Yasufuku, N.: Traffic loading and environmental effects on asphalt pavement rutting. Memoirs-Faculty of Engineering Kyushu University 56 (3), 149-170 (1996).
9. Moazami D, Muniandy R, Hamid, H., Yusoff, Z. M.: "Developing a comprehensive pavement management system in Tehran, Iran using Micro PAVER. Electron. Journal of Geotechnical Engineering, (15)1782-1792.
10. Shahin, M. Y.: Pavement management for airports, roads, and parking lots, Kluwer Academic Publishers, Norwell, Massachusetts (1994).
11. U.S. Army Engineering Research and Development Center-Construction Engineering Research Laboratory (ERDC-CERL). (2004), Micro PAVER Pavement Management System, www.cecr,army.mail/paver.

Investigating the Tensile Properties of Geocell Reinforced Pavement System Using a 2D FE Model

Yalcin Karakaya[1][0000-0003-1036-7941], Dilay Yildirim Uncu[2][0000-0001-8660-2114], Adem Ozer[3][0000-0002-3447-3901]

[1] Manisa Celal Bayar University, Civil Engineering Department, Manisa, Turkey, yalcin.karakaya@cbu.edu.tr
[2] Manisa Celal Bayar University, Civil Engineering Department, Manisa, Turkey, dilay.yildirim@cbu.edu.tr
[3] Manisa Celal Bayar University, Civil Engineering Department, Manisa, Turkey, adem.ozer@cbu.edu.tr

Abstract. The use of geocells is one of the most effective methods to increase the support beneath pavement where the existing soil is weak. Several studies in literature have shown that the bearing capacity of granular material is increased by the use of geocells. However, the effect of this modulus increase on the overall pavement performance has not been fully investigated. In this study, the tensile properties of a simple pavement system are investigated when the geocell is incorporated into the base course. The 2D FE model with plane strain was created in ABAQUS. The three-layer pavement system is modeled with a viscoelastic HMA layer, a linear elastic base layer, and a subgrade with Mohr-Coulomb plasticity. The effects of using geocells are simulated using modulus improvement factors from the literature. In addition, the effects of different subgrade conditions are also studied to see the improvement of geocells under different conditions. The results have shown that the use of geocells in the base course reduces the vertical deformations by up to 22% at the surface and up to 20% at the top of the subgrade. A reduction in horizontal stresses and strains of up to 71% and 61%, respectively, was observed at the bottom of the HMA layer. In addition, the effect of geocell improvement was higher when the subgrade was weak. In general, the higher the CBR value of the subgrade, the lower the percentage reductions in the tensile properties of the system.

Keywords: Geocell, 2D Finite Element Model, Prony Pairs, Pavement, Tensile Properties.

1 Introduction

Flexible pavements flex with traffic loads, making them less susceptible to damage and requiring less frequent maintenance. The amount of deflection can be quite large, especially if the existing soil is weak and cannot adequately support the pavement. When the tensile stresses reach the material limit, cracking of the pavement occurs. One of the most effective methods of increasing the bearing capacity of the pavement is the

use of geocells. Geocell is a type of geosynthetic manufactured in the form of three-dimensional honeycomb-like structures made from high-density polyethylene (HDPE) or other plastic materials [1, 2]. Due to their porous and clamped structure, geocells are distinguished from other improvement methods by creating a compacting effect and limiting the soil they are used in [3]. In weak soils where geocells are used, it compresses the soil towards the cells and acts like a reinforced material with the ground, limiting lateral movement [4].

Cellular lateral confinement, which was designed to improve the bearing capacity of poorly graded sand, was first developed and tested by the US Army Corps of Engineers in the 1970s [2]. These cells are interconnected and filled with aggregate, soil or other materials, creating a stable and permeable foundation for a variety of transportation infrastructure projects. The utilization of geosynthetic reinforcement has resulted in augmented bearing capacity and modulus, decreased base thickness requirements, prolonged pavement lifespan, lowered operational expenses, and decreased maintenance needs [5, 6]. It also saves the use of a new filling material by keeping the low-quality filling material in the field [7-10]. As a result of limiting lateral deformation, geocells increase the stabilization of the soil by showing an additional cohesion formation to the soil structure [11-13]. Due to its three-dimensional structure, geocells increase the load carrying capacity by acting as a raft foundation and distributing the pavement, ground, traffic and surcharge loads over a wide surface. Depending on the increase in the bearing capacity, the layer thickness and the amount of ground subsidence decrease [14].

Geocells can be used in a number of different transportation applications such as roadway construction, bridge abutments, slope stabilization, parking areas and railways. Geocell applications in transportation infrastructure have been developed in recent years in field and laboratory tests, performance evaluation, computer modelling and case studies actually [1, 15-19]. In the case of pavement consisting of unbound granular materials, it is known that the modulus of elasticity of these layers is directly affected by the modules of the underlying subgrade [20]. Therefore, understanding the behavior of unbound granular materials in the pavement structure is part of recognizing how the geocell can behave in this environment, improving overall pavement structural performance [21]. The majority of the existing research has also concentrated on examining the response of geocell-reinforced bases when exposed to static loading. However, geocells used in pavement applications are subjected to cyclic loading. There has been a scarcity of investigations carried out to evaluate the effectiveness of geocell-reinforced bases under repeated loading [1]. This is because modeling the stress caused by traffic on the pavement layer system is a highly complex process. Various variables are involved in determining the pressure caused by traffic, such as the vehicle's mass, the number of axles and wheels, the spacing between the axles, and the tire's contact patch.

In this study, information about pavement layer system, traffic loading conditions, material properties, finite element modelling and analyses was discussed in finite element chapter. The data obtained as a result of the analysis were examined in the results and discussion chapter.

2 Finite Element Modelling

2.1 Geometric Model

To evaluate the effect of geocell reinforcement on the overall pavement performance, an example pavement layer system was created. In this system, three different layers were distinguished: HMA layer, base layer and subgrade. These layers and the selected thicknesses are shown in Figure 1. At the top, the HMA layer was created with a thickness of 15 cm to simulate the asphalt concrete layer in a typical pavement system. Below, the base course, which represents the foundation layer of granular material in the field, was selected with a thickness of 25 cm. Finally, the subgrade layer, representing the existing soil, was created with a thickness of 2 m. Although the general theory assumes that the existing soil goes to infinity, it was decided that a soil layer of only 2 m was sufficient. Since this study investigates the stresses and strains at the top of the subgrade, a layer thickness of 2 m was considered sufficient to prevent stress accumulation at the lower boundary. For the same reason, the horizontal dimension of the geometric model was set at 5 m in total.

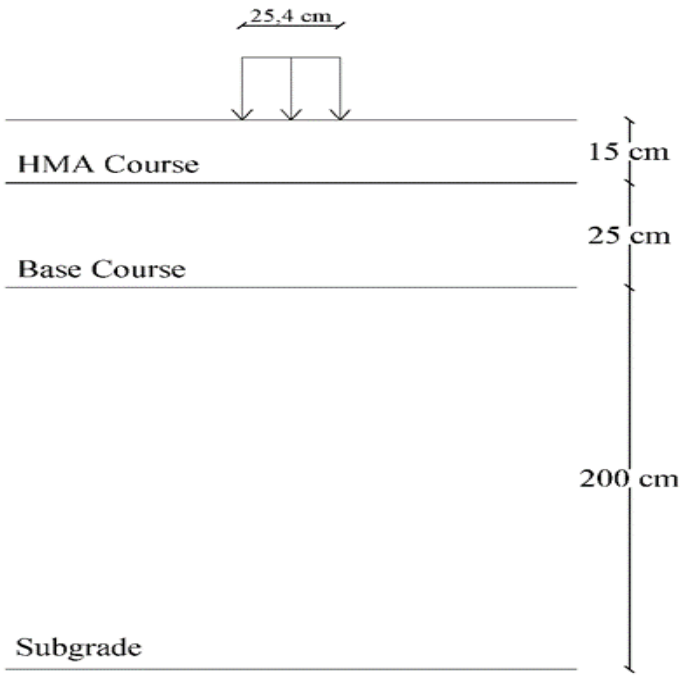

Fig. 1. Pavement layer system created in ABAQUS.

2.2 Loading

Simulating the traffic load acting on the top of the pavement layer system is a very complicated procedure. Several factors play a role in determining the traffic load pressure, such as the weight of the vehicle, the number of wheels and axles, the distance between the axles, and the contact area of the tires. In this study, the AASHTO tire contact area was chosen, which is assumed to be a rectangle with a width of 20" and a length of 10" [22]. In the same AASHTO guide, the road load is divided into four different classes. For this study, the loading type HS -20 was selected and applied to the previously selected tire contact area. A standard axle load of 32 kips (16 kips wheel load) was selected for the HS loading, so a stress level of 80 psi (0.55 MPa) was applied to the top surface of the pavement structure.

2.3 Materials

In the FE model, the HMA layer represents the asphalt concrete layer that exhibits viscoelastic behavior. Therefore, a viscoelastic material model was needed. In this context, the time-domain VE material model of ABAQUS was used in the form of Prony series coefficients. The method uses the following generalized Maxwell model equations to simulate VE material behavior using Prony series coefficients:

$$G_{(t)} = G_0\left(1 - \sum_{k=1}^{n} G_i(1 - e^{-t/\tau_i}\right) \quad (1)$$

$$K_{(t)} = K_0\left(1 - \sum_{k=1}^{n} K_i(1 - e^{-t/\tau_i}\right) \quad (2)$$

where G(t) is the relaxation shear modulus; K(t) is the bulk modulus; G0 is the instantaneous shear modulus; K0 is the instantaneous bulk modulus; G_i, K_i, and τ_i are the input coefficients. Gu et al. (2016) implemented this method in their 2D FE pavement model to simulate the viscoelastic material behavior of a HMA layer section. In this study, the Prony series coefficients calculated by fitting the dynamic modulus test results are used (see Table 1) [23]. In the elastic part of the VE material behavior, the instantaneous elastic modulus is calculated from the instantaneous shear modulus, and the Poisson's ratio was assumed to be 0.3 (approximate value for asphalt concrete). The other material properties estimated for each type of layer can be found in Table 2. In the analysis, 4-node, liner and quadrilateral elements were used to model the different layers. In addition, the problem was simulated in the 2D FE environment using plane strain theory.

Table 1. Prony series model coefficients after Gu et al. 2016.

Prony Series Coefficients		
G_1 = 0.362	K_1 = 0.362	τ_1 = 4.09E-06
G_2 = 0.363	K_2 = 0.363	τ_2 = 2.56E-04
G_3 = 0.177	K_3 = 0.177	τ_3 = 7.71E-03
G_4 = 0.074	K_4 = 0.074	τ_4 = 2.10E-01
G_5 = 0017	K_5 = 0.017	τ_5 = 3.88E+00
G_6 = 0.006	K_6 = 0.006	τ_6 = 6.53E+01

Table 2. Material properties for each layer type.

Layer	Material Behavior	Properties
HMA Course	Viscoelastic	γ = 2400 kg/m^3 E_0 = 18,130 Mpa ν = 0.30
Base Course	Linear Elastic	γ = 2100 kg/m^3 E = 50 Mpa ν = 0.35
Subgrade	Mohr Coulomb Plasticity	γ = 1600 kg/m^3 E = 1.502 MPa ν = 0.4 ϕ = 30° ψ = 1

2.4 Sensitivity Analysis

Meshing is of great importance when simulating real-world problems in a finite element environment. While the appropriate mesh size determines the accuracy, convergence, success and speed of the simulation, finer meshes take more time to solve. There is a point at which the mesh is fine enough to accurately calculate the results, and beyond that, additional computational effort is unnecessary. Sensitivity analysis in ABAQUS is about balancing accuracy and computational effort. To this end, when building the geometric model, an attempt is made to determine the optimal mesh size by examining the effects of different mesh sizes on the model results. Figure 2 below shows the effects of different mesh sizes on the maximum vertical deformation values at the top of the pavement. As can be seen from the figure, the effect of mesh size on the results is minimized after less than 5 mm. Therefore, the optimum mesh size in the model is set to 5 mm, resulting in a total number of 480,480 elements.

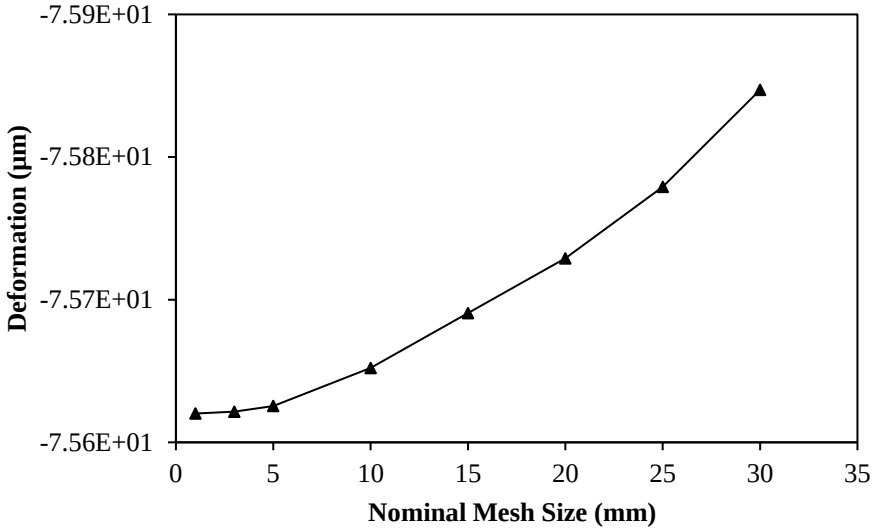

Fig. 2. The effect of mesh size on vertical deformation.

2.5 Analyses

The model is encastered at the bottom and the deformations of the sides were prevented in the horizontal direction (U1 = 0). The analysis were performed using the "visco" step type and the time-dependent load was applied to the viscoelastic HMA surface layer in one second. The results for stress, strain and deformation were assumed to be maximum values. An example of the model output is given in Figure 3. Three of the most important tensile properties, i.e., the vertical deformation at the top of the HMA layer, the vertical deformation at the top of the subgrade, and the horizontal strain at the bottom of the HMA layer, are evaluated under different conditions.

The effect of geocell reinforcement on overall pavement performance was simulated by considering modulus improvement in the granular base course. The initial modulus value of the unreinforced base course was estimated to be 50 MPa. Based on the literature review in the first chapter, the geocellular modulus improvement factors were set to 1.2, 1.5, 2.0, 2.5, and 3.0. In addition, the impact of the subgrade was evaluated using different CBR values, i.e., 2%, 5%, 10%, 20%, and 30%. Generally, geocell reinforcement is used in weak subsoil conditions. The effects of bearing capacity of the subgrade on the results of geocell reinforcement were also investigated in a stepwise manner up to a CBR value of 30%. However, in ABAQUS, the California Bearing Ratio values had to be converted to the corresponding Elastic Modulus (E) values. There are several methods in the literature that correlate the CBR value of the subgrade to the E value. The following equations are used to convert the subgrade CBR values to elastic modulus values [24].

$$E = 863.82\ CBR\ (kPa), \nu = 0 \quad (3)$$

$$E = 840.53\ CBR\ (kPa), \nu = 0.3 \quad (4)$$

$$E = 751\ CBR\ (kPa), \nu = 0.4 \quad (5)$$

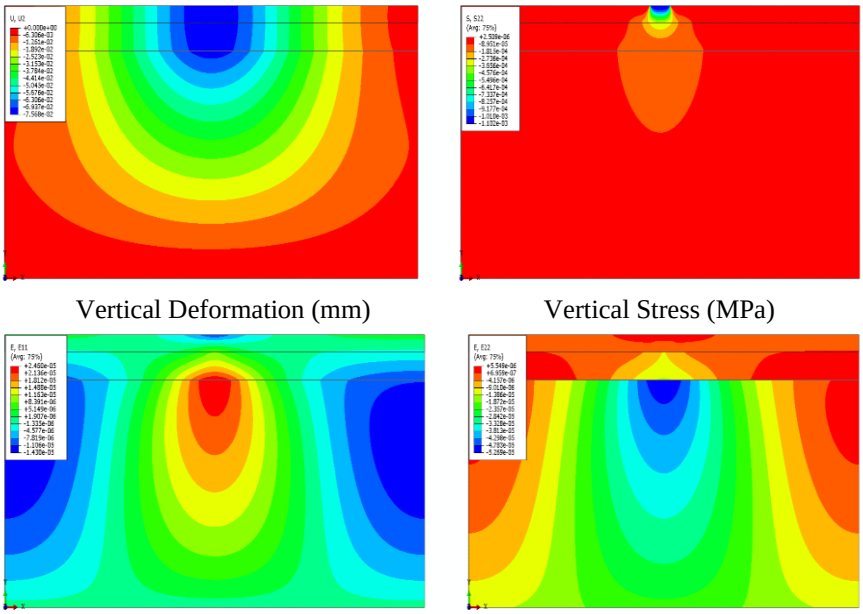

Vertical Deformation (mm) Vertical Stress (MPa)

Horizontal Strain (mm/mm) Vertical Strain (mm/mm)

Fig. 3. FE model results.

3 Results and Discussion

3.1 Vertical Deformations

Vertical deformations in pavement are very critical in two places, at the surface, where vertical stresses are greatest, and at the top of the subgrade, which is the weakest structure in the system. One of the main factors in causing these vertical deformations is inadequate support under the asphalt layer. Insufficient bearing capacity or insufficient thickness of the base course leads to an increase in these vertical deformations both at the surface and at the top of the subgrade.

Figure 4 shows the maximum vertical deformations at the top of the HMA layer. The modulus improvement factors represent the improvement of the geocells in the granular base course, i.e., 1.0 means unreinforced, 1.2 corresponds to a 1.2-fold increase in the

elastic modulus of the base course, etc. In addition, the effects of Geo cellular improvement under different subgrade conditions with different CBR values are also indicated in the figure. It can be seen that the improvement of maximum vertical deformations by the geocell is better when the subgrade is weak. The stronger the subsoil becomes, the lower the improvement of deformation.

Table 3 shows the effect of geocell reinforcement in the granular base course on the maximum vertical deformations under the standard axial load in percent. These percentages are the comparative values for how much the deformation decreases compared to the unreinforced section. When the subgrade is weak (CBR 2%), the use of geocells reduces surface settlement by up to 22%. Even if the improvement factor is moderate, i.e., about 1.5 times, the application of geocells can reduce surface settlement by about 9%. In addition, the contribution of geocells to vertical settlement decreases as the subgrade becomes firmer.

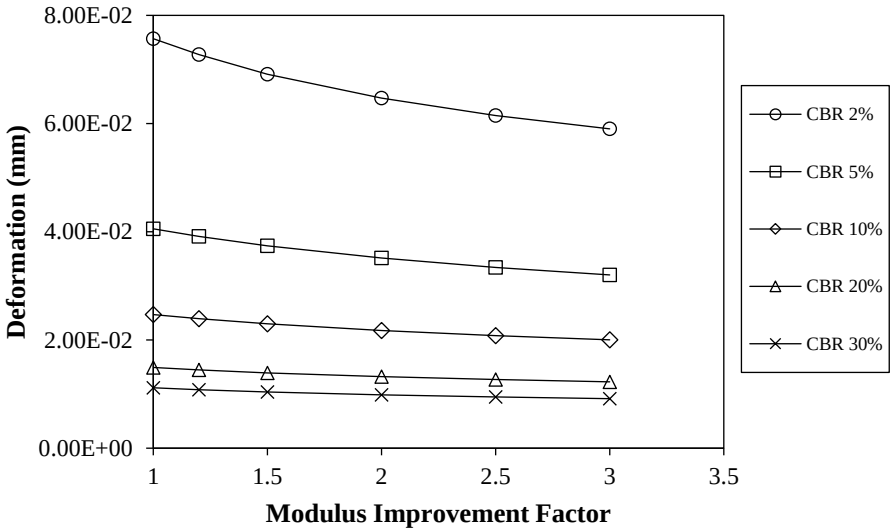

Fig. 4. Maximum vertical deformations at the surface.

Similar trends were also observed for the maximum vertical deformations at the top of the subgrade. The corresponding results are shown in Table 4. Again, the maximum settlements at the top of subgrade are reduced by up to 20% when the subbase is reinforced with geocells. These improvements are higher when the subgrade is weak. In addition, the improvements in maximum vertical deformations at the surface are higher than those at the top of the subgrade. This indicates that the application of geocells affects the settlements at the top of the pavement better than at the bottom.

Table 3. Geocell improvement in maximum vertical deformations at the surface.

Improvement Factor	% Reduction of the Vertical Deformations				
	CBR %2	CBR %5	CBR %10	CBR%20	CBR %30
1.2	3.88	3.43	3.24	3.06	3.03
1.5	8.67	7.73	7.05	6.89	6.80
2.0	14.53	13.33	11.89	11.45	11.33
2.5	18.78	17.61	15.77	15.28	14.93
3.0	22.02	21.02	18.90	18.06	17.79

Table 4. Geocell improvement in maximum vertical deformations at the top of subgrade.

Improvement Factor	% Reduction of the Vertical Deformations				
	CBR %2	CBR %5	CBR %10	CBR%20	CBR %30
1.2	3.64	3.03	2.40	1.86	1.59
1.5	8.17	6.91	5.53	4.33	3.72
2.0	13.72	12.04	9.80	7.76	6.72
2.5	17.77	16.03	13.22	10.56	9.20
3.0	20.86	19.22	16.04	12.90	11.28

3.2 Horizontal Stresses and Strains

Traffic loading causes flexible pavements to flex or sag, making them less susceptible to damage and requiring fewer repairs over time. When the HMA layer flexes, the highest tensile stresses occur at the bottom of the layer, where the tensile stresses are greatest. However, when these stresses exceed the tensile strength of the HMA, they cause cracking, from which various other pavement damages originate. Therefore, controlling the horizontal stress and strain values at the bottom of the HMA layer is very important for pavement construction.

The resulting maximum horizontal stresses at the bottom of the HMA layer are shown in Figure 5. Similar trends were observed in the results for horizontal stresses. First of all, the application of geocells has a stronger influence than the previous results. Similar to the vertical strain results, geocell reinforcement increases the support under the HMA layer and consequently reduces the maximum horizontal strains at the bottom of the HMA. As the factors to increase the modulus of elasticity increase, the reduction in tensile stresses continues. However, as the CBR value of the subgrade increases, the effect of the geocell improvement factor decreases. At about 3 times the initial modulus of elasticity of the base course, the horizontal stresses at the bottom of the HMA layer are very similar for the different CBR values of the subgrade. This indicates that geocell improvement increases the elastic modulus of the base course beyond a certain point to

the point where subgrade soil conditions have minimal effect on the maximum horizontal tensile stresses at the bottom of the HMA layer.

The percent reduction in horizontal stress and strain values at the bottom of the HMA layer is given in Table 4 and 5, respectively. The effect of geocell application is higher than the previous deformation results for both results. The maximum horizontal stress and strain at the bottom of the HMA layer are reduced by up to 71% and 61%, respectively. It can be seen that the percentage reduction is higher for the stress values than for the strain values. Similarly, the contribution of geocells decreases as the strength of the subgrade increases, indicating that the application of geocells is more effective when the bearing capacity of the subgrade is weak.

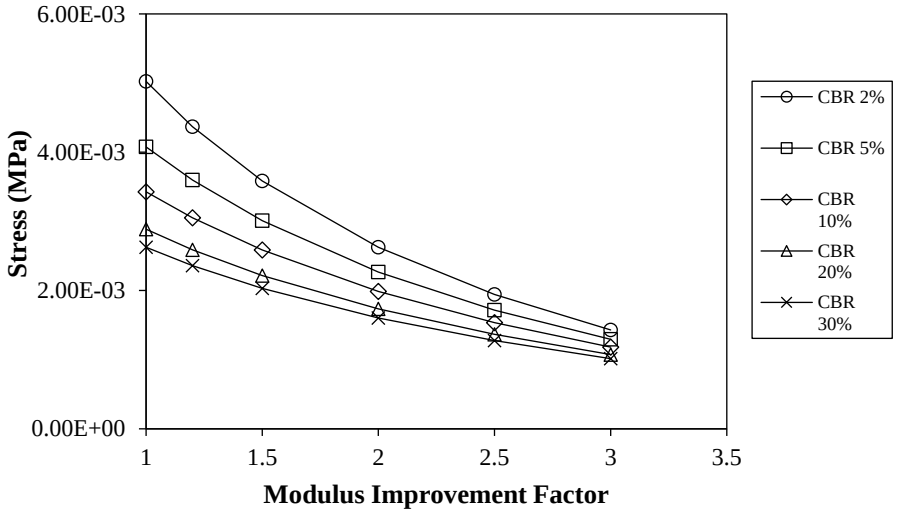

Fig. 5. Maximum horizontal stresses at the bottom of the HMA layer.

Table 5. Geocell improvement in maximum horizontal stresses at the bottom of HMA.

Improvement Factor	% Reduction of the Horizontal Stresses				
	CBR %2	CBR %5	CBR %10	CBR%20	CBR %30
1.2	13.03	11.74	10.94	10.33	10.10
1.5	28.66	26.16	24.54	23.21	22.66
2.0	47.73	44.39	42.02	39.92	38.94
2.5	61.34	57.87	55.20	52.69	51.42
3.0	71.54	68.26	65.53	62.80	61.35

Table 6. Geocell improvement in maximum horizontal strains at the bottom of HMA.

Improvement Factor	% Reduction of the Horizontal Stresses				
	CBR %2	CBR %5	CBR %10	CBR%20	CBR %30
1.2	10.88	9.59	8.80	8.20	7.97
1.5	24.12	21.54	19.86	18.53	17.96
2.0	40.56	36.90	34.32	32.11	31.07
2.5	52.51	48.45	45.41	42.65	41.26
3.0	61.59	57.49	54.23	51.12	49.48

3.3 Pavement Depth

The effect of geocell reinforcement on vertical deformations along the pavement depth is shown in Figure 6. In the figure, the results are based on the weak subgrade conditions (CBR 2%) since the improvement due to the geocells had previously peaked. It can be seen that the application of geocells on the base course not only reduces the vertical settlements at the top, but the reduction is significant throughout the pavement depth. Vertical deformations are similarly reduced in both HMA and base course as the modulus improvement factor increases. In the subgrade, the effect of the geocells decreases with increasing depth. In addition, the accumulated strain values in the HMA and base course are close to each other (see Figure 7). However, higher modulus improvement factors result in lower vertical strains at the top of the subgrade.

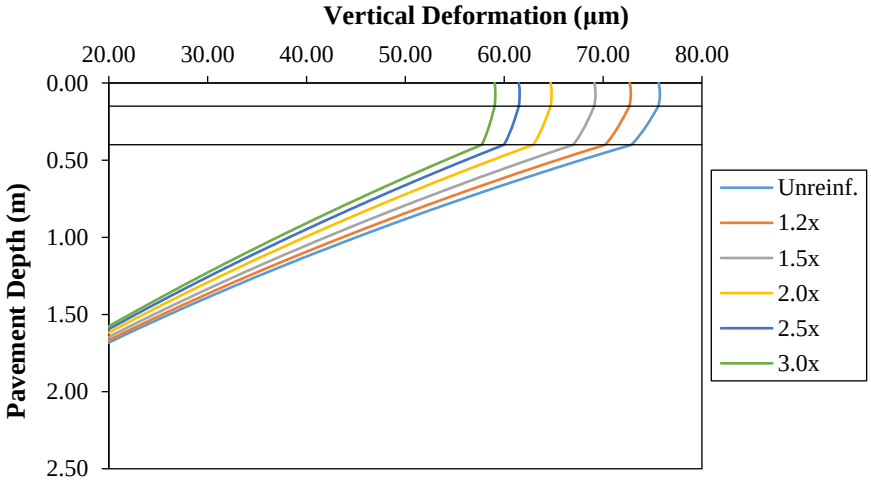

Fig. 6. Vertical deformations along the pavement depth (subgrade CBR 2%).

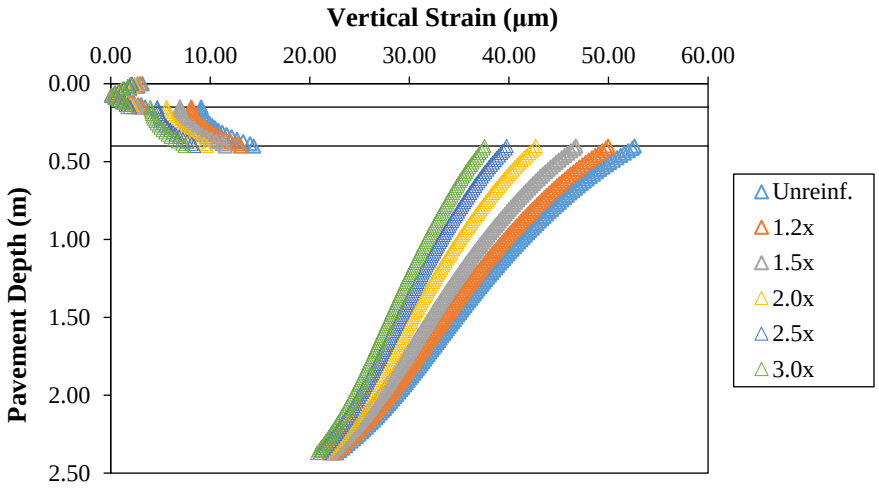

Fig. 7. Vertical strains along the pavement depth (subgrade CBR 2%).

4 Conclusions

In this study, the effect of using geocells in a layered pavement system was investigated using a 2D finite element model with plane strain. The basic pavement system was modeled with a viscoelastic HMA layer, a linear elastic base layer, and a subgrade with Mohr-Coulomb plasticity. All material properties used in ABAQUS were estimated from literature. Then, the effect of improving the geocells in a granular base course was simulated by increasing the elastic modulus of the course with an improvement factor. Similarly, the modulus improvement factors of the geocell application were selected based on several empirical tests from the literature. While the effects of different improvement factors and bearing capacities of the subgrade were investigated, the other parameters of the system remained constant. A standard axle load (AASHTO HS -20) was applied, and the resulting various tensile properties were analyzed. The following results can be summarized:

- Vertical deformations at the top of the pavement were reduced by up to 22% when the base course was reinforced with geocells. While the greatest improvement was observed at the lowest subgrade conditions (CBR 2%), the effect of geocell reinforcement decreased with increasing subgrade bearing capacity.
- Similarly, vertical deformations at the top of the subgrade were reduced by up to 20% when the geocell improvement factor was highest and the subgrade had the lowest CBR value. The percentage reduction in vertical deformations decreased when the subgrade had higher CBR values.
- The percent reduction in horizontal stresses and strains at the bottom of the HMA layer was up to 71% and up to 61%, respectively. The reductions were more

significant with weak subgrade. Even with strong subgrade, the improvement in horizontal stresses and strains due to the geocells was quite high.

- Vertical deformations through the pavement depth were significantly reduced even though the geocells were applied only to the base course. While the vertical strain values were close at the surface, the greatest improvement was observed at the top of the subgrade.

Only a single load was applied in the 2D model FE, and the resulting maximum deformations, stresses and strains were calculated. The viscoelastic material behavior of the HMA layer requires a more detailed time-dependent cyclic loading that can simulate the real traffic load. Therefore, it is recommended to investigate the effect of geocell improvement by loading and unloading cycles to more clearly identify the elastic and plastic deformations in the pavement system.

The authors declare that they have no known competing financial interests or personal relationships that could have appeared to influence the work reported in this paper.

References

1. Pokharel, S.K., Han, J., Leshchinsky, D., Parsons, R.L.: Experimental evaluation of geocell-reinforced bases under repeated loading. International Journal of Pavement Research and Technology 11, 114-127 (2018).
2. Pokharel, S.K., Han, J., Manandhar, C., Yang, X., Leshchinsky, D., Halahmi, I., Parsons, R.L.: Accelerated pavement testing of geocell-reinforced unpaved roads over weak subgrade. Transportation Research Record: Journal of the Transportation Research Board 2204, 67-75 (2011).
3. Akyıldız, M.H., Adar, K., Özdemir, S.S.: Usage of cell filling systems in civil engineering applications. Dicle University Journal of Engineering 13(3), 551-555 (2022).
4. Zhou, H., Wen, X.: Model studies on geogrid- or geocell-reinforced sand cushion on soft soil. Geotextiles and Geomembranes 26(3), 231-238 (2008).
5. Giroud, J.P., Han, J.: Design method for geogrid-reinforced unpaved roads. I. Development of design method. ASCE, Journal of Geotechnical and Geoenvironmental Engineering 130 (8), 775-786 (2004).
6. Giroud, J.P., Han, J.: Design method for geogrid-reinforced unpaved roads. II. Calibration of applications. ASCE, Journal of Geotechnical and Geoenvironmental Engineering 130 (8) 787-797 (2004).
7. Tanyu, B.F., Aydilek, A.H., Lau, A.W., Edil, T.B., Benson, C.H.: Laboratory evaluation of Geocell reinforced gravel subbase over poor subgrades. Geosynthetics International 20(2), 47-61 (2013).
8. Gurbuz, A., Mertol, H.C.: Interaction between assembled 3-D honeycomb cells produced from high density polyethylene and a cohesionless oil. Journal of Reinforced Plastics and Composites 31, 828-836 (2012).
9. Biabani, M.M., Indraratna, B., Ngo, N.T.: Modelling of geocell-reinforced subballast subjected to cyclic loading. Geotextiles and Geomembranes 44, 489-503 (2016).
10. Hegde, A., Sitharam, T.G.: Experiment and 3D numerical studies on soft clay bed reinforced with different types of cellular confinement systems. Transportation Geotechnics 10, 73-84 (2017).

11. Yünkül K., Gürbüz A.: Hücresel Dolguların Kullanım Alanları ve Çalışma Mekanizması. In: SETSCI. International Symposium on Innovative Approaches in Smart Technologies, pp. 354-360 Antalya, Türkiye (2018).
12. Latha G.M., Murthy V.S.: Effect of reinforcement form on the behaviour of geosynthetic rein forced sand. Geotextiles and Geomembranes 25, 23-32 (2007).
13. Chen R.H., Huang Y.W., Huang F.C.: Confinement effect of geocells on sand sample sunder triaxial compression. Geotextiles and Geomembranes 37, 35-44 (2013).
14. Akyıldız M.H.: Geosentetik türlerinin inşaat mühendisliğindeki uygulamaları ve sağladığı kolaylıklar. DÜMF Mühendislik Dergisi 10(2), 791-796 (2019).
15. George, A.M., Banerjee, A., Puppala, A.J., Saladhi, M.: Performance evaluation of geocell-reinforced reclaimed asphalt pavement (RAP) bases in flexible pavements. International Journal of Pavement Engineering 22, 181-191 (2021).
16. Han, J., Pokharel, S.K., Yang, X., Manandhar, C., Leshchinsky, D., Halahmi, I., Parsons, R. L.: Performance of geocell-reinforced RAP bases over weak subgrade under full-scale moving wheel loads. Journal of Materials in Civil Engineering 23, 1525-1534 (2011).
17. Han, J., Yang, X., Leshchinsky, D., Parsons, R.L.: Behavior of geocell-reinforced sand under a vertical load. Transportation Research Record 2045, 95-101 (2008).
18. Navaratnarajah, S.K., Indraratna, B., Ngo, N.T.: Influence of under sleeper pads on ballast behavior under cyclic loading: experimental and numerical studies. Journal of Geotechnical and Geoenvironmental Engineering 144(9) (2018).
19. Schary, Y.: Case studies on geocell-based reinforced roads, railways and ports. In: Springer Transactions in Civil and Environmental Engineering, pp. 387-411 Singapore (2020).
20. NCHRP.: Proposed enhancements to pavement ME design: Improved consideration of the influence of subgrade and unbound layers on pavement performance. Transportation Research Board, Washington (2019).
21. Zipoli, L.L.R., Avesani Neto, J.O.: Evaluation of back-calculated elastic moduli of unreinforced and geocell-reinforced unbound granular material from full-scale field tests. Geotextiles and Geomembranes 50, 910-921 (2022).
22. American Association of State Highway and Transportation Officials (AASHTO).: Standards Specifications for Highway Bridges. 16th ed., Washington D.C. (1996).
23. Gu, F., Luo, X., Zhang, Y., Lytton, R., Sahin, H.: Modeling of unsaturated granular materials in flexible pavements. In: EDP Sciences. 3rd European Conference on Unsaturated Soils (E3S Web of Conferences), 9(20002) (2016).
24. Eka, E., Putri, N., Rao, S. K., Mannan, M. A.: Evaluation of modulus of elasticity and modulus of subgrade reaction of soils using CBR test. Journal of Civil Engineering Research 2(1) (2012).

An Evaluation of Electric Vehicle Performance in Extreme Weather Conditions and HVAC Use

Hazal Ergül[1][0000-0003-3064-8476] and Hediye Tuydes-Yaman[2][0000-0003-2053-992X]

[1] Middle East Technical University, Engineering Faculty, Ankara, Türkiye, e173908@metu.edu.tr
[1] Middle East Technical University, Engineering Faculty, Ankara, Türkiye, htuydes@metu.edu.tr

Abstract. The transition from conventional vehicles with electric vehicles (EVs) plays an important role in achieving the sustainable transportation goals. However, EV range anxiety, has been a major concern for potential buyers. Even though advances in battery technologies have increased the range to 240 km-480 km, today, charging duration is still around 30 min. with the fast-charging stations. Furthermore, EV range can be decreased due to the energy for auxiliary services, such as lighting, radio, window opening or HVAC. EV range values published by the manufacturers are obtained generally under the most desirable conditions, such as 20ºC-25ºC, trim levels and no HVAC use. But it is known that the extreme weather conditions effect the battery negatively, and thus decrease the EV range significantly in real life use. This study focuses on the estimation of the range of an EV used in hot climatic regions in Turkey, such as Antalya, Adana, Şanlıurfa or Lefkoşa in Cyprus. In order to estimate the range reduction, the models developed by the previous studies on the performance of EVs in hot and cold weather conditions is considered. The change in EV performance due to the ambient temperature throughout May-September and December-February is analyzed. The results show that up to 40% of range reduction is experienced during cold weathers, 30% range reduction is also observed for hot weathers. This evaluation can help to better evaluate the climate change mitigation of EV related policies in these hot regions in Turkey and Cyprus.

Keywords: Electric Vehicle (EV), EV energy consumption; EV range; Extreme weather.

1 Introduction

Use of alternative-fuelled vehicles is one of the solutions against pollution and Greenhouse Gas (GHG) emission increase in cities. In recent years, electric vehicles (EVs) have gained significant attention as a promising alternative to traditional internal combustion engine (ICE) vehicles and due to their potential for reducing carbon emissions; however, their range is the major concern in the shift to EVs as detected in a survey in the UK [1]. Although increasing the battery capacity could be a solution, it

causes an extra weight on the vehicle, which leads to higher energy consumption (EC), and significantly increases the price. Furthermore, current EV batteries still do not provide a constant range, as they can significantly deteriorate in different environments.

The factors affecting the EV range include route elevation, driving speed, driving conditions such as traffic or driver aggressiveness, total weight and all the on-board energy consuming services (also referred to as auxiliary loads) such as heating, ventilation and air conditioning (HVAC), radio, lighting, etc. [2][3][4][5]. The conventional ICE-powered vehicles supply the energy requirement for the on-board services through the accumulator charged by the engine; EVs supply this energy directly from the battery, which i) creates an extra load on the battery, ii) significantly increases the EC, and thus, reduce the range. Based on GPS observations of 68 EVs in Japan, 9.66% electricity can be saved per km by eradicating unreasonable EV auxiliary loads [6]. Also, the same study showed that most economic temperatures for EVs are observed between 21.8ºC-25.2ºC, which proved the effect of temperature on the EV batteries. This is mainly due the fact that extreme weather conditions effect the EV battery efficiency negatively, both in extreme hot and cold weather.

To specifically identify the energy requirements for the auxiliary loads due to climatic conditions, only a few studies provided analytical estimations on EC by HVAC systems, which mostly include complex models [5]. Lee et al. concluded that the air conditioning causes an average of 33% decrease in the driving range in general [7]. Monitoring 24 EVs to evaluate the parameters, Dost et al. showed an increase up to 60% in EC in moderate wintry weather with a temperature of 10ºC [8]. Yüksel & Michalek characterized the effect of regional temperature differences on EV efficiency, range and CO_2 emissions through 7000 trips by Nissan Leaf users in USA [9]; on the coldest day of the year, the average range dropped to 113 km on the Pacific Coast and less than 72 km in the Upper Midwest. Similarly, Sagaria et al. reported that the range is reduced 25-35% for low temperatures compared to normal conditions [10]. Al-Wreikat et al. defined the moderate temperatures as 15-25ºC and estimated a range drop of 28% in urban EV operations at low temperatures from 0-15ºC [11].

The literature also discusses the difference in EC in the EVs during summer and winter. Jung et al. reported that the fuel economy drops by 19 ± 5% for the summer driving condition with air conditioner on and 47 ± 7% for the winter driving condition [12]. Hao et al. provided the most straight forward estimation for the effect of outside temperature on EC for EVs: when the temperature is lower than 10ºC, EC increases 2.4 kWh/100km for every 5ºC decrease in temperature, and when it is higher than 28ºC, EC increases 2.3kWh/100km for every 5ºC increase in temperature.

The increased use of EV in the northern countries, such as Canada, Finland, Norway has led to evaluation of EV range under extreme cold weather conditions, however, evaluation under extreme hot weather conditions has been rather limited. A study by Hamwi et al. gathered over 3000 EV journeys in Kuwait under temperatures that reach above 50ºC, and presented a model for EC applicable for temperatures between 10-50ºC. While the estimated EC at 20-23 ºC is 135Wh/km which is the optimum value, the EC increases to 240 Wh/km at 50 ºC.

Due to “zero emissions” goal by 2050 in Turkey, the policies for transportation sector heavily focuses on shift to EVs. EV range will also be a major concern to Turkish

drivers, which may change by various climatic conditions observed in Turkey. This study focuses on the estimation of the range reduction in an EV used in hot climatic regions such as Antalya, Adana, Şanlıurfa and Lefkoşa in North Cyprus. The potential range reduction is calculated based on models provided by Yüksek & Michalek and Hamwi et al. in the literature. The analysis is completed for both summer (May-September) and winter (December-February) conditions of four selected cities to see the climatic effect. To set a reference, the results for Ankara, which has a relatively moderate climate, are also obtained.

2 Methodology

To estimate the EC based on the ambient temperature, the models proposed by Hamwi et al.[13] and Yüksel & Michalek. [9] are used together as summarized in Equation 1: The model for EC estimation for temperatures between 10-50ºC is taken from of Hamwi et al., whereas for temperatures below 10 ºC, the EC estimation is achieved by the model represented by Yüksel & Michalek.

$$EC(T) = \begin{cases} 287.313 - 16.025T + 0.502T^2 - 0{,}004T^3 & T < 10 \\ 0.211 - 2.805 \times 10^{-3}T - 5.467 \times 10^{-5}T^2 & T \geq 10 \\ +2.653 \times 10^{-6}T^3 1.292 \times 10^{-7}T^4 - 2.432 \times 10^{-9}T^5 & \end{cases} \quad (1)$$

where T is the ambient temperature in degree Celsius and EC is the energy consumption in kWh per km. The resulting augmented model is visualized in Fig. 1. As the ambient temperatures are above and below 20-24ºC (the optimum temperatures for EV use), the EC increases and therefore the range decreases. The maximum range is observed when the EC is minimum. Note: For higher temperatures, Hamwi et al. graph is accepted as it worked with high temperatures and has more recent technology in the EVs.
EC increase also causes a range reduction, proportionally, which can be represented as a function of minimum EC value.

$$Range\ Reduction\ (RR)\ (\%) = \left(1 - \left(\frac{EC_{min}}{EC}\right)\right) \times 100 \quad (2)$$

To create a positive-valued RR parameter, EC_{min}/EC is reduced from the maximum range and represented in % values.

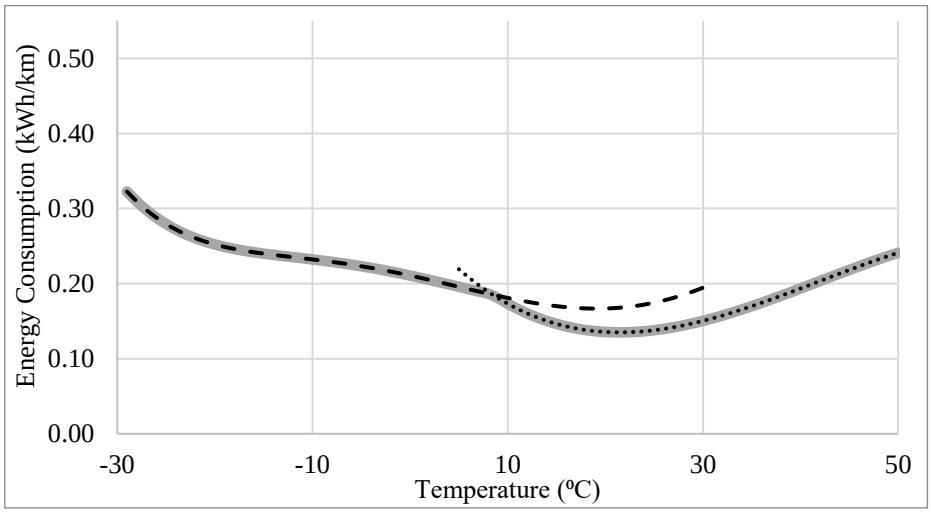

Fig. 1. Energy consumption per km vs. ambient temperature

The range reduction is calculated for the average and the most unfavourable situations which are a) the maximum ambient temperature during summer and b) the minimum during winter. Since the temperatures in Ankara during summer are close to the optimum values referred in the literature, Ankara is selected as a base case to obtain reference values for EC and RR in Turkey. Fig. 2 shows the daily temperatures and range reduction in the EVs during summer and winter. During summer the average ambient temperatures are between 10-26ºC. In May and September, the calculated range reduction using the average temperature is higher than the range reduction calculated using the maximum temperature. This is because the observed maximum temperatures are closer to the optimum operation temperatures, while the average temperatures are lower. During winter both the average and minimum temperatures are below the optimum temperatures. Therefore, it is clearly seen that as the temperatures get lower, the EC increases and therefore the range reduction increases. For Ankara, the maximum reduction in range is observed during winter reaching up to 42%. The maximum range reduction during summer is calculated as 20%.

Finally, the average range reduction is plotted for months in the selected cities. According to Statista, the estimated average battery capacity in electric vehicles worldwide from 2017-2025 ranges from 41-45 kWh [14]. For the estimation of the difference in range, a vehicle with 40 kWh battery is considered in the analysis. The results are compared for summer and winter months for the selected five cities. This analysis shows the suitability of EV use in cities pointing out the fact that both temporal and spatial evaluation for the EV use is necessary when planning the implementation.

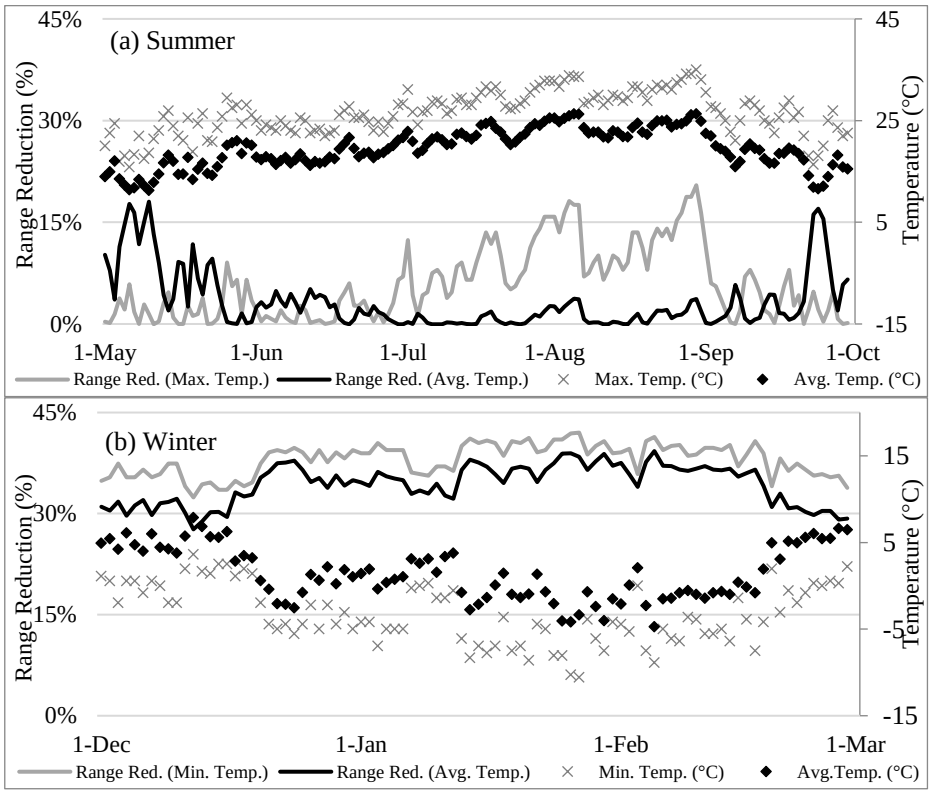

Fig. 2. Range reduction and temperature relationship (a) in Summer and (b) in winter

For Lefkoşa, Adana, Şanlıurfa and Antalya the daily average and maximum temperatures are gathered for the analysis considering the available data for the past two years (Fig. 3). The temperature data is gathered from an open-source Weather Underground website [15]. The average of the observed daily maximum, average and minimum values are calculated for the analysis. While the average temperatures for Lefkoşa, Antalya and Adana during summer range between 20-34ºC, the maximum temperatures reach up to 35-40 ºC. Şanlıurfa is the city with highest observed temperatures during summer, where the average and maximum temperatures reach to to 37ºC and 43 ºC respectively. During winter, the observed temperatures for the cities range between -2ºC -15ºC, showing that harsh weather conditions are not observed.

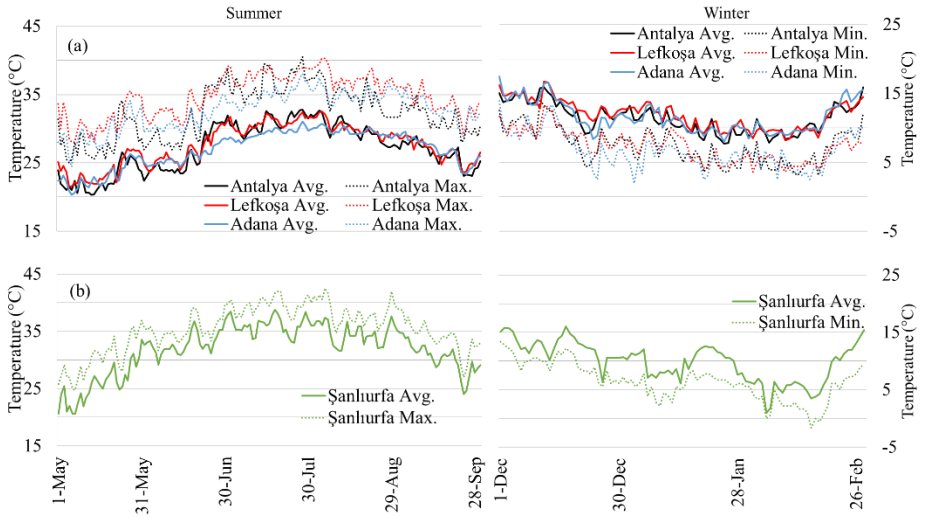

Fig. 3. Daily average and maximum temperatures during winter and summer for (a) Lefkoşa, Antalya and Adana (b) Şanlıurfa

3 Results and Discussion

Among the four hot climatic cities, Şanlıurfa showed the most significant impact of the ambient temperature on the EV energy consumption, thus, highest reduction in the range. The highest energy consumption is observed in during summer reaching 0.20 kWh/km (see Fig. 4). The range reduction reaches above 30% for the maximum ambient temperature analysis due to temperatures reaching above 40°C. The difference between the average temperature and the maximum temperature is not very significant as the humidity level of the city.

For Adana the summertime temperature is expected to cause a RR up to 10% during July and August according to average temperatures, while the RR in Lefkoşa and Antalya can reach up to around 15%. But, for these three cities, historical weather data shows a potential of larger maximum temperature values, which signals a risk of RR in up to 30%, reaching the expected RR in Şanlıurfa case. For Lefkoşa, Adana and Antalya the range reduction considering the average temperatures is almost zero up to the mid-June and increases in July and August. When the maximum observed ambient temperatures are considered, the range reduction reaches above 30% in Şanlıurfa, almost 30% in Antalya and Lefkoşa and up to 25% in Adana.

The range reduction analysis for winter is presented in Fig 5. For Antalya, Adana and Lefkoşa, similar results are obtained. While the RR during December is below 10% for these cities, it is higher than 10% in Şanlıurfa. The maximum estimated range reduction is almost 30% for all four cities. The main difference between Şanlıurfa and other three cities is the duration of colder weather conditions that causes an increase in range reduction up to 30%.

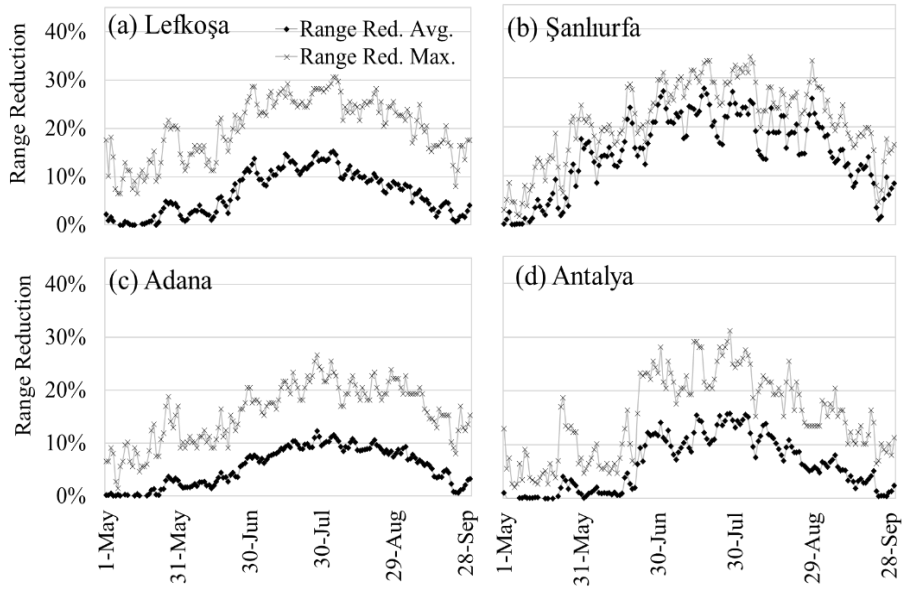

Fig. 4. The relationship between range reduction and ambient temperature in May-September for (a) Lefkoşa; (b) Şanlıurfa; (c) Adana and (d) Antalya

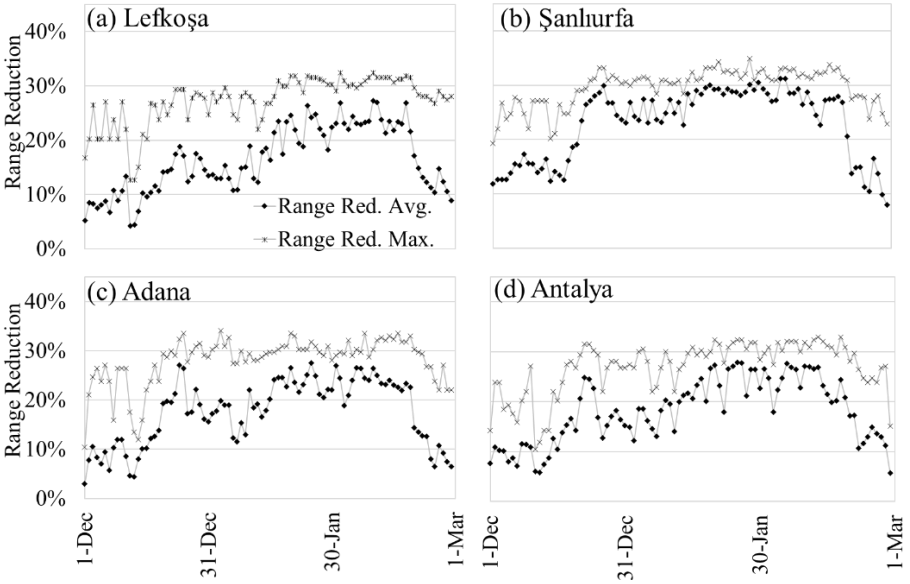

Fig. 5. The relationship between range reduction and ambient temperature in December-February for (a) Lefkoşa; (b) Şanlıurfa; (c) Adana and (d) Antalya

To better illustrate the impact of temperature in range reduction, a numerical example is prepared for a vehicle with 40kWh battery with a maximum range of 296 km in optimum conditions as in July and August for Ankara (see Fig. 6). In June, while the ranges in Lefkoşa, Adana and Antalya almost reach to Ankara value of 289 km, which is 284 km, driving range in Şanlıurfa is reduced to 248 km already. During July and August, all four cities showed bigger range reductions (reaching 228 km in Şanlıurfa), corresponding to a 12%-22% range reduction.

In winter season, the range reduction in Ankara is more severe with almost 36% loss leaving an active range of 189km- 198km. Among the four study cities, Lefkoşa, Adana and Antalya enable a driving range of 233 km- 256 km, which corresponds to a range reduction of 21%-13% on average. Şanlıurfa driving conditions however allows mostly a range of 215km – 240km during winter.

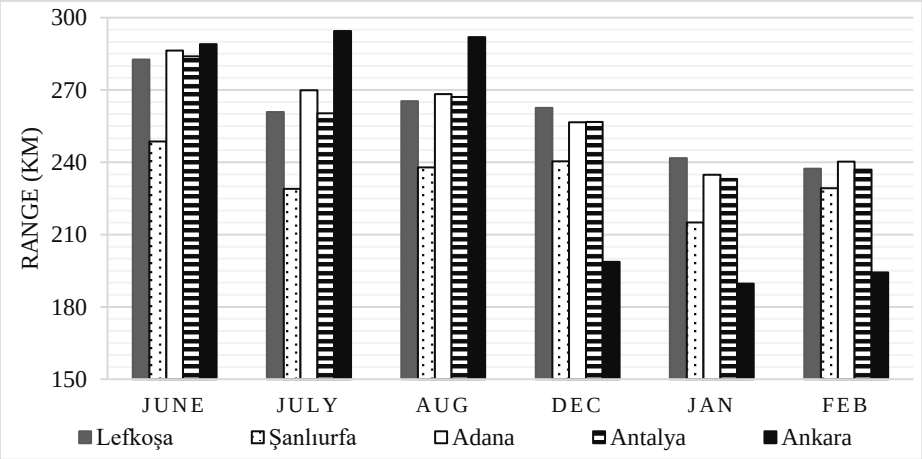

Fig. 6. Range changes during summer and winter months based on average temperature

4 Conclusions

Despite the almost constant ranges of the traditional (ICE) vehicles, the range in the EVs today can be affected significantly from the climatic conditions negatively during both hotter and colder days than the optimum driving conditions. This directly creates a range reduction, which is known to be a critical factor affecting the desirability of the EVs. The day-by-day change of EV range based on the daily temperatures makes it harder for the EV users to plan their daily routines and cause higher anxiety.

In the southern cities of Turkey (Adana, Antalya and Şanlıurfa) and Lefkoşa, these range reductions can be as high as 30% (corresponding to apprx. 90km), which would increase the range anxiety in the EV drivers. However, EV use can be more advantageous in overall in hot climates, if the winter is mild. During summer, to decrease the EC due to ambient temperature; the HVAC use can be limited, pre-cooling can be performed or especially during day times, the inside car temperature can be decreased by not leaving the car in a closed space or under the sun.

Today's average EV range of 300 km can be sufficient in strict urban use, and when supplied with widely available fast charging stations. But range reductions can be significant for suburban travels or commutes in large cities such as İzmir, İstanbul, Antalya where a big urban sprawl exists. People also do not buy separate cars for urban and intercity travels. Thirdly, charging is more expensive as well as not recommended by the EV manufactures due to battery degradation.

The battery technology has been constantly improving and the range of the EVs are expected to continue increasing in the future. Rapid deployment of fast and slow charging stations will definitely encourage the penetration of EVs in the vehicle park, if affordability of them increases by technological advances as well as financial incentives by the government.

References

1. N. Berkeley, D. Jarvis, and A. Jones, "Analysing the take up of battery electric vehicles: An investigation of barriers amongst drivers in the UK," Transp. Res. Part D Transp. Environ., vol. 63, no. June, pp. 466–481, 2018, doi: 10.1016/j.trd.2018.06.016.
2. J. Laurikko, R. Granström, and A. Haakana, "Realistic estimates of EV range based on extensive laboratory and field tests in Nordic climate conditions," 2013 World Electr. Veh. Symp. Exhib. EVS 2014, pp. 1–12, 2014, doi: 10.1109/EVS.2013.6914919.
3. Y. Al-Wreikat and J. R. Sodre, "Evaluating the Energy Consumption of an Electric Vehicle under Real-World Driving Conditions," SAE Tech. Pap., pp. 1–8, 2022, doi: 10.4271/2022-01-1127.
4. J. Vepsäläinen, K. Otto, A. Lajunen, and K. Tammi, "Computationally efficient model for energy demand prediction of electric city bus in varying operating conditions," Energy, vol. 169, pp. 433–443, 2019, doi: 10.1016/j.energy.2018.12.064.
5. P. Iora and L. Tribioli, "Effect of ambient temperature on electric vehicles' energy consumption and range: Model definition and sensitivity analysis based on Nissan Leaf data," World Electr. Veh. J., vol. 10, no. 1, pp. 1–15, 2019, doi: 10.3390/wevj10010002.

6. K. Liu, J. Wang, T. Yamamoto, and T. Morikawa, "Exploring the interactive effects of ambient temperature and vehicle auxiliary loads on electric vehicle energy consumption," Appl. Energy, vol. 227, no. January 2017, pp. 324–331, 2018, doi: 10.1016/j.apenergy.2017.08.074.
7. J. T. Lee, S. Kwon, Y. Lim, M. S. Chon, and D. Kim, "Effect of air-conditioning on driving range of electric vehicle for various driving modes," SAE Tech. Pap., vol. 1, no. December, pp. 5–9, 2013, doi: 10.4271/2013-01-0040.
8. P. Dost, P. Spichartz, and C. Sourkounis, "Temperature influence on state-of-the-art electric vehicles' consumption based on fleet measurements," Electr. Syst. Aircraft, Railw. Sh. Propulsion, ESARS, vol. 2015-May, no. 12 V, pp. 1–6, 2015, doi: 10.1109/ESARS.2015.7101504.
9. T. Yuksel and J. J. Michalek, "Effects of regional temperature on electric vehicle efficiency, range, and emissions in the united states," Environ. Sci. Technol., vol. 49, no. 6, pp. 3974–3980, 2015, doi: 10.1021/es505621s.
10. S. Sagaria, R. C. Neto, and P. Baptista, "Modelling approach for assessing influential factors for EV energy performance," Sustain. Energy Technol. Assessments, vol. 44, no. October 2020, p. 100984, 2021, doi: 10.1016/j.seta.2020.100984.
11. Y. Al-Wreikat, C. Serrano, and J. R. Sodré, "Effects of ambient temperature and trip characteristics on the energy consumption of an electric vehicle," Energy, vol. 238, 2022, doi: 10.1016/j.energy.2021.122028.
12. H. Jung, R. Silva, and M. Han, "Scaling trends of electric vehicle performance: Driving range, fuel economy, peak power output, and temperature effect," World Electr. Veh. J., vol. 9, no. 4, pp. 1–14, 2018, doi: 10.3390/wevj9040046.
13. H. Hamwi, T. Rushby, M. Mahdy, and A. S. Bahaj, "Effects of High Ambient Temperature on Electric Vehicle Efficiency and Range: Case Study of Kuwait," Energies, vol. 15, no. 9, 2022, doi: 10.3390/en15093178.
14. Statista Research Department, "Estimated average battery capacity in electric vehicles worldwide from 2017 to 2025, by type of vehicle," 2023. [Online]. Available: https://www.statista.com/statistics/309584/battery-capacity-estimates-for-electric-vehicles-worldwide/.
15. Weather Underground, "Daily Temperature Data." [Online]. Available: https://www.wunderground.com/.

Developing a Decision Support System for Roadside Restraint Systems (RRSs) Design

Ege Cem Saltık [1[0000-0001-8201-6468]], Abdurrahman Sinan Alemdar [2[0009-0001-1388-8075]], Hediye Tuydes-Yaman [3[0000-0003-2053-992X]]

[1] Middle East Technical University, Civil Engineering Department, Ankara, Türkiye, e153105@metu.edu.tr
[2]EMAY Uluslararası Mühendislik ve Müşavirlik A.Ş.,İstanbul, Türkiye, salemdar@emay.com
[3] Middle East Technical University, Civil Engineering Department, Ankara, Türkiye, htuydes@metu.edu.tr

Abstract. Road restraint systems (RRSs) aim to enhance road safety by minimizing casualties and property damage, particularly in Run-of-Road (RoR) accidents. They consist of components like crash cushions, vehicle restraints, and terminals, working to keep vehicles on the road and reduce the impact of accidents on occupants, infrastructure, and nearby facilities. RRS selection depends on local regulations, road design standards, safe zones, Road Safety Audits, and disparities in road hierarchy between countries. In Turkey, RRS performance is categorized into seven containment levels according to the TS EN 1317 standard, aligned with the EU standard. Different restraints are designed for passenger cars (N1-N2) and loaded trucks (H4a/b), even in limited roadside widths as seen on bridges. Previously, the General Directorate of Highways (GDH) relied on rule-of-thumb methods for RRS choices, but a comprehensive decision-tree model has been introduced. It considers factors like geometric attributes, corridor speed, traffic volume, composition, and local threats. To support this decision-making process, a Geographic Information System (GIS)-based decision support system (DSS) tool has been proposed. It utilizes the GDH database to automatically retrieve traffic volume and composition data. RRS design engineers input threat and geometric design information, and the tool provides corresponding risk and containment levels. GDH engineers conducted a preliminary evaluation of the GIS-based DSS tool along an 82.66 km road corridor in Zonguldak, Turkey. This study aims to leverage GIS technology for improved selection and design of RRSs, ultimately enhancing road safety outcomes.

Keywords: Road Restraint Systems, Decision Support Systems, Vehicle Restraint.

1 Introduction

1.3 million people are losing their lives, and 20-50 million people are facing non-fatal injuries in the world each year due to road traffic injuries [1]; and these victims include both drivers and vulnerable road users (pedestrians, cyclists, motorcyclists, etc.). Road traffic injuries impacts on national economies are reported to be 3% of countries annual gross domestic product [2], which is much higher at developing countries [3]. The possibility of road traffic accidents in non-developed countries is found three times higher than in developed countries due to driver behavior, lack of security systems in vehicles, and traffic safety awareness of countries [4]. Despite extensive literature on global traffic safety, there is a lack of knowledge and consensus on decision-making regarding roadside safety. This is crucial for developing countermeasures for to Run-off Road (RoR) accidents, which were the second largest accident group with 34,400 accidents (14.47%) in 2022 in Turkey.

In a RoR accident, when an errant vehicle runs off the road, it poses a severe hazard to third parties (i.e., other transportation systems, other road traffic users, pedestrians, cyclists, etc.). RoR accidents exhibit clustering in specific areas of the road network, which is mostly associated with excessive speed. As a countermeasure, road designers introduced the concept “safe zone” in the roadside design, as well as increased use of road restraint systems (RRSs) elements including guardrails, crash cushions, terminals, etc. However, due to differences in geometric design codes and practices across difference countries, there is still not globally accepted “roadside design codes”, which are mostly customized according to the traffic safety priorities and local needs in a country, mostly detected by Road Safety Audit (RSA) mechanisms. The RSA also enables a flexible tool to foresee and address the complex relations between the threats/risk's factors of the RoR accidents and the performance indicators of RSSs.

In the absence of a national RSA legislation in Turkey, the General Directorate of Highways (GDH) performs a traffic safety evaluation internally as a part of their road design procedures. More recently, the GDH also published an RSS design guideline to be used in their road network. Yet, there is still no national-level legislation addressing the roadside safety issues of the municipal road network. Thus, development of a decision support system (DSS) guiding the RSS selection is necessary to improve safety and minimize human errors in roadside designs.

1.1 Scope of the Study

This paper summarizes the data needs and the capabilities of a DSS developed for RSS decision-making in Turkish road networks. The definitions of key concepts such as “safe zone” and “threat/hazard” and how they can be estimated using the available traffic and RoR accident data in Turkey are explained as a part of the proposed DSS framework. These concepts are associated with the containment levels defined in the EN1317 Design Standard, which is also the legislation applied in Turkey. Furthermore, the GIS-based representation of the data and interpretation of the traffic conditions are discussed as a separate aspect of the proposed DSS tool. The user-friendly design of

the proposed tool is aimed to support not only the experienced engineers, but also the novice engineers.

2 Literature Review

While improving traffic safety, countries focused on engineering, enforcement and education, originally defining the 3Es of traffic safety. A nation-wide program with "zero traffic deaths" goal of Sweden (named Vision Zero) was launched in 1994, had a specific component dedicated as "safer roads", which was later adopted by Netherlands in 1997 and by Norway in 1999 [5][6]. This concept has recently been generalized to the Safe Systems approach [7] endorsed by the UN, which included five key dimensions: safe roads, safe speeds, safe vehicles, safe users, and post-crash care [8]. This shows the critical need to manage the road design and speed together in a successful road safety program.

2.1 Road and Roadside Safety Aspects in Europe

Over the years, road safety evaluations have aided determination of the relation between road design components and accident risk and led to compilation of best practices [9]. Safe road design is composed of improving safety of various design elements, such as horizontal and vertical curves, hydraulic design, and visibility.

Later, roadside safety design included design of RSS elements (i.e. barriers, cushions, motorcycle protection systems, etc.) [10]. Use of RSS element in UK was minimal until the 1960s. Initially, steel rope and guardrails were limited to bridges, steep embankments, and the Preston By-Pass Road opened in 1958. The 1960s witnessed the introduction of crash tests to assess the cost-effectiveness and performance of vehicle restraint systems (VRS). Early studies focused on accidents involving median crossings and opposite lane crossings, revealing a higher injury rate and increased fatality risk compared to other accidents [11][12]. Analysis further indicated that areas with low traffic density had a lower risk of head-on collisions, requiring an Average Annual Daily Traffic (AADT) of over 60,000 vehicles for such accidents to occur [13]. Subsequent studies suggested using barriers when the AADT exceeded 35,000 [14]. In the USA, safety barriers were first implemented in various road sections in the 1950s, and a similar trend was observed in England with the presence of bridge-side barriers [15]. Germany has been using road safety systems like steel guardrails and concrete crash barriers since the 1950s. Targeted development and improvement of steel guardrail systems took place in the 1960s and 70s, accompanied by crash tests. The "Passive Safety Rules" directive (RPS 1989) was implemented in 1989, later replaced by the "Vehicle Restraint Systems for Passive Road Safety" directive (RPS 2009), which remains in use today.

According to the RPS 2009 manual in Germany, roadside risk is divided into four hazard levels for both third-party endangerment and risks to vehicle occupants. Hazard Level 1 includes high-risk areas like chemical plants, heavily trafficked locations, rapid transit lines with speeds exceeding 160 km/h, and structures prone to collapse. Hazard

Level 2 comprises areas with a specific risk to third parties, such as busy walkways, bicycle paths, rail lines with over 30 trains passing daily, and roads with an Average Traffic Density (ATD) exceeding 500 vehicles daily. Hazard Level 3 covers obstacles endangering vehicle occupants, such as non-deformable extensive obstacles, individual non-deformable objects, noise barriers, steep slopes, intersecting ditches, and bodies of water deeper than 1m. Hazard Level 4 includes similar obstructions but with a higher risk to vehicle occupants. In the UK, obstacles are categorized based on their impact on user groups, including roadside obstructions, hazards that road users may encounter, and hazards that may affect others. In the US, hazards are categorized using a severity index, and their impact is assessed through hazard diagrams considering factors like hazard size, location, dimensions, vehicle size, speed, and angle of departure. Various charts have been developed to determine appropriate barriers for different roadside geometries, including trench shapes, slope inclinations, and fill heights. The RISER EU project established a hazard and accident database, revealing that both point hazards and distributed hazards can lead to severe or fatal injuries [16].

2.2 Roadside Safety in Turkey

According to the data of the General Directorate of Security (GDS) for 2022, out of 485,048 traffic accidents, there were 1919 fatality accidents and 195,015 injury accidents. The most common accident type was side impact accidents (31.96% share), followed by pedestrian accidents (17.0%). RoR accidents constituted the third major group (14.47%).

In 2005, the GDH prepared and published a handbook on highway design in Turkey. This handbook comprehensively elucidates and provides information on various stages of road design. The 7th chapter of this manual focuses on roadside design and the application of RRSs. This chapter directly translates the content from the AASTO 1996 Roadside Design Guide, 2nd Edition. However, the current approach and practices for designing roadsides are influenced by German standards. In Germany, the regulations for RRS were initially published by FGSV (Road and Transport Research Association) in 1989, with subsequent additions in 1996. The RPS 2009, titled "Guidelines for passive protection on roads by vehicle restraint systems regulation," was developed. The German guidelines for VRS application include charts that are based on assumptions about site conditions. Additionally, designers often rely on rule of thumb in their practical application. GDH handbook focuses on potential threats and hazards to external users and vulnerable road users based on existing road risks. The threat/hazard levels for external users are classified as high or low, taking into account vehicle and human density and traffic volume, especially in situations where removal or relocation is not feasible. For vehicle users, threat/hazard situations are evaluated at a single level due to the lack of prioritization among different types of dangers. However, there is a lack of clear definitions or widely accepted standards for defining threats or hazards internationally, hindering collaboration and coordination. Therefore, the study's observations are based on Turkish road conditions. Fig. 1 illustrates the threat and hazard situations occurring within the safe zone for vulnerable road users and vehicle users.

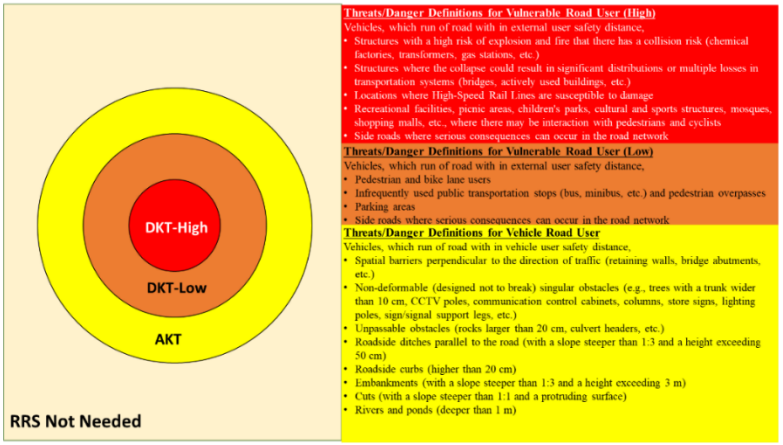

Fig. 1. Threats/hazard definitions for vulnerable and vehicle road users

3 Methodology

The primary decision in roadside safety design is to be able to produce a targeted solution for the function expected from roadside units, which have some duties for life and property safety of people on roads. Although EU standards have been developed for roadside elements, the principles and procedures regarding where and how these elements are used could be differentiated in each country. This has led to different cross-country approaches to roadside safety devices themselves. Examining the roadside safety systems and practices of Germany, England and the United States of America in the development of the application method has made significant contributions to the roadside safety approach to be developed for Turkey. This study provides a GIS-based decision support system for the selection of VRS, which is implemented by the GDH in Turkey. In this study, VRS decision-making processes can be monitored by decision makers and utilized decision trees in conjunction with existing applications on the right side.

To determine the distance at which such a vehicle poses a threat to road users, it is essential to establish at what distance a vehicle that has run off the road can safely stop or safely return to the road. In this study, the safe zone distance is considered in relation to design and operating speed, traffic volume, and geometric characteristics. Safe zone distance is evaluated differently for vehicle users and external road users, and the assumptions are shown in the Fig. 2.

To analyze the corridor effectively, it is necessary to determine geometric and design inputs, such as design speed, curve radius, lane numbers and widths, roadside slope parameters, and station kilometer information. Additionally, structures like bridges, overpasses, and areas with heavy pedestrian traffic should be located along the studied corridor. Traffic volume inputs, both for all vehicles and heavy-duty vehicles, need to be recorded in kilometers to assess accident potential. Accident statistics from the past three years are automatically retrieved to define safe zones based on speed limits. The

GIS-based DSS interface, integrated with GDH servers, displays accident data and allows for evaluating accident potential and vehicle density along the corridor.

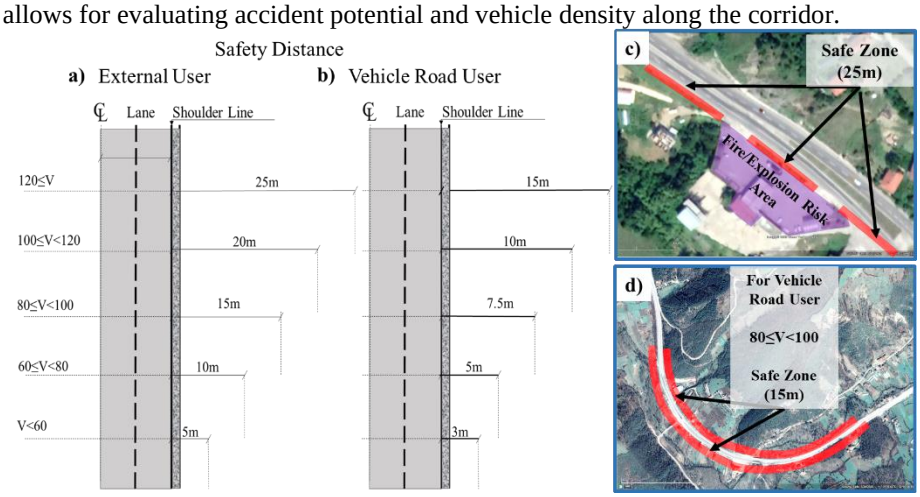

Fig. 2. Safe zone distance a) for external user b) vehicle road user

This study focuses on motorways, divided roads, and intercity roads under GDH responsibility. The roads are denoted as A or B based on kilometer increase or decrease, with median sections represented by E. Geometric information, volume data, and accident information are extracted from the system for the selected corridor. User intervention is allowed for adjustments and new data entry, including correction factors for geometric information. Safe zone definitions are made for both vulnerable road users and vehicles based on speed information. Hazard and threat situations are identified by the system, considering geometric data and user observations. Risk assessment and containment level determination are conducted, with seven containment levels implemented in Turkey (ranging from N1/N2 to H4a/H4b). The risk level is evaluated on a scale of 1 to 7 and matched with corresponding containment levels. Fig. 3 illustrates the parameters involved in the RRS process, which is performed by the GIS-based DSS.

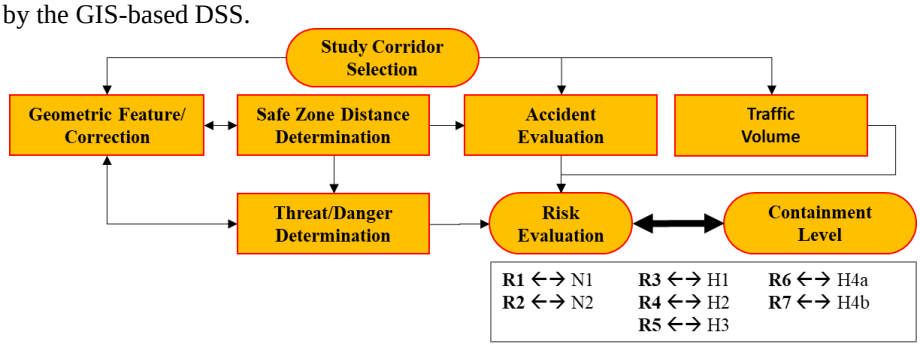

Fig. 3. Framework of RRS containment level selection by GDH

3.1 Need for a GIS-based User Interface

GIS-based tools are essential for traffic safety as they integrate and analyze spatial datasets, including road networks, traffic, and road conditions. This integration allows for pattern identification and correlation analysis, enhancing our understanding of traffic safety issues.

To improve traffic safety, GIS-based studies should be capable of creating buffers based on safety zone distances. This feature is currently lacking in existing systems, hindering adjustments in areas where vehicles run off the road and require space to safely return. Moreover, it is crucial to make arrangements and precautions in high traffic volume and heavy vehicle areas. Visualizing areas that pose risks and implementing safety measures based on current traffic conditions is essential. Consideration should be given to the distance of these areas from the roadside, as well as collision scenarios that threaten life and property. GIS-based visualization should encompass high-risk locations like gasoline stations, areas with pedestrian and passenger traffic, and hazardous conditions such as cut and fill areas lacking sufficient distance. Fig. 2 c) and d) illustrates the expectation that GIS-based systems will facilitate decision-making and enable the implementation of necessary measures in highlighted areas during the decision-making process.

A GIS-based decision support system (DSS) tool is developed to assist engineers and decision makers in determining suitable road restraint systems (RRS) based on geometric attributes, corridor speed, traffic volume, and road threats. Therefore, DSS tool helps

i. Filling the legislative gap regarding functional road classification and roadside "safe zone" in Turkey.
ii. Systematically addressing threats and hazards caused by run-off-road incidents.
iii. Considering the distribution and clustering of run-off-road accidents on intercity road networks
iv. Striving for a reasonable risk level by considering factors influencing accident occurrence and past accident results.

The GIS-based DSS tool is designed for roads, divided highways, medians, and bridges. It operates on GDH servers, providing real-time vehicle restraint application information and updating required data for the DSS. Historical accident data and site information from the past three years are integrated into the system. Speed information, including design, operational, and 85th percentile speeds, is considered to determine safe zone distances. However, the DSS tool allows users to adjust safe distances for different road sections. Threat and hazard analysis within a safe distance is automatically performed for roadsides, medians, and bridges. Traffic volume data, including Average Annual Daily Traffic (AADT) for both passenger and heavy vehicles, is retrieved from GDH.

The DSS tool retrieves geocoded information from the GIS environment, ensuring integrated and dynamic data updates. It supports various map bases and offers manual data entry for user convenience. It generates reports on VRS types and application lengths, reducing reporting time and expediting evaluation and decision-making

processes. The DSS provides easy access for defined users via the internet, enabling local governments and companies to conduct their own digital road safety studies. This accessibility and reporting capabilities enhance the efficiency and accessibility of vehicle restraint applications.

4 A Case Study using GIS based DSS Interface

A 2x2 divided road with the KKN number 750-01 in Zonguldak province was selected for analysis. The road is 82.66 km long and consists of 6 sub-sections. Traffic density information for each segment based on vehicle type was provided by GDH. The table below shows the accident statistics for the route. Out of a total of 169 accidents, 65 were run-off-road accidents, including 2 fatal accidents and 63 injury accidents. Specifically, there were 49 run-off-road injury accidents in 2017 and 46 in 2016. In 2016, there were also 2 fatal accidents and 44 injury accidents according to police records.

4.1 GIS-based User Interface Operations

Using KKN 750-01, relevant properties such as road name, speed limit, and section length are retrieved from GDH servers and displayed in the DSS screens. The starting point of the road, indicated by the lowest km information, is marked with a flag to ensure data accuracy. Analysis can be initiated by selecting the road and clicking the plus button in the DSS screens. Additionally, volume and accident information from GDH servers can be displayed on the map background in the filter section.

The user interface tool assigns codes (A, B, and E) to indicate the side of the road where vehicle restraints are applied (right, left, or median). Information regarding superstructures for VRS applications, including their start and end km, must be entered for risk and hazard assessments. The DSS retrieves capacity, velocity, and accident data from GDH's GIS servers, presenting them in both map and list view formats based on kilometer values. Past 3-year accident information is listed for each 250-meter interval.

Given the absence of reports or studies on road safety audits in Turkey, on-site observations become crucial for evaluating vehicle restraint applications. The user interface tool allows for the addition or removal of data based on field observations or experiences. Geometric design parameters obtained from GDH servers are cross-checked and corrected as necessary. Threats and hazards are defined separately for vehicle users and vulnerable road users according to GDH specifications, and users can add additional situations posing threats or hazards. Km-based information and distances from the verge are specified to define conditions important for risk analysis (Fig. 4).

Once metadata is entered into the system, the containment level of vehicle restraints can be viewed on the DSS screens as a result of the analysis. In the case study area, the containment level for the initial 250 meters is determined as N2. AADT, heavy vehicle capacity, and the occurrence of two injury accidents necessitate the need for vehicle restraints in the study area. The presence of fatality accidents within specific kilometer ranges increases the risk level, leading to the determination of containment levels such

as H4a. The remaining study area is evaluated to have threats/hazards for vulnerable road users, resulting in an N2 containment level. Detailed results regarding the containment level of the study area are displayed on the DSS screen.

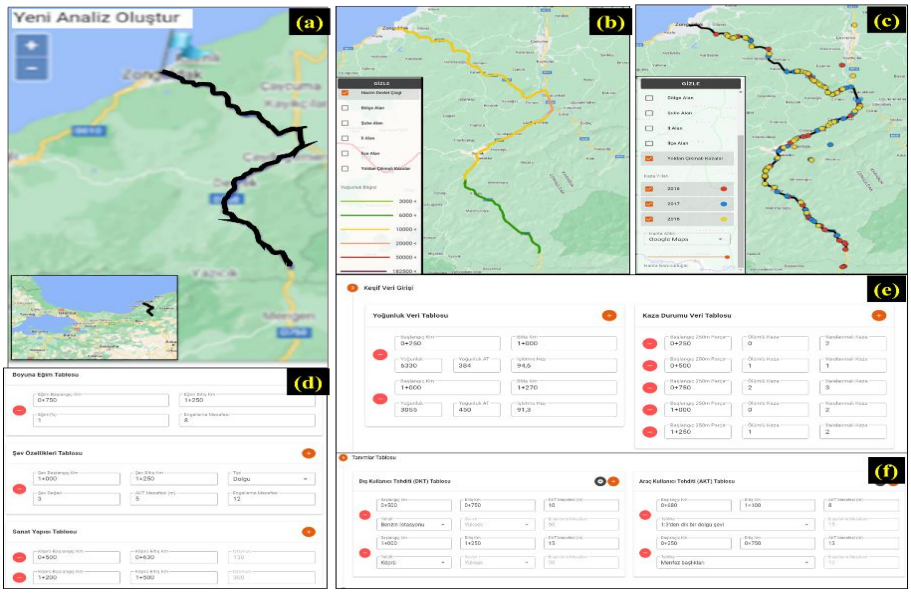

Fig. 4. a) View of study area b) traffic volume of the study area c) traffic accident data d) geometric design properties of the study area e) volume and accident menu f) threat/hazard menu

5 Conclusion

Countries have unique practices, regulations, and priorities in traffic management and safety, leading to differences in the implementation of safety precautions like vehicle restraints. Although road safety audit studies are currently lacking in Turkey, GDH has conducted some studies on vehicle restraint applications. Moreover, this research introduces a decision-making system that considers road threats for both vulnerable road users and vehicle drivers. It incorporates factors such as run-off-road accidents and historical accident data on intercity road networks. The system utilizes a GIS-based tool to support decision-making and focuses on the RRS decision-making system of GDH. Furthermore, The DSS aids users or decision makers in evaluating sites under various conditions. The system allows for dynamic and manual data entry, facilitating decision-making processes for authorities. Given the absence of road safety audits in Turkey, the DSS expedites evaluations for determining containment levels and implementing vehicle restraints. Additionally, the DSS enables reporting of these studies. It only requires an internet connection, ensuring easy access for defined users from any location with internet access.

Seeing all the relevant data as well as detected risk and containment levels along a long road corridor simplified the RRSs decisions as well as cost calculations for the engineers. The automatic reporting as well as data archiving for future road maintenance and repair helped to create systematic RRSs decision-making. As an added value, the tool not only decreased the risks of improper RRSs designs by inexperienced engineers, but it also provides opportunities to train them in roadside design. Also, a list of recommendations could be made for future improvements to the DSS tool.

References

1. World Health Organization (WHO), https://www.who.int/health-topics/road-safety#tab=tab_1, last accessed 2023/04/18
2. World Health Organization (WHO).: Global Status Report On Road Safety 2018. (2018).
3. Jadaan, K.,Al-Braizat,E.,Al-Rafayah,S.,Gammoh,H.,Abukahlil, Y.: Traffic Safety in Developed and Developing Countries: A Comparative Analysis. Journal of Traffic and Logistics Engineering Vol. 6, No. 1. (2018).
4. Betus,Y.: A Comparıson Of Roadsıde Desıgn Approaches In Terms Of Road Safety To Improve Turkısh Roadsıde Safety Standards. (2022).
5. Fahlquist, J.N.: Responsibility ascriptions and Vision Zero. Accident Analysis and Prevention, 1113–1118 (2006).
6. Cushing,M., Hooshmand,J., Pomares, B., Hotz,G.: Vision Zero in the United States Versus Sweden: Infrastructure Improvement for Cycling Safety. Journal Public Health, (2016).
7. Evenson,K.R.,Lajeuneese,S.,Keefe,E.,Naumann,R.B.: Mixed-methods approach to describing Vision Zero initiatives in United States' municipalities. Accident Analysis and Prevention 184 (2023).
8. U.S. Department of Transportation, What is a Safe System Approach?, https://www.transportation.gov/NRSS/SafeSystem, last accessed 2023/06/27.
9. European Commision, Mobility & Transport Road Safety, https://road-safety.transport.ec.europa.eu/statistics-and-analysis/statistics-and-analysis-archive/roads/getting-initial-safety-design-principles-right_en, last accessed 2023/04/18.
10. American Association of State Highway and Transportation Officials (AASHTO).: Roadside Design Guide (4th ed.). (2011).
11. Newland,V.J.,Newby,R.F.: Changes in Accident Frequency after the Provision of By-Passes, Traffic Engineering and Control. (1962).
12. Newby,R.F.,Johnson,H.D. Changes in number of Accidents and causalities on main roads near the London-Birmingham Motorway. (1964).
13. Moskowitz,K., Schaeffer,W.E.: California median study:1958. Highway Research Board, 266,34-62.(1960).
14. Moore, V.M., J. Dolinis and A. J. Woodward.: Vehicle speed and risk of a severe crash. (1995).
15. Berg, N.: Muting the Freeway. How roadside noise barriers are designed to absorb sound and evade attention. https://medium.com/re-form/muting-the-freeway-e18ee195bd38, last accessed 2023/06/27.
16. Thomson, R., Fagerlind, H., Martinez, A. V., Amengual, A., Naing, C. L., Hill, J., Hoschopf, H., Dupre, G., Bisson, O., Kelkka, M., van der Horst, R., & Gracia, J. M.: Roadside infrastructure for safer European roads: D06 European best practice for roadside design: guidelines for roadside infrastructure on new and existing roads. (2006)

Investigation of the Usability of Basalt and Limestone Aggregates Obtained from Bitlis Region in Porous Asphalt Construction

Alev Akilli el[1] [0000-0003-0158-9008] and Mehmet Yilmaz[2] [0000-0002-2761-2598]

[1]Bitlis Eren University, Technical Sciences Vocational School, Civil Department Bitlis, Turkey, aakilli@beu.edu.tr
[2]Fırat University, Engineering Faculty, Civil Engineering, Elazığ, Turkey
mehmetyilmaz@firat.edu.tr

Abstract. Porous asphalt is an innovative road pavement technology that is widely used around the world. It is a special-purpose wear layer built to increase road safety, especially in rainy weather. High amount of coarse gradation aggregates is used in porous asphalt mixtures. Therefore, determining the properties of aggregates used in the mixture significantly affects the performance of porous asphalt mixtures. In this study, the usability of volcanic-origin basalt aggregate and sedimentary-origin limestone aggregate obtained from Bitlis region in porous asphalt construction was investigated. Aggregates used within the scope of the study were performed that Sieve analysis, Flakiness index, Micro-Deval, Freeze-thaw durability ($MgSO_4$), Methylene Blue and Stripping tests. As a result of the experiments, it was determined that each aggregate meets the porous asphalt design conditions given in the Highways Technical Specifications.

Keywords: Porous Asphalt, Basalt, Limestone, Bitlis.

1 Introduction

Porous asphalt is a type of pavement with permeable structure with an air void content of approximately 20% [1]. These structural differences are to porous asphalt; It provides functionalities such as superior rainwater management, pollution control, anti-skid performance, improved driving safety and reduced traffic noise [2,3,4].

Today, porous asphalt pavement is widely used in European countries, including the Netherlands, Germany, Denmark, Switzerland, and Austria, as well as in Asian countries such as Japan, China, South Korea, and Singapore [5]. More than 90% of major highways in the Netherlands and 67% of the existing road surface in Japan are covered with porous asphalt concrete, and conventional single-layer porous asphalt pavement has been reported to be in good condition even after 15 years of use [6].

Poros asphalt is a creative road construction technology. It allows water to pass through the asphalt layer, thanks to the air gaps in its structure. This type of pavement reduces traffic noise and the slipperiness of the road surface [7]. The effectiveness of a

porous asphalt pavement depends on the characteristic factors of the design, such as air voids trapped in the pavement layers, and the technology used in it. This type of coating can also be used in heavy traffic conditions with its high design properties [8].

Porous asphalt has a special hollow skeleton structure that results from the interlocking of coarse aggregates. Aggregate quality has a significant impact on the loading capacity and overall performance of porous asphalt concrete [9-10]. In general, basalt and limestone (limestone) aggregate are granular materials commonly used in asphalt pavements. Basalt is an igneous rock type. It makes up more than 90% of volcanic rocks. Limestone, on the other hand, is a relatively common sedimentary rock that forms lime [11]. Limestone is widely used in the construction of roads, buildings and cement production due to its longevity and greater reserves. Limestone is alkaline and adheres strongly to asphalt, which is usually weakly acidic. Limestone has poor wear resistance. For this reason, if it is used in porous asphalt pavement, it may adversely affect the slip resistance and durability. Basalt aggregate has high mechanical properties and is therefore a preferred type of aggregate for the surface layer of the pavement. However, it cannot be used much due to the high price and limited resources [12].

Asphalt pavement can be considered as a mixture of three types of distributed systems; aggregate structure, asphalt binder and air void. These three systems are important for the pavement performance of the asphalt pavement, as well as for the porous asphalt pavement mixtures [13]. In this study, the properties of the aggregate used in porous asphalt mixtures are emphasized.

As a particulate composite material, more than 90% of porous asphalt mixes are aggregates excluding air voids. Aggregate gradation is important to control void content and ensure the performance of a porous asphalt pavement [14]. Generally, discontinuous gradation type is used in porous asphalt pavements. Because more than 60% of the aggregate gradation used in the mixture should contain coarse aggregate and the fine aggregate ratio should be low. This ratio is at a level that prevents the air gaps formed by coarse aggregates from closing. However, porous asphalt mixtures are more susceptible to deformation at high temperature compared to dense asphalt mixtures due to their high air void content [15]. For this, greater strength and stability of the skeletal structure developed with coarse aggregates is required. In addition, the structure of the aggregate affects the pavement performances of porous asphalt mixtures, such as low temperature resistance and water stability. Therefore, it is very important to optimize the aggregate gradation for porous asphalt mixtures and to know the strength mechanisms of the aggregate structure.

The coarse aggregate content of the porous asphalt mix is higher than the conventional asphalt mix and the contact area between the aggregates is approximately 25% less [2]. This means that the contact points will be subjected to higher stresses. For this reason, properties such as structure, shape, grain size and classification of the aggregate used in porous asphalt have a significant effect on the performance of the mixture [16-17].

Firstly, the coarse aggregate used in porous asphalt must have enough wear resistance to withstand external loads and must provide the necessary friction for driving safety. If aggregates with low wear resistance are used, aggregate fragmentation

may occur during the production of the mixture and compaction in situ. At the same time, the percentage of flat and long particles of the aggregates used in the mixture should be controlled in detail. The ratio of minimum diameter to maximum width in all directions of the particle shape should be less than a certain value (usually 0.3) [18]. Irregular particles can be easily broken or even crushed by the compactor or heavy vehicles, thus obtaining a fractured surface on the asphalt. In addition, if there are too many straight and long grains in the coarse aggregate, it can seriously affect the durability and function of the porous asphalt mixture.

In addition, similar to conventional asphalt mixes, the amount of asphalt absorption significantly affects the performance of the porous asphalt mix. Therefore, it is preferred to use aggregates with less than 2% water absorption. However, if locally available highly absorbent aggregates are used, the optimum asphalt content must be selected highly within specification limits to account for the mix's absorption during fabrication, placement and service [2].

The properties of the aggregates used in the porous asphalt mixtures according to the technical specifications of the highways are given in Table 1 and Table 2.

Table 1. Properties of coarse aggregate used in porous asphalt (19)

Experiment	Specification limits	Test Standard
Micro-Deval (Abrasion Test)% Loss	≤20	TS EN 1097-1
Weathering Resistance (loss with MgSO4)%	≤10	TS EN 1367-2
Flatness index%	≤20	BS 812
	≤15	TS EN 933-3
Peel Strength Test %	≥80	TS EN 12697-11
Water absorption %	≤2	TS EN 1097-6

Table 2. Properties of fine aggregate used in porous asphalt

Experiment		Specification limits	Test Standard
Plasticity Index		N.P	TS-1900-1
Organic Matter %		Negatif	TS EN 1744-1
Water absorption %		≤2	TS EN 1097-6
Methylene blue g/kg	0/2 mm of fine aggregate	≤1,5	TS EN 933-9
	0/2 mm of the ground magmatic aggregate	≤3	

In the study, it was aimed to determine the usability of basalt and limestone aggregates obtained from Bitlis region in porous asphalt mixtures as a result of experiments carried

out in the laboratory environment. In the scope of the study, sieve analysis, flatness index, methylene blue, sand equivalence determination, Micro-Deval abrasion resistance, frost resistance ($MgSO_4$ loss) and peel strength tests were performed on the aggregates supplied. The results of the experiments were compared with the Porous Asphalt mixture limits specified in the Highways Technical Specifications and information on the usability of aggregates in porous asphalt pavement mixtures was given.

2 Experimental Studies

Two types of aggregates, basalt and limestone, were used for the study. Type 2 was chosen to obtain a homogeneous mixture within the particle sizes indicated in the technical specifications of highways for porous asphalt. The necessary experiments were conducted to determine each aggregate's properties and compare their effects on the mixture. The basalt aggregates to be used was obtained from BAYSAN INS. MAD. LTD. STI in Seke village in the Bitlis-Ahlat district and the limestone aggregate was obtained from the MERMER quarry in the Bitlis region.

Table 3. Grading and limits of porous asphalt (KTŞ, 2013)

Elek Boyutu		**Tip-1**	**Tip-2**	**Tip-3**	**Tip-4**	**Tolerens Limitleri**
İnç, No	mm	Geçen %	Geçen %	Geçen %	Geçen %	%
3/4”	19	100	100	100	-	-
1/2"	12,5	5-15	90-100	85-95	100	±4
3/8”	9,5	-	63-77	5-15	85-95	±4
No.4	4,75	5-12	11-35	5-15	5-12	±3
No.10	2.00	5-10	10-20	5-10	5-10	±3
No.80	0,180	-	5-10	-	-	±3
No.200	0,075	3-5	3-7	3-5	3-5	±2

2.1 Sieve Analysis

The test to determine the aggregate particle size was carried out according to the standard TS EN 933-1. This test separates the aggregate by particle size [20]. In the test method, sieves are used from the largest to the smallest to determine the particle size of an aggregate pile. During the sieve analysis test, the sample weights on the sieve are limited because overloading the sieve will cause problems in particle size distribution. As a result of the test, the amount of aggregate remaining on each sieve is weighed, and the gradation curve is obtained by calculating the amount of aggregate passing through each sieve as a percentage (Figure 1).

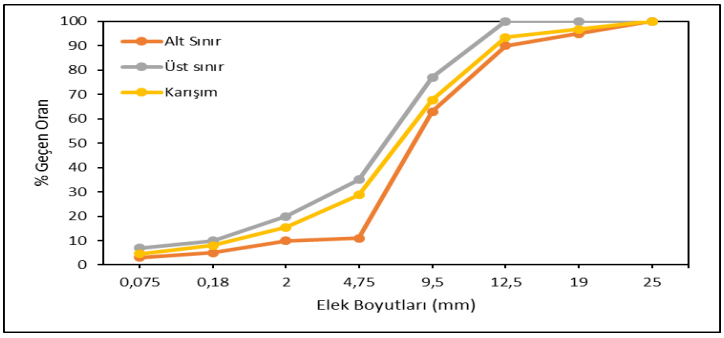

Fig. 1. Gradation curve as a result of sieve analysis

2.2 Flatness Index

For the aggregate to be classified as flat, the thickness of the aggregate must be less than 0.6 of its nominal size. Special template rulers are used for the flatness index experiment. The experiment was performed according to the standard BS 812 [21]. Aggregate sizes larger than 6.3 mm and smaller than 63 mm are selected. The test is performed by passing each aggregate particle through the aperture, indicating its particle diameter, one by one, from the special template ruler used to determine the flatness index (Figure 2).

Fig. 2. Flat index template used and aggregates with gradation distribution

According to the technical specifications of highways, the flatness index of aggregates used in porous asphalt (according to BS 812) should be ≤20%.

2.3 Micro-Deval (Abrasion Test)

The micro-deval test determines the aggregate's wear resistance and durability due to the materials' abrasion against each other using water, aggregate and steel balls with a diameter of 9.5 mm in a given drum. It was conducted according to the standard TS EN -1097-1 [22]. In this experiment, 2.5 liters of water with 500 g of aggregate and 5000 g of spherical steel balls are used in a hollow drum with an inner diameter of 200±1 mm (Figure 3).

Fig. 3. Micro-Deval drum, aggregate, steel ball and water mixture

The rotation of the steel drum is set to 12000 revolutions and runs at a speed of 100±5 revolutions per minute. At the end of the revolution process, the aggregates are separated from the water and the balls and washed and sieved through a 1.6 mm sieve. The average mass loss is calculated in % and reported as the micro-deval coefficient. The experiment was conducted twice for each sample, and the average value was determined. According to the Highways Technical Specifications, the wear resistance loss (micro-deval) of the aggregates used in Poroz asphalt is ≤ 20%.

2.4 Weathering Resistance (loss with $MgSO_4$)

Within the scope of the study, the test standard TS EN 1367-2 2010 was used. This standard deals with the weathering effect due to growing crystals pressurizing the pores of aggregates with magnesium sulfate salt [23]. Two test samples were prepared from each aggregate, 500 g from the aggregate samples with 10 mm and 14 mm grain sizes (Figure 4).

Fig. 4. Freeze-Thaw test sample, magnesium sulfate and its solution

The experiment was repeated for 5 cycles. Each sample is washed out of the solution with barium chloride. Then the samples are sieved through 10-mm sieves, and the magnesium sulfate value is determined.

According to the Technical Specification for Highways, the percentage loss of resistance to weathering ($MgSO_4$) of aggregates used in porous asphalt is ≤10.

2.5 Methylene Blue Experiment

Clay materials in aggregate expand based on the moisture content. The methylene blue test is a test that provides this information accurately and quickly. The test was performed according to the standard TS EN 933-9 [24]. The test is performed in a beaker containing 200 g of rock sample with 0-2 mm grain size and 500 ml of water and mixed at 600 rpm for 5 minutes. The device is stopped, then 5 ml of methylene blue solution is added to the mixture and mixed at 400 rpm for 1 minute. At the end of this time, the mixture is dropped onto the filter paper and moire is observed. This cycle is repeated 5 times and determines if the material is clean (Figure 5).

Fig. 5. Methylene blue mixture and moiré

According to the technical specifications of highways, the methylene blue value of fine aggregates used in porous asphalt is ≤1.5.

2.6 Peel Strength Test

The peel strength test is used to study the effects of adhesion between aggregates and bitumen. In this study, the test standard TS EN 12697-11 was used [25]. For the test, 200 g of material is taken from the aggregate sample remaining between 9.5 mm-4.75 mm sieves, washed and placed in the oven. The bitumen mixture of the aggregate was kept in the oven at 60 ºC for 24 hours. Equal amounts of the aggregates were poured into Petri dishes and analyzed independently. Distilled water was added to the Petri dishes containing the aggregate to cover the surface. The lids were sealed and left in an oven at 60 ºC for 24 hours. At the end of the period, the water in the sample containers removed from the oven was emptied, distilled water was added, and the aggregate surfaces were examined (Figure 6).

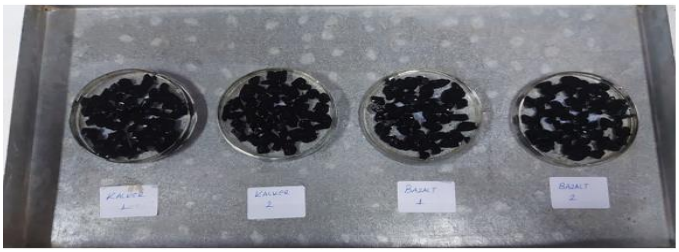

Fig. 6. The use of aggregates as a result of the peel strength test

The peel strength is determined by the ratio of the surfaces covered with bitumen to the total aggregate surface. Since the test was performed twice for each sample, the peel strength and the average value were calculated. The highway technical specifications state that the peel strength of aggregates used in porous asphalt (the surface area of the aggregate covered with bitumen) should be ≥ 80.

3 Results and Evaluation

The more the aggregate to be used in the mixture is exposed to crushing action, the more the proportion of diagonal in its structure increases. Since basalt is an aggregate of volcanic origin, its strength is quite high. Basalt is a harder material than limestone aggregate. Therefore, machines and crushers with a strong structure should be preferred for crushing in quarry crushers. Basalt aggregates are less angular when the rock pieces from the quarry enter the crushers. The flatness index value of aggregates used in porous asphalt mixtures should be ≤20%, according to BS 812. The flatness index of the basalt and limestone aggregates used in the study were 16% and 20%, respectively. The results were used to determine the usability of both aggregates in porous asphalt mixtures.

As a result of the Micro-Deval test, which was performed to determine the abrasion resistance of the aggregates, a loss of 17.41% was determined for basalt aggregates and 19% for limestone aggregates. In the Technical Specification for Highways, the percentage loss of wear resistance (micro-deval) of aggregates used in porous asphalt is ≤ 20. Based on the test results, it was determined that basalt and limestone aggregates meet the limits of the specification and can be used in porous asphalt mixtures.

A $MgSO_4$ solution was used for weathering resistance testing. It was conducted to determine the resistance of the aggregates to crumble under the effect of frost. The test results showed a loss of 4.5% for basalt aggregates and 8% for limestone aggregates. In the technical specifications of highways, the loss of aggregates to be used in porous asphalt with $MgSO_4$ is ≤ 10%. Both aggregates used were found to meet the specification limits.

In the methylene blue test to determine the clay content in fine aggregates, the basalt and limestone aggregates contained very little clay material and could be considered clean aggregates. The technical specifications established a methylene blue limit of ≤ 1.5 g/kg for the 0/2 mm portion of the fine aggregate in the porous asphalt mixtures and ≤ 3 g/kg for the 0/2 mm portion of the ground igneous aggregate. As a result of the

experiment, it was found that both aggregates had a methylene blue value of 0.5 g/kg and could be used in the mix.

A significant part of the road surface deterioration in bituminous pavements is due to the loss of adhesion of the aggregate with the bitumen under the abrasive action of water. The same is true for porous asphalt pavements. According to the design criteria for porous asphalt in the highway technical specifications, the peel strength of the bitumen-covered surface of the aggregate used in the mix after soaking in 60 ^{o}C water for 24 hours is specified as $\geq$ 80%. The result of the experiment was that the aggregates of basalt and limestone showed almost the same performance and that the aggregates met the specification limits of the bitumen-covered surfaces.

4 General Evaluation and Conclusions

More than 90% of porous asphalt mixtures are aggregates without air voids. Aggregates are very important in controlling gradation, void content and determining the performance of porous asphalt pavements. In this regard, it is very important to determine the physical and mechanical properties of the aggregates used in the mix beforehand and select the aggregate accordingly. This study investigated the usability of basalt and limestone aggregates from the Bitlis region in porous asphalt mixtures. As a result of the experiments, it was found that each aggregate meets the specified limits and can be used in the porous asphalt mixture.

NOTE

This study has been produced from the Ph. D. thesis title “Investigation of Mechanical Properties of Porous Asphalt and Semi-Rigid Pavements Prepared with Different Binders” studies of A. AKILLI EL.

References

1. Li, M., Tyre-road noise, surface characteristics and material properties, Doctoral Thesis, Dalian University of Technology, China, 2013.
2. Zhang, Z., Sha, A., Liu, X., Luan, B., Gao, J., Jiang, W., & Ma, F. State-of-the-art of porous asphalt pavement: Experience and considerations of mixture design. Construction and Building Materials, 262: 119998, 2020
3. Liu, M., Huang, X., & Xue, G. Effects of double layer porous asphalt pavement of urban streets on noise reduction. International Journal of Sustainable Built Environment, 5(1), 183-196, 2016
4. Chu, L., & Fwa, T. F. Functional sustainability of single-and double-layer porous asphalt pavements. Construction and Building Materials, 197, 436-443, 2019.
5. Wang, D., & Oeser, M. Interface treatment of longitudinal joints for porous asphalt pavement. International Journal of Pavement Engineering, 17(8), 741-752, 2016.
6. Takahashi, S. Comprehensive study on the porous asphalt effects on expressways in Japan: Based on field data analysis in the last decade. Road Materials and Pavement Design, 14(2), 239-255, 2013.
7. Karmakar, D., Pal, M., Majumdar, K., Suresh, M., & Roy, P. K. Utilization of porous asphalt material in road construction for reducing the vehicular noise. Materials Today: Proceedings, 65, 3602-3609, 2022.
8. Alber, S., Ressel, W., Liu, P., Wang, D., & Oeser, M. Influence of soiling phenomena on air-void microstructure and acoustic performance of porous asphalt pavement. Construction and Building Materials, 158, 938-948, 2018.

9. Chen, T., Ma, T., Huang, X., Ma, S., Tang, F., & Wu, S. Microstructure of synthetic composite interfaces and verification of mixing order in cold-recycled asphalt emulsion mixture. Journal of Cleaner Production, 263, 121467, 2020.
10. Tong, J., Ma, T., Shen, K., Zhang, H., & Wu, S. A criterion of asphalt pavement rutting based on the thermal-visco-elastic-plastic model. International Journal of Pavement Engineering, 23(4), 1134-1144, 2022.
11. Kong, D., Xiao, Y., Wu, S., Tang, N., Ling, J., & Wang, F. Comparative evaluation of designing asphalt treated base mixture with composite aggregate types. Construction and Building Materials, 156, 819-827, 2017.
12. Hu, J., Ma, T., Zhu, Y., Huang, X., & Xu, J. A feasibility study exploring limestone in porous asphalt concrete: Performance evaluation and superpave compaction characteristics. Construction and Building Materials, 279, 122457, 2021.
13. Ren, J., Xu, Y., Huang, J., Wang, Y., & Jia, Z. Gradation optimization and strength mechanism of aggregate structure considering macroscopic and mesoscopic aggregate mechanical behaviour in porous asphalt mixture. Construction and Building Materials, 300, 124262, 2021.
14. Xu, Y., Jiang, Y., Xue, J., & Ren, J. Investigating the effect of aggregate characteristics on the macroscopic and microscopic fracture mechanisms of asphalt concrete at low-temperature. Materials, 12(17), 2675, 2019.
15. Ma, X., Wang, H., & Zhou, P. Novel gradation design of porous asphalt concrete with balanced functional and structural performances. Applied Sciences, 10(20), 7019, 2020.
16. Moriyoshi, A., Jin, T., Nakai, T., Ishikawa, H., Tokumitsu, K., & Kasahara, A. Construction and pavement properties after seven years in porous asphalt with long life. Construction and Building Materials, 50, 401-413, 2014.
17. Xiaowei, W., Xingyu, G., Qiao, D., & Jiangtao, W. Effects of flat and elongated aggregateson the performance of porous asphalt mixture. Journal of Southeast University (English Edition) 34(1), 2018.
18. ASTM, S. D. Standard test method for flat particles, elongated particles, or flat and elongated particles in coarse aggregate. D4791-10, 2010.
19. Karayolları Genel Müdürlüğü. Karayolu Teknik Şartnamesi. Ankara, Türkiye, KTŞ, 2013.
20. TS EN 933-1, Agregaların geometrik özellikleri için deneyler-Bölüm 1: Tane büyüklüğü dağılımının tayini- Elek Yöntemi. Türk Standartları Enstitüsü, Ankara, 2012.
21. BS 812, Methodsfor Determination of Particle Shape: Flakiness Index", British Standarts, 1989.
22. TS EN 1097-1, Agregaların mekanik ve fiziksel özellikleri için deneyler bölüm 1: Aşınma Direncinin tayini (Mikro-Deval), Türk Standartları Enstitüsü, Ankara, 2011.
23. TS EN 1367-2, Agregaların termal ve bozunma özellikleri için deneyler Bölüm 2: Magnezyum Sülfat Deneyi, Türk Standartları Enstitüsü, Ankara, 2010.
24. TS EN 933-9, Agregaların geometrik özellikleri için deneyle-Bölüm 9: İnce tanelerin tayini-Metilen mavisi deneyi, Türk Standartları Enstitüsü, Ankara, 2010.
25. TS EN 12697-11, Bitümlü karışımlar-Deney Metodları-Sıcak karışımlı asfalt için-Bölüm 11: Agrega ile bitüm arasındaki bağlanmanın tayini, Türk Standartları Enstitüsü, Ankara,2020.

Investigation of Rutting Performance of Asphalt Binder Modified with New Boron-Containing Additive

Merve Gülfer Bozdemir[1], Hacer Yeşilçiçek[2], Şeref Oruç[3]

[1]Department of Civil Engineering, Engineering and Architecture Faculty, Erzurum Technical University, Erzurum, Turkey, merve.ozcan@erzurum.edu.tr, 0000-0001-5868-6613

[2]Department of Civil Engineering, Engineering Faculty, Karadeniz Technical University, Trabzon, Turkey, haceryesilcicek@ktu.edu.tr, 0000-0001-5474-7415

[3]Department of Civil Engineering, Faculty of Technology, Karadeniz Technical University, Trabzon, Turkey, oruc@ktu.edu.tr, 0000-0001-5788-890X

Abstract. Polymer additives are used in asphalt modification in order to bring in various rheological properties to the asphalt binder. However, recently, it has become important to use low-cost and environmentally friendly additives equivalent to existing additives in asphalt modification, since additives are costly, require a special mixing facility and cause environmental pollution. In this study, a new asphalt modifier was produced under laboratory conditions by synthesizing boron oxide, one of the boron derivatives of which our country has an important reserve, and rosin (colophon resin) naturally produced from pine trees. Modification was carried out by adding the produced additive to the asphalt binder at different rates. The resistance of modified asphalt binders to rutting was determined by the DSR test. As a result of experiments on unaged and short-term aged samples, it was determined that the rutting resistance of the modified asphalt binders increased significantly compared to the original asphalt binder, and the additive increased the PG grade of the original asphalt.

Keywords: Asphalt modification, Resin, Boron, Rutting.

1 Introduction

Asphalt pavements are more preferred than concrete roads due to their comfortable driving and easy repair and maintenance opportunities. The binder used at low rates in asphalt pavements significantly affects the performance and service life of the pavement. Due to the increase in traffic volume and unfavorable environmental conditions, the frequency of deterioration of asphalt pavements is increasing. For this reason, asphalt binder is modified with many different additives in order to extend the life of the pavement and improve the performance of the asphalt binder [1-4].
Polymer-type additives are commonly used to modify binders. The most common of these are styrene-butadiene-styrene (SBS) and plastomeric ethylene-vinyl-acetate (EVA). The addition of SBS polymer to the binder has been reported to improve the

resistance of asphalt to rutting and cracking at low temperatures [5-8]. Similarly, viscoelastic and rheological properties of asphalt have been reported to be improved with EVA polymer additives [9-12]. While polymer additives improve the performance of the binder, it has been reported that phase separation occurs over time and polymer modified binders cause additional costs during construction [13]. In addition, due to the fact that most of the polymers used as modifiers are not biodegradable, serious environmental impacts occur and therefore, it has become important to investigate biodegradable additives in studies.

Resin and its derivatives are used as modifiers due to similarities in the chemical structure of the asphalt binder [14]. Epoxy resin increases the viscosity of the binder and decreases its temperature sensitivity [15-16]. Polyester resin has been reported to improve the elastic behavior of asphalt and make it more resistant to deformations [17-18].

Boron and its derivatives, which rank first in the world in terms of reserves in our country, are used in many sectors. Boron and its derivatives are also used as modifiers in asphalt pavements. It has been reported that boron wastes can be reused as road materials and increase pavement performance [19-22] and boric acid improves the penetration and softening point values of the binder [23-24].

In this study, it was aimed to synthesize a new additive that combines the adaptability of boron derivatives with high molecular hydrocarbon derivatives and the high adhesion and strength properties of the resin and to determine the resistance of the obtained additive against rutting of asphalt binder.

2 Materials and Method

2.1 Materials

The rosin used in this study was obtained from Belplas Ankara Termoplastic and Maintenance and Repair Services Inc. and its features are given in Table 1.

Table 1. Properties of the rosin.

Purity	**% 95-97 min.**
Molar mass	302,45 gr/mol
Melting temperature	72-75℃
Specific weight	1,06-1,07 gr/cm^3

The boron oxide used in this study was obtained from an enterprise located in Balıkesir/Bandırma, Turkey and affiliated to Eti Maden Operations General Directorate. The properties of the boron oxide are given in Table 2.

Table 2. Properties of the boron oxide.

Components	**Amount**
B_2O_3	% 98.00min.
SO_4	500 ppm max
Cl	10 ppm max.
Fe	35 ppm max.
+0.315 mm [size]	%75.00 min.

In this study, the PG 64-16 asphalt cement (penetration grade 50/70) acquired from the Turkish Petroleum Refinery (Izmit) was used. Traditional tests were carried out to determine the properties of base asphalt, which are given in Table 3.

Table 3. Properties of the base asphalt.

Properties	**Test Methods**	**Value**	**Requirements**
Penetration (25°C, dmm)	ASTM D-5	56	50-70
Softening point (°C)	ASTM D-36	50	46-54
Flash point (°C)	ASTM D-92	249	≥ 230
Specific weight (gr/cm^3)	ASTM D-70	1.028	1.0-1.1
Viscosity (135°C, Pa. s)	ASTM D-4402	0.5	≤ 3

2.2 Preparation of Modified Asphalt

The synthesis process of colophony resin consisting of abietate type resin acids and boron oxide was based on the methods used in previous studies [25-27]. Before synthesis, the colophony resin was dissolved in acetone to remove impurities. The synthesis was carried out in the laboratory in the presence of a catalyst. The obtained additive (Boron Added Resin Compound-BARC) is a dark colored hard material and has a short production process.

The additive was added to the asphalt binder in different proportions. The modification process was carried out using a high shear mixer for 30 minutes at 2000 rpm at 150 ± 5 °C. The additive ratios of the binders obtained are given in Table 4.

Table 4. Preparation parameters of modified asphalt samples.

Samples	BARC (%)
BA	0
BA1.0	1
BA3.0	3

2.3 Rolling Thin Film Oven Test, RTFOT

The rotational thin-film heating test (RTFOT) simulates the short-term aging of hot asphalt mixtures during production and construction in the laboratory. In the experiment, 8 special glass bottles are used, each filled with 35 grams of asphalt binder. The bottles filled with asphalt binder are placed horizontally in an oven at 163 °C. The bottles are rotated in the oven for 75 (EN 12607-1) or 85 minutes (ASTM D2872, AASHTO T240). At the same time, the samples are exposed to an air flow of 4000 ml/min from an air blower located in the oven during rotation. Under the influence of temperature and rotation, the asphalt binder covers all surfaces of the bottles, forming a thin film. The combined effect of heat and air on this film layer better represents short-term aging under field conditions [28-30].

2.4 Dynamic Shear Rheometer, DSR

Dynamic shear rheometer test is performed to characterize the viscous and elastic behavior of asphalt binder under a certain temperature and shear stress. DSR test is performed according to AASHTO T 315 standard. The test determines the rutting and fatigue resistance of the asphalt binder. To determine the performance class and rutting resistance of asphalt binders, unaged (base) and short-term aged specimens after RTFOT are used. In the experiment, 25 mm diameter parallel plates were used and gaps between the plates were set at 1 mm. under controlled stress, 120 Pa constant stress were applied to the samples at a frequency of 1.59 Hz (10 rad/s) (ASTM T 315) [30-31].

3 Results and Discussion

3.1 DSR results

The performance levels of unaged base and modified asphalt binders at high temperatures were determined by DSR testing. Asphalt binders were tested at 3 different temperatures (58, 64 and 70°C), at a frequency of 1.59 Hz (10 rad/s) and under controlled stress (120 Pa). The specimen was placed in the device with a 1 mm gap between 25 mm parallel plates. As a result of the experiment, the G*/sinδ rutting parameter values were found and given in Figure 1.

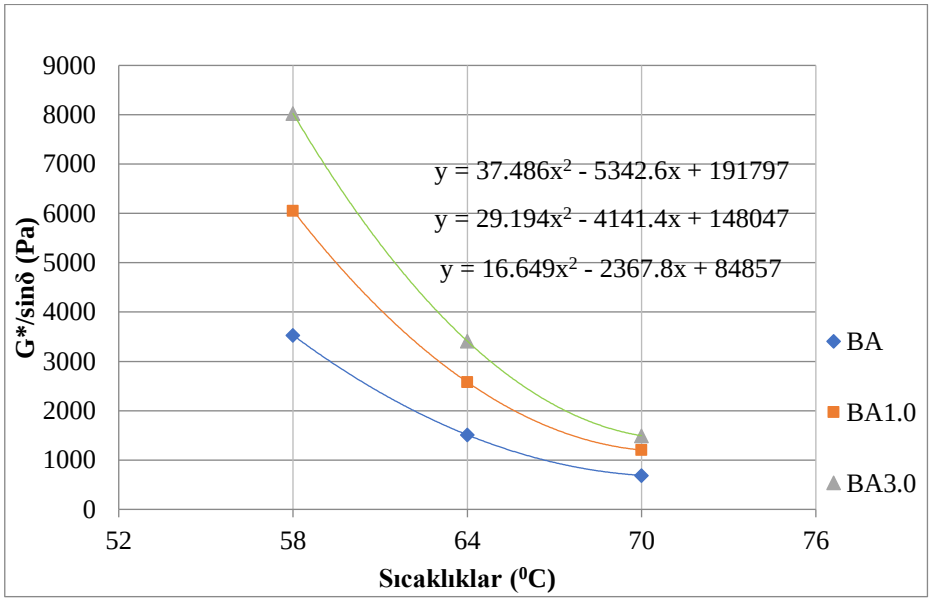

Fig. 1. G*/sinδ values of the base and modified asphalts at high temperatures

When the rutting strength parameters (G*/sin δ) are analyzed in Figure 1, it is seen that the values increase with the use of additives at 64 °C. According to the Superpave method, the specification limit value of 1000 Pa rutting strength for base asphalt binders was achieved at 64 °C for pure asphalt and 70 °C for modified asphalt binders. It was determined that the rutting strength of pure asphalt binder increased with the use of additives.

3.2 DSR Results After RTFOT

The base and modified asphalt binders were subjected to RTFOT test to represent short-term aging of asphalt binders. After the RTFOT test, the binders were subjected to DSR test and G*/sin δ parameter values were determined. The test was performed at 64°C and 70°C under controlled stress (120 Pa) at a frequency of 1.59 Hz (10 rad/s). The short-term aged specimen was placed in the machine with a 1 mm gap between 25 mm parallel plates. The test temperatures were selected based on the temperature values provided by the specification in the DSR test applied to unaged specimens. The data related to the test results are given in Table 18.

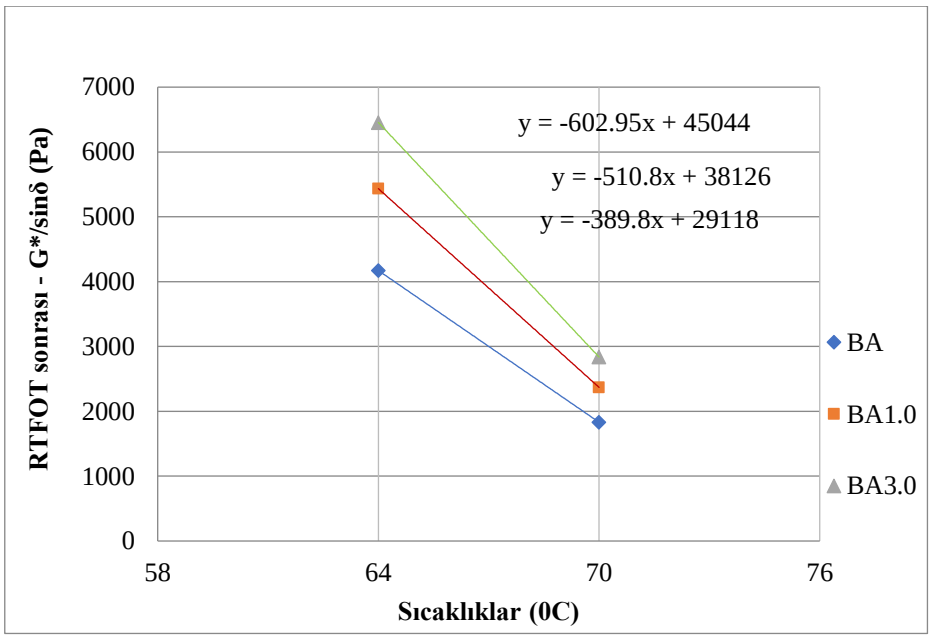

Fig. 2. Rutting (G*/sinδ) values after RTFOT

Figure 2 shows that all modified asphalt binders except base asphalt binder meet the specification limit of 2200 Pa after RTFOT. In order to determine the performance class of asphalt binders according to the Superpave method, unaged and short-term aged binders must meet the required specification limits at the same temperature. In this case, the performance class of the base asphalt binder is PG 64-X and the modified asphalt binders are PG 70-X. It was found that the performance class of the base asphalt binder was moved to a higher level with the use of additives and the rutting resistance of the base asphalt binder increased.

4 Conclusions

In this study, a new boron-containing additive was obtained and its effect on the rutting parameter of the pure binder was investigated. The obtained results of those experiments can be summarized as follows:

- From the results of the DSR test applied to unaged base and modified binders, it was concluded that the rutting strength parameter values increased with the use of the additive and the additive improved the elastic properties of the binder.

- The rutting strength parameter values obtained after short-term aging were also found to be better than the base binder. Considering the specification limit of the unaged and after RTFOT specimens, it was observed that the high temperature performance level of the base binder increased from PG64-Y to PG 70-Y with the use of the additive.

References

1. Song, R., Sha A., Shi K., Li J., Li, X., Zhang F., Polyphosphoric acid and plasticizer modified asphalt: Rheological properties and modification mechanism, Construction and Building Materials, vol. 309, (2021).
2. Dai, J., Ma, F., Fu, Z., Li, C., Jia, M., Wen, Y., Wang, W., Applicability assessment of stearic acid/palmitic acid binary eutecticphase change material in cooling pavement, Renewable Energy, 175, 748-759, (2021)
3. G. Polacco, J. Stastna, D. Biondi, L. Zanzotto Relation between polymer architecture and nonlinear viscoelastic behavior of modified asphalts, Curr. Opin. Colloid Interface Sci., pp. 230-245, 11 (4) (2006).
4. Zhou, H.-Y.; Dou, H.-B.; Chen, X.-H. Rheological Properties of Graphene/Polyethylene Composite Modified Asphalt Binder. Materials, 14, 3986, 2021.
5. Tayfur, S., Özen, H., Aksoy, A., Investigation of rutting performance of asphalt mixtures containing polymer modifiers, Construction and Building Materials, 328–337, 21 (2007).
6. Sengül, E. C., Oruç, S., Iskender, E., Aksoy, A., Evaluation of SBS modified stone mastic asphalt pavement performance, Construction and Building Materials, 777–783, 41 (2013).
7. G.D., Airey, Rheological properties of styrene–butadiene–styrene polymer modified road bitumens, Fuel, pp. 1709-1719, 82 (2003).
8. Yildirim, Y, Polymer modified asphalt binders, Constr. Build. Mater., 66-72, 21 (1) (2007).
9. O. González, M.E. Muñoz, A. Santamaría, M. García-Morales, F.J. Navarro, P. Partal, Rheology and stability of bitumen/EVA blends, Eur Polym J, pp. 2365-2372, 40 (10) (2004).
10. Garcia-Morales, M., Partal, P., Navarro, F. J., Martinez-Boza, F., Gallegos, C., Gonzales, N., Munoz, M.E., Viscous properties and microstructure of recycled EVA modified bitumen. Fuel, 31–38, 83 (2004).
11. W.-Q. Luo, J.-C. Chen, Preparation and properties of bitumen modified by EVA graft copolymer, Constr. Build. Mater., pp. 1830-1835, 25 (4) (2011).
12. W. Stark, M. Jaunich, Investigation of Ethylene/Vinyl Acetate Copolymer (EVA) by thermal analysis DSC and DMA, Polym. Test., pp. 236-242, 30 (2) (2011).

13. Zani., L., Giustozzi, F., Harvey J., Effect of storage stability on chemical and rheological properties of polymer-modified asphalt binders for road pavement construction, Construction and materials, 326-335, 145 (2017).
14. .Kejian Yao, Renewable Bio-Based Polymers and Degradable Functional Polymers, 2013.
15. Gao, J., Liu, Y., Yang, L., Thermalstability of boron-containing phenol formaldehyde resin, Polymer Degradation and Stability, Volume 63, Issue 1, Pages 19-22, January 1999.
16. Deng, P., Shi, Y., Liu, Y., Liu, Y., Wang, Q., Solidifying process and flame retardancy of epoxy resin cured with boron-containing phenolic resin, Applied Surface Science, Volume 427, Part A, Pages 894-904, 1 January 2018.
17. Ahmedzade, P., Yılmaz, M. ve Yılmaz, M., Polyester Reçinenin Bitümlü Bağlayıcıların Yüksek Sıcaklık Performans Seviyesi Üzerindeki Etkisi, Erciyes Üniversitesi Fen Bilimleri Enstitüsü Dergisi 24 (1-2) 227 – 240, 2008.
18. Ahmedzade, P. ve Yılmaz, M., Effect of Polyester Resin Additive on The Properties of Asphalt Binders and Mixtures, Construction and Building Materials, 22, 481-486, 2008.
19. Zhang, Y., Guo, Q., Li, L., Jiang, P., Jiao, Y., & Cheng, Y. Reuse of Boron Waste as an Additive in Road Base Material. Materials (Basel, Switzerland), 9(6), 416, 2016.
20. Gürer, c., Selman, G. Ş., Investigation of Properties of Asphalt Concrete Containing Boron waste as mineral filler, Materials Science, 22(1), 2016.
21. T Kütük-Sert, S Kütük, Physical and marshall properties of borogypsum used as filler aggregate in asphalt concrete, Journal of Materials in Civil Engineering 25 (2), 266-273.
22. Keskin, M., Karacasu, M., Effect of boron containing additives on asphalt performance and sustainability perspective, Construction and Building Materials, Volume 218, Pages 434-447, ISSN 0950-0618, 2019.
23. Lentz, Alfred P., Asphaltic Compound, United States Patent Office, Patent No: 2375117, 1945.
24. Oruç, Ş., Yılmaz, B. ve Bostancıoğlu, M., Borik Asitin Asfaltın Fiziksel Özelliklerine Etkisi, 6. Ulusal Asfalt Sempozyumu ve Sergisi, Ankara, 297-306. Kasım 2013.
25. Zhang, W., Liu, C., Ying, Y., Dong, W., The preparation and characterization of boron-containing phenolic fibers, Materials chemistry and physics 121, 89-94, (2010).
26. Arslan, D., Gürü, M., Çubuk, K. M., Performans Assesment of Organic-Based Synthetic Calcium and Boric Acid Modified Bitumens, Fuel, 102, 766-772, (2012).
27. Arslan, D., Gürü, M., Çubuk, M.K., Çubuk, M., Improvement of bitumen and bituminous mixtures performances by triethylene glycol based synthetic polyboron, Construction and Building Materials, Volume 25, Issue 10, Pages 3863-3868, October 2011.
28. Geçkil, T., Siyah Karbonun Bitümlü Sıcak Karışımların Özelliklerine Etkisinin Araştırılması, Doktora Tezi, Fırat Üniversitesi, Fen Bilimleri Enstitüsü, Elâzığ, 2008.
29. Yılmaz, B., Bor İçerikli Organik Katkıyla Modifiye Edilen Asfaltın Performans Özelliklerinin Araştırılması, Doktora Tezi, Karadeniz Teknik Üniversitesi, Fen Bilimleri Enstitüsü, Trabzon, 2016.
30. Zaniewski, J. P. ve Pumphrey, M. E., Evaluation of Performance Graded Asphalt Binder Equipment and Testing Protocol, West Virginia University, Morgantown, 2004.
31. McGennis, R. B., Shuler, S., & Bahia, H. U., Background of superpave asphalt binder test methods, National Asphalt Training Center Demonstration Project 101, Publication No. FHWA-SA-94-069, Asphalt Institute, Lexington, 91 s, 1994.

SPONSORS

Doğu Akdeniz Üniversitesi Rektörlüğü

BEM (Boğaz Endüstri ve Madencilik LTD)

Tüfekçi Group

KTMMOB-İMO (İnşaat Mühendisleri Odası)

Kıbrıs Türk İnşaat Müteahhitleri Birliği (KTİMB)

KKTC Merkez Bankası

Kıbrıs Türk Otelciler Birliği

Ekin Adademir İthalat & İhracat Şirketi

Kıbrıs Türk Kooperatif Merkez Bankası Ltd.

DAÜ-PERSEN

DAÜ-SEN

EKOR Un Ürünleri Sanayi Ltd.

Petek Pastahanesi

Deniz Plaza

https://ace2023.emu.edu.tr/en